SATNAC 2021

Southern Africa Telecommunication Networks and Applications Conference (SATNAC) 2021

20-23 November 2021
Champagne Sports Resort, Central Drakensberg, KwaZulu-Natal, South Africa

2021 Proceedings

Hosted by Telkom

Accelerated Digitalisation - Current and Future Ways of Working

Venue: Champagne Sports Resort, Central Drakensberg, KwaZulu-Natal, South Africa
Date: 20 - 23 November 2021

Publication Information

Title:	Southern Africa Telecommunication Networks and Applications Conference (SATNAC) 2021
Proceedings format:	Printed
ISBN:	
Editors:	Martin Smuts and Ronald Moorcroft
Date of print:	November 2021
Version:	Preliminary

SATNAC is the flagship of the Telkom Centre of Excellence (CoE) Programme.

Hosted by Telkom

Contents

SATNAC 2021 Conference Sponsors

The SATNAC 2021 committee would like to recognise the following sponsors:

Diamond Sponsors

Gold Sponsors

Silver Sponsors

SATNAC 2021 Review Process

A formal *Call for Papers* was issued, inviting anyone interested to submit a paper within categories specified by the Organising Committee. Authors uploaded their papers via web interface to a database. Papers were assigned to the review panel in the field to judge on the possible acceptance of the submission, based on the scope and depth of the subject matter.

The review process is based on the international de facto standard for blind paper reviews, and was undertaken by at least three experienced and well respected individuals. Papers were scrutinised by a panel of reviewers, consisting mainly of respected South African academics, as well as several international experts. The reviewers were asked to provide specific feedback, both positive and negative. This was the only information from the review process disclosed to the authors; all other information was kept confidential.

Reviewers used a 5 point scale to rate the following criteria:

- Originality
- References
- Technical quality
- Presentation style

Reviewers gave an overall rating and were asked to provide comprehensive comments, which assists the authors in improving and correcting their papers.

The reviewers submitted their scoring and comments via web interface to the database and the Technical Programme Committee (TPC) drew reports and aggregated the individual scores. The papers were ranked on their average weighted score, and the programme dictated the number of papers that could be accepted. Papers were submitted to an online plagiarism database, before being accepted.

The reviewers' comments were forwarded to the authors, with a request to submit a final revised version. Only those papers of high enough quality, as recommended by the respective reviewers, are included in the SATNAC 2021 proceedings as full reviewed papers.

Martin Smuts
Chairperson
Technical Programme Committee
SATNAC 2021

Organising Committee

Ms Mmaki Jantjies (Chairperson)
Mr Gys Booysen (Secretariat)
Mr Hugo van Zyl
Ms Marti Beukes
Mr Pushkar Gokhale

Technical Programme Committee

Dr Martin Smuts (TPC Chairperson), Openserve
Mr Ronald Moorcroft (TPC Vice Chairperson), Openserve
Mr Gys Booysen, Openserve

Mr Emmanuel Adigun, ABSA
Dr Rodolfo Martinez, Centro de Investigaciones en Óptica
Dr Samuel van Loggerenberg, MTN
Dr Lester Cowley, Nelson Mandela University
Dr Anthea Van der Hoogen, Nelson Mandela University
Dr Dieter Vogts, Nelson Mandela University
Dr Ifeoluwapo Fashoro, Nelson Mandela University
Prof Janet Wesson, Nelson Mandela University
Dr Frederik Vorster, Nelson Mandela University
Mr Ross Dix-Peek, Nelson Mandela University
Dr MC du Plessis, Nelson Mandela University
Dr Leda van der Post, Nelson Mandela University
Prof Andrew Leitch, Nelson Mandela University
Mr Ian Durston, NetScout Systems (UK) Ltd
Dr Melvin Ferreira, North-West University
Prof Albert Helberg, North-West University
Prof Tiny Du Toit, North-West University
Prof Hennie Kruger, North-West University
Mr Herman Blackie, North-West University
Mr Brite Devassy, Openserve
Mr Dirk Coetsee, Openserve
Mr John Manamela, Openserve
Mr Lucky Ramasila, Openserve
Mr Thato Mokoena, Openserve
Ms Noluthando Khuzwayo, Openserve
Mr Sabelo Yalezo, Openserve
Ms Asavela Sigonya, Openserve
Ms Tarika Balmahoon, Openserve
Ms Tipharah van Dyk, Openserve
Ms Yamnkelani Pipile, Openserve
Dr James Whitehead, Reutech Communications
Dr Zelalem Sintayehu Shibeshi, Rhodes University
Prof Alfredo Terzoli, Rhodes University
Dr Dane Brown, Rhodes University
Prof George Wells, Rhodes University

Mr James Connan, Rhodes University
Prof Karen Bradshaw, Rhodes University
Prof Nomusa Dlodlo, Rhodes University
Prof Philip Machanick, Rhodes University
Dr Yusuf Motara, Rhodes University
Mr Stones Dalitso Chindipha, Rhodes University
Ms Tapiwa Chindeka, Telkom
Mr Derwin Ngomane, Telkom
Mr Jabulani Msimango, Telkom
Mr Thembani Phaweni, Telkom
Mr Kyle van Wyk, Telkom
Ms Khanyisa Noganta, Telkom
Prof Anish Kurien, Tshwane University of Technology
Prof Karim Djouani, Tshwane University of Technology
Prof Thomas Olwal, Tshwane University of Technology
Dr Emmanuel Migabo, Tshwane University of Technology
Dr Bessie Malila, University of Cape Town
Dr David Johnson, University of Cape Town
Prof Hussein Suleman, University of Cape Town
Dr Josiah Chavula, University of Cape Town
Dr Joyce Mwangama, University of Cape Town
Dr Lateef Akinyemi, University of Cape Town
Prof Melissa Densmore, University of Cape Town
Mr Neco Ventura, University of Cape Town
Mr Sunday Oladejo, University of Cape Town
Dr Daniel Ramotsoela, University of Cape Town
Prof Albert Lysko, University of Cape Town
Mr Stephen Ekwe, University of Cape Town
Prof Khulumani Sibanda, University of Fort Hare
Dr William Vambe, University of Fort Hare
Mr Michael Grobler, University of Johannesburg
Mr Bashan Naidoo, University of KwaZulu-Natal
Dr Farzad Ghayour, University of KwaZulu-Natal
Prof Hongjun Xu, University of KwaZulu-Natal
Prof Jules-Raymond Tapamo, University of KwaZulu-Natal
Dr Narushan Pillay, University of KwaZulu-Natal
Dr Pradeep Kumar, University of KwaZulu-Natal
Prof Thomas Odhiambo Afullo, University of KwaZulu-Natal
Dr Tahmid Quazi, University of KwaZulu-Natal
Prof Viranjay Srivastava, University of KwaZulu-Natal
Mr Madimetja Jonas Manamela, University of Limpopo
Dr Thipe Modipa, University of Limpopo
Dr Peter Akuon, University of Nairobi, Kenya
Prof Herman Myburgh, University of Pretoria
Prof Mbuyu Sumbwanyambe, University of South Africa
Dr Ewald van der Westhuizen, University of Stellenbosch
Prof Thomas Niesler, University of Stellenbosch
Prof Anthony Krzesinski, University of Stellenbosch
Mr Andre Henney, University of the Western Cape
Prof Isabella Venter, University of the Western Cape

Prof Louise Leenen, University of the Western Cape
Dr Mehrdad Ghaziasgar, University of the Western Cape
Dr Michael Norman, University of the Western Cape
Dr Omowunmi E. Isafiade, University of the Western Cape
Mr Reginald Dodds, University of the Western Cape
Dr Olasupo Ajayi, University of the Western Cape
Dr Clement Nyirenda, University of the Western Cape
Prof Olutayo Oyerinde, University of Witwatersrand
Prof Fambirai Takawira, University of Witwatersrand
Prof Ling Cheng, University of Witwatersrand
Mr Shamin Achari, University of Witwatersrand
Dr Chabalala Chabalala, University of Witwatersrand
Prof Jules Moualeu, University of Witwatersrand
Ms Siphelele Fakude, University of Zululand
Mr Ayotuyi Tosin Akinola, University of Zululand
Mrs Ijeoma Noella Ezeji, University of Zululand
Mr Isaiah Oluwabunmi Adebayo, University of Zululand
Prof Matthew Adigun, University of Zululand
Mrs Sizakele Mathaba, University of Zululand
Ms Nombuso Sibeko, University of Zululand
Mr Paul Tarwireyi, University of Zululand
Dr Pragasen Mudali, University of Zululand
Prof Johan Bekker, Vaal University of Technology
Dr Olukayode Oki, Walter Sisulu University
Mr John Lewis, Xavant Technology

SATNAC 2021 Technical Programme

Access Network Technologies

Converged Services

Core Network Technologies

Data Centre & Cloud

Internet Services & End User Applications

Limited Range Communications

Management

Standards, Regulatory & Environmental

Access Network Technologies

Towards Achieving an Efficient ADR Scheme for LoRaWAN: A Review of the Constrained Optimisation Approach

Rachel Kufakunesu[1], Gerhard P. Hancke[1,2], Adnan M. Abu-Mahfouz [1,3]

[1]*Department of Electrical, Electronic and Computer Engineering, University of Pretoria, Pretoria 0002, South Africa*

[2]*Nanjing University of Posts and Telecommunications, Nanjing 210023, China*

[3]*Council for Scientific and Industrial Research (CSIR), Pretoria, 0184, South Africa*

[1]rachel.kufakunesu@tuks.co.za

Abstract—**Long Range Wide Area Network (LoRaWAN) is a networking technology that is rapidly growing in the Internet of Things (IoT) implementations under Low Power Wide Area Networks (LPWAN). The main goal of LoRaWAN is to optimise the coverage range, capacity, cost and battery life of the network. A vital LoRaWAN characteristic is the Adaptive Data Rate (ADR) algorithm that minimises energy utilisation and maximises throughput by regulating the bit rate, based on the link budget for individual end devices in the LoRaWAN. ADR regulates the transmission parameters, specifically Bandwidth (BW), Spreading Factor (SF), Transmission Power (TP) and Coding Rate (CR). The current spurt in IoT deployments has resulted in diverse QoS requirements, metrics, and implementation strategies. We present a comprehensive review of the constrained optimisation methods used to enhance ADR schemes for LoRaWAN technology. We highlight the strengths and drawbacks and computational complexity of the approaches. We provide a comparison of the optimisation techniques and identify research challenges and potential future study.**

Keywords— **Adaptive Data Rate, Computational Complexity, Constrained Optimisation, Internet of Things, LoRaWAN,**

I. INTRODUCTION

Numerous organisations in various industries are increasingly adopting the Internet of Things (IoT) to improve their functionality and improve decision making to improve the customer experience. Consequently, an accretion in devices connecting to the internet has ensued. These end devices (EDs) are required to have the capability of acquiring an Internet Protocol (IP) address and capable of data transfer over a network. Long Range Wide Area Network (LoRaWAN) is a Low Power Wide Area Network (LPWAN) that operates in the unlicensed industrial, scientific, and medical (ISM) frequency bands connected in a star network topology. A characteristic of LoRaWAN is low power consumption, low data rate (small data packets) and long-range communication up to five kilometres in urban locations and up to forty kilometres in rural locations [1].

The LoRaWAN network incorporates five core elements: the end devices also called end nodes, the gateway (GW), the network server (NS), the Join Server (JS) and application servers (AS) configured in a star topology architecture as shown in Fig I. The LoRa ED consists of a wireless transceiver and sensor nodes that send packets to several GWs within its locality utilising LoRa radio frequency (RF) modulation. GWs draw their power from the mains and can connect to the internet and comprise of radio components with transmitters and microprocessors for information processing. The cloud-based NS receives data packets from each GW which it consecutively transmits to the characteristic Application Server (AS). Where multiple GWs are available in a network, it is possible for one ED to send data to all the GWs. GWs are capable of concurrently listening to multiple frequencies in each SF.

The Adaptive Data Rate (ADR) scheme is an essential feature in LoRaWAN. Its objective is to minimise power utilisation and maximise throughput by regulating the bit rate depending on the link budget for each ED in the LoRaWAN. ADR regulates the transmission parameters, specifically transmission power (TP), spreading factor (SF), bandwidth (BW) and coding rate (CR) depending on the link budget. Optimising the ADR reduces airtime and increases network capacity and improves energy efficiency. The upsurge in IoT implementations has resulted in a wide variety of quality of service (QoS) specifications, benchmarks, and deployment methods. As such, ADR schemes have been implemented using different approaches. This paper looks at the constrained optimisation methods used to enhance the ADR schemes for LoRaWAN technologies. The key contributions of this paper are defined as follows:

- An overview of the ADR scheme and a comprehensive review of its parameters.
- An investigation of the constrained optimisation techniques that enhance the ADR schemes which are proposed in literature.
- A discussion of the strengths, drawbacks, and computational complexity of the optimisation techniques.
- Identification of research challenges and open issues for farther study.

The remainder of the paper is organised as follows: Section II provides an overview of the ADR scheme in LoRaWAN, describing how the algorithm works. Section III describes a typical system model, Section IV presents a review of the constrained-optimisation techniques. Section V features a discussion of strengths, drawbacks, and computational complexity of the optimisation method. Section VI concludes this paper.

II. TECHNOLOGICAL OVERVIEW

The ADR scheme was developed into LoRaWAN to enable the management of the ED transmission parameters to increase

the packet delivery ratio (PDR). The uplink (UL) data transmitted from the ED to the GW is determined by the transmission parameter settings that are controlled by the ADR algorithm. The ADR algorithm manages the data rate and TP of EDs centred on the link budget approximation in the UL data packet and the maximal signal-to-noise ratio (SNR) essential for correctly decoding data packets at the current data rate.

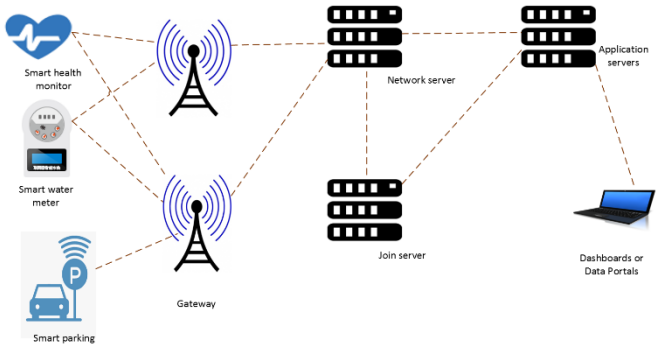

Figure I. LoRaWAN Architecture[2]

Where stationary EDs are concerned, ADR is managed by the NS subject to the historical information of the UL packets received from the EDs, termed "Network-managed ADR or Static ADR". This network-regulated ADR scheme would not function with mobile EDs due to channel degradation that arises when the mobile ED changes position. Where mobile EDs are considered, the ADR mechanism is effected "blindly" on the ED side, called "Blind ADR". In LoRaWAN networks, GWs use adaptive modulation techniques with multi-channel multi-modem transceivers in order to receive several data packets from the channels. Every distinct signal utilises a different SF, with the spread spectrum providing the orthogonal separation. This method offers advantages in managing the data rate [3].

In LoRaWAN, the ADR algorithm adaptively adjusts the transmission parameters attempting to extend the battery lifespan and maximise throughput. That is achieved by adjusting the data rate and TP for each ED in the LoRa network. Varying the SF adjusts the data rate, thus optimising the network performance. Past performance of each ED is the basis of data rate selection dependent on the transmission parameters. By optimising the data rates, time on air (ToA) and energy consumption, battery life is prolonged, and the overall capacity of the network is enhanced, thus increasing the lifespan of the EDs. The ADR algorithm is implemented in the LoRaWAN network to independently regulate the TP and data rate for all the EDs. LoRaWAN network performance is directly affected by power consumption in the EDs since the end devices have limited battery capacity. Because of the LoRaWAN Regional Parameters and Specifications [4, 5] EDs must cater for specific data rates farther compounding the power constraint predicament since the SNR values must cross certain thresholds and power levels. Because the EDs must respond to the channel conditions in the network, it implies they must be able to control the data rates and TP accordingly.

There is a procedure that EDs must follow to achieve optimal data rates [5]. Firstly, the ED requests the NS to manage data rate adaptation by selecting the ADR bit in an UL message header. Thereafter, the ED receives LinkADRReq MAC commands from the NS which specify the adjustment of its SF and TP and hence its data rate. The ED then confirms to the NS each part of the requested settings in a LinkADRAns MAC command. If the ED does not receive any DL packet within the ADR_ACK_LIMIT uplinks and the existing data rate is higher than the minimal data rate, all successive ULs are transmitted with an ADR acknowledgment request bit (ADRACKReq) set. If no DL message is received from the NS the ED does not receive any DL within ADR_ACK_DELAY successive ULs, the ED attempts to recover connectivity by shifting to the subsequent lower data rate delivering an expanded range. Consequently, whenever the ADR_ACK_DELAY is attained, the ED lowers the data rate by one step. The ED utilises its internal counter (ADR_ACK_CNT) which is reset whenever it receives a DL message from the NS. The transmission parameters that need to be allocated in order to optimally adjust the data rate are explained below.

A. *Bandwidth*

Bandwidth is a significant variable in LoRa modulation. LoRa symbols comprise of 2^{SF} chirps, spreading the entire frequency domain. BW is defined as a series of frequencies inside some specified transmission band [6]. Large figures of BW provide larger transmission data rates that imply smaller ToAs, resulting in diminished sensitivity due to the auxiliary noise incorporated. A smaller BW delivers greater sensitivity though it realises decreased data rates. While the choice of BW could range between 7.8 kHz and 500 kHz, the standard LoRaWAN operates at either 500 kHz, 250 kHz, or 125 kHz (BW500, BW250 and BW125) depending on the regional parameters [4].

B. *Spreading Factor*

SF is the number of raw bits that is encoded to a symbol to improve the signal-to-noise ratio (SNR), which improves sensitivity and range. However, SF results in increased ToA. The formulation 2^{SF} symbolizes the number of chips held by each symbol [2]. The spreading factor symbolises the correlation between the chip rate and the baseband data rate. The SF values for LoRaWAN range from 7 to 12, implying that, increasing the SF value increases the strength of the wireless signal which in turn increases the sensitivity of the GW, decreasing the data rate consequently. Contrastingly, reducing the SF results in an increase in the data rate, causing the data packets being transmitted to require higher TP for proper decoding at the GW. When the data signal is faint, EDs use a larger SF resulting in a longer ToA as shown in Table 1, using 125khz bandwidth and 20 bytes payload and a code rate of 4/5.

The value of SF is also affected by the distance from the GW. The farther away the ED is from the GW the weaker the data signal and hence the greater the SF value. In general, increasing the bandwidth decreases the receiver sensitivity,

while increasing the spreading factor improves the receiver sensitivity. SF is the significant parameter that improves QoS[7]. Theoretically spreading factors are orthogonal but in real deployments there are interferences that are experienced which decrease performance levels. Co-SF interference is interference emanating from EDs utilising the same SF on the same channel, while inter-SF interference results from EDs on the same channel but using different SFs [8].

TABLE I
EFFECT OF SPREADING FACTOR ON BIT RATE, TIME ON AIR AND SENSITIVITY

Spreading Factor	Bit Rate(kb/s)	Time on Air(ms)	Receiver Sensitivity(dBm)
7	5.47	61.7	-123.0
8	3.13	113.2	-126.0
9	1.76	205.8	-129.0
10	0.98	370.7	-132.0
11	0.54	695.5	-132.5
12	0.29	1318.9	-137.0

C. Code Rate

LoRa uses Forward Error Correction (FEC) error coding to increase the strength of the wireless link. This form of error correction introduces extra bits in the LoRa payload which is dependent on the CR variable in the PHY layer. The LoRa modem utilises CR to render enhanced insulation from spurts of interference and decoding errors. LoRa allows CR specifications to be either 4/5, 4/6, 4/7 or 4/8. Fixing a high CR value denotes larger number of error correction bits, providing improved protection for the message sent. Nevertheless, the drawback is an increase in ToA which results in decreased battery lifespan. GWs that maintain SF and BW constant while varying CR, can still communicate with the EDs by the use of explicit headers, given that the payload's CR is resident in the packet header. The default CR setting is 4/5 [9]. Equation (1) below states the link between data transmission rate, CR, BW, and SF [10].

$$R_b = SF * \frac{BW}{2^{SF}} * CR, \quad (1)$$

where:
SF = spreading factor
BW = modulation bandwidth
CR = code rate.

By tuning the transmission parameters mentioned earlier, the end-to-end attributes, namely, data rate, communication range, error correction capacity become variable [9]. Theoretically, it is possible to configure SF, BW and CR, but practically according to the LoRaWAN regional parameters specifications, the SF and BW combination forms the data rate [9]. The regional parameters paper stipulates the different regulatory requirements of LoRaWAN dependent on the network locale.

III. SYSTEM MODEL

A typical LoRaWAN system consists of a NS, GWs and EDs. EDs connect to the GWs within their vicinity and are configured with SF-TP combinations available from the ADR algorithm. The NS manages the spreading factor and transmission power of the EDs through the ADR commands so that packets can be correctly decoded from the GW. As such, the ADR algorithms are run on the NS. The EDs are stationary and can be homogenous or heterogenous (depending on the application) and generate data packets at a given rate. Interference is considered in the form of imperfect orthogonality and the capture effect. The EDs can be randomly or uniformly distributed around the GW which is located in the centre with a certain radius of coverage. To ensure successful transmission, the signal-to-noise ratio (SNR) must be above the reception threshold, the signal-to-interference ratio (SIR) must exceed the co-SF and inter-SF capture threshold in the presence of co-SF and inter-SF interference, respectively. In the event of packet collision of different SFs, a single signal will be successfully received if it's SIR is above its inter-SF capture threshold. If there are several signals with the same SFs transmitting on the same frequency simultaneously, the LoRa GW will successfully receive one of them provided its SIR exceeds 6dB for any SF. Channel propagation can be modelled using the different propagation models, for example Okumura-Hata model, Free Space Path Loss or Log-Distance Path Loss. An optimised ADR algorithm ensures proper ST and TP allocations resulting in an efficient network.

IV. REVIEW OF CONSTRAINED OPTIMISATION TECHNIQUES

Several optimisation methods have been developed for solving different types of optimisation problems. Because LoRaWAN has restrictions in terms of resource allocations, due to regional parameter regulations [4], constrained optimisation is a befitting method to improve ADR decision algorithms. The goals for LoRaWAN network determine what constraints the scheme will consider. Some networks want to optimise throughput, scalability, power consumption, communication robustness, coverage, and energy efficiency among other metrics. We review a body of work that utilises constrained optimisation to improve resource allocation that results in efficient ADR schemes.

The authors in [11] established a joint SF and TP assignment problem to maximise the minimum UL throughput of the EDs, based on co-SF and inter-SF interferences and TP constraints. Their SF allocation scheme hinges on the matching theory. After SFs have been assigned to EDs, the power distribution parameters are optimised to maximise the minimum throughput attained for each SF. The authors managed the intractability of the joint SF and power distribution problem by separating it into two distinct sub-problems: SF distribution while TP is constant, and TP allocation with constant SFs. The authors make the non-linear inequalities a tractable feasibility problem by implementing linear and quadratic approximation. Despite serious co-SF and inter-SF interferences, the results indicated that, the presented algorithms outperformed state-of-the-art algorithms, regarding minimal ED data rates, fairness, and mean ED throughput. Nonetheless, the model does not examine the optimisation of carrier frequencies (CFs) and the reduction of energy consumption according to the SF choice. Future work could consider load balancing and extending the proposed approach to multi-cell LoRaWANs which would assign EDs to the best GW in the case of multiple GWs.

The ADR mechanism that can efficiently optimize the packet error rate (PER) fairness within a LoRaWAN cell was proposed in [12]. The authors optimised the SF and TP per ED whilst avoiding near-far problems by assigning EDs lying on the edge of the cell to different channels. EDs pathloss values were used to arrange the EDs and divide them into homogenous clusters corresponding to the number of available channels. Each cluster was assigned a particular channel while within the cluster the proportion of EDs utilising the SFs is relative to $s/2^s$. This corresponds to the solution of the optimisation problem which seeks to minimise the maximum collision probability among all the spreading factors. The ADR mechanism computes the optimum SF assignment to apply for the purpose of minimising the collision probability. The algorithm allocates SFs and TP values optimally to EDs within a LoRaWAN cell such that there is no interference between the EDs. This scheme improves the PER of EDs farther from the GW. The results indicate that the PER can be decreased up to fifty percent for EDs farther away from the GW in a moderate contention setup. The global network PER is lowered by 42%. Energy consumption is reduced, and a wide network coverage provided, reducing the number of GWs required. The EDs are uniformly distributed around the GW and every ED can use all SFs and TPs. This means every ED in the network can reach the GW with each SF and each TP configuration. In a real-life network, this setup would be problematic because specific EDs can only employ a portion of the configuration settings which are prescribed by the radius from the GW. Future work could examine randomly distributed EDs and acknowledged traffic as they study unacknowledged traffic in this work.

In [13] the authors developed a method that reduces data collision and energy usage. This approach increased the data extraction rate (DER) and improved QoS of the LoRaWAN. They generated optimum SF and CF settings using the Mixed Integer Linear Programming (MILP) optimisation method. They demonstrated the effectiveness of the method for different network sizes using LoRaSim simulation. Their system model presumed that BW and CR are held constant whilst varying CF and SF to compute ToA to maximise packet success probability. They used the following assessment metrics to evaluate the network performance, such as, DER, number of collisions and system energy utilisation. The results proved that MILP optimised the allocation of SF and CF pairs giving more than six percentage increment in DER in contrast to the benchmark LoRaWAN ADR while the number of collisions were found to be thirteen times less. The overall energy usage of the network decreased nearly threefold compared to the equal-distribution and random dynamic allocation strategies. The strength of their approach lies in its backward compatibility with the standard ADR scheme, indicating that the solution can be implemented in off-the-shelf LoRa designs. Farther study could involve expanding the optimisation technique to much wider coverage and a greater number of GWs.

An investigation of energy efficient resource allocation was performed in [14]. The authors jointly optimised SF and TP allocation to maximise system energy efficiency (SEE) and minimal energy efficiency (MEE)of individual EDs. They constructed two optimisation problems, farther decomposing them into three sub-problems constituting user scheduling, SF allocation and TP assignment. They used an iterative power assignment process derived from the general fractional programming and proposed a sequential convex programming. The results demonstrate that the propositioned matching algorithm and power assignment scheme outperforms the current schemes regarding SEE and MEE.

MARCO is a Mixed Integer Linear Programming optimisation model for resource allocation for LoRaWAN introduced in [15]. They also introduce CORRECT, a heuristic for adaptive resource allocation which dynamically adjust the LoRaWAN parameters to reduce interference and packet collisions, thus maximising channel utilisation and delivered packets. They use a heuristic and an optimisation framework for resource allocation which models transmission parameters to maximise channel utilisation, minimising collisions meanwhile considering signal strength utilising the ED location. The simulation results obtained demonstrated that the CORRECT heuristic produces results approximating the optimum achieved by the MARCO model, optimising the assignment of transmission parameters reducing collisions and improving the overall network performance. Particularly, the CORRECT heuristic improves DER almost twelve percent compared to the ADR heuristic, and for other heuristics, this difference is even more considerable. CORRECT reduces the number of collisions up to three times compared to the standard ADR scheme adopted for LoRaWAN. Although the heuristic CORRECT shows the best DER results, the energy consumption is substantial in comparison.

The gradient projection optimisation method was employed in [16] to enhance the ADR scheme to optimise throughput. The authors propose a contention-aware ADR scheme which achieves considerably higher throughput than the standard ADR because of load balancing. The data rate is regulated by way of incrementing the number of EDs in the network using small SFs. Even though this scheme improves gross throughput, the drawback is that transmission success ratio declines which renders it unideal for applications that have reliability as a QoS requirement.

The authors in [17] proposed a LoRa network slicing and configuration mechanism to optimise resource allocation. They employed a slice-based SF and TP configuration optimization. The authors developed a novel slicing optimisation technique termed TOPG which is formulated on the Technique for Order of Preference by Similarity to Ideal Solution (TOPSIS) and Geometric Mean Method (GMM). The proposed method efficiently configures SF and TP parameters improving the performance of each slice with respect to QoS, reliability and power utilisation. From the results the authors illustrated that TOPG outperformed static and adaptive configuration strategies, improved the performance of LoRa slices in terms of reliability as well as the proportion of EDs that achieved their throughput and delay requirements. The drawback is that this approach performing slicing over LoRaWAN introduces overheads, resulting in reduction in network resources. The authors did not do the computational cost analysis of their proposed algorithm.

In [18] they investigated power allocation, and propositioned an algorithm centred on Markov decision process (MDP). They formulate a user grouping problem using a many to one matching problem. They grouped EDs into available channels and used a Markov Decision Process-based algorithm to allocate power to achieve an optimal throughput for each ED in the same channel. They develop transmission parameter assignment in wireless powered Internet of Things systems into a joint optimisation problem that optimises channel assignment and dynamic power distribution, where MDP is implemented to model the uncertainty of the harvested energy and channel conditions. To make the problem tractable, it is divided into two segments: a) allocation of EDs to available channels and b) optimising TP allocation of EDs allocated to a corresponding channel in the same time frame. The results showed that the propositioned method achieved close to optimum performance and is superior to methods that use random channel allocation but still maintains much lower computational complexity. In this paper, the authors solve the MDP-based power allocation using dynamic programming which requires known model information. Future research could look into model-free methods to solve MDP problems.

Narieda *et al.* in [19] present a performance improvement method utilising SF allocations for LoRaWAN. The authors construct the optimisation problem for the SF assignment to maximise the packet reception probability (PRP) encompassed in the average energy utilisation constraint per ED and the sensitivity constraint. By solving the optimisation problem, the network performance is improved under these constraints considering each ED individually. The authors developed a method that solves the optimisation problem using distributed genetic algorithm, a method which is metaheuristic. This method enhances the system performance by allocating the SFs to ED under the given constraints. It assumes static EDs whose quantity is constant in the network. The authors consider imperfect orthogonality of the SF in the derivation of the PRP in the LoRaWAN. The results obtained show that the PRP performance of the developed approach is more proficient and utilises a reduced mean energy for all the EDs in comparison with existent algorithms. Farther study could focus on energy usage per ED instead of averaging all the EDs.

V. DISCUSSION

Different performance metrics are used to optimise transmission parameters to achieve specific objectives such as throughput [11, 16-18], scalability [12] and energy consumption [13, 15, 19] . Table II highlights the different objectives and metrics used in the optimisation approaches under review. Energy and throughput efficiency are common objectives for optimisation while the RSS and coverage stand out as metrics. Multi-objective optimisation requires the formulated problem to divided into subproblems in order to deal with intractability[11, 14, 18]. For the references whose objective is throughput, [17] outperforms the rest of the algorithms because of the dynamic inter-slicing configuration whose performance is superior, followed by the contention aware ADR algorithm in [16] due to the load balancing effect using the gradient projection method. This is then followed by [18] whose proposed channel allocation algorithm outperforms the random channel assignment approach by ninety percent while offering better time efficiency. [11] is ranked the least performing as it achieves throughput fairness but because the approach does not optimise CFs, it compromises energy consumption. For the energy efficiency objective, the approach in [15] makes gains in the global network performance, but loses for having a higher energy consumption compared to the other approaches being considered. Ref [13] results are very closely optimum, although the runtime becomes more protracted as the number of EDs in the network increases. The algorithm proposed by [19] is superior as it presents the best PRP performance with the least average energy consumption.

Looking at the computational complexity of the approaches reviewed in this paper, Ref [11]shows the running time of the proposed SF algorithm is upper bounded by $\boldsymbol{O(NM + Q^2 + M)^2}$. When considering a real life LoRaWAN network, the complexity of the matching algorithm is not a limitation since the algorithm functions on the network server whose computational capability is extensive. In [12] they capped the amount of EDs at one thousand as a result of the computer memory restriction. All the parameters required to be transmitted to the EDs result in a $\boldsymbol{O(n^2)}$ memory utilisation. In [13] the Approximation Algorithm sustains a linear complexity time $\boldsymbol{O(n) = 111n + 57}$ in the worst-case scenario. The design of the algorithm is such that it functions in the LoRaWAN Application Layer with EDs that have a time complexity equal to the ADR algorithm, such that the suggested optimisation problem would not trigger any significant computation overhead, neither in the EDs nor in the NS. Ordinarily, the implementation of the algorithm utilises below 20 kB of memory, 4 kB in most cases while 20 kB would be the worst-case scenario. This is inconsequential considering that most commercial off-the-shelf EDs include at least 128 kB of flash memory [20].

TABLE II
COMPARISON OF THE OPTIMISATION TECHNIQUES

Ref	Objective	Metrics	Constraints
[11]	Throughput	Channel fading, RSS	Co-SF, inter-SF, TP
[16]	Throughput	RSS, ToA	Number of EDs, TP
[17]	Throughput	RSS, PER, slice priority	Channel reservation, TP, data rate capacity
[18]	Throughput	Data rate, ToA	TP, time slots per frame, users that can access the channel
[12]	Scalability	Coverage range	SINR
[13]	Energy efficiency	DER	SF, CF
[15]	Energy efficiency	PDR, DER	Sensitivity, Number of EDs
[19]	Energy efficiency	Channel contention, PDR	Sensitivity, current consumption

The computational complexity in [14] is such that for the energy efficient power allocation for SEE the whole complexity to solve SEE is $\boldsymbol{O}(\boldsymbol{L}_{\boldsymbol{max}}^{(1)} + (\boldsymbol{N}+\boldsymbol{1})^{3.5}\boldsymbol{\delta}^{(1)})$ where $L_{max}^{(1)}$ is the maximum iteration number and δ is the number of bits required to symbolise the entries in the optimisation problem. Concerning MEE, the computational complexity is $\boldsymbol{O}\left(\boldsymbol{log}_2\left(\boldsymbol{\epsilon}^{-1}(\boldsymbol{\eta}_{\boldsymbol{m,l}}^{\boldsymbol{max}} - \boldsymbol{\eta}_{\boldsymbol{m,l}}^{\boldsymbol{min}})\right)\boldsymbol{L}_{\boldsymbol{max}}^{(2)}(\boldsymbol{N}^{3.5}\boldsymbol{\delta}^{(2)})\right)$, where $\eta_{m,l}$ is energy efficiency per ED. In [17], because the adaptive slicing and spreading factor-transmission power configuration algorithm is simple, it has a constant complexity of $\boldsymbol{O}(\boldsymbol{1})$. Notwithstanding, the global complexity of the proposed dynamic adaptive slicing and SF-TP algorithm and TOPG algorithm is $\boldsymbol{O}(\boldsymbol{n}^{\boldsymbol{2}})$. Complexity is decreased in TOPG as a consequence of the server narrowing the search space to SF values that acknowledge the guaranteed bit rate threshold. The computation time is shortened without the QoS performance being significantly affected.

VI. CONCLUSION

ADR schemes are continually being developed because numerous end devices are being added to the IoT network daily, resulting in new QoS requirements emerging. It is crucial in LoRaWAN to allocate transmission resources optimally as demands for scalability, throughput and energy efficiency and QoS requirements continue to grow. Different applications have different objectives and constraints and thus require unique resource allocation optimisation mechanisms to accomplish the desired optimisation goals. This paper reviewed several existing ADR schemes that employ constrained optimisation techniques and considered their strengths and drawbacks and how they impact network performance. The research lays the foundation for more efficient and efficacious ADR algorithms. The study revealed that although transmission parameters are standard, many different approaches are constantly being proposed to improve network performance and provide efficiency. Gaps in the literature were identified and future work on enhancing ADR schemes was proposed.

ACKNOWLEDGMENT

This work is based on the research supported in part by our industry partner Telkom. The grant holder acknowledges that opinions, findings and conclusions or recommendations expressed in any publication generated by this research are that of the authors, and that our industry partners accept no liability in this regard.

REFERENCES

[1] M. Centenaro, L. Vangelista, A. Zanella, and M. Zorzi, "Long-range communications in unlicensed bands: The rising stars in the IoT and smart city scenarios," *IEEE Wireless Communications*, vol. 23, no. 5, pp. 60-67, 2016.

[2] L. Alliance, "LoRa and LoRaWAN-A Technical Overview," *White paper*, 2019.

[3] C. El Fehri, M. Kassab, S. Abdellatif, P. Berthou, and A. Belghith, "LoRa technology MAC layer operations and Research issues," *Procedia computer science*, vol. 130, pp. 1096-1101, 2018.

[4] L. Alliance, "LoRaWAN 1.1 regional parameters," *Technical Specification*, 2017.

[5] L. Alliance. "LoRaWAN 1.0. 3 specification." https://lora-alliance.org/resource-hub/lorawanr-specification-v103 (accessed May, 2021).

[6] A. Augustin, J. Yi, T. Clausen, and W. M. Townsley, "A study of LoRa: Long range & low power networks for the internet of things," *Sensors*, vol. 16, no. 9, p. 1466, 2016.

[7] M. A. Ertürk, M. A. Aydın, M. T. Büyükakkaşlar, and H. Evirgen, "A Survey on LoRaWAN Architecture, Protocol and Technologies," *Future Internet*, vol. 11, no. 10, p. 216, 2019.

[8] A. Waret, M. Kaneko, A. Guitton, and N. El Rachkidy, "LoRa throughput analysis with imperfect spreading factor orthogonality," *IEEE wireless communications letters*, vol. 8, no. 2, pp. 408-411, 2018.

[9] R. Sanchez-Iborra, J. Sanchez-Gomez, J. Ballesta-Viñas, M.-D. Cano, and A. F. Skarmeta, "Performance evaluation of LoRa considering scenario conditions," *Sensors*, vol. 18, no. 3, p. 772, 2018.

[10] Semtech, "Modulation basics application note AN1200. 22. Semtech Corporation-Wireless Sensing and Timing Products Division," Semtech, , 2015.

[11] L. Amichi, M. Kaneko, E. H. Fukuda, N. El Rachkidy, and A. Guitton, "Joint allocation strategies of power and spreading factors with imperfect orthogonality in LoRa networks," *IEEE Transactions on Communications*, 2020.

[12] B. Reynders, W. Meert, and S. Pollin, "Power and spreading factor control in low power wide area networks," in *2017 IEEE International Conference on Communications (ICC)*, 2017: IEEE, pp. 1-6.

[13] E. Sallum, N. Pereira, M. Alves, and M. Santos, "Improving Quality-of-Service in LoRa Low-Power Wide-Area Networks through Optimized Radio Resource Management," *Journal of Sensor and Actuator Networks*, vol. 9, no. 1, p. 10, 2020.

[14] B. Su, Z. Qin, and Q. Ni, "Energy Efficient Uplink Transmissions in LoRa Networks," *IEEE Transactions on Communications*, vol. 68, no. 8, pp. 4960-4972, 2020.

[15] J. Moraes *et al.*, "An Efficient Heuristic LoRaWAN Adaptive Resource Allocation for IoT Applications," in *2020 IEEE Symposium on Computers and Communications (ISCC)*, 2020: IEEE, pp. 1-6.

[16] S. Kim and Y. Yoo, "Contention-aware adaptive data rate for throughput optimization in LoRaWAN," *Sensors*, vol. 18, no. 6, p. 1716, 2018.

[17] S. Dawaliby, A. Bradai, and Y. Pousset, "Joint slice-based spreading factor and transmission power optimization in LoRa smart city networks," *Internet of Things*, p. 100121, 2019.

[18] X. Liu, Z. Qin, Y. Gao, and J. A. McCann, "Resource allocation in wireless powered IoT networks," *IEEE Internet of Things Journal*, vol. 6, no. 3, pp. 4935-4945, 2019.

[19] S. Narieda, T. Fujii, and K. Umebayashi, "Energy Constrained Optimization for Spreading Factor Allocation in LoRaWAN," *Sensors*, vol. 20, no. 16, p. 4417, 2020.

[20] Semtech. "MCU Memory Security and System Partitioning Considerations for Sensors for LoRaWAN® Networks." Semtech. https://lora-developers.semtech.com/library/tech-papers-and-guides/mcu-memory-management/download-mcu/ (accessed 5 June, 2021).

Rachel Kufakunesu received her BTech and MTech degrees in Electrical Engineering from the University of South Africa. She is currently pursuing a PhD in Electronic Engineering at the University of Pretoria. Her research interests are wireless sensor networks and low power wide area networks.

Slice Admission Control by Resource Auction Game in 5G Network with Reinforcement Learning

Mourice O. Ojijo*, Dismas O. Ombuya†
*Department of Electrical Engineering, University of Cape Town South Africa
†Department of Computer Science, Kabarak University Kenya

[1]ojjmou1@myuct.ac.za
[2]dombuya@kabarak.ac.ke

***Abstract*—Competition for network resources is anticipated to ensue as connectivity to 5G wireless network increases and demand for network slicing rises. Through network slicing, virtual resources will be allocated to 5G slice tenants on demand. This will be followed by online evaluation of the most valuable resource buyer in a competitive manner. One way of dealing with such resource competition is to apply an auction mechanism. However, the slice providers will have to deal will massive and granular data in order to determine the most valuable resource buyer to admit. In this regard, a slice provider must determine a policy for selecting the best buyer. In this paper we propose a slice admission control incorporating an auction game based on reinforcement learning that maximizes the slice provider's revenue. In this model, resource scarcity and quality of service requirements is considered. We later demonstrate that our model has an improved control on slice admission while maintaining fairness when compared existing models such as greedy and random strategies.**

***Index Terms*—Slice Admission Control, Resource Auction, Reinforcement Learning**

I. Introduction

The Fifth Generation (5G) network heterogeneous design is expected to implement virtual network function (VNF) and network function virtualization (NFV) under what is known as network slicing [1]. The need to sell network slices and admit corresponding tenants leading to resource allocation will depend on network resource availability, resource demand and expected revenue by the infrastructure network provider (InP) [2].The designers of 5G network have proposed three slice categories namely: enhanced mobile broadband (eMBB) for high bandwidth constraint services, massive machine type communication (mMTC) and ultra reliable low latency (uRLLC) for massive connectivity and mission critical services [3].

Hierarchically, the InP owns the physical infrastructure which hosts the virtual resources. A virtual network operator (VNO) can purchase virtual resources from the InP and further sell to end users. In a multi-tenant environment, the InP must deal with multiple requests for common resources, this consequently brings about resource competition. While the InP may choose to continually sell to tenants/VNOs who promise high revenue, this technique may be unfairly greedy. Intelligent resource auctioning allows InPs to evaluate tenants and sell resources to the most deserving buyers. A technique used by governments to auction telecommunication spectra [4].

In resource auctioning, there is a bidder who is in need of network resources and a seller who has limited network resources to sell but wants to maximize revenue. The information provided by the bidder informs the seller about bidder's value and preference. The rapid growth in the number of connected devices implies that a large volume of data containing the bidding information must be autonomously analyzed in order to make smart decisions [3]. Generally, the winning bid is resolved by its ability to meet the slice admission objective set by the InP.

There are two main objectives solved when resource auctioning is instantiated. First one is the more general economic problem of maximizing social welfare of the auctioneers/sellers, second improving technical efficiency through resource allocation and fairness [5]. We contribute to these solutions by considering the less investigated aspect of quality of service(QoS) requirement.

In auctioning, a bidding information vector is mapped to RL state attributes. The learning agent in RL resolves the best bid based on these attributes during the learning process. Many bidding strategies such Vickrey-Clarke-Groves strategy have bidders with dominant strategies based on incentive compatibility. We align our model to such universal models while allowing bidders to still maintain their own preferences and evaluate a non greedy policy intended to maximize utility while efficiently considering resource constraint and fairness.

II. Related Works

Recently, researchers have proposed theories for 5G resource management and auctioning models. The work in [2] proposes an online auction-based resource allocation for network slicing (ORANS). The concept provides a model for online resource allocation which include determining the winning bid followed by a strategy for payment. The proposed algorithm assumes a bidding mechanism where each bid is specific to a given slice. This assumption however, considers a strict adherence to a slice which may be technically challenging.

In [5], the authors proposed a two level cloud radio access network (C-RAN) resource auction: an auction between the

end user and the virtual network operator and an auction between the virtual network operator and the C-RAN operator, this consideration requires the auctioneer to coordinate two levels of auctioning at the same time which introduces further complexity in the resource auction process.

Liu et al in [6] and *Zhu et al* in [7] considered an online combinatorial auctioning based on resource allocation and pricing mechanism for 5G slices where an exclusive OR (XOR) mechanism was applied to maximize social welfare, the authors assumed static resource pricing which is less practical as resource pricing may change as scarcity become severe. A closely related work is proposed in [8].

Tadayon et al in [9] and *Zhao et in* [10] proposed resource auctioning and allocation for only spectral resource. Further, Vickrey-Clarke-Groves (VCG) [11] [12] mechanism which has been widely adopted to solve resource auctioning problem, relies on utilitarian welfare function whereeach bidding agent reports its value from which the optimal option is calculated, in such cases, some agents may still report untruthful values.

While auctioning mechanisms are obvious choices for fair network resource allocation, they also provide the ability to model interactions between InP and VNOs, ease of optimization, analysis and revenue maximization [13]. On that note we combine resource auctioning with reinforcement learning so as to obtain an optimal policy for slice admission control.

Our contribution in this work is summarized as follows:

- We model the auction mechanism as a sequential decision process problem and solve it using RL.
- We present our analysis from simulations to prove that RL based technique has improved control over slice admission while maintaining fairness and acceptable QoS.

III. System Model

A. Network Model

In this setup, a VNO sends slice resource requests to the InP after obtaining them from a set of underlying users. The InP employs a bidding controller as part of slice admission control mechanism. Users with similar requirements are placed in the same virtual group, this allows a slice request and the bidding information to be uniquely aligned to a specific resource bundle. A slice is then orchestrated.

We consider a user $u \in \mathcal{U}$ associated to a base station $v \in V$. Users are considered uniformly distributed within the network. The VNO provides grouping $i \in I$ as a slice class for users with similar latency requirement ω. The latency requirement for user u in group i under base station v is given by $\omega^u_{v,i}$. The maximum transmit power from the base station v to user u in group i is given by $P^u_{v,i}$. Each user is allocated a fraction of bandwidth $b^u_{v,i}$. There is a VNO $n \in N$ competing for similar resources from the InP. The overall assumption is that, the channel state information is known.

In a realistic time varying environment with user interference, the signal to noise ratio (SNR) is given by equation (1)

$$SNR_u = \frac{P^u_{v,i} h^u_v}{\mathcal{N}_o} \tag{1}$$

where $\mathcal{N}_o$ is the noise power. The total ergodic downlink throughput for a user u belonging to a VNO n can therefore be defined according to [14] in equation 2 as.

$$r^u_n = b^u_{v,i} B log_2(1 + SNR_u) \tag{2}$$

where B is the total bandwidth per base station. The total data rate per slice is therefore given by;

$$r_{tot,i,n} = \sum_{u \in \mathcal{U}} r^u_n \tag{3}$$

Each virtual group i is served by a slice having data rate $r_{tot,i,n}$.

B. Computing Resource Model

The computing resource requirements within a slice include memory, central processing units (CPU) core, and random access memory (RAM). In our grouping model, users in the same group require similar computing resources. Each virtual resource allocation per group is considered complete if it can be fully orchestrated. Assume each user resource requirement occupies a portion of $z \in Z$ finite memory and RAM $g \in G$. The InP refreshes the memory periodically such that there is no fragmentation hence improving memory and RAM usage efficiency. The computing resource availability indicator $d = 1$ meaning computing resource is available while $d = 0$ indicates no computing resource is available; hence $d \in \{0, 1\}$ is a two state Markov model [15] given by.

$$d_t = \begin{bmatrix} d_{t=0} & d_{t=1} & d_{t=2} & ... & d_{T-1} \end{bmatrix} \in [0, 1] \tag{4}$$

where t denotes the instantaneous time for which the computing resource is required. The total memory and RAM requirement per slice is therefore denoted by

$$\rho_{mem,i,n} = \sum_{u=1}^{\mathcal{U}} \sum_{t=0}^{T-1} d_t z^u_t \tag{5}$$

$$\rho_{ram,i,n} = \sum_{u=0}^{\mathcal{U}} \sum_{t=0}^{T-1} d_t g^u_t \tag{6}$$

where T is the total duration of memory occupancy per user u.

The computational model comprises of the size of task and the number of CPU core required per slice . We denote a CPU task as $\Omega\{o_t, q_t\}$, where o_t is the instantaneous size of the task and q_t is the task size per CPU. The computational capacity given by word size per CPU cores assigned to a slice n is therefore given by β_i. The numbers of CPUs per slice is given by 7:

$$f_i = \mathcal{U} \sum_{t=0}^{T-1} \frac{\Omega(o_t)}{\beta_n \Omega(q_t)} \times d_t \tag{7}$$

IV. Problem Formulation

A. Auctioning Mechanism

In a typical auctioning environment, consumers cannot express preference, they can only bid what the seller offers, this is highly inefficient as most consumers have specific demands. In our model, the tenant is explicitly allowed to have a bidding preference since the background resource demand is based on user requirement, however, to obtain a network resource, the tenant resource request must be subjected a competitive bidding process. Each VNO has a set of users associated to a particular slice. The VNO addresses the slice demand problem by buying a resource block from the InP for the subscribed users. To obtain a slice, the VNO enters resource action game controlled by an agent (auctioneer). The auction process is double sided where both the VNO and the InP send their valuations $\mathfrak{V}_{bid}$ and $\mathfrak{V}_{ask}$ to the agent respectively. A positive utility $\mathfrak{U}^{+} = \mathfrak{V}_{bid} - \mathfrak{V}_{ask}$ is achievable when the VNO *bid* is higher than the InP *ask*. To participate in auction game, the VNO sends its slice valuation alongside the bidding information. We define $\phi_{bid,n} = (r_{tot,i,n}, \rho_{mem,i,n}, \rho_{ram,i,n}, f_{i,n}, T_{i,n}, \mathfrak{V}_{bid,i,n}, l_i)$ as the bidding information containing the total resources required and the bidding price, T_n is the slice duration and $l_i = \frac{1}{\mathcal{U}} \sum_{u \in \mathcal{U}} \omega^{u}_{v,i}$ is the average latency named as QoS index requirement per slice. The profitability of the auctioning game is achieved by maximizing the positive utility given by equation (8)

$$\max_{n \in \mathcal{N}} \mathfrak{U}^{+}_{i,n} = \max \sum_{i=1}^{I} \sum_{n=1}^{\mathcal{N}} (\mathfrak{V}_{bid,i,n} - \mathfrak{V}_{ask,i,n}) \tag{8}$$

and the selling price given by equation 9 as:

$$\max_{n \in \mathcal{N}} \eta_{i,n} = \max \sum_{i=1}^{I} (\sum_{n=1}^{\mathcal{N}} \eta_{opt,i,n} - \sum_{j \neq n}^{J} \eta_{i,j}) \tag{9}$$

subject to:

$$C1 : \omega^{u}_{v,i} < \omega_{th} \tag{10}$$

$$C2 : d_t \in \{0, 1\} \tag{11}$$

$$C3 : \mathfrak{U}_{i,n} > 0 \tag{12}$$

$$C4 : \sum_{i \in I} [\rho_{mem,i,n} + \rho_{ram,i,n}] < \rho_{tot} : \quad \forall n \in \mathcal{N} \tag{13}$$

Where $\mathcal{N}$ is the total number of VNO (bidders) and $\mathfrak{U}_{\mathrm{n}}{}^{+}$ is the n^{th} utility, $\eta_{opt,i} = \frac{1}{l_i}(r_{tot,i,n} + \rho_{mem,i,n} + \rho_{ram,i,n} + f_{i,n}, T_{i,n})\mathfrak{U}^{+}_{i,n}\beta_i$ is the optimum selling price per slice class i and η_j represents other valuations as if the winning bidder was absent, β_i is the unit price per slice. Equation 9 conforms to the VCG auctioning model [16]. Constraint $C1$ represent the QoS threshold required by each slice. The control variable for slice admission in the cloud network for computing resources is $C2$. The constraint $C3$ indicates that the social welfare must remain positive for the maximization of profit. The overall computing memory resources allocation per slice is denote by constraint $C4$.

The auctioning process outcome combined with resource constraints are limiting parameters that periodically control slice admission process which leads to the dominant strategy and optimality. In this work, the dominant strategy is achieved when bids with positive utility as well as resource requests that pay more for short term contracts are admitted. In this regard we define a parameter known as the *value indicator (VI)* given by $\mathcal{VI} = \frac{\textit{Total slice cost}}{\textit{Total slice duration}}$ which is applied so that if a bidder pays more for a short term slice then *VI* is improved. When a resource block or slice is sold at selling price $\{\eta_{i,n} = \bar{\eta}_{i,n}\}$ [16], under dominant strategy then the agent is said to be on track to reach optimality. where $(\bar{\eta}_n \geq \mathfrak{V}_{ask})$ is known as the hammer price.

B. Incentive Compatibility and The Nash Equilibrium(NE)

Resource buyers may provide untrue bidding information in order to win a bid, this is an unfair strategy. As a result, a valuable bidder may be bypassed. If a resource buyer changes its valuation $\mathfrak{V}_{bid}$ with the intention of winning, our approach enforces fairness by providing the Nash equilibrium (NE) which goes as follows. The QoS indicator l_i is used as a weight balancing controller between the latency requirement of a slice and the resource valuation. For instance, the higher the valuation the smaller the latency requirement. We illustrate this in equation (14)

$$\mu = \log\left(\frac{\mathfrak{V}_{bid}}{li}\right) \tag{14}$$

where l_n is the average slice latency requirement. It should be noted that, any bidder cannot alter the bidding information without affecting the QoS index requirement and the InP's response. To explain this concept further consider a bidder who wishes to maintain the same QoS index but unfairly increases the valuation in order to win a bid. Equation 14 will not be satisfied without reducing the latency requirement, furthermore such a move is likely to violet the SLA between the VNO and the InP. Finally the fairness index [16] [17] is defined by equation (15) as

$$D(\mathfrak{U}) = \frac{\left(\sum_{i=1}^{I} \mathfrak{U}_i\right)^2}{I(\sum_{i=1}^{I} \mathfrak{U}_i^2)} \tag{15}$$

where $\mathfrak{U}_i$ is the utility obtained after each successful bid, auction and slice admission. The fairness index is a parameter used to evaluate how a strategy is.

C. Reinforcement Learning: State, Action and Reward Function

Reinforcement learning (RL) relies on a Markov decision process (MDP) formed as tuple $\{\boldsymbol{s, a, r, s'}\}$ where $\boldsymbol{s}$ is the observed state, $\boldsymbol{a}$ is the action taken, $\boldsymbol{r}$ is the reward obtained and $\boldsymbol{s'}$ is the next state under state transition model [18].

To apply RL in our work, the system environment must be defined. The environment comprises states, possible actions,

reward value. Since Q-leaning is employed, the algorithm is an off-policy and state transition is dependent on state arrival and not transition probability.

1) System State: The system states is modeled from the bidding information provided by each tenant n at discrete time $t = \{0, 1, 2, ...T-1\}$ which is given by a tuple in equation (16)

$$\boldsymbol{s}(t) = \{\phi_{bid,i,n}(t), \mathfrak{V}_{ask,i,n}(t), \Gamma_n\} \tag{16}$$

where $\phi_{bid,i,n}(t), \mathfrak{V}_{ask,i,n}(t), \Gamma_n$ are the bidding information, the InP's asking price and the total remaining resource units at time t respectively.

Between time $t = 0$ to $T-1$ the InP reads M requests from a holding queue. We assume that each bidding information forms a part of a finite state space $\boldsymbol{s} \in \boldsymbol{S}$. The dynamic state space $\boldsymbol{S}$ changes during each iteration as it must be updated to reflect the total available resources. Similarly, the ability to meet the QoS requirement after each admission must also be updated. The InP cannot admit a slice when resources are depleted hence the agent must learn this strategy, anything contrary is subjected to a penalty.

2) Action Space: The action space is modeled as a binary variable $\mathbf{a}(t) = \{\mathbf{a}(0), \mathbf{a}(1) \dots \mathbf{a}(T-1)\}$ such that $\boldsymbol{a}(t) \in \{0, 1\}$ represents an action at time t where 1 indicates a successful resource auction and an eventual slice admission and 0 otherwise. After every action $\mathbf{a}(t)$ the agent obtains the corresponding reward $\mathbf{r}(t)$ which is used to update the Q-values in the Q-table [18].

3) Reward: Intuitively, RL is used to maximize the reward by evaluating the value of each action. The reward function is modeled to optimize action selection (slice admission control) while considering all constraints. A reward $\mathbf{r}(t) = \chi$ is maximum when a good action is taken and minimum otherwise.

In order to assure complete slice isolation, the InP must guarantee all resources required to instantiate a slice. Let $\lambda = 1$ denote full resource availability and successful auction, 0 otherwise. The reward function employed can therefore given by equation (17 and 18)

$$\mathbf{r} = \mathbf{a}(t) log(\eta_{opt,i}) \mu VI: \quad \text{if } \lambda = 1 \tag{17}$$

else

$$\mathbf{r} = (1 - \mathbf{a}(t)) log(\eta_{opt,i}) \mu VI: \quad \text{if } \lambda = 0 \tag{18}$$

D. Q-Learning Model

The objective of Q-learning in **Algorithm** 1 is to build a map of optimal actions and their corresponding states $\boldsymbol{s} \in S$. This however, is not complete until this map is retrieved. The retrieval of this mapping is known as policy retrieval. Once the policy retrieval is complete the system is now aware of all possible bids under resource constraint for slice admission control. The policy retrieval algorithm is given in **Algorithm** 2. The Q-learning is built based in the classical Bellman's equation given in 19.

$$Q(\boldsymbol{s},\boldsymbol{a}) = (1-\alpha) q(\boldsymbol{s},\boldsymbol{a}) + \alpha\{\mathbf{r}_t + \gamma \max_{a'} q(\boldsymbol{a'},\boldsymbol{s'})\} \tag{19}$$

Where α is the learning rate, γ is the discount factor and R long-term reward. $Q(\boldsymbol{s},\boldsymbol{a})$ is the Q-value at action $\boldsymbol{a}$ after visiting state $\boldsymbol{s}$

Algorithm 1: Q-Learning

Result: Q-Table,RewardPerEpisode,
Input: Initialize learning parameters($\gamma, \alpha, \epsilon_{max}$)
Input: Initialize environment parameters
$(\phi_{bid,i,n}(t), \mathfrak{V}_{ask,i,n}(t), \Gamma_n, \mathbf{r}(t), \mathbf{a}(t))$
Input: Initial Q-table ($[Q]^{K \times M} = 0$)
while *inEpisode* **do**
  GetInitialState($\phi_{bid,i,n}(t=0), \mathfrak{V}_{ask,i,n}(t=0), \Gamma_n(t=0)$);
  for *m=0 to M-1* **do**
    Get Random *exploration rate* ;
    if *exploration rate* $> \epsilon$ **then**
      take greedy action
    end
    else
      Choose random action($\mathbf{a} \in [0, 1]$)
    end
    Update Γ_n;
    Find next-state($\mathbf{s} = \mathbf{s}_{t+1}$);
    Obtain reward (by Eq 17 or 18);
    Update Q-table by Eq.19;
    m=m+1;
  end
  Update Exploration rate using
  $(\epsilon = \epsilon_{min} + (\epsilon_{max} - \epsilon_{min}) e^{-\delta \times \text{episode}})$;
end
Return Q-table

Algorithm 2: Q-Learning Policy Retrieval

Result: Table of actions and states
Input: Initialize states
while *inState and Action Space* **do**
  GetInitialState;
  Obtain Optimal Action and Corresponding State;
  Obtain next state;
  m=m+1;
end
Return optimal actions and corresponding states

V. Simulation and Results

We based our simulation on 5G new radio(NR) FR2 parameters considering the time division duplex (TDD) major bands on single tier macro base station. The maximum achievable cell bandwidth is 400MHz at maximum subcarrier bandwidth of 120kHz, this follows a maximum of 264 subchannels. FR2 offer two subcarrier spacing frequencies of 60kHz and

TABLE I
SIMULATION PARAMETERS

Hyper parameters	
Parameter	Value
Discount rateγ	0.09
Learning rate α	0.001
Maximum exploration rate ϵ_{max}	1
Minimum exploration rate ϵ_{min}	0.001
Exploration decay rate δ	0.01
Number of episodes	1000
Other parameters	
Parameter	Value
Latency range	1ms-100ms
Carrier Frequency	400MHz
Subcarrier bandwidth	60KHz,120KHz
Thermal noise	-174dBm
Task per cpu	10GB
Path loss	72+30log (d) [19]

120kHz. The computational resources requested per slice is divide in terms of CPU cores, RAM usage per hour and hard disk storage per hour normalize off as resource unit blocks. In our simulation we assumed a single task is 10 gigabytes requiring 10^6 cycles per second. We started our simulation by determining how probable a slice request will be accepted given a Poisson request distribution. In Fig 1 it is clear that all the schemes (Learning,Greedy and Random based admission LBA,GBA,RBA) had no similar request admissions. The agent however, reduced the possibility of admitting a request once resources were deemed to have run out at around request number 1500. To determine how fair each scheme were, we calculated the fairness index according to Eq. 15 and shown that LBA was the most fair followed RBA then GBA as show in Fig. 2

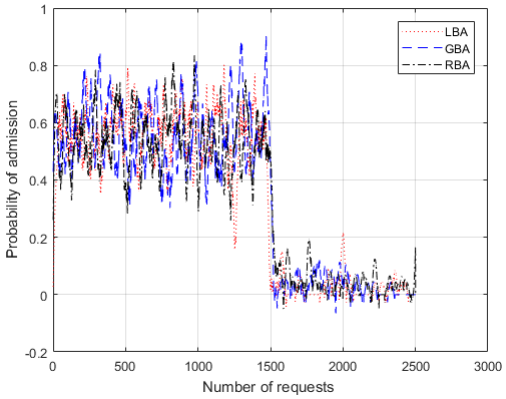

Fig. 1. Admission probability of each scheme

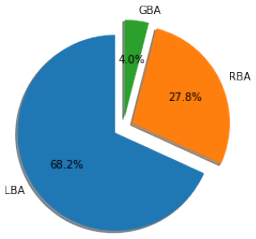

Fig. 2. Fairness percentage for each slice admission scheme

Any slice admission is mapped to the revenue obtained. We compared all the slice admission schemes based on the revenue obtained by the InP. From the simulations LBA promised the highest overall revenue followed by RBA the GBA. The intuition is that, LBA learned to determine which requests would offer higher revenue considering the rewards obtained during learning. This, in turn resulted into higher projected cumulative revenue as shown in Fig. 3. The dip in revenue towards the end of the graph is due to penalties incurred due to SLA violation for admitting slices during resource outage.

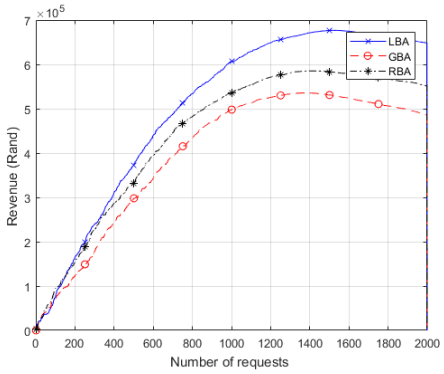

Fig. 3. Revenue accumulation considering resource constraint

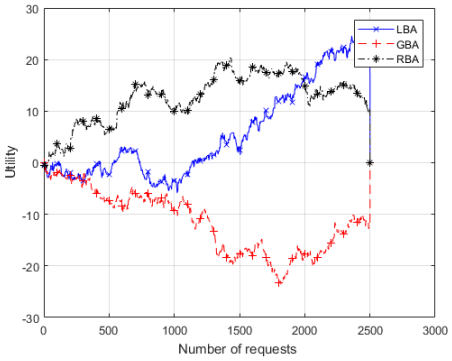

Fig. 4. Projected social welfare

In Fig. 4, we show the effect of auctioning by determining the social welfare which is the cumulative utility over all episodes. The RBA scheme had higher social welfare prediction in the beginning due to many successful random auctions and admissions. This however deteriorated in the long term as further random auctions did not produce positive utilities. The LBA however gradually learned when to auction and admit slice requests. The GDA performed poorly due to consistent exploitation of non optimal states leading to largely negative utilities. These results are shown in Fig. 4

After every slice admission the InP must check its ability to meet the QoS for remaining admissions. This ability is calculated as a function of the a quantity which represents the remaining resources known as the QoS index show in Fig. 5. The QoS index deterioration is considerably similar in all the scheme, however LBA still performs better than the other two schemes.

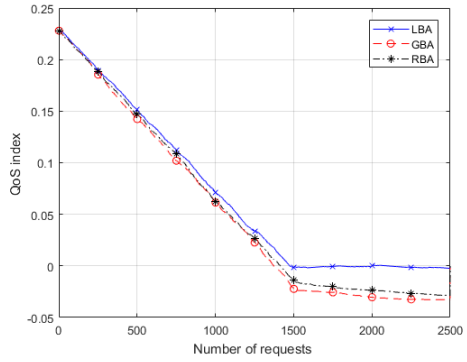

Fig. 5. QoS Index vs slice admission

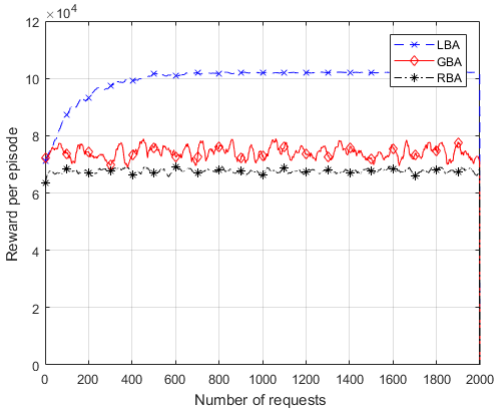

Fig. 6. Illustration of average reward build up during learning

In Fig 6 we finally demonstrate that LBA achieves optimal goal at around episode 600. This contrast both GBA and RBA which remains non optimal through all iterations. It is clear that LBA performs better for the tested events meeting the goals set at the beginning of this paper.

VI. Conclusion

To address the challenge of slice admission control and efficient resource allocation, we presented an auction based slice admission control to provide a QoS aware admission control while maximizing revenue. We have shown that, compared to RBA or GBA, the LBA scheme has greater control on admission selection enabling valuable resource tenants to be admitted. We have shown that the proposed algorithm allows the InP to limit losses by restricting slice admission to those that can achieve the auction goal and have the highest value.

Our proposed algorithm however, has limitation. The algorithm was based on finite state space which does not depict some real scenarios. Some of the parameters in 5G resource allocation are continuous and become memory intensive during learning leading to an extremely large Q-table. The application of value approximation with deep artificial neural networks is a tractable approach to be explored in our future work.

References

[1] M. O. Ojijo and O. E. Falowo, "A Survey on Slice Admission Control Strategies and Optimization Schemes in 5G Network," *IEEE Access*, vol. 8, pp. 14 977–14 990, 2020.

[2] L. Liang, Y. Wu, G. Feng, S. Member, X. Jian, and Y. Jia, "Online Auction-Based Resource Allocation for Service-Oriented Network Slicing," *IEEE Trans. Veh. Technol.*, vol. 68, no. 8, pp. 8063–8074, 2019.

[3] V. P. Kafle, Y. Fukushima, P. Martinez-Julia, and T. Miyazawa, "Consideration On Automation of 5G Network Slicing with Machine Learning," *2018 ITU Kaleidosc. Mach. Learn. a 5G Futur. (ITU K)*, pp. 1–8, 2019.

[4] B. Kasberger, "Can Auctions Maximize Welfare in Markets After the Auction?" *Mimeo*, no. NOeG, pp. 1–44, 2017.

[5] M. Morcos, T. Chahed, L. Chen, J. Elias, and F. Martignon, "A Two-level Auction for C-RAN Resource Allocation," *2017 IEEE Int. Conf. Commun. Work. (ICC Work.*, pp. 516–521, 2017.

[6] X. Liu, Q. Qiu, and L. Linyun, "An Online Combinatorial Auction Based Resource Allocation and Pricing Mechanism for Network Slicing in 5G," *2019 IEEE 19th Int. Conf. Commun. Technol.*, pp. 908–913, 2019.

[7] K. Zhu and E. Hossain, "Virtualization of 5G Cellular Networks as a Hierarchical Combinatorial Auction," *IEEE Trans. Mob. Comput.*, vol. 15, no. 10, pp. 2640–2654, 2016.

[8] X. Zhang, H. Qian, K. Zhu, and R. Wang, "Virtualization of 5G Cellular Networks : A Combinatorial Double Auction Approach," 2017.

[9] N. Tadayon and A. Sonia, "Radio Resource Allocation and Pricing : Auction-Based Design and Applications," *IEEE Trans. Signal Process.*, vol. 66, no. 20, pp. 5240–5254, 2018.

[10] F. Zhao, Y. Zhang, and Q. Wang, "Multi-Slot Spectrum Auction in Heterogeneous Networks Based on Deep Feedforward Network," *IEEE Access*, vol. 6, pp. 45 113–45 119, 2018.

[11] M.-t. Pons, N. Afraz, A. Elrasad, and M. Ruffini, "DBA Capacity Auctions to Enhance Resource Sharing across Virtual Network Operators in," *2018 Opt. Fiber Commun. Conf. Expo.*, pp. 1–3, 2018.

[12] M. Harishankar, S. Pilaka, P. Sharma, N. Srinivasan, C. Joe-wong, and P. Tague, "Procuring Spontaneous Session-Level Resource Guarantees for Real-Time Applications : An Auction Approach," *IEEE J. Sel. Areas Commun.*, vol. 37, no. 7, pp. 1534–1548, 2019.

[13] U. Habiba and E. Hossain, "Auction Mechanisms for Virtualization in 5G Cellular Networks : Basics , Trends , and Open Challenges," *IEEE Commun. Surv. Tutorials*, vol. 20, no. 3, pp. 2264–2293, 2018.

[14] S. Swain, N. Mishra, S. Rath, and B. P. S. Sahoo, "Spectrum Sharing for D2D Communication in 5G Cellular Networks : An Auction-Based Model."

[15] F. R. Yu and Y. He, *Deep Reinforcement Learning for Interference Alignment Wireless Networks*, 2019.

[16] Y. Zhang, C. Lee, D. Niyato, and P. Wang, "Auction approaches for resource allocation in wireless systems: A survey," *IEEE Commun. Surv. Tutorials*, vol. 15, no. 3, pp. 1020–1041, 2013.

[17] M. A. Rostom, A. H. A. El-malek, M. Elsabrouty, and M. Abo-zahhad, "Cognitive Radio Users Admission and Channels Allocation in 5G HetNets : A College-based Matching and Auction Game Approach," *2019 Int. Conf. Wirel. Mob. Comput. Netw. Commun.*, pp. 1–6, 2019.

[18] Q. Sun, C.-L. I, Z. Zhao, H. Zhang, X. Chen, C. Yang, R. Li, and M. Zhao, "Deep Reinforcement Learning for Resource Management in Network Slicing," *IEEE Access*, vol. 6, pp. 74 429–74 441, 2018.

[19] J. Deng, O. Tirkkonen, R. Freij-Hollanti, T. Chen, and N. Nikaein, "Resource Allocation and Interference Management for Opportunistic Relaying in Integrated mmWave/sub-6 GHz 5G Networks," *IEEE Commun. Mag.*, vol. 55, no. 6, pp. 94–101, 2017.

VII. Biographies

Mourice O. Ojijo is a PhD. student at the department of electrical engineering, University of Cape Town. He is also a student member IEEE.

Dismas O. Ombuya is a PhD. student at Jaramogi Oginga Odinga University of Science and Technology. School of Informatics and Innovative Systems (SIIS) and a lecturer at Kabarak University. He is also a student member IEEE

A Spectrum Management Strategy for Visible Light Communications Using an Adaptive Threshold Approach

Stephen S. Oyewobi[1], Karim Djouani [1, 2], Anish Mathew Kurien [1].*

[1]F'SATI/Tshwane University of Technology, Pretoria 0001, South Africa,

[2]University Paris-Est Creteil (UPEC)/LSSI Lab Creteil, France.

**Correspondence: oyewobistephen@gmail.com; Tel.: +2773 925 9362*

Abstract— **The accessibility of network resources is the primary criteria used to perform handover in existing handover strategies in communication systems. Moreover, the access technique approach implemented in visible light communications (VLC) which utilizes the availability of the channel as the sole criteria for handover instead of the capacity of the channel to support QoE of nodes leads to frequent handovers and poor QoE performance. In this work, the use of adaptive threshold-fixing is proposed to dynamically fix the trigger threshold for handover to match the minimum QoE constraints of the VLC node. Therefore, a node will remain in its current channel as long as the minimum QoE requirements are supported by the present channel. Hence, nodes will only handover if the current channel does not support the least QoE constraints of specific node applications and new channels with better QoE are available. To achieve this, the proposed algorithm dynamically adjusts the handover triggering threshold based on link information extracted from channel at discrete time to meet the minimum QoE constraints of node applications instead of switching to a new available channel. The proposed alogorithm is implemented using Monte Carlo simulations of different VLC scenarios and is compared with a reactive spectrum handoff strategy. Simulations results of the proposed strategies demonstrate a significant reduction of spectrum handoffs while maintaining better throughput for node applications.**

Keywords*— *adaptive spectrum handoff, visible light communication, cognitive radio, channel condition, dynamic spectrum access.

I. INTRODUCTION

Spectrum mobility (SM) is an aspect of communication systems which allows nodes equipped with software defined radio (SDR) or cognitive radio (CR) capabilities to make opportunistic use of unoccupied portions of licensed frequency spectrum of the primary users (PU) for their communication [1]. However, this opportunistic usage is on a condition that their communication does not cause harmful interference to the activity of the high priority PU. Therefore, by implementing a process known as spectrum handoff (SH) a SDR node or CR user must immediately vacate a channel it is opportunistically using whenever a PU arrives on the channel. As a result, the arrival of a PU and/or availability of new channels are the triggers for SH in cognitive radio networks (CRNs). So, typically a CR user or SDR node that is on an on-going communication is interrupted until it can establish a new link to complete its transmission. However, unlike CRNs, in VLC, this approach will introduce long delays which is contrary to the high speed and high data rates of VLC networks. Also, unlike CRNs, channel attenuation due to massive multipath fading and shadowing effects from large metallic obstacles instead of PU arrival in VLCs can be responsible for a large percentage of spectrum mobility [2]. Therefore, to eliminate long delays due to frequent and sometimes unnecessary handovers a coherent decision to linger in the current channel by adapting to channel conditions as long as the minimum QoE requirements of node applications are met to prevent frequent and unnecessary SHs is incorporated into a new proposed algorithm which is the main contribution of this paper. The tradeoffs on the choice to linger in the channel is calculated using a cost function which weighs the level of signal attenuation due to channel behavior to QoE constraints of node applications. As a result, the channel behavior is observed during node communication at discrete time. Based on this information, the proposed algorithm implements link adaptation by adaptively fixing the threshold to meet the minimum acceptable throughputs. SM is a resource management technique that allows network resources to be utilized effectively. The rest of the paper is organized as follows. In Section II, related work is discussed; this is followed by the system model in Section III; Section IV provides details on the proposed scheme. In Sections V, simulation results are presented and discussed. In Section VI future work is identified with conclusions provided.

II. RELATED WORKS

In this Section, an overview of related contributions on the application of VLC for IoT and other applications in literature is provided. While a number of papers have discussed the application of VLC for diverse wireless technologies only a few have highlighted VLC for IoT applications. In [3], the fundamentals and challenges of indoor VLC systems was investigated. Additionally, the authors identified the characteristics of channel models in indoor VLC as well as presented the theoretical details of channel modelling. In [4], the authors propose a VLC system design for IoT by integrating VLC in the dark and OFDM to overcome the limitations of traditional VLC for data transmission. In a similar contribution [5], VLC-over-UART systems is proposed, and bit error rate analysis was used to evaluate the performance of the proposed system. In another contribution [6], an overview on the potential of LiFi in transforming indoor lighting into the backbone of wireless communications was carried out. In [7], the concept of VLC was introduced and the application of VLC as well as some of the challenges facing VLC are discussed. In [8], the authors discussed the approach for resource allocation in hybrid cognitive VLC. Similarly, different mobility management schemes and resource allocations strategies are developed in [9]. However, none of the reviewed journals considers resource management using an

adaptive threshold-fixing approach and channel quality as a factor for resource management.

III. SYSTEM MODEL

In this Section, the system model model considered is presented.

A. System model and Assumptions

In this study, a cluster-based VLC network based on the IEEE 802.15.7 standard is assumed with each cluster having a VLC gateway as its cluster-head evenly distributed in the network. As illustrated in Figure 1, each cluster has partially overlapping coverage areas consisting of both PUs and VLC nodes equipped with SDR existing side-by-side. The VLC nodes have capabilities to perform SH due to the equipped SDR. It is assumed that the PUs communicate with each other using N channels licensed bands through a synchronous slot structure. It is considered that each channel has a bandwidth $B_i(i.e., i = 1,2, \dots \dots \dots, N)$ and that the network state is designated by time slot *t*, such that [10]:

.

$$t = [S_1(t), \dots \dots S_N(t)], \tag{1}$$

where $S_i(t) \in \{0(unoccupied), 1(occupied)\}$.It is assumed that the VLC nodes use VLC communications for downlink and RF communication for uplink by opportunistic transmission in the licensed band of the PUs through overlay transmission. It is considered that channel capacity is characterized by signal-to-interference-plus-noise ratio (SINR) at the receiver of N VLC nodes as depicted in (2) [11]

$$SINR_i = \frac{h_{ii}(t)x_i(t)}{\sum_{j\in\{N/i\}} h_{ji}(t)x_j(t)+n_i(t)} \tag{2}$$

where $x_j(t)$ represents the signal transmitted from a VLC node j, $h_{ji}(t)$ is the channel gain of transmission when VLC node i is transmitting. It is assumed that $h_{ji}(t)$ is stochastic due to channel attenuation, multipath fading, and shadowing effects which are indicative of the VLC wireless environment, $n_i(t)$ represents noise at VLC node i. Therefore, the received signal at any VLC nodes is denoted by $y_i(t)$ in (3):

$$y_i(t) = \sum_j h_{ij}(t)x_j(t) + n_i(t) \tag{3}$$

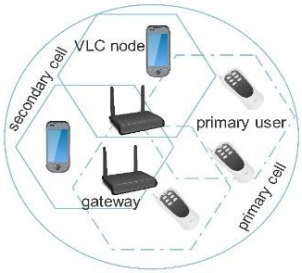

Figure 1. Proposed Network Model.

The VLC gateways are also equipped with SDR with exclusive functions which includes (1) keeping statistical history of PU's communication pattern; (2) performing spectrum sensing to update the network database of channel availability; (3) ranking the available channel base on SINR level; (4) supplying communicating pair of VLC nodes with an updated available channel list; and (5) acquiring information about the quality of the communication link using the received signal strength indicator (RSSI).

IV. PROPOSED ADAPTIVE SPECTRUM HANDOFF PROTOCOL WITH TARGET CHANNEL SELECTION SCHEME.

In this work, two major criteria are used as trigger for the handover technique. These include (1) the presence or absence of a PU signal on the channel being opportunistically used by a VLC node; and (2) current channel quality of a VLC. That is if the channel quality of a VLC node link can support the minimum QoE requirements of the node application or not.

A. Presence or absence of PU signal on target channel

In the case of presence or absence of PU signal on the channel being deployed opportunistically by a VLC node, a clear channel assessment approach with energy detection and carrier sensing approach is adopted. This approach is similar to the one used in IEEE 802.11 [12] where a PU signal is detected when a CR node senses an energy level above a pre-defined threshold. In the design proposed in this study, in order to trigger an SH process, a VLC node must listen to the gateway broadcast for the current updated target channel list. Based on this information, and in addition to the SINR of available channels, a pair of communicating VLC nodes rendezvous to acknowledge the new channel on which to continue on-going CR communication. The gateway continuously updates the backup channel list by periodically performing spectrum sensing for presence or absence of PU signal on the licensed bands. In (4) and (5), it is illustrated how this approach is implemented.

.

$$H_0: y_i(t) = n_i(t) \tag{4}$$

$$H_1 : y_i(t) = h_{ij}(t)x_j(t) + n_i(t), \tag{5}$$

where $y_i(t)$ is the received signal of the VLC node, $x_j(t)$ is the signal transmitted from PU transmitter, $n_i(t)$ is the noise at VLC node i, and $h_{ij}(t)$ is the fading channel co-efficient. H_0 signifies the absence of a PU signal, while H_1 denotes the presence of the PU signal. Nevertheless, after the condition H_0 above is tested to be true for each free channel, the gateway still deploys *closed-loop power control* [13] to rank each identified unoccupied channel based on the SINR level in the bandwidth of the channel. Therefore, VLC nodes by anticipating continuous SH task listen for the updated list from the gateway and select the available channel based on channel availability as well as channel quality.

B. Channel capacity of VLC nodes current channel

The capacity of the current channel to support the minimum level of QoE requirements of node applications is the other criterion used to trigger SH in this work. Therefore, SH is executed if channel quality in the current channel falls below the predefined QoS threshold for certain VLC applications. The details of how channel attenuation affects the capacity of

the channel and how conditions of the channel state are adapted to meet the QoE requirements are implemented is discussed below.

1) Channel model to characterize signal attenuation in the VLC node current channel.

In this work, the behavior of the current channel is characterized by the state of the channel in discrete time. Assume that the channel switches between three states characterized by the following models:

- Regime 1: A *log-normal shadowing model* describing large-scale fading due to large metallic objects.
- Regime 2: A *Rice distribution* representing temporal variations due to rapid changes in multipath profile of the current channel.
- Regime 3: A *Rayleigh distribution* representing channel fading profile of the current channel when the *K* factor of the Rice distribution is zero.

The transition matrix **P** represents the VLC link with each element P_{ij} of the matrix denoting the probability of transition from state *i* to *j* such that

$$\boldsymbol{P} = \begin{bmatrix} P_{AA} & P_{AB} & P_{AC} \\ P_{BA} & P_{BB} & P_{BC} \\ P_{CA} & P_{CB} & P_{CC} \end{bmatrix} \quad (6)$$

where the stationary state vector π is determined by using Markov processes which is represented by (7), (8) and (9) as

$$\pi = (\mathbf{I} - \mathbf{P}) = 0 \quad (7)$$

$$\pi e = 1 \quad (8)$$

$$e = [1\ \ 1 \ldots]^{\mathrm{T}} \quad (9)$$

where **I** is an identity matrix, and **P** is the transition matrix. Therefore, the stationary vector is

$$\pi = (\pi_A, \pi_B, \pi_C) \quad (10)$$

with each element of π_i signifying the fraction of the total time the channel remains in state i. The probability density function of the signal in this state is subject to a Rayleigh distribution such that

$$f_x(x) = \frac{x}{\sigma^2} . exp\left[-\frac{x^2}{2\sigma^2}\right] \quad (11)$$

in which the *N* order origin moment of the envelope of the received signal is described in (12) as

$$E[x^n] = n\sigma^2\, E[x^{n-2}], n \geq 2 \quad (12)$$

Similarly, if it is considered that the envelope of the received signal in channel state i consists of both LOS and multipath signals, then the probability density function of the signal is subject to a Rican distribution in which

$$f_r(r) = \frac{r}{\sigma^2} . exp\left[-\frac{r^2+z^2}{2\sigma^2}\right] I_0\left(\frac{rz}{\sigma^2}\right), \quad (13)$$

where the *N* order origin moment of the envelope of the received signal is represented in (14) as

$$E(r^n) = (2\sigma^2)^{\frac{n}{2}} . exp(-K) . \Gamma\left(1+\frac{n}{2}\right) . F(1 + \frac{n}{2}, 1, k) \quad (14)$$

Finally, assuming the envelope of the received signal in channel state i consists of only heavily shadowed signals, then its probability density function is subject to a Lognormal distribution as represented in (15)

$$f_z(z) = \frac{1}{z\sqrt{2\pi d_0}} exp[-\frac{[ln(z)-\mu]^2}{2d_0}] \quad (15)$$

such that the *N* order origin moment of the envelope of the signal is given in (16) as

$$E[z^n] = \exp[n\mu + \frac{n^2}{2}\sigma^2], \quad (16)$$

where the amplitude of the multipath signal is represented by *x*, the amplitude of LOS signal as *r*, amplitude of shadow signal is represented by *z*, and σ^2 represents the average multipath power, *k* is the Rican factor, while Γ(.) is the Gamma function, *F*(.) is flow and hypergeometric function, μ and d_0 are mean and variance of $ln(z)$ respectively. Therefore, the semi-Markov channel model can be represented by a new transition matrix *Y*, where

$$Y_{ij=} \quad \frac{P_{ij}}{1-P_{ii}} \quad for\ y \neq j\ and\ y_{ii} = 0 \quad (17)$$

Figure 2 shows the Markov diagram of the channel model.

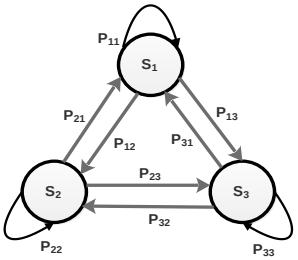

Figure 2. VLC channel model.

The behavior of the model described in Figure 2 is a discrete-time stochastic process such that the conditional probability that VLC signal will experience a poor QoE performance at discrete time instant X_t for $t = 0,1,2, \ldots . N$ and for all states i is

$$P(X_{t+1} = i_{t+1} | X_t = i_t, X_{t-1} = i_{t-1}, \ldots . X_1 = i_1, X_0 = i_0) = P(X_{t+1} = i_{t+1} | X_t = i_t) \ , \quad (18)$$

where the probability distribution of the state at time $t+1$ depends exclusively on the state at time t, and not on the state prior to time t. Therefore, the probability that channel will be in state j at time $t+1$, given that at time t it is in state i, is

$$P(X_{t+1} = j|X_t = i,) = P(X_t = j|X_{t-1} = i) = \cdots = P(X_1 = j|X_0 = i) = P_{ij} \quad (19)$$

From (19), the signal attenuation due to channel behavior can be observed at discrete instants in time. Based on this observation, the scheme (implemented on the SDR equipped VLC node) adaptively fixes the threshold to still match the minimum QoE constraints of VLC application to guarantee connectivity in the prevailing channel conditions. Until new channels with better SINR are available the VLC node lingers in the current channel.

2) Conditions for fixing threshold to adapt to channel condition for minimum QoE performance

In real VLC environments, channel conditions are extremely time-variant due to environmental influences and heterogeneous networks operating on the same frequency and may require fast adaptation rate. Therefore, it is important for the SH algorithm to adapt fast enough to variations in radio environments to benefit from an adaptation process before subsequent changes in the radio environment makes another adaptation necessary [14]. There is a tradeoff between tolerating low packet rate when lingering on the channel by fixing threshold and reducing communication delay when switching to a new channel. Therefore, the balance is determined by a cost function in (20) denoted by C_A [15] which is used to estimate the impact of channel attenuation on the QoE requirement of VLC applications. The gateway acquires several values of the RSSI for the VLC environment from its transceiver to estimate C_A. For periods with poor packet reception rate C_A is estimated as follows.

$$C_A = 1 - \frac{\sum_{i=0}^{i<n} Q_i}{n} \quad , \quad (20)$$

where Q_i is equal to 0 or 1 depending on the value of τ, as indicated by (21) in which

$$Q_i = \begin{cases} 0 & if\ R_i < \tau \\ 1 & if\ R_i \geq \tau \end{cases} \quad , \quad 21$$

where τ, is a threshold which is adaptively fixed by the algorithm depending on the impact of signal attenuation on the amplitude of the signal in the channel state i, n is number of signal samples used to calculate Q_i, and R_i is RSSI from the i^{th} signal sample in the channel state i.

3) Decision-making

The SH decision making is a major and fundamental step in every SH procedure. It plays a vital role in realizing users' needs, coordinating network resources and their application and making best usage of network performance [16]. Every SH scheme is different by the nature of trigger in the handoff algorithm that enables the activation of SH decision procedure. To have a robust SH procedure/technique, it better to combine one or more criteria for the handoff decision-making process. In this work, *the capacity of the link to support minimum QoE constraints of nodes applications in the current channel* and *presence or absence of PU signal on the target channel* are the two criteria used in decision-making for SH procedure. Firstly, the algorithm must establish if channel quality in channel states i supports QoE constraints of VLC nodes or not. The hypothesis is tested as presented in (22):

$$\begin{cases} H_3 & if\ C_A < 0 \\ H_4 & if\ C_A = 1 \end{cases}, \quad 22$$

Hypothesis H_3 means that the quality of a link in channel state does not support VLC node QoE requirements and VLC nodes should perform SH. On the other hand, hypothesis H_4 implies that the quality of a link in channel state does support VLC node QoE requirements and VLC nodes should continue with on-going transmission. The critical decision to determine if a transmitting pair of VLC nodes should continue on-going communication in a new channel or remain on current channel is taking by testing for all conditions in (23) as well as (4) and (5) in (23).

$$\begin{cases} H_3 & if C_A < 0, \\ H_4 & if\ C_A = 1, \\ H_0\ if\ y_i(t) = n_i(t), & \\ \quad and, & \\ H_1\ if\ y_i(t) = h_{ij}(t)x_j(t) + n_i(t) & \end{cases} \quad (23)$$

V. Simulation Results and Discussion

A. Simulation set-up

In this work, the performance of the proposed algorithm is investigated by extensive MATLAB simulations. The simulation setup is presented in Table 1.

TABLE 1. SIMULATION SETUP

Parameter	Value
Unlicensed band	
Frequency	2.4GHz ISM band
Transceiver	CC2420
Number of active nodes (ns)	20
Bandwidth	50KHz
Number of channel (nc)	nc=(ns*(ns-1)/2)
Packet rate	Poisson distribution
SINR	5dB
Licensed band	
Frequency	470-890MHz
Number of channel	5-20
Packet rate	Poisson distribution
SINR	1-15dB

B. Simulation Result

In this section, the simulation results to validate the proposed algorithm are presented. The performance of proposed algorithm is evaluated by comparing it with conventional reactive SH model with sequential spectrum sensing (RSHSS). Again, the number of SHs and throughput, which are very significant performance metrics are used to validate the performance of the proposed algorithm. In this paper, the number of SHs is the total number of SHs from the start of simulation which represents the start of transmission, to the end of simulation which signifies the end of the VLC transmission. During this period, several interruptions may occur due to low SINR and/or arrival of PU on the channels. Similarly, throughput represents data rates of VLC node during

entire transmissions which includes periods between data buffering and channel switching during period of SHs. Figure 5a shows the throughput performance of the proposed algorithm and RSHSS while Figure 5b shows the throughput performance under different bandwidths for the proposed algorithm and RSHSS. Based on the number of simulations, each simulation point on the x-axis represents 5000 Monte Carlo simulations.

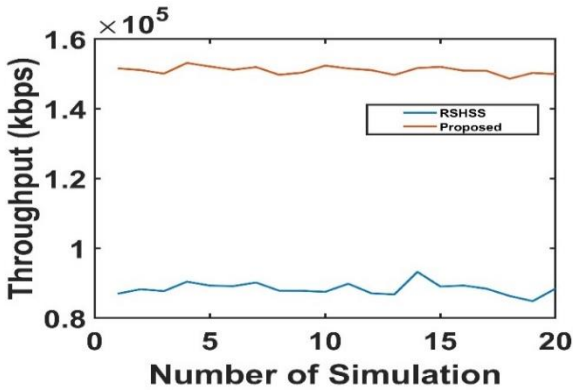

Figure 5a. Throughput performance.

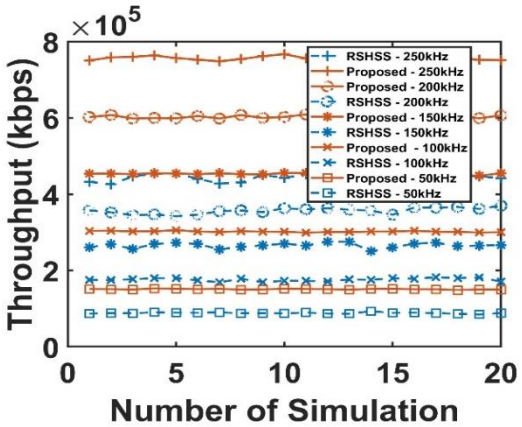

Figure 5b. Throughput performance in sub-channel bandwidth.

As shown in Figure 5a it is seen that the proposed algorithm outperforms RSHSS in terms of higher throughput. Similarly, throughput performance under varying bandwidth in Figure 5b shows related trends of higher throughput performance similar to Figure 5a. For instance, deploying the proposed algorithm at sub-channel bandwidth of 150KHz, VLC nodes achieved an average throughput performance of 450Kbps while using RSHSS at the same channel bandwidth gives 270Kbps average throughput performance. There is a 40% improvement in throughput performance which is attributed to the fact that the channel condition is adapted using adaptive threshold fixing prior to performing SH to a new channel with a better SINR in the proposed algorithm. In RSHSS, SH is initiated the instant SINR is low in the current channel, and data is buffered while waiting to join a new channel.

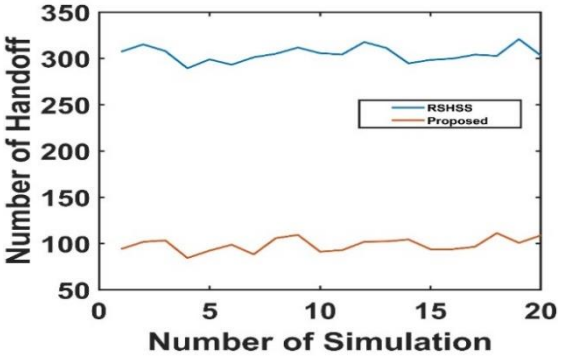

Figure 6a. Number spectrum handoffs.

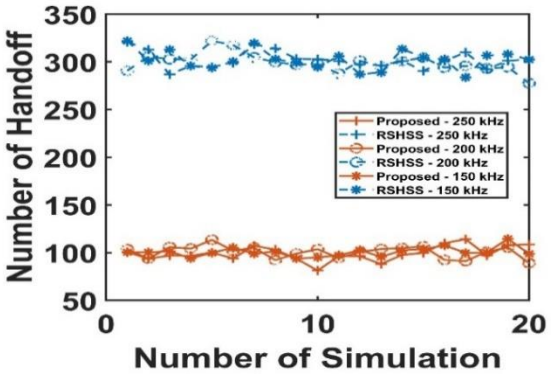

Figure 6b. Number of spectrum handoffs in sub-channel bandwidth.

Figure 6a shows the number of SHs for the proposed algorithm and RSHSS. Meanwhile, Figure 6b compares the number of SHs for different values of sub-channel bandwidth for both RSHSS and the proposed algorithm. In Figure 6a, it is seen that for the duration of the entire transmission, the proposed algorithm maintained an average of 130 SHs while RSHSS returned an average of 320 SHs. Therefore, the proposed algorithm reduced the number of SHs by 190 SHs which represents a 59% reduction in the proposed approach. The reason for this reduction is due to the fact that RSHSS operates sequential spectrum sensing for a target channel while in the proposed algorithm in this study, the VLC nodes listen and select the channel with the best SINR from updated target channel list supplied by the gateway.

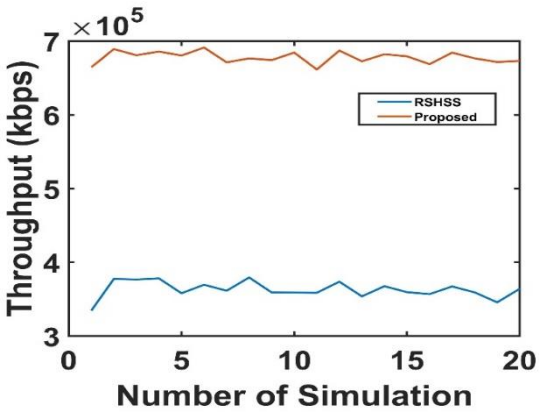

Figure 7a. Throughput performance.

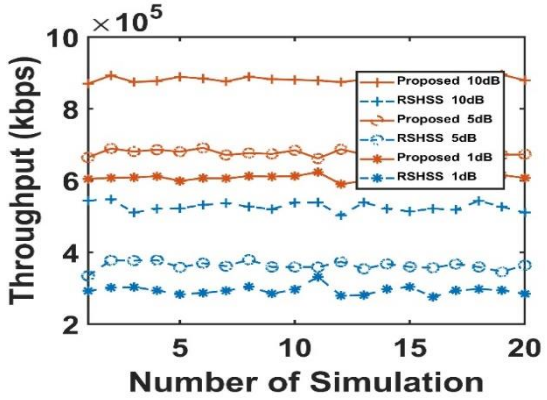

Figure 7b. Throughput performance in terms of SINR.

Figure 7a. shows the throughput performance for RSHSS and the proposed algorithm at SINR of 5dB in the unlicensed band. Figure 7b shows the throughput performance of the proposed algorithm at 1dB as well as 10dB which is compared with throughput performance of RSHSS under the same conditions. It can be noticed that in Figure 7a, the proposed algorithm performs better than RSHSS in terms of higher throughput. In Figure 7b, it can be seen that both approaches performed poorly in very bad channel conditions particularly at 1dB SINR. However, the proposed algorithm performed better than RSHSS.

VI. Future Work and Conclusion

VLC is a promising and emerging technology that has the potential of solving the challenges of wireless communication technology. However, there are still challenges in using light waves for uplink data communication in VLC networks. This is due to the expected high intensity and glare of the light wave from the source node, e.g. the screen of the smartphone. In this paper, a SH scheme that adapts to the link condition by observing the behavior of the link and dynamically fixes a threshold for SH to match the minimum QoE of VLC node has been developed. Based on the results presented, it is shown that the developed SH scheme outperforms conventional SH strategy in terms of throughput performance and number SHs. This work also serves a basis for future research direction. Therefore, in the future, work will be conducted on a hybrid VLC system which deploys light wave for downlink and LoRa for the uplink to increase the speed of data transmission and to improve performance of the VLC network.

.

Acknowledgment

This research was funded in part by the National Research Foundation of South Africa (Grant Number: 90604). Opinions, findings, and conclusions or recommendations expressed in any publication generated by the NRF supported research are those of the author(s) alone, and the NRF accepts no liability whatsoever in this regard. The authors would like to also thank the Telkom Centre of Excellence (CoE) for their support.

.

References

[1] S. S. Oyewobi and G. P. Hancke, "A survey of cognitive radio handoff schemes, challenges and issues for industrial wireless sensor networks (CR-IWSN)," *Journal of Network and Computer Applications*, vol. 97, no. Supplement C, pp. 140-156, 2017/11/01/ 2017.

[2] S. S. Oyewobi, K. Djouani, and A. M. Kurien, "A review of industrial wireless communications, challenges, and solutions: A cognitive radio approach," *Transactions on Emerging Telecommunications Technologies*, p. e4055, 2020.

[3] T. Cevik and S. Yilmaz, "An overview of visible light communication systems," *arXiv preprint arXiv:1512.03568*, 2015.

[4] K. Kadam and M. R. Dhage, "Visible light communication for IoT," in *2016 2nd International Conference on Applied and Theoretical Computing and Communication Technology (iCATccT)*, 2016, pp. 275-278: IEEE.

[5] C.-W. Chen *et al.*, "Visible light communications for the implementation of internet-of-things," *Optical Engineering*, vol. 55, no. 6, p. 060501, 2016.

[6] C. Jurczak, "LiFi: enlightening communications," *arXiv: 1802.01471 v2, physics. app. ph*, 2018.

[7] S. N. Ismail and M. H. Salih, "A review of visible light communication (VLC) technology," in *AIP Conference Proceedings*, 2020, vol. 2213, no. 1, p. 020289: AIP Publishing LLC.

[8] K. Danesh, S. Vasuhi, and R. Varshney, "Resource Allocation Approach for Hybrid Cognitive Visible Light Communication," in *2021 5th International Conference on Trends in Electronics and Informatics (ICOEI)*, 2021, pp. 891-898: IEEE.

[9] M. S. Demir, "mobility management and resource allocation strategies for visible light communication networks," Ozyegin University, 2021.

[10] M. P. Tran, T. P. T. Minh, L. Hea-Min, and D. S. Kim, "Effective spectrum handoff for cognitive UWB industrial networks," in *2015 IEEE 20th Conference on Emerging Technologies & Factory Automation (ETFA)*, 2015, pp. 1-4.

[11] A. M. Wyglinski, M. Nekovee, and Y. T. Hou, "Cognitive radio communications and networks," *IEEE Communications Magazine*, vol. 46, no. 4, pp. 209, 2008.

[12] T. M. Chiwewe and G. P. Hancke, "Cognitiva — A cognitive industrial wireless network protocol: Protocol design and testbed implementation," in *2016 IEEE International Conference on Industrial Technology (ICIT)*, 2016, pp. 2042-2047.

[13] N. Son Duc, P. Tung-Linh, and D. S. Kim, "Dynamic spectrum handoff for industrial cognitive wireless sensor networks," in *2013 11th IEEE International Conference on Industrial Informatics (INDIN)*, 2013, pp. 92-97.

[14] Y. Zhang, J. Zheng, and H.-H. Chen, *Cognitive radio networks: architectures, protocols, and standards*. CRC press, 2016.

[15] R. D. Gomes, D. V. Queiroz, A. C. Lima Filho, I. E. Fonseca, and M. S. Alencar, "Real-time link quality estimation for industrial wireless sensor networks using dedicated nodes," *Ad Hoc Networks*, vol. 59, pp. 116-133, 2017.

[16] A. Ahmed, L. M. Boulahia, and D. Gaiti, "Enabling vertical handover decisions in heterogeneous wireless networks: A state-of-the-art and a classification," *IEEE Communications Surveys & Tutorials*, vol. 16, no. 2, pp. 776-811, 2014.

Stephen S. Oyewobi is currently undertaking a research fellowship at FSATI/Tshwane University of Technology, Pretoria, South Africa. His research interest including, Advanced sensor Networks, Internet of Things, Energy Managements, Congestion control in network nodes, and Industrial Wireless Sensors Networks.

Karim Djouani (M'87).is a Full Professor, a Scientist, and a Technical Group Supervisor of pattern recognition, soft computing, networking systems, and robotics. Since January 2014, he has been the DST/NRF SARChI Chair in Enabled Environment for Assistive Living. He is a Full Professor at French South African Institute of Technology (F'SATI), Tshwane University of Technology, Pretoria, South Africa. His research interests include development of novel and highly efficient algorithms for reasoning systems with uncertainty as well as optimization, for distributed systems.

Anish M. Kurien (M'04) received the D.Tech. degree in electrical engineering from the Tshwane University of Technology (TUT), Pretoria, South Africa, and the Ph.D. degree in computing (through co-tutelle) from the University ParisEst, Champs-Sur-Marne, France, in 2012. He is currently the Node Director of the French South African Institute of Technology, TUT, development. His research interests include feature extraction and pattern recognition algorithms applied to mobile network subscriber classification.

Exploring CNN-Based Automatic Modulation Classification Using Small Modulation Sets

Andrew Oosthuizen*†, Marelie H. Davel*†, Albert Helberg*
*School of Electrical, Electronic and Computer Engineering, North-West University
†Centre for AI Research (CAIR), South Africa
aj.oosthuizen.ao@gmail.com
marelie.davel@nwu.ac.za
albert.helberg@nwu.ac.za

***Abstract*—We investigate the effect of a reduced modulation scheme pool on a CNN-based automatic modulation classifier. Similar classifiers in literature are typically used to classify sets of five or more different modulation types [1] [2], whereas our analysis is of a CNN classifier that classifies between two modulation types, 16-QAM and 8-PSK, only. While implementing the network, we observe that the network's classification accuracy improves for lower SNR instead of reducing as expected. This analysis exposes characteristics of such classifiers that can be used to improve CNN classifiers on larger sets of modulation types. We show that presenting the SNR data as an extra data point to the network can significantly increase classification accuracy.**

***Index Terms*—Automatic Modulation Classification, In-phase and Quadrature-phase (I/Q) symbols, Deep learning**

I. Introduction

In this paper we investigate a deep learning based approach to automatic modulation classification (AMC). AMC is used in the telecommunications field to identify transmission modulation schemes without this information being explicitly communicated between transmitters and receivers. AMC reduces overhead in communication and allows for effective switching between modulation schemes in cognitive radio applications. In the past, AMC has been implemented with statistical [3] and machine learning methods, such as clustering [4] and support vector machines [5]. In recent years deep learning architectures such as multilayer perceptrons (MLPs) and convolutional neural networks (CNNs) have been applied to the problem and have shown better performance over the more traditional approaches with regard to both accuracy and speed [6].

This paper investigates classification behaviour of deep neural networks on modulation types under additive white Gaussian noise (AWGN), by classifying between two modulation schemes, both varying in type and order. By using a reduced modulation pool for classification, we are able to better understand how a CNN interacts with an AMC task.

II. Related work

There exist several methods to approach AMC using deep learning models [7]. Most approaches supply some constellation data obtained from raw signal data to a neural network. How the constellation data is presented to the neural network does, however, vary depending on the method. Popular methods include presenting the quadrature and in-phase data points of constellation diagrams in a $2 \times N$ array, where N is the number of data points [2], or presenting the constellation plots as images [8]. The last method often contains several stages of feature extraction and pre-processing before the data is presented to the network.

CNNs are typically used for AMC problems [7] and function by presenting the input data to convolutional layers. The convolutional layers extract features from the data by making use of filters, also known as kernels. After feature extraction, the convolutional layers are flattened and passed to dense layers that make use of the previously extracted features to perform classification [9], [10].

For our study we use a CNN structure, similar to the network used by Yongshi et al. [2], that receives constellation data points rather than images as inputs. The reason for this is to simplify the investigation of the neural network, since pre-processing and presentation of image data to CNNs add extra levels of analysis to the process. We make use of 16th order quadrature amplitude modulation (16-QAM) and 8th order phase-shift keying (8-PSK) modulation schemes as input, as both the order and method of modulation differ between the two.

III. Experimental setup

A. Data

The data is presented as complex values of the signal constellation in the I/Q plane generated using Matlab version 2020b. A random bit stream source is modulated in baseband using one of two modulation types (8-PSK or 16-QAM). The modulated data is sent over an additive white Gaussian noise (AWGN) channel with varying normalised signal-to-noise (SNR) ratios (E_b/N_o) with an average signal power of 1W over 1Ω. The complex valued channel symbols are then grouped into samples containing 1024 constellation points of each symbol's in-phase and quadrature component. Thus, each sample consists of 1024 32-bit real and 1024 32-bit imaginary data points to create a 2×1024 sized data set.

The SNR, E_b/N_o, is discretely stepped over the range of -15 dB to 5 dB in 1 dB increments to create training, validation

and evaluation sets respectively. The number of generated data samples per E_b/N_o is listed in Table I.

TABLE I
NUMBER OF DATA SAMPLES GENERATED PER E_B/N_O OF A MODULATION SCHEME, AS WELL AS THE TOTAL SET SIZE OVER 21 SNR RANGE.

Modulation	Train	Validation	Test
8-PSK	1 000	500	1 000
16-QAM	1 000	500	1 000
Total set size	42 000	21 000	42 000

The training and validation sets are used in the training process as described below, while the evaluation sets are kept separate to evaluate the performance per E_b/N_o level.

B. Baseline architecture

The classifier architecture is based on that of Yongshi et al. [2], but with fewer nodes in the hidden dense layer. The hidden dense layer is reduced to 100 nodes, as the number of modulation types to classify has been reduced. This change is made to improve the training time and throughput of the network. The network consists of two convolutional layers that are ReLu-activated [11], makes use of batch normalisation, has no padding and a stride of 1. A max pooling layer, with a stride of 2, is placed between the convolutional layers to reduce the complexity of the network. After the convolutional layers a linear layer with 100 nodes is placed, followed by the classification layer (also a linear layer) with 2 outputs [2].

C. Training protocol

The same training protocol is followed for all networks. Networks are trained with the Adam [12] optimiser using a cross-entropy loss function. Adam is selected for its ability to adapt the learning rate of different parameters, and cross-entropy loss is used for its good performance in classification problems [9], [10]. Since ReLU activation functions are used, the weights of the network are initialised using a uniform Kaiming initialisation [13].

The following hyperparameters are optimised: learning rate, batch size, and weight decay (L2 penalty). We selected these hyperparameters, as preliminary tests showed that they have noticeable effects on the model's performance. Hyperparameter tuning is performed using grid searches on the predefined CNN architecture, by comparing the networks' results on the validation data set. The grid search is performed over different learning rates $\{0.01, 0.001, 0.0001\}$, batch sizes $\{32, 512\}$, weight decay values $\{0, 0.001, 0.01\}$ and 3 random initialisation seeds. The initialisation seeds are used to ensure a particularly strong or weak network initialisation does not affect the results. We also make use of a grid search over the architecture by varying the convolution kernel width $\{4, 16, 32, 64\}$ and amount of dropout $\{0, 0.5\}$ hyperparameters [14].

To ensure the network trains until it convergences, the network is trained for a minimum of 50 epochs, after which the training is terminated when no improvements in validation accuracy is found in the last 20% of epochs. Early stopping is then implemented by selecting the epoch at which the model achieved its highest classification accuracy on the validation set.

IV. Analysis and Results

A. Classification performance

The goal of this experiment is to analyse the behaviour of a CNN classifier on two modulation schemes of different types and orders that exposes fundamental characteristic when using a data point driven constellation diagram input.

From the classification accuracy and average class recall of the baseline architecture network in Figure 1, we can see that the model classifies well for SNRs above 0 dB. At lower SNRs the accuracy decreases as the signal falls below the noise floor. We also see an increase in accuracy when the number of kernels is increased to 36 kernels. Varying other hyperparameters revealed that adding dropout and using a weight decay value of 0.01 also increases accuracy and that the model generalises better on the validation set. The final hyperparameters for the baseline architecture can be found in Table II.

TABLE II
HYPERPARAMETERS OPTIMISED FOR THE BASELINE ARCHITECTURE.

Parameter	Value
Learning rate	0.0001
Batch size	32
Dropout	0.5
Weight decay	0.01
Kernel width	36

An interesting observation to make from Figure 1 is the unexpected improvement of the declining 8-PSK classification accuracy at very low SNR. The 16-QAM classification also increases slightly, but not as much as 8-PSK. This observation is strange, as we usually expect modulation classifiers to show reduced classification ability as noise increases until a reliable classification can no longer be made and the network shows 50% classification accuracy.

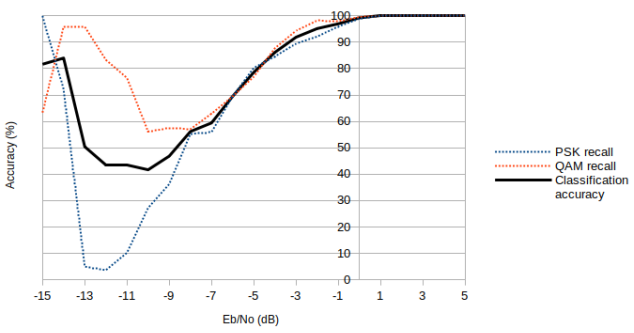

Fig. 1. Average classification accuracy (over 3 seeds) of the baseline architecture using optimised hyperparameters, for the evaluation data set with range of -15 dB to 5 dB. The average recall of 16-QAM and 8-PSK, respectively, is also shown.

B. Analysis of low SNR artefact

In order to find out why this increase in accuracy at lower E_b/N_o exists, we investigate whether this effect is due to the boundaries of the range of SNRs evaluated. Using the same training hyperparameters, the network was retrained for two ranges of the SNR, namely [-20;0] and [-10;10]. This investigation is also used to establish if the improvement in accuracy is tied to certain SNRs, or to a E_b/N_o position in the range. In addition, we investigate the effect of architectural changes to the neural network to ensure the artefact is not caused by lack of representational ability. The neural network will be adapted in the following ways:

- Increasing the dense layer node count from 100 to 1 000
- Changing the convolution layer kernels from 36 to 512
- Adding an extra convolution layer

To ensure well-defined results, each one of these changes is applied independently from the other.

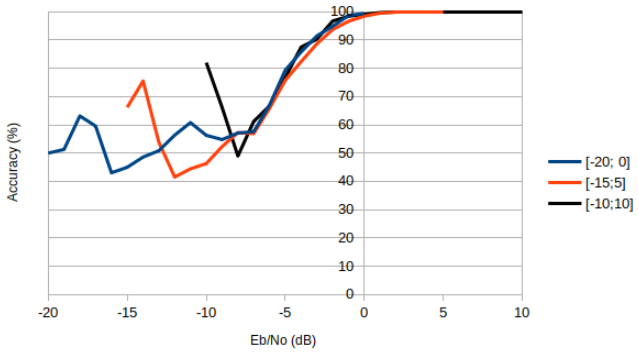

Fig. 2. Baseline network evaluation set performance when the network is trained on -20 dB to 0 dB, -15 dB to 5 dB and -10 dB to 10 dB SNR ranges, respectively.

When using the same baseline architecture as before but changing the E_b/N_o range, Figure 2 shows a similar trend to that observed before. Figure 2 indicates that the increase in accuracy occurs at lower E_b/N_o values, irrespective of the input data range. However, it is observed that the accuracy increase does not appear at a specific E_b/N_o. It should be noted that accuracy fluctuations only appear after the 0 dB accuracy descent and results near and above the noise floor increase gradually as expected.

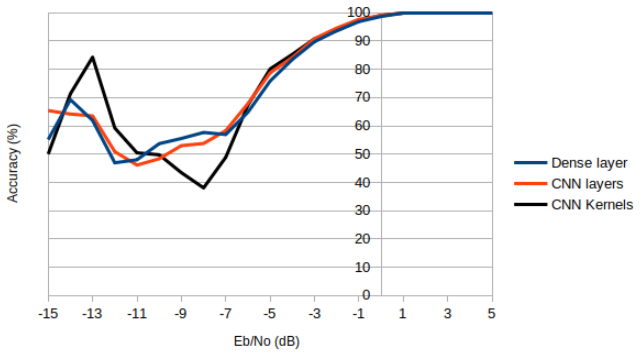

Fig. 3. Evaluation set performances when the dense layer of the baseline network is increased to 1 000 nodes ('Dense layer'), the baseline network's convolutional layers are increased from 2 to 3 ('CNN layers') and the baseline network's convolution kernels are increased to 512 ('CNN kernels').

When increasing the size and complexity of the network, Figure 3 shows a similar trend to that observed in the baseline architecture, except for variations in the average validation accuracy. Some of the methods change the shape and intensity of the accuracy increase in the E_b/N_o range, but all still exhibit the same artefact.

C. SNR-specific training

When observing Figure 1, we note that the increase in accuracy at lower E_b/N_o resembles models trained with SNR pairs selection [15]. With pairs selection, the network is only trained using two E_b/N_o data sets, instead of the entire range. In some instances this may cause an increase in accuracy surrounding the selected E_b/N_o pairs, especially in the low E_b/N_o range. To determine if this training method can give insight into the occurrence of the increase at low SNRs, we test how well the network can classify a single SNR's data by training baseline networks on only single SNR data sets. We also test the generalisation of each network over the entire SNR range to identify the classification abilities of our network on low SNR data.

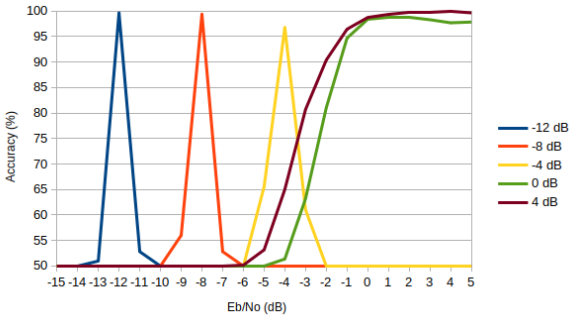

Fig. 4. The performance of five baseline networks, each trained on a specific dB value of SNR data and evaluated on the evaluation set.

From the classification accuracy of five baseline networks, in Figure 4, obtained from SNR-specific training, we see that each E_b/N_o could be classified above 90% accuracy over the -15dB to 5dB range, showing that the network can classify between the two modulation types, even when large amounts

of noise is added, if the task is restricted to a narrower noise range. Furthermore, this shows that the network is indeed able to classify accurately at lower E_b/N_o levels.

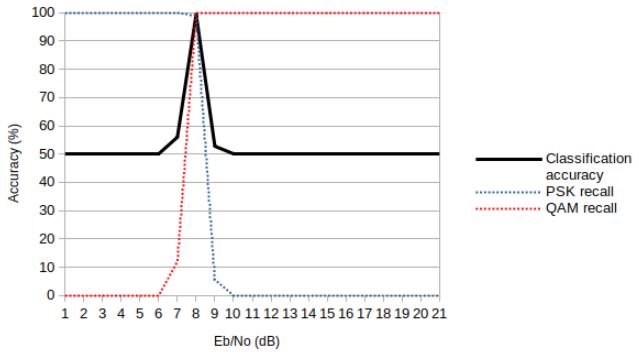

Fig. 5. Classification accuracy of a baseline network trained using only -8 dB data and evaluated on the evaluation set. The recall of 16-QAM and 8-PSK, respectively, is also shown.

From the classification accuracy and class recall of a baseline network trained on -8 dB data as shown in Figure 5, it is seen that networks trained on lower E_b/N_o data tend to generalise poorly to neighbouring E_b/N_o values and only show accuracy above 50% for one to two neighbouring E_b/N_o ranges before falling into a bias classification of 50%. Networks trained on E_b/N_ovalues above 0 dB E_b/N_o, however, show good generalisation, especially to higher E_b/N_o ranges than the E_b/N_o it is trained on. Accuracy of networks trained on high SNR data do however decrease when approaching and passing the noise floor at 0 dB E_b/N_o.

The knowledge that the network can accurately classify at any SNR level in our entire range, but then does not generalise well to other ranges, leads us to the observation that different classification criteria are being utilised for each SNR level, especially at lower SNRs. We can also see on which E_b/N_o level the network classifies accurately, not only by the increase in accuracy but also by the point where the network bias switches from 16-QAM to 8-PSK. This is also seen in our original network (Figure 1), where accuracy increases due to 16-QAM and 8-PSK classifications crossing over at lower E_b/N_o levels. These observations suggest the hypothesis that the network is prioritising certain E_b/N_o levels, or classification criteria, over others in the training process. By prioritising certain lower E_b/N_o levels the network increases the average validation accuracy.

D. Adding SNR as a feature

Knowing that the model can achieve an accuracy near 100% for any of the E_b/N_o levels within our range and the hypothesis that the network is selecting specific E_b/N_o ranges to optimise for, we turn to literature to find possible clarification of this behaviour. Several deep learning AMC networks [1] show increased accuracy when the E_b/N_o dB of the given constellation diagram is provided to the network to aid in classification. Providing the E_b/N_o level might allow the network to better optimise for the entire range, as it will not be blindly selecting an area in the E_b/N_o range to optimise for.

We provide the oracle E_b/N_o dB value to the network to test if this additional information aids the network in optimising better in the lower E_b/N_o range. The E_b/N_o value is provided to the linear layer of the network after the initial feature extraction has taken place in the convolutional layers, and prior to classification based on the extracted feature maps. By providing the E_b/N_o values, we test if the network will be able to adapt the classification criteria based on the E_b/N_o level.

From the classification accuracy of the network provided with SNR data in Figure 6, we observe a substantial increase in the validation accuracy across the entire E_b/N_o range. By providing the network with oracle E_b/N_o values, the network is able to adjust its classification criteria based on the amount of noise on the constellation data points.

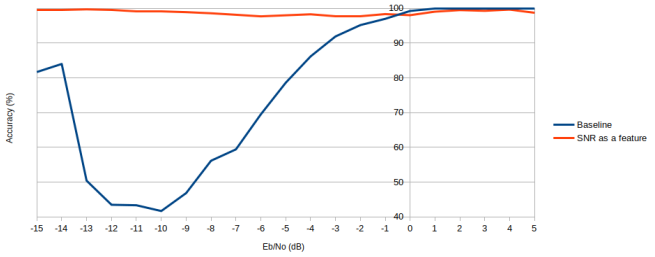

Fig. 6. Classification accuracy on the evaluation set, comparing the baseline network and a network where the SNR of the modulation scheme is presented to the network as a feature.

E. Effect of SNR estimation accuracy

By providing the oracle E_b/N_o data, we create a much-improved classifier for our binary classification problem. We do, however, know that the performance greatly relies on the provision of E_b/N_o values using SNR estimation at the receiver. This affects the implementation of this network in practical applications as noise level estimation accuracy tends to decrease at lower E_b/N_o levels [2]. To further understand the robustness and generalisation of the SNR-tagged network, we performed a sensitivity analysis.

The sensitivity analysis is conducted by generating statistical noise within a given range, as if an error was made when estimating the E_b/N_o value of the received signal, and adding that to the provided E_b/N_o data point when making a classification. The evaluation set and best performing baseline network is used for this analysis.

The results of the sensitivity analysis results for the baseline architecture is shown in Figure 7. We observe that variations within a 0.5 dB E_b/N_o range do not affect classification accuracy substantially, since all E_b/N_o still achieve above 95% accuracy. It is only after variation over 1 dB is introduced that the network's classification accuracy is noticeably reduced, especially at lower E_b/N_o levels.

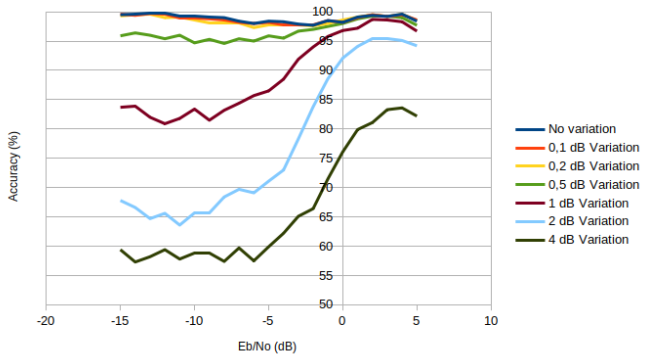

Fig. 7. A sensitivity analysis of SNR-tagged networks where the SNR input is corrupted with increased levels of stochastic variance. This mimics the effect of inaccurate SNR estimators.

This reduction in accuracy can be attributed to the network being trained with E_b/N_o step sizes of 1 dB, since as the provided SNR value moves closer to a neighbouring value, the generalisation of the classification criteria is reduced. The generalisation effect can also be observed at higher E_b/N_o levels as high accuracy levels are still achieved, even at high E_b/N_o variation. This observation once again highlights the specificity of the classification criteria needed to classify accurately at low E_b/N_o levels as opposed to above the noise floor.

V. Conclusion

This paper uncovers and investigates an artefact that occurs when implementing a modulation classifier for two modulation schemes, which provides constellation diagram data points as input to a CNN. It is found that the network can classify accurately at low SNR levels when only trained using specific E_b/N_o's data and that it generalises poorly to neighbouring E_b/N_o values. Knowing that the problem does not lie with the representational capacity of the network but rather with how the network models the task, the SNR values are provided as an additional input feature. This technique significantly increases accuracy at low E_b/N_o values as the network now has reference to the classification criteria to select when making a prediction. A sensitivity analysis of the effect when the additional input features are corrupted shows the weak generalisation of the classification criteria by highlighting the drop in performance when SNR estimation accuracy is low. This means that this network will only be of use if a SNR estimator that can accurately predict E_b/N_o at low SNR is used. Moving forward, this network and method could be further researched to improve AMC for low SNR environments.

Acknowledgement

The authors gratefully acknowledge the financial support of this study by the Telkom CoE at the NWU and Hensoldt South Africa.

References

[1] X. Xie, Y. Ni, S. Peng, and Y.-D. Yao, "Deep learning based automatic modulation classification for varying SNR environment," in *2019 28th Wireless and Optical Communications Conference (WOCC)*, 2019, pp. 1–5.

[2] W. Yongshi, G. Jie, L. Hao, L. Li, W. Zhigang, and W. Houjun, "CNN-based modulation classification in the complicated communication channel," in *2017 13th IEEE International Conference on Electronic Measurement Instruments (ICEMI)*, 2017, pp. 512–516.

[3] J. L. Xu, W. Su, and M. Zhou, "Likelihood-ratio approaches to automatic modulation classification," *IEEE Transactions on Systems, Man, and Cybernetics, Part C (Applications and Reviews)*, vol. 41, no. 4, pp. 455–469, 2011.

[4] J. P. Mouton, M. Ferreira, and A. S. Helberg, "A comparison of clustering algorithms for automatic modulation classification," *Expert Systems with Applications*, vol. 151, p. 113317, 2020. [Online]. Available: https://www.sciencedirect.com/science/article/pii/S0957417420301421

[5] Y. Wei, S. Fang, and X. Wang, "Automatic modulation classification of digital communication signals using SVM based on hybrid features, cyclostationary, and information entropy," *Entropy*, vol. 21, no. 8, 2019. [Online]. Available: https://www.mdpi.com/1099-4300/21/8/745

[6] F. Meng, P. Chen, L. Wu, and X. Wang, "Automatic modulation classification: A deep learning enabled approach," *IEEE Transactions on Vehicular Technology*, vol. 67, no. 11, pp. 10 760–10 772, 2018.

[7] S. A. Ghunaim, Q. Nasir, and M. A. Talib, "Deep learning techniques for automatic modulation classification: A systematic literature review," in *2020 14th International Conference on Innovations in Information Technology (IIT)*, 2020, pp. 108–113.

[8] S. Peng, H. Jiang, H. Wang, H. Alwageed, Y. Zhou, M. M. Sebdani, and Y.-D. Yao, "Modulation classification based on signal constellation diagrams and deep learning," *IEEE Transactions on Neural Networks and Learning Systems*, vol. 30, no. 3, pp. 718–727, 2019.

[9] I. Goodfellow, Y. Bengio, and A. Courville, *Deep Learning*. MIT Press, 2016, http://www.deeplearningbook.org.

[10] A. Zhang, Z. C. Lipton, M. Li, and A. J. Smola, *Dive into Deep Learning*, 2020, https://d2l.ai.

[11] A. F. Agarap, "Deep learning using rectified linear units (ReLU)," 2019, preprint on webpage at https://arxiv.org/abs/1803.08375.

[12] D. P. Kingma and J. Ba, "Adam: A method for stochastic optimization," 2017, preprint on webpage at https://arxiv.org/abs/1412.6980.

[13] K. He, X. Zhang, S. Ren, and J. Sun, "Delving deep into rectifiers: Surpassing human-level performance on imagenet classification," 2015.

[14] G. E. Hinton, N. Srivastava, A. Krizhevsky, I. Sutskever, and R. R. Salakhutdinov, "Improving neural networks by preventing co-adaptation of feature detectors," 2012, preprint on webpage at https://arxiv.org/abs/1207.0580.

[15] S. Ramjee, S. Ju, D. Yang, X. Liu, A. E. Gamal, and Y. C. Eldar, "Fast deep learning for automatic modulation classification," 2019, preprint on webpage at https://arxiv.org/abs/1901.05850.

Andrew Oosthuizen received his B.Eng Computer and Electronic Engineering degree in 2020 and is currently a first year M.Eng student at the North-West University in South Africa. He is working as a dual member of the TeleNet research group in the Telkom CoE, and of MuST, a CAIR-affiliated research group at NWU specialising in deep learning.

Estimating LTE Path-loss Model Parameters from End-user Device Measurements

Johan Fick, Albert Helberg, Melvin Ferreira
School of Electrical, Electronic and Computer Engineering, North-West University, Potchefstroom Campus, South Africa
[1]25867350@student.nwu.ac.za
[2]albert.helberg@nwu.ac.za
[3]melvin.ferreira@nwu.ac.za

***Abstract*—Path-loss models describe the power loss when a radio frequency signal propagates from a receiver to a transmitter. Developing such a model usually entails an extensive path-loss measurement campaign and fitting of the data. Using these models with the obtained parameters can indicate the expected path-loss at a distance from the transmitter. However, these models do not always generalise well to different areas due to the varying complexity of the propagation environments. Furthermore, newer generations of cellular networks are also starting to use higher frequencies, making some of the older path-loss models obsolete since higher frequencies result in more significant path-loss. This paper presents mobile devices as measurement tools for the path-loss experienced by mobile users in LTE networks. The paper shows the feasibility of using ground-truth propagation model parameters by fitting a log-normal model to the measurement data with good results.**

***Index Terms*—Path-loss model, multi-path fading, signal to noise ratio, log-normal path-loss, ground-truth measurements.**

I. INTRODUCTION

The evolution of mobile cellular networks allows for greater bandwidth, higher peak data rates, improved spectral efficiencies, and lower latency. With the advent of Cognitive Radio, a radio that can detect and adapt to changes in a network environment in a dynamic manner, it is essential to predict accurate network parameter values and continuously monitor them so that the software-defined radio can make intelligent cellular adjustments on the fly. To accommodate the aforementioned, base station antennas have to operate at higher frequencies, typically ranging in the ultra-high frequency (UHF) band (300 MHz - 3 GHz) for 4G, with newer generations targeting even higher frequencies [1]. Well-known path-loss models such as Okumura-Hata and COST231 were developed by using path-loss measurements of transmitters operating at 900 MHz, limiting these models' use to the UHF band's lower end. Furthermore, these models are usually specific to the measurement environments, city sizes, and the type of category of each city. For example, the author in [2] states that the model is valid for cities like Tokyo, Japan, which creates the ambiguous task of determining if a city is like Tokyo. Two of the typical approaches reported in the literature to formulate these models are statistical or deterministic methods. These methods typically use large-scale path-loss measurement data. With the vast number of cellular network users, the opportunity to acquire large-scale path-loss measurements using mobile devices becomes feasible. This paper presents a cost-effective method for acquiring these measurements using a mobile device as the measurement tool. Furthermore, this study explores the feasibility of using ground-truth parameter values specifically for LTE networks using the log-normal path-loss model.

The rest of the paper is organised as follows: Section II briefly introduces path-loss and the path-loss models considered in the paper. Section III discusses related work. Section IV describes the architecture of the measurement instrument and essential measurement parameters for an LTE network. Section V describes a centroid method to estimate the locations of the LTE base stations. Section VI details the measurement methodology and values captured by the measurement instrument. Section VII shows how the measurements can serve to estimate ground truth propagation parameters. Finally, in Section VIII a conclusion is drawn, and future work is proposed.

II. BACKGROUND

The free-space path-loss model describes the attenuation a radio frequency (RF) signal will experience when travelling through free-space [3]. The equation for free-space path-loss is given by (1), with d the distance in km and f being the frequency in MHz.

$$L_{FSL} = 32.4 + 20\log_{10} d + 20\log_{10} f \tag{1}$$

Even though air is a good approximation for free-space, real-world measurements typically deviate from this ideal model. However, large scale measurement campaigns have confirmed that the signal strength curves follow a power-law dependence d^{-M} where M varies between 3 and 4 [4]—indicating that external attributes are influencing the path-loss experienced in a real-world environment. Examples of identified attributes are diffraction, scattering, reflection, penetration, atmospheric refractive index changes, rain, and temperature. Continuous research efforts have developed methods to determine the loss associated with each attribute mentioned above [5]. Currently, the complexity and interconnectivity of mobile environments are on the rise, creating a more dynamic environment that at any stage can experience a multitude of these attributes.

A. Okumura/Hata

The Okumura/Hata model is based on many measurements made in Tokyo, Japan, by Okumura. The measurements served as the basis for obtaining path-loss curves for an urban environment. Several correction factors were introduced to improve the curves for other propagation conditions [2].

Hata derived formulas to fit the curves. The derived formulas are for urban, suburban, and rural areas, respectively. The valid input ranges are given in Table I , and the formula for the urban model is given below in (2).

$$L_{urban} = 69.55 + 26.16\log_{10} f_c + (44.9 - 6.55\log_{10} h_b)log_{10}d - 13.82\log_{10} h_b - a(h_m) \quad (2)$$

With f_c the operating frequency in MHz of the antenna, d the distance in km, h_b the height of the base station in m, h_m the height of the mobile antenna in m. Finally, $a(h_m)$ a correcting factor for the mobile antenna height for large (3) and small/medium-size cities (4).

$$a(h_m) = \begin{cases} 8.29(\log_{10}(1.54h_m))^2 - 1.1; & f_c \leq 200MHz \\ 3.2(\log_{10}(11.75h_m))^2 - 4.97; & f_c \geq 400MHz \end{cases} \quad (3)$$

$$a(h_m) = (1.1\log_{10} f_c - 0.7)h_m - (1.56\log f_c - 0.8) \quad (4)$$

The suburban model is given below in (5).

$$L_{suburban} = L_{urban} - 2\log_{10}(\frac{f_c}{28})^2 - 5.4 \quad (5)$$

Finally, for rural areas, the formula is given in (6).

$$L_{rural} = L_{urban} - (4.78(\log_{10} f_c)^2 - 18.33\log_{10} f_c + 40.94) \quad (6)$$

TABLE I
SUMMARY OF PARAMETRIC RANGES APPLICABLE TO OKUMURA/HATA

Parameter Name	Range
Frequency	$f \in [150, 1500]MHz$
Distance	$d \in [1, 20]km$
Base station height	$h_b \in [30, 200]m$
Mobile station height	$h_m \in [1, 10]m$

B. COST 231-Walfisch-Ikegami

The popularity of this model was sparked by the ever-decreasing distance between the base stations in urban environments for each new mobile generation. The model is a combination of three main path-loss components; the free-space path-loss L_{FSL}, a rooftop diffraction component accounting for the loss experience as the signal diffracts/scatters off multiple rooftops L_{rts}, and a multi-screen diffraction loss L_{ms} corresponding to the diffraction experienced as the signal moves from wall to wall formed by the buildings surrounding the streets [6]. Each of these components contributes to the total path-loss given by the equation as seen in (7) below.

$$L_{COST231} = L_{FSL} + L_{rts} + L_{ms} \quad (7)$$

With L_{FSL} the free-space path-loss (1), L_{rts} the rooftop to street diffraction and scatter loss (8) and L_{ms} the multiscreen loss (9) respectively, all in dB. The valid input ranges are given in Table II.

$$L_{rts} = -16.9 - 10\log_{10}\Psi + 10\log_{10} f_c + 20\log_{10}\Delta h_m + L_0 \quad (8)$$

where:

$\Psi =$ street width (m)
$\Delta = hr - h_m$ (m)
$L_0 = -10 + 0.354\phi$ $0° \leq \phi \leq 35°$
$L_0 = 2.5 + 0.075(\phi - 35°)$ $35° \leq \phi \leq 55°$
$L_0 = 4 - 0.114(\phi - 55°)$ $55° \leq \phi \leq 90°$
$\phi =$ incident angle relative to the street

$$L_{ms} = L_{bsh} + k_a + k_d\log_{10} d + k_f\log_{10} f_c - 9\log_{10} b \quad (9)$$

where:

$b =$ building separation distance (m)
$d =$ distance (km)
$L_{bsh} = -18\log(11 + \Delta h_b)$ $h_b \geq h_r$
$L_{bsh} = 0$ $h_b \leq h_r$

where: $\Delta h_b = h_b - h_r$, $h_r =$ average building height (m)

$k_a = 54$ $h_b > h_r$
$k_a = 54 - 0.8h_b$ $d \geq 500; h_b \leq h_r$
$k_a = 54 - 0.8\Delta h_b\frac{d}{500}$ $d < 500; h_b \leq h_r$

Note that both L_{bsh} and k_a increase path-loss with lower base station antenna heights.

$k_d = 18$ $h_b < h_r$
$k_a = 18 - \frac{15\Delta h_b}{\Delta h_m}$ $h_b \geq h_r$
$k_f = 4 + \alpha(\frac{f_c}{925} - 1)$

With α equal to 0.7 for a mid-size suburban city area with moderate tree density and α equal to 1.5 for a metropolitan area.

The error associated with the model is governed by the relationship between h_b and H_B. Good path-loss estimates are found when $h_b > H_B$.

TABLE II
SUMMARY OF PARAMETRIC RANGES APPLICABLE TO COST 231

Parameter Name	Range
Frequency	$f \in [800, 2000](MHz)$
Distance	$d \in [0.02, 5](km)$
Base station height	$h_b \in [4, 50](m)$
Mobile station height	$h_m \in [1, 3](m)$
Distance between building centres	$w_B \in [20, 50](m)$
Street Width	$w_s \in w_B/2(m)$
Incident angle relative to street	$\alpha = 90°$
Average Building height	$H_B = 3 \times (\#floors) + H_{roof}(m)$
Rooftop type	$\mathrm{H}_{roof} = \begin{cases} 3, & pitched(m) \\ 0, & flat(m) \end{cases}$

C. Log-normal

The log-normal path-loss model (11) extends the log-distance path-loss model in (10) by adding a random variable X_σ to the path-loss.

$$L_{logdistance} = L_{FSL}(d_0) + 10n \log_{10}(\frac{d}{d_0}) \qquad (10)$$

With $L_{FSL}(d_0)$ the free-space loss in dB at the reference distance d_0 in km.

The random value has a zero-mean and standard deviation of σ, following a log-normal distribution. The added variable is used to capture random shadowing effects caused by diverse levels of clutter using numerous measurement locations with the same base station and mobile station separation [5].

$$L_{lognormal} = L_{FSL}(d_0) + 10n \log_{10}(\frac{d}{d_0}) + X\sigma \qquad (11)$$

With n the path-loss exponent (PLE) and X_σ the random variable accounting for shadowing effects. If the reference distance is 1 km, the equation reduces to (12).

$$L_{lognormal}(1km) = 10n \log_{10} d + 20 \log_{10} f + 32.45 + X_\sigma \qquad (12)$$

Typical values for the PLE can be found in Table III below.

TABLE III
SUMMARY OF TYPICAL PATH-LOSS EXPONENT VALUES ADOPTED FROM [5]

Environment	path-loss Exponent
free-space	$n = 2$
Urban area cellular radio	$n \in [2.7, 3.5]$
Shadowed urban cellular radio	$n \in [3, 5]$
Inside a building (LOS)	$n \in [1.6, 1.8]$
Obstructed in building	$n \in [4, 6]$
Obstructed in factory	$n \in [2, 3]$

D. IMT-2000 Vehicular Environment

This model forms part of a subset of models generally known as the IMT-2000 models. The key benefit of using the IMT-2000 models is predicting path-loss in environments where relative time delay is important [7]. The governing equation is given by (13).

$$L_{vehicular} = 40(1 - 4 \times 10^{-2}\Delta h_b) \log_{10} d - 18 \log_{10}(\Delta h_b) + 21 \log_{10} f + 80 \qquad (13)$$

Where Δh_b is the change in average rooftop height to base station height in m, d the the distance to the transmitter in km and f the operating frequency in MHz.

III. RELATED WORK

Some of the related work worth mentioning in the literature are:

- Enami $et\ al.$ in [8] lay a good foundation for the typical issues regarding crowd-sourcing LTE networks using mobile devices. It is shown that using mobile devices as measurement tools can give a PLE value within 0.1 of advanced equipment. Unfortunately, the study did not present the overall system architecture used to capture their data.
- Mankowitz $et\ al.$ in [9] present a possible system architecture similar to the presented one in this paper. The study showed that it is possible to use off-the-shelf mobile devices to capture LTE network data. However, the study did not give any insight into the feasibility of using the captured data to determine ground-truth propagation model parameters.
- Neidhardt $et\ al.$ in [10] explored different methods used to estimate the location of base stations using crowd-sourced data. They indicate that a grid-based approach is best to determine the location of the base stations from measurement data. This study did not explore all of the possible attributes available for an LTE network to help determine the location of the base station.

Our study builds on the work above, with emphasis placed on the attributes captured for LTE networks using our proposed system architecture and how these attributes apply to classic path-loss models. Furthermore, the feasibility of using ground-truth propagation parameters is investigated for the data captured.

IV. MEASUREMENT INSTRUMENT

The dual objective of the measurement device is to capture real-world user experienced path-loss values and be cost-effective. To satisfy these objectives, an off-the-shelf LTE-capable mobile device is used as the measurement instrument since it can provide all of the needed functionality with the added advantage of having a flexible library base to help capture all of the required information. A mobile device allows capturing parameters and data of different cellular

network generations, depending on the device-specific chipset and firmware present on the mobile. An android application is developed to access the telecommunications specific data of the device and some other useful information. Table IV shows a summary of the most important data extracted for an LTE network.

TABLE IV
SUMMARY OF CELLULAR LTE AND DEVICE DATA

Extracted data	Description
(Longitude, Latitude)	Device GPS coordinates
rsrp	Reference signal received power
Quality Level	Abstract quality level for overall signal
rsrq	Reference signal received quality
rssi	Received signal strength indication
rssnr	Reference signal signal-to-noise ratio
Timing Advance	timing advance value for LTE
EARFCN	Unique identifier for operating frequency
Enb	Unique identifier for base station (eNodeB)

For large-scale measurements to be made, the architecture in Figure 1 is proposed and implemented. The tower represents a base station of which the path-loss is to be evaluated. The mobile device captures these measurements in an SQLite database. When a WiFi connection is available, the data stored in the SQLite database is sent to an Amazon EC2 instance. Next, the Apache module is used as a reverse proxy to send the request to the flask app. Finally, a connection between the flask app and the SQL database is used to insert the data. The entries can then be used to perform all of the required analyses by selecting the relevant data from the database.

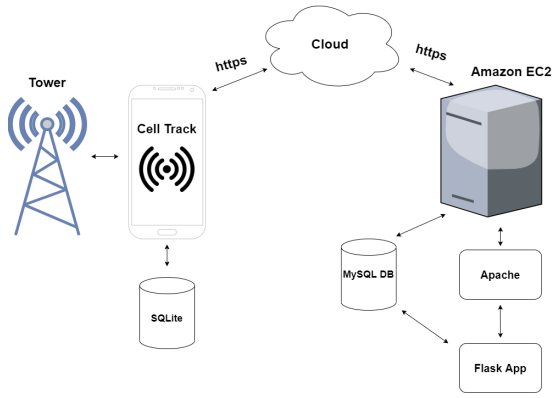

Figure 1. Overall measurement instrument architecture

An important assumption when using the above architecture pertains to LTE power control in the downlink. Two types of power control are distinguished in the downlink: fixed and dynamic. Fixed power control applies to the transmission of cell-specific information to the mobile device and which is received on port 0. The reference signal received power (RSRP) is calculated from 12 symbols' elements and serves as the downlink channel estimation reference. Since there is no stream of data from the device, it will not make use of dynamic power control, and the transmission power of the base station is therefore assumed to be fixed [11].

V. TOWER LOCALISATION METHOD

Since the path-loss depends on the distance between base station transmitter and mobile receiver, both the measurement and the base station locations are needed to determine the path-loss at a distance d. If both the locations are known, they can be substituted into the Haversine formula [12] to calculate the distance. However, since only information regarding the measurement location is known (i.e the mobile device location), the method proposed in [10] is used to estimate the location of the base station by making use of the idea of centroids. The underlying principle of the method is quite simple: if it is possible to connect the measurements in such a way as to form a polygon around an omnidirectional antenna, then the centroid of the polygon can serve as the estimated location of the antenna. If the number of measurements increases, the polygon formed will approach an ideal polygon describing the emission pattern. This will cause the estimated centroid to follow the same behaviour and give a better result as the number of measurements increase [10]. In Figure 2 the estimated base stations locations (green), estimated error (yellow), and the measurement locations (red) are shown for our area of interest.

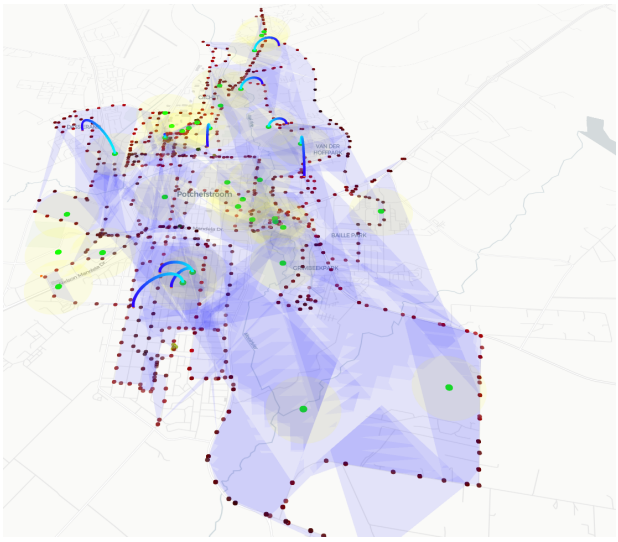

Figure 2. Visualisation of measurements and estimated base station locations.

One of the drawbacks of using this method is that if the antenna does not form an omnidirectional pattern, the above method will not hold. Using this method can thus introduce a deviation in the path-loss calculations due to the variance in the base station location estimation. Some ideas to help improve the above method are using the received signal strength values to form different signal strength regions. Combining these regions with a simple gradient descent approach will help select points closest to the tower. Using these points in the centroid estimation will mitigate not having an omnidirectional emission pattern and reduce the base station location error. The best solution is using highly accurate base station locations provided by cellular operators, although this information may be proprietary and not freely available. To get an idea of the error associated with the above centroid-based method, ten base stations were randomly selected, and

the estimated and actual coordinates were compared to get some idea of the error associated with the above centroid-based method. The mean error of the distance is 489.87 m, and the standard deviation is 235.41 m.

VI. METHODOLOGY

We conducted a small measurement campaign in a suburban area to test the feasibility of using android devices as measuring tools. A single mobile device acting as the measurement instrument connected to an Amazon EC2 t3.nano instance, shown in Figure 1, was used to capture the measurements. To help emulate real-world signal strength values, as experienced by end-users, no rigid sampling method was deployed since mobile users will use their devices at varying times and locations. Therefore the study used the approach of sampling signal strength during random periods in the day, at random measuring time-frames, and by varying the locations. Lastly, different degrees of mobility was also introduced when capturing measurements. Mobility is broadly classified into three categories: stationary, slow-moving (walking or riding a bicycle), or fast-moving (driving a car). The measurement approach resulted in 25171 LTE signal strength measurements captured for a mobile network in a suburban area over a few weeks.

After capturing the data, the first step was to determine the locations of the base stations from the measurement data. This was accomplished by making use of the tower localisation method as set out in Section V. Since both the coordinates of the measurements and the towers are known, it is possible to calculate the distance for each measurement to the tower. The distance to the tower and the accompanying signal strength is then used to fit a log-normal curve to the data yielding a path-loss exponent n and stochastic variable value $X\sigma$ for a specific set of tower measurements.

Table V broadly summarises some of the variables captured by the overall system for current and future usage.

TABLE V
SUMMARY OF IMPORTANT VARIABLES CAPTURED BY THE SYSTEM

Extracted data	**Current/Future Usage**
Device/Tower location	Distance calculations.
Unix Time Stamp	General; acquiring date-specific weather data per location.
Weather Data	Exploring effects of weather on a mobile network.
Device Orientation	Possibly useful for indoor/outdoor path-loss predictions according to [13].
Device Temperature	Explore the effect of battery temperature on measurements.
Device Speed	Determine how speed affects the measured signal.
Device Bearing	Explore how bearing relative to tower affect the measured signal.
Device Altitude	Explore how altitude affects measured signal.
Device Hardware	Usage is to create a possibly calibrated measurement device.

VII. ANALYSIS EXAMPLE

The feasibility of using the mobile measurement data for path-loss modelling was investigated next by selecting a well-measured transmitter. Figure 3 below shows the received signal strength plotted against the distance from the base station for 10191 measurements of the tower 313021 (eNodeB) operating at a frequency of 2120 MHz.

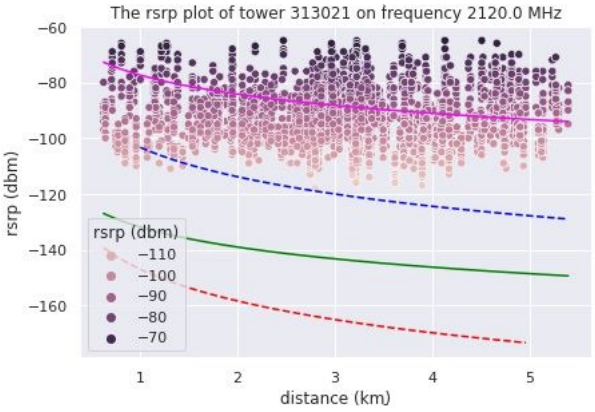

Figure 3. The rsrp data of tower 313021 (eNodeB) with path-loss models plotted - log-normal (magenta), Okumura/Hata (blue), COST 231 (red), IMT-2000 (green).

The magenta line is the path-loss curve formed by fitting a log-normal path-loss model to the data. A log-normal path-loss model was assumed as it is well described and has been applied to model path-loss in similar environments accurately, as discussed in section II of this paper. The best fit values for the log-normal parameters were found to be $n = 2.28$ with $X_\sigma = -21.62$, by applying non-linear least-squares fitting to the data. The background section shows that this value of n is smaller than the range of values reported for an urban environment. The reason is that the investigated environment of the tower for which our data was collected matches a typical suburban environment that has lower buildings further apart than in an urban environment, hence the lower value of n. It is also worth noting that the typical values used in the reference models for the PLE are for European environments, which boast more complex urban and suburban environments than typically found in South Africa.

An important consideration when interpreting the results is that the distances used in the calculations are based on estimates of the tower position, as derived by applying the centroid calculation method. If the estimated tower location error is large relative to the tower's coverage area and the tower has a radial emission pattern, points closer to the actual tower location might mistakenly be shown as points farther away and vice versa. It should also be noted that the measurements were taken on different radii from the tower, each associated with a different path profile. The above factors lead to a high variation in measured signal strengths at various distances from the tower, possibly explaining why the measurements in Figure 3 seem to form a flattened profile where the signal strength does not seem to reduce as much as expected with increase in distance from the tower. These factors can be compensated for by obtaining accurate tower

positions, antenna heights, and by taking many long term measurements, to establish a large data-set.

The green line resembles the IMT-2000 path-loss model for a vehicular environment. The IMT-2000 model is overestimating the path-loss by roughly 30 dBm. A possibility is that the calculated value for the change in average rooftop height to base station height might not resemble the actual scenario well. Again it can be argued that the model is designed for European environments with more complex clutter, therefore overestimating the path-loss. The dotted lines, blue and red, are the Okumura/Hata (rural and small) and COST 231 (suburban and medium) models, respectively. Being dotted indicates the tower frequency is not in the specified operating ranges of these models. However, they emphasise the deviation from the measured data and the need to investigate the feasibility of using ground-truth path-loss values for models such as the log-normal model.

VIII. Conclusion

The continuous advancement of cellular networks drives the need to predict and monitor crucial network parameters. Therefore, deploying large-scale, low-cost measurement campaigns will help design and maintain future networks. The measurement architecture presented in this paper shows the feasibility of using mobile devices as low-cost measurement tools with the ability to scale. Furthermore, the analysis sections show that it is possible to determine ground-truth propagation parameters from the measurement data for the log-normal propagation models with reasonable accuracy. On the other hand, the significant deviations of the other path-loss models from the measured data show their inability to predict accurate path-loss values for frequencies and environments not implicitly modelled.

The study also concluded that it is possible to blindly estimate base station locations with a tolerable degree of accuracy using the measurement data. Using highly accurate base station locations provided by a cellular network operator will be essential to determine the exact distance of each measurement from the base station, thus mitigating the error introduced by blindly estimating the locations. Furthermore, using these accurate locations will lead to a deeper insight into the effect of the associated error on the ground-truth propagation parameters. These newly formed insights might lead to estimating highly accurate ground-truth propagation parameters using a base station localisation method.

In this paper, we used the device and tower locations to estimate PLE values for a mobile network, leaving the rest of the variables as shown in Table V open for investigation in future research.

Acknowledgement

The authors gratefully acknowledge the financial support of this study by the Telkom CoE at the NWU and Hensoldt GEW. The authors also wish to thank the reviewers for their constructive feedback.

References

[1] L. Doyle, *Essentials of cognitive radio*. Cambridge University Press, 2009.

[2] M. Hata, "Empirical formula for propagation loss in land mobile radio services," *IEEE Transactions on Vehicular Technology*, vol. 29, no. 3, pp. 317–325, 1980.

[3] C. Haslett, *Essentials of radio wave propagation*. Cambridge University Press, 2008.

[4] J. Walfisch and H. Bertoni, "A theoretical model of uhf propagation in urban environments," *IEEE Transactions on Antennas and Propagation*, vol. 36, no. 12, pp. 1788–1796, 1988.

[5] O. O. Erunkulu, A. M. Zungeru, C. K. Lebekwe, and J. M. Chuma, "Cellular communications coverage prediction techniques: A survey and comparison," *IEEE Access*, vol. 8, pp. 113 052–113 077, 2020.

[6] L. M. Correia, "A view of the cost 231-bertoni-ikegami model," in *2009 3rd European Conference on Antennas and Propagation*, 2009, pp. 1681–1685.

[7] V. K. Garg, *Wireless communications and networking*. Morgan Kaufmann, 2007.

[8] R. Enami, Y. Shi, D. Rajan, and J. Camp, "Pre-crowdsourcing: Predicting wireless propagation with phone-based channel quality measurements," *Computer Communications*, vol. 132, pp. 96–110, 2018. [Online]. Available: https://www.sciencedirect.com/science/article/pii/S0140366418304158

[9] J. D. Mankowitz and A. J. Paverd, "Mobile device-based cellular network coverage analysis using crowd sourcing," in *2011 IEEE EUROCON - International Conference on Computer as a Tool*, 2011, pp. 1–6.

[10] E. Neidhardt, A. Uzun, U. Bareth, and A. Küpper, "Estimating locations and coverage areas of mobile network cells based on crowdsourced data," in *6th Joint IFIP Wireless and Mobile Networking Conference (WMNC)*, 2013, pp. 1–8.

[11] 3GPP, "Evolved Universal Terrestrial Radio Access (E-UTRA); Physical layer procedures," 3rd Generation Partnership Project (3GPP), Technical Specification (TS) 36.331, 09 2021, version 14.2.2. [Online]. Available: https://www.3gpp.org/

[12] "Iii. recherches sur les principaux problemes de l'astronomie nautique," *Philosophical Transactions of the Royal Society of London*, vol. 87, p. 43–122, 1797.

[13] Y. Boussad, M. N. Mahfoudi, A. Legout, L. Lizzi, F. Ferrero, and W. Dabbous, "Evaluating smartphone accuracy for rssi measurements," *IEEE Transactions on Instrumentation and Measurement*, vol. 70, pp. 1–12, 2021.

Johan Fick received his B.Eng in Computer and Electronic Engineering degree in 2019 and is currently a first-year M.Eng student at the North-West University in South Africa. Some of his research interests are cellular propagation models and machine learning.

A Comparison of Shared Access Licenses for Private Wireless Access Networks

Cilliers Schultz, Melvin Ferreira
School of Electrical, Electronic and Computer Engineering, North-West University, Potchefstroom Campus, South Africa
[1]26059754@student.g.nwu.ac.za
[2]melvin.ferreira@nwu.ac.za

***Abstract*—Spectrum sharing is increasingly becoming more important due to the increasing demand for available spectrum. Licensed shared access (LSA) is one example of such a spectrum sharing architecture. However, the dimensioning of these networks are still not well understood due to the multiple degrees of freedom that the licenses allow the licensee. In this paper, a simulation model was constructed to act as a framework to compare the low- and medium-power licenses available in the 4 GHz band, using OFCOM's shared access license (SAL) regulations. Results indicate SAL secondary system utility, including theoretical coverage area and capacity expectations.**

***Index Terms*—Spectrum Sharing, Licensed shared access (LSA), Private Wireless Access Networks, Dynamic Spectrum Access (DSA), Network Capacity and Coverage, Shared Access License (SAL)**

I. Introduction

Radio spectrum is a limited resource, and reusable spectrum is a desired commodity. Spectrum use is managed at both national and international levels, which means that each country is responsible for managing the frequencies in their borders. However, national regulators are subject to international regulators. The highest level of spectrum management is the International Telecommunications Union (ITU), an agency in the United Nations that is responsible for international radio regulations.

Historically, regulators have decided which users are allowed to transmit on specific frequency bands [1]. This tight control on the use of spectrum meant easier control over any excessive interference, but this might be an inefficient way to use spectrum.

Secondary users require additional spectrum that is not available using the traditional spectrum allocation paradigm [2]. The concept of spectrum sharing has been identified as a possible solution to the spectrum famine where spectrum can be shared by current primary users with secondary users allowing coexistence in the same spectrum band without significant or harmful interference to each other. One such spectrum sharing mechanism that has been proposed is Dynamic Spectrum Access (DSA), where spectrum is allocated dynamically in real-time as needed. Recent developments in DSA have resulted in the TV White Space (TVWS), LSA and Citizens radio broadband service (CBRS) spectrum sharing architectures.

The first spectrum sharing architecture regulated was TVWS that reuses the television bands for secondary users. The problem with TVWS is that new radio interfaces are required for transmitters and receivers, which increases the cost of new TVWS networks. LSA and CBRS present alternative approaches to spectrum sharing in the bands where current radio technologies like Long Term Evolution (LTE) and fifth generation of commercially automated cellular (5G) already have chipset support for the transceivers. Using existing technologies lowers the cost of setting up a network with these spectrum sharing architectures.

Despite an interest in spectrum sharing architectures and a need for private networks, little has been published on the utility, sizing and application of LSA networks. Furthermore, spectrum sharing architectures have many parameters and degrees of freedom that makes it challenging to ensure that these networks are feasible, even under desirable SAL pricing plans, as in the United Kingdom (UK) [3].

In this paper, a private campus network using LSA is simulated using the two LSA licensing schemes in the 3.8-4.2 GHz band. The two available licenses are the low-power and medium-power systems. A comparison is then drawn between the appropriateness of the licensing schemes for the application in a private campus network in terms of capacity and coverage.

The rest of the paper is organised as follows: Section II introduces the shared access license (SAL) and evaluates the low- and medium-power licenses available under SAL. Section III details related work. Section IV details the model constructed to evaluate utility in terms of coverage and capacity. Section V details the research method. Section VI discusses the results, and finally, the paper concludes with Section VII.

II. Shared access license

On 25 July 2019, Office of Communications (OFCOM) set out two new licensed products described in [3] to make it easier for a broader scope of secondary users in the UK to access radio spectrum. One of these licensed products is the SAL which allows the use of four spectrum bands that support mobile technology. SAL is a licensing scheme for the LSA concept that allows secondary users to coexist in shared spectrum.

Candidate use cases envisioned by OFCOM are Utilities, Industrial Internet of Things (IoT), Logistics and Distribution, Mining and Agriculture. SAL is marketed as a means to

provide connectivity to a business or campus site, affording more security than unlicensed technologies like Wireless Fidelity (WiFi) while being a feasible alternative to other solutions from mobile network operators (MNOs) that still allows for Quality of service (QoS).

When applying for a SAL, the secondary user applies for either a low-power or medium-power license, giving information that includes the location, desired frequency band, and in the case of a the medium-power license, details concerning the antenna installation.

1) SAL frequency bands: The SAL architecture has been rolled out over four bands of spectrum. The four bands are shown in Table I with the allowed bandwidths indicated for each band. In this this paper, the 4 GHz band is evaluated since it exists in the C-band and allows for comparison to other spectrum sharing architectures such as CBRS. The 4 GHz band sits just above the 3.6-3.8 GHz mobile band, which means chipsets with 5G support for this band already exist. In addition, it is the only band where fixed wireless access is allowed outdoors. Other bands under SAL regulations are only allowed fixed wireless access indoors.

TABLE I
TECHNICAL PARAMETERS REQUIRED TO APPLY FOR A SAL

Frequency band name	Frequency ranges	Channel bandwidths
1800 MHz	1781.7-1785 MHz 1876.7-1880 MHz	3.3 MHz
2300 MHz	2390-2400 MHz	10 MHz
4 GHz	3.8-4.2 GHz	10, 20, 30, 40, 50, 60, 80, 100 MHz
lower 26 GHz	24.25-26.5 GHz	50, 100, 200 MHz (only low-power)

2) Low-power license: The envisioned use case for the low-power license is for industrial campuses and enterprises wanting to deploy private networks. The low-power license allows the licensee to deploy as many base stations as required in a circular area within a radius of 50m centred on the licensed coordinate. Secondary users can move base stations around within the circular area without any further coordination requested from OFCOM. In cases where secondary users may want more flexibility with base station placement, they may apply for multiple low-power licenses, either contiguous or spaced out over a larger area. Figure 1 graphically depicts how the low-power license works. Note that licenses are given per circle, represented in orange, and requires a separate license application for each circle. The blue circles represent the coverage of the base stations. Multiple mobile or fixed terminals are allowed for each base station.

3) Medium-power license: The medium-power license is for secondary users who need a long transmission range from a fixed base station. An envisioned use case is the frequency wireless access (FWA) services in rural areas and industrial or enterprise services over bigger areas allowing wireless communication services to geographically spread campuses like ports, agriculture or forestry. This license only allows for a single base station which in turn can connect to fixed or

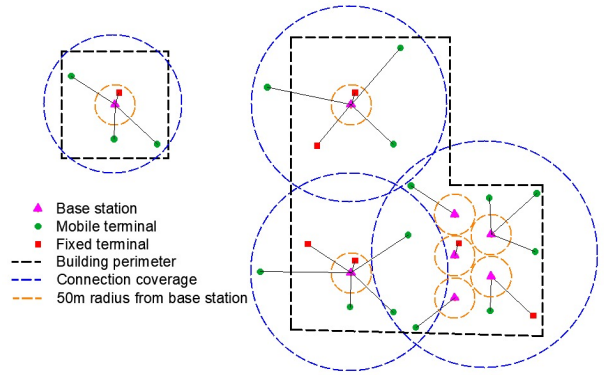

Figure 1. Low-power SAL adopted from [3]

mobile terminals. Due to an increased power allowance and larger transmit range, these licenses are only permitted in rural areas since they may prevent low power secondary users from deploying in the area. Figure 2 shows how a medium-power license may be set up with fixed and mobile terminals.

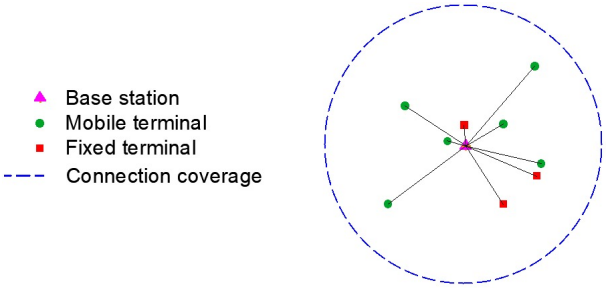

Figure 2. Medium-power SAL adopted from [3]

Table II shows the important technical parameters of both SAL types and the differences between these two license types.

TABLE II
LIMITATIONS FOR SAL IN THE 3.8-4.2 GHZ BAND

Technical Parameter	Low-power license	Medium-power license
Base station power limit	24 dBm / carrier for carriers $<$ 20 MHz 18 dBm / 5 MHz for carriers $>$ 20 MHz	42 dBm / carrier for carriers $<$ 20 MHz 36 dBm / carrier for carriers $>$ 20 MHz
Terminal Power limit (EIRP for fixed) (TRP for mobile)	28 dBm	28 dBm TRP 35 dBm / 5 MHz EIRP
Antenna height	10 m above ground	10 m above ground
Authorised Bandwidth	10, 20, 30, 40, 50, 60, 80 or 100 MHz	10, 20, 30, 40, 50, 60, 80 or 100 MHz
Permitted Deployment	Indoor or outdoor only	Outdoor only in rural areas

III. Related work

Studies were done to test the early regulations and possible improvements on the LSA concept. Mustonen *et al.* [4] describe the first live demonstration of the LSA concept that was shown in Finland in 2013. Critical factors of the architecture and their effects are discussed. The effect on the incumbent users are the main focus of this study and whether the regulations are sufficient.

Yrjola *et al.* [5] discusses system enhancements for antenna systems and the regulation changes required for the enhancements. LSA is discussed before possible active antenna enhancements are provided. The technical parameters of LSA are explained as well as integration between current systems and LSA.

A field trial was done for LSA using TD-LTE in the 2.3 GHz band in [6]. The field trial is described in terms of the environment and two use cases that were tested in the field trial. The trial concludes that dynamic availability of the LSA bands can be handled with existing real-world network equipment and some additional components.

A different field trial was done and discussed in [7] with reference to resource optimisation and incumbent protection. According to [7] the inclusion of small cells will allow the network operator to serve secondary users even when incumbent users request use of the spectrum.

[8] describes the LSA architecture, and a testbed is evaluated for the management system of LSA. It is concluded that the newly proposed regulatory approach shows promise to give better QoS and inclusion into the 3rd Generation Partnership Project (3GPP) 5G context.

[9] discusses a multi-objective optimisation approach for dynamic LSA systems. Optimisations are proposed for: Spectrum efficiency, energy efficiency, performance metrics of the wireless network in LSA and sharing between the incumbent and secondary user. Results indicate that using optimal power allocation can improve efficiency during the period when the incumbent is using the spectrum.

Yrjola *et al.* [10] discuss how LSA enables high-quality wireless networks and compares LSA and CBRS, discussing how the different spectrum sharing frameworks are implemented. The paper further discusses the evolution of LSA and utility.

Yrjola *et al.* in [11] further create a model to simulate the dynamic priority changes in different spectrum sharing architectures. Applying the spectrum allocation simulation, an evaluation is made on the efficiency of dynamic spectrum allocations between different sharing architectures.

Matinmikko *et al.* [12] make a similar comparison between spectrum sharing frameworks and compare different tiers of sharing in different sharing schemes. Very early iterations of the CBRS sharing architecture are discussed by looking at changes in US spectrum sharing regulations. This paper compares the LSA and Collective use of spectrum approach and the decisions made by regulators.

Kalliovaara *et al.* [**?**] evaluate LSA evolution and how it can be used to provide DSA for novel 5G use cases. The development of LSA is discussed and its application for mobile networks. The spectrum access system, which is the spectrum control system for CBRS, is discussed. Finally, a comparison is made between the regulation of the two architecture types.

Höyhtyä *et al.* [13] describe an LSA field trial and a testbed for satellite communications before discussing possible research directions for 5G communications.

We next introduce the system model used for our evaluation of the two SAL license types.

IV. Experimental model

An experimental model is developed in Matlab 2020b to evaluate the SAL utility. The basic components of a wireless network simulation such as transmitters, receivers, path loss (PL) or prediction models, transmission parameters and a defined area of interest, are defined. Then, the model calculates the capacity of multiple connections and plots the coverage of the network, which will be used as a basis for comparison.

A. Campus network map setup

A map is made where all the terminals are placed around the transmitter at regular intervals to disperse the terminals evenly in a circular pattern. The prediction radius of the circle for each license type is chosen based on the coverage of a transmitter using free-space loss.

B. Radio-frequency propagation model

A survey of propagation models presented in [14] is used to find a suitable propagation model for this study. The Longley-Rice Irregular Terrain Model (ITM) was chosen since it best fits the criteria of the simulation as provided in Table III, which shows the experimental parameters used for the simulation. The experimental parameters are derived from the regulations for the SAL [3]. What makes the Longley-rice ITM model a good estimation tool for PL is that it takes terrain, frequency and distance into account when predicting the PL of a signal.

The Longley-Rice ITM is implemented using a Matlab implementation of Signal Propagation, Loss, And Terrain (SPLAT!) [15], an application that uses a terrain model to calculate the losses due to terrain scattering. Version 3 of the Shuttle Radar Topology Mission (SRTM) dataset is used as a digital terrain model (DTM).

The Longley-Rice model is limited to distances between 1 and 20 km and frequencies between 20 MHz and 20 GHz. All receivers below 1 km use free-space loss for PL estimation. The free space loss (FSL) is calculated using (1):

$$L_{FSL} = 32.4 + 20\log_{10}(d) + 20\log_{10}(f) \qquad (1)$$

Where d is the distance between transmitter and receiver in km and f is the frequency of the signal in MHz.

C. Capacity calculations

The distance between the transmitter and each receiver can be calculated using the Haversine formula [16] that calculates the distance of an arc over the surface of a sphere such as the earth. As explained in section IV-A, multiple receivers around the transmitter with different distance increments are used. For each receiver, the propagation model is applied to find the PL from the transmitter. The received signal power, P_r, can be calculated at each receiver using (2):

$$P_r = P_{TX} + G_{TX} + G_{RX} - PL \tag{2}$$

Where P_r is the received signal power, P_{TX} is the signal power at the transmitter, G_{TX} and G_{RX} are the transmitter and receiver gain, respectively, and PL is the path loss as calculated by SPLAT! [15], all measured in dB. To calculate the signal to noise ratio (SNR) of the signal, a noise figure is required. An additive white Gaussian noise (AWGN) is added to the signal and the thermal noise is calculated at the receiver which can be used to calculate the SNR in (3).

$$SNR = \frac{P_r}{N_{awgn} + kTB} \tag{3}$$

Where P_r is received signal power and N_{awgn} is the AWGN both in watt. The second term in the denominator is the thermal noise in watt, where k is Boltzmann's constant, T is the temperature in Kelvin, B is the bandwidth of the signal in Hz.

For this study, other sources of interference are ignored to facilitate comparison between the two license types. The SNR is used to calculate the capacity using Shannon's capacity formula (4):

$$C = Blog_2(1 + SNR) \tag{4}$$

Where B is the channel bandwidth measured in Hz and SNR is the ratio as calculated above. The calculation results in C, the capacity of the signal in bits per second. C is known as the Shannon capacity and is an upper bound of how much information can be sent over a channel [17]. The capacity of the channel decreases as the distance and PL increases between the transmitter and the receiver. Thus, it can be used to compare networks using different input parameters that affect the signal loss.

V. Research method

We use a simulation to compare the utility of low- and medium-power SALs. A single transmitter and multiple receivers are simulated to calculate network characteristics such as coverage area and capacity. Table III shows the experimental parameters used in the simulation.

TABLE III
Experimental model parameters

Parameter	value
Frequency	3.8 GHz
Channel Bandwidth	10 MHz
Transmit power	250 mW for Low-Power license 4000 mW for Medium-Power license
Residual noise floor	-70 dBm
TX Latitude (degrees)	26.6883 S
TX Longitude (degrees)	27.0929 E
TX antenna height	10 m
TX Gain	10 dBm
Amount of receivers	1000
Maximum receiver distance	3 km for Low Power license 10 km for Medium Power license
Distance increment	100 m for Low power license 500 m for Medium power license
RX antenna height	1.5 m
RX Gain	10 dBm
Propagation models	Longley-Rice ITM, Free-space loss
Digital terrain model	SRTM

The chosen transmitter latitude and longitude is the North-West University (NWU) administration building F1 as a reference to using the private network on campus. The transmission parameters are chosen by considering the SAL regulations for the 4 GHz band, as shown in Table II. The best-case scenario for both the low- and medium-power licenses are simulated, assuming the highest power output allowed. In the case of antenna height, the base stations are 10 m high, but the receiver height is limited at 1.5 m, a typical height used for user equipment (UE) in LTE. A thousand receiver locations are used to maintain a statistically significant amount of samples to support the results. The maximum distance of the receivers from the transmitter is chosen to keep within the range where the SNR is larger than 0 using FSL.

For control results, only the FSL of the signal is used for calculations to allow for an extra degree of analysis in the work. The FSL model represents an ideal propagation environment, which will, under most propagation conditions, not be achievable by a practical network subject to attenuation and interference. Coverage and capacity calculations performed using FSL approaches the Shannon capacity upper bound.

Receivers are placed in concentric circles around the transmitter location at an incremental distance given in Table III. Each receiver is used to calculate PL [15], received power (2), SNR (3) and capacity (4) at the receiver coordinates. The capacity values are then grouped based on the received SNR. The groups are based on typical LTE signal strength ranges for the minimum SNR required to receive and demodulate the signal successfully.

VI. Results and analysis

First, graphs are constructed plotting SNR over the distance from the transmitter. These graphs show how SNR decreases as the distance increases. Next, complementary cumulative distribution function (CCDF) plots are constructed from the simulation results based on how many receivers have an SNR value above the threshold levels. The theoretical capacity is used to compare the utility of the low- and medium-power

licenses in the simulation. Finally, the coverage area of both license types is provided for a coverage comparison.

A. Performance evaluation based on SNR

The SNR is plotted for all incremental distances from the transmitter as calculated using both FSL and the PL calculated with the Longley-Rice propagation model.

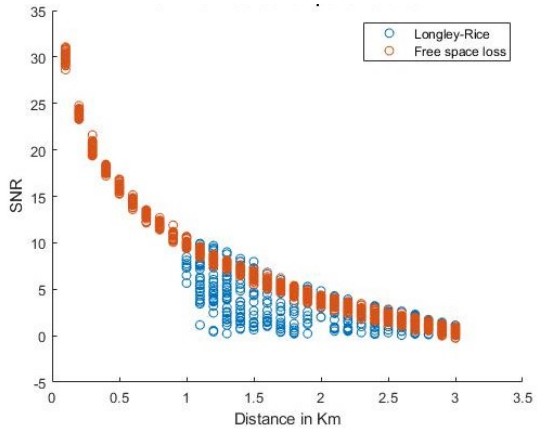

Figure 3. SNR vs Distance for the low-power SAL

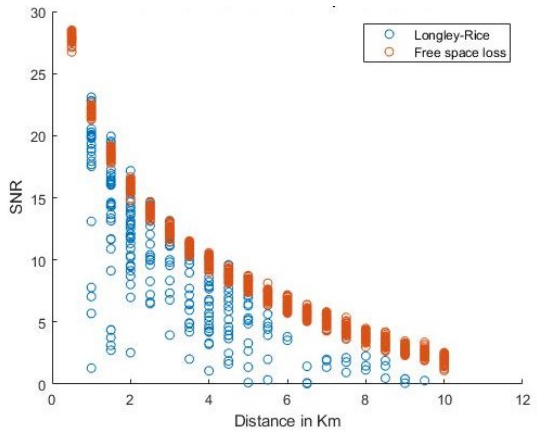

Figure 4. SNR vs Distance for the medium-power SAL

Figure 3 and 4 show the calculated SNR as a function of distance. It can be seen that the SNR calculated using FSL gives the upper band that is possible using the Longley-Rice ITM model. For the first kilometre from the transmitter, only the red circles that represent FSL are shown. This is because the Longley-Rice ITM is limited to distances above 1 km, and FSL is used as a substitute at these distances. The Longley-Rice ITM includes signal loss due to terrain, thus decreasing the possible SNR around the transmitter. For this reason, the Longley-Rice ITM plot is spread out below the FSL.

B. Performance evaluation based on capacity calculations

A CCDF graph is made by adding the number of points that reach above a given SNR threshold. Each point that is added increases the probability of achieving the corresponding capacity above the SNR threshold.

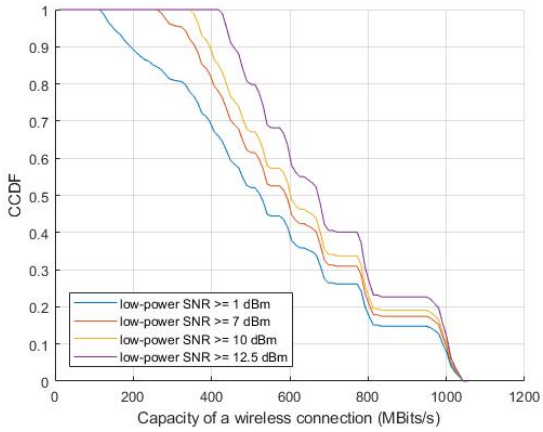

Figure 5. CCDF for the low-power SAL

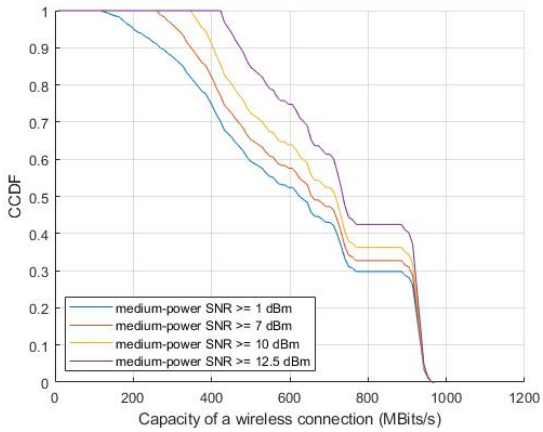

Figure 6. CCDF for the medium-power SAL

The CCDF figures represent the probability that a signal can have a capacity based on the SNR threshold in the simulation. Higher SNR values result in a higher probability of achieving a higher capacity. Figure 5 and 6 show that the probability of achieving a higher capacity increases for higher SNR values. Note that SNR decreases over larger distances as shown in Figure 3 and 4, so the CCDF graphs also show that capacity decreases as the distance increases.

C. Evaluation of coverage

The coverage of a single transmitter is calculated to show the difference in utility between the low- and medium-power licenses by comparing the coverage area of both. We assume there are enough measurements taken in the circular area so that each receiver location represents roughly an equal surface area. This is why the receiver results appear evenly spaced in Figure 3 and 4. Since the step sizes are small with regard to the total radius of the circle and that the circle radius itself is relatively small, the receiver positions representing a specific area are used to calculate coverage area by dividing the number of receivers that have SNR values above the thresholds by the total sample size.

TABLE IV
COVERAGE IN (km^2) OF THE SAL NETWORKS USING LONGLEY-RICE

SAL type	SNR (dB)		
	$\geq$ **7**	$\geq$ **10**	$\geq$ **12.5**
Low-power	8.9	8.7	6.6
Medium-power	80.9	66.6	50

TABLE V
COVERAGE OF THE SAL NETWORKS USING THE FREE-SPACE MODEL

SAL type	SNR (dB)		
	$\geq$ **7**	$\geq$ **10**	$\geq$ **12.5**
Low-power	12.8	8.9	6.6
Medium-power	166.9	116.4	83.5

Table IV and V show that using the Longley-Rice ITM produced smaller coverage than the FSL model. This is because the ITM takes the DTM into account and shows that the terrain around the transmitter attenuates the signal. The FSL model only represents the distance the signal will travel before attenuating below the minimum detectable signal or noise floor. It can also be seen that the medium-power system loses much more coverage due to terrain but still has a much larger terrain coverage than the low-power system because the medium-power system has a larger transmission power.

VII. SUMMARY AND CONCLUSION

Comparing the SNR values between the low- and medium-power license schemes shows that the medium-power license allows for a better signal reception than the low-power license at larger distances. The medium power license covers much greater distances than the low-power license. However, its use is limited to rural areas, and a medium-power license only covers a single fixed base station outdoors. The low-power license may have a much smaller coverage area but has a larger degree of freedom with more flexible capabilities. When considering the smaller area covered with high SNR levels by the low-power license, it has more utility indoors and for smaller campuses.

SAL would be the easiest approach in South Africa since regulations in ITU region 1 have already been rolled out. It is compatable with current chipsets and can realistically be used for spectrum sharing.

For future work, the simulation can be improved to include other sources of interference for terminals, using signal to interference and noise ratio (SINR) instead of SNR, and an indoor propagation scheme can be used to predict network behaviour of low-power SAL indoors. Dimensioning of the secondary network within the allocated shared spectrum remains an open challenge. Further studies are required to make a comparison between LSA, TVWS and CBRS. The unlicensed user tier in CBRS can be compared to the licensed tier of other spectrum sharing schemes.

ACKNOWLEDGEMENT

The authors gratefully acknowledge the financial support of this study by the Telkom CoE at the NWU. The authors also wish to thank the reviewers for the constructive feedback.

REFERENCES

[1] M. Cave, C. Doyle, and W. Webb, *Essentials of Modern Spectrum Management*, W. Webb and S. Dixit, Eds. Cambridge University Press, 2007.

[2] M. Lazarus, "The great spectrum famine," *IEEE Spectrum*, pp. 26 – 31, Oct. 2010.

[3] OFCOM. (2019, Jul.) Shared access lisence guidence document. OFCOM. [Online]. Available: https://www.ofcom.org.uk/__data/assets/pdf_file/0037/157888/local-access-licence-guidance.pdf

[4] M. Mustonen, M. Matinmikko, M. Palola, S. Yrjölä, J. Paavola, A. Kivinen, and J. Engelberg, "Considerations on the licensed shared access (lsa) architecture from the incumbent perspective," in *2014 9th International Conference on Cognitive Radio Oriented Wireless Networks and Communications (CROWNCOM)*, June 2014, pp. 150–155.

[5] S. Yrjölä and E. Heikkinen, "Active antenna system enhancement for supporting licensed shared access (lsa) concept," in *2014 9th International Conference on Cognitive Radio Oriented Wireless Networks and Communications (CROWNCOM)*, June 2014, pp. 291–298.

[6] M. Palola, M. Matinmikko, J. Prokkola, M. Mustonen, M. Heikkilä, T. Kippola, S. Yrjölä, V. Hartikainen, L. Tudose, A. Kivinen, J. Paavola, K. Heiska, T. Hänninen, and J. Okkonen, "Description of finnish licensed shared access (lsa) field trial using td-lte in 2.3 ghz band," in *2014 IEEE International Symposium on Dynamic Spectrum Access Networks (DYSPAN)*, April 2014, pp. 374–375.

[7] M. Matinmikko, M. Palola, M. Mustonen, T. Rautio, M. Heikkilä, T. Kippola, S. Yrjölä, V. Hartikainen, L. Tudose, A. Kivinen, H. Kokkinen, and M. Mäkeläinen, "Field trial of licensed shared access (lsa) with enhanced lte resource optimization and incumbent protection," in *2015 IEEE International Symposium on Dynamic Spectrum Access Networks (DySPAN)*, Sep. 2015, pp. 263–264.

[8] M. Bavaro, P. Viaud, J. Chareau, P. Chawdhry, and E. Angiuli, "A laboratory testbed for licensed shared access," in *2015 IEEE International Symposium on Dynamic Spectrum Access Networks (DySPAN)*, Sep. 2015, pp. 281–282.

[9] S. O. Onidare, K. Navaie, and Q. Ni, "On the spectrum and energy efficiency in dynamic licensed shared access systems: A multiobjective optimization approach," *IEEE Access*, vol. 7, pp. 164 517–164 532, 2019.

[10] S. Yrjola and H. Kokkinen, "Licensed shared access evolution enables early access to 5g spectrum and novel use cases," *EAI Endorsed Transactions on Wireless Spectrum*, vol. 3, p. 153463, 12 2017.

[11] S. Yrjola. (2018, Nov.) Results of the demonstration of shared spectrum access of different user groups and changing priorities. Wireless Innovation Forum Conference. [Online]. Available: https://www.researchgate.net/publication/328982301_Results_of_the_Demonstration_of_Shared_Spectrum_Access_of_Different_User_Groups_and_Changing_Priorities

[12] M. Matinmikko, M. Mustonen, D. Roberson, J. Paavola, M. Höyhtya, S. Yrjölä, and J. Röning, "Overview and comparison of recent spectrum sharing approaches in regulation and research: From opportunistic unlicensed access towards licensed shared access," in *2014 IEEE International Symposium on Dynamic Spectrum Access Networks (DYSPAN)*, April 2014, pp. 92–102.

[13] M. Höyhtyä, M. Majanen, M. Hoppari, P. Järvensivu, H. Kokkinen, J. Ojaniemi, A. Reis-Kivinen, O. Pellay, D. Pham-Minh, and M. Guta, "Licensed shared access (lsa) field trial and a testbed for satellite-terrestrial communication including research directions for 5g and beyond," *International Journal of Satellite Communications and Networking*, 09 2020.

[14] C. Phillips, D. Sicker, and D. Grunwald, "A survey of wireless path loss prediction and coverage mapping methods," *IEEE Communications Surveys Tutorials*, vol. 15, no. 1, pp. 255–270, First 2013.

[15] J. Magliacane. (1997) Splat. [Online]. Available: https://www.qsl.net/kd2bd/splat.html

[16] J. Renfree. (2021, Jun.) Distance calculation using haversine formula. MATLAB Central File Exchange. [Online]. Available: https://www.mathworks.com/matlabcentral/fileexchange/27785-distance-calculation-using-haversine-formula

[17] C. Shannon, "Communication in the presence of noise," in *Proc. IRE*, vol. 37, no. 1, Jan. 1949, pp. 10–21.

Cilliers Schultz received his B.Eng in Computer and Electronic Engineering in 2020. He is currently a second-year M.Eng student working on the comparison between spectrum sharing architectures in the Telkom CoE at the North-West University.

Applications of Terahertz Communication System in 6G Era: A Review

Akinyemi, L.A*†, Oladejo, S.O.†, Ekwe, S.O.†, Ajibare, A.T.†, Ventura, N.†, Shoewu,O.O*
* *Department of Electronic and Computer Engineering, Lagos State University, Lagos, Nigeria*
† *Department of Electrical Engineering, University of Cape Town, South Africa*
[1]ltfaki001@myuct.ac.za ; [2]oldsun002@myuct.ac.za
[3]ekwste001@myuct.ac.za; [4]ajbade004@myuct.ac.za
[5]neco.ventura@uct.ac.za
[6]oluwagbemiga.shoewu@lasu.edu.ng

***Abstract*—The extraordinary increase in size of wireless data traffic has championed the exploration of appropriate era in the radio spectrum chart to fulfil users ever-increasing demands and permit the utilisation of huge capacity and gargantuan connectivity. Hence, judging by this current radio allocation bandwidth, it is practically impossible to achieve such huge radio spectrum less than 0.09 Terahertz (THz). The THz frequency band has gained tremendous and observable attention among the research communities in recent times as a perfect candidate for cases entailing high-speed communication in sixth generation (6G) network. Hence, in this study, it is aimed at surveying cutting-edge studies to examine essential and critical ideas related to the THz system organisation. Therefore, this survey will be a good platform towards investigating novel areas for the future of wireless communications system.**

***Index Terms*—6G, Terahertz, frequency, wireless communication**

I. Introduction

The future networks characterised by trivial latency, ultra-high bandwidth and seamless communication are envisaged as potentials that will transform the process by which the global communities generate, allocate, and utilize data in form of information in the near future. More importantly, by year 2030 upwards, it is projected that the future networks will witness applications and services such as holographic calls, autonomous driving, bio-inspired internet-of things, and unmanned mobility devices. Different from present-day case in which bandwidth in the range of Megahertz (MHz) is inadequately enough to operate the aforementioned services and applications, the next generation network termed 6G will need bandwidth in the range of Terahertz (THz) to operate optimally [1]–[5].

Currently, the regularisation of the fifth generation (5G) technology has been concluded and placement has started in a number of cities around the world. The current deployed 5G technology will be unable to meet the ultra-low latency and data rates among other demands of these services and applications. These issues are taken into consideration as a major driver in the direction of design and development of telecommunication networks to a new phase of future radio networks termed 6G [1]–[3].

The move to improve human life through the expansion and development of various high-technologies is gaining a swift stride in different areas and at several levels. Regarding the micro integrated circuit area, the move centres on advancing several micro-transistors on the substrate (wafer) area, that is by trial and error forecast by the famous Moores Law [1]. In the field of telecommunication engineering, the desire is gradually tending towards increasing the data rates to meet various ever-growing service demands, which is predicted by the notable Edholms law of bandwidth [2]. Digital wireless traffic has been gaining tremendous and exceptional growth during the last few years. Although mobile data traffic is expected to increase seven times in a period of 2016 and 2021.

Notwithstanding, the video traffic is witnessing a three-time rise at about the same time [3]. The THz is a promising technology that will be operating frequency in 6G. It lies between the microwave/millimetre waves (mm Waves) and Infrared region from (1-10) THz with wavelength range (3mm-30m), respectively. This THz is going to last or sustain for a very long distance due to high frequency capability and wide bandwidth. This is an operating frequency gap between the electronics and photonics Indeed, the traffic of both the mobile and wireless devices is forecast to constitute about 70-71% of the overall traffic experienced by the year 2022 [4]–[6].

Moreover, by the year 2030, it is anticipated that the wireless data rates will be sufficiently enough to keep up with the wired broadband counterpart favourably. Such fundamental important increase of wireless utilisation has made community of researchers and scientists to study suitable areas in the radio frequency spectrum to meet the ever-increasing and demands of mobile users in the world [5], [6]. Hence, the THz has started gaining huge attention among the research communities globally. Some of the characteristics of the THz are limitless bandwidth, stable data transfer, split seconds latency, superfast and ultra-high-speed download among others making it an ideal candidate as the operating frequency in 6G era. These features are extraordinary and ensure transformation and changes the pattern via which human being and devices access information and disseminate it as well.

The underlying goal of 6G communications system is basically to enhance the performance of users data rates

and reduction of latency. Additionally, the 6G network will employ a new approach allowing new communication phenomenon to emerge with connectivity happening ubiquitously. Nevertheless, from all the technological applications and services concerning the future network (6G), the artificial intelligence (AI) and THz are shown to be new technologies in the area of radio networks. Besides, the 6G communication network will provide services and applications that are outside mobile internet including the support of AI from the backbone (core) network involving the devices and data centres via transmission backhauls. It is therefore anticipated that AI will be play a pivotal role in the planning, design, and optimisation of 6G network [6]–[11].

The question now arises that why employing THz in 6G technology? The answer to this is that THz is a good and perfect candidate which offers a significant growth of wireless usage. The THz band (0.1-10 THz) starts to gain noticeable attention from the researchers within the world community and our society due to the services it can support such as seamless data transfer, unlimited bandwidth, micro second latency, and ultra-fast download which are the characteristics of services the 6G tends to support and achieve based on users requirements and demands when fully deployed and implemented [5]–[7].

Furthermore, it also assures comprehensive throughput thereby leading to capacities in the order of Terabits per second (Tbps). Thus, compact wireless technologies above 10THz are unable to support Tbps links. An Infrared (IR) free-space optics (FSO) communication system is able to support 10Gbps wireless links in case of line-of-sight (LOS) propagation for wireless local area networks (WLANs). However, wireless technologies below 0.1THz are unable to support Tbps links.

In Long Term Evolution-Advanced (LTE-A) networks, peak data rates are in the order of 1Gbps when using a 4x4 Multiple Input Multiple Output (MIMO) scheme over 100MHz aggregated bandwidth. A 60GHz millimetre wave (mm-wave) communication system can support data rates in the order of 10Gbps within one metre. The usable bandwidth is limited to less than 7GHz, which effectively imposes an upper bound constraint on the data rates [6], [7].

II. Architecture of THz in 6G

There are three fundamental architectural designs for THz in 6G namely: THz Astronomy, THz Satellite Communication and Reconfigured Intelligence Surface (RIS) supported THz inter-Satellite link, which have been captured and shown in Figs. 1, 2, and 3, respectively.

III. Possibilities and Challenges of THz: 6G THz Wireless Communication Systems

There are several advantages of THz applications which have been stated in previous section of this review. Despite these merits of THz in relation to 6G technology, below are some of the possibilities in terms of its area of applications and possible problems that may arise.

A. Channel modelling

This involves the design and modelling such as multipath channel, 3D channel, ultra-massive MIMO channel, and time-varying channel to mention a few as regards to THz.

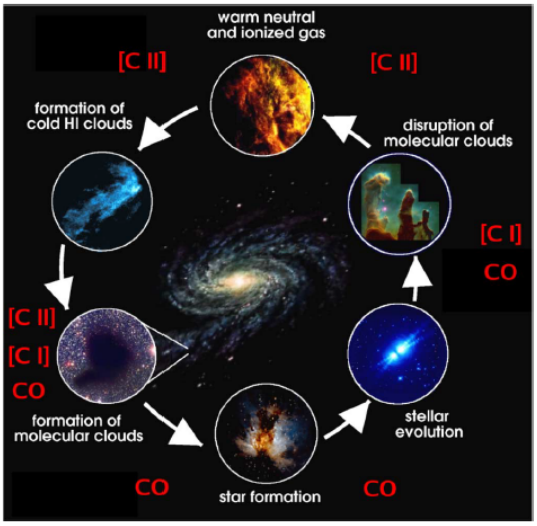

Fig. 1. Terahertz communication in 6G era for astronomy [12]

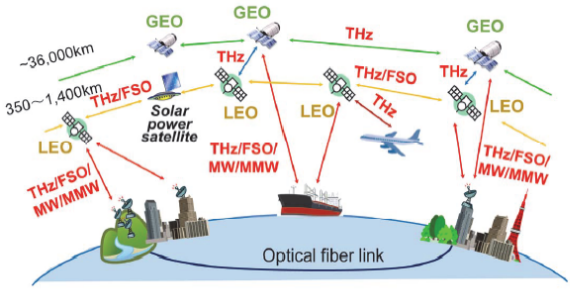

Fig. 2. Terahertz in 6G era for satellite communication [13]

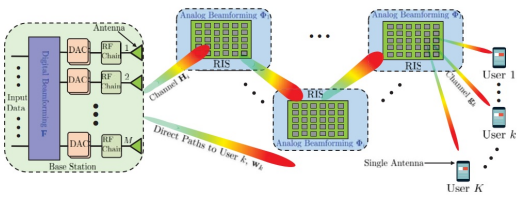

Fig. 3. Reconfigurable intelligent surface (RIS) terahertz communication in 6G era [14]

B. Physical Communication

This requires modulation scheme, synchronization, resource allocation, ultra-massive MIMO Beamforming, and Coding to be designed, formulated and afterwards implemented for the THz as the existing schemes may not work perfectly in 6G era. Furthermore, transmission distance is limited due to atmospheric attenuation as THz waves undergo

great absorption by water vapour and oxygen molecules in the atmosphere. Catering for this loss, there will be reduction of material absorption used in the design of the measurement equipment [15].

C. Wireless Networking

This includes Interface, medium access, alignment and tracking, congestion control, routing and cross-layer frame work to be designed and implemented.

D. Interdisciplinary Application cases

Such applications for THz are in sensing and imaging, joint radar and communications, THz localization, THz space communication, internet-of nano-things, internet-of-micro things, and internet-of macro things.

E. Device and Testbed Applications

Detection (Detector), power amplification, signal generator, antenna and array, machine learning, and physical and experimental testbed.

F. Challenges of THz

- Very high path loss at THz band frequencies, which poses major drawback on the communication distance.
- Development of effective and efficient ultra-broadband antennas at THz band frequencies.
- Implementation of compact high-power THz band transceivers.
- Characterization of the frequency-selective path loss.
- Development of new modulation, transmission schemes, communication protocols.
- The THz band is unregulated yet.
- THz channel modelling.

IV. Application of THz at Macro-Scale region

In this section, some of the exciting applications that THz will offer if fully employed in 6G will be briefly discussed.

- THz Band communication system can be in next generation small cells (i.e., femto, pico and so on) such as part of cellular networks or heterogeneous network.
- Directional THz band link can be employed to offer an ultra-high speed wireless backhaul to small cells.
- Implementation of compact high-power THz band transceivers.
- It enables seamless interconnection between ultra-high speed wired networks, fibre optical links and wireless devices i.e., computers, phones (tablet-like) and so forth.
- Terabit wireless personal area network which transfers the equivalent content of a slice-ray device to a tablet-type device might take less than one second with a 1Tbps link, improving the data rates of the existing technologies as Wi-Fi and so on [16].
- Secure Terabit Wireless Communication-Very narrow, beams which significantly limit the probabilities of eavesdropping by unwanted users.
- Radio Astronomy and Planetary Science-Has the great potential and capability to demonstrate about the planetary atmosphere, surface and sub-surface water, and iced contents from the space platform.
- Support fourth industrial revolution (4IR) system.

V. Application of THz at Nano-Scale region

In this section, some of the interesting applications that THz will offer if fully employed in 6G will be briefly discussed.

- Health monitory system using nano-sensor network.
- Internet of nano-things-nano transceiver and nano-antennas inserted or rooted in every object to allow them to be perpetually connected to the cyberspace (internet).
- Ultra-High-speed on-chip communication provides efficient and scalable features and means of inter-communication in wireless on-chip networks and planar nano-antennas.

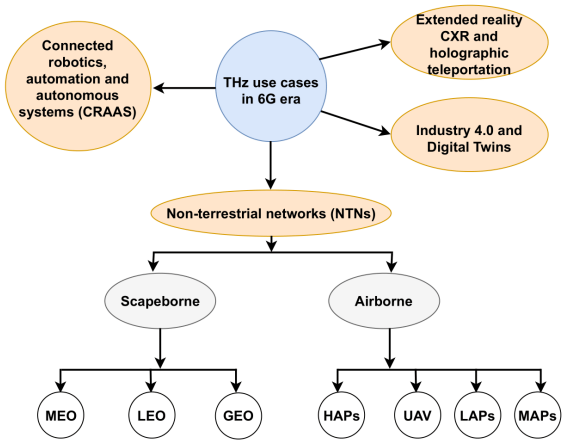

Fig. 4. Use cases for enable terahertz communication in 6G era.

VI. Use case for THz communication in 6G era

Some of the use cases and application that will be fully supported by THz are summarily depicted in Fig. 4. The service and applications that will be primarily supported by THz in 6G era use case are non-terrestrial networks (NTNs), which can be further divided into scapeborne (medium earth orbit (MEO), low earth orbit (LEO), and geostationary earth orbit (GEO)) and airborne such as high altitude platform (HAPs), unmanned aerial vehicle (UAV), low altitude platforms (LAPs) and medium altitude platform (MAPs), connected robotics, automatic and autonomous systems (CRAAS), extended reality (XR), holographic teleportation, industry 4.0, and digital twin technology [17].

In [17], the following interesting areas were covered and reiterated partially or in detail as related primarily to applications of THz in 6G domain: nanocommunications and networking; channel measurement and modelling using THz as an operating frequency; design of modulation scheme, channel estimation, detection and equalisation; hybrid-based

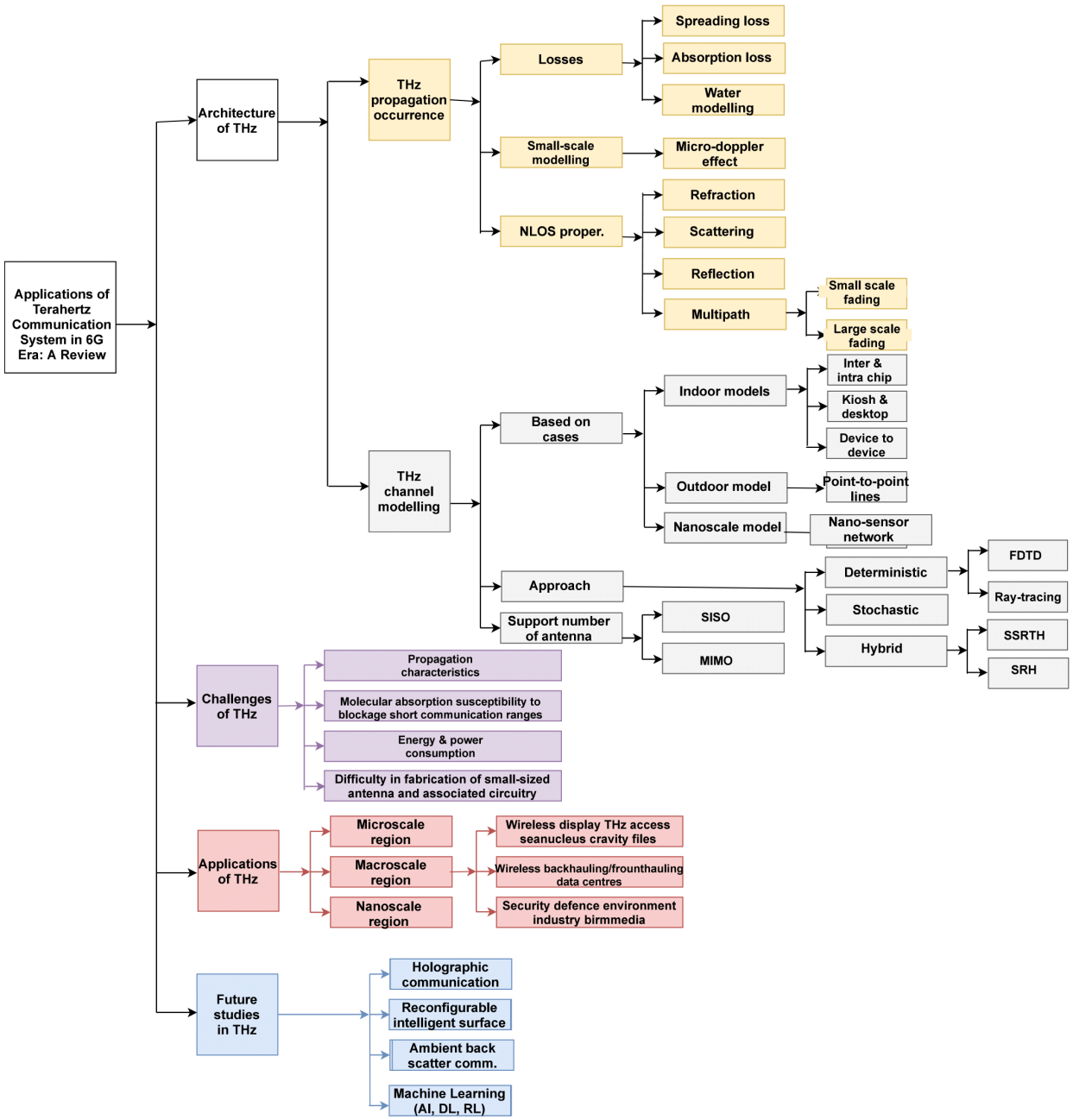

Fig. 5. Taxonomy of the application for terahertz communication system in 6G era.

beamforming and aerial communication system; device modelling and circuits for THz transceivers; and networking aspects and protocols. Hence, wireless communications and communications networks in the THz domain are nevertheless a developing and in its infancy field and kind of problems still exist that need to be addressed in the near future.

VII. Future Study Directions in THz

As THz communication is gaining increasing research interest, several research areas still need to be adequately addressed. In this section, we highlight below these interesting topics for researchers to investigate [18]–[20].

- THz-imaging.
- THz-ultra-massive MIMO.
- Implementation of compact high-power THz band transceivers.
- THz virtual reality (VR), augmented reality (AR), extended reality (XR) perception through cellular network.
- THz communication for mobile heterogeneous networks (HetNets).
- THz 3D beamforming techniques.
- THz communication for urban environment.
- THz automotive applications.
- THz security measures.
- Hybrid THz-optical wireless communication links.
- THz for enhanced data centre performance.
- Losses and validity of transmission distance

TABLE I
SUMMARY OF KEY IDEAS OF THZ IN 6G ERA

Variables	Reliance in Frequency	Effect on 6G THz in Communication System	THz versus others
Shinning impacts	Improves with frequency	Resistant in THz space-based communication systems	No lucid impact at others, such as millimetre waves, microwaves. THz is less affected than Free Space Optics (FSO)
Meteorological conditions impacts	Frequency-reliant flying/area with scattering particles	THz open-air communication is characterized by high limitation with huge rain attenuation	Better than others, poorer than FSO
Atmospheric loss	Frequency-reliant pathloss crest occur	Frequency-reliant spectral windows with different bandwidth	No obvious impact at microwave level, both oxygen and water molecules are form at THz region
Line-of-sight (LOS) probability, shadowing effect and diffraction	Insignificant diffraction, penetration losses and shadowing effects, vary with frequency arithmetically, LOS probability is frequency-dependent	High rate of sparsity, limited or restricted multiple path effect and dense spacial re-utilisation	Better than microwave but poor and weaker than FSO

VIII. CONCLUSION

To meet the needs for higher data rates by users with help services of different pattern, new and effective wireless communication technologies for a range of communication connections need to be formulated and designed. While 5G network systems that are being implemented in several parts across the world employing the concept of millimetre wave frequency band, the society of academics and scientists is examining the significance of THz frequency as a perfect candidate to provide solution to support above 5G network technology and allow applications that are unable to be implemented via the 5G technology owing to unanticipated challenges. In this survey paper, an all-inclusive review has been advanced regarding the THz wireless communication system in an effort to review the channel models, devices and as well as advantages in terms of its applications related to the advancement of THz architectural designs. With the arrival of THZ communication services, communities will have to be expectant of limitless wireless link with abilities to expand the present technological network system (5G). The likes of applications and services such as autonomous systems, holographic calls, high-definition streaming, virtual, augmented and extended reality alongside smart cities will be made possible via the use of THz frequency band in 6G era. This is the reason the traditional cellular communication system has failed appropriately and satisfactorily to characterise these novel services and applications. Hence, state-of-the-art techniques in the context of optimisation and network planning by the scientists and engineers will be in demand.

ACKNOWLEDGEMENT

The authors would like to thankfully appreciate the financial support received from TELKOM SA via the Telkom Centre of Excellence (CoE) in Broadband Networks and Application at the University of Cape Town, and the Department of Electronics and Computer Engineering, Lagos State University, Lagos, Nigeria.

REFERENCES

[1] G. E. Moore, "Cramming more components onto integrated circuits," *Proceedings of the IEEE*, vol. 86, no. 1, pp. 82–85, 1998.
[2] S. Cherry, "Edholm's law of bandwidth," *IEEE spectrum*, vol. 41, no. 7, pp. 58–60, 2004.
[3] C. V. N. Index, "Cisco visual networking index: Forecast and methodology 2015-2020," *White paper, CISCO*, 2015.
[4] G. Forecast, "Cisco visual networking index: global mobile data traffic forecast update, 2017–2022," *Update*, vol. 2017, p. 2022, 2019.
[5] H. Elayan, O. Amin, B. Shihada, R. M. Shubair, and M.-S. Alouini, "Terahertz band: The last piece of rf spectrum puzzle for communication systems," *IEEE Open Journal of the Communications Society*, vol. 1, pp. 1–32, 2019.
[6] R. Li, "Towards a new internet for the year 2030 and beyond," in *Proc. 3rd Annu. ITU IMT-2020/5G Workshop Demo Day*, 2018, pp. 1–21.
[7] T. S. Rappaport, Y. Xing, O. Kanhere, S. Ju, A. Madanayake, S. Mandal, A. Alkhateeb, and G. C. Trichopoulos, "Wireless communications and applications above 100 ghz: Opportunities and challenges for 6g and beyond," *Ieee Access*, vol. 7, pp. 78 729–78 757, 2019.
[8] K. B. Letaief, W. Chen, Y. Shi, J. Zhang, and Y.-J. A. Zhang, "The roadmap to 6g: Ai empowered wireless networks," *IEEE Communications Magazine*, vol. 57, no. 8, pp. 84–90, 2019.
[9] S. Chen, Y.-C. Liang, S. Sun, S. Kang, W. Cheng, and M. Peng, "Vision, requirements, and technology trend of 6g: How to tackle the challenges of system coverage, capacity, user data-rate and movement speed," *IEEE Wireless Communications*, vol. 27, no. 2, pp. 218–228, 2020.
[10] I. F. Akyildiz, J. M. Jornet, and C. Han, "Terahertz band: Next frontier for wireless communications," *Physical Communication*, vol. 12, pp. 16–32, 2014.
[11] M. H. Alsharif, M. A. Albreem, A. A. Solyman, and S. Kim, "Toward 6g communication networks: Terahertz frequency challenges and open research issues," *Computers, Materials & Continua*, vol. 66, no. 3, pp. 2831–2842, 2021.
[12] C. Kulesa, "Terahertz spectroscopy for astronomy: From comets to cosmology," *IEEE Transactions on Terahertz Science and Technology*, vol. 1, no. 1, pp. 232–240, 2011.
[13] T. Nagatsuma and A. Kasamatsu, "Terahertz communications for space applications," in *2018 Asia-Pacific Microwave Conference (APMC)*. IEEE, 2018, pp. 73–75.
[14] C. Huang, Z. Yang, G. C. Alexandropoulos, K. Xiong, L. Wei, C. Yuen, and Z. Zhang, "Hybrid beamforming for ris-empowered multi-hop terahertz communications: A drl-based method," *arXiv preprint arXiv:2009.09380*, 2020.
[15] X. Jiang, M. Sheng, N. Zhao, C. Xing, W. Lu, and X. Wang, "Green uav communications for 6g: A survey," *Chinese Journal of Aeronautics*, 2021.
[16] Y. Zhao, W. Zhai, J. Zhao, T. Zhang, S. Sun, D. Niyato, and K.-Y. Lam, "A comprehensive survey of 6g wireless communications," *arXiv preprint arXiv:2101.03889*, 2020.
[17] I. F. Akyildiz, T. Kawanishi, W. Gerstacker, X. Dong, and A. Babakhani, "Guest editorial special issue on thz communications and networking," *IEEE Journal on Selected Areas in Communications*, vol. 39, no. 6, pp. 1499–1505, 2021.

[18] C. De Alwis, A. Kalla, Q.-V. Pham, P. Kumar, K. Dev, W.-J. Hwang, and M. Liyanage, "Survey on 6g frontiers: Trends, applications, requirements, technologies and future research," *IEEE Open Journal of the Communications Society*, vol. 2, pp. 836–886, 2021.

[19] Y. Zhao, J. Zhao, W. Zhai, S. Sun, D. Niyato, and K.-Y. Lam, "A survey of 6g wireless communications: Emerging technologies," in *Future of Information and Communication Conference*. Springer, 2021, pp. 150–170.

[20] W. Jiang, B. Han, M. A. Habibi, and H. D. Schotten, "The road towards 6g: A comprehensive survey," *IEEE Open Journal of the Communications Society*, vol. 2, pp. 334–366, 2021.

Lateef Adesola Akinyemi received a B.Sc (LASU) Electronic and Computer Engineering, Lagos, an M.Sc (LASU) in Electronic and Computer Engineering, and M.Sc (UNILAG) in Electrical and Electronics Engineering(Communication Engineering Option) and PhD in the Department of Electrical Engineering, UNiversity of Cape Town. His research areas are Wireless Communications, Computational Electronics Analysis, Wavelets and Frames, Electromagnetic fields and Waves, Radio Wave propagation, Antennas, Microwave Engineering and Quantum Electrodynamic Applications to Plasmonic, Photonic and Mesoscopic devices.

Sunday Oladayo Oladejo received the B.Eng degree in electrical and electronic engineering from the Federal University of Technology, Akure, Nigeria, in 2004 and the M.Eng degree in communication engineering from the Federal University of Technology, Minna, Nigeria, in 2016. He is currently pursuing a PhD degree in electrical engineering at the University of Cape Town, South Africa. From 2007 to 2017, he was Senior Core Network Engineer with Glo Mobile, Nigeria. His research interest includes radio resource management in wireless networks, and artificial intelligence.

Stephen Obono Ekwe received the B.Eng degree in Electrical and Electronic Engineering from the Cross River University of Technology, Calabar, Nigeria, in 2008 and the M.Sc. degree in Personal, Mobile and Satellite Communication from the University of Bradford, West Yorkshire, England, in 2013. He is currently a Doctoral Candidate in Electrical Engineering at the University of Cape Town, South Africa. His research interest includes 5G, Internet of Things, Social Network Analytics, Machine Learning, and Resource Optimization and Management in Wireless Communication Networks.

Oluwagbemiga Omotayo Shoewu B.Sc. (Electronic and Computer Engineering). M.Sc. (Electronics and Communications), PhD (Electronics and telecommunications), MIAENG, MIEEE, MIET, MCPN, MNCS, MNSE, MNIEM, MNIEEE, MMEACSE. SMIRED, MIACSIT, MIAJC, MSDIWC, MIAASSE. He is a lecturer at the faculty of Engineering, Lagos State University, and his research interests are Electronics, Signal Propagation, Telecommunications, Embedded Systems and Computational Analysis.

Slice-Aware User Association and Resource Allocation in Integrated Terrestrial and Non-Terrestrial Networks

Denise J. Birabwa*, Daniel Ramotsoela*, Neco Ventura*
*Department of Electrical Engineering
University of Cape Town, Rondebosch 7700, South Africa
Email: brbden001@myuct.ac.za, daniel.ramotsoela@uct.ac.za, neco.ventura@uct.ac.za

***Abstract*—The integration of terrestrial with non-terrestrial networks (NTNs) promises a truly ubiquitous and seamlessly connected network. However, this integration will comprise different radio access networks (RANs) with diverse constraints and capabilities to meet the user's contrasting requirements. Therefore, optimally mapping the user's needs to the appropriate RAN presents a challenge in the radio resource management of the Integrated terrestrial and non-terrestrial network (ITNTN). In this paper, a slice-aware user association and resource allocation problem for the ITNTN is formulated. A heuristic algorithm that maximizes the spectrum efficiency of the network is proposed; it associates and allocates resources to users based on their quality of service (QoS) requirements and prioritizes the use of NTNs for highly mobile users. To analyze the performance of the proposed algorithm, we first compare three access node (AN) selection criteria; maximum signal-to-interference-plus-noise-ratio (SINR), least load, and random association. Results show that association based on SINR yields the highest spectrum efficiency (SE) and a relatively high user acceptance ratio (AR). Then, the proposed slice-aware user association and resource allocation algorithm is compared to the slice-unaware scheme. Simulation results reveal that the proposed algorithm achieves higher overall network SE and user AR.**

***Index Terms*—RAN user association, resource allocation, terrestrial networks, non-terrestrial networks, spectrum efficiency**

I. Introduction

The integration of terrestrial networks (TNs) with non-terrestrial networks (NTNs) has been proposed as one of the key enabling features that will facilitate ubiquitous and seamless broadband connectivity in the sixth generation of wireless networks (6G) [1]. The considered NTNs in this integration are the satellite communications (SatComs) and the unmanned aerial vehicles (UAVs), which can be categorized into the high altitude platforms (HAPs) and the low altitude platforms (LAPs) [2] Different use-cases of the integrated terrestrial and non-terrestrial network (ITNTN) have been defined, including the communication and resilience use-case, in which the NTNs are deployed to assist the TNs during periods of traffic overload [2].

Similar to [3], [4], this paper considers the communication and resilience use-case. In such a usage scenario, there exists a large number of users that cannot be supported by the TN access nodes (ANs), necessitating direct radio access to all available radio access networks (RANs), including the NTNs. The problem that arises then is how to map the different user requirements to the appropriate RAN. According to [1], the envisaged use-cases in 6G will include further enhanced mobile broadband (feMBB), enhanced ultra-reliable and low-latency communications (euRLLC), ultra-massive machine-type communications (umMTC), long-distance and high-mobility communication (LDHMC), and extremely low-power communications (ELPC). Associating such users with different QoS requirements to the appropriate RAN in the ITNTN is rigorous and complex, given that the RANs have different characteristics and constraints. For instance, the TN has higher throughput and lower latency when compared to the NTNs. Still, it has limited resources to support an increased number of users in situations of traffic overload [5]. Moreover, TN's coverage per base station (BS) limitation results in an increased number of handoffs for the LDHMC service group. Therefore, using the NTNs that have wider coverage for such applications will limit the number of handoffs, consequently reducing the handoff signaling overhead, delays, and probability of handoff failure, thus increasing the QoS for such applications [6]. On the contrary, Satcoms' long propagation delay makes it unsuitable for delay intolerant users in the euRLLC service group. Similarly, the UAV networks have a limited number of channels; thus, it is essential to prioritize their use for traffic whose QoS requirements may not be met satisfactorily by the other RANs [5].

Recent proposals in the literature on resource management in the ITNTN do not address the RANs' different capabilities and limitations in meeting the diverse user QoS requirements. Moreover, many do not account for the differences in users' QoS needs and do not consider integrating all four RANs, i.e., TN, LAP, HAP, and SatComs. Consequently, this work addresses the need for a user association and resource allocation algorithm that considers the strengths and limitations of the different RANs and optimally maps user requirements to the appropriate RAN. The differences in user QoS requirements are considered by introducing slice awareness in the user association decision. Three use-cases: feMBB, euRLLC, and LDHMC, are considered in this work. In addition, service provisioning to the euRLLC service group is prioritized, and its access to the Satcoms is limited. Also, the work prioritizes the use of NTN RAN over the TN for long-distance and highly mobile applications.

To determine the best AN a user should associate with,

we compare three AN selection criteria. One is based on connecting a user to an appropriate AN with the highest SINR. The other to an AN with the least load, while the third associates a user randomly to any available but appropriate AN. According to the simulation results, association using SINR matching achieves the highest spectrum efficiency (SE) at a comparatively high user acceptance ratio (AR). The performance of our proposed slice-aware algorithm is then compared with the slice-unaware algorithm that does not consider the; (i) heterogeneity in user traffic types and (ii) uniqueness in the capabilities and limitations of the RANs. Simulation results show that the slice-aware algorithm outperforms the slice-unaware scheme in overall network SE and AR. The key contributions of this work are therefore summarized as:

- Formulation of a novel slice-aware user association and resource allocation problem that maximizes the spectrum efficiency of the integrated terrestrial-aerial-space network subjected to limited resource budget, power budget, and minimum user QoS requirements constraints.
- Prioritization of the mission-critical slice and the use of NTNs over TNs for long-distance and highly mobile users.
- Presentation of numerical results that compare different AN selection criteria and the slice-aware algorithm to the slice-unaware algorithm. The results show that our proposed algorithm yields better overall network SE and user AR.

II. Related Work

In recent times, several works have addressed user association and resource allocation in the ITNTN. In [7], the authors propose a resource allocation problem that maximizes the overall sum rate of the integrated terrestrial and UAV RANs together with the macro BSs and satellite backhaul links. The authors supplement this work in [3] by considering the limited life endurance of UAVs and the energy consumption costs of the ANs. In [8], the authors propose a load balancing algorithm for a TN and satellite network. Traffic from an overloaded terrestrial cell is offloaded first to neighboring terrestrial cells and then to the satellite cell. Only delay-tolerant traffic is offloaded to the satellite network. The authors in [9] propose an algorithm that optimizes the throughput of users and location of HAPs in an integrated satellite, airborne and terrestrial network. The authors in [10] propose an algorithm that maximizes the energy efficiency of an integrated satellite/terrestrial cache-enabled RAN. In [4], the authors propose an optimization problem that maximizes the network capacity while ensuring QoS in terms of minimized interference between a large number of users in an integrated terrestrial and satellite network. The authors in [11] maximized the minimum ergodic achievable rate of a user-UAV link subjected to constraints on UAV's transmit power, tolerable interference, UAV velocity, and acceleration, UAV height, terrestrial and satellite backhaul capacity, and maximum allowable energy consumption of the UAV.

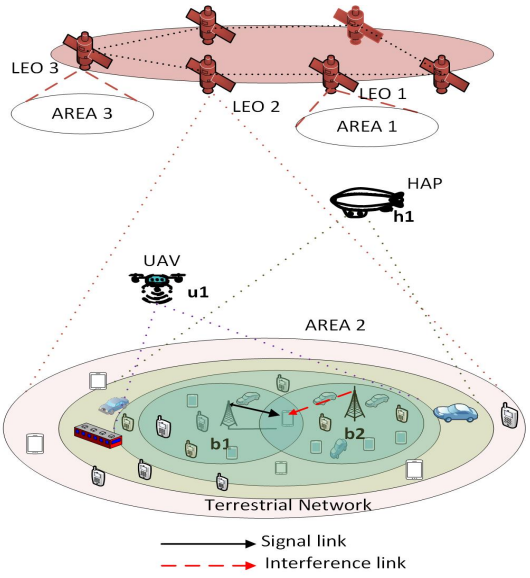

Fig. 1. System Model.

All the works in [3], [4], [7]–[11] did not consider the idea of 6G, which is to have all four RANs, that is, space (satellite), aerial (LAPs and HAPs), and the TN ANs concurrently provide radio access to users. Moreover, they do not use the concept of slicing to differentiate different use-cases and thus effectively and flexibly associate users to appropriate RANs depending on their QoS requirements. [8] did not consider power constraint, which is critical especially to NTNs such as LAPs and HAPs, which are limited by power.

III. System Model and Assumptions

A. General Model

The downlink transmission of an ITNTN that supports a set of users $\mathcal{I} = \{1, 2, 3, ..., |\mathcal{I}|\}$ is considered. The ITNTN comprises four tiers namely LAP, HAP, SatComs, and a Macro tier as depicted in Fig. 1. A LAP access node (AN) belonging to the LAP tier is indexed as $u \in \mathcal{U}$. Similarly, a HAP AN in the HAP tier is denoted as $h \in \mathcal{H}$ and a satellite AN in the SatComs network is represented as $s \in \mathcal{S}$. Likewise, a macro base station (MBS) in the TN is indexed as $b \in \mathcal{B}$. The system is considered to support three slice use-cases, namely; feMBB, euRLLC, and LDHMC, denoted by $\mathcal{E}$, $\mathcal{R}$, and $\mathcal{D}$ respectively. The sets of users demanding the slice cases $\mathcal{E}$, $\mathcal{R}$, and $\mathcal{D}$ are denoted by $\mathcal{I}_{\mathcal{E}}$, $\mathcal{I}_{\mathcal{R}}$, and $\mathcal{I}_{\mathcal{D}}$ respectively, such that, $i_{\mathcal{E}} \in \mathcal{I}_{\mathcal{E}}$, $i_{\mathcal{R}} \in \mathcal{I}_{\mathcal{R}}$, $i_{\mathcal{D}} \in \mathcal{I}_{\mathcal{D}}$, $\mathcal{I} = \mathcal{I}_{\mathcal{E}} \cup \mathcal{I}_{\mathcal{R}} \cup \mathcal{I}_{\mathcal{D}}$ and $\mathcal{I}_{\mathcal{E}} \cap \mathcal{I}_{\mathcal{R}} \cap \mathcal{I}_{\mathcal{D}} = \emptyset$. Without loss of generality, this work assumes that the users in $\mathcal{I}_{\mathcal{E}}$ and $\mathcal{I}_{\mathcal{R}}$ are static while those in $\mathcal{I}_{\mathcal{D}}$ are mobile. It is further assume that each user $i \in \mathcal{I}$ can access any of the available tiers $j \in \{\mathcal{B}, \mathcal{U}, \mathcal{H}, \mathcal{S}\}$ within its coverage. An AN of the j^{th} tier $o_j \in \mathcal{O}$ where $\mathcal{O} = \{\mathcal{B} \cup \mathcal{U} \cup \mathcal{H} \cup \mathcal{S}\}$, is considered to own a set $\mathcal{C}_j$ of basic bandwidth units (BBUs), with each BBU $c_j \in \mathcal{C}_j$ having a bandwidth denoted by $\mathcal{T}_{c_j}$. The total bandwidth of the ITNTN is denoted by Φ.

The system model used for the LEO SatComs tier is similar to that used in [10]. Since the LEO satellite provides access

over a given area for only a certain limited period, it is assumed that each non-overlapping terrestrial area is served by one satellite at a time, as illustrated in Figure 1. Consequently, a user can access one satellite at any given time. Each satellite follows a predictable pattern in which it periodically views one area after another, well-controlled by the Network Control Center [10]. The handover process between satellites is out of the scope of this work and hence shall not be considered.

B. Channel model

The coordinate of a user i is denoted by $t_i = \{[x_i, y_i]^T \in \mathbb{R}^2 | i \in \mathcal{I}\}$, while the ground projection of an NTN AN $o_j \in \{\mathcal{U}, \mathcal{H}, \mathcal{S}\}$ is denoted as $t_{o_j} = \{[x_{o_j}, y_{o_j}]^T \in \mathbb{R}^2\}$. The height of an NTN AN $o_j \in \{\mathcal{U}, \mathcal{H}, \mathcal{S}\}$ is denoted as z_{o_j}. Consequently, the distance $d_{o_j,i}$ of user i to the NTN AN o_j is given as

$$d_{o_j,i} = \sqrt{\|t_i - t_{o_j}\|_2^2 + z_{o_j}^2} \quad \forall j \in \{\mathcal{U}, \mathcal{H}, \mathcal{S}\},\ \forall i \in \mathcal{I}\ , \quad (1)$$

where $\|.\|_2$ is the 2-norm operator. It should be noted that for the MBS tier, $z_{o_j} = 0$ in (1).

Path loss modelling is classified into three categories: (i) TN, (ii) UAV, i.e., HAPs and LAPs and, (iii) SatComs.

1) Terrestrial Network Path loss model: The Path loss of a user i located at a distance $d_{o_j,i}$ meters from an urban MBS $o_j \in \mathcal{B}$ and communicating via the BBU $c_j \in \mathcal{C}_j | j \in \mathcal{B}$ is given by [12]

$$PL_{o_j,i,c_j} = 40(1 - 4 \times 10^{-3} h_{o_j}) \log_{10}(\frac{d_{o_j,i}}{1000}) - 18 \log_{10} h_{o_j} + 21 \log_{10} f_{o_j,c_j} + 80 + \tau_{o_j}\ , \quad \forall\ j \in \mathcal{B},\ \ \forall\ i \in \mathcal{I}\ . \quad (2)$$

The term f_{o_j,c_j} is the carrier frequency in MHz, h_{o_j} is the MBS height in meters while τ_{o_j} is the path loss due to shadow fading assumed to be a zero-mean random variable.

2) UAV Path loss model: The path loss model used for signal propagation from a UAV AN to a user is defined in [13]. A user i located at a distance $d_{o_j,i}$ from a UAV AN $o_j \in \{\mathcal{U} \cup \mathcal{H}\}$ experiences path loss given by

$$PL_{o_j,i,c_j} = \begin{cases} PL^{LoS}_{o_j,i,c_j} = 20 \log_{10} d_{o_j,i} + 20 \log_{10} f_{o_j,c_j} \\ -27.55 + \eta_{LoS},\ \text{Line of sight (LoS) scenario} \\ PL^{NLoS}_{o_j,i,c_j} = 20 \log_{10} d_{o_j,i} + 20 \log_{10} f_{o_j,c_j} \\ -27.55 + \eta_{NLoS},\ \text{non LoS (NLoS) scenario}\ , \end{cases} \quad (3)$$

where f_{o_j,c_j} is carrier frequency in MHz, $d_{o_j,i}$ is distance in meters determined using (1), η_{LoS} or η_{NLoS} is the additional loss due to shadowing, scattering and reflections caused by buildings, foliage etc., which is dependent on whether the propagation is LoS or NLoS [13].

3) SatCom path loss model: The path loss of a user i a distance $d_{o_j,i}$ from an AN $o_j \in \{\mathcal{S}\}$, assuming clear sky conditions is given by [2]

$$PL_{o_j,i,c_j} = 20 \log_{10} d_{o_j,i} + 20 \log_{10} f_{o_j,c_j} - 27.55 + \tau + CL + PL^k + PL^e + PL^y,\ \ \forall\ o_j \in \mathcal{S}\ . \quad (4)$$

The range $d_{o_j,i}$ is in meters and can be determined using (1). The term τ in (4) accounts for shadow fading while CL depicts clutter loss caused by surrounding buildings and objects on the ground. Both terms are dependent on whether the propagation is LoS or NLoS. The terms PL^k, PL^e, and PL^y denote attenuation due to atmospheric gases, ionospheric or tropospheric scintillation and building entry loss respectively.

4) Channel gain: Having derived the large scale fading effects of path loss and shadowing in the preceding sections III-B1 to III-B3, the linear channel gain between the AN $o_j \in \mathcal{O}$ where $j \in \{\mathcal{B}, \mathcal{U}, \mathcal{H}, \mathcal{S}\}$ and user i, communicating via a bbu c_j is given by [12]

$$\Gamma_{o_j,i,c_j} = 10^{-\frac{PL_{o_j,i,c_j}}{10}}\ . \quad (5)$$

The signal-to-interference-plus-noise (SINR) ratio experienced by the user i is then given by

$$\gamma_{o_j,i_q,c_j} = \begin{cases} \dfrac{P_{o_j,i_q,c_j}\ \Gamma_{o_j,i_q,c_j}}{\sigma^2 \quad + \sum\limits_{\substack{l_j \in \mathcal{O} \\ l_j \neq o_j}} P_{l_j,i_q,c_j}\ \Gamma_{l_j,i_q,c_j}} \\ \forall i_q \in \{\mathcal{I}_\mathcal{E} \cup \mathcal{I}_\mathcal{R}\},\ \forall j \in \{\mathcal{B}, \mathcal{U}, \mathcal{H}, \mathcal{S}\}\ \text{static user} \\ \dfrac{P_{o_j,i_q,c_j}\ \Gamma_{o_j,i_q,c_j} |\beta_{o_j,i_q,c_j}|^2}{\sigma^2 \quad + \sum\limits_{\substack{l_j \in \mathcal{O} \\ l_j \neq o_j}} P_{l_j,i_q,c_j}\ \Gamma_{l_j,i_q,c_j}\ |\beta_{l_j,i_q,c_j}|^2} \\ \forall i_q \in \mathcal{I}_\mathcal{D},\ \forall j \in \{\mathcal{B}, \mathcal{U}, \mathcal{H}, \mathcal{S}\}\ \ \text{mobile user}\ , \end{cases} \quad (6)$$

where β_{o_j,i_q,c_j} and β_{l_j,i_q,c_j} denote the small-scale fast fading component that accounts for mobility of a user and is assumed to be independent and identically distributed (i.i.d) as $\mathcal{CN}(0,1)$ [14]. P_{o_j,i_q,c_j} is the transmit power from an AN/BS o_j to a user i_q using bbu c_j. The transmit power P_{o_j,i_q,c_j} is assumed to be fixed and uniformly allocated to each bbu c_j. On the other hand, P_{l_j,i_q,c_j} is the interfering transmit power from another AN l_j in the j^{th} RAN reaching the same user i_q, on the same bbu c_j. For simplicity, only co-tier interference is considered, as described by eq. (6).

The data rate achieved by the user $i \in \mathcal{I}$ on the bbu c_j is given by the Shannon capacity as

$$\mathcal{L}_{o_j,i,c_j} = \mathcal{T}_{c_j} \log_2(1 + \gamma_{o_j,i,c_j})\ , \quad (7)$$

where $\mathcal{T}_{c_j}$ is the bandwidth for bbu $c_j \in \mathcal{C}_j$.

IV. Problem Formulation

The slice-aware resource allocation and user association problem is formulated as an SE maximization problem. Mathematically, SE is the ratio of the entire network's sum rate to total bandwidth [15], as shown in (8).

$$\Omega = \frac{1}{\Phi} \sum_{j \in \{\mathcal{B},\mathcal{H},\mathcal{U},\mathcal{S}\}} \sum_{o_j \in \mathcal{O}} \sum_{i \in \mathcal{I}} \sum_{c_j \in \mathcal{C}_j} \pi_{j,i}\ \mu_{o_j,i}\ \omega_{o_j,i,c_j} \mathcal{L}_{o_j,i,c_j} \quad (8)$$

where $\pi_{j,i}$ and $\mu_{o_j,i}$ are association factors and ω_{o_j,i,c_j} is a resource allocation factor. $\pi_{j,i}$ specifies the RAN $j \in \{B, U, H, S\}$ a user $i \in \mathcal{I}$ is associated to, $\mu_{o_j,i}$ indicates the specific AN $o_j \in \mathcal{O}$ onto which this user is attached while ω_{o_j,i,c_j} indicates whether a bbu $c_j \in \mathcal{C}_j$ is allocated to the user i.

The objective is to maximize the overall network SE, constrained to limited resource budget, power budget and QoS

requirements. Consequently, the optimization problem can be formulated as:

$$\max_{\pi_{j,i},\ \mu_{o_j,i},\ \omega_{o_j,i,c_j}} \quad \Omega \tag{9}$$

s.t.

$$C1: \pi_{j,i} = \{0,1\},\ \mu_{o_j,i} = \{0,1\},\ \omega_{o_j,i,c_j} = \{0,1\},$$
$$\forall\ j \in \{\mathcal{B},\mathcal{H},\mathcal{U},\mathcal{S}\},\ \ \forall\ o_j \in \mathcal{O},\ \ \forall c_j \in \mathcal{C}_j,\ \ \forall\ i \in \mathcal{I} \tag{9a}$$

$$C2: \sum_{j\in\{\mathcal{B},\mathcal{H},\mathcal{U}\}} \pi_{j,i}\mu_{o_j,i}\omega_{o_j,i,c_j} = 1, \quad \forall\ i_R \in \mathcal{I}_R \tag{9b}$$

$$C3: \quad \psi_{o_j} \sum_{j\in\{\mathcal{U},\mathcal{H},\mathcal{S}\}} \pi_{j,i}\mu_{o_j,i}\omega_{o_j,i,c_j}$$
$$\psi_{o_j}=1 \Big| \sum_{i\in\mathcal{I}}\sum_{c_j\in\mathcal{C}_j} \pi_{j,i}\mu_{o_j,i}\omega_{o_j,i,c_j}\mathcal{T}_{c_j} \le \Phi_{o_j}$$
$$+ \quad \delta_{o_j} \sum_{j\in\{\mathcal{B}\}} \pi_{j,i}\mu_{o_j,i}\omega_{o_j,i,c_j} \leqslant 1, \ \ \forall\ i_D \in \mathcal{I}_D \tag{9c}$$

$$C4: \psi_{o_j} = \{0,1\}, \delta_{o_j} = \{0,1\} \quad \forall\ o_j \in \{\mathcal{B}\cup\mathcal{U}\cup\mathcal{H}\cup\mathcal{S}\} \tag{9d}$$

$$C5: \psi_{o_j} + \delta_{o_j} = 1 \quad \forall\ o_j \in \{\mathcal{B}\cup\mathcal{U}\cup\mathcal{H}\} \tag{9e}$$

$$C6: \sum_{j\in\{\mathcal{B},\mathcal{H},\mathcal{U},\mathcal{S}\}} \pi_{j,i}\mu_{o_j,i}\omega_{o_j,i,c_j} \leqslant 1, \ \ \forall\ i_E \in \mathcal{I}_E \tag{9f}$$

$$C7: \pi_{j,i}\mu_{o_j,i}\omega_{o_j,i,c_j}\left[L_{o_j,i,c_j} - L^v_{thres}\right] \geqslant 0\ ,$$
$$\forall\ i \in \mathcal{I},\ \ \forall\ v \in \{\mathcal{E},\mathcal{R},\mathcal{D}\} \tag{9g}$$

$$C8: P_{o_j,i,c_j} \geqslant 0, \quad \forall\ c_j \in \mathcal{C}_j \tag{9h}$$

$$C9: \sum_{i\in\mathcal{I}}\sum_{c_j\in\mathcal{C}_j} \pi_{j,i}\mu_{o_j,i}\omega_{o_j,i,c_j}P_{o_j,i,c_j} \le P^{thres}_{o_j}, \quad \forall\ o_j \in \mathcal{O} \tag{9i}$$

$$C10: \sum_{i\in\mathcal{I}}\sum_{c_j\in\mathcal{C}_j} \pi_{j,i}\mu_{o_j,i}\omega_{o_j,i,c_j}\mathcal{T}_{c_j} \le \Phi_{o_j}, \quad \forall\ o_j \in \mathcal{O} \tag{9j}$$

In the optimization problem depicted in (9), Constraint C1 indicates that the decision variables $\pi_{j,i}$, $\mu_{o_j,i}$ and $\omega_{o_j,i,c_{o_j}}$ are either zero or one. When $\pi_{j,i}$ is zero, then the user i is not associated to the j^{th} network, and one implies otherwise. On the other hand, if $\mu_{o_j,i}$ is zero, then the user isn't associated with the AN o_j, while one means association. In the same manner, $\omega_{o_j,i,c_{o_j}} = 1$ implies the BBU is allocated to user i while $\omega_{o_j,i,c_{o_j}} = 0$ implies otherwise. Since slice $\mathcal{R}$ serves mission-critical applications for which denial of service has adverse consequences, constraints C2 indicates that users in this slice must be attached to the network, with each user associated to only one of either the MBS, LAP, or HAP AN at a time. In constraint C3, the use of the NTN ANs over the TN MBS, for slice $\mathcal{D}$ users is prioritized by introducing priority factors ψ_{o_j} and δ_{o_j}. The priority factor $\psi_{o_j} = 1$ only when there exists sufficient resource budget in the NTN ANs to meet the slice $\mathcal{D}$ user QoS requirements. When $\psi_{o_j} = 1$, then using constraint C5, the priority factor $\delta_{o_j} = 0$, hence the user will only be associated with an NTN AN. On the other hand, when the NTN resource budget is depleted, then $\psi_{o_j} \neq 1$, hence from constraint C4, $\psi_{o_j} = 0$, making $\delta_{o_j} = 1$, consequently associating a slice $\mathcal{D}$ user with the MBS. Constraint C6 indicates that users attached to the feMBB slice can be associated with only one of the available RANs at a time. A user is guaranteed a minimum QoS in terms of data rate through constraint C7. L^v_{thres} is the minimum expected data rate of the slice in which i belongs. Constraints C8 and C9 ensure that the total transmit power allocated to all users associated to an AN $o_j \in \mathcal{O}$ where $j \in \{\mathcal{B},\mathcal{U},\mathcal{H},\mathcal{S}\}$ must not exceed the AN's power budget $P^{thres}_{o_j}$ while C10 ensures that the resource budget of an AN $o_j \in \mathcal{O}$ is not exceeded.

V. User Association and Resource Allocation Algorithm

To solve the user association and resource allocation problem, a heuristic slice-aware algorithm is developed. Three factors are considered in the association process: 1) the mission-critical slice $\mathcal{R}$ is prioritized, 2) Users are prioritized depending on the number of ANs within their coverage, and 3) NTNs are prioritized over TNs for slice $\mathcal{D}$ users. The association of users to an appropriate AN is evaluated based on three criteria; maximum SINR matching, least load, and random access. The maximum SINR criterion associates a user to an appropriate AN with the highest SINR, the least load to an AN with the lowest load, while the random access randomly associates a user to any appropriate AN. Resource allocation is done concurrently with user association by ensuring that users are attached to ANs whose available number of BBUs, $\mathcal{N}^{bbu}_{o_j}$ is greater than the minimum number of BBUs $\mathcal{N}^{bbu}_i$ required by user i, given by

$$\mathcal{N}^{bbu}_i = \frac{L^v_{thres}}{\mathcal{L}_{o_j,i,c_j}}, \ \ \forall\ v \in \{\mathcal{E},\mathcal{R},\mathcal{D}\}, \forall i \in \mathcal{I},$$
$$\forall o_j \in \mathcal{O}, \forall j \in \{\mathcal{B},\mathcal{U},\mathcal{H},\mathcal{S}\}\ . \tag{10}$$

The pseudo-code of the proposed heuristic algorithm given in Algorithm 1 is based on the snapshot model [16] and uses maximum SINR matching as the association criterion. Lines 3-8 of Algorithm 1 determine user i's path loss, channel gain, SINR, and data rate, and after that, store all ANs in whose coverage i lies in a set $Cov^i_{o_j}$. Line 9 sorts users in each slice to prioritize them according to the number of ANs within their coverage. Users in slice $\mathcal{R}$ are serviced in lines 11-31. Lines 32-49 associate and allocate resources to users in the $\mathcal{D}$ slice while ensuring that access to HAPs or UAVs or SatComs is prioritized over the MBSs. Users of slice $\mathcal{E}$ are provisioned through lines 50-52. Line 54 returns a list $Assoc^i_{o_j}$ containing the AN o_j serving user i, and the number of BBUs $\mathcal{N}^{bbu}_i$ allocated to the user.

VI. Results and Performance Evaluation

To evaluate the performance of the proposed algorithm, we consider a square of 10 km $\times$ 10 km of an urban environment covered by the LEO satellite. Within this region are 14 MBSs, 3 UAVs and 1 HAP, with each tier having radius of 1 km, 2 km and 4 km respectively. Users and ANs are uniformly and randomly distributed. It is assumed that the propagation for the NTNs is LoS. Other parameters used in the simulation are given in Table I [2], [9], [12], [13].

Figure 2 depicts spectrum efficiency (SE) and the user acceptance ratio (AR) versus the number of users. The user AR is defined as the ratio of users accepted into the network to the total number of users. First, user association based on three criteria; maximum SINR, least load, and random access, is analyzed. Figure 2(a) shows that the maximum SINR association criterion achieves the highest SE since such an association technique is based on maximum SINR. On the other hand, an association based on least load gives the least SE since it puts users on ANs with the least load regardless

Algorithm 1 Slice-Aware user association and resource allocation algorithm

Input: f_{o_j}, $P_{o_j}^{thres}$, $\mathcal{N}_{o_j}^{bbu}$, z_n, L_{thres}^{v}, $\mathcal{T}_{c_j}$
Output: User association and resource allocation set, $Assoc_{o_j}^{i}$

procedure USER ASSOCIATION AND RESOURCE ALLOCATION
Initialise: $Assoc_{o_j}^{i} = \emptyset$
  for Each user $i \in \{\mathcal{I}_R, \mathcal{I}_E, \mathcal{I}_D\}$ **do**
    for Each AN $o_j \in \mathcal{O}$ **do**
      Calculate PL_{o_j,i,c_j}, Γ_{o_j,i,c_j}, γ_{o_j,i,c_j}, and $\mathcal{L}_{o_j,i,c_j}$
      Add o_j to $Cov_{o_j}^{i}$ if i is within o_j's coverage
    end for
  end for
  sort $\{\mathcal{I}_R, \mathcal{I}_E, \mathcal{I}_D\}$ according $|Cov_{o_j}^{i}|$
  for Each user $i \in \{\mathcal{I}_R \cup \mathcal{I}_D \cup \mathcal{I}_E\}$ **do**
    if $user\ i \in \mathcal{I}_R$ **then**
      if $Cov_{o_j}^{i} == \emptyset$ **then**
        $\pi_{j,i}\mu_{o_j,i}\omega_{o_j,i,c_j} = 0\ \forall j \in \{\mathcal{B}, \mathcal{U}, \mathcal{H}, \mathcal{S}\}$
      else
        sort $Cov_{o_j}^{i}$ according γ_{o_j,i,c_j}
        $\pi_{j,i}\mu_{o_j,i}\omega_{o_j,i,c_j} = 0$
        for $o_j \in Cov_{o_j}^{i}$ **do**
          if $o_j \in \mathcal{S}$ **then**
            pass
          else
            if $\mathcal{N}_{o_j}^{bbu} < \mathcal{N}_{i}^{bbu}$ **then**
              pass
            else
              $\pi_{j,i}\mu_{o_j,i}\omega_{o_j,i,c_j} = 1$
              Deduct $\mathcal{N}_{i}^{bbu}$ from $\mathcal{N}_{o_j}^{bbu}$
              Append $[i, o_j, \mathcal{N}_{i}^{bbu}]$ to $Assoc_{o_j}^{i}$
              break
            end if
          end if
        end for
      end if
    else if $user\ i \in \mathcal{I}_D$
      steps 12-16
      Extract lists of $\{\mathcal{U} \cup \mathcal{H} \cup \mathcal{S}\}$ and $\{\mathcal{B}\}$ from $Cov_{o_j}^{i}$
      if $|\{\mathcal{U} \cup \mathcal{H} \cup \mathcal{S}\}| > 0$ **then**
        for $o_j \in \{\mathcal{U} \cup \mathcal{H} \cup \mathcal{S}\}$ **do**
          steps 21-28
        end for
        if $\pi_{j,i}\mu_{o_j,i}\omega_{o_j,i,c_j} == 0$ **and** $|\mathcal{B}| > 0$ **then**
          for $o_j \in \mathcal{B}$ **do**
            steps 21-28
          end for
        end if
      else
        if $|\mathcal{B}| > 0$ **then**
          steps 40-42
        end if
      end if
    end if
    if $i \in \mathcal{I}_E$ **then**
      steps 12-17, 21-28,29-31
    end if
  end for
  Return $Assoc_{o_j}^{i}$
end procedure

of the transmission power and path loss. From Figure 2(b), it is observed that all three schemes have almost similar user AR, with the least load criterion having a slightly higher AR as the number of users increases.

Next, the proposed slice-aware algorithm is compared with the slice-unaware algorithm. Both algorithms associate users based on maximum SINR since it outperforms the least load and random user association criteria in SE yet still has a high AR. Like the slice-aware approach, the slice-unaware prioritizes users according to the number of ANs within their coverage but does not consider the heterogeneity in user QoS requirements and RAN capabilities in meeting these needs.

TABLE I
SIMULATION PARAMETERS AND VALUES

Parameter	Value
$f_{o_B}, f_{o_U}, f_{o_H}, f_{o_S}$	[4, 2, 3, 5] GHz
$\mathcal{T}_{c_\mathcal{B}}, \mathcal{T}_{c_\mathcal{U}}, \mathcal{T}_{c_\mathcal{H}}, \mathcal{T}_{c_\mathcal{S}}$	[0.18, 0.18, 1, 2] MHz]
Number of BBUs for $[o_B, o_U, o_H, o_S]$	[50, 50, 100, 200]
$[P_{o_B}^{thres}, P_{o_U}^{thres}, P_{o_H}^{thres}, P_{o_S}^{thres}]$	[40, 25, 100, 250] Watts
$x,\ y,\ \eta_{LoS},\ \eta_{NLoS}$	[10.39, 0.05, 1, 20]
Shadow fading $[\mathcal{B}, \mathcal{S}]$	[8, 4] dB
$[CL,\ PL^k,\ PL^y]$	[0, 0, 23 dB]
NTN AP height $[z_U, z_H, z_S]$	[2,17,600] km
Slice user ratio $[\lvert\mathcal{I}_\mathcal{E}\rvert : \lvert\mathcal{I}_\mathcal{R}\rvert : \lvert\mathcal{I}_\mathcal{D}\rvert]$	[0.6:0.3:0.1]
$L_{thres}^{v} v \in [\mathcal{E}, \mathcal{R}, \mathcal{D}]$	[1000,500,1000] kbps
Noise spectral density	-174 dBm

In Figure 2(c), the slice-aware scheme admits over 90% of mission-critical users, the other 10% being users outside the coverage of capable radio ANs. On the other hand, the acceptance ratio of mission-critical users is lower in the slice-unaware algorithm and keeps reducing as the number of users increases. This difference in performance arises from the fact that the slice-aware algorithm prioritizes mission-critical users and associates them only to tiers that meet their needs. In comparison, slice-unaware does not distinguish users based on their QoS needs, and neither does it consider the limitations of the different RANs. This results in a reduced acceptance ratio of the $\mathcal{R}$ slice since these are not prioritized and are also associated with RANs that cannot meet their needs. The valley in the slice-unaware scheme is because satellite resources are still available at a lower number of users. Hence, the number of dropped euRLLC users due to association with the satellite is high. As the satellite resources get depleted, this number reduces, increasing AR at about 300 users.

In Figures 2(d) and 2(e), both algorithms have acceptance ratios of $\mathcal{E}$ and $\mathcal{D}$ at 100% for a smaller number of users when resources are still available. As the number of users increases, resources reduce, and hence the acceptance ratio decreases. The slice-unaware algorithm performs better in this case since this did not prioritize mission-critical users and the use of NTNs for slice $\mathcal{D}$. Therefore, slice $\mathcal{E}$ and $\mathcal{D}$ users were able to use up resources that are prioritized for slice $\mathcal{R}$ users in the slice-aware algorithm. Also, the slice $\mathcal{D}$ users can associate to the MBS if it has a better SINR to achieve better SE even if its coverage is limited. However, Figures 2(g) and 2(f) show that even with the priorities subjected to the slice-aware algorithm, its overall SE and user acceptance ratio is better than the slice-unaware algorithm. Therefore, the slice-aware algorithm prioritizes mission-critical applications, whose rejection results in adverse consequences, prioritizes the use of wider coverage NTNs for highly mobile users, and at the same time, maximizes the number of admitted users and the network SE.

VII. CONCLUSION

This paper introduces a slice-aware user association and resource allocation problem that maximizes SE in an IT-NTN. The optimization problem is solved using a heuristic algorithm that prioritizes delay-sensitive mission-critical users and the use of NTNs over MBs for long-distance and high-

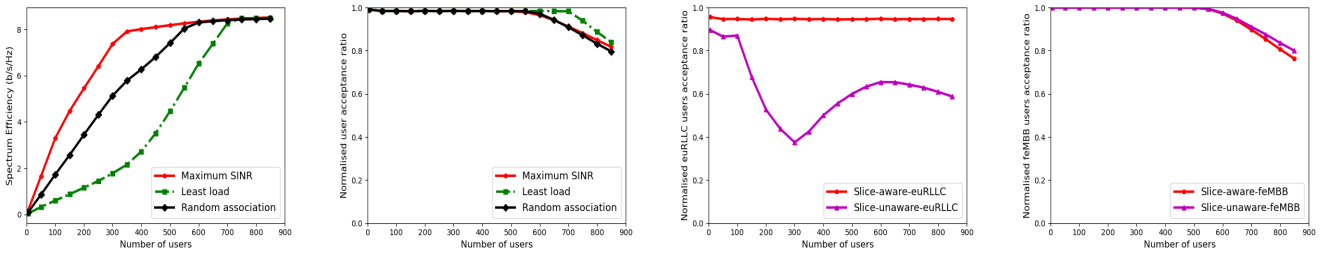

(a) SE of different AN selection criteria (b) User AR of different AN selection criteria (c) euRLLC AR; slice-aware vs. slice-unaware (d) feMBB AR; slice-aware vs. slice-unaware

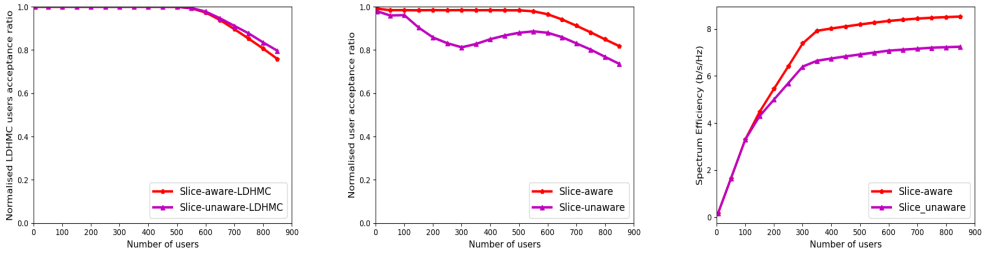

(e) LDHMC AR; slice-aware vs. slice-unaware (f) Network acceptance ratio; slice-aware vs. slice-unaware (g) Spectrum Efficiency; slice-aware vs. slice-unaware

Fig. 2. Performance against number of users

speed users. Simulation results have shown that the slice-aware algorithm has a better performance than the slice-unaware algorithm. In the future, we shall improve the work to show the user mobility model, handoff analysis, and consider fairness between high and low SINR users.

ACKNOWLEDGEMENT

The authors are thankful for the support received from Kyambogo University, Uganda, the University of Cape Town and the Telkom Centre of Excellence (COE) in Broadband Networks, South Africa.

REFERENCES

[1] Z. Zhang, Y. Xiao, Z. Ma, M. Xiao, Z. Ding, X. Lei, G. K. Karagiannidis, and P. Fan, "6g wireless networks: Vision, requirements, architecture, and key technologies," *IEEE Vehicular Technology Magazine*, vol. 14, no. 3, pp. 28–41, 2019.

[2] 3GPP, "Technical Specification Group Radio Access Network; Study on New Radio (NR) to support non-terrestrial networks (Release 15) ," 3rd Generation Partnership Project (3GPP), Technical Specification (TS) 38.811, 09 2019, version 15.2.0.

[3] Y. Hu, M. Chen, and W. Saad, "Joint access and backhaul resource management in satellite-drone networks: A competitive market approach," *IEEE Transactions on Wireless Communications*, vol. 19, no. 6, pp. 3908–3923, 2020.

[4] B. Deng, C. Jiang, J. Yan, N. Ge, S. Guo, and S. Zhao, "Joint multi-group precoding and resource allocation in integrated terrestrial-satellite networks," *IEEE Transactions on Vehicular Technology*, vol. 68, no. 8, pp. 8075–8090, 2019.

[5] J. Liu, Y. Shi, Z. M. Fadlullah, and N. Kato, "Space-air-ground integrated network: A survey," *IEEE Communications Surveys & Tutorials*, vol. 20, no. 4, pp. 2714–2741, 2018.

[6] H. Tabassum, M. Salehi, and E. Hossain, "Fundamentals of mobility-aware performance characterization of cellular networks: A tutorial," *IEEE Communications Surveys & Tutorials*, vol. 21, no. 3, pp. 2288–2308, 2019.

[7] Y. Hu, M. Chen, and W. Saad, "Competitive market for joint access and backhaul resource allocation in satellite-drone networks," in *2019 10th IFIP International Conference on New Technologies, Mobility and Security (NTMS)*. IEEE, 2019, pp. 1–5.

[8] S. M. Shahid, Y. T. Seyoum, S. H. Won, and S. Kwon, "Load balancing for 5g integrated satellite-terrestrial networks," *IEEE Access*, vol. 8, pp. 132 144–132 156, 2020.

[9] A. Alsharoa and M.-S. Alouini, "Improvement of the global connectivity using integrated satellite-airborne-terrestrial networks with resource optimization," *IEEE Transactions on Wireless Communications*, vol. 19, no. 8, pp. 5088–5100, 2020.

[10] J. Li, K. Xue, D. S. Wei, J. Liu, and Y. Zhang, "Energy efficiency and traffic offloading optimization in integrated satellite/terrestrial radio access networks," *IEEE Transactions on Wireless Communications*, vol. 19, no. 4, pp. 2367–2381, 2020.

[11] X. Li, W. Feng, Y. Chen, C.-X. Wang, and N. Ge, "Maritime coverage enhancement using uavs coordinated with hybrid satellite-terrestrial networks," *IEEE Transactions on Communications*, vol. 68, no. 4, pp. 2355–2369, 2020.

[12] A. Moubayed, A. Shami, and H. Lutfiyya, "Wireless resource virtualization with device-to-device communication underlaying lte network," *IEEE Transactions on Broadcasting*, vol. 61, no. 4, pp. 734–740, 2015.

[13] A. Al-Hourani, S. Kandeepan, and S. Lardner, "Optimal lap altitude for maximum coverage," *IEEE Wireless Communications Letters*, vol. 3, no. 6, pp. 569–572, 2014.

[14] L. Liang, J. Kim, S. C. Jha, K. Sivanesan, and G. Y. Li, "Spectrum and power allocation for vehicular communications with delayed csi feedback," *IEEE Wireless Communications Letters*, vol. 6, no. 4, pp. 458–461, 2017.

[15] M. Adedoyin and O. Falowo, "Joint optimization of energy efficiency and spectrum efficiency in 5g ultra-dense networks," in *2017 European Conference on Networks and Communications (EuCNC)*. IEEE, 2017, pp. 1–6.

[16] D. Fooladivanda and C. Rosenberg, "Joint user association and resource allocation in heterogeneous cellular networks: Comparison of two modeling approaches," in *2019 31st International Teletraffic Congress (ITC 31)*. IEEE, 2019, pp. 66–74.

Denise Joanitah Birabwa is a Ph.D student with the Department of Electrical Engineering in the University of Cape Town, South Africa.

QoE-Aware Q-Learning Resource Allocation for Spectrum Reuse in 5G Communications Network

Stephen Ekwe*, Sunday Oladejo*, Lateef Akinyemi*, Neco Ventura *
*Department of Electrical Engineering, University of Cape Town, South Africa
[1]ekwste001@myuct.ac.za; [2]oldsun002@myuct.ac.za; [3]ltfaki001@myuct.ac.za; [4]neco.ventura@uct.ac.za;

***Abstract*—This paper presents a Q-learning resource allocation scheme for spectrum re-use in a 5G communications network. The scheme aims to maximise the quality of experience (QoE) of users using reinforcement learning techniques. It exploits the social similarities of users to enable coexistence between primary and secondary user equipments on the same frequency band. Consequently, it is assumed that the available spectrum resources meant for primary users can be re-used by secondary users. Hence, a QoE model is formulated as a utility maximisation problem with a cost function for secondary users willing to coexist, howbeit under strict power and interference constraints. An optimal social-aware policy learning model is constructed to regulate transmission power while improving user QoE. The simulation results show the efficiency of the proposed scheme relative to the independent, policy averaging, and similar traffic reinforcement learning solutions.**

***Index Terms*—Interference mitigation, quality of experience, social-aware, Q-learning,**

I. Introduction

The fifth-generation (5G) communications network seeks to satisfy the increasing user demand for spectrum resources by supporting the growing variety of user devices and service requirements across several vertical industries [1]. Cisco's visual networking index report on South Africa in 2016 predicted the number of mobile-connected devices to be 68% in 2021, with machine-to-machine (M2M) module accounting for 28% (46.1 million). In 2018, they predicted that the global popularity of M2M applications would increase tremendously, with about 50% (14.7 billion) of the globally connected devices expected to be M2M connections by 2023. Similarly, there is an expected growth in the use of mobile applications (i.e., about 300 billion downloads), Wi-Fi hotspots (i.e., nearly 628 million), and mobile users (i.e., 66% of the global population) [2].

This rapid growth in wireless connectivity and data service pushes the boundaries of the communication network's capability. Although 5G proposes several enabling technologies (such as massive-user MIMO, non-orthogonal multiple access (NOMA) techniques, device-to-device communication, etc.) that try to improve spectrum utilization via shared resources, there are still limitations owing to the inability of current radio resource management schemes to dynamically scale during peak traffic periods while still ensuring the QoE of users. Additionally, there is a prevailing concern of interference, which increases with user demand. Motivated by this, it has become imperative to embrace big data and artificial intelligence (AI) to ensure adaptability, scalability, and optimum resource utilization in 5G communications network [3].

Accordingly, Y. Shi et al. presented a reinforcement learning (RL) based solution to dynamically allocate spectrum, power, and computing resource stochastically on the arrival of network slice requests in [4]. The authors proposed a Q-learning solution to maximise network utility in terms of the total weight of granted network slicing requests over time, subject to communication and computational constraints. Their result showed that the Q-learning based solution scales well with an increase in the number of users. W. Alsobhi et al. in [5] proposed a cooperative approach to address the problem of spectrum resource allocation within a two-tier HetNet. The authors explored the application of RL in a femtocell deployment and network interference management. Their results revealed the impact of interference on users within femtocells. S. He et al. in [6] proposed a multi-agent to single-agent RL scheme for QoE-aware resource allocation in NOMA wireless multimedia communications network. Their results provide evidence for enhanced performance in the NOMA downlink system with increased power budget. Likewise, the authors in [7], [8] presented similar Q-learning based algorithms to achieve optimum solutions that maximised the network QoE performance metric.

Hence, this study presents a lightweight QoE-aware Q-learning resource allocation scheme for spectrum re-use in a 5G communications network. Specifically, we formulate the problem as a utility maximisation problem that ensures the QoE of users while mitigating interference. To take advantage of big data within the communications network, we construct a social-aware policy to exploit the similarities of users and improve the reward of the agent in any given state. The following are the main contributions of this study:

- To quantitatively analyse the QoE perceived by users a mathematical QoE model is formulated as a utility function.
- To efficiently solve the formulated QoE problem, a cooperative RL scheme is developed to determine the optimum learning policy of a newcomer secondary user.
- To exploit the similarities of users on the network, a social-aware policy is designed based on the concept of social-awareness in wireless networks. The goal is to minimise the interaction time of an agent in a stochastic environment while maximising reward.
- To present the impact of specific system parameters on network performance and evaluate the proposed scheme by comparing with other RL models from literature.

The rest of this study is presented as follows: Section II

describes the system model, which summarises the assumptions made in this study. Section III explains the problem formulation. Section IV presents the RL Q-learning model used. Section V discusses the results and analysis, and Section VI concludes the paper.

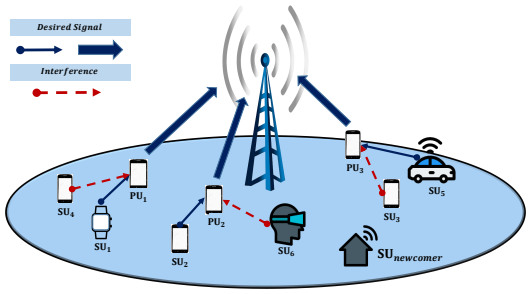

Fig. 1: Deployment of a Su newcomer in a 5G communication network

II. System Model

A. Deployment Scenario

This study carefully considers the uplink of a single-tier 5G communications network illustrated in Fig. 1, which comprises of a remote radio head (RRH), a set of primary user devices denoted by $Pu = \{1, 2, \ldots, |Pu|\}$, and a set of secondary users devices denoted by $Su = \{1, 2, \ldots, |Su|\}$. Where $|Pu|$ and $|Su|$ represent the cardinality of each set. The RRH allocates each primary users a separate physical resource block (PRB) denoted by $n \in N$, where $n \in \mathbb{N}^+$, with a transmission bandwidth B_n. Such that the total transmission bandwidth B is characterised by $B_n \times N$ [9]. To re-use a channel, each SU most adapt its transmission parameters to satisfy the interference requirements from other PUs and SUs. Under this assumption, a newcomer SU can estimate its channel gain through actively learning the channel state information of other SUs. The transmission environment considered is affected by the pathloss (PL) (i.e., PL = $d^{-\varphi}$), having a large scale fading (φ). Without loss of generality, the following assumptions are considered:

1) All users transmit using the adaptive modulation and coding scheme, which dynamically adapts to the time-varying frequency fading channel to maximise throughput of the transmission link.
2) A secondary user (SU) is allowed to re-use the spectrum resource of a primary user (PU) under strict signal-to-interference and noise ratio (SINR) requirements. This is done to fully utilise spectrum resource.
3) The transmit power, channel, and additive white Gaussian noise (AWGN) of the network is quasi-static. This is to enable the SU to deduce the channel state information (CSI) through active learning on the network.
4) SU has sensory capabilities to discover and respond to other users within its neighbourhood via proximity-based services (ProSe) as stated in 3GPP TS 23.303.

B. Social Similarity

This is a measure of commonality between any given pair of nodes. In communications network, the similarity index can be in terms of service request, geo-location, channel availability, or a combination of either one [10]. In this study, the social similarity index between users is obtained as the weighted link of a pair of vertices in a two-dimensional graph $\mathcal{G} = (\mathcal{U}, \phi, \alpha_{(u,\overline{u})})$. Where $\mathcal{U}$, ϕ, and $\alpha_{(u,\overline{u})}$ denote the set of vertices, links, and their weights, respectively. Thus, for a pair of vertices u and $\overline{u}$ it is obtained as,

$$\alpha_{(u,\overline{u})} = \begin{cases} \dfrac{|\aleph_{(u)} \cap \aleph_{(\overline{u})}|}{|\aleph_{(u)} \cup \aleph_{(\overline{u})}|}, & \text{if } u \text{ and } \overline{u} \text{ are connected} \\ 0, & \text{otherwise} \end{cases} \quad (1)$$

where $|\aleph_{(u)} \cap \aleph_{(\overline{u})}|$ denotes a set of common neighbours between vertices with respect to their total number of neighbour [11]. The expression in (1) determines the likelihood of an association between users, with a degree of freedom ranging from 0 to 1, the latter being the highest achievable similarity index. Figure 2 depicts the neighbourhood graph of users in a two-dimensional space.

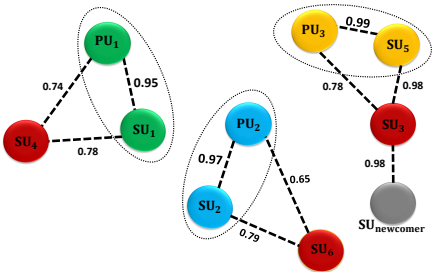

Fig. 2: Graph $\mathcal{G} = (\mathcal{U}, \phi, \alpha_{(u,\overline{u})})$ of set PU and SU with weighted links indicative of the likelihood of an association.

C. Channel Model

To fully utilise the available spectrum resources of the network the newcomer SU listens to the RRH for transmit parameters and learns the channel state information of other users, however, under strict signal to interference and noise ratio (SINR) requirement. Thus, the SINR of the PU and SU as experienced at the RRH is expressed as,

$$\Upsilon_{Pu_i} = \frac{P_{Pu_i} \lambda_{Pu_i,m}}{\sigma^2 + \sum\limits_{j \in Su} P_{Su_j} \lambda_{Su_j,m}}, \quad \forall i \in Pu, \ \forall j \in Su, \quad (2)$$

$$\Upsilon_{Su_j} = \frac{P_{Su_j} \lambda_{Su_j,m}}{\sigma^2 + \sum\limits_{i \in Pu} P_{Pu_i} \lambda_{Pu_i,m} + \sum\limits_{\substack{j' \in Su \\ j' \neq j}} P_{Su_{j'}} \lambda_{Su_{j'},m}}, \quad \forall i \in Pu, \ \forall j \in Su, \quad (3)$$

where σ^2 denote the AWGN power experienced on the network, P_{Pu_i} and P_{Su_j} denote the transmit power of the PU and SU, respectively, while $\lambda_{Pu_i,m}$ and $\lambda_{Su_j,m}$ denote their

channel gain to the RRH. Accordingly, the achievable data rate of the newcomer SU can be expressed as [12],

$$\Delta_{Su_j} = \sum_{n=1}^{N} \vartheta_{Su_j,n} B_n \log_2 \left(1 + \frac{1.5\Upsilon_{Su_j}}{-\ln(5\Pi_{Su_j})}\right), \quad \forall n \in N,\ \forall j \in Su, \tag{4}$$

where $\vartheta_{Su_j,n}$ denotes the decision variable for allocated PRB's, and Π_{Su_j} is the target bit error rate of the SU.

III. Problem Formulation

This study aims to improve the QoE of a user in the uplink of a single-tier 5G communications network. Hence, we formulate a QoE-aware resource allocation problem as a utility maximisation problem, using a two-level logarithmic model as in [6] and expressed in (5) as,

$$\underset{\alpha_{i,j}}{\text{maximise}}\ \mathrm{U}(\Delta_{Su_j}) = log_2(1 + \Delta_{Su_j}) - \eta_n \Gamma_{Su_j}, \tag{5}$$

Subject to:

$$\text{C1:}\ \sum_{n\in N} \vartheta_{Su_j,n}\Delta_{Su_j} \geq \Delta_{min},\quad \forall n \in N,\quad \forall j \in Su,$$

$$\text{C2:}\ \sum_{n\in N} \vartheta_{Su_j,n}\Gamma_{Su_j} \leq P_{max},\quad \forall n \in N,\quad \forall j \in Su,$$

$$\text{C3:}\ \Gamma_{Su_j} > 0,\quad \forall j \in Su,$$

$$\text{C4:}\ \sum_{n\in N} \Upsilon_{Su_j} \geq \Upsilon_{min},\quad \forall n \in N,\quad \forall j \in Su,$$

$$\text{C5:}\ 0 \leq \alpha_{i,j} \leq 1,\quad \forall i \in Pu,\quad \forall j \in Su,$$

$$\text{C6:}\ \sum_{n\in N} \vartheta_{Su_j,n} \leq 1,\quad \forall n \in N,\quad \forall j \in Su,$$

$$\text{C7:}\ \vartheta_{Su_j,n} \in \{0,1\},\quad \forall n \in N,\quad \forall j \in Su,$$

Constraint C1 guarantees the quality-of-service of a user given the service application. Constraints C2 and C3 are power constraints. C2 ensures that the transmit power of a user does not exceed a given threshold in each PRB, whereas C3 ensures that the transmit power is non-negative. Constraint C4 enforces strict SINR requirements for users. Constraint C5 ensures that the similarity index indicative of the probability of an association between Pu and Su is within a normalised range. C6 ensures that a resource is allocated to at most one user. Finally, C7 relax the function in (5).

In constraint C2 and C3, $\Gamma_{Su_j} = P_{Su_j}/\alpha_{(i,j)}$ is used to denotes the actual transmit power of the Su, given the likelihood $\alpha_{(i,j)}$ of an association, while $\eta_n \Gamma_{Su_j}$ denotes the cost of the spectrum resource, while η_n is the coefficient per-unit price of the spectrum resource. Since QoE has a logarithmic relationship with the achievable data rate, maximising the data rate will also improve their QoE. However, the transmit power component in that relationship will also increase interference on the channel. Hence, the rationale behind the cost function introduced in (5).

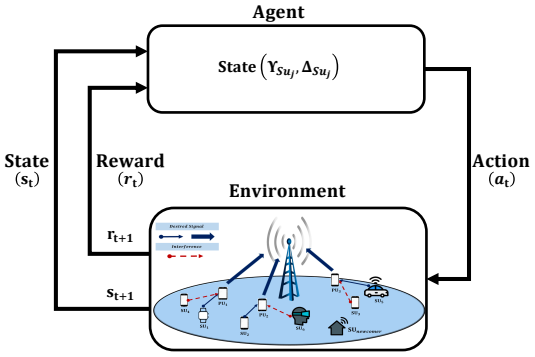

Fig. 3: Illustration of the reinforcement learning model.

IV. Reinforcement Q-Learning Model

A. Overview

The RL approach like most intelligent-based algorithms seeks to find a balance between exploration and exploitation. Fig. 3 shows a basic single-agent model, where an agent interacts with the environment by taking actions and then perceiving the effects of those actions. A new state after action and the received reward determine if some set goal has been reached. The objective of the agent is to maximise its total rewards (i.e., the sum of all rewards received after a number of actions). This formal single-agent model is called a Markov decision process (MDP). An MDP is a tuple $\{S, A, T, R\}$, which comprises a set of bounded states, actions, transition function, and rewards, respectively. Where $s_t \in S$ gives the state of an agent in an environment at a discrete time-slot t. The agent observes the state and takes an action $a_t \in A$ to the next possible state (s_{t+1}) based on a transition probability function T. The agent receives a reward $r_t \in R$ during transition. The agent's action selection is determined by its policy (π), and its expected cumulative reward is given by,

$$Q(s,a) = \mathbb{E}\left[\sum_{t=0}^{\infty} \gamma^t r(s_t, \pi(s)) s_0\right] = s, \tag{6}$$

where γ denotes the discount factor that regulates the agent's reward in the Q-function, and $Q(s,a)$ is the corresponding Q-value. When the selected action a is the optimal action $\pi(s)$, then $Q(s,a)$ is considered to be the optimal state, and is obtained using Bellman optimality equation [13],

$$Q^*(s_t,a_t) = (1-\beta)Q(s,a) + \beta(r_t + \gamma \max_{b\in A} Q_t(s_t,b)), \tag{7}$$

where $\beta \in (0,1)$ is the learning rate. Hence, the objective of the agent is to find the optimal policy that maximises the expected cumulative discounted reward over time, while updating its Q-table recursively as follows,

$$\widehat{Q}(s_{t+1},a_{t+1}) = (1-\beta_t)\ Q^*(s_t,a_t) + \beta_t(r_{t+1} + \gamma \max_a Q(s_{t+1},a_t^*)). \tag{8}$$

B. Proposed Solution

In this study, Q-learning is used to obtain the optimal policy given a finite state of target SINR. The goal is to maximise the QoE utility function of a newcomer SU. The parameters of the Q-learning is defined as follow

Agent: This is the newcomer SU who desires to re-use the spectrum resource of the PU (i.e., $j \in Su$, $j \neq 0$).

State: In any given state, the agent observes two critical components: SINR and data rate, i.e. $s_t = \left(\Upsilon_{Su_j}, \Delta_{Su_j}\right)$.

Action: The actions of the agent is to find an optimum transmit power strategy based on a policy, while satisfying the constraints in (5) (i.e., $a_t = \pi|_{t+1}$).

Reward: This is the QoE utility under the new power allocation strategy of the agent (i.e., $r_t = \mathrm{U}(\Delta_{Su_j})|_{t+1}$). After an action by the agent, the changes on the system and to the transmission of the agent is observed and rewarded if the the QoE is maximised with minimal interference or penalised otherwise.

Hence, we propose a lightweight QoE-aware Q-learning solution that allows newcomer learner agents to use the information from expert agents based on the state and similarity index of the agent. This social-aware policy is treated as a decentralised learning system with a user-centric view. It is based on a generalisation that users with a higher likelihood of association will be more willing to share their resources. Consequently, a user device with sensing capabilities can intelligently regulate its transmit power (i.e., $P_{Su_j} \rightarrow \Gamma_{Su_j}$) when sharing spectrum resources based on the similarity index obtain in (1). Furthermore an agent can improve its reward by learning the actions of experts with high similarity index in similar states using (9),

$$a_t = \left[\arg\max Q(s_t, a_t), a_t \in \pi^* \mid \forall\ \alpha_{i,j} \geq \alpha_{min}\right]. \quad (9)$$

This social strategy reduces the complexity of the algorithm by decreasing the exploration time of the agent while increasing exploitation. Without loss of generality, the proposed social-aware policy is constructed as follows:

i) The optimal power allocation of a newcomer $j \in Su$ will be affected by the channel availability of $i \in Pu$ given $\alpha_{(i,j)} \geq \alpha_{min}$.

ii) The optimal power allocation of a newcomer, Su_j in state (s_t) will depend on the information of Su_{j-1} given $\alpha_{(j-1,j'-1)} \geq \alpha_{min}$.

iii) The optimal power allocation of a newcomer, Su_j will utilize the SINR, actual transmit power, and similarity index of expert (i.e. $Su_{j-1}, Su_{j-2}, \therefore, Su_{j-k}|_{k+j}$).

The expert agent learns the environment individually using a distributed Q-learning scheme that first initialising and pre-allocating the Q-Table, apply a greedy strategy to select the best reward within an iterative loop, select the state (s_{t+1}) after an action (a_t), observe and generate reward (r_t) or penalty $(-r_t)$ based on the action, and update the calculated Q-value on the Q-Table [13]. Note that Algorithm 1, is proposed to take advantage of the expert information on the environment.

Algorithm 1: Q-Learning on Social Policy

```
Input Q-Table Q*(s_t, a_t), α_{i,j}
Initialize learning rate (β), discount factor (γ)
for iteration time: t = 0 : T do
    if Similarity Index: α_{i,j} ≥ α_min then
        Let agent select action (a_t) as in 9
        Observe power strategy and reward (r_t);
        Update Q-value, Q̂(s_{t+1}, a_{t+1}) as in 8
    end
end
output: Mean QoE: U(Δ_{Su_j});
```

TABLE I: System Parameters

Parameters	Values
Channel bandwidth: B	10 MHz
Cell radius:	300m
Neighbour radius:	30m
AGWN: σ^2	-174 dBm/Hz
No. of secondary users: Su	{10 : 10 : 70}
SINR: Υ_{Su_j}	{-5 : 2 : 15} dB
Bit error rate: Π_{Su_j}	10^{-5}
Max transmit Power: P_{max}	23 dBm
large scale fading: φ	2.8 dB
Min Similarity index: α_{min}	95%
Learning rate: β	0.1
Discount factor: γ	0.4
Iteration:	10000
Episodes:	500

V. Results and Analysis

This section presents simulation results to substantiate the proposed solution. The implementation of our proposed scheme is performed on MATLAB. We considered that a PU occupies a single channel bandwidth with a target SINR set at 10 dB. Both SUs and PUs are randomly distributed within a macrocell radius 300m. In the proposed RL model, each newcomer SU is a learning agent who is expected to choose an SINR from a finite set based on its power allocation strategy. The algorithm assumes the same learning rate and discount factor for all SU's. The proposed solution was studied through a Monte Carlo simulation consisting of 10000 iterations per 500 episodes, for which the average results are captured. To evaluate the performance, our results are compared to three different RL models from literature, which assumed a similar system model: independent policy (IP), policy averaging (PA) [14], and similar traffic policy (STP) [12] algorithm.

A. Impact of Social Similarity on Network performance

Figure 4 shows the variation in the optimal resource allocation results attained by an expert and leaner agent using the IP and proposed algorithm, respectively. The results compare the learning efficiency of both algorithms under strict SINR requirements. It is seen that the learner agent achieves about a 3% increase in mean QoE score at SU = 10 and about 2.4% at SU = 30 when comparing the median of their distributions. Even with a slightly skewed distribution for the learner agent when SU = 30, it still attained a much higher mean QoE score due to the shared knowledge of highly social expert

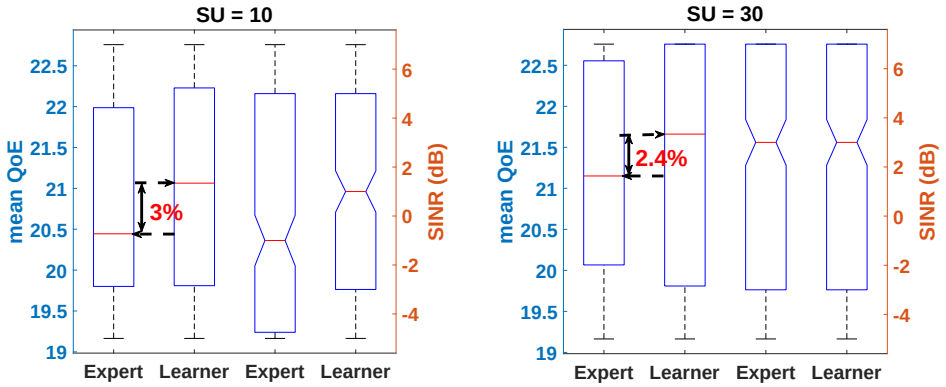

Fig. 4: Performance evaluation of SU newcomer learning using the RL social-aware policy resource allocation scheme

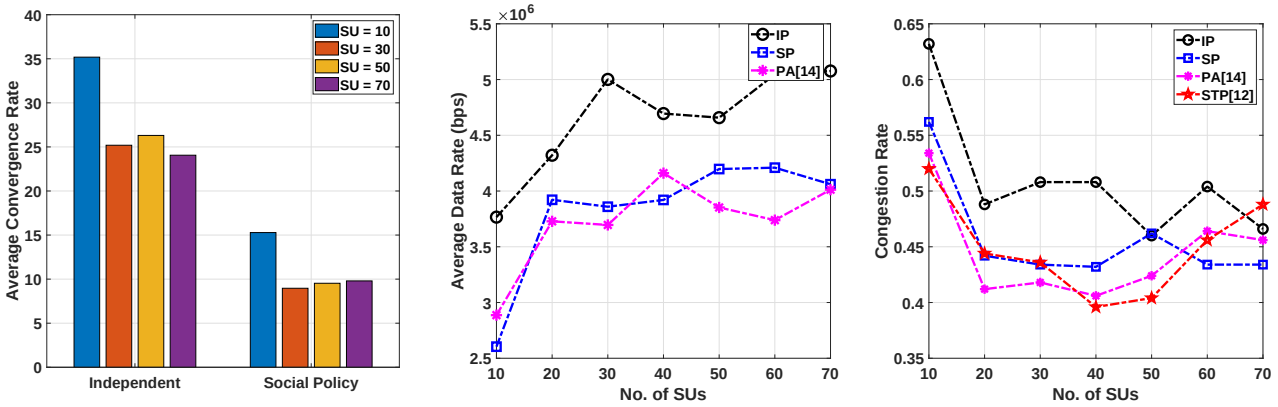

(a) (b) (c)

Fig. 5: Performance of social-aware policy under quasi-static channel condition with increasing SU density. The proposed scheme is evaluated based on (a) average convergence, (b) average data rate, and (c) congestion ratio

agents. The results clearly show that the proposed algorithm can maximise reward even for sparse user density with fewer social agents. The expert and learner agent also achieved a median SINR score of (-1, 1) dB at SU = 10 and (3, 3) dB at SU = 30, respectively, all within the required constraints.

B. Impact of User Density on Network Performance

From Fig. 5a, it is observed that the newcomer SU utilises the social awareness of its environment to achieve lower average convergence. It shows that the number of iterations needed to achieve convergence reduced by about 60% on all use cases when compared to the IP algorithm. It is also worthy of note that the issue of fewer social agents is seen when SU = 10 since it takes the proposed algorithm slightly longer to converge.

In further evaluating the performance, Fig. 5b shows the average data rate of an agent for various algorithms. In retrospect, the proposed solution achieved a lesser average data rate compared to the IP algorithm despite its lower convergence rate. However, this trade-off is expected given the relevance placed on exploitation over exploration within the network environment. Compared to the PA algorithm, the proposed algorithm performance slightly better, with few dips in performance at SU = 10 and 40.

Figure 5c tells about the congestion level of the network. It shows the performance of the algorithms as the number of scheduled users increases. However, this can also be an indicator for mobile operators to admit more users to the network given a predefined allowable congestion rate.

C. Impact of RL model on Network Performance

Figure. 6 shows the mean QoE achieved under different RL models by the learning agent for four different user deployment use cases. It is observed that the proposed algorithm easily outperforms PA and STP algorithms, while match IP in performance, with both having similar distributions and a median score of 20.44 at SU = 10. The IP algorithm performs best in sparse use cases, however, other algorithms can match its QoE performance in more dense user deployment use cases, such as at SU = 50 and 70.

Thus, the onus is on the network operator to decided the best learning policy for users upon spectrum request. This may depending on key performance indicators, such as

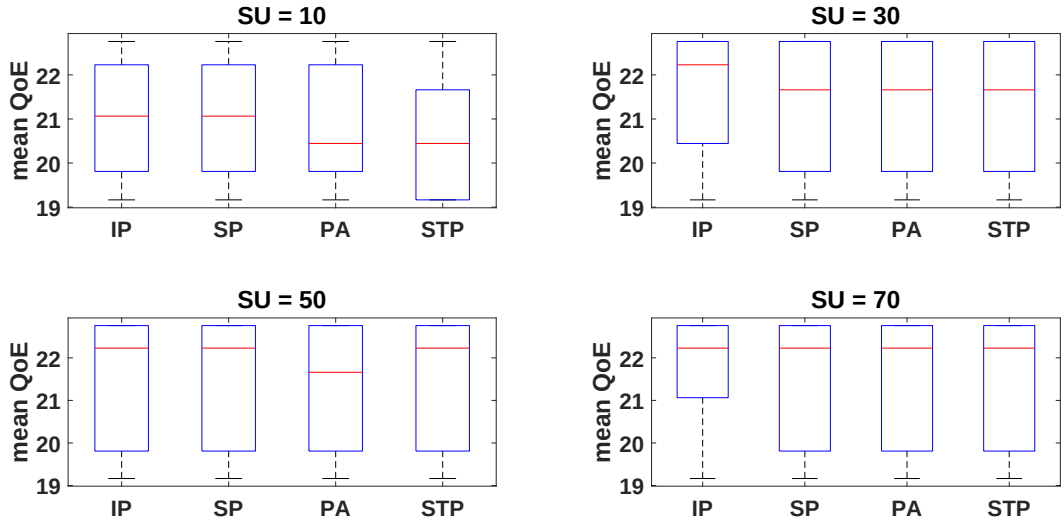

Fig. 6: QoE performance evaluation under different resource allocation policies

convergence rate, congestion rate, spectrum availability, and user QoE.

VI. Conclusion

In this study, we have investigated the uplink of a single-tier 5G communications network to address the interference that arises from spectrum re-use amidst growing demand. A QoE-aware Q-learning resource allocation algorithm is proposed to measure the QoE of secondary users that seek to coexist on the same frequency band as the primary user, howbeit under strict power and SINR requirement. The QoE problem is formulated as a utility maximisation problem with a cost function to mitigate interference to the primary user. A social similarity index is used to establish the likelihood of possible association between users. A social-aware policy is proposed for optimal resource allocation, which allows a newcomer secondary user to leverage the knowledge of socially experienced users to improve its QoE. The simulation results show that the proposed solution outperforms other RL algorithms, although with few exceptions. The trade-off of the proposed algorithm is between the exploration and exploitation of the learning environment, which affirms the need for balance even within model-free RL systems.

Acknowledgment

The authors would like to thankfully appreciate the support received from TELKOM SA via the Telkom Centre of Excellence (CoE) in Broadband Networks and Application at the University of Cape Town, and the Department of Physics, University of Calabar, Nigeria.

References

[1] A. Morgado, K. M. S. Huq, S. Mumtaz, and J. Rodriguez, "A survey of 5g technologies: regulatory, standardization and industrial perspectives," *Digital Communications and Networks*, vol. 4, no. 2, pp. 87–97, 2018.

[2] U. Cisco, "Cisco annual internet report (2018–2023) white paper," 2020.

[3] Z. Xiong, Y. Zhang, D. Niyato, R. Deng, P. Wang, and L.-C. Wang, "Deep reinforcement learning for mobile 5g and beyond: Fundamentals, applications, and challenges," *IEEE Vehicular Technology Magazine*, vol. 14, no. 2, pp. 44–52, 2019.

[4] Y. Shi, Y. E. Sagduyu, and T. Erpek, "Reinforcement learning for dynamic resource optimization in 5g radio access network slicing," in *2020 IEEE 25th International Workshop on Computer Aided Modeling and Design of Communication Links and Networks (CAMAD)*. IEEE, 2020, pp. 1–6.

[5] W. AlSobhi and A. H. Aghvami, "Qos-aware resource allocation of two-tier hetnet: a q-learning approach," in *2019 26th International Conference on Telecommunications (ICT)*. IEEE, 2019, pp. 330–334.

[6] S. He and W. Wang, "Qoe-aware q-learning resource allocation for noma wireless multimedia communications," *IET Networks*, vol. 9, no. 5, pp. 262–269, 2020.

[7] J. Chen, Y. Wang, Y. Li, and E. Wang, "Qoe-aware intelligent vertical handoff scheme over heterogeneous wireless access networks," *IEEE Access*, vol. 6, pp. 38 285–38 293, 2018.

[8] S. Colonnese, F. Cuomo, G. Pagliari, and L. Chiaraviglio, "Q-square: A q-learning approach to provide a qoe aware uav flight path in cellular networks," *Ad Hoc Networks*, vol. 91, p. 101872, 2019.

[9] S. O. Ekwe, S. O. Oladejo, L. A. Akinyemi, and N. Ventura, "A socially-inspired energy-efficient resource allocation algorithm for future wireless network," in *2020 16th International Computer Engineering Conference (ICENCO)*. IEEE, 2020, pp. 168–173.

[10] S. Ekwe and N. Ventura, "Community-aware pricing game for utility maximization in 5g heterogeneous networks," in *2019 IEEE International Conference on Advanced Networks and Telecommunications Systems (ANTS)*. IEEE, 2019, pp. 1–6.

[11] S. Tariq, M. Saleem, and M. Shahbaz, "User similarity determination in social networks," *Technologies*, vol. 7, no. 2, p. 36, 2019.

[12] F. S. Mohammadi and A. Kwasinski, "Qoe-driven integrated heterogeneous traffic resource allocation based on cooperative learning for 5g cognitive radio networks," in *2018 IEEE 5G World Forum (5GWF)*. IEEE, 2018, pp. 244–249.

[13] S. Messaoud, A. Bradai, and M. Atri, "Distributed q-learning based-decentralized resource allocation for future wireless networks," in *2020 17th International Multi-Conference on Systems, Signals & Devices (SSD)*. IEEE, 2020, pp. 892–896.

[14] W. Shi, S. Song, and C. Wu, "High-level tracking of autonomous underwater vehicles based on pseudo averaged q-learning," in *2018 IEEE International Conference on Systems, Man, and Cybernetics (SMC)*. IEEE, 2018, pp. 4138–4143.

Stephen Ekwe is a Ph.D. candidate at the Department of Electrical Engineering, University of Cape Town, South Africa. He received his B.Eng in Electrical and Electronics Engineering from Cross River University of Technology, Nigeria, and his M.Sc in Personal Mobile and Satellite communication from the University of Bradford, United Kingdom. His research interest includes Radio Resource Management, Network Theory, Machine Learning, and 5G.

An Evolutionary Game-Based Random Access Scheme For Machine Type Communication Networks

Paul Orim*, Neco Ventura†, Joyce Mwangama*
*Dept. of Electrical Engineering, University of Cape Town
[1]ormpau001@myuct.ac.za
[2]Neco.Ventura@uct.ac.za
[3]jb.mwangama@uct.ac.za

***Abstract*—The critical challenge of deploying massive machine-type communication devices (MTCDs) on the cellular network without proper access control leads to severe congestions and network overload. The introduction of clustering of MTCDs within the macro cell helps to reduce network overload. However, an attempt to reduce network overload could lead to an increase in the energy consumed by MTCD during the random access procedure. To meet the latency requirement of MTCDs at reduced energy consumed, we propose an evolutionary game-based random access scheme. This scheme combines MTCD clustering and an effective access mode selection using the evolutionary game to distribute access requests. Thus, it enables the reduction of congestion in the network while reducing the energy consumed. Performances of the Evolutionary game-based access scheme show an improvement in the delay and energy consumed when compared to the ordinary Access Class Barring (ACB).**

***Index Terms*—Massive access, Random access, Evolutionary Game, Energy consumed, Cellular network.**

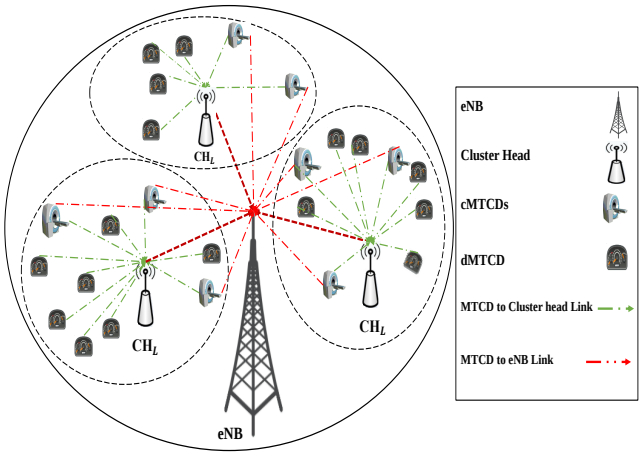

Fig. 1: Illustration of a Random Access Network

I. Introduction

Machine Type Communication (MTC) has become an important component of the Internet of Things (IoT) systems as it enables automated communication of Machine Type Communication Devices (MTCDs) with little or no human input. The existing cellular networks play a crucial role in providing the necessary platform for the connectivity of MTCDs. However, in contrast to the mostly downlink cellular traffic, machine-type communication (MTC) traffics are uplink-dominated. Also, their small data size means that they can be transmitted during the random access (RA) procedure. Nonetheless, the massive deployment of MTCDs over cellular infrastructure will require the densification of these devices. These will bring about technical challenges such as congestion and network overload especially over the air interface where random access is performed. Due to the limited air interface resource which is the random access channel (RACH), the massive number of MTCDs will also lead to waste of resources, quality-of-service (QoS) degradation, and in extreme cases, it may cause service unavailability. Furthermore, the requirement that MTCDs depend mostly on battery power, raises the concern of an increase in the energy consumed by these devices during Random Access (RA) procedure [1]. Consequently, there is a need for efficient control of massive access of MTCDs to allow for fair network access by these devices. The requirement to optimize the connectivity of MTCDs over cellular networks to meet their latency requirement at reduced energy is the focus of this paper.

To alleviate network overload and congestion at reduced energy consumed, we propose an evolutionary game-based access scheme. In this scheme, MTCDs are clustered to reduce the number of access requests arriving at the evolved node B (eNB). Considering that MTCDs are self-interested and aim to improve their performance, we introduce an evolutionary game that enables the analyses of the behaviour of MTCDs and optimizes the access selection thereby connecting devices to meet their latency requirement which reduces the energy consumed. Since MTCDs are considered to be with bounded rationality, the evolutionary game-based model is suitable for its key features of simplicity and requiring a limited amount of information among devices for decision making. The access scheme tends to balance MTCD access requests among the eNB and their respective cluster.

II. RELATED WORK

Several schemes have been put forward to tackle the problem of congestion during RA procedure with 3rd Generation Partnership Project (3GPP) coming up with standards that are mostly inefficient during massive access but have constantly been improved upon and used for the design of other schemes [2]. The authors in [3] proposed an optimal scheme that dynamically adjusts the access class barring (ACB) factor and the number of RACH resources among clustered MTCDs. However, ACB schemes are limited in performance during massive access. Also, the energy consumed was not considered in the research. An investigation was done by [4] on the impact on the RACH procedure when a massive number of MTCD try to access the radio access network. They evaluated mixed traffic scenarios, one with only MTCDs and the other with a mixture of MTCD traffic and VoIP traffic. They concluded that massive access diminishes the RACH resources and the situation is worsened with the combination of other types of traffic.

A review of the various challenges associated with the support of massive access in cellular communication systems was done in [5]. They analysed common approaches proposed in literatures and deduced that clustering would assist in addressing the problem associated with PRACH overload. The author in [6] proposed a two-stage radio access scheme to alleviate collision for MTCDs while [7] subscribed for a 3GPP ACB and separate RACH access scheme. Both authors implemented a form of clustering in the access scheme to control access to the eNB which reduces congestion in the PRACH. The drawback in their scheme was the inadequacies during massive access and the lack of consideration for the energy consumed. The impact of MTCDs massive and simultaneous access of LTE network was studied in [8]. They analysed five of the 3GPP access schemes namely ACB, Separate RACH, Backoff Access, Dynamic RACH allocation, and Slotted Access scheme. Although they concluded that slotted access performed optimally. However, it does not meet the QoS requirement of MTCDs because they are required to perform the RA procedure only during their allocated slot. The next optimal was the ACB scheme as it gives room for MTCDs to meet their QoS requirement. The shortcoming in the authors' analysis is that they did not consider the energy consumed.

The authors in [9] separated the PRACH resources (Preambles) into three portions; Human type users, machine type users, and a hybrid of both users. Giving priority to the human-type users, they dynamically allocated the third slot using a game-theoretic framework to any of the two types of users as their various congestion increases. Their scheme did not consider the QoS requirement of critical MTCDs neither did they analyse the energy consumed by the MTCDs. A prioritized energy-efficient RA scheme for stationary IoT networks utilizing timing advance value was considered in [10]. The collision and average energy consumed by MTCDs were shown to improve under a practical simulated environment. The scheme gave priority to MTCDs farther away from the eNB over those closer without considering the QoS requirement of the latter. The authors in [11] proposed an evolutionary game-based ACB algorithm that helps MTCDs alleviates congestion and eliminate substantial defects on the ordinary ACB scheme. However, the energy consumed by MTCDs and the QoS requirements of the MTCDs were not considered. Therefore, we tackle the issues of congestion and the energy consumed in the RA process by using an effective clustering and evolutionary game-based access scheme that reduces the access delay and energy consumed of critical MTCDs thereby meeting their QoS requirement.

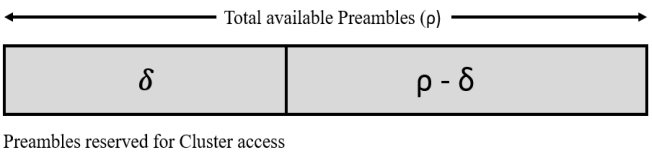

Fig. 2: Illustration of the preamble reservation technique

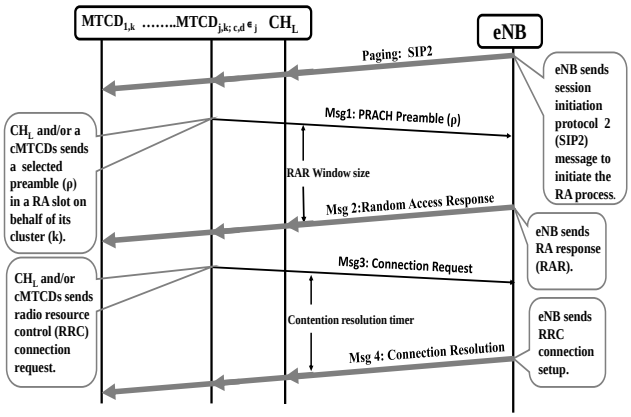

Fig. 3: Illustration of the clustered random access procedure

III. SYSTEM MODEL

We consider a single cell random access MTC served by an eNB where MTCDs are clustered as illustrated in Fig. 1. The MTCDs are classified into two types which are delay tolerant (dMTCDs) and critical MTCDs (cMTCDs). The RA procedure is as described in [12], however, preambles (ρ) are reserved for clustered access (δ) as shown in Fig.2. MTCDs are grouped into clustered with critical MTCDs allowed to access the δ preambles or transmit their preamble request directly to the eNB. We denote the cMTCD accessing the eNB as a cluster represented by e. The packet generation rate in a cluster for dMTCDs and cMTCDs follows a Poisson process at a rate of $\lambda_{d,k}$ and $\lambda_{c,k}$, respectively. To distribute access requests while considering the delay requirements of MTCDs, each cluster is designed to have a cluster head. The cluster head ($\mathcal{CH}_L$) is given the responsibility to initiate the RA procedure on the behalf of the group as shown in Fig. 3 [13]. MTCDs that send access requests directly to the eNB

do so using power ramping. This gives incentives to MCTDs not to perform their access request directly to the eNB as it will require higher preamble transmit power.

IV. Clustering and Random Access Process Analysis

To mitigate the effect of collision and meet the requirements of the different MTCDs, we design a scheme that gives cMTCDs the option of transmitting their access request either through the cluster head with a little delay or directly send their access request to the eNB which requires more preamble transmit power due to the implementation of power ramping. The scheme distributes access requests thereby reducing the number of such requests arriving at the eNB. The MTCDs are cluster in to $\mathcal{K}$ clusters where $\mathcal{K}$ = {1,2,3,..., k+1 }. We define a set of dMTCD in a cluster as $\mathcal{N}_{d,k}$ where $\mathcal{N}_{d,k} = \{1,2,3,...\mathrm{d_k}\}$. The set of cMTCD is also defined as $\mathcal{N}_{c,k}$ where $\mathcal{N}_{c,k} = \{1,2,3,..., \mathrm{c_k}\}$. A cluster head selection is implemented using the residual energy and the channel gain of the MTCDs within a cluster. The latency requirement of devices is taken into consideration when redistributing access requests between the eNB and the cluster head using the Evolutionary Game-based access selection mechanism. This enables the scheme to meet the QoS requirements at a reduced energy consumed for the devices within a cluster. The scheme is illustrated in three parts, namely, MTCDs clustering/cluster heads selection, random access and energy Consumption analysis, and the Evolutionary game-based access selection mechanism.

A. Clustering and Cluster head Selection

The MTCDs are clustered to reduce the number of concurrent channel access requests and increase the lifetime of the clustered MTCDs through less collision and lower preamble transmit power. However, the lifetime of the cluster head will be affected due to the increase in energy consumed in listening to the channels and initiating access requests. As illustrated in Fig. 2, for the purpose of cluster access a set of preambles is assigned for the use of intra-cluster access. The set of preambles can be used by other clusters due to the principles of preamble reuse [14]. The cluster head selection is based on a weighted cost function $\mathcal{A}_{\mathbf{w}}$ as derived in [15].The clustering and cluster head selection is as shown in Algorithm 1.

Algorithm 1 Clustering/Cluster heads selection Algorithm

1: Set maximum number of cluster k
2: Cluster MTCDs
3: Countdown 20secs
4: **if** Count == 0
5: For each cluster Calculate $\mathcal{A}_{\mathbf{w}}$
6: For each cluster $\mathcal{CH}_L$ == $\mathcal{A}_{\mathbf{w}}$
7: **end if**
8: **output** cluster, cluster head.

B. Random Access and Energy Consumption Scheme

We analyse the delay and average delay on the MTCD and its cluster with the understanding that MTCDs which access preamble directly through the eNB can be regarded as being in a cluster. When MTCD sends access requests to the cluster-head or eNB there will be collision as the number of MTCD increases. The probability of collision [4] of the RACH process for the cluster-access and eNB-access respectively can be calculated as:

$$\mathcal{Q}_{j,k} = 1 - e^{-\frac{\lambda_{j,k}}{\beta\rho}}, j \in \{\mathcal{N}_{d,k} \cup \mathcal{N}_{c,k}\}, \forall k \in \mathcal{K}, k \neq e, e \in \mathcal{K}. \tag{1a}$$

$$\mathcal{Q}_{c,e} = 1 - e^{-\frac{\lambda_{c,e}}{\beta(\rho-\delta)}}, \qquad c \in \{\mathcal{N}_{c,k}\}, \forall e \in \mathcal{K}, k \neq e, e \in \mathcal{K}. \tag{1b}$$

Where β denotes the total number of random access opportunities per second. The operation of the RA process is divided according to the mode of the MTCDs (i.e. Idle, transmission, and receiving modes). The RA process as described in [12] outlines stages of preambles exchanges. We assume the preamble requests are initiate immediately MTCDs generate data. The time taken to transmit message 1 and 3 is $\mathcal{T}_1$ and $\mathcal{T}_3$, respectively. $\mathcal{T}_p$ is the time taken when the MTCD pause before going into receiving mode, while the time taken to receive message 2 and 4 is denoted by $\mathcal{T}_2$ and $\mathcal{T}_4$, respectively. $\mathcal{T}_{idle}$ is the idle time of the device. The access delay for cluster-access and eNB-access is given by

$$\mathcal{D}_{j,k} = \frac{\mathcal{T}_1 + \mathcal{T}_2 + \mathcal{T}_3 + 2(\mathcal{T}_p)}{(\sum_{j=1}^{\alpha} \mathcal{Q}_{j,k})} + \frac{\mathcal{T}_1 + \mathcal{T}_2 + \mathcal{T}_3 + \mathcal{T}_4 + 2(\mathcal{T}_p)\psi}{(1 - \mathcal{Q}_{j,k})}, \tag{2a}$$

$$\mathcal{D}c, e = \frac{\mathcal{T}_1 + \mathcal{T}_2 + \mathcal{T}_3 + 2(\mathcal{T}_p)}{(\sum_{c=1}^{\alpha} \mathcal{Q}_{c,e})} + \frac{\mathcal{T}_1 + \mathcal{T}_2 + \mathcal{T}_3 + \mathcal{T}_4 + 2(\mathcal{T}_p)\psi}{(1 - \mathcal{Q}_{c,e})}, \tag{2b}$$

where *PreambleTransmax* (α_{max}) defines the maximum number of preamble re-transmission a MTCD can attempt after experiencing collision at the PRACH during eNB-access. we define α as the preamble collision counter where α = {1,2,3,..., α_{max} }. ψ is binary function that indicate congestion in the eNB-access. We express this function mathematically as:

$$\psi = \begin{cases} 1, if\ \alpha \\ 0,\ otherwise \end{cases}$$

The power consumed during the RA process for the idle, transmission, and receiving modes can be denoted by $\mathcal{P}_{idle}$, $\mathcal{P}_{PRACH}$, and $\mathcal{P}_r$ respectively. While the MTCD circuit power is denoted by $\mathcal{P}_{cir}$. We assume that the MTCDs are in an idle mode when not transmitting or receiving preamble messages. The power consumed for transmitting preamble [16] is given by

$$\mathcal{P}_{PRACH} = min\{\mathcal{P}_{MAX}, \mathcal{P}_{target} + \mathcal{PL}\}, \tag{3}$$

where $\mathcal{P}_{MAX}$ is the maximum configured MTCD transmit power, while pathloss ($\mathcal{PL}$) and the target power ($\mathcal{P}_{target}$) respectively are given by

$$\mathcal{PL} = 35.2 + \log d_{\mathrm{m}} \ , \tag{4a}$$

$$\mathcal{P}_{target} = \mathcal{P}_{P_target} + \theta + (\varrho - 1) * \varphi, \tag{4b}$$

Where Preamble_Received_Target_Power, Delta_Preamble, Preamble_Power_Ramping_Counter, and Preamble_Power_Ramping_Step are denoted by $\mathcal{P}_{P_target}$, θ, ϱ, and φ, respectively. The energy consumed by MTCD for cluster and eNB access respectively are given by

$$E_{j,k} = \begin{cases} \mathcal{D}_{j,k}(\mathcal{P}_{PRACH} + \mathcal{P}_r) + \mathcal{T}_{idle}\mathcal{P}_{idle}, k = e; k, e \in \mathbf{K} \\ \mathcal{D}j, e(\mathcal{P}_{PRACH} + \mathcal{P}_r) + \mathcal{T}_{idle}\mathcal{P}_{idle}, j = c, k \neq e, \\ k, e \in \mathbf{K}. \end{cases} \tag{5}$$

C. Evolutionary Game-based Access

We analyse the evolutionary game-based access scheme for the effective access of MTCDs. The replicator dynamics is used to model the strategy adaptation process while evolutionary equilibrium is considered as the solution of the formulated game. The evolutionary game is formulated as follows:

a) Set of players ($\mathcal{C}$): The set of cMTCDs who can choose among the two access modes are the players of this game. The dMTCDs are not involved in this game as they are programmed to access the network via their respective cluster head.

b) Strategy (s): The strategy is the selection of the access mode (i.e cluster-access (c) or eNB-access(e)) . Where (s) = { c, e } corresponds to the selection of an access mode. The players are interested in selecting a suitable access medium to meet their latency requirement at a reduced energy.

c) Population: The population is a set of players (cMTCDs) in the game. The population corresponds to each cluster-access area or eNB-access area. The total number of cMTCDs in an access area and the number of cMTCDs selecting a particular strategy can be denoted by $\mathcal{N}_k$ and n_{s}, respectively. Therefore, the frequency of strategy s used in the particular population also referred to as population share is given by

$$\mathbf{x}_{\mathrm{s}} = \frac{n_{\mathrm{s}}}{\mathcal{N}_k}. \tag{6}$$

d) Payoff function: This function quantifies the performance satisfaction level of a potential cMTCD strategy s which depends on the delay and the preamble transmit power $\mathcal{P}_{tr}$ of the cluster-access or eNB-access. The first component measures the utility of the cMTCDs in selecting an access mode, while the second component is the penalty (or reward) for such a strategy. We use $\pi_c(t)$ to denote the utility of players selecting strategy s and $\bar{\pi}(t)$ to denote the average utility of the said population. The replicator dynamics and the evolutionary equilibrium can be expressed as follow:

- Replicator dynamics: The replicator dynamics model the rate of strategy adaptation by which cMTCDs will adapt their strategy according to the received payoff. This strategy adaptation by cMTCDs will affect the population share leading the population to evolve hence the evolution of the game. The evolution of the population can be analysed by the replicator dynamics which is a set of the ordinary differential equation given by

$$\dot{x}(t) = x_j(t)(\pi_j(t) - \bar{\pi}(t)), \tag{7}$$

where $x_j(t)$ denote the population of cMTCDs in a cluster selecting a strategy s. The utility of a cMTCD $\pi_j(t) = \mathcal{U}(E_{j,k})$ while the utility of the of the population $\bar{\pi}(t) = \mathbb{E}[E_{j,k}]$

- Evolutionary equilibrium : The Evolutionary equilibrium is considered as the solution to the game where the proportion in each access group will be stable. When this stable point is reached, the payoffs of all cMTCDs in a cluster are identical and they will not be willing to change their access mode.

V. PERFORMANCE EVALUATION

The simulation was carried out according to the parameters highlighted in Table 1. MTCDs were designed to generate a maximum of 25 packets per second. We assumed that access requests are sent immediately after they are generated, therefore, no idle time between access generation and access requests. This is done to simulate the massive nature of MTCDs. ACB was implemented at the cluster for dMTCD and power ramping is implemented at the cMTCD to eNB access. We cluster the MCTDs into twenty (20) clusters based on the work in [15]. The clustering and cluster head selection was done as specified in Algorithm 1. We set δ = 18 . The percentage of dMTCDs and cMTCDs is as indicated in Table 1.

Algorithm 2 Evolutionary Game-based Random Access Algorithm

1: Initialize MTCD in terms of dMTCD and cMTCD
2: Execute Algorithm 1
3: Initialize **ALL** dMTCD to perform RA through the cluster-access
4: Initialize cMTCD˙pick randomly to pick either 1 or 2.
5: **if** cMTCD˙pick = 1
6: cMTCD perform eNB-access
6: **else if**
7: cMTCD˙pick = 2
8: cMTCD perform cluster-access
9: **end if**
10: Calculate E_{n_k}, $\mathbf{x}_{\mathrm{s}}$, π_c, $\bar{\pi}$ and $\dot{x}$
11: **if** $\dot{x} \leqslant 0$
12: Remain in initial Access mode
13: **else if**
14: Change in initial Access mode
15: Perform Evolutionary Game according to the utility function to achieve equilibrium
16: **end if**

A. Performance Metrics

The key performance indicators were evaluated to obtain our simulation results which show the effectiveness of our proposed scheme to that of the ACB scheme. The aim is to meet the QoS requirement of cMTCDs. The following parameters were evaluated:

- Average MTCD Access delay: The average time it takes for each type of MTCD to generate an access request to the time this request is either successful or failed. This access request can either be from the MTCD to the eNB or through the $\mathcal{CH}_L$ to the eNB.
- Average Energy Consumed: The average energy consumed by MTCDs during the RA process (i.e, request generation inclusive). As mentioned earlier it is for both successful and failed access.

TABLE I: SIMULATION PARAMETERS

Parameter	Values
PRACH configuration Index	5
Number of Preambles	54
PreambleTransMax (α_{max})	5
ACB factor (Q)	variable
Back off time (T_{K})	10subframe
Number of resource block per slot	6RBs
Max MTCD transmission Power	23dBm
Power ramping Step	2dBm - 6dBm
MTCD circuit power	10dBm
% of dMTCD	60
% of cMTCD	30
Pathloss(MTCD to $\mathcal{CH}_L$)	127 + 30$\log_{10} d$, d in km [17]
Pathloss(MTCD to $\mathcal{CH}_L$)	35.2 + 35$\log_{10} d$, d in km [10]

B. Performance Result

The effectiveness of our simulation result is shown in comparison with the ACB scheme. We concentrate on the QoS of cMTCDs as we wish to appraise the effect of massive access on the delay and energy consumed by cMTCDs. The results as presented in Figs. 4, 5, and 6 shows the effect of the aforementioned performance metrics given 20 cluster formations. When considering the average delay for 20 cluster formation, our evolutionary game-based access scheme outperforms the ACB scheme especially as the number of MTCDs increases. In Fig. 4, the access delay for our scheme raised from around $7.24ms$ with 200 MTCDs to $114.81ms$ with 2000 MTCDs while for the same number of MTCDs the access delay of the ACB scheme raised from $10.45ms$ to $150ms$. We also observed higher energy consumed for the ACB scheme compared to our scheme.

The dynamics of the utility for eNB-access and clustered-access modes is shown in Fig. 6. The evolutionary equilibrium was attended for each type of access which is that stable utility where no MTCDs will change their current access mode. This is the case as changing access mode at this stage will not yield to a higher utility for the said MTCD.

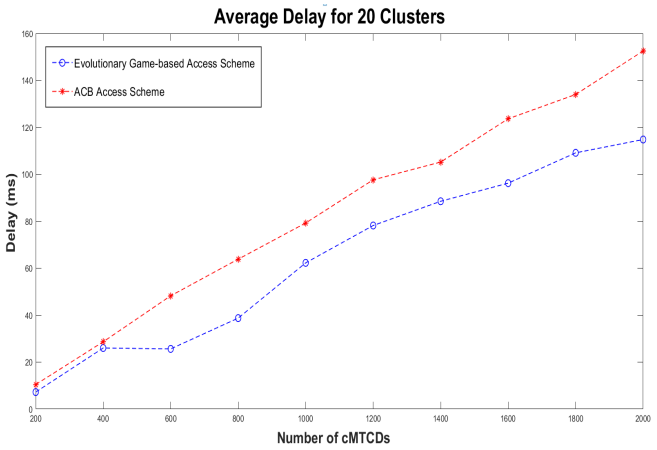

Fig. 4: Average delay for evolutionary game-based access and ACB access for 20 clusters

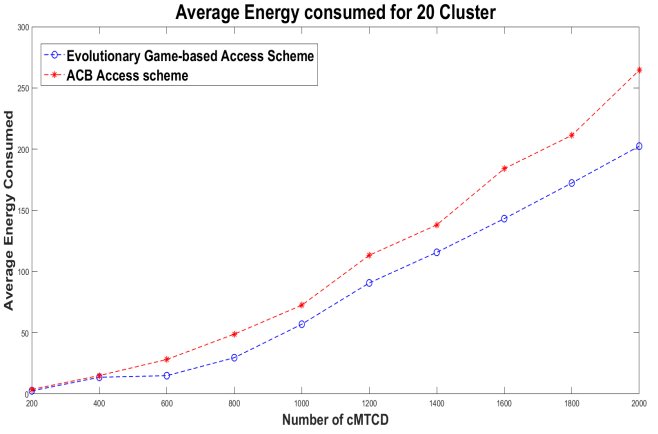

Fig. 5: Average energy consumed for evolutionary game-based access and ACB access for 20 clusters

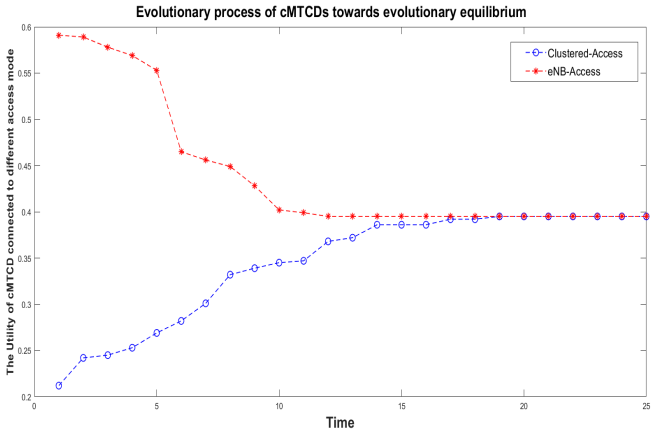

Fig. 6: Average utility for evolutionary game-based access and ACB access for 20 clusters

VI. CONCLUSION

In this paper, we have proposed an Evolutionary game-based access scheme that redistributes access requests of MTCDs thereby improving the delay and energy consumed of MTCDs in comparison with the 3GPP ACB scheme. The choice of evolutionary game was due to its low complexity considering that MTCDs require their battery life to last for 10 years when deployed. We clustered MTCDs into 20 cluster formations and using power ramping and evolutionary game-based access, the QoS of MTCDs was achieved at reduced energy consumed. Future research direction will be geared towards applying suitable machine learning to give the MTCDS some degree of intelligence at reduced complexity.

ACKNOWLEDGEMENT

The authors acknowledge the support received from TELKOM SA via the Telkom Centre of Excellence (CoE) in Broadband Networks Applications at UCT, as well as the University of Calabar, Nigeria.

REFERENCES

[1] M. Hasan, E. Hossain, and D. Niyato, "Random access for machine-to-machine communication in lte-advanced networks: Issues and approaches," *IEEE communications Magazine*, vol. 51, no. 6, pp. 86–93, 2013.

[2] H. Althumali and M. Othman, "A survey of random access control techniques for machine-to-machine communications in lte/lte-a networks," *IEEE Access*, vol. 6, pp. 74 961–74 983, 2018.

[3] N. Li, C. Cao, and C. Wang, "Dynamic resource allocation and access class barring scheme for delay-sensitive devices in machine to machine (m2m) communications," *Sensors*, vol. 17, no. 6, p. 1407, 2017.

[4] N. S. Bezerra, M. Wang, C. Åhlund, M. Nordberg, and O. Schelén, "Rach performance in massive machine-type communications access scenario," in *2018 IEEE Wireless Communications and Networking Conference (WCNC)*. IEEE, 2018, pp. 1–6.

[11] T. Jiang, X. Tan, X. Luan, X. Zhang, and J. Wu, "Evolutionary game based access class barring for machine-to-machine communications," in *16th International Conference on Advanced Communication Technology*. IEEE, 2014, pp. 832–835.

[5] A. Biral, M. Centenaro, A. Zanella, L. Vangelista, and M. Zorzi, "The challenges of m2m massive access in wireless cellular networks," *Digital Communications and Networks*, vol. 1, no. 1, pp. 1–19, 2015.

[6] W. Li, Q. Du, L. Liu, P. Ren, Y. Wang, and L. Sun, "Dynamic allocation of rach resource for clustered m2m communications in lte networks," in *2015 International Conference on Identification, Information, and Knowledge in the Internet of Things (IIKI)*. IEEE, 2015, pp. 140–145.

[7] H.-W. Kao, Y.-H. Ju, and M.-H. Tsai, "Two-stage radio access for group-based machine type communication in lte-a," in *2015 IEEE International Conference on Communications (ICC)*. IEEE, 2015, pp. 3825–3830.

[8] M. Ouaissa, M. Benmoussa, A. Rhattoy, M. Lahmer, and I. Chana, "Performance analysis of random access mechanisms for machine type communications in lte networks," in *2016 International Conference on Advanced Communication Systems and Information Security (ACOSIS)*. IEEE, 2016, pp. 1–6.

[9] Y.-C. Pang, S.-L. Chao, G.-Y. Lin, and H.-Y. Wei, "Network access for m2m/h2h hybrid systems: A game theoretic approach," *IEEE Communications Letters*, vol. 18, no. 5, pp. 845–848, 2014.

[10] E. Park, J. Bae, Y. Choi, and Y. Han, "Energy-efficient random access for lte-based stationary iot networks," *IEEE Communications Letters*, vol. 23, no. 2, pp. 346–349, 2018.

[12] P. Orim and N. Ventura, "Dynamic massive access for machine type communication in lte/lte-a," in *Proceedings of the 2018 Southern Africa Telecommunication Networks and Applications Conference (SATNAC-2018*, 2018, pp. 92–97.

[13] G. Farhadi and A. Ito, "Group-based signaling and access control for cellular machine-to-machine communication," in *2013 IEEE 78th vehicular technology conference (VTC Fall)*. IEEE, 2013, pp. 1–6.

[14] H. R. Mazandarani and S. Khorsandi, "Preamble reuse for massive machine-type communications in lte networks," in *Electrical Engineering (ICEE), Iranian Conference on*. IEEE, 2018, pp. 1652–1657.

[15] P. Orim, N. Ventura, and J. Mwangama, "Cluster-based random access scheme for 5g urllc," in *2019 IEEE International Conference on Advanced Networks and Telecommunications Systems (ANTS)*. IEEE, 2019, pp. 1–6.

[16] T. ETSI, "136 213 v14. 2.0 (2017-04)," *LTE; Evolved Universal Terrestrial Radio Access (E-UTRA); Physical layer procedures*.

[17] S. Ekwe and N. Ventura, "Joint user association and power allocation in a social-aware 5g multi-cell network."

Paul Orim is currently studying for his PhD in the Department of Electrical Engineering, Telkom Centre of Excellence in Broadband Networks at the University of Cape Town, South Africa.

Non-Orthogonal Multiple Access For Virtualised Networks: A Deep Neural Network Approach

Oladejo, S.O*, Ekwe, S.O.*, Akinyemi, L.A*†, Ventura, N.*
* *Department of Electrical Engineering, University of Cape Town, South Africa*
† *Department of Electronic and Computer Engineering, Lagos State University, Lagos, Nigeria*
[1]oldsun002@myuct.ac.za ; [2]ekwste001@myuct.ac.za
[3]ltfaki001@myuct.ac.za; [4]neco.ventura@uct.ac.za

***Abstract*—The 5G mobile networks are required to meet the ever-increasing user demands. However, the rise in the user density accompanied by diverse user requirements places a heavy burden on the existing multiple access techniques, their complexity, and the tractability of mobile networks. Consequently, this leads to the optimum system capacity problem faced by the networks and experienced by the users. Motivated by this shortcoming, a deep neural network (DNN) based non-orthogonal multiple access (NOMA) model for virtualised 5G premised on the power-domain variant of NOMA is presented in this study. Thus, a network resource allocation problem is formulated as a capacity maximisation optimisation problem and decomposed into a user-pairing and joint power-radio resource allocation problem. The coverage area of the macrocell is segmented and users are categorised and paired according to geographical location. Also, a power splitting factor is introduced in the allocation of transmit power. The DNN-NOMA based model is trained with data captured by over $200,000$ runs of Monte-Carlo simulations for different network scenarios. We compare the performance of the DNN-NOMA based model with the traditional NOMA scheme. Our findings reveal that the DNN-NOMA based model outperforms the traditional NOMA scheme.**

***Index Terms*—NOMA, DNN, 5G, capacity, user-pairing**

I. Introduction

Cisco reported [1] that by 2023, there would be 3.6 networked devices/connections per person and nearly 10 devices and connections per household, leading to a projection of 30 billion networked devices by 2023, up from 18.4 billion in 2018. Consequently, the explosive growth rate will place huge capacity burdens on mobile networks. However, the fifth generation (5G) networks will play a critical role in meeting the growing and diverse demands of these futuristic subscribers [2]. Also, the 5G networks are expected to meet various requirements of verticals such as latency, security, data rates, energy consumption, reliability, massive connection.

The two broad approaches to 5G network research are: the evolutionary and the service-oriented views [3]. In the evolutionary approach, new technologies such as massive-user MIMO, beamforming, new multiple access technique (such as non-orthogonal multiple access (NOMA)) are employed to enhance network performance. The service-oriented view entails redesigning the architecture of the 5G network and therefore adopts technologies such as cloud computing, network function virtualisation (NFV), and network slicing (NS) [4]. Motivated by the increasing number of users/devices and the growing reliance on the mobile network for human transactions during and post-COVID19 pandemic, in this work, both approaches are applied to solve the optimum capacity problem of a 5G slice network. The viewpoint in this study is to implement a 5G slice network in a deep learning-based NOMA environment.

In NOMA, the idea is to assign more than one user at the same time to a resource block which can either be a time slot, a sub-channel, or a spread code. Hence, it meets the requirements of massive connectivity and higher spectrum efficiency. Moreover, users are distinguished by their power levels, which is made possible by employing successive interference cancellation (SIC) both at the transmitter and receiver [5], [6]. However, in orthogonal multiple access (OMA), users are assigned resource blocks that are orthogonal in time, code space, frequency in such a manner to prevent interference. Unlike NOMA, in OMA systems, a resource block is assigned to only one user irrespective of the user's channel conditions. Figure 1 illustrates the NOMA environment.

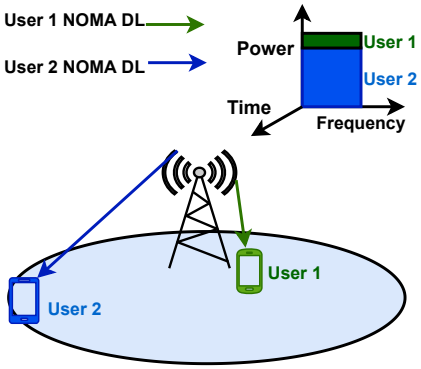

Fig. 1. Illustration of NOMA.

Although NOMA improves network performance such as the number of connections, spectral efficiency, nevertheless it requires high computational power and complex SIC algorithms. Additionally, the increasing diversity and complexity of mobile network architectures have made the designing, monitoring and operation of resource allocation schemes intractable. Therefore, incorporating the intelligence of machine learning is imperative to keep mobile networks efficient and automated [7]. Moreover, with the recent breakthroughs in deep neural networks (DNN) and the rapidly decreasing cost of graphic processing units and tensor processing units, DNNs can be applied to NOMA systems to enhance network

intelligence, reduce the required computing power and complexity of SICs in the implementation of NOMA systems [8], [9]. Additionally, DNNs possess powerful learning and universal approximation abilities, and to this end, they can simulate complex communication systems [10]. DNNs have the capability of handling geometric data (i.e., multivariate data) of mobile networks [7]. In this work, DNN is engaged in the pairing of mobile users, channel estimation, and resource allocation in a NOMA-based slice network to optimise the network capacity and eventually spectral and energy efficiencies.

A critical problem in the implementation of network slicing in virtualised multi-tenancy environment is the challenge of optimum system capacity. The key contributions of this paper are as follows :

- A DNN-based NOMA resource allocation model is proposed to achieve optimum system capacity utilisation. The DNN-based NOMA resource allocation model carries out channel estimation, pair slice users, and allocates network resources. The inputs features of the model consist of the coordinates of the slice user, the power budget of the gNodeB, and coverage radius of the gNodeB.
- An optimal system capacity optimisation sliced network in a virtualised multi-tenant environment is formulated. Moreover, we employed an efficient pairing scheme to associate certain slice users to the same radio resource. An efficient and yet simple power allocation strategy that relies on slice user positioning is proposed.
- The system capacity is investigated by varying network parameters such as the cell radius, power budget of the gNodeB, number of cell users, and convergence of the model.
- A DNN-based NOMA resource allocation model is proposed to enhance network capacity, and compared with a traditional NOMA approach.

II. System Model

A. General Model

We describe the system model considered in this paper, as depicted in Fig. 2. The considered scenario assumes the downlink of a single-tier network whose physical resources are owned by an infrastructure provider (InP). The InP provides services to a set of mobile virtual network operators (MVNOs) $\mathcal{H} = \{h|h \in \mathcal{N}, 1 \leq h \leq |\mathcal{H}|\}$. Each MVNO, $h \in \mathcal{H}$ is uniquely independent of each other; that is, $h \neq h^{'}$, and h has its own set of network slice use cases, $\mathcal{S}_h$, it offers to its slice users. However, $\mathcal{S}_h = \{\mathcal{E} \cup \mathcal{M}\}$, in which $\mathcal{E}$ denotes the eMBB slice user case and $\mathcal{M}$ indicates the mMTC slice use case. It is essential to state that the users of an MVNO, h, are categorised according to their requested slice use case $\{\mathcal{E} \cup \mathcal{M}\}$ and geographical position in the multi-tier network. The system bandwidth is composed of equal-sized physical resource block RBs in the frequency domain.

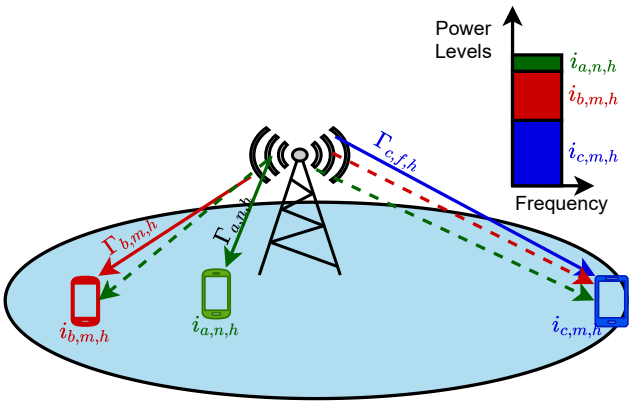

Fig. 2. Illustration of the system model.

B. Slice User Categorisation

Considering the slice use-case requested by QoS requirement and the geographical location of the users, we categorise users into three:

1) **Cat. I:** $\mathcal{E}_{h,n}$ is the set of eMBB users belonging to MVNO h, nearest to the gNodeB, i.e., lies within a distance range $0 \leq d_n$. In addition, the set of users requesting mMTC slice belonging to MVNO h nearest to the gNodeB, i.e., lies within a distance range $0 \leq d_n$, is denoted by $\mathcal{M}_{h,n}$.
2) **Cat. II:** The set of MVNO h eMBB users in the coverage of a macro cell, however fairly distant from the gNodeB within the distance range $d_n < d \leq d_m$, is denoted as $\mathcal{E}_{h,m}$ and similarly, $\mathcal{M}_{h,m}$ for the set of mMTC slice users.
3) **Cat. III:** For the set of slice users belonging to MVNO h, that is beyond distance d_m from the gNodeB, is denoted as $\mathcal{E}_{h,f}$. Likewise, $\mathcal{M}_{h,f}$ denotes the set of mMTC slice users which are beyond distance d_m from the gNodeB.

The Categorisation of slice users according to their geographical location plays a critical role in the pairing of users allocated to the same resource.

C. Channel Model

Specifically, our paper draws on the downlink of a single-tier NOMA-based system model given in [11], [12]. Without loss of generality, we assume mMTC and eMBB slice users are static and moderately mobile users. We consider a slice user i_h with a path loss in dB given as [13]

$$\rho_{i,j,h} = 30 + 35\log(d_{i,j,h}), \qquad \forall\ i_h \in \{\mathcal{E}_{h,j}, \mathcal{M}_{h,j}\}, \quad j \in \{n, m, f\}, \quad (1)$$

where $d_{i,j,h}$ denotes the distance in metres of the slice user, i_h, belonging to MVNO, h within the distance range, $j \in \{n, m, f\}$. For clarity, n,m, and f are from the categorisation in subsection II-B. $\Gamma_{i,j,h}$ denotes the channel gain of a slice user which belongs to an MVNO, h, and given as,

$$\Gamma_{i,j,h} = 10^{-\frac{\rho_{i,j,h}}{10}}, \quad (2)$$

where $\rho_{i,j,h}$ denotes the path loss given (1).

D. Non-Orthogonal Multiple Access (NOMA)

In this work, we consider a power-domain NOMA (PD-NOMA) system. In PD-NOMA systems, slice users allocated to the same frequency resource (i.e., PRB) are distinguished by the respective power levels. The complexity of the SIC circuitry in decoding users increases as the number of slice users allocated the same resource increases. However, in practice, the number of slice users on the same resource is limited to 3.

For a NOMA system with 3 slice users on a resource block, such that the channel gains of the 3 users are $\Gamma_{a,n,h}$, $\Gamma_{b,m,h}$, and $\Gamma_{c,f,h}$, belonging to the same MVNO h, however with different distances in the categorisation of near, mildly far, and far, respectively. Employing the SIC, the data rate of the respective slice users is given as

$$\gamma_{i,j,h} = \begin{cases} \log_2(1 + \dfrac{P_{a,n,h}\Gamma_{a,n,h}}{N_o B}), \quad \forall\ a, i \in \{\mathcal{E}_{h,n}, \mathcal{M}_{h,n}\}, \\ \qquad\qquad\qquad\qquad j = n \\ \log_2(1 + \dfrac{P_{b,m,h}\Gamma_{b,m,h}}{N_o B\ +\ P_{a,n,h}\Gamma_{b,m,h}}), \\ \qquad\qquad \forall\ b, i \in \{\mathcal{E}_{h,m}, \mathcal{M}_{h,m}\},\ j = m \\ \log_2(1 + \dfrac{P_{c,f,h}\Gamma_{c,f,h}}{N_o B\ +\ P_{a,n,h}\Gamma_{c,f,h} +\ P_{b,m,h}\Gamma_{c,f,h}}), \\ \qquad\qquad \forall\ c, i \in \{\mathcal{E}_{h,f}, \mathcal{M}_{h,f}\}, \quad j = f, \end{cases} \tag{3}$$

where $P_{a,n,h}$, $P_{b,m,h}$, and $P_{c,f,h}$ denote the downlink transmit power for users $i_{a,n,h}$, $i_{b,m,h}$, and $i_{c,f,h}$, respectively. Herein, $\Gamma_{a,n,h} > \Gamma_{b,m,h} > \Gamma_{c,f,h}$ and $P_{a,n,h} > P_{b,m,h} > P_{c,f,h}$ according to the principles and concepts of NOMA.

III. Problem Formulation

In this section, the problem of maximum capacity in a multi-tenant single-tier virtualised 5G Network in a network slicing scenario is examined. To fully maximise the capacity of the network, we formulate a joint power-resource allocation problem in (4).

$$\max_{P_{i,j,h}, \alpha_{i,j,c}} \quad \sum_{h \in \mathcal{H}} \left[\quad \sum_{c \in \mathcal{C}} \sum_{i_h \in \mathcal{I}_h} \alpha_{i,h,c}\ \mathcal{B}_{c,h}\ \gamma_{i,j,h} \right] \tag{4}$$

s.t.

C1: $\sum_{i_h \in \mathcal{I}_h} \alpha_{i,h,c} = k, \quad \forall\ h \in \mathcal{H}, \ \forall\ c \in \mathcal{C}, \ 2 \leq k,$

C2: $\sum_{h \in \mathcal{H}} \sum_{c \in \mathcal{C}} \sum_{i_h \in \mathcal{I}_h} \alpha_{i,h,c}\ \mathcal{B}_{c,h} \leq k\mathcal{B}, \ 2 \leq k,$

C3: $\sum_{i_h \in \mathcal{I}_h} \alpha_{i,h,c} P_{i,j,h} \leq P_c, \ \forall h \in \mathcal{H}, \ \forall c \in \mathcal{C}, \ j \in \{n, m, h\},$

C4: $\sum_{h \in \mathcal{H}} \sum_{c \in \mathcal{C}} \sum_{i_h \in \mathcal{I}_h} \alpha_{i,h,c} P_{i,j,h} \leq P_{max}, \quad j \in \{n, m, h\},$

C5: $P_{i,j,h} \geq 0, \ \ \forall i_h \in \mathcal{I}_h, \ \ \forall h \in \mathcal{H}, \ \ j \in \{n, m, h\},$

C6: $\alpha_{i,j,h} \in \{0, 1\}, \ \ \forall i_h \in \mathcal{I}_h, \ \ \forall h \in \mathcal{H}, \ \ j \in \{n, m, h\},$

The throughput of each MVNO is the summation of the throughput of the three categories of slice users explained in subsection II-B and therefore, the network's total throughput is the maximisation of the several MVNOs throughput which is given in the objective function of (4). As shown in (4), $\mathcal{I}_h = \{\mathcal{E}_{h,n} \cup \mathcal{M}_{h,n} \cup \mathcal{E}_{h,m} \cup \mathcal{M}_{h,m} \cup \mathcal{E}_{h,f} \cup \mathcal{M}_{h,f}\}$. $\mathcal{B}$ and $\mathcal{C}$ denote the PRB size and set of PRB. Constraint C1 ensures the total number of users allocated the resource block does not exceed the defined threshold k. For NOMA systems, to reduce the complexity of the SIC circuitry k, is usually set at values not greater than 3. Constraint C2 ensures that the bandwidth capacity of the gNodeB is not exceeded. Moreover, C2 takes into consideration the number of users allocated to the same resource block. Additionally, constraint C3 ensures that the transmit power limit for each resource block is not violated by the users allocated the same resource block. Similar to C3, constraint C4 ensures the power budget of the gNodeB is not exceeded. Constraints C5 and C6 ensure the transmit power $P_{i,j,h}$ is a positive quantity and the resource allocation variable $\alpha_{i,j,h}$ is either 0 or 1. The value of $\alpha_{i,j,h}$ is 1 if and only if the resource block is allocated to a particular user and 0 otherwise.

IV. Proposed Solution

In this section, we present the detailed description of the proposed solution to the maximum capacity resource allocation problem in a NOMA-based virtualised network stated in (4). First, we perform the user-pairing process which is critical to the operation of the SIC in NOMA systems.

A. User-Pairing Process

We propose a user-pairing scheme that segments the gNodeB's coverage area into k regions, where k is the number of users that can be paired to the same resource (i.e., PRB in this case). Moreover $k \geq 2$, however, to reduce the complexity of the SIC circuitry, it is such that $2 \leq k \leq 3$. This is illustrated in Fig. 3. The pseudo-code of the user-pairing scheme is described in Alg. 1. Furthermore, we simplify (4) by transforming the objective function into a tractable expression. The transformed expression is a summation of the capacity of the MVNOs in the network. The power allocation is critical to the capacity maximisation in NOMA-based systems.

B. Joint Power-Radio Resource Allocation Scheme

A joint power-radio resource allocation scheme is proposed that takes into consideration the constraints in (4) to ensure the

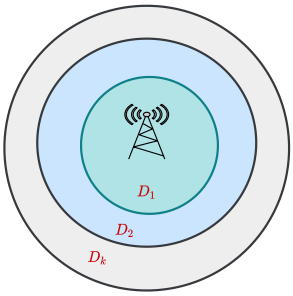

Fig. 3. Coverage region segmentation for the user-pairing.

Algorithm 1 User-Pairing Scheme

Segment the coverage area into k
Set the distances threshold for k segment
Create a pairing table (PT)
for $h \leftarrow 1$ to $|\mathcal{H}|$ **do**
  Determine the distance of users from the gNodeB
  for $c \leftarrow 1$ to $|\mathcal{C}|$ **do**
    Pair users from different segments in step 6
    Update the PT
  end for
end for
return PT

efficient allocation of both transmit power and radio resource blocks to slice users. The power allocation to slice users is dependent on the location of the slice users and the application of a power-splitting factor, β_q. The power-splitting factor is dependent on the number of distance segments described in subsection IV-A, such that,

$$\sum_{q=1}^{k} \beta_q \leq 1, \qquad \beta_q \in \{0, 1\}. \tag{5}$$

The pseudo-code of the joint power-radio resource allocation scheme is given in Alg. 2.

Algorithm 2 Joint Power-Radio Resource Allocation Scheme

Set the number of resources $\mathcal{C}$
Set the power-splitting factor $\boldsymbol{\beta} = \{\beta_1, \beta_2, \cdots, \beta_k\}$
Set the Power budget of the gNodeB, P_{max}
for $h \leftarrow 1$ to $|\mathcal{H}|$ **do**
  Set the max. power for each PRB, P_c
  $P_c = P_{max}/|\mathcal{C}|$
  Attribute β_k to users based on their distance threshold
  for $c \leftarrow 1$ to $|\mathcal{C}|$ **do**
    For users paired: $P_{i,k,h} = \beta_q P_c$
  end for
end for

C. DNN NOMA-Based Model

Deep learning is a branch of machine learning that employs neural networks (otherwise known as DNNs) as function approximators, with a particular emphasis on stacking many layers of structurally similar components such as neurons, activations, biases, weights, and layers in order to define the multilayer perceptron (MLP), a simple model that is iteratively composed of these basic components [14]. As illustrated in Fig. 4, the DNN is made up of many hidden layers whose weights are trained by the data set feed into the DNN. In this work, our DNN-NOMA based model is designed following the stages depicted in Fig. 5.

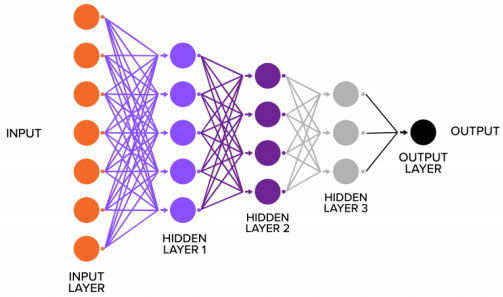

Fig. 4. DNN with hidden layers [15].

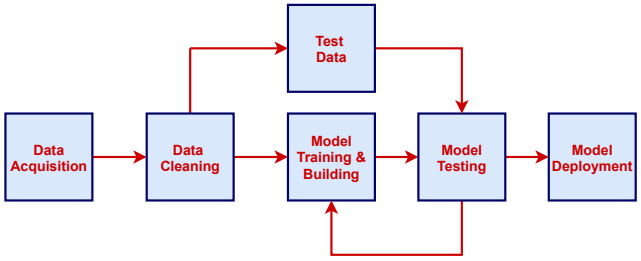

Fig. 5. DNN NOMA based model generation process.

1) Data Acquisition: Herein, the data used in modeling the DNN-NOMA based model is generated with the aid of the Monte Carlo process (i.e., over 200000 runs) in MATLAB environment. The deployment of the NOMA-based network was performed in the MATLAB environment, with several scenarios of network simulated to determine an average value of the network performance metric. Furthermore, the throughput of each user per scenario is captured in the data set. The input data is of the form given by

$$input = \{\delta_1,\ \delta_2,\ \delta_3,\ \delta_4,\ \delta_5,\ \delta_6\}, \tag{6}$$

where δ_1 and δ_2 denote the position coordinates of the user; δ_3 and δ_4 denote the coverage radius and number of users in a cell. The power budget and resource capacity of the gNodeB is denoted as δ_5 and δ_6,respectively. The throughput of each user is represented as δ_7 is the target in this case. The data is stored in CSV format.

2) Data Cleaning: The cleaning process in this work is performed in a python pandas environment. The cleaning is done using data wrangling to clean null cells and other data engineering processes.

3) Model Building and Training: In building the model, we employed the tensorflow framework [16], keras [17], and scikit-learn libraries [18] in a python environment. The model is designed using a sequential model owing to its simplicity with 3 hidden layers. Each layer is made up of 6 rectified linear unit (relu) [19] activation neurons. Owing to the large data set used in training, a batch mode technique of capturing the data set is employed, with the epoch set at 300. We chose an Adam-based optimization algorithm [20] which can replace the classical stochastic gradient descent owing to fast convergence, superior handling of memory and sparse gradients. It is a first-order optimisation algorithm that optimises the loss function by iteratively updating the weights of the neurons based on the training data. A simplistic pseudo-code of Adam optimiser is described in Alg.3.

Algorithm 3 Adam Optimiser

```
Initialise moment vectors
i ← 0 Initialise step
while Parameters not converged do
    i ← i + 1
    Get gradients at step i
    Update biased moment estimates
    Compute bias-corrected moment estimates
    Update parameters
end while
```

4) Test Data: Using the train-test-split technique from sklearn libraries, we split the data set into training and test data. In this work, 70% of the data set is used for the model training and the remaining 30% is then used for performing the test process.

V. Results and Discussion

In this section, we evaluate the performance of the DNN-NOMA based model in a python environment. We considered a single-tier network with one MVNO. The slice users were uniformly distributed across the coverage of the gNodeB. The gNodeB is assumed to have a bandwidth capacity of 5MHz (i.e., 25 PRBs). Besides, the proposed scheme can be deployed in networks with larger bandwidth size.

A. Impact of Power Budget on Network Capacity

First, we investigate the performance of the DNN-NOMA based model with number of slice users set at 14 and cell radius varied at 500m and 750m, respectively in Fig. 6. We observe that network throughput increases as the power budget increases. Moreover, the DNN-NOMA follows the same increasing trend as that of the NOMA based scheme. However, the DNN-NOMA based scheme outperforms the NOMA scheme.

B. Impact of Number of Slice users on Network Capacity

Figure 7 presents the impact of the slice user on the total network throughput. In Fig. 7, we set the power budget of the gNodeB to 40W and the coverage radius of the cell to 150m, while the number of slice users is varied. From Fig. 7,

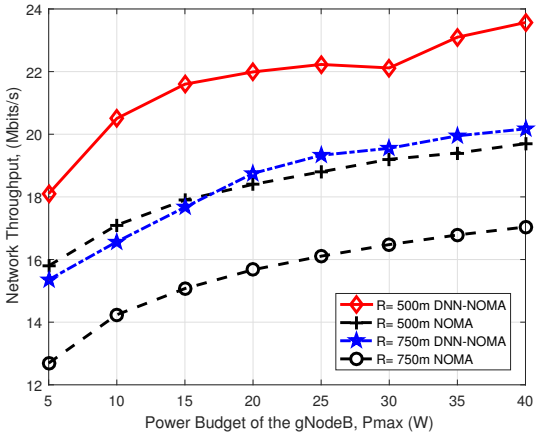

Fig. 6. Impact of power budget on network capacity.

we can observe that the total network throughput increases as the number of slice users increases. This is as a result of the increase in the demand for radio resources by users on the network. Moreover, the DNN-NOMA follows the increasing trend of the NOMA scheme.

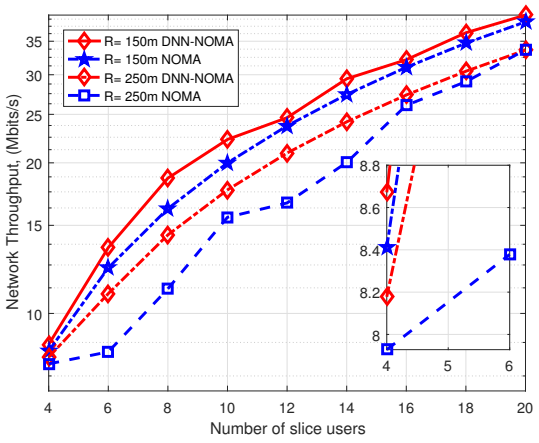

Fig. 7. Impact of number of slice users on network capacity.

C. Impact of Cell Radius on Network Capacity

Figure 8 shows the impact of the cell radius on the network throughput. Herein, we vary the cell radius from 100m to 500m and set the number of slice users to 20 and the gNodeB's power budget to 40W. We observe that the network throughput decreases as the cell radius increases. This is owing to the effect of distance on the path loss and consequently the channel gain. Additionally, the DNN-NOMA based model outperforms the NOMA scheme.

D. Convergence of the DNN Model

In Fig. 9, we investigate the convergence of the DNN-NOMA based scheme after training the model. The DNN-NOMA is observed to converge fast at about the 10th to 20th iteration. Although DNNs are known to converge fast,

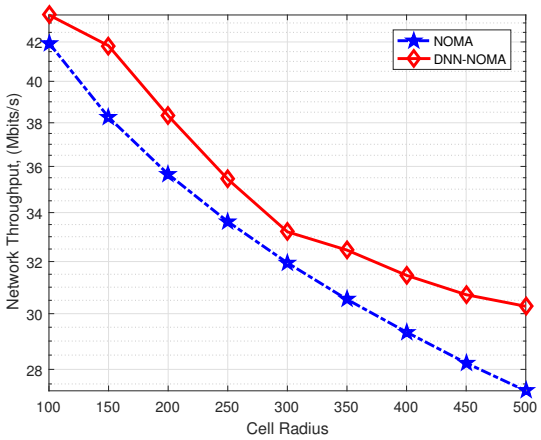

Fig. 8. Impact of cell radius on network capacity.

however, the choice of the adam optimization algorithm enhances the convergence of the DNN-NOMA model.

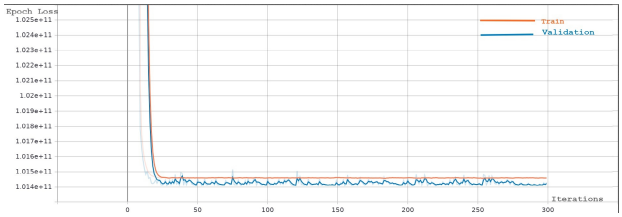

Fig. 9. Convergence of the DNN-NOMA based Model.

VI. Conclusion

In this paper, we have proposed a DNN-NOMA based model that considers the maximum capacity of the network in a virtualised 5G network. The DNN model was trained using data generated via over 200000 runs of Monte-Carlo simulation for each network scenarios. Different network scenarios were randomly chosen to enhance the learning capabilities of the DNN-NOMA based model. The DDN-NOMA based model is shown to have outperformed the traditional NOMA approach.

Acknowledgement

The authors acknowledge the support received from TELKOM SA via the Telkom Centre of Excellence (CoE) in Broadband Networks and Applications at the University of Cape Town.

References

[1] Cisco, *Cisco Annual Internet Report (2018-2023)*. Cisco White Paper, March 2020. [Online]. Available: https://www.cisco.com/c/en/us/solutions/collateral/executive-perspectives/annual-internet-report/white-paper-c11-741490.pdf

[2] E. J. Oughton, W. Lehr, K. Katsaros, I. Selinis, D. Bubley, and J. Kusuma, "Revisiting wireless internet connectivity: 5g vs wi-fi 6," *Telecommunications Policy*, vol. 45, no. 5, p. 102127, 2021. [Online]. Available: https://www.sciencedirect.com/science/article/pii/S030859612100032X

[3] X. Foukas, G. Patounas, A. Elmokashfi, and M. K. Marina, "Network slicing in 5G: survey and challenges," *IEEE Comms. Mag.*, vol. 55, no. 5, pp. 94–100, May 2017.

[4] F. Boccardi, R. W. Heath, A. Lozano, T. L. Marzetta, and P. Popovski, "Five disruptive technology directions for 5G," *IEEE Comms. Mag.*, vol. 52, no. 2, pp. 74–80, February 2014.

[5] Z. Qin, X. Yue, Y. Liu, Z. Ding, and A. Nallanathan, "User association and resource allocation in unified noma enabled heterogeneous ultra dense networks," *IEEE Communications Magazine*, vol. 56, no. 6, pp. 86–92, 2018.

[6] P. I. Tebe, K. Ntiamoah-Sarpong, W. Tian, J. Li, Y. Huang, and G. Wen, "Using 5g network slicing and non-orthogonal multiple access to transmit medical data in a mobile hospital system," *IEEE Access*, vol. 8, pp. 189 163–189 178, 2020.

[7] C. Zhang, P. Patras, and H. Haddadi, "Deep learning in mobile and wireless networking: A survey," *IEEE Communications Surveys Tutorials*, vol. 21, no. 3, pp. 2224–2287, 2019.

[8] I. Sim, Y. G. Sun, D. Lee, S. H. Kim, J. Lee, J.-H. Kim, Y. Shin, and J. Y. Kim, "Deep learning based successive interference cancellation scheme in nonorthogonal multiple access downlink network," *Energies*, vol. 13, no. 23, p. 6237, 2020.

[9] C. Lin, Q. Chang, and X. Li, "A deep learning approach for mimo-noma downlink signal detection," *Sensors*, vol. 19, no. 11, p. 2526, 2019.

[10] M. K. Hasan, M. Shahjalal, M. M. Islam, M. M. Alam, M. F. Ahmed, and Y. M. Jang, "The role of deep learning in noma for 5g and beyond communications," in *2020 International Conference on Artificial Intelligence in Information and Communication (ICAIIC)*, 2020, pp. 303–307.

[11] Y. Saito, Y. Kishiyama, A. Benjebbour, T. Nakamura, A. Li, and K. Higuchi, "Non-orthogonal multiple access (noma) for cellular future radio access," in *2013 IEEE 77th Vehicular Technology Conference (VTC Spring)*, 2013, pp. 1–5.

[12] A. Benjebbour, Y. Saito, Y. Kishiyama, A. Li, A. Harada, and T. Nakamura, "Concept and practical considerations of non-orthogonal multiple access (noma) for future radio access," in *2013 International Symposium on Intelligent Signal Processing and Communication Systems*, 2013, pp. 770–774.

[13] S. O. Oladejo and O. E. Falowo, "Latency-aware dynamic resource allocation scheme for multi-tier 5g network: A network slicing-multitenancy scenario," *IEEE Access*, vol. 8, pp. 74 834–74 852, 2020.

[14] R. Collobert and S. Bengio, "Links between perceptrons, mlps and svms," in *Proceedings of the twenty-first international conference on Machine learning*, 2004, p. 23.

[15] Smartboost, "Deep learning vs neural network: What's the difference?" 2020, Accessed on: 2021-06-20. [Online]. Available: https://https://smartboost.com/blog/deep-learning-vs-neural-network/

[16] M. Abadi, A. Agarwal, P. Barham, E. Brevdo, Z. Chen, C. Citro, G. S. Corrado, A. Davis, J. Dean, M. Devin, S. Ghemawat, I. Goodfellow, A. Harp, G. Irving, M. Isard, Y. Jia, R. Jozefowicz, L. Kaiser, M. Kudlur, J. Levenberg, D. Mané, R. Monga, S. Moore, D. Murray, C. Olah, M. Schuster, J. Shlens, B. Steiner, I. Sutskever, K. Talwar, P. Tucker, V. Vanhoucke, V. Vasudevan, F. Viégas, O. Vinyals, P. Warden, M. Wattenberg, M. Wicke, Y. Yu, and X. Zheng, "TensorFlow: Large-scale machine learning on heterogeneous systems," 2015, software available from tensorflow.org. [Online]. Available: https://www.tensorflow.org/

[17] F. Chollet *et al.*, "Keras," https://keras.io, 2015.

[18] F. Pedregosa, G. Varoquaux, A. Gramfort, V. Michel, B. Thirion, O. Grisel, M. Blondel, P. Prettenhofer, R. Weiss, V. Dubourg *et al.*, "Scikit-learn: Machine learning in python," *Journal of machine learning research*, vol. 12, no. Oct, pp. 2825–2830, 2011.

[19] X. Glorot, A. Bordes, and Y. Bengio, "Deep sparse rectifier neural networks," in *Proceedings of the fourteenth international conference on artificial intelligence and statistics*. JMLR Workshop and Conference Proceedings, 2011, pp. 315–323.

[20] D. P. Kingma and J. Ba, "Adam: A method for stochastic optimization," in *International Conference for Learning Representations*, San Diego, MA, USA, May 2015.

Sunday Oladejo is currently a Ph.D candidate at the Centre of Excellence in Broadband Networks at the University of Cape Town, South Africa.

Stephen Ekwe is a Ph.D. candidate at the Department of Electrical Engineering, University of Cape Town, South Africa. He received his B.Eng in Electrical and Electronics Engineering from Cross River University of Technology, Nigeria, and his M.Sc in Personal Mobile and Satellite communication from the University of Bradford, United Kingdom.

Lateef Akinyemi received a B.Sc (LASU) Electronic and Computer Engineering, Lagos, an M.Sc (LASU) in Electronic and Computer Engineering, and M.Sc (UNILAG) in Electrical and Electronics Engineering (Communication Engineering Option) and PhD in the Department of Electrical Engineering, University of Cape Town.

A Radiofrequency Electromagnetic Wave Radiation Exposure Minimization Method in 5G Network: A Perspective of QoS Trade Offs

Adedotun Temitope Ajibare*, Daniel Ramotsoela*
*Department of Electrical Engineering, University of Cape Town, Cape Town, South Africa
[1]ajbade004@myuct.ac.za; [2]daniel.ramotsoela@uct.ac.za

***Abstract*—Radiofrequency (RF) electromagnetic fields (EMF) radiation exposure to human, most especially the mobile device users has been a serious concern in wireless network. Therefore there is a need to address and afterwards increase the health awareness regarding the radiation exposure of wireless networks to the public. This paper investigates the effect of minimizing the exposure index (EI) and specific absorption rate (SAR) induced in fifth generation (5G) wireless networks and its impact on the quality of service (QoS) of the users in the network. With the aim of minimizing the EI on mobile user, we propose a power control algorithm that solves an optimization problem formulated to minimize the EI while guaranteeing the QoS requirement of users. Given that the radiated SAR and EI are characterized by power density in the wireless network, the proposed algorithm controls the transmit and received powers subject to interference, power and QoS constraints. Simulation results show that the proposed scheme reduces the effect of both SAR and EI on users in 5G network while satisfying the required QoS in terms of the data rate. Furthermore, the results reveal that both SAR and EI are tolerable and fall within the threshold set by the International Commission on Non-Ionizing Radiation Protection (ICNIRP) when compared with the ICNIRP standard.**

Keywords*—5G, RF-EMF exposure, QoS, SAR, exposure index, radio frequency interference, power control.

I. Introduction

Fifth generation (5G) network is expected to improve the quality of service (QoS) of users in its network. To achieve this high gigabit-per-second (Gbps) data rates, 5G networks have been operating around the frequency of 6GHz. It is expected that future 5G networks will be deployed using the promising millimetre wave (mm-wave) communications band of 28 and 39 GHz. Operating with such high frequencies will reduce the coverage areas of the access points (APs) in 5G network. Therefore, proper network planning is necessary and a large number of small cells is expected so as to make up for the reduced coverage area especially in crowded areas in the heart of the cities. This proliferation of APs and antenna such as massive MIMO brings about the needed signal to interference-noise ratio (SINR) in the network along with corresponding increase in the power density and unfortunately the challenges of increase in the interference and exposure in the network as presented in Fig. 1 [1], [2]. However, compared to the previous generation of wireless generation networks, i.e. the existing third and fourth generation networks, the maximum transmit power is lower in 5G than the mobile device power levels [3].

RF-EMF exposure metric known as exposure index (EI) [4] is evaluated using the electric field strength, magnetic field strength, power density, specific absorption rate (SAR), as well as considering the variability of other factors such as environment, the conductivity and the mass density of tissue. The radiation emitted from APs and mobile devices is analysed and compared with the limits set by the International Commission on Non-Ionizing Radiation Protection (ICNIRP) [5].

It is therefore necessary to manage EM radiation in 5G wireless networks using both green and blue wireless communications. Green communication reduces the energy cost, increase the energy efficiency of base stations, and also increase the battery life of user device, whereas, blue communication reduces the SAR, exposure and time of transmission. In both green and blue wireless communications; less energy, less cost, less power, and transmission time are used especially in the uplink transmission [6].

Fig. 1. An architecture depicting radiation exposure in an ultra-dense 5G network

In exposure management, there are many methods of reducing exposure such as transmission time reduction, power density minimization, beamforming technique and data usage reduction etc. However, in 5G networks, it will be practically impossible to reduce the radiation exposure by minimizing data usage since 5G is expected to solve the problem of data explosion. Therefore, this research focused on minimising the transmission time and power/energy since the impact of

power control in the network will reduce UE transmit power, hence, minimize EMF exposure and at the same time reducing the interference [7] in the network. The reduction factor for radiation exposure index (EI) in our work is evaluated as the power density. The proposed power control and optimization algorithm minimizes the characterised EI in the form of the power density in a simulated 5G network. In this paper, to achieve a reasonable tradeoff between radiation exposure and needed QoS amongst users in the network, we investigated the effects of lower transmit power and lower SINRs in the network, we maintained acceptable QoS with low EMF in both uplink (UL) and downlink (DL) transmissions, and we developed a scheme that uses effective power control mechanism in reducing the RF-EMF radiation exposure in a 5G network. The performance of the proposed schemes was evaluated through simulations, and the results show reduced users' interference and radiation exposure in the network while satisfying the users' target QoS. This research work again increase the health awareness concerning radiation exposure of 5G wireless networks.

A. Contributions

The main contributions of the paper are as follows:

- We evaluated the specific absorption rate and exposure index of the users in the 5G network.
- We formulate an optimization problem to minimize the total exposure index of users in the network.
- We propose an EI power control algorithm (EIPCA) that minimizes the EI through the transmit and received powers in the network that solves the radiation exposure problem.
- Through simulation analysis, we evaluate and validate the proposed algorithm with the target QoS values and IC exposure thresholds.

The rest of the paper is organised as follows. In Section II, we briefly review the related works. The proposed system model is discussed in Section III, the problem formulation is defined in Section IV. The proposed solution (algorithm) and its performance evaluation are presented in Sections V and VI respectively. Finally, Section VII concludes the paper.

II. Related Works

RF-EMF radiation exposure induced by wireless networks has garnered increasing attention recently, most especially after many conspiracy theories linking COVID 19 and 5G network. Several works in the literature have investigated this research area differently. In this section, recent and relevant studies regarding RF-EMF radiation in wireless networks are reviewed.

In [6], the author presented a study on the quality of experience (QoE) and EMF trade-off and how to reduce exposure index in 5G mobile networks. Sarrebourse et al. in [8] proposed a new exposure metric EI, and deployed low-complexity dosimeters to measure and provide the exposure information in the city. In [9], the authors presented a study on whole-body and localized SAR and dose prediction. They calculated the absorbed doses with the measured SAR values by multiplying the time duration of the exposure and showed the influence of phone call duration on the total absorbed dose. The authors concluded that SAR is lowered when more base stations with lower transmit power are installed. However, the absorption due to UL transmission of the other users is not accounted for. Authors in [10] presented the strategies of reducing the global EMF exposure, their exposure is strongly linked to user's behaviour e.g. mobility of user increases exposure, since a user experience frequent handovers and mobility increases signalling. Other factors presented that influence exposure are; user profile, type of services, and duration.

In [11], the authors minimized EMF exposure while achieving a target QoS and maximize the network capacity while remaining below the legal thresholds. The EMF exposure is characterised with UL transmit power and DL power density, the small cells' inter-site distance (ISD) were varied using 50m, 100m, and 200m with the optimal network parameters. A 50m & 100m ISD cause a strong reduction on the DL EMF exposure. UL EMF exposure improve significantly when the distance between users and small-cells (SC) decreases. The authors concluded that 5G network brings APs closer to the user, and reduces UL transmit power using smaller BSs. D. Plets et al. [12] presented an exposure prediction method based on the measured values, the power was then used in calculating and predicting the SAR values and also the EIs. The authors compared the induced exposure of UMTS macrocell, UMTS femtocell, and WiFi VoIP. It was concluded that WiFi radiates more exposure due to no power control algorithm. Macrocell is better and femtocells is the best in term of exposure emission. Authors in [13] suggested ways of managing and reducing EMF levels without compromising the users' QoS. Some of the methods suggested include; efficient handover management, RATs, populations, and power control. In [14], the authors proposed a user scheduling scheme for reducing Electromagnetic emission in the UL. They formulated a user scheduling/power allocation scheme that minimized the EM exposure of users by minimizing the total energy dissipated towards each user subject to transmitting a target number of bits.

In this work, the radiofrequency electromagnetic fields (RF-EMF) radiation exposure induced in a 5G network is characterized by EI and evaluated with the power flux densities between the users and the access points (APs) in the network. We therefore propose an RF-EMF emission exposure reduction scheme to reduce the total exposure index in the system. The optimization problem is solved by minimizing the total EI subject to transmit power, QoS, interference and other constraints. We validate the performance of our proposed scheme through simulations, with RF-EMF and QoS metrics. Also, the results are compared and discussed with the established global limits recommended by ICNIRP.

III. System Model

The system model considered in this paper is illustrated in Fig.2. The considered scenario assures a typical ultra-dense 5G network. The users are crowded with a high numbers of access points L as expected in any urban centre. These access points propagate radio wave signals to a set of users U that are assumed to be immobile, hence, these users are susceptible to radiation exposure within a distance d_u^l, and cross-sectional area A_u^l . We denote the signalling power of user u to the

serving AP l in the uplink transmission as $P^{Tx}_{u,c,l}$, and $P^{Rx}_{u,c,l}$ is the received power of user u from the serving AP l in the downlink transmission. The exposure radiation on each of the users is equivalent to the sum of the interfering power densities generated both the APs and the user's device at that particular location. The spectral power density, S^l_u (W/m^2) which is

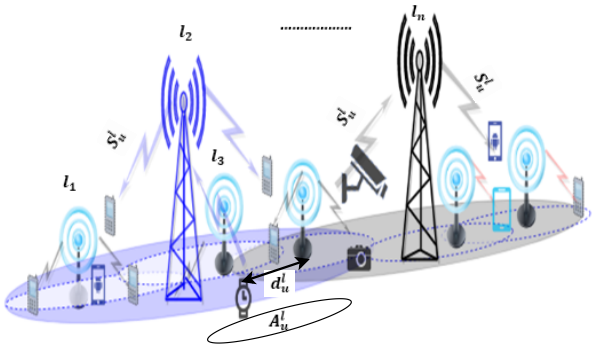

Fig. 2. System model of a typical ultra-dense 5G

the ratio of EIRP incident perpendicular to a surface and the cross-sectional area (A^l_u) of the surface of the radiated radio wave. The power density closed-form expression is given as [15],

$$S^l_u = \frac{P_T * G_T}{4\pi {d^l_u}^2} = \frac{P_T * G_T}{A^l_u} = \frac{|E^l_u|^2}{Z_o} \quad (1)$$

where Z_o is the characteristic impedance of vacuum (free space) which is 120πΩ = 377Ω. E^l_u (V/m) is the electric field strength of the radiated radiofrequency electromagnetic wave. Therefore, E^l_u is expressed as.

$$E^l_u = \sqrt{Z_o * (\frac{P_T * G_T}{4\pi {d^l_u}^2})} \ . \quad (2)$$

The SAR[W/kg] is the rate of energy absorbed by or deposited per unit mass per unit time and it is derived from the induced electric field strength using the electrical conductivity of the tissue σ (S/m) and the tissue density ρ (kg/m³), which are assume constant for all the users in the network. Consequently, SAR^l_u is expressed as

$$SAR^l_u = |E^l_u|^2 * \frac{\sigma}{\rho} = \left| \sqrt{Z_o * \left(\frac{P_T * G_T}{4\pi {d^l_u}^2} \right)} \right|^2 * \frac{\sigma}{\rho}. \quad (3)$$

Finally, the EI is evaluated in (4) as the ratio of the evaluated SAR taken for an average duration of 6 minutes interval or local exposure or 30 minutes interval for whole-body exposure and the corresponding maximum limit [16].

$$EI^l_u = \frac{SAR^l_{uevaluated}}{SAR_{\max limit}} \quad (4)$$

The ICNIRP defined the SAR maximum limits to be 2w/kg for a local exposure and 0.08w/kg for the whole-body exposure.

IV. Problem Formulation

We consider the uplink of multiuser 5G networks, as depicted in Fig. 2 where single-antenna APs communicate with U uniformly distributed single antenna users. The system uses a total bandwidth B divided into C equal subcarriers. We assume that time is split into T, each of length t. A subcarrier can be allocated to at most one user in a time domain but a user can have more than one subcarrier in a T i.e. more than one physical resource block (PRB) $(T * C)$. Hence, the throughput located to a user u in RAT l can be expressed as [17]:

$$R^l_{u,c} = \sum_{t=1}^{T} \sum_{c=1}^{C} x^l_{u,c}(t) b^l_{u,c}(t) log_2 \left(1 + \frac{p^l_{u,c}(t) \left| h^l_{u,c} \right|^2 (t)}{N_0 + I^l_{u,c}(t)} \right) \quad \forall u \in U \quad (5)$$

where $b^l_{u,c}(t)$ denotes the bandwidth of a subcarrier, $p^l_{u,c}$ (t) and $\left| h^l_{u,c} \right|^2 (t)$ represent the transmit power and channel gain, respectively, of user u on subcarrier c in RAT l at time t. The parameter $x^l_{u,c}(t)$ represents the subcarrier allocation index of user u, such that $x^l_{u,c}(t) = 1$ if subcarrier c is allocated to user u in RAT l at time t, otherwise, $x^l_{u,c}(t) = 0$. N_0 is the noise power per subcarrier. Additionally, $I^l_{u,c}(t)$ accounts for the interference from users transmitting on subcarrier c at time domain t in the neighbouring cells such that

$$I^l_{u,c}(t) = \sum_{v=1,\ v \neq l}^{L} p^v_{u,c}(t) \left| h^l_{u,(v),c} \right|^2 (t) \quad (6)$$

where $\left| h^l_{u,(v),c} \right|^2 (t)$ denotes the channel gain of user u on the subcarrier c in cell v to the BS in RAT l, while L represents the number of RATs in the system.
The total EI exposure of the system can be expressed as in [6]

$$EI^l_u = \sum_{t}^{N_{period}} \sum_{u}^{N_{indiv}} \sum_{l}^{N_{RATs}} \left[T^{UL}_{u,t,l} * SAR^{Tx}_{u,l} \frac{P^{Tx}_{u,c,l}}{P^{Tx}_{ref}} + T^{DL}_{u,t,l} * SAR^{RX}_{u,l,} \frac{P^{Rx}_{u,c,l}}{P^{Rx}_{ref}} \right] \quad (7)$$

where EI^l_u denotes the contribution of user u in sector RAT l to the EM exposure index. $SAR^{TX}_{u,l}$ is the localised averaged SAR of the u user mobile device (from UL). $SAR^{RX}_{u,l,}$ is the whole-body averaged SAR of the u user mobile device (from DL), while P^{Tx}_{ref} and P^{Rx}_{ref} represent the incident reference transmit and received powers. $P^{Tx}_{u,c,l}$ is the signalling power of user the u to the serving AP l in the uplink transmission, $P^{Rx}_{u,c,l}$ and is the received power of user the u from the serving AP l in the downlink transmission. $T^{UL}_{u,i,j,k}$ is the time of exposure and posture accounted for in the uplink, while $T^{DL}_{u,i,j,k}$ is the time of exposure and posture accounted for in the downlink. Moreover, the signalling power $P^{Tx}_{u,c,l}$ and the received power $P^{Rx}_{u,c,l}$ can be computed using power control as stated below [18]:

$$P^{Tx}_{u,c,l} = min\{ P^{\ max}_{UE} ; P_o + 10 log_{10} M + \alpha * PL_u + \partial_{mcs} + f(\Delta_i) \} \quad [d_{Bm}] \quad (8)$$

$$P^{Rx}_{u,c,l} = P_o + \alpha * PL_u \quad [d_{Bm}] \quad (9)$$

where $P_{max\ UE}$ depends on the UE and is the maximum power allowed in uplink transmission. M is the number of PRBs allocated per user. P_o is cell-specific and is the power contained in one PRB. α is the pathloss compensation factor and ranges between 0 and 1. PL_u is the estimated pathloss for the UE. ∂_{mcs} is the modulation code scheme dependent offset and it is UE specific. $f(\Delta_i)$ is the closed-loop correction function.

Consequently, our RF-EMF emission exposure reduction scheme aims at reducing the total exposure index (EI) in the network, the objective function of the optimization problem is stated in (10),

$$\min_{P,t} \sum_{l}^{L} \sum_{u}^{U} (EI_u^l) \tag{10}$$

Subject to

$$\text{C1}: b_{u,c}^l \sum_{u}^{U} \sum_{c}^{C} x_{u,c}^l(t)\, log_2 \left(1+\frac{p_{u,c}^l(t)\left|h_{u,c}^l\right|^2(t)}{N_0+ I_{u,c}^l(t)}\right) \leq B$$

$$\text{C2}: \sum_{u=1}^{U} \sum_{c=1}^{C} x_{u,c}^l(t)\ P_{u,c}^l(t) \leq P_u^{max} \qquad \forall t,$$

$$\text{C3}: \sum_{u}^{U} x_{u,c}^l(t) \leq 1,$$

$$\text{C4}: \sum_{x_{u,c}^l(t)}^{U} \left(I_{u,c}^l(t)\right) \leq I_u^{max} \qquad \forall c \in C,$$

$$\text{C5}: R_u^{min} \leq R_{u,c}^l \qquad \forall u \in U.$$

C1 is the total bandwidth constraint set across the total PRBs for all users. C2 is the power constraint, it indicates that the total power budget is lesser than the maximum power threshold. C3 is the subcarrier allocation constraint. C4 is the interference constraint, it ensures that the interference threshold, I_u^{max} is not exceeded, and C5 is the target data rate constraint for each user u. The objective function in (10) is formulated as a Mixed Integer Non-Linear Program (MINLP) and EI power control algorithm solves the problem by minimizing the exposure index without compromising the QoS of the users.

V. Proposed Algorithm

In the proposed algorithm, we solve for the optimization problem in (10) by determining the feasible power solution needed to achieve the needed SINRs that give the required data rates for each user. Since EI is a function of power and time of transmission, the EI is minimized by optimising the transmit power and the transmit time. More importantly, for all users in the network, there is an agreed minimum data rate need for the class of service/slice/use-case the mobile device is offered. Therefore, while the objective is to reduce both the transmit power and the transmission time of signals to minimize the total exposure index of the user as given in (10), the required data rate must be satisfied according to constraint C5. The total bandwidth constraint set across the whole PRBs for all the users in the network must also be satisfied as in C1. The objective function in (10) also ensures that the total power budget is less than the maximum power limit as specified in C2. This is made possible with the pathloss compensation factor (α) and power control in (8) and (9). Consequently, the subcarrier binary allocation and interference threshold constraints must be satisfied while optimizing the exposure index as described Algorithm 1.

Algorithm 1 EI Power Control Algorithm (EIPCA)

Inputs: G_T, Z_o, P_o, α, B, f_c, λ, h_g, D, U, L, C, d_u,
Outputs: S_u^l, SAR_u^l, E_u^l, $R_{u,c}^l$, $I_{u,c}^l$, EI_u^l

1. Given the set U where $u \in U$
2. **for** each user *u* **do**
3. Initialize the values of P_u^{max}, ρ, σ, and $SAR_{\text{max}limits}$
4. Set $I_{u,c}^l = 0$, $t = T$, and $\forall c = 1, 2, 3, \ldots . C$
5. **while** $P_{u,c}^l \leq P_u^{max}$ $\forall$ APs and u **do**
6. $I_{u,c}^l \leq I_u^{max}$
7. $\sum_c^C b_{u,c}^l(t) \leq B$
8. $R_u^{min} \leq R_{u,c}^l$
9. **end while** $\forall u \in U,$
10. Solve for the EI_u^l as in Eq. 10.
11. **if** $R_u^{min} \leq R_{u,c}^l$ **then**
12. Determine EI_u^l
13. Terminate if the optimal solution is found
14. **else**
15. Increase $p_{u,c}^l$ or set $p_{u,c}^l = P_u^{max}$
16. **end if**
17. **end for**

VI. Performance Evaluation

In this section, we simulate our system model and evaluate the performance of our proposed exposure index power control algorithm. The simulation parameters used for the experiment are as shown in Table I.

A. Simulation Environment

We simulated a wireless network with 5G RATs and 4G RATs as the umbrella network in a MATLAB [19] environment. Random number of users were uniformly distributed in the coverage area of radius 50m for the 5G APs (gNobeB) and 500m for the 4G APs (eNobeB). The radiated SAR, EI to each of the network users were evaluated using the system parameters. The proposed algorithm minimized the overall EI of these users taking into consideration the received and transmit powers, minimum data rate, and other QoS constraints.

B. Simulation Results

In this sub-section, we discuss the performance of the proposed scheme and for comparison, we assume a conventional 5G network algorithm where the evaluated users' EI is not optimized to benchmark our proposed algorithm. The simulation results are presented with different performance metric below.

1) Impact of Network Interference Level on Users: As the number of users increase in the network, it leads to additional interference in the network that affects the users. The result in Fig. 3 shows that the interference level is higher in the conventional 5G network when compared with the optimized value for the same number of UEs/APs. Also, the interference

is lower than the tolerable interference limit of -116dBm ($2.5*10^{-15}$w). This further shows that the interference is proportional to the RF-EMF radiation in the network. It also means that minimizing the RF-EMF radiation exposure reduces the interference in the network as well.

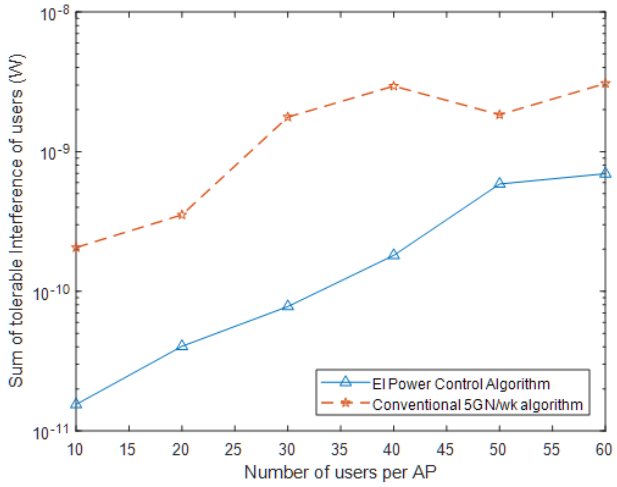

Fig. 3. Tolerable interference of users vs. number of users

TABLE I
SIMULATION PARAMETERS AND VALUES

Parameter	Value
Number of RATs	3
Number of APs/RAT	2
Number of Users	Random
Spectrum allocation	80 MHz
Carrier frequency	6 GHz
Channel model	3GPP
Data rate linit (R_s^{min})	2.5Mbps
Max UE power (P_u^{max})	0.25 W [24dBm]
Max AP Tx power	20 W [43dBm], 0.25 W [24dBm]
P_{ref}	1 W
Tolerable interference (I_u^{max})	-116dBm
UE thermal noise density (N_0)	10^{-13}W [-100 dBm]
Slot duration (T)	1 ms
Scheduling frame	10ms
Overall interval	20s
Cell-level user distribution	Uniform
Conductivity of the tissue (σ)	0.97 S/m
Mass density of the tissue (ρ)	1000 kg/m³
Characteristic Impedance (Z_o)	$120\pi\Omega$ = 377Ω
Power Control	Open-loop
Pathloss exponent ()	0.7
Antenna height	35m, 50m
UE height	1.5m
UE thermal noise density (N_0)	10^{-13}W [-100 dBm]
Log-normal shadow fading	8 dB standard deviation
Cell coverage radius	50m, 500m

2) Effect of Power Density on the entire network: There is a rising complexity in the future of 5G and next generation networks (NGN). It is evident from Fig. 4 that as the users and access points increase in the network, the power density experienced by a user at a point and the radiation exposure increase. From this, it is depicted that the denser the network, the higher the power density and radiation exposure. Therefore, the main issue concerning RF-EM radiation of an area is more of the ultra-denseness of the network (such as massive MIMO) than the radio access technology (RAT) in that location. Although next generation RATs use higher frequency such as millimetre wave frequency, but it has been shown that the higher frequency is compensated for by its shorter wavelength [20]. Furthermore, the Fig. 4 shows that the highest power density experienced at any point in the network is lower than the limit of 10W/m^2 set by U.S Federal Communications Communication (FCC) for frequency above 6GHz [20].

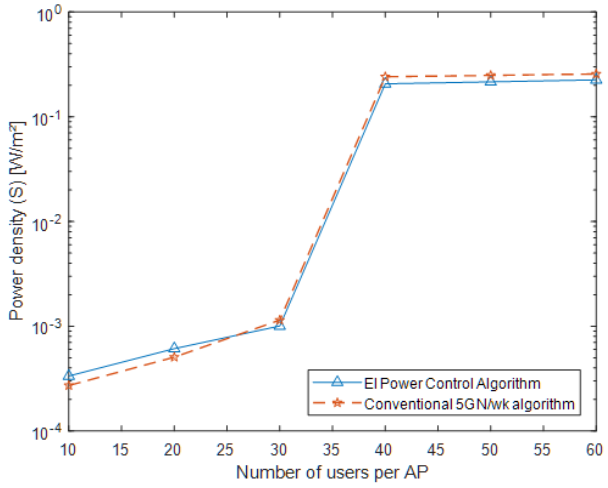

Fig. 4. Power density of users vs. number of users per AP

3) Impact of QoS (in terms of Data Rate) trade-offs on Users: Figure 5 shows the graph of data rate (QoS) of users in the network against the EI. The data rate is lower in the proposed algorithm as compared with the conventional 5G network. However, the proposed algorithm offers more data rate than the needed QoS limit of 2.5Mbps for all the users. Also, the EI is quite lower in the proposed algorithm as compared with the benchmark algorithm. Therefore, it can be inferred that our proposed algorithm offers better QoS (required data rate and lower EI) in the network. It is worthy of note that all of the exposure indexes calculated are lower than the standard limits recommended by the IEEE [22] and the ICNIRP [5].

4) Impact of Specific Absorption Rate (SAR) on Network: The specific absorption rate in the network is presented in Fig. 6. Similar to the QoS metric in Fig. 5, the SAR of the different users is reduced in the proposed algorithm compared with the conventional 5G network algorithm. This shows a relationship between the power density (W/m^2), SAR (W/kg) and the exposure index radiated in wireless networks. More importantly, the SARs are much lower than the recommended limit of $0.08W/kg$ advised by ICNIRP.

VII. Conclusion

In this paper, we presented a proposed power control algorithm that minimizes the radiation exposure in 5G networks.

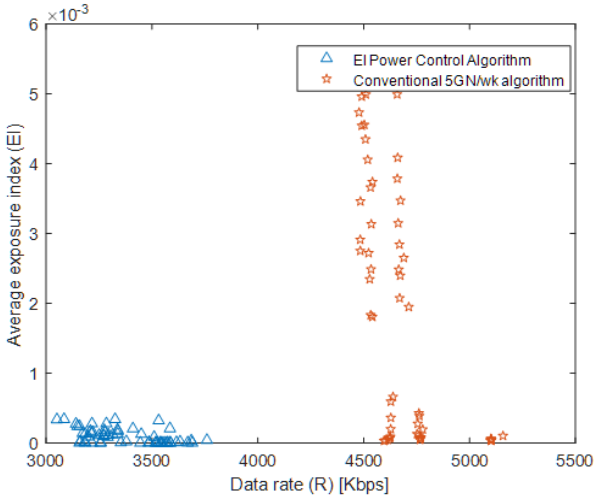

Fig. 5. Average users' data rate (QoS) vs. users' EI

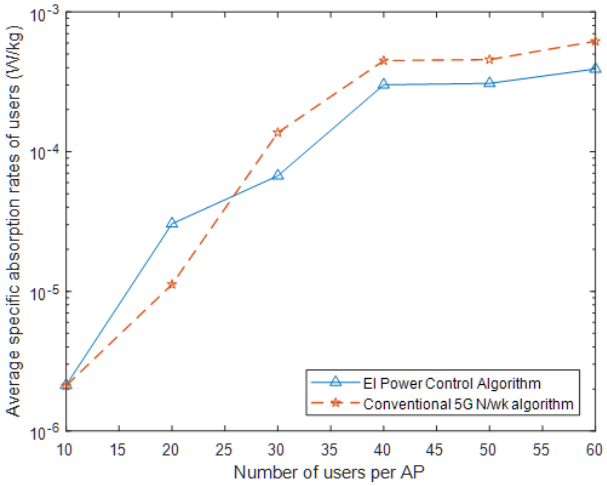

Fig. 6. Specific absorption rates of users vs. number of users

The algorithm solves an optimization problem that minimizes the RF-EMF radiation in the network taking into account the QoS constraints such as the data rate, power and interference limits. We employed the EI, power density, SAR and the data rate to evaluate the performance of the proposed scheme. Simulation results show that the EI and SAR radiated in the network can be minimized using the transmit power without compromising the QoS of the users. Results also demonstrate that the recommended exposure limits advised by the ICNIRP [5] and IEEE [22] are complied with in the simulated 5G network.

REFERENCES

[1] A. M. El-Hajj and T. Naous, "Radiation Analysis in a Gradual 5G Network Deployment Strategy," in 2020 IEEE 3rd 5G World Forum (5GWF), 2020.

[2] M. Celaya-Echarri, L. Azpilicueta, J. Karpowicz, V. Ramos, P. Lopez-Iturri and F. Falcone, "From 2G to 5G Spatial Modeling of Personal RF-EMF Exposure Within Urban Public Trams," IEEE Access, vol. 8, pp. 100930-100947, 2020.

[3] B. Thors, D. Colombi, Z. Ying, T. Bolin and C. Törnevik, "Exposure to RF EMF From Array Antennas in 5G Mobile Communication Equipment," IEEE Access, vol. 4, pp. 7469-7478, 2016.

[4] N. Varsier et al., "D2.6: Global Wireless Exposure Metric definition v2," 2013. [Online]. Available: http://www.lexnet.fr/project-progress/publicdeliverables.html. [Accessed 23 01 2020].

[5] The International Commission on Non-Ionizing Radiation Protection, "ICNIRP Guidelines for limiting exposure to electromagnetic fields (100kHz to 300 GHz)," Health Phys, vol. 118, no. 5, pp. 483-524, 2020.

[6] T. Brown, "Containing exposure in 5G networks, a perspective from LExNet," in 5G Radio Technology Seminar. Exploring Technical Challenges in the Emerging 5G Ecosystem, 2015.

[7] A. T. Ajibare and O. Falowo, "Dynamic Slicing and Scheduling for 5G Networks Using Joint Power and Sub-Carrier Allocation," in Southern Africa Telecommunication Networks and Applications Conference (SATNAC), Hermanus, 2019.

[8] T. Sarrebourse et al., "Towards EMF exposure assessment over real cellular networks: An experimental study based on complementary tools," in 2014 11th International Symposium on Wireless Communications Systems (ISWCS), 2014.

[9] D. P. e. al., "Whole-body and Localized SAR and Dose Prediction Tool for Indoor Wireless Network Deployments," in 2014 11th International Symposium on Wireless Communications Systems (ISWCS), 2014.

[10] M. Popović, M. Tesanovic and B. Radier, "Strategies for Reducing the Global EMF Exposure: Cellular Operators Perspective," in 2014 11th International Symposium on Wireless Communications Systems (ISWCS), 2014.

[11] J. Stephan, M. Brau, Y. Corre and Y. Lostanlen, "Joint Analysis of Small-cell Network Performance and Urban Electromagnetic Field Exposure," in The 8th European Conference on Antennas and Propagation (EuCAP 2014), 2014.

[12] D. Plets, W. Joseph, K. Vanhecke and L. Martens, "Downlink Electric-Field and Uplink SAR Prediction Algorithm in Indoor Wireless Network Planner," in The 8th European Conference on Antennas and Propagation (EuCAP 2014), 2014.

[13] M. Tesanovic et al., "The LEXNET Project. Wireless Networks and EMF: Paving the Way for Low-EMF Networks of the Future," IEEE Vehicular Technology Magazine,, vol. 9, no. 2, pp. 20-28, June 2014.

[14] Y. A. Sambo, F. Heliot and M. A. Imran, "A User Scheduling Scheme for Reducing Electromagnetic (EM) Emission in the Uplink of Mobile Communication Systems," in 2014 IEEE Online Conference on Green Communications (OnlineGreenComm), 2014.

[15] IARC, Non-ionizing Radiation, Part 2: Radiofrequency Electromagnetic Fields. IARC Monographs on the Evaluation of Carcinogenic Risks to Humans, vol. 102, Lyon: International Agency for Research on Cancer, 2013, pp. 1-481.

[16] A. Gati, M. Wong and J. Wiart, "Duality Between Uplink Local Downlink Whole-Body Exposures In Operating Networks," IEEE Transactions on Electromagnetic Compatibility, vol. 52, no. 4, pp. 829-836, 2010.

[17] A.T. Ajibare and O. Falowo, "Resource Allocation and Admission Control Strategy for 5G Networks Using Slices and Users Priorities," in 14th IEEE Africon International Conference, Accra, 2019.

[18] E. Tejaswi and B. Suresh, "Survey of Power Control Schemes for LTE Uplink," International Journal of Computer Scienece and Information Technologies, vol. 4, no. 2, pp. 369-373, 2013.

[19] MATLAB, version 9.6.0.1072779 (R2019a). The Mathworks Inc., 2019.

[20] A. T. Ajibare et al., "RF EMF Radiation Exposure Assessment of 5G Networks: Analysis, Computation and Mitigation Methods," in 2021 IEEE Africon International Conference, Arusha, pp. 215-220, 2021.

[21] R. Rodríguez-Cano, S. Zhang, K. Zhao and G.F. Pedersen, "User Body Interaction of 5G Switchable Antenna System for Mobile Terminals at 28 GHz," in 2019 13th European Conference on Antennas and Propagation (EuCAP), Krakow, 2019.

[22] IEEE, "IEEE Standard for Safety Levels with Respect to Human Exposure to Electric, Magnetic, and Electromagnetic Fields, 0 Hz to 300 GHz," IEEE Std C95.1-2019 (Revision of IEEE Std C95.1-2005/ Incorporates IEEE Std C95.1-2019/Cor 1-2019), pp. 1–312, 2019.

Towards Next-Generation Network and Haptic-Enabled Internet Architectures: The Shift from QoS to QoE / QoT Perspectives

Maradona Gatara[#], Mjumo Mzyece[#]

[#]*Technology and Operations Management Unit, Wits Business School (WBS), Johannesburg, South Africa*

[1]maradona.gatara@wits.ac.za

[2]mjumo.mzyece@wits.ac.za

***Abstract*—Next-generation digital communications networks will likely precipitate a shift from traditional technical system-centric to more dynamic user-centric network architectures of the future. To this end, there has been a concerted effort to integrate Quality of Experience (QoE) requirements into the 5G ecosystem to emphasise the importance of integrated network design with the end-user at its epicentre, and the transition from more traditional Quality of Service (QoS) dimensions. One particular area where QoS dimensions will be mapped onto QoE is that of haptic-enabled Internet technologies. These technologies are envisioned to leverage the Ultra-Reliable Low-Latency Communication (URLLC) characteristics of 5G Networks. The anticipated shift from content-centred to control-based user-centred network architectures will result in the augmentation of the experience of human end-users who will be capable of performing a set of tasks through the manipulation of real and virtual objects via wireless communication channels. Beyond network-centric QoS, user-centric QoE will augment human-in-the-loop (HITL) use cases which will increasingly become a core component of next-generation digital network-enabled technology applications. This QoE approach will also have implications for emergent Quality of Task (QoT) dimensions, owing to the task-sensitive nature that will become synonymous with future URLLC-supported haptic-enabled Internet architectures. In this paper, we explain the shift from the traditional system-oriented QoS to the user-centric QoE-oriented next-generation digital networks by drawing on the example of emergent 5G (URLLC) and haptic-enabled Internet architectures for remote task performance applications. Further, we explain the significance of the HITL component, and describe the link between QoE and emergent QoT concepts.**

***Keywords*—Quality of Service (QoS), Quality of Experience (QoE), Next-Generation Digital Communication Networks, Haptics, 5G, Ultra-Reliable Low-Latency Communications (URLLC), Human-in-the-Loop (HITL), Quality of Task (QoT)**

I. INTRODUCTION

Despite the promise of next-generation networks like 5G [1], 6G [2], and quantum communications [3], there is still uncertainty about their successful diffusion. One particular question for which there is currently no conclusive answer is that of what consumers would expect of next-generation network-enabled technologies. The factors that would play a critical role in ensuring that consumer expectations are fulfilled must be identified [4]. There is a degree of consensus among researchers and practitioners on the technical requirements of next-generation communication networks that have been formally standardised, e.g. 5G. Historically, performance monitoring and management in communication network standards has been focused on the key performance indicators (KPIs) linked to Quality of Service (QoS) based technical requirements. However, for next-generation networks, this paper argues that, in order to adequately address consumer expectations in emerging use cases, it is important to shift focus from a traditional network-centric QoS perspective to a user-centric Quality of Experience (QoE) / Quality of Task (QoT) perspective.

There has been a concerted effort to integrate QoE requirements into the 5G ecosystem to emphasise the importance of network design with the end-user at its epicentre [5]. To achieve this, it is, therefore, necessary to identify and analyse those essential attributes with which researchers and practitioners can contribute towards shaping QoE-centric networks as part of the broader future network ecosystems (e.g. 5G) [5]. This will ensure consistency, transparency, personalisation, and differentiation in service delivery, which are all core aspects of next-generation networks, the first of which will be 5G [4]. As such, a move towards a QoE-based network and user-centric architecture would be a key differentiator heralding the transition from 4G to 5G and future networks.

Future 5G networks will support three generic services, namely Extreme Mobile Broadband (eMBB), Massive Machine-Type Communication (mMTC), and Ultra-Reliable Low-Latency Communication (URLLC). For each of these generic services, there are specific requirements such as data rates in eMBB, number of devices in mMTC, and latency and reliability for URLLC. A key driver of future digital neworks in the era of 5G and beyond will be the anticipated QoE from the perspective of the end-user. This is expected to be an essential feature of next-generation digital network-enabled applications.

Increasingly, the notion of user centricity will require digital networks that support URLLC use-case applications, which will be critical to enabling the required QoS for optimal user QoE levels [6]. One particular area where QoS dimensions will increasingly be mapped onto QoE is emergent haptic-enabled technologies. These technologies are envisioned to leverage 5G URLLC capabilities, signifying a paradigm shift from content-centric to control-based network architectures to empower human end-users as task performers who will be able to manipulate real and virtual objects through wireless communication channels or information transfer media [7]. In other words, URLLC 5G and future network and haptic-enabled technologies could remotely enable physical experiences and real-time control, to transform the more

traditional current content delivery-based communication channels into task-oriented skillset delivery-based networks [8], [9]. Next-generation digital networks such as 5G must account for the diversity of existing and emerging use cases as well as the various demands for numerous service types. These requirements would only be addressed by a shift from system-centric to user-centric architectures e.g. haptic-enabled Internet for remote task performance. With the customer personalisation and service differentiation that will be synonymous with 5G and future networks, different use cases or services will demand various QoE requirements. End users do not have uniform QoE requirements. As such, QoS in the more conventional pre-5G network services e.g. 4G LTE, is an insufficient dimension with which to capture such distinct modalities. These can only be adequately represented via QoE-oriented network and application management approaches. Inevitably, QoE must be infused into 5G systems and beyond. User experience as QoE requires that the human operator is infused into the assessment process. Beyond QoS, QoE will bring into focus the human-in-the-loop (HITL) component, which will increasingly become a core attribute of next-generation digital network-enabled technology applications. For future use case scenarios where, for instance, an Internet based on remote physical interaction is to be realised, the HITL must be a key player. QoE will also have implications for the emergence of QoT dimensions which will stem from QoE, owing to the task-dependent nature that will come to characterise URLLC-supported 5G and haptic-enabled remote physical interactions that will be typical of future communication network applications. QoE refers to how much a physical interaction across a network compares to the same manipulation if performed in a real-world environment, accounting for discrepancies in physical interaction and relating to the transparency of the system [10], [11], whereas QoT denotes the precision with which a haptic-enabled user can perform a given task using a system or tool support function [12]. Thus, for digital communication networks of the future, the traditional QoS-driven measurement models in their current state will no longer suffice. The purpose of this paper is to highlight, using the example of emerging 5G URLLC network and haptic-enabled Internet architectures, a shift from the traditional system-oriented QoS, to more dynamic and interactive user-centric QoE-sensitive next-generation digital networks of the future. There are three main contributions of this paper. First, we discuss a paradigm shift from traditional system-oriented QoS to more dynamic and interactive user-centric networks of the future. Second, we draw on proposed future 5G (URLLC) network and haptic-enabled Internet architectures and examples of related real-world use cases. Third, we propose methods through which their applications can be empirically tested and validated. The rest of this paper is organised as follows. Section II discusses concepts of QoS, the emergent QoE paradigm, and within it QoT. Section III highlights future applications synonymous with 5G URLLC network and haptic enabled future Internet architectures and related use case examples. Section IV describes the HITL aspects of a haptic-enabled Internet and the link between QoE and QoT. Section V outlines future research directions and, finally, Section VI provides the conclusions to the paper.

II. THE SHIFT FROM QUALITY OF SERVICE TO QUALITY OF EXPERIENCE

In the telecommunications sector, there has been a heavy reliance on QoS as a metric of overall performance, yet its measurement is focused only on technical network performance. With emerging next-generation digital network applications, such as 5G URLLC, there is a gradual shifting towards quality improvement through a more user-centric approach [13]. It will, therefore, be necessary to incorporate QoE in currently QoS-focused network technologies. This linkage will be contingent upon integrating technical-level QoS with user experience dimensions. Consequently, the question of how to integrate QoS and QoE from a user-centric perspective will become more critical. In the near future, user behaviour must be mapped to technical network QoS-oriented features and specifications [13]. According to the ITU Telecommunication Standardisation Sector ITU-P.10/G.100, QoE is broadly defined as a measure of the "level of user acceptance towards an application and service" [14]. This must necessarily be a subjective dimension, which can be difficult to quantify. Services rendered with very low levels of QoE can result in user dissatisfaction, whereas the over-use of service resources may occasion resource-wastage. A comparison between these components is, therefore, necessitated. When QoE is attained and maximised by the user, then maintaining consistent QoE levels becomes increasingly important. In general, QoE is a non-linear function of QoS such that if network optimisation is based solely on QoS, it may not necessarily lead to optimal QoE. This makes the definition of a relationship between the technical QoS affecting QoE less linear. Thus, QoE cannot be directly captured using network measurements. QoE is, instead, a metric of satisfaction levels associated with the service and application, and must, therefore, incorporate user perception characteristics in given task environments. The environment involves the user task performance setting or those domains in which services in a given framework must operate. Thus, transitioning from a QoS to QoE-centric network management would signify a change from more traditional networks such as 4G LTE to more dynamic digital networks of the future such as 5G with URLLC capabilities [15]. Apart from QoS, which is typically a technical, objective concept, user-focused dimensions such as cost, availability, utility, and usability, directly affect user satisfaction, and by extension, perceptual QoE. A common assumption is that QoS, which is primarily focused on the optimisation of network attributes, will automatically lead to the rapid adoption of ICT products or services on the part of the user-consumer. However, QoS typically has little influence on the end-user. Although higher QoS can lead to improved QoE in some instances, there is no guarantee that attaining certain pre-defined QoS thresholds will necessarily result in high(er) user QoE. QoE not only accounts for observed technology performance above and beyond QoS, but also for what users can do with a particular tool or system, what they expect from it, what their expectations are, how much these expectations are met, and in what task domain or context they use given technology tools and systems. Notably, the QoE dimension of "usability", observed as user behaviour when using technology, indicates the degree of effectiveness, efficiency, and satisfaction with technology. The higher the usability, the easier it is for the user to perform a given set of

tasks. As such, if a product or service is difficult to use, users will likely not adopt it and assess it in terms of a low QoE, even if it considered state-of-the-art from a technical QoS perspective. Emerging future Internet applications must impose high requirements, thus requiring networks which allow ultra-reliable and low-latency communication to meet the challenge of rendering the QoS needed to maintain optimum user QoE levels [6]. A key challenge posed in the development of mobile 5G neworks is the rendering of low-latency transmissions with adequate user QoE. As such, the assessment of QoE in haptic-enabled Internet applications warrants further investigation [6]. In a 5G URLLC network and haptic-enabled Internet, performance-related measures can incorporate the QoE, QoT, and QoS dimensions, interlinked as shown in Figure 1. Note that an additional dimension Quality of Control (QoC) can be included in the application layer of this schematic and linked to QoS. Extending Beyond HITL (QoE) requirements, QoC is useful where the use of immersive perception applications is needed (e.g. autonomous cameras for live simultaneous localisation and mapping) [6].

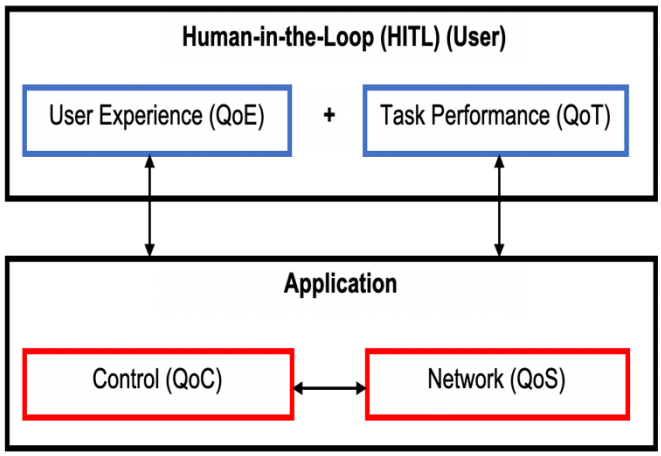

Figure 1: Various Performance-Related Dimensions for the Evaluation of Combinative Quality of Experience and Quality of Task (QoE + QoT), and Quality of Service (QoS) and Quality of Control (QoC) Measures

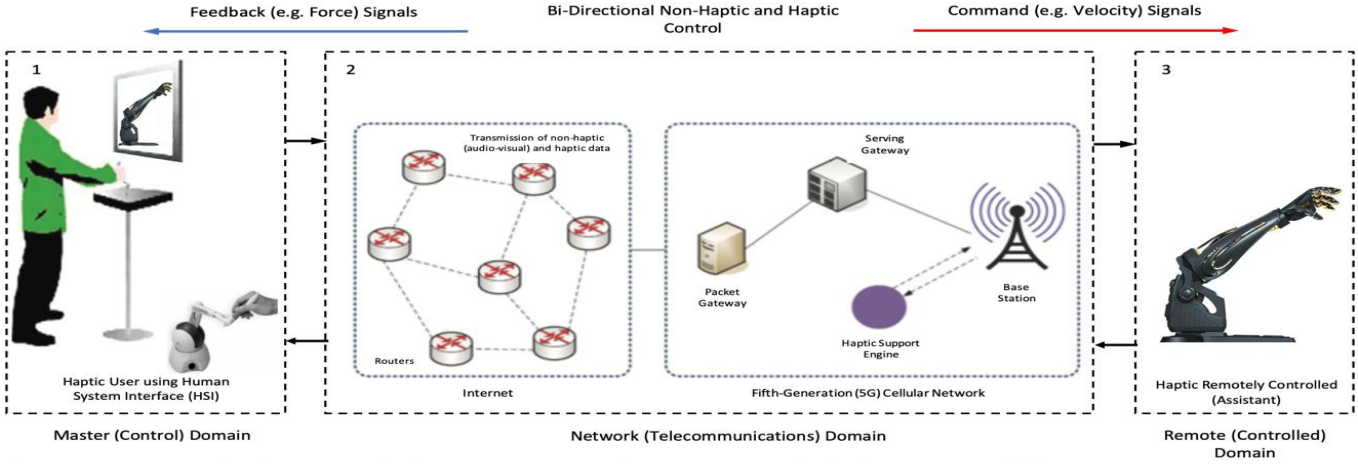

Figure 2: 5G Network and Haptic Communication-Enabled Internet Architecture

To highlight QoE, we draw on the example of Haptic-enabled Internet architectures that will be powered by next-generation digital networks such as 5G with URLLC characteristics. User QoE would infuse all the known core attributes of conventional audio and visual communication, while extending audio-visual perception to a third dimension, that of haptic communication, which would enable the real-time and interactive transmission of touch-based sensations. In a 5G URLLC network and haptic-enabled Internet of the future, the user experience would be influenced by certain network conditions (e.g. delay, jitter, and packet loss), the control scheme in use, and the task orientation (e.g. free space versus contact or soft object versus rigid surface). However, it will be important to consider factors and develop models that will enhance the accuracy of QoE-related performance to better guide numerous applications e.g. the preferred control scheme of a given task in a pre-specified QoS setup [11]. QoE can be a useful alternative to QoS because it incorporates user-focused decision processes and mechanisms. As such, with monitoring and control through the application of "QoE-sensitive" algorithms, the phenomenon of "over-engineering" is avoided, thereby ensuring more resource-efficent networking. Thus, QoE will become increasingly important in the design and planning of a future network, as well as its testing, maintenance, and improvement [16]. Typically, QoS is oriented towards purely technical characteristics and does not incorporate human user-focused factors that can impact quality. As such, the same QoS level may not guarantee the same QoE level for two distinct human users. Other than technical system features, dimensions including usage context, user characteristics, and delivered content, will all have an effect on user-perceived QoE [16]. QoS is also not reflective of the effect that technical dimensions have on user-perceived QoE. There is, therefore, an increasing need to close the QoS-QoE gap by mapping QoS-level parameters to overall assessed QoE values [16]. The QoE is not only restricted to the system. Instead, it is infused and activated when users interact with technologies. In essence, it resides in the user's domain such that an overall perceived QoE is contingent upon user acceptance, experience and interaction with the technology [13]. QoE is a subjective measure from the user's perspective of the overall value of the service provided, and thus does not replace, but extends end-to-end (E2E) QoS by providing the quantitative link to user perception [17]. With user-perceived

QoE data, telecom operators will be able to predict the behaviour of end users when new services are offered to them and to ensure service provisioning and management that is "fit" for user needs [17] or task requirements. A focus on QoE therefore assumes a shift from network-centric to user-focused management, combining control of network performance with customer-related feedback [17].

III. THE EMERGENCE OF A HAPTIC-ENABLED INTERNET ARCHITECTURE AND APPLICATIONS

The first and original Internet, a global network of computers, marked a paradigm shift that revolutionised the economies of the 20th century. The initial Internet, was followed by the Mobile Internet, which has connected billions of mobile devices and computers, reconfiguring entire economic sectors in the first decade of the 21st century [18]. Today, we have the Internet of Things (IoT), which is projected to connect trillions of smart devices and set to redefine economies of the next decade. These Internets will, however, be transcended by the emergence of a Haptic Internet, whereby highly reliable and responsive networks will enable the transmission of touch sensations remotely, adding a novel dimension to human-machine interaction through which real-time interactive system technologies will be designed and developed [8]. As the Haptic Internet will be expected to service some of the most crucial segments of society, it will not only have to be ultra-reliable, but also render capacity to enable large numbers of smart devices to simultaneously inter-communicate. It will also have to support extremely low end-to-end latencies to enable real-time haptic communication whereby mobile technologies will be enhanced to remotely control and manipulate real objects. As its core application, this novel Internet must support haptic communications [19], thereby providing a medium for real-time transmission of touch and actuation sensations, in addition to conventional audio-visual data. Haptic data typically comprises two primary feedback typologies. The first is kinaesthetic feedback, which provides data on dimensions such as force, torque, position, and velocity. The second, tactile or cutaneous feedback, provides information on dimensions such as surface, texture, and friction. The haptic sensations of touch and actuation will link the human user to a remote or virtual environment in a manner similar to the senses of sight and sound. Unlike these senses, however, the transmission of haptic sensations will be bi-directional. In other words, touch will be detected by imposing motion on an environment and feeling via a distortion or reactionary force. Haptics will provide an added dimension over conventional audio and visual communication for the support of truly immersive motion and control in remote environments. Haptic control will be essential to the realisation of this future Internet. As depicted in Figure 2, a Haptic-Internet architecture will comprise three domains, namely the (1) Master (control), (2) Network (Communication), and (3) Remote (Controlled) domains. First, the master (control) domain typically comprises a human user using a Human System Interface (HSI). This HSI functions as a haptic device that transmutes the human input using coding mechanisms. This haptic device allows the user to touch, feel, and handle objects in a remote environment. Second, the network (communication) domain provides a channel for bi-directional communication between the master (control) domain and a remote environment, and thus, can by means of haptic transmission, link the human user remotely. Elementally, the human user is fully immersed in the remote environment [6], [8]. Third, the remote (controlled) domain consists of an assistant robot that is directly controlled by the human user in the master (control) domain through various command signals. The robot then interacts with elements in the remote environment. According to the International Mobile Telecommunications – 2020 (IMT – 2020) 5G network standard, a key generic application use case is URLLC. URLLC is suited to use cases with stringent requirements on reliability and latency e.g. task performance in remote robotic surgery applications. As an example, the use case of remote robotic surgery depends on the URLLC and time synchronization capabilities of 5G to enable precise time-critical information sharing and control of treatment devices that support remote task performance [6].

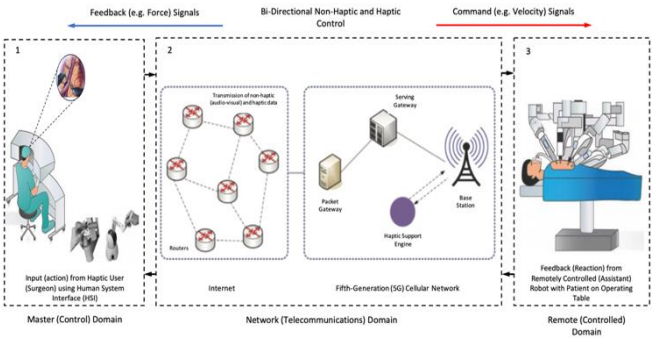

Figure 3: Architecture of 5G URLLC Network and Haptic-Enabled Internet for Remote Robotic Surgery

The 3rd Generation Partnership Project (3GPP) provides a set of concurrent technical specifications for the implementation of the 5G New Radio (NR) standards. The current 3GPP 5G NR standard, Release 16, enhances support for URLLC services by enabling latency in the range of 0.5 to 1 ms and improved reliability with a target error rate of 10^{-6}. Building on the enhancement of URLLC in the 5G core network expected with Release 16, the specifications of 3GPP Release 17, currently in development and to be finalised in 2021, are expected to address the communication service requirements for Critical Medical Applications (CMED), among others. Release 17 is thus expected to expand the reach of 5G for URLLC-supported mission critical use cases, including robotic telesurgery (Fig. 3), with further reduced latency [20].

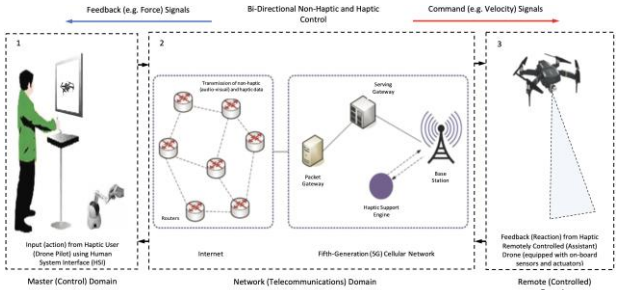

Figure 4: Architecture of 5G URLLC Network and Haptic-Enabled Internet for Unmanned Aerial Vehicle (UAV) Control in Remote Sensing/Monitoring

Similarly, the coming 3GPP 5G NR standard Release 17 is expected to address Enhancement for Unmanned Aerial Vehicles (UAVs) through application requirements for communication latency, mobility, and reliability [21]. The low latencies of URLLC-supported 5G, would be suited to real-time scenarios such as remote UAV control in the performance of remote sensing and monitoring tasks (Fig. 4).

IV. THE HUMAN-IN-THE-LOOP IN A HAPTIC-ENABLED INTERNET AND THE LINK BETWEEN QUALITY OF EXPERIENCE AND QUALITY OF TASK

The human-in-the-loop (HITL) central to a Haptic-Enabled Internet is the link between the master (control) domain and remote (controlled) environment in which skilled users interact with physical objects to perform specific tasks remotely. Thus, even if a particular task requirement were to be defined, various manoeuvres executed by the human user would result in changes in position, relayed from the remote (controlled) domain as force feedback signals. These signals would then affect the actions and therefore, position, of the task-performing human user [18] in the master (control) domain. The Haptic-Enabled Internet as the convergence of haptics, 5G networks, AI, and robotics, will augment the human user experience enabling task performance via the manipulation and control of objects in remote environments. This will transform traditional content delivery-based communication channels into task-oriented networks for the delivery of skill-sets [8, 9]. Thus, in effect, the transmission of human user skills for remote task performance in real-time will indicate the emergence of a 5G (URLLC) and haptic-enabled Internet of Skills (IoS), signifying a paradigm shift in augmented technology user experience. With the emergence of a user-centric 5G (URLLC) and haptic-enabled IoS, a Quality of Experience (QoE)-focused evaluation becomes particularly important, as this would advance the development of quality performance metrics. The QoE-oriented modeling of a human haptic user interaction is, thus, necessitated [11]. In evaluating human user QoE, it is equally imperative to consider the Quality of Task (QoT) dimension, which denotes the precision with which a haptic-enabled IoS user can perform a particular task using a given technological system or tool support function. This is owing to the task dependent nature of a user-centric haptic-enabled IoS.

V. FUTURE DIRECTIONS

A. *Task-Technology Fit Modelling for a QoE and QoT Perspective of Future Internet Architectures*

This research is extensible to future papers. The next phase of this research can incorporate a number of approaches to inform QoE and QoT perspectives of future Internet applications. For instance, one novel way to evaluate a 5G (URLLC) and haptic-enabled Internet applied to mission-critical use cases such as remote robotic surgery (Fig. 3) and remote-controlled UAV (drone) sensing and monitoring applications (Fig. 4) from the perspective of QoE and QoT, is by applying Task-Technology Fit (TTF) modelling techniques. TTF is the extent to which functional capacities of a tool or system converge with the user's needs in performing the task-at-hand [22]. Its premise is that technologies will be used and lead to gains in user task performance if functional support characteristics fit use requirements. The presence of a "fit" between task and technology will result in utilisation and performance outputs [22].

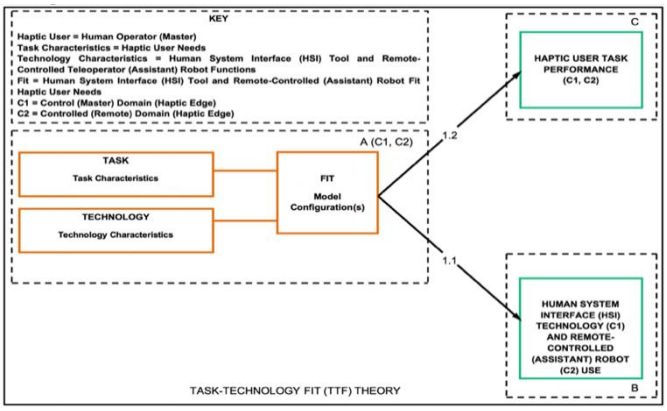

Figure 5: Conceptual Task-Technology Fit (TTF) Model of User Experience in Master (Control) and Remote (Controlled) Domains of a 5G URLLC Network and Haptic-Enabled Internet

TTF models would typically link the task the user performs and the technology used, and the "fit" of their respective characteristics, which in turn would have effects on use and user performance outcomes. This paradigm would be particularly useful in the context of a 5G and haptic-enabled Internet where a conceptual model (Fig. 5) would be developed to link human user task and HSI and remote assistant robotic technology characteristics, and use and user performance outcomes, in both master (control) and remote (controlled) domains (Figs. 3-4). In so doing, we would benefit from a novel QoE and QoT perspective corresponding with a HITL layer linking user experience with task performance dimensions (Fig. 1) to supplement network characteristics in the application layer (QoS). QoE and QoT would map onto the HITL interacting with the technology in both the master (control) and remote (controlled) domains of future Internet architectures (Figs. 3-4), mediated by QoS mapped onto their network (telecommunications) domains (Figs. 2-4).

B. *Description of Proposed Methodology (Analysis Techniques)*

An explanatory and predictive (hypothetico-deductive) research design can be used to examine and explain relationships between conceptual TTF model constructs (Fig. 5). TTF, which can be configured in numerous ways, will be tested for its use and user effects. Partial Least Squares – Structural Equation Modelling (PLS-SEM) will be used to analyse data. This will involve robust, component-based, second-generation path analysis, based on Ordinary Least Squares (OLS) regression. Additionally, Polynomial Regression with Response Surface Methodology will be used to test the possible non-linear impacts of a 5G network and haptic-enabled Internet architecture. This Internet will potentially enable a number of mission-critical real-world applications. Scenarios such as the use cases of remote robotic surgery (Fig. 3) and remote UAV (drone) control in sensing and monitoring (Fig. 4) would benefit from TTF modelling (of the interactions between critical support functions and user needs). To do so, empirical data in such usage contexts would be collected (using a set of developed Likert scale perceptual

instrument survey measures) from human users (task performers) (e.g. surgeons in the use case of remote robotic surgery) and analysed. This would allow for (i) the initial testing and subsequent validation of TTF models for a particular 5G (URLLC) network and haptic-enabled Internet user environment, and (ii) empirical observation and explanation of real-time immersive task performance scenarios, thereby demonstrating QoE and QoT centred perspectives for the augmentation of the human user experience.

VI. CONCLUSIONS

The QoE perspective is increasingly becoming useful for evaluating how users subjectively perceive a technology service. It provides a more holistic view of factors beyond just the technical system-centric dimensions attributed to the traditional QoS. As next-generation digital communication networks of the future (e.g. 5G with URLLC capabilities) will infuse network architectures with high-end user-centred services, it is imperative that QoS and QoE dimensions must be integrated. Whereas researchers and practitioners have attempted to link user behaviours to technical network attributes and QoS parameters, evidence-based research on QoE and QoS has been limited, particularly in the context of emerging next-generation digital network technologies. Thus, technical-level QoS must be integrated with user-oriented QoE for a more holistic perspective. This highlights a need to further investigate the relationships between network-centric QoS and user-oriented QoE, and by extension QoT for augmented human (task performer) user experience use cases. Based on recent advances in 5G, particularly in ultra-reliable low-latency communication (URLLC), we contribute to explaining the emerging paradigm shift from content-delivery networks to skillset-delivery networks enabled by the emerging and future network architectures (e.g. a 5G URLLC and haptic-enabled Internet), that will be more human user-centric, but mediated through human-to-machine/robot (H2M/R) interactions.

REFERENCES

[1] A. Osseiran, J. F. Monserrat, and P. Marsch, *5G Mobile and Wireless Communications Technology*, Cambridge, UK: Cambridge University Press, 2016.

[2] M. Giordani, M. Polese, M. Mezzavilla, S. Rangan, and M. Zorzi, "Toward 6G Networks: Use Cases and Technologies," *IEEE Communications Magazine*, vol. 58, pp. 55-61, Mar. 2020.

[3] R. Bassoli, H. Boche, C. Deppe, R. Ferrara, F. H. P. Fitzek, G. Janssen, and S. Saeedinaeeni, *Quantum Communication Networks*, Cham, Switzerland: Springer, 2021.

[4] A. Seetharaman, A, I. Niranjan, V. Tandon, S. Devarajan, M. K. Moorthy, and A. S. Saravanan, "What do Customers Crave in Mobile 5G?," *IEEE Consumer Electronics Magazine*, vol. 6, pp. 52-66, Jul. 2017.

[5] L. Pierucci, "The Quality of Experience Perspective Toward 5G Technology," *IEEE Wireless Communications*, vol. 22, pp. 10-16, Aug. 2015.

[6] K. Antonakoglou, X. Xu, E. Steinbach, T. Mahmoodi, and M. Dohler, "Toward Haptic Communications Over the 5G Tactile Internet," *IEEE Communications Surveys and Tutorials*, vol. 20, pp. 3034-3059, Fourth Quarter. 2018.

[7] G. P. Fettweis, "The Tactile Internet: Applications and Challenges," *IEEE Vehicular Technology Magazine*, vol. 9, pp. 64-70, Mar. 2014.

[8] A. Aijaz, M. Dohler, H. Aghvami, V. Friderikos, and M. Frodigh, "Realizing the Tactile Internet: Haptic Communications over Next Generation 5G Cellular Networks," *IEEE Wireless Communications*, vol. 24, pp. 82-89, Apr. 2017.

[9] S. K. Sharma, I. Woungang, A. Anpalagan, and S. Chatzinotas, "Toward Tactile Internet in Beyond 5G Era: Recent Advances, Current Issues, and Future Directions," *IEEE Access*, vol. 8, pp. 56958-56991, Mar. 2020.

[10] X. Xu, B. Cizmeci, C. Schuwerk, and E. Steinbach, "Model-Mediated Teleoperation: Toward Stable and Transparent Teleoperation Systems," *IEEE Access*, vol. 4, pp. 425-449, Mar. 2016.

[11] Q. Liu and T. Zhao, "Quality-of-Experience in Human-in-the-Loop Haptic Communications," *ZTE Communications*, vol. 17, pp. 48-55, Mar. 2019.

[12] J. Sachs, L. A. A. Andersson, J. Araujo, C. Curescu, J. Lundsjo, G. Rune, E. Steinbach, and G. Wikstrom, "Adaptive 5G Low-Latency Communication for Tactile Internet Services," *Proceedings of the IEEE*, vol. 107, pp. 325-349, Feb. 2019.

[13] D.-H. Shin, "Conceptualizing and Measuring Quality of Experience of the Internet of Things: Exploring How Quality is Perceived by Users," *Information and Management*, vol. 54, pp. 998-1011, Dec. 2017.

[14] ITU-T, "Vocabulary for Performance, Quality of Service and Quality of Experience," ITU-T P.10/G.100 – Amendment 1, 2019.

[15] N. Banovic-Curguz, D. Ilisevic, and D. Budimir, "Towards Digital Transformation with 5G Technology," *International Journal of Electrical Engineering and Computing*, vol. 2, pp. 101-109, 2018.

[16] E. Lioutou, D. Tsolkas, and N. Passas, "A Roadmap on QoE Metrics and Models," *Proc. 23rd International Conference on Telecommunications (ICT 2016)*, Thessaloniki, Greece, 16-18 May, 2016.

[17] M.D. Stojanoovic, M.M. Vukasinovic, and V.M.R. Djoogatovic, "Approaches to Quality of Experience Management in the Future Internet," *12th International Conference on Advanced Technologies, Systems and Services in Telecommunications (TELSIKS 2015)*, Niš, Serbia, 14-17 Oct. 2015.

[18] M. Dohler, "The Future and Challenges of Communications – Toward a World Where 5G Enables Synchronized Reality and an Internet of Skills," *Internet Technology Letters*, vol. 1, pp. 1-3, Feb. 2018.

[19] E. Steinbach, S. Hiche, M. Ernst, F. Brandi, R. Chaudhari, J. Kammerrl, and I. Vittorrias," Haptic Communications," *Proceedings of the IEEE*, vol. 100, pp. 937-956, Apr. 2012.

[20] 3GPP, "Study on Communications Services for Critical Medical Applications (Release 17)," Tech. Rep. TR 22.826, V17.2.0, 2021.

[21] 3GPP, "Enhancement for Unmanned Aerial Vehicles (Release 17)," Tech. Rep. TR 22.829, V.17.1.0, 2019.

[22] M.T. Dishaw and D.M. Strong, "Supporting Software Maintenance with Software Engineering Tools: A Computed Task-Technology Fit Analysis," *The Journal of Systems and Software*, vol. 44, pp. 107-120.

Maradona C. Gatara is Wits Business School (WBS) Postdoctoral Research Fellow in Technology and Operations Management at the, University of the Witwatersrand (Wits) in Johannesburg, South Africa. His research interests include haptics, next-generation digital networks, health informatics, and technology service delivery systems. He holds a Ph.D. degree in Information Systems.

Mjumo Mzyece is Associate Professor of Technology and Operations Management at Wits Business School (WBS), University of the Witwatersrand (Wits), in Johannesburg, South Africa. His research interests include next-generation digital networks, technology policy, strategy, and management. He holds a Ph.D. degree in Mobile & Wireless Communications Engineering.

Deep Learning And Blockchain-based Dynamic Routing For Neighbourhood Area Network Communication

Tatenda Trust Gotora[1], Neco Ventura[2] , Mqhele Dlodlo[3]
Department of Electrical Engineering, University of Cape Town, Cape Town, South Africa
[1]gtrtat002@myuct.ac.za
[2]neco.ventura@uct.ac.za
[3]mqhele.dlodlo@nust.ac.zw

***Abstract*—Blockchain technologies have disrupted the data storage capability and brought decentralization in transaction processing. From handling business to governance, Blockchain continues to promote shared digital ledger systems, transparency and secure data delivery between transacting entities. Wireless network transactions are no exception as determination of a routing table, channel selection and decentralizing traffic control are issues which Blockchain can address. Smart grids are currently facing two-way transmission problems due to demand for accommodating flexible prosumer demands, smart city initiatives and distributed renewable energy integration. The study seeks to explore the potential application of deep learning based smart contracts in determining the route path of traffic in a Neighbourhood Area Network (NAN). This will be first of its kind as this will lead to establishment of a viable Blockchain-Licensed Assisted Access smart grid architecture that will provide smooth switching between LTE/5G and Television whitespace access points in a NAN. This will lessen the data processing burden on NAN gateway and smart meters. Future work seeks to test the proposed concepts in a real test bed in a rural area set up and compare with other adhoc routing protocols.**

Keywords—Blockchain, Smart Grid, Routing, Licensed Assisted Access, Smart Contracts.

I. INTRODUCTION

A Blockchain (BC) can be viewed as a distributed ledger system that stores data records or transactional data which is linked and tamperproof. [1] places more emphasis on the point of a Blockchain consisting of cryptographically signed transactions stored as blocks which are linked securely one after the other, only when validation and a consensus resolution has been done by nodes in the shared ledger system. This makes the blocks secure, verifiable by consensus protocols and unmodifiable. Although, there are various consensus protocols that determine how blocks or tokens are authenticated in Blockchain, these include proof of stake (PoS), proof of authority (PoAu), proof of work (PoW) and proof of concept (PoC) etc. Blockchain technology is applicable in various sectors including; business, banking, mining, education and governance. Although Blockchain technology is mostly popular in modern day world in the creation of crypto-currency[1] e.g. Bitcoin, Ethereum etc., it can also be used in Smart Grids to address a lot of issues like energy trading[2], secure communication[3], [4], channel selection and route determination[5], [6]. The decision engine in a Blockchain is implemented by the Smart Contract (SC) and it is this crucial element which determines the efficiency in a Blockchain system.

In [7] a smart contract is defined as a user-defined program stored in a public ledger which is associated to a blockchain address with the goal to carry out a certain task. [2] also mentions the SC has the ability to determine what can be written in the public ledger. In this research, a smart contract will be considered a set of rules that describe how autonomous entities operate and what decision criteria exists between them when routing. Blockchain networks can be permission-less or permissioned depending on the level of trust required by the transacting entities, with permissioned networks proving to be computationally faster and cheaper [1], [2].

Power grids on the other hand have enjoyed centralized control by utility bodies and service providers in a country but the rise of increased energy demand and greenness shift has promoted renewable energy producers and Independent Power Producers (IPPs) initiatives. SGs being the next intelligent power grids are eager to incorporate distributed renewable energy sources (DRES), optimized demand response management (DRM) techniques, secure communication and two-way communication between prosumer and utility centre. SG communication networks are made up of three major sections Home Area Network (HAN), Neighbourhood Area Network (NAN) and Wide Area Network (WAN) [8], [9]. These three subnetworks are going to contain smart meters, sensors and synchrophasors to collect data for effective decisions to be made. The data will be voluminous in nature and might require unorthodox data mining abilities to extract meaningful information while striking a balance between energy consumed and delay. To the best of the researchers knowledge not much exploration has been carried out on Blockchain based dynamic routing in the NAN. Routing is the establishment of a path when transmitting data amongst nodes or hosts using a fixed or intelligent decision matrix and a routing table. Next Generation Networks especially Software Defined Networks (SDNs) and Fifth Generation (5G) technology seeks to decouple the control and data planes using network function virtualization. Likewise in SG networks the routing control can be managed by an autonomous and independent SC while transfer of data is handled by wireless networks like Licensed Assisted Access (LAA) technologies.

This study seeks to explore the potential application of deep learning-based smart contracts in determining the route path of traffic in a NAN. Most researches have investigated the aspects of wireless communication and energy provisioning separately when these two are actually directly related. This will be first of its kind as this will lead to establishment of a viable hybrid Blockchain-Licensed Assisted Access smart grid architecture that will provide smooth switching between LTE/5G and Television whitespace (TVWS) access points in a NAN while aiding dynamic energy provisioning.

II. NAN ROUTING TECHNIQUES

Many routing optimization techniques have been suggested and some perform exceptionally well in different scenarios [10]–[16] but a lot of exploration needs to be carried out in line with Blockchain-enabled routing for Smart Grid Networks. Passive neighbor discovery is an essential process in wireless networks which allows communicating devices to

learn about their current neighbors after actively listening to their communication[17]. Using deterministic discovery methods the speed of discovery and excellent reliability is only suitable for single-channel scenarios rather than asynchronous multi-channel needs brought by wireless technologies operating in different bands. LAA uses more than one frequency band attributed to unlicensed and licensed access. To solve this problem [17] uses previous scanning history and accelerating discovery of neighbors with lesser beacon durations of a set with beacon orders for each channel contained in a channel pool i.e. listening-scanning scheduling technique through linear programming (LP) optimization. However, the conditions were ideal as no channel switching, no interference and no beacon transmission time was considered. Furthermore a switched optimized solution to cater for switching times was also compared to the passive discovery technique and proved to be more effective in first and last discovery times which are much needed in SG routing for effective real-time communication in a NAN.

In their study [6] mention the common problems faced by Autonomous systems (AS) (i.e. a collection of linked routers or switches with prefixes and routing policies offered by Internet Service Providers (ISPs)), one of which is Border Gateway Protocol (BGP) hijacking on the internet. [6] goes on to suggest use of a Routechain a Blockchain-based routing protocol to solve the BGP security issue leveraging on policy management and already present ISP infrastructure unlike many solutions like BGPSec which need a costly infrastructure revamp. A PoAu consensus protocol called Clique was used to provide trust amongst AS entities to improve the BGP weak trust model and cryptographically secure routing information which proved to be tamper-proof and resilient to hijacking when tested under YouTube 2008 case study conditions[6]. They only focused on external BGP connections more like NAN to NAN connections in the SG scenario leaving out internal problems unresolved, when these are actually also key to having smooth prosumer to prosumer interaction in a NAN and hence better energy provisioning.

Routing Protocol for Low power and Lossy Networks (RPL) was designed for IPv6 which constructs its own destination oriented directed acyclic graph (DODAG) information object (DIO) message to maintain and control interconnection. RPL can be optimized by changing the objective function metrics like link/network metrics, such as delay, energy metrics such as residual energy, node metrics include hop count, and power metrics.[18]. RPL with a self-configuring ability is suggested in one study applied in a NAN which uses TVWS for smart metering to transmit data and control instructions between fixed smart meters (SMs) in a wireless mesh network with a concentrator [19]. The self-organizing ability is enabled by a radio environment maps and geo-location database for channel allocation and smooth switch over. SMs associates with a particular concentrator and scan for incumbent user (IU) occupancy as they transmit data. The switch over time is on average 15 seconds as PU arrival increases leading to frequent leads to network overhead as the switching between channels increases [19]. One major drawback is meter nodes are fixed depending on the powerline communication to transmit data and if an outage occurs there will be connectivity problems during multi-hop.

Moreso, the authors in [18] and [20] make adjustments to the RPL. Simulations in [18] demonstrate that by using ETEN-RPL algorithm which combines the expected transmission time (ETX) and residual energy metrics improvements are observed in the network link stability, lifeline of nodes, packet delivery ratio (PDR) by 1.2% and average energy consumption (AEC) by 5.4% in comparison to the ordinary RPL. On the other hand in [20], Green-RPL algorithm prioritizes route selection based on energy efficiency over virtual distance amongst nodes thereby improving the total node energy consumption, packet delivery ratio and coordination overhead. This is due to use of micro frames for transmitting acknowledgement messages and protecting PUs considering the collision risk factor when compared with RPL and other modified RPL. All protocols showed degradation in performance as number of nodes increased. Yang et al. propose a reinforcement learning based scheduling routing algorithm for wireless sensor networks which leverages on a BC network used for storing the routing network state information [21]. The authors go on to apply a PoAu consensus algorithm to validate transactions where server nodes are the validators and routing nodes are the miners. This model proved to be effective than back pressure (BP) and back pressure-Blockchain routing algorithms in terms of average packet delay which was reduced by 81% even when malicious nodes where 50% of the routing nodes. The learning ability of the routing algorithm made it dynamically robust. A comparison of PoAu and PoW was also done to measure the reinforcement learning-based algorithm efficiency. The PoAu performed remarkably well reducing token transaction latency by 44% and showed a stable average transaction consumption of 35,660 gas amounting around USD$0.0613 for both PoAu and PoW [21].

III. SYSTEM MODEL

Considering $S = \{s_1, s_2 \dots, s_n\}$ as a set of SM nodes or secondary users (SUs) which are cognitive-enabled, occupying a service area denoted by $\mathcal{A}$ measuring d^2, where d represents the square edge length. The SM nodes are Poisson distributed with mean value λ. The nodes are located in a geographic space g and have transmission radius of r.

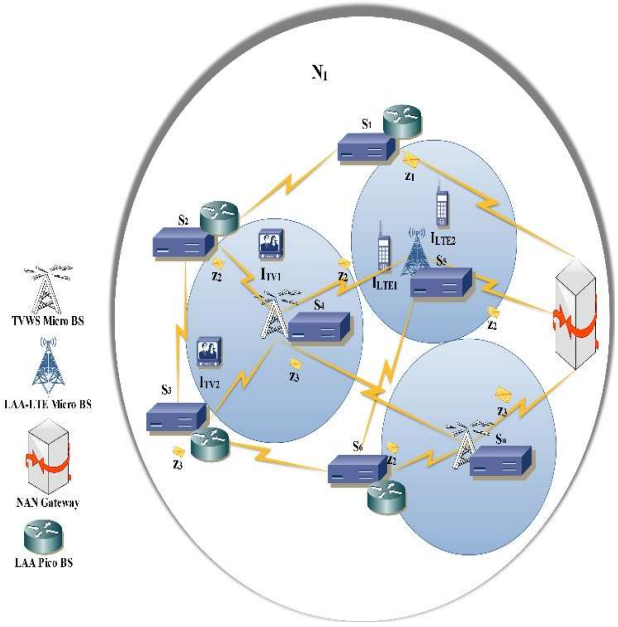

Figure 1: System Model

The NAN is also considered to have $B = \{b_1, b_2 \dots, b_q\}$a set of micro base stations (MBS) which operate in the TVWS, LAA and LTE network bands with transmission times

denoted as t_{TVWS}, t_{LAA} and t_{LTE} respectively. Let $Y = \{y_1, y_2 \ldots, y_m\}$present a set of NAN clusters where, a cluster $Y \subseteq \mathcal{A}, \forall\, i \in Y,\ \forall\ \cup_{i=1}^{m} y_i = \mathcal{A}$ and $\cap_{i=1}^{j} \mathrm{Y}_i = w$ are satisfied. w denotes an interference threshold for any two adjacent i and j NANs. If $\mathrm{C} = \{c_1, c_2 \ldots, c_k\}$ is a set of vacant channels left by active incumbent users (IUs) assigned via the base stations or NAN gateway (NGW), a set of occupied channels will be represented by $O = \{o_1, o_2 \ldots, o_k\}$ which enable connectivity in the service area. The system model is shown in Fig 1 above. Data will be sent between any given nodes depending on its class or level of importance denoted by $\mathcal{Z} = \{z_1, z_2, z_3\}$ as defined in [16].

IV. Problem Formulation

Suppose we want to ensure incumbent user protection and dynamically allocate channels to SMs depending on routing node location and transmission cost. Let's assume the incumbent and primary users occupy the TVWS, LAA and LTE channels at varying time intervals. The channel status denoted as $\mathrm{u}_\mathrm{q}^\mathrm{t}$ is determined by spectrum sensing or TVWS Geolocation database (T-GDB). When an SU is occupying a TVWS channel and an IU arrives, the SU releases channel before the base station relocates it to another free one. The research assumes the LTE will give priority to IUs but if an intelligent scheduler is available the unused channels can be allocated to SUs. This might result in co-tier or adjacent channel interference considering LAA, TVWS and LTE will be operating in the same band of 700 to 900Mhz, which leads to transmission delay. If RPL is used channel status will be sent by parent node as a DIO message to other routing nodes and which need to be ranked for efficient forwarding to transpire. The ranking value for a node i can be obtained using formula mentioned in [20] and adding an interference factor $I_c(i,j)$:

$$r_i = \min\{r_j + (w * I_c(i,j))\} \quad (1)$$

Where r_j represents the rank of parent node j, w is the weight given to node transmission, $I_c(i,j)$ is the interference factor between node i and j in the cth channel.

$$I_c(i,j) = 1 - min\left(g_{ij}, D(c_i, c_j)\right)/D(c_i, c_j) \quad (2)$$

Where g_{ij} is the actual distance between node i and j from finding the Euclidean distance $|g_j - g_i|$. $D(c_i, c_j)$ is the channel interference range between channel i and channel j. For effective routing to occur the node i should select channel with minimum interference. Upon receiving the DIO message the smart meter or access point will create its own forwarder set considering a particular priority in this case link cost over virtual distance during a particular time slot $(C(t)_{lv})$ function expressed as:

$$C(t)_{lv} = L_{ij}^t / v_{ij} \quad (3)$$

Where L_{ij}^t, is the link cost required to transmit data between node i and j at time slot t. v_{ij} is the virtual distance computed by $|r_j - r_i|$. The goal is to minimize $C(t)_{lv}$ by selecting the optimal path from j to i, reducing energy transmission cost and interference while improving channel allocation. Through applying deep learning and Blockchain this can become a reality. The link cost between node i and j can be computed as follows:

$$L_{ij}^t = \left(x_{ij}^t * E_{xij}^t\right) + \left(s_{ij}^t * E_{sij}^t\right) + \left(b_{ij}^t * E_{bij}^t\right) \quad (4)$$

Where infrastructure transmission cost is denoted as x_{ij}^t, E_{xij}^t is the energy consumed when transmitting data between i and j, spectrum sensing cost is denoted by s_{ij}^t, E_{sij}^t is the energy used in channel sensing and selection, b_{ij}^t is the blockchain cost to transact between i and j, while E_{bij}^t represents the energy used per transaction.

$$\min_{c_{ij}^t, g_{ij}} \sum_{t=1}^{24} \sum_{q=1}^{Q} C(t)_{lv} * \mathrm{u}_\mathrm{q}^\mathrm{t} \quad (5)$$

Subject to:

$$|r_j - r_i| > 0 \quad (6)$$

$$m_{ji} = m_j - m \quad (7)$$

$$m_{ij} = m_i + m \quad (8)$$

$$E_{xij}^t + E_{sij}^t + E_{bij}^t \leq 0 \quad (9)$$

$$I_c(i,j) \leq I_{thres} \quad (10)$$

$\mathrm{u}_\mathrm{q}^\mathrm{t}$ represent binary variable that indicates the channel state for each running index q at time slot t, idle or busy i.e. $\{\mathrm{u}_\mathrm{q}^\mathrm{t} \in 0,1\}$. m_{ji} represent the packet balance verified by BC when m data is transferred from j to i. m_{ij} is the packet balance verified by BC after m data is received from j by i. E_{Tx}^t is the total energy consumed when transmitting data from smart meter on prosumer to BS. E_I^t is the energy used in processing the information on SM. E_{BC}^t is the energy needed to send and receive blocks from BC per given transaction obtained from the Ethereum Blockchain platform.

V. Methodology

Data packets were randomly generated using Scapy python library tool for 10 smart meter nodes located in a NAN, which measured 10 by 10 square kilometers in a typical suburban or rural set up. The physical distance between nodes was assumed to range between 100 and 1 000 metres apart. The smart contract was designed using solidarity in the truffle project environment and deployed in the Ganache Blockchain development platform. The deep learning-based smart contract was then invoked in a python script to perform routing between any given nodes i and j. Each NAN was assumed to have at least two TVWS base stations which are 10 000 metres apart and one LTE base station stationed at the 5 000 metres radius.

A. Proposed Deep Reinforcement Learning and Blockchain (DLBC) Algorithm

Step 1: let $S = \{s_1, s_2 \ldots, s_n\}$ *be N input nodes with defined IP addresses and fixed data packets (e.g. message "Hello").*
Step 2: Initialize t = 1, i = 1, j =0, q = 1, $E_{sij}^t = 0$ *and* $r_j = 0$.
Step 3: Select an action ***a*** *for each node based on the node rank.*
Step 4: Compute the node rank $r_i = min\{r_j + (w * I_c(i,j))\}$
Step 5: For i to N do:
increment i by 1;
update r_i*;*
route(i, j);
record $m_{ji} = m_j - m$*;*
$validate\ m_{ij} = m_j + m$;
For t =1 to 24 do:
Compute $L_{ij}^t = \left(x_{ij}^t * E_{xij}^t\right) + \left(b_{ij}^t * E_{bij}^t\right)$
Increment t by 1;
End For;

End For;
Step 6: *For t =1 to 24 do:*
For q = 1 to 10 do:
Compute $C(t)_{lv} * u_q^t$;
update u_q^t *for each action*
increment q by 1;
End for;
increment t by 1;
End for;
Step 7: Stop

B. Proposed DLBC Routing Model

The model shows the data packets will be transmitted between SMs and blockchain nodes. The deep learning engine will be stored in a cloud or local blockchain network where the smart contract resides. The channel allocation and selection manager is supposed to liaise with the T-GDB to get a collection of all available channels to be used for transmission. For purposes of this research the manager was not implemented but random channels were assumed to be free or occupied.

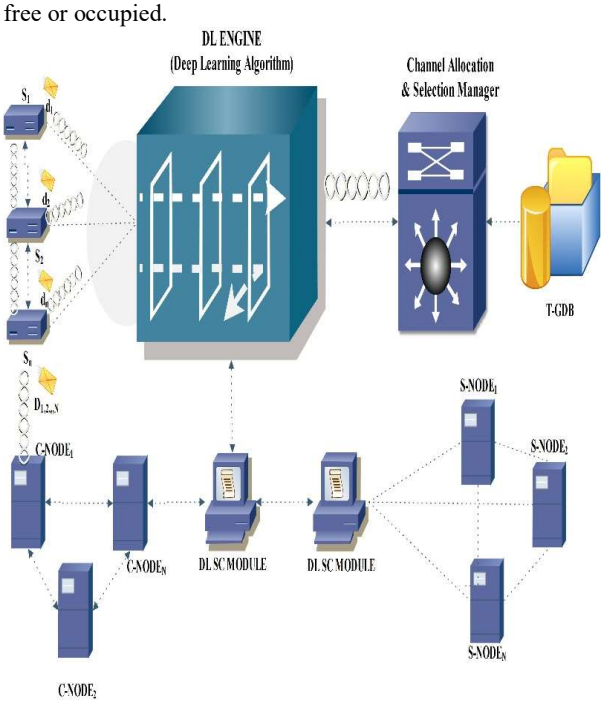

Figure 2: Proposed Deep Learning and Blockchain Network

VI. RESULTS AND DISCUSSION

From the routing and blockchain transaction simulations carried in this research results show that the DLBC-based routing algorithm outperformed normal RPL, in terms of packet delivery ratio and transmission delay between nodes. As shown in table I and table II respectively. In table I, DLBC is presented as being at par with RPL in short distances and superseding RPL in long distances. But the DLBC consumes more energy when compared to RPL due to transmission of data to and fro blockchain platform which can be reduced by placing renewable energy on HANs. In table II it is shown that for both transmission control protocol (TCP) and user datagram protocol (UDP) high priority message tend to have less delay than low priority messages despite the distance in consideration.

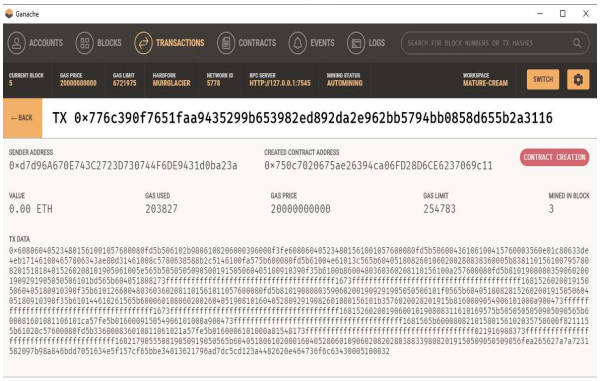

Figure 3: Blockchain Transaction captured in Ganache

Figure 3 shows how a transaction is recorded on the Ganache development platform and the corresponding data packets between nodes were simulated using Scapy library as they got recorded in Wireshack.

TABLE I. PDR VS NODE DISTANCE

Distance (m)	Packet Delivery Ratio%	
	DLBC	***RPL***
100	0.96	0.93
500	0.93	0.93
1000	0.87	0.93
2000	0.86	0.80
5000	0.85	0.75
10000	0.80	0.70

TABLE II. END TO END DELAY VS NODE DISTANCE

Distance (m)	Transmission Protocol	Message Type (Priority)	End to End Delay %	
			DLBC	***RPL***
100	UDP TCP	HIGH	1.3 1.2	1.4[20] 1.4
500	UDP TCP	LOW	3.3 3.0	3.5 3.0
1000	UDP TCP	MID	2.8 2.5	2.6 2.5
2000	UDP TCP	MID	4.6 4.7	5.0 5.2
5000	UDP TCP	HIGH	3.0 3.1	3.4 3.3
10000	UDP TCP	LOW	10 15.5	12 17

VII. Conclusion And Future Work

Blockchain technology is bringing transparency and security to many sectors including smart grid. Although it consumes more computational energy, through use of deep learning and renewable energy the energy and transmission costs can be greatly reduced. Applying deep learning and blockchain in NAN improves packet delivery ratio, delay and channel switching ability for smart meter nodes. Future work will consider comparing with more bio-inspired algorithms like cat swarm optimization, ant colon and hybrid ones. The algorithm needs to be tested in a real test bed environment with real time SM data.

Acknowledgment

The authors acknowledge the support received from Telkom SA via Telkom Centre of Excellence (CoE) in Broadband Networks and Applications hosted at the department of Electrical Engineering at University of Cape Town. Special thanks also go to Midlands State University (MSU) located in Zimbabwe for the financial support and resources availed to Tatenda.

References

[1] D. Yaga, P. Mell, N. Roby, and K. Scarfone, "Blockchain technology overview," National Institute of Standards and Technology, Gaithersburg, MD, NIST IR 8202, Oct. 2018. doi: 10.6028/NIST.IR.8202.

[2] M. Andoni *et al.*, "Blockchain technology in the energy sector: A systematic review of challenges and opportunities," *Renew. Sustain. Energy Rev.*, vol. 100, pp. 143–174, Feb. 2019, doi: 10.1016/j.rser.2018.10.014.

[3] K. Singh and S. C. Choube, "Using blockchain against cyber attacks on smart grids," in *2018 IEEE International Students' Conference on Electrical, Electronics and Computer Science (SCEECS)*, Feb. 2018, pp. 1–4. doi: 10.1109/SCEECS.2018.8546891.

[4] Q. Xia, E. B. Sifah, K. Huang, R. Chen, X. Du, and J. Gao, "Secure Payment Routing Protocol for Economic Systems Based on Blockchain," in *2018 International Conference on Computing, Networking and Communications (ICNC)*, Mar. 2018, pp. 177–181. doi: 10.1109/ICCNC.2018.8390309.

[5] Y. Liu *et al.*, "A novel routing verification approach based on blockchain for inter-domain routing in smart metropolitan area networks," *J. Parallel Distrib. Comput.*, vol. 142, pp. 77–89, Aug. 2020, doi: 10.1016/j.jpdc.2020.04.005.

[6] M. Saad, A. Anwar, A. Ahmad, H. Alasmary, M. Yuksel, and A. Mohaisen, "RouteChain: Towards Blockchain-based Secure and Efficient BGP Routing," in *2019 IEEE International Conference on Blockchain and Cryptocurrency (ICBC)*, May 2019, pp. 210–218. doi: 10.1109/BLOC.2019.8751229.

[7] A. Pinna, S. Ibba, G. Baralla, R. Tonelli, and M. Marchesi, "A Massive Analysis of Ethereum Smart Contracts. Empirical study and code metrics," *IEEE Access*, 2019, doi: 10.1109/ACCESS.2019.2921936.

[8] A. A. Khan, M. H. Rehmani, and M. Reisslein, "Cognitive Radio for Smart Grids: Survey of Architectures, Spectrum Sensing Mechanisms, and Networking Protocols," *IEEE Commun. Surv. Tutor.*, vol. 18, no. 1, pp. 860–898, Firstquarter 2016, doi: 10.1109/COMST.2015.2481722.

[9] H. Gözde, M. C. Taplamacıoğlu, M. Arı, and H. Shalaf, "4G/LTE technology for smart grid communication infrastructure," in *2015 3rd International Istanbul Smart Grid Congress and Fair (ICSG)*, Apr. 2015, pp. 1–4. doi: 10.1109/SGCF.2015.7354914.

[10] K. Lakshminarayanan, D. Adkins, A. Perrig, and I. Stoica, "Securing User-Controlled Routing Infrastructures," *IEEEACM Trans. Netw.*, vol. 16, no. 3, pp. 549–561, Jun. 2008, doi: 10.1109/TNET.2007.903980.

[11] D. Lin, B. Shi, X. Lu, Y. Tang, Z. Cheng, and H. Zhao, "Opportunistic routing for heterogeneous micro-power network in smart grids," in *2016 IEEE International Conference of Online Analysis and Computing Science (ICOACS)*, May 2016, pp. 327–329. doi: 10.1109/ICOACS.2016.7563107.

[12] A. I. Sabbah, A. El-Mougy, and M. Ibnkahla, "A Survey of Networking Challenges and Routing Protocols in Smart Grids," *IEEE Trans. Ind. Inform.*, vol. 10, no. 1, pp. 210–221, Feb. 2014, doi: 10.1109/TII.2013.2258930.

[13] S. Alam, A. N. Malik, I. M. Qureshi, S. A. Ghauri, and M. Sarfraz, "Clustering-Based Channel Allocation Scheme for Neighborhood Area Network in a Cognitive Radio Based Smart Grid Communication," *IEEE Access*, vol. 6, pp. 25773–25784, 2018, doi: 10.1109/ACCESS.2018.2832246.

[14] J. Kim, J. Han, Y. B. Ko, and F. Filali, "Interleaving-based orphan channel Scanning for the IEEE 802.15.4m in TVWS smart grid networks," in *2015 Seventh International Conference on Ubiquitous and Future Networks*, Jul. 2015, pp. 89–94. doi: 10.1109/ICUFN.2015.7182506.

[15] Z. H. Wei and B. J. Hu, "A Fair Multi-Channel Assignment Algorithm With Practical Implementation in Distributed Cognitive Radio Networks," *IEEE Access*, vol. 6, pp. 14255–14267, 2018, doi: 10.1109/ACCESS.2018.2808479.

[16] M. Gupta, S. K. Dhurandher, and P. Nicopolitidis, "Intelligent and Efficient Channel Allocation in Smart Grid Neighhorhood Area Network," in *2018 International Conference on Computer, Information and Telecommunication Systems (CITS)*, Jul. 2018, pp. 1–5. doi: 10.1109/CITS.2018.8440135.

[17] N. Karowski, A. C. Viana, and A. Wolisz, "Optimized asynchronous multi-channel neighbor discovery," in *2011 Proceedings IEEE INFOCOM*, Apr. 2011, pp. 536–540. doi: 10.1109/INFCOM.2011.5935221.

[18] L. Gao, Z. Zheng, and M. Huo, "Improvement of RPL Protocol Algorithm for Smart Grid," in *2018 IEEE 18th International Conference on Communication Technology (ICCT)*, Oct. 2018, pp. 927–930. doi: 10.1109/ICCT.2018.8600162.

[19] S. Subramani, Zhong Fan, S. Gormus, P. Kulkarni, M. Sooriyabandara, and Woon Hau Chin, "WISEMEN: White Space for Smart Metering," in *2012 IEEE PES Innovative Smart Grid Technologies (ISGT)*, Jan. 2012, pp. 1–6. doi: 10.1109/ISGT.2012.6175796.

[20] Z. Yang, R. Han, Y. Chen, and X. Wang, "Green-RPL: An Energy-Efficient Protocol for Cognitive Radio Enabled AMI Network in Smart Grid," *IEEE Access*, vol. 6, pp. 18335–18344, 2018, doi: 10.1109/ACCESS.2018.2812191.

[21] J. Yang, S. He, Y. Xu, L. Chen, and J. Ren, "A Trusted Routing Scheme Using Blockchain and Reinforcement Learning for Wireless Sensor Networks," *Sensors*, vol. 19, no. 4, Feb. 2019, doi: 10.3390/s19040970.

Tatenda Trust Gotora is a PhD scholar studying at the Centre of Broadband Networks and Applications at UCT. He also serves as a lecturer and software engineering consultant at MSU in Zimbabwe. Tatenda is a hold of an MTech in Software Engineering from JNTUH, India, 2014. His research interests are in Smart Grid, Next Generation Networks, Big Data Analytics and Information Security. He has published numerous research papers in peer-reviewed journals and presented in International Conferences. He is also a professional member for IET (UK) and ZICT (Zimbabwe).

Preliminary Attenuation Measurement And Prediction for an Optical Wireless Communication Link in South Africa

Sabelo Q. Buthelezi [#], Thomas JO Afullo[#], Modisa Mosalaosi[*]

[#]*Discipline of EECE, School of Engineering, University of KwaZulu-Natal, Durban 4041, South Africa*

215021695@stu.ukzn.ac.za; afullot@ukzn.ac.za

[*] *Electrical, Computer, and Telecommunications Engineering, Botswana International University of Science & Technology, Private Bag 16, Palapye, Botswana*

[2]mosalaosim@biust.ac.bw

***Abstract*—The performance of Optical Wireless Communication (OWC) is strongly influenced by the atmospheric conditions in a given environment. In foggy, rainy, and clear weather conditions, optical signals are known to be attenuated due to absorption and scattering. In this paper, rain attenuation measurement is presented using an empirical method based on the relationship between the observed attenuation distribution and the related observed rain intensity distribution at 30-second integration period in Durban, South Africa. A distrometer is used to obtain the raindrop size and rain intensity, while an optical power meter is used to log the received optical signal power level, to evaluate the influence of rain on the signal transmitted over the 7-m link. The relationship between the received signal level, and the rain intensity for a particular weather condition at a specific time is then obtained. Analyses are then made, and compared against the French model at a wavelength of 850 nm. The measurement results show extremely high attenuation values compared to the French model, which thus calls for further investigations.**

***Keywords*— Optical Wireless Communications; Free Space Optics; FSO Measurements**

I. INTRODUCTION

Due to the unprecedented growth of high speed multimedia services and diversified applications initiated from the massive connectivity of IoT devices, 5G and beyond 5G (B5G) cellular communication systems, the existing electromagnetic spectrum under RF ranges is incapable of satisfying the enormous future data rate demands. Optical wireless communication (OWC), also known as Free Space Optics (FSO), which covers a wide range of unlicensed spectrum, has thus emerged as an efficient solution to mitigate conventional RF spectrum scarcity for communication ranges from tens of meters to several kilometers. The FSO communication system is one of the prominent wireless communication systems, which witnessed a massively increasing interest and vast development in the last decade [1]. The commercially available FSO is a wireless line-of-sight communication between two points. This type of communication can handle data at a rate of more than 1Gbps over a distance that may reach 4 km. FSO was originally developed to solve the "last mile bottleneck" with a cost effective way that avoids the high cost of fiber optic cables [2].

According to Umair et al [3], FSO systems are based on the transmission of data through the atmosphere within optical spectral windows that are free from molecular absorption. They note that FSO provides several advantages over normal RF links, including: very high bandwidths; narrow-beam transmission which improves frequency re-use and electromagnetic compatibility issues; and free spectrum (no license costs) [1] [3]. However, an FSO transmission is prone to the non-ideal conditions arising from unstable weather conditions. In other word, a single beam FSO system is susceptible to weather conditions whereby turbulence, rain, fog, haze and dust introduces attenuation to the light source or even block the propagation. Hence, an FSO system should be thoroughly investigated relative to weather conditions, to ensure that the received power is sufficient at the receiver for processing [1].

Under clear-air conditions, atmospheric turbulence is the major cause of optical signal fluctuations or fading in FSO systems, which in turn affects the link availability. The atmospheric turbulence effects are caused by the differences detected in the refractive index as a result of the in-homogeneities in temperature and also by fluctuations obtained in air pressure along the transmission pathway of the laser beam. Atmospheric turbulence is thus an atmospheric phenomenon generated by the temperature difference between the surface of the Earth and the atmosphere. According to Mohale et al, from their study of the South African environment, atmospheric turbulence disrupts the coherence of both laser radiation and optical wave during the entire day [4]. In FSOC systems, strongly divergent beams where the beam energy is redistributed across the beam width is the most significant source of turbulence. This condition of strongly diverged beams is also known as scintillation. On the other hand, under precipitation conditions, the optical laser beam propagating in such media undergoes deep fading due to scattering and absorption: in temperate regions, FSO signal fading is largely due to fog and heavy snow; while in tropical regions, the fading is mainly due to rain and haze [1, 5].

In South Africa, Mohale et al [4] have studied the feasibility of deployment of FSO communication (FSOC) links in South Africa based on atmospheric losses under average and worst case atmospheric conditions. Their results show that Ermelo has the highest optimal FSOC link distance of 7.5 km at an overall atmospheric loss of 2.8 dB under average conditions, while Durban has the shortest FSOC link distance at 2.6 km at an overall atmospheric loss of 12 dB under worst

case conditions. This finding was reached by the authors based on theoretical analysis of long-term atmospheric data consisting of average visibility, wind speed, and altitude. In [6], Layioye *et al* report on the Visibility Range Distribution (VRD) for FSO applications within South Africa (Durban), noting that the behavior of optical signals in the atmospheric channel depends on the magnitude of the visibility which in turn is the most important parameter required to achieve an optimal link performance and optical signal availability at 99%. In the same vein, Kolawole et al [7] present regression models based on meteorological factors to reliably estimate atmospheric visibility for FSO links in South Africa. The meteorological factors used are relative humidity, temperature, fractional sunshine, atmospheric pressure and wind speed for Cape Town, South Africa. However, FSO link attenuation or fading due to rain has not been addressed for South Africa.

In [3], a model for the prediction of attenuation due to rain over FSO links is presented, with particular focus on tropical Pakistan. The model utilizes local rain statistics for the site of interest as inputs, in addition to incorporating the dependence of raindrop size distribution and related multiple scattering effects on FSO signal attenuation. The DSD is modeled with a gamma function, with the latter only being dependent on the shape parameter, μ, and the rain rate, *R*. They note that the DSD impact depends on R: for example, they show that at R=50 mm/h, the specific attenuation obtained is 10 dB/km for μ=-2, to 25 dB/km for μ=7. They also point out that the specific attenuation due to rain in the optical band (0.78 μm & 1.55 μm) is of the same order of magnitude as in the V-band (40-75 GHz). In [5], Suriza *et al* present an analysis of rain attenuation measurement over a terrestrial FSO link in Malaysia. They compare their results to those due to the ITU-R model which was developed based on measurements performed in France and Japan. They conclude that both models, which are based on parameters of temperate regions, are unable to predict FSO attenuation measured in a tropical climate, hence they recommend further research to develop an appropriate model for the tropics.

Finally, Singh and Mittal [8] present a performance analysis of an FSO link under rainy weather conditions for inland and coastal zones of India. Using values of k *and* α for specific attenuation due to rain as 1.076 and 0.67 respectively, they determine that, under average rain weather conditions, with Mumbai recording a rain rate of 7.3 mm/h, while Hyderabad records a rain rate of 2.35 mm/h, the corresponding values of specific attenuation are 4.08 dB/km and 1.91 dB/km, respectively. On the other hand, under worst rain weather conditions, the corresponding rain rates are 177.6 mm/h for Mumbai, and 37.7 mm/h for Hyderabad; with the corresponding values of specific rain attenuation being 34.6 dB/km and 12.2 dB/km, respectively. As Al-Gailani also states, both Japan and Europe models do not take into account the higher rain intensities which occur in tropical countries, thus the link attenuation estimated by these models are not applicable in the tropical regions [1].

The power law given in (1) represents the specific rain attenuation, which is the fundamental quantity in determining attenuation due to rain for terrestrial and earth space links.

$$\gamma_{rain} = k \times R^{\alpha} \tag{1}$$

Where γ_{rain} is specific attenuation due to rain; R is the rain intensity; k *and* α are rain coefficients.

The coefficients k *and* α depend on the carrier frequency of FSO systems, and on the characteristics of rain such as raindrop size distribution (DSD) and polarization, as well as the location [5, 9]. Both coefficient values can be obtained from ITU-R P.838-3 [10]. Since raindrops are assumed to have a spherical form, estimates of k *and* α do not depend on vertical or horizontal polarization [5]. The following formula was presented by Charbonneau for French model [11] [12]:

$$\gamma_{rain} = 1.076 \times R^{0.67} \left[\frac{dB}{km}\right] \tag{2}$$

This equation is for drizzle rain (up to 5 mm/h), and it will be used to compare against the measured attenuation, and the specific attenuation, from Durban, which is the focus of this paper, using the drizzle rain intensity.

II. Measurement Equipment

A. Optical Power Measurement Setup

The measurement setup requires two computers, each displaying the data for each transceiver, as illustrated in Fig. 1. The Gigabit Ethernet Media Converter, which is utilized as an electrical-to-fiber optic converter or a fiber optic-to-electrical converter, is shown in Fig. 2. The Ethernet cable C85 with an RJ45 connector on the right (RIGHT) is used for sending or receiving electrical signals. The fiber cable with LC connection on the left (LEFT) in Fig. 2 is responsible for receiving or sending fiber optic signals. The two transceivers, (transmitter and receiver) are 7 meters apart, as shown in Fig. 3. Signal transmission is carried out using infrared lasers, which are efficient and reliable. Lasers with an optical wavelength of 850nm are utilized for transmission. The Avalanche Photodiode Detector (APD), a very sensitive detector, is used at the transceiver to detect the signal.

B. Distrometer Measurement Setup

To analyse the fluctuation of signals based on different weather conditions, such as clear weather, fog, and rain, weather data is commonly used. A distrometer is a device that measures the size of raindrops as well as the rainfall intensity. The velocity and size of each particle in each drop are calculated and recorded. The distrometer used is the Vaisalla RD-80 which captures drop size measurements using a personal computer. The distrometer detects the size distribution of raindrops falling on the sensor's sensitive surface. Using this information, it is possible to calculate the actual drop size distribution in a volume of air [13].

The diameters of the raindrops that can be measured range between 0.3 and 5.4 millimetres. Drops smaller than 0.3 mm cannot be measured due to the measuring equipment's practical limits, and are normally of minimal relevance in the applications for which the device is designed. Due to the volatility of big drops, which promotes drop break-up, drops larger than 5.4 mm are extremely rare [13]. 127 drop diameter channels are distinguished by the RD-80. To limit the amount of data and get statistically relevant samples, the 127 drop size channels are re-grouped into 20 drop size groups that are spread more or less exponentially over the available spectrum

TABLE I
OWC SYSTEM PARAMETERS

Parameter	Value
Wavelength	850, 950, and 1550 nm
Transmit Power	16 dBm (40 mW)
Light Source	Laser
Receiver Sensitivity	-38 dBm
Transmit and Receiver Systems losses	2 dB
Receiver Aperture Diameter	16 cm
Eye Safety	Class 1M
Receiver Field of View	10 mrad
Detector	Avalanche Photodiode (APD)
Transmit Beam Divergence Angle	2.8 mrad
Data Rate	1.25Gbps

TABLE II
INFORMATION OBTAINED FROM RD-80 DISTROMETER FOR THE PERIOD OF MEASUREMENT

CATEGORY	NUMBER OF SAMPLES
Monthly	
August	647
September	1141
October	3119
November	9492
December	2251
January	195
Seasonal	
Winter	647
Spring	13752

of drop sizes. The translation into 20 classes is handled by the data logging software. As a result, every 30 seconds, the raindrop diameter and intensity are monitored, allowing them to be stored and presented on the PC screen as seen in Fig. 4 [13].

The first column in Fig. 4 displays the sampling time intervals, which in this case vary by 30 seconds; the second column indicates the number of drops measured in each drop size class (class 1-20) during time interval t, which in this case is 30 seconds. The last two columns show R, which is the intensity at which the drops hit the Styrofoam (in mm/h), and the rainfall accumulated, RT (in mm), the real-time cumulative weight of the drops every 30 seconds. The results in Fig. 4 are used to calculate the rain intensity by using the following formula [13]:

$$R = \frac{\pi}{6} \cdot \frac{3.6}{10^3} \cdot \frac{1}{F \cdot t} \cdot \sum_{i=1}^{20} \left(n_i \cdot {D_i}^3\right) \left[\frac{mm}{h}\right] \quad (3)$$

Where:
F is size of the sensitive surface of the sensor, which is equal to 0.005 m^2; t is time interval for data logging; n_i is the number of drops measured in drop size class i during time interval t; and D_i is the average diameter of drops in class i.

Equation (3) is used to calculate the rain intensity [13]. Fig. 4 shows measured values, which are recorded and saved in tab-delimited ASCII format, and can be imported into other programs, like spreadsheet programs, for further analysis.

C. FSO Link Losses and Fade Margin

For the FSO link in question, the link parameters are shown in Table 1.

For a line-of-sight link, the free space loss is given by:

$$FSL = 10\, log_{10}(\frac{4\pi d}{\lambda})^2 = 20\ log_{10}(\frac{4\pi d}{\lambda}) \quad (4)$$

Substituting d, the distance between the transceivers, which in this case is 7 m, and the free space wavelength of 850 nm, the FSL is determined to be:

$$FSL = 20\ log_{10}\left(\frac{4\pi(7)}{(850\times10^{-9})}\right) = 160.3\ dB \quad (5)$$

Now, the actual received signal level at the FSO receiver is determined from:

$$P_r(dBm) = P_t(dBm) + G_T + G_R - FSL - FL - OL - EL \quad (6)$$

Where P_r is received signal level (dBm), P_t is transmit signal level (dBm), G_T is transmit lens gain (dB), G_R is receive lens gain (dB), FL is the total feeder (system) loss (dB), OL is optical loss (dB), EL is excess loss, which covers scintillation, atmospheric loss, and fog loss.

Thus, our P_t is 16 dBm, while the lowest acceptable value for P_r or P_{rmin} is -38 dBm.

$$G_T = 20\ \log_{10}\left(\frac{126.491}{\theta}\right) \quad (7)$$

Where θ is the transmit beam divergence angle in radians, which is given as 2.8 mrad is this case, hence:

$$G_T = 20\ \log_{10}\left(\frac{126.491}{2.8\times10^{-3}}\right) = 93.1\ dB \quad (8)$$

For a lense of diameter D, which is 16 cm in this case, the gain of the receive lens is given by:

$$G_R = 20\ \log_{10}\left(\frac{31.623\pi D}{\lambda}\right) \quad (9)$$

Hence:

$$G_R = 20\ \log_{10}\left(\frac{31.623\pi(0.16)}{(850\times10^{-9})}\right) = 145.4\ dB \quad (10)$$

FL is given in Table 1 as 2 dB. The geometric or optical loss, OS, is caused by the optical beam diverging from its path. For this link with d=7 m, this loss is given by:

$$OL = 20\ \log_{10}\left(\frac{D}{d\theta}\right) = 20\ \log_{10}\left(\frac{0.16}{7(2.8\times10^{-3})}\right) = 18.2dB \quad (11)$$

Therefore, after substituting the above values, P_r is given by:

$$P_r(dBm) = 74.2\ (dBm) - EL\ (dB) \quad (12)$$

EL can then be determined from link measurements.

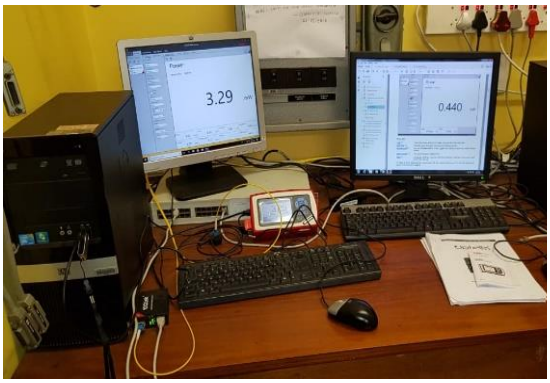

Fig. 1: Current set up and equipment used for FSO link infrared signal level measurement Network

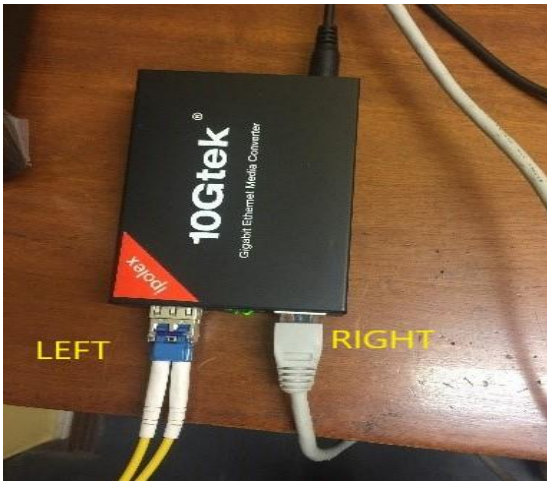

Fig. 2: Electrical-to-Fiber or Fiber-to-Electrical Converter

Fig. 3: Fibre Optic Link of Length 7 meters

III. Link Attenuation Measurement

The maximum power recorded (dBm) at the transceiver, during the period of the experiment, which is mid-August 2019 to mid-February 2020, was 5.7603 dBm - which value was recorded on 1st September 2019 at 08:52 am. However, this value is not fixed for a given rain event. At any time, the "unfaded" received signal level varies, depending on whether there is fog, scintillation, or rain. Therefore, the signal power recorded at a certain time should be subtracted from the maximum value recorded during that particular period of measurement (or measurement event) to determine the attenuation in dB as shown in equation (13):

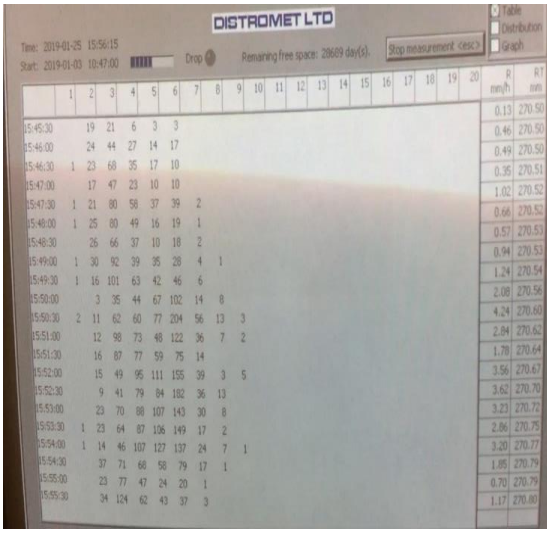

Fig. 4: Distrometer Display

$$\text{Loss(dB)} = P_{max}\,(\text{dBm}) - P_{received}\,(\text{dBm}) \quad (13)$$

The measured attenuation is calculated between the two transceivers with respect to a fixed distance (L) in kilometers, and the specific attenuation is then determined as attenuation with respect to distance in (dB/km). It is calculated as follows:

$$\text{Specific Attenuation(dB/Km)} = \frac{Loss(dB)}{L(km)} \quad (14)$$

In this particular case, the link length of 7 meters or 0.007 kilometers is used. Thus, in (14), L is equal to 0.007 for all the calculations.

IV. Measurement Results and Analysis

South Africa has a variety of climatic changes that are reliant on seasonal cycles. These are: Summer (December to February); Autumn (March to May); Winter (June to August); and Spring (September to November) [14]. The data for this study was obtained during three seasons, namely, winter, spring, and summer. However most of the data was collected during spring, which, together with summer, is Durban's rainiest season [14]. This section focuses on the analysis of the results obtained from measurements taken between August 2019 and January 2020. These findings will be used to study the relationship between rain intensity and attenuation due to rain, as well as the specific attenuation.

A. Plots of Rain Intensity versus Received Optical Power

The rain intensity time series and the equivalent optical received signal time series of the drizzle events on September 13th, 2019 and December 4th, 2019, respectively, are shown in Figures 5 and 6. It can be seen that when the rainfall rate rises or falls, there is a change in the received power, and this difference is what constitutes rain attenuation. For example, in Fig. 5, between 12:20:00 and 12:25:00 on September 13th, 2019, the received signal is attenuated, as the rain intensity

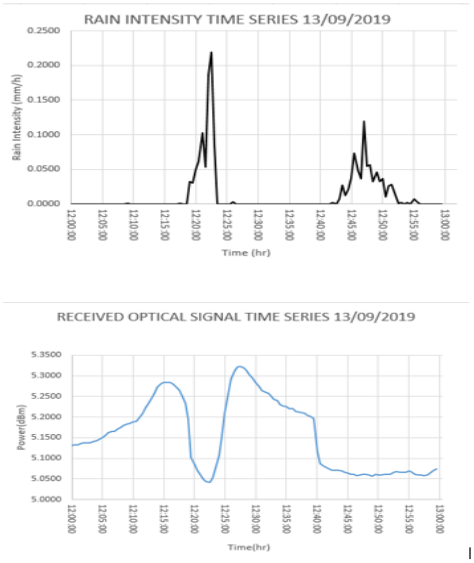

Fig. 5: Rain Intensity and Received Optical Signal time series for drizzle event on the 13th of September 2019, in Durban

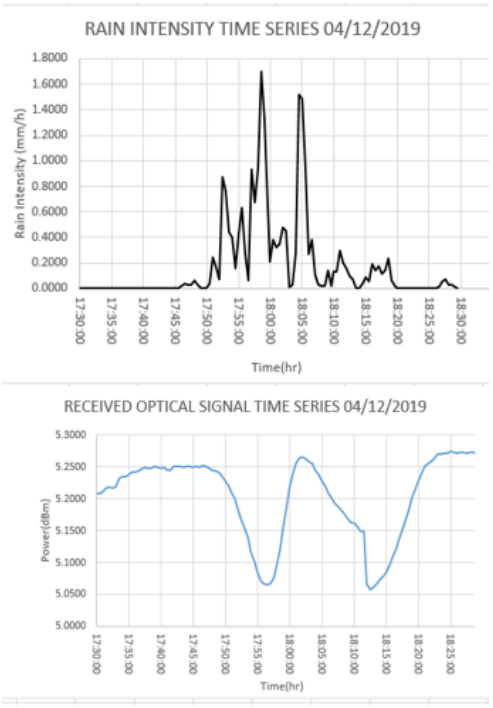

Fig. 6: Rain Intensity and Received Optical Signal time series for drizzle event on the 4th of December 2019, in Durban

rises from 0 to around 0.22 mm/h, and then recovers to its maximum value when the rain intensity goes back to zero. This shows that there was attenuation due to rain during that period. The received signal is attenuated again as the droplets begin to fall with a small intensity, leading to the conclusion that the received signal attenuation on that specific day was primarily due to rain.

It is important noting that the rain intensity was quite low during these days, but there was still attenuation. This implies that, in addition to the rain intensity, there are other factors affecting the received signal, such as fog, alignment, scintillation, and possibly the raindrop diameter. This will only be verified through further research.

Fig. 6 shows the attenuated signal recorded on the 4th of December 2019, between 17:30:00 and 18:30:00. The received signal was consistent for the first 20-25 minutes. The signal became attenuated as soon as the rain intensity increased, i.e. as it started drizzling. With the progression of time, it can be observed that the received signal fluctuates to its lowest value at some point, with a high rain intensity recorded; while it again rises, with the low rain intensity recorded. The recorded received signal showed attenuation of about 0.22 decibels, and the drizzle rain intensity reached its highest value of about 1.7 mm/h.

A total of 16845 rainfall events were analysed throughout the measurement period, and they are classified into monthly (August 2019 to January 2020) and seasonal (Winter, Spring and Summer) categories in Table 2.

B. Plots of Attenuation and Specific Attenuation due to Rain

The relationship between specific attenuation in dB/km and rain intensity in mm/h, as well as the relationship between attenuation in dB and rain intensity, are shown in the plots in Figures 7 and 8. As shown in the figures, the rain regime considered for this reporting is the drizzle type, with rain intensities ranging from 0.2 to 5 mm/h. The trend-lines in the two figures show a rise in rain attenuation as well as specific attenuation, as the rain intensity increases, with a maximum rain intensity of slightly less than 5 mm/h. For example, in August 2019, the "measured" attenuation equation is $y = 88.763x^{0.0029}$, where y is the specific rain attenuation and x is the rain intensity. The k *and* α coefficients are 88.763 and 0.0029, respectively. From the measured attenuation in both Figures 7 and 8, one sees a constant value of about 0.62 dB over the link. The measured attenuation is seen to be practically independent of the rain rate. This implies that there is a high possibility of the presence of fog alongside the drizzle. Indeed, from the work of Mohale et al [4], it is shown that of all the cities in South Africa, Durban has the lowest visibility, a parameter which is closely related to the fogginess.

For comparison, the French prediction model for FSO rain attenuation is also plotted alongside the scatterplots for the measurements, to give the predicted attenuation due to rain in Durban, and check if they were in correlation with other existing models. The ITU-R rain attenuation prediction model for FSO system provided the k *and* α coefficients for the French model [9]. It is also important to note that the French model for FSO attenuation is for drizzle rain [9], that is for rain intensity of less or equal to 5 mm/h. The French model plots indicate that, for drizzle rain type, attenuation follows a rising trend as opposed to the Durban measurements where the attenuation follows almost a flat line. The other marked difference is that the attenuation values plotted for Durban are much higher than that due to the French model. This calls for further investigation in Durban, as there seems to be an obvious underlying attenuation factor alongside the rain attenuation for FSO links. This is thus the subject of further work.

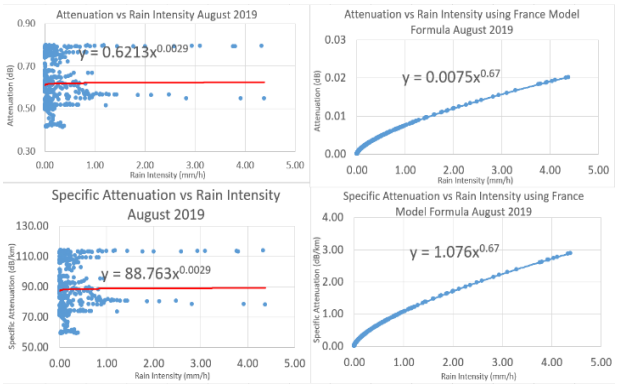

Fig. 7: Specific Attenuation as well as Attenuation vs Rain Intensity graphs for August 2019

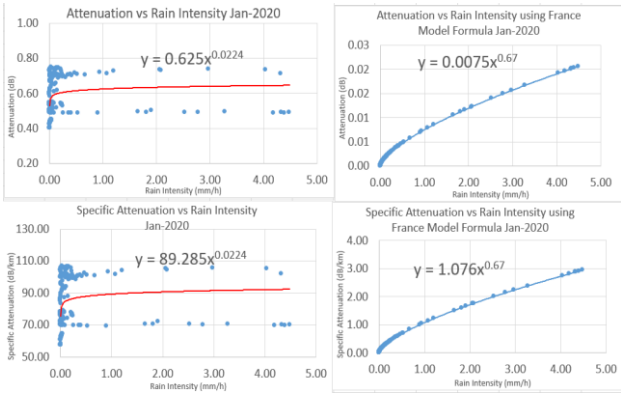

Figure 8: Specific Attenuation as well as Attenuation vs Rain Intensity plots for January 2020

V. Conclusion

A study of the performance of the FSO link under drizzle rainfall regime in Durban reveals that the received optical signal time series and rain intensity time series plots shows that there is attenuation that is almost constant. The attenuation due to rain is almost two orders of magnitude higher than the French model prediction. This shows that during a drizzle rain event, attenuation is not solely dependent on rain intensity, implying that other parameters play an active role during a rain event in Durban. This therefore calls for further analysis of these subterranean influences.

Acknowledgment

The authors wish to gratefully acknowledge the support of Telkom-SA and the Telkom Centre for Radio Access & Rural Technologies (CRART) of the University of KwaZulu-Natal for supporting the lead author in this work.

References

[1] S. A. Al-Gailani *et al.*, "A Survey of Free Space Optics (FSO) Communication Systems, Links, and Networks," in *IEEE Access*, vol. 9, pp. 7353-7373, 2021, doi: 10.1109/ACCESS.2020.3048049.

[2] Mohammad H. Alrasheedi: A Low-Cost, Man-Portable Free-Space Optics Communication Device for Ethernet Applications, MSc Thesis, Naval Postgraduate School Monterey, California, December 2005.

[3] U. Korai, L. Luini and R. Nebuloni, "Model for the Prediction of Rain Attenuation Affecting Free Space Optical Link," Electronics, vol. 7, 407, 2018.

[4] A. Z. Suriza, I. M. Rafiqul, W. Al-Khatteb and A. W. Naji, "Analysis of Rain Effects on Terrestrial Free Space Optics Based on Data Measured in Tropical Climate," IIUM Engineering Journal, vol. 12, no. 5, pp. 45-51, 2011.

[5] J. Mohale, M.R. Handura, T.O. Olwal, and C. N. Nyirenda, Feasibility study of free space optical communication for South Africa, Optical Engineering, 0001;55(5):056108. doi:10.1117/1.OE.55.5.056108, 2016.

[6] O. A. Layioye, T. J. O. Afullo and P. A. Owolawi, "Visibility range distribution modeling for free space optical link design in South Africa: Durban as case study," *2017 Progress in Electromagnetics Research Symposium - Fall (PIERS - FALL)*, 2017, pp. 2732-2741, doi: 10.1109/PIERS-FALL.2017.8293601.

[7] O. Kolawole, TJO Afullo, M. Mosalaosi, "Visibility Modeling and Prediction for Free Space Optical Communication Systems for South Africa," International Journal on Communications Antenna and Propagation (IRECAP) Vol 10, No 3 (2020), August 2020.

[8] H. Singh and N. Mittal, "Performance Analysis of Free Space Optical Communication System Under Rain Weather Conditions: A Case Study for Inland and Coastal Locations of India," Optical and Quantum Electronics, Vol.53 (2021), pp1-21.

[9] Samir A. Al-Gailan, Abu Bakar Mohammad, Usman U. Sheikh, Redhwan Q. Shaddad, "Determination of rain attenuation parameters for free space optical link in tropical rain," *Optic*, vol. 125, pp. 1575-1578, 2014.

[10] Recommendation, I. T. U. R. P, 838-3., "Specific attenuation model for rain for use in prediction methods," 2005.

[11] Vladimir Brazda, Vladimir Scheijbal, and Ondrej Fiser , "Rain Impact on FSO Link Attenuation Based on Theory and Measurement," *6th European Conference on Antennas and Propagation (EUCAP)*, pp. 1239-1243, 2012.

[12] T. Carbonneau, D. Wisley, "Opportunities and challenges for optical wireless; the competitive advantage of free space telecommunications links in today's crowded market place," in *SPIE Conference on Optical Wireless Communications*, 1998.

[13] Distromet "*DISDROMETER RD-80, User Guide for DISDRODATA 4.0*," DISTROMET LTD, 15 January 2018. [Online]. Available: http://www.ictinternational.com/content/uploads/2018/07/Disdrodata-User-Guide-4.0-January-2018.pdf. [Accessed 18 April 2021].

Sabelo Qiniso Buthelezi received the BSc in Electronic Engineering from the University of KwaZulu-Natal in 2018. He is currently doing his MSc in Electronic Engineering at UKZN.

Thomas J.O. Afullo holds the BSc(Hon.) from University of Nairobi, MSEE from University of West Virginia, and PhD in Electronic Engineering from VUB, Belgium. He is currently a Professor of Electronic Engineering, University of KwaZulu-Natal, South Africa. His research interests include RF propagation, FSO and PLC.

Modisa Mosalaosi holds BSc, MScEng, and PhD degrees in Electronic Engineering from the University of KwaZulu-Natal, Durban, South Africa. He is a Lecturer at the Department of Electrical, and Telecommunication Engineering, Botswana International University of Science and Technology. His research interests include power line communications, RF propagation and FSO

Converged Services

M2M Device Scheduling With GW-MAC Virtualisation in Large-Scale Internet of Things

Prosper Zanu Sotenga*, Karim Djouani*, Anish Kurien*
* *Department of Electrical Engineering/F'SATI, Tshwane University of Technology, Pretoria, South Africa*
[1]zanuzy05@hotmail.com
[2]djouani@gmail.com
[3]kurienam@tut.ac.za

***Abstract*—Large-Scale IoT (LS-IoT) networks are generally characterised by the existence of an enormous number of heterogeneous Machine-to-Machine (M2M) devices connected to the internet through a Gateway (GW) device. This creates congestion in the GW node due to the massive number of device transmissions that need to be managed at both the Physical (PHY) layer and the Media Access Control (MAC) layer. Virtualisation of the Gateway's MAC (GW-MAC) can be used to improve the scalability of LS-IoT networks, supported by a robust and seamless concurrent PHY layer multiplexing. However, the GW-MAC virtualisation may introduce additional delay when scheduling devices. Therefore, this paper evaluates the impact of the GW-MAC virtualisation on a classical Carrier Sense Multiple Access with Collision Avoidance (CSMA/CA) random MAC scheduling protocol by using a modified throughput model which incorporates the effects of the GW-MAC virtualisation process for a non-saturated network. The results obtained in this study suggest that the GW-MAC virtualisation reduces the throughput of the network. However, the results show that the reduction in throughput can be improved by the creation of multiple virtual GW-MAC instances supported by multiple independent collision domains in the PHY layer multiplexing.**

***Index Terms*—Media Access Control (MAC), CSMA/CA, Virtualisation, Gateway (GW), Large-Scale IoT (LS-IoT)**

I. Introduction

The proliferation of Machine-to-Machine (M2M) devices associated with numerous Internet of Things (IoT) applications require large-scale networks akin to the cellular network infrastructure. In fact, LS-IoT networks in the future may require a much larger access network than cellular networks. As such, new technologies and standards have been developed to address the increase in IoT network size with an emphasis on the Media Access Control (MAC) layer. One example of these standards is the IEEE 802.11ah standard [1] which proposes a novel Restricted Access Window (RAW) MAC mechanism and hierarchical scheduling combined with the classical Carrier Sense Multiple Access with Collision Avoidance (CSMA/CA) random access technique referred to as the Distributed Coordination Function (DCF). Another issue with LS-IoT is that the Gateway (GW) nodes experience congestion problems which is sometimes eminent at the MAC layer. Some PHY layer improvements exist to provide a seemingly concurrent transmission. However, the GW-MAC acts like a bottleneck in a LS-IoT scenario [2].

Virtualisation of the GW-MAC is one of the approaches that can be used to ease the congestion of the GW-MAC and improve the scalability of the network. This can be achieved by offloading the GW-MAC functions externally to a remote edge (eDC) for execution. However, this process may affect the ability of devices to perform a random MAC scheduling procedure. This effect has not been widely investigated in literature. Therefore, in this study we present a throughput model based on [3] and [4] which is based on the CSMA/CA random MAC scheduling procedure like the DCF used in the 802.11 networks. We consider the non-saturated condition since most M2M devices in IoT networks do not always have traffic to be transmitted because IoT traffic is usually event-driven and less bursty. Therefore, the non-saturated model is ideally suited for representing IoT networks. Based on this model the GW-MAC virtualisation cost is introduced to arrive at a GW-MAC virtualised throughput model for a single instance and multiple instances which is used for the analysis.

The rest of the paper is organised as follows: Section II presents related works on the GW-MAC virtualisation. Section III presents the MAC device scheduling throughput model, first without the virtualisation delay and followed by the introduction of the virtualisation delay. Section IV then presents the numerical computation of the model, the results obtained, and the analysis thereof. Section V concludes the paper by consolidating all the key aspects studied in this paper.

II. Related Work

The virtualisation of the lower layers (PHY and MAC layers) of a wireless communication protocol stack has barely been studied. Very few studies on the virtualisation of GW-MAC exist irrespective of the type of wireless application. In this section, some of the few related works on the general MAC virtualisation are reviewed and their shortfalls are highlighted to motivate the need for analysing the impact of GW-MAC virtualisation in LS-IoT networks.

In [5] a concept for virtualising the MAC functions in an Access Point (AP) is proposed by splitting the physical AP such that the physical AP is transparently connected remotely to a machine hosting the virtual MAC through a tunnel over Ethernet. The results of the proposed concept indicate a fairly small drop in throughput due to the virtualisation of the MAC with improved flexibility in managing the MAC of the AP. However, the study does not investigate the impact of using multiple instances of the virtual MAC which could improve the throughput performance. Also, the study does not

consider the large-scale nature of the network to establish the extent of the degradation in throughput performance. In [6], Caeiro et al. proposed an algorithm for addressing network capacity constraints through virtualising the wireless access mechanism. They proposed a concept of a differentiated virtual base station instantiation within a given coverage area. Their algorithm encompasses various radio resources management activities which include the MAC scheduling of devices in a wireless channel. In their results, the number of virtual base stations is compared with the average data rate of a cluster of devices which indicates a minor difference between the maximum deviation of the average data rate and the number of virtual based stations. Though the work studies the effect of virtualisation on the average data rate, it does not specifically focus on large scale M2M or IoT traffic types. In [7] a generic approach is proposed for virtualising the MAC in heterogeneous networks with different radio access technologies. The author uses a novel approach to offload resources for mobility and device scheduling. The results obtained in their work suggest that resource utilisation can be enhanced by virtualising the MAC function of the radio access component. However, the results are not based on M2M or IoT traffic types. In [8] the authors conducted an experiment based on the deployment of virtual MAC protocols in a shared network. They used a software program called MAClets to provide real-time virtualisation of the CSMA/CA based MAC scheduling of devices in an IEEE 802.11 network. The results obtained in the study merely indicate a saturation of the throughput level of the virtual MAC as additional devices join the network. However, the experiment was based on only 3 best effort devices which do not represent a LS-IoT network.

In general, from the related works, there is very little focus on studying the effects of GW-MAC virtualisation on the scheduling of devices in LS-IoT based networks. However, the move towards GW-MAC virtualisation must be evaluated with emphasis on the scalability (throughput performance versus the number of devices) of the network rather than the mere benefits of flexibility in managing the GW nodes.

III. Media Access Control Model with GW-MAC Virtualisation

A. Basic Random Access Mechanism based on CSMA/CA

We first consider a large number of M2M devices connected to a GW node. A group of devices contend for a transmission opportunity in a single channel. The contention is based on the CSMA/CA mechanism which is the basis for some MAC protocols in IoT networks such as the Distributed Coordination Function (DCF) used in the IEEE 802.11ah standard for device scheduling in time slots [9]. A device that has data in its MAC buffer to be transmitted first senses the communication channel to detect if the channel is free from any ongoing transmission. If the device senses that the channel is idle within a period called an Inter-frame Spacing (IFS), the device then initiates the transmission of the data packet. On the other hand, if the device senses that there is an ongoing transmission in the channel during the IFS period, the device continues to monitor the channel until the channel is idle for the duration of the IFS. When the channel is idle, the device enters a random back-off (BO) procedure before transmitting the data packet. The random BO procedure in this case serves as a collision avoidance mechanism during transmission. The random BO procedure does not completely avoid collisions. However, it reduces the probability of having multiple transmissions in one channel. The random BO is selected over a range of 0 to CW, where CW is referred to as the contention window, starting with the minimum contention window CW_{min}. After randomly selecting a BO time, the device then initiates a down counter until it reaches zero before transmitting a packet. If the transmission is unsuccessful after the BO timer reaches zero, possibly due to a collision, then the contention window is increased to $2^i CW_{min}$ upon each failed transmission attempt until the maximum contention window value CW_{max}. The parameter i represents the current BO stage. The BO procedure is executed so long as the channel is idle. However, it is frozen when a transmission is detected and resumed when the channel is idle again for an IFS period.

The time duration for transmission after the IFS period is divided into time slots, t_{slot}. Devices therefore may only transmit at the beginning of a timeslot. The duration of the time slot is therefore very critical in the performance of the LS-IoT network. This is because the time slot is shared amongst all other devices contending for channel access. Hence, a heterogeneous LS-IoT network of devices that results in several random device scheduling events at different times with different traffic rates can potentially impact the throughput level. To describe such a situation, a non-saturated throughput model is adequate which is presented in the following subsections.

B. Non-saturated CSMA/CA Probabilities

In order to estimate the throughput of the non-saturated network, some key probabilities need to be established. These are the conditional collision probability denoted as p, the probability that there is at least one active transmission in a time slot denoted as P_{tr}, the probability that there is a successful transmission in a time slot denoted as P_{suc} and the probability that a device initiates a transmission in a time slot denoted as τ. We first present the equations for the probabilities p, P_{tr} and P_{suc} based on the saturated model presented in [4] which still applies for a non-saturated network. We then present the probability τ based on [3] which conforms with a non-saturated network hence can be used to describe a LS-IoT heterogeneous network that schedules devices based on the CSMA/CA random access technique. The models in [4] and [3] have been widely applied in other works due to their accuracy.

The conditional collision probability p is defined in 1 and is based on the probability that, in a given time slot at least one of the remaining $d-1$ devices may transmit some packet.

$$p = 1 - (1 - \tau)^{d-1} \tag{1}$$

The probability that there is at least one active transmission in a time slot P_{tr} is defined in 2 and is based on the fact

that there are d number of devices that contend for a transmit opportunity based on the probability τ.

$$P_{tr} = 1 - (1 - \tau)^d \tag{2}$$

The probability that there is a successful transmission in a time slot P_{suc} is defined in 3 and is based on the fact that there is at least one device and exactly one device transmitting in the channel.

$$P_{suc} = \frac{d\tau(1-\tau)^{d-1}}{P_{tr}} \tag{3}$$

The probability τ that a device initiates a transmission in a time slot is the fundamental part of the throughput model. This is because τ describes the contention process which occurs before the attainment of a transmit opportunity. In addition, the probability that a device initiates a transmission depends on the packet arrival rate from the upper MAC (part of the MAC that interacts with the Logical Link Control sublayer) of the device for transmission. Therefore, to obtain τ, a Markov model that defines the CSMA/CA contention process for the non-saturated network (the rate at which packets arrive for transmission) can be used. There are numerous Markov models proposed in literature for non-saturated networks such as [10] and [11]. However for accuracy and ease of computation we adopt the Markov model proposed by [3] which yields the equation for τ depicted in 4 and 5.

$$\tau = \frac{1/(1-p)}{\frac{W_0+1}{2} + \frac{P_{NA}}{q} + 1 + \frac{W_0-1}{2}P_{BA}P_{NA} + \alpha + \frac{p^m}{1-p}\frac{W_m+1}{2}} \tag{4}$$

$$\alpha = \sum_{i=1}^{m-1} p^i \frac{W_i + 1}{2} \tag{5}$$

The parameter W_0 is the contention window of the initial BO stage obtained as $CW_{min} + 1$, W_i is the i^{th} contention window represented as $2^i CW_{min}$ and m is the number of backoff stages. As presented in 4 and 5, the model considers the probability P_{BA} where the channel is busy when a packet arrives for transmission or during the initial IFS period and the probability P_{NA} where no packet arrives for transmission. Also, the probability q where a new packet arrives for transmission during a time slot is considered. The probability P_{BA} is given in 6 which is based on the probability that there is at least one busy instance in an IFS period. The busy instance is described by the probability of a collision and a successful transmission during the average slot duration $\overline{t_{slot}}$. The parameter $\overline{t_{slot}}$ here represents the average slot duration covering the slot activities including idleness, collisions and successful transmissions.

$$P_{BA} = 1 - e^{-\frac{1-(1-\tau)^d \times T_{IFS}}{\overline{t_{slot}}}}. \tag{6}$$

The probability P_{NA} is given in 7 which is simply derived based on the utilisation (λ/μ) of the MAC queue in the device. Thus, when the utilisation of the queue increases, the lower the probability of having an empty queue which indicates no packet arrivals. λ is the rate of packet arrivals for transmission and μ is the service rate of the packets defined as $1/(n_{slot} \times \overline{t_{slot}})$, with n_{slot} being the number slots used for transmission.

$$P_{NA} = \begin{cases} 1 - \lambda/\mu & \lambda/\mu < 1 \\ 0 & \lambda/\mu \geq 1 \end{cases} \tag{7}$$

The probability q that at least one packet arrives during $\overline{t_{slot}}$ is given as

$$q = 1 - e^{-\lambda \overline{t_{slot}}}. \tag{8}$$

The equations 1, 4, 6, 7 and 8 represent a system of non-linear equations which can be solved numerically to obtain the p, τ, P_{NA}, P_{BA} and q.

C. GW-MAC Virtualisation Throughput

Binachi presented a model for estimating the throughput S of a saturated network in [4] based on the CSMA/CA protocol in 802.11 networks which is presented in 9. This also applies to a non-saturated network. In 9, L_{PLD} is the average length of the packet payload in bits, T_{tx} is the duration of a busy channel due to an active transmission and T_{col} is the duration of a busy channel due to a collision.

$$S = \frac{P_{suc}P_{tr}L_{PLD}}{(1-P_{tr})t_{slot} + P_{suc}P_{tr}T_{tx} + P_{tr}(1-P_{suc})T_{col}} \tag{9}$$

We now introduce the virtualisation component into 9. It is important to highlight that 9 estimates the throughput without any explicit indication of the type of MAC scheduling mechanism employed. The expression in the denominator of 9 defines the average time slot value $\overline{t_{slot}}$. In order to introduce the random access mechanism and the virtualisation delay in the throughput equation, the parameters T_{tx} and T_{col} are defined based on the slot activities and access scheme illustrated in Fig. 1. To obtain this, we assume a basic access mechanism and that the GW-MAC virtualisation delay is the same for both uplink and downlink. We also assume that the duration of the IFS is the same for all types of packet transmissions or devices including the GW and that the packet size is fixed. Based on these assumptions, the duration of a successful transmission T_{tx} is defined as

$$T_{tx} = T_{HDR} + T_{PLD} + T_{ACK} + 2(T_{IFS} + T_{PG} + T_{VR}). \tag{10}$$

Equation 10 describes the activities that happen in an average slot duration for successful transmission. The device transmits the available packet for a duration T_{HDR} proportional to the length of the packet's header as well as a duration T_{PLD} proportional to the length of the payload carried by the packet. The transmitted packet will encounter some propagation delay between the device and the GW which is represented as T_{PG}. Once the packet arrives at the GW node, the GW does not process the packet at the MAC. Since the MAC is externally virtualised or deployed in a remote eDC, the delay imposed by the virtualisation process T_{VR} is added to the average duration of the transmission. Once the packet is successfully received at the eDC and processed for forwarding onto the IP network, an acknowledgement (ACK) frame is generated in which the duration of the ACK frame T_{ACK} is proportional to the length of the ACK frame. The ACK frame is sent back to

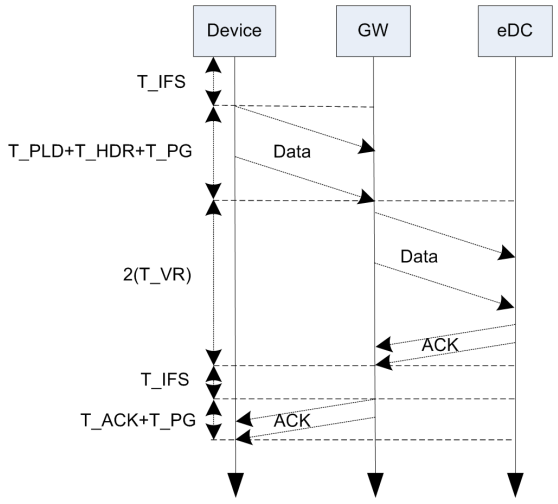

Fig. 1. Timing diagram of a CSMA/CA algorithm for uplink access with GW-MAC virtualisation

the GW which approximately doubles the virtualisation delay. The GW then sends the ACK to the device after an IFS period denoted by T_{IFS} which also doubles the propagation delay. After receiving the ACK, the device waits for another IFS period before it attempts to transmit the next packet which doubles the IFS period.

The duration of a collision or an unsuccessful transmission T_{col} is defined in 11. With a collision, there is no activity performed by the GW hence the activities of the GW are not considered. This means that there is no ACK transmitted back to the device. However, the device will still expect an ACK frame until a $T_{ACK_{TO}}$ time out has reached. Therefore, the duration of the collision is defined by the ACK time out value, the duration of the packet transmission (header and payload), the IFS period for the next transmission attempt and the propagation delay.

$$T_{col} = T_{HDR} + T_{PLD} + T_{IFS} + T_{ACK_{TO}} + T_{PG}. \quad (11)$$

We now consider that there are multiple instances of the virtualised GW-MAC deployed at a remote eDC. In this case, the idea is that each instance of the GW-MAC serves a group of devices that contend for channel access in a single frequency channel. This means that the number of virtual MAC instances is equal to the number of collision domains. With this consideration, the throughput model can be modified based on the number of virtual GW-MAC instances. Another important consideration is that, when the number of MAC instances increases, the traffic load on the virtualisation process increases which means that the virtualisation delay will increase. For convenience, we assume that the virtualisation delay increases exponentially with the number of MAC instances. This is because the virtualisation process can be represented as a queueing system with traffic arrivals based on a Poison distribution. Therefore this is likely to produce a virtualisation delay that grows exponentially based on the number of virtual GW-MAC instances. Therefore T_{VR} is modified such that it becomes $T^*_{VR} = (T_{VR})^{n_v}$ where n_v is the number GW-MAC instances. The parameter T^*_{VR} is replaced with T_{VR} in 10 to give S^*_v for a single collision domain. Considering all the assumptions, the virtualised throughput S^{ins}_{VR} based on the number of GW-MAC instances can be derived as the superposition of the throughput for each collision domain as depicted in 12.

$$S^{ins}_{VR} = \sum_{v=1}^{n_v} S^*_v \quad (12)$$

IV. Numerical Computation, Results and Analysis

A. Experimental Setup

The initial parameters used for the numerical evaluation of the model are shown in I and are based on the IEEE 802.11ah standard for LS-IoT as summarised in [12] and [13]. The computation of the model was performed using MATLAB. For all the results obtained, the number of devices was varied between 1 and 1200. A PHY layer channel rate of 130 $Mbps$ was used to obtain the transmission duration of the header and payload which conforms with 64-QAM modulation and 2 Spatial streams in a 16 MHz channel bandwidth. A slot duration of 500 μs was also used which corresponds to the minimum restricted access window slot duration in the IEEE 802.11ah standard. The IFS duration was chosen such that it is equal to the longest 802.11ah IFS duration of 264 μs for basic channel access. The length of the header used was 16 bytes, corresponding to the maximum length of the short MAC header for uplink access. The minimum and maximum contention window values used are 15 and 1024 respectively which gives 6 maximum BO stages.

TABLE I
Model Evaluation Parameters

Parameter	Value
MAC header length	16 $Bytes$
ACK frame length	26 $Bytes$
IFS duration	264 μs
Propagation delay	1 μs
Slot duration	500 μs
ACK time out	300 μs
number of BO stages	6
Minimum Contention Window	15

To evaluate the extent of the effects of the GW-MAC virtualisation, four different arbitrary values for the virtualisation delay T_{VR} were used to generate the results which are: 20 ms, 5 ms, 200 us and 50 us. We also define four different types of IoT traffic classes based on the length of the payload and interarrival time of packets as shown in Table II. This is to evaluate and verify the model based on the different traffic arrival rates. The rate at which packets are generated by the device for transmission in terms of bits per second can easily be derived by dividing the payload length by the interarrival time. The traffic classes are characterised by the type of IoT applications which are: Industrial Automation (IA), Logistics and Transportation (LT), Agricultural Monitoring (AM) and Smart Metering (SM). As depicted by the values in Table II, the IA application typically has more data to be transmitted at relatively short intervals. This is followed by LT applications which typically have shorter data payload and longer transmission intervals than IA. AM applications also have a much

shorter data payload and much longer transmission interval than IA and LT. Lastly, SM applications are attributed to very short data payload and very long transmission interval than IA, LG and AM applications.

TABLE II
IoT DEVICE TRAFFIC ARRIVAL CHARACTERISATION

IoT Application	Payload size (bytes)	Interarrival time (seconds)
IA	150	0.01
LT	100	0.1
AM	50	15
SM	20	60

B. Analysis of Results

At first glance one can observe the classical throughput behaviour of a basic CSMA/CA random access scheme in Fig. 2, Fig. 3 and Fig. 4. Thus, the throughput rises with the increasing number of devices almost linearly until a certain point where there is no longer an increase in the throughput. This point is the maximum throughput of the system which is the peak of the curve. The increase in throughput before the peak is signified by a very low probability of collision hence minimal packet losses. It can also be observed that the results with the highest maximum throughput exhibit the steepest decline in throughput after saturation. This is attributed to the increased load on the network or the probability of a collision as the number of devices increases. We now discuss the results of the individual plots. We first analyse the throughput results based on the different traffic characterisation to verify the behaviour of the model.

In Fig. 2 the throughput for a single virtualised GW-MAC instance is plotted against the number of devices for different IoT traffic classes characterised by different traffic arrival rates in the device. A virtualisation delay of $50\ us$ corresponding to the least virtualisation delay value in the set-up was used to obtain the results. It can be observed that IA generally has the highest throughput followed by LT, AM and SM. This is an anticipated behaviour that is attributed to the differentiation of traffic arrival rates. The IA traffic class has the highest arrival rate as can be deduced in Table II. This, therefore, increases the probability of having at least one packet arrival in a slot for transmission. As a result, devices that generate the IA traffic class will have more chances of transmission than the other types yielding a maximum throughput value that is higher than the other traffic classes. The same effect can be said for behaviour seen with the LT, AM and SM traffic types.

We now discuss the effects of the virtualisation delay. The results presented in Fig. 3 show the throughput for a single virtualised GW-MAC instance which is plotted against the number of devices. The payload size and the interarrival time for the IA traffic class are used to obtain the result presented. The throughput for the different virtualisation delay values is also plotted and compared with the results obtained when the virtualisation is not considered. It can be observed that when there is no delay imposed due to virtualisation, the maximum throughput versus the number of devices is higher than when

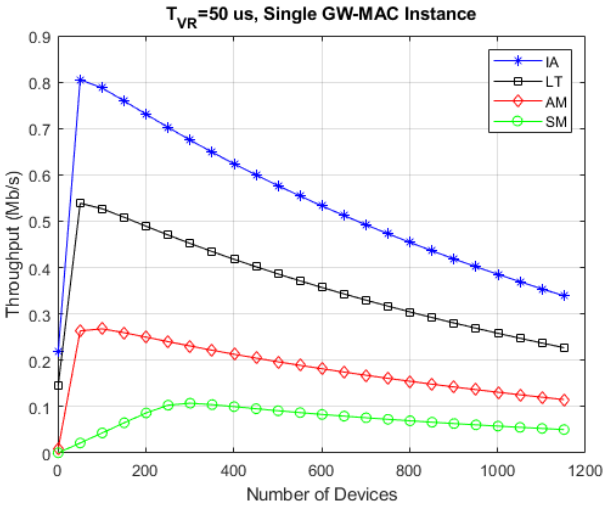

Fig. 2. Throughput results plotted against the number of devices for the different IoT traffic classes

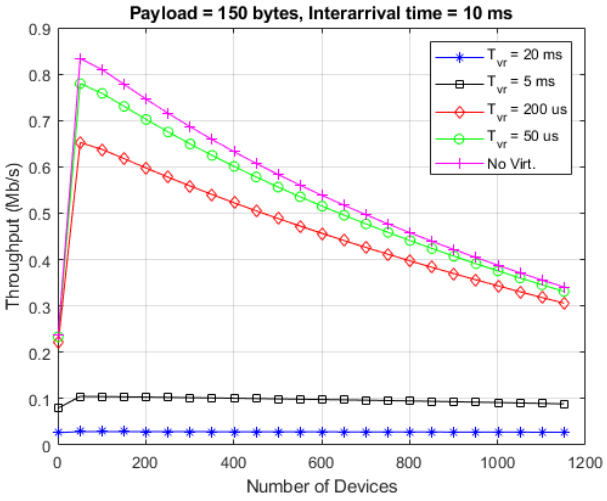

Fig. 3. Throughput results plotted against the number of devices for the different GW-MAC virtualisation delay values.

the delay imposed due to virtualisation is considered. It can also be observed that when the virtualisation delay is introduced, the throughput drops as can be seen with results for $20\ ms$, $5\ ms$, $200\ \mu s$ and $50\ \mu s$. Thus, the throughput reduces as the virtualisation delay increases as can be seen from the fact that the throughput is at its lowest and almost constant at $20\ ms$, which is the highest virtualisation delay considered. These observations are expected because the average slot transmission time is minimised due to the absence of the virtualisation process by the GW-MAC hence more devices can access the channel as a result of a reduced possibility of finding the channel busy. In addition, the average slot transmission is increased when the virtualisation delay is also increased hence the probability of collision or finding a busy channel is higher which results in much lower throughput.

In Fig. 4 the throughput results versus the number of devices are presented and compared with three situations. The first situation is when there is no virtualisation of the GW-

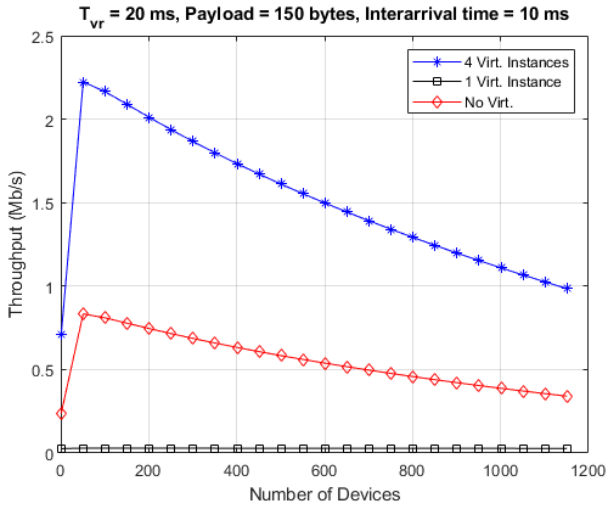

Fig. 4. Throughput results plotted against the number of devices compared with the absence of GW-MAC virtualisation, the presence of 1 GW-MAC instance and 4 GW-MAC instances.

MAC, the second is when there is only one instance of the GW-MAC virtualisation, and the third is when there are multiple instances of the virtualised GW-MAC. For both single and multiple instances the highest virtualisation delay value of 20 ms is used to represent the worst-case scenario. It can be observed in Fig. 4 that the throughput is lowest for the single virtual instance but higher with no virtualisation. Note that this is similar to the behaviour observed in Fig. 3. However, the interest here is the comparison with the behaviour when there are multiple instances. It is observed that with 4 instances, the throughput is significantly higher as anticipated. This is due to the consideration that each instance is served on a separate collision domain represented as different channels, and hence, the superposition of the throughput of all instances increases the overall throughput. This suggests that to counter the effects of the virtualisation delay as seen with the single virtual instance and to significantly improve the throughput, it will be necessary to employ a strategy to create multiple GW-MAC instances where each instance is mapped to a group of devices using different channels.

V. Conclusion

In this paper, a reference MAC scheduling throughput model was presented and modified to evaluate the effects of offloading the GW-MAC functions to a remote eDC in the context of a non-saturated LS-IoT network. The virtualisation delay was introduced as part of the average transmission time in a given slot for a CSMA/CA MAC scheduling scheme for M2M devices. The results obtained in the study conform with the classical throughput behaviour of the CSMA/CA scheduling scheme. The results further showed that for a heterogeneous (IoT traffic classes) non-saturated network the maximum throughput is highest for IA traffic classes and drops for LT, AM and SM traffic class in that order. However, the rate of reduction in throughput is highest for IA traffic due to the increased traffic load on the network when compared to the other traffic classes. In terms of the effect of virtualisation, the results obtained suggest that the throughput is higher when there is no GW-MAC virtualisation compared to when there is one instance of a GW-MAC. However, it was shown that creating more instances of the virtual GW-MAC significantly improves the throughput under the condition that each GW-MAC instance serves a group of devices in a separate channel. Proposed future work will be to model the virtualisation delay based on the different virtualisation processes involved to ascertain a more accurate representation of the effects of the GW-MAC virtualisation.

References

[1] M. Park, "IEEE 802.11 ah: sub-1-ghz license-exempt operation for the internet of things," *IEEE Communications Magazine*, vol. 53, no. 9, pp. 145–151, 2015.

[2] P. Z. Sotenga, K. Djouani, and A. M. Kurien, "Media access control in large-scale internet of things: a review," *IEEE Access*, vol. 8, pp. 55 834–55 859, 2020.

[3] N. T. Dao and R. A. Malaney, "A new markov model for non-saturated 802.11 networks," in *2008 5th IEEE Consumer Communications and Networking Conference*. IEEE, 2008, pp. 420–424.

[4] G. Bianchi *et al.*, "Performance analysis of the IEEE 802. 11 distributed coordination function," *IEEE Journal on selected areas in communications*, vol. 18, no. 3, pp. 535–547, 2000.

[5] J. Vestin, "Cloudmac: access point virtualization for processing of wlan packets in the cloud," *Bachelor Thesis*, 2012.

[6] L. Caeiro, F. D. Cardoso, and L. M. Correia, "Wireless access virtualisation: Addressing virtual resources with different types of requirements," in *2014 European Conference on Networks and Communications (EuCNC)*. IEEE, 2014, pp. 1–5.

[7] B. Fan, H. Tian, Y. Zhang, and Y. Zhang, "Virtual MAC concept and its protocol design in virtualised heterogeneous wireless network," *IET Communications*, vol. 11, no. 1, pp. 53–60, 2017.

[8] D. Garlisi, F. Giuliano, I. Tinnirello, P. Gallo, F. Gringoli, and G. Bianchi, "Deploying virtual MAC protocols over a shared access infrastructure using MAClets," in *2013 IEEE Conference on Computer Communications Workshops (INFOCOM WKSHPS)*. IEEE, 2013, pp. 17–18.

[9] O. Raeesi, J. Pirskanen, A. Hazmi, T. Levanen, and M. Valkama, "Performance evaluation of ieee 802.11 ah and its restricted access window mechanism," in *2014 IEEE international conference on communications workshops (ICC)*. IEEE, 2014, pp. 460–466.

[10] J. V. Sudarev, L. B. White, and S. Perreau, "Performance analysis of 802.11 CSMA/CA for infrastructure networks under finite load conditions," in *2005 14th IEEE Workshop on Local & Metropolitan Area Networks*. IEEE, 2005, pp. 1–6.

[11] D. Malone, K. Duffy, and D. Leith, "Modeling the 802.11 distributed coordination function in nonsaturated heterogeneous conditions," *IEEE/ACM Transactions on networking*, vol. 15, no. 1, pp. 159–172, 2007.

[12] V. Banos, M. S. Afaqui, E. Lopez, and E. Garcia, "Throughput and range characterization of IEEE 802.11 ah," *IEEE Latin America Transactions*, vol. 15, no. 9, pp. 1621–1628, 2017.

[13] W. Sun, M. Choi, and S. Choi, "IEEE 802.11 ah: A long range 802.11 WLAN at sub 1 ghz," *Journal of ICT standardization*, vol. 1, no. 1, pp. 83–108, 2013.

Prosper Z. Sotenga is a lecturer with the Tshwane University of Technology (TUT). He is currently pursuing the D.Eng. degree in electrical engineering with TUT and the Ph.D. degree in computer science (on the co-tutelle program) with Universit Paris-Est Crteil (UPEC), Crteil, France. His research areas include IoT, M2M and computing amongst others.

Karim Djouani is a full professor at University Paris Creteil, and full professor at Tshwane University of Technology (TUT), Pretoria, South Africa. His research interests include pattern recognition, soft computing, networking systems and Robotics amongst others.

Anish M. Kurien is a full professor at Tshwane University of Technology (TUT), Pretoria, South Africa and the Node Director of FSATI at TUT. His research focus areas include Feature Extraction, Pattern Recognition, Data Mining and Knowledge Discovery amongst others.

Axial Induction Optimization Using Particle Swarm And Interior Point Optimizer

Mfon Charles*, David T. O. Oyedokun*, Mqhele Dlodlo†
*Department of Electrical Engineering, University of Cape Town
[1]chrmfo001@myuct.ac.za
[2]davoyedokun@ieee.org
†National University of Science and Technology (NUST), PO Box AC 939, Bulawayo, Zimbabwe
[3]mqhele.dlodlo@nust.ac.zw

***Abstract*—Increasing the turbine density in wind plants allow for an increase in power density and increases accessibility to the individual turbines due to the shorter distances between them. It also has the capability to reduce length of interconnecting cables depending on the communication architecture and topology employed, resulting in reduced maintenance costs over the duration of the wind plant lifetime. The resulting shorter inter-turbine distances lead to increased wake interactions between turbines that negatively affect the plant efficiency and increase turbulence intensities at downstream turbines. In modern-day wind plants, turbine-level control as well as plant-wide setpoint optimization is needed to maximize plant power while minimizing loads on turbines to improve plant efficiency. In this study, an axial-based plant-wide power maximization is carried out using particle swarm optimization (PSO), a heuristic algorithm and interior point optimizer (IPOPT), an exact solver. Results suggest that applying either optimizers, impressive wind plant power increments are possible with turbulence intensity levels kept below 15%, for wind inflow conditions as low as 7 m/s.**

***Index Terms*—Axial induction, wind power maximization, plant-wide optimization, PSO, IPOPT.**

I. Introduction

Wind plants allow more active electrical power to be generated from a given area by increasing the number of turbines deployed within the area. This can reduce operation and maintenance (O&M) costs [1] by reducing access constraints to individual turbines and reducing length of interconnecting cables. The drawback, however, is the resulting increased aerodynamic interactions known as wakes between operating turbines, which could negatively impact plant power production [1] due to wake velocity deficits. These interactions also has the capacity to increase the turbulence intensity levels at individual turbines within the wind plant [2], making turbine wake modeling a crucial objective to the reduction of power losses and overall improvement of plant efficiency [3].

In the literature, analytical models such as the Park model in [4] have shown simplicity yet exhibited effectiveness in wake modeling, while also offering low computational costs in wind plant power prediction. Experimental and numerical models provide a better insight to turbine wake modeling, attempting to capture more wake characteristics such as wake meandering and wind shear and offering high-fidelity solutions compared to analytical methods [3]. The problem, however, is that they are slow and computationally expensive compared to analytical models [5], [6]. Increasing turbulence levels increase turbine fatigue loads and can affect plant lifetime [6]. This induces a possible increase in capital costs from turbine support structures. Studies have shown that optimizing turbine set-points could provide better results than completely shutting down individual turbines [6].

Many studies in the literature that employ static analytical models apply both gradient-free and gradient-based methods to obtain turbine set-points, based on a static thrust coefficient (C_t) table. The sequential non-linear optimizer (SNOPT), a gradient-based method that yields local optimal solutions to constrained non-linear problems is used in [7], [8], The authors in [9] employ sequential convex programming using CVX, a MATLAB-based global optimization tool, for turbine set-point optimization. Game theoretic methods are explored in [10] for plant power optimization using each turbine's axial induction factor a_i as the optimization variable. Heuristic methods such binary PSO and genetic algorithms (GA) have also been applied by [11] and [12] respectively to solve the plant power maximization problem. In [11] the PSO is used in a distributed architecture for plant power maximization with turbine axial induction factor and yaw angle as the optimization variables.

This study focuses on exploring the PSO, a heuristic method, and IPOPT, an exact method available through the GEKKO optimization suite [13] in a centralized architecture for axial induction-based plant power maximization.

II. Methodology

In this study, an already existing analytical wake and turbulence model are incorporated to predict power generation at individual turbines in a wind plant. To account for multiple wake effects on a single downstream turbine, the study applies to the chosen single wake model, a superposition principle based on the inter-turbine distances in the wind plant. A regular turbine deployment where turbines are statically positioned within a fixed area following a regular hexagonal pattern is employed. The focus of the optimization is to improve overall wind plant power production by first increasing turbine density while ensuring that the resulting increase in turbulence intensity levels does not exceed 20% (TI^{max}), and then applying optimization techniques to further maximize the wind plant power production for wind inflow conditions considered. Following a 12-bin wind rose, optimization is carried out

for a single direction and for three inflow conditions; 7 m/s, 8m/s, and 10 m/s. Also, three inter-turbine distances; $4D$, $5D$, and $6D$ are studied and their optimized plant power productions are compared to that of a $7D$ non-optimized spacing. The study assumes that at a $7D$ inter-turbine distance is large enough for wakes to sufficiently recover, hence, an insignificant deficit downstream. Such inter-turbine distances are regarded as conventional [14], needing no optimization. Hence, any optimization effort for such spacing will only be impacting negatively on both capital costs and O&M costs. By nD, it is implied that the hexagonal sides on whose vertices and centre turbines are deployed, are n rotor diameters long.

A. Wake Model

A continuous single wake model presented in [15]; an extension to the familiar Park model [4], is employed to ensure velocity continuity at the boundary of the wake zone. The single wake model defined by [4] is derived using an ambient-based methodology and multiple wakes are combined using the root sum square superposition method. Due to the close inter-turbine spacings studied, it was necessary to re-define the single wake model as a rotor-based model while retaining the root sum square method for combination of multiple wakes. Assuming a uniform flow at each turbine's rotor plane, Equation (1) expresses the wake velocity at each turbine in the wake zone of an extracting upstream turbine.

$$U_{b,\kappa,j} = U_{b,\kappa}^{free}(1 - U_{b,\kappa,i}^{def\_t}) \tag{1}$$

where $U_{b,\kappa}^{free}$ (also known as U_∞) is the free wind inflow and $U_{b,\kappa,j}^{def\_t}$ is the total deficits suffered due to wakes from all the upstream turbines, and is dependent on the affected turbine j, time instance κ, and wind direction b, as given in (2).

$$U_{b,\kappa,i}^{def\_t} = \sqrt{\sum_{i=1}^{\mathcal{T}} \left[\frac{2a_{b,\kappa,i}}{(1 + (\frac{2\alpha x_{b,\kappa,i}}{D_i}))^2} \exp\left(-(\zeta)\right) \right]^2} \tag{2}$$

where the term enclosed in brackets represents a single wake velocity deficit, a_i and D_i is the upstream turbine(s) axial induction factor(s) and rotor diameter(s) respectively. The parameter α is the decay constant which determines how fast the wake spreads and can be expressed in terms of the roughness length z_{r_l} of the plant site and the considered turbine's hub height z_0. The term ζ is given in (4) while the divergence of the wake is then estimated from (5). The parameters x in (2) and (4), and r in (4) are both distance parameters (in meters) and represent the distance of turbine j from each upstream turbine $i \in \mathcal{T}$ in the longitudinal and perpendicular directions, respectively.

$$\alpha = \frac{0.5}{\ln \frac{z_0}{z_{r\_l}}} \quad , \tag{3}$$

$$\zeta = \frac{r_{b,\kappa,i}}{\frac{D_i}{2} + \alpha x_{b,\kappa,i}} \quad , \tag{4}$$

$$\gamma = 2\tan^{-1}(\alpha) \quad . \tag{5}$$

B. Turbulence Intensity Model

At such close deployments investigated, the study assumes that the wake-generated turbulence presented by Frandsen's simplified WT model [16] and given in (6) is dominant, encapsulating any ambient turbulence effects.

$$TI_j = \frac{\sigma_{0,wake}}{U_j} \tag{6}$$

where $\sigma_{0,wake}$ is the representative standard deviation.

$$\sigma_{0,wake} = \sqrt{\frac{U_j^2}{\left(1.5 + 0.8\left(\frac{x^{norm}}{\sqrt{C_j^{thrust}}}\right)\right)^2} + \sigma_{mean,0}^2} \tag{7}$$

where x^{norm} is the longitudinal distance between the nearest upstream turbine i' and turbine j normalised with the rotor diameter D_j, and $\sigma_{mean,0}$ is the time-averaged value of standard deviations for the wind plant site. The parameter C_j^{thrust} is the thrust coefficient of turbine j corresponding to U_j, as opposed to U_∞ proposed by the simplified WT model. This is done to prevent its less conservative nature of predicting TI, considering the close inter-turbine deployments.

C. Wind Plant and Turbine Characteristics

Turbines are deployed within a fixed dimension following a hexagonal pattern. As part of a wider study that aims to improve the annual energy production of a wind plant site whose wind information is provided with a 12-bin wind rose, a hexagonal deployment has been followed to deliberately create bins of sufficiently large inter-turbine distance, enhancing a no-optimization in these bins. Fig. 1 depicts a 12-bin wind rose with sample hexagonal deployments.

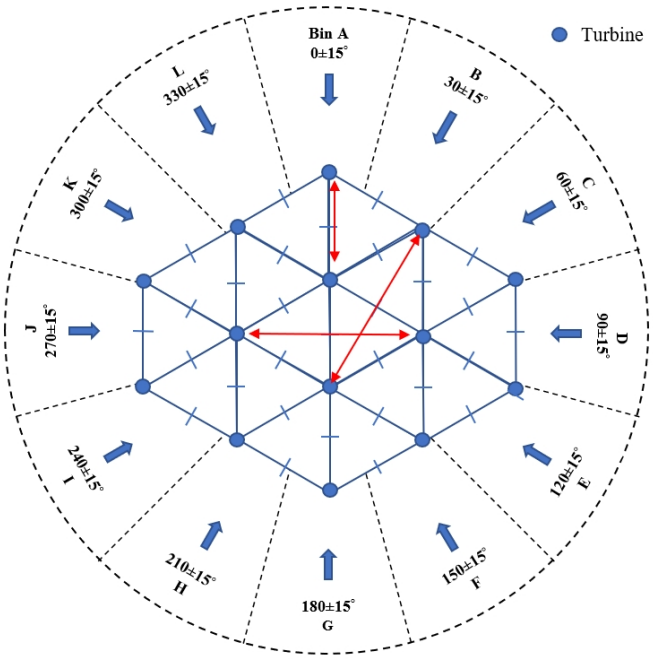

Fig. 1. Hexagonal deployment on 12-bin wind directions. [17]

With respect to Fig. 1, sufficiently large inter-turbine spacing can be created for bins B, D, F, H, J, and I. As demonstrated in Table I for the different inter-turbine distances investigated, the $4D$ deployment would have an inter-turbine spacing of approximately $6.92D$ which is very close to a $7D$ inter-turbine spacing, hence, ignoring optimization in these bin directions.

TABLE I
INTER-TURBINE DISTANCES IN ROTOR DIAMETERS

Deployment (D)	**Inter-turbine Distances** (D) **Bin** $B = D = F = H = J = I$
7	$\approx$ 12.12
6	$\approx$ 10.4
5	$\approx$ 8.66
4	$\approx$ 6.92

Figure 2 and Table II (values approximated to 3 d.p) provide details about the turbine used for the investigation.

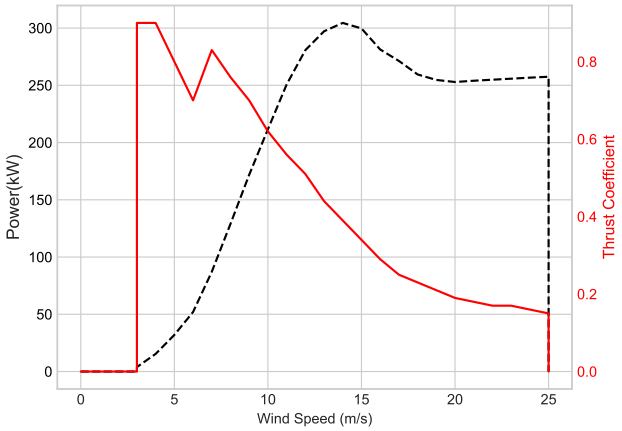

Fig. 2. Power and Thrust Curve: Power (kW) and thrust coefficient (C_t) versus wind speed (m/s) of the Bonus 300 kW MkIII wind turbine generator with U_{in} = 3 m/s, U_r = 14 m/s, U_{out} = 25 m/s, D = 31m, and z_{hub} = 30m, $C_{p_{max}}$ = 0.5923 [18].

TABLE II
TURBINE AXIAL DATA (U_{in} TO U_r).

$U(m/s)$	3	4	5	6	7	8
a	0.342	0.342	0.276	0.226	0.294	0.255
$U(m/s)$	9	10	11	12	13	14
a	0.226	0.192	0.168	0.15	0.126	0.109

D. Power Modeling

The power at a controlled turbine can be computed from (8) according to the modeling in [19]. Wind plant power optimization is then obtained through a coordinated distribution of control set-points across all the turbines in the plant.

$$P(U) = \begin{cases} 0, & \text{if } U < U_{in} \\ \frac{1}{2}\rho A U^3 C_p, & \text{if } U_{in} \leq U < U_r \\ \frac{1}{2}\rho A U^3 {C_p}^*, & \text{if } U_r \leq U < U_{out} \\ 0, & \text{if } U_{out} \leq U \quad . \end{cases} \tag{8}$$

where C_p and ${C_p}^*$ are the power coefficients in the design and optimized forms, respectively. Furthermore, U_{in}, U_r and U_{out} are the cut-in, rated, and cut-out wind speeds, respectively.

$$C_p = 4a(1-a)^2 \tag{9}$$

III. MATHEMATICAL FORMULATION

Here, the study presents a formulation to effect a coordinated and centralized control on wind turbines in a wind plant using PSO and IPOPT, with the aim of finding optimal set-points for each turbine in a major wake zone (MWZ) that yields an improved overall plant power compared to a counterpart non-optimized base case.

Consider an inflow into a fixed dimension wind plant as shown in Fig. 3. Let $\mathcal{N}$ be a set of all turbines in the wind plant, $\mathcal{M} \subseteq \mathcal{N}$ is a set of MWZs, m, and $\mathcal{T}$ is a set of turbines in m. Because the area of the plant is fixed, values of $\mathcal{M}$ and $\mathcal{N}$ decrease as minimum deployment distance increases.

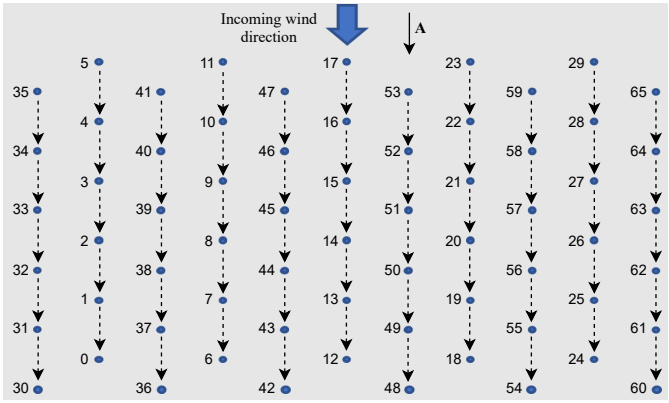

Fig. 3. A regular hexagonal layout showing direction of inflow.

Consider a major wake zone m of $\mathcal{T}$ turbines with power productions $\{P_i\}_{i\in\mathcal{T}}$ and control settings $\{a_i\}_{i\in\mathcal{T}}$ that are standing in the wake of each other, with a free-stream inflow U_∞ from the direction illustrated on Fig. 3. The optimization variable considered in this study for plant power maximization is the axial induction factor a, hence, an adjustment in a of any $i \in \mathcal{T}$ in m, affects turbine i's power production and those of others in its downstream. Optimal settings of a $\forall i \in \mathcal{T}$ and $\forall m \in \mathcal{M}$, will thus produce a maximized plant power output per instance of time. For simplicity, let each m be identified by the number of the uppermost upstream turbine $w.r.t$ the wind inflow direction in Fig. 3.

The optimization problem can thus be formulated as:

$$\max_{(U_{m,i},P_{m,i})} \quad \sum_{m=1}^{\mathcal{M}} \sum_{i=1}^{\mathcal{T}} \beta_{m,i} U_{m,i}^3 \qquad \forall i \in \mathcal{M}$$
$$\text{s.t.} \quad a_{m,i} \leq a_{max} \qquad (10)$$
$$0 < \beta_{m,i} U_{m,i}^3 \leq P^{max}$$
$$TI \leq TI^{max}$$

where U is given in Eqn (1) and β in Eqn (11)

$$\beta_{m,i} = \frac{\rho A C_{p_{m,i}}}{2} \qquad (11)$$

Constraint 1 prevents the axial induction factor of each turbine from exceeding the manufacturer's maximum design power coefficient (obtainable at U_{in} for the turbine model studied). Constraint 2 ensures that no turbine power in the plant exceeds that which it would generate at the mean free-stream inflow U_∞ and at the design axial induction factor synonymous with that free-stream inflow, while also making sure that all turbines in the plant generate power. Constraint 3 ensures that the turbulence intensity level at each turbine is below a set maximum of 20% (TI^{max})

With the following parameters, 300 iteration runs were conducted for each optimizer and results presented - IPOPT (m.solver_options = ['linear_solver mumps','mu_strategy adaptive','max_iter 1000', 'tol 1.0e-5']); PSO(Particles = 30, c1 = 2, c2 = 2, wMax = 0.9, wMin = 0.2)

IV. Results

Considering Fig. 3, all MWZs in the direction considered contain the same number of turbines with equal separation distances. Hence, results from a single MWZ are reported in Figs. 4 - 7 to demonstrate the performance of both optimizers in maximizing power and managing TI levels. Considering a single MWZ (MWZ 5), results of wind speed, power, and TI levels at each turbine are presented for all deployment distances for a single wind inflow (i.e 7 m/s).

The base case operation depicts the normal behaviour of the turbines with the investigated wake and turbulence models. The optimized operation (PSO and IPOPT) shows the turbine behaviour when a plant-wide coordinated control is implemented.

Figures 4 - 7 show the performance of both optimizers compared to the base case/non-optimized case, with an inflow of 8 m/s. As seen, both optimizers show a similar degree of power increment on the individual turbines and consequently, MWZ and overall plant power, for all inter-turbine spacings investigated. These power increments is accompanied with significant decrements in turbulence intensity levels experienced by each turbine in each MWZ.

For each of Figs. 8 - 10, it is also observed that overall plant power increment for both optimizers decrease with increasing deployment distance as expected, and this is consistent for all wind inflows investigated. This justifies the popular choice to not employ any optimization scheme on turbine set-points if deployment distances are sufficiently large.

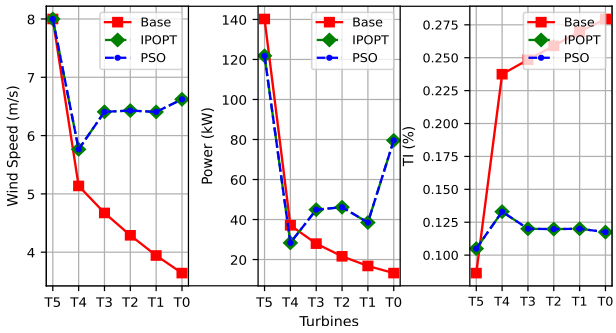

Fig. 4. $4D$ deployment distance at 8 m/s mean wind speed.

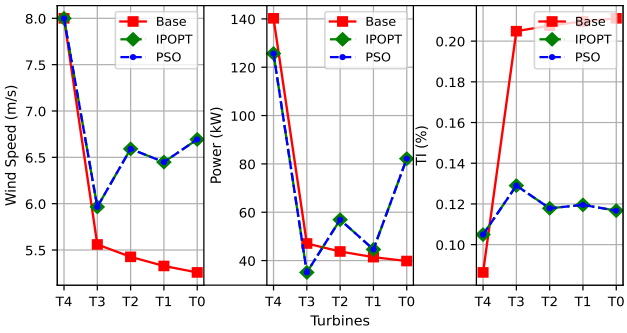

Fig. 5. $5D$ deployment distance at 8 m/s mean wind speed.

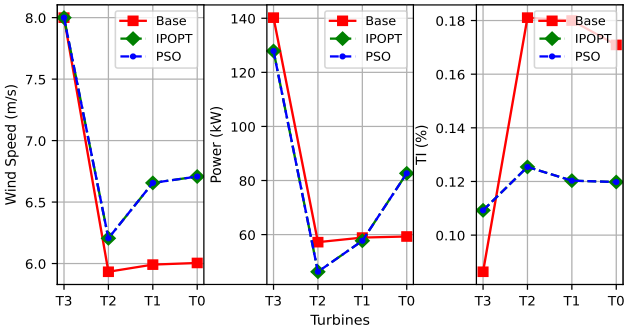

Fig. 6. $6D$ deployment distance at 8 m/s mean wind speed.

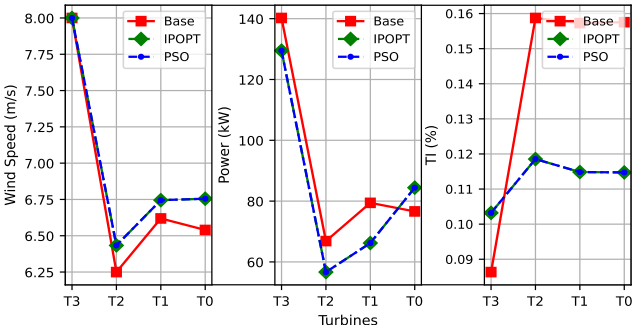

Fig. 7. $7D$ deployment distance at 8 m/s mean wind speed.

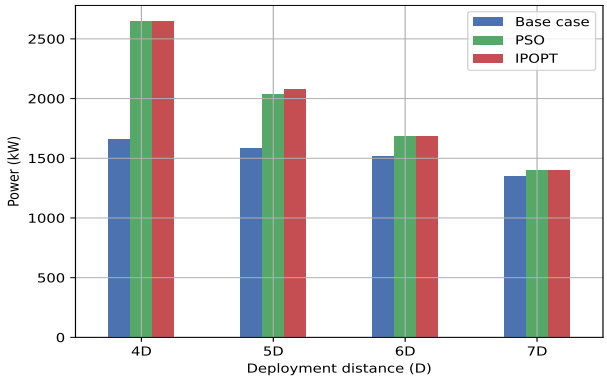

Fig. 8. Total plant power for all deployments, at 8 m/s mean wind speed.

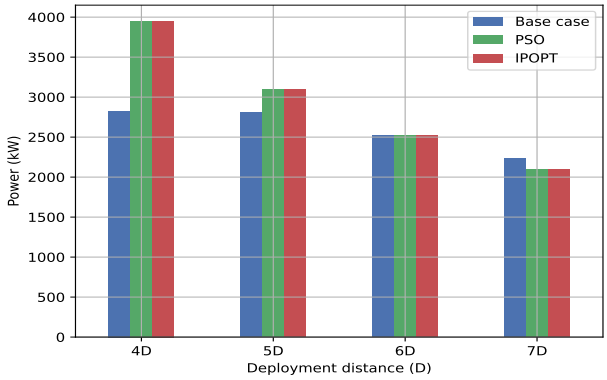

Fig. 9. Total plant power for all deployments, at 8 m/s mean wind speed.

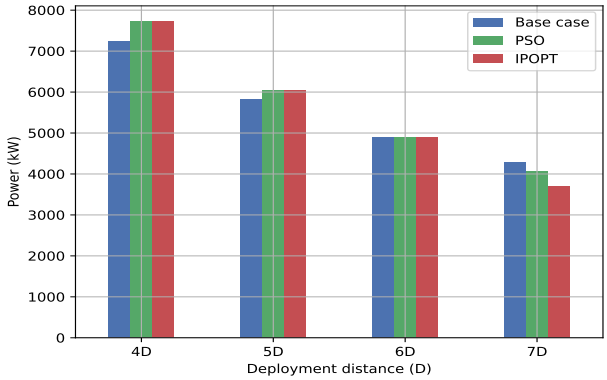

Fig. 10. Total plant power for all deployments, at 10 m/s mean wind speed.

It can also be observed from Figs. 11 - 14 that overall power does not only change with inter-turbine distance, but with varying wind inflow, decreasing as wind inflow increases. At 7 m/s inflow, a plant power increase of approximately 37.4% is achieved with both optimizers for a $4D$ deployment, reducing to 22.1% and 23.5% respectively for PSO and IPOPT at $5D$, respectively. A further decrease in overall power increment to 9.89% and 3.95% is noticed with $6D$ and

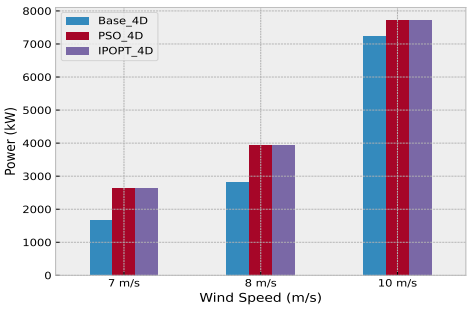

Fig. 11. Total plant power for all inflow conditions, for 4D deployment.

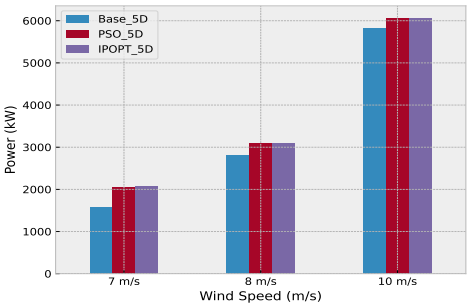

Fig. 12. Total plant power for all inflow conditions, for 5D deployment.

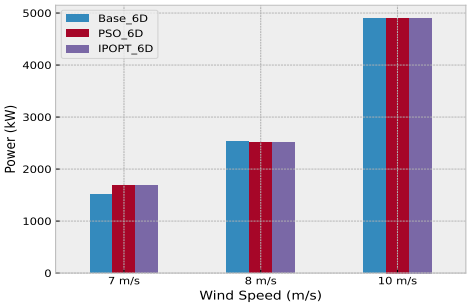

Fig. 13. Total plant power for all inflow conditions, for 6D deployment.

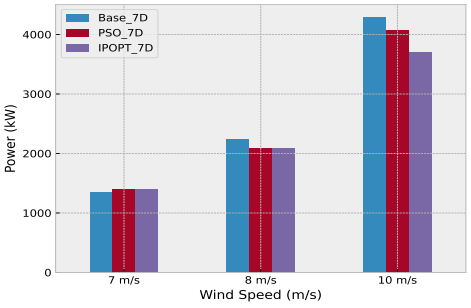

Fig. 14. Total plant power for all inflow conditions, for 7D deployment.

$7D$ deployments, respectively. These are shown graphically on Fig. 8. These power increments and accompanying TI decrements are summarized in Table III.

TABLE III
MWZ POWER INCREMENTS AND AVERAGED TI DECREMENTS.

Scenario	Power Change(%): PSO	Power Change(%): IPOPT	Max TI(%)
7 m/s	+37.4	+37.4	14.9
$4D$: 8 m/s	+28.5	+28.5	13.3
10 m/s	+6.31	+6.31	11.4
7 m/s	+22.1	+23.5	13.9
$5D$: 8 m/s	+9.34	+9.34	12.9
10 m/s	+3.69	+3.69	10.9
7 m/s	+9.89	+9.89	14.4
$6D$: 8 m/s	-0.35	-0.35	12.5
10 m/s	+0.05	+0.05	10.9
7 m/s	+3.95	+3.95	13.5
$7D$: 8 m/s	-7.25	-7.25	11.9
10 m/s	-3.79	-11.3	10.7

V. DISCUSSION

The study demonstrates the ability of the PSO algorithm and IPOPT solver to improve plant power, given a fixed area of hexagonally deployed turbines. It is shown that plant power increment is possible even for a $6D$ deployment. However, with such a deployment ($6D$) the resulting annual energy production of the plant may not be comparable with that of the benchmark (non-optimized $7D$ scenario). The PSO being stochastic in nature and the IPOPT although an exact method, but mostly settling to a local minima, have shown capability to improve plant power with the $4D$ and $5D$ scenarios. From presented results, both algorithms offer comparable solutions to the problem. However, the IPOPT solver (which implements the interior point algorithm) converges faster and would be a preferred option for real-time solutions, which is the case in wind farm set-point optimization.

Furthermore, a close observation of Fig. 8 indicates that the gains achieved from axial-based plant-wide optimization using these optimizers would totally lose significance at wind inflows above 10 m/s regardless of the inter-turbine spacing. Although this is dependent on the turbine model(s) and other factors such as ground surface roughness effects from the plant site, it will be necessary to employ more sophisticated exact solvers that specifically find global solutions.

VI. CONCLUSION

By considering three different mean wind inflows, the study has demonstrated that increasing the mean wind inflow reduces the gains that can be achieved with a combination of turbine density increment and plant-wide optimization. It has shown that impressive power increments are possible while keeping turbulence intensity levels below 15% at a low wind inflow of 7 m/s for the turbine and inter-turbine spacing investigated. In future smart wind farms, hexagonal layouts can be exploited to create a combination of close and sparse inter-turbine distances, taking advantage of close spacings to maximize power productions at low wind inflows, while also exploiting the large spacings to conserve computational resources and communication bandwidth by neither optimizing nor disseminating turbine set-point updates across the smart wind plant.

ACKNOWLEDGEMENT

Special appreciation goes to the Centre for Broadband Networks, Department of Electrical Engineering, University of Cape Town for her constant financial and moral support.

REFERENCES

[1] T. Ahmad, O. Coupiac, A. Petit, S. Guignard, N. Girard, B. Kazemtabrizi, and P. C. Matthews, "Field implementation and trial of coordinated control of wind farms," *IEEE Transactions on Sustainable Energy*, vol. 9, no. 3, pp. 1169–1176, 2017.

[2] G.-W. Qian and T. Ishihara, "Wind farm power maximization through wake steering with a new multiple wake model for prediction of turbulence intensity," *Energy*, vol. 220, p. 119680, 2021.

[3] A. Niayifar and F. Porté-Agel, "Analytical modeling of wind farms: A new approach for power prediction," *Energies*, vol. 9, no. 9, p. 741, 2016.

[4] I. Katic, J. Højstrup, and N. O. Jensen, "A simple model for cluster efficiency," in *European wind energy association conference and exhibition*, vol. 1, 1986, pp. 407–410.

[5] S. Chowdhury, J. Zhang, A. Messac, and L. Castillo, "Optimizing the arrangement and the selection of turbines for wind farms subject to varying wind conditions," *Renewable Energy*, vol. 52, pp. 273–282, 2013.

[6] E. Bossanyi and T. Jorge, "Optimisation of wind plant sector management for energy and loads," in *2016 European Control Conference (ECC)*. IEEE, 2016, pp. 922–927.

[7] P. Gebraad, J. J. Thomas, A. Ning, P. Fleming, and K. Dykes, "Maximization of the annual energy production of wind power plants by optimization of layout and yaw-based wake control," *Wind Energy*, vol. 20, no. 1, pp. 97–107, 2017.

[8] A. P. Stanley, J. King, and A. Ning, "Wind farm layout optimization with loads considerations," in *Journal of Physics: Conference Series*, vol. 1452, no. 1. IOP Publishing, 2020, p. 012072.

[9] T. G. Hovgaard, L. F. Larsen, J. B. Jørgensen, and S. Boyd, "Sequential convex programming for power set-point optimization in a wind farm using black-box models, simple turbine interactions, and integer variables," in *10th European Workshop on Advanced Control and Diagnosis*, 2012.

[10] J. R. Marden, S. D. Ruben, and L. Y. Pao, "A model-free approach to wind farm control using game theoretic methods," *IEEE Transactions on Control Systems Technology*, vol. 21, no. 4, pp. 1207–1214, 2013.

[11] N. Gionfra, G. Sandou, H. Siguerdidjane, D. Faille, and P. Loevenbruck, "Wind farm distributed pso-based control for constrained power generation maximization," *Renewable energy*, vol. 133, pp. 103–117, 2019.

[12] Y. Chen, H. Li, K. Jin, and Q. Song, "Wind farm layout optimization using genetic algorithm with different hub height wind turbines," *Energy Conversion and Management*, vol. 70, pp. 56–65, 2013.

[13] L. D. R. Beal, D. C. Hill, R. A. Martin, and J. D. Hedengren, "Gekko optimization suite," *Processes*, vol. 6, no. 8, 2018. [Online]. Available: http://www.mdpi.com/2227-9717/6/8/106

[14] B. Sanderse, "Aerodynamics of wind turbine wakes-literature review," 2009.

[15] J. Park and K. H. Law, "Layout optimization for maximizing wind farm power production using sequential convex programming," *Applied Energy*, vol. 151, pp. 320–334, 2015.

[16] P. Argyle, S. Watson, C. Montavon, I. Jones, and M. Smith, "Modelling turbulence intensity within a large offshore wind farm," *Wind Energy*, vol. 21, no. 12, pp. 1329–1343, 2018.

[17] M. Charles, D. T. Oyedokun, and M. Dlodlo, "Wind farm density effects on turbulence intensity for large hexagonal farm arrays," in *2020 6th IEEE International Energy Conference (ENERGYCon)*. IEEE, pp. 1–6.

[18] "WAsP wind assesment program," https://www.wasp.dk/wasp#educational-wasp, accessed: 2018-06-15.

[19] J. F. Manwell, J. G. McGowan, and A. L. Rogers, *Wind energy explained: theory, design and application*. John Wiley & Sons, 2010.

Mfon Charles holds an MSc in Information and Communications Engineering from the University of Leicester, UK. He is passionate about clean energy and seeks to explore wired communication topologies for future smart farms that will conserve bandwidth, and possibly reduce capital costs and O & M costs through improved power generation and reduced inter-turbine cabling.

Early Dehydration Detection Using Infrared Imaging

Louise Poole*, Dane Brown†, James Connan‡
*Department of Computer Science, Rhodes University, Grahamstown, South Africa
[1]louisecarmenpoole@gmail.com
[2]d.brown@ru.ac.za

***Abstract*—Crop loss and failure have devastating impacts on a country's economy and food security. Developing effective and inexpensive systems to minimize crop loss has become essential. Recently, multispectral imaging — in particular visible and infrared imaging — have become popular for analyzing plants and show potential for early identification of plant stress. We created a directly comparable visible and infrared image dataset for dehydration in spinach leaves. We created and compared various models trained on both datasets and concluded that the models trained on the infrared dataset outperformed all of those trained on the visible dataset. In particular, the models trained to identify early signs of dehydration yielded 45% difference in accuracy, with the infrared model obtaining 70% accuracy and the visible model obtaining 25% accuracy. Infrared imaging thus shows promising potential for application in early plant stress and disease identification.**

***Index Terms*—Machine Vision, Image Classification, Infrared Imaging, Image Database**

I. Introduction

Crop loss and failure directly impact not only a country's economy but also a country's food security, often to devastating effects. For example, the rice blast disease alone destroys, per year, enough rice to feed the entire population of Italy [1]. This is a constant pressure placed on the agriculture sector that only increases during plant epidemics which cause greatly exaggerated losses.

Once discovered, infected plants must be removed, and in the case of many plants such as grapes and vineyards, new plants must be planted. These plants, in turn, take around five years to reach full production. Essentially, any plant loss that occurs often affects many years of food production. As such, the importance of not only successfully detecting plant diseases once they have appeared but to do so as early in their development as possible is essential to minimize disease spread and damage to crop production [2].

In recent years, with the development of and increase in ease of access to new equipment and technology, the use of spectroscopy in the early detection of plant diseases has become notably popular. This is due to the increase in demand for inexpensive, rapid and non-invasive applications for plant disease detection and classification [3].

Visible and infrared spectroscopy has been extensively studied and effectively applied to systems designed to determine the quality of agricultural products [4]. However, a limited amount of the current literature focuses on its use for, or application in, the detection of plant stress and diseases [5, 6]. Furthermore, there is not much literature determining its effectiveness in early disease detection.

This paper aims to show the difference in stress classification performance of a system using NIR image input versus a system using visible image input. The stress chosen was dehydration, and established dehydration classification and early dehydration classification performances were also compared.

This study was funded by National Research Foundation (120654). This work was undertaken in Distributed Multimedia CoE at Rhodes University.

II. Multispectral Imaging

The use of spectroscopy and multispectral imaging in early detection of plant diseases has recently become notably popular due to its potential for inexpensive, rapid and non-invasive application in plant disease detection and classification [3].

Spectroscopy is the study of electromagnetic (EM) waves and their interaction with matter. Electromagnetic waves include the ultraviolet (UV), visible (VIS) and infrared (IR) spectra [7], as shown in Figure 1 [8]. Multispectral imaging is an analytical technique based on spectroscopy where images are captured within specific wavelength ranges across the electromagnetic spectrum. The majority of multispectral sensors for remote sensing capture visible (VIS) and near-infrared (NIR) regions of the EM spectrum [9].

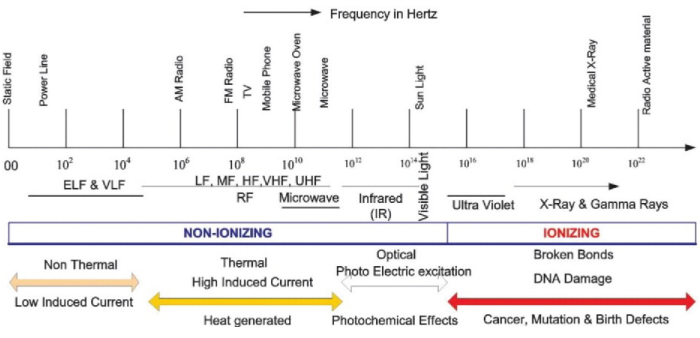

Fig. 1. Electromagnetic Spectrum

Due to their many advantages over other analytical techniques, visible and infrared (VIS-IR) spectroscopy, with wavelengths of 400 - 100 000nm, are considered one of the most promising and extensively accepted non-invasive techniques used for plant analysis [5]. As such, current literature mainly focuses on the use of VIS-IR for determining the quality of

agricultural product [4] and does not effectively explore the combination of computer vision and VIS-IR imaging for its use in the detection of plant stress and diseases [5, 6].

A. Spectral Reflectance of Plants

Research has shown that there exists a relationship between specific absorbance-reflectance patterns for the photoactive pigments in a leaf, mainly chlorophylls and carotenoids, and the physiological state of the leaf [10].

Both of these photoactive pigments play a vital role in a plant's ability to photosynthesize by working together to absorb and convert the light energy that reaches the leaf [11]. Changes in chlorophyll concentration and proportions are triggered by stress, ageing and other factors directly related to the production rate of the plant [12]. Thus significant changes in reflectance in the leaf due to stress caused by strain or pathogens and diseases can be observed in both the visible range of 380 - 750nm and the far-red range of 690 - 720nm, with the far-red range indicating early infection before other regions of the electromagnetic spectrum do [13].

Specific wavelength ranges sensitive to the stress experienced by the plants depend on the specific combination of diseases and plant species in question. Various plant species and diseases are thus explored below.

B. Related Studies

Many studies have been conducted to determine the wavelengths that provide the most significant changes in leaf reflectance when infected or under stress for various plant species and diseases/stresses. The following studies all compare the VIS and NIR ranges and smaller ranges found within them.

Xu et al. [14] studied Leaf Miner damage on Tomato leaf and found the NIR ranges of 800-1100nm and 1450-1900nm provided the most useful data for infection severity.

Ausmus and Hilty [15] studied both the maize dwarf mosaic virus and *Helminthosporium maydis* diseases and their effect on the reflectance of corn leaves. They found that infected and healthy leaves possessed similar reflectance in the visible range of 400-750nm but significantly different reflectance in the NIR range of 800-2600nm.

Malthus and Madeira [16] studied the reflectance properties of field bean infected by the fungus *Botrytis fabae* over the VIS-IR wavelength range of 400-1100nm. They found that wavelengths around 800 nm had the greatest response to the changes caused within the leaf by the fungus.

Bravo et al. [17] studied yellow rust on wheat plants and found that using four wavebands from the VIS/NIR ranges of the spectrum, namely 543 ± 10, 630 ± 10, 750 ± 10 and 861 ± 10, they were able to obtain a 96% classification success rate between the healthy and infected wheat plants.

Riedell and Blackmer [18] studied the effect of Russian wheat aphids and greenbugs on the reflectance spectra of wheat. They determined that the wavelengths most responsive to the crop stress caused by these pests were 625-635nm and 680-695nm.

One limitation of the above-listed studies is that they use specialized and expensive equipment to gather their data. The equipment list includes mounted spectrographs, specialized spectrometers etc.

This paper focuses on the wavelengths obtainable by more affordable visible and infrared cameras and relies on machine learning to make the final classifications. Due to the majority of the compared literature selecting various wavelengths in the far-red and NIR ranges, input covering both ranges will be used in this research.

III. Machine Learning

Machine learning (ML) is a small subset of the field of Artificial Intelligence and can be defined as the automated learning done by a program to make predictions without explicitly being programmed to make those predictions. This is done through the use of learning algorithms which use available data to create an estimation of some unknown mapping between system inputs and outputs. This can be used to generate future predictions based on the previously observed samples. One of the most widely researched fields of machine learning is supervised learning. Data samples with both known inputs and known outputs are used during supervised learning [19].

Traditional ML approaches require the application of feature extraction to the data prior to the model receiving it. This focuses the model, allowing it to learn only the relevant features by removing the confusion that unnecessary and unrelated information introduces. The development of Deep Learning (DL) has significantly decreased the need for a model to rely on accurate feature extraction. Deep Learning is a subfield of machine learning that is identifiable by its use of at least more than 3 layers: an input layer, one or more hidden layers and an output layer. A popular class of deep machine learning algorithms is known as Convolutional Neural Networks (CNN).

A CNN is a deep neural network algorithm that utilizes convolutional layers [20]. Convolutional layers are considered to be more specialized and efficient than fully connected layers.

In a fully connected layer, each neuron within the layer is connected to every neuron in the layer before. Each connection also has its own weight. This makes using fully connected layers computationally expensive and memory heavy.

In contrast, in a convolutional layer, every neuron within the layer is connected to only a few local neurons in the previous layer. This proves to be very useful for spatial data where features are locally clustered. It is also useful for allowing CNN to prioritize notable features and ignore what is unnecessary for categorizing the input. Thus other feature extraction on input data is often not necessary. The same set of weights are used for every neuron's set of connections. This is useful when features are equally likely to be found

anywhere in the input. Hence why CNNs are a popular choice for learning image datasets.

In general, a CNN architecture is comprised of a combination of one or more convolutional, pooling and fully connected layers. One of the most popular architectures for image datasets is ResNet [21].

ResNet was proposed by He et al. [21]. They make use of a deep residual learning framework in their architecture in order to combat the degradation issue that arises with high network depth. This is done by using 'shortcut connections' [22], or residual links, which allows connections to skip one or more layers. In this case, these shortcut connections are simple identity mappings where their outputs are added to the outputs of the stacked layers. The system learns residual functions without adding computational complexity and thus makes the deep network easier to optimize and faster to compute. A visual representation of the residual block found in the ResNet architecture that uses a shortcut connection is given in Figure 2 [21].

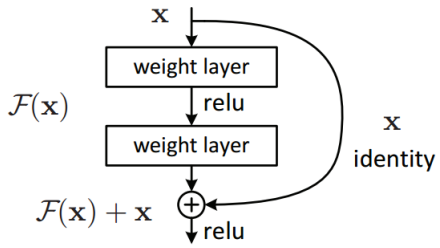

Fig. 2. The ResNet residual block.

He et al. [21] compare their proposed architecture to popular existing state-of-the-art architectures such as VGG-16, GoogLeNet and PReLU-net. They performed the comparison using the ImageNet 2012 classification dataset [23]. This image dataset consists of 1000 classes and over 1.4 million images. They used just over 1.2 million images for training, 50k for validation and 100k for testing. Comparing the top-5 error rates of the models generated for each architecture, ResNet obtained consistently lower error rates than the other architectures considered. The top performing existing architecture models obtained an error equal to the poorest performing ResNet model. The ResNet models showed a trend of decreasing error rate with increasing layer depth. The 152 layer ResNet model obtained the lowest error rate of 4.49%.

In this research, a ResNet model of 30 layers will be used.

IV. Experimental Setup

The following section describes the structure and setup of the experiments conducted.

A. Data Collection

The plant species chosen to collect data from was spinach. This was chosen due to the plant's ability to grow year-round, allowing it to be flexible to the needs of the data collector, its quick nature in developing and displaying symptoms and stress and its ease at recovering when the stress is removed. This allows for multiple opportunities to collect data from the same plant.

The data was collected over a period of seven days, with the plants receiving no water starting on day 1. This was to initiate the process of dehydration in the plants. Images were taken on day 1 to collect healthy plant images, day 5 to collect images containing early signs of dehydration and day 7 for images of established dehydration.

Two datasets were collected simultaneously: one using infrared images and the other using visible images. The infrared images were taken on a Canon EOS 800D with its internal visible wavelength filter removed and an external NIR filter added. The chosen NIR filter added was the Kolari Vision K665. This filter allows for far-red light and NIR wavelengths greater than $665\ nm$ to reach the camera's sensor.

For the visible images, a Canon EOD 700D was used with no alterations made.

All images were taken outdoors using the sun as a natural light source. They were taken with complex backgrounds of soil, pots, walls and other unrelated plants. This was to assist in duplicating the real-life input the system would receive from an end user.

To allow the separate datasets to be as directly comparable as possible, the following steps were followed:

- Both cameras were equipped with EFS 18-55mm lenses set at 35mm zoom. This allowed for minimal differences in focal distances and background blur between the datasets.
- For each leaf image taken by the infrared camera, the same leaf was photographed immediately after by the visible camera. This enabled minimal changes in natural light intensities present between the datasets.
- The angle to and distance from the leaf of the infrared camera when taking the infrared image was immediately duplicated as closely as possible by the visible camera. This allowed for minimal differences in image composition, angle of light reflectance etc.

Example images from the infrared and visible datasets are given in Fig. 3 and 4. They demonstrate the minimal differences strived for between the datasets.

Fifty photos were taken with each camera on days 1, 5 and 7. This created two balanced datasets of 150 photos each. For the various experiments listed in Section IV-D, the datasets were divided as shown in Table I.

TABLE I
Breakdown of Datasets Used

Dataset Name	Days	Total Images
Full Dataset	1, 5, 7	150
Identification Dataset	1, 7	100
Early Identification Dataset	1, 5	100

Fig. 3. Image from the visible dataset

Fig. 4. Image from the infrared dataset

B. Measuring Model Performance

In the majority of plant classification research papers available, classification accuracy was the chosen metric for comparing the performance of the machine learning models developed.

Accuracy is a measurement for the system's overall correctness and is found by calculating the ratio between the number of correctly classified samples and the total number of input samples.

$$Accuracy = \frac{\text{number of correct classifications}}{\text{total number of classifications attempted}}$$

This gives a true reflection of a given model's overall performance if the test data used is balanced.

C. Parameter Tuning

A hyperparameter optimizer developed by the Google team called KerasTuner [24] was used to determine the best parameter values for the ResNet models created. The optimizer used was Hyperband [25]. However, Hyperband is based on the popular Random Search optimizer but with early stopping and adaptive resource allocation to decrease the system's computational expense, thereby increasing the tuning speed of the system. The chosen parameters for tuning were *learning rate* and *optimization algorithm*.

D. Test Models

For each test model generated, the system first underwent parameter tuning, followed by the retraining of the model with the chosen parameters and finally testing on the test data.

Each dataset was split into three sections for this process: training, validation, and test data. The training data was used for parameter tuning, with the validation data used to evaluate the comparative performance of each of the tuner's models. Validation loss was chosen as the value to be optimized during training. Once the best combination of parameters was determined on the validation data, a new model was trained once again. This final model was tested on the unseen test data to reflect the model's unbiased performance accurately. Furthermore, data contamination was avoided during data augmentation as it was applied only to the training data and not to the test data. A visible overview of the process described above is shown in Fig. 5.

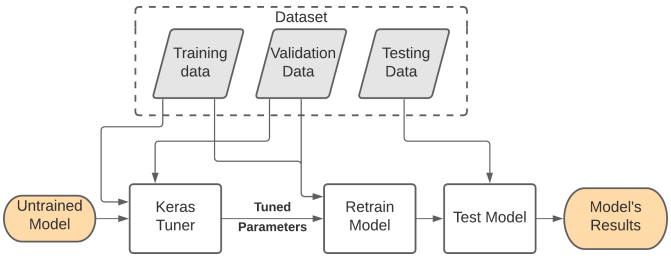

Fig. 5. Overview of system used to test the models.

A train:test split of 80:20 was used. The training data includes the validation data used during tuning. Six models were trained for the respective experiments listed below:

- Experiment 1 - Compare the performance of the models trained and tuned on the infrared and visible full datasets
- Experiment 2 - Compare the performance of the models trained and tuned on the infrared and visible identification datasets
- Experiment 3 - Compare the performance of the models trained and tuned on the infrared and visible early identification Datasets

V. Results and Discussion

A. Parameter Tuning

For the parameter tuning of each model, 20 trials and 100 epochs were used to find the best learning rate and optimization algorithm. Learning rates of $1e^{-3}$ to $1e^{-8}$ were explored. The optimization algorithms considered during tuning were Adam and Stochastic Gradient Descent (SGD). The parameters that produced the best models per dataset-architecture pairing are given in Table II.

TABLE II
Best Parameters Determined With Keras Tuner

	Dataset	**Best Parameters**	
		Learning Rate	***Optimization***
Infrared	Full	$1e^{-7}$	SGD
	Identification	$1e^{-3}$	SGD
	Early Identification	$1e^{-5}$	Adam
Visible	Full	$1e^{-6}$	SGD
	Identification	$1e^{-6}$	Adam
	Early Identification	$1e^{-7}$	Adam

B. Experiment 1

Experiment 1 trains and tests the models produced on the infrared and visible full datasets with the relevant parameters determined in section V-A. The results are given in Table III.

TABLE III
PERFORMANCE OF MODELS TRAINED ON THE FULL DATASETS.

Dataset	Training		Testing	
	Loss	*Accuracy*	*Loss*	*Accuracy*
Visible	1.1658	34.86%	1.5637	36.67%
Infrared	1.2014	40.37%	1.3735	40.00%

It can easily be deduced that neither model performed well on the full dataset. However, comparatively speaking, the model using infrared input performed slightly better than the visible input model.

By inspection of the confusion matrix produced by the Infrared model and given in Fig. 6, out of the 30 test images, 25 were labelled as 'Early Dehydration'. This shows that the model does not discern the degree of dehydration well. The 'middle ground' provided between the two classes confuses the model's overall classification. This would likely be corrected by the use of a much larger dataset to train and test on. However, to break down where the model struggles on this small dataset being used, we need to compare the model's performance on classifying healthy and dehydrated against healthy and early dehydration. This is done in Experiments 2 and 3.

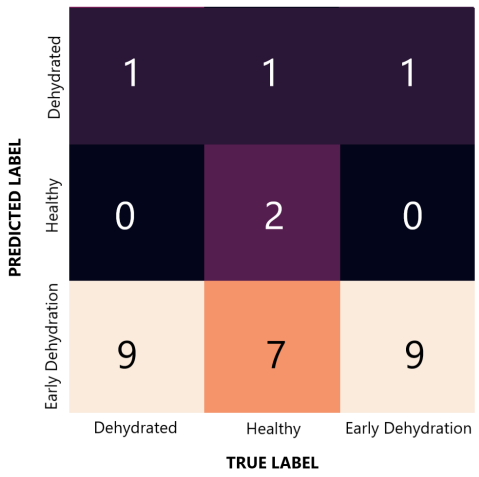

Fig. 6. Confusion Matrix of the Infrared Model

C. Experiment 2

Experiment 2 trains and tests the models produced on the infrared and visible identification datasets with the relevant parameters determined in section V-A. The results are given in Table IV.

It is observed that both of the models perform well when classifying healthy versus dehydrated leaves. This suggests that the confusion encountered by both models in Experiment 1 were caused by uncertainty around the early identification

TABLE IV
PERFORMANCE OF MODELS TRAINED ON THE IDENTIFICATION DATASETS.

Dataset	Training		Testing	
	Loss	*Accuracy*	*Loss*	*Accuracy*
Visible	0.3282	81.08%	0.3577	80.00%
Infrared	0.116	95.95%	0.0718	95.00%

day (day 5) and that by removing that class, the models both perform exceptionally better. The infrared model outperforms the visible model by an impressive 15%.

D. Experiment 3

Experiment 3 trains and tests the models produced on the infrared and visible early identification datasets with the relevant parameters determined in section V-A. The results are given in Table V.

TABLE V
PERFORMANCE OF MODELS TRAINED ON THE EARLY IDENTIFICATION DATASETS.

Dataset	Training		Testing	
	Loss	*Accuracy*	*Loss*	*Accuracy*
Visible	0.7142	54.17%	1.1818	25.00%
Infrared	0.2814	93.06%	1.5406	70.00%

Due to the poor performance of the models in Experiment 1, it was expected for both models to underperform when conducting early identification. This expected poor performance can be seen in the visible model's accuracy of 25%. What was interesting to note, and as was suggested in the literature reviewed in Section II, the Infrared model performed significantly better than the visible model with an accuracy of 70%.

This implies that NIR imaging is ideal for when early identification is required and suggests the confusion in Experiment 1 falls between early and late dehydration and not in the classification of dehydration as a whole. However, to make a single system that works accurately for multiple stages of dehydration, more data is required for training, or multiple smaller systems need to be combined, i.e. run input through the models from both Experiments 2 and 3, taking the most 'dehydrated' classification as the final classification.

VI. CONCLUSION

Overall, there was a stark difference between the various models' performances on the visible dataset. Visible input can be concluded to be only viable for classification of established dehydration and does not perform well whenever early classification is introduced.

On the other hand, the various models produced on the infrared dataset performed significantly better than the visible models did with classifying both established and early dehydration. It fell short when distinguishing between the stages of dehydration but performed well when asked to classify the dehydration regardless of its stage. This has lots of practical

implications. Like dehydration, plant diseases also cause plant stress and affect the chlorophyll levels inside the leaves, thus provides a promising avenue for future infrared research.

REFERENCES

[1] R. A. Dean, N. J. Talbot, D. J. Ebbole, M. L. Farman, T. K. Mitchell, M. J. Orbach, M. Thon, R. Kulkarni, J.-R. Xu, H. Pan, N. D. Read, Y.-H. Lee, I. Carbone, D. Brown, Y. Y. Oh, N. Donofrio, J. S. Joeng, D. M. Soanes, S. Djonovic, E. Kolomiiets, C. Rehmeyer, W. Li, M. Harding, S. Kim, M.-H. Lerbun, H. Bohnert, S. Coughlan, J. Butler, S. Calvo, L.-J. Ma, R. Nicol, S. Purcell, C. Nusbaum, J. E. Galagan, and B. W. Birren, "The genome sequence of the rice blast fungus magnaporthe grisea," *Nature*, vol. 434, no. 7036, pp. 980–986, 2005.

[2] W. Yang, J. Chen, G. Chen, S. Wang, and F. Fu, "The early diagnosis and fast detection of blast fungus, magnaporthe grisea, in rice plant by using its chitinase as biochemical marker and a rice cdna encoding mannose-binding lectin as recognition probe," *Biosensors and Bioelectronics*, vol. 41, pp. 820–826, 2013.

[3] M. M. López, E. Bertolini, A. Olmos, P. Caruso, M. T. Gorris, P. Llop, R. Penyalver, and M. Cambra, "Innovative tools for detection of plant pathogenic viruses and bacteria," *International Microbiology*, vol. 6, no. 4, pp. 233–243, 2003.

[4] D.-W. Sun, *Infrared spectroscopy for food quality analysis and control*. Academic press, 2009.

[5] A. Y. Khaled, S. Abd Aziz, S. K. Bejo, N. M. Nawi, I. A. Seman, and D. I. Onwude, "Early detection of diseases in plant tissue using spectroscopy–applications and limitations," *Applied Spectroscopy Reviews*, vol. 53, no. 1, pp. 36–64, 2018.

[6] F. Martinelli, R. Scalenghe, S. Davino, S. Panno, G. Scuderi, P. Ruisi, P. Villa, D. Stroppiana, M. Boschetti, L. R. Goulart *et al.*, "Advanced methods of plant disease detection. a review," *Agronomy for Sustainable Development*, vol. 35, no. 1, pp. 1–25, 2015.

[7] D. L. Pavia, G. M. Lampman, G. S. Kriz, and J. A. Vyvyan, *Introduction to spectroscopy*. Cengage learning, 2014.

[8] A. Zamanian and C. Hardiman, "Electromagnetic radiation and human health: A review of sources and effects," *High Frequency Electronics*, vol. 4, no. 3, pp. 16–26, 2005.

[9] K. Navulur, *Multispectral image analysis using the object-oriented paradigm*. CRC press, 2006.

[10] D. A. Sims and J. A. Gamon, "Relationships between leaf pigment content and spectral reflectance across a wide range of species, leaf structures and developmental stages," *Remote sensing of environment*, vol. 81, no. 2-3, pp. 337–354, 2002.

[11] J. S. Amthor, "From sunlight to phytomass: on the potential efficiency of converting solar radiation to phytoenergy," *New Phytologist*, vol. 188, no. 4, pp. 939–959, 2010.

[12] G. A. Blackburn and J. G. Ferwerda, "Retrieval of chlorophyll concentration from leaf reflectance spectra using wavelet analysis," *Remote Sensing of Environment*, vol. 112, no. 4, pp. 1614–1632, 2008.

[13] G. A. Carter and A. K. Knapp, "Leaf optical properties in higher plants: linking spectral characteristics to stress and chlorophyll concentration," *American journal of botany*, vol. 88, no. 4, pp. 677–684, 2001.

[14] H. Xu, Y. Ying, X. Fu, and S. Zhu, "Near-infrared spectroscopy in detecting leaf miner damage on tomato leaf," *Biosystems Engineering*, vol. 96, no. 4, pp. 447–454, 2007.

[15] B. S. Ausmus and J. W. Hilty, "Reflectance studies of healthy, maize dwarf mosaic virus-infected, and helminthosporium maydis-infected corn leaves," *Remote Sensing of Environment*, vol. 2, pp. 77–81, 1971.

[16] T. J. Malthus and A. C. Madeira, "High resolution spectroradiometry: spectral reflectance of field bean leaves infected by botrytis fabae," *Remote Sensing of Environment*, vol. 45, no. 1, pp. 107–116, 1993.

[17] C. Bravo, D. Moshou, J. West, A. McCartney, and H. Ramon, "Early disease detection in wheat fields using spectral reflectance," *Biosystems Engineering*, vol. 84, no. 2, pp. 137–145, 2003.

[18] W. E. Riedell and T. M. Blackmer, "Leaf reflectance spectra of cereal aphid-damaged wheat," *Crop Science*, vol. 39, no. 6, pp. 1835–1840, 1999.

[19] P. Cunningham, M. Cord, and S. J. Delany, "Supervised learning," in *Machine learning techniques for multimedia*. Springer, 2008, pp. 21–49.

[20] A. Krizhevsky, I. Sutskever, and G. E. Hinton, "Imagenet classification with deep convolutional neural networks," *Communications of the ACM*, vol. 60, no. 6, pp. 84–90, 2017.

[21] K. He, X. Zhang, S. Ren, and J. Sun, "Deep residual learning for image recognition," in *Proceedings of the IEEE conference on computer vision and pattern recognition*, 2016, pp. 770–778.

[22] B. D. Ripley, *Pattern recognition and neural networks*. Cambridge university press, 2007.

[23] O. Russakovsky, J. Deng, H. Su, J. Krause, S. Satheesh, S. Ma, Z. Huang, A. Karpathy, A. Khosla, M. Bernstein *et al.*, "Imagenet large scale visual recognition challenge," *International journal of computer vision*, vol. 115, no. 3, pp. 211–252, 2015.

[24] T. O'Malley, E. Bursztein, J. Long, F. Chollet, H. Jin, L. Invernizzi *et al.*, "Keras tuner," https://github.com/keras-team/keras-tuner, 2019.

[25] L. Li, K. G. Jamieson, G. DeSalvo, A. Rostamizadeh, and A. Talwalkar, "Efficient hyperparameter optimization and infinitely many armed bandits," *CoRR, abs/1603.06560*, vol. 16, 2016.

Louise Poole is a student at Rhodes University completing her final year of MSc in Computer Science. Interests: image processing and machine learning.

Dane Brown obtained his PhD and is a Senior Lecturer at Rhodes University. Interests: image processing, machine learning, security and GPGPU.

James Connan is a Senior Lecturer at Rhodes University. Interests: image processing and machine learning.

Core Network Technologies

Overview of Resource Allocation in Imperfect D2D Cooperation in LTE-Advanced Pro Systems

Sarisha Padayachee, Tshidiso Marabutse, Olutayo Oyerinde

School of Electrical and Information Engineering, University of the Witwatersrand, Johannesburg, South Africa

[1]2287216@students.wits.ac.za

[2]0710218J@students.wits.ac.za

[3]Olutayo.Oyerinde@wits.ac.za

Abstract—**This paper focusses on providing an overview of resource allocation in imperfect device-to-device (D2D) cooperation in LTE-Advanced Pro Systems. The various characteristics and interworking of D2D cooperation and resource allocation are discussed. The benefits of D2D cooperation are increased throughput, spectral efficiency, reduced latency and power efficiency. The resource allocation algorithm usually aims to improve one or more of these objectives, it can also aim to minimize interference and ensure fairness is achieved between cellular users and D2D pairs. A criterion is tabulated to evaluate the investigated algorithms to determine the most effective one. Seven resource allocation algorithms each with their specific objective were investigated and analysed based on the tabulated criteria. The algorithms investigated are simulated in LTE-Advanced (LTE-A) and LTE-Advanced Pro (LTE-A Pro) networks. The Weighted Efficiency Interference-Aware (WEIA) algorithm met most of the criterion requirements for effective resource allocation for D2D cooperation and was simulated in an LTE-A network. Therefore, it is proposed for resource allocation in LTE-A Pro networks for imperfect D2D cooperation.**

***Keywords*— LTE-Advanced Pro, Resource Allocation, D2D.**

I. INTRODUCTION

Research conducted by the 3rd Generation Partnership Project (3GPP) to improve Long Term Evolution (LTE) from Release 8 is presented in [1]-[3], and the milestones are the Release 12 of LTE-Advanced and the publishing of LTE-Advanced Pro in Release 14 as 5G intermediary and termed 4.5G. 4.5G is a more energy efficient and has flexible spectrum utilization than 4G. This is achieved through efficient bandwidth algorithms such as multicarrier load distribution technique that reduces signalling loading by differentiating handovers in idle and connected modes. Massive Carrier Aggregation (MCA) is used for flexible channel allocation and wider bandwidth control and together with massive MIMO (Multiple Input Multiple Output) these techniques improve 4.5G data rates. 4.5G data rates will reach 3Gpbs, increased carrier bandwidth of 640MHz and reduced latency of 2ms. Like the previous LTE-Advanced, 4.5G is managed by the Software Defined Networks (SDN) and Self Organizing Networks (SOA) platforms, for agility and unified framework control.

With Release 12 of LTE-Advanced came the concept of Device-to-Device (D2D) communication as presented in [4], [5]. D2D has become very popular due to it providing increased throughput and spectral efficiency. It can also save power in transmission from the base station due to the shorter range of communication.

One of the objectives of 5G is to roll out Machine Type Communications (MTC) and Vehicle to Everything (V2X) communications. D2D communication in the LTE-A Pro network is the foundation upon which MTC and V2X will be enhanced.

However, D2D communication is not without its challenges. In imperfect D2D the channel state is not always known by the base station due to it being bypassed in some cases. There is also limited bandwidth and power in cooperative links. If there is not an efficient method of allocating cellular resources, it can lead to network congestion and interference between the cellular users and the D2D pairs. To effectively enhance MTC and V2X communication, resource allocation needs to be optimized due the imperfect nature of the channel and limitations in bandwidth and power. This is what motivates the research conducted in this paper.

This paper provides an insightful overview of D2D Cooperation and Resource Allocation in relation to D2D. A criterion is tabulated to evaluate resource allocation algorithms. Seven resource allocation algorithms are investigated and analysed using the criterion for D2D cooperation in imperfect conditions. The algorithms investigated are simulated in LTE-A and LTE-A Pro. The rest of the paper is organized as follows. Section II describes D2D cooperation, Section III focuses on resource allocation techniques, algorithms and analysis of the most efficient investigated algorithm. Conclusions are drawn in Section IV.

II. DEVICE-TO-DEVICE (D2D) COOPERATION

D2D communication is defined in [6], [7] as the capability of mobile devices within proximity to one another to establish direct links of communication with or without the use of the base station (eNodeB). D2D communication offers improvement in energy efficiency, throughput, latency and enhances spectral efficiency as well as the overall system capacity.

D2D can use licensed spectrum (Inband) or unlicensed spectrum (Outband). For Inband there are two types of communication, underlay and overlay as shown in Fig. 1. In underlay the links are set up using the cellular spectrum, whereas for overlay a dedicated portion of the available spectrum is used for D2D communication. Underlay has

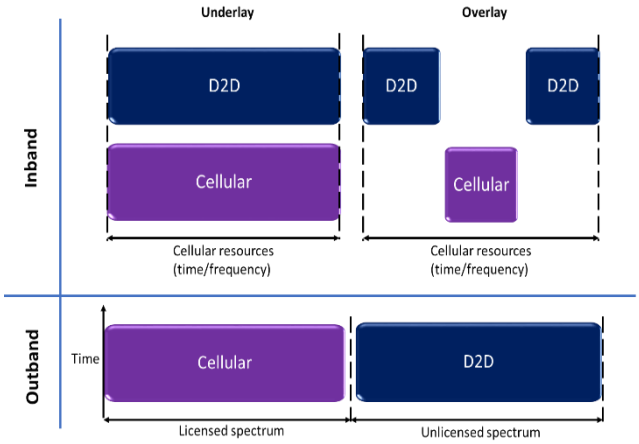

Figure 1: Comparison of D2D types [7]

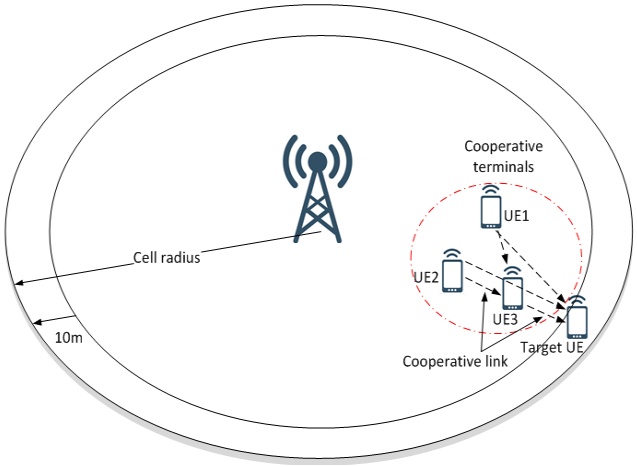

Figure 2: D2D Cooperation [5]

interference between the D2D pairs and the cellular users (CUs) whereas overlay does not have interference but has no spectral efficiency gain. Outband experiences no interference with cellular users as Inband does, but it requires an additional radio interface (e.g., Wi-Fi Direct, ZigBee or Bluetooth) to perform the coordination.

D2D communication can be used in the format of direct communication between UE controlled by the base station or by the devices themselves and it can also be used in the format of user equipment (UE) relaying information to another UE and can be controlled by either the base station or the devices themselves. In the case of relaying the aim is to improve the system performance within the last 10m of a cell site.

The relaying of information from one device to the target device requires cooperation between devices, as shown in Fig. 2. In this scenario UE1 is relaying information to UE3 as well as the target UE, UE2 is relaying information to UE3 and the target UE and UE3 is relaying its inputs from UE1 and UE2 to the target UE.

D2D communication can be carried out in the uplink, downlink or in both. In the case of uplink D2D communication the base station experiences interference from the D2D users but can be managed using advanced digital signal processing at the base station. D2D users are also affected by CUs. When D2D communication is in the downlink the D2D users are affected by interference from CUs and D2D users also negative affect the CUs reception. Due to some regions implementing regulatory restrictions on the reuse of downlink resource most studies investigate uplink resource utilization for D2D communication.

In cooperation the transmission is divided into two time slots. In the first time slot the base station transmits to both the target UE and the D2D relay user. If it is found that the cooperative link is beneficial then the D2D device uses a superposition coding scheme to transmit to the target UE in the second time slot. With the superposition coding scheme, the D2D users' own signal (x) and the signal for the target CU (y) are linearly combined and then transmitted as

$$t = ax + by \quad (1)$$

where a and b are constants and t is the transmitted output.

For cooperation to be beneficial to the target UE the achievable rate with cooperation must be greater than that of the achievable rate without cooperation. For it to be beneficial for the D2D user the power spent on transmitting the signal to the target UE must be minimized.

Mobile devices in the D2D network use batteries which are limited power sources and must be preserved. Device transmit mode selection is presented in [8], [9] that is available via the eNodeB and on devices. D2D mode selection also preserves transmit power of the eNodeB when a cellular connection is handed over to a D2D link for cellular offloading.

To ensure efficient resource allocation the number of relays and relay selection needs to be optimized. With base station cooperation the X2 interfaces between base stations, and the S1 interface between the base station and the core network make use of optical fibre or Gigabit Ethernet which provides enough bandwidth for transmission.

With D2D cooperation the link is now wireless which has limited bandwidth and power capabilities. One of the key challenges with D2D cooperation underlay is radio resource allocation to ensure there is no interference with the cellular users. These factors are what we define as imperfect D2D communication

III. RESOURCE ALLOCATION

A. *Overview*

Resource allocation algorithms are used to allocate throughput and power resources efficiently in D2D. For an optimised D2D network the UE are assumed to have capabilities of transmit mode selection and the eNodeB must control the transmission power of D2D links to meet the minimum interference for the minimum required quality of service (QoS). There are three types of resource allocations for D2D communications that have been researched: centralized, distributed and hybrid and these are defined in [6], [8]-[10].

Centralized: In this mode the radio resources are coordinated by the eNodeB (LTE base station) via UE1 request.

When the target UE requests D2D communication, the UE1 sends a request to the eNodeB to set up a session. The Mobility Management Entity (MME) and Non-Access Stratum (NAS) configures the signalling parameters and setup up a D2D bearer to be used by UE1 and the target UE. The second alternative is when the Packet Data Network Gateway can identity two IP source addresses that share the same eNodeB, and if a D2D link provides higher data rate and UE1 has enough transmit power, then a seamless handover from the cellular uplink to D2D link takes place.

Distributed: This an autonomous scenario applicable for broadcast of out of coverage UE. Resource pool for scheduling is pre-configured on the devices. UE1 shares the configured resources with the target UE during transmission.

Hybrid: The eNodeB allocates the initial resource but the communication is carried by the UE. This mode allows for centralised control of the resources and interference but also reduces eNodeB signal overheads as it allows autonomous communication.

The network model for a resource allocation methodology can be an instantaneous or statistical approach, and this is defined in [7]. The instantaneous approach makes use of link distances and channel gains to formulate the problem. This methodology assumes that the base station has all the channel state information for decision making. The decisions in terms of power and channel allocations and criteria for mode selection are made instantaneously based on the information at the base station. This methodology is mainly used for understanding the potential gains in network performance but comes with high overheads and computational complexity. The statistical methodology uses statistical information, assumed to be valid for longer time spans, on the distribution of users, channel gains and base stations. This methodology is also used for optimal decision making.

Once the network model and the methodology is chosen the algorithm for resource scheduling is used to solve the problem. The model and the algorithm are usually then put through simulation in order to test and verify its validity.

In [10] LTE networks use three resource scheduling algorithms which are Round Robin (RR), Maximum Rate (MR) and Proportional Fair (PF).RR schedules resource blocks to all users at the same time, and the result is users with poor Channel State Information (CSI) cannot receive and transmit. Transit power of the relay devices is also wasted. MR uses CSI strength as a priority criterion for recipients of resources. The result is also that users with poor CSI are at a disadvantage. PF is the algorithm that balances high throughput and fair allocation. This is achieved by computing the average latency between RR and MR and using the moving average throughput at the average latency for all the users.

In this overview the following requirements are defined for the most effective algorithm as:

- Spectral efficiency
- Improves throughput
- Minimizes overall interference
- Minimizes transmission power
- Improves latency
- Fair resource allocation between CUs and D2D pairs
- Complexity

B. Algorithms

There has been significant research into various resource allocation methods for imperfect D2D cooperation in LTE-A but not many specifically for LTE-A Pro. Seven resource allocation algorithms are investigated and documented as follows.

A greedy heuristic scheduling algorithm is proposed for LTE-A in [10] The simulation parameters were a single hexagonal cell of 500 m, omni-directional single-input-single-output antenna, and bandwidth of 10 MHz, the D2D receivers' range was varied from 5 m up to 50 m in steps of 5m around the D2D transmitters. The access scheme for the uplink was Single Carrier-Frequency Division Multiple Access (SC-FDMA) and downlink was Orthogonal Frequency Division Multiple Access (OFDM). This algorithm makes use of knowledge of the channel gains between the CUs and the base station (eNodeB), as well as the interfering link gains between D2D users and the CUs and between eNodeB and D2D users to perform resource allocation for D2D pairs. For every sub-frame, the CU that has a high channel quality indicator shares its resource blocks with the D2D pair which causes minimum interference to it. This algorithm demonstrated an increase in both throughput and spectral efficiency whilst maintaining QoS for the CU and D2D users.

A second algorithm is also presented for LTE-A in [10] termed proportional fair. The simulation parameters were the same as the greedy heuristic scheduling algorithm except the bandwidth changed to 5 MHz and the D2D receivers' range was varied from 10 m up to 100 m in steps of 10 m around the D2D transmitters. With this algorithm the scheduling of resources for CUs is performed at the base station and these resources are reused for the D2D users. The CUs get the minimum required rate to maintain their QoS. Maximum weight bipartite matching (MWBP) was used to allocate single as well as multiple resource blocks to D2D users. Excess signal-to-interference-plus-noise ratio (SINR) of CUs are used to allocate power to D2D pairs. A high throughput and fairness for D2D users was achieved.

Similarly, [12] proposed a resource allocation method based on weighted efficiency interference-aware (WEIA) mechanism for LTE-A. The algorithm was evaluated by averaging 500 independent experiments. The main parameters were system area of 500 m, transmit distance of 50 m, 50 mW transmit power of CUs and sub-channel bandwidth of 100 kHz. A power control procedure is implemented to limit the interference from D2D users to a specified threshold. The transmit power of the D2D pairs are determined using a distributed power control method and the D2D pairs are assigned to clusters (user sets of resource blocks) based on the threshold of SINR. The weighted efficiency interference-aware algorithm is used to optimize the matching of D2D pairs and resource blocks. With this algorithm each D2D pair is weighted based on the SINR to compete for the priority of resource blocks fairly. The simulated results show that the

SINR of CUs performs well when D2D pairs reuse the resource blocks. The system throughput increases as the number of D2D users increases. It outperformed the alternative schemes of interference-aware and random allocation in terms of throughput.

In [5], a novel resource allocation algorithm is proposed. They aimed to maximize the LTE-A Pro systems achievable rate by using a three-step process. The first step is optimizing the artificial noise vector. The second step is to optimize the link resource allocation vector. The last step is to optimize the UE group and subcarrier. The simulation first analyses the influence of the cooperative link. The parameters used were: 2 eNodeBs with 10 users uniformly placed around them. The antenna configuration for users was 2 and the moving speed of the users was set to 1 m/s. Other parameters were set to standard 3rd Generation Partnership Project, Technical Report 36.942 which details the system scenarios for radio transmission and reception. The simulation results showed a comparison between the proposed algorithm with random allocation method, distance aware allocation and proportional fairness algorithm using a 20MHz cooperative link. The proposed algorithm showed a 7% gain in throughput when the cumulative distribution function (CDF) is 75% and 2% gain when the CDF is 50% over the distance aware allocation which had the second-best performance. In terms of spectrum efficiency, the proposed algorithm outperformed the distance aware algorithm.

For link capacity below 4 Mbps the spectrum was 1 bit/Hz greater than the distance aware algorithm, for 4 Mbps they were equal, but above 4 Mbps the proposed algorithm was able to increase in spectral efficiency where the distance aware method plateaued. This was due to the compress and forward method employed as opposed to transmitting the original data.

Another method of matching based two-timescale resource allocation is proposed for LTE-A Pro by [13]. The two-timescale resource allocation was proposed in order to reduce overhead. The pairing between CUs and D2D users is determined at a long timescale and the cooperation policy to allocate transmission time for the D2D link and CU link is done at a short timescale. The CSI is used for the long timescale pairing and the instantaneous CSI is used for the short timescale transmission time. A matching game-based method is used to solve the two-timescale resource allocation problem and resulted in an optimal cooperation policy to characterize the long-term payoff for each potential pairing of CU and D2D. For their simulation, they considered the scenario where the eNodeB is deployed in the cell centre with the radius of the cell set to 500 m. The CUs are distributed uniformly at the cell edge and the D2D pairs are uniformly distributed in the area with a distance of 200 m to 400 m from the eNodeB. The noise power was set to -100 dBm, transmit power of the CU and D2D transmitters was 20 mW, the distance of the D2D link was uniformly distributed in between 10 and 30 m. The sum rate of D2D pairs versus the number of D2D pairs is evaluated in comparison with other schemes and the performance is near the optimal performance scheme. Their proposed scheme also had very similar outage percentages as the optimal scheme.

A game theory approach is considered in [4] for resource allocation in LTE-A. In the system model employed the CUs require permission form a single base station for transmission. The D2D pairs also need to request permission from the base station. A payment method is used for resource allocation, where the base station determines the price for resource parameters with the goal of optimizing efficiency as its profit. The UEs can accept or decline the service based on the base stations price. This study also examines the scenario of when the channel quality is unknown as is the case in imperfect conditions. In this scenario the UEs are allowed to lie about their channel quality, hence the base station does not know their exact channel qualities. A linear search algorithm is used to find the optimal profit by comparing the base station profit with each possible device. In this simulation they used a. For their simulation the efficiency of the system was analysed by comparing the performance between the optimal situation and the scenario under Unknown Quality Base Station-centric game. In this simulation they used the satisfactory weighting factor of 1000, a cost weighting factor of 5, 19 cells with 150 UEs and 75 D2D pairs in the central cell. They also account for inter-cell interference by using calculated values for $SINR_{cellular} = 19.5361\,dB$ and $\sigma_{SINR} = 10\,dB$. From the simulation results the system efficiency is very close to that of the perfect condition scenario where the channel state information is known.

The hybrid scheme, [14], resource allocation algorithm combined the centralised interference mitigation and distributed power allocation algorithms. This is also a three-step process that reduced the interference and transmit power in an LTE-A. The CU interference in the downlink is cancelled using multi-cell cooperation techniques. Then the D2D pair interference is reduced by controlling the transmit power of the channel. Lastly the power distribution is modelled on game theory to achieve optimised power for the UE. The simulation parameters used were: the cell radius is 1000 m, the intercell distance is 1800 m, the maximum D2D transmission distance is 50 m, the maximum transmission power of CUs is the same as D2D pairs, i.e. 200 mW (23 dBm), the constant circuit power is 100 mW (20 dBm), and the thermal noise power is 10^{-7} W, the number of cells is 6, the number of CUs and D2D pairs in each cell is 10 and the power amplifier efficiency is 35%. The simulated results showed that energy efficiency performance increased by 71% for CUs and 65% for D2D pairs when QoS requirement was 0.7 bits/s/Hz. The simulation also measured the infeasibility ratio (how infeasible it is to achieve the QoS requirement) against the QoS requirement. The hybrid scheme achieved an infeasibility ratio of almost zero for all the QoS requirements set, which indicates it is very feasible.

C. Analysis

From the schemes that were investigated, each had their own specific objectives. From the resource allocation methods investigated the greedy heuristic algorithm focussed most on increasing throughput and spectral efficiency and whilst the QoS of the CUs is maintained, the algorithm is unfairly focussed on the D2D users.

The proportional fair algorithm can potentially be used with any cellular resource allocation scheme and can adapt to time

TABLE I
COMPARISON OF ALGORITHMS

Algorithm	Spectral Efficiency	Interference	Throughput	Transmit Power	Latency	Fair Distribution	Complexity
Greedy	Increased	Minimised	Increased	N/A	N/A	Unfair	Medium
Proportional Fair	Increased	N/A	Increased	Controlled	N/A	Fair	High
WEIA	Increased	Minimised	Increased	Controlled	N/A	Fair	Low
Novel 3-Step	Increased	N/A	Maximised	N/A	N/A	N/A	Low
2 Timescale	Increased	N/A	Near optimal	N/A	Reduced	Fair	Low
Game Theory	Increased	Considered	N/A	N/A	N/A	Fair	Low
Hybrid Scheme	Increased	Minimised	N/A	Controlled	N/A	N/A	High

and location varying channels. It can achieve a very high throughput increase from the existing LTE throughput and good fairness between CUs and D2D users. The simulations were performed using an LTE-A model and not necessarily an LTE-A Pro but could possibly provide similar results.

The WEIA method is simulated for an LTE-A, but much fewer D2D pairs are introduced into the simulated network. WEIA shows a promising increase in throughout of the system as the D2D pairs increase. It is also stable over various parameters of channel states and users. It can increase spectral efficiency, minimise interference and control the transmit power whilst ensuring the resource allocation is fair.

The matching based two-timescale resource allocation looks at reducing the overhead incurred for pairing CUs and D2D pairs in a short timescale, which is applicable to LTE-A and LTE-A Pro network. This scheme does not look at the overall network throughput but instead the sum rate of D2D pairs which was found close to optimal performance.

The novel 3-step resource allocation method is simulated in LTE-A Pro system and is the closest to the focus of this paper, as it also factors in the limited capacity of the cooperative link as found in real scenarios. It shows an increase in spectral capacity for link capacity over 4Mbps and a 7% gain in throughput.

The game theory approach for LTE-A takes into consideration the imperfect D2D communication scenario of when the channel conditions are not always known. It can nearly match the resource utilization efficiency of that where the channel state is known and is able to allocate resources fairly.

Lastly, the hybrid scheme can increase spectral efficiency while minimising interference and transmit power in an LTE-A network.

From the analysis a comparison between each algorithm and the defined requirements for the most effective algorithm is tabulated in Table I. Complexity of the algorithms was determined based on the computation processing to be performed by the eNodeB. The WEIA algorithm meets the highest amount of the requirements for effective resource allocation for D2D cooperation. For future improvements it should be simulated in LTE-A Pro and 5G networks and aim to decrease latency.

IV. CONCLUSION

The paper presents an overview of resource allocation in an imperfect D2D cooperation. D2D communication can provide increased throughput, spectral efficiency, reduced latency and power efficiency. The challenges of D2D are that the channel state is not always known by the base station and there is limited bandwidth and power in cooperative links. If there is no efficient method of allocating cellular resources, it can lead to network congestion and interference between the cellular users and the D2D pairs. Seven resource allocation algorithms, each with their own specific performance objectives, were investigated and analysed on a tabulated criterion. The most effective algorithm was found to be the Weighted Efficiency Interference-Aware as it meets six out of seven of the criteria. It was simulated in an LTE-A network and is the proposed algorithm for resource allocation in an LTE-A Pro network in imperfect D2D coordination. For future work it should be optimized to decrease latency in LTE-A Pro and 5G network.

REFERENCES

[1] E. H. S. Haidine A, "LTE-A Pro (4.5G) as Pre-Phase for 5G Deployment: Closing the Gap Between Technical Requirements and Network Performance," in 2016 International Conference on Advanced Communication Systems and Information Security, Marrakesh, 2016.

[2] S. K. Routray S.K., "4.5 G: A Milestone Along The Road To 5G," in IE2016 International Conference on Information Communication and Embedded Systems (ICICES), Chennai, 2016.

[3] R. Jain, "Introduction of LTE-Advance Pro (4.5)," Washington University, Saint Louis, 01 02 2019. [Online]. Available: https://www.cse.wustl.edu/~jain/cse574-18/ftp/j_19lap.pdf. [Accessed 12 05 2020].

[4] B.-Y. Huang, S.-T. Su, C.-Y. Wang, C.-W. Yeh and H.-Y. Wei, "Resource Allocation in D2D Communication – A Game Theoretic Approach," in 2014 IEEE International Conference on Communications Workshops, Sydney, 2014.

[5] Y. Gao, X. Li, H. Ao, Q. Zou, W. Zhou, L. Yi, S. Cheng, Z. Xiong and K. Wang, "A Novel Resource Allocation in Imperfect D2D Cooperation in LTE-Advanced Pro Systems," in 2016 IEEE 7th Annual Information Technology, Electronics and Mobile Communication Conference, Vancouver, 2016.

[6] P. Gandotra and R. K. Jha, "Device-to-Device Communication in Cellular Networks: A survey," Journal of Network and Computer Applications, vol. 71, pp. 99-117, 2016.

[7] S. Shalmashi, "Device-to-Device Communications for Future Cellular Networks: Challenges, Trade-Offs, and Coexistence," KTH Royal Institute of Technology, Stockholm, 2015.

[8] S. Lopez, "An Overview of D2D in 3GPP LTE Standard," Orange Labs. Indo-French Workshop on D2D Communications for 5G and IoT Networks, 21 June 2016. [Online]. Available: http://d2d-4-5g.gforge.inria.fr/Workshop-June2016/slides/Overview_LTE_D2D.pdf. [Accessed 10 05 2020].

[9] K. Doppler, M. Rinne, C. Wijting, C. Ribeiro and H. K, "IEEE Communications Magazine," Device-To-Device Communication As An Underlay To LTE-Advanced Networks, vol. 47, no. 12, pp. 42-49, 2009.

[10] I. Mondal, “Resource Allocation for Device-to-Device Communication Underlaying Cellular Network,” INDIAN INSTITUTE OF TECHNOLOGY BOMBAY, Bombay, 2016.
[11] P. Phunchongharn, E. Hossain and D. Kim, “Resource Allocation For Device-To-Device Communications Underlaying LTE-Advanced Networks,” IEEE Wireless Communications, vol. 20, no. 4, pp. 91-100, 2013.
[12] J. Li, X. Zhang, Y. Feng and K.-C. Li, “A Resource Allocation Mechanism Based on Weighted Efficiency Interference-Aware for D2D Underlaid Communication,” Sensors, vol. 19, no. 14, p. 3194, 2019.
[13] Y. Yuan, T. Yang, Y. Hu, H. Feng and B. Hu, “Matching Based Two-Timescale Resource Allocation for Cooperative D2D Communication,” in 2019 11th International Conference on Wireless Communications and Signal Processing, Xi'an, 2019.
[14] Z. Zhou, M. Dong, Z. Chang and B. Gu, “Combined Centralized and Distributed Resource Allocation for Green D2D Communications,” in 2015 IEEE/CIC International Conference on Communications in China, Shenzhen, 2015.

Sarisha Padayachee completed her Bachelor of Science in Electronic Engineering from University of Kwa Zulu-Natal in 2012 and has completed a Master of Engineering (Professional) degree from the University of the Witwatersrand in 2020. She is a Specialist in Strategy, Alignment and Standards at Openserve, a division of Telkom SA SOC Ltd.

Tshidiso Marabutse completed his Bachelor of Science in Electrical Engineering in 2012 and is enrolled for a Master of Engineering (Professional) degree from the University of the Witwatersrand. He works as an Operations Specialist in Network Engineering and Build for Openserve, a division of Telkom SA SOC Ltd.

Numerical Solutions as Applied to Quantum-Inspired Electromagnetic Problem in Photonic and Plasmonic Devices: A Conservative Finite Difference Method Standpoint

Lateef Adesola Akinyemi*, Sunday Oladayo Oladejo†, Stephen Obono Ekwe ‡
*†*Department of Electronic and Computer Engineering, Lagos State University, Epe Campus, Nigeria*
†*Department of Electrical Engineering, University of Cape Town, Cape Town, South Africa*
[1]lateef.akinyemi@lasu.edu.ng; ltfaki001@myuct.ac.za;
[2]oldsun002@myuct.ac.za; [3]ekwste001@myuct.ac.za;

***Abstract*—Schrödinger equation (SE) can be cast in differential form. For solving real problems, the differential equation needs to be discretised and solved numerically. Although the standard finite difference method (SFDM) is relatively straightforward to implement, both the boundary element method (BEM) and finite element method (FEM) are more tractable in discretising uneven geometry. The shortcoming of SFDM, BEM, and FEM is that they neither preserve nor conserve some of the features of the original operator which is remedied to ensure these features are well-taken care of by employing conservative finite difference method (CFDM). The CFDM as applied to the Schrödinger equation, for the first time, promises to have opened up avenues for further research in the field of small-scale (nano) photonic and plasmonic device applications for future networks.Hence, thhe CFDM provides a straightforward-to-execute approach for a big class of real-life challenges in biomedical engineering, science-based problem, computational engineering and telecommunications engineering. Hence, by construction, the CFDM preserves and conserves the properties such as energy, different other laws, frequency-dependent dielectric function, susceptibility, refractive index of electronic, photonic, and plasmonic devices that work "logically" instead of a geometrically rectangular grid-system. This scheme is premised on a support operator originally designed by Favorskii et al. In this present study, we demonstrate the application of CFDM to electromagnetic field challenges in photonic and plasmonic devices. Furthermore, this work examines the optical properties of metallic materials of a one-and two-dimensional geometry. To this end, the Schrödinger equation is employed and solved numerically using CFDM.**

***Index Terms*—Schrödinger equation, CFDM, Discretisation, Photonics, Plasmonic**

I. Introduction

The extreme reduction of photonic, nanophotonic, plasmonic and electronic devices in recent times needs the incorporation of energy occurrences (phenomena) in modelling and simulation procedures. This study aims to create a stage for the numerical solution as applied to electromagnetic-inspired problems in photonic and small-scale plasmonic devices. The fundamental of this work is the application of conservative finite difference method (CFDM) to compute optical properties such as frequency-dependent dielectric function employed in nanophotonics and nanoplasmonic fields of study with quantum-based models for these properties.

Furthermore, it has been studied in the literature [1] in which Maxwell's equation (ME) can be modelled in differential or, differently, diverse corresponding integral forms [2]. In this regard, the CFDM scheme has been employed analytically to demonstrate its significance to provide solutions to surface acoustic wave (SAW) but the issue of numerical solution has not been examined to our best of knowledge . To solve realistic or real problems, the integral or differential equation for ME must be discretised and solved same way for the Schrödinger equation (SE). Although the standard finite difference method better known as finite difference method (SFDM) [3], [4] is relatively and reasonably easy to realise. The FEM and BEM are more tractable in discretising unpredictable or rough geometry than SFDM. Then, numerous questions emerge such as: Is it feasible to merge the straightforwardness of SFDM execution with the tractableness of BEM or FEM? What happens regarding the conservativeness of basic features in the primary continuum paradigm after the discretisation process must have taken place? Additionally, to be more specific, to what extent or degree can the gradient, divergence , curl, conservation of energy and so forth be preserved or kept in distinct variant of the original continuum problem?

Similarly, it is our desire and goal to understand how the solidity, lustiness, robustness and ruggedness of the numerical solutions without impacting or undermining the flexibility and straightforwardness of the discrete scheme. Thus, the CFDM offers compelling and definite answers to the aforestated questions and more importantly, a straightforward-to-execute scheme for a big class of practical challenges or real-life cases especially computational engineering, biomedical engineering, and bio-inspired research. In addition, adequate application of CFDM preserves the hermiticity of Hermitian operators after being discretised. This capability of designing and developing conservative numerical scheme is outstanding feature, which has not been duly appreciated in computational community, partially owing to its comparatively cumbersome implementation. It relies on the method of support-operators

initially developed and designed [5], [6]. CFDM employs the integral relationships which include operators and their corresponding adjoints. Hence, to utilise the CFDM for photonic and plasmonic problems, it is necessary to construct adjoint operators of different operators that emerge from the governing equations using Schrödinger equation [5], [6]. In the present study, it is demonstrated that the CFDM technique is an ideal and good candidate to proffer solutions to well-posed small-scale photonic and plasmonic problems by computing specifically the frequency-dependent dielectric function based on quantum models such as Drude, Lorentz, and so on [7]–[10].

In [7], [8], the aims were to go beyond solving simple and complex boundary value problem. Alternatively, the following objectives were implemented: 1) Introduction of Sinc functions has been applied to ensure numerical well-posedness of the computation and robustness; 2) Derivation of closed form expressions derived in detail for frequency-dependent dielectric function and matrix elements; 3) The calculations of eigenpair of the underlying canonical and associated perturbed quantum system are calculated and employed for the computation of dielectric function; and 4) Galerkin scheme employed to dicretise the boundary value problem.

In this work, we adopt the CFDM to further solve this similar problem with a different scheme. Nevertheless, a considerable effort has been initiated to make the current work self-reliant and self-sufficient. In spite of the fact that most formulae in this paper have been derived in closed-form, inconveniently. To facilitate the discussion and understanding, appropriate ideas, explanations and references have been cited in this work.

The contributions of this paper are as follows:

- A conservative finite difference method is designed, formulated and applied to solve photonic- and plasmonic-based real life problem using numerical techniques.
- A customised scheme is developed to solve any regular and irregular geometries of interest to compute the optical properties of the materials used in small-scale plasmonic devices.
- Numerical results are presented which evaluate the performance of the method (CFDM) employed and compared with the SFDM in this study.

II. Theory of Schrödinger Equation

Numerical modelling and simulation of quantum mechanical-based devices remains ongoing issue in the field of photonics, electronics, and plasmonics as the miniaturisation of devices continues unabatedly. One of the underlying problems in this procedure is to calculate the intial states for the simulation. To this end, the solutions of the time-dependent Schrödinger equation must be obtained [7],

$$H\Psi(r,t) = i\hbar\frac{\partial}{\partial t}\Psi(r,t), \tag{1}$$

here,$\Psi(r,t)$, $\hbar$, H, and i represent the time-dependent eigenstate, reduced planck constant, Hamiltonian operator, and the imaginary unit, respectively. Further, the solutions to the time-independent Schrödinger equation are expressed as

$$H\psi(\mathbf{r}) = E\psi(\mathbf{r}), \tag{2}$$

where ψ, E, and $\mathbf{r}$ denote the time-independent eigenfunction, the energy, and the position vector comprising all the coordinates in such a way that $\mathbf{r} = (\mathbf{x_1}, \mathbf{x_2}, \cdots)$, respectively.

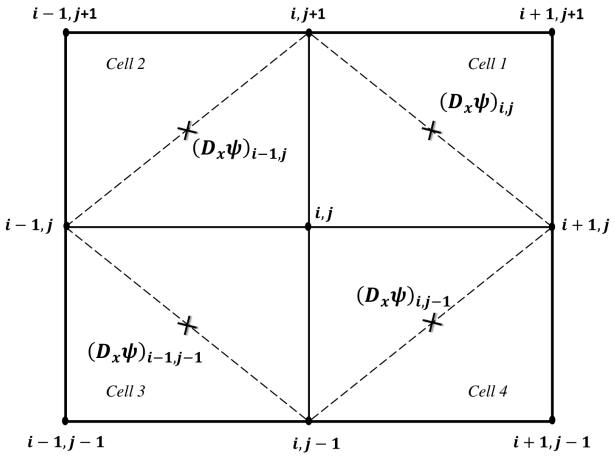

Fig. 1. CFDM Discretisation geometry

A. Discretisation of 1-D Boundary Value Problem Applying CFDM

To typify the utilisation of CFDM, consider the 1-D Schrödinger equation with vanishing potential energy term, $V(x)$; i.e., (2) can be recast as

$$-\frac{\hbar^2}{2m}\nabla^2\psi(x) = -\frac{\hbar^2}{2m}\frac{d^2}{dx^2}\psi(x) = E\psi(x), \tag{3}$$

where m, $\hbar$, and $\psi(x)$ represent the mass of the particle, planck constant, and wavefunction of the particle, respectively.

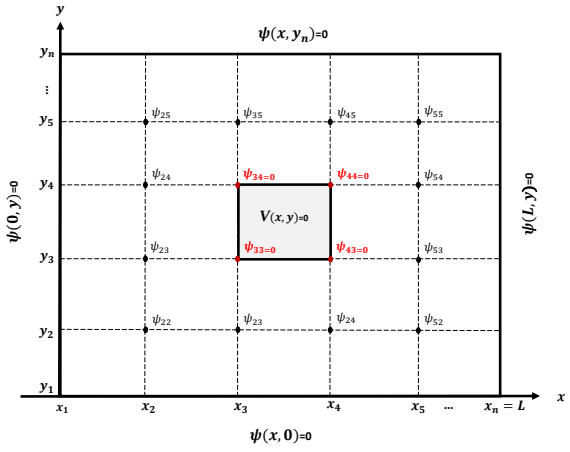

Fig. 2. The grid used for the implementation of the SFDM and CFDM subject to Dirichlet boundary conditions

Furthermore, to discretise this ordinary differential equation (ODE), the following steps must be taken into consideration.

To emphasise some of the outstanding characteristics of CFDM, the expression for $\partial/\partial y$ will be provided [6].

- Construct an expression for the first-order derivative using trapezoidal rule for Green's formula for x-axis or y-axis, as the case may be; $\frac{\partial \psi}{\partial x} = \frac{\oint_c \psi \, \partial y}{A}$, $\frac{\partial \psi}{\partial y} = -\frac{\oint_c \psi \, \partial x}{A}$
- Obtaining the second-order derivative, it requires four first-order derivatives or can be expressed in terms of first-order of another variable; i.e., $\partial^2\psi/\partial x^2 = \partial^2\psi/\partial x^2 = \partial\phi/\partial x$, where $\partial\psi/\partial x = \phi$.

By applying these steps alongside the concept of CFDM support-operators as proposed by Favorskii et al. to discretise (3), it gives

$$\frac{d^2}{dx^2}\psi(x) \cong \frac{(D_x\psi)_n - (D_x\psi)_{n-1}}{0.5(x_{n+1} - x_n) - 0.5(x_n - x_{n-1})}, \quad (4)$$

where $(D_x\psi)_n$ refers to the discrete derivative of ψ with respect to x, and evaluated at the n^{th} grid point or cell-centre. Moreover, the $\cong$ shows that the expression at the right-hand side is a discrete representation for the differential form at the left-hand side. It is expeditious that the Schrödinger equation corresponding to the interior point n becomes

$$-\left(\frac{\psi_{n+1} - \psi_n}{x_{n+1} - x_n} - \frac{\psi_n - \psi_{n-1}}{x_n - x_{n-1}}\right) = \frac{2mE\left[(0.5(x_{n+1} - x_{n-1})\right]}{\hbar^2}\psi_n \quad (5)$$

This equation is logical and well-founded for general non-uniform grids. In this paper, a uniform grid has been assumed to simplify the discussion. Letting $k_1 = 1/(x_{n+1} - x_n)$, $k_2 = 1/(x_n - x_{n-1})$ and $\bar{\omega} = \hbar^2/(2m\delta x)$, and simplifying

$$\bar{\omega}[-k_2\psi_{n-1} + (k_1 + k_2)\psi_n - k_1\psi_{n+1}] = E\psi_n \quad (6)$$

with $\bar{E} = E/\bar{\omega} = \eta$, and considering the equation associated with all interior points, we obtain the eigenvalue matrix equation as

$$\bar{L}\psi = \eta\psi. \quad (7)$$

The matrix entries from $\bar{L}$ are non-dimensional. Next, the scheme CFDM is tested to ascertain the veracity of (5) with internal nodes of the uniform grid system ranging from 5 to 10 for demonstration purpose for this study. In 1-D case, the generating matrix for CFDM agrees with the SFDM but not shown here because of paucity of space.

B. Problem of the Study

As a result of incomplete numerical schemes for modelling and simulation of photonic, nanophotonic, nanoplasmonic and plasmonic applications and specifically pocket-size devices owing to scaling of solid state devices from macroscopic to nanoscopic region, there is a critical demand for examination of different models appropriate in this area of study. In this paper, attempts are being made towards handling this research gap by employing novel numerical scheme, the Conservative Finite Difference Method to the modelling and simulation of frequency-dependent dielectric function in photonic, nanophotonic and pocket-size device application for the next generation. Consider the two-dimensional Schrödinger equation

$$\left.\begin{aligned} -\frac{i\hbar\partial\psi(x,y)}{\partial t} = -\frac{\hbar^2}{2m}\left[\frac{\partial^2\psi(x,y)}{\partial x^2} + \frac{\partial^2\psi(x,y)}{\partial y^2}\right] \\ \frac{2mE}{\hbar^2}\psi(x,y) = -\nabla^2\psi(x,y) \\ \tilde{E}\psi(x,y) = -\nabla^2\psi(x,y) \\ \tilde{A}\psi(x,y) = \lambda\psi(x,y) \end{aligned}\right\} . \quad (8)$$

For the range in consideration, the geometry of study is: x-axis and y-axis are given as [0, a] and [0, b], respectively. The boundary conditions using Dirichlet for $\psi(x,y) = \psi$ are stated explicitly as: $\psi(x = 0, y) = 0 \implies \psi(0) = 0, \psi(x = a, y) = 0, \psi(0) = 0$, $\psi(x, y = 0) = 0 \implies \psi(0) = 0, \psi(x, y = b) = 0, \psi(0) = 0$. For both the interior and external geometries as shown in Fig. 2, these Dirichlet boundary conditions hold. For simplicity, we assume that the potential cage (energy) is zero i.e., $V(x,y) = 0$, then, it gives

$$-\frac{i\hbar\partial\psi(x,y)}{\partial t} = -\frac{\hbar^2}{2m}\left[\frac{\partial^2\psi(x,y)}{\partial x^2} + \frac{\partial^2\psi(x,y)}{\partial y^2}\right]. \quad (9)$$

The expression in (9) represents the two-dimensional (2-D)space for the BVP which will be discretised using CFDM and resulting compactly as

$$-\frac{\hbar^2}{2m}\nabla^2\psi(x,y) = -\frac{\hbar^2}{2m}\frac{d^2}{dx^2}\psi(x,y) = E\psi(x,y) \quad (10)$$

Upon applying CFDM, it gives

$$\begin{aligned}
\tilde{E}\psi_{i,j}Vn_{i,j} = {} & \frac{y_{i-1,j} - y_{i,j-1}}{2}\left\{\frac{(\psi_{i,j} - \psi_{i-1,j-1})(y_{i-1,j} - y_{i,j-1}) - (\psi_{i-1,j} - \psi_{i,j-1})(y_{i,j} - y_{i-1,j-1})}{2Vc_{i-1,j-1}}\right\} \\
& - \left(\frac{y_{i,j+1} - y_{i+1,j}}{2}\right)\left\{\frac{(\psi_{i+1,j+1} - \psi_{i,j})(y_{i,j+1} - y_{i+1,j}) - (\psi_{i,j+1} - \psi_{i+1,j})(y_{i+1,j+1} - y_{i,j})}{2Vc_{i,j}}\right\} \\
& - \left(\frac{y_{i+1,j} - y_{i,j-1}}{2}\right)\left\{\frac{(\psi_{i+1,j} - \psi_{i,j-1})(y_{i,j} - y_{i+1,j-1}) - (\psi_{i,j} - \psi_{i+1,j-1})(y_{i+1,j} - y_{i,j-1})}{2Vc_{i,j-1}}\right\} \\
& + \frac{y_{i,j+1} - y_{i-1,j}}{2}\left\{\frac{(\psi_{i,j+1} - \psi_{i-1,j})(y_{i-1,j+1} - y_{i,j}) - (\psi_{i-1,j+1} - \psi_{i,j})(y_{i,j+1} - y_{i-1,j})}{2Vc_{i-1,j}}\right\} \\
& + \frac{x_{i-1,j} - x_{i,j-1}}{2}\left\{\frac{(\psi_{i,j} - \psi_{i-1,j-1})(x_{i-1,j} - x_{i,j-1}) - (\psi_{i-1,j} - \psi_{i,j-1})(x_{i,j} - x_{i-1,j-1})}{2Vc_{i-1,j-1}}\right\} \\
& - \left(\frac{x_{i,j+1} - x_{i+1,j}}{2}\right)\left\{\frac{(\psi_{i+1,j+1} - \psi_{i,j})(x_{i,j+1} - x_{i+1,j}) - (\psi_{i,j+1} - \psi_{i+1,j})(x_{i+1,j+1} - x_{i,j})}{2Vc_{i,j}}\right\} \\
& - \left(\frac{x_{i+1,j} - x_{i,j-1}}{2}\right)\left\{\frac{(\psi_{i+1,j} - \psi_{i,j-1})(x_{i,j} - x_{i+1,j-1}) - (\psi_{i,j} - \psi_{i+1,j-1})(x_{i+1,j} - x_{i,j-1})}{2Vc_{i,j-1}}\right\}
\end{aligned} \quad (11)$$

$$+\frac{x_{i,j+1}-x_{i-1,j}}{2}\left\{\frac{(\psi_{i,j+1}-\psi_{i-1,j})(x_{i-1,j+1}-x_{i,j})-(\psi_{i-1,j+1}-\psi_{i,j})(x_{i,j+1}-x_{i-1,j})}{2Vc_{i-1,j}}\right\}$$

The notational explanation regarding the details of (11) can be found in [8] for further reading and insight. Equation (11) can be compactly represented in an eigenvalue problem as,

$$\mathbb{H}\Psi = E\Psi. \tag{12}$$

The algorithm 1 shows the generation of matrix $\mathbb{H}$ to compute eigenpair using SFDM approach.

Algorithm 1 Generation of matrix $\mathbb{H}$ for Eigenpair for SFDM 2-D case

Set $\Delta x = X_f/(M+1)$, $\Delta y = Y_f/(M+1)$
Set $\mathbb{H} \leftarrow M \times M$
$\mathbb{H}_{1,1}, \mathbb{H}_{1,1} \leftarrow 2/\Delta x^2, 2/\Delta y^2$
$\mathbb{H}_{1,2}, \mathbb{H}_{1,2} \leftarrow -1/\Delta x^2, -1/\Delta y^2$
for $i, j \leftarrow 2$ to $M-1$ **do**
    $\mathbb{H}_{ii-1}, \mathbb{H}_{jj-1} \leftarrow -1/\Delta x^2, -1/\Delta y^2$
    $\mathbb{H}_{ii}, \mathbb{H}_{jj} \leftarrow 2/\Delta x^2, 2/\Delta y^2$
    $\mathbb{H}_{ii+1}, \mathbb{H}_{jj+1} \leftarrow -1/\Delta x^2, -1/\Delta y^2$
    Update the $\mathbb{H}$
end for
$\mathbb{H}_{MM-1}, \mathbb{H}_{MM-1} \leftarrow -1/\Delta x^2, -1/\Delta y^2$
$\mathbb{H}_{MM-1}, \mathbb{H}_{MM-1} \leftarrow 2/\Delta x^2, 2/\Delta y^2$
return $\mathbb{H}$

C. The Quantum-based models employed in Photonics and Plasmonics

Further effects of size can be obtained by modifications in the frequency-dependent dielectric function of the metallic material itself. Considering the structure of the Drude model dispersion relation in [7], [9], [10],

$$\varepsilon(\omega) = \varepsilon_\infty - \frac{\omega_p^2}{\omega^2 - i\gamma\omega}, \tag{13}$$

where w_p, γ, and w denote plasma frequency of the particle, damping constant and operating frequency, respectively. The desired modifications can be implemented. For metallic particles in which their size is lower than $100\mathring{A}$, scattering of the particles away from the surface of the particle allows the contribution to the overall damping constant be modelled as [9], [10]

$$\gamma = \gamma_{bulk} + \frac{v_F}{L}, \tag{14}$$

here, γ, v_F, and L denote the damping constant which is the inverse of the lifetime of the particle, Fermi velocity of the particle, and the length of the particle that depends on the particle's size, respectively.

Finally, the frequency-dependent dielectric function of an electron in metallic nano-particle (photonic or plasmonic device) can be computed using the eigenpairs obtained in (11), subject to the effect of electromagnetic wave, with direction of polarization being in z-axis, and, the frequency ω [7], [9], [10],

$$\varepsilon(\omega) = \varepsilon_\infty + \frac{\omega_p^2}{N}\sum_i\sum_f \frac{s_{if}(F_i - F_f)}{\omega_{if}^2 - \omega^2 - i\omega\gamma_{if}}, \tag{15}$$

with the terms ε_∞, s_{if}, ω_{if}, γ_{if}, $(F_i - F_f)$, and N being interband effect, oscillator strength of initial to final states of the particle, change in frequency as a result of different state, damping factor for change of state and Fermi-Dirac probability distribution characterising the initial to final states of the particle, respectively. The concept is explained rigorously in [7], [8]. The flowchart of the process employed in the numerical simulation and implementation of CFDM is depicted in Fig. 3.

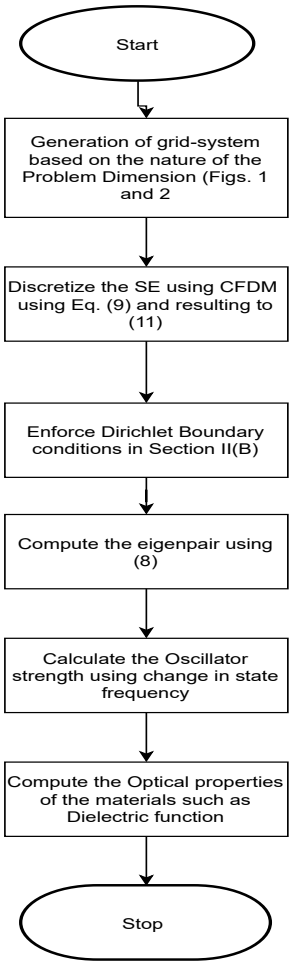

Fig. 3. The flowchart of the process employed in the numerical simulation and implementation of CFDM scheme

III. Results and Discussion

In the section, the numerical results for both the SFDM and CFDM are presented. The numerical solutions using the SFDM and CFDM with and without holes have been achieved and depicted in Figs. 4 and 5 .The following values are employed for simulating the frequency-dependent dielectric function for a gold (Au) metallic structure. The length, Fermi velocity, plasma frequency, Fermi frequency, and damping and bulk constant are given as $L = 30\times10^{-9}m$, $V_F = 1.39\times10^6 m/s$, $1.36\times10^{10} rad/s$, $\gamma_{bulk} = 0.016eV$, respectively. The values of a and b are assumed to be 5

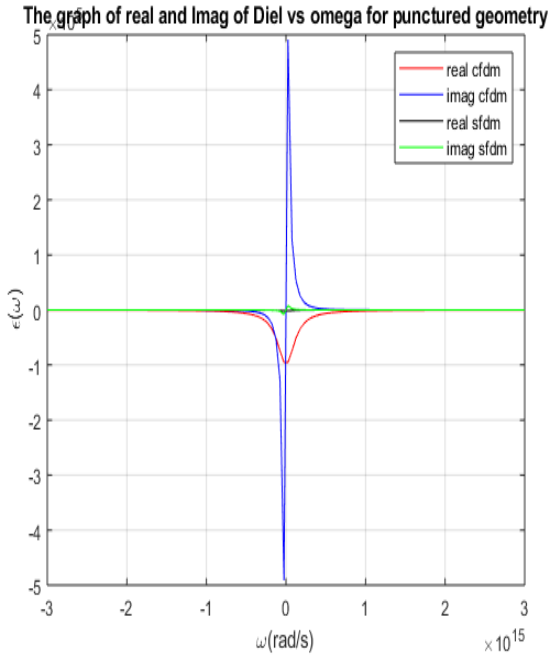

Fig. 4. Comparison of proposed scheme CFDM with SFDM: Dielectric function

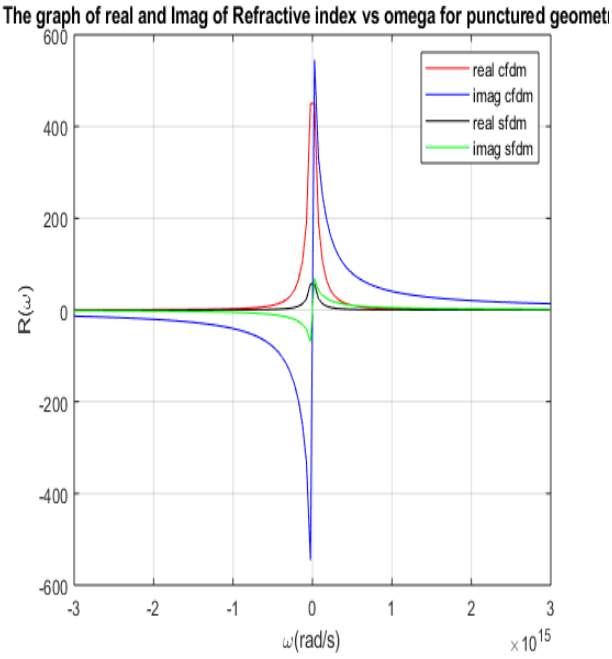

Fig. 5. Comparison of proposed scheme CFDM with SFDM: Refractive index

in nm. Owing to the paucity of space in this paper, the results of punctured system are presented. Figures 4 and 5 present results of geometries with internal holes. The results show the real-and imaginary parts of frequency-dependent dielectric function, and refractive index for CFDM with a factor approximately ten times that of SFDM. This reveals the conservative nature of CFDM as against the SFDM after going through the discretisation process. The discrete solution is highly oscillating as depicted in Figs. 4 and 5. The performance of CFDM is superior to SFDM, as expected owing to its conservativeness. Furthermore, the numerical comparison has been successfully made between the SFDM and CFDM in this paper and both schemes have employed with and without an internal puncture (These results are no presented here). The model employed (Figs. 1 and 2) consists of a uniform grid along both x- and y-axes for simplicity. A grid of N-by-N points is applied. This geometry has been chosen to demonstrate the differences between the methods without unreal overstatement; improved differences can easily be achieved by using a more robust scheme. The numerical equations were solved on an ACER computer system with core i7, 20G RAM, 1 Terabyte of Hard drives, 250 GB Solid-state drive (SSD). The computation was nearly the same for the 1-D system in terms of setting up the system matrix , apart from the few cases that have to do with the computation of coefficients using both methods. However, the difference is appreciable and conspicuous in the case of 2-D, as shown in Figs. (4- 5). As expected, the higher the number of grid points or equivalently, the smaller the mesh size, the smoother the resulting data (curves).

IV. Conclusion

Using the Conservative Finite Difference Method concept, Schrödinger equation and rectangular grid system with Dirichlet boundary conditions imposed on the 1-and 2-D photonic and plasmonic geometry, has been modelled, developed and simulated using quantum-based models such as Drude, Lorentz for the computational analysis of optical properties such as frequency-dependent dielectric function. The numerical scheme and solutions essential using CFDM based on impingement of electromagnetic wave on the surface of the metallic device in modern miniaturised photonic-and plasmonic based devices have been constructed, simulated and their behavioural optical properties such as frequency-dependent dielectric function, susceptibility have been discussed in great detail. In this study, CFDM has been employed to solve a well-posed Boundary value problem with Dirichlet Boundary conditions for photonic and plasmonic devices. The underlying physics here is the use of quantum-inspired models such as Drude and Lorentz to examine some of the optical phenomena features of the materials at nano scale. Notwithstanding, further details have not been expounded expressly in this paper due to paucity of space. It should be stated that the origin of this employed scheme in this work, has been in existence for awhile yet to be applied in nanophotonic and plasmonic research areas with quantum-based model which are the future making it first time such scheme will be utilised in computational community.

Acknowledgement

The lead author LAA would like to thank the support of the the Departments of Electronic & Computer Engineering, Lagos State University. All authors would like to graciously

acknowledge the support received from Telkom SA and the Jasco Group via the Telkom Centre of Excellence (CoE) in Broadband Networks at the University of Cape Town.

REFERENCES

[1] A. Baghai-Wadji, "6a-6 conservative finite difference method as applied to electromagnetic radiation problems in saw devices," in *2006 IEEE Ultrasonics Symposium*. IEEE, 2006, pp. 100–103.

[2] R. F. Harrington, *Field computation by moment methods*. Wiley-IEEE Press, 1993.

[3] S. Datta, "Ece 659 quantum transport: Atom to transistor," *energy*, vol. 2, no. 1, p. 2, 2009.

[4] ——, *Quantum transport: atom to transistor*. Cambridge university press, 2005.

[5] A. Favorskii, A. Samarskii, V. Tishkin, and M. Shashkov, "On constructing fully conservative difference schemes for gas dynamic equations in eulerian form by the method of basic operators," *Preprint Keldysh Inst. of Appl. Math. the USSR Ac. of Sc*, vol. 63, pp. 13–21, 1981.

[6] M. Shashkov and S. Steinberg, *Conservative finite-difference methods on general grids*. CRC press, 2018.

[7] L. A. Akinyemi and A. Baghai-Wadji, "Quantum physics-based modelling of frequency-dependent dielectric function for small-scale devices in optical communications," in *2017 Global Wireless Summit (GWS)*. IEEE, 2017, pp. 78–82.

[8] L. A. Akinyemi, "Quantum-based modelling and simulation of materials used in small-scaled plasmonic devices," 2021.

[9] M. Zapata-Herrera, Á. S. Camacho, and H. Y. Ramírez, "Influence of the confinement potential on the size-dependent optical response of metallic nanometric particles," *Computer Physics Communications*, vol. 227, pp. 1–7, 2018.

[10] L. Genzel, T. Martin, and U. Kreibig, "Dielectric function and plasma resonances of small metal particles," *Zeitschrift für Physik B Condensed Matter*, vol. 21, no. 4, pp. 339–346, 1975.

Lateef Adesola Akinyemi is a Lecturer and researcher of Electronic and Computer Engineering at the Department of Electronic and Computer, Faculty of Engineering, Lagos State University, Lagos, Nigeria. He obtained a B.Sc.(First Class Hons.) Electronic and Computer Engineering (Computational Electronics) at Lagos State University, Lagos, Nigeria , a Master of Science in Electronic and Computer Engineering at Lagos State University, Lagos, Nigeria and Master of Science in Electrical and Electronics Engineering (Communication Engineering Option), University of Lagos, Akoka, Nigeria, and PhD in Electrical Engineering, Department of Electrical Engineering, Faculty of Engineering and the Built Environment, University of Cape town, Western Cape, South Africa. His research areas are Wireless Communications and its Applications, Computational Electronics and Analysis, Wavelets and Frames, Electromagnetic Fields and Waves, Numerical Techniques (SFDM, CFDM, DFT), Modelling and Simulations of Quantum- and Bio-inspired Nano-particles and Devices, Microwave Engineering and Antennas.

Sunday Oladayo Oladejo received the B.Eng degree in electrical and electronic engineering from the Federal University of Technology, Akure, Nigeria, in 2004 and the M.Eng degree in communication engineering from the Federal University of Technology, Minna, Nigeria, in 2016. He is currently pursuing a PhD degree in electrical engineering at the University of Cape Town, South Africa. From 2007 to 2017, he was Senior Core Network Engineer with Glo Mobile, Nigeria. His research interest includes radio resource management in wireless networks, and artificial intelligence.

Stephen Obono Ekwe received the B.Eng degree in Electrical and Electronic Engineering from the Cross River University of Technology, Calabar, Nigeria, in 2008 and the M.Sc. degree in Personal, Mobile and Satellite Communication from the University of Bradford, West Yorkshire, England, in 2013. He is currently a Doctoral Candidate in Electrical Engineering at the University of Cape Town, South Africa. His research interest includes 5G, Internet of Things, Social Network Analytics, Machine Learning, and Resource Optimization and Management in Wireless Communication Networks.

Measuring SANReN Performance: An Internal and External View

Luqmaan Salie*, Josiah Chavula†
Computer Science Department, University of Cape Town
*SLXLUQ002@myuct.ac.za, †jchavula@cs.uct.ac.za

***Abstract*—Internet systems in developing regions experience various performance challenges due to inadequate infrastructure and resources. In this study, we conduct measurements using Speedchecker and perfSONAR to determine network performance when accessing the South African Research and Education Network (SANReN) from within the network and from outside the network. Our analysis finds that SANReN has performance challenge in and around Port Elizabeth (PE), as universities in these cities experienced the highest delays and page load times. We find that PE uses circuitous routes for traffic flows to Johannesburg and Pretoria, causing high delays and high page load times.**

***Index Terms*—NRENs, Active Measurements, Delay, Page Load Time**

I. Introduction

Network scalability, reliability, performance, and quality of experience (QoE) are among the most common issues faced by network administrators [1], [2]. These issues are amplified in the context of developing regions such as Africa, with many ISPs having low inter-connectivity between each other, resulting in high round-trip times (RTT) [3]. In addition, Chetty et al. [3] showed that South African broadband users regularly do not achieve the bandwidth speeds that are expected on their respective internet connections. The Covid-19 pandemic added extra stress on the networks, resulting in an increase in latencies as well as a decrease in video streaming quality as perceived by Facebook users [4]. Previous research on Africa's National Research and Education Networks (NRENs) showed that over 75% of traffic between African universities used primarily circuitous routes [5]. In this study, we focus on exploring performance issues faced by the South African National Research Network (SANReN). We employ active network measurements to investigate performance challenges and factors that impact performance for users of the network.

The main contribution of the study is to find the performance issues within SANReN and evaluate the reasons. We carry out network performance tests to analyse the quality of service (QoS) when accessing zero-rated websites hosted in SANReN. More specifically, active measurements focus on performance disparities when accessing these educational websites from different locations and networks in South Africa. Active measurements also focus on the performance of accessing these educational websites from within SANReN, compared to accessing them from outside the network. One of the key metrics used for the comparison is page load time (PLT) – which is the average time taken from the time the user enters the URL in the browser, until the page is completely loaded. The other metrics used are end-to-end packet delay, and throughput. The location of web servers, inter-connection between network operators and SANReN, and consequently, the network paths followed by packets from source to destination are among the factors that are investigated.

II. Background and Related Work

A. SANReN

SANReN is the South African nation-wide network that supplies universities, science councils, science projects such as the Square Kilometre Array (SKA), and various other projects and institutions with broadband internet connectivity [6]. It is operated by the Tertiary Education and Research Network of South Africa (TENET) [7], and primarily funded by the Department of Science and Technology (DST) [8]. Figure 1 shows the topology of SANReN, a nation-wide network that spans across multiple universities around South Africa. Most universities are connected via either 100 Gbps, 10 Gbps, or 1 Gbps links across the land, supplied by telecommunication companies such as Telkom, Neotel, and DFA. There are multiple 10 Gbps undersea cables supplied by West Africa Cable System (WACS), SEACOM, and Eastern Africa Submarine Cable System (EASSy) that link universities via London and Amsterdam [6]. Universities within close proximity are linked wirelessly or share a metropolitan network.

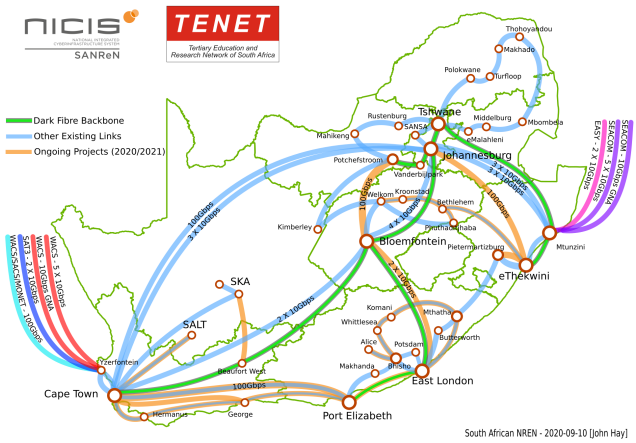

Fig. 1. SANReN backbone map [6].

B. Active Measurements

Active network measurements consists of injecting packets to assess network performance in terms of delay, packet loss and bandwidth capacity [9], [10], [11], [12]. Our study carries out the active measurements using existing tools, leveraging the advantages of both Speedchecker [13] and perfSONAR [14] to target specific source and destination combinations.

PerfSONAR is a global network measurement framework that operates within NRENs. PerfSONAR has dedicated tests for delay (ping), page load time, traceroute, and throughput. PerfSONAR includes tools such as Bandwidth Test Controller (BWCTL) [15], One-Way Ping (OWAMP) [16], and Network Diagnostic Tool (NDT) [17], and these allow perfSONAR to conduct tests for specific types of traffic such as bulk data transfer and video transfer. A *big data* study done by Zurawski et al. [18] shows the potential of perfSONAR in applying it to determine the source of congestion between Brown University (in the United States) and the Large Hadron Collider at the European Organization for Nuclear Research (CERN). Another project making use of perfSONAR for network monitoring is the US ATLAS [19], [20].

Speedchecker [13] is a global network measurement in which software probes are installed on end-user devices, including home routers, PCs, and wireless devices. The Speedchecker platform exposes an API that allows one to issue measurements such as ping, traceroute, and HTTP GET. The measurements can be launched from specific locations (countries and cities), and this allows measurement of internet quality of service from the vantage point of those locations. Recent studies [21], [22] have used Speedchecker to study Africa's internet infrastructure. Chavula et al. [22] studied the effects of cross-border infrastructure and logical interconnections on intra-country and cross-border latency in Africa. They conducted Speedchecker ICMP pings between countries using Speedchecker and applied a community detection algorithm to group countries based on round trip times (RTTs) between countries. The study was expanded in Formoso et al. [21] who carried out a large-scale mapping of inter-country delays in Africa. Their analysis further revealed clusters of countries with lower delay interconnectivity among themselves. Arnold et al. [23] conducted a study using Speedchecker to measure the impact of a private WAN on cloud performance.

III. Methodology

We used two platforms to conduct active performance measurements: Speedchecker [13] and perfSONAR [14]. We undertook a 2-week active measurements study, runnting test both from within SANReN (internal performance) and from outside SANReN (external performance).

A. Network Delay and Page Load Time

Network delay is one of the key metrics used to assess network performance because it directly impacts user experience. In this study, we conduct delay (ping) tests to various zero-rated websites[1] that are hosted within SANReN. We also conduct Page load time (PLT) test to measure the total time it takes to load a page from when the user enters the URL in a browser. PLT is a key metric in finding the QoS of websites because it shows the network performance when actual data is requested by an end-user [24]. We load the same websites from different cities, both within and from outside SANReN. This is done to observe the performance from different locations, and compare performance from outside SANReN and from within [25].

We also conduct traceroute tests to the websites and use the results to explain the delays and PLTs. We attempt to find gaps in the network and identify congestion prone paths. The traceroute also helps to identify if the routes that are used are circuitous. The dependent variable for these tests is the number of IP hops it takes to travel from each source to the specified destination. We only consider successful traceroutes as being the ones that reach the target websites' ASNs. We use MaxMind's ASN database [26] to lookup the ASN of each target website, as well as the last IP hop reached by a traceroute.

B. Throughput

Throughput tells us how fast the network transfers data between two points [27], [28]. For external tests, we calculate throughput from the page load time tests by using the total number of bytes downloaded for each test. We define throughput for these tests as the number of total downloaded bytes (TDB) divided by the result of total page load time minus time-to-first-byte (TTFB), i.e.: $Throughput = \frac{TDB}{PLT-TTFB}$. For the internal tests, we use Iperf3 [29] to measure the throughput.

We run tests from Cape Town, Johannesburg, Durban, Port Elizabeth, and Pretoria to websites at the universities as listed in Table I. The universities were chosen because they are seven of the biggest universities in South Africa and are spread out across the country. The websites that we used as destinations are zero-rated websites from each of the universities, and their locations were checked using IP-API [30] and IPWHOIS [31].

TABLE I
DESTINATION UNIVERSITIES USED IN THIS STUDY.

Abbreviation	Name	Location
UCT	University of Cape Town	Cape Town
UWC	University of the Western Cape	Cape Town
WITS	University of the Witwatersrand, Johannesburg	Johannesburg
UJ	University of Johannesburg	Johannesburg
DUT	Durban University of Technology	Durban
UNISA	University of South Africa	Pretoria
NMU	Nelson Mandela University	Port Elizabeth

We ran daily tests for two weeks between each city and university. In order to comply with Speedchecker's fair-usage policy, we limited our tests to 14 per day per destination

[1]South African Zero-rated Content: https://docs.google.com/spreadsheets/d/1d3HciexwZQndqHULEILwk_g4F1RRwUMlQjVVPc80BsI/edit?usp=sharing

university. Tests were conducted in the morning (9AM), afternoon (3PM), and night (9PM) to get a measure of the network performance.

IV. Results

We group our active measurement results by experiment type and split them into external Speedchecker experiments conducted from outside of SANReN, and internal perfSONAR experiments conducted from within SANReN. We present the data as box plots and show the distribution of data for each city and each university. We use scatter plots to display the relationship between page load time and delay. We also show the number of IP hops taken by the traceroute to reach each destination from the source cities. After presenting the internal and external results, we present a comparison thereof.

A. Packet Delay Results

1) Packet Delay from Outside of SANReN: Figure 2 presents a box plot of the delay from the five cities that were used as sources for testing. The cities with the lowest median delays to universities are Johannesburg with a median packet delay of 29ms, and Pretoria with a median delay of 35ms. Durban had a median delay of 47ms, Cape Town: 48ms, and PE: 53ms. In terms of the destination websites, WITS (which is within Johannesburg) had the lowest median delay: 37ms, followed by UNISA (in Pretoria) at 37.5ms. NMU, which is located in Port Elizabeth, had the highest median delay of 57ms, followed by UCT and UWC with 46ms and 43ms respectively. Both UCT and UWC are located in Cape Town.

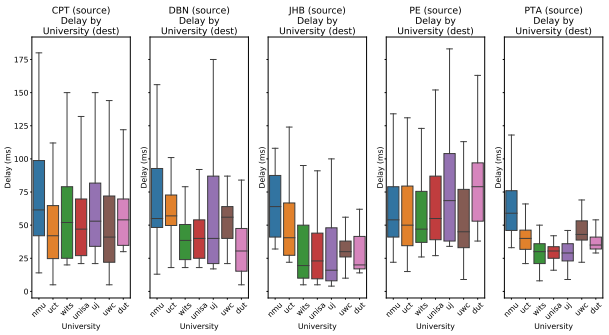

Fig. 2. External delay by destination university.

Overall, the delays appear to be in line with the distances between the universities and cities. For example, the delay from Durban to Cape Town universities was higher than the delay from Durban to universities in Johannesburg, Pretoria, and Durban. The median delay from Durban to UWC is 56 ms and Durban to UCT is 57 ms. Delay between Durban and the universities in Johannesburg, Pretoria and Durban is lower, with Durban to UJ: 40 ms, Durban to UNISA: 40 ms, Durban to WITS: 38.5 ms, and Durban to DUT: 30.5 ms.

2) Packet Delay from within SANReN: Results from the internal delay tests are presented in Figure 3. Here again we see that the delays follow the distance pattern. For example, the median delay from Cape Town to DUT is 27.05 ms, and from Durban to UCT and UWC, the median delays were 26.82ms and 27.35ms respectively.

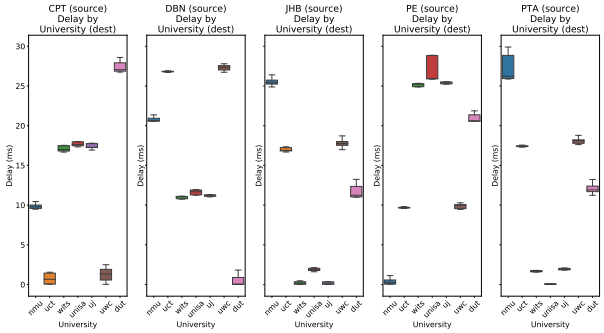

Fig. 3. Internal delay by destination university.

There is higher delay from Port Elizabeth (PE) to UJ and WITS, with median delays of 25.47 ms and 25.26 ms respectively. We also observe higher delays from Johannesburg to NMU (25.42ms). Similarly, we see relatively high delays between Pretoria to NMU (Port Elizabeth) of 26.24ms. In comparison, we see relatively lower median delays of 10ms between Cape Town and PE (and vice-versa).

3) External vs Internal Packet Delay: We combined and compared the results from the external and internal delay experiments. Figure 4 shows the overall delay to each university. We observe, as expected, that the internal tests have lower delays when targeting each of the universities. We also observe that NMU has the highest median delay from both external and internal sources, while WITS has the lowest median delay from both external and internal sources. UJ has the biggest IQR (53) and the highest value for the maximum delay from external sources (154 ms). The biggest difference between external and internal median is experienced by NMU with the difference being 36.4 ms (57 ms - 20.6 ms).

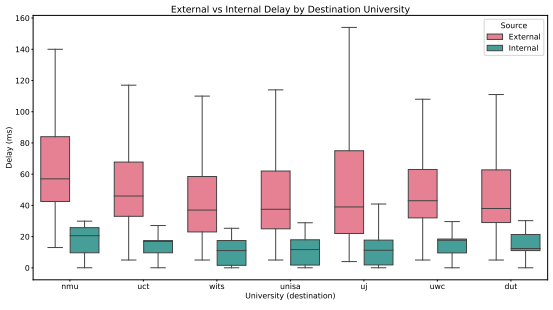

Fig. 4. External vs internal delay by destination university.

B. Page Load Delay Results

1) Page Load Delay from outside SANReN: Results from the page load time tests conducted by Speedchecker (external vantage points) to SANReN-based websites are presented below. In Figure 5, we observe that results are similar for four of the source cities, with again PE being the outlier. PE experiences higher PLTs for SANReN websites than the rest

of the cities, with a median PLT of 1727 ms. In contrast, Johannesburg had the lowest median PLT of 315ms, followed by Durban with 472ms, Cape Town with 496ms, and Pretoria with 534ms.

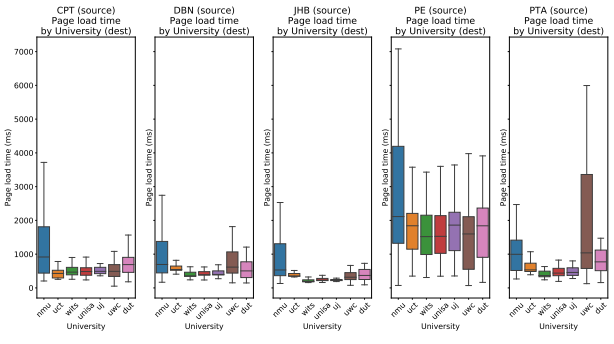

Fig. 5. External page load times by destination university.

In terms of target websites, NMU (again Port Elizabeth) has the highest PLTs with an overall median of 899ms from all cities. In comparison, DUT, UWC, and UCT have median PLTs of 594.5ms, 527ms, and 516ms respectively. WITS, UNISA, and UJ had the lowest overall median PLTs of 387ms, 404ms, and 426ms respectively. When focusing on specific pairs of source city and target university, we see that although NMU resides in Port Elizabeth, the highest median PLT of any source and target pair is experienced when trying to reach NMU from Port Elizabeth, with 2112.91 ms. Moreover, PE has an overall IQR of 1244.5, showing that the PLTs are inconsistent to all the universities targeted. For comparison, Cape Town has an IQR of 322, Durban: 312, Johannesburg: 193, and Pretoria 526.

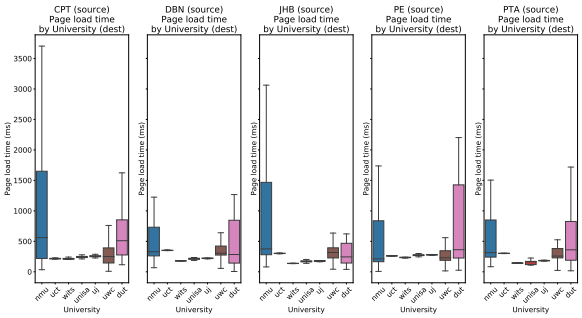

Fig. 6. Internal page load time by destination university.

2) Page Load Delay from within SANReN: Figure 6 presents the results for page load times from within SANReN. We see that NMU and DUT have the highest median PLTs across all the source cities, with NMU having a PLT of 329.75 ms and DUT having a PLT of 341.82 ms. The rest of the universities experience lower PLTs, with UCT having an overall median PLT of 300.8 ms, UWC: 275.48 ms, UJ: 223.11 ms, UNISA: 215.68, and WITS: 179.55 ms. The next highest median PLT to DUT is 362.75 from Port Elizabeth.

3) External vs Internal Page Load Delay: We combine the results from our external and internal page load time experiments and present them in Figure 7. We observe that parts of the external and internal quartiles for NMU, DUT, and UWC overlapping. We see high page load times to universities even from within the cities in which they are located, indicating possibility of congestion in the paths used to transfer data.

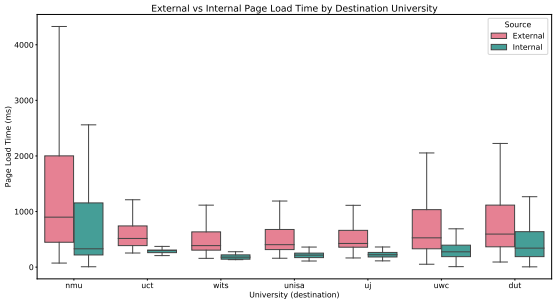

Fig. 7. External vs internal page load time by destination university.

More specifically, we see a difference of 569.25 ms when comparing the external and internal median PLTs to NMU, a difference of 252.68 ms when comparing DUT's external and internal PLTs, and a difference of 251.52 ms when comparing UWC. We observe a difference of 215.2 ms between UCT's median PLTs, 207.45 ms between WITS', 188.32 ms between UNISA's, and 202.89 ms between UJ's median PLTs. With the exception of WITS, all the universities have a difference of over 200 ms between their external and internal PLTs.

4) External and Internal Page Load Delay vs Packet Delay: We combined and compared the results from our external and internal page load time experiments. Figure 8 shows the overall results compared to one another. We notice that high delays are common when using external sources, with 20.53% of the data points having delays higher than 75 ms. We also observe that the page load times are similar for a large number of tests, with 93% of internal tests having PLTs under 1000 ms, whereas only 77.42% of external tests have PLTs under 1000 ms. This suggests that delay from external sources could be improved, and that throughput in the network is sufficient as page load times from inside the network are similar to that of external sources.

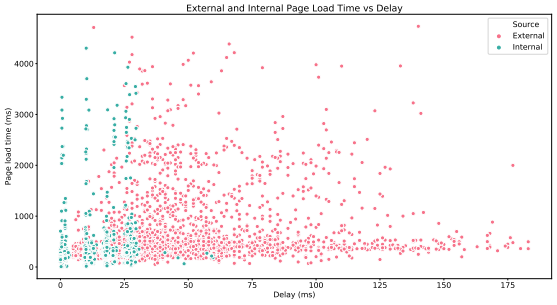

Fig. 8. External and internal page load time vs delay.

C. Traceroute Results

We conducted traceroute tests from the source cities to each target website, and we make the following observations. The highest median number of hops among the target universities when using PE as the source is 17 from PE to NMU. We observe that the overall median number of hops to universities from PE is 14. We observe that from our external experiments, DUT is the university with the biggest difference between external and internal median values, with external tests taking 14 hops and internal tests taking 6 hops. NMU's internal and external results have a big difference in their median values as well, with the internal and external tests taking 8 and 15 hops respectively. PE is the only city where the university with the highest median number of hops is located in the source city itself. Figure 9 presents a comparison of number of hops to each university.

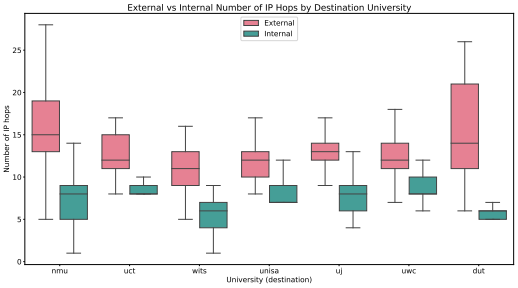

Fig. 9. Number of IP hops for traceroute by destination university — external vs internal sources.

We observe that, for the external tests, the highest number of hops of any source and target pair is 17 from PE to NMU. For the internal tests, the highest number of hops for a source and target pair is 11 from PE to UNISA and from Pretoria to UWC.

D. Throughput Results

It has to be noted that the internal (perfSONAR) throughput measurements reflect the capacity of the core SANReN infrastructure, whereas the external results reflect the throughput when SANReN resources are accessed from outside the SANReN. Figure 10 shows the comparison between the sets of measurements. For throughput measurements conducted from outside SANReN (using Speedchecker), we observe Johannesburg has the highest overall median throughput with a value of 0.01404Gbps, with the highest values being 0.02206 Gbps from Johannesburg to DUT. PE experiences the lowest throughput with an overall median value of 0.00234, with the lowest being from PE to UJ at 0.00104Gbps.

Internal throughput tests conducted using perfSONAR from within SANReN show inter-university median throughput values between 4.91Gbpss and 8.005 Gbps. The lowest throughput was from Durban to UCT at 4.91Gbps. However, Durban experienced the highest overall median throughput of 8.005 Gbps, followed by Pretoria with 7.64 Gbps, Johannesburg with 7.55 Gbps, and PE with 7.53 Gbps.

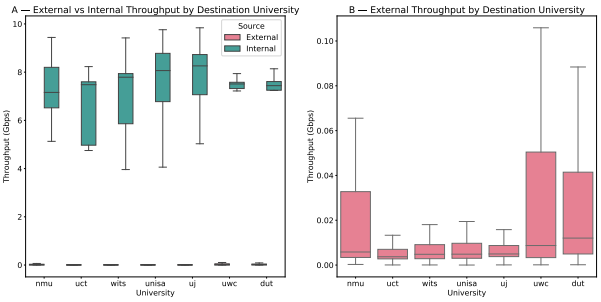

Fig. 10. External vs internal throughput by destination university.

V. Discussion

This study has focused on evaluating network quality of service (QoS) when accessing content hosted in SANReN. We conducted active measurements to study disparities between internal and external access to SANReN, especially when accessing zero-rated educational websites. A key metrics for our comparison was page load time, which is used to represent user's quality of experience when accessing the network. Our results show the difference in the nature of network paths followed by packets from source to destination, and that this is an important factor differentiating delay and page load times between internal and external access. We observe that other ISPs take more circuitous routes to different universities in the SANReN, with 11 as the median number of hops from other ISPs (South Africa based) to SANReN. In comparison, internal SANReN paths have a median is hop count of 6, which is just about 1/3 of number of hops for external access. This indicates sub-optimal interconnection between SANReN and other ISPs in South Africa. This is likely to be a result of the interconnections happening in only one or two locations, and thus traffic being forced to follow circuitous routes through these locations.

The observed performance differences also appear to be different depending on location. For example, the delay to reach a website hosted by NMU from outside of SANReN (57ms) is 35.71% higher compared to the overall median for reaching universities from outside of SANReN (42ms). For the external tests, the overall median delay from PE to the universities tested is 53ms, which is 26.19% higher than the median of all the source cities combined (42ms). For internal delays, PE's delays are 107.59% higher than the overall median. We also see that the delay when targeting NMU is 71.81% higher than the overall median. These high delays seem to be due to circuitous routing, as traceroute analysis shows traffic from Port Elizabeth to Johannesburg travelling via Cape Town, which means that the paths to Johannesburg via East London and Bloemfontein are ignored. Our results also show that PE has higher page load times. The external results when accessing NMU produced a median page load time of 1727 ms, compared to the overall median from cities at 491ms.

The impact of this sub-optimal interconnection is also observed in the differences in median latencies measured from

within and from outside SANReN. We observe median latency difference of up to 36 ms between measurements taken from external and internal sources.

We observe a big difference between page load times when accessing webservers from within SANReN compared to accessing them from other ISPs, with the differences being over 500 ms. We observe that the page load times are in general higher for external sources, with up to 23% of external tests having PLTs of over 1000 ms, whereas only 7% of internal tests had PLTs over 1000 ms. This suggests that delay from external sources could be improved through better interconnection with other ISPs.

VI. Conclusion

In this study, we focused on evaluating the internal and external performance differences for SANReN by using active measurements. Our measurements showed a big difference between delays experienced when accessing SANReN webservers from within the network compared to accessing them from other ISPs. Our analysis shows that the high delays and higher page load times experienced outside the SANReN are caused by traffic flowing via circuitous routes, using Cape Town as an interconnection point. This is problematic considering that Cape Town is located far from the rest of the cities in the network, and thus, introduces delays.

For future work, we will expand the number of cities and universities tested. We will also explore and experiment with traffic engineering solutions that could be employed in SANReN.

Acknowledgement

That authors would like to acknowledge and appreciate the financial support from the UCT Centre of Excellence (CoE) in Broadband Networks and Applications.

References

[1] S. Sezer, S. Scott-Hayward, P. K. Chouhan, B. Fraser, D. Lake, J. Finnegan, N. Viljoen, M. Miller, and N. Rao, "Are we ready for sdn? implementation challenges for software-defined networks," *IEEE Communications Magazine*, vol. 51, no. 7, pp. 36–43, 2013.

[2] H. Kim and N. Feamster, "Improving network management with software defined networking," *IEEE Communications Magazine*, vol. 51, no. 2, pp. 114–119, 2013.

[3] M. Chetty, S. Sundaresan, S. Muckaden, N. Feamster, and E. Calandro, "Measuring broadband performance in south africa," in *Proceedings of the 4th Annual Symposium on Computing for Development*, 2013, pp. 1–10.

[4] T. Böttger, G. Ibrahim, and B. Vallis, "How the internet reacted to covid-19: A perspective from facebook's edge network," in *Proceedings of the ACM Internet Measurement Conference*, 2020, pp. 34–41.

[5] J. Chavula, N. Feamster, A. Bagula, and H. Suleman, "Quantifying the effects of circuitous routes on the latency of intra-africa internet traffic: a study of research and education networks," in *International Conference on e-Infrastructure and e-Services for Developing Countries*. Springer, 2014, pp. 64–73.

[6] "South african national research network (sanren)," https://sanren.ac.za/, accessed: 2021-01-22.

[7] "Tertiary education and research network of south africa (tenet)," https://www.tenet.ac.za/, accessed: 2021-01-22.

[9] J. L. de Vergara, M. Ruiz, L. Gifre, L. Vaquero, J. Zazo, S. López-Buedo, O. G. de Dios, and L. Velasco, "Demonstration of 100 gbit/s active measurements in dynamically provisioned optical paths," 2019.

[8] "Department of science and technology (dst)," https://www.dst.gov.za/, accessed: 2021-01-22.

[10] R. van Rijswijk-Deij, M. Jonker, A. Sperotto, and A. Pras, "A high-performance, scalable infrastructure for large-scale active dns measurements," *IEEE Journal on Selected Areas in Communications*, vol. 34, no. 6, pp. 1877–1888, 2016.

[11] A. Nikravesh, H. Yao, S. Xu, D. Choffnes, and Z. M. Mao, "Mobilyzer: An open platform for controllable mobile network measurements," in *Proceedings of the 13th Annual International Conference on Mobile Systems, Applications, and Services*, 2015, pp. 389–404.

[12] S. Sonntag, L. Schulte, and J. Manner, "Mobile network measurements-it's not all about signal strength," in *2013 IEEE Wireless Communications and Networking Conference (WCNC)*. IEEE, 2013, pp. 4624–4629.

[13] "Speedchecker," https://www.speedchecker.com/, accessed: 2021-01-07.

[14] A. Hanemann, J. W. Boote, E. L. Boyd, J. Durand, L. Kudarimoti, R. Łapacz, D. M. Swany, S. Trocha, and J. Zurawski, "Perfsonar: A service oriented architecture for multi-domain network monitoring," in *International conference on service-oriented computing*. Springer, 2005, pp. 241–254.

[15] "Bandwidth test controller (bwctl)," https://software.internet2.edu/bwctl/, accessed: 2021-01-14.

[16] "One-way ping (owamp)," https://software.internet2.edu/owamp/, accessed: 2021-01-14.

[17] "Network diagnostic tool (ndt)," https://software.internet2.edu/ndt/, accessed: 2021-01-14.

[18] J. Zurawski, S. Balasubramanian, A. Brown, E. Kissel, A. Lake, M. Swany, B. Tierney, and M. Zekauskas, "perfsonar: On-board diagnostics for big data," in *1st Workshop on Big Data and Science: Infrastructure and Services. Co-located with IEEE International Conference on Big Data*. Citeseer, 2013.

[19] "Atlas," https://po.usatlas.bnl.gov/, accessed: 2021-01-14.

[20] S. McKee, A. Lake, P. Laurens, H. Severini, T. Wlodek, S. Wolff, and J. Zurawski, "Monitoring the us atlas network infrastructure with perfsonar-ps," in *Journal of Physics: Conference Series*, vol. 396, no. 4. IOP Publishing, 2012, p. 042038.

[21] A. Formoso, J. Chavula, A. Phokeer, A. Sathiaseelan, and G. Tyson, "Deep diving into africa's inter-country latencies," in *IEEE INFOCOM 2018-IEEE Conference on Computer Communications*. IEEE, 2018, pp. 2231–2239.

[22] J. Chavula, A. Phokeer, A. Formoso, and N. Feamster, "Insight into africa's country-level latencies," in *2017 IEEE AFRICON*. IEEE, 2017, pp. 938–944.

[23] T. Arnold, E. Gürmeriçliler, G. Essig, A. Gupta, M. Calder, V. Giotsas, and E. Katz-Bassett, "(how much) does a private wan improve cloud performance?" in *IEEE INFOCOM 2020-IEEE Conference on Computer Communications*. IEEE, 2020, pp. 79–88.

[24] X. S. Wang, A. Balasubramanian, A. Krishnamurthy, and D. Wetherall, "Demystifying page load performance with wprof," in *10th {USENIX} Symposium on Networked Systems Design and Implementation ({NSDI} 13)*, 2013, pp. 473–485.

[25] D. N. da Hora, A. S. Asrese, V. Christophides, R. Teixeira, and D. Rossi, "Narrowing the gap between qos metrics and web qoe using above-the-fold metrics," in *International Conference on Passive and Active Network Measurement*. Springer, 2018, pp. 31–43.

[26] "Maxmind," https://www.maxmind.com/en/geoip2-services-and-databases, accessed: 2021-01-12.

[27] S. A. Jyothi, A. Singla, P. B. Godfrey, and A. Kolla, "Measuring and understanding throughput of network topologies," in *SC'16: Proceedings of the International Conference for High Performance Computing, Networking, Storage and Analysis*. IEEE, 2016, pp. 761–772.

[28] W. Luan, D. Sharp, and S. Lancashire, "Smart grid communication network capacity planning for power utilities," in *IEEE PES T&D 2010*. IEEE, 2010, pp. 1–4.

[29] M. Mortimer, "iperf3 documentation," 2018.

[30] "Ip-api," https://ip-api.com/docs, accessed: 2021-01-12.

[31] "Ipwhois," https://ipwhois.io/documentation, accessed: 2021-01-12.

Luqmaan Salie is a Masters in Computer Science student at the University of Cape Town (UCT). His research is on Analysis of Internet Traffic Flow in SANReN using Active and Passive Measurements.

Josiah Chavula is a lecturer and researcher in Computer Science at the University of Cape Town. He received a PhD in Computer Science from UCT (2017), and an MSc in Networking and Internet Systems from Lancaster University (2011). His research focuses on performance of internet systems in Low Resource contexts.

Design, Implementation and Evaluation of an Intelligent Secure 5G and Beyond Digital Health Testbed for Digital Health Applications and Services in Africa

Alinafe Kaliwo[1], Tinashe Mutsvangwa[2], Bessie Malila[3]

[1, 2, 3]*Division of Biomedical Engineering, Department of Human Biology, Faculty of Health Sciences, University of Cape Town, Anzio Road, Observatory, Cape Town 7935*

[1]klwali001@myuct.ac.za

[2]tinashe.mutsvangwa@uct.ac.za

[3]bessie.malila@uct.ac.za

Abstract— **The need for novel digital health applications and services has prompted the re-evaluation of Africa's mobile network infrastructure. The introduction of the fifth generation and beyond networks allows researchers to leverage digital health applications to solve the most pressing health challenges on the continent. This growth in innovations calls for the need for a launchpad platform for such technologies. This paper argues the need for Africa to have its own 5G and beyond digital health testbeds. The paper further proposes the design of a testbed that uses readily available open-source technologies in its implementation. The layers of the communication systems in relevant domains, namely: the data acquisition, access network, core network and data retrieval domains, are presented. A proposal for managing the security and privacy aspects of medical data through Blockchain and X-Road technologies is also outlined. In closing, the paper discusses the potential of deploying 5G-powered private networks in hospitals.**

Keywords— **5G, B5G, Core Network, Testbed, Digital Health**

I. INTRODUCTION AND MOTIVATION

Digital Health, which implies using communications technologies in healthcare, incorporates personalised and participatory healthcare models [1]. Transmission of medical data using mobile networks for health monitoring, well-being practices and preventive care expands the organisation and delivery of health-related services and activities beyond professional healthcare organisations. Africa's healthcare systems can be strengthened by integrating robust digital health applications, including electronic health (eHealth), mobile health (mHealth), telehealth and telemedicine. These solutions offer the potential to positively transform healthcare delivery [2], particularly in Africa, where there is a great need to enhance access to health information and distribution of routine, emergency health and diagnostic services [3].

The Coronavirus disease 2019 (COVID-19) pandemic has prompted an exploration of novel tools to mitigate some of the devastating effects of the disease on communities. As a result, attention has turned to the search for options to provide possible healthcare solutions using digital health applications in this time of unprecedented health crisis [4]. As a result, several digital health applications have successfully been implemented in Africa during the current pandemic, specifically focusing on telehealth and mHealth technologies [5]. For example, the South African government rapidly implemented the COVID-19 Alert SA App, which tracks people who tested positive for COVID-19 and those who had some contact with COVID-19 positive persons [6].

A. Challenges in Africa's Healthcare Systems

Africa's population continues to grow and is currently estimated to be about 1.369 billion people, with an annual growth rate of more than 2.5% [7]. Apart from having a low doctor-to-patient ratio, Africa is characterised by weak health systems, poor preparedness for health emergencies, poor road networks, poor quality of care and an overall inadequacy of drug supply, and hence continues to face serious challenges in providing good healthcare services to its people [8], [9]. However, many of these challenges can be solved using digital health applications.

Deployment of digital health applications and services has been a challenge because of several factors. Lack of proper training and documentation, lack of proper alignment to need, and inadequate mobile telecommunications infrastructure are some of the notable challenges encountered in implementing digital health technologies [10]. However, it is believed that 5G and Beyond 5G (B5G) technologies will solve the problem of inadequate mobile telecommunications infrastructure, enabling a new health ecosystem that connects Africa's healthcare systems accurately, efficiently, conveniently, and cost-effectively [11].

B. The Need for Digital Health Solutions for Africa's Healthcare Challenges

The Universal Health Coverage (UHC) stipulates the need for all nations to reach the targets as set in the Sustainable Development Goals (SDGs) of 2015 [12]. African countries have become good candidates for adopting digital health technologies in their health systems to reach up to one billion more people as set in UHC [13]. According to the United Nations Sustainable Development Goal (UNSDG) number 3, universal health coverage can reduce poverty [14]. The indicator in section 3.8.1 of the goal describes coverage of essential health as the average coverage of essential healthcare services like reproductive, maternal, newborn and child health, infectious diseases, non-communicable diseases, and service capacity and access, among the general populace and the most disadvantaged population [15]. Furthermore, the Global

Strategy on Digital Health 2020-2025 report by the World Health Organization (WHO) shows that the use and scaling of digital health solutions can revolutionise access to health among people worldwide. Moreover, digital health applications can help achieve higher health standards and access services to promote and protect health and well-being [15]. This section presents some ideas and suggestions on how digital health applications would solve some pressing issues in African healthcare systems.

Digital health interventions allow health systems to share and disseminate vital health information to the masses irrespective of geographical limitations. For example, by using mobile phone Short Message Service (SMS) applications, health content on COVID-19 has been disseminated via mobile SMS by different telecommunication companies and partners supporting the ministries of health in Africa [10]. The SMSs contained important information on different thematic areas, including awareness, prevention, testing, tracking, vaccination, and treatment. In addition, patients have been given a chance to consult with healthcare providers using telehealth remotely.

Digital health applications also have the potential to facilitate communication between workers in Africa's health systems. This channel of communication enables lower-level workers to expand their range of tasks and take on tasks that would previously be assigned to higher-level workers [17] by using virtual reality (VR) applications and video conferencing. A typical example can be a nurse performing a high-level diagnosis or treatment procedure on a patient at a remote health centre by following instructions from a doctor located at the district or referral hospital [16]. In this way, health workers working in rural and remote areas can appreciate the efficiency of digital health technologies in offering services through the applications. The technologies also present a better way of sharing vital medical and statistical data between remote sites and central or district offices. Health systems can share such important data with researchers, accelerating response to outbreaks and ailments [17].

However, to date, the possibility of such technologies is precluded on the African continent because of poor quality of coverage and inadequate data speeds capacities of the 2G, 3G and 4G [18]. This challenge is why African countries need to invest in mobile telecommunications infrastructure by embracing technologies like 5G (B5G). The deployment of 5G (B5G) systems and platforms for healthcare in hospitals and clinics will provide a route for improved healthcare provision.

From findings, 5G (B5G) networks provide a better opportunity to develop innovative solutions in the health sector. This opportunity is because 5G networks have ultra-low latency, are more reliable, have massive capacity, increased availability, and provide a more uniform user experience to more users [19]. Research shows that 5G networks have considerable high data transmission rates and provides dedicated channels for processing and delivering relevant biomedical data rates of up to 20Gbps [20]. In addition, small cell-based 5G networks operating in millimetre wave (mmWave) frequencies are energy-efficient and cost-effective compared with traditional base stations [21], [22]. This factor shows how 5G will be easier to deploy even in rural and remote areas. The sixth-generation (6G) wireless communication networks are expected to support many medical equipment and devices with ultra-low latency requirements [23]. These B5G networks will integrate the terrestrial, aerial, and maritime communications into robust networks which would be more reliable, fast and agile. Furthermore, these networks will deal with delays in accessing and transmitting data through digital health applications even in network congestion [28], enabling a better quality of service (QoS) and improved user experience in using the applications.

C. The Need for a 5G (B5G) Digital Health Testbeds in Africa

Healthcare challenges in Africa are unique, and solving them will require embracing the emerging technologies outlined above. The availability of 5G (B5G) testbeds will accelerate the design and development of digital health interventions that will use today and in future networks. The testbeds will also facilitate improved beta testing before actual deployments of such interventions and increase the probability of successful implementations. Testbeds also provide a good launchpad for notable scaling up of interventions by replicating workable models of deployment and technology support [24].

This paper investigates the design and implementation of a secure 5G (B5G) digital health testbed to evaluate and validate digital health applications and services. The testbed is currently being implemented in the Faculty of Health Sciences at the University of Cape Town, South Africa. The project uses open-source tools and applicable standards to develop a cost-effective, flexible and scalable 5G (B5G) digital health testbed. The rest of the paper is organised as follows: Section II reviews related work and literature. Section III narrates the methodology to be used; Section IV presents a summary of the proposed solution; Section V discusses the expected outcomes of the testbed research, and Section VI concludes the paper and discusses future work.

II. RELATED WORK

Research has shown that there are no 5G and B5G health testbeds in Africa. However, in recent years, several digital health testbeds have been implemented globally. In this research, three testbeds have been identified and analysed in their implementation architecture, use cases, and security and privacy features. The United Kingdom (UK), through the Department for Digital, Culture, Media & Sport of the National Health Service (NHS), funded various 5G digital health testbed implementations under the 5G Testbeds and Trials Programme (5GTT) project [25]. Three of such implementations under the UK5G project were the Liverpool 5G testbed [26], the West Mercia Rural 5G [27] and the West Midlands 5G [28]. However, from the UK5G project, only the Liverpool 5G testbed is reviewed due to its uniqueness in using low-cost open-source 5G network architectures, artificial intelligence, VR and IoT.

The Liverpool 5G project is a consortium of public sector health and social care suppliers, the NHS, university

researchers at the University of Liverpool, the City Council, organisations, SMEs and a leading UK 5G technology vendor, Blu Wireless. The testbed has been established as a private 5G small cell mesh network in the Kensington area of Liverpool. It combines the City's closed-circuit television (CCTV) fibre assets and street furniture, Blu Wireless's tailored 60GHz mm-Wave technology, WiFi and a low-power long-range wide-area network protocol (LoRaWAN) as illustrated in Fig. 1 below. The use cases implemented on the testbed are safe house, PAMAN, Push-to-Talk (PTT), VR headsets in palliative care, telehealth in a box and chromatic sensors [26]. The applications use the concepts of IoT, VR, video conferencing, AI and ML, which necessitated the need for high data rates achievable in 5G networks. Thus, the Liverpool 5G testbed is an example of a multi-application platform-based digital health testbed.

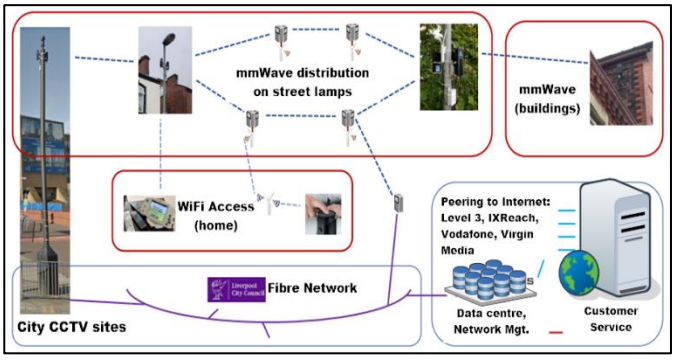

Figure 1: Liverpool 5G Testbed Network Deployment [35]

The second testbed reviewed is the 5G-Smart Diabetes testbed. This testbed was developed by researchers from Huazhong University of Science and Technology, the University of Oulu and the Korea Advanced Institute of Science and Technology. It combines state-of-the-art technologies such as wearable blood glucose monitoring devices, AI, ML, and big data to generate comprehensive sensing and analysis for patients who have diabetes [29].

Their implementation architecture is divided into layers, namely: the sensing layer, personalised diagnosis layer and data sharing layer. Furthermore, they developed a cloud platform using their data centre at their EPIC lab. All the collected data sets are offloaded to the cloud platform via the interface of the smart app. In addition, the results of the analyses and treatments are fed back through the app. To evaluate the performance of the testbed, Decision Tree, Support Vector Machine (SVM) and Artificial Neural Networks (ANN) machine learning algorithms are used [29]. The 5G-Smart Diabetes is an example of an application-specific use-case-based testbed.

The third testbed was developed by researchers at the Oulu University in the OuluHealth Labs. Using technologies such as health data management, efficient and ethical utilisation of AI, ML and 5G, they developed new predictive analytics for preventive medicine [30]. Their digital health testbed is integrated into the existing open 5G network through standardised architecture connected with test devices [31]. Their 5G New Radio (5G NR) network is 3GPP compliant, operating at 3.5GHz with a maximum of 100MHz bandwidth. It is envisaged that the non-standalone 5GNR supported by Long-Term Evolution (LTE) base station functions will later run in standalone mode [34]. Some of the projects being supported using the backbone 5G network at Oulu are DigiHealth, Nordic Arctic Co-creation Platform (NACCOP), Virtual Hospital 2.0, medical and dentistry digital learning (MEDigi), inDemand and HIPPA [32]. To tackle security and privacy issues, Oulu University launched a Secure-Connect project through the Centre for Wireless Communications to study the impact of 5G technologies in security and privacy [33].

A. Identified Research Gaps in the Related Work

Literature is not clear on how Liverpool 5G, 5G-Smart Diabetes and Oulu 5GTN testbeds leverage AI and ML in making the testbed core networks intelligent. Of the three, only Oulu 5GTN showcases some level of automation and monitoring of network traffic using NFV service-based slicing [34]. Furthermore, the three testbeds mentioned above did not showcase any notable use of X-Road, Blockchain, AI, and ML in tackling security and privacy issues. Blockchain can be used to establish secure, immutable and decentralised shared resources.

B. Suggested Solutions Proposed by Other Researchers

J. Kaur et al. (2021) propose Deep Learning (DL) for use on 5G&B5G networks because of its capabilities in achieving learning from scenarios that are more close to humans [20]. Using deep learning methods of AI and ML can solve the uncertainty, time variations, and complexity of a secure 5G (B5G) digital health network [35]. MedBlock is an example of an AI-enabled and Blockchain-driven medical healthcare system developed to secure Electronic Health Records (EHRs) of COVID-19 patients [36].

III. THE PROPOSED INTELLIGENT SECURE 5G AND BEYOND DIGITAL HEALTH TESTBED

The proposed research activities will be carried out in four stages. The first stage will involve designing and implementing a 5G campus network system in the Faculty of Health Sciences. The access network will consist of WiFi access points, Ethernet and 4G small cell base stations, which provide an interface for medical devices to share data with the core network. The digital health testbed network will be allocated its virtual network resources on the core network. Using Mobile Edge Computing (MEC) technology to improve applications' performance on the testbed, the network resources will be allocated as EDGE nodes for easy access and integration [37].

AI and ML algorithms will be programmed using PyCharm [38], Google's Colab and a library called TensorFlow [39] to automate the service instantiation of containers on the testbed. The MEC system, comprised of the virtual data processing and virtual storage machines (VMs), will be implemented in the same unit and connected to the 5G core system using network

adapter methods in the VirtualBox. Software-defined networking (SDN) will be used to decouple the control plane and the data plane of the testbed for better optimisation [40]. Once successfully installed, the end-to-end performance of the network infrastructure will be evaluated using Iperf [41], [42] and Wireshark [43], both open-source software tools used to validate network performance characteristics, i.e., latency, throughput and jitter. Two virtual machines will be installed to emulate online servers for data storage and processing. In addition, two Android phones and a laptop will be used as data retrieval devices.

The second stage will involve identifying and integrating digital health applications services that will act as preliminary use cases to test the testbed's performance. Five concepts have been targeted for the preliminary evaluation of the testbed. These are in areas of the internet of medical things (IOMT), augmented/virtual reality (AR/VR), image processing, tuberculin skin testing (TST) and tele-ultrasound.

The third stage of this project will involve designing and implementation the security framework. The Blockchain network will be implemented using Ethereum Blockchain technology, with the Blockchain smart contracts being implemented in the Solidity programming language [44]. The interplanetary file system will emulate the decentralised file storage in Blockchain, which is also characteristic in connected health systems when setting up storage servers on the testbed [45]. A blockchain client will be implemented in all Android devices to allow secure communication with the Blockchain system. The X-Road system will be implemented using open-source software provided under the MIT licence, with technical support available online from the Nordic Institute of Interoperability Solutions, an organisation supporting international X-Road deployments, with whom the authors are collaborating. This stage will also involve integrating the security framework onto the 5G network infrastructure. The network and medical devices secured using Blockchain and X-Road will be connected to the network.

The fourth stage will involve full integration of system units and run-time assessment of all the installed applications and services. Then, further evaluation of the testbed's ability to allow secure exchange of health data between mobiles devices and a server will be carried out to validate its security and privacy capacities.

IV. PROPOSED ARCHITECTURE FOR IMPLEMENTATION

The proposed testbed network will be comprised of four main domains, as shown in Fig. 2 below.

1) Data Acquisition Domain: This domain is where medical devices will be installed. These devices will collect patient health information and act as a point of entry of data into the digital health testbed. Other mobile applications that are used to capture data will also be used in this domain.

2) Access Network Domain: In this domain, access is given to the devices to share data with the core network infrastructure for processing storage and retrieval. Here, WiFi access points will be installed to connect WiFi-enabled equipment and devices for data transmission to and from the core network. An LTE Evolved Node B based small cell base station will also be installed. Ethernet connections to computers and Ethernet-enabled equipment will also be provided by installing a hub switch to extend the ethernet capability of the network.

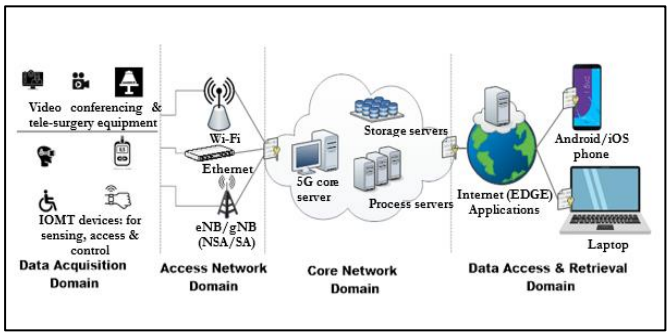

Figure 2: A proposed generic 5G-enbaled health network showing different system domains.

3) Core Network Domain: The core network will be the hub of all data transactions. This domain is where the 5G core Virtual Machine (VM) will be installed. The VMs will be comprised of the Mobility Management Entity (MME), Home Subscriber Server (HSS), Policy and Charging Rules Function (PCRF), Serving Gateway Control Plane (SGWC), Serving Gateway User Plane (SGWU), Packet Gateway Control Plane/ Session Management Function (PGWC/SMF) and the Packet Gateway User Plane/ User Plane Function (PGWU/UPF). Data processing and storage facilities, applications and services will be implemented using virtualisation (VMs) and containerisation (containers).

4) Data Retrieval Domain: This is where monitoring services and applications will be implemented. Computer, web-based, and smartphone (Android & IOS) applications will be installed on PC and mobile phones connected to the core network through the access network.

V. EXPECTED OUTCOMES

The research outcomes include a working testbed platform for the validation of digital health applications developed at UCT. The testbed will be open and accessible for other universities from South Africa and other African countries for their researchers to perform trials of their digital health applications. The testbed will become a very important blueprint in modelling the emerging concept of 5G-connected hospitals [50] in Africa through replication.

The testbed will also work as a catalyst for fast-tracking translation of research results in digital health applications to deployable commercial products and solutions. The testbed will be equipped with all the parametric capabilities to mimic the deployment environments. The applications will be tested using selected medical devices, mobile phones, computers, and servers connected to the testbed. The testbed will provide a

practical modelled environment for testing, reducing the failure rate during deployment while in service. As a result, these well-matured digital health applications will bring a tremendous positive impact on healthcare service delivery.

The testbed architecture will also become a blueprint in installing 5G (B5G) private networks or 5G campus networks, facilitating the introduction of local 5G-powered hospitals in Africa [46]. The 5G architecture will comprise of such unique technical features of 5G/6G such as the New Radio (NR) interface, 5G core (5GC) network, network slicing as well as the use of AI and ML in 5G (B5G) networks.

VI. CONCLUSIONS AND FUTURE WORK

This paper proposes the design, development and evaluation of an intelligent, secure 5G (B5G) digital health testbed used as a centre of research for digital health interventions in Africa. The paper advocates for the need for Africa to have its digital health testbed that provides a platform of collaboration and continual research in the subject matter. The proposed testbed will meet the intended outcomes and help improve the testing and delivery of digital health applications in 5G (B5G) networks in Africa.

ACKNOWLEDGEMENT

The South Africa National Research Foundation (NRF) Grant No. 980000001090 and Telkom South Africa support this research via the Telkom Centre of Excellence (CoE) in Broadband Networks at the University of Cape Town and a grant from Carnegie Corporation of New York. The statements made and views expressed are solely the responsibility of the authors.

REFERENCES

[1] M. Herselman, A. Botha, H. Toivanen, J. Myllyoja, T. Fogwill, and R. Alberts, 'A Digital Health Innovation Ecosystem for South Africa', in *2016 IST-Africa Week Conference*, May 2016, pp. 1–11.

[2] C. Guo, H. Ashrafian, S. Ghafur, G. Fontana, C. Gardner, and M. Prime, 'Challenges for the evaluation of digital health solutions—A call for innovative evidence generation approaches', *Npj Digit. Med.*, vol. 3, no. 1, Art. No. 1, Aug. 2020.

[3] T. Folaranmi, 'mHealth in Africa: challenges and opportunities', *Perspect. Public Health*, vol. 134, no. 1, pp. 14–5, Jan. 2014.

[4] A. Kapoor, S. Guha, M. Kanti Das, K. C. Goswami, and R. Yadav, 'Digital healthcare: The only solution for better healthcare during COVID-19 pandemic?', *Indian Heart J.*, vol. 72, no. 2, pp. 61–64, 2020.

[5] M. Okereke, A. O. Babatunde, S. T. Samuel, I. O. Ogunkola, Y. G. Mogessie, and D. E. Lucero-Prisno, 'Applications of telemedicine in the supply and distribution of COVID-19 vaccines in Africa', *J. Glob. Health*, vol. 11, Mar. 2021.

[6] ICLG, 'International Comparative Legal Guides', *International Comparative Legal Guides International Business Reports*, 2021. https://iclg.com/practice-areas/digital-health-laws-and-regulations/south-africa (accessed Jun. 18, 2021).

[7] Worldometer, 'Population of Africa (2021) - Worldometer', May 18, 2021. https://www.worldometers.info/world-population/africa-population/ (accessed May 19, 2021).

[8] J. Michel *et al.*, 'Achieving universal health coverage in sub-Saharan Africa: the role of leadership development', *J. Glob. Health Rep.*, vol. 4, p. e2020037, Jun. 2020.

[9] O. O. Oleribe *et al.*, 'Identifying Key Challenges Facing Healthcare Systems In Africa And Potential Solutions', *Int. J. Gen. Med.*, vol. 12, pp. 395–403, Nov. 2019.

[10] L. H. Kamulegeya, J. M. Bwanika, D. Musinguzi, and P. Bakibinga, 'Continuity of health service delivery during the COVID-19 pandemic: the role of digital health technologies in Uganda', *Pan Afr. Med. J.*, vol. 35, no. 43, Art. No. 43, May 2020.

[11] PwC, '5G In Healthcare', *PwC*, 2020. https://www.pwc.com/gx/en/industries/tmt/5g/5g-in-healthcare.html (accessed May 19, 2021).

[12] WHO, 'Universal health coverage (UHC)', Apr. 01, 2021. https://www.who.int/news-room/fact-sheets/detail/universal-health-coverage-(UHC) (accessed May 18, 2021).

[13] R. Lozano *et al.*, 'Measuring universal health coverage based on an index of effective coverage of health services in 204 countries and territories, 1990–2019: a systematic analysis for the Global Burden of Disease Study 2019', *The Lancet*, vol. 396, no. 10258, pp. 1250–1284, Oct. 2020.

[14] UN, 'Goal 3 | Department of Economic and Social Affairs', Sep. 2015. https://sdgs.un.org/goals/goal3 (accessed May 17, 2021).

[15] WHO, 'Global strategy on digital health 2020-2025', World Health Organization, Geneva, 2021. Accessed: Jun. 08, 2021. [Online]. Available: https://cdn.who.int/media/docs/default-source/documents/gs4dhdaa2a9f352b0445bafbc79ca799dce4d.pdf?sfvrsn=f112ede5_75

[16] J. M. Winters and J. M. Winters, 'Videoconferencing and Telehealth Technologies Can Provide a Reliable Approach to Remote Assessment and Teaching Without Compromising Quality', *J. Cardiovasc. Nurs.*, vol. 22, no. 1, pp. 51–57, Feb. 2007.

[17] Z. Allam and D. S. Jones, 'On the Coronavirus (COVID-19) Outbreak and the Smart City Network: Universal Data Sharing Standards Coupled with Artificial Intelligence (AI) to Benefit Urban Health Monitoring and Management', *Healthcare*, vol. 8, no. 1, Art. No. 1, Mar. 2020.

[18] A. Kaliwo, C. Mikeka, H. Gombachika, S. Kaunda, and C. Mlangeni, 'Analysis of Mobile Telecommunication Networks' Coverage and Internet Capacity to Support mHealth Applications in Blantyre City: A Case of TNM and Airtel Networks', *South Asian Res. J. Eng. Technol.*, vol. 01, no. 03, pp. 87–97, Nov. 2019.

[19] M. Bennis, M. Debbah, and H. V. Poor, 'Ultrareliable and Low-Latency Wireless Communication: Tail, Risk, and Scale', *Proc. IEEE*, vol. 106, no. 10, pp. 1834–1853, Oct. 2018.

[20] J. Kaur, M. A. Khan, M. Iftikhar, M. Imran, and Q. Emad Ul Haq, 'Machine Learning Techniques for 5G and Beyond', *IEEE Access*, vol. 9, pp. 23472–23488, 2021.

[21] A. Mesodiakaki, A. Kassler, E. Zola, M. Ferndahl, and T. Cai, 'Energy-efficient line-of-sight millimetre wave small cell backhaul: 60, 70, 80 or 140 GHz?', in *2016 IEEE 17th International Symposium on A World of Wireless, Mobile and Multimedia Networks (WoWMoM)*, Jun. 2016, pp. 1–9.

[22] B. Malila, N. Ventura, and O. Falowo, 'Design of a Cognitive Small Cell Backhaul System for Non-Line-of Sight Deployment in Urban Canyons', p. 6, 2017.

[23] M. W. Akhtar, S. A. Hassan, R. Ghaffar, H. Jung, S. Garg, and M. S. Hossain, 'The shift to 6G communications: vision and requirements', *Hum.-Centric Comput. Inf. Sci.*, vol. 10, no. 1, p. 53, Dec. 202.

[24] L. Olsen, D. Aisner, and J. M. McGinnis, *Developing the Test Bed—Linking Integrated Service Delivery Systems*. National Academies Press (US), 2007. Accessed: Jun. 18, 2021. [Online]. Available: https://www.ncbi.nlm.nih.gov/books/NBK53485/

[25] UK DCMS, '5G Testbeds and Trials Programme', *GOV.UK*, Mar. 26, 2021. https://www.gov.uk/guidance/5g-testbeds-and-trials-programme (accessed Jun. 16, 2021).

[26] UK5G, 'Liverpool 5G Testbed', Mar. 10, 2018. https://uk5g.org/discover/testbeds-and-trials/liverpool-5g-testbed/ (accessed Jun. 16, 2021).

[27] UK5G, 'West Mercia Rural 5G', Mar. 01, 2020. https://uk5g.org/discover/testbeds-and-trials/west-mercia-rural-5g/ (accessed Jun. 16, 2021).

[28] UK5G, 'West Midlands 5G', Sep. 01, 2018. https://uk5g.org/discover/testbeds-and-trials/west-midlands-5g/ (accessed Jun. 16, 2021).

[29] M. Chen, J. Yang, J. Zhou, Y. Hao, J. Zhang, and C.-H. Youn, '5G-Smart Diabetes: Toward Personalised Diabetes Diagnosis with Healthcare Big Data Clouds', *IEEE Commun. Mag.*, vol. 56, no. 4, pp. 16–23, Apr. 2018.

[30] S. Hazlegreaves, 'The future of healthcare is created in the OuluHealth ecosystem in Finland', *Open Access Government*, Mar. 21, 2019. https://www.openaccessgovernment.org/healthcare-ouluhealth-ecosystem-finland/61288/ (accessed Jun. 17, 2021).

[31] Oulu, 'Open 5G connection in Finland's test network now in use', May 16, 2019. https://www.oulu.fi/university/news/open-5g-connection (accessed Jun. 17, 2021).

[32] OuluHealth, 'Testing & Co-creation', *OuluHealth*. https://ouluhealth.fi/services/testing-co-creation/ (accessed Jun. 14, 2021).

[33] A. Miettinen, 'Security in 5G networks is a building block for a safer future', Feb. 21, 2018. https://www.oulu.fi/cwc/node/45500 (accessed Jun. 17, 2021).

[34] M. Arif, O. Liinamaa, I. Ahmad, A. Pouttu, and M. Ylianttila, 'On the Demonstration and Evaluation of Service-Based Slices in 5G Test Network using NFV', in *2019 IEEE Wireless Communications and Networking Conference Workshop (WCNCW)*, Apr. 2019, pp. 1–6.

[35] Y. Dai, D. Xu, S. Maharjan, Z. Chen, Q. He, and Y. Zhang, 'Blockchain and Deep Reinforcement Learning Empowered Intelligent 5G Beyond', *IEEE Netw.*, vol. 33, no. 3, pp. 10–17, May 2019.

[36] C. Mistry *et al.*, 'MedBlock: An AI-enabled and Blockchain-driven Medical Healthcare System for COVID-19', in *ICC 2021 - IEEE International Conference on Communications*, Jun. 2021, pp. 1–6.

[37] D. Adib, 'Mobile Edge Computing (MEC): What is Mobile Edge Computing?', *STL Partners*. https://stlpartners.com/edge-computing/mobile-edge-computing/ (accessed Jun. 25, 2021).

[38] JetBrains, 'PyCharm: the Python IDE for Professional Developers by JetBrains', *JetBrains*, 2021. https://www.jetbrains.com/pycharm/ (accessed Aug. 27, 2021).

[39] TensorFlow, 'TensorFlow', *TensorFlow*, 2021. https://www.tensorflow.org/ (accessed Aug. 27, 2021).

[40] A. Gopalasingham, L. Roullet, N. Trabelsi, C. S. Chen, A. Hebbar, and E. Bizouarn, 'Generalised software-defined network platform for Radio Access Networks', in *2016 13th IEEE Annual Consumer Communications Networking Conference (CCNC)*, Jan. 2016, pp. 626–629.

[41] iPerf, 'iPerf - The TCP, UDP and SCTP network bandwidth measurement tool'. https://iperf.fr/ (accessed Jun. 17, 2021).

[42] Md. T. Islam, N. Islam, and Md. A. Refat, 'Node to Node Performance Evaluation through RYU SDN Controller', *Wirel. Pers. Commun.*, vol. 112, no. 1, pp. 555–570, May 2020.

[43] C. Sanders, *Practical Packet Analysis, 3rd Edition: Using Wireshark to Solve Real-World Network Problems*. No Starch Press, 2017.

[44] Team Solidity, 'Solidity Programming Language', *Solidity Programming Language*. https://soliditylang.org// (accessed Jun. 21, 2021).

[45] D. C. Nguyen, P. N. Pathirana, M. Ding, and A. Seneviratne, 'Blockchain for 5G and beyond networks: A state of the art survey', *J. Netw. Comput. Appl.*, vol. 166, p. 102693, Sep. 2020.

[46] A. Rostami, 'Private 5G Networks for Vertical Industries: Deployment and Operation Models', in *2019 IEEE 2nd 5G World Forum (5GWF)*, Sep. 2019, pp. 433–439.

Alinafe Kaliwo is a PhD student in Biomedical Engineering at the University of Cape Town. He obtained his MPhil (Eng.) in Telecommunications from the University of Malawi. His research interests include 5G and beyond networks, Internet of Things, Cloud Computing, Artificial Intelligence and Machine Learning.

Tinashe Mutsvangwa is an Associate Professor for Biomedical Engineering at the University Cape Town, South Africa. He holds a BSc in Electrical/Electronic Engineering and an MSc and PhD in Biomedical Engineering, all from the University of Cape Town.

Bessie Malila is a junior research fellow in Biomedical Engineering at the University of Cape Town. She holds a PhD and MSc in Telecommunications from the University of Cape Town and a BSc in Electrical and Electronic Engineering from the University of Zimbabwe.

Data Centre & Cloud

Selecting Datasets for Evaluating an Enhanced Deep Learning Framework

Kudakwashe Dandajena[1], Isabella M. Venter[2], Mehrdad Ghaziasgar[2], and Reg Dodds[2]
[1,2]*Department of Computer Science, University of the Western Cape*
[1]3986658@myuwc.ac.za, [2]{iventer,mghaziasgar,rdodds}@uwc.ac.za

***Abstract*—A framework was developed to address limitations associated with existing techniques for analysing sequences. This work deals with the steps followed to select suitable datasets characterised by discrete irregular sequential patterns. To identify, select, explore and evaluate which datasets from various sources extracted from more than 400 research articles, an interquartile range method for outlier calculation and a qualitative Billauer's algorithm was adapted to provide periodical peak detection in such datasets. The developed framework was then tested using the most appropriate datasets. The research concluded that the financial market-daily currency exchange domain is the most suitable kind of data set for the evaluation of the designed deep learning framework, as it provides high levels of discrete irregular patterns.**

***Index Terms*—Sequential analysis artefacts, deep learning framework for irregular sequential analysis, sequential prediction environment, enhanced deep learning framework, and irregular sequential patterned dataset.**

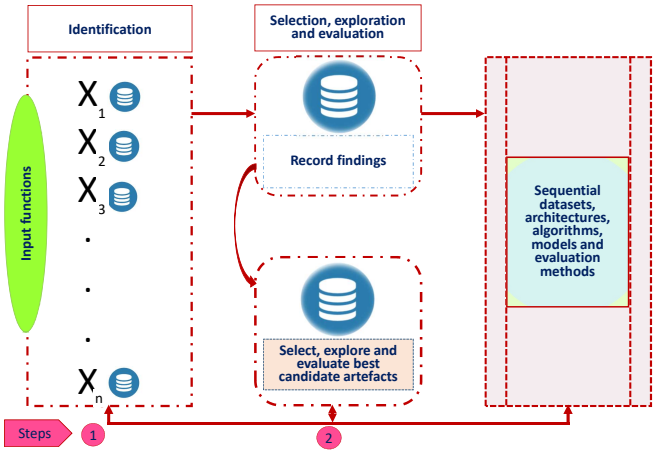

Fig. 1. SeLFISA framework dataset selection process

I. Introduction

The current technological transformation, named the fourth industrial revolution (4IR) [1] has positively transformed society by its: abundance of data; enhanced connectivity; industrial and workplace automation; autonomous and intelligent agents; artificial intelligence (AI) solutions; the Internet of things (IoT) technologies, etc. [2]. Every other industrial revolution, produced a different type of cutting-edge technology which had its own challenges. Institutions and individuals are investing in a considerable amount of resources such as capital, human talent, infrastructure, hardware platforms, environments and software tools to remain competitive and sustainable. It is important to note that research within 4IR, is assisting science to improve the lives of people. This can be validated by how researchers such as Geoffrey Hinton, Yoshua Bengio, Ian Goodfellow, Andrew Ng, etc., have leveraged developments for the advancement of AI [3].

The underlying challenges associated with existing deep learning frameworks for the analysis of discrete irregular patterned complex sequences were identified [4]. Specific concerns raised were: performance robustness; transparency of the methodology; literature consistency; internal and external architectural design and configuration issues. Inconsistencies and discord in the literature highlight some of the challenges associated with existing approaches to the analysis of irregular sequences and makes it possible to address them. It was suggested that addressing these challenges might lead to a systematic, accurate, stable, explainable and repeatable deep learning framework for the analysis of these types of datasets. The explainability of any system is determined by the ability to present and explain its underlying features in a way that can be understood [5]. The relationship between data and deep learning solutions has become important for the development of better artefacts for analysis [6]. Current interest in innovative developments in the field of AI is often driven by large scale data. Data is both a push and a pull factor for the development of AI technologies, which are producing and consuming an unprecedented abundance of data. For example data is produced by financial markets, social media, astronomy, weather, traffic, surveillance, etc. [7]. There is an emerging trend that datasets are characterised by a high level of irregularities as a result of incompleteness, extreme randomised patterns and noise [8]. Dealing with such massive datasets remains challenging.

This paper builds towards a framework named the *Systematic enhanced deep Learning Framework for Irregular Sequential Analysis (SeLFISA)* for the analysis of these kinds of datasets. The framework will be a combination of architectures, algorithms and models aimed at predicting the future behaviour of complex sequences. The intention is to produce an explainable and straightforward framework as part of a solution within the 4IR space. The initial step of such a framework involves selecting suitable and appropriate datasets, which is the focus of this paper. The dataset selection process of the intended SeLFISA framework is shown in Fig. 1. As such, the aim of this research is to address the question: *How should such a dataset be identified to evaluate the SeLFISA framework?* A design science research methodology guided the research.

Referring to the process in Fig. 1, a class of datasets with irregular patterns were identified as a key stage of developing better deep learning artefacts for sequential analysis. Seventy three sequential datasets from eight domains of different sources were extracted from 400 research articles, by means of a systematic literature review process [4]. Datasets, characterised with the most irregular patterns, were then identified for the evaluation of the deep learning framework. The daily financial market currency exchange domain provided high levels of discrete irregular patterned environments and the Pound to Dollar exchange rate was used for the evaluation.

II. Materials and Methods

The implementation process of the SeLFISA framework illustrated in Fig. 1 involves detailed activities at each step to create a systematic, and repeatable way of analysing irregular discrete patterns in sequential environments.

The two steps in the framework shown in Fig. 1 were:

Step 1—Identify existing sequential datasets, analysis artefacts, and an evaluation mechanism using the systematic literature review process (SLR): This stage creates an initial node that receives input from the SLR guided by reporting items for systematic reviews and meta-analyses (PRISMA) [9]. Artefacts in the form of algorithms and models provide hints to guide the choice of implementation approaches, datasets and performance evaluation techniques. This stage focuses on trying to find initial answers to the following questions:

1) *Which datasets are sequential in nature with irregular characteristics?*
2) *Which artefacts in the form of algorithms and models have been applied elsewhere to analyse such datasets?*
3) *How were those artefacts evaluated in terms of determining their performance?*

This step also creates a precondition for implementing the SeLFISA framework by ensuring that it produces repeatable and reliable output.

Failure to satisfy the initial condition will not only affect the entire development process of better artefacts to analyse such datasets but will negatively affect substantiation of the results.

Step 2—Select, explore and evaluate candidate requirements: Here identified datasets, classical algorithms for irregular sequential analysis, and evaluation mechanisms were loaded into a database of records. This was done to implement an ecosystem comprising high performance computing resources coupled with specific software libraries and tools. An analysis that considered different dimensions had to be made and applied to add insights into eradicating elements of inconsistency and ambiguity that may affect future implementation steps and procedures. Once this analysis was done, a selection process commenced based on the following:

1) **Datasets**—Select a dataset with most irregular patterns. Determine the number of irregular patterns of datasets by combining both descriptive numerical and visualization approaches. Check the levels of irregularity of selected datasets by considering the following:
   a) *Box and whisker plot*: apply statistical descriptive analysis of irregular patterns on all datasets by considering the interquartile range (IQR) outlier calculation [10]. This approach illustrates the minimum and maximum values of any dataset. The first, second and third quartiles Q1, Q2 and Q3 of the data are shown in the in the box plot. The difference between the minimum and maximum provides the range of values within the dataset. Finally, the difference between Q3 and Q1 provides an inter-quartile range (IQR) given by Equation (1):

   $$IQR = Q3 - Q1 \tag{1}$$

   Outliers in irregular patterns can easily be detected as those data points that are either one and a half times IQR below Q1 or above Q3, i.e. :

   $$\text{Below } = Q1 - 1.5 \times IQR \tag{2}$$

   $$\text{Above } = Q3 + 1.5 \times IQR \tag{3}$$

   b) *Billauer's algorithm* is used to validate outcomes of the box and whisker plot results and to detect local maxima and minima in a signal [11]. It provides a graphical visualization analysis of peaks to measure the degree of irregularity of the original data environment. The algorithm is then customised to provide irregular-pattern peak period detection (IPPD) which detects discrete peak values by searching for values that are surrounded by lower or larger values for maxima and minima across the y-axis and corresponding x-axis. A look-ahead value for determining the look-ahead distance for a potential peak needs to be a set as a specific value to provide a maximum number of discrete peaks.
   c) *Further exploratory data analytics* then needs to be conducted for insights into how variables of the chosen sequential dataset are connected to each other. Data description, data pre-processing, data munching, data cleaning, and exploratory data analysis all are executed under this umbrella procedure to understand a dataset in detail.
2) **Artefacts**—Candidate artefacts were then selected, based on their intrinsic design, application, context and veracity. At this stage, attention has to be focused on topical issues associated with common, debatable and contradicting issues highlighted by different authors. Attention was also paid to the search space through variable clipping.
3) **Evaluation**—Evaluation allowed for the development of a narrow list of multidimensional performance criteria. This was done to find the best metrics for each criterion that captures the requirements of the sequential analysis challenge. The multidimensional criteria encompass a basket of factors covering complexity accuracy, efficiency, stability, straightforwardness, explainability and repeatability.

TABLE I
A SUMMARY OF IDENTIFIED SEQUENTIAL DATASETS, ANALYSIS ARTEFACTS, AND EVALUATION MECHANISMS

Sequential Models and Architectures	Sequential Datasets	Evaluation Techniques
$\geq$ 34 architectures	$\geq$ 73 datasets from 8 domains of different sources.	6 evaluation techniques
See Section VI for Annexure_1_Results.pdf in GitHub.		

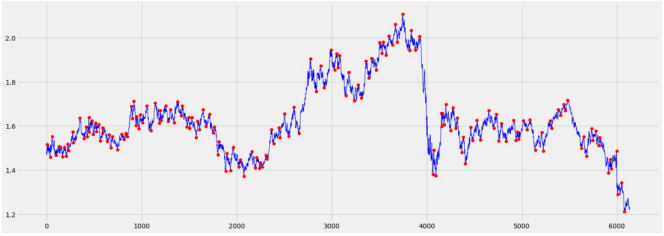

Fig. 2. IPPD visualisation analysis of daily exchange data between the GB Pound and the US Dollar from 1990 to 2016 [12]

III. RESULTS

A summary of the results for these implementation steps is given below:

Step 1—The identification of existing sequential datasets, analysis artefacts, and evaluation criteria. This step is an extension of the systematic literature review work [4] which reviewed over 400 research articles from year 2015 to 2020 and narrowed them to the 33 most relevant articles. A summary of identified sequential models, architecture, datasets and evaluation techniques is shown in Table I.

Step 2—The selection, exploration and the evaluation of candidate requirements

i **Datasets**—At this stage, all datasets identified were collected into a bank of datasets—see Section VI Annexure_2-Datasets_Models in GitHub. A hybrid high-end computational processing environment was provided by the South African Centre for High Performance Computing which provides NVIDIA GeForce MX130 graphical processing units (GPUs) and random access memory ranging between 20–210 GB, 10 TB HDD; a CUDA toolkit for GPU deployment; Anaconda distribution software with Python and Jupyter Notebook, and the Keras, TensorFlow, Pandas and other libraries.
This dual mathematical and visualisation approach identified a dataset of financial daily exchange data between the GB Pound and the US Dollar from 1990 to 2016 [12] with the highest number of irregular patterns, i.e. 639 from 6135 daily records. The financial daily exchange data between the Japanese Yen and the US Dollar from the same period has around 24 irregular patterns from 5000 daily records.
Applying Billauer's algorithm produced irregular patterns peak period detection (IPPD) visualisation analysis of the daily exchange data between the GB Pound and the US Dollar. See Fig. 2. The financial daily exchange rate data between the GB Pound and the US Dollar became our primary candidate dataset for the SeLFISA framework evaluation, and the daily exchange rate data between the Japanese Yen and the US Dollar became the elected validation dataset to test performance stability and consistency.

ii **Algorithms**—The experimental process identified 12 implementable or executable algorithms for sequential analysis from different authors which became the candidate artefacts. The selection process considered a combination of architecture uniqueness and referenced performance properties. Some of these algorithms were based on gated recurrent neural networks (RNN), autoencoders, convolutional neural networks, bidirectional mechanisms, attention mechanisms, ensemble techniques, deep and vanilla architectures.
Specific architectural design features of these 12 selected algorithms were: the gated LSTM architecture suggested [13], [14] and [15]; the bidirectional mechanism combined with both LSTMs and GRUs influenced [16]; the attention mechanism combined with gated neural networks [17]; deep convolutional neural network (CNN) ensemble with LSTM and an attention mechanism [18]; a GRU [19] autoencoders combined with LSTM [20] and finally a deep gated recurrent neural network architectures made up of both GRU and LSTM [21].

iii **Evaluation**—The following factors were considered as potential performance evaluation criteria with specific metrics: complexity measure through the total number of built parameters of every architecture, accuracy considered a *mean absolute error* (MAE) which is robust in environments associated with discrete irregular patterns when measuring the average magnitude of the errors in a set of predictions, without considering their direction. *Mean squared error* (MSE) provided an accuracy performance measure of the variance of the residuals and a quadratic scoring rule of *root mean squared error* (RMSE) which gives a relatively high weight to large errors. The R^2 measures how well the independent variables in the linear regression model predict the dependent variable. The lower the value of MAE, MSE and RMSE the more favourable the performance accuracy of the implemented model. Higher R^2 values indicate better performance.
Efficiency was measured as a ratio of execution time and the total number of parameters—whilst explainability and repeatability were identified qualitatively.

IV. DISCUSSION

There is still not much agreement on how to solve the challenges posed by the analysis of irregular sequential datasets [4]. Contrary to existing frameworks—which are skewed towards probabilistic randomization or ad-hoc design approaches, which are prone to accuracy, stability, explainability and repeatability deficiencies—the SeLFISA framework aims at addressing these deficiencies [22]. To test the developed framework, appropriate datasets had to be identified.

A. Datasets

This paper has shown that analysing discrete irregular patterns or behaviour in sequential environments is more centred on a framework approach beyond just an architecture- or an algorithm- or a model-approach. The framework provides guidance for developing a robust analysis artefact. The suggested SeLFISA framework has proved to be useful—as it integrates outputs and outcomes from a wide range of research approaches to provide a systematic way to address performance, robustness, literature inconsistencies, straightforwardness and design limitations associated with existing sequential analysis techniques. Iterative steps of the SeLFISA framework deliver an explainable and understandable way of determining the levels of irregularity of such datasets. It applied Billauer's algorithm and mathematical and interquartile range outlier calculations to select, explore and evaluate a variety of sequential datasets [11]. The daily exchange rate data between the GB Pound and the US Dollar has been identified as a dataset which is very suitable for learning because of high irregularity [12]. The daily exchange between the Japanese Yen and the US Dollar data can then be used as a validation dataset.

B. Algorithms

On the other hand, models and algorithms designed through gated sequential architectures in the form of LSTMs and GRUs have been widely used in such analysis environments [13], [14], [15]. Thus the guidance from the SeLFISA framework will influence the development of deep learning with artefacts that may demonstrate better performance over these suggested gated models.

C. Evaluation

This framework is useful when evaluating performance criteria with specific metrics for a particular analysis artefact. SelFISA provides a multidimensional perspective for examining critical design aspects and properties of chosen artefacts.

V. Conclusion and Future Recommendations

The SelFISA framework was developed to address limitations associated with existing sequential analysis techniques. The identification, selection, exploration and evaluation of datasets characterised by irregular discrete sequential characteristics using the SeLFISA framework provides a starting point towards the design of better performing, straightforward, explainable and understandable deep learning analysis artefacts. It creates a consistent shareable technical and literature platform which consists of a knowledge bank of implemented irregular sequential analysis frameworks, datasets, algorithms and literature.

A literature bank of financial sequential datasets with varying complexity was created. This provides a source to the solution of existing literature inconsistencies and deficiencies in explaining the performance of deep learning artefacts for modelling irregular sequential behaviour see Section VI.

It is recommended to further develop the SeLFISA framework to create a consistent shareable technical and literature platform. The framework will consist of a knowledge bank of implemented irregular sequential analysis frameworks, datasets, algorithms and literature.

VI. Annexures

The annexures of results and datasets can be found on GitHub: https://github.com/Dandajena/SATNAC_2021_Paper.

VII. Acknowledgment

This work is funded by the Research Committee of the University of the Western Cape and Telkom/Aria Technology Africa Centre of Excellence. The work received computational processing environment support from the South African Centre for High Performance Computing.

References

[1] K. Schwab, *The Fourth Industrial Revolution*. New York, NY: Crown Business, 2017.

[2] J. Lee, H. Davari, J. Singh, and V. Pandhare, "Industrial artificial intelligence for industry 4.0-based manufacturing systems," *Manufacturing Letters*, vol. 18, pp. 20–23, 2018.

[3] I. J. Goodfellow, Y. Bengio, and A. Courville, *Deep Learning*. Cambridge, MA: MIT Press, 2016.

[4] K. Dandajena, I. M. Venter, M. Ghaziasgar, and R. Dodds, "Complex sequential data analysis: A systematic literature review of existing algorithms," in *Conference of the South African Institute of Computer Scientists and Information Technologists 2020*, Cape Town, 2020, pp. 44–50.

[5] F. Doshi-Velez and B. Kim, "Towards a rigorous science of interpretable machine learning," *arXiv:1702.08608*, vol. [stat.ML], pp. 1–13, 2017.

[6] S. S. Sarmah, "Concept of artificial intelligence, its impact and emerging trends," *International Research Journal of Engineering and Technology*, vol. 6, no. 11, pp. 2164–2019, 2019.

[7] N. Srivastava, G. Hinton, A. Krizhevsky, I. Sutskever, and R. Salakhutdinov, "Dropout: A simple way to prevent neural networks from overfitting," *Journal of Machine Learning Research*, vol. 15, pp. 1929–1958, 2014.

[8] W. Souma, I. Vodenska, and H. Aoyama, "Enhanced news sentiment analysis using deep learning methods," *Journal of Computational Social Science*, vol. 2, pp. 33–46, 2019.

[9] D. Moher, A. Liberati, J. Tetzlaff, and D. G. Altman, "Preferred reporting items for systematic reviews and meta-analyses: the PRISMA statement," *Epub*, pp. 123–130, 2009.

[10] K. M. Myat and S. S. M. Win, "Analysis of outlier detection on structured data," in *Proceedings of 2020 the 10th International Workshop on Computer Science and Engineering*, Yangon, Myanmar, 2020, pp. 16–21.

[11] J. Xiao, H. Li, X. Wang, and S. Yuan, "Traffic peak period detection from an image processing view," *Journal of Advanced Transportation*, vol. 2018, pp. 1–10, 2018.

[12] Y.-Y. Chang, F.-Y. Sun, Y.-H. Wu, and S.-D. Lin, "A memory-network based solution for multivariate time-series forecasting," *arXiv:1809.02105*, vol. [cs.LG], pp. 1–8, 2019.

[13] A. Azlan, Y. Yusof, and M. F. M. Mohsin, "Determining the impact of window length on time series forecasting using deep learning," *International Journal of Advanced Computer Research*, vol. 9, no. 44, pp. 260–267, 2019.

[14] M. Glenski, T. Weninger, and V. Volkova, "Improved forecasting of cryptocurrency price using social signals," *arXiv:1907.00558*, vol. [q-fin.ST], pp. 1–11, 2019.

[15] C. Chalvatzisa and D. Hristu-Varsakelis, "High-performance stock index trading: making effective use of a deep long short-term memory network," *arXiv:1902.03125*, vol. [q-fin.ST], pp. 1–30, 2019.

[16] M. Sardelicha and S. Manandhar, "Multimodal deep learning for short-term stock volatility prediction," *arXiv:1812.10479*, vol. [q-fin.ST], pp. 1–40, 2018.

[17] S. Huang, D. Wang, X. Wu, and A. Tang, "DSANet: Dual self-attention network for multivariate time series forecasting," in *CIKM '19*, Beijing, 2019, pp. 2129–2132.
[18] M. Mäkinen, J. Kanniainen, M. Gabbouj, and A. Iosifidis, "Forecasting of jump arrivals in stock prices: New attention-based network architecture using limit order book data," *arXiv:1810.10845*, vol. [q-fin.TR], pp. 1–29, 2018.
[19] H. Qin, "Comparison of deep learning models on time series forecasting: A case study of dissolved oxygen prediction," *arXiv:1911.08414*, vol. [eess.SP], pp. 1–16, 2019.
[20] W. Wei, H. Wu, and H. Ma, "An autoencoder and LSTM-based traffic flow prediction method," in *Sensors*, Beijing, 2016, pp. 1–16.
[21] S. Bai, J. Z. Kolter, and V. Koltun, "Deep equilibrium models," in *33rd Conference on Neural Information Processing Systems (NeurIPS 2019)*, Vancouver, 2019, pp. 1–16.
[22] V. Kuleshov, N. Fenner, and S. Ermon, "Accurate uncertainties for deep learning using calibrated regression," *arXiv:1807.00263*, vol. [cs.LG], pp. 1–9, 2018.

Kudakwashe Dandajena is a Ph.D. student in Computer Science at the University of the Western Cape, investigating the optimisation of deep learning algorithms in discrete irregular sequential patterns. He is program manager for the community of scientists of the Next Einstein Initiative at the African Institute for Mathematical Sciences Global Secretariat in Rwanda. Kuda holds a Master's degree in Computer Science. Mobile: +25078 582 1565.

Isabella M. Venter is an Emeritus Professor in Computer Science at the University of the Western Cape, South Africa and the Chair of the Management Committee of the Telkom/Aria Technologies Africa Centre of Excellence. Her research interests include: computer science education, human computer interaction and information communication technologies for development. Mobile: +2782 202 3520.

Mehrdad Ghaziasgar holds a PhD in Computer Science and is a Senior Lecturer in Computer Science at the University of the Western Cape. He heads up the Assistive Technologies Research Group at the Department which investigates applications of computer vision and machine learning to novel assistive technologies. Tel: +2721 959 3012.

Reg Dodds has lectured in Computer Science at Stellenbosch, Natal, Port Elizabeth Universities and at the University of the Western Cape.

Linux Networking Performance Profiling Towards Network Function Virtualisation Improvements

Tariro Mukute*, Joyce Mwangama*, Albert A. Lysko† *
*Department of Electrical Engineering, University of Cape Town
[1]mkttar001@myuct.ac.za
[2]joyce.mwangama@uct.ac.za
†Council for Scientific and Industrial Research, South Africa
[3]alysko@csir.co.za

***Abstract*—The mobile networking industry has proposed the adoption of network function virtualisation in the various components of the core network, including the Gi-LAN which houses a large set of network functions. However, virtualisation introduces performance cost or additional processes that degrade the performance of the resultant network functions. In this work we consider the network stack for the most common virtualisation technology, Linux. We model the Linux networking stack based on the detailed analysis and monitoring of the performance of the various processes that occur in the network stack as the packets are forwarded to the network functions for processing. Based on the resultant model, we suggest and evaluate approaches for reducing the performance cost or avoiding unnecessary processes, in the context of Gi-LAN network functions.**

***Index Terms*—performance, profiling, networking, VNF, Virtual Network Function, Linux, eBPF, extended Berkeley Packet Filter, bpftrace**

I. Introduction

The recent growth in mobile networking traffic and the preceded diversity of the traffic coupled with the high Capital Expenditure (CAPEX) in the telecommunication industry have promoted the re-engineering of the current and future communication technologies [1]. Among these re-engineering efforts is the migration from expensive hardware-based communication Network Functions (NF) to software based NF deployed on cheaper standard off-the-shelf hardware/servers. Migrating to flexible software-based NF entails running the NF on virtualised platforms. Virtualisation often degrades the performance of the resultant Virtual Network Function (VNF). However, in order to serve this increased growth in network traffic whilst solving for the lower CAPEX, the re-engineered virtualised platforms need to either maintain or improve the performance of the current and emerging communication networks. This entails a deep dive and understanding of the networking of the most common virtualisation technology, the Linux kernel.

The kernel's primary function is to enable the sharing of the hardware resources. This results in the virtualisation of each hardware resource so that it can be accessed by multiple competing processes in execution. The networking consists of the network drivers and the network stack. The network drivers are responsible for moving the packets from the Network Interface Controller (NIC) hardware to the kernel, and the network stack allows the sharing of the NIC hardware resources by maintaining multiple per connection queues and per-NIC queues. To maintain memory isolation between the queues and to absorb the different processing speeds the data is copied across the NIC queues and connections queues. The resultant virtualisation of hardware resources up for competing access; the multi-queue per NIC and per connection approach; the data copies and the context separation between the processes mentioned earlier and VNF form a complex system that affects the performance of the deployed VNF. In order to lessen performance degradation, it is valuable to identify the key sources of reduced performance, e.g., via profiling of the performance of the various processes mentioned above. Such quantification needs to be drawn down first. The results allow to put an extended focus on either improving these processes or adapting them to the context of operation. This can be particularly important in the telecommunication industry where some of these generic networking processes can be omitted or modified resulting in overall improvement.

The profiling of the above functions means tracing the processes inside the kernel. There are a several tracing tools with different levels of observability of the underlying kernel. In order to get a good performance profiling, the tools need to offer high observability. This study will use the observability capability offered by the extended Berkeley Packet Filter (eBPF) to the Linux kernel. The eBPF allows safely executing untrusted user-defined eBPF programs inside the kernel. These programs can be written to collect metrics and can be attached to different points in the kernel. The possible attachment points to collect metrics are: i) Kernel functions with *kprobes*, ii) userspace functions with *uprobe*, iii) system calls with *seccomp*, and iv) *tracepoints*. The high observability feature becomes particularly important in the performance profiling as most of the kernel processes mentioned in the earlier paragraph are kernel functions with *kprobes* and/or *tracepoints* as we will illustrate in the later sections.

This study gives a detailed analysis of the networking of the recent Linux kernel version 5.4. We detail the receive path of the network traffic/packets and state the various kernel functions and processes applied to the network traffic/packets, from the point it is received on the NIC hardware to the destined application. Thereafter we profile the performance of these functions and processes using our custom eBPF programs that we attach to the *kprobes* and *tracepoints* of

these functions and processes. We define performance using the metrics frequency and time taken to execute each of the kernel functions and processes. These metrics are collected by our eBPF programs. We collect the metrics at different network bandwidths whilst the CPU is operating at full load. Lastly, this study presents the performance profiling of the networking of the Linux kernel version 5.4 and recommendation on processes that can be improved or omitted in the context of the telecommunication industry applications like, Firewalls etc.

The following section gives a detailed analysis and models the receive path of the Linux kernel networking based on the study and reference of the Linux source code. Thereafter Section III introduces eBPF tracing and the different attachment points used in this study. The next is Section IV, which describes the set-up for collecting the metrics, i.e., traffic generation and the System Under Test (SUT). Section V then presents and discusses the collected performance profile. Lastly, Section VI gives recommendations and offers conclusions on the study.

II. Related Works

Performance profiling of the Linux kernel has been an ongoing methodology for understanding the Linux kernel for years. This methodology has been enabled by the various tracing tools that were developed over the years, which including *SystemTap* [2], *top*, *iostat* and *vmstat* [3] among many other tools. On top of these tools, the profiling can also be derived from reading and monitoring the statistics collected into system files by the kernel. For example, reading and monitoring the `/proc/interrupts` can help us see how the number and rate of hardware interrupts change as packets arrive. However, these tools generally have limited observability of the Linux kernel. They cannot trace some parts of the Linux kernel, limiting the effectiveness of the performance profiling methodology. In addition, Linux will process a fair number of packets in the context of whatever is running in the CPU when Software Interrupt Request (SoftIRQ) is handled. Therefore, in most cases, system accounting will attribute those CPU cycles to the process that was running at that moment. For example, *top* can report that a process is using 99+% CPU while maybe 60% of that time is spent process packets. Only when there is more work for New API (NAPI) and the work is deferred to another SoftIRQ cycle that the system becomes more transparent and processes the packets under the context of SoftIRQ [4].

The authors in [5] describe the networking receive path of the Linux kernel version 2.6. The NIC and Device Driver Processing are modelled as a token bucket algorithm and the rest modelled as queuing processes. The authors look at the key factors that affect Linux systems' network performance correlating it to the models. During this process, the tracing is limited to the number of used packet descriptors and the transmit and receive rates of the system. Limited information is provided regarding the performance of the various functions and processes identified during the analysis of the networking receive path of the Linux kernel.

Another study by Joe Damato [6] considers the receive path of the Linux kernel version 3.13.0 and Intel's *igb* network driver. In addition to giving a detailed description of the functions and processes that occur as a packet transvers through the receive path, the author states the system files that can be monitored for performance profiling. Although the author provides more observability of the Linux kernel than the previous study, the observability can still be improved. Additionally, the author only gives a description and does not present any results.

In this study, we analyse the Linux kernel version 5.4 and Intel's *i40e* network driver. We use the eBPF programs for tracing, which we attach to the Kernel functions' *kprobes* and *tracepoints* to collect metrics for performance profiling. The eBPF programs can be attached to monitor most kernel functions (through *kprobes* and *tracepoints*) hence allow for better observability as compared to other tools and methods mentioned earlier. Additionally, because we author these eBPF programs, we control the metrics we collect, and how we collect them. There are various ways of writing the eBPF programs [7]. Another important attribute is that by using eBPF programs, we can obtain the time that has been spent on a particular packet processing function and that we do not need to rely on the context the CPU is running under. From the eBPF programs, we can also tell in which program's context the packet processing is occurring.

In this study, we make use of *bpftrace* to write our eBPF programs. *Bpftrace* was created by Alastair Robertson. It uses LLVM [8] as a backend to compile scripts to BPF-bytecode and makes use of BPF Compiler Collection (BCC) for interacting with the Linux BPF system, as well as existing Linux tracing capabilities: kprobes, uprobes, and tracepoints [7]. We use *bpftrace* because it makes writing eBPF tracing programs easier and is well suited for short scripts and ad-hoc investigations [7]. These benefits fit the scope of our work.

III. Linux Networking Stack

The Linux networking stack on packet ingress carries the packet through various functions in order to deliver it to the destination application. This process can generally be dived into three parts:

- Packet is read from the NIC and put into kernel buffers for further processing (*NIC and Device Driver Processing*).
- The packet goes through protocol processing and is delivered to the destination socket (*Packet Protocol Processing*).
- The application listening on the destination socket receives the packet (*Application Processing*).

During these processes, the packets are applied to different functions defined across the networking stack, which either drop the packet or continue with processing. Fig 1 depicts the network stack, from packet arriving on the NIC and being delivered to the destination socket being read by the intended application. These processes are described in detail in the following subsections.

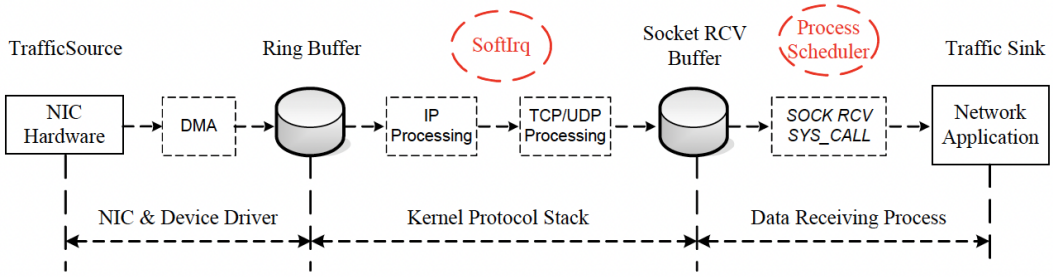

Fig. 1: Linux Networking Subsystem: Packet Receiving Process [5], from receiving by network interface card (NIC) to passing the received data to Network Application, via various stages in the kernel. DMA stands for direct memory access. SoftIrq stands for soft interrupt request. SOCK RVC denotes socket receive. SYS_CALL points to system call(s).

A. *NIC and Device Driver Processing*

This is the initial part of the network stack for processing network packets. The network packets are received by the NIC and transferred into kernel buffer network data structure (`struct sk_buff`) for further processing up the network stack. The process is managed and controlled by the NIC and device driver. Packets are first transferred from the NIC using Direct Memory Access (DMA) into a DMA-able region on the Random Access Memory (RAM). The memory region for receiving the packets is a ring, `rx_ring`, divided into buffers, `rx_buffer`, referenced by packet descriptors. The `rx_ring` is allocated $\mathcal{D}$ buffers and the respective packet descriptors of each buffer, δ, where the received packets are transferred to. The number of packet descriptors, $\mathcal{D}$, is a design parameter of the NIC and driver. To be able to receive packets, the packet descriptors should be in a ready state, meaning they should be initialised and pre-allocated. When a packet is received (rx), it is transferred into the packet descriptors with a ready state, and if none of the packet descriptors are in ready state, the packet is dropped. Once in the `rx_buffer`, the packet is copied across to the `sk_buff` in the kernel. The packet descriptors are refilled as the used `rx_buffer` is read during NAPI poll and prepared for reuse/recycle. Therefore, the packets are dropped when `rx_buffer` are not cleaned out timely.

The process described above is triggered by a hardware Interrupt Request (IRQ), raised to let the system know that there is a packet in the `rx_ring`. The IRQ is processed by an interrupt handler which does minimal work and leaves the rest of the packet reception to a SoftIRQ handler.

Hardware interrupts tend to be expensive in terms of central processing unit (CPU) usage. The NAPI was designed to mitigate this by allowing the driver to go into polling mode instead of being hardware interrupted on every packet. The interrupt is only raised when NAPI [9] needs bootstrap, i.e., when it's not enabled. In this case, `napi_schedule` is called, which wakes up the NAPI subsystem to read packets from DMA'd memory region. During this step, further IRQ is disabled to allow the NAPI subsystem to process packets without interruption from the device. The NAPI function `napi_schedule` then raises a SoftIRQ (`NET_RX_SOFTIRQ`), which run the registered SoftIRQ handler (`net_rx_action`) to poll the packets using the device driver's NAPI poll function. Before finally copying the packets into `sk_buff`, early packet processing functions can be applied to the packet using eXpress Data Path (XDP). These are user-defined dynamically loaded hook functions.

To detail the above process, we look at the source code for the device driver from intel *i40e*. The IRQ is handled by the function `i40e_intr` shown in Listing 1. The function handles the different types of interrupts (Legacy/MSI/MSI-X) and ultimately enables NAPI using the function `napi_schedule_irqoff` an alias for `napi_schedule` as can be seen in Listing 2. The handler and the NAPI do minimal work and triggers SoftIRQ to do the heavy lifting as shown in Listing 2. The triggered SoftIRQ then runs the handler function `net_rx_action`, which uses NAPI to read packets. If the network packets are not exhausted, another SoftIRQ is raised. The effective poll function called by `net_rx_action` is `i40e_napi_poll` and is defined by the device driver shown in Listing 3. This function, as shown, reads the packets from the `rx_ring` and ensures that the budget (i.e., the number of packets read in a single poll) is not exceeded. From the code, we can see that the packets can be polled using zero copy (`i40e_clean_rx_irq_zc`), allowing for early actions to be performed on the packet without copying it into `sk_buff`. Alternatively, early actions can be performed on the packet after copying it into the kernel.

When zero copy is enabled, the driver runs the XDP hook function(s) without copying the packets to an `xdp_buff`. XDP functions can return four types of responses, `XDP_PASS`, `XDP_DROP`, `XDP_TX`, `XDP_REDIRECT`, `XDP_ABORTED`. As shown in the Listing 5, the `sk_buff` is only created when the XDP returns `XDP_PASS`, saving packet processing time and overheads for certain packets. Once that is done, the `napi_gro_receive` function is called to perform Generic Receive Offloading (GRO). If zero copy is not enabled in (please refer to Listing 6), the driver starts by creating and copying the packet to an `xdp_buff`. It then runs the XDP function and, depending on the response, it can either create a `sk_buff` (build/construct) or continue to the next packet in the `rx_ring`. When the XDP action is `XDP_PASS`, after creating the `sk_buff`, the `napi_gro_receive` function is called to perform GRO. This polling process is repeated until either the budget has been finished or there are no more packets. When the polling process is done, `napi_complete_done` is called, which passes that packet for protocol processing as detailed in the next

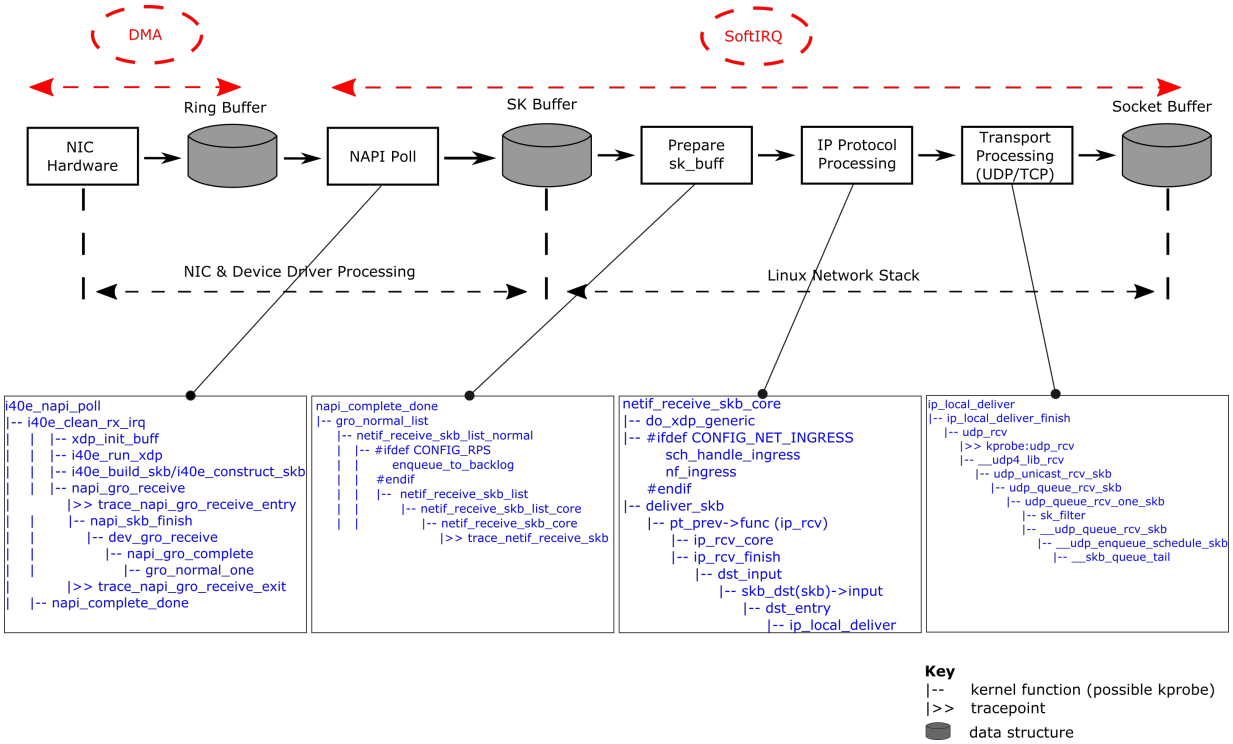

Fig. 2: Linux Receive Packet Processing Flow, with details around bufferisation and related functions NIC refers to the network interface card. DMA stands for direct memory access. SoftIRQ stands for soft interrupt request.

subsection. This packet flow, along with the packet flow processing described in the next subsection, is depicted in Figure 2.

B. *Packet Protocol Processing*

This processing follows after the packet has been copied into the `sk_buff`. The network packets in the `sk_buff` are delivered to packet taps devices or the protocol layer before queuing the packet data to a socket `sock`. This packet protocol processing can be initiated by SoftIRQ when interrupts, IRQ, are enabled through the function `netif_receive_skb` (see Listing 8). It can also be initiated when `napi_poll` completes through `napi_complete_done` (see Listing 7). *The first case happens when the scheduler has preempted the NAPI poll function has been preempted by the scheduler before passing all the packets (`sk_buff`) up the networking stack.* During this process, for each IP packet that is dequeued from the `rx_ring`.

The steps start by checking if Receive Packet Steering (RPS) is enabled and enqueues the `sk_buff` on another CPU where RPS is enabled. We will focus on the case when RPS is not enabled. In this case, if the system is having a generic XDP function(s) defined, the XDP hook functions are applied to the packet, and the packet is either dropped or continued up the stack, depending on the action returned by the XDP function. The XDP functions here run after the packets have been copied and to `sk_buff`. Thereafter, if required, the packet is delivered to the tap device. Following this, if `CONFIG_NET_INGRESS` is enabled, Linux traffic control (TC) classification and actions are applied to the packet. This function can be defined using eBPF or Linux tc command. Right after, netfilter ingress functions are applied to the packet as well. If the packets are not dropped by TC or netfilter, the packet is delivered to the protocol layer by calling `deliver_skb`. This process is shown by the extracted code shown in Listing 8.

The protocol functions to call depend on the packet type. In our case, we will consider IP protocol, which is thereby called by `deliver_skb` through `pt_recv->func`, which calls `ip_rcv`. The Listing 9 shows the processing functions for the IP protocol. The function `ip_rcv_core` does the heavy lifting, in processing and is called from within the `ip_rcv` entry function. The receive function is ended with a call to `ip_rcv_finish`, which is executed through a Netfilter hook function. If netfilter doesn't drop the packet, the process continues in `ip_rcv_finish`. This continues the processing, depending on the destination of the packet. If the packet's destination is the local system, `dst_entry` calls the `ip_local_deliver` function, which calls the network transport function depending on the type of the packet. Like earlier, this function is called from a Netfilter hook (`NF_HOOK`); therefore, it's only called if the packet is not dropped by Netfilter. The register network transport functions can be seen from the Listing 10.

We will consider the UDP transport protocol. As shown from the Listing 10, the handler function for UDP is `udp_rcv` and it relies on `__udp4_lib_rcv` to do the heavy lifting. The Listing 11 with function `__udp4_lib_rcv` shows that is the destination socket was predetermined the packet is delivered to that socket; otherwise, the destination socket is looked up first. The process subsequently calls

`udp_queue_rcv_one_skb` which first applies socket level eBPF program through `sk_filter_trim_cap`. If the socket level eBPF called in `__udp_queue_rcv_skb` doesn't drop the packet, `__skb_queue_tail` is called, which will put the packet on the receiving socket. The processing listening on the socket is then notified that the packet is now available.

IV. Experiment Set Up

In order to collect our results, we set up two servers, Server 1 and Server 2, on the same subnet, both running Linux kernel version 5.4. Server 1 serves as our System Under Test (SUT) and Server 2 serves as our traffic generator. We generate the traffic using IPerf [10]. As mentioned earlier in Section II, Linux processes packets in the context of whatever program is in the CPU when IRQ is handled. We use two different approaches to this problem. First, we use of eBPF programs, which provide better observability, by monitoring specific packet processing functions. Second, we infer the networking overhead using *openssl speed*, which is a well-known workload that reports how much CPU access it gets. We pin the *openssl speed* to a particular CPU, and we use NIC traffic steering to send all traffic from IPerf to the CPU running *openssl speed*. Additionally, in our eBPF programs, we also collect metrics for the CPU that *openssl speed* is pinned on. The CPU will be same CPU IPerf packets are being processed on. We collect context switching overhead which we measure across all CPUs.

In our eBPF programs, we collect the following metrics:

- **total packet poll time**: this is the amount of time spent getting the packets from the `rx_ring` to an `skb_buff`. This is measured from the time `net_rx_action` is called to poll packets, to when `napi_complete_done` is called, which is called when the budget has finished or there are no more packets.
- **skb-ip prep time**: this is the time taken to prepare the `skb_buff` created earlier for processing to the IP protocol. This is measured from when `napi_complete_done` is called to when `netif_receive_skb` is invoked.
- **total IP processing time** this is the time taken to apply IP protocol-based functions to the `skb_buff`/packet plus the time taken to execute functions that decide where the packets are to be delivered. Just before the process starts, the following hooks can be applied in the following order: i) generic XDP, ii) tc, iii) net-filter ingress. When the hooks functions are defined, the time the take to execute affects the **total IP processing time**. The textbftotal IP processing time is recorded from when `netif_receive_skb` is called to when `ip_local_deliver` is invoked.
- **total total IP to transport protocol time protocol time**: this the time taken from the moment the packet is set to be delivered locally until the transport protocol to use has been established. In our experiment, this is from the instance `ip_local_deliver` was called, to when `udp_rcv` has been invoked.
- **total ip processing**: is the sum of the times above.
- **cs time**: this is the total amount of time taken processing context switching across all the CPUs
- **total packet processing time**: this is the CPU time that has been from the *openssl speed* due to packet processing. This includes both the receive and transmit path of the networking.

We assume and approximate the receive and transmit path to be asynchronous. We then verify the results from the eBPF programs (first approach) with the results inferred from the *openssl speed* (second approach). The first approach gives the CPU time taken by the receive path processes. The is reported by **total IP processing**. The second approach gives the CPU time taken by both the receive and transmit path processes. This is reported by (**total packet processing time**). Therefore, the **total IP processing** CPU time reported by the eBPF programs should be approximately half of the CPU time reported by *openssl speed*, **total packet processing time**.

V. Results and Discussion

We run our experiment as described in the earlier section. The summary results from the experiment can be shown in Figure 3. From the results in Figure 3, we can see that the processing of IP packets to their respective transport protocol, UDP in this case, takes the most time. This is an example of a packet processing that can be omitted for certain use cases in the core network. For example, consider NF like firewalls which can be deployed in core network. These NF (applications) may not require a continued session as they block the initial packets of a TCP or UDP session and therefore can do without this part.

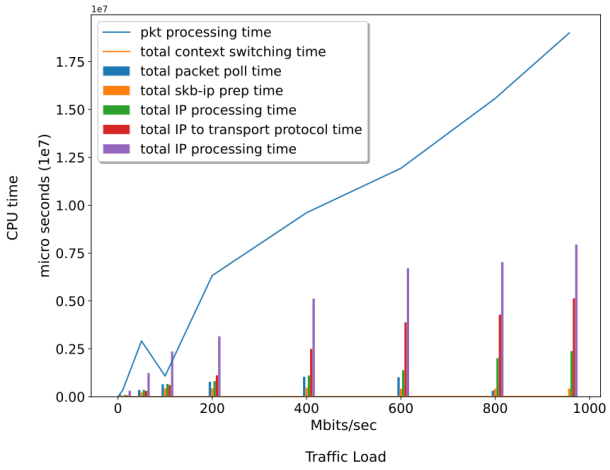

Fig. 3: Linux networking performance profile

Another observation is the **total packet poll time** goes down as the bandwidth increases. This may be because, under high bandwidth, most packets are processed in a single NAPI poll as part of the same budget. Therefore, the NAPI poll function is not called many times. This means that the virtual deployments should be on a path with a network bandwidth above a certain amount, in this case, 800 Mbits per second.

The **total IP processing time** and the **total IP to transport protocol time** increase linearly with the increase in network

bandwidth. This observation can be used to approximate the CPU time of those processes under different network bandwidth, enabling better VNF deployment decisions as well as hardware resources provisioning decisions.

An additional observation that does not show up in Figure 3 explicitly is how context switching overhead increases as the bandwidth increases. We show these results in Figure 4. The context switching can be seen to take a lower overhead. However, since it increases linearly, context switching can, at a certain bandwidth, account for a significant part of the CPU cost of networking in the Linux kernel.

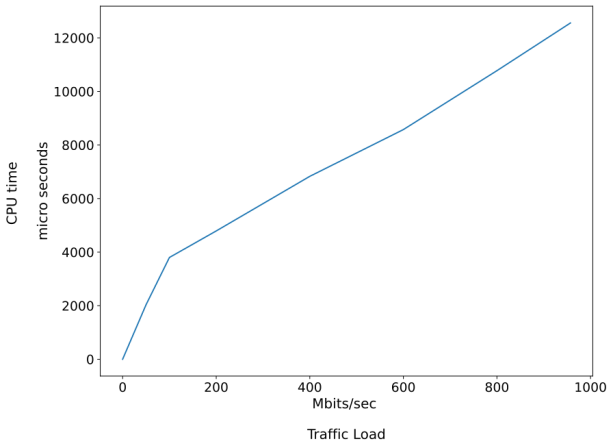

Fig. 4: Linux networking context switching

VI. Conclusion

In this study, we considered the migration to virtual network function in the telecommunication industry, i.e., deploying NF on virtualised platforms, using the Linux kernel. However, virtualisation degrades the performance of the resultant network functions. We considered the need to maintain or improve the virtual deployments' performance to serve the growing traffic. To address this need, we attempt to quantify the performance degradations in various parts of the networking of the Linux kernel. We adopted performance profiling, reading and understanding the source code. Related works that used performance profiling, have had limited visibility/observability of the underlying functions and processes of the Linux networking. In our study, we used eBPF programs that we attach to Kernel function *kprobes* or *tracepoints*. We write these programs to collect metrics, which we then use for performance profiling. We also make use of inferred performance profiling, where we run a user program and compare its CPU time before and after network traffic. We then use these results to verify the results obtained from our eBPF programs.

Based on our results, we identify processes that take the most time and the processes that can be omitted or modified in the context of the telecommunication industry. In our future work, we plan to attempt to model performance profiling mathematically to approximate the CPU time of networking at different loads across different parts of the Linux networking.

Acknowledgement

The authors acknowledge the support received from TELKOM SA via the Telkom Centre of Excellence (CoE) in Broadband Networks Applications at UCT.

References

[1] J. Costa-Requena, J. L. Santos, V. F. Guasch, K. Ahokas, G. Premsankar, S. Luukkainen, O. L. Perez, M. U. Itzazelaia, I. Ahmad, M. Liyanage, M. Ylianttila, E. M. de Oca, "SDN and NFV integration in generalized mobile network architecture," in *2015 European Conference on Networks and Communications*, June 2015, pp. 154–158.

[2] F. C. Eigler and R. Hat, "Problem solving with systemtap," in *Proc. of the Ottawa Linux Symposium*. Citeseer, 2006, pp. 261–268.

[3] B. Gregg, "Linux performance analysis and tools," Technical report, Joyent, Tech. Rep., 2013.

[4] D. Ahern, "The CPU Cost of Networking on a Host," 2020, accessed on Jun 2021. [Online]. Available: https://people.kernel.org/dsahern/the-cpu-cost-of-networking-on-a-host

[5] W. Wu, M. Crawford, and M. Bowden, "The performance analysis of linux networking–packet receiving," *Computer Communications*, vol. 30, no. 5, pp. 1044–1057, 2007.

[6] J. Damato, "Monitoring and tuning the linux networking stack: Receiving data," 2016, accessed on Jun 2021. [Online]. Available: https://blog.packagecloud.io/eng/2016/06/22/monitoring-tuning-linux-networking-stack-receiving-data/

[7] C. Cassagnes, L. Trestioreanu, C. Joly, and R. State, "The rise of eBPF for non-intrusive performance monitoring," in *NOMS 2020-2020 IEEE/IFIP Network Operations and Management Symposium*. IEEE, 2020, pp. 1–7.

[8] C. Lattner and V. Adve, "LLVM: A compilation framework for lifelong program analysis & transformation," in *International Symposium on Code Generation and Optimization, 2004. CGO 2004.* IEEE, 2004, pp. 75–86.

[9] The Linux Foundation. "napi". Accessed on Jun 2021. [Online]. Available: https://wiki.linuxfoundation.org/networking/napi

[10] A. Tirumala, "Iperf: The TCP/UDP bandwidth measurement tool," *http://dast. nlanr. net/Projects/Iperf/*, 1999.

Tariro Mukute received his BSc degree in Electrical and Computer engineering in 2016 at the University of Cape Town. He is currently pursuing a PhD in the Department of Electrical Engineering at the University of Cape Town, Cape Town, South Africa.

Configuring a Single-board Parallella Cluster for Parallel Execution of Benchmarks

Matthew D. Lewis*, Karen Bradshaw†
Computer Science Department, Rhodes University, South Africa
[2]k.bradshaw@ru.ac.za

***Abstract*—Traditional compute clusters are very expensive, require a lot of power and take up a lot of space, and as such are only available to large research groups and industry. Clusters consisting of single-board computers, however, are more affordable for smaller companies and even individuals to own.**

Using the Parallella single-board computer option, this research seeks to ascertain to what extent a cluster comprising these single-board computers can be useful for high-performance computing. For the cluster, four Parallella nodes were set up with relevant frameworks and libraries, while a Raspberry Pi controller node, external to the cluster, was set up to perform supporting functions for the cluster including DHCP, NFS and NAT. For benchmarking, a sequential matrix multiplication program was adapted to use Open MPI, and this was executed on the cluster, with a slightly different version run on a single Epiphany node and also an i-5 Intel processor for comparison. The results showed a 1.5× to 2.5× speedup on the 4-node cluster relative to the single-node, but the standard modern CPU had a 4× speedup relative to the cluster.

***Index Terms*—High performance computing, Clusters**

I. Introduction

Traditional computer clusters, consisting of a number of computers connected in parallel such that they act as a single computing resource, are widely used because they come at a much lower cost than a single computer of comparable performance. Using a cluster also removes the reliance on a single computing resource. These clusters are extremely useful for parallelisable workflows such as weather forecasting. However, as traditional computer clusters are very expensive, require a lot of power and take up a lot of space, they are available only to large research groups and industry.

Single-board computers, a functionally complete computer built onto a single circuit board, can be used as an alternative to traditional computers and come at a significantly cheaper cost and power draw. Clusters consisting of these single-board computers are more affordable for smaller companies and even individuals to own.

Using the alternative Parallella single-board computer (SBC) option discussed above, this research set out to ascertain to what extent a cluster comprising these single-board computers can be useful for high-performance computing. Specifically, the following sub-objectives were considered:

- to determine whether four Parallella boards could be combined to form a small computer cluster,
- to find a suitable software framework for the Parallella cluster,
- to ascertain the capabilities of the cluster by running HPC benchmarks, and
- to ascertain the limitations of the cluster.

The rest of this paper includes a section on related work as well as two background sections covering high performance computing in general and the specifications of the Parallella. Section 5 introduces the methodology and design overview of the cluster, Section 6 takes a more detailed look at the implementation of this, and Section 7 introduces the benchmarks that were run and discusses the results of these. Finally, in Section 8, the research is summarised and a breakdown of the extent to which the objectives were achieved is given.

II. Related work

There have been many different projects in which Raspberry Pis have been used. One such project, by Coutier et al. [1], was a cluster consisting of 24 Raspberry Pi 2 nodes which were designed to research the detailed per-node power measurement. This cluster was capable of over 15 GFLOPs of performance. Another project, by Cox et al. [2], involved setting up a cluster consisting of 64 Raspberry Pis (original variant). The purpose of this cluster, dubbed Iridis-Pi, was for implementing educational applications to teach high performance computing and data handling for complex problems. This cluster was able to deliver a peak performance of 1.14 GFLOPS with its memory capacity limiting the addressable problem size.

Richie et al. [3] explored the use of MPI for programming a single Parallella node and tested the bandwidth and performance of the Epiphany architecture using several benchmarks, including matrix multiplication and a 2D FFT. Their results showed that the Parallella node achieved 33% and 13% of the theoretical peak, respectively, whilst executing these two benchmarks. The authors in [4] compared two SBC clusters to assist in password cracking. The first cluster consisting of an 8-node (i.e. 128-core) Parallella SBC was shown to outperform the second cluster, consisting of 32 Raspberry Pi 2 (4-core) processors, while cracking 5000 commonly used weak passwords. Both clusters were able to outperform a quad-core Intel i7 CPU.

III. High Performance Computing

High performance computing (HPC) is a term that is used to refer to the computing environment in which "supercomputers and computer clusters [are utilised] to address complex

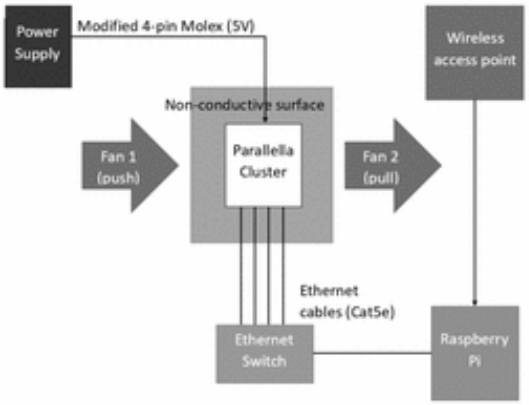

Fig. 1. Physical layout of cluster and how it all 'fits together'

computational requirements, support applications [that have] significant processing time requirements, or require processing of significant amounts of data" [5, p. 37].

Traditional HPC systems come in the form of specialised supercomputers that utilise multiprocessors and custom memory architectures which have been heavily optimised for numerical calculations [5]. To receive the performance benefits of supercomputers, special parallel programming techniques must be used. Although traditional supercomputers are extremely powerful, they come at a great expense in the form of the initial purchase price, hardware maintenance costs and operational costs (electricity) and therefore, over the years the popularity of cluster computers has grown. These cluster computers are far more flexible because they can consist of many average consumer-grade computers while still reaching very high levels of performance, parallelism and scalability. Determining the effectiveness of these systems is not simple. Many factors may affect this, including the application for which it will be used, the specific algorithm, the scale of the problem, the specific high- or low-level language used to implement the program and how it is implemented, the depth and effectiveness of the optimisations done by the developer of the specific program as well as by the compiler itself, the specific operating system used, the architecture of the computer and the hardware characteristics of the computing resource [6]. Benchmarks seek to simplify matters by providing metrics that give an idea of how well the system performs, though careful consideration must be given as to which benchmarks to use for them to be effective in determining the best system for a particular use [7]. The results of a benchmark, however, should not be treated as a measure of the total performance of a system (unless considerable analysis has shown a correlation of the benchmark to the workload of interest), but rather as a reference point for further evaluations.

IV. Parallella

The Parallella is an SBC equipped with a 32-bit Zynq-Z7010 dual-core ARM A9 processor that handles all basic operations, 1 Gb of DDR3 RAM, gigabit Ethernet and, most importantly, a 16-core Epiphany Co-processor [8]. The co-processor has an efficient general-purpose instruction set and excels in compute-intensive applications. The co-processor's memory space is mapped into the Zynq (host processor) memory space. This allows for data and resources to be shared between the CPUs via this shared memory. The co-processor consists of 16 superscalar floating-point RISC CPUs, known as eCores, with peak theoretical performance of 2 GFLOPS each [9].

V. Methodology & Design Overview

The cluster consists of four Parallella nodes with a separate Raspberry Pi controller node that fulfils services required by the cluster itself. The physical setup of the cluster, as seen in Figure 1, includes:

- Conductive spacers used to stack the nodes on top of one another for portability and power delivery.
- A non-conductive mat for the cluster to rest atop (necessary because of the conductive spacers used to power it).
- A switch to provide a communication route among the nodes and between the nodes and the Pi.
- 2 x 140mm case fans in a push-pull configuration (one fan is pushing air onto the cluster and one is pulling it away) for greater cooling.
- A desktop power supply used, in conjunction with the conductive spacers, to power the cluster and the fans.
- A Raspberry Pi 3 B+ used to perform various services needed by the cluster.
- Four Parallella worker nodes.

The conductive spacers and modified Molex cable used to power the cluster were completed by Kruger [10].

A. Controller Node

The Raspberry Pi fulfils the following primary services required by the cluster: dynamic host configuration protocol (DHCP), network file system (NFS), and network address translation (NAT). DHCP is used to provide IP addresses to the nodes so that they may communicate with one another and the Raspberry Pi. NFS is used to provide a shared directory through which the Pi and nodes can all access the same files and will be used by Open MPI to send the exact same copy of code to each of the nodes. NAT is used to provide Internet access to the Parallellas (via the Raspberry Pi's onboard wifi) whilst still allowing them to exist on their own closed network through the switch they are connected to. Internet speed and access are of secondary importance to the cluster's function (as it is only used to download various packages and frameworks, after which it is not needed), and thus it is not detrimental to use NAT on the Pi to provide the cluster with access to the Internet. The provision of these services is discussed in greater detail in Section VI.

B. Worker Nodes

The Parallella nodes were installed with an OS called Parabuntu [11]. This OS is based on Ubuntu 15.04 and is the stable version of Parabuntu. Parabuntu was chosen because of its integrated support with the Parallella through the Epiphany

SDK (ESDK) which comes pre-installed alongside other useful libraries and frameworks such as COPRTHR, and Open MPI [9]. The nodes also had to be able to remotely access one another and had to be remotely accessible from another device (the Pi) as they are not equipped with any video output. Besides this and some other basic system software, the nodes were also set up as NFS clients so that they could access the shared storage created by the Pi.

The cluster made use of frameworks & libraries to parallelise its programs; this was done at the cluster-level (whereby the workload and data are split equally among the nodes) and node-level (whereby the workload given to each node is split further through the use of the Parallella's Epiphany co-processor). For cluster-level parallelisation, Open MPI, an MPI implementation, was used due to its popularity and thus widespread support for it which is particularly important due to the relatively poor software support and documentation for the Parallellas. For node-level parallelisation, the Epiphany SDK (included with Parabuntu), was used in to allow the offloading of work onto the Epiphany's cores. In conjunction with the base Epiphany SDK, the Epiphany Bulk-synchronous parallel (EBSP) library can be used which allows the BSP model to be used with the Epiphany [12].

VI. Software Configuration

A. Setup of the Controller Node

Since the Raspberry Pi would be running multiple servers, a static IP for its Ethernet interface (*eth0*) had to be set up. To achieve this, the netplan configuration file (/etc/netplan/50-cloud-init.yaml) was edited to disable DHCP for *eth0* and to set up the static IP to which the Raspberry Pi will receive on boot up.

To set up the DHCP server, *dhcpd* was installed. This daemon reads the /etc/dhcp/dhcpd.conf config file on startup and uses the IP pool given in that file to automatically provide IP addresses on the selected interface (in this case the /etc/default/isc-dhcp-server config file was edited to provide DHCP services only on the *eth0* interface). The dhcpd.conf file was edited to provide IP addresses in the range of 10.0.1.120 to 10.0.1.150, but was also later set up to provide fixed addresses (outside of the regular DHCP range) to each of the Parallella nodes as this made it easier to work with the cluster and allowed for entries to be made into the /etc/hosts file which can be used to translate hostnames or domain names provided into IP addresses (such as using the hostname node1 instead of the IP address of that node).

To set up the NAT service, the Pi was first connected to the internet through its onboard wifi using the /etc/netplan/50-cloud-init.yaml file which allows takes in various details about the network(s) you are connecting to and uses that to automatically connect to the wireless network(s) specified in the file). Next the /etc/sysctl.conf file was edited to allowing the forwarding of IpV4 packets and the *Iptables* package was downloaded to dictate how the packets are filtered. Next, several *Iptables* commands were used to forward any traffic received from the Parallella nodes on the *eth0* interface to the *wlan0* interface and to direct traffic intended for Parallella nodes from the *wlan0* to the *eth0* interface.

To set up the NFS server, the *nfs-kernel-server* package was installed and the /etc/exports file was edited to allow access to the folder to be shared to the nodes and the details and permission they would have. All nodes were given read/write access that is synchronised (nodes have to take turns when accessing files within the shared folder).

B. Setup of the worker nodes

To remotely access the Parallella nodes, secure shell (*SSH*) was set up. This allows for the remote execution of commands on the nodes. For ease-of-use passwordless *SSH* was set up through the use of public/private keys which uses a known public key to encrypt the connection and a secret private key to decrypt on the other end. The key pair is generated through the use of the following command, run on the device that will be remotely accessing the Pi:
`ssh-keygen -t rsa` and then the keys are copied to the remote server (in this case the Pi) using the command:
`ssh-copy-id parallella@node<1 to 4>`
Thereafter, the same is done for the root user. Doing this allows any node to access any other node in the cluster (which is useful for OpenMPI).

To enable access to the shared files on the NFS server, the *nfs-common* package was downloaded. Next, the
`showmount -e nfs-server`
command was run on a Parallella node to check that the export list for the NFS server was set up correctly. After confirming that the export list is correct, the /etc/fstab file was edited to allow the NFS folder to automatically mount on boot:
`10.0.1.100:/shared /shared nfs auto 0 0`

VII. Benchmarking & Results

Preliminary cluster test results are given in this section.

A. NetPIPE

Network Protocol Independent Performance Evaluator (*NetPIPE*) is a package that makes use of varying sized messages to obtain a measure of the performance of a network [13]. It does this by sending increasingly larger messages between two processes within a system or between two nodes across a network. For small messages, the overhead involved in setting up the communication is greater than the latency involved in sending the message (thus the transmission of small messages is latency bound). For larger messages, the overhead in setting up the communication becomes an insignificant factor and the transmission of the message becomes limited by the bandwidth available (the bandwidth available is determined by the PCI bus, network card link, or network switch depending on the method used to send the message). NetPIPE can be used to test a variety of systems including Open MPI and the transmission control protocol (TCP).

NetPIPE can be used to test a variety of systems including Open MPI and TCP. NetPIPE TCP tests the network interconnect speeds by sending messages between two nodes on the network. One node is set up to be a receiver and another is set up to be a transmitter. The transmitter then makes use of TCP to send varying sized messages (as mentioned above) to the receiver. This process is repeated numerous times to get a good measure of the network bandwidth available. In the case of the Parallella cluster, the maximum bandwidth available is 100 Mbps due to limitations in the Ethernet switch used.

NetPIPE Open MPI makes use of the Open MPI interface to send messages between two specified nodes or processes again with messages of varying sizes. This test, which was used to determine whether Open MPI had been configured correctly, was run by invoking the following command:

```
mpirun --hostfile machinefile -np 2
NPopenmpi
```

In this case, `machinefile` contained the IP address of two nodes only. For smaller messages, it is expected that smaller transmission rates will be attained due to the overhead involved in sending messages via Open MPI. Larger messages, on the other hand, are bound by the interface being used (in this case transmissions cannot exceed 100 Mbps).

B. Matrix Multiplication Benchmark

A basic matrix multiplication example program (also referred to as Matmul), using the *EBSP* library, was adapted to give a measure of the performance of the cluster. The original example program was included with the *EBSP* library files [12]. This program takes as input two square matrices, A & B, with dimensions $Rows \times Columns$ and performs the dot product, the result of which is stored in the output matrix, C.

At its base, the host program consists of setting up various data streams, necessary because the matrices used are too large for the local memory of the Epiphany. These data streams make use of the much larger (and much slower) external memory [14]. A `downstream` contains data that is needed by an eCore. In the case of this program, the A and B matrices were first split up into 16 $times$ 16 smaller blocks and then the streams for A & B were filled with the data from this smaller blocks of the A & B matrices. These streams are used to copy the data onto the eCores.

There are various mechanisms and arguments that can be used to optimise this dataflow, such as the *double_buffer* argument, which makes use of the DMA channels available on the Parallella to process two streams simultaneously. This process, however, takes up twice as much memory as when processing the streams sequentially. On the host, an `upstream` was also created, which allows the results that are calculated on the eCores to be sent back to the host on the Parallella.

1) Adapting the example program: The first change made to the original example code was to create a build script to compile the program on the actual cluster. This build script was created by adapting a build script from a Parallella example program. Secondly, a basic run script that called the compiled version was created (this was found to be particularly useful at a later stage once the Open MPI calls had been made). Next, numerous changes to the code were needed to make it suitable to benchmark the cluster. Firstly, a timer was added to get some measure of the cluster's performance versus a single node's performance. This was implemented using the *Sys/time* library.

To get the program running with Open MPI, it first had to be altered to work with non-square matrices. In the original program, the data that was split up and sent off to the eCores was $N \times N$ dimensional data. Originally it was intended to adjust the underlying logic to work with $N \times M$ dimensional matrices, but due to time constraints, this was not possible. Instead, the program was altered such that the initial A and B matrices were of $N \times M$ and $M \times N$ dimensions, respectively, with the resultant C matrix having dimensions $N \times N$. This meant that when the data is split up by Open MPI, both A and B will be of $M \times M$ dimensions and thus will be square matrices that will have no issue working with the underlying logic.

First, the basic Open MPI commands, such as *MPI_Init* and *MPI_Comm_rank* were added to the code. Next matrix A was split up using the *MPI_Scatter* function which takes as parameters the array to be scattered, how many elements to scatter and another array to store said elements. The elements of matrix A are then scattered row-wise such that each node ends up with a quarter of the rows of A (where the first node has the first quarter and the last node has the last quarter). A copy of matrix B was sent to all the nodes as each portion of matrix A will require the entirety of matrix B, and thus to calculate a full partial solution on a node, a portion of matrix A and the entirety of matrix B are needed. Matrix B was copied using the *MPI_Bcast* function which utilises the head node to send an exact copy of the array given to all the nodes. Finally, after the nodes had calculated the partial C solutions, these then had to be compiled into a single C matrix. The *MPI_Gather* function is essentially the inverse of the *MPI_Scatter* function. It was used to gather up the partial C matrices present on each of the nodes into a single C matrix on the head node.

Finally, the program then performed the matrix multiplication sequentially on the head node and compared these results with the C matrix calculated by the cluster. This was used to confirm that the cluster was performing the calculations and gathering the data correctly.

2) Limitations of Matmul: Ideally, the code would be altered so that the underlying logic for the eCores works with non-square matrices (instead of altering the program such that it takes in non-square matrices and splits these up into square matrices to be split up further for the with the existing code for the eCores). This would allow for a more optimised solution with less of a reliance on EBSP streams and thus memory usage and communication overhead. This would also enable the cluster to run much larger matrices, which would likely result in a larger speedup relative to a single-node.

TABLE I
RESULTS OF MATMUL PROGRAM EXECUTED ON A SINGLE EPIPHANY NODE, THE 4-NODE CLUSTER, AND A SINGLE CPU CORE

Matrix dimensions (rows x columns)	Single-node time (s)	Cluster time (s)	Standard CPU time (s)	Speedup of cluster relative to single-node
256 x 64	3.24766	1.2780	0.01125	2.5412
512 x 128	4.00465	1.8332	0.09500	2.1845
768 x 192	5.71325	3.1861	0.33733	1.7932
1024 x 256	8.78199	5.63615	0.81733	1.5582
1280 x 320	13.44266	9.34067	1.54567	1.4392
1344 x 336	n/a	10.48012	1.76500	n/a
1408 x 352	n/a	11.89527	2.02033	n/a
1472 x 368	n/a	13.23628	3.30752	n/a

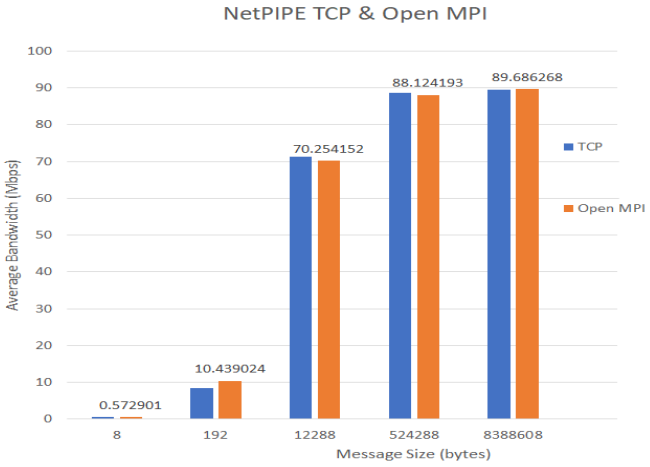

Fig. 2. NetPIPE benchmark results

In its current state, the program works but the speedup is not optimal and there is a lot of communication overhead involved (first at the cluster-level and then again at the Epiphany-level with all the data streams).

C. Benchmark Results

1) NetPIPE Results: The results of executing NetPIPE Open MPI and NetPIPE TCP can be seen in Figure 2. (Note that the NetPIPE benchmark gave the throughput (in Mbps) for many different sized messages, but the graph shows only a few of these message sizes with the throughput attained for that particular message.) NetPIPE TCP & Open MPI tend to have similar throughput, with TCP usually being marginally higher than Open MPI. These results are expected as Open MPI, in a cluster setup, is ultimately limited by the bandwidth of the interconnect selected, and thus will, never exceed 100 Mbps (the bandwidth limitations of this particular cluster setup). Since both TCP and Open MPI (in a cluster setup) make use of the network, they should return similar results.

2) Matmul Results: The results of executing the matrix multiplication program are given in Table I and Figure 3.

To obtain these results, different matrix sizes were run on three different platform configurations: a single Epiphany node of the cluster (henceforth referred to as the single-node platform), the 4-node cluster itself (henceforth referred to as the cluster platform), and a single core of a 9th generation Intel i5-processor (henceforth referred to as a standard CPU platform). The timings were obtained by averaging the results of 5 runs per configuration. The program executed on the standard CPU was an altered version (for sequential execution) of the Matmul program run on the cluster.

The single-node version of the program consisted of similar code to the cluster version, albeit without the Open MPI calls. The data was also split up on this version so that all the eCores on the Epiphany could assist in performing the necessary calculations, however, due to memory limitations of the single-node, the partial results calculated on the Epiphany were not compiled back into a complete solution to save on memory usage. The single-node was also unable to compute matrix sizes above (1280 x 320) due to memory limitations.

These results show a marginal speedup for the cluster relative to a single-node. The speedup is quite small, however, as the cluster would ultimately only see big speedups for larger matrix sizes but due to memory limitations, the single-node cannot compute programs with matrices larger than 1280×320. The cluster is also ultimately limited by memory for this program since the matrix sizes are too large for the Parallella's shared memory, and thus the much slower main memory (of which each node is only equipped with 1 Gb) must be used.

For early entries in the table, the speedup of the cluster (relative to a single-node) is quite high compared to later entries in the table, this is due to the overhead involved in setting up the BSP environment and the streams for the Epiphany (the single-node version of the program requires more streams as the entirety of the data has to be used).

The standard CPU performed matrix multiplication using a single core and for a 1472×368 matrix saw a $4\times$ speedup relative to the cluster.

To put these results into context, the laptop consisted of a 9th generation i5 CPU which had a base clock of 2.4 GHz (with a boost clock of 4.1 GHz) and 16 Gb of DDR4 memory running at 2667 MHz, compared to the Epiphany co-processor running at 500 MHz (with a peak of 600 MHz) and 1 Gb of DDR3 memory (the exact speed of this memory is unfortunately not specified by Adapteva, but is likely to be significantly lower than that of the laptop as it is using the DDR3 standard). This means that a cluster would need to consist of closer to 8 nodes to compare to that of a modern CPU due to the communication overheads involved at the cluster-level whereby data will be split up and sent through the use of a parallel framework (such as Open MPI) and then

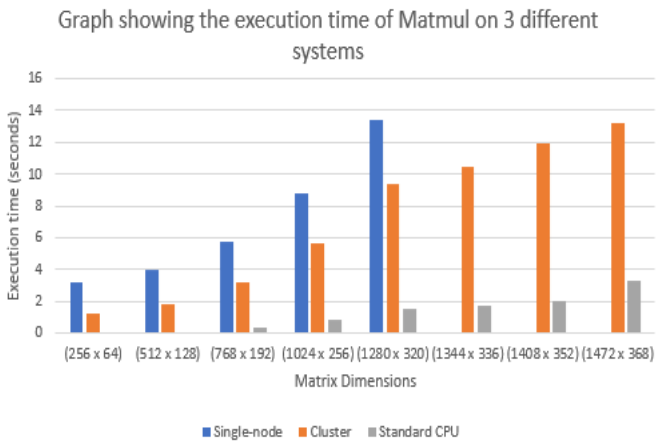

Fig. 3. Matmul benchmark results

again the node-level, whereby data will be split up further and sent to the Epiphany for processing. The size of the computation also plays a part in the weaker performance of the cluster compared with that of the CPU as shown by the decreasing slowdown from the smallest matrix dimensions (19× slowdown) to the largest (4× slowdown).

VIII. Conclusion

The research began with a review of available literature, through which important decisions were made regarding the methodology to be used, including which parallel frameworks to employ. Following this, a Parallella node was set up with an operating system and configured to run as intended (this included changes to configuration files to allow installation of packages, and the installation of the *SSH* package). This image was then cloned to the rest of the boards, with the only difference being the *hostname* of each node and a slightly different *SSH* list). Next, the Raspberry Pi was set up and configured with an *NFS* and *DHCP* server to provide shared file storage and IP addresses to the nodes, and *NAT* to provide Internet to the cluster. Finally, the nodes were set up with the *EBSP* library and a Matrix multiplication program was adapted for use as a benchmark. The results from this program were used to draw some conclusions on the capabilities and limitations of the 4-node Parallella cluster.

The first objective namely, to determine whether four Parallella boards could be combined to form a small computer cluster, was achieved by connecting all the components together and then testing that these components could talk to each other and access the shared storage and memory. This was tested using *NetPIPE TCP* which confirmed that the nodes could communicate with one another.

The second objective of finding a suitable software framework for the Parallella cluster was achieved through the use of *Open MPI* and the *EBSP* library which allowed a parallel benchmark to be run that showed a speedup relative to execution on a single Epiphany node.

The third objective related to ascertaining the capabilities of the cluster. This was not achieved as typical HPC benchmarks were not run due to limited time. Moreover, the cluster consisted of only 4 nodes and thus, its performance was nowhere near HPC-levels of performance as reiterated by Richie et al. [3] who state: “The raw performance of currently available Epiphany coprocessors is relatively low compared to modern high performance CPUs and GPUs”.

The final objective to ascertain the limitations of the cluster was, to some extent, achieved. Running the matrix multiplication benchmark showed the limitations of the shared Epiphany memory, and the main memory in general. It also showed the computational limitations of this small cluster which did not measure up to the processing power of a standard CPU. The cluster also has hardware limitations in the form of the Epiphany co-processor which lacks hardware support for floating-point division and other higher-complexity arithmetic.

Acknowledgement

This work was undertaken in the Distributed Multimedia CoE at Rhodes University, with financial support from Telkom SA and Infinera. The authors acknowledge that opinions, findings and conclusions or recommendations expressed here are those of the author(s) and that none of the above mentioned sponsors accept liability whatsoever in this regard.

References

[1] M. F. Cloutier, C. Paradis, and V. M. Weaver, “A Raspberry Pi cluster instrumented for fine-grained power measurement,” *Electronics*, vol. 5, no. 4, p. 61, 2016.
[2] S. J. Cox, J. T. Cox, R. P. Boardman, S. J. Johnston, M. Scott, and N. S. O’brien, “Iridis-Pi: a low-cost, compact demonstration cluster,” *Cluster Computing*, vol. 17, no. 2, pp. 349–358, 2014.
[3] D. Richie, J. Ross, S. Park, and S. D, “Threaded MPI programming model for the Epiphany RISC array processor,” *Journal of Computational Science*, vol. 9, pp. 94–100, 2015.
[4] S. J. Matthews, R. W. Blaine, and A. F. Brantly, “Evaluating single board computer clusters for cyber operations,” in *2016 International Conference on Cyber Conflict (CyCon US)*. IEEE, 2016, pp. 1–8.
[5] A. Middleton and P. Solutions, “HPCC systems: Introduction to HPCC (high-performance computing cluster),” *White Paper, LexisNexis Risk Solutions*, 2011.
[6] K. Dowd and C. Severance, *High Performance Computing*, 3rd ed. Rice University, 2010.
[7] J. J. Dongarra, P. Luszczek, and A. Petitet, “The Linpack benchmark: past, present and future,” *Concurrency and Computation: Practice and Experience*, vol. 15, no. 9, pp. 803–820, 2003.
[8] Adapteva, “Parallella board,” Online, 2014, accessed on 21 February 2020. [Online]. Available: https://www.parallella.org/board/
[9] ——, “Epiphany datasheet,” Online, 2014, accessed on: 29 March 2020. [Online]. Available: https://adapteva.com/docs/e16g301_datasheet.pdf
[10] M. J. Kruger, “Building a Parallella board cluster,” *Bachelor of Science Honours Thesis, Rhodes University, Grahamstown, South Africa*, 2015.
[11] Adapteva, “Parabuntu,” Online, 2016, accessed on: 10 June 2020. [Online]. Available: https://github.com/parallella/parabuntu/releases
[12] CODUIN, “Epiphany BSP Library,” Online, 2017, accessed on: 5 October 2020. [Online]. Available: https://github.com/coduin/epiphany-bsp
[13] Q. Snell, A. Mikler, G. Helmer, and J. Gustafson, “NetPIPE,” Online, 2019, accessed on 21 October 2020. [Online]. Available: http://manpages.ubuntu.com/manpages/cosmic/man1/NPlam.1.html
[14] CODUIN, “Getting started with EBSP,” Online, 2018, accessed on: 5 October 2020. [Online]. Available: https://jwbuurlage.github.io/epiphany-bsp/basic.html

Matthew Lewis completed his B.Sc(Honours) in the Department of Computer Science at Rhodes in 2020.

Towards Cloud-based Multi-operator Core Networks (MOCN) for Infrastructure Sharing

Lusani Mamushiane*,‡, Joyce Mwangama †, Albert Lysko*,†, Lawrence Mboweni *, Hlabishi Kobo*, Sabelo Dlamini ‡

*Council for Scientific and Industrial Research (CSIR), Pretoria, South Africa
†University of Cape Town (UCT), Cape Town, South Africa
‡State Information Technology Agency (SITA), Pretoria, South Africa
[1]RVHLUS001@myuct.ac.za

***Abstract*—The cost associated with telecommunication infrastructure acquisition and deployment remains a primary inhibitor to market entry by new operators who lack the capital to deploy competitive infrastructure. This entry barrier has resulted in the monopolisation of the telecommunication industry by established network operators. To cope with the growing user demands, existing operators are looking for strategies to cost-effectively expand and improve their existing infrastructures. Network virtualisation and technologies for infrastructure sharing play important roles in reducing the deployment and operational costs of future mobile networks and fostering healthy competition in the market. The prospects of reducing the cost of network deployment offers some flexibility in adjusting retail prices and extending broadband access to rural areas. This paper proposes a network sharing architecture called cloud-based multi-operator core networks (C-MOCN), derived from a well-known specification where the radio access network (RAN), and spectrum, are shared among multiple mobile network operators. The technical implementation details of the architecture and acceptance tests conducted to ensure strong traffic isolation are described. The test results show that it is possible for multiple operators to co-exist on the same RAN while ensuring strong traffic isolation and high quality of experience for end-users.**

***Index Terms*—Infrastructure sharing, Multi-operator core networks (MOCN), Spectrum sharing, Isolation**

I. Introduction

The telecommunications industry has a great potential of driving the socio-economic transformation in the country. It also plays a critical role in digitalisation. However, the current telecommunication landscape in South Africa is largely vertically integrated, i.e., it is dominated by few players with their own end-to-end infrastructures. The telecommunication infrastructure is broadly composed of a core and a radio access network (RAN), where the former is located at the head office, and it is typically run from specially developed hardware servers. The RAN is the visible part of the network that is installed on masts across the country, and finally, these are connected by a backhaul network to the core. Each operator in the incumbent network owns the entire network elements from its core to RAN. This leads to inefficient usage of both external resources (power and spectrum) and infrastructural resources (compute, networking and storage), resulting in high cost of deploying and running a network. By extension, this contributes to high cost of broadband to the end-user.

Network infrastructure sharing has been cited as a silver bullet solution towards reducing network deployment costs and opening up barriers to market entry for small, medium and micro enterprises (SMMEs) [1]. This cost reduction is achieved by allowing SMMEs to fold their operations into a shared network infrastructure. This sharing will potentially stimulate service-level competition (instead of infrastructure-level competition) and innovation, resulting in a better quality of service and lower cost of broadband services [2].

The concept of network sharing is not entirely new. It was introduced in the earlier generations of mobile communication. However, its implementation has always been confined to passive infrastructure such as site locations, radio equipment, and masts. As such, it was never fully explored from the technology perspective. In recent times, the network sharing concept has and continues to find prominence due to mobile technologies' advancement and evolution. It finds expression in the multi-tenancy [3] networking paradigm, which is driven by recent and emerging technologies such as network function virtualisation (NFV)[4] and software-defined networking (SDN) [5]. Network sharing is anticipated to accelerate network rollouts and open new business opportunities for mobile virtual network operators (MVNO), over-the-top providers (OTT) and other vertical industry players.

This paper demonstrates a practical implementation of a 3GPP compliant network infrastructure sharing testbed, which we have codenamed 'cloud-based multi-operator network (C-MOCN)'. C-MOCN was developed using cloud native core network functions running as microservices and proprietary RAN. C-MOCN was developed to allow multiple network operators (each having its own core network) to co-exist on the same RAN by adopting both the active and passive RAN sharing models, where multiple operators not only share the passive radio infrastructure but also share active radio elements such as spectrum and computing resources.

A. Contribution

To date, there have been numerous research studies directed towards the network infrastructure sharing paradigm. Table I summarises the contributions of the research works related to infrastructure sharing testbed implementations found in

TABLE I: Related Work

References	Main Contribution
Kokku et al. [6]	Proposed a remote RAN sharing solution by inserting a slice scheduling broker between the RAN and core networks. A testbed was built using simulation.
Ksentini et al. [7]	Proposed a dynamic RAN sharing architecture design and admission control approach. The design was implemented on an emulation platform called OpenAirInterface.
Lin et al. [8]	Proposed a transparent RAN sharing approach by inserting a "RAN proxy" which acts as a broker between the RAN and multiple core networks. The authors also tested a scenario where multiple RAN proxies are deployed, one between the small cell and macrocell and the other between the macrocell and core network.
Turk et al. [9]	Tested the effects of RAN sharing on a live LTE network with two sharing partners.
Markendahl et al. [10]	Carried out a techno-economic analysis of RAN network sharing for indoor deployments using femtocells and distributed antenna systems.
Calero et al. [11]	Conducted an empirical study of the techno-economic and performance implications of sharing the RAN infrastructure between multiple network operators.
Alaez et al.[12]	Proposed an open-source testbed design to demonstrate RAN sharing. The network components were simulated using NS-3.

the literature. However, most studies relied on emulation and simulation tools for their testbed implementation. This includes simulated LTE stacks such as base stations and air interfaces which does not fully represent a real service provider environment. Also, these works do not provide information on the acceptance tests they conducted to ensure strong traffic isolation between mobile network operators. This paper describes the acceptance tests carried out on C-MOCN to make sure that it meets the basic isolation requirements in a typical shared network environment. The main contributions of this paper can be summarised as follows:

- Provides an architecture for RAN sharing leveraging virtualization technologies
- Presents the acceptance test plan for traffic isolation in shared RAN environment
- Highlights the benefits and beneficiaries of RAN sharing

B. Organisation

The paper is organised as follows. Section II describes different network sharing architectures ratified by the 3rd Generation Partnership Project (3GPP). Section III presents the key building blocks of our C-MOCN and reveals the implementation details. Section IV describes the acceptance tests that we performed. Section V discusses the results from the acceptance tests. Finally, Section VI concludes the paper and provides future research direction.

II. Network Sharing Architectures

3GPP has ratified and defined two architectures with varying degrees of sharing, namely the multi-operator core networks (MOCN) and multi-operator RAN (MORAN). The MOCN architecture enables a mobile network operator to provide services to its subscribers as one of the multiple operators that share both the radio carriers and passive radio equipment, while the core network remains proprietary to each operator. With MORAN, only the passive elements of the RAN, except for the radio carries, are shared between multiple operators. A prerequisite when entering into the MORAN contract is for each operator to have acquired a dedicated spectrum license, making MORAN resource inefficient. MOCN brings incremental benefits over MORAN in that it offers mobile operators the opportunity to pool and share their spectrum allocations for better utilisation of resources and improved trunking efficiency. For both these sharing approaches, mobile operators can decide whether or not to share the backhaul connecting to their respective core networks. Table II summarizes the differences between MOCN and MORAN architectures.

TABLE II: A comparison summary between MORAN and MOCN

Component	MORAN	MOCN
Civil works	Shared	Shared
Frequency spectrum	Independent	Shared
Network operations and management	Independent	Shared
Core Network	Independent	Independent
RAN equipment	Shared	Shared
Backhaul	Shared or Independent	Shared or Independent
Feature deployment (e.g. transmission power cell range, interference)	Independent	Shared

III. C-MOCN Design and Implementation

C-MOCN (as depicted by Figure 1) constitutes four main components, namely, the user equipment (UE), the RAN, the backhaul and core networks. The design and implementation details of these components are outlined in the following sections.

1) Cloud Platform: Our testbed uses OpenStack to host virtualised network functions of the core networks. OpenStack is an open-source cloud computing platform used to build and manage public and private clouds. Our OpenStack deployment was designed to handle core cloud-computing services such as compute, networking, storage, identity, image and orchestration services. The hardware specification of the commercial off the shelf (COTS) servers used to deploy OpenStack is as follows: 1008.3GB RAM, 10TB storage, and 208 virtual CPUs.

2) Core Networks: To study the multi-operator core network (MOCN) architecture, two multi-vendor virtual core networks were deployed. These core networks are cloud-native solutions designed using microservices for each network function. Both these core networks were deployed on top of OpenStack virtual machines. The first core network

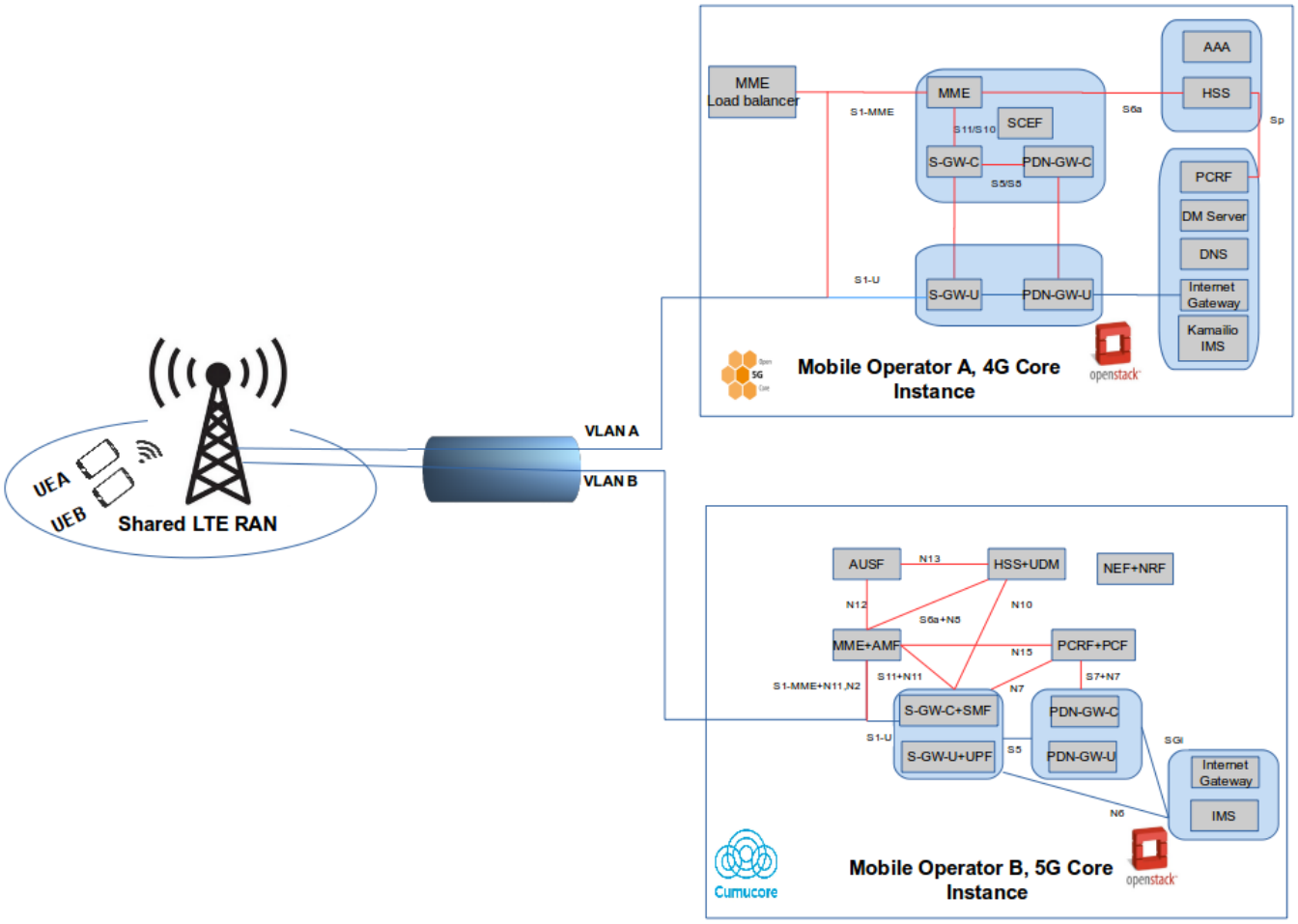

Fig. 1: C-MOCN high level architecture

is from Cumucore, and supports 5G non-standalone (NSA) mode. The second core network is open-source and is from Fraunhofer and supports 4G (LTE) functionality. The virtual machines were each allocated 2GB RAM, 2 virtual CPUs and 60GB storage. To maintain isolation between the mobile operators, there was no interconnection between the two core networks. The network functions of each core network were configured to communicate with each other over localhost. The packet gateway network function of each core network was configured to connect to the local internet service provider with DHCP and NAT enabled. The use of virtualised core networks has the potential to create unprecedented business cases in that instead of operators being locked to vendors, they can utilize open-source solutions which run on commodity hardware, offering operators an opportunity to add new features on-demand and decrease time-to-market new services.

3) RAN: The RAN was deployed using a real Flexi Zone Indoor LTE pico cell from Nokia, operating in the 1800Hz (indoor R&D license) band. The base station supports a maximum of 840 active users with a coverage of 200 meters. The base station was commisioned using the BTS element manager from Nokia [13]. The configured base station parameters included tracking area codes (TAC), public land mobile network (PLMN) identities, application addresses (user planes, control planes and management planes for each operator), NTP servers, routing, transport networks and so forth.

4) User Equipment(UE): For the UE, two Android smartphones from Samsung were used. Each smartphone was equipped with a programmable USIM card from Sysmocom. The USIMs were programmed with subscriber and authentication information. The carrier-specific configuration (such as the PLMN and access point name (APN)) were also added to each UE.

5) Backhaul Network: An Ethernet backhaul connection was used to connect the base station and the core network.

6) Isolation: Network traffic for each operator is segregated from the radio access network all the way to the backhaul. Further, unique network settings of each mobile network operator ensure that unintended network access by a subscriber of one operator to another is not possible. These unique settings include PLMN identities, authentication keys and operator-encrypted codes provisioned in the home subscriber servers (HSS). Our testbed capitalizes on the power of VLANs to segregate traffic of each mobile network operator. In order to integrate the two core networks to the

shared base station, two virtual LAN (VLAN) interfaces were created on the virtual machines running the core networks and on the base station's backhaul interfaces.

IV. Acceptance Test Plan

Considering the need for traffic isolation, the VLAN technique is applied to separate traffic (both control and user traffic) between the core networks. This means that each core network can only register users connected to the VLAN interface that have the same shared type of VLAN (same VLAN ID). To achieve this, two different acceptance tests were executed to validate the VLAN isolation mechanism. This section describes the acceptance tests conducted and the expected outcomes. The admission control procedure is also outlined.

A. Test Case 1: vEPC isolation

In this setup, each mobile network operator activates its own core network services using different virtual machines hosted on a cloud platform. This test case is used to demonstrate that each network operator uses their own mobile core network. Therefore, when the core network is shutdown, all subscribers associated with it must fail to connect.

1) Test procedure:

- Start-up only one mobile core network belonging to network operator A.
- Use UEA (subscriber belonging to network operator A) to establish a connection to the network.
  Expected results: Connection should succeed.
- Use UEB to establish a connection to the network.
  Expected results: Connection should fail.
- Start up mobile core network belonging to network operator B and attach UEB.
  Expected output: Connection should succeed.
  Note: Repeating the above setup using mobile core network B should give the same results.

B. Test Case 2: Isolation on the backhaul

The C-MOCN only has one backhaul from within the core. This test is used to demonstrate that there is a strong isolation of packets from one network to the next.

1) Test procedure:

- Attach UEA and UEB. Expected results successful connection to the respective networks.
- Generate traffic from UEA.
- Connect network packet sniffers (Wireshark or tcpdump) on VLAN of network B on the interface connecting the core network to the backhaul. **Expected results** no packets of UEA should be visible.
- Connect network packet sniffers (Wireshark or tcpdump) on VLAN of network A on the interface connecting the core network to the backhaul. **Expected results** only packets of UEA should be visible.
  Note: Repeating the above setup using network B should yield the same results.

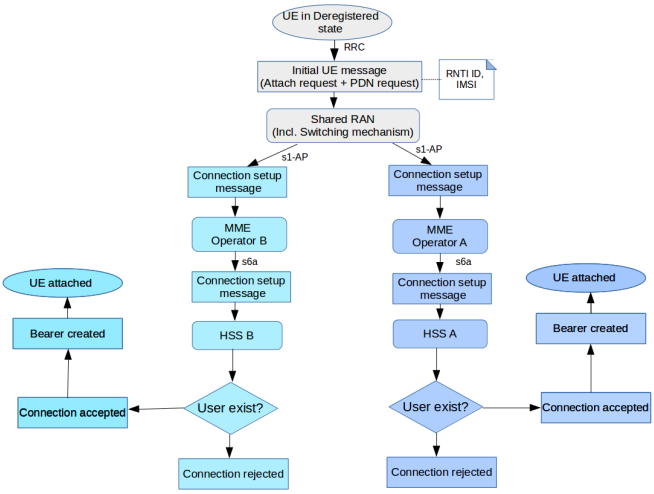

Fig. 2: C-MOCN admission control procedure

C. Admission Control

The target of the admission control procedure is to register the UE to its home network and for the UE to be able to send and receive data to and from the packet data network (PDN). The admission control procedure (see Figure 2) for C-MOCN in 4G mode is as follows: first the UE is initially in deregistered state, meaning it is not connected to the network. The UE sends a radio resource channel (RRC) connection request to the base station on random access channel (RACH) to establish a signalling radio bearer. After succesful creation of the radio bearer, the UE then sends an initial UE message, containing an attach request and PDN connectivity request, subscription information (such as the IMSI), and security information to the MME via the base station. In order to send the connection request to the correct MME, the base station checks its PLMN, and VLAN application address configurations and make sure the configuration matches the values embedded in the attach request. The communication between the MME and base station is using s1 application (S1-AP) protocol. Upon receipt of the connection request, the MME uses Diameter transport protocol (over s6a interface) to forward the connection request to the HSS. The HSS then checks if the UE has been provisioned in its database. If the UE exists, then the connection request is accepted and a bearer (tunnel) between the UE and MME is created. At this stage, the UE is now connected to the network and its status changes to registered. Once registered, the UE can start consuming broadband services. If the HSS could not authenticate the UE on its database, then the connection request is rejected.

V. Results

This section discusses the results observed after executing the test cases described in section IV. The subnet mask details of each operator are as follows: mobile operator A is allocated a subnet mask of 11.0.0.0/24, whereas mobile operator B's allocation is 12.0.0.0/24. The IP address of the configured VLAN interface on the virtual machine running operator A's core network is 11.0.0.111, and the corresponding VLAN

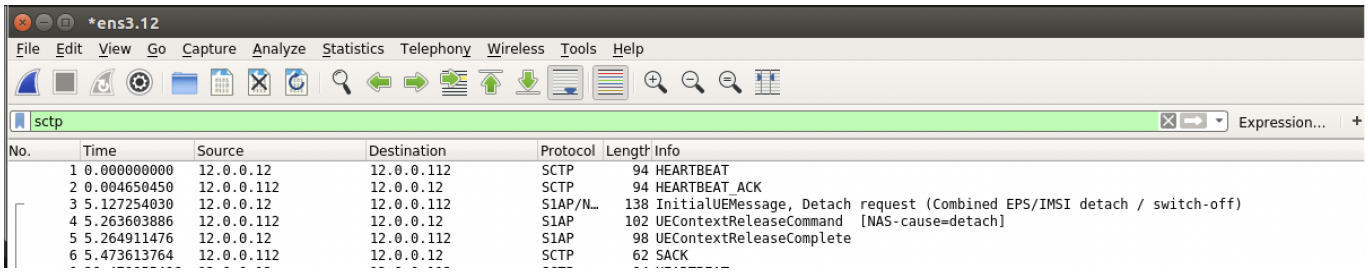

Fig. 3: Packet capture (PCAP) Logs with Wireshark on Core Network A

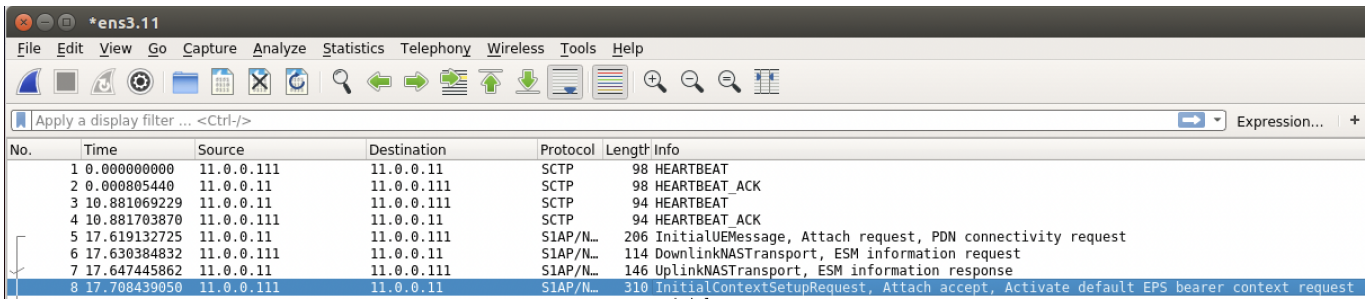

Fig. 4: Packet capture (PCAP) Logs with Wireshark on Core Network B

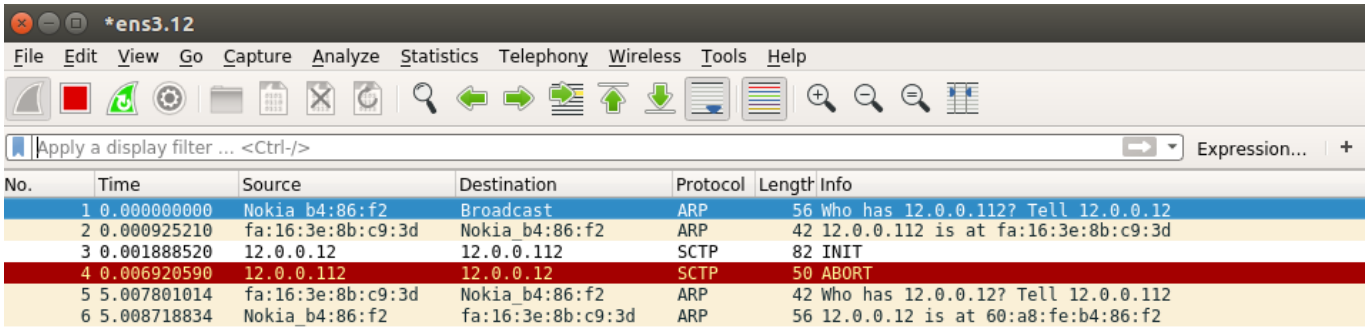

Fig. 5: Packet capture (PCAP) Logs with Wireshark on Core Network B

interface on the base station is assigned an IP address of 11.0.0.11. Similarly, operator B's core network and its corresponding base station VLAN interface are assigned 12.0.0.112 and 12.0.0.12 respectively. As shown in Figure 3 and Figure 4, C-MOCN passed the isolation on the backhaul test (see section IV-B). The UE attach requests are only visible to the operators each UE is subscribed to and not to others.

On execution of Test Case 1 (section IV-A), the base station could not attach to operator B's core network resulting in an SCTP ABORT message from the core network. Subsequently, UE B could not connect to the network and remained in a deregistered state. As expected, the PCAP logs on Operator B's core network (see Figure 5) did not include any packets from UE B. This validated the strong isolation levels in C-MOCN.

In order to evaluate the end-user quality of experience (QoE) on C-MOCN, we performed video streaming, web browsing and voice over IP (VoIP) tests and compared the test results with the QoE delivered by commercial networks. The test results indicated no visible performance differences. However, it is noteworthy that C-MOCN was deployed in a semi-sterile indoor environment with direct line of communication, and negligible interferences in the air interface. Thus, different results may be observed under a fair benchmarking environment.

Fig. 6: LTE speed test results

Speed tests were also conducted to measure the upload and download speeds of each sharing mobile network operator. The tests were carried out using the an LTE speed test application called SpeedTest [14]. The speed tests were performed in parallel. The results are as shown in Figure 6).

Both core networks produced the same download speed and almost the same upload speeds.

VI. Conclusion

This paper demonstrated the paradigm of network infrastructure sharing (including spectrum sharing) by building a prototype based on MOCN architecture. There is a general consensus that infrastructure sharing presents the possibility of reducing the cost of network acquisition, deployment and operation which is likely to stimulate small and medium businesses penetration to the telecoms business market and foster a healthy competition. Our paper presents the emperical validation of the network sharing architecture leveraging virtualization technologies in core network deployment and traffic isolation. The performance evaluation of the sharing architecture was also conducted based on quality of experience. The beneficiaries of the results of our work include small operators, incumbent operators, regulatory bodies who can use this work as evidence of the technical feasibility of infrastructure sharing to unlock cost savings and to improve broadband penetration rates in developing countries that are still plaqued by the digital divide.

Our work primarily employed VLANs as a traffic isolation mechanism.The VLAN-based sharing mechanism is still highly vendor-dependent and lacks transparency in terms of QoS management and allocation between sharing partners. In future we plan to extend our testbed with an open RAN capability running on commercial off the shelf hardware to build a full-fledged multi-RAN virtualised solution.

Acknowledgement

The authors acknowledge the support received from TELKOM SA via the Telkom Centre of Excellence (CoE) in Broadband Networks Applications at UCT.

References

[1] D.-E. Meddour, T. Rasheed, and Y. Gourhant, "On the role of infrastructure sharing for mobile network operators in emerging markets," *Computer networks*, vol. 55, no. 7, pp. 1576–1591, 2011.

[2] J. Hou, L. Sun, T. Shu, Y. Xiao, and M. Krunz, "Economics of strategic network infrastructure sharing: A backup reservation approach," *IEEE/ACM Transactions on Networking*, 2020.

[3] K. Samdanis, X. Costa-Perez, and V. Sciancalepore, "From network sharing to multi-tenancy: The 5g network slice broker," *IEEE Communications Magazine*, vol. 54, no. 7, pp. 32–39, 2016.

[4] B. Yi, X. Wang, K. Li, M. Huang *et al.*, "A comprehensive survey of network function virtualization," *Computer Networks*, vol. 133, pp. 212–262, 2018.

[5] D. Kreutz, F. M. Ramos, P. E. Verissimo, C. E. Rothenberg, S. Azodolmolky, and S. Uhlig, "Software-defined networking: A comprehensive survey," *Proceedings of the IEEE*, vol. 103, no. 1, pp. 14–76, 2014.

[6] R. Kokku, R. Mahindra, H. Zhang, and S. Rangarajan, "Cellslice: Cellular wireless resource slicing for active ran sharing," in *2013 Fifth International Conference on Communication Systems and Networks (COMSNETS)*. IEEE, 2013, pp. 1–10.

[7] A. Ksentini and N. Nikaein, "Toward enforcing network slicing on ran: Flexibility and resources abstraction," *IEEE Communications Magazine*, vol. 55, no. 6, pp. 102–108, 2017.

[8] Y.-D. Lin, H.-T. Chien, H.-W. Chang, C.-L. Lai, and K.-Y. Lin, "Transparent ran sharing of 5g small cells and macrocells," *IEEE Wireless Communications*, vol. 24, no. 6, pp. 104–111, 2017.

[9] Y. TÜRK and E. ZEYDAN, "On performance analysis of multioperator ran sharing for mobile networkoperators," *Turkish Journal of Electrical Engineering & Computer Sciences*, vol. 29, no. 2, pp. 816–830, 2021.

[10] J. Markendahl and A. Ghanbari, "Shared smallcell networks multi-operator or third party solutions-or both?" in *2013 11th International symposium and workshops on modeling and optimization in mobile, Ad Hoc and wireless networks (WiOpt)*. IEEE, 2013, pp. 41–48.

[11] R. M. Alaez, J. M. A. Calero, F. Belqasmi, M. El-Barachi, M. Badra, and O. Alfandi, "Towards an open source architecture for multi-operator lte core networks," *Journal of Network and Computer Applications*, vol. 75, pp. 101–109, 2016.

[12] R. Marco Alaez, J. M. Alcaraz Calero, Q. Wang, F. Belqasmi, M. El Barachi, M. Badra, and O. Alfandi, "Open-source based testbed for multioperator 4g/5g infrastructure sharing in virtual environments," *Wireless Communications and Mobile Computing*, vol. 2017, 2017.

[13] "Bts site manager," 2020. [Online]. Available: https://bts-site-manager.updatestar.com/en

[14] "Speed test," 2020. [Online]. Available: https://www.speedtest.net/apps

Lusani Mamushiane received the B.Eng. degree in Electrical and Electronic Engineering from the University of Johannesburg, South Africa in 2014. In 2015, she joined Microsoft where she worked as an Electronic and Telecoms Engineer for Intelligent Traffic Systems. In 2016, she joined the Cloud Networks and Architecture Services (CNAS) research group under the Next Generation Enterprise Institution cluster (formally known as Meraka Institute), at CSIR as a Researcher. She holds a Masters degree in Electrical Engineering, specializing in Software Defined Wide Area Networks (SDWAN) from University of Cape Town (UCT), and is currently pursuing a PhD at UCT under the supervision of Dr Joyce Mwangama and Dr Albert Lysko. She is now working as a Senior Researcher at State Information Technology Agency (SITA). Her research interests include but not limited to Programmable Networks leveraging Software Defined Networking (SDN) and Network Function Virtualization (NFV), Cloud Computing, Internet of Things (IoT), Artificial Intelligence, and other 4IR accelerators.

Internet Services & End User Applications

Improving Smart Grid Reliability Using Software-Based Networking

Gerhard Brown, Neco Ventura, Joyce Mwangama

Department of Electrical Engineering, Faculty of Engineering and the Built Environment

University of Cape Town, P. Bag X, Cape Town 7700

brwger006@myuct.ac.za

neco.ventura@uct.ac.za

joyce.mwangama@uct.ac.za

Abstract— **Smart grid is a combination of technologies that emerged in response to the rapid changes in the way humans generate, transfer, distribute and use energy. An important characteristic of smart grid is its improved reliability, enabled by better use of grid knowledge and the distribution of grid intelligence. Currently, utilities face new challenges in developing networks that can meet more stringent communication requirements while limiting cost and complexity. This study proposes a new software-based networking platform, based on Industrial Internet of Things (IIoT) technology, which aims to improve smart grid reliability by enabling more reliability-centred smart grid systems and by reacting immediately to communication problems while using real-time monitoring techniques. Using the principles of Software Defined Networking (SDN), Network Functions Virtualisation (NFV) and Machine-to-Machine Communication (M2M), this design aims to provide a more flexible and affordable approach to developing and maintaining large-scale grid communication networks while offering several features that improve grid reliability and performance. By using a topology based on a model of a real city distribution grid, this architecture was implemented in an emulated network environment. Results from the experimental evaluation show that these networks are easy to set up, maintain and scale using virtual machines. Furthermore, the results show that these networks can automatically detect and recover from several types of simulated communication failures without affecting smart grid operations. The results also demonstrate their capability to reduce network congestion. From these results, we conclude that software-based networking can offer promising design alternatives for smart distribution grids, capable of improving the grid's overall reliability.**

Keywords— **Internet of Things, Smart Grids, Software Defined Systems, Machine-to-Machine.**

I. INTRODUCTION

In the past decade, electricity supply disruptions have inconvenienced the daily lives of people around the world. Many of these disruptions can be attributed to failures in electricity grid infrastructure and there is thus a need to make the current grid more reliable, efficient, and secure. By using a two-way flow of electricity and information to create an automated, widely distributed energy delivery network, the next-generation power grid, i.e., the smart grid, aims to achieve these goals [1]. The system-wide intelligence that characterises smart grid is only feasible if the information exchange among its various functional units is expedient, reliable, and dependable. A communication network that is fast, reliable, and secure is therefore one of the keys enabling technologies of a smart grid. However, the current communication capabilities of existing electric power grids are limited and because the world is currently still in a transitional phase of shifting to smart grids, since research on the communication architectures that will support various automated and intelligent grid management systems is still in its early stages. Furthermore, although the energy industry has shown great interest in smart grid, its adoption by utilities has been slower than anticipated. This is especially true for nations with developing economies that do not have access to resources for major grid improvements [2]. Besides the regulation, standardisation, socio-economic and economic challenges utilities face with implementing smart grids, there are also various technical challenges that are awaiting solutions [3].

Reliable communication is one of the problem areas identified for further research into communication architectures for smart grid [4]. For a network to be considered reliable it must ensure that each message reaches its destination correctly and timely, thus minimising the probability of system faults occurring in the grid. Some smart grid applications make use of messages that have critical timing requirements, which means the communication network reliability should be evaluated under strict timing constraints. Communication problems can be reduced, but they can never be eliminated. Reliable smart grid communication networks must therefore also limit the impact communication faults have on the whole power system by restoring dysfunctional components to their normal working status without delay, thereby improving communication resilience. Unfortunately, due to the associated unpredictability, the cost, as well as the complexity associated with developing large-scale electricity distribution networks that rely on the use of advanced communication hardware infrastructure, it may be very difficult for network architects to provide the required assurances that their network designs will meet these requirements.

Using a model of a real city distribution grid as reference, the main objective of this work is to design and implement a communication network platform based on SDN, NFV and M2M that can potentially improve a distribution grid's reliability. In particular, the following research questions will be explored: What would the key requirements and design considerations be for a software-based communication network that aims to improve the reliability of a distribution grid? Can software-based networking principles be used to design a platform, hosted on a desktop or laptop computer, that can streamline the set up and evaluation of smart grid

communication network designs for distribution grids? Will an implemented software-based communication network be able to support and enable a reliable smart grid application, i.e., an Enterprise Asset Management (EAM) application that relies on automated batch data acquisition functions? Can network functions and services implemented in this network reduce the probability of communication failures as well as communication delays, and finally, can these functions be automated to reduce the overall network repair time?

The rest of this paper is structured as follows: Section 2 will explore the requirements for reliable data communication in smart grids. Section 3 will consider existing approaches to improving smart grid communication reliability, focussing on work that has been done in terms of Internet of Things (IoT) based approaches. This will be followed by a description of the proposed architecture section 4. Section 5 will describe the implementation of the proposed architecture in an emulated network platform along with the tests that were performed to evaluate this network's reliability. Section 6 will offer an evaluation of the test results. This paper will be concluded in section 7 with answers to our research questions as well as a discussion of further work.

II. Requirements For Reliable Smart Grid Communication

Because most of the systems in a smart grid depend on automated and intelligent grid management systems, the reliable flow of power will in many cases depend on the reliable flow of information. For example, consider a power supply disruption detected by a sensor in a transmission substation that triggers a failover signal to another substation in a distribution grid, which will allow it to switch over to local solar photovoltaic (PV) plants. A damaged fibre-optic cable in the communication network may prevent this failover signal from reaching the other substation, thus leading to a supply disruption. Furthermore, if a malfunctioning network switch delays the transfer of grid status information, it may delay operators from manually intervening to correct the fault or cause them to manually switch over supply to underperforming PV plants. This could extend the duration of the supply disruptions even further. The fact that these networks need to accommodate various smart grid applications and devices that depend on different message types, adds another layer of complexity to their design. In the distribution domain, the IEC 61850 standard has been widely adopted for substation communications and stipulates the typical design considerations for networks carrying different messages [5]. Table 1 summarises these considerations.

TABLE I
Communication Network Considerations For Different Message Types Used For Substation Communication [5].

Message Type	End-to-end Latency	Message Size
Fast messages	< 3 ms - 100 ms	1 bit
Medium speed messages	< 100 ms	1 bit -16 bits
Low speed messages	< 500 ms	16 bits – 1024 bits
Raw data messages	< 3 ms - 10 ms	12 bits – 18 bits
File transfer functions	> 1000 ms	512 bits – 200 kilobits

Designing smart distribution grids with functions that improve communication reliability to meet these requirements is therefore vital to improving the overall reliability of the power grid. To design reliable smart grid communication networks, three important communication requirements need to be considered. These requirements are summarised in Table 2.

TABLE II
Summary Of Requirements For Reliable Smart Grid Communication.

Requirements	Contributing Factors	Related Smart Grid Objectives
Reduce the probability of lost messages	Link and node failures; source and destination unavailability; and network isolation	Increase the probability of meeting communication service requirements that will ensure grid functions are executed successfully
Reduce the probability of delayed messages	Underperforming and overloaded network devices	Increase the probability of meeting communication service requirements that will ensure grid functions are executed on time
Reduced the mean time to repair network problems	Delays in time to detect, locate, analyse, repair communication issues	Shorten recovery times to reduce the probability of extended periods of failures and delays, thereby reducing the probability of failed or delayed grid functions

III. Existing Solutions

Inspired by successes in the telecommunications and information technology sectors, more studies are focussing on solving the problem of developing IoT based communication network architectures that can meet the stringent requirements of various smart grid systems. A recent survey provides an overview of several SDN based smart grid communication (SDN-SG) architectures that have been proposed and implemented [6]. Other studies that have made noteworthy contributions to this work are listed in Table 3.

TABLE III
Existing Solutions That Contributed To This Work.

Solutions	Contributions
[7] Dorsch et al., 2016	Proposed an architecture that combines the benefits of reactive and proactive Fast Failover Recovery (FFR) for smart grids using SDN.
[8] Niedermeier et al., 2016	Offers a model that supports the benefits of NFV for smart grid applications in large-scale distributed networks.
[9] Nafi et al., 2018	Offers a reference topology for SDN-based smart grid Neighbourhood Area Networks (NANs) as well as insight into the number of controllers and switches needed for a NAN in a residential area.
[10] Sydney et al., 2014	Demonstrated the flexibility and speedy implementation of SDN based FFR and load balancing functions in a real-world, geographically distributed platform called GENI.
[11] Guo et al., 2016	Proposed an architecture that buffers, schedules, and aggregates data using SDN to support big-data acquisition in smart grids.
[12] Meloni et al., 2016	Proposed an architecture with virtual grid devices and virtual application entities that can aggregate and schedule data for transfer as a service.

[13] Molina et al., 2015	Proposed an architecture with SDN applications to monitor and control smart grid networks that use non-SDN protocols. Implemented the network on a single computer using Mininet [14].
[15] Jararweh et al., 2017	Proposed an architecture that uses virtualisation and Software Defined Systems (SD-Sys) to provide functions and services in the network edge.

IV. PROPOSED DESIGN

Considering the architectures and models described by other researchers along with their potential benefits and shortcomings, a smart grid communication architecture that aimed to improve the reliability of smart distribution grids was proposed in this work. This architecture is presented in Fig. 1 in terms of the four smart grid zones that are most relevant to the distribution domain [16]. Note that, although this architecture is designed with the electricity distribution domain in mind, it may also be adapted for use in other smart grid domains.

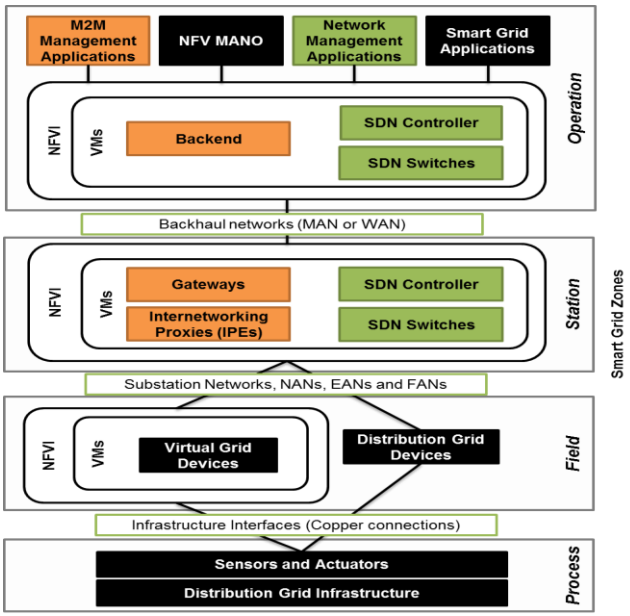

Figure 1: Architecture of the proposed system

A. Architecture

From the bottom up, the process zone represents the distribution grid infrastructure that supports the electricity distribution processes. This includes electricity infrastructure, machines, and buildings. In distribution grids, this layer will describe the distribution substations and other distribution field equipment. The sensors and actuators connected to the distribution infrastructure are also included in the process zone. Next, these sensors and actuators are connected to devices in the field zone. In most cases, these connections are physical copper connections that transfer electrical signals. The field zone will contain the devices that transform these signals into data for transfer using the distribution grid's communication networks. Smart grid devices in this grid zone of a distribution grid may include stand-alone computers, laptops, mobile devices and in many cases, devices that are integrated directly with the grid infrastructure as part of a "smart" unit. Devices located in and around substations will be equipped with hardware for data processing, storage, and communication. Many of the functions performed by these devices can be virtualised, which is why Network Functions Virtualisation Infrastructure (NFVI) and Virtual Machines (VMs) are included in the field zone of this architecture. The devices in the field zone will communicate among themselves and with elements in the station zone using internal substation networks and NANs, Extended Area Networks (EANs) and Field Area Networks (FANs). The communication nodes in these networks, i.e., the network switches, are contained in the station zone. By implication, the devices in higher tier substations and other facilities acting as NFVI for virtual switches and SDN controllers will become the distribution grid edge network's "hot spots". The NFVI in the station zone will connect the distribution grid's field components to the grid's Metropolitan Area Networks (MANs) or Wide Area Networks (WANs) by providing interfaces to the grid's backhaul networks. The NFVI in the station zone will also include instances of M2M Internetworking Proxy Entities (IPEs) that act as interfaces for non-M2M devices, and in some cases M2M Gateways that provide edge networks service needed at specific points in the distribution grid. The operation zone contains the NFVI that hosts the domain level SDN switches and controllers for the distribution grid's core communication networks. VMs hosted on this NFVI also contain the M2M Backend services. The distribution grid's smart grid applications, network management applications and M2M management applications are also located in the operation zone with interfaces to the relevant NFVI and VMs. This includes the SDN applications for network monitoring and automated network control functions. The NFV Management and Orchestration (MANO) also operates in the operation zone, where it manages the provisioning, updating, resourcing and termination of all VMs on available NFVI in the network.

B. Network Design

Using this architecture, a design for a software-based communication network that aimed to improve the reliability of a section of the City of Cape Town's distribution grid was developed. The architecture of this proposed design is shown in Fig. 2.

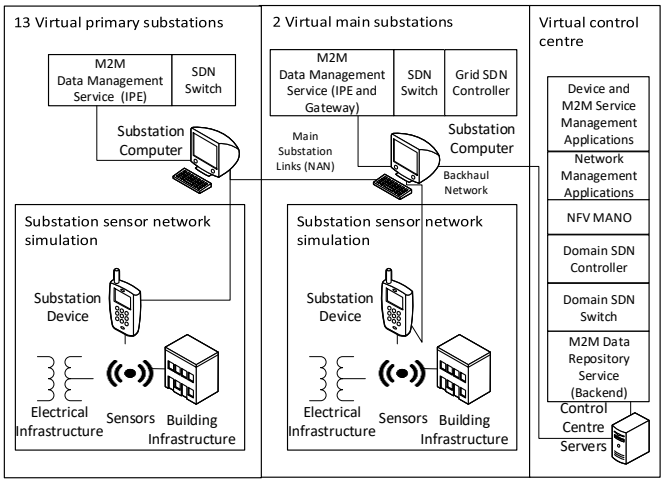

Figure 2: Example of how a software defined communication network design can be implemented in an electricity distribution grid

For this design, a substation computer was placed in each primary and main substation to act as the station and field zone NFVI. These substation computers function as the network "hot-spots" for the distribution grid devices near them, offering network connectivity via the SDN switches that they will host as VMs. Each substation also has at least one substation device that will have direct interfaces to sensors that collect data about the grid infrastructure. The primary substations in the distribution grid are the main network interfaces for devices in smaller secondary substations, mini-substations and other distribution grid field infrastructure that do not have their own substation computers. In addition to hosting an SDN switch, the primary substation computers also host M2M IPE services that transform all data received from the distribution grid devices to a common data model used by M2M data acquisition services. The IPE also manages the low-level data aggregation and storage of received sensor data.

The substation computers located in the main substations host the M2M Gateway services, which provide another level of data aggregation in the edge networks, along with other network service functions. Distribution grid SDN controllers are also hosted on these main substation computers to provide edge network control in the NANs. Servers located in the distribution grid's control centre serve as the NFVI in the operation zone. These servers host VMs for the domain SDN controllers and the Backend M2M services, which will be the central repository for the acquired grid data. Running alongside these VMs will be the smart grid applications themselves that will access this stored data when needed. Applications that manage the distribution grid devices and remote storage also run on these servers, along with the NFV MANO that provision the required VMs and manage their resources. Most important for managing the functions that aim to improve the distribution grid's communication reliability will be the network management applications that also run on these servers.

Included in this design are network functions that automatically discover the entire network topology and update the topology information when the network configuration changes. These functions also ensure that the shortest routing paths are maintained for each discovered network switch. Applications that support automatic FFR and traffic scheduling with flow aggregation are also included, with the potential to add more network functions that support communication reliability at a later stage. FFR functions are the main recovery mechanism for communication link and node failures. Automated traffic scheduling functions are implemented as M2M services and configured to support automated failover to back-up devices to manage destination device unavailability. Lastly, applications that support real-time network monitoring and run-time network control are included in the design, with a graphical user interface (GUI) that provides an easy-to-use presentation of network information to users. Real-time network monitoring and control functions play a crucial role in improving the communication reliability for functions that cannot be automated. These applications will provide users with live monitoring metrics of the global network status and that can be recorded for historical trends analysis.

V. IMPLEMENTATION

To evaluate the proposed design, a virtual network was implemented using a network emulation system called Mininet [14], hosted on a single desktop computer. The scope of this implementation was limited to two main substations and 13 primary substations, each connected to 13 sensors interfacing with a smart substation device and a substation computer. It also included a control centre server. The network topology therefore consisted of 15 virtual network switches connected to NAN in the network edge, with two interfaces to a backhaul network in a MAN. The network was controlled by three virtual SDN controllers. Network functions for FFR, automated SDN controller failover, automated host failover, data buffering and traffic scheduling were implemented using SDN application interfaces and M2M services. The ONOS Tutorial VM Version 1.15.0 [17] was chosen for this testbed because it came preconfigured with Mininet, ONOS SDN controllers and various other applications needed for creating virtual SDN networks. A high-level architecture of the implemented testbed is shown in Fig. 3.

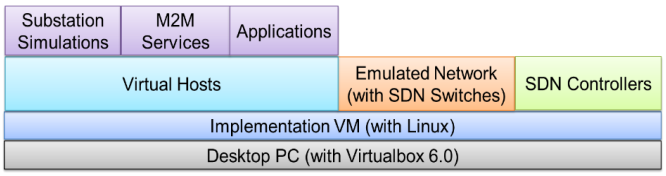

Figure 3: Implementation testbed architecture

A. Substation Simulations and M2M Service Platforms

Using the OpenMTC IPE-sensors demo application examples [18] as a reference, Python programs were developed to function as simulations that generate data from smart grid devices connected to substation sensors. The programs were also implemented to acquire data by functioning as M2M service platforms. The procedures executed by these programs are shown in Figs. 4-5.

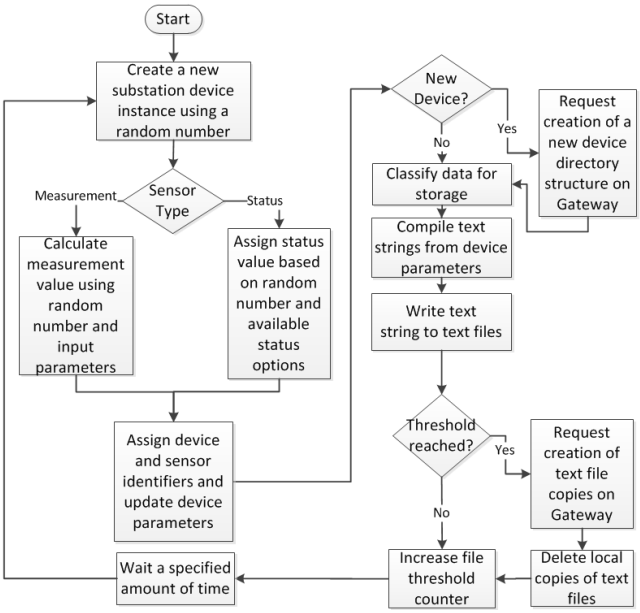

Figure 4: Algorithm for substation data generation and data acquisition using a Machine-to-Machine gateway service

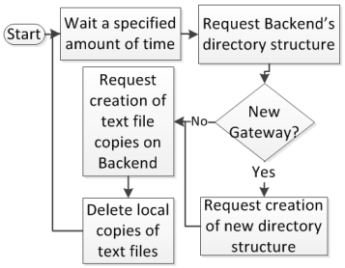

Figure 5: Algorithm for data acquisition using a Machine-to-Machine backend service

Python programs were also developed to offer M2M functions for data storage and organisation, data transfer using FTP communication, traffic scheduling and automated failovers to back-up devices. To observe the effects of communication issues on these simulations acting as running smart grid applications, these programs were configured with status logging messages that informed users of each function the program executed and alerted them to any problems with the execution of these functions. The communication was monitored using the ONOS GUI [19] and the Wireshark [20] network packet analyser.

B. Network reliability tests

Next, a series of tests were conducted to evaluate the reliability of the implemented network. These tests focused on answering the following two questions: Could the implemented software-based network provide the communication functions and services needed to support a reliability focussed EAM system? Would the network functions and M2M services implemented in this design improve the communication reliability of the modelled distribution grid when subjected to various communication problems? These tests therefore focussed on the ability of these network functions and services to support the uninterrupted operation of a reliability focussed smart grid application, while reducing the probability of communication failures and communication delays and reducing the mean time to repair any communication problems. The network functions that were tested included fast failover recovery, automated SDN controller failover, automated host failover, as well as data buffering and traffic scheduling. To test these network functions, the network was subjected to a series of failure simulations from which it had to recover automatically without interrupting a data acquisition process. The points of simulated failures introduced in the network during testing are illustrated by the red bolts in Fig. 6.

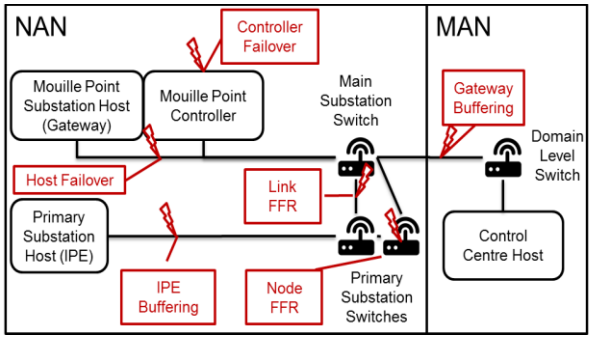

Figure 6: Simulated failure points in the implemented network

VI. VERIFICATION

The Fast Failover Recovery functions were tested first by disabling network links and nodes in the NAN. Within milliseconds, the network functions detected these failures and diverted traffic to alternative flow paths without interrupting the executing EAM functions and without any data loss. The automated SDN controller failover functions also caused no data loss or interruptions after a controller failure was simulated by disabling it. The functions again detected the failure, and reassigned mastership of the impacted switches to backup controllers until the failed controller was automatically restarted. When one of the Gateway hosts was disconnected from the network during data acquisition, the M2M service platforms ensured that data transfers from impacted IPE hosts were rerouted to a backup Gateway host. This ensured that the EAM functions were not interrupted and that none of the captured data was lost. However, each switchover to a backup Gateway introduced a slight delay in the data transfer step. Automated data buffering functions were tested by disconnecting a substation from the NAN and by disconnecting the NAN from the MAN respectively. After a substation was disconnected, the generated data was buffered on an IPE host using text files. The buffered data then automatically transferred to a Gateway host as soon as a connection was re-established. Similarly, the Gateway host showed that it could buffer data intended for the Backend host until the connection to the MAN was re-established. The data buffering functions allowed the EAM functions to continue without interruption or data loss, but delays in data transfers were observed each time the network connections were re-established. These delays were attributed to network congestion caused by the reconnecting hosts attempting to clear their buffer backlogs.

Lastly, traffic scheduling functions that aimed to overcome these sorts of congestion problems were tested by overloading network resources with large file transfers. The Round-Trip-Latency (RTL) of ping messages that were sent across the congested network before and after the traffic scheduling functions activated, were then measured to observe the effectiveness of these network functions. The result was that the amount of network traffic reduced substantially each time the scheduling service activated, resulting in improved RTL for the ping messages. The measured RTL for ping messages before and after the traffic scheduling service activation was plotted in the graph shown in Fig. 7.

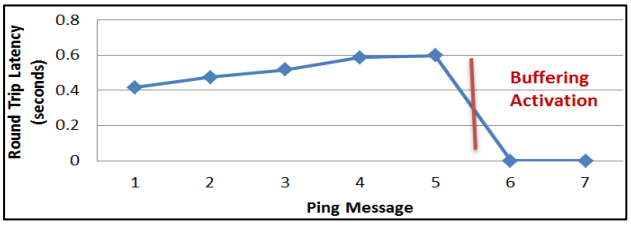

Figure 7: Improvement in round trip latency due to traffic scheduling

VII. CONCLUSIONS

This research aimed to determine if software-based communication networks could offer a means to improve the reliability of smart grids in the distribution domain. Based on

the results obtained, it can be concluded that communication networks based on the IoT frameworks of SDN, NFV and M2M indeed have the potential to improve the overall reliability of a distribution grid. These results show that this improvement in grid reliability can be achieved by using network functions to reduce the probability of communication failures and communication delays, while minimising communication fault restoration time. The results also show that software-based networks can better enable communication dependent smart grid functions, such as the functions required by EAM systems by providing specific communication services, e.g. data management. This work therefore supports the benefits that software-based networking architectures can offer smart grid designers. It also demonstrates new opportunities to integrate customised network applications into network designs. This adds a new degree of flexibility to the network, which may help to overcome various challenges, especially those utilities faced with limitations posed by supplier specific solutions and technologies. Furthermore, this work demonstrated how a software-based communication network, based on a model of a real city's distribution grid can be implemented and evaluated on a single desktop or laptop computer using a network emulation system. These virtual networks can be created in a matter of minutes and allow for the simulation of network problems that can offer valuable information that will assist network designers with improving their designs. This is a major benefit over conventional hardware-based networking approaches, which may take days, weeks or even months to set up and evaluate. The ability to monitor and control these networks with a decoupled control plane is also favourable over conventional on-site network maintenance. Although not implemented in this work, related literature supports the fact that the VMs used in these network emulation systems can also be deployed in existing distributed infrastructure. Overall, the opportunities demonstrated by this research to improve a distribution grid's reliability and streamline its development may offer utilities a means to develop better electricity distribution grids that are also more economically viable to implement. These benefits will likely encourage the uptake of smart grid by utilities and promote the use of technologies that can integrate with smart grid networks to grid users. In the long term, this may also result in better uptake of more cost effective and energy efficient technologies that may help to reduce the world's carbon footprint.

Further research may consider the use of this architecture for the improvement of ICT security in smart distribution grids as well as the enablement of other smart grid systems beyond EAM. There is also potential to expand this design to include other communication networks in the distribution domain or even other smart grid domains. Finally, to better understand the implications of implementing the proposed architecture in a distributed environment, future research should consider implementation in a distributed testbed environment and potentially a real world implementation, as part of a case study.

VIII. ACKNOWLEDGMENT

The authors are grateful to the City of Cape Town for providing grid information used in this study and acknowledge that the views of the authors are not regarded as official City of Cape Town policy. The authors further acknowledge the support received from TELKOM SA via the Telkom Centre of Excellence (CoE) in Broadband Networks at the University of Cape Town.

IX. REFERENCES

[1] X. Fang, S. Misra, G. Xue and D. Yang, "Smart Grid - The New and Improved Power Grid: A Survey," in IEEE Communications Surveys & Tutorials, vol. 14, no. 4, pp. 944-980, Fourth Quarter 2012.

[2] K. Folly, "Challenges in implementing smart grid technologies in Africa," presented at Africa Utility Week, 13 May 2013.

[3] Z. Fan et al., "Smart Grid Communications: Overview of Research Challenges, Solutions, and Standardization Activities," in IEEE Communications Surveys & Tutorials, vol. 15, no. 1, pp. 21-38, First Quarter 2013.

[4] W. Wang, Y. Xu and M. Khanna, "A survey on the communication architectures in smart grid," Computer Networks, Vol. 55, no. 15, pp. 3604-3629, 2011.

[5] IEC, "Communication networks and systems in substations – Part 5: Communication requirements for functions and device models," IEC standard 61850-5, 2003.

[6] M. H. Rehmani, A. Davy, B. Jennings and C. Assi, "Software Defined Networks based Smart Grid Communication: A Comprehensive Survey, " in IEEE Communications Surveys & Tutorials, 2018.

[7] N. Dorsch, F. Kurtz, F. Girke, and C. Wietfeld, "Enhanced fast failover for software-defined smart grid communication networks," in IEEE Global Communications Conference (GLOBECOM), Dec 2016, pp. 1–6.

[8] M. Niedermeier and H. de Meer, "Constructing Dependable Smart Grid Networks using Network Functions Virtualization," Journal of Network and Systems Management, vol. 24, issue 3, pp. 449–469, July 2016.

[9] N. Nafi, K. Ahmed, M. Gregory and M. Datta, "Software defined neighbourhood area network for smart grid applications," Future Generation Computer Systems, vol. 79, part 2, pp. 500–513, 2018.

[10] A. Sydney, D. Ochs, C. Scoglio, D. Gruenbacher, R, "Using GENI for experimental evaluation of Software Defined Networking in smart grids," Computer Networks, vol. 63, pp. 5-16, 2014.

[11] W. Guo, V. Mahendran and S. Radhakrishnan, "Achieving throughput fairness in smart grid using SDN-based flow aggregation and scheduling," 2016 IEEE 12th International Conference on Wireless and Mobile Computing, Networking and Communications (WiMob), New York, NY, 2016, pp. 1-7.

[12] A. Meloni, P. A. Pegoraro, L. Atzori and S. Sulis, "An IoT architecture for wide area measurement systems: A virtualized PMU based approach," 2016 IEEE International Energy Conference (ENERGYCON), Leuven, 2016, pp. 1-6.

[13] E. Molina, E. Jacob, J. Matias, N. Moreira and A. Astarloa, "Using software defined networking to manage and control IEC 61850-based systems," in Computers and Electrical Engineering, Vol. 43, pp. 142–154, April 2015.

[14] (2019) The Mininet website. [Online]. Available: http://www.mininet.org/

[15] Y. Jararweh et al., "Software-Defined System Support for Enabling Ubiquitous Mobile Edge Computing," The Computer Journal, vol. 60, issue. 10, pp. 1–15. October 2017.

[16] CEN-CENELEC-ETSI Smart Grid Coordination Group, "Smart grid reference architecture", European Commission DG ENER Publications, Technical Report, 2012.

[17] (2019), The ONOS Tutorial web page. [Online]. Available: https://wiki.onosproject.org/display/ONOS/Basic+ONOS+Tutorial

[18] Fraunhofer Focus, "OpenMTC IPE-sensors demo app", Available: https://www.openmtc.org/doc/training/training-ipe-sensors.html

[19] The ONOS web GUI webpage. [Online]. Available: https://wiki.onosproject.org/display/ONOS/The+ONOS+Web+GUI

[20] (2019), The Wireshark website. [Online]. Available: https://www.wireshark.org/

Gerhard Brown (Pr Eng) received his MSc in Electrical Engineering in July 2021. He is a Principal Engineer at the City of Cape Town and part of the Centre for Broadband Networks at the University of Cape Town. His research interests are Smart Grids and IoT applications.

Colour-Based Encoding Schemes for Improved Human Pose Recognition Using a Convolutional Neural Network

J.S. du Toit[1], J.V. du Toit[2], H.A. Kruger[3]

School of Computer Science and Information Systems
North-West University, Potchefstroom Campus
Private Bag X6001, Potchefstroom, 2520, South Africa
Tel: +27 18 2992548, Fax: +27 18 2992570

[1]Jaco.DuToit@nwu.ac.za

[2]Tiny.DuToit@nwu.ac.za

[3]Hennie.Kruger@nwu.ac.za

Abstract—**The goal of computer vision is to provide computers with the perceptual capability to process and understand visual data and is achieved by synthesizing information from raw videos and images. Humans are among the most frequently analysed subjects of computer vision because activity recognition and pose identification are applicable in various critical industries. This study examines a novel data augmentation technique that can aid in the machine-learned interpretation of the human form for improved pose recognition by superimposing joint markers on humans detected in video footage. The joint locations are derived from a pose estimator and are supplemented with additional information through the use of colour. The keypoint colour augmentations are applied based on either a radial or ringed colour wheel, which is notionally intended to encode spatial information based on the position of the joint. An improvement in classification accuracy of up to 11 percentage points over a baseline model was achieved when applied to a pose dataset and classified using a convolutional neural network. Furthermore, different augmentation schemes were found to favour the recognition of certain poses over others. These augmentation schemes can be diversely applied in human activity recognition and tailored to foster improved accuracy for pose-dependent classification tasks.**

Keywords—**Convolutional neural network, Data augmentation, Image classification, Pose estimation, Pose recognition.**

I. INTRODUCTION

Automated human activity and human pose recognition are among the technologies used to assist and cooperate with humans in meaningful ways. Human-orientated machinery and assistive technology systems often apply person recognition to enable systems that involve patient monitoring and health evaluation [1], human-computer interfacing [2], smart home technology [3], and limb and recovery rehabilitation therapy [4]. These systems operate by acquiring situational awareness through scene understanding based on the presence and actions of humans in the immediate environment [5]. Depending on the nature of the task, these systems often need to operate in real-time. Video-based human activity recognition (HAR) is one such application that is frequently relied upon for time-critical tasks, especially in healthcare monitoring. A HAR solution operates by learning the routine activities of daily life to recognise any abnormal behaviour, like a person falling down. An event of this kind should ideally be met with immediate assistance to the victim.

HAR achieves scene understanding by synthesising information in video footage [5]. To date, attempts to identify visual cues have relied on body shape analysis, where deformations in the silhouette of a person are measured to infer a specific action or movement. This involves monitoring changes in the proportions of a projected bounding box drawn around the individual. Alternatively, contemporary model-based approaches obtain cues by encoding a human pose as a compact feature vector which maintains a measure of similarity with a database of known poses, thus allowing for comparative distance measurements when estimating new pose instances [5]. Preserving pose similarity makes it possible for known poses to be easily recognised and unknown poses to be readily estimated. Similarly, modern machine learning methods maintain pose similarity by mapping an abstracted feature space to a common class label as is the case for a Convolutional Neural Network (CNN).

This paper investigates the use of data augmentation in pose recognition to compose a favourable feature encoding that a machine-learned classifier can leverage for improved classification accuracy. The augmentation techniques embed spatial information into each input instance and consequently encourage class similarity among similar poses. This approach entails identifying individuals in an incoming video feed and plotting a skeletal mapping of keypoints across their approximated silhouette. The keypoints are assigned colours based on their position, thereby supplementing the visual information available to the classifier. These descriptors can be leveraged during feature extraction and thereby enhance the discriminative cues for pose recognition within the CNN feature space.

Two colour wheel configurations are proposed for the positional assignment of each keypoint colour, namely a radial and a ringed structure, which are presented in Section IV. The distinct colour arrangement of each wheel helps to encode cues for silhouette deformation (ringed) and orientation changes (radial). The fixed position of keypoints on the colour wheel results in identical poses expressing a similar range of keypoint colours. Ultimately, this approach allows a pose classifier the freedom to selectively learn which visual cues are salient features that best describe a pose based on either the isolated human silhouette or the colour-encoded keypoints.

The remainder of this paper is organised as follows. Section II provides an overview of advances in pose estimation and recognition and how colour has been discovered to be a salient feature in image classification. Insight into how a CNN functions and performs image recognition is presented in Section III. Section IV contains details on the experimental design, the dataset, the colour-based augmentation techniques, and the structure of the implemented CNN. The evaluations performed on each keypoint colour encoding are summarised in Section V, whereafter the study is concluded in Section VI.

II. Related Work

Different approaches exist for human pose estimation which is decided by the choice of sensors and the intended application. The kinematic configuration, or pose, of the human body is often only approximated given the complexity of its articulation within 3D space [5]. Simplifying the human form to an abstract shape or a set of keypoints in 2D space makes for a practical approach to estimating a pose. This is because a 2D representation is subject to a reduced search space and is the result of forgoing contextual and spatial information that would otherwise be captured in 3D imaging [5].

Pons-Moll and Rosenhahn [6] identified a selection of keypoints to model a 3D representation of the human body. Their approach relied on depth sensors and the complex coordination of multiple cameras aligned to observe the same scene. This 3D abstraction allowed for an accurate representation of a pose as it relates to the real-world configuration of the human body. However, accurately modelling the human form in 3D affords a greater degree of freedom in permissible poses and consequently more opportunity for possible errors. Additionally, optimising such a representation to adapt to incoming instances for pose estimation is computationally expensive. For these reasons, a simplistic 2D representation is often preferred given its realistic potential for real-time applications, albeit at the expense of 3D information that would otherwise support greater accuracy. Therein lies the motivation of this study: to experimentally enhance a 2D pose representation with a pose-sensitive descriptor that can mimic forfeited 3D information. Colour is a prime candidate for this type of enhancement given recent insights into the functionality of CNNs and how colour has been discovered to be a valuable feature in image classification.

A recent study showcases how adept CNNs are in processing colour. Buhrmester *et al.* [7] examined the effects of colour omission when classifying images from multiple datasets. The significance of colour-dependency among samples was most prominently expressed in an image dataset of different terrains that depict desert, forest, snow, and urban scenery. Samples from the desert and snow classes were among the most dependent on colour information, likely due to the similarity in their appearance. Their identical landscapes prompted the classifier to learn characteristic hues of warm or cool colours as distinguishing features between them. Interestingly, the urban category was least affected by the omission of colour, suggesting that perhaps colours varied too often among its samples and thus learnt characteristic objects and shapes within the cityscapes as cues for that class. These findings suggest that CNNs learn adaptively based on the most discriminate features of each class, including colour. This study capitalises on this insight by introducing colour-based keypoint mappings that act as cues in the classification of human poses. These mappings are based on a fixed geometrical shape that simulates 3D spatial information regarding variations in the orientation and shape deformation of the human body.

III. Convolutional Neural Network

A CNN is a multi-layer neural network that effectively learns visual patterns directly from images. The initial layers in the CNN act as a hierarchical feature extractor where a set of learnt filters sequentially convolve across the entirety of an image to yield a feature vector that is iteratively refined as it is passed through each layer. This connection structure essentially performs feature filtering on the output of each preceding layer to help isolate salient features that suggest the input class. The filters are adapted during training to become sensitive to discriminative patterns and activate when a valuable feature is detected.

Convolution is traditionally followed by a sub-sampling layer, such as pooling, which reduces the dimensionality of the feature vector and instils the classifier with translation invariance. This makes the classifier robust against minor distortions and variations for the sought features in an image [8]. The effect is a consequence of condensing the feature vector to contain only the most significant features that contribute to the input's eventual classification. Translation invariance is advantageous for pose recognition because a person can be positioned in any location and in various poses within the recorded video frames.

A CNN concludes in either a single or a set of fully connected layers that acts as a general-purpose classifier over the extracted features. These layers learn an association between a collection of features and its predefined class. This association is self-elected and can be based on a concentration of certain abstracted textures, shapes, or even colours in the compiled feature vector [7]. For this study, adopting data augmentation as a pre-processing step is intended to benefit the classifier by providing it with more freedom in electing a favourable class association. This would improve the classification accuracy for easily confused classes such as the sitting (on a chair) and crawling pose which are identical except in their orientation. Given the translation invariance inherent in a CNN, it is not sensitive to differentiating classes based on the position or orientation of a pose. However, encoding such positional and orientational cues using colour-based augmentations may equip the classifier with this capacity.

IV. Experimental Design

This section contains an overview on each aspect of the experiments conducted in this study, including the dataset of human poses, the method used for human detection and silhouette extraction, how keypoints are identified and augmented to encode additional information through colour, and finally the CNN structure that facilitates pose recognition.

A. Dataset

The dataset was obtained from Adhikari *et. al* [9], which was compiled for their own fall detection experiments. It consists of five different poses (sitting, standing, laying, bending, crawling), which allows for the influence of colour-based augmentations to be observed on each of these poses. The five poses were manually labelled for each captured video frame that was recorded using a Microsoft Kinect sensor. Variability within the dataset was also minimised by limiting real-world complications such as extreme occlusions, changes in the background of the scene, and the possibility of multiple people within a scene. However, out of frame observations were retained, which naturally occur as an individual walks into and out of the camera's field of view, resulting in a sixth class free of any pose and labelled as an empty instance.

The resolution of the Kinect sensor yields frames of 640 x 480 pixels and captures both Red Green Blue (RGB) and depth images. These were recorded from a vantage point of approximately 2.4m above ground which is the height of the ceiling for each room in which the recordings were made. A total of five different participants were monitored from eight distinct viewing angles within selected rooms. The training set of 14,938 frames features two participants whose movements were recorded in separate rooms. The validation set of 3,063 frames again features one of these participants but recorded from a different viewing angle not contained within the training set. The remaining three participants make up the test set of 2,344 frames recorded in a room not included in either the training or validation sets. Combining these different angles, rooms, and participants into the dataset helps ensure that it expresses various perspectives for all of the five poses.

B. Silhouette Extraction

The first step toward pose estimation entails detecting any humans in the video footage using static background subtraction. It is a simple technique that discounts the changeless elements in a scene to identify motion and extract a silhouetted person from the video frame. The method is typically only applied when monitoring a controlled environment to avoid any confusion that pets, or other moving objects, may introduce. Adaptive background subtraction is a similar but more advanced technique that helps counteract irrelevant scene changes such as shifting shadows by weighting incoming observations in a video feed more heavily than preceding observations [10]. Using this technique, the dataset is pre-processed to extract the silhouette of any person present in each video frame. The original video frames in the RGB and depth footage are depicted alongside their background subtracted counterparts in Fig. 1 and Fig. 2, respectively.

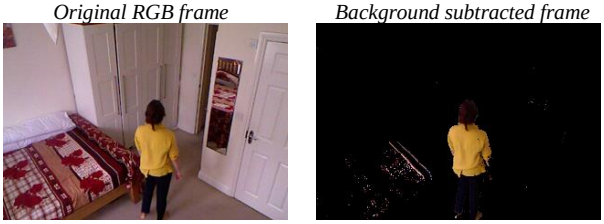

Figure 1: Example of recorded RGB frame (left) alongside its background-subtracted counterpart (right).

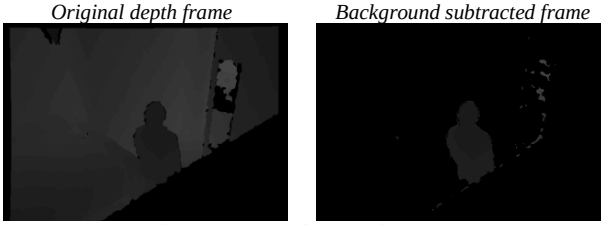

Figure 2: Example of recorded depth frame (left) alongside its background-subtracted counterpart (right).

The information loss suffered by RGB images due to scene variations and changes in lighting during background subtraction is supplemented by depth images, which are robust against these influences. Depth imaging is, however, subject to a limited viewing range given the sensor's observable distance (typically less than 5m for the Kinect). Both sets of images are complementary in the information they provide and including both in the dataset allows the pose classifier the opportunity to utilise RGB information when depth imaging is affected by its distance limitation. Similarly, it can rely on depth information when RGB imaging is affected by a malformed silhouette caused by variations in lighting and shadows.

C. Keypoint Colour-based Augmentation

OpenPose [11] is a reliable vision-based pose estimator used to derive a set of 25 skeletal keypoints from each identified person in the dataset. It performs this estimation using an iteratively refined heat map of the most probable locations for every joint of the human body. The positional likelihood of each joint is refined by considering its relation to surrounding joints. In the end, the pixels associated with the highest degree of probability for their associated joint are then output as a set of XY coordinates. These represent the keypoints that are mapped onto the human silhouettes and assigned a colour based on their position within a projected colour wheel. Fig. 3 illustrates the four colour wheels used to this end. In addition, the extracted human silhouettes are used to establish a comparable baseline dataset without keypoint mappings to further highlight the effectiveness of this approach. Finally, the baseline images and applied augmentations yield five separate datasets that are comparatively evaluated in Section V.

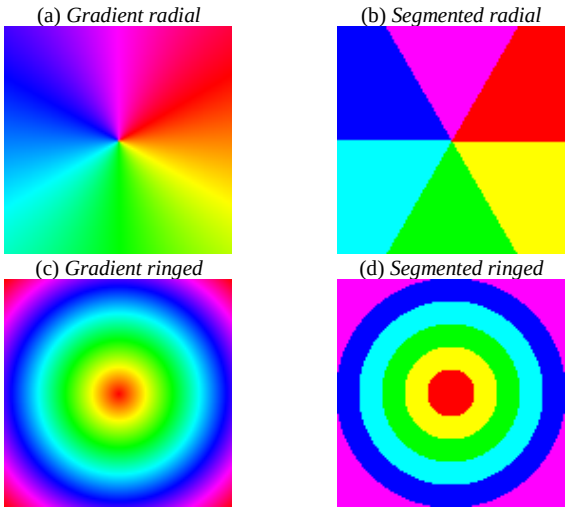

Figure 3: The proposed colour wheels that are used to assign keypoint colour based on their position within the colour wheel.

Using the obtained OpenPose XY coordinates, the given colour wheel is fixed to the centre of a person's torso when assigning colours to the keypoints. Examples of this mapping are illustrated in Figs. 4-7. The type of information encoded through each of the colour wheels is determined by the available spectrum of colours and the structural arrangement of those colours. The gradient-based colour wheels in Fig. 3(a) and Fig. 3(c) supports greater granularity that emphasizes slight changes in a pose through the use of 360 distinct colours. The segmented colour wheels in Fig. 3(b) and Fig. 3(d) instead account for only six colours, helping to disregard any insignificant movement between poses. Using less granularity through a limited spectrum of colours helps to encourage CNN generalisation among poses of the same class. This is best illustrated in Fig. 4 where the projected keypoint mapping of various standing poses will mostly express the same six colours for the same joints across most instances. In contrast, varying gradients of similar colours will instead be expressed in the same set of joints when encoded using a gradient colour wheel as demonstrated in Fig. 5.

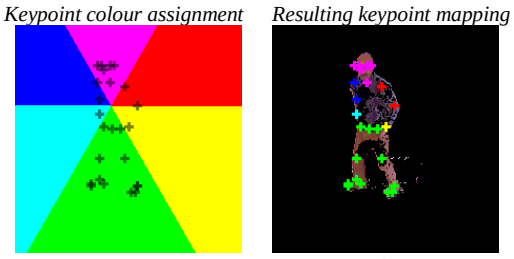

Figure 4: Positional keypoint colour assignment for a standing pose is demonstrated on a colour wheel of low colour granularity (left) alongside its projected mapping onto a human silhouette (right).

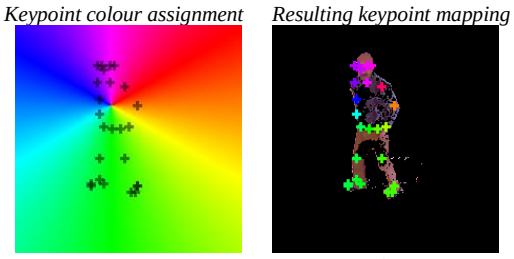

Figure 5: Positional keypoint colour assignment for a standing pose is demonstrated on a colour wheel of high colour granularity (left) alongside its projected mapping onto a human silhouette (right).

The structural arrangement of colours in the colour wheel helps to mimic spatial cues that denote postural changes that would otherwise go unrecorded in the abstracted feature space of a CNN. The radial colour wheels in Fig. 3(a) and Fig. 3(b) are to help encode changes in the orientation of a pose, whereas the ringed colour wheels in Fig. 3(c) and Fig. 3(d) are to help capture silhouette deformations. Encoding any orientation changes should assist the classifier in distinguishing poses that share the same silhouette, such as sitting (on a chair) and crawling. Fig. 6 illustrates this in that a crawling pose will align horizontally with the colour wheel, thus saturating the keypoints of similarly oriented poses with the same colours: cyan and yellow. Again, a standing pose will align vertically and adopt mostly green and magenta keypoints.

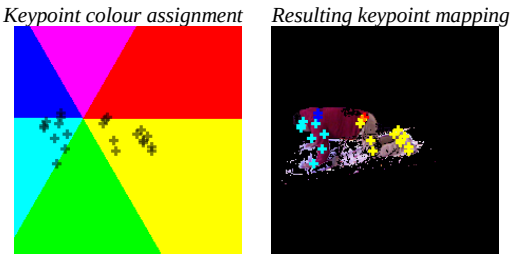

Figure 6: Positional keypoint colour assignment for a crawling pose is demonstrated on a radial colour wheel that encodes orientation (left) alongside its projected mapping onto a human silhouette (right).

On the other hand, the ringed colour wheel is expected to help capture size deformations related to the surface area that a pose assumes within a frame (e.g. standing compared to sitting). As demonstrated in Fig. 7, the range or number of colours expressed in the keypoint mapping is dependent on the size of the pose. The keypoint colours of a shrunken pose such as sitting will tend to be limited to colours in the inner rings of the colour wheel, whereas a larger pose will capture colours in the outer rings. However, unlike the radial colour wheel, the ringed representation is easily affected by size distortions caused by the distance between the subject and the camera. This influence can be limited by recording poses in a controlled environment, like in the given pose dataset [9], where consistent distances are maintained throughout all instances.

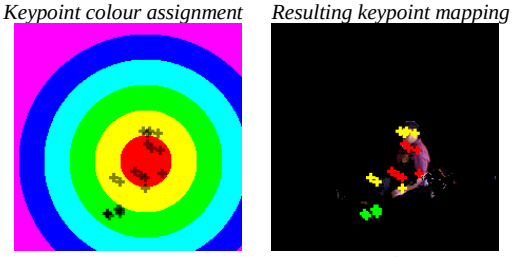

Figure 7: Positional keypoint colour assignment for a sitting pose is demonstrated on a ringed colour wheel that encodes size deformation (left) alongside its projected mapping onto a human silhouette (right).

In the end, the final output image is resized to 156 x 108 pixels to help reduce the computational load when training and executing the classifier. The images were also adapted to include four channels. The first three accommodate the RGB colour information for the background-subtracted image and encoded keypoint markers, like the resulting mappings illustrated in Figs. 4-7. The fourth channel accommodates the background-subtracted depth image, shown earlier in Fig. 2. Keypoint markers are also superimposed onto the silhouette depth images to highlight the points of interest that the CNN can use to classify the instances.

D. Convolutional Neural Network Architecture

The structure of the CNN is based on that of Adhikari *et. al* [11], which performed pose recognition on the same dataset. Their CNN was inspired by the VGGNet [12] which outperformed all other submissions in the ImageNet Challenge 2014 for image classification. As illustrated in Fig. 8, the input layer of the network accepts an input image of size 156 x 108 x 4. The remainder of the network replicates the VGGNet with only its hyperparameters adjusted to favour the pose dataset.

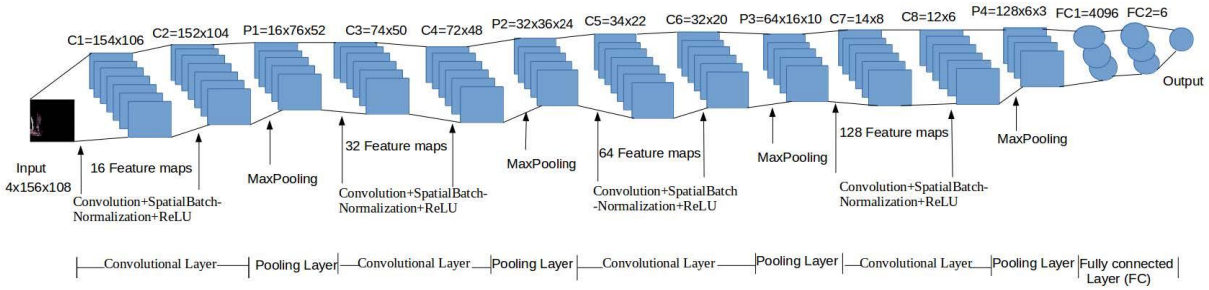

Figure 8: The composition of the CNN used to perform pose recognition as an image classification task in this study [9].

V. Results

The performance results for the colour-based augmentation schemes in pose recognition are documented in this section. The scores are evaluated against a baseline measure of non-augmented pose representations to denote the improvements in classification accuracy.

A. Validation Loss During Training

The averaged validation loss performance for 20 training epochs for the five types of CNN classifiers are shown in Fig. 9. Each classifier was trained on separate datasets augmented with a chosen augmentation scheme represented by each line in the graph. These and succeeding metrics presented in this section were computed using a stratified ten-fold cross-validation strategy where the dataset was divided into ten subsets. Each set consisted of approximately the same number of data samples and an equally representative distribution of classes according to an approximate 75% train, 15% validation split, and a held-out 10% testing split. Fig. 9 reveals a steady performance improvement as the models are optimised with every training epoch. All models achieve convergence by the 17th epoch.

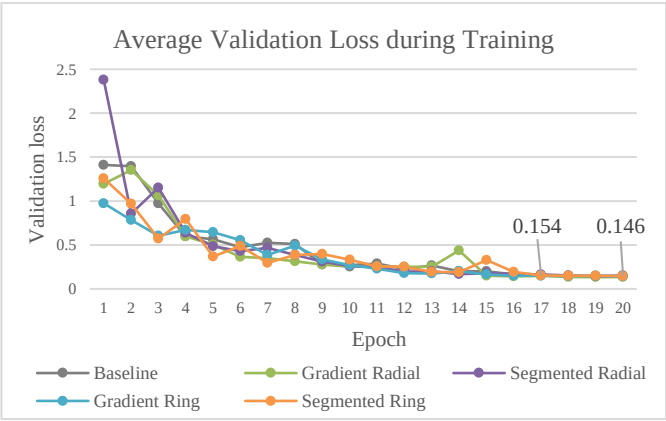

Figure 9: Averaged ten-fold cross-validation loss for each model type trained on their respective datasets.

B. Pose Classification Accuracy

The averaged classification accuracy for the ten-fold models measured on a single set of 2,344 test images is shown in Fig. 10. The baseline models achieved performance scores in the range of 66% to 76%, with an average score of 70.48%. Each colour-based augmentation improves on the baseline scores and in the case of the segmented radial wheel improves performance by up to 11 percentage points (81.61%). However, these improvements are concentrated in specific classes since each augmentation tends to favour the recognition of certain poses over others.

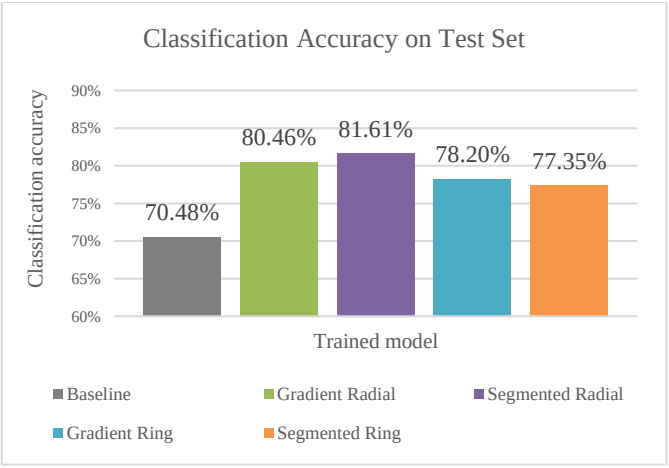

Figure 10: Averaged test accuracy performance scores across all ten-fold cross-validation models trained on each augmented dataset.

C. Pose Class Recall

The improvements that colour-coded keypoint markers afford classification accuracy is most obvious when observed using the averaged recall values depicted in Fig. 11. This illustrates how each augmentation scheme facilitates a model's improved sensitivity toward certain poses. The baseline scores show marginal support for the bending (3%) and crawling (7%) poses. They are also the least represented poses in the dataset but evidently benefit the most from the applied augmentation schemes. Keypoint colours assigned based on the ringed colour wheel provide the greatest increase in recall likely due to its support for encoding size deformations. Since these poses demonstrate a more compact silhouette than any of the other poses, their keypoints acquire a greater concentration of colours within the inner rings of the colour wheel. This results in a unique colour set for the crawling and bending class instances.

The radial colour-based augmentation scheme does not afford much improvement in classification sensitivity. This reveals that the most distinguishing attribute of bending and crawling poses is their compact shape, rather than their orientation. Improvements in recall for other poses namely, standing, sitting, and laying are not as significant because the classifier is likely well attuned to recognising these poses given the abundance of training instances. Thus, any minor improvement in sensitivity may be attributed to fewer poses being confused or falsely classed as one of these prevalent classes.

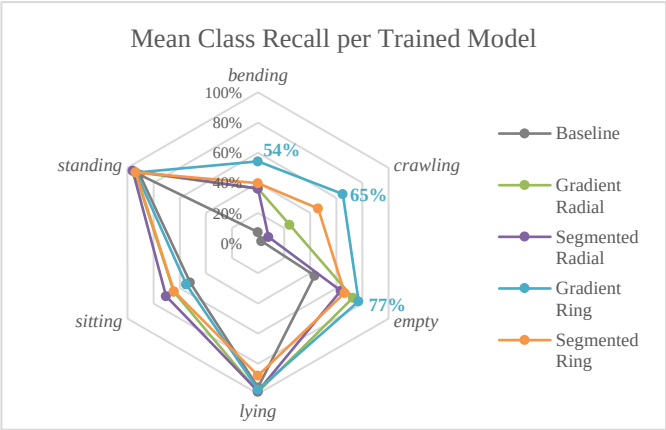

Figure 11: Mean recall performance on the test set for each pose across all ten-fold cross-validation models per augmented dataset.

D. True Positive Class Count

Examining the true positive count can further demonstrate how assigning a colour to keypoints based on a colour wheel encodes discriminative features into the pose representation. The counts are compiled in Table 1 and reveal how the structural arrangement of colours supports the classifier in learning to recognise poses that are mainly differentiated based on orientation or body shape deformation. The bending and crawling instances have the highest true positive counts when represented using the ringed augmentation scheme, given its aptitude for encoding variations in silhouette size. Laying and standing poses have the highest counts when keypoints are assigned colours from the radial colour wheel which encodes the characteristic vertical or horizontal orientation of these poses. Interestingly, sitting poses seem to benefit from the radial colour wheel augmentation scheme instead of the expected ringed colour wheel. It would appear that size deformation is not considered a significant feature in its classification and thus demonstrates an underlying and unknown feature set and class association learnt by the CNN.

TABLE I
TRUE POSITIVE COUNTS ON TEST DATASET

Class	Baseline	Gradient Radial	Segmented Radial	Gradient Ring	Segmented Ring
Crawling (37)	1	9	3	**24**	17
Bending (83)	6	30	30	**45**	33
Empty (205)	89	149	130	**158**	136
Lying (577)	552	**570**	567	561	507
Standing (657)	595	621	**631**	614	616
Sitting (785)	409	507	**552**	431	504

VI. CONCLUSION

Pose recognition conducted as an image classification task is encumbered by the loss of spatial information given the nature of 2D imaging. The experiments conducted as part of this study show that it is possible to augment the representation of a pose to partially recover lost spatial cues related to the orientation and changes in the shape of the human body. The projection of keypoints onto a human silhouette and positional colour association within a colour wheel demonstrates the ability to mimic spatial cues. These cues emphasise postural changes that would otherwise go unnoticed in the abstracted feature space of a CNN image classifier. The structural arrangement of these colours in either a radial or ringed pattern encodes a similarity among instances of respective pose classes based on changes in orientation or shape. These colour-based signals can be leveraged by a CNN to better recognise poses that are characterised by these features. In addition, this form of augmentation can be readily applied to an incoming data stream, thereby helping to enhance a pose-dependent implementation that may require accurate and real-time classification when performing a time-critical task.

The influence that the level of granularity (facilitated by the number of colours) has on classification performance could not be demonstrated using this dataset. Its influence would likely be most apparent when combating the distortion of different viewing angles that the placement of a camera may introduce. An inclined viewing angle from a high vantage point diminishes the cues for silhouette deformation while emphasising changes in orientation. Incorporating more granularity into the projected keypoint colours may offer more differentiation among poses that the viewing angle negates.

REFERENCES

[1] T. Banerjee, M. Enayati, J. M. Keller, M. Skubic, M. Popescu, M. Rantz, "Monitoring patients in hospital beds using unobtrusive depth sensors", in 2014 36th Annual International Conference of the IEEE Engineering in Medicine and Biology Society, 2014, pp. 5904-5907.

[2] K. Lai, J. Konrad, P. Ishwar, "A gesture-driven computer interface using Kinect", in 2012 IEEE Southwest Symposium on Image Analysis and Interpretation, 2012, pp. 185-188.

[3] T. Sato, T. Harada, T. Mori, "Environment-type robot system 'Robotic Room' featured by behavior media, behavior contents, and behavior adaptation, *IEEE/ASME Transactions on Mechatronics*, vol 9, no. 3, pp. 529-534, Sep. 2004.

[4] R. Komatireddy, A. Chokshi, J. Basnett, M. Casale, D. Goble, T. Shubert, "Quality and quantity of rehabilitation exercises delivered by a 3-D motion controlled camera: A pilot study", *International Journal of Physical Medicine & Rehabilitation*, vol. 2, no. 4, pp. 1-14 , 2014.

[5] M. Stommel, M. Beetz, W. Xu, "Model-Free detection, encoding, retrieval, and visualization of human poses from kinect data", *IEEE/ASME Transactions on Mechatronics*, vol. 20, no. 2, pp. 865-875, Apr. 2015.

[6] G. Pons-Moll, B. Rosenhahn, Model-based pose estimation. In *Visual analysis of humans*, London, England, Springer-Verlag, 2011, pp. 139-170.

[7] V. Buhrmester, D. Münch, D. Bulatov, M. Arens, "Evaluating the Impact of Color Information in Deep Neural Networks", in Iberian Conference on Pattern Recognition and Image Analysis, 2019, pp. 302-316.

[8] I. Goodfellow, Y. Bengio, A. Courville, Deep learning, London, England: MIT press, 2016.

[9] K. Adhikari, H. Bouchachia, H. Nait-Charif, "Activity recognition for indoor fall detection using convolutional neural network", in 2017 Fifteenth IAPR International Conference on Machine Vision Applications, 2017, pp. 81-84.

[10] Z. Zivkovic, F. Van Der Heijden, "Efficient adaptive density estimation per image pixel for the task of background subtraction", *Pattern Recognition Letters*, vol. 27, no. 7, pp. 773-780, May 2006.

[11] Z. Cao, G. Hidalgo, T. Simon, S. E. Wei, Y. Sheikh, "OpenPose: realtime multi-person 2D pose estimation using Part Affinity Fields", *IEEE Transactions on Pattern Analysis and Machine Intelligence*, vol. 43, no. 1, pp. 172-186, July 2018.

[12] K. Simonyan, A. Zisserman, "Very deep convolutional networks for large-scale image recognition", in International Conference on Learning Representations, 2014.

Jaco du Toit received his B.A. in Language Technology in 2017 and his B.Sc. Hons. In Computer Science in 2018 from the North-West University, Potchefstroom Campus. He is presently studying towards his Master of Science degree at the same institution in the field of Artificial Intelligence.

A Sustainable Mobile Money Prototype for Rural Communities

Nobert Jere*, Kehinde Aruleba†
*†*Walter Sisulu University*
*njere@wsu.ac.za
†arulebak@gmail.com

***Abstract*—Rural dwellers face challenges in collecting money due to the lack of banking services in their communities. In many countries, Mobile Money applications have been developed to enhance financial transactions. The mobile money concept allows people to transact money digitally without having a formal bank account. COVID-19 pandemic has worsened the situation with regulations such as social distance, limitations on people's movement and the importance of avoiding gatherings. This paper proposes a Mobile Money application for rural people. This secure application allows users to send money either through cash, EFT or card and also allows them to redeem vouchers at local shops. A community in the Eastern Cape Province of South Africa was engaged. Participants were engaged through online participatory design. Results show that over 90% of subjects are interested in using mobile money systems to improve their living standards. Participants would prefer a simple and easy-to -use mobile application that is very reliable. A mobile money prototype was designed and tested within the same community. Evidently, mobile money has the potential to address travelling and financial access challenges facing rural communities of South Africa. Government departments could use the proposed mobile money for payment of government grants and COVID-19 relief funds to minimise travelling and overcrowding in towns.**

***Index Terms*—Mobile money; Rural community; COVID-19**

I. Introduction

The unavailability of financial institutions in remote areas has had a tremendous impact on financial resources for rural dwellers. Several solutions have been proposed and introduced to enable access to finance for rural people; unfortunately, the gaps remain. The rise of mobile money as a business model and as a development tool has been propelled by the need for financial inclusion in remote communities by assisting them to access financial banking systems [1]. Although there are various definitions of mobile money, the widely accepted definition is 'electronic financial services executed using a mobile phone' [2], [3]. Unlike mobile banking that involves much formal documentation and interaction with banks, mobile money services encompass basic banking, transfers and payments [3]. It utilises basic cellular systems through Unstructured Supplementary Serves Data (USSD) and Short Message System (SMS), making mobile money accessible regardless of how simple a mobile phone is.

Mobile money has its history in Africa dated back to 2007 with M-Pesa, an initiative powered by Safaricom and Vodafone, Kenya. As of 2017, the M-Pesa model was a success, with 96% of the households in Kenya using the service [1]. Since then, other countries such as Uganda and Zimbabwe have introduced similar Mobile Money platforms in their cities and extended them to rural communities. The growth of mobile banking in Africa is further necessitated because over four in every five people do not have an account with a formal banking institution [4]. As a result, the use of mobile money expanded to other parts of Africa, where it has successfully improved financial inclusion. The paper introduces a mobile money application that allows small businesses to grow and provides easy access to basic services for rural communities without incurring too much costs of travelling to town. Most of the people in these communities are unemployed and live below the poverty line; a convenient and straightforward transaction system such as our proposed application is needed by these residents. The paper has been motivated by the current COVID-19 pandemic regulations, which mainly include minimising travelling and keeping social distances. We argue that if rural communities could be supported with efficient and reliable mobile financial services, there would be less travelling and congestion in nearby towns.

The structure of the paper is as follows: Section II discusses related work, and the methodology section is presented in Section III. Finally, Section IV shows the paper's conclusions.

II. Related Work

The recent COVID-19 pandemic, which has resulted in a large-scale shutdown worldwide with governments calling for social distancing to reduce transmissions of the coronavirus, has also impacted the mobile money industry. Physical financial transactions such as handing out cash were highly discouraged, which created an opportunity for the digital money market [5]. As a result, 2020 saw a growth in the number of mobile money subscribers by 12.7%. Besides, changes in consumer behaviour during 2020 influenced growth in account activity, with over 300 million active accounts monthly [4]. While the global increase in the number of users is apparent, 13% of subscribers who registered during the pandemic cited that they did so due to the pandemic itself [6]. The first deployment of mobile money was pioneered in the Philippines through Smart Money in 2001. It was a collaborative effort of Smart Communications, a telecommunications company and a bank, Banco de Oro. Smart money was established to bridge the gap created by the restricted reach of banks. Mobile money depends on a cash-in, cash-out system. Central to this system are merchants or agents who are designated to accept cash, which is then deposited into a wallet (cash-in) or allows the

wallet holder to convert the electronic value into cash (cash-out) [2].

The Financial Access Initiative of 2009 revealed that more than 2.5 billion individuals, translating to more than half of the world's population, have no subscription to a formal banking system, with the most significant proportion (62%) being the residents of Asia, Africa, Latin America and the Middle East [7]. Therefore, financial inclusion challenges mostly affect developing regions. Of the 1.2 billion individuals who have access to banking services, two in every three people live below USD5 per day [7]. Financial inclusion in poor communities is exacerbated by factors such as the cost of opening a formal bank account, long distances to banks from remote areas and lack of documentation that is required to open a bank account [3].

Most rural areas in developing countries are far from ATMs or banks, which are mostly places in urban areas where human traffic is high. Most banks require an identity document, proof of residence, or employment letter [8]. Many adults in marginalised communities do not have these documents, thereby disqualifying them from having accounts with formal banking institutions. Without mobile money platforms, remote communities rely on saving their money as cash or buy assets such as livestock which they can sell when they have an immediate need for money. The challenge of keeping money in these forms is that they are susceptible to losses through theft. Also, there are chances of mortality in livestock. Again, when there is an immediate need for money, it may be difficult to quickly sell large biological assets such as cattle. Hence, lack of access to money will increase vulnerability because of the absence of an emergency buffer. Usually, banking fees are high for low-income households. The operation costs of banks have limited their establishment in remote areas. High transaction costs and minimum balances accompany accessibility challenges of banks to communities in rural areas. Thus, formal banking proves to be unaffordable to people living below the poverty datum line.

Mobile money has addressed most of these drawbacks encountered by residents of these rural communities. For example, since the introduction of mobile money in Zimbabwe in 2009, the industry has seen significant growth in terms of subscriptions and the number of services mobile money offer. Mobile Money has since grown from offering the primary person-to-person (P2P) transactions and cash-in, cash-out services to providing bill payments, buying airtime, disburse and receiving salaries, cross-national remittances, payment of taxes and bank-mobile money transfers [4], [9].

The mobile money industry in Zimbabwe was introduced because it was believed that most people who resided in rural areas had no formal bank accounts [10]. The industry is operated by three mobile money giants namely Econet Wireless, Telecel and Netone. Ecocash, operated by Econet wireless, was launched in 2011, OneMoney by Netone, established in 2011 and Telecash by Telecel, launched in 2014. As of 2016, Ecocash had the highest number of active accounts (97.5%), followed by OneWallet (2%) and then Telecash with 0.2% [11]. The mobile money industry is sustained by existing mobile phones infrastructure. As such, 6720 cellphone towers have been erected in the whole of Zimbabwe, and almost 30% are positioned in rural areas [11]. As of 2019, ten years into Zimbabwe, the proportion of adults with mobile money accounts (77%) surpassed that of those who hold formal bank accounts (43%), showing invasive growth.

Apart from consumer behaviour naturally shifting towards mobile money use, policymakers and mobile money operators worked together to create a conducive environment for the utilisation of mobile money to reduce physical transactions. For example, in Uganda, mobile money operators reduced fees for payments made through merchants, cancelled fees, either partially or fully, for P2P transactions and extended transaction limits [4]. Although there is a reported increase in the use of mobile money services, there is a significant interruption reported during the beginning of the pandemic. Most governments imposed a complete shutdown of day-to-day economic activities, except for essential services. In so doing, some businesses that acted in the capacity of merchants were liquidated, thereby reducing the number of merchants available [6]. Those whose businesses remained open after the complete shutdown faced a shortage of float [12]. These negative interactions brought about disruptions of mobile money services.

III. Methodology

A qualitative approach using the participatory design technique was adopted. Participants living 20 or more kilometres out of East London Central Business District (CBD) were considered. These were classified as either community members, spaza shop owners or community leaders. Due to COVID-19, only two trips to the communities were made to engage the participants, especially the app's testing physically. However, most engagements were done online and five sessions were held online with each group of participants. Then, an online questionnaire was distributed after the sessions for the participants to complete individually. In the study, participation was voluntary, and internet through data bundles was provided.

This section also introduces the proposed cross-platform system for mobile money transfer. With that in mind, the system supports multiple devices, from desktops to mobile devices. Figure 1 shows the architecture of the proposed system. The architecture is in three components, i.e., the user, the system itself and the bank. All the components are dependent on each other to function properly. Figure 2 presents the high-level use case of the mobile money system.

A. Survey

To understand if mobile money systems were needed and beneficial to the rural communities, we conducted a survey in various communities within the Buffalo City Metropolitan Municipality (BCMM) between November 2020 to February 2021. The survey focuses on how residents make use of services provided by small businesses in their area. In the study, community members and Spaza shop owners were the subjects. Spaza shops that were part of this study operate seven days a week, and their operating hours range from 12

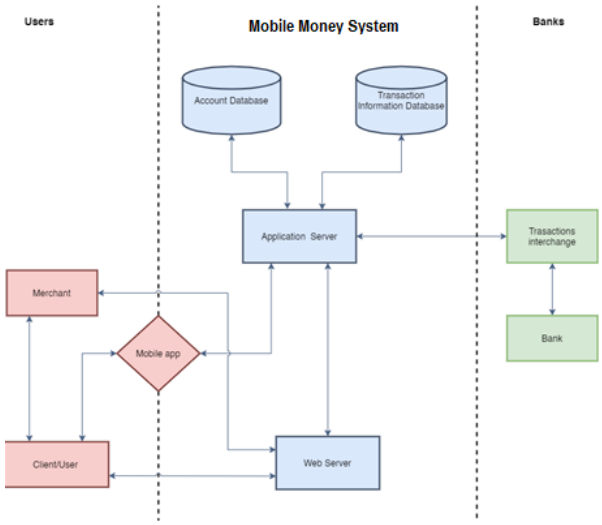

Fig. 1. System Architecture

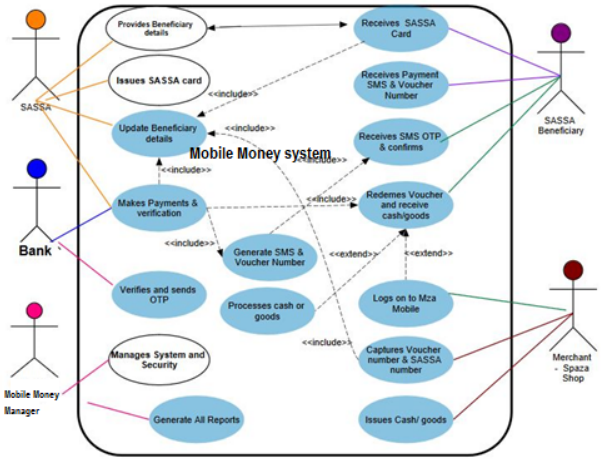

Fig. 2. Mobile money use-case

to 15 hours daily. Results gathered showed that all the Spaza shops do not offer any cash withdrawal facilities and do not sell prepaid electricity. Also, over 97% of Spaza shops sell prepaid airtime and data to a majority of their customers. Customers buying in these Spaza shops range from an average of 20 customers per day, with one Spaza citing an approximate figure of 40 customers daily. The high number of customer interactions demonstrates the opportunity for Spaza shops to expand and automate their processes to provide convenience to customers.

Through an application such as mobile money, residents would have all the convenient essential services within reach. Over 90% of Spaza shop owners showed a sincere interest in subscribing to the proposed mobile money platform; 100% of responses cited 'Yes' when asked if they would be merchants. Spaza shops would be better positioned to conveniently offer community members transactions such as sending and receiving money, buying prepaid airtime, data, electricity, groceries, and other prepaid items through this system. Figure 3 illustrates the key activities we propose for spaza shops.

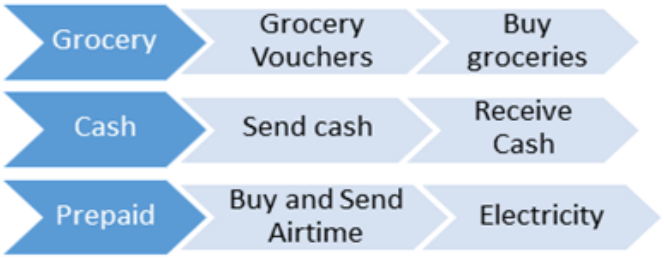

Fig. 3. Spaza shops key components

A few community members were also approached to be part of the study to probe and understand some of the daily activities and challenges people encounter regarding access to basic services and buying everyday household items. A majority of approached members of the community are unemployed individuals who depend on SASSA social grant and pensioners grant; 100% of individuals who participated in this study highlighted that they go to town, in East London at least once a week, and some, unfortunately, spend roughly R30 to R60 in travelling costs. The most commonly mentioned reason for travelling to town is to withdraw cash, i.e., to have access to money. The findings from the survey show a need for better and convenient services by Spaza shops for residents within townships. Most of the respondents stated that they deem this platform a beneficial application, and they are willing to be subscribers.

B. Technologies

The mobile money platform was built as two docker images, i.e., the front-end and back-end, developed on Google Cloud Platform. Ionic and Angular frameworks were used alongside Nginx, a web server used for reverse proxy for the front-end development. We used angular material components for constructing consistent, attractive, and functional UIs. Also, docker, a platform that uses OS-level virtualisation, was used to deliver the system in packages. For the back-end, Scala and Cassandra, an open-source NoSQL database management system were used. Lagom framework was also used alongside Twilio, an API to send and receive SMS, MMS, and OTT messages. The feedback and comments from the participants were considered for the design and development of the prototype. What came out strongly were issues around its simplicity, security and ease to use.

C. User Interface

We developed our UI as text-free because of the accessibility barrier posed by most computer applications to those who can not read fluently as most residents in these communities. Text-free UIs are simple to understand and contain little or no text and graphics for visual information. This will allow more illiterate and semiliterate residents to subscribe to the platform. Below are some of the selected UI of the developed

TABLE I
KEY ASSUMPTIONS

	Main Actors
1	The sender The merchant - Spaza shop, and service station The recipient/ beneficiaries The marketer – The sender, merchant, and marketer must be registered and have a bank account – The merchant gets R1 per transaction – The marketer gets 10% of the R8 on each transaction by a referral – When the sender does the transaction – a voucher number is generated
2	Key stakeholders SASSA, Bank, Merchant and beneficiaries understand mobile payment and want to use the mobile money app
3	Recipients/Beneficiaries have a mobile number and a mobile phone – even the basic phone
4	Senders have mobile money app installed
5	The bank will be willing to modify the message sent to the beneficiaries to include the voucher number
6	The bank already has the list and updated payment details from SASSA
7	The merchant, i.e. Spaza shop has a working mobile money app on the tablet
8	The merchant, i.e. Spaza shop already has a bank account with the bank making SASSA payments
9	The merchant, i.e. Spaza shop has stock enough to cater for the common grocery needed by the beneficiaries

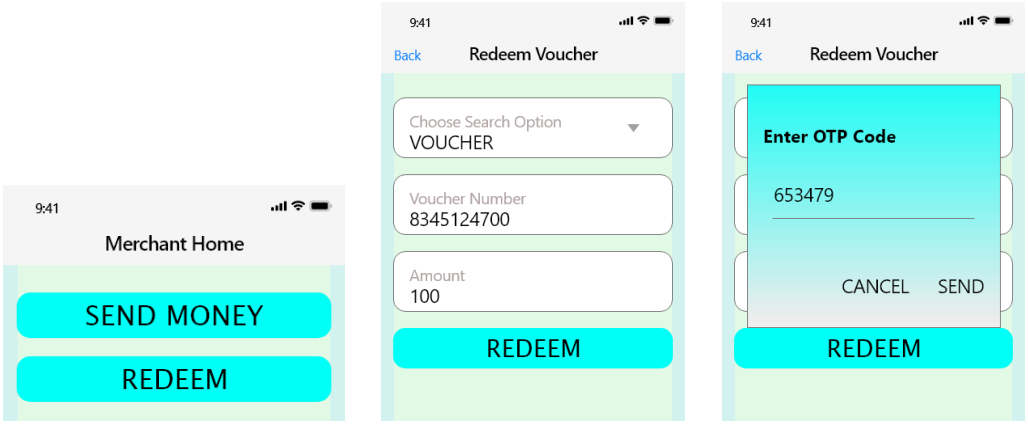

(a) Transaction page (b) Transaction page (c) Transaction page

Fig. 4. Mobile money voucher transaction user interface

system. Table I shows the key assumptions that were made during the development of the mobile money prototype.

Users can redeem vouchers through the system, as presented in Figure 4(a). We have incorporated a security system that allows users to get an OTP before proceeding with their transactions, as shown in Figure 4(c). From Figure 5(a), the user is presented with an interface to select the customer type. We identified three types of users or customers: business, individual and beneficiary as shown in Figure 5(b). Once a user has identified the type of customer they are, they can then register on the system and login using their mobile number as their username, as shown in Figures 5(e) & 5(c), respectively. Figures 5(a), 5(f) - 5(h) illustrate the process of sending money. Money senders have the privilege to do any of these: send cash, make an EFT payment or use their Debit/Credit card, see Figure 5(g).

After the development of the mobile money prototype, participants were engaged. All the participants indicated that the prototype was straightforward. They were pleased with the SMS which was received during the demonstrations.

D. Testing

The mobile money system was tested on multiple devices. We engaged potential users who were mainly accessible to the technical team as we were complying with COVID-19 regulations. Mobile money applied and complied with the COVID-19 procedures during the testing of the App process, mainly on the Tablets. Also, we engaged other participants online and presented the mobile money application for the participants' input, mainly related to testing. Feedback from the participants was captured and considered for the improvement of the app. The presented version of the mobile money app has accommodated users comments and feedback. The prototype testing focused on requirements such as App functionality, App Usability, App User Interface, Cross-Platform Compatibility and App Integration. The feedback from the participants was mainly that the app is simple to use and follow and serves the purpose.

1) Functionality Testing: The test was geared towards designated and non-designated tasks for the mobile money app. The tests looked at different operating conditions, func-

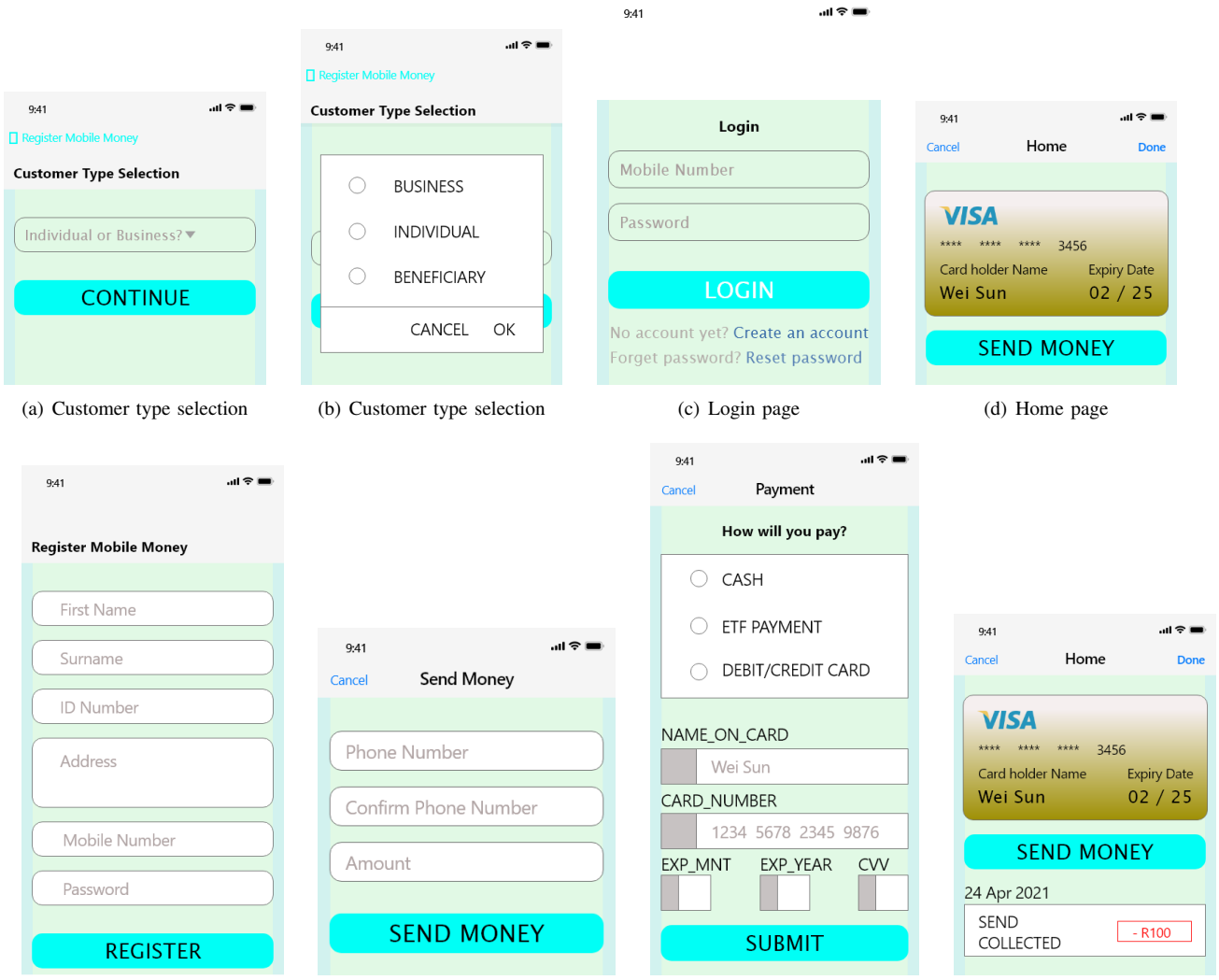

(a) Customer type selection (b) Customer type selection (c) Login page (d) Home page

(e) User registration page (f) Transaction page (g) Transaction page (h) Transaction page

Fig. 5. Mobile money user interface

tional options and the consistency of the mobile money app. Besides, the tests carried covered adequate prevention from the performing of undesired actions.

2) Performance Testing: The test covered key performance issues for the mobile money app. The tests looked at the time to launch, mobile money app performance of peak load conditions and continual user input entry, integration of the mobile money app with other apps on the test device, display of error messages and app performance with network variability.

3) Security Testing : This test covered user security and privacy of user data. The tests also covered the security of network protocols in use and breach in security, error reporting, and automatic application lockout upon continuously entering invalid credentials.

4) Usability Testing: The usability test was to ensure the client's comfort in the Mobile Money app. The test covered aspects of the app responsiveness, visual feedback for user actions and easy navigation across different screens.

IV. Conclusion

This paper presents a mobile money application that allows people to send money and redeem vouchers. Through an extensive survey involving all stakeholders and about 48 hours of interaction with rural communities, we discovered several issues around financial transactions that were incorporated into the work that we believe could apply to other rural communities in developing nations. Some of these issues were highlighted in Section II. Our survey results also showed that most residents in these areas seriously need mobile money systems. The proposed prototype provides opportunities for small-scale businesses where people can register as merchants and perform transactions. Merchants receive a commission for each transaction they facilitate. These will reduce the unemployment rate. According to Nakouwo and Akplehey [12], mobile money systems have created about 90% of jobs across sub-Saharan Africa for small businesses. Also, governments and humanitarian organisations can now reach vulnerable groups in remote areas through our system. Social or relief grants and humanitarian cash transfer schemes can now be

distributed to targeted people through the system. In the future, we plan to improve the system usability by adding local languages voice assistants and conducting a user study of the system.

V. Acknowledgement

We would like to thank the engaged researchers and the entrepreneur who initiated the idea. We appreciate the feedback and comments from the engaged community that helped with the design and development.

References

[1] S. C. Rea and T. C. Nelms, "Mobile money: the first decade," *Institute for Money, Technology and Financial Inclusion Working Paper*, vol. 1, 2017.

[2] K. Donovan, "Mobile money for financial inclusion," *Information and Communications for development*, vol. 61, no. 1, pp. 61–73, 2012.

[3] M. Subia and N. Martinez, "Mobile money services: A bank in your pocketoverview and opportunities," *ACP Observatory on Migration, Brussels*, 2014.

[4] S. K. Andersson-Manjang and N. Naghavi, "State of the industry report on mobile money 2021," 2021, accessed: 25 May 2021. [Online]. Available: https://www.gsma.com/mobilefordevelopment/wp-content/uploads/2021/03/GSMA_State-of-the-Industry-Report-on-Mobile-Money-2021_Full-report.pdf

[5] N. V. Loayza and S. Pennings, "Macroeconomic policy in the time of covid-19: A primer for developing countries," 2020.

[6] GSMA, "Assessing mobile money consumer trends in the wake of the covid-19 pandemic," 2021, accessed: 16 June 2021. [Online]. Available: https://www.gsma.com/mobilefordevelopment/wp-content/uploads/2021/03/GSMA_Assessing-mobile-money-consumer-trends-in-the-wake-of-the-COVID-19-pandemic-2.pdf.

[7] A. Chaia, A. Dalal, T. Goland, M. J. Gonzalez, J. Morduch, and R. Schiff, "Half the world is unbanked: Financial access initiative framing note," *McKinsey & Company*, 2009.

[8] E. Flores-Roux and J. Mariscal, *The development of mobile money systems*. Centro de Investigación y Docencia Económicas, División de Administración , 2011.

[9] M. Lwanga Mayanja and A. Adong, "A pathway to financial inclusion: mobile money and individual savings in uganda," Tech. Rep., 2016.

[10] G. Munyoro and M. Matinde, "The significance of plastic money to the hospitality industry: A case study of rainbow towers group of hotels (rtg): Research journalis journal of economics," 2016.

[11] M. Willis, "Can e-transfers promote financial inclusion in emergencies: A case study from zimbabwe," 2016, accessed: 14 June 2021. [Online]. Available: https://www.mercycorps.org/sites/default/files/202001/ETransfersFinInclusionCaseStudyZimbabwe2017.pdf.

[12] S. N. Nakouwo and F. N. Akplehey, "Covid-19 and mobile money agents in ghana," *African Journal of Emerging Issues*, vol. 2, no. 12, pp. 75–85, 2020.

Smart Health Systems' Design Guidelines: The Case of An Information Sharing and Diagnostic Assistance System To Support Healthcare Practitioners During Virtual Encounters

Themba Makubalo[1], Brenda Scholtz[2], Temitope Tokosi[3]

Computing Sciences & Information Systems Department, Nelson Mandela University, University Way, Summerstrand, Gqeberha, 6001

[1]s216682886@mandela.ac.za

[2]brenda.scholtz@mandela.ac.za

[3]toksymoore@gmail.com

Abstract— **The integration of personal health record (PHR) systems, which manage a patient's entire health history with smart health, provides better assistance to practitioners in making diagnostic-related decisions about a patient's healthcare. This integration will encourage patients to be more involved in the diagnostic process, and more accurate results will be provided. Unfortunately, currently, PHR and smart health systems exist as separate entities, and are not used in virtual encounter contexts. This paper provides a set of guidelines for the design of a smart health system that provides diagnostic assistance for practitioners during virtual encounters. A qualitative literature review covering the requirements and design of personal health records, smart health and clinical decision support systems, was performed, analysing the studies through the lens of Meaningful Use. The findings revealed five important characteristics for allowing PHR and smart health systems to integrate with each other. These are: Communication; Customisability; Portability; Automated Data Collection, Information Transformation and Health Information. Each characteristic has related guidelines. An extant systems analysis of four systems was conducted using the recommended guidelines to identify the strengths and weaknesses thereof. This analysis successfully served as an exploratory study into the applicability of these guidelines.**

Keywords— **Personal Health Records, Smart Health, Clinical Decision Support Systems, Virtual Encounters**

I. INTRODUCTION

Many nations consider the provision of access to quality healthcare for their citizens to be a basic human right. However, it is still one of the major challenges that each nation faces [1], [2]. The growth of the global population has led to an increased demand for healthcare; however, the number of healthcare practitioners has not risen to accommodate the demand [3]–[5]. South Africa's healthcare system has been governed in a chaotic and fragmented fashion, with resources being managed inadequately [1]. Fragmentation has led to healthcare bodies directing most of their resources towards tertiary healthcare. This has left South Africa's healthcare system being inequitable, expensive and inefficient to those who need it [2], [6]. These problems have necessitated the need for patients to receive efficacious solutions to health and wellness monitoring [7].

African research into access to healthcare has primarily focused on distance-based models, as researchers understand that it is a key factor in healthcare access [6]. Virtual encounters have been researched as a solution to the healthcare access problem. Virtual encounters provide remote healthcare through audio-visual technology, allowing clinical encounters to occur across great distances [8]. They can take the form of various systems such as live interactive video, transferral of health information and consultation, diagnostic assistance and treatment recommendation [9]. Unfortunately, virtual encounters lack the affordances that are available during face-to-face clinical encounters, and are therefore not truly effective [8], [10]. Firstly, a practitioner lacks access to a patient's medical history. Secondly, a practitioner would be unable to perform hands-on examinations on a patient to assist in making diagnoses and recommending treatments [11], resulting in reduced confidence in the reliability of the healthcare being delivered.

A preliminary review of literature in the field of virtual encounters revealed a gap in research related to the design of systems that can integrate Personal Health Records (PHRs), smart health and Clinical Decision Support Systems (CDSSs). This paper addresses this gap and proposes guidelines for designing smart health systems that can support and assist practitioners in making a diagnosis during, or after, a virtual encounter.

The paper is structured as follows: Section II describes the theory and concepts of Meaningful Use, and how it is used to qualitatively review the literature. Section III identifies and discusses design characteristics and guidelines for PHR systems. Section IV discusses smart health and CDSSs. Section V provides a qualitative extant system review on smart health systems using the proposed characteristics and guidelines and evaluates each characteristic by importance for the design of a diagnostic support system for virtual encounters. Section VI concludes this paper and highlights some recommendations and shortcomings.

II. METHODS

Meaningful Use is a concept that was originally presented by the Medicare and Medicaid Electronic Health Record Incentive Program of the United States of America [12]. The goal of Meaningful Use is to make improvements in healthcare by achieving certain criteria through e-health systems. The organisation established the five pillars of health outcomes priorities for Meaningful Use [13]: 1) Improve quality, safety, efficiency, and reducing health disparities; 2) Engage patients and families in their health; 3) Improve care coordination. 4) Improve population and public health; 5) Ensure adequate privacy and security protection for personal health information.

To satisfy all five pillars, it is believed that the use of e-health systems by all health professions is required, to progress through a series of stages from data capture and sharing to the use of e-health systems to advance clinical processes and improve patient outcomes [12]. These stages are defined by subdividing the pillars into three Stages [12], [14]. The Stage 1 criteria highlight the importance of health information, focusing on health information being recorded in a standardised manner, and being communicated to coordinate patient care. For example, reporting on and tracking of information about key clinical conditions, clinical quality and public health, and using this information to help patients/families with health care. Stage 2 criteria focus on health information exchange, including the increase in requirements concerning e-prescribing and reporting of laboratory results. The work done in Stage 2 includes the transmission of electronic patient care summaries across settings, and the provision of opportunities for patients to control more of their data. Stage 3 criteria address the need for improved safety, quality, and efficiency. In this stage, CDSS tools for practitioners, patient self-management tools, comprehensive health information exchange and public health are essential to Stage 3 work. Meaningful Use is projected to accomplish restructure the way healthcare is conducted, by redesigning healthcare processes using e-health as a vehicle [13]. The Meaningful Use of e-health by patients could lead to improved health outcomes. Proper patient involvement is considered an important component towards ensuring that the use of e-health systems is of profound importance to patients for personal health management [12], [15].

III. Design of Personal Health Record (PHR) Systems

The limitations of traditional healthcare processes, new developments in healthcare practice and the ever-growing requirements for amenable access to health information, have resulted in a persistent demand on e-health systems everywhere, specifically PHR systems [16]–[18]. PHR systems use secure information systems that allow patients to store and retrieve their health information and ensure that the information contained is up-to-date and available whenever required [18]. PHR systems intend to provide systematic digitisation and restructuring of medical information to enhance provider services and patient care. The restructuring of medical information produces a more efficient medical workflow, as well as standardising information dissemination and data exchange into clinically relevant protocols and practices [17].

[19] reported that the most likely individual to keep their records up to date would be those that are highly motivated. In addition, it would be unlikely for a PHR that depends only on patient input to be a reliable medium for exchanging health information during patient-practitioner interactions. Many consumers have become interested in personal health management, which has resulted in a multitude of questions being asked about the meaningful ways in which health consumers should be using PHR systems [12].

Discovery Health, a South African medical aid organisation, has developed Discovery HealthID, a mobile electronic health record system that allows doctors to access patients' health information [20]. The goal of the system is to reduce the chances of serious medical errors occurring and performing duplicate or unnecessary pathology tests. The functionalities the system provides to practitioners are access to the patient's personal details and previous medical records, prescribing medication, practitioner referrals and the completion of discharge forms. Discovery HealthID requires practitioners to attain the consent of the patient to access these functionalities. However, patients do not have any access to their own medical records, nor do they have the option of selecting which pieces of health-related information their practitioner should have access to. Information access is entirely decided by Discovery Health. The lack of patient access and control in the management of their health history results in patients being passive and disengaged participants in their own healthcare [12], [21]. This may undermine the communication and collaborative spirit that is at the heart of Meaningful Use.

[16] conducted a study that analysed the basic requirements for a customisable and extendable PHR system. The authors identified that the two significant characteristics of such systems are the software and platform. Their first recommendation was that PHRs should be facilitated by Open-Source Software (OSS). The concept of OSS intends to do away with all restrictions of proprietary software, such as distribution limitations, instead, allowing for software to be modified according to the needs and requirements of the developers and users [22]. OSS solutions usually bring about better quality and technical support, simply due to having a worldwide involved community. Solutions that come about due to the application of OSS in the field of e-health often guarantee full access to the source code, a reduction in business-related risks, and a free license to copy, distribute and change the software according to healthcare environment needs [16]. The second recommendation made is the use of a web-based PHR system, which allow for use and interoperability flexibility. Web-based solutions allow users to access data anywhere, anytime, provided they have an internet connection and a browser. This enhances accessibility and eliminates the need for downloading and installing software. [23] notes that it is unacceptable for a PHR to be unavailable at any time as it defeats the purpose of being lifelong and may put a patient's health at risk. The ability to access health information that is more accessible and portable allows for PHR' systems to be easily integrated with mobile communication devices, thus, accessing a PHR can also be done through a smartphone or a tablet PC [16], [18]. The new emerging area of mobile health (m-health) further supports this requirement [24].

The application of PHR in this way potentially allows for the transformation, quality enhancement, accessibility, and delivery of healthcare. The findings of the literature review revealed five main characteristics of a PHR system that should be included in their design. These are Communication; Customisability; Portability; Automated Data Collection and Information Transformation (ADCIT) and Health Knowledge. To verify these characteristics and guidelines, they were viewed and analysed according to the pillars and stages of Meaningful Use. This analysis is summarised in Table I.

The guidelines for each characteristic are described as follows:

- **Communication**: **Guideline 1 -** Collaborative decision making between patient and practitioner should be achieved by utilising different forms of communication.

- **Customisability: Guideline 2** By using best practice standards and ensuring proper documentation during the development of the system, it should still be possible to add on new features in later versions of the system or allow other systems to connect and communicate with it. This should be achieved relatively simply, without compromising the confidentiality of the sensitive information stored on the system.
- **Portability**: **Guideline 3 -** Patients and practitioners should be able to access a PHR at any time or location. This is best realised by incorporating mobile computing in conjunction with the internet and cloud computing in the design and creation of a PHR system.
- **Automated Data Collection and Information Transformation (ADCIT): Guideline 4 -** Patients should not have to manually input health data into the system unnecessarily, as they may make mistakes, or may not be health literate. Therefore, wherever possible, the system must be able to collect data automatically by being able to communicate with other systems. In addition, the system should also be able to transform the data into useful information that can be understood by both the patient and practitioner.
- **Health Knowledge**: **Guideline 5** - Patients can gain greater access to general health information and, in turn, enrich their health awareness and wellbeing if their PHR receives regular guidelines and health activities from a reliable source such as their practitioner, a web portal hosted by the government or a local health clinic.

TABLE I: CHARACTERISTICS OF PHR SYSTEMS

Characteristic	Meaningful Use Pillar	Meaningful Use Stage
Communication	1, 2, 3	1
Customisability	1, 2, 3, 5	1, 2, 3
Portability	1, 2, 3, 4	1, 2
Automated Data Collection and Information Transformation (ADCIT)	1, 2, 3	1, 2, 3
Health Knowledge	1, 2, 3, 4	1, 2

IV. DESIGN OF SMART TECHNOLOGIES AND CLINICAL DECISION SUPPORT SYSTEMS

Despite PHR systems being of great assistance in solving common problems faced by patients and practitioners during clinical encounters, several issues persist within healthcare that they cannot solve on their own. The healthcare industry has taken advantage of smart systems to increase the speed of health diagnostics and treatment. Smart Systems make use of sensing, actuation, and control to analyse a particular set of circumstances, and to make predictive or adaptive decisions based on available information [25], [26]. These systems have provided innovative services for patient health monitoring and medical automation in different situations and environments (such as hospitals, offices, homes). This has resulted in a considerable decline in practitioner visit costs, and an overall improvement of patient care quality [27]. Reduction in practitioner visits is achieved by utilising networked sensors that simultaneously collect multiple physiological signals and wireless connectivity to share the collected signals directly to a cloud server, where diagnostic algorithms can be performed. From this cloud server, practitioners can conduct further analysis and clinical review. Furthermore, the Internet-of-Things (IoT) enabled remote monitoring applications, and can significantly reduce travel, cost and time in long-term monitoring applications [27]–[29]. Wearable sensors allow patients to pursue time-efficient and economical treatment and recovery options, as opposed to traditional healthcare processes. They can collect physiological signals over protracted periods of time, which is impractical during traditional clinical encounters. Thus, wearable sensors are of great benefit to people living in remote and rural areas who have limited access to medical services. As a result of an ageing population, several healthcare and social challenges could be addressed by wearable sensors, and act as a catalyst in the current transition to personalised digital medicine. Virtual encounters and digital technologies may serve as a source of support for enhancing the efficacy of healthcare services and may join the larger body of potential solutions to existing healthcare challenges. These challenges include a rapidly ageing population; limited access to primary healthcare, beds in hospitals, nursing homes, specialists, and other healthcare services; or unexpected circumstances [30].

Smart health can be used in conjunction with CDSS to counteract specific clinical challenges and improve patient care [31], [32]. Challenges and improvement may include efficiency, cost-effectiveness, or guideline-concordance [32]. A strong underlying foundation results in a well-functioning CDSS. Therefore, an appreciation of how to frame decision-making, regardless of the CDSS tools being used, is a useful starting foundation. The following principles of decision-making have been proposed [33]: 1) a distinction between rational-analytic vs. naturalistic-intuitive decision-making styles; 2) the utility of a flexible, adaptive, robust, approach that considers multiple criteria and possibilities (often reflected as alternative scenarios); 3) and the notion of appropriate levels of trust in recommendations.

[34], [35] believe that clinical decision support delivered through IS in conjunction with some form of PHR system as the platform, will finally provide decision-makers with tools, making it possible to achieve large gains in performance, narrow gaps between knowledge and practice, and improve safety. Early reviews by [32], [36] suggested that performance improvements can be made by CDSSs, however, this has not always been the case. [34], [36] have summarised the evidence that CDSSs works, based partially on the evidence domain. The key in CDSS design is to offer sufficient evidence that provides decision-makers with a comprehensive view that does not overburden them with too much information [33]. Additionally, the possibilities that a CDSS offers to the decision-maker must be viewed with a suitable level of responsibility – such as the system is performing as it should be or, whether it has the appropriate content and configuration to provide applicable recommendations for the given circumstances, or not [31], [33]–[35].

V. EXTANT SYSTEM REVIEW

A qualitative extant system review of the functionality of four smart health systems was conducted using the characteristics and guidelines proposed in Table I. A summary of the findings for the systems reviewed is provided in Table

II, Table III and Table IV. The first of these systems [37] was a real-time electrocardiogram (ECG) monitoring, analysis and diagnostic system, which used Bluetooth and Zigbee networks, as these wireless sensor standards were the most optimistic. Bluetooth and Zigbee provide advantages in that they have a relatively low-energy consumption rate, a low data rate and had a limited amount of delay. The major flaw with their system is the requirement of a desktop PC, which prevents the system from being portable (Guideline 3). The second system reviewed [38] was an alternative system that uses mobile phones instead of PCs, thus solving the portability problem.

Despite this, both systems have other flaws that limit their Meaningful Use. The first flaw is that they have bulky graphical user interfaces (GUIs) with an unequal distribution of different pieces of information being displayed to the user. This leaves the user confused and having to closely examine what is being displayed to fully understand the information. This limits the amount of Health Knowledge that is received by patients (Guideline 5). The second flaw is that the data is not aggregated over time, resulting in an inability to transform the data into useful information. This results in an ineffective CDSS, as practitioners are not given a comprehensive view of the patient's health overall health status that would help guide them towards making the correct diagnosis (Guideline 4). Finally, there is no mention of the systems' customisability, making it unknown if either system would be able to integrate well with other smart health or PHR systems (Guideline 2). A lack of customisability prevents the system from accessing data from other sources, thereby increasing the amount of health information that can be provided to users and limits the extent to which the system could be used.

[39] proposed a system that used dedicated smart health sensors with Bluemix and Raspberry Pi to monitor a patient's vital signs, such as pulse and body temperature. Remote health monitoring was attained by storing the collected data on a Bluemix cloud where it could be later retrieved by a practitioner for analysis, thus allowing for anomalies to be detected more easily. The system has a few shortcomings. Firstly, the wires and connection points of the sensors and Raspberry Pi are exposed. Without the inclusion of protective covering, it is very easy for accidents that result in either damage to the system, or corrupt data being stored in the system to occur (Guideline 4). Secondly, there is a lack of clarity in the information that is displayed to the user, particularly the patient (Guideline 4 and 5). The information displayed to the user makes it unclear whether the vital signs are bad or good. Thus, practitioners would be wasting time attempting to decipher the meaning of the information, while patients would not understand the information resulting in a lack of Health Knowledge.

[29] proposed a Raspberry Pi and IoT health monitoring system that monitors and informs practitioners of the current health status of their patient, wherever the patient may be. The system utilises sensors that collect the patient's vital signs such as heart rate, blood pressure, and pulse rate. It also utilises a live camera feed to monitor the patient through a Raspberry Pi kit, which is used as a data aggregator as well as a processor. The information collected is then stored on a medical server from which both the patient and practitioner can access, as they both have access to the IP server address. The patient will receive an emergency alert whenever the sensor value exceeds a certain threshold. This system possesses potential security flaws as it is unclear if simply knowing the IP address is all that is required to gain access to the server. If so, this puts the patient at risk as it now becomes easy for third parties to access or manipulate the patient's sensitive health data (Guideline 4). The practitioner is not notified if the patient's vital signs are below the threshold. Thus, practitioners are not given complete information to assist them in making healthcare decisions. The information that is displayed to the user is not very clear as the vital signs lack the units for which they are being measured. Similarly, to the system in [39], this affects the time taken to decipher meaning for practitioners and the Health Knowledge gained by patients. Also, a customisable system would not be able to use the data contained in this system, as using data with unknown units does not provide any meaningful data (Guideline 2).

TABLE II: SHORTCOMINGS AND SOLUTIONS FOR SYSTEMS IN [37], [38]

Shortcoming	Solution	Characteristic	Meaningful Use Pillar
Bulky GUI and unequally information distribution.	Make effective use of the screen real-estate by using best practice user experience guidelines	Health Knowledge	1, 2, 4
Unaggregated data.	Implement algorithms that can take the collected data and transform it into useful information	ACIDT	1, 2, 3, 4
Non-customisable	Incorporate open-source principles into the design of the system	Customisability	1, 2, 3, 5

TABLE III: SHORTCOMING AND SOLUTIONS FOR SYSTEMS IN [39]

Shortcoming	Solution	Characteristic	Meaningful Use Pillar
Exposed wires and connection points	Use protective coverings	ACIDT	5
Unclear information display	Make effective use of the screen real-estate by using best practice user experience guidelines.	ACIDT, Health Knowledge	1, 2, 3, 4

TABLE IV: SHORTCOMINGS AND SOLUTIONS FOR SYSTEMS IN [29]

Shortcoming	Solution	Characteristic	Meaningful Use Pillar
Security and authentication	Ensure that the best security practices are always being used. Periodically check that the system is not vulnerable to attacks.	ACIDT	1, 5
Unnotified practitioner	Alert the practitioner in addition to the patient.	Communication	1, 3
Unclear units of measure	Specify all units of measure and indicate how close or far off the patient is from the threshold.	Health Knowledge, Customisability	1, 3, 4, 5

VI. CONCLUSIONS

In this paper, literature on PHR systems, smart health systems and CDSS were reviewed utilising the concept of Meaningful Use to derive a set of characteristics and guidelines for designing a diagnostic assistance tool to assist practitioners during virtual encounters. The five characteristics (Communication; Customisability; Portability; ADCIT and Health Knowledge) were identified as characteristics that should be included in the design of such systems, so that they fulfil the five pillars of Meaningful Use. These guidelines are a contribution to designers of such systems and will promote patient health monitoring and better coordination of primary healthcare. As a result, practitioners can be more effectively supported by information sharing and diagnostic assistance. In addition, these guidelines can be used by systems analysts to evaluate the strengths and weaknesses of existing systems and determine where improvements are required. Researchers can use the guidelines as a foundation for other research aimed at improving the design of other e-health systems, such as those found in m-health. The shortcomings of the paper are that it was an exploratory study only. It is recommended that future research be conducted by implementing the guidelines in the development of a system and then evaluating it to determine if it can overcome the affordances lacking in virtual encounters. A second limitation is that only a handful of systems were evaluated. Future research should investigate a wider range of health devices and systems that could be incorporated into virtual encounters.

ACKNOWLEDGMENT

The authors would like to thank Nelson Mandela University, particularly the Department of Computing Sciences, for providing the opportunity to pursue this research study, as well as the Telkom Centre of Excellence for helping fund the study.

REFERENCES

[1] S. Katuu, "Transforming South Africa's health sector," *J. Sci. Technol. Policy Manag.*, vol. 7, no. 3, pp. 330–345, Oct. 2016, doi: 10.1108/JSTPM-02-2016-0001.

[2] S. Katuu, "Healthcare systems: typologies, framework models, and South Africa's health sector," *Int. J. Heal. Gov.*, vol. 23, no. 2, pp. 134–148, Jun. 2018, doi: 10.1108/IJHG-10-2017-0054.

[3] E. AbuKhousa, N. Mohamed, and J. Al-Jaroodi, "e-Health Cloud: Opportunities and Challenges," *Futur. Internet*, vol. 4, no. 3, pp. 621–645, Jul. 2012, doi: 10.3390/fi4030621.

[4] A. Amadi-Obi, P. Gilligan, N. Owens, and C. O'Donnell, "Telemedicine in pre-hospital care: a review of telemedicine applications in the pre-hospital environment," *International Journal of Emergency Medicine*, vol. 7, no. 1. Springer-Verlag London Ltd, 05-Jul-2014, doi: 10.1186/s12245-014-0029-0.

[5] S. B. Baker, W. Xiang, and I. Atkinson, "Internet of Things for Smart Healthcare: Technologies, Challenges, and Opportunities," *IEEE Access*, vol. 5, no. January 2018, pp. 26521–26544, 2017, doi: 10.1109/ACCESS.2017.2775180.

[6] A. H. Neely and A. Ponshunmugam, "A qualitative approach to examining health care access in rural South Africa," *Soc. Sci. Med.*, vol. 230, no. April 2018, pp. 214–221, 2019, doi: 10.1016/j.socscimed.2019.04.025.

[7] X. Ma, Z. Wang, S. Zhou, H. Wen, and Y. Zhang, "Intelligent Healthcare Systems Assisted by Data Analytics and Mobile Computing," *Wirel. Commun. Mob. Comput.*, vol. 2018, pp. 1–16, Jul. 2018, doi: 10.1155/2018/3928080.

[8] J. M. Khan, "Virtual Visits — Confronting the Challenges of Telemedicine," *N. Engl. J. Med.*, vol. 372, no. 18, pp. 1684–1685, 2015, doi: 10.1056/NEJMp1502419.

[9] X. Fang *et al.*, "Clinicians' perspectives about the feasibility and effectiveness of using telemedicine in first aid: A qualitative study," *Int. J. Gen. Med.*, vol. 14, pp. 3343–3353, 2021, doi: 10.2147/IJGM.S314901.

[10] N. R. Armfield, S. K. Edirippulige, N. Bradford, and A. C. Smith, "Telemedicine - Is the cart being put before the horse?," *Med. J. Aust.*, vol. 200, no. 9, pp. 530–533, Jun. 2014, doi: 10.5694/mja13.11101.

[11] M. M. Ward, M. Jaana, and N. Natafgi, "Systematic review of telemedicine applications in emergency rooms," *International Journal of Medical Informatics*, vol. 84, no. 9. Elsevier Ireland Ltd, pp. 601–616, 21-Dec-2014, doi: 10.1016/j.ijmedinf.2015.05.009.

[12] M. S. Househ, E. M. Borycki, W. M. Rohrer, and A. W. Kushniruk, "Developing a framework for meaningful use of personal health records (PHRs)," *Heal. Policy Technol.*, vol. 3, no. 4, pp. 272–280, Dec. 2014, doi: 10.1016/j.hlpt.2014.08.009.

[13] Centers for Disease Control and Prevention, "Introduction | Meaningful Use | CDC," *CDC*, 17-Sep-2020. [Online]. Available: https://www.cdc.gov/ehrmeaningfuluse/introduction.html. [Accessed: 02-Nov-2020].

[14] C. Showell, "Barriers to the use of personal health records by patients: A structured review," *PeerJ*, vol. 2017, no. 4, 2017, doi: 10.7717/peerj.3268.

[15] M. A. Clarke, R. M. Schuetzler, J. R. Windle, E. Pachunka, and A. Fruhling, "Usability and cognitive load in the design of a personal health record," *Heal. Policy Technol.*, vol. 9, no. 2, pp. 218–224, Jun. 2020, doi: 10.1016/j.hlpt.2019.10.002.

[16] I. Genitsaridi, H. Kondylakis, L. Koumakis, K. Marias, and M. Tsiknakis, "Towards intelligent personal health record systems: Review, Criteria and extensions," in *Procedia Computer Science*, 2013, vol. 21, pp. 327–334, doi:

10.1016/j.procs.2013.09.043.
[17] R. Brandt and R. Rice, "Building a better PHR paradigm: Lessons from the discontinuation of google health™," *Heal. Policy Technol.*, vol. 3, no. 3, pp. 200–207, Sep. 2014, doi: 10.1016/j.hlpt.2014.04.004.
[18] N. Mostert-phipps, M. Korpela, and D. Pottas, "Improving continuity of care through the use of electronic records : a South African perspective Improving continuity of care through the use of electronic records : a South African perspective," *South African Fam. Pract.*, vol. 54, no. 4, pp. 326–331, 2014, doi: 10.1080/20786204.2012.10874244.
[19] H. S. Park *et al.*, "A worker-centered personal health record app for workplace health promotion using national health care data sets: Design and development study," *JMIR Medical Informatics*, vol. 9, no. 8. JMIR Publications Inc., 01-Aug-2021, doi: 10.2196/29184.
[20] Discovery, "HealthID: The technology that puts your patients' health records in your hands.," *Discovery Health*. [Online]. Available: https://www.discovery.co.za/medical-aid/health-id. [Accessed: 19-Mar-2019].
[21] N. Archer, U. Fevrier-Thomas, C. Lokker, K. A. McKibbon, and S. E. Straus, "Personal health records: A scoping review," *Journal of the American Medical Informatics Association*, vol. 18, no. 4. J Am Med Inform Assoc, pp. 515–522, Jul-2011, doi: 10.1136/amiajnl-2011-000105.
[22] GNU, "What is free software? - GNU Project - Free Software Foundation," *GNU*, 30-Jul-2017. [Online]. Available: https://www.gnu.org/philosophy/free-sw.html. [Accessed: 02-Nov-2020].
[23] A. Mxoli, N. Mostert-Phipps, and M. Gerber, "Personal Health Records: Design considerations for the South African context," *Des. Dev. Res.*, vol. 16, no. 8, pp. 124–245, 2014.
[24] M. Rajak and K. Shaw, "Evaluation and selection of mobile health (mHealth) applications using AHP and fuzzy TOPSIS," *Technol. Soc.*, vol. 59, Nov. 2019, doi: 10.1016/j.techsoc.2019.101186.
[25] S. Alter, "Making Sense of Smartness in the Context of Smart Devices and Smart Systems," *Inf. Syst. Front.*, vol. 22, no. 2, pp. 381–393, Apr. 2020, doi: 10.1007/s10796-019-09919-9.
[26] M. Romero, W. Guédria, H. Panetto, and B. Barafort, "Towards a Characterisation of Smart Systems: A Systematic Literature Review," *Comput. Ind.*, vol. 120, p. 103224, 2020, doi: 10.1016/j.compind.2020.103224.
[27] L. Greco, G. Percannella, P. Ritrovato, F. Tortorella, and M. Vento, "Trends in IoT based solutions for health care: Moving AI to the edge," *Pattern Recognit. Lett.*, vol. 135, pp. 346–353, Jul. 2020, doi: 10.1016/j.patrec.2020.05.016.
[28] U. Satija, B. Ramkumar, and S. M. Manikandan, "Real-Time Signal Quality-Aware ECG Telemetry System for IoT-Based Health Care Monitoring," *IEEE Internet Things J.*, vol. 4, no. 3, pp. 815–823, 2017, doi: 10.1109/JIOT.2017.2670022.
[29] E. N. Ganesh, "Health Monitoring System using Raspberry Pi and IOT," *Orient. J. Comput. Sci. Technol.*, vol. 12, no. 1, pp. 08–13, Apr. 2019, doi: 10.13005/ojcst12.01.03.
[30] E. Kańtoch and A. Kańtoch, "What Features and Functions Are Desired in Telemedical Services Targeted at Polish Older Adults Delivered by Wearable Medical Devices?—Pre-COVID-19 Flashback," *Sensors*, vol. 20, no. 18, p. 5181, Sep. 2020, doi: 10.3390/s20185181.
[31] K. Miller *et al.*, "Interface, information, interaction: a narrative review of design and functional requirements for clinical decision support," *J. Am. Med. Informatics Assoc.*, vol. 25, no. 5, pp. 585–592, May 2018, doi: 10.1093/jamia/ocx118.
[32] J. Austrian *et al.*, "Applying A/B testing to clinical decision support: Rapid randomized controlled trials," *J. Med. Internet Res.*, vol. 23, no. 4, Apr. 2021, doi: 10.2196/16651.
[33] H. W. Wu, P. K. Davis, and D. S. Bell, "Advancing clinical decision support using lessons from outside of healthcare: An interdisciplinary systematic review," *BMC Medical Informatics and Decision Making*, vol. 12, no. 1. 2012, doi: 10.1186/1472-6947-12-90.
[34] J. K. Greenberg *et al.*, "Electronic clinical decision support for children with minor head trauma and intracranial injuries: a sociotechnical analysis," *BMC Med. Inform. Decis. Mak.*, vol. 21, no. 1, Dec. 2021, doi: 10.1186/s12911-021-01522-w.
[35] S. Agarwal *et al.*, "Decision-support tools via mobile devices to improve quality of care in primary healthcare settings," *Cochrane Database Syst. Rev.*, vol. 2021, no. 7, Jul. 2021, doi: 10.1002/14651858.CD012944.pub2.
[36] L. Shahmoradi, R. Safdari, H. Ahmadi, and M. Zahmatkeshan, "Clinical decision support systems-based interventions to improve medication outcomes: A systematic literature review on features and effects," *Med. J. Islam. Repub. Iran*, vol. 35, p. 27, Apr. 2021, doi: 10.47176/mjiri.35.27.
[37] B. Kim, Y. Kim, I. S. Lee, and I. You, "Design and implementation of a ubiquitous ECG monitoring system using SIP and the zigbee network," *Proc. Futur. Gener. Commun. Networking, FGCN 2007*, vol. 2, pp. 599–604, 2007, doi: 10.1109/fgcn.2007.97.
[38] B. Yu, L. Xu, and Y. Li, "Bluetooth Low Energy (BLE) based mobile electrocardiogram monitoring system," in *2012 IEEE International Conference on Information and Automation*, 2012, no. June, pp. 763–767, doi: 10.1109/ICInfA.2012.6246921.
[39] A. Kaur and A. Jasuja, "Health monitoring based on IoT using Raspberry PI," *Proceeding - IEEE Int. Conf. Comput. Commun. Autom. ICCCA 2017*, vol. 2017-Janua, pp. 1335–1340, 2017, doi: 10.1109/CCAA.2017.8230004.

Themba Makubalo is a Master's scholar at Nelson Mandela University, currently doing the second year of an MSc degree in Computer Sciences and Information Systems.

A Review of Automated Cow Body Condition Scoring Approaches Using 3d Feature Extraction

Gary I. Summerfield*, Herman C. Myburgh*, Allan de Freitas*
*Department of Electrical. Electronic and Computer Engineering, University of Pretoria, South Africa
[1]u17012822@tuks.co.za
[2]herman.myburgh@up.ac.za
[3]allan.defreitas@up.ac.za

***Abstract*—Automated Cow Body Condition Scoring (BCS) will provide farmers with cost-effective, reliable, and consistent body condition scores for large dairy cow farms. This is important for ensuring optimal milk production and cow health in the long run. In this paper, various approaches to automated body condition scoring are reviewed and compared. The two general models used are regression-based and Convolutional Neural Network (CNN) based models. It was found that the angles and the angularity of the cow's body in both 2D and 3D yielded very good results for several researchers. The use of CNNs to predict BCS values shows good results and potential for a commercial automated BCS system. More research and models are needed in the field of CNN-based automated BCS systems.**

***Index Terms*—Automated Cow Body Condition Scoring, Convolutional Neural Network, Regression**

I. Introduction

Body condition scoring (BCS) is an objective scoring method in which an animal's health is evaluated. It was found that there is a correlation between the BCS of a cow and milk production, long-term health, and ease of calving [1]. Therefore it is important to determine and track a cow's BCS over time to ensure optimal milk production in the long run.

Automated BCS is becoming vital to large commercial dairy farms as it will help the owners score their cows more often and more consistently compared to manual methods and scorers [2]. Automated BCS systems provide the benefit of frequent BCS evaluations whilst being cost-effective. In this review, a brief explanation of how manual BCS works is given. Various existing regression-based and CNN-based models are then reviewed. The various body features used and the results of the models are compared. Existing commercial BCS systems are also briefly discussed.

II. Manual Body Condition Scoring Methods

There are two cow BCS methods, the 5-point BCS and the 9-point BCS [2]. The most popular method used is the 5-point scale, which scores cows from one to five in increments of 0.25. The models reviewed in this paper primarily used the 5-point system. A low BCS value indicates that a cow is underweight while a high BCS value indicates that a cow is overweight. Both of these are unhealthy and negatively impact milk production and yield. Most automated cow BCS systems are based on the scoring system derived by Ferguson et al. [3]. The researchers based their scoring system on the work by Edmonson et al. [4]. The main difference is that in [3] seven anatomical features are used while in [4] eight are used to score cows. These eight regions are given in Table 1. The method described in [4] looks at whether these regions fit certain predetermined profiles. This is primarily done by looking at how the skin wraps around the bones as well as visually and physically inspecting these regions for how much subcutaneous fat and muscle is under the skin. Usually, overweight cows are more rounded around these regions while underweight cows are more angular due to protruding bones. This indicates how much subcutaneous fat and muscle is built up in these regions and is a visual indicator as to how underweight or overweight a cow is.

Table 1 was reproduced from the work of Edmonson et al. [4] and shows how a trained scorer would produce a body condition score by examining a cow both visually and physically. The eight body features presented in [4] are shown in Figure 1.

The researchers in [3] noted that it is difficult to accurately distinguish between BCS values lower than 2 or greater than 4. Therefore, it may be useful to develop a system that simply classifies a cow with a BCS value below 2 as "too thin" and one above 4 as "too fat". Additionally, this may simplify the models used since there would be fewer classes used for classification.

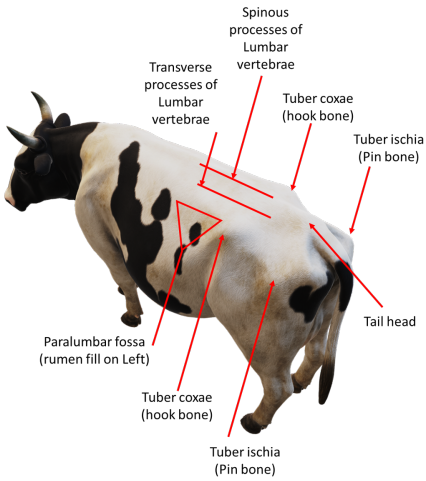

Fig. 1. Important anatomical features for BCS on a Holstein cow, adapted from [4]

TABLE 1
BCS Chart for Holstein Cows, adapted from [4]

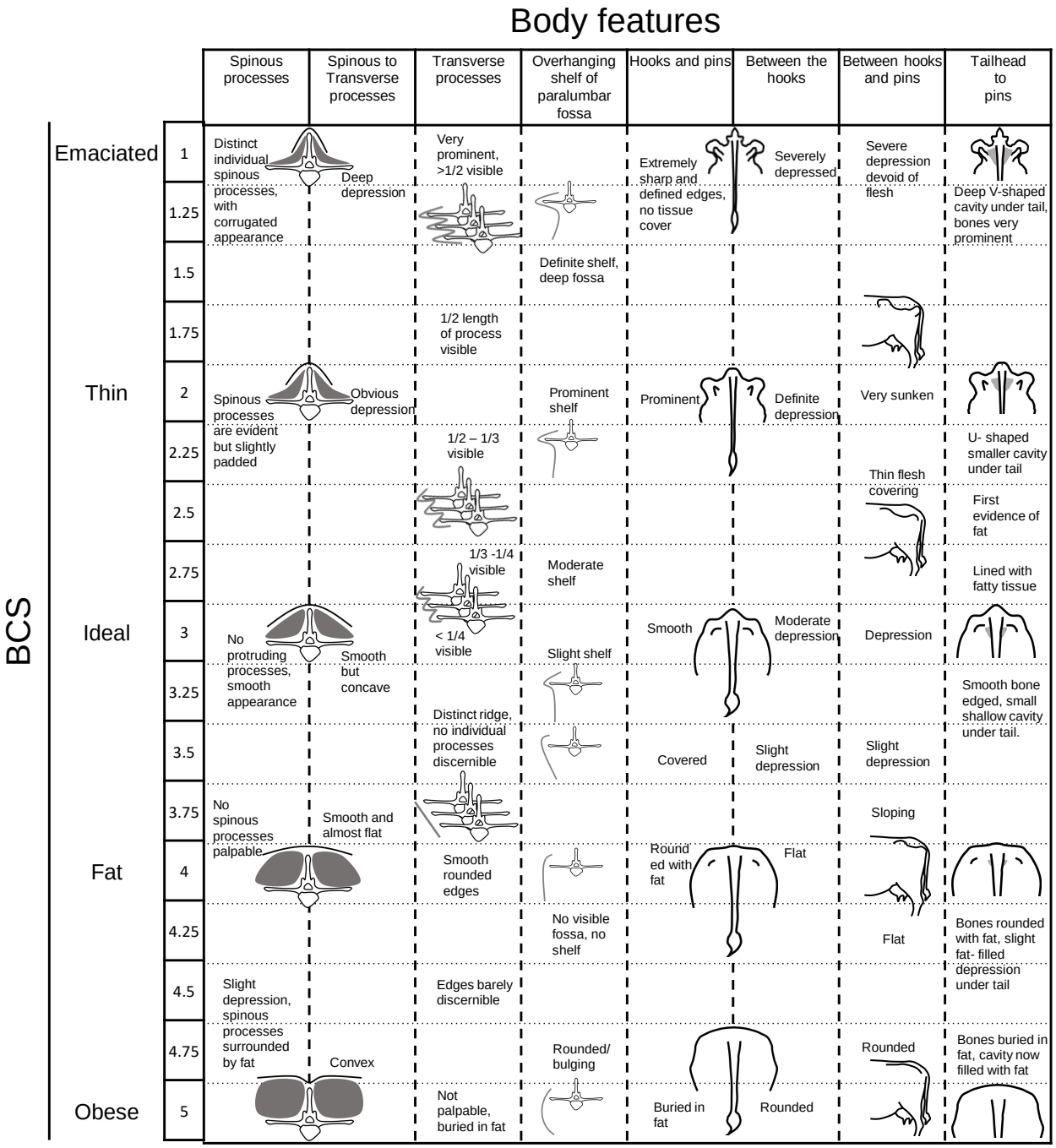

Since the original BCS methods require at least some physical examination of the cow, it is a difficult to accurately determine the BCS of a cow by only visually examining the important anatomical regions. Nevertheless, the majority of manual scoring systems rely heavily on visually inspecting these regions. This is the reason why automated BCS models not only exist but are fairly accurate [5]. The systems extract the important anatomical regions and various features of a cow and predict the BCS. The models are trained by fitting the extracted features with manually determined BCS values to accurately predict the BCS of any given cow.

III. Automated Body Condition Scoring Methods

A. Regression Based Models

A common approach to automated BCS scoring is using a regression based model. This involves extracting features from a cow digitally and then fitting these features to the manually labelled BCS values through various regression techniques. These regression-based models can then be used to predict the BCS of a never before seen cow. The following systems were based on models which used regression to fit the extracted features to the manually produced BCS values.

One of the first approaches to automate BCS for cows was developed by Bewley et al. [2]. The approach involved using 15 different angles between 23 anatomical points around the cow. These angles are produced when the skin wraps around the hook bones, the posterior and the tail of the cow.

The researchers in [2] used a 2D greyscale image of each cow which was taken from above at a weigh station. The images included most of the cow's back, from the neck backwards. The 23 key anatomical points were manually identified and mapped. Both the US 9-point BCS and the UK 5-point BCS systems were used. A total of 1601 cows were used for the data collection where the researchers extracted 3332 images of the cows moving under a weight station. Due to various factors such as movement and bad lighting, not all the images contained all the necessary anatomical points. This limited the number of training samples for certain angles. The actual BCS values were produced by two experienced farm employees.

Two models were used by the researchers in [2]. The first used only the angles of the skin around the hook bones and the second used angles from both the hook bones and the rear of the cow. Both models used first-order auto-regression to fit the angles to the manual BCS values for prediction. The researchers were able to correctly predict 99.87% of the UK BCS values to within 0.5 BCS points of the actual BCS value and 89.95% were within 0.25 points of the actual BCS value. It was found that the angles which formed around the rear of the cow had very little impact on the predicted BCS score and therefore had little impact on the accuracy of the model as a whole. Though the models which were used showed very good results, the system did not operate in real-time and had very little automation since the anatomical points had to be manually mapped from the 2D images. Once the points were mapped the system could produce a very accurate and reliable BCS value. The researchers also noted that it is sometimes difficult to map the points around a predominately black cow. The fact that humans sometimes struggle with the task of selecting the 23 points on predominately black cows does not show much promise for an automated version of this 2D system. Perhaps using 3D depth data to extract the outline of the cow would mitigate the colour problems.

One of the first fully automated real-time regression based cow BCS systems was created by Hansen et al. [6]. The method developed did not use specific anatomical features of the cow. Instead, the 3D image was processed to quantify the angularity of the surface of the cow's back. The idea is that a skinny cow would have more angles due to the bones sticking through whilst a fatter cow would have far fewer angles. The quantified angularity was then related to the 5-point scoring system using regression. The researchers used a Microsoft Kinect camera which was mounted above the ground looking down at the cow's back. This allowed the researchers to obtain a 3D image of the back of a cow as the cow walked through a narrow walkway. An RFID tag was used to identify each cow as it walked under the camera. The researchers automatically scored 119 cows. Three trained staff scored the cows manually to produce the manual BCS values.

The researchers in [6] used a very simple model in which a novel rolling ball image processing algorithm was used to quantify the angularity of the back of a cow. This allowed the researchers to accurately determine how skinny or fat a cow was based on how visible the bones were. The researchers achieved a Mean Absolute Error (MAE) of 0.21 with 80% of the cows being scored to within 0.34 of the manual BCS. The MAE is calculated by finding the mean of the absolute difference of a set of predicted and observed values. The results were promising and showed that automated real-time cow body condition scoring with a 3D camera can be done.

Another important model is that of Spoliansky et al. [7]. The model used 14 features of a cow to determine the BCS score. The first six were related to anatomical features of the back of a cow. The rest related to the height, weight, and age of a cow. This makes the model different from most other models since the features used are not limited to anatomical features. A Microsoft Kinect v1 was used to obtain the 3D data and was placed 2.5 meters above the floor looking down at the cow's back. A sensor would trigger when there is a cow in the walkway and the camera would start capturing the 3D frames at 30 frames per second for 4 seconds.

Polynomial regression using quadratic terms was used to correlate the 14 extracted features with the BCS. The model achieved an accuracy of 74% within 0.25, 91% within 0.5, and 100% within 1 BCS value of the actual BCS values for the cows. The system also yielded a coefficient of determination of 0.75 and an MAE of 0.26 BCS. The fact that the actual BCS values came from only one expert is questionable since it could lead to inconsistent and unreliable baseline BCS values. The model achieved very good results and this may be one of the reasons it was used in the commercial DeLaval system [8].

Song et al. looked at 8 anatomical regions of the cow from 3 angles [9]. These features were extracted and processed further so that the values describing them could be used for the model. The system used three 3D cameras looking from the top, side, and rear of the cows. The researchers aimed to show that using multiple 3D cameras would yield good results. The model consisted of a K-nearest neighbor approach. The 8 automatically extracted features were used to train the nearest-neighbor model to predict the BCS values of cows. The model achieved a sensitivity of 0.72 and an MAE of 0.15. This model produced good results and was one of the few systems where multiple 3D camera angles were used. The very low MAE shows promise for improving automatic BCS accuracy by using the extra features from multiple angles.

B. CNN Based Models

A newer approach to automated cow BCS is using Convolutional Neural Networks (CNN). The first automated cow BCS scoring system which used a CNN-based model was developed by Alvarez et al. [5]. The model uses a 3D scan of the back of a cow. No specific anatomical features were extracted or examined as the model itself effectively extracted the features and shapes as needed. The researchers used a Microsoft Kinect v2 3D camera to capture the training data. The Kinect v2 cameras capture depth images with a resolution of 512 x 424. According to the researchers, the Microsoft Kinect v2 is better for outdoor use than the original Microsoft Kinect camera since it is less affected by direct sunlight. The researchers used 1661 cows and each was evaluated by only one expert to obtain the manual BCS values.

The researchers used 70% of the images (1158) for training the model and 30% (503) for validating the model. The researchers captured the data at three farms under similar environmental conditions to reduce the influence of external factors. Only the depth layer from the 3D camera was used by the researchers. While the data was being captured an expert evaluated the cows to produce manual BCS values. The dataset contained cows ranging from 1.75 to 4.5 on the 5-point BCS scale. Since it is quite difficult to create a dataset with an equal number of images for each BCS value class, the images were weighted according to the number of images available in each class for training. This meant that images on the upper or lower end of the spectrum were weighted higher during training. This was done by scaling the error during training by the class weight. After the 3D image was captured, it was processed to remove unwanted depth noise and isolate only the back of the cow. To remove the background a background image was subtracted from the captured image. Next, any pixels located above a set threshold above the ground were removed since these pixels are likely noise and not part of the cow. Next, the pixel values were re-scaled to be between 0 and 255. This highlighted body shape variability and made the images independent of animal size.

The input image to the CNN consisted of three channels, a depth channel, an edge channel, and a Fourier channel. The researchers used SqueezeNet [10] to implement the CNN model used in the research. SqueezeNet is a very accurate lightweight CNN architecture which uses fifty times fewer parameters than a conventional CNN. This means that the model uses much less memory and processing time during training, allowing the model to train faster on conventional GPUs without compromising the accuracy of the model. The researchers also made use of data augmentation. Data augmentation is a technique that increases the number of training images without obtaining actual new images [11]. This is done by creating fake images through techniques such as cropping, padding, and horizontal flipping. Data augmentation also reduces overfitting and produces a more generalized model. The researchers used the Keras library to develop and train the CNN model.

The model achieved an accuracy of 94% within 0.5 BCS, 78% within 0.25 BCS and 40% were exact. The model outperformed all automated regression-based models. This shows that a simple CNN approach has good potential for a commercial automated real-time BCS system. The fact that the actual BCS scores came from only one expert is questionable since it could lead to inconsistent and unreliable baseline BCS values. The researchers suggested that a larger dataset may result in improved performance. The researchers also found that using training images of cows from different farms helped to improve the general accuracy of the system.

The researchers later improved on their results by introducing two new techniques [12]. The first is transfer learning. Transfer learning is where a very good performing previously trained model is adapted for a new task and retrained on the new task. This technique allows a model to be trained for a specific task with very few training samples for each class. This applies to the current case of predicting BCS values with only around 200 cows per BCS value at best. In transfer learning the first "n" layers of the base network become the first "n" layers of the new network. The remaining layers are then randomly initialised and trained as usual. The researchers used the VGG16 model [13], which is a well-trained image classifier, as their base network.

The second technique is called model ensembling. This is where several models are trained, either in the same manner or using different techniques, and the predicted outputs are combined. It is preferred that different types of models are used so that each model looks at different aspects. This allows the end prediction to be a combination of various perspectives, features, and predictions.

The researchers developed 7 models. Model 1 was trained from scratch using only the depth data. Model 2 used both the depth and the edge data. Model 3 used the depth, edge, and Fourier data similar to [5]. Models 4 to 7 consisted of different implementations of transfer learning. It was found that Model 2 performed the best yielding an accuracy of 96.8% within 0.5 BCS, 81.3% within 0.25 BCS and 39.6% were exact. Model 3 performed the second-best yielding an accuracy of 95.8% within 0.5 BCS, 77.1% within 0.25 BCS and 35.8% were exact. Models 4 to 7 produced poor results in comparison. These results showed that using transfer learning in this application lowered the accuracy. This may be because the dataset was still too small for this technique to work.

The researchers then used model ensembling, by combining Models 2, 3, 6, and 7, to improve the results. The combined ensembled model yielded an accuracy of 97.4% within 0.5 BCS, 81.5% within 0.25 BCS and 41.1% were exact. Both Model 2 and the ensembled model showed improved accuracy in comparison to the model developed by the researchers in [5].

These results once again show that the CNN-based models have good potential for automated real-time BCS systems. The researchers produced one of the best-performing models for an automated body condition scoring system. The researchers used the same preprocessing and dataset as in their previous paper, which shows that the improved results came solely from the improved models.

In [14], the same model and features were used as in [5]. The paper proposed a new method for manual BCS scoring which is more consistent and precise. This more accurate BCS scoring system was then used to develop the training data for the CNN-based approach. The thickness of body fat under the skin of each cow was measured with a portable ultrasound instrument by a professional. The fat thickness was then correlated to the manual BCS scores using regression. It was investigated how well this technique would work for obtaining the actual BCS score in all the cows. The 686 cows used in the research were manually scored by two experts. The correlation coefficient for the ultrasound BCS technique was calculated as 0.94. This is very high which shows that using a portable ultrasound machine to measure the subcutaneous fat thickness is a consistent and accurate method for obtaining manual BCS values for cows. The CNN model used yielded an accuracy of 98% within 0.5, 77% within 0.25 and 45% were exact. This is a good accuracy for a BCS approach. These results also support the results obtained in [5]. While the ultrasound technique is accurate and consistent, it requires the use of an expensive machine by a professional. It is also not real-time and requires the cow to be relatively still. This makes it a poor candidate for a commercial BCS system. It is still a very reliable method for obtaining the actual BCS values for training automated models.

C. Commercial Systems

To date, there are currently three commercially available automated cow BCS systems. These are the DeLaval system from DeLaval International, the BodyMat F (BMF) system from Ingenera, and the 4DRT-Alpha from Biondi Engineering. Only two of the three have been independently validated. All three systems use 3-dimensional image-based approaches.

The commercial DeLaval system was evaluated in [8]. Since the DeLaval system is a commercial system, the exact details of how the system works are a trade secret. The system uses features and models based on [3] and [7]. This means that the system most likely looks at how anatomical features of the cow, and more importantly, the cow's back relate to each other. To evaluate the commercial system, three trained staff members manually scored 343 cows. The consistency and reliability of the staff members were assessed by calculating the Pearson correlations. It was found that the staff scored very similar to each other, meaning that there was high inter-observer reliability. The DeLaval system uses a 3D camera that captures 32 000 3D points at 30 FPS, similar to the system used in [7]. The researchers in [8] found that the manual and automated scores were strongly correlated with a correlation score of 0.78 and a mean error of 0.1. The system performed well for BCS values between 3.00 and 3.75 but accuracy drops at the upper and lower ends of the scoring system, so for fatter and thinner cows.

In [15] a validation study of a new commercial BCS system called the BodyMat F (BMF) was performed. Similar to the DeLaval system, there is no clear information on exactly how the system works. All that is known is that the system uses 3D image analysis of the back of a cow to predict the BCS. The validation study found that the BMF system was more accurate than the DeLaval system. The BMF validation results showed that 95% of the BMF scores were within 0.3 of the actual scores while the DeLaval system produced 95% of the scores within 0.5 of the actual scores. Based on these confidence intervals the BMF system outperforms the DeLaval system and produced similar accuracy to some of the most successful models. Another area where the BMF system outperforms the DeLaval system is with under-conditioned cows. The BMF appears to be more successful when scoring under-conditioned cows than the DeLaval system. The BMF does however struggle with over-conditioned cows similar to the DeLaval system. The researchers suggest that this could be due to reduced variation in the back shape of over-conditioned cows. This is why some manual BCS methods require palpitation of the back of the cow to more accurately score over-conditioned cows. It should be noted that both studies were carried out on Holstein cows only.

Although these two systems are commercially available, they are not the most accurate. There are several other systems and algorithms which have been developed recently which show much higher accuracy across all BCS values. This research still needs to be commercialised to provide very high accuracy real-time cow BCS to farmers.

IV. Discussion

The literature shows that using the outline of the cow as seen from the top is a very good feature to use for BCS prediction. In general, using the angularity of a cow in both 2D and 3D yielded very good results for several researchers. If some of the better-performing systems were automated they would have good potential for a commercial application.

The use of CNNs to predict BCS values shows good results and potential for a commercial automated BCS system. Since effectively the same model was used for all three CNN-based approaches there is plenty of room for new CNN-based models and approaches. Using the angles and outline of the cows from above is a popular and effective method [2], [16]. The angles of the external structure of a cow seem to play the biggest role when it comes to digital BCS scoring.

It should be noted that it is difficult to compare different models and systems since not all papers provide the same

performance metrics. Some provide accuracy, some provide MAE and some provide correlation coefficients. Therefore models were compared where possible using any performance metrics the researchers shared.

In all of the referenced literature, only 1 to 3 scorers were used to produce the manual BCS scores. A larger number of trained scorers, say 5, would be beneficial since it will minimise errors and variations in the manual scores.

V. CONCLUSION

In this study various existing digital cow Body Condition Scoring (BCS) models and systems were reviewed. The various features and models used were investigated and the results of the systems were compared. Several prominent regression-based models made use of the angles the skin formed around the bones of the back of a cow. There are still several research gaps in this field, especially using CNNs, which will hopefully lead to improved results.

Large strides in automated real-time BCS have been made in recent years. This is largely due to the improvements in 3D camera technology as well as algorithmic innovation. Automated BCS systems will soon become vital to large commercial dairy farms. Automated BCS systems provide the benefit of frequent BCS evaluations whilst being cost-effective, reliable, and consistent. This will enable more farmers to accurately track the health of their cows. Farmers will more easily be alerted of sick cows sooner. Farmers will also be able to track and manage the health and weight of cows to safely increase milk production.

REFERENCES

[1] M. Klopčič, A. Hamoen, and J. Bewley, *Body condition scoring of dairy cows*. Biotechnical Faculty, Department of Animal Science, 2011.

[2] J. Bewley, A. Peacock, O. Lewis, R. Boyce, D. Roberts, M. Coffey, S. Kenyon, and M. Schutz, "Potential for estimation of body condition scores in dairy cattle from digital images," *Journal of dairy science*, vol. 91, pp. 3439–53, Oct 2008.

[3] J. Ferguson, D. Galligan, and N. Thomsen, "Principal descriptors of body condition score in holstein cows," *Journal of dairy science*, vol. 77, pp. 2695–703, Oct 1994.

[4] A. Edmonson, I. Lean, L. Weaver, F. TB, and W. GA, "A body condition scoring chart for holstein dairy cows," *Journal of Dairy Science - J DAIRY SCI*, vol. 72, pp. 68–78, Jan 1989.

[5] J. Rodriguez Alvarez, M. Arroqui, P. Mangudo, J. Toloza, D. Jatip, J. Rodriguez, A. Teyseyre, C. Sanz, A. Zunino, C. Machado, and C. Mateos, "Body condition estimation on cows from depth images using Convolutional Neural Networks," *Computers and Electronics in Agriculture*, vol. 155, pp. 12–22, Dec 2018.

[6] M. Hansen, M. Smith, L. Smith, K. Jabbar, and D. Forbes, "Automated monitoring of dairy cow body condition, mobility and weight using a single 3D video capture device," *Computers in Industry*, vol. 98, pp. 14–22, June 2018.

[7] R. Spoliansky, Y. Edan, Y. Parmet, and I. Halachmi, "Development of automatic body condition scoring using a low-cost 3-dimensional Kinect camera," *Journal of Dairy Science*, vol. 99, Jun 2016.

[8] I. Mullins, C. Truman, M. Campler, J. Bewley, and J. H. Costa, "Validation of a commercial automated body condition scoring system on a commercial dairy farm," *Animals*, vol. 9, p. 287, May 2019.

[9] X. Song, E. Bokkers, S. Mourik, P. P. Groot Koerkamp, and P. Tol, "Automated body condition scoring of dairy cows using 3-dimensional feature extraction from multiple body regions," *Journal of Dairy Science*, vol. 102, Mar 2019.

[10] F. Iandola, M. Moskewicz, K. Ashraf, S. Han, W. Dally, and K. Keutzer, "Squeezenet: Alexnet-level accuracy with 50x fewer parameters and textless1mb model size," Feb 2016.

[11] A. Krizhevsky, I. Sutskever, and G. Hinton, "Imagenet classification with deep convolutional neural networks," Jan 2012, pp. 1097–1105.

[12] J. Rodriguez Alvarez, M. Arroqui, P. Mangudo, J. Toloza, D. Jatip, J. Rodriguez, A. Teyseyre, C. Sanz, A. Zunino, C. Machado, and C. Mateos, "Estimating body condition score in dairy cows from depth images using convolutional neural networks, transfer learning and model ensembling techniques," *Agronomy*, vol. 9, Feb 2019.

[13] K. Simonyan and A. Zisserman, "Very deep convolutional networks for large-scale image recognition," *CoRR*, vol. abs/1409.1556, 2015.

[14] S. Yukun, H. Pengju, W. Yujie, C. Ziqi, L. Yang, D. Baisheng, L. Runze, and Z. Yonggen, "Automatic monitoring system for individual dairy cows based on a deep learning framework that provides identification via body parts and estimation of body condition score," *Journal of Dairy Science*, vol. 102, Sep 2019.

[15] N. O Leary, L. Leso, F. Buckley, J. Kenneally, D. Mcsweeney, and L. Shalloo, "Validation of an automated body condition scoring system using 3D imaging," *Agriculture*, vol. 10, Jun 2020.

[16] A. Fischer, T. Luginbühl, L. Delattre, J. Delouard, and P. Faverdin, "Rear shape in 3 dimensions summarized by principal component analysis is a good predictor of body condition score in holstein dairy cows," *Journal of dairy science*, vol. 98, May 2015.

Gary Summerfield received his BEng in Computer Engineering in 2020 at the University of Pretoria. He is currently completing his honours and plans to complete his masters next year.

Computationally Efficient Note Activation Classifier for Multiple-Instrument Automatic Music Transcription

Pieter C. Kok*, J. Pieter Jacobs*
*Department of Electrical, Electronic and Computer Engineering, University of Pretoria, Pretoria, South Africa
[1]pc.kok@tuks.co.za
[2]jpjacobs@up.ac.za

***Abstract*—Multiple-instrument transcription is a relatively unexplored problem in automatic music transcription (AMT). This paper presents a machine learning model to extract instrument stream-level transcriptions of multiple-instrument polyphonic music from posteriogram transcriptions for each instrument. Posteriograms are obtained from non-negative matrix factorization (NMF) transcription, which extracts activations for each note of each instrument in each time frame of a magnitude spectrogram using pre-extracted frequency templates. A feed-forward neural network (FFNN) is used as a classifier to convert these posteriograms to piano roll transcriptions for each instrument. Additionally, frame segments are considered to enable temporal note continuity in transcription and mel-frequency cepstral coefficients (MFCCs) are used to improve instrument separation. The algorithm is based on assuming the instrumentation that is being transcribed is a common combination (for example a quartet) and that a specialised model can be trained for such common instrumentations in order to take advantage of using neural network classifiers for post-processing. The TRIOS dataset is used for training and testing with a mix of violin, clarinet, saxophone and bassoon parts. The proposed algorithm achieved similar accuracy to state-of-the-art algorithms for stream-level transcription that were also evaluated on comparable classical music datasets. The algorithm is also highly efficient due to consigning most of the processing to pre-training.**

***Index Terms*—Multiple-instrument transcription, stream-level transcription, posteriogram, non-negative matrix factorization, feed-forward neural network classifier.**

I. Introduction

Multiple instrument transcription or stream-level transcription is a problem in music information retrieval (MIR) that has only recently been explored [1]. More focus has been put into the comparatively easier, but similar task of single instrument polyphonic transcription. There are large datasets for training and testing, such as the MIDI Aligned Piano Sounds (MAPS) dataset [2], and the problem has effectively been solved for many instruments to a high degree of accuracy, although improvements are still made. Annotated multiple-instrument transcription datasets have emerged as the need arose in the new problem domain of transcribing multiple instruments and assigning instrument streams [3]–[7].

Early instrument transcription algorithms used mathematical models of sounds to account for and track harmonics and so estimate fundamental frequencies (F0s). F0s can be found from peaks in time-frequency representations and can be refined by correlation with expected harmonic or note shapes [8]–[10], but later algorithms found more success for instrument specific transcription using note templates.

Non-negative matrix factorization (NMF) is a form of unsupervised learning. It has been applied to automatic music transcription (AMT) by factorizing a time-frequency representation in matrix form into a frequency event template and an activation matrix that contains the transcription of the event times. The frequency event matrix can be pre-learned templates of instrument notes to transcribe a specific instrument [11].

Probabilistic latent component analysis (PLCA) can be seen as an extension of NMF, using a probabilistic framework. It makes it easier to generalize models or incorporate priors. PLCA models have been used for transcription and have included extensions such as shift-invariance, sound state modeling for the temporal evolution of notes and instrument sources, which has been used for stream-level transcription [12].

Hidden Markov models (HMMs) are often used for post-processing transcriptions. It is useful for enforcing continuity in transcribed notes. Algorithms like Viterbi decoding and iterative conditional modes are used to find the most probable hidden states for active notes or sources [10], [12], [13].

Frame-level note classification is also possible with supervised machine learning. Using machine learning models to transcribe music requires annotated training data. Models transcribe frame-wise features into posteriograms, which give the probabilities of notes in a frame being active. Different features and models have been used for single instrument transcription. Time-frequency representations are common input features with magnitude spectrograms [13], [14] and constant-Q transforms [14]–[16] being the most common. Simple models, such as support vector machines with HMM post-processing have been shown to work [13], but deep learning models such as deep neural networks (DNNs), convolutional neural networks (CNNs) and recurrent neural network (RNN) have shown more success in transcribing to posteriograms [14], [16] as well transducing clean transcriptions from posteriograms [15], [16].

Stream-level transcription is a relatively unexplored problem domain. Common approaches are to estimate F0s and to then assign them to instrument streams. Mel frequency

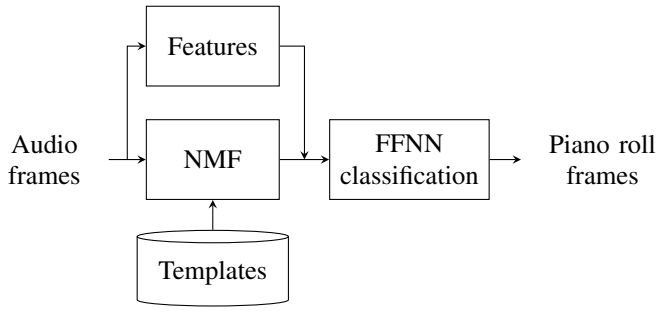

Fig. 1. An overview of the proposed system

cepstral coefficients (MFCCs) are used as timbre features to group F0s that are most likely from the same instrument source. This is done using PLCA to estimate F0s and then using an HMM to enforce temporal continuity of notes and timbre similarity in streams [10] or as a post-processing algorithm that clusters existing F0s using an iterative clustering algorithm to minimise the timbre variance in stream clusters [17]

Machine learning approaches to multi-instrument transcription have been limited. Recent success has been had by an approach of using an encoder-decoder CNN model to transcribe multiple instruments simultaneously for both frame-wise and note-wise transcription by training a model on a set combination of instruments [18].

In Section II we propose a system for transcribing multiple instruments playing simultaneously from posteriogram inputs. We elaborate on the feed forward neural network (FFNN) classifier design and training in Section III. Our experiments and results are given in Section IV.

II. System Overview

The proposed system uses posteriograms obtained from NMF transcription, along with timbre features as inputs to a classifier FFNN that for each output node classifies the corresponding instrument note as active or inactive in the input audio frame. Figure 1 shows the details of the system architecture.

A time-frequency representation is used as input to both the NMF posteriogram transcription and MFCC timbre features. A short-time Fourier transform magnitude spectrogram is computed with a 46 ms Hamming window, 10 ms hop size and 2048 point fast Fourier transform. Audio is sampled at $F_s = 44.1$ kHz.

A. Non-negative Matrix Factorization Posteriograms

NMF posteriograms are obtained by transcribing the spectrogram representation of the input audio using an NMF multivariate analysis algorithm. NMF factorizes a $K \times N$ non-negative matrix $\mathbf{V}$ into a $K \times P$ template matrix $\mathbf{W}$ and a $P \times N$ event matrix $\mathbf{H}$ such that $\mathbf{V} \approx \mathbf{W} \cdot \mathbf{H}$. $\mathbf{A} \cdot \mathbf{B}$ denotes matrix multiplication between two matrices $\mathbf{A}$ and $\mathbf{B}$. $\mathbf{W}$ and $\mathbf{H}$ are estimated using multiplicative update rules [19]:

$$\mathbf{H}_{ij}^{t+1} = \mathbf{H}_{ij}^{t} \frac{[(\mathbf{W}^t)^T \cdot \mathbf{V}]_{ij}}{[(\mathbf{W}^t)^T \cdot \mathbf{W}^t \cdot \mathbf{H}^t]_{ij}}, \tag{1}$$

$$\mathbf{W}_{ij}^{t+1} = \mathbf{W}_{ij}^{t} \frac{[\mathbf{V} \cdot (\mathbf{H}^{t+1})^T]_{ij}}{[(\mathbf{W}^t) \cdot \mathbf{H}^{t+1} \cdot (\mathbf{H}^{t+1})^T]_{ij}}, \tag{2}$$

where t is an iteration timestep. $\mathbf{W}$ and $\mathbf{H}$ are initialised to non-negative values and are updated iteratively for a set number of iterations or until a cost function reaches a minimum.

Factorizing a time-frequency representation of music results in a transcription of P events, which are each characterized by a frequency template of K frequency bins in a column of $\mathbf{W}$ and for which the corresponding row of $\mathbf{H}$ shows the energy of the event in each of N time frames.

For implementations where the dimension N can be of any size and where an approximation of real-time processing is desired, $\mathbf{V}$ can be factorized for one column at a time. The template matrix $\mathbf{W}$ can also be pre-computed and kept constant, which also has the advantage of fixing the rows in $\mathbf{H}$ to specific events The update rule becomes [11]:

$$\mathbf{h}^{t+1} = \mathbf{h}^{t} \otimes \frac{(\mathbf{W} \otimes (\mathbf{v}\mathbf{e}^T))^T (\mathbf{W}\mathbf{h})^{\cdot \beta - 2}}{\mathbf{W}^T (\mathbf{W}\mathbf{h})^{\cdot \beta - 1}}, \tag{3}$$

where $\mathbf{e}$ is a vector of ones and β is a β-divergence parameter, which is set to $\beta = 2$ to correspond with the Euclidean distance cost function. The cost function

$$C = \sum_{i=1}^{K} \sum_{j=1}^{N} |\mathbf{V} - \mathbf{W} \cdot \mathbf{H}|_{ij}^2, \tag{4}$$

is minimised during the iterative updates. To estimate the posteriogram of a musical exerpt, its spectrogram is factorized one frame at a time. A column vector of P note activations is uniformly randomly initialized and update for 200 iterations or until the cost reduces to below a threshold of $\tau_C = 0.001$, using a fixed $\mathbf{W}$ dictionary. This results in a posteriogram frame of salience values correlating to the probability of each instrument note being active in the frame.

The $\mathbf{W}$ dictionary is pre-computed by factorizing recordings of instrument notes separately for each potential instrument note with the P dimension set to 1. The resulting $\mathbf{H}$ matrix is discarded and the $\mathbf{W}$ matrix is concatenated into the larger dictionary. Lower resolution is needed for compiling the dictionary, which improves generalization of the samples, so a 30 ms window, and a 25 ms hop size is used.

III. FFNN Activation Classifier

A single hidden layer FFNN is used as a classifier to determine instrument note activations for each frame of the input posteriograms. A single layer FFNN is a relatively simple neural network compared to state-of-the-art deep learning models that are now commonly applied to machine learning problems — the network is kept simple in order to investigate whether posteriogram features can compensate for a complex network architecture. The input vector contains a number of

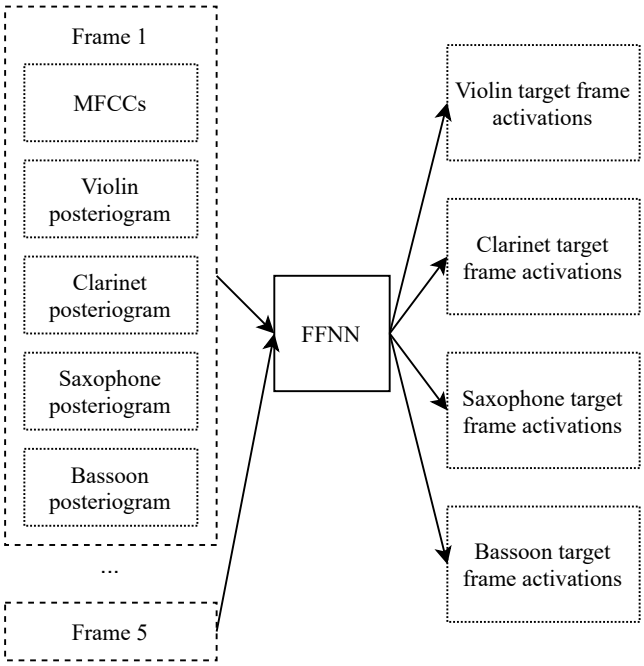

Fig. 2. The FFNN inputs and outputs.

features for a segment of consecutive frames. $F = 875$ input features are obtained from the segmented posteriogram frames of each instrument's NMF transcription and the MFCCs. Each frame contains 165 posteriogram note activations spanning all the instruments and notes, as well as 10 MFCCs. The 175×5 feature frame segment is flattened to obtain the classifier input for the target frame. $D = 256$ hidden neurons are fully connected to the input layer, with ReLu activation functions, which in turn feed into each of the $P = 165$ network outputs with sigmoid activations. The number of hidden neurons and frame segments were chosen based on 5-fold cross-validation and selected as the parameters at which the increase in F-score for larger parameters is less than 1 % The network input and output vectors are shown in Figure 2. Each output corresponds to the activation of one instrument note in a frame. The network is applied to all frames of the posteriogram transcription to obtain a full transcription of each instrument for each frame.

A. Mel-frequency Cepstrum Coefficient Features

MFCCs are often used as timbre feature and are useful features in instrument recognition [20]. They are the amplitudes of cepstrums obtained from the type-II inverse cosine transforms of a series of bandpass filter powers. The filters are L triangular filters with centers which are equally spaced on the mel scale between 0 Hz and $F_s/2$ with half their bandwidths overlapping. $L = 50$ filters are used. 10 coefficients are used as features, excluding the average signal energy 0^{th} coefficient.

B. Higher Level Segmentation

Frame segments are used to take multiple frames into account at once and better capture continuous F0s over note durations without CNNs or RNNs. Segmentation consists of a number of frames to either side of the target frame being added to the feature vector. Zero-padding at the beginning and end of the input signal feature frame matrix is used to keep the total number of frames consistent. Segments of 5 frames are used.

C. Training

The binary cross-entropy (BCE) loss is minimised during training, which gives the average error over the weights, $\mathbf{w}$, as

$$E(\mathbf{w}) = \frac{-1}{N} \sum_{n=1}^{N} \Big[y_n \log \hat{y}_n + (1 - y_n) \log(1 - \hat{y}_n) \Big], \quad (5)$$

for N approximations $\hat{\mathbf{y}}$ of N true binary classifications $\mathbf{y}$. The output layer of the activation classifier outputs binary activations for the frame instrument notes. Models are trained using the Adam optimizer [21] with parameters $\alpha = 0.001$, $\beta_1 = 0.9$, $\beta_2 = 0.999$ and $\epsilon = 1e-07$. Training is done over 300 epochs in batches of 32, which are shuffled each epoch. Early stopping on the validation loss is used with $\Delta = 0.0001$ and the best model weights are saved.

D. Post-processing

The sigmoid activation functions for the FFNN outputs an approximate probability of each instrument note being active in a frame. A binary piano-roll representation is desired for evaluation using an F-score. The output posteriograms of the FFNN are converted to a final binary piano-roll by thresholding the FFNN output. All instrument note frame activations larger than a threshold of $\tau_a = 0.5$ are set as active in the frame; all others are set as inactive.

IV. Evaluation

A. Datasets

Train, test and validation data is compiled from mixes of the violin, clarinet, saxophone and bassoon parts of excerpts of real instruments recorded in isolation. Not all combinations of excerpt parts span the entire musical range of the instruments, so mix excerpts are randomly generated using notes spanning the range of each instrument from the University of Iowa Musical Instrument Samples (MIS) dataset [22]. Mixing is done by playing a single note sample from each instrument at any given time (for a maximum polyphony of 4) with a Poisson distributed interval of 10 ms on average between instrument samples. All available samples for each instrument are repeated twice and ordered randomly.

Training and testing data is compiled from the TRIOS dataset, which contains five recordings of trios consisting of pieces for threefold combinations of clarinet, violin, cello, viola, piano, French horn, trumpet, bassoon, saxophone and drums. The excerpts were recorded live for each instrument separately and manually aligned MIDI files are provided for ground truth recordings [4]. All relevant parts for the violin, clarinet, saxophone and bassoon are mixed in all possible

TABLE I
STREAM-LEVEL TRANSCRIPTION RESULTS ON THE TRIOS DATASET WITH MIXED PARTS FROM ALL EXCERPTS.

Instrument	Precision (%)	Recall (%)	Accuracy (%)	F1 (%)
Violin	78.8	47.9	42.4	59.6
Clarinet	92.7	62.8	59.8	74.9
Saxophone	80.3	50.7	45.1	62.1
Bassoon	69.7	19.7	18.1	30.7
All instruments	82.5	48.9	44.3	61.4

TABLE II
REPORTED RESULTS ACHIEVED IN MULTIPLE INSTRUMENT STREAM-LEVEL TRANSCRIPTION FOR OTHER CLASSICAL MUSIC DATASETS OF COMPARABLE POLYPHONY.

Model	Dataset	Polyphony	Accuracy (%)	F1 (%)
Shift-invariant PLCA [12]	MIREX	5	—	45.49
Stream clustering [17]	Bach10	4	53	—
Multiple F0 estimation [10]	Bach10	4	61.3	62.4

combinations for a total of 28 excerpts. A random mix of instrument notes from the MIS dataset [22] is added to the dataset. The compiled dataset contains 172773 audio frames. It is split into training, testing and validation sets by assigning the frames to batches of 500 frames (roughly 5 seconds of audio). These batches of frames are in turn randomly allocated to each subset. A training to testing split of 80 % to 20 % is used with the training set further split into 80 % purely training samples and 20 % validation samples.

B. Metrics

Accuracy ($\mathcal{A}$) and the F1 score are used as the evaluation metrics. Accuracy is a common metric used for evaluating transcription problems [23] and is given by

$$\mathcal{A} = \frac{TP}{TP + FP + FN}. \tag{6}$$

The F1 score is commonly used to evaluate binary classification problems and is the harmonic mean of precision ($\mathcal{P}$) and recall ($\mathcal{R}$):

$$\mathcal{P} = \frac{TP}{TP + FP}, \tag{7}$$

$$\mathcal{R} = \frac{TP}{TP + FN}, \tag{8}$$

$$F_1 = \frac{2}{\mathcal{P}^{-1} + \mathcal{R}^{-1}}. \tag{9}$$

True positives (TP) are taken as active notes in a frame that are correct for both the pitch and instrument, false positives (FP) are active instrument pitches in a frame that are not active in the ground truth transcription and false negatives (FN) are instrument notes from the ground truth frame that are absent in the algorithm transcription. Both metrics are presented, so results can easily be compared to other state-of-the-art implementations.

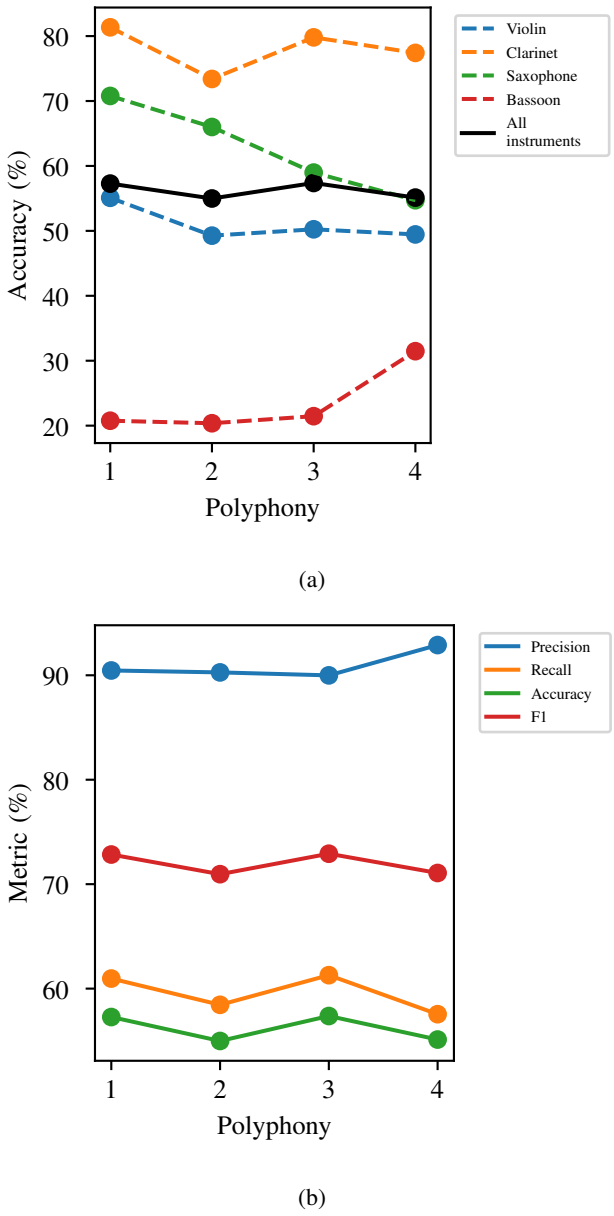

Fig. 3. Stream-level transcription (a) accuracy for different instruments and (b) evaluation metric results for different numbers of polyphony on the TRIOS dataset.

C. Results

A model was trained and evaluated on the TRIOS dataset. These results are shown in Table I. These results do not perform as well as state-of-the-art neural network models for multiple-instrument AMT [18] but compare favourably to results reported by F0 clustering methods [10], [17], although recall is not as good, which indicates a lot of missed note transcriptions.

An example transcription was computed on an excerpt of the training set with the proposed FFNN instrument transcription algorithm. The instrument stream transcriptions can be seen in Figure 4. Clarinet parts are clearly transcribed the best and bassoon the worst. Note that many of the false positives and negatives are only single frames and are often octave

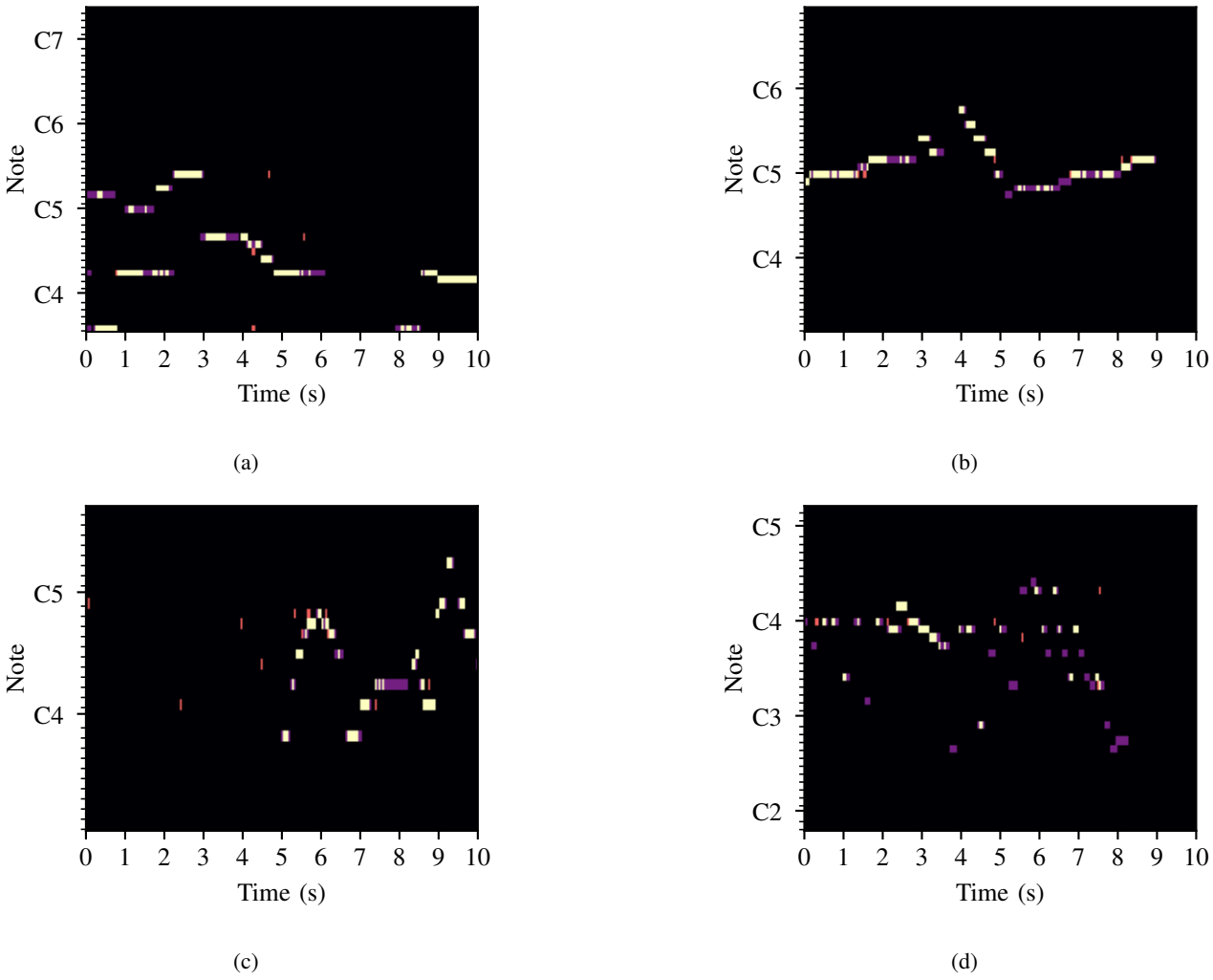

Fig. 4. Transcriptions of an excerpt from the TRIOS dataset. The assigned instrument streams are (a) violin, (b) clarinet, (c) saxophone and (d) bassoon. True positives are indicated in white, false positives are indicated in red and false negatives are indicated in purple.

errors.

1) Performance and Trade-offs: When compared to results reported by other implementations in Table II, our implementation outperforms or performs similarly to other multiple-instrument AMT methods that do not use supervised learning. As discussed in Section I, estimating F0s has been solved effectively, but assigning F0s to instruments is a much harder problem that can reduce accuracy significantly through incorrect stream assignment. Blind stream assignment through clustering has the disadvantage of potentially assigning the wrong number of streams if not all streams are active, but our system solves this by explicitly looking for specific instrument notes in a posteriogram (see Figure 3). This also has the advantage that instrument streams do not need to be matched to instruments after transcription.

This implementation is not computationally intensive, with most of the online computation needed for the NMF posteriograms. The algorithm was tested on a laptop with a 3.2 GHz CPU, 32 GB of RAM and a NVIDIA GeForce RTX 3060 GPU. The mean computation time of the main algorithm parts are shown in Table III with standard deviations noted in brackets. The NMF is much slower than the FFNN, but can be optimised further by downsampling the input to reduce the number of frames to be computed or by reducing the number of iterations of the update rule. There is a lot of room to trade off accuracy for a faster computation time. Even so, most of the processing is done in training, so the approach is well suited to online implementations. A trade-off for this is the FFNN model weights (approximately 1.1 megabytes for the features used) and instrument note dictionary (approximately 1.4 megabyte for 4 instruments) that need to be stored. This will of course scale for more instruments.

TABLE III
COMPUTATION TIMES PER FRAME FOR DIFFERENT PARTS OF THE ALGORITHM.

Algorithm block	CPU time per frame (ms)
NMF	63.2 (1.6)
FFNN	0.262 (0.207)

2) Polyphony and Instrumentation: Examining Figure 3 shows no significant change in accuracy as polyphony increases. Some instruments, like saxophone decreases, while

others, like bassoon increases. On the whole there is not a significant decrease in accuracy with an increase in polyphony, with the exception of saxophone, so more instruments could potentially be added without too much loss in accuracy. A more generally useful implementation beyond this specific instrumentation could have more instruments in the training set implementation and would perform well for transcribing music for which the instrumentation is a subset of the training set instrumentation.

V. Conclusion

This paper has shown the potential of multiple-instrument AMT using simple machine learning classifiers on existing single-instrument posteriogram features. It also shows that NMF posteriogram features are effective for classifying instrument note activations. The proposed system performs similarly to clustering methods for instrument-stream transcription that were also evaluated on classical music datasets with a similar polyphony. This method has the advantage over clustering methods of having the instrument streams inherently assigned.

The proposed network architecture is relatively simple and can be trained on a small dataset of annotated music. The NMF posteriogram extraction algorithm has been shown to be able to run in near real-time [11], so the overall system has the potential to be practically applicably for transcribing recorded audio with a known instrumentation mix.

Further research needs to be done to determine how resilient the system is for higher polyphony and unknown instruments or percussion in the mix. Investigation is also needed into the potential of deeper neural networks, such as RNNs and CNNs to improve performance, especially on cross-dataset evaluation.

Acknowledgement

This work is based on research supported in part by Telkom. The grant holder acknowledges that opinions, findings and conclusions or recommendations expressed in any publication generated by this research are that of the author(s), and that our industry partners accept no liability in this regard.

References

[1] E. Benetos, S. Dixon, Z. Duan, and S. Ewert, "Automatic Music Transcription: An Overview," *IEEE Signal Processing Magazine*, vol. 36, no. 1, pp. 20–30, 2019.

[2] V. Emiya, R. Badeau, and B. David, "Multipitch estimation of piano sounds using a new probabilistic spectral smoothness principle," *IEEE Transactions on Audio, Speech and Language Processing*, vol. 18, no. 6, pp. 1643–1654, 2010.

[3] Z. Duan, B. Pardo, and C. Zhang, "Multiple fundamental frequency estimation by modeling spectral peaks and non-peak regions," *IEEE Transactions on Audio, Speech and Language Processing*, vol. 18, no. 8, pp. 2121–2133, 2010.

[4] J. Fritsch, "High Quality Musical Audio Source Separation," Master's thesis, UPMC / IRCAM / Telecom Paristech, 2012.

[5] M. Miron, J. J. Carabias-Orti, J. J. Bosch, E. Gómez, and J. Janer, "Score-informed source separation for multichannel orchestral recordings," *Journal of Electrical and Computer Engineering*, vol. 2016, no. January 2017, 2016.

[6] J. Pätynen, V. Pulkki, and T. Lokki, "Anechoic recording system for symphony orchestra," *Acta Acustica united with Acustica*, vol. 94, no. 6, pp. 856–865, 2008.

[7] B. Li, X. Liu, K. Dinesh, Z. Duan, and G. Sharma, "Creating a Multitrack Classical Music Performance Dataset for Multimodal Music Analysis: Challenges, Insights, and Applications," *IEEE Transactions on Multimedia*, vol. 21, no. 2, pp. 522–535, 2019.

[8] A. de Cheveigné and H. Kawahara, "YIN, a fundamental frequency estimator for speech and music," *The Journal of the Acoustical Society of America*, vol. 111, no. 4, pp. 1917–1930, 2002.

[9] A. Loscos, Y. Wang, W. Jie, and J. Boo, "Low level descriptors for automatic violin transcription," in *ISMIR 2006 - 7th International Conference on Music Information Retrieval*, 2006, pp. 164–167.

[10] V. Arora and L. Behera, "Multiple F0 estimation and source clustering of polyphonic music audio using PLCA and HMRFs," *IEEE/ACM Transactions on Audio Speech and Language Processing*, vol. 23, no. 2, pp. 278–287, 2015.

[11] A. Dessein, A. Cont, and G. Lemaitre, "Real-time polyphonic music transcription with non-negative matrix factorization and beta-divergence," *Proceedings of the 11th International Society for Music Information Retrieval Conference, ISMIR 2010*, pp. 489–494, 2010.

[12] E. Benetos and S. Dixon, "Multiple-instrument polyphonic music transcription using a temporally constrained shift-invariant model," *The Journal of the Acoustical Society of America*, vol. 133, no. 3, pp. 1727–1741, 2013.

[13] G. E. Poliner and D. P. W. Ellis, "A Discriminative Model for Polyphonic Piano Transcription," *EURASIP Journal on Advances in Signal Processing*, vol. 48317, 2007. [Online]. Available: http://www.piano-midi.de/.

[14] R. Kelz, M. Dorfer, F. Korzeniowski, S. Böck, A. Arzt, and G. Widmer, "On the potential of simple framewise approaches to piano transcription," *Proceedings of the 17th International Society for Music Information Retrieval Conference, ISMIR 2016*, pp. 475–481, 2016.

[15] S. Sigtia, E. Benetos, and S. Dixon, "An end-to-end neural network for polyphonic piano music transcription," *IEEE/ACM Transactions on Audio Speech and Language Processing*, vol. 24, no. 5, pp. 927–939, 2016.

[16] A. Ycart, D. Stoller, and E. Benetos, "A comparative study of neural models for polyphonic music sequence transduction," in *Proceedings of the 20th International Society for Music Information Retrieval Conference, ISMIR 2019*, 2019, pp. 470–477.

[17] Z. Duan, J. Han, and B. Pardo, "Multi-pitch streaming of harmonic sound mixtures," *IEEE Transactions on Audio, Speech and Language Processing*, vol. 22, no. 1, pp. 138–150, 2014.

[18] Y. T. Wu, B. Chen, and L. Su, "Multi-Instrument Automatic Music Transcription with Self-Attention-Based Instance Segmentation," *IEEE/ACM Transactions on Audio Speech and Language Processing*, vol. 28, pp. 2796–2809, 2020.

[19] D. D. Lee and H. S. Seung, "Algorithms for Non-negative Matrix Factorization," in *Advances in Neural Information Processing Systems 13: Proceedings of the 2000 Conference*. MIT Press, 2001, p. 556–562.

[20] S. Theodoridis and K. Koutroumbas, *Pattern recognition*, 4th ed. Academic Press, 2009.

[21] D. P. Kingma and J. L. Ba, "Adam: A Method for Stochastic Optimization," in *3rd International Conference for Learning Representations*, San Diego, 2015, pp. 1–15.

[22] "University of Iowa Electronic Music Studios." [Online]. Available: http://theremin.music.uiowa.edu/mis.html

[23] S. Dixon, "On the computer recognition of solo piano music," in *Proceedings of Australasian Computer Music Conference*, 2000, pp. 31–37.

Pieter Kok received a degree in Computer Engineering from the University of Pretoria in 2019 and an honours degree in 2020. He is studying with the Intelligent Systems Group in the Department of Electrical, Electronic and Computer Engineering of the University of Pretoria.

Pieter Jacobs holds a PhD in electronic engineering from the University of Pretoria and a doctorate in musical arts from Yale University. He is currently an associate professor in the Department of Electrical, Electronic and Computer Engineering at UP. His research interests include music information retrieval and electromagnetic modeling.

Automatic Language Identification in Paired Tsonga and English Texts

Ntiyiso Baloyi*, Madimetja JD Manamela*, Thipe I Modipa*
*Department f Computer Science, University of Limpopo, Limpopo, south Africa
[1]ntiyisontiyiso2@gmail.com
[2]jonas.manamela@ul.ac.za
[3]thipe.modipa@ul.ac.za

***Abstract*—The development of a language identifier that effectively detects a language of a sentence or word in a code-switched text can help in many natural processing tasks. Tasks such as subjecting only the documents of the relevant languages to further processing, indexing documents by using their languages, data collection in the internet, detecting the language of a document prior to translation, and corpus creation. This paper presents exploratory results of automatic language identification of -English language pair. First, a dataset is collected on Twitter and Tsonga short stories, and novels. The data is then combined and annotated manually. Four supervised machine learning models are then used to carry out language identification task at word-level. The models are then evaluated using weighted F_1-score, precision and recall. The best performing model is used to build the automatic language identification interface for paired Tsonga and English text.**

***Index Terms*—language identification, automatic language identification, code-switching, code-switching detection.**

I. Introduction

Code-switching refers to a phenomenon of alternating between different languages in a single utterance. Code-switching has become a reality in day-to-day forms of human-to-human communication episodes in many multilingual societies [1]. Code-switching is being used in almost all social media platforms, such as Twitter, Facebook and Instagram [2]. For machines to partake in these communication episodes, code-switching trends need analysis and development of tools and techniques that can handle it appropriately whenever it is encountered.

Code-switching detection refers to the detection of language switches in code-mixed utterances. There have been little effective attempts at code-switching detection for communication episodes that involve under-resourced languages [3]. This is due to lack of code-switched training speech and text datasets to train reliable models that can accurately recognise uttered words and its language. Another limitation imposed on building code-switching models is the lack of annotated code-switched datasets to train supervised models.

In the design and development of automatic code-switching detection systems for Tsonga speakers, automatic language identification becomes a relevant study. Automatic language identification (LI) is the task of identifying the natural language of a written text [4]. The task of LI at a word level is identified as a special case of text classification, where tokens are mapped into one of the assigned classes. LI for Tsonga-English language pair is the first step in automatically detecting code-switching in this language pair. The results in automatic LI task will be used to create Tsonga-English corpus, automatically annotate Tsonga-English corpus, and will be merged with the code-switching detection task to predict code-switching in real time.

The rest of this paper is organised as follows. In Section 2, we discus the work related to this research word. Section 3 describe of how the data was collected and how the corpus was formed. It also gives an exploratory analysis of the data-set and shows how the data-set was then annotated. Section 4 is the experimental setup and evaluation. Section 5 is the results and analysis, and lastly is conclusions.

II. Related Work

Several studies have been conducted on automatic language LI for both speech and written texts languages [5] [4] [6]. In written text, LI has been conducted at both document-level and word-level standpoint [7] [8] [9]. Paul McNamee [10] described LI as a solved problem which is to be carried out by undergraduate instruction. There are still issues related to language identification which needs to be addressed, this includes LI of multilingual documents, open-class LI, etc [11]. Classifying texts at a word level is a very challenging task [12]. The task of classification at a word-level has been carried out using character n-gram models, word dictionaries, and machine learning algorithms [13].

Nina Dongen [14] explored five models for automatic LI. These models include the baseline model, rule-based algorithm,and three supervised machine learning models. These models were developed and trained on Dutch and English pair tweet data, and the best performing model was to be combined the task of code-switching detection for fully automation. It was found that the Decision Tree model outperforms other supervised machine learning models. The DT model was then combined with the rule-based dictionary lookup model. The performance of the two combined models was 20.1%, 32% and 24.6% for Precision, recall and F_1-score respectively. These did not qualify to be used in a real-life setting.

N Nguyen and A. Seza [7] On their experiments of word-level language identification with online multilingual discussions, they used language models and dictionaries to tag the language of individual tokens, then integrate context to improve the performance. Precision, recall, accuracy, Pearson's

correlation, Mean Absolute Error and F_1-score were used to evaluate the performance at word and post levels. This study achieved 98% accuracy.

III. Corpus development

Tsonga is a Bantu language spoken in Southern Africa by Tsonga people. It is an official language in South Africa (SA), Zimbabwe as Shangani and in Mozambique. It is also used in Swaziland but not as the official language. Tsonga has a total population of 7.3 million with 2 615 000 speakers in South Africa, 4 525 000 million speakers in Mozambique, 24 000 speakers in Swaziland, and 136 000 speakers in Zimbabwe [15]. In South Africa, many of Tsonga speakers live in Limpopo Province, Mpumalanga Province, Gauteng Province, and North West Province [16]. The South Africa's Census 2011 shows that the Tsonga first language speakers form 4.5% of the SA population [16]. The Census 2011 also reveals that the Tsonga language is spoken by black Africans, Coloureds, Indians or Asians, and Whites in South Africa. Many of Tsonga speakers are multilingual and they often switch from one language to another during their conversational episode [17]. Their switching from one language to another is influenced by the commonplace multilingualism in the provinces of South Africa.

A. Data collection

The data was collected on twitter using the Twitter Search API and on selected Tsonga short stories and novels [18]. Tsonga keywords were used to search and collect Twitter messages. One keywords was used per trial. Keywords were first selected based on their high frequency in NCHLT Tsonga speech corpus transcriptions, but these keywords produced tweets that belong to other languages (Shona, Sepedi, IsiZulu, etc.) instead of Tsonga and English tweets. Keywords were then selected randomly based on their uniqueness to Tsonga language. The list of keywords used consists of the following words: nwina, vulavula, ndzi, vona, swona, endla, sweswi, kombela, rhandza, swinene, vutomi, leswi, leswo, ndza, rirhandzu and khensa. For Tsonga short stories and novels, we collected texts from chapters and sections where code-switching of Tsonga and English occurred. The data is highly imbalanced, the corpus is dominated by Tsonga texts, but English phrases are also occasionally observed. Inter-Sentential, Intra-Sentential and Extra-Sentential code-switching was observed in the collected text. Below are few examples that illustrate switches between Tsonga-English language pair within the same post.

The first two examples (Example 1 and Example 2) denote Inter-Sentential code switching,where users are switching from English to Tsonga and vice versa. In Example 1, code switching occurred between the words 'you!' and 'wa', where a user switched from English to Tsonga. Example 2, code switched occurred between the words 'thekisi' and 'I' where a user was switching from Tsonga to English.

Example 3 denotes the Intra-Sentential code-switching where Code-switched occurred in the middle of a sentence. User switched from Tsonga to English and vice versa by including a word 'experience' in the middle of Tsonga text.

Example 4 denotes the Extra-Sentential or tag code-switching where a user switched from Tsonga to English by simply using a phrase 'isn't it?'.

Lastly, Example 5 denotes the code switch at a word level. The word 'robe' is a mixed word, where the first part, 'rob' belongs to English language and the last part, 'e' belongs to Tsonga language.

1) : **I will hit you! Wa ndzi twa?** (I will hit you! do you hear me?)

2) : **Wena khandziya thekisi, I will walk.** (You take a taxi, I will walk.)

3) : **Mina ndzo lava experience ntsena eka ntirho lowu.** (I only want experience in this job)

4) : **ka hisa, isn't it?** (It is hot, isn't it)

5) : Mageza i **robe** xitolo xa ka Mabunda. (Mageza robbed Mabunda's tuck-shop.)

B. Data Filtering

Most of tweets duplicates are filtered out during data extraction. Table I below display the list of keywords with the number of tweets extracted per keyword.

TABLE I
NUMBER OF TWEETS PER KEYWORD

Keyword id	Keyword	keyword in English #	Tweets
1	nwina	you	65
2	vulavula	speak, talk	16
3	ndzi	I	57
4	vona	them, they, view, see	417
5	swona	these	54
6	endla	do, does, make, create, handle, produce	55
7	sweswi	immediate, now	24
8	kombela	ask, please, request	23
9	rhandza	love	33
10	swinene	decent, good	23
11	vutomi	life	354
12	leswi	these, this	43
13	leswo	that	3
14	ndza	I	23
15	rirhandzu	affection, love	34
16	khensa	thank, thanks	37
Total			1261

C. Data Annotation

From the 1261 tweets extracted from Twitter, 589 tweets contain code-switched. The 589 code-switched tweets are combined with the 240 code-switched texts from Tsonga short stories and novel to form a corpus. This corpus consists of 829 sentences. Six classes will be used and tokens (9990 in total) will then be assigned one of these classes. The classes are Tsonga, English, Named Entity, Mixed, Other, and unknown. A native Tsonga speaker who is fluent in both Tsonga and English was then asked to manually annotate the corpus. The classes are fully described below with one example for each class.

Tsonga(TSO) All Tsonga words are tagged Tsonga (TSO)

- **U ndzi xisile u ku u ta ndzi thola.** (You deceived me and said you will hire me)

English(ENG) All English words in the corpus are tagged English ENG

- **Sorry boss**, a ndzi nga ha engeti (Sorry boss, I won't repeat)

Named Entity(NE) All words that belongs to proper nouns, names, places, companies, and organizations, etc. are tagged as Named Entity(NE).

- A mi yi tivi hinkwenu **Irish Coffee**? (Don't you all know Irish Coffee?)

Tsonga-English mixed word(MIX) these are words that contain code switch of Tsonga and English at a word-level. They don't belong to Tsonga or English language.

- Ndzi ta ku **texta** loko ndzi fika ekaya. (I will text you when I get home.)

Other (OTHER) this class includes all words that belongs to onomatopoeia, numbers, hashtags,unclear words, and URLs, etc.

- **Ohhhhh!!** I mali hinkwayo leyi! (Ohhhhh!! Is this real money!)

unknown (UNK) this class includes all words that are unknown, words that belongs to other languages

- My favourite lady misava hinkwayo **jikelele**. (My favourite lady in the whole world jikelele)

Words that are in both Tsonga and English (e.g. "hi", "a", "to", "he") are tagged in relation to words that surround them.

D. Statistics

The corpus have a total of 829 sentences with 9990 words. Table II below shows the mapping of tokens onto the set of six classes (TSO, ENG, NE, MIX, OTHER, and UNK as stated in the previous section) . Tokens labeled TSO dominate the entire dataset with 72.8%¿, followed by the English (ENG) class with 23.1%. The third class (labeled Named Entity (NE)) contains 3.7% . The last two classes (MIX and OTHER) contain less than 1% of the dataset.

TABLE II
TSONGA-ENGLISH DATASET

Class id	Class	Token #	Percentage
1	TSO	5 697	57.03%
2	ENG	3 780	37.84%
3	NE	351	3.51%
4	MIX	30	0.30%
5	OTHER	101	1.01%
6	UNK	31	0.31%
Total		9 990	100%

The dataset is divided into three sets: validation set, training set and testing set. Training and testing sets consist of 85% of the entire dataset. The remaining 15% was reserved for the validation of the models.

IV. EXPERIMENTAL SETUP

A. Models

The total of 4 supervised machine learning models were evaluated in this paper. Models are: Conditional Random Field (CRF), Decision Tree (DT), Multinomial Naive Bayes (NB), and Support Vector Machine (SVM). These models were selected based on their capabilities for word identification and for their popularity, they have been used in multiple text classification tasks.

Decision Tree classifier uses probabilistic decision rules to predicts a class of a word deduced and acquired from given sample data.

Multinomial Naive Bayes emanate from the Bayes theorem. It forecast a class of a word using probabilistic methods. The algorithm returns a tag with a highest value after it has calculated the probability of every tag in given data features. In NB, features are independent [19].

Support Vector Machine (SVM) classifier separate data points by drawing a straight line (hyper-plane) between classes to help classify data points. It uses LSVM algorithm to select a hyper-plane that separates these classes with the largest amount of margin between them.

Conditional Random Field classifier is a probabilistic graphical model which implements dependencies between the predictions. It takes into account contextual information when predicting a label.

B. Features

To predict the language of a word, we create a list of features that are meaningful from words. Table III below presents a list of features extracted from words. All features are associated with a word. The first feature (Feature 1) is a word itself.

Feature 2 gives the length of in a word. This features return the number of characters in a word. The length of a word can give important information about the label of the word. If a word is very long, this may mean it is a URL or onomatopoeia, which can be classified as OTHER.

Feature 3 is a Diphthong (a syllable with a two vowels). English allows syllables with a combination of two vowels. This feature might help the classifier to classify any word that contains diphthong as English, since all words in Tsonga do not contain diphthong. Feature 8 assign 1 to a word with diphthong and zero otherwise.

Feature 4 to feature 10 check the initialization and the termination of a word to help determine if a word belongs to Tsonga or English. Tsonga syllables are of type two, allowing syllables of the form: Consonant (C) followed by Vowel(V) (CV), and V. English is of type four, allowing syllables of the form: CV, C, CVC, and VC [20]. All words from Tsonga end with a vowel, and English words may end with a consonant. Having a feature that checks the last character of a word can help in determining whether a word belongs to Tsonga or English class. English permits complex codas

[20]. This means English words can have a maximum of four consonant segments in a coda, for example, a word 'strength'. However,there are no words in Tsonga that have coda or complex coda. Therefore, words with coda(s) will be assigned to English class. Feature 4 assign the value 1 to a word that ends with a consonant or coda, and zero otherwise.

Feature 11 to Feature 16 use dictionaries to check if the word belong to English or Tsonga. Text transcriptions of the National Centre for Human Language Technology (NCHLT) Speech corpora (Tsonga and English) were used to create lists of words called Tsonga dictionary and English dictionary [21]. A word is checked against these two dictionaries separately. If the word appears in a dictionary, it is assigned a value of 1, and zero otherwise. This is repeated to word n-1, and n-2. These Features help in identifying the language that the word might belong.

TABLE III
WORD FEATURES

Feature ID	Feature Description	F-score Coefficient	P-Value	Rank
1	Word (n)	3841.994615	0.00e+00	1
2	Length of n	28.188433	3.34e-05	12
3	Diphthong of n	21.261730	7.23e-04	14
4	n suffix-1 is char	73.828900	1.63e-14	8
5	Prefix-1 of n	35.663883	1.11e-06	10
6	Prefix-2 of n	691.743923	2.99e-147	4
7	Prefix-3 of n	691.743923	2.99e-147	3
8	Suffix-1 of n	325.467241	3.34e-68	6
9	Suffix-2 of n	373.810804	1.30e-78	5
10	Suffix-3 of n	818.546328	1.12e-174	2
11	n in Tsonga dict.	113.311401	8.17e-23	7
12	n-1 in Tsonga dict.	31.486410	7.51e-06	11
13	n-2 in Tsonga dict.	4.938643	4.23e-01	16
14	n in English dict.	71.571456	4.82e-14	9
15	n-1 in English dict.	28.011325	3.62e-05	13
16	n-2 in English dict.	6.534334	2.58e-01	15

C. Feature analysis

To identify the most relevant and less significance features from the list of features above, we perform univariate statistical tests. These statistical test are used to test the independence of features to the response (H0: Null hypothesis). Features are selected based on their heavily dependent to the response (H1: Alternate hypothesis). The F_1-score and P-value are calculated for every feature. When features are highly independent to the response, the value of F_1-score is smaller. When F_1-score is smaller, we fail to reject the null hypothesis, and conclude that features are independent to the response. However, if the F_1-score is high, we reject the null hypothesis, and conclude that features highly depended on the the response.

In this study, the null hypothesis refers to: no feature have the influence in identifying the labels (TSO, ENG, MIX, NE, OTHER, and UNK). The null hypothesis is rejected if features have influence in identifying the labels. Table III gives all the details of feature analysis and ranking them based on their performance on F_1-score and p-value. The p-value is set to p < 0.01.

Features that have significant influence in identifying the labels of the two language are #1, #10, #7, #6, and #9. These features yield F_1-score of greater than 370 and p-value of less than 0.000001.

The second best performing set of features that have greater influence in identifying the labels are #8, #11, #4, #14, #5,#12, #2, #15, and #3 with F_1-score of greater than 20 and p-value of less than 0.001. As expected, token(n) in Tsonga, token(n) English language dictionary, and end suffix of the token being consonant, have a greater influence in identifying the labels.

The last set of features that have less significance in identifying the labels are #16, and #13 with F_1-score < 10 and p-value > 0.01. These features are discarded in training and testing models.

D. Evaluation and Performance

The dataset is highly imbalanced, more tokens belong to Tsonga class. Accuracy will not be able to provide enough information about the performance of the models. Therefore, we used a score method named balanced F_1-score. This score takes into account Precision and recall. Precision in this context is defined as: considering the tagged words, how many were correctly tagged. Recall is defined as: considering the tagged words, how many words were really correctly tagged. F-score is then calculated using Precision and recall. F_1-score is the harmonic mean of the two.

V. RESULT

All four machine learning models were trained and tested using 85% of the entire dataset in a 3fold cross validation. 15% of the remaining dataset was set aside for validation purposes. The parameter K in cross validation was set to 3 based on the MIX label which had 3 observations on the validation set after the data was split into validation and training sets. Classes were split up equally on the three folds to deal better with the imbalanced class distribution. Precision, recall, and F_1-score are used to measure model performance on automatically allocated labels. The result of 4 machine learning models are shown in Table IV to table IX below.

Labels were trained using the top 5, top 10, and all the features (excluding feature #13 and #16) listed in Table III in section IV.B. All machine learning models yielded zero percent in the UNK label. Therefore, the results of this label are not shown in this paper.The results of the labels NE and OTHER are also not shown in this paper. The results of TSO, ENG, and MIX labels are displayed in Table IV to table IX below.

Table IV and Table V display the results of the Tsonga (TSO) label. The TSO label performs very well in all the feature sets (i.e top 5 features, top 10 features and all the features) and all the models with a precision, recall and F_1-score greater than 80%.

The performance of the English(ENG) label is displayed in Table VI and Table VII. The Decision Tree (DT) outperforms the Multinomial Naive Bayes and Support Vector machine (SVM) when trained on all the features and the top 10

features. The MNB precision dropped from 80% to 77%, and the MNB recall remains constant at 74% as more features are added. This caused the MNB F_1-score to drop from 77% to 75%. The dropping of MNB precision due the addition of more features may be due to the fact that these features contribute less to predicting the language of a token as shown in Table III above. The Conditional Random Field model yields the best results, with precision, recall and F_1-score greater than 94%. These results are not surprising, since CRF takes content information into account, which is forbidden in other models (DT, SVM and MNB).

In Table VIII and Table IX, the results of Tsonga-English mixed(MIX) label are recorded. The DT model perform best in all the feature sets (top 5, top 10 and all features) compared to all other models (SVM, MNB, and CRF). The SVM and CRF models have 0% precision, recall, and F_1-score in all the feature sets.

TABLE IV
RESULTS OF THE MNB AND DT FOR TSO LABEL

TSO	**DT**			**MNB**		
Label	**P**	**R**	F_1	**P**	**R**	F_1
Top 5	0.93	0.89	0.91	0.91	0.81	0.86
Top 10	0.94	0.91	0.93	0.90	0.81	0.85
All Features	0.94	0.90	0.92	0.90	0.81	0.85

TABLE V
RESULTS OF THE SVM AND CRF FOR TSO LABEL

TSO	**SVM**			**CRF**		
Label	**P**	**R**	F_1	**P**	**R**	F_1
Top 5	0.82	0.86	0.84	0.938	0.977	0.957
Top 10	0.82	0.88	0.85	0.942	0.982	0.962
All Features	0.82	0.88	0.85	0.948	0.982	0.965

TABLE VI
RESULTS OF THE NB AND DT FOR ENG LABEL

ENG	**DT**			**MNB**		
Label	**P**	**R**	F_1	**P**	**R**	F_1
Top 5	0.78	0.89	0.83	0.80	0.74	0.77
Top 10	0.81	0.91	0.86	0.78	0.74	0.76
All Features	0.81	0.91	0.86	0.77	0.74	0.75

TABLE VII
RESULTS OF THE SVM AND CRF FOR ENG LABEL

ENG	**SVM**			**CRF**		
Label	**P**	**R**	F_1	**P**	**R**	F_1
Top 5	0.68	0.72	0.70	0.950	0.977	0.964
Top 10	0.72	0.73	0.73	0.959	0.971	0.965
All Features	0.72	0.73	0.72	0.958	0.971	0.964

TABLE VIII
RESULTS OF THE NB AND DT FOR MIX LABEL

MIX	**DT**			**MNB**		
Label	**P**	**R**	F_1	**P**	**R**	F_1
Top 5	0.57	0.14	0.23	0.06	0.57	0.11
Top 10	0.67	0.21	0.32	0.08	0.57	0.14
All Features	0.38	0.21	0.27	0.07	0.54	0.13

TABLE IX
RESULTS OF THE SVM AND CRF FOR MIX LABEL

MIX	**SVM**			**CRF**		
Label	**P**	**R**	F_1	**P**	**R**	F_1
Top 5	0.00	0.00	0.00	0.00	0.00	0.00
Top 10	0.00	0.00	0.00	0.00	0.00	0.00
All Features	0.00	0.00	0.00	0.00	0.00	0.00

VI. DISCUSSION OF RESULTS

The Decision Tree perform very well when trained on the first two feature sets (best 5 and best 10) in labels TSO, ENG, and MIX. However, when trained on all features, the results (precision, recall, and F_1-score either drop or remain the same.

The CRF gives best performance when identifying TSO and ENG labels when trained on all feature sets. However, it fails to identify the MIX label in all feature sets.

The Conditional Random Field is the best model in identifying TSO and ENG labels, followed by Decision Tree model. The third model to yield great results in identifying TSO and ENG labels is MNB. The SVM is the least model in identifying TSO and ENG labels is MNB.

Supervised machine learning models provide promising results in automatic language identification. If more features can be added and the dataset can be increased to deal better with all classes. These models can yield much better results for Tsonga-English language pair.

VII. SYSTEM DESIGN

In this section, the best performing model is used to build the automatic language identification interfaces for paired Tsonga and English texts. Conditional Random Field performed best on identifying TSO, ENG labels as seen in the previous section.

Gradio is used to build the interfaces for our model. Gradio open-source Python package that generates visual interfaces for machine learning models [22]. Our interface is divided into two sections. The first section is where the user is asked to enter sentence. The second part returns the sentence tagged as output.

The sentence entered by the user is passed to the model for tagging. The model process the sentence entered by the user and automatically tag it using TSO, ENG, NE, MIX, OTHER and UNK labels. The tagged sentence is then returned to the user as an output.

The remaining set of tweets (not tagged) after data annotation is used in these examples. Other examples of code-switched texts are from Facebook posts, where Tsonga and English code-switched is observed. These examples were carefully selected to cover almost all types of code-switching.

In Fig. 1. we see the inter-sentential and intra-sentential code switching in one sentence. All words are properly tagged with TSO, ENG, and OTHER labels. This is not surprising, since our model was the best model in these labels.

The performance outcomes yielded by the CRF model in tagging sentences with labels is very good in inter-sentential, intra-sentential code switching, extra-sentential. This classifier does not tag tokens that belong to MIX label, since it produced 0% precision, recall and F_1-score in MIX label in section VI above.

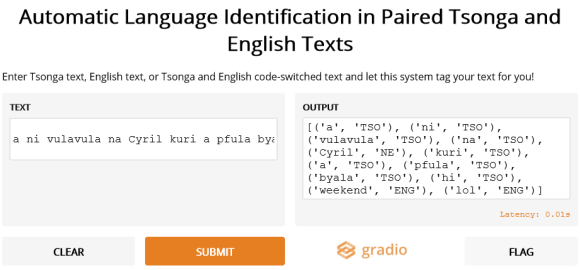

Fig. 1. Inter-Sentential code switching Example

VIII. Conclusion and Future Work

The task of language identification is a constrain in many Natural Language Processing tasks. The results of this work will be used in Tsonga-English corpus creation, corpus annotation, and will be used together with the code-switching detection to fully automate the task of prediction in Tsonga-English language pair.

In this paper, we presented exploratory experiments and results of automatic language identification at a word-level in paired Tsonga and English texts. First, we collected from Twitter, and from Tsonga short stories and novels. We then annotated the data corpus manually. In this paper, six labels were used to identify Tsonga, English, Named Entity, Tsonga and English mixed, other, and unknown. Four supervised machine learning models were evaluated, and 14 selected from 16 features to train the supervised machine learning models. The CRF model performed best on TSO and ENG classes compared to other models. The Decision Tree perform very well when trained on the first two feature sets (best 5 and best 10) in labels TSO, ENG, and MIX. Moreover, all models were unable to identify the UNK class, F_1-score of 0%. The best performing model (CRF) was used to build the automatic language identification interfaces for paired Tsonga and English texts.

Future work will focus on adding more features to the dataset in other to make the classifiers more robust. The automatic language identification will be used together with a code-switching detection task in other to fully automate the prediction task.

Acknowledgement.

I would like to express my special thanks of gratitude to the Telkom Centre of Excellence (CoE) at the University of Limpopo who gave me the golden opportunity to carry out this research work. I would also like to thank my supervisor and core-supervisor for a continuous support and commitment towards the success of this research work.

References

[1] S. Sitaram, K. Chandu, S. Rallabandi, and A. Black, "A survey of code-switched speech and language processing," 03 2019.
[2] M. Aulia and M. Laksman-Huntley, *Indonesian-English Code-switching on Social Media*, 12 2017, pp. 791–796.
[3] Q. Wang, E. Yılmaz, A. Derinel, and H. Li, "Code-switching detection using asr-generated language posteriors," 09 2019, pp. 3740–3744.
[4] T. Jauhiainen, M. Lui, M. Zampieri, T. Baldwin, and K. Lindén, "Automatic language identification in texts: A survey," *Journal of Artificial Intelligence Research*, vol. 65, 04 2018.
[5] R. Lins and P. Gonçalves Jr, "Automatic language identification of written texts," 01 2004, pp. 1128–1133.
[6] M. Adikari, A. Perera, and W. Wiharagoda, "Spoken language identification," Ph.D. dissertation, 07 2013.
[7] D. Nguyen and A. S. Doğruöz, "Word level language identification in online multilingual communication," in *Proceedings of The 2013 Conference on Empirical Methods in Natural Language Processing*. Seattle, Washington, USA: Association for Computational Linguistics, Oct. 2013, pp. 857–862. [Online]. Available: https://www.aclweb.org/anthology/D13-1084
[8] K. Hoxha and A. Baxhaku, "Albanian language identification in text documents," 01 2019.
[9] M. Dahiya, "Word-level language identification in bilingual text and back-transliteration," *International Journal of Advanced Research in Computer Engineering Technology*, vol. 6, pp. 887–889, 06 2017.
[10] P. Mcnamee, "Language identification: A solved problem suitable for undergraduate instruction," *Journal of Computing Sciences in Colleges*, vol. 20, pp. 94–101, 01 2005.
[11] N. Akosu and A. Selamat, "Word-length algorithm for language identification of under-resourced languages," *Journal of King Saud University - Computer and Information Sciences*, vol. 28, 09 2015.
[12] T. Baldwin and M. Lui, "Language identification: The long and the short of the matter," in *Human Language Technologies: The 2010 Annual Conference of the North American Chapter of the Association for Computational Linguistics*. Los Angeles, California: Association for Computational Linguistics, Jun. 2010, pp. 229–237. [Online]. Available: https://www.aclweb.org/anthology/N10-1027
[13] T. Gottron and N. Lipka, "A comparison of language identification approaches on short, query-style texts," vol. 5993, 03 2010, pp. 611–614.
[14] N. Dongen, "Analysis and prediction of dutch-english code-switching in dutch social media messages," *Master's Thesis, Universiteit Van Amsterdam, Amsterdam, Netherlands*, 2017.
[15] J. Project, "The tsonga people group is reported in 4 countries." [Online]. Available: https://joshuaproject.net/people_groups/15596
[16] S. S. Africa, "Census 2011: Census in brief, statistics south africa," 2011.
[17] M. T. Babane and M. T. Chauke, "Xitsonga in language shift: A sociolinguistic approach," *Journal of Social Sciences*, vol. 47, no. 1, pp. 49–57, 2016. [Online]. Available: https://doi.org/10.1080/09718923.2016.11893543
[18] H. D. Baloyi, "The use of code-switching from xitsonga to english as a conversational strategy," Ph.D. dissertation, 2010.
[19] Shriram, "Multinomial naive bayes explained: Function, advantages disadvantages, applications in 2021," 01 2021. [Online]. Available: https://www.upgrad.com/blog/multinomial-naive-bayes-explained/
[20] A. Vratsanos and M. Kadenge, "Hiatus resolution in xitsonga," *STELLENBOSCH PAPERS IN LINGUISTICS PLUS*, vol. 52, 04 2017.
[21] M. Davel, E. Barnard, C. Van Heerden, F. Wet, and J. Badenhorst, "The nchlt speech corpus of the south african languages," 05 2014.
[22] A. Abid, A. Abdalla, A. Abid, D. Khan, A. Alfozan, and J. Zou, "Gradio: Hassle-free sharing and testing of ml models in the wild," *arXiv preprint arXiv:1906.02569*, 2019.

Ntiyiso Baloyi is currently a second-year student of MSc in Computer Science at the University of Limpopo (UL). His research interests are Machine Learning, Speech and Language Processing.

Madimatja Jonas Manamela is a Senior Lecturer in the Department of Computer Science and Head of the CoE for Speech Technology at the UL. His research interests are Speech Processing Technology, Information and Communication Technology for Development and Machine Learning

Thipe Modipa Thipe Modipa is a Senior Lecturer in the Department of Computer Science and Programme Manager for the Centre of Artificial Intelligence Research at the UL. His research interests are Speech Recognition, Data Science and Artificial Intelligence.

Security for networked smart healthcare systems: A systematic review

Nyamwezi Parfaite Ndarhwa[1], Bessie Malila[2]

[1,2]*Division of Biomedical Engineering, University of Cape Town, 7th Floor Anatomy Building, Observatory, Cape Town*

[1]ndrnya002@myuct.ac.za
[2]bessie.malila@uct.ac.za

Abstract— **Smart healthcare systems are connected to the Internet and use mobile platforms which allow them to utilize technologies such as wearable devices and Internet of Things (IoT) to dynamically connect people to health services and provide access to information related to healthcare. To secure and protect the sensitive medical information, several mitigation measures have been implemented and others have been proposed. Examples include data encryption and biometrics. Emerging security technologies such as Blockchain and X-Road, are expected to address the distributed and decentralized architectures of smart healthcare systems. This study reviewed studies that have addressed end-to-end security risks in smart healthcare systems. Most studies focused on the protection of patient's data from attackers who may cause harm. However, there is lack of studies that focus on protection data in cases where the intruder has already accessed the system.**

Keywords—**5G, security, smart healthcare, Blockchain, X-Road.**

I. INTRODUCTION

Smart healthcare systems are interconnected infrastructures comprising medical devices, health systems, and embedded technologies that are used for monitoring patients and deliver healthcare services [1]. Smart healthcare systems are set to transform healthcare, for example, through the use of applications installed on mobile devices which can be equipped with sensors for collecting physiological signals and health data. Smart healthcare services include teleconsultation, delivery of health information to practitioners, patients and healthcare service providers such as pharmacies, insurers, and researchers; remote real-time monitoring of vital signs; and training and collaboration of healthcare workers [2-4].

Mobile networks constitute one of the cornerstones of smart healthcare systems. Smart healthcare applications are installed on devices that use mobile networks. Mobile networks have experienced exponential growth over the years, the current fifth-generation networks (5G), will further drive the increased adoption of smart healthcare systems [5].

Certain security measures should be implemented to mitigate the security risks associated with connected health systems [6]. Security requirements for connected smart healthcare systems can be broken down into three key components, i.e. confidentiality, integrity, and availability. Confidentiality refers to the protection of data from being exposed to unauthorized users; data integrity refers to different measures taken to protect the content of the message and its accuracy; and availability refers to the accessibility of information by authorized users [6-8]. Furthermore, to guarantee the effectiveness of these security components, two additional features are required, namely authentication, which verifies the identity of the user, and authorization, which ensures that the user has the right to perform the tasks they wish to perform within the system [7]. To secure and protect sensitive medical information in connected healthcare systems, several mitigation measures have been implemented and others have been proposed. Examples include data encryption, use of cryptographic keys, biometrics and implementation of system-wide frameworks based on technologies such as Blockchain and X-Road [9-11]. These security measures are being used in systems that are not 5G-based. The 5G architecture is designed to be widely distributed and decentralized, allowing the public to have more access to the system through the use of cloud-based storage and processing servers, sensors, and smart phones[12]. 5G systems are expected to be the main drivers for the adoption of smart healthcare systems, thus enabling distributed and decentralised smart healthcare system architectures requiring new security solutions such as Blockchain and X-Road whose architectures are decentralized and distributed.

Although these security measures have shown potential to improve the delivery of smart healthcare by ensuring the security of data, there are still many security risks that cause vulnerabilities in smart healthcare systems. These include denial of service attacks performed on processing and storage servers, reverse engineering attacks[13] - a process by which a device is deconstructed to reverse its initial design, bots - a malicious software installed on mobile or medical devices for stealing medical information, eavesdropping on wireless or wired communication links and unauthorized access to data[14]. Attackers target vulnerabilities in these systems, and the attacks on health systems can have serious physical, social, and economic effects, and can potentially result in patient deaths [15].

This study aims to systematically review literature about security issues in emerging smart healthcare systems, with a focus on the security requirements, potential security risks, the measures currently being proposed to mitigate these risks, and the effectiveness of these measures. Preliminary results of the systematic literature review are presented.

A thorough examination of recent research was piloted, and we found that, Hameed et al. [16] conducted a systematic review on the security and privacy of Internet of Medical Things (IoMT) and their respective solutions by using machine learning techniques. Authors found that Machine learning techniques have been considerably deployed for device and network layer security; however, most studies barely represented IoMT systems.

Similarly, Liao et al. [17] performed a systematic review to analyse the security of IoT devices using mobile computing. Their systematic review only focussed on mobile computing particularly smart phones and therefore disregarded all other IoT based devices such as medical devices.

The main motivation that led to pursue this research was due to the strong security need for smart healthcare systems which was encouraged by the above gaps found in recent related work. Therefore, this necessitates for a systematic review to be conducted on studies that focuses on the security and privacy of smart healthcare systems which encompasses the Internet of medical things.

The main research question for the systematic review is: what are the security issues related to the acquisition, transmission, storage and sharing of patient health data in in Smart Healthcare systems? The systematic reviews aims to answer the following sub-questions: (a) What are the security requirements for secure acquisition, transmission, storage and sharing of patient health data in networked Smart Healthcare systems, (b) What are the security risks during the acquisition, transmission, storage and sharing of patient health data in networked Smart Healthcare systems, (c) What solutions have been proposed in literature to mitigate these security risks (d) How effective are the proposed security solutions.

II. METHODOLOGY

The review strategy used in this systematic review is the PICO, i.e., problem, intervention, comparator and outcome (PICO) systematic review search strategy. The problem addressed in this study is how to ensure the security and privacy of patient data smart healthcare systems. The intervention is the security measures that have been proposed to address the problem. The comparator is not applicable for this systematic review because this review focuses on the security measures available and in this case the comparator intervention is non-existent. The outcome is improved security in smart healthcare systems for patient data during acquisition, storage and while in transit.

The strategy included assessment of the security requirements for smart healthcare systems and the security measures that have been proposed to ensure the privacy and security of health data. The study also assessed the effectiveness of the proposed security measures in improving the security of patient data sharing, storage, and access. The systematic review has been registered with PROSPERO (the International Prospective Register of Systematic Reviews). This study has also adhered to PRISMA guidelines, an evidence-based set of items that aim to assist researchers improve the reporting of systematic reviews and meta-analyses [18]. PRISMA focuses on ways in which authors can ensure the complete and transparent reporting of systematic review studies [19]. The study is not restricted to any geographical setting.

The process and results of the study selection process was supported by the PRISMA flowchart shown in Fig. 1. The systematic review involved an exhaustive search of databases including Scopus, PubMed, Web of Science, Medline, CINAHL, Ebscohost and the Cochrane Library. Throughout the search only 3 databases yield results: Scopus, Web of science and Medline. The key search words and was carried out to identify studies that addressed the problem of security in smart healthcare systems and proposed solutions. The process of study selection was conducted with the use of the inclusion and exclusion criteria as shown in Table 1.

TABLE I
INCLUSION AND EXCLUSION CRITERIA TABLE

Characteristic	Inclusion Criteria	Exclusion Criteria
Problem	Articles on security in smart healthcare systems for patient data sharing, storage, acquisition and access control.	Articles that do not focus on health-related topics are excluded.
Intervention	Studies focusing on the security mechanisms used to mitigate against data breaches in smart healthcare systems.	Articles that do not demonstrate data protection during acquisition, transmission, storage, access and sharing are excluded.
Outcome	Studies that show improved security of smart healthcare systems for patient data sharing, storage, sharing and access control.	Studies that did not demonstrate end-to-end security in smart healthcare systems data sharing, storage and access control were excluded.

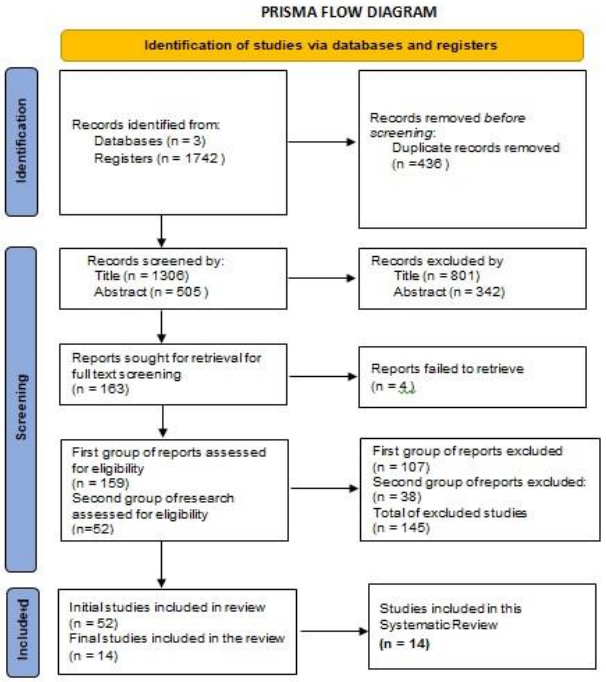

Figure 1: The PRISMA flowchart

III. FINDINGS AND RESULTS

Studies were screened for relevance using the study titles and abstracts, and consideration was given only to studies that addressed the problem of security in smart healthcare systems. The Final screening was carried out by reading full texts of the studies, and their relevance was defined by the reported PICO characteristics in each study. Excluded articles included those articles that did not focus on health-related topics, and articles that did not demonstrate end-to-end security in smart healthcare.

This systematic review identified a total of 1742 records through an exhaustive and comprehensive search from three electronic databases. Before performing screening, 436 records were identified as duplicates and they were removed. Using titles and abstracts, the remaining 1306 studies (after removing duplicates) were screened focusing on studies relating to the security of smart healthcare systems. From these 1306 articles, 801 records were excluded as they did not report security or smart healthcare system in their title, leaving a total of 505 articles. These 505 were further

screened based on their abstracts and 342 records were excluded after abstract screening leaving a total of 163 articles. Of the remaining 163 full texts, 4 records could not be found in all databases, at the University of Cape Town library, or even after contact the authors who were unreachable. Hence the remaining 159 full text articles were screened for eligibility. Of these 159 potentially eligible studies, 107 were initially excluded based on publication type such as analysis papers; and study focus such as studies focusing on the design of a system rather than its security. This initially led to 52 studies being eligible for inclusion in the study.

After further analysis by both reviewers, the remaining 52 studies were reassessed to focus the scope of this systematic review on end-to-end security. In order to be considered for inclusion, these studies needed to focus on improved end-to-end security in smart healthcare systems for patient data sharing, storage and access control. This led to the exclusion of 38 studies which were mostly focussing solely on wireless body area network as well as authentication and disregarded all other security requirements, i.e. these studies were not focussed on end-to-end security. A total of 14 studies were included in this systematic review.

1) Analysis based on research questions

The studies were classified into different subsections and analysed while trying to answer the research questions as follow:

a) What are the security requirements for networked Smart Healthcare systems?

First analysis was conducted based on security requirements stated in the studies. This question intended to provide a solution towards identifying different security requirements that are relevant for the full functionality of smart healthcare systems. Studies reported a number of security requirements that the proposed smart healthcare systems need to ensure the security of patient data. Studies reported the same security requirements i.e. confidentiality, integrity, availability, authorisation and authentication. These security requirements guide innovators when designing and implementing security measures that can provide robustness against data breaches.

Some examples of implemented security measures to meet the confidentiality security requirement were user registration, login and authentication phase to verify the user's identity thus ensuring that only authorised users have access to the system (3) (9) (11) (12) (13) (14). In some of the proposed solutions (1) (5) (7) (8) (10); the system needed to verify and validate the collected raw data and compare it to encrypted data stored in the cloud and the system had to follow some security procedures such as a mutual authentication between users and sensors according to secret keys generated to ensure the security, integrity and accessibility of data in the system Other studies have demonstrated that through the implementation of authentication schemes, several security features are enabled between patients, devices and healthcare providers to allow resilience to possible attacks by integrating anonymous authentication services (2) (4) (6). Likewise, blockchain technology can be used in smart healthcare systems to provide the protection of medical data and guarantees user authentication, integrity and confidentiality. It also ensures the protection, availability and allows data integrity preservation as blockchain keeps record of system access and user accountability. Hence the need for compatibility between the healthcare devices with the block chain technology in order to maintain the security of medical data (4).

b) What are the security risks in networked Smart Healthcare systems?

This question intended to identify reported security risks which could potentially result in the violation of the security of patient data.

The main security risk reported by several studies is the risk to confidentiality of data. These included eavesdropping in wireless communication mediums, and impersonation attacks. Secondly, the risk to the integrity of data was reported. These included data fabrication attack and message modification attack. i.e. modification of a patient's data and replacing it with incorrect data. Thirdly, other security risks reported were threat to the availability of data through denial-of-service attack (3) (9) (11) (12) (13) (14).

These reported security risks have the potential to cause harm to the patient, the data, and the healthcare system as a whole. A number of studies reported potential of security risks which are different attacks that could be launched to cause harm to patient's data, network, or the healthcare system such as authentication vulnerabilities, data security, access and privacy issues, data sharing and transmission issues as well as malware attacks (1) (5) (7) (8) (10). An example is when there is an unauthorised access to patient's data which happens when the attacker attempts to modify patient's data and replaces it with incorrect data. Consequently, incorrect data could lead to misdiagnosis which may affect patient health (10).

c) What solutions have been proposed in literature to mitigate these security risks?

Thirdly, studies reported different types of mitigation measures. For studies that focused on the security issues, such as end-to-end security as well as access control in EHR integrated into IoT; Authors reported solutions such as a security framework used for isolation of patient health data using network slicing techniques and user authentication (3). An end-to-end security scheme for IoT healthcare was proposed in order to provide end-to-end security from data acquisition, transmission access on servers and sharing of data (9). Three-tier hierarchical m-health system architecture has been proposed. It has a sensor network tier to collect patient's vital signs, a mobile computing network to process and route the data and a back-end network tier to analyse patient's medical data (11). Additionally, Authors proposed a healthcare system framework which is designed for data collection, data storage and data transmission through a wireless network infrastructure and published using a security gateway (12). A secure and privacy-preserving protocol for health data processing in mobile healthcare network is proposed for patient's data privacy (13). Cloud-based encryption architecture is proposed, it uses three types of encryption techniques: Advanced data encryption, Attribute-based encryption as well as proven data possession (14).

Moreover, studies that focused on data integrity and privacy of EHRs reported solutions such an architecture which combines biometric-based blockchain technology with the EHR system (2); A security model is proposed that allows protection of medical data using blockchain technology (4); as well as an innovative user cantered data sharing solution using blockchain technology (6).

Furthermore, studies focused on data sharing, exchange and transmission over the network in smart healthcare systems reported solutions such as symmetric encryption keys to encrypt the wireless communication from medical devices by avoiding wireless key exchange (1); An efficient data sharing scheme is proposed (MedChain). This Scheme uses block chain technology, peer-to-peer network and digests chain to overcome efficiency issues (5). Additionally, (7) proposed a trustworthy access control mechanism is achieved with the use of smart contracts to achieve security of EHR amongst patients and healthcare providers. A secure data transmission method using a complex encryption transmitting healthcare related data over the network by devices with resource constraint, as well as prevention of EHR modification by a third party (8); and finally, (10) an IoT-based smart healthcare security model framework is proposed to help design security areas for IoT services.

d) How effective are the proposed security solutions?

Included studies have demonstrated the effectiveness of the proposed mitigation measures in securing smart healthcare systems. These measures have shown potential to mitigate attacks in the systems and provide security protection. The effectiveness is guaranteed through the provision of security to patient's data and devices as well as the hospital devices. Some examples of reported the effectiveness are described below.

An end-to-end security as well as access control in EHR integrated into IoT reported the effectiveness as follows: The proposed security framework is shown to be effective by isolating the health traffic from general traffic. This is achieved through the implementation of a healthcare network slice reserved for caregivers and healthcare personnel. As well as a smart home network slice that provides connectivity to the elderly home (3). Another proposed security framework is shown to be effective by providing 97% more energy efficiency and was 10% faster. Authors also reported that the session redemption approach has 8.1% and 98.7% improvement on client-side and processing time respectively (9). Furthermore (11) reported that the system architecture has demonstrated its effectiveness using stochastic geometry, by showing how the transmitter is able to communicate with its neighbours with a higher average secrecy probability without the need of secure protocols such as RF Fingerprinting. The transmitter was able to extend its secure communication range by learning user's behaviour and trustworthiness. Also, being equipped with information on possible eavesdropping attack, the system is able to better perform in terms of secrecy and latency. Likewise, (12) proposed a healthcare system framework and reported its effectiveness in three areas. Namely, it uses easily deployed and low-cost wireless sensor networks, addresses the issue of achieving a direct communication between user's mobile and embedded medical devices, and also, it allows the enforcement of privacy preserving strategies and attains satisfactory performance. Hence, the proposed framework provides a significant component of the informationization of medical industries. Alex, et al. (13) reported that the proposed security framework was effective by through a comparison to Meshram's scheme described in the study; in terms of resource consumed and computational energy conception needed for access check depending on the number of users. Authors reported that as the number of helpers increases in the system, the required resources in requesting user's smart devices are reduced. Hence, the proposed protocol drastically reduces user's resource consumption and therefore decreases the resource conception ratio. And finally, (14) reported that the proposed security measure was shown to be effective by its ability to check and validate whether data is correctly encrypted and stored in the system. This is done by comparing the encrypted data stored in the cloud to the raw data input using advanced encryption methods such as attribute-based encryption, advanced encryption standards and provable data possession method. Authors concluded that this has resulted in an increase in data security, privacy and integrity; security and lower processing power.

Additionally, studies that focused on data integrity and privacy of EHRs such as (2), reported the effectiveness by comparing the use of secret and private keys to the proposed use of biometric based mechanism such as fingerprints. This proposed mechanism allows reduction in computational overhead required from patients, compared to the use of secret keys. The use of fingerprints also shows effectiveness in providing better audit logs for activities in the system and therefore analyses and prevents unauthorized activities; and provides a much more secure exchange and synchronization of the HER among healthcare providers. Also, (4) the security model security model is shown to be effective by evaluating the system performance based on its scalability and efficiency in data processing. The results shows that with a range of 10 to 10 000 requests, the system showed the average of 4.27 seconds response time with 10 0000 requests simultaneously. Also, regarding user permission grant/denial, the system responded with an average of 4.13 seconds response time per 10 000 user request simultaneously (grant) and 2.35 seconds response time (denial). Authors concluded that with these results, users can effectively manage the access to their data, as the system has demonstrated the ability to support high load of requests. This allows the system to perform transactions in a very effective way by granting and denying permissions to the rest of the participants. Then (6) demonstrated the effectiveness of the proposed solution by measuring its performance in terms of scalability and efficiency. With the focus on proof generation, data validation and data integrity, the system tested a number of concurrent records and concluded that it could handle s large data set at low latency. This indicates the effectiveness in scalability and efficiency of data.

Other studies focused on data sharing, exchange and transmission over the network in smart healthcare systems such as (1); reported that the proposed security framework is shown to be effective by analysing and testing the random

key generation. The key generation is tested based on two points. Namely, the stop-time in the system which is unknown to the adversary, and the number of iterations needed to produce the key. This leads to obtaining different key values resulting to a drastic sequence change of the generated key. Authors demonstrated that the security and randomness in the generated keys is achieved by using the proposed encryption technique. Hence the security of the encrypted message that is communicated between devices is achieved. (5) Showed how the proposed scheme MedChain was effective by analysing the system performance compared to existing blockchain-based solutions in terms of communication and storage overhead (5). The results show that in terms of the communication overhead in data access this approach facilitates integrity check in data access since it encodes the digest of data stream into a digest chain from blockchain and this allows validation of data integrity. Similarly, in terms of storage overhead, existing schemes stores all the data on the blockchain. However, for MedChain only stores the fingerprints and the rest of the data is stored on the directory servers which are mutable and the data can be removed from the servers only when the session is revoked. Hence MedChain guarantees less storage overhead.

Furthermore, (7) showed that the proposed system is shown to be effective by the author's performance analysis. Authors discuss that the proposed system is designed with its ability to provide flexibility as it is deployed on mobile platform and can be accessible to any authorize user with a smartphone. Additionally, authors measure the effectiveness of this system by its ability to provide high level of availability of health data anytime anywhere. They conclude that it uses a decentralized storage system which avoids single point of failure and also guarantees high security of data, integrity and privacy with the use of blockchain and smart contracts. (8) Measure the effectiveness by analysing the two-level encryption framework (Strong encryption done on the cloud and a light weight encryption done by the user) is shown to be effective by encrypting the whole image before sending it to the cloud, rather than the encryption of a portion of the image. This way, a lesser encryption time is achieved as compared to previous scheme such as the Saijjad scheme. To measure the effectiveness of the proposed framework in comparison to the Saijjad scheme, values of the encrypted data such as (Size of the compressed image, Pick signal ration, similarity index between old and new image and the number of changing pixel rate NPCR) should be as low as possible. Authors concluded that smaller values on the encrypted data was achieved, For example, I the case of medical image 1, Image dimensions were 256x256, when encrypting with the Saijjad scheme, the NPCR was 0.5784 and the proposed method yield the NCPCR of 0.6404. This method allows the preservation of the authenticity of the image as well as a lower encryption time, thus validating the effectiveness of the proposed encryption scheme. Finally, (10) demonstrated how the proposed security framework is shown to be effective by comparing the CPU and Memory performance with variation in the number of hosts in a network. The test results show that when the number of hosts is small, the CPU and Memory usage is high. However, as the number of hosts increases, the CPU and Memory usage does not increase linearly, but shows a small increase. This illustrated in the graph as follows: for memory usage, single system usage for 3 hosts is 12% and 11%; and for 8 hosts and 30% for 22% for distributed system. For CPU usage the figures are 6% and 7.8% for 3 hosts and 14% and 10% for 8 hosts.

IV. DISCUSSION AND CONCLUSIONS

The included articles described the smart healthcare system and identified the security requirements, security risks and solutions to mitigate the risks. Each study also explained the effectiveness of their proposed security solution. However, it was evident that some studies briefly reported the effectiveness of their proposed solution and this was considered poor reporting. Of the 14 studies included in the final selection, most of them focused on detecting security risks that have potential to cause harm to user authorization, data authentication, confidentiality, integrity and availability. However, while doing the study selection, it was evident that most of the excluded studies only focussed on user authorisation and authentication, hence they were excluded because they paid no attention to the rest of the security data journey which is securing data at the acquisition device, over the network while the data is being transferred as well as ensure the security of data at the storage device. Most studies have proposed measures such as biometrics, data encryption and blockchain technology to address security threats within the smart healthcare systems. These proposed measures have the potential to transform the security of smart healthcare systems and therefore to providing security of data from the point of acquisition, while being transferred through mobile networks, and during storage.

The limitation of this research is that it was carried upon a few selected online databases (3) namely Scopus, Medline and Web of Science due to other databases yielding result of 0 studies after the search queries were performed. Additionally, A few articles (4) could not be retrieved for full text analysis.

It is evident that the issue of securing data throughout its process from the acquisition, while being transferred through the network as well as at the storage has been resolved by providing end-to-end security of data. Studies have achieved this security by ensuring adherence to the proposed mechanisms. For example, by using the biometrics (fingerprints) mechanism for access control on the EHR, this eliminates the risk of permanent loss of identity and access control to EHRs and further assures patients data privacy (13). Another example is, with the use of a physical layer security scheme that was proposed for mobile computing tier in m-Health, patients medical data can be transferred with secrecy and delay constraints can be overcome (11). Also, by using MedChain, users exchange data through the blockchain technology which allows transaction of data without the need for a decentralized third party. This scheme is proven to provide efficient data sharing without any security compromise (5).

The results of the study are set to inform security system designers on the best approaches and policies for developing security mechanisms in smart healthcare systems. The results may also be useful to network operators in showing the potential risks to health information as it traverses mobile networks. The results could further be useful to conscientise

departments of health in the potential risks of publicly shared health data, possible mitigation measures, and potential solutions. Hence, this will positively impact the security for smart healthcare system as whole.

All the included studies reported the effectiveness of their mitigation measures against security risks in smart healthcare systems. These studies focused on the protection of patent's data from attackers who may cause harm. However, there is lack of studies that focuses on protection data in cases where the intruder has already accessed the system. This leaves a gap for researchers to consider exploring the area of security of healthcare systems by detecting the attacker who has already gained access into the system as well as the protection of data after intrusion. Recommendations for future research and open research issues include the need for future studies to focus on intrusion detection within smart healthcare systems.

ACKNOWLEDGMENT

This research is supported in party by the South African Research Chairs Initiative of the Department of Science and Technology and the National Research Foundation of South Africa (Grant No. 98788), Telkom South Africa via the Telkom Centre of Excellence (CoE) in Broadband Networks at the University of Cape Town and a grant from Carnegie Corporation of New York. The statements made and views expressed are solely the responsibility of the authors.

REFERENCES

[1]. Tian, S., et al., *Smart healthcare: making medical care more intelligent.* Global Health Journal, 2019. **3(3)**(3): p. 62-65.

[2]. Jagadeeswari, V., et al., *A study on medical Internet of Things and Big Data in personalized healthcare system.* Health Information Science and Systems, 2018. **6(1)**(1): p. 14.

[3]. Luna, R., et al., *Cyber threats to health information systems: A systematic review*. Technology and Health Care, 2016. **24(1)**(1): p. 1-9.

[4]. Ahmed, I., et al., *Wireless Communications for the Hospital of the Future: Requirements, Challenges and Solutions.* International Journal of Wireless Information Networks, 2020. **27**(1): p. 4-17.

[5]. Samaoui, S., et al., *Wireless and mobile technologies and protocols and their performance evaluation*, in *Modeling and Simulation of Computer Networks and Systems: Methodologies and Applications*. 2015. p. 3-32.

[6]. Al-Janabi, S., et al., *Survey of main challenges (security and privacy) in wireless body area networks for healthcare applications.* Egyptian Informatics Journal, 2017. **18(2)**(2): p. 113-122.

[7]. Crosby, G., *Wireless Body Area Networks for Healthcare: A Survey.* International Journal of Ad hoc, Sensor & Ubiquitous Computing, 2012. **3(3)**(3): p. 1-26.

[8]. Tan, C.C., et al. *Body sensor network security: An identity-based cryptography approach*. in *WiSec'08: Proceedings of the 1st ACM Conference on Wireless Network Security*. 2008.

[9]. Ramli, S.N., et al. *A biometric-based security for data authentication in Wireless Body Area Network (WBAN)*. in *International Conference on Advanced Communication Technology, ICACT*. 2013.

[10]. Memon, Q.A. and A.F. Mustafa, *Exploring mobile health in a private online social network.* International Journal of Electronic Healthcare, 2015. **8(1)**(1): p. 51-75.

[11]. Malila, B. and T.E.M. Mutsvangwa, *Security architecture for a 5G mHealth system.* Global Health Innovation, 2019. **2(1)**(1): p. 1.

[12]. Mwangama, J., et al., *What can 5G do for healthcare in Africa?* Nature Electronics, 2020. **3(1)**(1): p. 7-9.

[13]. Imane, S., M. Tomader, and H. Nabil. *Comparison between CoAP and MQTT in Smart Healthcare and Some Threats*. in *International Symposium on Advanced Electrical and Communication Technologies, ISAECT 2018 - Proceedings*. 2019.

[14]. Kumar, P., et al. *Addressing a secure session-key scheme for mobility supported e-Healthcare systems*. in *International Conference on Advanced Communication Technology, ICACT*. 2014.

[15]. Sridharan, K., *Security Vulnerabilities In Wireless Sensor Networks: A Survey*. Journal of Information Assurance and Security, 2010. **5(1)**: p. 31-44.

[16]. Hameed, S.S., et al., *A systematic review of security and privacy issues in the internet of medical things; the role of machine learning approaches.* PeerJ Computer Science, 2021. **7**: p. 1-44.

[17]. Liao, B., et al., *Security Analysis of IoT Devices by Using Mobile Computing: A Systematic Literature Review*. IEEE Access, 2020. **8**: p. 120331-120350.

[18]. Moher, D., et al., *Preferred Reporting Items for Systematic Reviews and Meta-Analyses: The PRISMA Statement.* PLOS Medicine, 2009. **6**(7): p. e1000097.

[19]. Liberati, A., et al., *The PRISMA Statement for Reporting Systematic Reviews and Meta-Analyses of Studies That Evaluate Health Care Interventions: Explanation and Elaboration.* PLoS Medicine, 2009. **6(7)**(7): p. 1000100.

Nyamwezi Parfaite Ndarwha recieved her BTech in Information and Communication Technology at Capetown University of Technology. She is an MPhil student in Health Innovation at the University of Cape Town.

Bessie Malila is a junior research fellow in Biomedical Engineering at the University Cape Town. She holds a PhD, and MSc in Telecommunications from the University of Cape Town and BSc in Electrical and Electronic Engineering from the University of Zimbabwe. Her research interests include security in in digital health systems and application of 5G and beyond technologies in digital health.

Bootstrapping the Development of Services for Wireless Community Networks

Keegan White*, David Johnson*, Melissa Densmore*, Hafeni Mthoko†
*Department of Computer Science, University of Cape Town, South Africa
[1]keeganthomaswhite@gmail.com
[2]david.lloyd.johnson@gmail.com
[3]melissa.densmore@uct.ac.za
†Office of the Pro-Vice Chancellor: Research, Innovation and Development, University of Namibia, Namibia
[4]hafenimthoko@gmail.com

***Abstract*—Affordable Internet access has been critical for continued remote education and work-from-home environments during the COVID-19 pandemic. However, localized services made available through a community network can also provide high value for education, work and entertainment in communities that lack affordable access. Creating these localized services is technically challenging and in this paper, we take the first attempt at describing the development issues faced when creating these services as well as the first attempt at fostering a collaborative approach to developing community networks in Africa. We examine a case study relating to the development of a localized service followed by detailing an improved containerised architecture for easily bootstrapping new localized services using a combination of a virtual machine, Docker containers and the Traefik HTTP reverse proxy. Through the creation and subsequent sharing of our codebase and containerised architecture, we aim to set a precedent for resource sharing and collaboration amongst developers in the African wireless community network space.**

***Index Terms*—Wireless Community Networks, Open Source Development, Virtualisation**

I. Introduction

As South Africa continues to develop, access to the internet has become an ever more pivotal tool and resource for many population members. However, mobile data usage in low-income areas in South Africa is limited. This is due to the high cost of data relative to the per capita income in these areas and variable mobile signal coverage, which results in low-quality connections [1] [2] [3]. As a result, a large portion of the country's population is left with limited or no access to the internet.

To rectify the above disparities, there has been an increase in the creation of Wireless Community Networks (WCNs) throughout South Africa. WCNs are created to connect communities to the internet while also offering zero-rated local services [4]. However, this movement struggles from a lack of collaboration and subsequently a lack of shared resources to educate and build off of. Rey-Moreno et al. [5] examined over thirty WCNs based in Africa, where more than sixty percent were based in South Africa and found that the majority of parties involved in the creation of WCNs were unaware of other projects similar to their own. He concluded that there is the need for collaboration and resource sharing to facilitate a collective movement towards bringing communication technology to resource-constrained environments [5]. Creating a starting point for collaborative development in this space is the main contribution of this paper. By sharing our entire codebase we aim to set a precedent and motivate other WCN owners to do the same, thus forming a collaborative ecosystem for WCN development. While there have been numerous papers addressing the benefits of WCNs in Africa and examining their architecture [5] [6] [7] [8], to the best of our knowledge, this is the first attempt at examining the development process taken on by contributors to an open source WCN platform and a first attempt at documenting a freely available containerised WCN server. Thus, there is no relevant related work to our project.

This paper will focus on the iNethi project, an open source platform that allows communities to quickly bootstrap a community-built internet service provider (ISP) developed with Docker containers. iNethi was started by a group of researchers, developers, entrepreneurs, and community activists. It aims to facilitate the development of WCNs simply and intuitively while also abstracting the complex networking knowledge needed to carry out such a task. Furthermore, by facilitating an easier and more efficient way to produce a WCN, these networks can become community-owned entities and, thus, create a sense of ownership and control over users' services and data. There is an active deployment of iNethi in Ocean View (OV), a low-income area in Cape Town, South Africa. There are currently ten Libremesh WiFi access points in the community, which roughly three-hundred residents use to access local services or the internet at R20 per gigabyte.

The open source nature of this project means that the code for the system is openly available online, with anyone able to contribute to the project. Students at the University of Cape Town have been actively participating in the expansion of iNethi, with numerous postgraduate projects being based on the OV network and the university's Developers' Society actively recruiting members to participate in iNethi. Such projects have shown a need for a simple and efficient way to set up a development environment that contributors can work on individually and test their services before adding them to the code base. We will examine a case study developed using the original HAProxy architecture to illustrate the Docker container architecture development process and challenges encountered, followed by an improved architecture that sim-

plifies configuration complexity. This case study outlines the need for a testing environment that nullifies the expansive knowledge of networking needed to participate in WCN service development while also emphasising the importance of WCNs in addressing the digital divide in low-income areas in South Africa. Additionally, it highlights the complex nature services can adopt when catering for the needs of members of low-income areas.

To solve the aforementioned issues, we modified our deployment environment's architecture and built an Ubuntu-based Virtual Machine (VM), that is freely available online and mirrors the OV deployment environment. The pre-configured nature of the VM allows contributors to start developing immediately and nullifies the need for a complex understanding of the deployment environment. Therefore, the VM facilitates collaboration through simplification and improves the chances of successful deployments by mitigating potential differences between development and deployment environments. Additionally, the open source nature of the configuration files and code used to create this VM makes the process of creating a functional WCN server as simple as running pre-existing build scripts. The VM uses Dnsmasq and Traefik Docker containers to route traffic and create the links needed throughout the Docker network to build a working environment.

The remainder of this paper is organised as follows: Section II outlines the background of the iNethi project, Section III motivates the need for the VM system in open source projects like iNethi, Section IV presents an iNethi case-study that exemplifies the need for the VM, Section V describes the VM framework, and section VI concludes the paper.

II. Background

This paper focuses on the iNethi deployment in OV, which launched in 2018. The network is owned by OVCOMM Dynamic, an entirely community-owned cooperative. The directors of OVCOMM Dynamic come from various backgrounds, including education, art and media, youth development, and radio communication. In addition, they live in OV and are therefore representative of the community.

The iNethi infrastructure consists of several Libremesh-based WiFi access points located in the community. Libremesh allows the network to make use of layer-two and layer-three mesh protocols. This makes it possible for users to move between access points without losing their connection. Additionally, it creates room for network expansion and accommodates scalability as the mixture of the two routing approaches allows inter-cluster links to be established over dedicated radio links. The aforementioned community access points allow users to utilise the iNethi network and internet through a voucher-based system. Vouchers cost R20 per gigabyte, making them at least five times cheaper than the lowest one-gigabyte data bundle offered by South African mobile service providers [9].

WCNs, such as the deployment of the iNethi in OV, are important pillars in societal communication architecture. The creation of WCNs lessens the digital divide by establishing more affordable internet access and communication technologies. This has become even more important in under-resourced areas in light of the COVID-19 pandemic. E-learning has become an important tool in combating the spread of COVID-19 in South Africa. At OV secondary school, a staggering 36 percent of respondents to a school-wide survey could not access online learning material during the nationwide lockdown [9]. This led to the creation of the iNethi NextCloud platform, an open source cloud hosting service similar to Dropbox that can be hosted on Linux servers, such as the server located in OV. iNethi runs a global and local instance of NextCloud that allows teachers to upload content to the global server even when they are not within the confines of the community. This content is synced with the local instance on NextCloud, and students can access it via an app or through a browser-based interface.

The creation of iNethi NextCloud stemmed from a need within the community and was expanded upon in community-led workshops with OV-based educators. This is an important aspect of iNethi and its principles; all service creation and additions to the network must stem from a need identified by those within the community rather than a project which an outside source deems interesting or useful.

The creation of iNethi and the local content distributed within the community draws on the concept of locality of sharing that Phokeer et al. [1] found apparent in low-income areas, with OV being one of the areas they examined. This concept highlights how members of such communities communicate with people within their locality. This has motivated iNethi to be a means of access to the global internet and offer locally-hosted messaging, file sharing, video streaming, music sharing, and the aforementioned e-learning platform to community members. Instead of using the most popular mainstream applications to message a neighbour via an international expanse of networks, users' can use a locally-hosted service. This thereby nullifies the need for a message to be sent via expensive external data links. This is a key factor in reducing the cost of communication and media consumption within low-income areas. Therefore, sharing the code and framework used to create and host features such as iNethi NextCloud will allow other WCNs to adopt such a service, thus benefiting the global WCN ecosystem as a whole.

There are currently few contributors to the iNethi project, meaning that there are numerous important services that the community has requested that have not been started and numerous projects that have been started but never reached deployment. The lack of continued involvement by contributors and the number of unfinished projects can be attributed to the skill gap that many contributors face and a general tendency towards a lack of commitment. These are issues that have already been documented in many other open source projects [10] [11] [12].

III. Motivation

Up until now, there have only been a handful of long-term contributors to the iNethi project. There have been many

students from the University of Cape Town that have tried to contribute. However, the complex nature of the network has led to a skill gap that many have not been able to overcome. To set up an adequate test environment, contributors need to have experience with low-level network configuration and a good understanding of traffic routing within a network. This is the main issue students, and other contributors face when trying to help contribute to iNethi. In turn, this has made collaborating with new contributors very difficult as the few active contributors have to answer a myriad of questions before these developers can start on projects. While this is possible, active contributors do not always have time to upskill new developers. These issues are best exemplified by examining previous student contributions. In 2020, four honours students attempted to create bespoke services for the iNethi project. Considerable time investment was required for integration and this was only achieved by one student. Another student then was able to leverage this work to create a plausible iNethi-hosted service, while the other two students failed to integrate their solution with the deployment environment.

The aforementioned issues have led to the development of a fully functional VM replica of the iNethi server in OV. The VM uses Dnsmasq and Traefik Docker containers to make up the networking architecture. In addition, the scripts used to set up the VM are also available online so that contributors can build an iNethi environment on their own servers, VMs or machines. While this not only equips contributors with an adequate test environment, it also allows the iNethi project to be easily reproducible. This allows more people to adopt this architecture and thereby is a step towards addressing the lack of shared resources amongst African WCN owners and developers [5].

Traefik is a Hypertext Transfer Protocol (HTTP) reverse proxy and a load balancer designed to deploy microservices, such as Docker containers [13]. It configures itself automatically and dynamically, abstracting the complex network knowledge needed to set up a WCN test environment. Dnsmasq further simplifies this process by acting as a Domain Name Server (DNS) within the VM, resolving requests for services hosted by the VM. In addition, Dnsmasq is preconfigured in the VM and does not require user intervention to run even when new services are added.

Thus, using Traefik in conjunction with Dnsmasq allows a contributor that is new to Docker and networking to start a hosted service with a Docker compose file easily. Consequently reducing the skill gap required to contribute to iNethi.

IV. iNethi Case Study

In 2020 we conducted an honours project that focused on creating a tailor-made music sharing service for the iNethi architecture in a co-design fashion. This project was proposed by members of the OV community and aimed to create the aforementioned music sharing service with specific features to allow local artists to share their music with residents of their community and people residing outside of OV in a simple, cost-effective and data-efficient way. The purpose of this website was not only to encourage local content creation and celebrate the local talent but also to stimulate the local economy by providing the musicians with a way of making money and marketing themselves online. This was addressed by incorporating social media style profiles where artists can advertise themselves, accept donations and share contact details. Additionally, the platform included an e-commerce component that allowed users to purchase coupons to access restricted content or download music marked as freely downloadable.

Background research was done before interviews with OV-based musicians to gather context and design well-refined questions. Three musicians were interviewed, and an OV-COMM Dynamic director who has a passion for music and interacts with the artists regularly.

This project set out to solve an important problem specific to low-income areas in South Africa, exemplifying the significance of not only iNethi but WCNs in general.

A. Background and Community Insights

From interviews with the musicians based in OV, it was apparent that the biggest issue faced by South African musicians in low-income areas is their inability to share their music. This is due to a lack of an established platform that aligns with the data restraints they and their fellow community members face.

This has lead to music sharing in low-income areas being dominated by Bluetooth and WhatsApp file sharing [14] [15]. There has only been one previous attempt to facilitate music sharing in these communities, which resulted in the development of a website called KasiMP3. It was designed for use on feature phones with data constrained users in mind [15] [16]. At its peak, KasiMP3 had over fifty-thousand artists on their platform. However, this platform is no longer running.

During the feature selection process, the OV-based musicians suggested that the music sharing system incorporated a feature that allowed them to sell access codes, referred to as coupons, for the music they chose to place behind a paywall. This would replace their need to sell compact discs at live performances, which they said had become less lucrative over the years as digital music consumption has become more prevalent.

B. Implementation

To allow musicians to grow their audience outside of OV, two instances of the music sharing website were created. The first was a version that would only be seen when someone accessed the website using a wireless access point within the community. The second was hosted on an Amazon Web Services (AWS) server and was accessible by anyone. These two versions will be referred to as the local and global deployments, respectively. Each site only differed in terms of feature accessibility. The global website only allowed users to sign up as a customer and download music. In contrast, the local website allowed users to sign up as customers or musicians and upload their music.

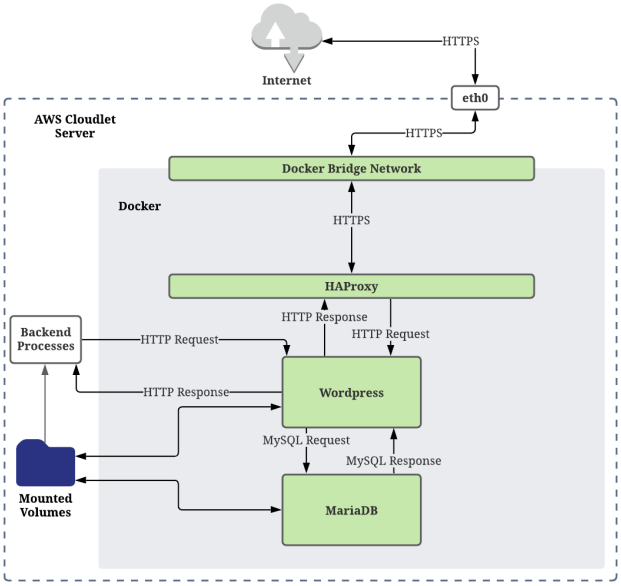

Fig. 1. Architecture of the global music sharing website

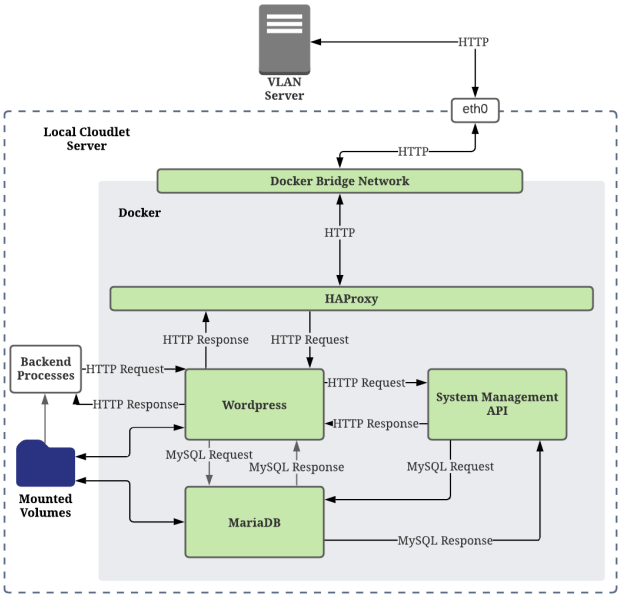

Fig. 2. Architecture of the local music sharing website

These websites were built using various Docker containers. The website front-end was built using WordPress to allow for easy customisation from someone without computer science knowledge. This aligns with the goal of iNethi to build community-owned networks. In essence, much of this project was built in the simplest way possible to allow for community maintenance and ownership. The system consists of a WordPress Docker container, a MariaDB Docker container, and a custom-built Python flask-based Application Programming Interface (API) housed within a Docker container, known as the system management API. The system management API handles the coupon creation process and updates the download statistics for each song.

When the system is built, the Docker containers are connected to a Docker bridge network, which allows them to communicate with each other. An HAProxy Docker container was run as a reverse proxy server on both the AWS and local servers. This takes in Hypertext Transfer Protocol Secure (HTTPS) requests for the AWS server, verifies and decrypts them and then passes them to the WordPress Docker container as an HTTP message, see Fig. 1. In the local network, the HAProxy container routes HTTP messages to the WordPress container or system management API, see Fig. 2.

On both servers, the WordPress container carries out the request and returns an HTTP response to the HAProxy container, which is then encrypted in the case of the AWS server and sent as an HTTPS response back to the user. In the case of the local server, the process is the same, except the response is sent in HTTP format. Optionally, the WordPress container queries the connected MySQL database, hosted in a MariaDB container, if data is needed from it.

The aforementioned request pattern includes actions like downloading music and browsing the site. These requests are handled by the containers and are thus architecture-independent and run on any server that can run Docker. However, in more complex cases where custom-built solutions are needed to handle user requests, the system management API or server will play a role in carrying out a portion of the request. The two core features of the website fall into these categories. Both the music upload process and coupon creation process are handled by the server and API, respectively.

The music upload process uses backend processes run on the server to coordinate product creation between the local and global server, i.e. creating an entry for a song in the e-commerce store that acts as the music library. These processes include updating the file name, moving the file into a permanent location, syncing files between the servers, reading from the database to get the user's submitted information and then using the WordPress WooCommerce API, the e-commerce store used on the website, to create the product locally and globally.

The coupon generation process uses the system management API to process user input and coordinate coupon creation between the local and global servers. The API uses calls to the WordPress WooCommerce API and information gathered from the local database to create a coupon.

C. Deployment Issues

Although the system was successfully tested throughout development within a local environment, the architecture-dependent nature of the song upload process meant the deployment on the local server was unsuccessful. This was due to compatibility issues with the libraries used for the backend processes. In addition to this, integrating the service's Docker containers, which were architecture-independent, into the deployment environment was difficult and time-consuming. The manual and environment-specific configuration that HAProxy required led to friction when trying to deploy this service be-

fore testing could take place. When this phase was completed, the testing phase brought to light the library compatibility issues.

V. Virtual Machine Framework

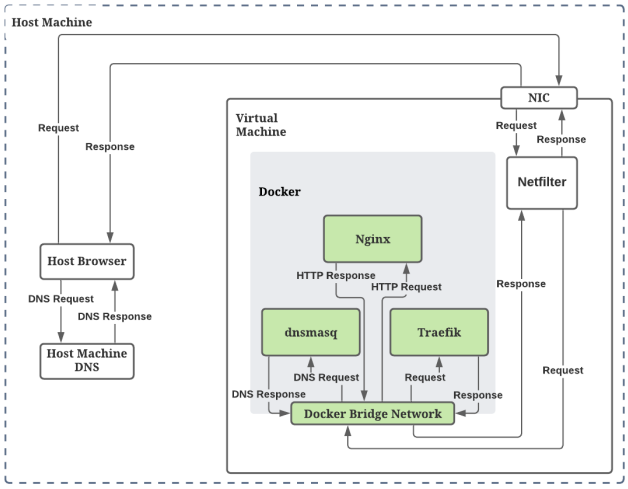

Fig. 3. Architecture of the VM

After the conclusion of the music sharing project, we had seen the shortcomings of the current software development life cycle employed in the iNethi project. It was noted that the chance of an unsuccessful deployment of the music sharing service could have been significantly reduced if we had a development environment that mimicked that of the iNethi deployment environment. To stop projects from experiencing issues similar to those observed during this honours project, the aforementioned VM was created.

The VM is built using Oracle's VirtualBox, a free and open source hosted hypervisor for x86 and AMD64/Intel64 virtualisation [17]. The VM itself runs the same OS as the OV server, a 64-bit Ubuntu 18.0.4 long term support OS. By mirroring the OS and the rest of the network within the VM, we ensure that there will be no unexpected software or library incompatibilities when deploying a new service.

Docker is pre-installed on the VM, and the architecture is pre-configured. When Docker is installed, it creates two custom Iptables chains named 'DOCKER-USER' and 'DOCKER' [18]. It also ensures that incoming packets are always initially checked by these two chains. This allows the host machine and the VM to access the services hosted on the VM without any complex manual configuration. Iptables is a pre-installed firewall system that interfaces with the kernel's Netfilter packet filtering framework. It interacts with traffic through packet filtering hooks in the Linux kernel's networking stacks. Whether incoming or outgoing, every packet will trigger these hooks allowing specific associated programs to interact with these packets at key points in the networking process.

Two Docker containers are pre-configured on the VM to facilitate the networking needed to use the VM as a development environment. Traefik is set up as a reverse proxy, and Dnsmasq acts as the DNS.

Traefik was chosen as it is a simple and easily configurable reverse proxy that eliminates the need for configuration of each route to connect paths and subdomains to their microservices. Instead, this is done automatically as services are started and removed. It intercepts and routes incoming requests to the corresponding backend services using service discovery to configure itself dynamically from these services. Additionally, Traefik does not need to restart every time a service is added, thereby minimising the overhead of adding new services to the development environment. Furthermore, this choice was motivated by the shortcomings of the old HAProxy architecture as it was difficult to use and required manual configuration to deploy a new service successfully.

Dnsmasq is used as it is a lightweight application that is suitable for resource-constrained environments. Thus, the DNS virtualisation will not take up computing power that can otherwise be used for development [19]. Furthermore, using Dnsmasq means that the VM can act as a self-contained development environment because the hosted services can be accessed from the VM's browser. It also allows the host device to access the VM's hosted services with minimal configuration on the host machine. The Dnsmasq configuration file does not need to be edited by users, which abstracts knowledge of DNS services and network traffic routing that a contributor may otherwise need.

The first step in interacting with the VM's services involves domain name resolution, whether that be for a request sent from the browser of the host machine or from within the VM, see Fig. 3. Incoming requests on port 53 will be sent to the internal Internet Protocol (IP) address of Dnsmasq. This will act as a DNS and confirm that the request has reached the VM. Any request on port 83 or 8080 is forwarded to Traefik, which uses a wild card configuration to ensure that any Uniform Resource Locator (URL) ending in '.inethihome.net' is forwarded to the relevant Docker container's internal IP address where the request will be processed. For example, if a user were to search for 'splash.inethihome.net' in the internet browser on their host machine, the request would be sent to their local DNS and resolve to the IP address of the VM, see Fig. 3. This request is then be sent to the VM via its Network Interface Card (NIC). The incoming packets will activate the hook for port 53 in the Docker chain. This packet will be sent to Dnsmasq, which sends a confirmation response packet to the host machine via the NIC. Following this, the subsequent packets will activate the port 80 hooks in the Docker chain and be sent to the internal IP address of Traefik, which will subsequently send them to the Nginx Docker container. The Nginx Docker container is used to host the 'splash' page - the web page a member of the OV community would see when they first connect to an access point.

This means developers only need to add Traefik labels to their Docker compose file to integrate a service with the environment. Once these are added, the above processes will facilitate their service's networking requirements, and they will be able to test their services in a quasi-iNethi deployment

environment. Once the service has been tested on the VM, it can easily be deployed on the local or global instance without modification.

The VM is also pre-loaded with shell scripts used to build the iNethi environment. A 'build all' script allows the user to select what services they wish to have running on their machine. This script then automatically configures the network and other settings needed to mirror the iNethi deployment environment. Furthermore, these services can be stopped and resumed with other scripts that are freely available online. Therefore the creation of the VM is more than just an effort to allow contributors to test their services. It is a fully configured containerised version of iNethi and allows the machine running it to utilise the VM as a pseudo access point. Because the scripts to build this system are made available to the public, this will allow people to build an iNethi server effortlessly with no manual configuration. This is a significant step in making iNethi a product rather than just a project in the eyes of potential network administrators, as the code that was used to set up the VM can be run on any Ubuntu-based machine to set up a replica of the OV deployment server. Therefore, we are facilitating the first step towards creating a collaborative WCN ecosystem in Africa by facilitating simple external deployments of our framework.

VI. Conclusions

Open source projects can struggle to gain traction and contributors when there is a significant learning curve needed to understand the codebase and deployment environment. Due to the complex networking knowledge and understanding of Docker that is needed to grasp the intricacies of iNethi, there has been an issue in maintaining long-term contributors' interest in the platform and deploying projects. This has led to a small team of contributors and a slow code output rate compared to other open source projects. These factors motivated the development of a VM that imitates the deployment environment of iNethi in OV. This will allow contributors to focus on their individual projects without spending time configuring a suitable development environment. By abstracting the networking knowledge that would otherwise be needed, the skills required to work on iNethi are less specific, and projects that work on a developer's local machine have an increased chance of successfully integrating with the deployment environment in OV.

Additionally, making this code freely available online facilitates the creation of more WCNs similar to iNethi and allows other networks to use our code in pre-existing infrastructures. Ultimately this will allow for developers and network administrators from different WCNs to create collaborative relationships. This is a vital step in addressing the lack of resource sharing and tools available in the African landscape for deploying WCNs and building services for them.

Acknowledgements

This work was supported in part by the Telkom Centre of Excellence for Broadband Networks and Applications as well as the Telecom Infra Project.

References

[1] A. Phokeer, M. Densmore, D. Johnson, and N. Feamster, "A first look at mobile internet use in township communities in south africa," in *Proceedings of the 7th Annual Symposium on Computing for Development*, 2016, pp. 1–10.

[2] A. Phokeer, D. Johnson, and M. Densmore, "Characterisation of mobile data usage in township communities," *Southern Africa Telecommunication Networks and Applications Conference (SATNAC)*, 2016.

[3] S. Hadzic, A. Phokeer, and D. Johnson, "Townshipnet: A localized hybrid tvws-wifi and cloud services network," in *2016 IEEE International Symposium on Technology and Society (ISTAS)*. IEEE, 2016, pp. 1–6.

[4] L. Maccari and R. Lo Cigno, "A week in the life of three large wireless community networks," *Ad Hoc Networks*, vol. 24, pp. 175–190, 2015, modeling and Performance Evaluation of Wireless Ad-Hoc Networks. [Online]. Available: https://www.sciencedirect.com/science/article/pii/S1570870514001474

[5] C. Rey-Moreno and M. Graaf, "Map of the community network initiatives in africa," *L. Belli, Community connectivity: building the internet from scratch*, pp. 149–169, 2016.

[6] S. J. N. Noutat, T. D. Ndié, and C. Tangha, "Wireless community network services: Opportunities and challenges for dcs: Case of rural cameroon," in *International Conference on e-Infrastructure and e-Services for Developing Countries*. Springer, 2012, pp. 308–317.

[7] K. Sibanda, H. N. Muyingi, and N. Mabanza, "Building wireless community networks with 802.16 standard," in *2008 Third International Conference on Broadband Communications, Information Technology Biomedical Applications*, 2008, pp. 384–388.

[8] A. Phokeer, S. Hadzic, E. Nitschke, A. Van Zyl, D. Johnson, M. Densmore, and J. Chavula, "inethi community network: A first look at local and internet traffic usage," in *Proceedings of the 3rd ACM SIGCAS Conference on Computing and Sustainable Societies*, 2020, pp. 342–344.

[9] A. van Zyl and D. L. Johnson, "inethi: locked down but not locked out," *XRDS: Crossroads, The ACM Magazine for Students*, vol. 27, no. 2, pp. 54–57, 2020.

[10] I. Steinmacher, G. Pinto, I. S. Wiese, and M. A. Gerosa, "Almost there: A study on quasi-contributors in open-source software projects," in *2018 IEEE/ACM 40th International Conference on Software Engineering (ICSE)*. IEEE, 2018, pp. 256–266.

[11] G. Hertel, S. Niedner, and S. Herrmann, "Motivation of software developers in open source projects: an internet-based survey of contributors to the linux kernel," *Research policy*, vol. 32, no. 7, pp. 1159–1177, 2003.

[12] J. Coelho and M. T. Valente, "Why modern open source projects fail," in *Proceedings of the 2017 11th Joint Meeting on Foundations of Software Engineering*, 2017, pp. 186–196.

[13] T. Labs. (2021, jun) traefik proxy. [Online]. Available: https://traefik.io/traefik/

[14] A. Schoon, "Digital hustling: Ict practices of hip hop artists in grahamstown," *Technoetic Arts*, vol. 12, no. 2-3, pp. 207–217, 2014.

[15] ——, "Distributing hip-hop in a south african town: From the digital backyard studio to the translocal ghetto internet," in *Proceedings of the First African Conference on Human Computer Interaction*, 2016, p. 104–113.

[16] M. Mapaya, "Download currency - the kasimp3 story," Johannesburg, 2018. [Online]. Available: https://www.iafrikan.com/publications/DownloadCurrency.pdf

[17] Oracle. (2021, jun) Virtualbox. [Online]. Available: https://www.virtualbox.org/

[18] D. Inc. (2021, jun) Docker and iptables. [Online]. Available: https://docs.docker.com/network/iptables/

[19] S. Kelley. (2021, jun) Dnsmasq. [Online]. Available: https://thekelleys.org.uk/dnsmasq/doc.html

Keegan White is studying his MSc. Computer Science at the University of Cape Town, focusing his research on machine learning in software defined networks.

David Johnson is an adjunct senior lecturer in computer science at the University of Cape Town and the director and founder of iNethi.

Melissa Densmore is an associate professor in computer science at the University of Cape Town and a co-founder of iNethi.

Hafeni Mthoko is a researcher in the Office of the Pro-Vice Chancellor: Research, Innovation and Development at the University of Namibia.

An Evaluation of Machine Learning Methods for Classifying Bot Traffic in Software Defined Networks

Joshua van Staden[1] and Dane Brown[2]
Computer Science, *Rhodes University*
Grahamstown, South Africa
[1]g14v2805@campus.ru.ac.za, [2]d.brown@ru.ac.za

***Abstract*—Internet security is an ever-expanding field. Cyber-attacks occur very frequently, and so detecting them is an important aspect of preserving services. Machine learning offers a helpful tool with which to detect cyber attacks. However, it is impossible to deploy a machine-learning algorithm to detect attacks in a non-centralized network. Software Defined Networks (SDNs) offer a centralized view of a network, allowing machine learning algorithms to detect malicious activity within a network.**

The InSDN dataset is a recently-released dataset that contains a set of sniffed packets within a virtual SDN. These sniffed packets correspond to various attacks, including DDoS attacks, Probing and Password-Guessing, among others. This study aims to evaluate various machine learning models against this new dataset. Specifically, we aim to evaluate their classification ability and runtimes when trained on fewer features. The machine learning models tested include a Neural Network, Support Vector Machine, Random Forest, Multilayer Perceptron, Logistic Regression and K-Nearest Neighbours.

Cluster-based algorithms such as the K-Nearest Neighbour and Random Forest proved to be the best performers. Linear-based algorithms such as the Multilayer Perceptron performed the worst. This suggests a good level of clustering in the top few features with little space for linear separability. The reduction of features significantly reduced training time, particularly in the better-performing models.

***Index Terms*—Machine Learning, Software Defined Networks, Security**

I. Introduction

Bots are typically seen as a problem in various services, specifically in social networks. These bots come about from compromised machines, which form part of a zombie botnet. These bots can then perform any number of illegal activities based on instructions sent to them by the owner of the bot. With multiple bots in a botnet, coordinated attacks can be done to, for example, execute a Distributed Denial-of-Service (DDoS) on a server.

These bot-coordinated attacks are difficult to detect at the router level, as the router can only see its specific portion of the network. Software Defined Networks (SDNs) offer a global, centralized view of the network. This provides an opportunity for Machine Learning models to identify the pattern of a DDoS attack and block the relevant IP addresses.

This study was funded by National Research Foundation (120654). This work was undertaken in the Distributed Multimedia CoE at Rhodes University.

This study offers a comparison of various forms of machine learning for identifying malicious bot activity on a network. We aim to examine the machine learning algorithms best suited for classification of malicious activity with very limited data. Our hope is that this will give insight into these forms of activity and pave the way for more efficient forms of machine learning for malicious activity classification.

Section II provides an overview of the literature surrounding this topic. In Section III, we discuss each form of classification using machine learning. Section IV explores a recently-released dataset, InSDN, identifying various bot-related malicious activities. Section V describes the experiment design for evaluating the machine learning models. Finally, Section VI applies these machine learning algorithms to bot-related activities and evaluates each algorithm for its ability to classify malicious coordinated activity.

II. Related Work

Wu *et. al.* [1] provide a comparison of various forms of unsupervised learning to detect bots using traffic analysis. The authors used datasets gathered from real-world malicious bots. Specifically, they were aiming to classify Zeus, Waledac and Storm attacks. The authors used three clustering algorithms to classify these bots: Simple K-Means, X-Means and EM clustering. They did some careful feature extraction and achieved accuracy results ranging from 0.89 to 0.96.

Tuan *et. al.* [2] provide a comparison of various forms of machine learning algorithms for DDoS traffic detection. The algorithms compared include the Support Vector Machine (SVM), Decision Trees, Naive Bayes, Artificial Neural Networks and various forms of unsupervised learning. It was found that unsupervised learning produces the best results when classifying DDoS attacks.

Cusack *et. al.* [3] used a Random Forest classifier to detect ransomware over a network forwarding HTTPS traffic. Specifically, they classified various Cerber ransomware attacks over an SDN. From this, they achieved a high F1 score of 0.94 with a low false-positive rate.

Zhang *et. al.* [4] created a botnet detection framework for Peer-to-Peer (P2P) architectures. The proposed pipeline involves filtering Transmission Control Protocol (TCP) packets and extracting the relevant features. They further reduce the

features down to 10 before passing it across to the classification. The authors used multilayer neural networks to classify the packets as either a legitimate connection or a botnet detection. The chosen datasets were the ISOT dataset [5] for malicious bots, and the ISCX dataset [6] for non-malicious traffic. The proposed approach achieved a precision of 98.32% and an F-measure of 98.69%. Additionally, the false-positive rate achieved was 0.75%.

III. Classification Algorithms

A. Logistic Regression

Logistic regression is an algorithm that aims to separate linearly separable data. This is done by fitting a logistic sigmoid function to the data and classifying each resulting value below 0 to the negative class and each value above 0 to the positive class.

This algorithm creates a simple model with very few parameters. As a result, training and inference are fast. The logistic regression results can also be fairly informative, as they measure the correlation coefficient and direction of association of two variables. It is, however, not restricted to bivariate classification and can easily be extended to multinomial regression. The only downside to logistic regression is that it is restricted to linearly separable data and cannot learn complex relationships.

B. Support Vector Machines

The SVM [7] is a form of linear classification. The algorithm aims to minimize the number of data points falling within a certain margin, set as a hyperparameter. The smaller the margin, the higher the likelihood of overfitting.

SVMs can classify non-linear data through the use of a kernel trick. This is done by projecting the data across an extra dimension defined by a specific kernel. Some examples include a radial basis function, polynomial kernel, linear kernel, among others. The separation line is thus calculated in this extra dimension and then downsampled to the previous dimension. As a result, various shapes can be predicted by the SVM, defined by the kernel.

C. Random Forests

The Random Forest algorithm [8] is an algorithm based on an ensemble of Decision Trees. A single Decision Tree is an algorithm that models the data using simple decision rules. These decision rules are updated based on the training data.

The Random Forest algorithm takes the ensemble of Decision Trees trained and merges them to get a more accurate result. This is usually trained through the bagging method [8]. Bagging is done by taking the aggregation of each bootstrap estimation of the Decision Tree means. This is useful as it is robust to high variations in the data.

The Random Forest algorithm benefits Decision Trees by reducing overfitting while improving accuracy. It is also robust to missing values in the data.

D. K-Nearest Neighbours

K-Nearest Neighbours (KNN) is a supervised clustering algorithm [9]. Classification in this algorithm is done by inspecting the classes of the nearest k neighbours relative to a point in the feature space. The point is assumed to belong to the class with the highest count in these nearest neighbours.

E. Multilayer Perceptrons

A single perceptron is a single unit that can classify data by determining a line of best fit. While this can classify linearly-separable bi-variate data, more complex data containing higher dimensionality tends to be beyond the scope of a single perceptron. A Multilayer Perceptron (MLP) extends this to multivariate data. The MLP resembles a neural network but is designed for linearly separable data in higher dimensions.

The use cases of MLPs are similar to those of SVMs. However, MLPs tend to work better with data containing more than two output classes.

F. Neural Network

Neural Networks [10] form a large basis behind deep learning. While it is not the only form of deep learning, it is relatively popular in the machine learning community. The premise behind neural networks is to simulate the human brain, with certain activations being sent to various neurons.

Neural Networks consist of three main parts: an input layer, one or more hidden layers and an output layer. Each layer consists of several neurons. The number of neurons in the input layer is determined by the number of features in the data. The output layer neurons are determined by the number of classes, and the number of neurons in the hidden layers can vary in number. The output of each neuron is the weighted sum of the output of each neuron in the previous layer, with an activation function applied.

IV. The InSDN Dataset

The InSDN Dataset [11] is a recent dataset containing labelled packets for various attacks within and SDN controller. The data was simulated as an Open vSwitch (OVS) with three networks attached. The first network is an attacker network running Kali Linux. The second network contains regular Mininet users to generate regular traffic. The final network contains the vulnerable Linux server, running on a Metasploit 2 framework. We investigate 6 different attacks made on the vulnerable server: Brute Force Attacks (BFAs), BotNet Attacks, Denial-of-Service (DoS), Distributed Denial-of-Service (DDoS), Probe, and Web-Attack.

A BFA is when the attacker attempts to log in to another user's profile by guessing passwords. This particular type of password-cracking guesses every combination of the valid password tokens, hashes them and checks against the server.

A BotNet attack is a class of attack executed by botnets in a network. A botnet is a host that has been infected by the attacker and executes commands from the hacker. In the InSDN Dataset, the Kali Linux machine performs this by infecting two hosts from the Mininet network.

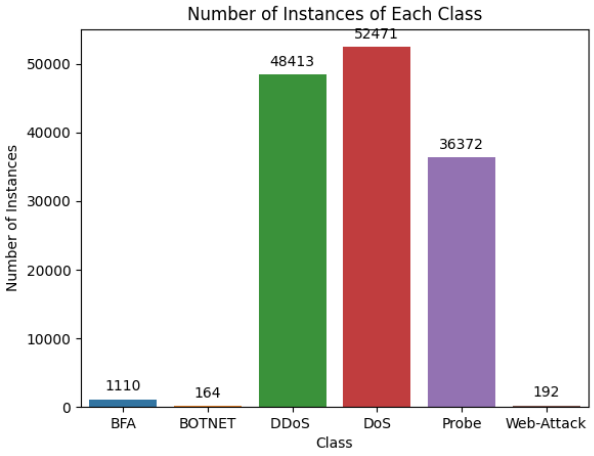

Fig. 1. The number of instances of each class in the InSDN Dataset.

The Probe attack class arises from the hacker scanning the vulnerable host for weak points. The attacking network scans the Mininet hosts as well as the Metasploit server.

Web-Attacks refer to attacks on the webserver itself and attacks at the application layer. The specific attacks used were Cross-Site Scripting (XSS) and SQL Injection attacks, which are two of the most common attacks [12].

The DoS and DDoS attacks both refer to an attack that renders the network unavailable for regular users. This is done by flooding the servers with spoofed packets that cause the server to stall for prolonged periods. The DDoS achieves the same goal but through using multiple botnets to flood the bandwidth of the victim server.

Figure 1 illustrates the number of instances of each class present in the dataset. The three highest classes are the DDoS, DoS and Probe attacks. Considering this imbalance of classes, this might introduce some bias in the results.

A. InSDN Features

The InSDN consists of Wireshark packet captures. In total, there are 83 features in the dataset. These features can be categorized as follows [11]:

- Network identifier attributes: Basic information about the source and destination.
- Packet-based attributes: Information related to the packets, such as the total number of packets in a forward and backward direction.
- Bytes-based attributes: Information related to the bytes in the forward and backward direction.
- Interarrival time attributes.
- Flow timers attributes.
- Flag attributes: Attributes related to the flags, such as SYN and RST.
- Flow descriptors attributes.
- Subflow descriptors attributes.

B. Baseline Results

The authors of [11] included a set of baseline results with which to compare models. These baseline results used all of the same models used in this study, with the exception of the Neural Network and Logistic Regression models. Before training, the authors removed any socket data and standardized the numerical data to the range $[0 : 1]$. Training was done on all remaining features of the dataset. These results are summarized in Table I.

TABLE I
BASELINE RESULTS FROM THE INSDN DATASET [11].

Model	Precision	Recall	F1-Score	Training Time (ms)
KNN	99.9	99.9	99.9	1,391,163
MLP	99.9	99.9	99.9	806,736
Random Forest	99.9	99.9	99.9	231,436
SVM	99.8	99.9	99.9	17,161,164

V. EXPERIMENT DESIGN

We test a set of ML models against the InSDN dataset. First, we preprocess the data to ensure that it more closely suits the needs of these algorithms. The models tested include a Neural Network, SVM, Random Forest, K Nearest Neighbours (KNN), Logistic Regression and MLP. These models are trained, fine-tuned and tested against a range of different input dimensionalities. For fine-tuning, we use a grid search and cross-validate the data with 5 folds. For testing, we extract 30% of the dataset.

We aim to test these models with respect to a decreasing feature space. According to the features listed in Figure 2, we extract the top 36, 18 and 8 features. We train and fine-tune each model separately on each of these feature sets and report on the achieved precision, accuracy and F1 score. To accurately measure the training times of the models, we instantiate a new model with the optimal hyperparameters and train it on the dataset again, without any cross-validation. We expect to see some drop in the scores achieved on lower dimensionality when compared to the baseline results, but hope that this comes with a significant decrease in training time.

A. Preprocessing

Due to the high dimensionality of the dataset, we aim to reduce the number of features to increase speed and reduce overfitting. Before feature selection, we first preprocess the data. This ensures that all values lie roughly within the same region and provides a more stable ground for evaluating the features. Firstly, we use a Robust Scaler to ensure that outliers are handled. Then we use a Min-Max Scaler to ensure that all feature values lie within the range of $[0 : 1]$. This results in non-negative values within the dataset. All scalers were fitted on the training data and applied on all data.

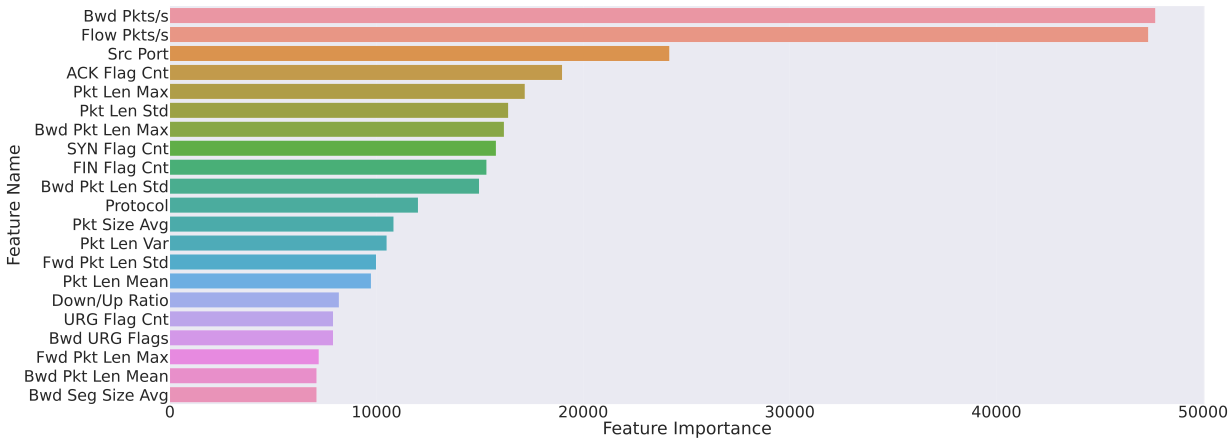

Fig. 2. The features ranked by their χ^2 score.

1) Feature Reduction: We first remove all string data within the dataset to reduce features, as we aim to classify based on numerical data. This resulted in 80 non-string features. Following this, we use the SELECTKBEST method included in the SCIKIT-LEARN package. We select based on the χ^2 criterion, as all features included are non-negative. The SELECTKBEST method was fitted on the training data and applied to all data. Figure 2 illustrates the χ^2 scores of the top 36 features. We find that these features hold the majority of the information. As a set of feature space sizes, we extract the top 36, 18 and 8 features, respectively.

In particular, we see a significant amount of significance in the top two features: the number of backwards-flowing packets per second (i.e. from the client to the OVS switch) and the number of packets per second in a given flow. Considering the attack classes in the dataset, particularly in DoS, DDoS and Brute Force attacks, these are logical features to consider. Among other important features, information such as packet length, protocol used and flag counts appeared to be significant.

B. Classification

For classification, we use various models from the SKLEARN package, as well as a deep neural network model from the KERAS package. To find optimal hyperparameters, we fine-tune each model using a grid search. This grid search cross-validated the data with 5 folds, which was optimal as detailed in [11]. The Neural Network used a combination of layers containing 32, 64, and 128 nodes. Some dropout was introduced into the network to introduce some regularization. All models were run on a 16-core AMD Ryzen 9 3950X processor. Each core averaged a clock speed of 2713 MHz.

VI. RESULTS

Table II details the achieved macro-averaged precision, recall and F1 score of each model. From the outset, we note that the skew classes shown in Figure 1 would have a large impact on the performance of these models. Furthermore, we aim to analyze these results with respect to their performance in a low-dimensional environment.

The highest performing models were the Random Forest and KNN models. These models achieved scores that were consistently within the 90$^{\text{th}}$ percentile. Similar to [3], the Random Forest model produced a lower False Positive Rate. Furthermore, reducing the feature space did not seem to have a significant impact on these scores. Imbalanced classes do not have an adverse affect on the KNN models, and its high performance in the top 8 features is indicative of the fact that these features are well-clustered. This aligns with [1], who also achieved good results with clustering algorithms. Similarly, the clear clustering of data would result in features that are categorized easily by the Random Forest algorithm.

The Neural Network and SVM models reported good results, with F1 scores ranging from the 50$^{\text{th}}$ percentile to the 80$^{\text{th}}$ percentile. While these models are well-equipped to learn complex relationships, and should therefore outperform all other models, the low dimensionality of the data had an adverse impact on the performance of these models. With similar preprocessing to that of [4], better results may have been achieved.

The lowest scoring models were the Logistic Regression and MLP models. These models are highly linear in nature, so separability in a low-dimensional space may be difficult. As shown in the baseline results, the MLP is able to achieve high results with all available features.

Figure 3 illustrates the training times of the models. As anticipated, there is a significant reduction in these timings when compared to the baseline results presented in [11]. However, a lower number of features does not always introduce a lower training time, as some instances illustrate. Interestingly, the KNN model, which was among the highest training times in the baseline, is among the lowest in Figure 3, indicating that

TABLE II
CLASSIFICATION RESULTS OF EACH MODEL WITH VARYING FEATURE SIZE.

Model	36 Features			18 Features			8 Features		
	Prec	Rec	F1	Prec	Rec	F1	Prec	Rec	F1
Neural Network	77.77	95.95	80.50	72.68	91.32	78.31	59.33	79.20	64.87
KNN	92.63	94.70	93.55	92.01	92.48	92.22	91.92	92.95	92.36
MLP	16.67	6.30	9.15	57.62	61.21	59.11	55.43	62.83	57.77
Logistic Regression	59.19	64.75	61.36	53.31	65.95	56.33	46.15	47.24	46.38
Random Forest	93.53	92.91	93.18	93.59	91.57	92.44	92.36	90.89	91.52
SVM	82.74	98.82	88.12	71.99	97.33	79.89	67.68	96.85	76.42

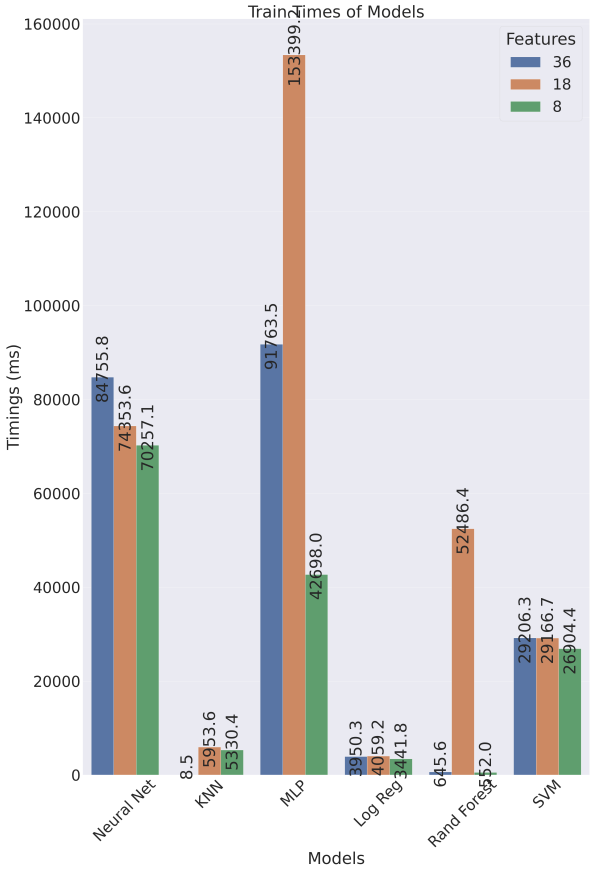

Fig. 3. Train times of the various models.

convergence is reached quicker with fewer dimensions. The Random Forest was also among the lowest in train times, with the exception of the train time using 18 features. This indicates that convergence may be difficult to reach in a certain feature space size. The Logistic Regression interestingly did not take long to train. However, this is due to the fact that the imposed maximum number of iterations were reached, hence all train times were similar.

The MLP and NN models were the longest to train. In the case of the MLP, its low classification result indicates that its long train time is due to the fact that sufficient convergence was not reached. For the Neural Network, the train time does not depend on convergence, but rather the number of epochs included. As a result, its train time is not significant.

The SVM did not take too long to train. Considering that this was the longest train time in the baseline results, this is a significant improvement. This indicates that, with a higher dimensional space that is still significantly lower than the total number of features in the dataset, this model will reach a good trade-off between train time and classification power.

VII. Conclusion

BotNet detection is a highly important aspect of making secure SDNs. Machine learning can be utilized in this environment as the SDNs offer a centralized view of the overall network. As a result, an evaluation of various machine learning methods is important to ensure that the best methods are always used in detecting botnets and cyber attacks. The recently-released InSDN dataset provides a fresh set of data to test various models on. This paper evaluates a set of machine learning methods against the InSDN dataset. Specifically, it examines their performance with a low feature space.

Various models were trained on the InSDN dataset. These models were trained using the top 36, 18 and 8 features. The optimal hyperparameters were found using a grid search with a 5-fold cross-validation.

We found that methods relying on well-clustered data performed well, showing a very small sacrifice in classification power when compared to models trained on all available features. This illustrates that the selected features are well-clustered. Additionally, the training time showed a marked decline in these models, resulting in a strong classifier with a high computational efficiency. Linear-based models suffered the most due to the reduction of the features.

Further exploration of these models performance in varying feature sizes would give insight into the perfect trade-off of speed and classification ability. Additionally, studying unsupervised forms of learning, such as that of [2], would potentially yield better results.

References

[1] W. Wu, J. Alvarez, C. Liu, and H.-M. Sun, "Bot Detection using Unsupervised Machine Learning," *Microsystem Technologies*, vol. 24, no. 1, pp. 209–217, 2018.

[2] T. A. Tuan, H. V. Long, R. Kumar, I. Priyadarshini, N. T. K. Son *et al.*, "Performance Evaluation of Botnet DDoS Attack Detection using Machine Learning," *Evolutionary Intelligence*, pp. 1–12, 2019.

[3] G. Cusack, O. Michel, and E. Keller, "Machine Learning-Based Detection of Ransomware using SDNs," in *Proceedings of the 2018 ACM International Workshop on Security in Software Defined Networks & Network Function Virtualization*, 2018, pp. 1–6.

[4] M. Alauthaman, N. Aslam, L. Zhang, R. Alasem, and M. A. Hossain, "A P2P Botnet Detection Scheme Based on Decision Tree and Adaptive Multilayer Neural Networks," *Neural Computing and Applications*, vol. 29, no. 11, pp. 991–1004, 2018.

[5] S. Saad, I. Traore, A. Ghorbani, B. Sayed, D. Zhao, W. Lu, J. Felix, and P. Hakimian, "Detecting P2P Botnets through Network Behavior Analysis and Machine Learning," in *2011 Ninth annual international conference on privacy, security and trust*. IEEE, 2011, pp. 174–180.

[6] A. Shiravi, H. Shiravi, M. Tavallaee, and A. A. Ghorbani, "Toward Developing a Systematic Approach to Generate Benchmark Datasets for Intrusion Detection," *computers & security*, vol. 31, no. 3, pp. 357–374, 2012.

[7] C. Cortes and V. Vapnik, "Support-Vector Networks," *Machine learning*, vol. 20, no. 3, pp. 273–297, 1995.

[8] L. Breiman, "Random Forests," *Machine learning*, vol. 45, no. 1, pp. 5–32, 2001.

[9] L. E. Peterson, "K-Nearest Neighbor," *Scholarpedia*, vol. 4, no. 2, p. 1883, 2009.

[10] W. S. McCulloch and W. Pitts, "A Logical Calculus of the Ideas Immanent in Nervous Activity," *The bulletin of mathematical biophysics*, vol. 5, no. 4, pp. 115–133, 1943.

[11] M. S. Elsayed, N.-A. Le-Khac, and A. D. Jurcut, "InSDN: A Novel SDN Intrusion Dataset," *IEEE Access*, vol. 8, pp. 165 263–165 284, 2020.

[12] Symantec, "Internet Security Threat Report," 2018. [Online]. Available: https://symantec-enterprise-blogs.security.com/blogs/

Joshua van Staden obtained his MSc and is pursuing a PhD at Rhodes University. His research interests are computer vision and machine learning.

Dane Brown obtained his PhD and is a Senior Lecturer at Rhodes University. His research interests are image processing, machine learning, information security and GPGPU.

Adaptive Network Intrusion Detection using Optimised Machine Learning Models

Hatitye Chindove*, Dane Brown†
*Department of Computer Science, Rhodes University, Grahamstown, South Africa
[1]hatitye@gmail.com
[2]d.brown@ru.ac.za

***Abstract*—Network intrusion detection system (NIDS) adoption is essential for mitigating computer network attacks in various scenarios. However, the increasing complexity of computer networks and attacks make it challenging to classify network traffic. Machine learning (ML) techniques in a NIDS can be affected by different scenarios, and thus the recency, size and applicability of datasets are vital factors to consider when selecting and tuning a machine learning classifier. The proposed approach evaluates relatively new datasets constructed such that they depict real-world scenarios. It includes empirical analyses of practical, systematic ML-based NIDS with significant network traffic for improved intrusion detection. A comparison between machine learning classifiers, including deep learning, form part of the evaluation process. Results on how the proposed approach increased model effectiveness for NIDS in a more practical setting are discussed. Recurrent neural networks and random forests models consistently achieved the best results.**

***Index Terms*—Computer Networking, Security, Network Intrusion Detection Systems, Machine Learning**

I. Introduction

As the world has become more dependent on computer systems, the infrastructure has experienced an increase in the scale of security attacks [1]. A 2019 IBM report[1] shows that successful attacks have an average detection time of 206 days, coupled with a 314-day life cycle to contain each security breach. As such, early detection can assist in improving response times for any system seeking to maintain a high-security posture [2]. It follows that intrusion detection is an essential part of monitoring computer events. A Network Intrusion Detection System (NIDS) is one such security tool that identifies an inside attack, outside attack and unauthorised access into a computer network.

NIDS use two methods for detection, namely, signature-based and anomaly-based detection. In signature-based detection, pre-installed rules for the attacker patterns are adopted as models to detect attacks. Anomaly-based detection uses traffic shape observations to measure the deviation from normal traffic [3]. Anomaly-based detection using machine learning (ML) has recently shown promising results [4].

This study was funded by National Research Foundation (120654). This work was undertaken in the Distributed Multimedia CoE at Rhodes University. Thank you to the Canadian Institute for Cybersecurity for making datasets used in this paper publicly available.

[1]www.all-about-security.de/fileadmin/micropages/Fachartikel_28/2019_Cost_of_a_Data_Breach_Report_final.pdf

A key characteristic of ML-based techniques is their ability to learn and improve their performance over time [5]. Common strategies for ML emphasise building a framework that enhances its execution based on previous results – changing execution strategy based on recently acquired data – to classify an intrusion. ML techniques have the advantage of adaptability and capturing of interdependencies when effectively implemented. However, an immediate challenge with ML is observed with the need to compromise between model complexity and training duration. Selecting an appropriate algorithm for NIDS is vital in addressing this problem.

The approach of using ML-based intrusion detection has potential. However, there are challenges and limitations associated with it that require comprehensive review before developing ML-based NIDS. These will form part of the basis of this paper.

II. Motivation and Contributions

In real-world systems, most network traffic is non-malicious; it follows that categorising irregular traffic may be challenging for NIDS. Furthermore, NIDSs inevitably encounter novel scenarios. As such, they should be able to adapt to these new traffic scenarios. A review of systematic NIDS development, that perform multi-class classification, is worth first exploring.

Hence, this paper addresses the above challenges and gaps in ML-based NIDS research by developing a multi-class NIDS that is effective on new/unseen data. Top-performing NIDS models are evaluated and contrasted against related systems found in the literature.

III. Literature Review

Supervised ML-based NIDS approaches are considered based on related studies. Subsequently, datasets are reviewed to reflect the intended contributions.

A. Related Work

This sub-section details related ML algorithms used in related studies to develop NIDS classifiers

1) K-Nearest N.eighbour (KNN): **KNN** assumes similarities exist at a close distance. The algorithm selects k entries in a dataset that is closest to the new data point. A majority vote of the prevalent classes among those k entries will be the class

of the new data point. Using the CICIDS 2017 dataset, Atefi et al. [6] achieved a 0.964 accuracy with the KNN model.

2) Support Vector Machines (SVM): **SVM** first maps the input vector into a higher dimensional feature space and obtains an optimal hyperplane in the higher dimensional feature space [7]. The hyperplane aims to separate two classes of data points by finding the largest margin between two points. Aksu et al. [8] used SVM to determine the effect of each feature on classification. The results show a selection of 30 features producing an f1-score of 0.656.

3) Decision Trees (DT): **DT** is based on a divide and conquer strategy, which utilises decision nodes and leaf nodes. In this, a test over one of the decision node attributes and a leaf node represents the class value [5]. Bisht and Ahmad [9] used DT and attained an f1-score of 0.831.

4) Random Forests (RF): **RF** is consists of a large volume of individual DT's that operate as an ensemble [10]. Each tree in the RF outputs a class prediction. When combined, the class with the most votes becomes the model's prediction. Bisht and Ahmad [9] used RF for NIDS and achieved a 0.809 f1-score, which was lower than the work DT finding for the same study.

5) Multi-layer Perceptrons (MLP): Artificial Neural Networks (ANN) incorporates a collection of connected units called artificial neurons, which have connections between each neuron with transmission ability to signal another neuron [11, 12]. **MLP** is a feed-forward ANN that has a series of algorithms that recognise underlying relationships in a dataset [11]. Typically, back-propagation is then used for training in a supervised manner. MLP is composed of activation functions that are chained together in a layer. The layers are fully connected as each unit in the layer is influenced by all previous units. Chuan-long et al. [13] utilised MLP in a multi-class classification NIDS and achieved an accuracy of 0.781.

6) Recurrent Neural Networks (RNN): **RNN** contains loops, allowing information storage within the network [11]. RNN also uses back-propagation learning through storing recurring time sequences. Therefore, if the input order were to be changed, the RNN model would become significantly different [13]. RNNs form part of deep learning methods. Chuan-long et al. [13] used an RNN model composed of 80 hidden nodes and a 0.1 learning rate. The model achieved an accuracy of 0.833 and 0.813 for binary and multi-class classification, respectively.

B. Datasets

The KDD 99 dataset has been most prominent for NIDS research and comprises 41 features [14]. Key challenges of this dataset lie with the redundancies present, which has made ML model training biased towards the most represented classes leading to poor classification for underrepresented classes. The KDD 99 dataset has several limitations which make the obtained results unrealistic [15]. Other datasets to supplement these limitations that are widely adopted datasets include UNSW-NB, Kyoto 2006+ and AWID. However, for this paper, these did not form part of this experiment.

This paper focused on using the CICIDS 2017 dataset as the training, validation partition and testing set. The CICIDS 2018 dataset for additional model training and testing without model validation. These datasets reflect real-world and practical scenarios in composition and data distribution. The CICIDS 2017 dataset was gathered by Sharafaldin et al. [16] using simulated attack and victim networks. The dataset was prelabeled by the authors of the dataset and adopted in this system. The output is statistical features calculated separately for a bidirectional network. The final dataset constitutes 83 statistical features and a classification label, each calculated for forward and reverse network traffic directions. The dataset is composed of 15 classes[2].

The CICIDS 2018 dataset follows a similar data gathering methodology as the CICIDS 2017 but in a different setting. Context data of the attacks is defined as scenarios in time windows provided by the dataset authors. The dataset includes some different attack scenarios from the CICIDS 2017 dataset and a distinct attacking infrastructure. This dataset is composed of 15 classes, but three of those classes are additional *DDoS* variants. Many classes are similar to CICIDS 2017 but CICIDS 2018 lacks *Heartbleed* and *PortScan*.

IV. Proposed Methodology

This section explains the proposed methodology and ascertains the top-performing approaches for NIDS that are optimised for macro f1-score. Macro-f1 is the harmonic mean between precision and recall, where the average is calculated per label and then averaged across all labels. If pj and rj are the precision and recall for all $\lambda_{\mathrm{j}} \in \mathrm{h}\,(\mathrm{xi})$ from $\lambda j \in y_i$, the macro-F1 is:

$$\text{macro-f1} = \frac{1}{Q}\sum_{j=1}^{Q}\frac{2 \times pj \times rj}{pj + rj}$$

Each classifier undergoes much experimentation – based on the literature review – for this paper. The approach for creating the proposed NIDS is illustrated in Figure 1.

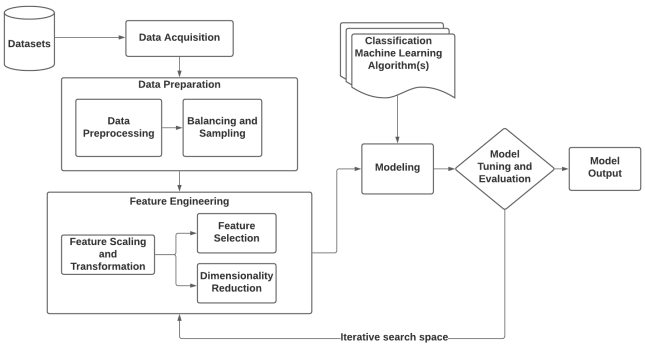

Fig. 1. Experiment Design Overview.

The system goes through several stages in the pipeline, namely; 1) Data Preparation, 2) Feature Engineering, and 3)

[2]Benign, Bot, DDoS, DoS(GoldenEye, Hulk, Slowhttptest, slowloris), Patator(FTP and SSH), Heartbleed, Infiltration, PortScan, Web (Brute Force, Sql Injection and XSS)

Model Evaluation and Tuning. ML processing pipelines are adopted to prevent data leakage in the test harness by ensuring that data preparation is constrained to each fold of the cross-validation procedure.

A. Data Preparation

During preliminary visualisation and testing for the CICIDS 2017 dataset, numeric features were loaded as floats and integers. By loading all data as integers except the 'Label' column, loading speeds were significantly improved across the different datasets. This was necessary to address time constraints and memory limitations during experimentation.

The extracted CICIDS 2018 data was used as semantic information to determine different variants of classes – both known and unknown – for labelling, using rules from regular expressions. The caveat of the approach is that sub-classes of attacks can be inaccurately labelled for unknown attacks in CICIDS 2018. Furthermore, the CICIDS 2018 dataset includes some different attack scenarios from the CICIDS 2017 dataset. Since most features are the same, the 69 common features in both datasets were tested.

1) Data Preprocessing: The data was first merged into a single dataset by loading all the CSV files from the CICIDS 2017 dataset into data frames and consolidating them into a single data frame. Note that the first field is typically a header containing the feature names per column. After merging, it was discovered that there are duplicate header fields throughout the CICIDS 2017 CSVs. These were removed, resulting in a total of 2,660,377 samples and 15 classes.

Data was prepared per the guidelines described in Reis et al. [10] and Rosay et al. [4] where CSV field headers and duplicate samples were removed, NaN values were mapped to –1 and class label strings were mapped to integers.

2) Balancing and Sampling: Stratified sampling was applied to the CICIDS 2017 dataset to separate training and test data. Post-strata, the sample is selected randomly in proportion with a seed of 42 for reproduction purposes. Training/test data splits of 10/90, 30/70 and 50/50 percentage were selected to observe the effect of the training data size on the models. There was a clear presence of a class imbalance in the CICIDS 2017 dataset. Note, a subset train set is used as the validation set.

The study defines minority classes as those with a representation of fewer than 5000 samples in a dataset. Synthetic Minority Oversampling Technique (SMOTE) was applied to synthesise 100 to 500 samples to minority classes. Two hundred synthetic samples produced optimal results during preliminary tests but yielded insignificant accuracy changes to classification performance. Random Undersampling was subsequently applied to remove excess samples from majority classes if they contained more than 50000 samples. Of note, SMOTE was applied only to the training data for a fair comparison – avoiding data contamination during cross-validation and testing.

SMOTE was thus applied without contaminating the cross-validation and test data for real-world applicability. Note, 10/90 – 10% training and validation data, and 90% testing data – was determined to be the *minimum distributable* split ratio (limited data). The assumption was that if a model performs well with this *limited data*, it may perform well on novel data. Furthermore, using this limited data can reflect the effectiveness of feature selection that is more applicable to real-world scenarios.

B. Feature Engineering

1) Feature Scaling and Transformation: Several feature scaling and transformation approaches are evaluated in the pipeline, where standardisation is applied to mitigate distance-based classifier problems. This step explored using Standard, Power, Quantile and Robust scaling techniques. Note, RF and DT – non-distance based classifiers– have cases where scaling/transformation is not adopted due to their scale-invariant nature.

2) Feature Selection and Dimensionality Reduction: Feature importance methods were evaluated for feature selection, namely, Gini Importance (GI) and Permutation Importance (PI). These methods were evaluated across all scalers. PI is adopted as a method that could be generally applied to some degree. Feature importance ranks the best features in each model by permuting over 34 (features / 2) iterations and explicitly selecting features with the best f1-score for a particular base model.

Alternate to feature selection, dimensionality reduction using the PCA method is adopted. PCA transforms data into a vector (eigen) space that can be scaled effectively for distance methods. Other subspace [3] methods were tested on the validation set but not presented in the results due to observed limitations, including the tendency to overfit, low classification performance, and high computational requirements. The first 26 principal components explain 0.99 of variance used to identify the number of required PCA components.

C. Model Tuning and Evaluation

The proposed method evaluates several supervised ML classifiers highlighted in Section III. As a training strategy, One versus All (OvA) is used. The strategy involves training a single classifier per class, with the samples of that class as positive samples and all other samples as negatives.

26PCA or 26PI – 26 components by PCA or 26 top-selected features by PI – represents the feature space reduction approach. Moreover, **Q-26PCA-MLP** represents a model application, where the first character represents the scaling method – Quantile as Q, Power as P – followed by the feature space reduction method – 26PCA – and finally the tuned classification algorithm – MLP.

While each ML classifier has diverse hyperparameter tuning parameters, Grid Search[4] was used for an exhaustive

[3] LDA, LLE, t-SNE and UMAP

[4] First Random Search is used to reduce search space, followed by Grid Search, which iterates exhaustively through the best subset of the hyperparameters of a target algorithm.

search with 5-fold cross-validation in the pipeline toolkit. A series of experiments were conducted for each tuned ML classifier against its best feature space reduction method. The performance metrics are used for contrasting purposes of each output ML model against related systems.

The macro-average is the adopted metric for this study because it gives all classes equal importance. As such, it computes the f1 metric independently for each class and averages them, whereas a micro-average aggregates the contributions of all classes.

Data from CICIDS 2018 were divided into two groups: group 1 contained data from classes previously seen in CICIDS 2017 and group 2 contained data of previously unseen classes. The models were updated using data from the unseen classes (group 2).

V. Results

A. Feature Engineering and Model Tuning Results

The model classifier parameter tuning process was initiated by finding the optimal features to adopt per base model through evaluating the CICIDS 2017 validation set taking from the 10% training set. Following the feature preprocessing steps in the proposed methodology, classifier base models are tuned by ranking their respective PI according to the 69 feature set, applicable to the real world. Model tuning results on the validation set are based on data scaling in combination with feature selection or dimensionality reduction approaches.

PI and PCA are compared to determine which approach effectively reduces feature space and improves classification accuracy. In general, feature selection had varying effects per ML model. Results show that this step was vital for RF, DT, KNN and MLP classifiers. When performing additional dimensionality reduction, PCA produced better results compared to other explored extraction methods.

The hyperparameters are based on the balance of the bias/variance trade-off by selecting the value where both training and cross-validation accuracy scores peak.

Table I shows classifiers with their respective most influential parameter. Tuning results show that the CICIDS 2017 dataset yields similar results for Quantile and Power transform methods, where Quantile is typically insignificantly better.

TABLE I
Most Influential Hyperparameters using 26PI.

Classifier	Parameter(s)	Accuracy
RF	n-estimators = 300 max-features = sqrt max-depth = 25	≈1
SVM	kernel = rbf gamma = 7 C = 100	≈1
MLP	solver = adam learning-rate = constant hidden-layer-sizes = (200, 200, 200) alpha = 0.0001 activation = relu	0.887
KNN	weights = distance n-neighbors = 1 metric = manhattan	≈1
DT	min-samples-split = 3 min-samples-leaf = 3 max-features = sqrt max-depth = 25 criterion = gini	0.93
RNN	epochs = 500 batch-size = 64 dropout-rate = 0.2 learn-rate = 0.001 neurons = 128	≈1

TABLE II
Best results minimum distributable train/test split ratio models.

Model	Accuracy	Precision	Recall	f1-score (macro)
26PI-RF	≈1	0.90	0.86	0.87
Q-26PI-KNN	≈1	0.80	0.86	0.82
Q-36PI-MLP	≈1	0.83	0.85	0.81
Q-26PI-SVM	≈1	0.82	0.84	0.81
S-16PI-DT	≈1	0.78	0.83	0.76
Q-69PI-RNN	≈1	0.74	0.82	0.73
S-36PI-NB	0.70	0.43	0.74	0.47

B. Validation Set Results

The best performing models used the minimum distributable train/test split ratio to prove efficacy against training data dependence in practice. Multi-class classification models are trained for all the classes in the CICIDS 2017 dataset.

Table II shows the best results for the NIDS models on *minimum distributable* data. All the models achieved a macro f1-score above 0.70. 26PI-RF achieves the best macro f1-score of 0.87 with a precision as high as 0.90.

1) RF: 26PI-RF yields the best results with limited data with a 0.87 macro f1-score plus a perfect (rounded) accuracy and micro f1-score, outperforming the 0.9648 accuracy achieved by Kurniabudi et al. [17], which was the best observed in the literature. For feature space reduction, RF prefers feature selection (26PI) over dimensionality reduction (26PCA) methods. The model performs exceptionally well for the major classes and improves the macro-level score even when minority classes may not be exceptional.

2) MLP: Q-36PI-MLP achieves the highest macro f1-score of 0.81. Chuan-long et al. [13] 's study achieved a recall of 0.78, which is lower compared to those achieved by all evaluated MLP models in this study. For optimal results, the model prefers more features than the RF, SVM, DT and RNN models.

3) SVM: Q-26PI-SVM is the best SVM model with a 0.81 macro f1-score. Interestingly, SVM results exhibit trends different to RF's, in that SVM's recall is significantly better in many cases, and conversely, precision is worse. Furthermore, differences in f1-scores are much lower across other feature selection combinations than RF. This indicates that the SVM is relatively sensitive to features included in the model.

4) DT: 16PI-DT is the best performing model with a macro f1-score of 0.76. An opposite model performance effect is observed for scaling and extraction methods. It is observed that Quantile performs better than both Power and Standard

when used with 26PCA. Of note, DT preferred fewer features in both validation and these experiments compared to the rest of the models evaluated.

5) RNN: Unlike the rest of the evaluated models, RNN was preferred all the features and did not undergo feature space reduction. Due to several factors such as the training approach, loop structure of the neural network, layers, dropout layers, the focus was placed on model tuning. Q-69PI-RNN has the best performance at a macro level for detection. The model was effective at anomaly detection due to near-perfect detection rates on major classes compared to the rest of the models but not for the minority classes.

Moreover, across the different train/test split ratios, the results show that more training data was not necessarily better in most cases. There is a lack of evidence that an increase in the training data would significantly improve most models. As such, the selection of features in the models was effective for real-world adoption.

C. Unseen Dataset Results

Table III shows novel results for the best CICIDS 2017 classifiers tested against the CICIDS 2018 dataset. Q-36PI-MLP achieves the best macro f1-score of 0.22.

TABLE III
CICIDS 2017 MODEL AGAINST CICIDS 2018 DATASET.

Model	Precision	Recall	f1-score (macro)	f1-score (micro)
Q-36PI-MLP	0.22	0.25	0.22	0.81
Q-26PI-SVM	0.29	0.18	0.19	0.9
Q-26PI-KNN	0.23	0.21	0.17	0.66
Q-69PI-RNN	0.14	0.15	0.13	0.78
16PI-DT	0.08	0.13	0.09	0.62
26PI-RF	0.06	0.07	0.06	0.81

All classifiers predict the *Benign* class with an excellent micro f1-score, greater than 0.80. The majority of classes were detected to some degree by MLP, SVM, KNN and RNN. However, all classifiers failed to predict the minority classes. Regardless of the low macro performance, MLP, SVM, KNN and RNN models show better detection of unmodelled data. These results from the proposed model address the motivation raised in Section II, where NIDS are expected to adapt to new scenarios.

Table IV shows the best models for each classifier after retraining with the 10% of the CICIDS 2018 dataset.

TABLE IV
CICIDS 2018 BEST MODEL PER CLASSIFIER.

Model	**Accuracy**	**f1-score** (macro)
Q-69PI-RNN	0.98	0.73
26PI-RF	0.78	0.72
Q-26PI-SVM	0.73	0.68
Q-26PCA-MLP	0.78	0.67
Q-26PI-KNN	0.77	0.66
16PI-DT	0.77	0.64

After model retraining, Q-69PI-RNN results are the best with a macro f1-score of 0.73 and remains similar to those from the previous dataset contrasted with other classifiers. RF was marginally lower with a 0.72 f1-score with a 0.16 decline against the 0.88 from the first model.

An interesting observation is that PCA with a Quantile transform performs well against the CICIDS 2018 dataset. This suggests that PCA may be transforming the data into a more uniform distribution[5].

In the table presented, there were no other results of significance observed for the other classifiers.

VI. CONCLUSION AND FUTURE WORK

This paper focused on ML-based NIDS development following a systematic multi-class analysis of classifiers. During the process, an identified challenge was categorising irregular traffic and adapting to novel malicious traffic. In response, several supervised ML classifiers, hyperparameter tuning, feature engineering and data preprocessing activities were explored.

As part of data preprocessing, the effect of Quantile transformation with uniform output on distance-based classifiers – KNN, MLP, SVM, RNN and NB – showed superiority in the macro f1 of the models. This suggests that a uniform distribution transform to the training dataset inherently benefits the models. The literature reviewed did not identify the need as part of the proposed methodology except for the Standard scaler used by Rosay et al. [4]. In practice, a computer network is likely to follow a uniform distribution in usage, thus likely why the transformation was as effective. Of note, None distance-based classifiers preferred no scaling and had lower accuracy when PCA was applied.

RNN was the best ML classifier in terms of average macro f1-score, followed by RF that performed marginally lower. RNN remains consistent when presented with new datasets, thus reflecting more stability from a macro f1-score perspective. RF does perform better at a micro-class discrimination level to the RNN model. The model is thus a better fit for diverse network traffic classification and novel scenarios compared to the rest of the model evaluated. At a macro level, the rest of the evaluated models perform well except for NB.

The macro f1-score was the most reliable metric for this imbalanced dataset as the other metrics – ROC curve, AUC, micro f1-score, accuracy – were hard to distinguish results for analysis. The literature reviewed did not describe the choice of metrics and their effectiveness on models evaluation, to a great extent for minority classes.

PI yielded favourable results over PCA for dimensionality reduction. As part of future work, a correlation matrix to identify correlated features during feature selection can be explored to contrast with PI. Given the widespread adoption of the KDD-99 dataset – which has different features extracted to the CICIDS 2017 and CICIDS 2018 datasets used in this paper – additional studies to consolidate features and labelling

[5]PCAs dominant components resulted in a uniform distribution.

across datasets can be developed to address limitations that are inherent in model development with different datasets.

REFERENCES

[1] B. Schneier, *Secrets and lies: digital security in a networked world*. John Wiley & Sons, 2015.

[2] D. E. Denning, "An intrusion-detection model," *IEEE Transactions on software engineering*, vol. 1, no. SE-13, pp. 222–232, 1987.

[3] M. A. Hayes and M. A. M. Capretz, "Contextual anomaly detection framework for big sensor data," *Journal of Big Data*, vol. 2, pp. 1–22, 2014.

[4] A. Rosay, F. Carlier, and P. Leroux, "Mlp4nids: An efficient mlp-based network intrusion detection for cicids-2017 dataset," in *Machine Learning for Networking*, S. Boumerdassi, É. Renault, and P. Mühlethaler, Eds. Cham: Springer International Publishing, 2020, pp. 240–254.

[5] C.-F. Tsai, Y.-F. Hsu, C.-Y. Lin, and W.-Y. Lin, "Intrusion detection by machine learning: A review," *expert systems with applications*, vol. 36, no. 10, pp. 11 994–12 000, 2009.

[6] K. Atefi, H. Hashim, and M. Kassim, "Anomaly analysis for the classification purpose of intrusion detection system with k-nearest neighbors and deep neural network," in *2019 IEEE 7th Conference on Systems, Process and Control (ICSPC)*, 2019, pp. 269–274.

[7] O. Chapelle, P. Haffner, and V. Vapnik, "Support vector machines for histogram-based image classification," *IEEE transactions on neural networks / a publication of the IEEE Neural Networks Council*, vol. 10, pp. 1055–64, 09 1999.

[8] D. Aksu, S. Ustebay, M. Aydin, and T. Atmaca, *Intrusion Detection with Comparative Analysis of Supervised Learning Techniques and Fisher Score Feature Selection Algorithm*. Cham: Springer International Publishing, 09 2018, pp. 141–149.

[9] N. Bisht and A. Ahmad, "Analysis of classifier ensembles for network intrusion detection systems," *Communications on Applied Electronics*, vol. 6, pp. 47–53, 02 2017.

[10] B. Reis, E. Maia, and I. Praça, "Selection and performance analysis of cicids-2017 features importance," in *International Symposium on Foundations and Practice of Security*. Springer, 2019, pp. 56–71.

[11] P. Muhuri, P. Chatterjee, X. Yuan, K. Roy, and A. Esterline, "Using a long short-term memory recurrent neural network (lstm-rnn) to classify network attacks," *Information*, vol. 11, p. 243, 05 2020.

[12] J. V. Tu, "Advantages and disadvantages of using artificial neural networks versus logistic regression for predicting medical outcomes," *Journal of Clinical Epidemiology*, vol. 49, no. 11, pp. 1225–1231, 1996. [Online]. Available: http://www.sciencedirect.com/science/article/pii/S0895435696000029

[13] Y. Chuan-long, Z. Yue-fei, F. Jin-long, and H. Xin-zheng, "A deep learning approach for intrusion detection using recurrent neural networks," *IEEE Access*, vol. PP, pp. 1–1, 10 2017.

[14] D. Aksu, S. Üstebay, M. A. Aydin, and T. Atmaca, "Intrusion detection with comparative analysis of supervised learning techniques and fisher score feature selection algorithm," in *Computer and Information Sciences*, T. Czachórski, E. Gelenbe, K. Grochla, and R. Lent, Eds. Cham: Springer International Publishing, 2018, pp. 141–149.

[15] E. K. Viegas, A. O. Santin, and L. S. Oliveira, "Toward a reliable anomaly-based intrusion detection in real-world environments," *Comput. Netw.*, vol. 127, no. C, pp. 200–216, Nov. 2017. [Online]. Available: https://doi.org/10.1016/j.comnet.2017.08.013

[16] I. Sharafaldin, A. H. Lashkari, and A. A. Ghorbani, "Toward generating a new intrusion detection dataset and intrusion traffic characterization." in *ICISSP*, 2018, pp. 108–116.

[17] Kurniabudi, D. Stiawan, Darmawijoyo, M. Y. Bin Idris, A. M. Bamhdi, and R. Budiarto, "Cicids–2017 dataset feature analysis with information gain for anomaly detection," *IEEE Access*, vol. 8, pp. 132 911–132 921, 2020.

Hatitye Chindove is currently pursuing his MSc. in Computer Science at Rhodes University. The focus of his research is network intrusion detection systems and machine learning.

Dane Brown obtained his PhD and is a Senior Lecturer at Rhodes University. His research interests are image processing, machine learning, information security and GPGPU.

Improving User Experience in Community Networks using a Browser Extension

Hilbert Muchatibaya[1], Alfredo Terzoli[2], Nomusa Dlodlo[3]

Department of Computer Science, Rhodes University
Drosty Rd, Grahamstown, Makhanda, 6139, South Africa

[1]hilbertmuna@gmail.com

Abstract— **Changes within ICT over the past decade required a review of the network solution deployed in the Siyakhula Living Lab (SLL), a joint venture between the Universities of Fort Hare and Rhodes, focussed on finding blueprints for sustainable e-infrastructure in poor communities. The review found that the in-network cache – Squid - is no longer effective, given the switch to HTTPS, the strong presence of advertising, and the data weight of current web pages. The issue can be cured leveraging Squid's 'bumping' and splicing features; deploying a browser extension to make picture download optional; and using Pi-hole, a DNS sinkhole. However, in this work, we report on the browser extension. The results show that, by blocking images and videos, we decrease the page weight and manage data usage, which improves user experience. The browser extension also aims to satisfy the important constraints of technical simplicity and financial viability within the 'broadband islands'.**

Keywords— **ICT4D, Broadband Island, access networks, user experience, page load time, bandwidth management.**

I. INTRODUCTION

The Siyakhula Living Lab (SLL) is a joint ICT for Development (ICT4D) venture between the Universities of Fort Hare and Rhodes in South Africa. From its start in 2005, its aim has been the practical development of blueprints for the sustainable deployment of the e-infrastructure in poor communities, both rural and peri-urban. The e-infrastructure model has three main components: one focusing on the network, one on computing and one on the applications.

Over the past decade rapid change has characterized ICT, which has affected network design across the industry. As a result, there was a need to review the blueprint for the network component of the SLL, to gauge the extent to which the change had affected it and suggest appropriate updates where necessary, to ensure that it remains a useful tool to allow access to the Internet to poor communities in South Africa. The results of the review showed that the switch from HTTP to HTTPS, among many other changes, has impacted the page weight and that has resulted in high bandwidth consumption.

The adoption of HTTPS was inevitable due to the rising concerns of security in a more personalized web2.0. This issue was addressed in two ways; leveraging Squid's 'bumping' and 'splicing' feature and deploying a browser extension to make picture download option. In this paper, we will discuss the latter issue.

II. BACKGROUND

A. *Research Background*

The network component of the Siyakhula Living Lab is based on a high-speed wireless local area network, called Broadband Island (BI), connecting a cluster of nearby schools and linked in redundant fashion, but at much lower speed, to the Internet. The advantages of this approach to network design are as follows: it provides high speed communication between entities and members of the community within the span of the Broadband Island, facilitating local collaboration; and it allows the community to share access to the Internet in a cost-effective manner [1], [2]. The high-speed local area network allows also the sharing of common services. An important service to the network component is a central cache, so that remote content is stored locally as much as possible to reduce bandwidth and data usage when reaching outside the Broadband Island

Within this model, local schools house digital access nodes, which are computing infrastructure points of presence. In practice, the network component comprises routers, switches, wireless access points, antennas, WiMAX CPEs and in some cases micro base stations[1], [2].

The actual deployment has been using WiMAX technology from Alvarion to share Internet access. The decision to use WiMAX was based on the promise, in 2006, of a new technology, described in both academic and consumer's literature as "Wi-Fi on steroids". WiMAX offered solutions to the problems of outdoor use of Wi-Fi at that time. It could be used natively over much longer distances, without the need of a clear line of sight, supported higher data throughput and was less susceptible to interference because of running in licensed bands [1], [2].

The original deployment was divided into cells, each of them hosting a WiMAX micro base station (μbs). The WiMAX μbs are wireless access point and were located at two schools. The μbs's worked together with the BreezeMAX CPEs housed in the other connected schools. The two WiMAX base stations were mounted, together with 13 dBi omni-directional antennas, on 12m masts in the schools' property. These μbs's were then connected to a core router responsible for routing traffic from the schools where the μbs's are hosted to the Internet [1], [2].

The links to the Internet were realized through VSATs (Very Small Aperture Terminal, a satellite-based technology).

The web cache service was realized using Squid, a well-known proxy server at the time of the initial deployment. Its presence improved drastically network performance, helped by the homogeneity of the community served by the Broadband Island. Also, Squid allowed good control on websites access, preventing for example access to inappropriate content, either

because of its nature or because its impact on the links to the Internet.

B. *The effects of recent technological trends on the page weight*

Over the last 10 years web browsing is has evolved at a very high pace. We have seen webpages evolve from simple text content from one server to complex dynamic web pages being served from multiple domains *[3], [4]*. The increase in page complexity is partly due to the introduction of Web2.0 and HTTP/2, which have dramatically influenced the nature of the content and how it is delivered. Web2.0 has resulted in more personalized dynamic web sites e.g., Social Media websites. In addition, we have seen an increase of the User's bandwidth over the years. According to Nielsen's Law of Internet bandwidth, the User's bandwidth grows by 50% per year and there is evidence that shows that the law fits data collected from 1983 to 2019 *[5]*. With the increase in resources i.e., user bandwidth, the introduction of more efficient content delivery protocols or technology, the demand for rich content and more functionality on Web sites has risen. Consequently, page complexity has had to increase consistently to meet user expectations.

As expected, there is anecdotal evidence of users being frustrated by the high page load times and increased bandwidth consumption [3]. It is clear that to an extent, this outcome is a result of conflicting expectations. Since in general, the heavier and more functional a webpage is, the higher its Page Load Time (PLT) because we then factor in computational overhead and the bandwidth bottleneck. In some instances, web masters have resorted to rendering web pages on the server and then simply serving the client with a fully rendered webpage. However, this also limits the number of requests servers can handle, depending on how much computation has to be done per request. However, it is worth noting that these issues mentioned have had solutions provided for them, such as edge caching, reverse caching and Server Push (an HTTP/2 feature).

HTTP/2 was recently standardized to optimize the Web by promising faster Page Load Times (PLT) as compared to the standard HTTP/1.1 [6] . In addition, the introduction of edge caching and CDNs, has allowed content providers to ensure that they provide fast delivery of their content by serving them from servers that are geographically closer to the end user. Therefore, it is clear that the increase in page complexity has been coupled with adequate improvements to handle the ever-increasing demands from the end user. However, these solutions fare well only in high resource environments where users have access to high bandwidth and are willing to pay extra for sophisticated infrastructure or faster internet.

Our observation is that in an environment where the user's resources i.e., disposable income, bandwidth and advanced devices, are not a limiting factor, the rate of data consumption is less likely to impact user experience. However, in low resource communities, with no access to high bandwidth due to financial constraints, the rate of data consumptions impacts user experience more significantly. To be clear, this does not imply that either environment would not have issues arising from PLT or general high data consumption. This only highlights the types of trade-offs likely to be taken in both environments based on the available resources.

The problems mentioned above could be observed during one of our experiments in a school, in Dwesa, Eastern Cape, point of presence of the SLL. The data usage from a simple lab experiment reflected that the rate of data consumption was not sustainable. Based on HTTPArchive, we have seen significant increase in the average page weight from the time that we initially setup the broadband islands network [7]. It is also highlighted those images and videos are the biggest contributors to this increase. To relate this to what we mentioned earlier, in a low resource environment like Dwesa, where there are limited financial resources, the rate of data consumption does not only impact user experience, but it also determines whether the solution as a whole is viable in the long run. Since it's already been established that images and videos contribute significantly to the problem, in this chapter we propose a browser extension that will reduce the page weight of each webpage by blocking unnecessary images and videos

C. Page Weight and User Experience

Page weight refers to the total size of a web page including all resources used to create the page. Page weight is important because it affects user experience [8]. Broadly speaking, user experience can be put into two categories: page load time and rate of data consumption. In this scenario however, we are more concerned lowering the rate of data consumption. In recent times, it is clear that images and videos constitute more of the total page weight as illustrated by the diagram below.

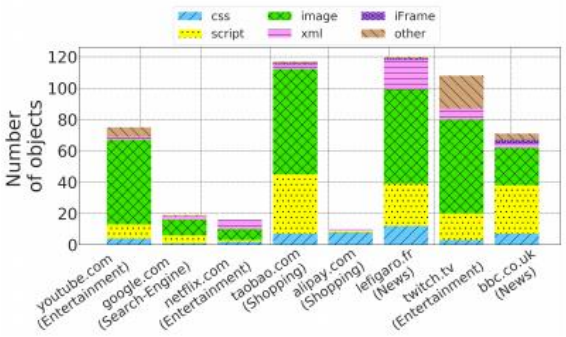

Figure 1: Type of resources contributing to page weight [4]

D. *Our Solution*

Now that we have established the degree to which images contribute to the dramatic increase in page weight., we will discuss one component of our solution: the image blocking browser extension. This solution is one part of a two-part solution, which involves leveraging Squids 'ssl-bumping' feature, to allow us to cache encrypted webpages. The image blocking extensions has 3 main processes:

(1) Intercept all get requests and then filter the request URL header(s) of each request and cancel all requests that contain images extensions.

(2) Storing the URL of the cancelled request

(3) Embedding the image URL(s) in a button the user can use to download the image later.

The following sections will explain the architecture of the browser and how we designed, implemented and tested the solution

III. Browser Architecture

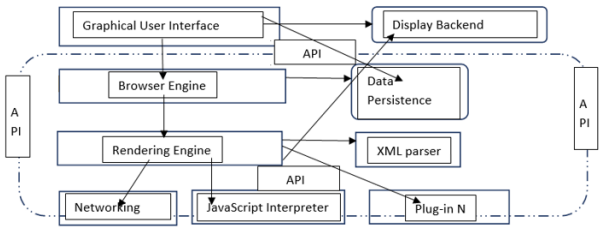

Figure 2: Modern web browser architecture [9]

A. *Graphical User Interface (GUI)*

The user interface in a browser, is the top bar in a browser and that is where the controls for the user lie. The user interface includes space to type in a URL, a refresh button and back/forward buttons. In addition, the user interface displays all active extensions [9].

B. *Browser Engine*

The browser engine is the bridge between the render engine and the user interface. Based on the inputs from the user, it queries and manipulates the render engine [9].

1. *Rendering Engine*

The render engine starts by getting contents of the requested document from the networking layer and then it goes through this four-step process:

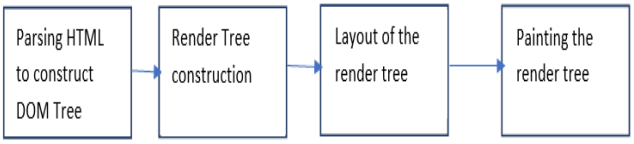

Figure 3: 4 stages of page rendering [10]

The render engine parses through the HTML document looking for HTML symbols and related attributes so that it can convert them into DOM nodes that can be traversed using JavaScript. The engine will also parse through CSS files (inline, embedded and external) to create a cascading style sheets object model (CSSOM). The styling information and the visual instructions from the HTML will create another tree called the render tree [9] [11] .

The layout process determines where each node will appear on the screen. Finally, the browser engine will traverse through the render tree and paint it below the GUI using the UI backend layer/Display backend [9] [11].

2. *Networking*

The networking components handles HTTP requests and all aspects of internet communications. In addition, it implements a cache of retrieved documents to reducing where possible network usage.

3. *The Request/Response Cycle*

At the core web is a series of requests and responses between clients and servers. A client is a software component that requests for services made available by the server. Normally, a client is a web browser but, in some instances, they can be API's making requests to another server. A client generates a text string containing specifications of the resources it needs from the server, this string is called an HTTP request. This request is containing a URL, which is a string that specifies the resource the client wants from the server [12] [13].

C. Plug-in N

1. *Browser Extensions*

A browser extension is a typical example of a plug-in. A plug-in is a software component that extends the features of an existing program without the need to modify its codebase. The browser extensions can take advantage of the same APIs that the browser uses on the web page and extend the features of the browser with its own set of APIs. Browser extensions enable third-party developers to create behaviours which extend the browser without the risk of them modifying the source code [9].

2. *How a browser renders a webpage*

First, the user types in the URL of the webpage or resource they need. The browser engine then uses the network process to create an HTTP GET request with the URL of the desired resource or web page. (The client then does a DNS Lookup to find the IP address of the host containing the resource specified in the URL [11], [14]). When the host server locates the resource, a HTTP response message is sent back to the browser. If the returned resource is a web page, the browsers render engine parses through the HTML file. Parsing means that the browser will derive the structure or layout of the webpage by processing the various components contained in the response. The HTML file contains the text content of the web page, the structure of the web page and links to other resources (URLs) [11]. As the render engine is parsing the HTML file, it communicates through IPC with the network component to fetch the other resources the web page needs. These resources include CSS (sets the rules for the structure of the page), JavaScript (describes the behaviour of the webpage) and media content which includes images and videos. After the browser parses through the HTML file, CSS files and decodes all media needed for the page, it renders the web page and displays it to the user. In addition, it creates an internal data structure called the document object model[11].

IV. *Browser Extension in SSL*

In the last section we described how the browser software component functions and we also described the role or purpose of browser extensions. In this section, this information will now be put into the context of SSL.

A. *SLL Browser Extension*

The SSL extension consists of 4 different, but cohesive, components. These components include, a background script, content script, UI elements and a JavaScript file that maintains its state globally and across different tabs. Based on the description of the SSL extension, this section will use a holistic approach to the analysis of the browser extension in order to emphasize how the constituent components of the extension correlate and are the sum of the system.

B. *Manifest File*

The manifest file fulfils provides metadata of the extension. This metadata includes information that specifies the most important files and the capabilities the extension might use.

C. *UI Elements*

The browser extension is expected to be used by various users, both technical and non-technical users, therefore, the user interface design has to be simple enough for the average user to understand but also offer complex enough information for the practitioners to use. As a rule, a browser extension must only have one clearly defined objective. The SLL extension has one objective, which is to block images and videos to allow the user to save data. To be clear, the SLL extension is not simply just blocking the image from being loaded on the user's webpage but it is ensuring that the images or videos are not transferred over the network or access link. This is a key point because the extension is offering an alternative to the proxy cache. The SLL extension doesn't not simply block images and videos, but it also offers the user the option to download specific images they may want to view. In addition, the browser extension will provide statistics to the user regarding the potential data saved and the total number of images that were blocked.

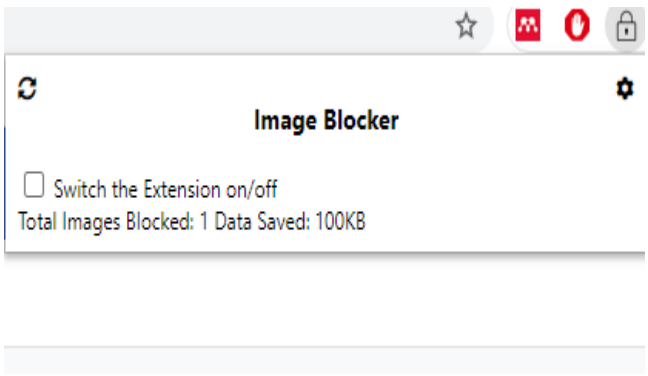

Figure 4: User Interface for SSL Browser extension

As illustrated above, the status of the browser extensions provides the user with regular feedback on the state of the system. Much of the design principles used for the user interface are based on Nielsen's 10 heuristics. For example, the choice to use the cog to represent systems settings and the circular arrows as the refresh button was to leverage the familiarity that comes with these icons as they are widely used in the majority of interfaces. Another example is the minimalistic design is to ensure that all information displayed on the UI is relevant, therefore, allowing the user to spend less time understanding the extension. Lastly, is the visibility of the system status, this is to ensure that the user is informed about what is going on.

D. *Background Scripts*

The background scripts of the SLL extension have a single purpose: to block images from being downloaded from the server. To do this, the scripts will make use of the web request api events in figure 5.

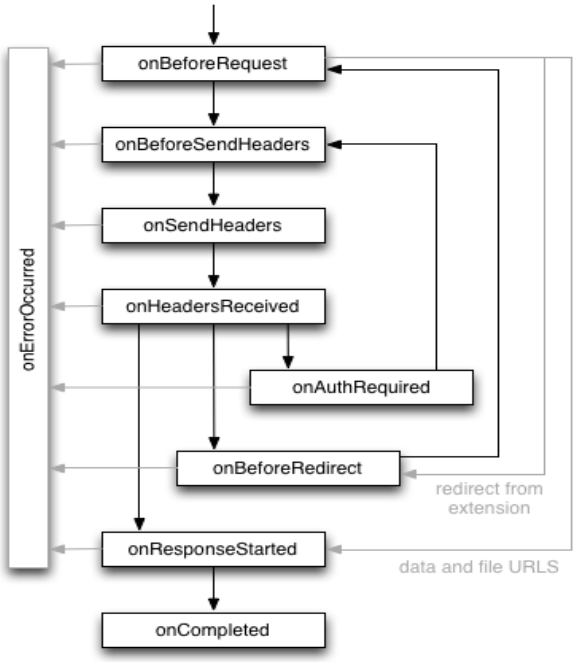

Figure 5: Web request API events [16]

Since the purpose of the SLL extension is to provide similar benefits to the proxy cache, a lot of the design decisions were based on architecture of a proxy cache. For example, the proxy stores remote content locally to ensure that the expensive access link is used sparingly, therefore, it makes sense that the browser extension would listen to network events before they are sent over the network. So, the SLL extension will be listening for the onBeforeRequest to allow it to filter out any URL's that are fetching images before the images are already transferred over the access link. This will use the URL filter policy that will cancel any request that has a URL containing an image extension or if the request type is an image. According to HTTP archive, the most common image extension types on the web have the following file extensions: - jpeg, webp, ico, svg. In addition, the policy will also cancel requests with a MIME type containing image [7], [16].

Also, the background script estimates the total data saved during each browsing session using the following equation:

$$\text{Estimated data saved} = \text{Average size of an image} \times \text{number of images blocked} \quad (1)$$

This is an estimate because it is not possible to know the size of the image unless it is transferred over the network. The average size of the image is based on the data provided by HTTP Archive that states that as of 2020 the average size of an image is 973.4 KB [7].

E. *Content Script*

Context scripts work in the context of the webpage; therefore, they are treated as if they are not part of the main extension [16] [17]. The content script of the SLL extension is will make changes to the webpages the user visits and it will listen to events and pass messages to the background extension. The goal of the extension is not only to block all images but to also allow the user to pick specific images they would like to view

Since the content script run in the context of the webpage, it uses a message passing API to communicate with the rest of the extension. This communication is done using an API for one-time requests or in certain instances long-lived connections. The content script will need to communicate with the background script throughout the duration of the users browsing session. This is because the extension will be continuously updating tab statistics for the user and also listening for click events in the case where the user needs to download an image. That is why the content script uses long-lived connections that allow a longer conversation between the background script and the content script.

F. *How it all works together:*

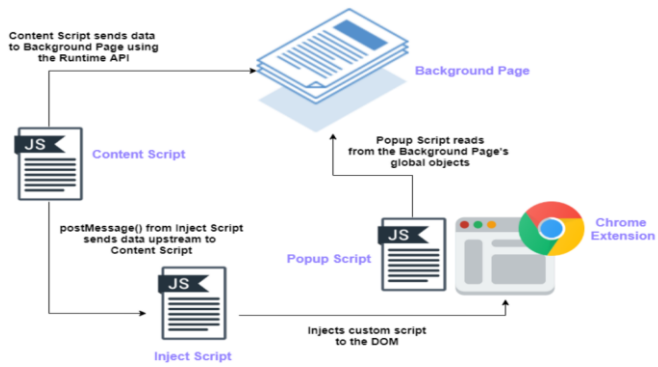

Figure 6: How all the browser components work together [18]

The diagram above shows how the different components of the browser extension all work together and communicate for the common goal.

When the page is loaded, the script executes code that traverses through the DOM and adds a download button to next to all blocked images or within the same parent node.

Figure 7: Images blocked by SSL extension

G. Functional Testing

Independent variable: Disabled/Enabled images in the browser

Dependent variable: Data Usage

Controlled variables: Browser cache (Always must be cleared at the beginning of each experiment), the experiments will all be done on the same website and each experiment will be done in Google Chrome.

Table 1. A SUMMARY OF THE RESULTS FROM THE EXPERIMENT

Website Name	Website Url	Data Transferred before	Data transferred	Data Saved	Data Saved
Khan Academy	khanacademy.org/	1600	299	1301	81,3
Code Academy	codecademy.com	1300	832	468	36,0
Apex Learning	apexlearning.com/	13400	4700	8700	64,9
Mobymax	mobymax.com/	2700	1300	1400	51,9
ABCya	abcya.com/	2200	1800	400	18,2
Achieve 3000	achieve3000.com/	1600	1021	579	36,2
Cool Math	coolmathgames.com/	2100	1500	600	28,6
PBS kids	pbskids.org/	5100	1300	3800	74,5
Hooda Math	hoodamath.com/	1100	384	716	65,1
Average Data Saved (%)	50,7				
Average Data Saved (KB)	1996				
Average Data Saved (MB)	2,00				

As illustrated on table 2, the average data saved per webpage is 50.7%. These results confirm that the browser extension is more effective than the browsers in-built image blocking function and this is mainly because the extension also blocks videos. Due to the blocked images and videos, the page weight of the web pages is reduced, as a result, less data is consumed.

H. UX Testing

The aim of this testing it to assess the effectiveness and efficiency of this browser extension. The criteria for the testing are accessibility, functionality and user interface. The browser extension was tested by colleagues and friends on various devices and below is the feedback we got.

I. Feedback

The users stated that the user interface of the extension has a very simple design which comprises of a single button that allowed them to either enable or disable the extension with ease. The extension automatically reloads the webpage when the state of the system changes i.e., the user starts or stops the extension and this improved the user experience for the users as they were provided with visual cues whenever they interacted with the system.

For those who were in a low-bandwidth setting, the user's experienced faster page load time, which significantly improved their user experience

Lastly, we expected that the lack of images during browsing would negatively impact the browsing experience, especially on websites where images are used to communicate or capture the user's attention. However, that was not the case, as the feedback from the users suggested that the majority of the images where merely placeholders and had no effect on the users overall browsing experience.

J. Porting the browser extension

The browser extension was designed and implemented on Google Chrome, therefore, there was a need for us to port it to other web browsers. Porting the extension from Google Chrome to Firefox and Microsoft Edge is a straightforward process because the Web Extension APIs are designed to support cross browser compatibility. This is because most of the Web APIs support call back functions under the chrome namespace. For this reason, the extension is a lightweight and easy to deploy software which is a crucial faction in this context. The browser extension improves user experience and this can be broadly put into two categories; page load time and data usage. Google has indicated that page load time or page speed is used as a ranking factor when it comes to user experience.

V. Conclusion

In conclusion, we built a browser extension for a low-bandwidth setting, to allow users to block images as a way to reduce data consumption, which would also improve user experience. The results from testing this extension showed us that individuals in a low-bandwidth setting, benefit more from making the trade-off between data consumption and blocking images from webpages. We also managed to port the browser extension on other browsers with no difficulty.

ACKNOWLEDGMENT

This work was undertaken in the Distributed Multimedia CoE at Rhodes University, with financial support from Telkom SA and Infinera. The authors acknowledge that opinions, findings and conclusions or recommendations expressed here are those of the author(s) and that none of the above-mentioned sponsors accept liability whatsoever in this regard.

REFERENCES

[1] A. Terzoli, I. Siebörger, and S. Gumbo, 'Community " Broadband Islands " for digital government access in rural South Africa', 2017.

[2] A. Terzoli, I. Siebörger, M. Tsietsi, and S. Gumbo, 'Digital Inclusion : A model for e-Infrastructure and e- Services in Developing Countries'.

[3] M. Butkiewicz, H. V. Madhyastha, and V. Sekar, *Understanding Website Complexity: Measurements, Metrics, and Implications*. 2011. [Online]. Available: http://www.cs.ucr.edu/~harsha/web_complexity/.

[4] A. Saverimoutou, B. Mathieu, and S. Vaton, 'A 6-month analysis of factors impacting web browsing quality for QoE prediction', *Comput. Netw.*, vol. 164, p. 106905, Dec. 2019, doi: 10.1016/j.comnet.2019.106905.

[5] W. L. in R.-B. U. Experience, 'Nielsen's Law of Internet Bandwidth', *Nielsen Norman Group*. https://www.nngroup.com/articles/law-of-bandwidth/ (accessed May 23, 2021).

[6] T. Zimmermann, B. Wolters, O. Hohlfeld, and K. Wehrle, 'Is the web ready for HTTP/2 server push?', *CoNEXT 2018 - Proc. 14th Int. Conf. Emerg. Netw. Exp. Technol.*, pp. 13–19, 2018, doi: 10.1145/3281411.3281434.

[7] 'HTTP Archive'. https://httparchive.org/ (accessed Nov. 15, 2020).

[8] M. Butkiewicz, D. Wang, Z. Wu, H. V. Madhyastha, and V. Sekar, 'KLOTSKI: Reprioritizing Web Content to Improve User Experience on Mobile Devices', p. 16.

[9] S. B. Matija Varga, Michal Mokrys, 'The evolution of web browser architecture', no. June, 2014.

[10] P. Silva, R. Monge, T. Federico, S. María, and E. B. Fernandez, 'A Reference Architecture for web browsers: Part II, A pattern for Web Browser Content Renderer', doi: 10.1145/3011784.3011813.

[11] 'Inside look at modern web browser (part 1) | Web | Google Developers'. https://developers.google.com/web/updates/2018/09/inside-browser-part1 (accessed Nov. 15, 2020).

[12] 'An overview of HTTP - HTTP | MDN'. https://developer.mozilla.org/en-US/docs/Web/HTTP/Overview (accessed Nov. 15, 2020).

[13] A. Brylinski, 'Overview of HTTP / 2', 2017.

[14] 'How the browser renders a web page? — DOM, CSSOM, and Rendering | by Uday Hiwarale | JsPoint | Medium'. https://medium.com/jspoint/how-the-browser-renders-a-web-page-dom-cssom-and-rendering-df10531c9969 (accessed Nov. 15, 2020).

[15] A. Barth, A. P. Felt, P. Saxena, and A. Boodman, 'Protecting Browsers from Extension Vulnerabilities', *Ndss*, vol. 147, pp. 1315–1329, 2010, doi: 10.1111/j.1365-2486.2006.01169.x.

[16] 'Getting Started Tutorial - Google Chrome'. https://developer.chrome.com/extensions/getstarted (accessed Nov. 15, 2020).

[17] 'Browser Extensions - Mozilla | MDN'. https://developer.mozilla.org/en-US/docs/Mozilla/Add-ons/WebExtensions (accessed Nov. 15, 2020).

[18] 'Chrome Extension Tutorial: How to Pass Messages from a Page's Context', *freeCodeCamp.org*, Feb. 24, 2021. https://www.freecodecamp.org/news/chrome-extension-message-passing-essentials/ (accessed Jun. 06, 2021).

BIOGRAPHY

Hilbert Muchatibaya is a final year Masters Student at Rhodes University. He is in the Department of Computer Science and he is a member of the Telkom Centre of Excellence. Hilbert has been

involved this programme to help grow local telecommunication and information technology skills in marginalized communities.

Performance of Mobile Money Fraud Detection Models on Imbalanced Datasets: The Effect of Sampling Techniques

Oluwatosin Elegbede[1], Khulumani Sibanda[2]

Department of Computer Science, University of Fort Hare

[1]tosinel12@gmail.com

[2]ksibanda@ufh.ac.za

Abstract—**Mobile money fraud detection is very important for users of the platform. The majority of the literature focuses on evolving and enhancing quantitative approaches to improve how well detection models perform. On a hugely imbalanced dataset, this work explores the influence of sampling approaches on the efficiency of machine learning algorithms. Using three sampling techniques, five quantitative algorithms are tested. Up-sampling, downsampling, and Synthetic minority oversampling (SMOTE) are the sampling techniques employed in this study. Decision trees, Naïve Bayes, k-nearest neighbors, gradient boosted trees and logistic regression are the five classification algorithms used. The juxtaposition of each algorithm performance on varied sample sets of the hugely skewed dataset was reviewed. According to the findings, the appropriate sampling method for developing detection algorithms is largely determined by the frequency of fraudulent transactions in the learning sample set.**

Keywords—**Classification, Mobile money, Skewed dataset, Up-sampling, Down-sampling, SMOTE**

I. INTRODUCTION

A. Background

Fraudulent activities in mobile money ecosystems have progressed at the same rate as the mobile money market's technological advancements. Fraudsters have taken advantage of flaws in mobile network providers' systems and processes. There have been a lot of methods that fraudsters use in taking advantage of mobile money platforms **[1]**. This may include malware installed on mobile devices or personal computers, impersonation of company representatives, vishing (voice calls), fraudulent emails and smishing (short message services), data transmission interception, Fraud in near-field communication, and denial of service attacks on mobile money systems. Owing to the restrictions necessitated by COVID 19, South Africa has of late, seen an exponential increase in mobile money fraud daily. This has led to huge losses of people's hard-earned money. Of course, this happens despite financial institutions putting in place several interventions which include prevention and detection. Prevention is always the first line of defense, with financial institutions implementing tactical measures such as multi-factor authentication, short message service alerts to subscribers, regularly cleaning malware as well as access control through HTTPS protocol. The second line of defense disposable to financial institutions is detection. Just like prevention strategies, there are several options for implementing fraud detection in mobile money systems, these include process behavior analysis **[2]**, machine learning techniques, neural network approach, Bayesian networks and many others. This work is only limited to fraud detection hence the discussions in this paper focus on financial fraud detection.

Financial fraud detection is a common classification problem from a statistical standpoint in which a transaction is categorized into a non-fraudulent or a fraudulent category based on its characteristics. Quantitative methods are typically used to detect a link between a service's fraudulent attacks and its mobile money transaction data from the previous fiscal year or other data from the same period revealing the platform's operating environment. This is commonly referred to as a mobile money fraud detection model (MMFDM), which is built using a portion of archival data and assessed using another portion of archival data. With the expectation that the connection will continue hereafter, the algorithm will be able to detect fraud henceforth using the platform's current data. Improving the mobile financial fraud detection model is based on data-fitting experimental findings, and the common model development method is depicted in **Figure 1.** The figure shows various factors that influence the performance of the model. The factors shown are sampling, feature selection, modeling, and evaluation criteria **[3]**.

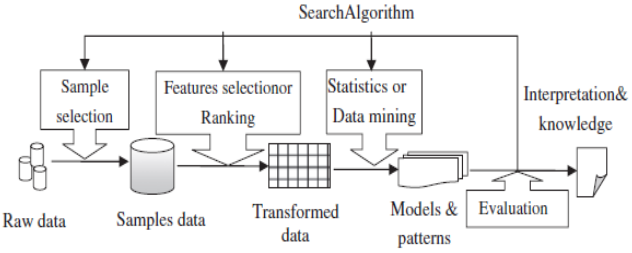

Figure 1: The process of creating an empirical fraud detection model

B. Related work

A great deal of research has gone into the selection of features in the development of MMFDMs.**[4]** identified 14 key ratios for detecting financial fraud and put them to test using a generic algorithm model on 7001 instances of fraudulent / non-fraudulent transactions. The empirical findings revealed that the most efficient attributes were "age of client", "merchant" and the "amount that is being transacted".**[5]** reviewed 10000 instances of fraudulent and legitimate transactions. The authors used a multilayer perceptron, support vector machine, and Naive Bayes algorithms to test 8 separate ratios recognized to be essential determinants for detecting fraud; The empirical findings revealed that the time gap between each transaction, the type of transaction, the amount transacted, the transaction originator's old balance before the transaction, the originator's final balance after the transaction, the recipient's old balance

before the transaction, amount transacted and the recipient's final balance after the transaction were the most decisive attributes that could accurately detect fraudulent activities. In the same vein, several quantitative approaches and techniques from data mining have been used to develop algorithms that can perform better. These include linear regression **[6]**, and decision trees **[7]** algorithms. Regardless of which approaches are used to develop better algorithms, how well a fraud detection model performs is influenced not only by the features chosen and the quantitative methods used but also by the volume of samples used to fit the model. The type of quantitative techniques employed determines the form of a model, but the algorithm parameters are decided by the data-fitting methods, and thus by the sample collection, **[8]** evaluated the performance of 4 models built using various quantitative methods and different feature sets chosen using different feature ranking techniques.

[9] compared the detection abilities of neural networks when the degree of imbalance was different: 30/100, 50/100, 70/100, and 100/100. They concluded that support vector machines outperformed convolutional neural networks in rightly classifying fraudulent and non-fraudulent transactions when given equal sample size in the learning phase. As can be noted, most of the research carried out to our knowledge focused on either determining the parameters that best detect fraudulent transactions or comparing the performance of models upon varying the degree of data imbalance. This paper aims to investigate the effects of varying learning sample sets and how that affects the performance of widely used fraud detection models.

The remaining sections are organized as follows: Section II presents the sampling strategies, section III presents the metrics of performance, section IV presents the methodology, and section V presents the empirical results.

II. SAMPLING STRATEGIES

The approach employed to resample the dataset in tackling the problem of data skewness has received some scrutiny in the machine learning community **[10-14]**. Down-sampling and up-sampling are two common resampling strategies. Down-sampling involves selecting a fraction of the class with higher data instances to attain a balance with the class having lesser data instances in the binary class. Let the class containing lesser data instances and the class with more data instances be denoted by $|Y_{min}|$ and $|Y_{max}|$ independently, the volume of the class with lesser data instances $|Y_{min}|$ is by far less than the volume of majority class with more data instances $|Y_{max}|$ in the skewed training dataset. Y stands for the learning dataset. **Table 1 [15]** is an illustration of a learning dataset for fraud detection. This illustration is only meant to demonstrate techniques for sampling, and it is unbalanced. Each observation has an N attribute and a transaction status that has been noted: whether transactions are fraudulent or not. In the ''isFraud" column, the fraudulent observation is marked with a value of 1, the legitimate observation is denoted with a value of 0. Each observation has its correspondence denoted by C. Fraudulent observations are denoted by the letter "J" and non-fraudulent observations are denoted by the letter "N". Fraudulent observations are in the minority in this example, while non-fraudulent observations are the class with more instances. As a result, the group of minorities $Y_{min} = \{J_1, J_2 J_3, J_4\}$ and $|Y_{min}| = 4$. Majority class's $Y_{max} = \{N_1, N_2, \dots, N_{10}\}$ and $|Y_{max}| = 10$.

TABLE I
AN EXAMPLE OF THE ORIGINAL TRAINING DATASET IN ITS SIMPLEST FORM.

C	G_1	G_2	…	G_M	isFraud
J_1	1.05	0.03	…	0.01	1
J_2	1.20	0.03	…	0.04	1
J_3	0.67	0.01	…	-0.12	1
J_4	0.57	0.21	…	-0.15	1
N_1	0.24	-0.57	…	-0.64	0
N_2	8.50	-0.13	…	0.88	0
N_3	12.47	-0.10	…	0.89	0
…	…	…	…	…	…
N_{10}	0.58	0.01	…	-0.10	0

A. Up-sampling

The extensively used up-sampling methods are Synthetic Minority Over-sampling Technique (SMOTE) and Random Up-sampling with Replication (RUWR). RUWR is a method for balancing skewed distribution by replicating the skewed class examples at random **[14]**.

Random Up-sampling with replication

Model 1: RUWR (Y_{min}, Y_{max})

Input: The class with lesser data instances Y_{min} and a representative class with more data instances Y_{max}

Output: evened class Y of volume 2| Y_{max}| sample set

i. Y = Y_{max}

ii. **for** i = 1 **to** | Y_{max}|

A random element a_i was chosen at random from the Y_{min} sample set.

Y = Y ∪{$\boldsymbol{b}_i$}.

endfor

The following is an illustration of the definitive learning set Y for the learning dataset shown in Table 1. { $J_4, J_2 J_1$, J_3, N_5, N_7, N_8} and has eight as size.

B. Synthetic Minority Over-sampling Technique

This technique is a revised up-sampling approach reviewed by **[14]**. Here, the class with lesser data instances is up-sampled by developing "synthetic" data instances as opposed to up-sampling with substitutes. The concept of SMOTE is to up-sample the class with lesser data instances by taking samples of the class containing lesser data instances and inserting synthetic samples along line portions linking unspecified or the entire k class with lesser data instances nearest neighbors. The following is a list of SMOTE's features **[14]**:

Model 2: SMOTE($|Y_{min}|, Q, l$)

Input: $|Y_{min}|$number of class containing lesser data instances samples Q percent of the class with lesser data instances is up-sampled; l is the number of closest neighbors. The class with more data instances set $|Y_{min}|$ and the (Q/100) * $|Y_{min}|$ synthetic minority class samples are combined.

i.**if** $\boldsymbol{Q}$ < 100 **then**

Sort the $|Y_{min}|$ minority class samples at random.

T = (Q/1 × 10^2) * $|Y_{min}|$
Q = 10^2
endif
ii.Q = (*int*)(Q/100)
iii.the sum of neighbours
iv.sumfeat= the sum of all the features
v.Instance[][]:the class containing lesser data instances
vi.newinstances = 0//records the instances produced
vii.Generated[][]: a collection of produced instances
viii.for *i* = 1 to $|Y_{min}|$
Calculate the indices for *i*'s *k* nearest neighbors and save them in the *qqarray*.
Fill in (*Q, i nnarray, Synthetic, and newindex*)
endfor
Fill in (*Q, i nnarray, Synthetic, and newindex*)
ix.while Q ≠0
qq = figures between 1 and *k* at random
for *feat*= 1 to *sumfeats*
dif = Sample[qqarray[qq]][feat] − Sample[qqarray[i]][feat]
void = a random figure that is either 0 or 1
Generated[newinstances][feat] = Sample[i][feat] + void × dif
endfor
newinstances **++**
Q = Q – 1
Endwhile

Assume the criteria in the SMOTE technique are set as $|Y_{min}|$ = 4, M = 300, k = 2, for the learning dataset presented in the above Table. SMOTE produces a learning set of twenty-two data instances, including twelve fraud data instances and ten legitimate data instances $\{N_1 \ldots, N_{10}\}$. Step 8 in the above SMOTE is the most important in generating the 12 fraud observations. Assuming G_j i represents the i^{th} feature of observation with correspondence of J_j . The eight-step generates another *Q*/100 = three data instances for each fraud observation, which are referred to as "synthetic" examples. If l_1 's two closest neighbors are l_2 and l_4 , and the random figures *qq* in SMOTE's step nine is two, then one synthetic data instances $\hat{I}_1^1$ for I_1 is obtained as follows:
G_{1-1} = 1.05, G_{1-2} = 0.03, … , G_{1-M} = 0.01
G_{4-1} = 0.57, G_{4-2} = 0.21, … , G_{4-M} = −0.15
ΔG_1 = 0.57 − 1.05 =−0.58, ΔF_2 = 0.21 − 0.03 = 0.18, …,
$\Delta G_i = G_{4-i} - G_{i-i}$,…, $\Delta G_m = G_{4-M} - G_{1-M}$
$(G_1, G_2, \ldots, G_i, \ldots, G_M)$ = (1.05, 0.03, … , $G_{1-i}, \ldots, 0.01$) + *Rand*() × $(\Delta G_1, \Delta G_2, \ldots, \Delta G_i, \ldots, \Delta G_M)$

C. Down-sampling
Random Down-sampling (RD)
The goal of random down-sampling is to make equal the class dispersion by randomly removing the class with more data instances **[16]**. The RD used in this paper is to incoherently choose a portion with more data instances to attain evenness that yields the same result.

Model 3 RD (Y_{min}, Y_{max})
Input: The class with lesser data instances class Y_{min} and class with more data instancesY_{max}.
Output: equal class Y of size 2$|Y_{min}|$ sample set
1. $Y = Y_{min}$
2. **for** *i* = 1 **to** Y_{min}
A random element $\boldsymbol{b_i}$ was chosen from the sample set.
Y_{max}
Y = Y ∪ $\{\boldsymbol{b_i}\}$.
endfor

Learning set Y was developed by RD for the dataset in Table 1 as follows: $\{J_1, J_2 J_3, J_4 N_8, N_3, N_7, N_5\}$ and has a size of eight

Down-sampling based on Nearest Neighbour Clustering (DBONNC)
The clustering problem inspired DBONNC, which splits the nodes into K clusters and picks the nodes that are closest to the middle region of every cluster to depict the entire cluster. A breakdown of DBONNC is analyzed below:

Model 4 DBONNC (Y_{min}, Y_{max})
Input: The class with lesser data instances class Y_{min} sample set and the class with more data instances Y_{max} sample set
Output: Evened class Y of proportion 2$|Y_{min}|$ sample set.
1. $Y = Y_{max}$
2. With the two phases that follow, separate the points in Y_{max} into $|Y_{min}|$ clusters **[17]**:
2.1. In a situation where every iteration consists of entire nodes being transferred to the center of the closest cluster at the same time and then cluster centroids being recalculated, batch updates are employed.
2.2 When nodes are reassigned independently, online updates are used.
3. **for** *i* = 1 **to** Y_{min}
Find the cluster i's mid-point $\boldsymbol{c}_i$.
Choose the node $\boldsymbol{b}_i$ that is closest to the node $\boldsymbol{c}_i$ in cluster *i*.
Y = Y ∪ $\{\boldsymbol{b_i}\}$.
endfor
Assume non-fraudulent observations in Table 1 are divided into four clusters as shown; $\{N_2, N_3, N_8\}$, $\{N_1, N_7, N_{10}\}$, $\{N_4, N_6, N_8, N_9\}$,$\{N_5\}$. The midpoint of each cluster is simple to calculate; the midpoint's coordinates are the median of the equivalent coordinates of all nodes in the cluster. Nearest nodes to the cluster's midpoint can then be evaluated.
$Y = \{J_1, J_2 J_3, J_4 N_2, N_7, N_6, N_5\}$

III. METRICS OF PERFORMANCE

To assess the models' performance, the following five common performance measures were chosen:
A. Sensitivity = $\frac{\text{NN}}{\text{NF+NN}}$
B. Specificity = $\frac{\text{FF}}{\text{FN+FF}}$
C. Accuracy = $\frac{\text{NN+FF}}{\text{NF+NN+FF+FN}}$

Where NN denotes non-fraudulent classification as fraudulent, NF denotes non- fraudulent classification as fraudulent, FF denotes fraudulent classification as fraudulent and FN denotes fraudulent classification as non-fraudulent.
D. F1-Score = 2 * $\frac{\text{Precision} * \text{Recall}}{\text{Precision} + \text{Recall}}$ **[18]**

Where Precision $= \frac{NN}{NN+FN}$, Sensitivity = recall. Precision indicates how many legitimate data instances were correctly classified as legitimate by the models, whereas Recall/ Sensitivity indicates how many real non-fraudulent observations were accurately classified as legitimate by the algorithms.

E. AUC stands for the area underneath the Receiver operating characteristic curve: Sensitivity serves as the Y-axis, while 1-Specificity serves as the X-axis. In a two-dimensional ROC graph, the relative arbitrate is depicted in a ROC graph (true non-fraudulent) and cost (false non-fraudulent). It's effective for building and visualizing classifiers, particularly in areas of expertise where class dispersion is skewed. The AUC of a model classifier is the likelihood that an arbitrary chosen positive instance will be rated above a randomly chosen negative instance **[19]**.

IV. METHODOLOGY

Within the confines of this study's domain, two methodologies can be implemented. These methodologies are CRISP-DM **[20]** and SEMMA. CRISP-DM stands for Cross Industry Standard Process for Data Mining. SEMMA methodology comprises five sequential stages that aid the implementation of data science tasks. These stages are "Sample, Explore, Modify, Model, and Assess" **[21]**. CRISP-DM methodology was chosen due to its capability of understanding the business domain. The SEMMA methodology shows a smaller focus on the initial planning stages of a data mining task. This is disadvantageous when building machine learning models because the performance evaluation of these algorithms is based on the business understanding of the use case.

A. THE DESIGN OF THE STUDY

The design consists of the total requirements for implementing a data science project. The stages of the CRISP-DM process made up the strategy for the data analysis.

1) Business understanding

The business understanding includes being aware of the goals and specifications of a project. This stage helps to select the best sampling technique applicable for making the best business decisions. Data sources and choice of software are necessities in this stage.

2) Data understanding

This stage involves data collection, description, and exploration. The entire procedure is described in the subsections that follow.

a) Data collection

Secondary data was adopted mainly to promote the confidentiality of mobile money customers, these records were obtained from a month's financial history of an organization. The dataset was obtained from Kaggle**[22]**. In the Kaggle dataset, a fraudulent transaction is denoted by 1 while a legitimate transaction is denoted by 0 in the ''isFraud" binary class.

b) Data description

The synthetic dataset was created by a simulator known as *paysim*. It is made up of 6,362,620 mobile money records and 11 attributes. The *step* attribute refers to the time interval between transactions where 1 step (total steps =744) equals 1 hour (total days =30); *type* refers to the nature of the transaction. It has 5 class attributes namely CASH-IN, CASH-OUT, DEBIT, TRANSFER, and PAYMENT; *amount* refers to the transaction amount in the local currency; *nameOrig* refers to the account name of the merchant who began the transaction; *oldBalanceOrig* refers to the initial balance in the merchants' account before the transaction occurred; *newBalanceOrig* refers to the new balance in the merchants' account after the transaction occurred; *nameDest* refers to the account name of the customer involved in the transaction; *oldBalanceDest* refers to the initial balance in the customer's account before the transaction occurred; *newBalanceDest* refers to the final balance in the customer's account after the transaction; *isFraud* refers to the instance of the transaction characterized as fraudulent equals 1 and non-fraudulent equals 0; *isFlaggedFraud* indicates transactions as fraudulent when there is an attempts to transfer more than 200000 in one transaction.

c) Data Exploration

Exploratory Data Analysis (EDA) is a technique for describing the features of the data. In the *type* feature, the *matplotlib* library was used to visualize the class attributes. The data frame method *type.value_counts*() in python was used to count the class attributes and it showed that CASH_IN comprised of 1399284 transactions, CASH_OUT comprised of 2237500 transactions, DEBIT comprised of 41432 transactions, PAYMENT comprised of 2151494 transactions, and TRANSFER comprised of 532909 transactions. To determine the fraudulent and non-fraudulent transactions in the class attribute of the *type* feature, the df.groupby function of the pandas data frame was invoked. The CASH_IN comprised of 1399284 non-fraud and 0 fraud transactions, CASH_OUT comprised of 2233384 non-fraud and 4116 fraud transactions, DEBIT comprised of 41432 non-fraud and 0 fraud transactions, PAYMENT comprised of 2151494 non-fraud and 0 fraud transaction, TRANSFER comprised of 528812 non-fraud and 4097 fraud transaction. The *isFraud* feature was also explored. The *seaborn* library was used to visualize the *isFraud* feature. The total number of non-fraud transactions was 6354407 and the total number of fraud transactions was 8213 which infers a highly imbalanced dataset. The *isFlaggedFraud* feature was also analyzed. The *isFlaggedFraud* feature flagged only 16 transactions.

3) Data preparation

Data preparation is important to make certain that the best independent features are applied to machine learning algorithms for optimum performance.

a) Feature selection

The minimum and maximum amount in the account of the merchant before transferring funds to the customer was analyzed. Using the *minmaxbalance*() in python, it was discovered that the minimum and maximum amount of the initial balance of the merchant before sending money (*oldBalanceOrig*) when the limit was set was 353874 and 19585040 respectively. After sending money (*newBalanceOrig*) when the limit was not set was 0 and 575668 respectively. In a scenario where the amount limit was not exceeded in a TRANSFER transaction and money was erroneously transferred to a fraudster, the amount will be unknown to *isFlaggedFraud* because it only flags transactions above the threshold amount. The new balance in

the merchants' account after sending money (*newBalanceOrig*) is updated when the transaction is completed. It was discovered that there were transactions that exceeded the threshold limit but were not flagged as fraudulent. Therefore (*newBalanceOrig*) shows no feature relationship with the *isFlaggedFraud* feature because it does not determine whether the limit of the transaction has been exceeded or not. In conclusion, the *isFlaggedFraud* feature has proven to be irrelevant and it will not be used in the further analysis because it has no relationship with variables of the dataset. Using the *str.contains*() in python, an analysis was done to check if merchants' were included in the account names that sent money to the customers (nameOrig) or received money from the customers (nameDest) concerning CASH_IN or CASH_OUT transactions. It was discovered that merchants' were involved in neither CASH_IN nor CASH_OUT transactions. Therefore it can be inferred that the *nameOrig* and *nameDest* do not show the existence of fraudulent transactions and on that basis, they will be excluded from further evaluations.

b) Data cleaning

A function was defined to perform the cleaning task. The name of the function was *cleaning*. *nameOrig*, *nameDest*, and *isFlaggedFraud* were removed. TRANSFER and CASH_OUT are discretized using CAIM (class attribute interdependency maximization). Missing values were also filled in the customer and merchants' accounts.

c) Feature engineering

Errors inherent in the merchant and customer accounts were recorded. Two new features were derived for this purpose to differentiate zero balances inherent in the features of the destination accounts from non-fraud transactions of the dependent variable class.

V. EMPIRICAL RESULTS

The RUWR technique simply duplicates instances in the minority class by varying the sample sizes from 10% to 100%. SMOTE creates new minority class instances and the samples sizes are also varied from 10% to 100%. To maintain equity in the binary class of the learning sample set, the RD technique down-sampled varied proportions of the non-fraudulent class. **Figure 2**, **Figure 3,** and **Figure 4** shows how well the implemented algorithms perform on AUC test data. The coding algorithm for upsampling and downsampling was adapted from **[23]**. The coding algorithm for SMOTE was adapted from **[24]**. According to the literature, AUC is the most appropriate evaluation metric for skewed datasets in the data mining community. Statistical comparisons of sampling techniques are visualized concerning the AUC score. As shown in **Figures 2**, the AUC score of down-sampling when decision tree model is implemented ranged from 62% to 72%, when gradient boosted tree model is implemented, it ranged from 65% to 67%, when k nearest neighbor model is implemented, it ranged from 58% to 61%, when the logistic regression model is implemented, it ranged from 58% to 60% and when Naïve Bayes model is implemented, it ranged from 34% to 35%. These scores are poor because the downsampling technique discards valuable insights used to train the data. As shown in **Figures 3**, the AUC score of up-sampling when decision tree model is implemented ranged from 90% to 91% when gradient boosted tree model is implemented, it ranged from 95% to 98%, when k nearest neighbor model is implemented, it ranges within 89%, when the logistic regression model is implemented, it ranged from 85% to 90% and when Naïve Bayes model is implemented, it ranged from 73% to 74%. These scores are better because the upsampling technique improves the resolution and signal-to-noise ratio, prevents phase distortion and information loss when used to train the data. As shown in **Figures 4**, the AUC score of SMOTE when the decision tree model is implemented ranged from 94% to 95%, when gradient boosted tree model is implemented, it ranged from 94% to 98%, when k nearest neighbor model is implemented, it ranged from 94% to 95%, when the logistic regression model is implemented, it ranged from 85% to 91% and when Naïve Bayes model is implemented, it ranged within 74%. These scores are better because the SMOTE technique eliminates overfitting. After all, samples are generated and not replicated when used to train the data. SMOTE and RUWR are better choices in terms of improving the model performance significantly. However, the computational time is overly increased. With RD, all five algorithms performed poorly even though the computational time is relatively small. With RUWR, gradient boosted trees performed best while with SMOTE, decision trees and gradient boosted trees performed better than the three other algorithms. The majority of previous studies used a random down-sampling method to train and test models with a balanced sample. However, in industry application use cases, the validation sample set is hugely skewed and as a result, using sampling techniques and also varying sample volumes before training and testing is important to observe improvements in model performance.

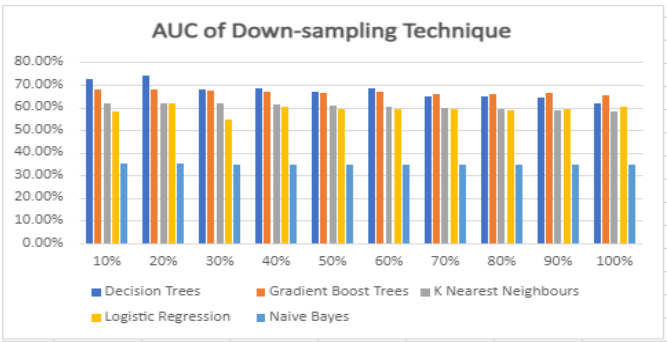

Figure 2: A graph of the AUC score of down-sampling technique versus varied sample sizes ranging from 10% -100%

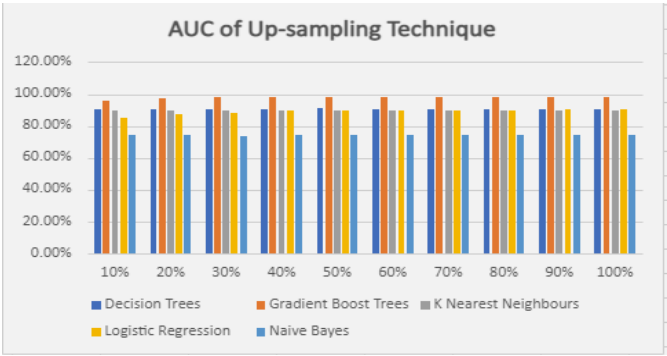

Figure 3: A graph of the AUC score of up-sampling technique versus varied sample sizes ranging from 10% -100%

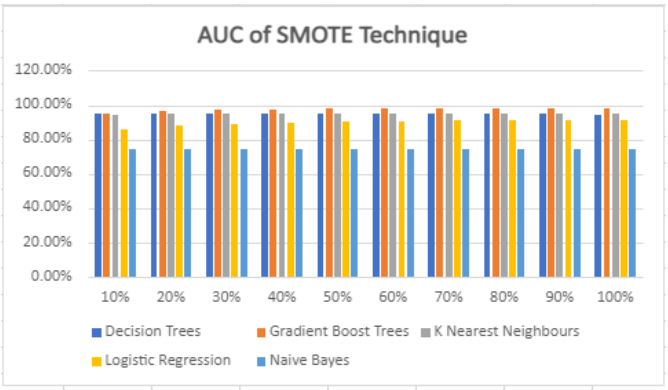

Figure 4: A graph of the AUC score of SMOTE technique versus varied sample sizes ranging from 10% -100%

B. Discussions and conclusions

The impact of different sampling techniques on mobile money imbalanced datasets is investigated. The experimental results show that when sample sizes are varied, SMOTE and RUWR are better sampling techniques in terms of improving the model performance significantly because varied learning instances of the class with fewer data instances in the binary class levels up with higher data instances in varied measures. Bias is not desirable in classification models but it cannot be avoided. Therefore the best sampling technique will exhibit a minimal probability of bias to the non-fraudulent class. However, the time complexity used in learning data instances is high as opposed to RD. In RD, because the class with higher data instances is downsampled, essential learning instances are cut out in varying degrees which negatively affects the model performance. However, because learning data instances have been down-sampled, computational time was fast. In RUWR and SMOTE, data instances are varied to determine the appropriate data instance with the best performance when evaluated on a model. Model performance varies depending on the sampling method used. The problem of overfitting was looked into and it was found that the model complexity was minimal because the best combination of input features was chosen for data training and it underwent cross-validation. For future work, there is still a need to ascertain if model accuracy and variability of a model can occur simultaneously.

REFERENCES

[1] Kioko, M. M. (2018). *Determination of Premiums Payable By Mpesa Agents*.

[2] Rieke R, Zhdanova M, Repp J, Giot R, Gaber C. 2013. Fraud Detection in Mobile Payments Utilizing Process Behavior Analysis. The 2nd International Workshop on Recent Advances in Security Information and Event Management, Sep 2013, France. pp.8. ffhal-00841002f.

[3] International, L. C., & Of, J. (2020). *DETECTING MOBILE MONEY LAUNDERING USING GENETIC ALGORITHM AS FEATURE SELECTION METHOD*.

[4] Ak, B. K., Dechow, P. M., Sun, Y., & Wang, A. Y. (2013). The use of financial ratio models to help investors predict and interpret significant corporate events. *Australian Journal of Management*, *38*(3), 553–598. https://doi.org/10.1177/0312896213510714

[5] Pech, R. (2019). Fraud detection in mobile money transfer as a binary classification problem. June. https://www.researchgate.net/publication/333755188

[6] Zhdanova, M., Repp, J., Rieke, R., Gaber, C., & Hemery, B. (2014). No smurfs: Revealing fraud chains in mobile money transfers. *Proceedings - 9th International Conference on Availability, Reliability, and Security, ARES 2014*, 11–20. https://doi.org/10.1109/ARES.2014.10

[7] Alali, A., & Alali, A. (2020). *Financial Fraud Detection using Machine Learning Techniques*.

[8] Botchey, F. E., Qin, Z., & Hughes-Lartey, K. (2020). Mobile money fraud prediction-A cross-case analysis on the efficiency of support vector machines, gradient boosted decision trees and Naïve Bayes algorithms. *Information (Switzerland)*, *11*(8). https://doi.org/10.3390/INFO11080383

[9] Hwang, J., & Kim, K. (2020). An Efficient Domain-Adaptation Method using GAN for Fraud Detection. *International Journal of Advanced Computer Science and Applications*, *11*(11), 94–103. https://doi.org/10.14569/IJACSA.2020.0111113

[10] S.J. Yen, Y.S. Lee, Cluster-based under-sampling approaches for imbalanced data distributions, Expert Systems with Applications 36 (2009) 5718–5727.

[11] H. He, E.A. Garcia, Learning from imbalanced data, IEEE Transactions on Knowledge and Data Engineering 21 (2009) 1263–1284.

[12] S. Kotsiantis, P. Pintelas, Mixture of expert agents for handling imbalanced data sets, Annals of Mathematics, Computing & TeleInformatics 1 (2003) 46–55.

[13] A. Estabrooks, T. Jo, N. Japkowicz, A multiple resampling method for learning from imbalanced data sets, Computational Intelligence 20 (2004) 18–36.

[14] N.V. Chawla, K.W. Bowyer, L.O. Hall, W.P. Kegelmeyer, SMOTE: synthetic minority over-sampling technique, Journal of Artificial Intelligence Research16 (2002) 321-357

[15] Zhou, L. (2013). Performance of corporate bankruptcy prediction models on the imbalanced dataset: The effect of sampling methods. *Knowledge-Based Systems*, *41*, 16–25. https://doi.org/10.1016/j.knosys.2012.12.007

[16] P. Pintelas, Mixture of expert agents for handling imbalanced data sets, Annals of Mathematics, Computing & TeleInformatics 1 (2003) 46–55

[17] MathWorks, Statistics Toolbox User's Guide, TheMathWorks, Massachusetts, 2012.

[18] M. Hall, E. Frank, G. Holmes, B. Pfahringer, P. Reutemann, I.H. Witten, The WEKA data mining software: an update, SIGKDD Explorations 11 (2009).

[19] T. Fawcett, Roc Graphs: Notes and Practical Considerations for Data Mining Researchers, HP Laboratories, Palo Alto, CA, USA, January 2003.

[20] Piatetsky, G., 2014. CRISP-DM, still the top methodology for analytics, data mining, or data science projects. KDD News.

[21] Azevedo, A.I.R.L and Santos, M.F., 2008. KDD, SEMMA, and CRISP-DM: a parallel overview. IADS-DM

[22] Kaggle.com., 2018., accessed 12 May 2020, <https://www.kaggle.com/ealaxi/paysim1>

[23] *Random Oversampling and Undersampling for Imbalanced Classification*. (n.d.). Retrieved June 20, 2021, from https://machinelearningmastery.com/random-oversampling-and-undersampling-for-imbalanced-classification/

[24] *SMOTE for Imbalanced Classification with Python*. (n.d.). Retrieved June 20, 2021, from https://machinelearningmastery.com/smote-oversampling-for-imbalanced-classification/

Oluwatosin Elegbede is a second-year MSc Computer Science student at the University of Fort Hare. He began his MSc in 2020. This paper is based on his MSc dissertation.

Measuring QoE Impact of DoE-based Filtering

Enock Samuel Mbewe, Josiah Chavula
Department of Computer Science , University of Cape Town, South Africa
{embewe,jchavula}@cs.uct.ac.za

***Abstract*—In this paper, we analyse the impact of DNS-based filtering on Quality of Experience (QoE). We use three DNS standard protocols: regular DNS (Do53), DNS over HTTPS (DoH) and DNS over TLS (DoT) on Quality of Experience. We conduct measurements against four open public DNS service providers (Cloudflare, CleanBrowsing, Adguard and Quad9) under three network conditions; Campus wired network, Eduroam and 4G. We aim to establish whether the filters from the same provider have statistically significant differences. This information could be used by Internet users and Internet Service Providers to make sound decisions when choosing DNS privacy services. The results show significant DNS response time and page load time differences between non-filtered and filtered DNS recursive resolvers from Cloudflare, Adguard and Quad9. We do not observe significant differences in page load times when CleanBrowsing resolvers are used despite observing significant differences in DNS response times. The results further show that some filters would provide better QoE than non-filtered counterparts.**

***Index Terms*—Internet performance, DNS privacy, DNS measurements, DNS filtering, QoE, QoP, DoH, DoT, Do53**

I. Introduction

Domain Name System (DNS)[1] is a fundamental component of the Internet that maps the human-readable names to their respective IP addresses of Internet resources. For most of the Internet's history, these services have been delivered in plaintext, providing a fertile ground for attackers to exploit and compromise Internet users' security and online privacy [2]. As a result, various efforts have been developed to encrypt DNS queries. These efforts have resulted in the development of different protocols such as DNS over TLS (DoT) [3], DNS over DTLS, DNS over QUIC, DNS over HTTPS (DoH)[4], DNSCrypt [5] and DNSCurve [6]. DNS over HTTPS (DoH) and DNS over TLS (DoT) are the two newer standard protocols requiring more studies to understand them fully. Both these protocols encrypt DNS traffic to improve the privacy of Internet users. Our study focuses on these two protocols as measured from end-user networks and devices. We collectively refer to these protocols as DNS-over-Encryption (DoE), a term that was introduced by Lu *et al.* [7]. We use DNS over port 53 (Do53) to refer to the regular, unencrypted DNS.

Given the recency of DoT and DoH, the Internet measurements research community is yet to establish the real performance cost of these protocols. At the writing of this paper, we know of very few measurement studies on the performance cost of DoT and DoH. An early preliminary study by Mozilla [1] found that DoH lookups are only marginally slower (6 ms) than conventional, unencrypted DNS over port 53 (Do53). Bottger *et al.* [8] studied the DoH ecosystem to understand the cost of the additional DNS security. Their findings indicate that the impact is marginal and does not heavily impact the page load times. In their works, Hounsel et al. ([9] and [10]) compared the cost of DoT and DoH measured from campus network and Amazon ec2 instances. Their results show that despite the lower resolution times of Do53, DoT and DoH can perform better than Do53 in terms of page load times. Lu *et al.* [7] conducted end-to-end DNS-over-Encryption measurements. They report that generally, the service quality of DNS-over-Encryption is satisfying in terms of accessibility and latency. In our prior work[2], we found that DoT and DoH negatively impact QoE, especially when the content is hosted offshore using offshore resolvers. We concluded the study by calling for ISPs and network operators to implement DoE and hosting services closer to their subscribers. In the current paper, however, we investigate whether using filters would improve QoE.

DoH, in particular, is attracting the attention of the research community due to its current centralised implementation. As a response, some works focus on de-centralising DoH so that no single provider has all the browsing information. Hoang *et al.* [11] propose K-resolver to slice user information to different decentralised DoH resolvers. This decentralisation, however, suffers from increased latency when the servers are geographically separated. A similar study is conducted by Hounsel *et al.*[12] which proposes a distributed DoH server architecture called M-DNS. However, none of the works so far has evaluated the cost and potential benefits of DoE-based filtering on Quality of Experience.

DNS-based filtering is one of the add-on services that Internet Service Providers (ISPs) have been offering to their subscribers to protect them from malware [13], adware, botnets [14], [15] phishing, cyberbullying and pornography. However, RFC 7258 [16] classifies such filtering mechanisms as pervasive monitoring. This leaves the ISPs in a dilemma since these mechanisms also protect their infrastructure apart from protecting their clients. This has led to resistance by ISPs from adopting DoH, which sends DNS transactions over HTTP traffic [17]. The Internet research community has tried and continues to measure the impact of DoE protocols on QoE. Analysing the ensuing performance impact of such protocols and their filtering services would be critical to both ISPs and the end-users.

This paper presents the results of DNS security measurement study taken from 13 vantage points located in 7 African countries (including the name of the Internet provider): Mada-

[1]See https://blog.nightly.mozilla.org/2018/08/28/firefox-nightly-secure-dns-experimental-results

gascar (Widecom), Zambia (MTN, Liquid telecoms), Uganda (Airtel, Orange), Kenya (Airtel), Nigeria (MTN), Malawi (TNM, Airtel) and South Africa (Vodacom, Eduroam, Campus wired network). We conduct the measurements on end-user devices against 11 resolvers from Four DNS providers; Adguard [AdGuard Nofilter (AGN), Adblock/Security filter (AGAd/AGS), AdGuard Family filter (AGF)], CleanBrowsing [CleanBrowsing Adult filter (CBA), CleanBrowsing Security filter (CBS), CleanBrowsing Family filter (CBF)], Cloudflare [Cloudflare Nofilter (CFN), Cloudflare Security filter (CFS), Cloudflare Family filter (CFF)], and Quad9 [9 Nofilter (Q9N), Quad9 Security Filter (Q9S)]. We compared the performance of these resolvers to the local, Do53 resolver provided by the network.

We perform these measurements on 4G, Eduroam and Wired networks. We compare the DNS response time and page load time when different filters are configured. We measure the performance of both filtered and non-filtered configurations on each recursive resolver on the three protocols; regular DNS (Do53), DoT and DoH. We further measure the performance of the local recursive resolver's non-filtered Do53 to serve as a baseline. The main objective of this study is to establish whether DNS filters from the same provider are significantly different. We further investigate the implication of DNS response times and page load times.

Contributions: The contributions of this study are as follows:

- *Performance analysis of DoE-based filtering (from the vantage point of access networks in Africa.)* We conduct baseline internet measurements from real access networks in Africa. The results from these measurements can inform the Internet community on the best DNS filter provider to use depending on their geolocation and network conditions. This contribution is two-fold: First, the ISPs can learn from the performance of these open public resolvers and implement their own local, filter-enabled DoE infrastructure, which would reduce latency to the DoE servers. This would lead to lower DNS response times and page load times. Secondly, the results from this study inform the user which filters would result in better QoE.
- *Observations.* Using the dataset collected, we compare the performance impact of DNS-based filtering using public DoE resolvers. For example, we observe higher DNS response times from Adguard's filters. This information may help the DNS providers to optimise their services for networks in Africa.

II. Methodology

The study uses Alexa's top 50 global websites for African countries and the top 50 local ones for each African country (hosted locally or operated by local entities). The local websites were particularly included to represent the websites serving African content and observe how DoT and DoH impact the browsing QoE on the local websites. We managed to get 1583 unique websites that we use in this study.

A. Experiment setup

To replicate web browser actions when a user visits a website, we use automated Firefox 67.0.1 to randomly visit the websites in our list in headless mode as discussed in prior works [9], [2] . This is a clean instance without any ad or pop-up blockers. We, however, install a plugin to export HTTP Archive (HAR) objects from each visited website. We store these HARs in a PostgreSQL database as JSON objects. Each browsing session uses a randomly selected configuration tuple of the form (domain, recursive resolver, DNS type [Do53, DoT, DoH]) to measure the QoE impact of each of the DNS protocols from the 11 public recursive resolvers from Four DNS providers; Adguard, CleanBrowsing, Cloudflare and Quad9. Of the four resolvers, two (Cloudflare and Quad9) negotiate TLS1.3 while CleanBrowsing and AdGuard negotiate TLS1.2

Firefox web browser natively supports Do53 and DoH. On the other hand, DoT has to be configured on the user's machine outside the browser. As such, we use *Stubby* for DoT resolution, a stub resolver based on the *getdns* library. *Stubby* listens on a loopback address and responds to Do53 queries. All DNS queries received by *Stubby* are then sent out to a configured recursive resolver over DoT. We modify /etc/resolv.conf on our measurement systems to point to the loopback address served by *Stubby*. This forces all DNS queries initiated by Firefox to be sent over DoT. This randomisation was done to avoid the potential effect of a query warming the resolver's cache for subsequent queries from the other protocols tested.

This measurements study was done in two blocks; 1 March 2020 to 30 August 2020 and 1 June 2021 to 17 June 2021) from 13 end-user vantage points located in 7 countries under three network conditions, 4G, Eduroam, wired campus network. We conducted the measurements continuously, with no delays between successive page loads. The researchers had access to the vantage points. We ran the measurements on i5 computers with 8GB of RAM running the Ubuntu 18.04 desktop version.

B. Metrics

This study aimed to understand the impact of DNS filtering on browsing Quality of Experience (QoE). The study considered network-level and browser-level metrics. These metrics are latency, DNS response time (in this paper referred to as DRT), DNS success and failure rates and page load time (PLT).

1) Latency: Several studies have pointed out that African networks suffer high latencies. Recent studies [18], [19], [20] have attributed these latencies to suboptimal routing, lack of peering and cache sharing. Other studies have attributed these latencies to offshore hosting and misconfiguration of DNS. However, none of these works has looked at the impact of security protocols on latency in the region. Latency determines the kind of applications that can run on affected networks. Therefore, it is important to understand how secure DNS protocols affect QoE to inform Internet users what

applications may run on a given network condition. Also, it is important to show which DNS providers respond with reasonable latency. This would aid users in the choice of DNS recursive resolvers. We conduct ping measurements to each of the resolvers and calculate the median RTT for each latency measurement.

2) DNS Resolution Time: DNS query response time is one of the major factors that affect the speed of page rendering in the browser. A web page normally contains several objects fetched from different servers. In this study, we measured DNS resolution time firstly for the main page. After that, we collected all the unique domains for components (i.e. images, JavaScript, CSS, among others) for each domain and measured their respective DNS Response time. We use *getdns* and *libcurl* C libraries to issue Do53, DoT, and DoH queries. *Getdns* provides an API that allows developers to perform DNS Do53 and DoT requests using different programming languages. Libcurl supports POST requests to be sent via HTTPS. This capability enables us to measure DoH response time. We could have gotten the DNS response times from the collected HARs; however, we noted that some of the timings were not correct and decided to use the *getdns*. It is important to note that the DNS responses were not cached by the browser used in the measurements to ensure that the subsequent transaction is not affected by the cache.

3) Page Load Time: Page load time is an important metric of browser-based QoE. It represents the time a user has to wait before the page is loaded in a browser. In this study, Firefox was used in headless mode to visit a set of websites. We collect HAR files in JSON format for each website containing timing information, including blocking information, proxy negotiation, DNS lookup, TCP handshake, SSL, Requests, Waiting and Content download. From the HAR files, we record the *onLoad* timing - the time taken to load the page together with its components completely.

C. Analysis

We use descriptive statistics to explore the data. We then apply Shapiro to test normality. Finally, we conduct a pairwise comparison of the DNS filters from the same provider using a T-test to explain their relationship. For example, Cloudflare provides two filters; security (CFS) and family (CFF) and one non-filter resolver (CFN) each of which provides three DNS protocols (Do53, DoH, DoT). In the study, we are interested in identical comparisons, Do53 against Do53, DoT against DoT and DoH against DoH. This gives us nine pairwise tuples {(CFN_Do53, CFF_Do53), (CFN_Do53, CFS_Do53), (CFF_Do53, CFS_Do53), (CFN_DoH, CFF_DoH), (CFN_DoH, CFS_DoH), (CFF_DoH, CFS_DoH), (CFN_DoT, CFF_DoT), (CFN_DoT, CFS_DoT), (CFF_DoT, CFS_DoT)) } on which we perform T-test.

III. Results

In total, we managed to successfully download and save $492,977$ HTTP Archive Record (HAR) files from which we obtain and analyse the page load times (PLT). Each successfully saved HAR had a number of objects, which we measured independently for DNS response time (DRT). This yielded $3,427,808$ unique domains, which translates to, on average, ≈ 7 domains referenced by a single HAR file.

A. Latency

We used ICMP ping to measure latency. Each successfully saved HAR file was accompanied by five ping measurements to the recursive resolver. This metric explains the differences in the DNS response times and page load times between resolvers from the same provider and between resolvers from different providers. As expected, we generally observe lower latencies to local resolvers provided by the Internet Service Providers. However, for some ISPs such as Telekom Networks Malawi, MTN Zambia and MTN Nigeria, we noted higher latencies than public resolvers such as Quad9 and Cloudflare. We posit that this might be the case under suboptimal routing. Also, this may be the case when ISPs choose not so highly cached DNS resolvers.

Observing from the network conditions' point of view, we find the lowest latency on wired (median RTT ≈ 87ms) network followed by Eduroam (median RTT ≈ 92ms) with the higher latencies observed under 4G (median RTT ≈ 446ms). We further observed differences in latencies under 4G; some countries had lower latencies than others. Comparing different resolvers, results indicate higher latencies to AdGuard resolvers with a minimum RTT of ≈ 750ms. In general, the latency results suggest that the resolvers from the same DNS providers are colocated.

B. DNS resolution Delay

DNS response time is one of the sources of delay in any online transaction that fetches resources from a remote location. A web transaction, in particular, comprises multiple name resolutions for page components such as images, scripts and cross-site components. This section presents summaries of DNS response times from all the measured resolvers, grouped by DNS provider and the network conditions. Due to space limitation, we focus our reporting on results from Cloudflare representing the fastest DNS provider observed in this study.

Figures 1, 2 and 3 show Cumulative Distribution Functions (CDFs) of DNS response times for the protocols and filters from Cloudflare. As expected, we note that Do53-based filters perform better than their corresponding DoE-based filters. This makes sense, considering the extra latency brought by the TLS handshakes. Comparing DoH and DoT from each resolver, we note that generally, DoT has higher DNS response times than DoH except for Cloudflare resolvers which show almost no difference. Also, we note in the 4G results (Figure 1) that the public Do53 perform better than the local Do53 provided by the Internet Service Providers. We note substantial differences in response times between filters and their respective protocols from three (Cloudflare, Adguard and Quad 9), with minimal differences noted from CleanBrowsing's filters. Comparing filters and non-filters, we note that the filters, especially DoH-based filters, provide lower response times than their non-filtered counterparts.

Comparably, Cloudflare resolvers perform better than the rest of the resolvers. Prior works [9], [21] have attributed this to the fact that Cloudflare resolvers do not support EDNS. In this work, we did not validate this claim. We also argue that Cloudflare has multiple points of presence in the region. This agrees with the latency results in which Adguard has the highest RTTs. Traceroute results show that Adguard resolvers are not present in Africa, hence the higher RTTs. When compared against each other, security filters outperform family filters. This pattern is helpful as it could inform the users of protocols or filters that would give them the best Quality of Experience.

Of peculiar notice is the performance of Quad9's DoT, which is consistently poorer regardless of network conditions. Prior works [9], [7], [2] have reported this observation. However, we have not engaged the provider to report or seek explanations as at writing this paper.

So far, we have observed using descriptive statistics that there are differences between resolvers from the same provider in terms of DNS response times. The question we ask is, are these differences significant? To answer this question, we conducted a T-test between the same protocols from different resolvers. Generally, we find that the results agree with the descriptive statistics as presented by the CDFs such as those presented in Figures 1, 2 and 3. We observe that the difference between filters from the same provider is mostly significant across recursive resolvers ($p < 0.001$) except for some fewer cases [(AGAd, AGF), (AGN, AGAd), (CBA, CBS), (CFF, CFS)] where the difference is not statistically significant.

On the other hand, we observe significant differences between DoE-based filters. Of the providers, Adguard and Quad9 show substantial differences (depicted by larger t values) than Cloudflare and CleanBrowsing. When we compare the filters, we note significant differences between the non-filter DoE resolvers and filtered resolvers. However, we note marginal differences between the filters (i.e. substantial differences between (CFN, CFS) and (CFN, CFF) and marginal differences between CFS and CFF). We also note that, under better network conditions, DoT filters are not statistically significant.

C. Page Load Times (PLT)

Pageload time is a more direct indication of how users experience web browsing. We have already seen the differences in query response times among the various DNS protocols under different network types across African vantage points. This section shows how the choice of filters and DNS providers would impact the quality of the browsing experience. We begin by comparing different filters with the local, non-filtered recursive resolver. This would inform the users of the cost they are likely to incur should they prefer open, public DoE filtering services to the Do53 service provided by their ISPs. Finally, we will compare the DoE-based filters with their Do53 counterparts.

Generally, we note a similar pattern between the latency, response time and page load time results. This is unsurprising considering that, to a greater extent, TLS-based security protocols are mainly determined by latency due to the extra overhead incurred during TLS handshake. Figure 4 shows the median page load time differences between public DNS providers and a local DNS recursive resolver. The difference is calculated by taking the median page load time for a website/user using one public, filter-enabled resolver minus the median page load time of the same website/user using a local, unfiltered resolver. Therefore, the difference is indicative of the extra cost a user would bear when using secure DNS protocols provided by public DNS resolvers compared to default Do53. From this Figure, we note that DoT performs better than DoH except for two cases (Cloudflare no filter and Quad9 no filter). Q9N's DoT displays extreme results with a mean page load difference of about seven seconds, concurring with the DNS response time results.

When we compare the providers, Cloudflare and CleanBrowsing fare consistently better than AdGuard and Quad9 with a page load difference of $\approx$ 2 seconds. We expected Cloudflare to perform comparably to Quad9, considering that both have multiple points of presence in Africa. We think that Quad9's DoE has some protocol design or infrastructural issues such as caching.

We also use Figure 4 to analyse the performance differences among DoE filters from the same provider with respect to the filter's Do53 performance. We note marginal differences between DoT and DoH-based filters with a median page load difference of up to 2 seconds except for Quad9's DoT, which we have already discussed in previous paragraphs. However, another aim of this study is to see whether these differences are statistically significant. We use a T-test to investigate the similarity and differences between filters and protocols from the same provider. We observe significant differences in the performance of Adguard, Cloudflare and Quad9 resolvers. Cloudflare (See Table I) generally sows significant differences in page load times except for DoT under wired network, suggesting that DoT's performance between CF's filters is not different under better network conditions. CleanBrowsing, however, does not show any significant differences between its resolvers across network conditions. This is in contrast to the DNS response time T-test results. CleanBrowsing's filters are not new, suggesting that they may have higher cache hits in Africa. On the other hand, Cloudflare's and Quad9's filters are new, and users and ISP's are yet to cache them hence the substantial difference. Adguard's performance is attached to the long distance from the vantage points to its points of presence which, from the latency measurements, indicate that they are situated offshore.

IV. Discussion and Implications

Thus far, we have presented results indicating significant differences in DNS response time and page load times exhibited by filter-enabled resolvers from the same public DNS provider. These differences are observed from all the measured network conditions; 4G, Eduroam and Campus wired broadband networks. The key role of DNS-based filtering

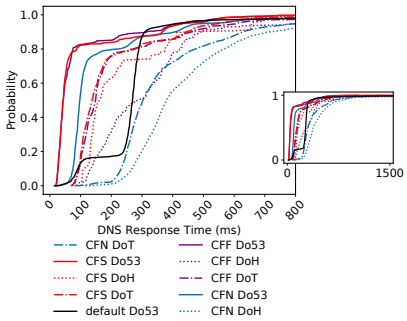

Fig. 1: DNS response time CDF for Cloudflare filters under 4G

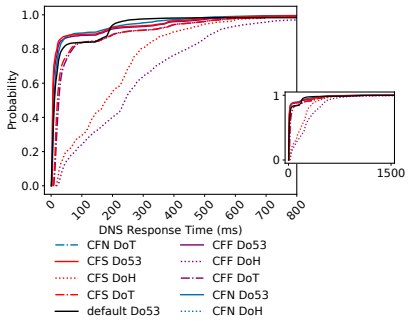

Fig. 2: DNS response time CDF for Cloudflare filters under Eduroam

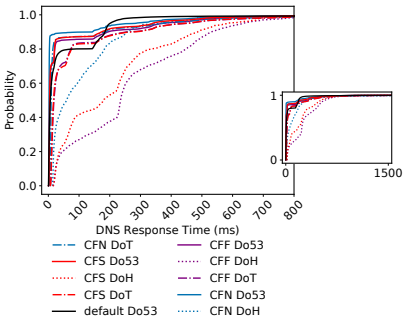

Fig. 3: DNS response time CDF for Cloudflare filters under wired network

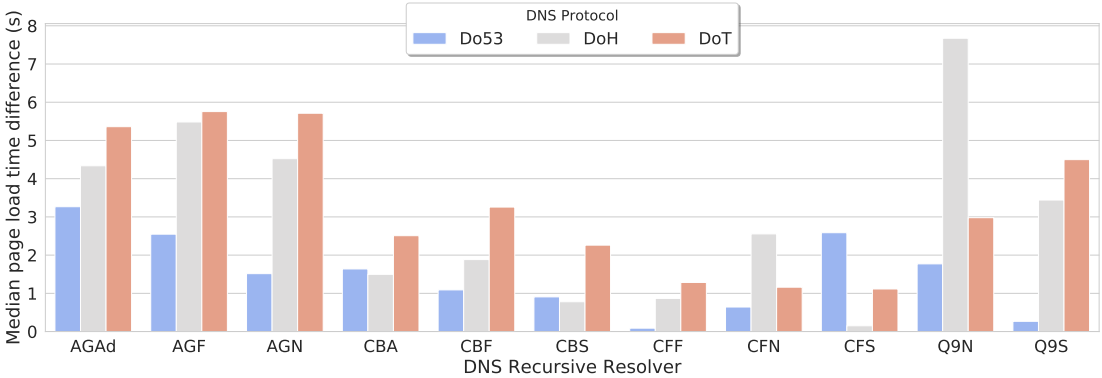

Fig. 4: Mean page load time difference between public and local recursive resolver

Pairwise PLT T-test-Cloudflare	Wired Network	Eduroam	4G
(CFN_Do53, CFF_Do53)	(t=14.931, p=0.000)*	(t=7.287, p=0.000)*	(t=6.928, p=0.000)*
(CFN_Do53, CFS_Do53)	(t=14.615, p=0.000)*	(t=7.473, p=0.000)*	(t=6.150, p=0.000)*
(CFF_Do53, CFS_Do53)	(t=-0.316, p=0.752)	(t=0.191, p=0.849)	(t=-0.549, p=0.584)
(CFN_DoH, CFF_DoH)	(t=2.651, p=0.008)*	(t=3.015, p=0.003)*	(t=2.090, p=0.036)*
(CFN_DoH, CFS_DoH)	(t=2.857, p=0.004)*	(t=2.809, p=0.005)*	(t=1.407, p=0.160)
(CFF_DoH, CFS_DoH)	(t=0.207, p=0.836)	(t=-0.244, p=0.807)	(t=-0.500, p=0.617)
(CFN_DoT, CFF_DoT)	(t=-0.432, p=0.666)	(t=2.234, p=0.026)*	(t=6.225, p=0.000)*
(CFN_DoT, CFS_DoT)	(t=0.318, p=0.750)	(t=3.210, p=0.001)*	(t=5.408, p=0.000)*
(CFF_DoT, CFS_DoT)	(t=0.766, p=0.443)	(t=1.136, p=0.256)	(t=-0.371, p=0.711)

TABLE I: T-tests for Cloudflare's Page load time

is to protect Internet users from malware, adware, phishing, cyberbullying and pornography. The results have also shown that DNS-based filters generally outperform their non-filter counterparts, implying that their usage would improve the Quality of Experience. Comparing the DNS providers, Adguard and Quad9 perform more poorly than Cloudflare and CleanBrowsing. Cloudflare performs consistently better across all network conditions. From these findings, we offer the following suggestions as possible remedies.

A. Implement local and regional DoE Infrastructure

ISPs widely use DNS level filtering as a value-added service to their customers to block malware, enforce parental controls, and prevent different cyber attacks. The problem with the Do53-based filtering was its invasive nature into the privacy of the subscribers described in the RFC [16] and various DNS attacks. The coming of the standard DNS privacy protocols is a relief to many security-conscious Internet subscribers. The limiting factor, however, could be the performance overhead incurred when using public resolvers. Also, other subscribers would not be comfortable using third-party DNS providers. This study and other prior works suggest that the closer the resolvers are to the end-user, the better the Quality of Experience. Therefore, we recommend that the ISPs and Network Operators implement DoE services. This would reduce the latency overhead and eventually improve QoE.

B. Offer configurable Quality of Protection to Internet Users

Internet is costly in edge networks. Because of this, paternalistic or stupid user implementation of Internet security services may negatively impact some users from these networks. On the other hand, the configuration of Internet security services is not straightforward [22] imposing security configuration overhead on the users. Consequently, most users have developed poor mental models around security, including DNS service, and they do not find the motivation to configure security on their Internet access devices. We are aware of recommendations by researchers to optimise secure DNS. Deccio C. and Davis J. [23], connection-oriented DNS by Zhu, *et al.* [24] proposed the usage of TCP Fast Open (TFO) and TLSv1.3. Hounsel *et al.* [9] propose opportunistic partial responses, wire caching and disabling of EDNS Client-Subnet.

One possibility is to introduce an integrated, easy-to-use cost-aware Internet security configuration framework that will enable users to choose their desired level of security, such as choosing the type of DNS filters in this case.

Finally, the results from this study enable both users and ISPs to make better DNS choices based on the measurement data and based on the trust they have in the DNS provider. The results also inform the DNS providers on the possible improvements and expansion of their services in Africa.

V. Conclusion and future work

This paper investigated the QoE impact of public Do53 and DoE-based filtering from African vantage points. The study has shown that users who use DNS filters would experience a better QoE. In some cases, the study has shown that DoE-based filtering performs even better than Do53-based filters. The results from this study assist Internet Service providers and Internet users to make sound decisions when choosing the DoE-based filters to implement. The choice of DNS filters would improve the Quality of Protection and Experience.

Acknowledgement

The authors are grateful for the financial support received from the Hasso Plattner Institute (HPI) through the HPI Research School at the University of Cape Town.

References

[1] Mockapetris, P. Domain Names - Concepts and Facilities. RFC 1034, IETF (1987). URL https://www.ietf.org/rfc/rfc1034.txt.

[2] Mbewe, E. S. & Chavula, J. On QoE Impact of DoH and DoT in Africa: Why a User's DNS Choice Matters. In Zitouni, R. *et al.* (eds.) *Lecture Notes of the Institute for Computer Sciences, Social-Informatics and Telecommunications Engineering, LNICST*, vol. 361, 289–304 (Springer International Publishing, Cham, 2021).

[3] Hu, Z. *et al.* Specification for DNS over Transport Layer Security (dotls). RFC 7858, IETF (2016). URL https://tools.ietf.org/html/rfc7858.

[4] McManus, P. H. . P. DNS Queries over HTTPS (DoH). RFC 8484, IETF (2018). URL https://tools.ietf.org/html/rfc8484.

[5] dnscrypt.info. DNSCrypt version 2 protocol specification. URL https://dnscrypt.info/protocol.

[7] Lu, C. *et al.* An End-to-End, Large-Scale Measurement of DNS-over-Encryption: How Far Have We Come? *Proceedings of the Internet Measurement Conference* (2019).

[6] dnscurve.org. DNScurve: Usable security for DNS. URL https://dnscurve.org/.

[8] Böttger, T. *et al.* An Empirical Study of the Cost of DNS-over-HTTPS. In *Proceedings of the Internet Measurement Conference*, IMC '19, 15–21 (Association for Computing Machinery, New York, NY, USA, 2019). URL https://doi.org/10.1145/3355369.3355575.

[9] Hounsel, A., Borgolte, K., Schmitt, P., Holland, J. & Feamster, N. Analyzing the costs (and benefits) of DNS, DoT, and DoH for the modern web. *Proceedings of the Applied Networking Research Workshop* (2019).

[10] Hounsel, A., Borgolte, K., Schmitt, P., Holland, J. & Feamster, N. Comparing the effects of DNS, DoT, and DoH on Web Performance. In *Proceedings of The Web Conference 2020*, WWW '20, 562–572 (Association for Computing Machinery, New York, NY, USA, 2020). URL https://doi.org/10.1145/3366423.3380139.

[11] Hoang, N. P., Lin, I., Ghavamnia, S. & Polychronakis, M. K-resolver: Towards Decentralizing Encrypted DNS Resolution. *ArXiv* **abs/2001.08901** (2020).

[12] Hounsel, A., Borgolte, K., Schmitt, P. & Feamster, N. D-DNS: Towards Re-Decentralizing the DNS. URL https://arxiv.org/abs/2002.09055. 2002.09055.

[13] Stalmans, E. & Irwin, B. A framework for DNS based detection and mitigation of malware infections on a network. In *2011 Information Security for South Africa*, 1–8 (2011).

[14] Alieyan, K. *et al.* DNS rule-based schema to botnet detection. *Enterprise Information Systems* **0**, 1–20 (2019). URL https://doi.org/10.1080/17517575.2019.1644673.

[15] Singh, M., Singh, M. & Kaur, S. Issues and challenges in DNS based botnet detection: A survey. *Computers & Security* **86**, 28–52 (2019). URL http://www.sciencedirect.com/science/article/pii/S0167404819301117.

[16] Farrell, S. & Tschofenig, H. Pervasive Monitoring is an attack. RFC 7258, IETF (2014). URL https://tools.ietf.org/html/rfc7258.

[17] Livingood, J., Antonakakis, M., Sleigh, B. & Winfield, A. Centralized DNS over HTTPS (DoH) Implementation Issues and Risks. Draft, IETF (2019). URL https://tools.ietf.org/id/draft-livingood-doh-implementation-risks-issues-03.html.

[18] Calandro, E., Chavula, J. & Phokeer, A. Internet Development in Africa: A Content Use, Hosting and Distribution Perspective. In Mendy, G., Ouya, S., Dioum, I. & Thiaré, O. (eds.) *e-Infrastructure and e-Services for Developing Countries*, 131–141 (Springer International Publishing, Cham, 2019).

[19] Formoso, A., Chavula, J., Phokeer, A., Sathiaseelan, A. & Tyson, G. Deep diving into Africa's inter-country latencies. In *IEEE INFOCOM 2018 - IEEE Conference on Computer Communications*, 2231–2239 (2018).

[20] Fanou, R. *et al.* Exploring and analysing the African Web ecosystem. *ACM Trans. Web* **12**, 22:1–22:26 (2018). URL http://doi.acm.org/10.1145/3213897.

[21] Knows, S. DNS-over-HTTPS performance (2019). URL https://www.samknows.com/blog/dns-over-https-performance.

[22] Borgolte, K. *et al.* How DNS over HTTPS is Reshaping Privacy, Performance, and Policy in the Internet Ecosystem. *SSRN Electronic Journal* (2019).

[23] Deccio, C. & Davis, J. DNS Privacy in Practice and Preparation. In *Proceedings of the 15th International Conference on Emerging Networking Experiments And Technologies*, CoNEXT '19, 138–143 (Association for Computing Machinery, New York, NY, USA, 2019). URL https://doi.org/10.1145/3359989.3365435.

[24] Zhu, L. *et al.* Connection-Oriented DNS to Improve Privacy and Security. In *2015 IEEE Symposium on Security and Privacy*, 171–186 (2015).

Enock Samuel Mbewe is a PhD candidate in the Computer Science at the University of Cape Town (UCT). His research is on configurable Internet security. In particular, his work investigates the use of a novel, cost-aware Internet security decision model to allow users, especially those with limited computing skills, to easily configure security options that can map to complex Internet security mechanisms to achieve Confidentiality, Integrity, Authentication and Privacy. He received MSc in Information Theory, Coding and Cryptography and a BSc in ICT from Mzuzu University, Malawi.

Josiah Chavula is a lecturer and researcher in Computer Science at the University of Cape Town. He received a PhD in Computer Science from UCT (2017), and an MSc in Networking and Internet Systems from Lancaster University (2011). His research focuses on performance of internet systems in Low Resource contexts.

Feasibility Study: Computing Confidence Interval (CI) for IBR Data Using Bootstrapping Technique

Stones Dalitso Chindipha*, Barry Irwin†*
*Computer Science Department, Rhodes University, South Africa
[1]s.chindipha@ru.ac.za
†Noroff University College, Kristiansand, Norway
[2]barry.irwin@noroff.no

***Abstract*—Statistical bootstrapping has been used in different fields over the years since it was introduced as a technique that one can use to simulate data. In this study, parametric and non-parametric bootstrapping techniques were used to create samples of different compositions from the baseline data. The bootstrap distribution of a point estimator of a population parameter has been used in the past to produce a bootstrapped confidence interval (CI) for the parameter's true value, if the parameter is written as a function of the population's distribution. Population parameters are estimated with many point estimators. The study used mean as the population parameter of interest from which bootstrap samples were created. This research was more interested in the CI side of bootstrapping and it is this aspect that this paper focused on. This is the case because the study wanted to offer a certain degree of assurance and reliability of IBR data to users who may not have access to a larger 'lens' of a network telescope to allow them to monitor security threats in their network. The primary interest in the dataset were source and destination IP (DSTIP) addresses, thus the study selected different size pools of DSTIP addresses to simulate bootstrap samples.**

***Index Terms*—Bootstrapping, Network Telescope, Confidence Interval (CI), Internet Background Radiation (IBR)**

I. Introduction

Internet Background Radiation (IBR) [1], [2] consists of non-productive data packets on the Internet, which target unused IP addresses or ports, where there is typically no functional network device to receive them [3], [4]. In theory, no traffic should ever arrive at such an IP address. However, when it receives traffic, it is marked as an anomaly, and recorded for analysis [2], [5], [6]. IBR data is collected by devices known as network telescopes [1], [7], [8]. The basis of a network telescope is to monitor blocks of IP address spaces on a network that are not utilised [5], [6], [8] and have no services running on them [3], [9]. The value of network telescopes has been dealt with extensively by other researchers to the point that its significance to cybersecurity research cannot be discounted [3], [5], [7]. Analysis of IBR traffic often shows evidence of either malicious activity or poor configuration [3], [10], the latter being either temporal or permanent [3], [10]. Given the fact that there are no legitimate hosts in an unused address block [8], [11], [12], then traffic must be the result of poor configuration, back-scatter from spoofed source addresses or scanning from worms and other probings [1], [4]. What makes IBR critical as part of a larger cybersecurity viewpoint is its ability to provide an early-warning detection mechanism for new threats and attacks [13].

This research was conducted with the overall objective of identifying the confidence interval for each of the datasets under study with the aim of offering confidence to the users of the dataset as to what range of values they would be expecting to get should they opt to work with a sample of the dataset presented to them. Essentially, the main question was, if a sample is taken from a baseline dataset what confidence does a telescope user have in the sample dataset in accurately representing it's baseline data.

In order to achieve this, the study had the following objectives in mind:

1) Identify a confidence interval technique that can be used to compute the values without being biased. Bootstrapping technique was identified as the ideal technique for this task.
2) Assess the confidence interval variations as the confidence level changes from 80% to 99%.
3) Assessing how representative different samples are to the baseline dataset after applying bootstrapping to the sample to impute a month's worth of data.
4) Identify the bootstrap technique that works best with IBR data.

The remainder of this paper is structured as follows: Bootstrapping is introduced in **Section II**. This is followed by **Section II-A** which justifies why bootstrapping in essential to this study. This is followed by **Section II-B** which explain the bootstrapping techniques that were considered for this study. Confidence Interval (CI) is introduced in **Section III** followed by the nature of the data used and its sources in **Section IV**. The research approach is laid in **Section V**, and results and discussion are found in **Section VI**. The papers closes with a conclusion and recommendations followed by future work in **Sections VII** and **VIII** respectively.

II. Bootstrapping

Bootstrapping works on the principle of starting with a dataset with an unknown underlying distribution from which a partially randomised sample of the available data is selected [14]–[16]. Using any specific population parameter of interest (it could be mean, standard deviation, variance, etc) a normal distribution is formulated by applying a statistical function to the parameter of interest [14], [17]–[19]. This study used *mean* as the statistical parameter of interest to bootstrap IBR data. This study identified *mean* as its population parameter

because it is an unbiased estimate of the corresponding population parameters [15], [20]. Thus the true population parameter of this study is the actual value of the mean that has been computed from the sample being studied. The re-sampled data, which approximates the normal distribution, is formulated through simulation of the original data using the statistical function of interest as the guiding population parameter of interest [14], [19], [21]. Essentially, bootstrapping eliminates the unknown variables (e.g. unknown data distribution, stationarity) that are presented in the original data by simulating the data to come up with known variables from which values like CI can be computed from using the plug-in-principle [19]–[22].

The plug-in-principle work on the notion of computing an estimate of the unknown variable and replacing that which is unknown in order to understand a population under study [20], [22]. Thus, the unknown parameter(s) is substituted for the one computed as an estimate of what was not known initially. Through the simulation process, using the identified population parameter estimator, the original data is reused through re-sampling to create a new data sample which is referred to as a bootstrap sample [14], [19]–[21]. With known variables being present in the bootstrap sample, CI can now be compute, as well as an estimate of the shape of the sampling distribution, and an estimate of the standard error of the quantity; an estimate of bias and P-value [14], [20], [23]. For the bootstrap samples, this study computed Standard Error of the Mean (SEM).

A. Bootstrapping Rationale

Bootstrapping is important to this study because the overall idea is that the study is working with the assumption that a user does not have access to a larger network telescope. As such, the network telescope user will only be able to collect IBR data with the IP addresses that the individual has. However, there is no telling how representable the data the user has collected is in relation to having more DSTIP addresses. With bootstrapping, this study aims to simulate various samples of the baseline data to mimic the number of data points observed in the baseline data.

Baseline dataset in this case represents a larger network telescope while the bootstrap samples represent the small network telescope. By simulating the samples to reproduce the baseline dataset, one can compute how different the bootstrap samples are from the actual baseline dataset. Using such differences between the bootstrap samples and the baseline dataset, the study will show how suitable simulating the IBR data is and how representable a smaller network telescope is to a larger one. This study has an advantage in that it has a baseline dataset with all the data points as such simulating samples from it will have a proper benchmark from which one can gauge from, something that a smaller network telescope user will not have.

This research was more interested in the CI side of bootstrapping and it is this aspect that this paper will focused on. This is the case because the study wanted to offer a certain degree of assurance and reliability of the bootstrap samples to whoever would find themselves in a scenario where they do not have access to a larger network telescope.

B. Types of Bootstrapping

In this study, bootstrapping was categorised into two parts: parametric and non-parametric bootstrapping. This section will expand more on what is involved in each bootstrapping technique.

1) Parametric Bootstrapping: Parametric bootstrapping involves the need to make parametric assumptions based on an underlying equation or any specific model while non-parametric bootstrapping involves none of such assumptions but rather based on an estimate of the standard error of the quantity [16], [17], [21], [23]. In parametric bootstrapping, assumptions are made regarding the underlying model or equation and the parameters of that model [17], [20], [22]. The bootstrap samples are then drawn from the assumed model together with the estimated parameters. It is worth noting that the estimated parameters are in no way a replacement of the baseline estimates, i.e the estimated *mean* cannot replace the baseline *mean* but rather allows inference to be made from such a computation to understand the unknown values of the baseline dataset [20], [22].

Note that with parametric bootstrapping, you either know or assume the function (or model) responsible for the distribution of your bootstrap sample coupled with unknown parameters that are revealed once the sample is computed [24]. In some cases, you do not use the model but explicitly state the distribution observed in the baseline data and use it as the base line. Either way, the bootstrap sample is generated by explicitly stating the assumptions and identifying whether it was done with replacement or without replacement [24]. More often than not the unknown parameters estimated offer maximum likelihood estimates to cover as much ground as possible [24].

2) Non-Parametric Bootstrapping: Non-parametric bootstrap on the other hand draws its samples from an empirical distribution samples generated from an estimate of the standard error of quantity [16], [20], [22]. Usually, this is the bootstrap that constitute large sample sizes and numerous simulations to get the appropriate bootstrap sample correctly [24]. It is also possible to make adjustments to a non-parametric bootstrap by ensuring that samples are done with replacement (usually referred to as bootstrap with replacement) [17], [25]. This was the approach that was taken in this case however, this study maintained the use of non-parametric because no assumptions were made regarding its distribution or parameters and thus still qualifies to be called non-parametric bootstrap, something that [25] partly alluded to in his work. This approach improves the accuracy of the results and some of the criticism offered in its lack of having statistical basis when formulating its bootstrap sample [25]. For this study, the *mean* of the individual datasets was chosen as the estimate of the standard error of the quantity. It is the result from this statistical function of mean (upon simulation) from which parameters of interest like the maximum likelihood CI and standard errors are computed from [20], [21], [24], [26].

It is worth noting that median, standard deviation, variance or any quantile can also be used as an estimate of the standard error of the quantity when creating a non-parametric bootstrap sample [22]–[24]. The main assumption when it comes to non-parametric bootstrapping is that the distribution of the bootstrap sample, more often than not, take the shape of the data from which it was taken from [22], [23]. The re-sampling with replacement involved in computing CI makes both parametric and non-parametric bootstrap to fall under the main category of percentile bootstrap [23], [24], [26].

III. Confidence Interval (CI)

According to Dixon, CI coverage is the probability that the CI includes the true parameter, under repeated sampling from the same underlying population [24]. Working with this definition, it essentially means that the value of interest after multiple re-sampling from the baseline data understudy, the parameter of interest ought to fall within the range generated by the bootstrap sample created.

The range computed from the bootstrap sample is what gives the user the level of confidence needed in the data in order to make informed decision(s). When computing CI, the quantile ranges are used in order to compute a specific CI [16], [27]. The rule of thumb is that for each CI, for the overall confidence level selected, the value is split into two to accommodate both the lower bound and the upper bound to mimic two standard deviations from the mean principle [24]. For instance, in a *95% CI*, the lower limit is defined as the 2.5th quantile of the bootstrap distribution, and the upper limit at the 97.5th quantile. If it changes to *99% CI*, the lower bound will be defined as the 0.5th quantile of the bootstrap distribution, and the upper bound at the 99.5th quantile [24], [28].

It is worth noting that empirical and theoretical studies of coverage and the author of bootstrapping acknowledged and showed that the percentile CI may not always give accurate results i.e. it works very well in some cases and in other cases the likelihood of one getting accurate results is very slim [29], [30]. Its accuracy is dependent on how the CI end points are calculated, the size of the bootstrap sample, the type of bootstrapping used (whether it is parametric or non- parametric), the statistical functions used as a parameter estimator and how the bootstrap samples are selected [23], [24]. Skewed sampling distribution tend to be less accurate as compared to symmetrical sampling distribution when calculating end points of CI [24], [30]. Increasing the size of the sample and the number of simulations when generating bootstrap sample boosts accuracy and confidence in the CI computed from the samples [17], [24].

IV. Data Source

The data used in this research was collected from one of the five of Rhodes University's network telescopes [31]. Since it is a feasibility study, it offers an opportunity to expand more on to other datasets for future research. Worth noting is that each of the five telescope's sensors consist of /24 net-blocks, routed to a collection server. Note also that there are a lot of similarities in the datasets that were collected from Rhodes University's telescopes as is shown in previous work [9], [10]. Thus in presenting the data from one of the five network telescope datasets, it gives outputs that are similar in more ways given previous work done on them.

A. Data Processing

Pre-processing of the raw Packet Capture (pcap) data was performed using a combination of standard UNIX text processing tools and a series of Python scripts that were used to pre-process the pcap data and convert it to a *.csv* file. The change in format made the data readable and easier to work with when analysing the data, be it for statistical or visual purposes. A breakdown of the traffic composition of the dataset used for this study is shown in **Table I**. The data dictionary table (**Table I**) shows the name of the network telescope, where the data was collected from, the number of packets from each of the major protocols identified in the dataset, when it was collected and the duration of data collection. It also shows the number of unique source IP (SRCIP) addresses contained in each dataset and how proportional these unique SRCIPs are to the overall traffic observed. The dictionary also show the breakdown of traffic based on the protocol used by each packet received.

This study focused mainly on TCP traffic because it was the largest dataset that was observed. Three months worth of data from a /24 IPv4 network telescoped were used, spanning from January to March. Unfortunately due to space limitation the study will only show how the results look like by using the month of January as a test case. In this study, this network telescope is referred to as 196/8 network telescope. The variables of interest for this research study were source and DSTIP addresses. SRCIP addresses were of interest because it gives a more accurate distribution of traffic by SRCIP address while the DSTIP addresses were needed because they are the recipient of the traffic and are the ones that a user has control over.

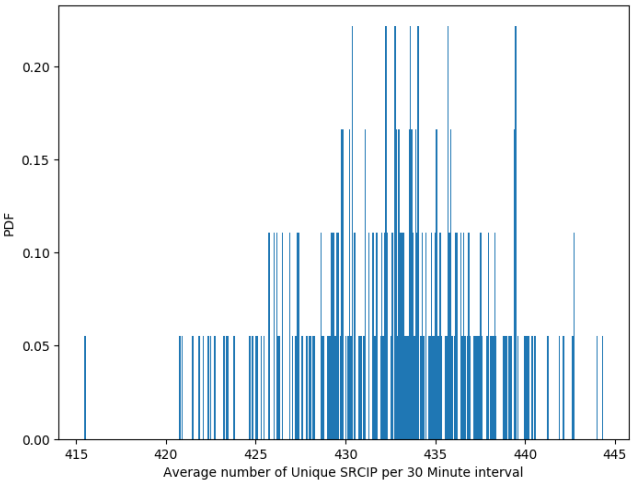

Fig. 1. 196/8 - A: Non - Parametric Bootstrapping at 95% CI

TABLE I
DICTIONARY 196/8-012021

Dictionary Name	196/8-012021		**Description**		
Start	Fri Jan 1 00:00:00 2021		**End**	Sun Jan 31 23:59:59 2021	
Duration	31 Days				
Total Traffic:	48,079,105	**Unique Sources:**	665,897	**Unique Destinations**	256
Protocols	pkts	%	Sources	Uniq src %	
TCP	42,043,059	87.44	538,891	80.93	
UDP	5,764,771	11.99	118,618	17.81	
ICMP	271,166	0.56	8,279	1.24	
Other	109	0.0002	109	0.016	

TABLE II
MONTHLY ACTIVE TCP DATASET: CI FOR NON PARAMETRIC COMPUTATION - SRCIP/HOUR

	CI Level			
Bootstrap sample	80%	90%	95%	99%
196/8 - /$_e$24	[793 - 806]	[791 - 807]	[790 - 809]	[787 - 812]
196/8 - /$_e$25	[399 - 406]	[398 - 406]	[397 - 407]	[396 - 409]
196/8 - /$_e$26	[199 - 202]	[199 - 203]	198 - 203]	[198 - 204]
196/8 - /$_e$27	[99 - 101]	[99 - 101]	[98 - 101]	[98 - 102]

TABLE III
MONTHLY ACTIVE TCP DATASET: CI FOR PARAMETRIC COMPUTATION - SRCIP/HOUR

	CI Level			
Bootstrap sample	80%	90%	95%	99%
196/8 - /$_e$24	[931 - 951]	[927 - 954]	[924 - 957]	[920 - 961]
196/8 - /$_e$25	[468 - 479]	[467 - 481]	[466 - 482]	[462 - 486]
196/8 - /$_e$26	[234 - 240]	[233 - 241]	[233 - 241]	[232 - 243]
196/8 - /$_e$27	[116 - 120]	[116 - 120]	[115 - 121]	115 - 121]

TABLE IV
MONTHLY NON-PARAMETRIC BOOSTSTRAP SAMPLE SUMMARY STATISTICS FOR TCP DATASETS - SRCIP/HOUR

Bootstrap Sample	Baseline Mean	Bootstrap Mean	Baseline SEM	Bootstrap SEM
196/8 - /$_e$24	799	800	4.84	4.84
196/8 - /$_e$25	403	402	2.52	2.52
196/8 - /$_e$26	100	100	0.70	0.70
196/8 - /$_e$27	201	201	1.32	1.32

V. RESEARCH APPROACH

Outliers were removed from each dataset to ensure that they do not affect the results. Using the Interquartile Range (IQR), this study identified a range that contained at least 80% of the data points in each dataset, thus any number falling outside this range was detected and treated as an outlier. Each baseline dataset contained all the 256 DSTIP addresses, from which 32, 64 and 128 DSTIP addresses were randomly selected to create new samples. It was from these samples that the bootstrap samples were generated and the computation of CI was conducted from it. These samples represent different sizes of the network telescope 'lens'. Each bootstrap sample contained 744 data points, the same data points that one would find in a baseline data where each hour within a month was considered a single data point.

The study opted to have all the bootstrap samples have the same number of data points as the original data as proposed in [14], [15], [19]. The reason for creating bootstrap samples of the same size as the baseline data was to ensure that there was comparability between the baseline data and the bootstrap samples [19], [20]. Secondly, by having a bootstrap sample be of the same size as the baseline, it eliminated the need of standardizing the bootstrap samples since it contained the same number of data points as the baseline [15]. This approach also ensured that the standard errors observed in the original dataset are reflected in the bootstrap sample as compared to having hypothetically larger or smaller samples [20]. This essentially meant that the number of observations was the same but the composition was different just as explained in Section II.

VI. RESULTS: UNDERSTANDING IBR DATA USING CONFIDENCE INTERVAL

As explained earlier in **Section III**, CI coverage is the probability that the CI includes the true population parameter, under repeated sampling from the same underlying population. The range computed from the bootstrap sample is what gives the user the level of confidence needed in the data in order to make informed decision(s). This section focused on interpreting the results and what they mean to this research.

To ease understanding of the results in this section , consider CI as a range of values defined by an upper bound being above the statistical mean of the sample under study and lower bound being below the statistic's mean of the same population. The CI is likely to contain an unknown population parameter being evaluated or examined. Thus the

true population parameter of this study is the actual value of the *mean* that has been computed from the sample being studied. The likelihood of finding this unknown *mean* in any sample under study is defined by the level of confidence used to compute the CI.

The study computed CI at different levels of confidence in order to offer a wider scope from which to work with. **Tables II** and **III** show the CI levels at which CI was computed and the number of unique DSTIP addresses contained in each bootstrap sample. **Tables II** and **III** also shows percentages of confidence at which different ranges of CI were computed. These have been labelled CI levels which range from 80% to 99%. Bootstrap samples are presented by using the name of the network telescope followed by the name of the subnet equivalent. Subnet equivalent because it is a random sample with the same number of IP addresses found in an actual subnet. For instance a /24 IPv4 baseline bootstrap sample for Network telescope **196/8** will be presented as **196/8 - /$_e$24** which means that this sample had *256* unique DSTIP addresses. A bootstrap sample from the same network telescope which had *128* unique DSTIP addresses will be presented as **196/8 - /$_e$25**. Depending on the nature of study, different fields use different levels of CI in order to attain their objectives. For instance, medical practitioners demand the highest level of confidence because they deal with life. In this study, the levels started at 80% confidence level until 99% CI. As the confidence level increased the CI range got wider meaning that the user gets more certain of how many unique SRCIP addresses one could get if the user bootstraps the IP addresses available in their network. Narrow CI at 80% CI level created more uncertainty of how many unique SRCIP addresses one could find in their sample. The more certain a user is the more confident they will have in the data to be used for more analysis and achieve their objective(s). A look at **Tables II** and **III** show that there are very slight variations between 95% and 99% CI level.

Another important detail to note is that CI changes with every new CI level of adjustment, i.e increasing the confidence level will increase the margin of error resulting in a wider interval. Standard Error of the Mean (SEM) tells you how accurate your estimate of the mean is likely to be, i.e SEM measures how much discrepancy there is likely to be in a sample's mean compared to the population mean [32]. **Table IV** shows how each bootstrap samples performed when compared to the baseline bootstrap. As the sample size of DSTIP addresses taken from the baseline data to create a bootstrap sample increased, SEM was increasing as well. This means that bigger samples created better bootstrap samples which were more representative of the overall baseline bootstrap thus the SEM got closer to the baseline bootstrap.

When DSTIP addresses were systematically sampled, the representation of the unique SRCIPs found in it was almost proportional, i.e the number of unique SRCIP addresses observed in a specific subnet, proportional wise, was approximately the same. This pattern is observed here too when looking at the CIs. As the sample size of DSTIP addresses taken from the baseline data to create a bootstrap sample increased, the CI increased by an equivalent proportion. Each time the sample size doubled, almost the same proportion was reflected in the CI. What this means is that whether the sample is randomly sampled or systematically sampled the proportionality of the unique SRCIP addresses between a subnet and its subnet equivalent is similar.

Fig. 1 shows a CI plot for non-parametric bootstrap plotted at 95% confidence level. What is observed in this plot is that most of the data points are concentrated between [428 - 441]. This shows that we are 95% confident that every hour the value of the average number of unique SRCIP addresses observed by a unique DSTIP address is between 428 and 441. The dispersion seen outside of this region just shows that the other 5% could fall outside of the [428 - 441] as CI computation acknowledges the likelihood of the actual population parameter falling outside of this region. With high CI levels the likelihood increases. However as shown in **Tables II** and **III**, the differences in CI between 95% CI and 99% CI are not significantly different compared to other CI levels in this IBR dataset. What this means is that if a user uses a small network telescope and gets values lower or higher than this range, given their corresponding number of unique DSTIP addresses, they may know with 95% certainty how many unique SRCIP addresses are missing from their dataset. The symmetrical nature of **Fig. 1** also entails the accuracy of our results as explain in **Section III**.

VII. Conclusion and Recommendations

The study has proven that bootstrapping can indeed be used to simulate IBR data to fill in the void left by those who do not have adequate resources to afford larger network telescope 'lens'. IBR data has shown results that were more reflective of the baseline bootstrap when working with non-parametric bootstrapping than parametric bootstrap thus the study recommends the use of non-parametric bootstrapping for future studies. The study has also confirmed observations made by [20] in his study as mentioned in **Section III**. The results are also consistent with what is expected in any inferential computation when it comes to the value of SEM.

The study also recommends the use of the data at least at 95% CI level because the variations between 95% and 99% CI level are not big, this way there will be a high chance of reflecting the reflections observed in the baseline data. A 95% or 99% CI for any given sample size means that the data user is 95% or 99% confident that each of the allocated sample will contain a specific average amount of unique SRCIP addresses in the available pool of DSTIP addresses. Confident to a point of knowing how much is not accounted for if the number observed are anything lower or higher than the indicated interval presented per network telescope 'lens' size. The number of unique SRCIP addresses observed in the DSTIP addresses of the host's network telescope is going to be different based on the duration of observation and the size of the network telescope 'lens'. Long observation period offer high volume of unique SRCIPs contained in the pool of unique DSTIP addresses observed. This is to say that if a 30 minute observation interval showed a few unique

SRCIP addresses as compared to hourly observation then a monthly interval would show more unique sources than a weekly observation. Also, a network telescope with 32 DSTIP addresses will show less unique SRCIP addresses than a 128 network telescope as illustrated in **Tables II** and **III**.

VIII. Future Work

Work that could not be added in this study due to limitations of space include the quantification of the differences that exist between the bootstrap samples and the baseline data using well known statistical tools like Mean Absolute Percentage Error (MAPE), Symmetric MAPE, Mean Absolute Scaled Error, Mean Absolute Eror. We have done work on quantifying the differences between baseline and subnet equivalents [33] but none links this work to bootstrapping samples. The researchers plan to continue to investigate what happens to these bootstrap samples if we were to use samples that have been collected over larger time periods, specifically to see if it affects the composition of the unique SRCIPs collected from the selected DSTIP addresses.

Acknowledgement

The authors would like to express their gratitude for financial support received from Telkom SA and Coriant. This work was undertaken as part of Distributed Multi- media CoE at Rhodes University. The authors acknowledge that opinions, findings, conclusions and recommendations are those of the authors and that none of the aforementioned sponsors accept liability whatsoever in this regard.

References

[1] E. Cooke, M. Bailey, Z. M. Mao, D. Watson, F. Jahanian, and D. McPherson, "Toward Understanding Distributed Blackhole Placement," in *Proceedings of the 2004 ACM Workshop on Rapid Malcode*, ser. WORM '04. New York, NY, USA: ACM, 2004, pp. 54–64.

[2] A. Guillot, R. Fontugne, P. Winter, P. Merindol, A. King, A. Dainotti, and C. Pelsser, "Chocolatine: Outage Detection for Internet Background Radiation," in *2019 Network Traffic Measurement and Analysis Conference (TMA)*. IEEE, 2019, pp. 1–8.

[3] R. Pang, V. Yegneswaran, P. Barford, V. Paxson, and L. Peterson, "Characteristics of internet background radiation," in *Proceedings of the 4th ACM SIGCOMM Conference on Internet Measurement*, ser. IMC '04. New York, NY, USA: ACM, 2004, pp. 27–40.

[4] E. Wustrow, M. Karir, M. Bailey, F. Jahanian, and G. Huston, "Internet Background Radiation Revisited," in *Proceedings of the 10th ACM SIGCOMM Conference on Internet Measurement*, ser. IMC '10. New York, NY, USA: ACM, 2010, pp. 62–74.

[5] D. Moore, C. Shannon, G. M. Voelker, and S. Savage, "Network telescopes: Technical report," University of California, San Diego, Tech. Rep., 2004, date Accessed: 20 November 2018. [Online]. Available: https://www.caida.org/catalog/papers/2004_tr_2004_04/tr-2004-04.pdf

[6] S. O. Hunter, B. Irwin, and E. Stalmans, "Real-Time Distributed Malicious Traffic Monitoring for Honeypots and Network Telescopes," in *2013 Information Security for South Africa*. Washington DC, USA: IEEE, Aug 2013, pp. 1–9.

[7] B. Irwin, "A Source Analysis of the Conficker Outbreak from a Network Telescope," *SAIEE Africa Research Journal*, vol. 104, no. 2, p. 38, 2013.

[8] J. Czyz, K. Lady, S. G. Miller, M. Bailey, M. Kallitsis, and M. Karir, "Understanding IPv6 Internet Background Radiation," in *Proceedings of the 2013 Conference on Internet Measurement Conference*, 2013, pp. 105–118.

[9] B. Irwin, "A Baseline Study of Potentially Malicious Activity Across Five Network Telescopes," in *2013 5th International Conference on Cyber Conflict (CYCON 2013)*. Tallinn, Estonia: NATO CCDCOE, June 2013, pp. 1–17.

[10] T. M. Nkhumeleni, "Correlation and Comparative Analysis of Traffic Across Five Network Telescopes," Master's thesis, Rhodes University, 2014. [Online]. Available: http://hdl.handle.net/10962/d1011668

[11] I. Polakis, G. Kontaxis, S. Ioannidis, and E. P. Markatos, "Dynamic Monitoring of Dark IP Address Space (Poster)," in *International Workshop on Traffic Monitoring and Analysis*. Springer, 2011, pp. 193–196.

[12] B. Irwin, "A Network Telescope Perspective of the Conficker Outbreak," in *2012 Information Security for South Africa*. Washington DC, USA: IEEE, Aug 2012, pp. 1–8.

[13] U. Harder, M. W. Johnson, J. T. Bradley, and W. J. Knottenbelt, "Observing Internet Worm and Virus Attacks with a Small Network Telescope," *Electronic Notes in Theoretical Computer Science*, vol. 151, no. 3, pp. 47–59, 2006.

[14] K. N. Kirby and D. Gerlanc, "BootES: An R Package for Bootstrap Confidence Intervals on Effect Sizes," *Behavior Research Methods*, vol. 45, no. 4, pp. 905–927, 2013.

[15] B. Efron and T. Hastie, *Computer Age Statistical Inference: Algorithms, Evidence, and Data Science*. Cambridge University Press, 2016, vol. 5.

[16] R. Marcaccioli and G. Livan, "Maximum Entropy Approach to Multivariate Time Series Randomization," *Scientific Reports*, vol. 10, p. 10656, 2020.

[17] M. A. Martin, "On Bootstrap Iteration for Coverage Correction in Confidence Intervals," *Journal of the American Statistical Association*, vol. 85, no. 412, pp. 1105–1118, 1990.

[18] A. Davison and D. Kuonen, "An Introduction to the Bootstrap with Applications in R," *Statistical Computing & Statistical Graphics Newsletter*, vol. 13, no. 1, pp. 6–11, 2002.

[19] N. Chamandy, O. Muralidharan, and S. Wager, "Teaching Statistics at Google-scale," *The American Statistician*, vol. 69, no. 4, pp. 283–291, 2015.

[20] T. C. Hesterberg, "What Teachers Should Know About the Bootstrap: Resampling in the Undergraduate Statistics Curriculum," *The American Statistician*, vol. 69, no. 4, pp. 371–386, 2015.

[21] A. M. Zoubir and D. R. Iskandler, "Bootstrap Methods and Applications," *IEEE Signal Processing Magazine*, vol. 24, no. 4, pp. 10–19, 2007.

[22] J.-P. Kreiss and S. N. Lahiri, "Bootstrap Methods for Time Series," in *Handbook of Statistics*. Elsevier, 2012, vol. 30, pp. 3–26.

[23] G. Rousselet, C. Pernet, and R. R. Wilcox, "A Practical Introduction to the Bootstrap: A Versatile Method to Make Inferences by Using Data-driven Simulations," *PsyArXiv*, 2019.

[24] P. M. Dixon, "Bootstrap Resampling," in *Encyclopedia of Environmetrics*. Wiley Online Library, 2006.

[25] L. Simar and P. W. Wilson, "Sensitivity Analysis of Efficiency Scores: How to Bootstrap in Non-parametric Frontier Models," *Management science*, vol. 44, no. 1, pp. 49–61, 1998.

[26] R. R. Wilcox, *Introduction to Robust Estimation and Hypothesis Testing*. Academic Press, 2011.

[27] G. A. Rousselet, C. R. Pernet, and R. R. Wilcox, "The Percentile Bootstrap: A Teaser with Step-by-Step Instructions in R," *Advances in Methods and Practices in Psychological Science*, vol. 4, no. 1, 2021.

[28] ——, "Beyond Differences in Means: Robust Graphical Methods to Compare Two Groups in Neuroscience," *European Journal of Neuroscience*, vol. 46, no. 2, pp. 1738–1748, 2017.

[29] R. J. Tibshirani and B. Efron, *An Introduction to the Bootstrap*. CRC press, 1993.

[30] A. C. Davison and D. V. Hinkley, *Bootstrap Methods and their Application*. Cambridge University Press, 1997.

[31] B. V. W. Irwin, "A Framework for the Application of Network Telescope Sensors in a Global IP Network," Ph.D. dissertation, Rhodes University, 2011. [Online]. Available: http://hdl.handle.net/10962/d1004835

[32] S. Seabold and J. Perktold, "Statsmodels: Econometric and Statistical Modeling with Python," in *9th Python in Science Conference*, 2010. [Online]. Available: https://pdfs.semanticscholar.org/3a27/6417e5350e29cb6bf04ea5a4785601d5a215.pdf

[33] S. D. Chindipha, B. Irwin, and A. Herbert, "Quantifying the Accuracy of Small Subnet-Equivalent Sampling of IPv4 Internet Background Radiation Datasets," in *Proceedings of the South African Institute of Computer Scientists and Information Technologists 2019*, ser. SAICSIT '19. Association for Computing Machinery, 2019, pp. 1–8.

Stones Dalitso Chindipha is undertaking a PhD in the department of Computer science and a member of SNRG at Rhodes University. His research interests are in the fields of data analytics, active and passive security, cyber security, network security and threat intelligence.

Automatic African Zulu Music Genre Classification Using Machine Learning and Signal Processing Techniques

Nomthandazo Mpanza, Siphiwe Cilo , Olutayo Oyerinde
School of Electrical & Information Engineering, University of the Witwatersrand, Private Bag 3, 2050, Johannesburg, South Africa
1407896@students.wits.ac.za
1124513@students.wits.ac.za
Olutayo.Oyerinde@wits.ac.za

***Abstract*—This paper presents the procedure undertaken to achieve automatic classification of 3 of the most popular Zulu music genres namely: Maskandi, Gqom and Gospel. A dataset consisting of 356 Zulu songs in *.mp3* format which belong to the three distinct genres was created. Clips of 15 $seconds$ were extracted from the collected data samples for usage in the feature extraction process. The songs were then renamed as part of manual labelling in the data-preprosessing stage for classification. Timbral, rhythmic and chroma frequency features were extracted from the clips for training the proposed voting classifier which ensembles k-Nearest Neighbours (KNNs), Support Vector Machines (SVMs), Linear Discriminant Analysis (LDA) and Decision Trees. This paper however, focuses on the contribution of KNNs and LDA to the achieved overall accuracy of 94 % for the voting classifier. The KNNs and LDA achieved accuracies of 83.3 % and 79.6 % respectively. Another proposed classification method employs a ResNet50 model which achieved an accuracy of 90.6 %. This model was trained on Spectrogram images generated from the audio clips. The models had difficulty distinguishing between Gqom and Maskandi genres. This is due to the strong correlation between the features extracted and similarity in perceptual and rhythmic features. A web application was implemented for demonstrating the classification.**

***Index Terms*—Automatic classification, Feature extraction, Gospel, Gqom, KNNs, LDA, Maskandi, ResNet50, Voting Classifier.**

I. Introduction

Numerous challenges arise when handling vast music collections that have to be retrieved and classified [1]. Audio classification systems can be employed in the generation of automatic recommended playlists. Humans created music genres as categorical labels used in the identification of different music styles. However, genres are now used as descriptors in the organization of large contents of digital music. The ability of machine learning to perform pattern recognition is useful when considering music genre classification, especially with the millions of search queries in the music database that occur on the internet. Certain characteristics are shared amongst members of the same genre. Automatic genre classification is popular in Western music, however, it has not been explored for African music. This paper aims to bridge that gap by presenting classification schemes for three distinct Zulu music genres namely: Gqom, Maskandi and Gospel.

This paper starts by providing the background on previous work that has been employed in automatic music genre classification using machine learning. It then provides the system overview followed by a detailed description of the design methodologies employed to achieve the automatic classification of Zulu music into distinct genres. The results obtained from evaluating the models are then presented and analyzed. This paper only focuses on the implementation of the ResNet50 classifier and the contribution of KNNs and LDA to the voting classifier. Details of the contribution of SVMs and Decision Trees to the voting classifier along with the details of the implemented web application can be found in [2].

II. Background

This paper draws from existing methods that have been used to successfully classify Western music. More specifically, the same features that were used to classify the Western music into different genres will be used in this paper to classify Zulu music.

The extraction of content-based features such as rhythmic, timbral and pitch content features has proven to lead to more accurate music genre classification schemes [3]. A combination of the aforementioned features is extracted and used in the creation of a feature vector used to train a classification model in [4]. This approach is adopted in the feature selection stage for the proposed voting classifier algorithms by using a combination of rhythmic, timbral and pitch content features. According to the knowledge of the author, automatic music genre classification has not been previously done for Zulu music. It has mostly been done for Western music. Careful attention is paid to the differences between African and Western music in order to analyze the features extracted and to distinguish their strengths on different genres.

Even though convolutional neural networks (CNNs) were created for classification of natural images, the use of spectrograms as image inputs to CNNs has become popular in recent times [5] with regards to audio classification. Deshpande in

[6] makes use of Mel-frequency cepstral coefficients (MFCCs) and spectrograms to transform audio data into images in the visual domain and employs a texture-of-textures approach to pick perceptually meaningful features from the images. This paper draws from [6] to focus on the conversion of audio into spectrogram images which will be used for training a ResNet50 model. A systematic study was performed by [5] to investigate the behaviour of pretrained ImageNet models when it comes to learning audio representations on ESC-50, GTZAN and UrbanSound8K datasets. In their findings, they concluded that the fine tuned standard deep CNN ImageNet pretrained models are applicable for use as strong baseline audio classification networks. Moreover, they require the smallest amount of work with regards to model design. The proposed ResNet50 classifier draws from the fine tuning process explored in [5].

III. SYSTEM OVERVIEW

The approach undertaken to achieve automatic classification of Zulu music into three different genres namely: Maskandi, Gqom and Gospel is depicted by the block diagram in Figure 1.

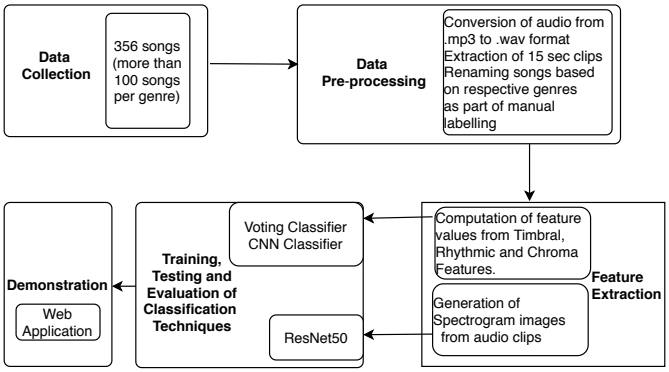

Fig. 1. Block diagram of system overview

IV. SYSTEM DESIGN AND IMPLEMENTATION

Both MATLAB and python have a wide variety of packages and libraries that are available for machine learning. In comparison to MATLAB, python is a free open-source programming language that requires less computational processing power. Moreover, its environment enables easier remote collaboration hence it was used in implementing the models. Two classification methodologies were developed, a Voting classifier which encompasses four algorithms namely: SVMs, KNNs, LDA and Decision Trees and a pretrained ResNet50 that was trained with Spectrograms. This paper focuses on two algorithms (KNNs and LDA) used in ensembling the voting classifier and the complete implementation of the ResNet50 classifier.

A. Zulu Music Dataset

1) Data Collection: A new dataset consisting of a total of 356 Zulu songs under three different genres namely: Maskandi (119 songs), Gqom (122 songs) and Gospel (115 songs) was created as there was no readily available Zulu music dataset that could have been used. Most of the music samples were collected from the *internet* and *youtube*.

2) Data Pre-processing: All the music samples collected were first converted from $.mp3$ to $.wav$ format. This was done because the $.wav$ format is uncompressed thus it enables better extraction of the content-based features that define the signal. The songs were then sampled and renamed for manual labelling based on the genre they belonged to. Moreover, 15 $seconds$ clips were extracted from each song. The 7.5 $seconds$ before and after the midpoint of the song were used to avoid capturing the song at any random moment. Furthermore, at the beginning and end of most Zulu songs there is usually ululating, praises, clapping or shouting which makes the required features to be more difficult to identify. In addition, this was done to make sure that while pre-processing the data, the perceptual properties of the music content are preserved. The music samples were then converted from stereo to monophonic format by averaging the stereo channels to make them fully ready for the feature extraction process.

B. Feature Selection and Extraction

The main challenge associated with pattern recognition systems is the construction of explanatory features which can be calculated as a solid numerical portrayal of the audio segment [7]. Features need to be extracted from audio signals in order to be fed into a classification system. This is because audio signals are naturally time-varying complex signals which are incompatible for being directly fed into classification systems due to their unclear representation. The efficiency and performance of any classification system is highly dependent on the features extracted. Too many features usually degrade the efficiency as they lead to increased computational space. Some features are also irrelevant, which diminishes model performance [8]. Similarly, too few features lead to failure in the process of sufficiently capturing useful information. The features that were selected are the most critical features because they define the genres of the songs being classified [9]. The features that were selected and extracted to form a feature vector are detailed below. The *librosa* library was used for the process of feature extraction. Furthermore, the mean and standard deviation of each feature was computed as it was assumed that the feature values follow a Gaussian distribution.

1) Timbral Features: These give the human ear the ability to differentiate between sounds having a similar loudness and pitch, as a result, they are used to characterize distinct traits in a tone.

- Spectral Roll-off - indicates the frequency below which 85 % of a signal's spectrum energy lies and is used to measure the shape of the signal. It serves as a useful discriminator between vocal and non-vocal sounds. Moreover, it is used in the approximation of the maximum signal frequency [7].

- Spectral Flatness - This feature differentiates between harmonic and noisy signals [7]. It uses a scale of *0-1* where a spectral flatness of *1* represents a perfectly flat power spectral density. It is measured as the magnitude of the signal's spectrum geometric to arithmetic mean ratio.

2) Rhythmic Features: Points out the structural elements in audio signals that are not recognized by timbral features. It is mainly about the repetitive patterns in audio signals.

- Tempogram - indication of distinct strength of the pulse of an audio signal over a time lag period. It indicates the pace at which a music piece is performed [7]. It provides the general sense of the music and attempts to convey different emotions (such as sadness, excitement etc). Furthermore, it is usually most dominant in African music [10].

3) Chroma Frequencies: Characterizes the pitch and harmonic content features in a music signal [7]. It obtains an audio spectrum and divides it into relevant chromatic chords then it marks them at the appropriate places where they occur. This enables the ability to denote similarities between two different music pieces.

4) Spectrograms Generation: The *plt.specgram* function from the *matplotlib.pyplot* library was used to generate the spectrogram image features from the audio samples. These are visual representation of the frequencies composed within each audio signal. Each extracted song clip was loaded in a mono format for a period of 5 $seconds$. No window was applied and *2048* datapoints were used per block in fast fourier transform computations. A frame skip of *128* was used to achieve increased time localization with a sampling rate of 22050 *Hz*.

C. Voting Classifier

A voting classifier is a type of ensemble classifier which have been proven to produce lower error values and are not prone to overfitting [11]. The voting classifier used in this paper, is part of Python's Machine Learning library scikit-learn. The classifier creates a combination of predicted outcomes for each genre, then all the algorithms are passed through a majority vote. Soft voting was chosen for this model because of its ability to improve the errors of each classification algorithm used [12]. Soft voting adds aggregates the predictions of each algorithm that is voting and then it makes a decision based on the higher aggregate.

Four different supervised machine learning algorithms were passed into a voting classifier for the novelty of the model. This paper focuses on only two of them, which are the KNNs and the LDA. Manually labelled data was used to train the aforementioned algorithms to classify unlabelled audio signals. The *sklearn* library from the *scikit-learn* package in Python was used for the training. *Scikit-learn* is an open-source machine learning package in Python [12].

1) KNNs: In this non-parametric supervised machine learning classifier, a decision is influenced by a small number of neighbours around a particular point [4], [13]. From the training set, each sample gets assigned a label based on the number of k nearest neighbours on the target feature vector. The model was trained with uniform weights (meaning that all the points in neighbouring positions were weighed equally).

The Euclidean distance formula is used to obtain the distances between the nearest neighbours. However, this method is highly sensitive to magnitudes thus the data is normalised using Max-Min Normalisation [14] in order to reduce all the feature values to the same scale. In this paper, the best k value was chosen based on an iteration of values from *1 to 10*. Higher k values are costly to compute and may underfit the data while very low values add noise to the results and may overfit data [15]. Consequently, the optimal k value of 5 is relatively small hence it provides faster computational time and a more flexible fit. Furthermore, choosing a smaller value leads to a decreased bias.

2) LDA: This is another supervised machine learning algorithm which obtains a linear transformation that separates different classes and then works in the transformed space to perform classification using a metric [13]. The separation is achieved through the computation of linear discriminants that are a representation of the axis between the different classes. Bayes Theorem is employed in the estimation of probabilities.

D. ResNet50 Classifier

It is a pretrained residual CNN with 50 layers. The choice of using a pretrained network was motivated by the fact that it is trained on more than one million ImageNet image data thus only requires fine tuning in order to classify the new datasets [5]. Moreover, the network does not have a gradient degradation problem since it uses shortcut connections and has increased accuracy with its depth [5]. The open-source *fastai version 2* library was used with the *datablock api* for increased efficiency. It was applicable for use because it is designed primarily for notebook-oriented interactive systems [16] and it has a flexible infrastructure.

1) Model Training: The spectrogram images generated were already pre-processed as a three-channel input as done in [17] and were directly fed into ResNet50. The weights of the model were not changed, however, they were frozen over all the layers just before the final hidden softmax classification layer and the final softmax was fine tuned. The *cnn_learner* function connects an Adam optimizer with the pretrained ResNet50 model and the data that the model was trained and validated on. The classification head of the model was replaced with the one proposed for Zulu music genre classification. The method followed for training is as follows: Only the last layer of the network was unfrozen and trained on the spectrogram images since it is responsible for the classification. After some training iterations, it was found that using 4 epochs yields the smallest training error. The model was then saved and reloaded with the added layer. In order to optimize it further, the entire model was then unfrozen and *model.lr_find()* was used to obtain the optimal learning rate. The model was then trained using that rate. The training and validation losses plot achieved over 100 iterations is depicted

by Figure 2 and it shows that the model does not underfit or overfit.

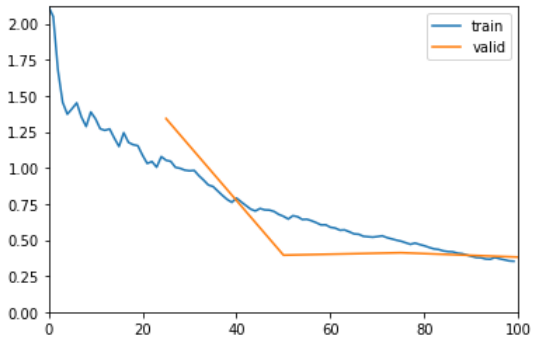

Fig. 2. Training and Validation loss

V. RESULTS AND ANALYSIS

A. Voting Classifier Results

A total of 356 songs were used from the dataset. The split between training and testing data was 80 % (284 songs) and 20 % (72 songs) respectively for the voting classifier model. Table I shows the different accuracies that were achieved from the models and machine learning algorithms trained.

TABLE I
MODEL ACCURACIES

Classification Method	Accuracy (%)
KNNs	83.3
LDA	79.6
Voting Classifier	94
ResNet50	90.6

The KNNs and LDA models struggled to differentiate between Gqom and Maskandi music as shown in Figure 3 and 4 respectively.

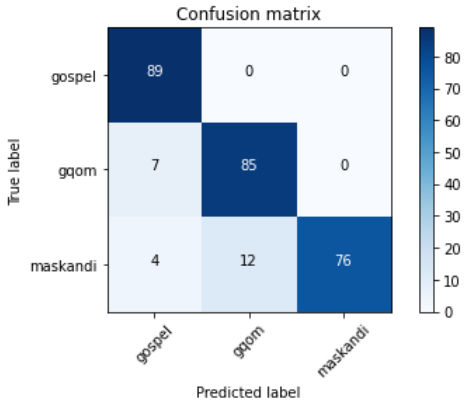

Fig. 3. KNN confusion matrix

It can be observed that the algorithms mostly incorrectly classified Gqom songs for Maskandi and vice versa than it did for Gospel. This is due to the similarities shown by the

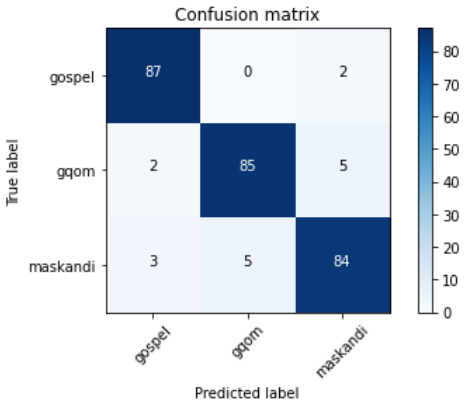

Fig. 4. LDA confusion matrix

features extracted. The KNN performed much better than LDA in classifying the Maskandi genre. The overall accuracy that resulted from the Voting Classifier was mainly affected by the independent results achieved from the different algorithms. The confusion matrix generated by the voting classifier is depicted by Figure 5. It shows that the overall accuracy improved and less songs were incorrectly classified as other genres. However, there exists a strong similarity in the features of Gqom and Maskandi which is evident in the confusion matrix from the LDA and KNN algorithms.

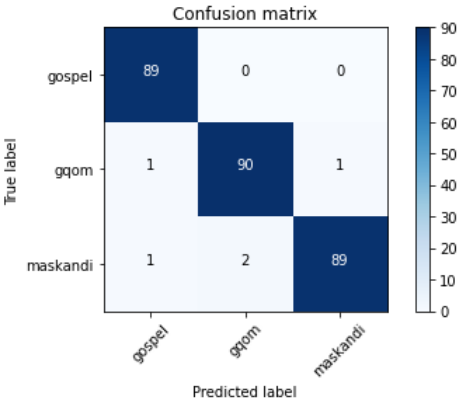

Fig. 5. Voting classifier confusion matrix

Figure 6 shows classification clusters from the model. A strong correlation exists between Maskandi and Gqom mainly due to the rhythmic, loudness and timbral features. As a result, except for Gospel, the voting classifier failed to make a clear distinction for Gqom and Maskandi genres.

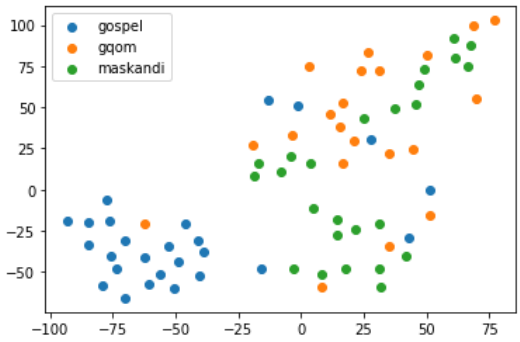

Fig. 6. KNN clusters for different genres

B. ResNet50 Classifier Results

Out of a total number of 326 spectrogram images, 64 were used for validating the ResNet50 model. These resulted from the 80 % to 20 % split for training and validation data. The confusion matrix obtained from the validation set is depicted by Figure 7. The model was able to correctly classify all Gqom songs. However, a few of both Gospel and Maskandi samples were confused for being other genres.

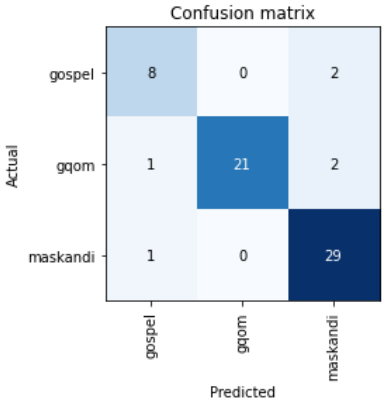

Fig. 7. ResNet50 confusion matrix

C. Critical Analysis

The dataset used for training the models is biased as there is no balance between the number of collected songs for each genre class. Moreover, this affects the results obtained due to the unequal songs used since the model seems to be routing for Gqom because it had the highest number of music samples. The procedure utilised for extracting the segments of the song is inadequate as audio is a time-variant signal and extracting only the middle part does not expose the time variation traits in the song. The essence and quality of the captured features are highly restricted by the data pre-processing stage.

Gospel can be subdivided into *worship* and *praise*. The tempo (rhythmic feature) in *praise* is much faster compared to *worship*. It explains why the KNNs and the ResNet50 would classify some of the Gospel songs as Gqom or Maskandi due to the similarity of the rhythmic features.

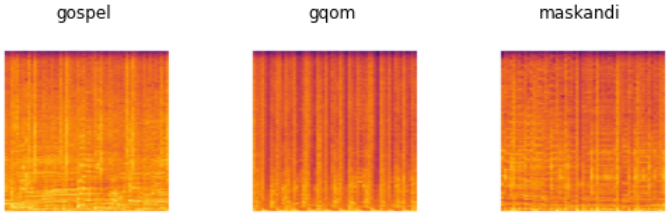

Fig. 8. Spectrogram images for different genres

Figure 8 shows different spectrogram images for each genre. The frequency bands represented in the images are much darker at the top for Gqom which indicates the absence of high frequencies. This is due to the instruments used in the production of this type of genre, the beats and the drums. Gospel spectrograms show a huge variation due to the different instruments that are used in its production. The upper part of these images has strong dark bands which indicate the absence of high transients on those parts. Overall, all these music genres have high frequencies on their lower and medium parts. However, some of the Maskandi songs seem to have the same bands on top which supports why the CNN would incorrectly classify Gospel for Maskandi with a probability of *0.26* (symbolising less confidence in classification) as shown in Figure 9.

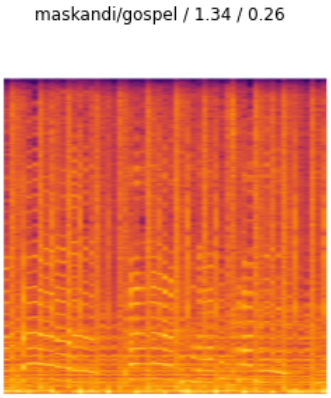

Fig. 9. Incorrectly classified Gospel sample

D. Comparison with Existing Solutions

An accuracy of 75 % was obtained by [6] using KNNs as a classification method for Jazz, Rock and Classical music. Table II shows the accuracy results obtained from methods previously used [3] for Western music genre classification. Only those with features mostly similar to those extracted in this work were considered.

The results obtained in this paper were within $\pm$ 5 % range of the accuracies obtained in existing solutions. This proves that features extracted for Western music are applicable to African Zulu music for classification. Furthermore, classification using ResNet50 achieved much higher accuracy compared to the AlexNet model with 78 % accuracy. There seems

TABLE II
MODEL ACCURACIES

Classification Method	Datasets of (Accuracy (%))	Number of genres
KNNs	GTZAN (86.67)	3
KNNs	McKay, Fujinaga's 3 root (75)	3
LDA	McKay, Fujinaga's 3 root (86.33)	3
AlexNet	GTZAN (78)	10

to be a promising future in classification using pretrained models. Provided with more data samples and a combination of more distinct features, the approaches proposed can achieve improved performance.

VI. CONCLUSION

Three distinct Zulu music genres namely: Gqom, Maskandi and Gospel, have been classified using a Voting classifier and a pretrained ResNet50 model. The classification accuracies obtained were 94 % and 90.6 % respectively. The models had difficulties with differentiating between Gqom and Maskandi music due to the strong similarities that exist between the two genres. Based on the combination of the features extracted, the results were within $\pm$ 5 % of the accuracies in existing solutions. There is no conclusive evidence that these algorithms can be applied to other distinct African music genres.

REFERENCES

[1] S. Oramas, O. Nieto, F. Barbieri, and X. Serra, "Multi-label music genre classification from audio, text, and images using deep features," 07 2017.

[2] N.Mpanza, "Automatic zulu music genre classification using cnn and voting classifier"," 2020.

[3] R.Ajoodha, "Automatic music genre classification"," Master's thesis, School of Computer Science, 2014.

[4] G. Tzanetakis and P. Cook, "Musical genre classification of audio signals," in *IEEE Transactions on Speech and Audio Processing*, 2016, pp. 293–302.

[5] K. Palanisamy, D. Singhania, and A. Yao, "Rethinking cnn models for audio classification," 07 2020.

[6] H. Deshpande, U. Nam, and R. Singh, "Mugec: Automatic music genre classification," 07 2001.

[7] B. to twoears.eu. Spectral features. http://docs.twoears.eu/en/latest/afe/available-processors/spectral-features/. Accessed: 2020-10-14.

[8] M. Banitalebi-Dehkordi and A. Banitalebi Dehkordi, "Music genre classification using spectral analysis and sparse representation of the signals," *Journal of Signal Processing Systems*, vol. 74, 02 2014.

[9] M. Müller, D. Ellis, A. Klapuri, and G. Richard, "Signal processing for music analysis," *Selected Topics in Signal Processing, IEEE Journal of*, vol. 5, pp. 1088 – 1110, 11 2011.

[10] J. Dickie, "Singing the psalms: applying principles of african music to bible translation," *Scriptura*, vol. 116, 04 2017.

[11] N. Chand, P. Mishra, R. Challa, E. Pilli, and M. Govil, "A comparative analysis of svm and its stacking with other classification algorithm for intrusion detection," 04 2016, pp. 1–6.

[12] F. Pedregosa, G. Varoquaux, A. Gramfort, V. Michel, B. Thirion, O. Grisel, M. Blondel, P. Prettenhofer, R. Weiss, V. Dubourg, J. Vanderplas, A. Passos, D. Cournapeau, M. Brucher, M. Perrot, and E. Duchesnay, "Scikit-learn: Machine learning in Python," *Journal of Machine Learning Research*, vol. 12, pp. 2825–2830, 2011.

[13] N. Scaringella, G. Zoia, and D. Mlynek, "Automatic genre classification of music content: a survey," *Signal Processing Magazine, IEEE*, vol. 23, pp. 133 – 141, 04 2006.

[14] O. A. Akanbi, I. S. Amiri, and E. Fazeldehkordi, "Chapter 4 - feature extraction," in *A Machine-Learning Approach to Phishing Detection and Defense*, O. A. Akanbi, I. S. Amiri, and E. Fazeldehkordi, Eds. Boston: Syngress, 2015, pp. 45–54. [Online]. Available: https://www.sciencedirect.com/science/article/pii/B9780128029275000046

[15] Palak. Deep Insights Into K-nearest Neighbors. https://medium.com/towards-artificial-intelligence/deep-insights-into-k-nearest-neighbors/-2c95c04728d9. Accessed: 2020-10-10.

[16] M. Wojczulis. Introduction To Deep Learning With Fastai: This Is Why Deep Learning Can Work For Everyone. https://dlabs.ai/blog/introduction-to-deep-learning/. Accessed: 2020-10-10.

[17] L. Wyse, "Audio spectrogram representations for processing with convolutional neural networks," 2017.

Siphiwe Cilo completed her Bachelor of Science in Electrical and Information Engineering from the University of the Witwatersrand in 2020. Her research interests are in machine learning and renewable energy. She is a junior Software Developer at Discovery in Discovery Health.

Nomthandazo Mpanza completed her Bachelor of Science in Electrical Engineering at the University of the Witwatersrand in 2020. She is a Junior Software Developer at Discovery Bank Limited. Her research interests are in machine learning and data analytics.

PSO-Based Workflow Scheduling: A Comparative Evaluation of Cloud and Cloud-Fog Environments

Dineshan Subramoney, Clement Nyirenda
Department of Computer Science,
Faculty of Natural Sciences,
University of the Western Cape,
Cape Town 7535, South Africa
[1]cnyirenda@uwc.ac.za
[2]dineshansubramoney@gmail.com

***Abstract*—This paper presents a comparative evaluation of cloud and cloud-fog environments for workflow scheduling using the classical Particle Swarm Optimization (PSO) algorithm. This paper also presents a weighted sum objective function based on three objectives: makespan, cost and energy. The recently proposed FogWorkflowSim is used as the simulation environment for the cloud and cloud-fog architectures. The results obtained for two well-known scientific workflows (Montage and CyberShake) show that the incorporation of the fog layer for the execution of workflows has the potential to improve processing efficiency and reduce energy consumption, motivating the cloud-fog computing paradigm. Future work will focus on the evaluation of other types of workflows such as Epigenomics, LIGO and SIPHT as well as increasing the number of tasks in a workflow.**

***Index Terms*—Workflow scheduling, Fog Computing, Cloud Computing, Particle Swarm Optimization**

I. Introduction

As cloud computing [1] becomes more and more established in the ICT industry, the possibility of conducting large-scale scientific computations, that could not be done on traditional computing systems is becoming a reality. Scientific workflows [2]–[4] are some of the data-intensive scientific applications that are really benefiting from the cloud computing revolution. In a nutshell, scientific workflow is characterized by interdependent tasks and computations that are aimed at achieving some scientific objectives. The cloud infrastructure offers a suitable platform for executing scientific workflows because these applications involve complex data and are also characterized by long sessions of computation. Furthermore, the cloud infrastructure offers other crucial attributes to workflow computations such as cost efficiency, high speed, accessibility, manageability, elasticity, and virtualization capabilities.

Scientific workflows are typically described as a directed acyclic graph (DAG), where the nodes are tasks and the edges denote the task dependencies [4]. The scheduling of these tasks for execution on cloud virtual machines presents huge challenges because of high computation and communication costs [5]. Population-based techniques such as Genetic Algorithm (GA), Particle Swarm Optimization (PSO) have been used for scheduling the tasks on the cloud infrastructure [5]–[10]. Currently, the PSO approaches seem to be the most favourite amongst these population-based techniques as evidenced by a recent extensive survey on PSO-based approaches [9]. The interest in PSO is sparked by its fast convergence and short run time.

While most of the aforementioned works have focused on workflow scheduling in the traditional two-tier cloud infrastructure, very few [10]–[12] have focused on the emerging three-tier infrastructure, which incorporates the fog devices between the cloud and the end devices. Fog computing extends the cloud computing model and acts as an intermediate layer. Any device with computing, storage and networking capabilities can be considered a fog device. Among other things, fog devices are characterised by the following advantages, compared to their cloud counterparts: lower latency, improved user experience, higher security, and energy efficiency.

A simulation toolkit, known as Fogworkflowsim [13], for workflow scheduling in fog computing was recently proposed. This work was inspired by the WorkflowSim [14], which has been used for simulating workflow scheduling in cloud environments for close to a decade. In [12], a comparative evaluation of population-based optimization algorithms for Workflow Scheduling in cloud-fog Environments has been conducted. The work developed a weighted sum objective function that incorporates makespan, cost, and energy consumption and proceeded to implement the Genetic Algorithm (GA), PSO, Differential Evolution (DE), and the PSO-GA algorithms in the Fogworkflowsim [13] toolkit.

The paper builds on the work in [12] by exclusively focusing on the PSO algorithm's workflow scheduling performance in two architectures: the traditional cloud environment and the emerging three-tier cloud-fog environment. To the best of our knowledge, no work has so far compared PSO workflow scheduling performance under the two environments. The work is preliminary in nature as it uses only two types of scientific workflows within the Pegasus framework, namely: Montage and CyberShake. Makespan, energy consumption, and cost are used as performance metrics.

The rest of the paper is organised as follows. Section II briefly describes the standard PSO algorithm. Section III presents the workflow Scheduling basics as well as the objective function, that was used in this work. Section IV presents the PSO optimization process for workflow scheduling, while Section V presents the performance evaluation. Section VI concludes the paper and presents future work.

II. Particle Swarm Optimization Algorithm

Particle swarm optimization (PSO) is a population-based stochastic optimization algorithm introduced by Kennedy and Eberhart [15]. The technique is used to solve optimization problems by emulating the social behavior of bird flocking, fish schooling and other animal societies that cooperate and share information to improve their position without relying on a leader. In this technique, a population of individuals, that are candidate solutions represented as particles, move in a given solution space according to its current position X_i^k, and current velocity V_i^k for the k^{th} iteration. The quality of each particle is measured using a defined fitness function depending on the optimization problem. Each particle's movement is based on its best known personal position $pBest_i$, and also moves towards the best known global position $gBest$ for the entire swarm. This process leads the swarm to the best position over a number of iterations in the search process. The particle's velocity and position are described below:

$$V_i^{k+1} = \omega V_i^k + c_1 r_1 (pBest_i - X_i^k) + c_2 r_2 (gBest_i - X_i^k) \quad (1)$$

$$X_i^{k+1} = X_i^k + V_i^k \quad (2)$$

where ω is the inertia weight, r_1 and r_2 are random numbers between (0,1), and c_1 and c_2 are the learning factors.

III. Workflow Scheduling Basics and Objective Function

This section begins by defining the workflow scheduling problem. Then, the weighted sum based objective function is presented for workflow scheduling.

A. The Concept of Workflows and Problem Formulation

The workflow application is represented as a Direct Acyclic Graph (DAG), defined by $G = (T, E)$, where T denotes the set of n tasks $\{t_1, t_2, \ldots, t_n\}$ and E is the set of edges, representing the dependencies between pairs of tasks [6], [7], [10], [12]. An edge can be illustrated by $d_{ij} =< t_i, t_j > \in E$, where d_{ij} is a positive value representing the output data from task t_i to t_j. Therefore, the execution of t_j cannot start until t_i has completed. A task t_i with no parent is known as a $start$ task and a task t_j with no child is known as an end task.

Workflow application scheduling in the cloud and cloud-fog environments are defined here as the problem of assigning computing resources with different characteristics to tasks of the workflow application, in order to minimize the total completion time, cost and energy of the workflow execution.

B. The Weighted Sum Objective Function

There are m computational resources which are of two types, namely cloud and fog servers. In the cloud setup, only cloud servers are considered, whereas the cloud-fog approach includes both cloud and fog servers. The source end devices are not considered as computational resources since the aim of this work is to evaluate the incorporation of the fog layer to the existing cloud paradigm. Next, the mathematical formulas are defined for makespan, cost and energy consumption, and finally the presentation of the weighted sum based objective function.

1) Makespan: The makespan MS is calculated as follows:

$$MS = max\{FT_{t_i}, t_i \in T\} - min\{ST_{t_i}, t_i \in T\} \quad (3)$$

where ST_{t_i} and FT_{t_i} are the starting time and finishing times respectively for task t_i in a workflow.

2) Cost: The computation cost and communication cost are considered in this work. The computational cost [10] when using computing resource r is

$$CE_i^r = pr * (FT_{t_i} - ST_{t_i}), \quad (4)$$

where pr is the unit processing cost. The communication cost for a particular task refers to the cost of sending a task output of size d_{ij} from the resource processing task i to the resource allocated to process task j.

$$CC_{ij} = trc_{ij} * d_{ij}, \quad (5)$$

Therefore, the total cost TC is

$$TC = \sum_{i=1}^{n}\sum_{j=1}^{n} CC_{ij} + \sum_{r=1}^{m}\sum_{i=1}^{n} CE_i^r. \quad (6)$$

3) Energy Consumption: The energy consumption model [16] is constructed using active E_{active}, that is energy consumed when a task is being executed, and idle E_{idle}, the energy used when a resource is idling. The active energy is calculated by using

$$E_{active} = \sum_{i=1}^{n} \alpha f_i v_i^2 (FT_{t_i} - ST_{t_i}), \quad (7)$$

where α is a constant; f_i and v_i are the frequency and voltage for the resource on which task i is being executed. The energy consumed during the idle period [16], [12] is determined by using

$$E_{idle} = \sum_{j=1}^{m} \sum_{idle_{jk} \in IDLE_{jk}} \alpha f_{min\ i} v_{min\ i}^2 L_{jk}, \quad (8)$$

where $IDLE_{jk}$ is a set of idling slots on resource j, $f_{min\ i}$ and $v_{min\ i}$ refer to the frequency and lowest supply voltage on resource j respectively; L_{jk} is the duration of idling time for $idle_{jk}$. The total energy TE consumed for the execution of the entire workflow is

$$TE = E_{active} + E_{idle}. \quad (9)$$

Therefore, using the three aforementioned objectives, the weighted sum objective function is defined by:

$$F(M) = w_1 * MS_{norm} + w_2 * TC_{norm} + w_3 * TE_{norm}, \quad (10)$$

where M is the assignment of the n tasks of a workflow to the m available computing resources. MS_{norm}, TC_{norm} and TE_{norm} are the normalized makespan, total cost and total energy respectively; w_1, w_2 and w_3 are the coefficient weights. Equal weighted coefficients are used here to obtain a balanced contribution of the three objectives since all are equally important in a good solution. Normalization is used here to eliminate any biases in the objective function and is described in our previous paper [12].

IV. The PSO Optimization Process for Workflow Scheduling

This section firstly describes the encoding of the particle for PSO and how this mapping is used to generate a task-resource schedule. The second part describes the PSO optimization process.

A. Description of the Particle for PSO

The workflows used in this work can be scheduled for execution at the fog server or at the cloud server. Each computational resource has its own computational capacity, power and bandwidth.

Since the scheduling of workflow tasks in a computing environment is a discrete problem, we use natural numbers to encode the individuals for the PSO algorithm. The individuals of the PSO are represented by the particles that are mappings of task-resource schedules. The dimension or length of each particle is n which is the total number of tasks in the workflow. Each position in the particle is a positive integer representing the task number. The value assigned to this position is the server ID that is allocated to execute the task. The ID numbers are selected from the servers available on the respective architecture tier. Suppose a workflow has 10 tasks which are scheduled for execution on 5 available servers. In this instance, the particle's length is 10 and each element is an integer between 1 and 5. An example task assignment of this particle can be expressed as {3,3,2,4,5,3,2,1,5,1}. This particle's possible schedule for the cloud and cloud-fog environments are illustrated in Table I and Table II.

Algorithm 1 illustrates the PSO optimization process. Parameters N and G denote the number of particles and the number of generations respectively. while the other parameters have already been defined in Section II. The algorithm starts with the initialization of N, c_1, c_2, ω, and G. It then proceeds by creating N particles, each of which is evaluated by running the respective workflow scheduling on the Fogworkflowsim [13] toolkit. The fitness function value is evaluated and the personal best and the global best values are determined. After that the algorithms goes into iterative process for G generations. It updates the global best and the personal best values whenever it gets better values.

TABLE I
Example of the Task-Resource Allocation using only the Cloud Layer

Layer	Cloud	Cloud	Cloud	Cloud	Cloud
Server ID	1	2	3	4	5
Assigned Task	8,10	3,7	1,2,6	4	5,9

TABLE II
Example of the Task-Resource Allocation on the Cloud and Fog Layers

Layer	Fog	Fog	Cloud	Cloud	Cloud
Server ID	1	2	3	4	5
Assigned Task	8,10	3,7	1,2,6	4	5,9

Algorithm 1: Particle Swarm Optimization (PSO) Algorithm

Input: N, c_1, c_2, ω, and G;
Output: $gBest$ and $F(gBest)$;
Randomly generate N particles;
$F(gBest) \leftarrow 0$;
for $i \leftarrow 1, N$ **do**
    Invoke the Fogworkflowsim workflow scheduler.;
    Compute the fitness function value, $F(x_i)$, for particle i, by using the Weighted Sum Objective Function from Section III (B) ;
    $pBest_i \leftarrow x_i$;
    $F(pBest_i) \leftarrow F(x_i)$;
    if $F(x_i) > F(gBest)$ **then**
        $gBest \leftarrow x_i$;
        $F(gBest) \leftarrow F(x_i)$;
$t \leftarrow 0$;
while $t \leq G$ **do**
    for $k \leftarrow 1, N$ **do**
        (1) Update v_k and x_k by using Eq. 1 and Eq. 2;
        (2) Invoke the Fogworkflowsim workflow scheduler. ;
        (3) Compute the fitness function value, $F(x_k)$, by using the Weighted Sum Objective Function from Section III (B);
        if $F(x_k) > F(pBest_k)$ **then**
            $pBest_k \leftarrow x_k$;
            $F(pBest_k) \leftarrow F(x_k)$;
        if $F(x_k) > F(g^b)$ **then**
            $gBest \leftarrow x_k$;
            $F(gBest) \leftarrow F(x_k)$;
    $t \leftarrow t + 1$;

V. Performance Evaluation

In this section, the workflow models are presented along with the simulation setup on the FogWorkflowSim tool [13], and finally, a discussion on the simulation results.

A. Workflow Models

This work uses two well-known scientific workflows that have been studied extensively in research, namely Montage and CyberShake [17]. The graphical representation of the workflows are shown in Fig. 1. The Montage workflow, created by NASA/IPAC, represents an astronomy application that combines multiple input images to create custom mosaics of the sky. It has a more sequential structure with a pipeline of tasks, while CyberShake requires more parallel processing of tasks for characterizing earthquake hazards threatening a region. Together, these workflows are composed of a variety of structures that provide a good basis for performance evaluations.

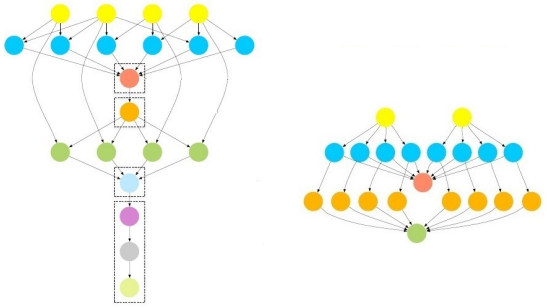

(a) Montage (b) CyberShake

Fig. 1. Scientific workflows [17]

B. Simulation Environment

The simulations are done using the FogWorkflowSim simulator. The simulator is executed using the Eclipse Java IDE on a computer with 64-bit Windows 10 operating system, Intel(R) Core(TM) i5- 5200U CPU @ 2.20GHz and 16 GB RAM. The population size of PSO is set to 50. The PSO learning factors C1 = C2 = 2. The inertia weight is 1. The number of iterations is 100. The weighted coefficients w_1, w_2 and w_3 are equal. The two scientific workflows with 500 tasks each are used as input where the workflow is a DAG XML file representation of the workflow generated by Pegasus [18]. The simulations are performed 10 times for each workflow and environment setup. The number of cloud servers and fog servers are 10 and 6, respectively. The characteristics of each server on the two tiers along with the parameter settings for the simulation environment are shown in Table III.

TABLE III
PARAMETER SETTINGS OF SIMULATION ENVIRONMENT

Parameters	Fog Server	Cloud Server
Processing rate (MIPS)	1000	2000
Task execution cost ($)	0.48	0.96
Communication cost ($)	0.01	0.02
Working power (mW)	700	1700
Idle power (mW)	200	1200
Uplink bandwidth (Mbps)	500	300
Downlink bandwidth (Mbps)	800	500

C. Simulation Results

In Figs. 2-4, the results for makespan, cost and energy consumption for the Montage workflow for 500 tasks are illustrated. The makespan is lower for the cloud-fog environment, as expected, due to the 6 additional fog servers used in the simulation. The cost metric is significantly better in the cloud-fog layers. This is likely due to the reduced processing and data transfer costs associated with the fog layer. The energy consumption is also reduced in cloud-fog as the larger size of the cloud requires more energy to remain online, and utilizing the fog with the cloud enables more efficient and distributed processing of the workflow tasks.

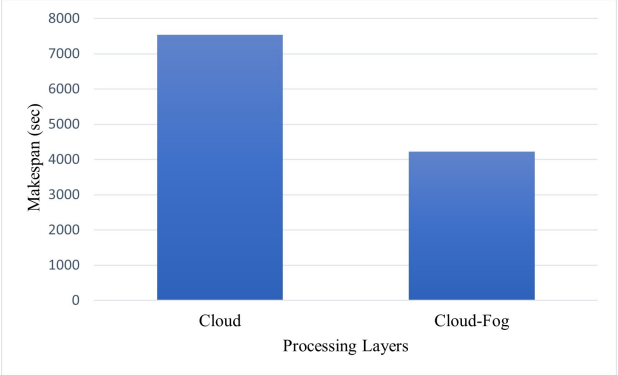

Fig. 2. Makespan for Montage

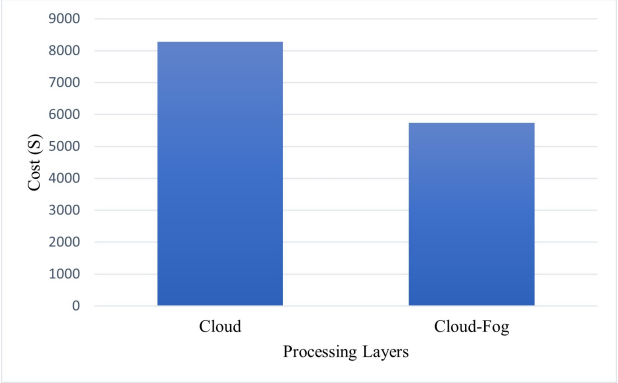

Fig. 3. Cost for Montage

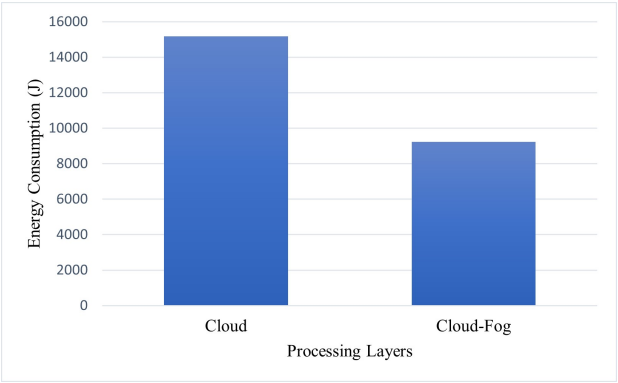

Fig. 4. Energy consumption for Montage

In Figs. 5-7, the results for makespan, cost and energy consumption for the CyberShake workflow for 500 tasks are illustrated. The performance metric comparative results for the cloud and cloud-fog are similar to what was observed

for the Montage workflow, however, the metric values are significantly higher. This is because the CyberShake workflow task sizes and task runtimes are much higher compared to Montage.

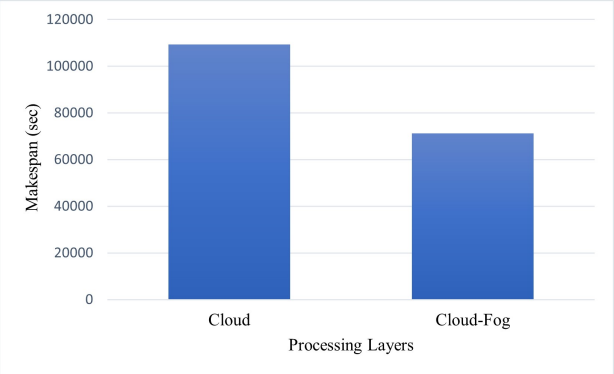

Fig. 5. Makespan for CyberShake

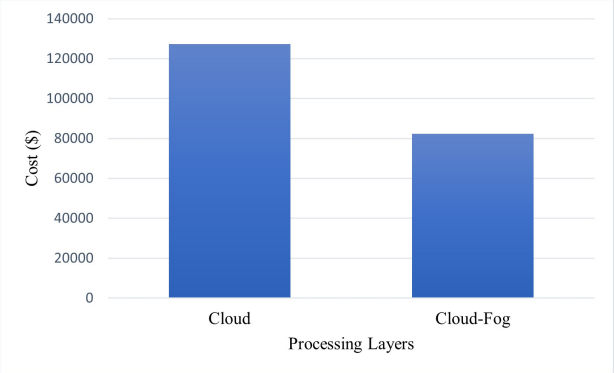

Fig. 6. Cost for CyberShake

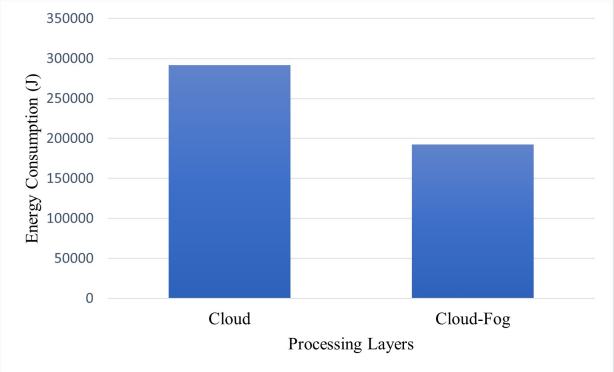

Fig. 7. Energy consumption for CyberShake

VI. Conclusion and Future Work

This paper has presented a comparative evaluation of workflow scheduling in cloud and cloud-fog environments using the classical PSO algorithm on the FogWorkflowSim simulator. A weighted sum objective function made up of makespan, cost and energy is described for workflow scheduling. Results show that the cloud-fog environment performed better than the cloud especially in terms of overall cost and energy consumption. Therefore, the incorporation of the fog layer for the execution of workflows has the potential to improve processing efficiency justifying the benefits of the emerging cloud-fog computing paradigm.

In future, the number of tasks in each of the workflows will be increased. Other types of workflows such as Epigenomics, LIGO and SIPHT will be evaluated. The number of fog servers, optimization objectives will be increased, and deadline and budget constraints will be incorporated.

References

[1] R. Buyya, S. Pandey, and C. Vecchiola, "Cloudbus toolkit for marketoriented cloud computing," *Proceedings of the 1st International Conference on Cloud Computing*, vol. 5931, pp. 24–44, 2009.

[2] W. Song, F. Chen, H.-A. Jacobsen, X. Xia, C. Ye, and X. Ma, "Scientific workflow mining in clouds," *IEEE Transactions on Parallel and Distributed Systems*, vol. 28, no. 10, pp. 2979–2992, 2017.

[3] Y. Zhao, Y. Li, I. Raicu, S. Lu, C. Lin, Y. Zhang, W. Tian, and R. Xue, "A service framework for scientific workflow management in the cloud," *IEEE Transactions on Services Computing*, vol. 8, no. 6, pp. 930–944, 2014.

[4] M. A. Rodriguez and R. Buyya, "A taxonomy and survey on scheduling algorithms for scientific workflows in iaas cloud computing environments," *IEEE Transactions on Parallel and Distributed Systems*, vol. 28(10), p. e4041, 2017.

[5] A. Verma and S. Kaushal, "A hybrid multi-objective particle swarm optimization for scientific workflow scheduling," *Parallel Computing*, vol. 62, pp. 1–19, 2017.

[6] A. Singh *et al.*, "A multi-objective workflow scheduling algorithm for cloud environment," in *2018 3rd International Conference On Internet of Things: Smart Innovation and Usages (IoT-SIU)*. IEEE, 2018, pp. 1–6.

[7] A. M. Manasrah and H. Ba Ali, "Workflow scheduling using hybrid ga-pso algorithm in cloud computing," *Wireless Communications and Mobile Computing*, vol. 2018, 2018.

[8] M. Farid, R. Latip, M. Hussin, and N. A. W. Abdul Hamid, "A survey on qos requirements based on particle swarm optimization scheduling techniques for workflow scheduling in cloud computing," *Symmetry*, vol. 12, no. 4, p. 551, 2020.

[9] M. Masdari, F. Salehi, M. Jalali, and M. Bidaki, "A survey of pso-based scheduling algorithms in cloud computing," *Journal of Network and Systems Management*, vol. 25, no. 1, pp. 122–158, 2017.

[10] Y. Xie, Y. Zhu, Y. Wang, Y. Cheng, R. Xu, A. S. Sani, D. Yuan, and Y. Yang, "A novel directional and non-local-convergent particle swarm optimization based workflow scheduling in cloud–edge environment," *Future Generation Computer Systems*, vol. 97, pp. 361–378, 2019.

[11] V. De Maio and D. Kimovski, "Multi-objective scheduling of extreme data scientific workflows in fog," *Future Generation Computer Systems*, vol. 106, pp. 171–184, 2020.

[12] D. Subramoney and C. N. Nyirenda, "A comparative evaluation of population-based optimization algorithms for workflow scheduling in cloud-fog environments," in *2020 IEEE Symposium Series on Computational Intelligence (SSCI)*. IEEE, 2020, pp. 760–767.

[13] X. Liu, L. Fan, J. Xu, X. Li, L. Gong, J. Grundy, and Y. Yang, "Fogworkflowsim: An automated simulation toolkit for workflow performance evaluation in fog computing," in *2019 34th IEEE/ACM International Conference on Automated Software Engineering (ASE)*. IEEE, 2019, pp. 1114–1117.

[14] W. Chen and E. Deelman, "Workflowsim: A toolkit for simulating scientific workflows in distributed environments," *8th IEEE International Conference on E-science*, pp. 1–8, 2012.

[15] J. Kennedy and R. Eberhart, "Particle swarm optimization in: Neural networks," in *Proceedings IEEE International Conference on 1995*, 1942, pp. 1942–1948.

[16] S. Yassa, R. Chelouah, H. Kadima, and B. Granado, "Multi-objective approach for energy-aware workflow scheduling in cloud computing environments," *The Scientific World Journal*, vol. 2013, 2013.

[17] S. Bharathi, A. Chervenak, E. Deelman, G. Mehta, M.-H. Su, and K. Vahi, "Characterization of scientific workflows," in *2008 third workshop on workflows in support of large-scale science*. IEEE, 2008, pp. 1–10.

[18] The Pegasus website, [Online]. Available: https://pegasus.isi.edu/. [Accessed 22 May 2021].

Clement N. Nyirenda received his PhD in Computational Intelligence from Tokyo Institute of Technology in 2011. His research interests are in Computational Intelligence paradigms such as Fuzzy Logic, Swarm Intelligence, and Artificial Intelligence and their applications in Communications.

Dineshan Subramoney received his Bachelors Degree (Honors) in Computer Science from the University of KwaZulu-Natal. He is currently working on his MSc in Computer Science at the University of the Western Cape. His research interest is in Workflow Scheduling using Population-based Algorithms such as Particle Swarm Optimization.

An Enhanced Data Analysis Framework

Luntha Kazembe*, Karen Bradshaw†
*Department of Computer Science, Rhodes University, Grahamstown 6140
[1]g19k4482@campus.ru.ac.za
[2]k.bradshaw@ru.ac.za

***Abstract*—This study seeks to improve the data analysis process for small business and individuals with limited resources by developing an easy-to-use data analysis framework that allows users to carry out data analysis effectively and efficiently with only basic understanding of the data analysis process. The framework was developed to analyse various alpha-numeric data formats by using a variety of statistical and mathematical techniques. As a proof of concept, an enhanced data analysis framework is created and subsequently tested using a typical analysis scenario on network packet data. Results of this testing show that typical network management decision-making requirements can be satisfied using the framework.**

In addition to supporting the general data analysis process, the framework is enhanced by two additional features to facilitate the process, particularly when analysing large volumes of data or carrying out repetitive processes. The two additional components are a modeller that is used to develop data analysis models and an iterator used to execute repetitive processes.

Further tests carried out on a large dataset show that analysis tasks can be run without needing specific data analysis skills. A further benefit is time saving in that the analyst no longer needs to be present during the execution as the enhanced framework can be used in a non-interactive mode.

***Index Terms*—Network Data Analysis, Network Management**

I. Introduction

Data is valuable as it can be processed to gain information about an object such as a person, organisation, or environment, for example. Data analysis is the process by which data is organized, for use in tasks that help to explain the past and predict the future [1]. A typical data analysis process includes the following processes: data collection, data preparation, data analysis and data visualisation. With big data now the norm for many organizations, data analytics plays a critical role in how the data is effectively leveraged to add value in various organizations and environments. Data analytics is the discovery, interpretation, and communication of meaningful patterns in data and involves a combination of computer tools (software and hardware), techniques and the data analysis process, which is an efficient and effective way of deducing information from data [2].

Two of the challenges when performing data analysis and analytics are that firstly, there are significant resources required, such as computing capacity and secondly, some level of specialised knowledge and skill is needed to use the tools and because of the dynamic nature of data requirements, there is no one approach to carrying out tasks [3], [4]. Thus, this research seeks to address these challenges by offering a simple solution for carrying out data analysis effectively and efficiently with only a basic understanding of the data analysis process and basic computing resources.

In this study, a proof-of-concept data analysis framework is developed that supports the traditional data analysis process but with the addition of two enhancements, specifically aimed at handling large volumes of data and carrying out repetitive processes. The research further explorers to what extent this framework can support generic data and so what level of automation can be carried out using open-source tools. Validation of the developed framework (both with and without using the enhanced features) is carried out using network packet data. The prototype framework does not support artificial intelligence (AI) nor machine learning (ML), methods as this study initially is concerned to address the two challenges stated earlier as a foundation. Additional techniques are envisaged as future work.

Network data can be collected from different sources depending on how a computer network is configured. Computer networking devices such as routers, switches, servers and firewalls are normally used for network data collection since network traffic travels through these devices before reaching a recipient. Networking devices store details of the traffic that passes through and this is the data that are normally analysed, although in some instances such as network security related, the actual data can also be examined [5].

The rest of this paper includes the following sections: a discussion of related work (Section II), the design (Section III) and implementation (Section IV) of the data analysis framework, some results (Section VI), and finally conclusions and suggestions for future work (Section VII).

II. Related Work

Data analytics is widely used to generally add value to business processes through identification and implementation of efficient and effective business process innovation and solutions by various entities and organizations, for example, organizations are able to develop new or improved products/services [4]. With various technology adoptions (different applications of computer technology to business processes) across industries and advances such as the internet of things, data is considered a key asset [6], [7]. Best data management practices are thus important to handling data and the data analysis process is the foundation for processing data. One of the greatest challenges organizations face is that, obtaining information from data often requires the execution of large-scale data analysis involving the execution of large number

of processes, primarily as a result of the ever increasing generation of data across multiple industries [8], [9].

A significant amount of related work has been done. A more general approach taken in the Automatic Statistician project aims to automate data science, producing predictions and human-readable reports from raw datasets with minimal human intervention by automating the construction of models for the dataset, a comparison of these models, and a software component that turns these results into natural language descriptions [9]. An exploratory case study undertaken by [10] explains the flexible and reprogrammable nature of big data analytics (BDA) technologies. Another approach by [13] in network analysis for malware information and defence. Features that are commonly used to improve more complex analysis include ML and AI, however, they the require capable computing resources, examples that these have been applied in include; extreme condition traffic forecasting [11] and next-generation wireless networks [12]. The validation testing of the proposed framework is based on some of the analyses used in these related works.

III. Methodology and Design of the Framework

To satisfy the objective of the study, a quasi-experimental approach was used for an iterative process of code implementation and framework refinement, followed by repeated experimentation to find patterns and anomalies within the dataset. Thus, a basic/generic data analysis software framework that supports the traditional data analysis process was implemented (with four main components of the data analysis process, data collection, data transformation/preparation, data analysis and data visualisation/presentation), and later refined to include two enhancements, a modeller and an iterator.

The modeller has two main components, a record and playback feature that allows recording (modelling) of data analysis steps taken for a specific analysis process and then rerun that process by using the recorded steps as input on a bigger or different dataset. The iterator facilitates the execution of repetitive tasks by the framework in a non-interactive mode by allowing the user to specify variables and conditions that specify how and which of the analysis tasks should be repeated.

These enhancements aim to provide scaling of data analysis tasks in an efficient way by limiting the interaction of the user in the process and using computing resources efficiently.

A. Design Considerations

The design of the system included some considerations that would improve the framework's scalability and resource utilization, namely, multiprocessing and multithreading. The framework needed to run in an efficient manner, taking advantage of available hardware resources by carrying out some processes in parallel wherever possible to enhance the data analytics process further.

Multiprocessing uses at a minimum two different central processing units (CPU) to run at least two processes at a time. Multiprocessing initiates multiple operating system processes for each separate process/task to allow them to run in parallel by separate processor cores [16]. For the framework, multi-processing was designed to run two or more data analytics processes at a time, one process in interactive mode and a number of processes in non-interactive mode (subject to hardware resources availability) because the processes would be independent (i.e. the data analysis processes would be separate).

With multithreading, multiple processing cores work on shared input data, threads work on different parts of a process with input/output (IO) bound processes [16]. Threading was designed into the system, created an effect of inter-living of tasks as is the case during data collection, once data has been stored in computer memory and is then being copied to the system database, data analytics operations can be carried out on the data by the user; for example, after the system copies data from source, the user will be asked to provide project, database and table names, after which the main menu will be displayed in order to process the data further using transformation, analysis and presentation components of the data analytics framework. When the copying of data to the database is completed, the user will be notified and can access that data at any time. Meanwhile a user will always process the data in memory, an option to save it to the database will be available (saving of data is designed to use multithreading) at the menus of all three components in order to maintain data integrity and to make it easy to roll-back if mistakes have been made. As the processed data for a project is saved using the same database provided earlier in the process, the user needs to note the table names used.

B. Implementation Considerations

Tool selection was based on several desired characteristics as determined by the researcher, such as, ease of use, the open-source nature and functional capabilities of the tools for data processing. The system was implemented using the Python[1] programming language with a MySQL database as the system's internal database.

Python was chosen because it offered flexibility and scalability on data handling especially with the power of the Pandas[2] library and the open-source nature of it was preferred as opposed to commercial tools to prevent limitations of functions that would go against the dynamic nature of data analytics.

The Pandas library was used to implement all data processes, as it provides an efficient dataframe for handling data, large or small. Other Python libraries such as NumPy[3] and SciPy[4] were used for data analysis functions, while Matplotlib[5] was used for data presentation. SQLAlchemy[6], a Python library, was used for handling interaction between the system and the Database Management System, MySQL (using

[1] https://www.python.org/
[2] https://pandas.pydata.org/
[3] https://numpy.org/
[4] https://www.scipy.org/
[5] https://matplotlib.org/
[6] https://www.sqlalchemy.org/

MariaDB[7] 10.4.6), SQLAlchemy interfaced with Python using MySQL.Connector[8], a Python library.

MairaDB is an enhanced, drop-in replacement for MySQL developed by the original developers of MySQL and guaranteed to stay open-source. It is fast, scalable and robust, with a rich ecosystem of storage engines, plug-ins and many other tools that make it very versatile for a wide variety of use cases. The framework utilizes the database system for storing data. For data collection from sources, the framework is able to interact with two types of sources, flat files such as Comma Separated Values (CSV), Microsoft excel files, text files etc. and Database Management Systems of which there are four types, namely, MySQL, Microsoft SQL, Oracle and PostgreSQL. The system can provide output (i.e. processed data) to either a database or CSV files or PDF files.

As execution infrastructure, the system requires minimum specifications as given in Table I.

TABLE I
MINIMUM SYSTEM SPECIFICATIONS

Operating System	Windows/Linux/MacOS with Python3
Python Modules	Pandas, SQLAlchemy, MySQL.Connector, Matplotlib, Scipy, Numpy, pdfkit
Database Management System	MySQL
Storage	1GB of free space on Hard Disk Drive (otherwise dependant on size of data being analysed)
Main Memory - RAM	8GB
Processor	Duo Core with 1.9GHz

C. Dataset for Validation

A network packet capture (PCAP) dataset was used for the framework validation. It contained 28,950,695 Internet Protocol (IP) address records with the following attributes: Time (for Time-stamp), SourceIP (Source IP Address), DestIP (Destination IP Address), TTL (for Time To Live), PakcetSize, Protocol, SPort (Source Port) and DestPort (Destination IP).

The PCAP dataset was chosen for this study because it provided records for a real world network data analytics environment and is free to use. Most functionality was tested, however, due to space limitations, not all content was made available in this paper. Each component of the framework adds value to the data analysis process, while log data and financial data have been used to validate the framework's generic application.

IV. FUNCTIONALITY OF THE GENERIC DATA ANALYSIS FRAMEWORK

Implementation of the proposed framework was done in two stages. First, a generic data analysis framework was developed and testing using a PCAP dataset with alphanumeric data formats and an analysis scenario. Thereafter, the two enhanced features, namely the modeller and iterator, were implemented and tested on large scale data. This section discusses the first phase implementation.

The generic framework supports the typical data analysis process that includes data collection, data preparation, data analysis and data visualisation. These stages are discussed below, with the exception of the data collection component as this merely involves retrieving data from a database or file and as such is not discussed in any more detail.

A. Data Preparation

Data preparation involves three processes, namely extraction, transformation and loading [7].

- Extraction copies data from the data source to a data store from where the next process can access it. In-situ or streamed data is captured into a temporary data store, where it is scanned to determine frequencies, size and formats, this is referred to as preprocessing. The data may be compressed to improve efficiency in the processes to come [17].
- In the transformation stage, the data is moved, cleaned, split, translated, merged, sorted and validated, then stored in a preparation data store. This is aimed at improving quality of analysis.
- The loading process deals with loading the data into another data store where analysis will occur for data exploration, where statistical methods are applied to the data. Data in the preparation data store can be replicated between data stores to allow for further analysis while maintaining data integrity thereby maintaining or improving quality of the results.

B. Data Analysis

The data analysis component offers statistical analysis methods that can be applied to data to retrieve values and information. Data analysis makes available statistical measures for gaining information from data. The input is data specified in the system database and is processed using statistical measures chosen for analysis to produce information as output. that can answer questions or meet set objectives. For example, adding up the number of times a particular event occurred, predicting when and how such an event can occur, measuring the relationship between two or more events in network traffic and to improve by taking appropriate action. In order to address common challenges such as scalability, data integrity, certain analysis measures might need to occur, like data sampling.

This component is split into six functional groups as stated below:

- Managing data, which provides for three options, sampling, sorting and filtering.
- Measures of central tendency, including mean, median and mode.
- Measures of dispersion, including range, variance and standard deviation.
- Measures of association, including correlation and regression.

[7]https://mariadb.org/
[8]https://pypi.org/project/mysql-connector-python/

- Other tools, such as, counting values, summary statistics, comparing columns and basic math operations such as addition, subtraction, multiplication and division.

C. Data Visualization

The data presentation component provides visualisations, i.e. methods for presenting information that is deduced from data. Pattern discovery, reporting and general awareness of the state of data is thus presented visually with this component. Data presentation component is used to represent information and data in readable forms using various tools such as charts and tables.

Analysed data can be presented using various methods that enhance the information deduced. Data being analysed can aid in identifying what visualisations to use [18] as most visualisations require specific properties from the data for the visualizations to be effective, for example, line charts are useful when showing changes over time, bar charts illustrate categorical data better, maps represent data based on a certain location or feature [18]. Experimenting with different visualizations can also help in identification of patterns and trends not previously thought of since there is no general approach that addresses all types of scenarios.

For this function, the input is data from the system database and visualisation options that are desired and visualisations are the output, the visualizations available are listed below:

- Charts include scatter plot, line graph, bar graph, pie chart, horizontal bar graph, histogram, density estimation plot and table view.
- Reports provide the capability of customised reporting saved as either PDF or CSV files.

V. Data Analysis Enhancements for the Framework

The second part of the implementation was to develop two enhancements to the framework: namely, record (also known as the modeller) and playback (also known as the iterator) features aimed at enhancing the data analytics process by improving usability, scalability and resource utilization. These characteristics were designed in the framework to add value to the way the framework executes. With regard to usability, the record and playback features should be able to make the data analysis process easier to use by among other things, minimizing user interaction and wherever there is interaction, it should be short and clear. Some degree of automation was identified to enhance the generic application of the framework by enabling a user to record steps for any data analytics process, from start to finish and then run that recorded input using the playback feature to repeat that process on a bigger dataset which would take more time and resources, thus improving the scalability. Another optional enhancement available is to be able to run a data analytics process repeatedly on different attributes of the data, for example, using different time periods. The record and playback feature was designed to be able to utilize computer resources effectively through multiprocessing and interleaving of tasks discussed in Section III-A to improve scalability and resource utilization.

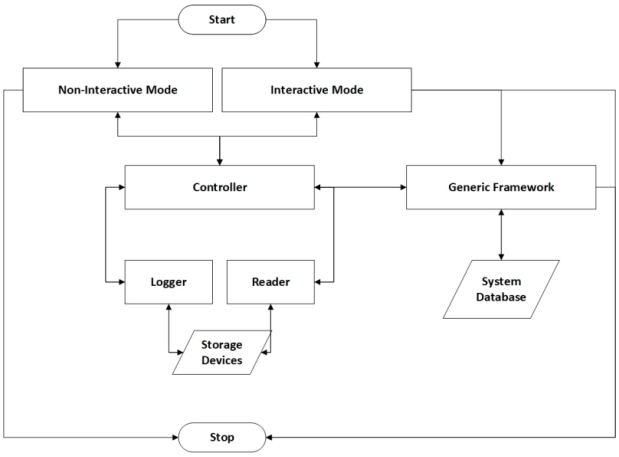

Fig. 1. High-Level System Design - The Record and Playback Feature

The record and playback feature was designed to include three main functions: a controller function, a logger function and a reader function, Figure 1. These functions are accessed by a user through one of two containers, namely interactive mode and non-interactive mode. Interactive mode is the default mode where the user interacts with the system step-by-step. In this mode the user can choose to use the system in the most basic form by just using the generic framework, or alternatively to use what is called the recording function, where by a log file is created that records the steps and input the user takes to carry out data analysis (recording occurs as the user carries out a data analysis process). The other mode is the non-interactive mode, which is used to run a data analysis process that has been recorded in a log file with user input on a full/larger dataset or on a data analysis process that is run repeatedly. In this mode the function uses multiprocessing wherever applicable while letting the user work in the interactive mode on other data analysis processes by going through the steps and input in a specified log file with the recorded user input. Thus an ideal approach would be a user choosing a sequence of analysis tasks, recording the steps while working on a small sample dataset, reviewing the log file to refine the data analysis process and finally running the recorded steps with the framework in non-interactive mode for data analysis of the full dataset.

A. Logger Function

One of the functions in the record and playback feature is the logger, which is responsible for the first of two main tasks in this feature, the recording.

This function requires pre-formatted data as input and produces a log file as output. The logger function records user input throughout a data analysis process. This function is available in the interactive mode. Logging is used to capture all user input and corresponding functions accessed, it carries out its processes in the background, recording input into a log file for use by the reader function (see below). Each log

record has the following format: date and time, user input, input format and function ID as shown in Fig 2.

```
Date_and_Time, Millisecond, Input, Format, Function_ID
2020-10-11 08:48:20,622, 1, <class 'int'>, DC1
2020-10-11 08:48:28,340, 1, <class 'int'>, DC2
2020-10-11 08:48:31,551, data/sample_net.csv, <class 'str'>, DC3
2020-10-11 08:48:38,663, 1, <class 'int'>, TRF1
2020-10-11 08:48:40,112, 4, <class 'int'>, TRF3
2020-10-11 08:48:49,212, Flow-Rate, <class 'str'>, TRF4
2020-10-11 08:48:54,058, 3, <class 'int'>, DP1
2020-10-11 08:48:58,455, 2, <class 'int'>, DP2
2020-10-11 08:49:12,322, Time, <class 'int'>, DP2
2020-10-11 08:49:21,172, Flow-Rate, <class 'int'>, DP2
```

Fig. 2. Sample Log

B. Reader Function

The second of the functions in the record and playback feature is the reader, which is responsible for the playback. This function plays back input to the framework when carrying out a data analytics process in the non-interactive mode.

The reader function reads a log file comprising user input (compiled by the logger function) to execute analysis tasks on a specified dataset. This function is accessed in the non-interactive mode and the only input required is the path of the input file. Each log record is executed using the input and function records and the processed data is then stored as various files and database tables depending on user choices. This function uses a function map module designed to call the respective modules/functions in the framework.

C. Controller Function

This is the main function that manages the logger and reader functions by interfacing the framework operations with the record and playback features. The interactive and non-interactive modes call this function and it is this function that manages what is passed to the logger function to be logged and what is read from the reader function to be fed the framework. During the recording of a data analytics process, as the user captures input, the logger captures it as well. Similarly, when using the non-interactive mode as the log file is being read as input, each input is passed to the framework at a time and in sync with processes happening in the framework.

D. The Modeller

The modeller works by creating a log file and adds a header (Timestamp, Input, Input Format and FunctionID) to the log file, this then initializes the logger function to log all steps the user takes in the data analysis process. At the end of the process the user can then review the steps and make changes if and where necessary.

E. The Iterator

The iterator works by executing the steps in a log file created by the modeller. In specific instances where a process needs to be repeated, using the interactive mode, there is an option for iteration. With this option a user goes through the step to be repeated while the logger logs the steps and then at the end the user specifies the condition that needs to hold during the iteration of the recorded step. Thus, this specific action can be enabled when modelling.

F. Scenario Design

The scenario is based on general network information that can be sought from a PCAP type of data. The scenario was divided into two parts, the first part to carry out an analysis of frequent source and destination IP addresses accessing the network with total packet size using one processor the second part carried out the same analysis using multiprocessing. Each of the parts requires a different approach to data analysis and thus determines what techniques and features are ideal for the analysis that can be utilized from the framework.

The data used for this study had 8 attributes, namely, time-stamp, source IP address, destination IP address, time to live, packet size, protocol, source port and destination IP. The data had 28,950,695 records recorded from 3rd December 2019 to 31st December 2019 (29 days). The data analysis made use of four attributes, time-stamp, source IP address, destination IP address and packet size to come up with information about frequent source and destination IP address for different time periods

VI. Results

The results were obtained by running each of the two parts of the scenario with and without enhancements while recording the time taken for execution.

Figure 3(a) shows top 10 frequent source IP addresses with total packet sizes for the whole duration the data represents and Figure 3(b) shows the top 10 frequent destination IP addresses with total packet size for the same period. When enhancements are applied by modelling this data analysis, users would save time in running such an analysis. When enhancements were included in the running, results showed a 53.70% saving in time spent carrying out the analysis. For a general analysis like this the enhancements might not be necessary if the analysis is not frequently required/run, for example, the time range in this analysis might be considered broad as such a drill down would be carried out.

A similar analysis process was carried out to produce Figure 3 by increasing the number of days in each run, i.e. repeating the the analysis steps for one to two days,three day, four days and so on. The repetitive tasks were that of collecting, processing and visualising of the data. The larger the number of repetitions the more the time savings would be realised, in this case it was an average of 9 seconds. In the case where the two parts are run simultaneously the savings are improved to 72.22%.

SourceIP	Count	Total Packet Size
185.156.73.45	726,281	29,051,240
185.175.93.101	639,523	25,580,920
45.141.86.154	400,032	16,001,280
45.141.84.40	369,700	14,788,000
45.141.86.146	318,586	12,743,440
185.40.4.46	316,429	12,657,160
45.141.86.156	304,951	12,198,040
45.141.86.149	298,251	11,930,040
146.88.240.4	244,213	16,186,297
91.217.254.37	197,049	7,881,960

(a) Top10 Source IP Addresses

DestIP	Count	Total Packet Size
192.192.192.1	171,027	8,602,209
192.192.192.251	139,660	22,540,705
192.192.192.153	136,505	7,938,713
192.192.192.245	136,418	20,405,221
192.192.192.114	129,677	7,548,492
192.192.192.130	129,523	7,619,365
192.192.192.227	128,781	7,514,023
192.192.192.40	127,584	7,464,945
192.192.192.172	125,127	7,416,474
192.192.192.33	124,371	7,332,359

(b) Top10 Destination IP Addresses

Fig. 3. Top 10 IP Address - Inbound and Outbound

In the second instance there would be more information gained from drilling down into more detail. For example, trend analysis could be done for each specific day, this could potentially lead to improved ways of managing a network.

VII. Conclusion

The results suggest that data analysts have the potential of saving 50% of the time spent processing repetitive processes through modelling and automating the running of the models. When two different repetitive processes are run concurrently the saving is about 70% of the time, assuming the hardware resources are adequate. If more than two processes are run the potential is slightly higher considering the resources. However, in an ideal situation, the improved time savings would be limited by the ability of the CPU can manage the concurrency. The time savings simply allow for one to make more use of it by doing more in a time period.

Acknowledgement

This work was undertaken in the Distributed Multimedia CoE at Rhodes University, with financial support from Telkom SA and Infinera. The authors acknowledge that opinions, findings and conclusions or recommendations expressed here are those of the author(s) and that none of the above mentioned sponsors accept liability whatsoever in this regard.

References

[1] H. Cuesta, *Practical data analysis*. Packt Publishing Ltd, 2013.
[2] H. Jean-Baptiste, M. Qiu, K. Gai, and L. Tao, "Meta meta-analytics for risk forecast using big data meta-regression in financial industry," in *2015 IEEE 2nd International Conference on Cyber Security and Cloud Computing*. IEEE, 2015, pp. 272–277.
[3] B. M. Balachandran and S. Prasad, "Challenges and benefits of deploying big data analytics in the cloud for business intelligence," *Procedia Computer Science*, vol. 112, pp. 1112–1122, 2017.
[4] Y. Duan, G. Cao, and J. S. Edwards, "Understanding the impact of business analytics on innovation," *European Journal of Operational Research*, vol. 281, no. 3, pp. 673–686, 2020.
[5] V. Joseph and B. Chapman, "Chapter 13 - performance monitoring and measurement," in *Deploying QoS for Cisco IP and Next Generation Networks*, V. Joseph and B. Chapman, Eds. Boston: Morgan Kaufmann, 2009, pp. 413 – 481.
[6] R. Elshawi, S. Sakr, D. Talia, and P. Trunfio, "Big data systems meet machine learning challenges: Towards big data science as a service," *Big Data Research*, vol. 14, pp. 1 – 11, 2018. [Online]. Available: http://www.sciencedirect.com/science/article/pii/S2214579617303957
[7] Y. Wang, L. Kung, W. Y. C. Wang, and C. G. Cegielski, "An integrated big data analytics-enabled transformation model: Application to health care," *Information & Management*, vol. 55, no. 1, pp. 64 – 79, 2018.
[8] E. Deelman, K. Vahi, G. Juve, M. Rynge, S. Callaghan, P. J. Maechling, R. Mayani, W. Chen, R. F. Da Silva, M. Livny *et al.*, "Pegasus, a workflow management system for science automation," *Future Generation Computer Systems*, vol. 46, pp. 17–35, 2015.
[9] C. Steinruecken, E. Smith, D. Janz, J. Lloyd, and Z. Ghahramani, "The automatic statistician," in *Automated Machine Learning*. Springer, Cham, 2019, pp. 161–173.
[10] C. Lehrer, A. Wieneke, J. Vom Brocke, R. Jung, and S. Seidel, "How big data analytics enables service innovation: materiality, affordance, and the individualization of service," *Journal of Management Information Systems*, vol. 35, no. 2, pp. 424–460, 2018.
[11] R. Yu, Y. Li, C. Shahabi, U. Demiryurek, and Y. Liu, "Deep learning: A generic approach for extreme condition traffic forecasting," in *Proceedings of the 2017 SIAM international Conference on Data Mining*. SIAM, 2017, pp. 777–785.
[12] M. G. Kibria, K. Nguyen, G. P. Villardi, O. Zhao, K. Ishizu, and F. Kojima, "Big data analytics, machine learning, and artificial intelligence in next-generation wireless networks," *IEEE access*, vol. 6, pp. 32 328–32 338, 2018.
[13] L. L. Rudman, "Netwioc: a framework for the automated generation of network-based iocs for malware information sharing and defence," text, Thesis, Masters, MSc, Rhodes University, Faculty of Science, Computer Science, 2018.
[14] T. Qiu, Z. Ge, D. Pei, J. Wang, and J. Xu, "What happened in my network: Mining network events from router syslogs," in *Proceedings of the 10th ACM SIGCOMM Conference on Internet Measurement*, ser. IMC '10. New York, NY, USA: ACM, 2010, pp. 472–484.
[15] W. Queiroz, M. A. Capretz, and M. Dantas, "An approach for sdn traffic monitoring based on big data techniques," *Journal of Network and Computer Applications*, vol. 131, pp. 28–39, 2019.
[16] T. Khot, "Parallelization in python," *XRDS: Crossroads, The ACM Magazine for Students*, vol. 23, no. 3, pp. 56–58, 2017.
[17] P. Paakkonen and D. Pakkala, "Reference architecture and classification of technologies, products and services for big data systems," *Big Data Research*, vol. 2, no. 4, pp. 166 – 186, 2015.
[18] J. Hoelscher and A. Mortimer, "Using tableau to visualize data and drive decision-making," *Journal of Accounting Education*, vol. 44, pp. 49–59, 2018.

Luntha Kazembe is currently studying towards his MSc at Rhodes University. His research interests include data science, information security and computational modelling.

Karen Bradshaw is an Associate Professor in the Department of Computer Science at Rhodes University. Her research interests include computational thinking, parallel processing including GPGPU and robotics.

An Analysis of False Positive Reduction in Maritime Detection In A Cluttered Environment

Nosiphiwo Nkele[1] Nyashadzashe Tamuka[2], Khulumani Sibanda,[3]

Department of Computing Sciences

University of Fort Hare, P.O Box X1314, Alice 5700

[1]201203131@ufh.ac.za

[2]201516429@ufh.ac.za

[3]ksibanda@ufh.ac.za

Abstract— **Target detection is a significant research area in computer vision with its applications in military, maritime surveillance, and defense and security. Maritime target detection during critical sea conditions produces several false positives when using the existing algorithms due to sea waves, dynamic nature of the ocean, camera motion, sea glint, sensor noise, sea spray, swell, and the presence of birds. The focus of this paper is to explore the reduction of false positives that are generated by many machine learning algorithms when used for object detection in maritime environments. Most of related studies on object detection still have challenges in addressing the problem of false positives and false negatives due to background clutter. Some researchers have already attempted to reduce the false positives by applying filters. However, filtering degrades the quality of an image leading to more false alarms during target detection. As much as radar technology has previously been the most utilized method, it still fails to detect very small objects and it may be applied in special circumstances. In this paper, visible images were retrained on a pre-trained Faster R-CNN with inception v2. The pre-trained model was retrained on five different sample data with increasing size. For the last two samples, data was duplicated to increase size. For testing purposes, 20 test images were utilized to evaluate all the models. The results showed that, deep learning method performed best in detecting maritime vessels and the increase of dataset improved detection performance and false positives were reduced. The duplication of images did not yield the best results; however, the results were promising for the first three models with increasing data.**

Keywords— **Object detection, Machine Learning, Neural Networks, Convolutional Neural networks, Computer Vision**

I. INTRODUCTION

Computer vision is a technology of machines that is intending to supply computers and machines with exceptional ability to perform. It is an interdisciplinary field that is capable of seeing, perceiving [1] and let computers to gain an extensive understanding from images and videos [2]. It is concerned with the automated extraction, understanding and the analysis of information from an image or images [2].

The application of image recognition, in a cluttered maritime environment is rapidly increasing [3] and it is significant in South African navy. Literature has revealed that ships and boats detection in the sea tends to produce a number of false positives due to factors affecting the detector [5]. False positives can be caused by sun-glint which appears like small targets [6]. The goal of this paper is to intelligently analyze and manipulate images or video frames to detect boats and ships in maritime environments.

II. RELATED WORK

Hall et al. [7] compared five adaptive background differencing techniques and the same public benchmark datasets were used by the detectors for evaluation. The compared methods were the (LOTS) Lehigh omnidirectional tracking system, the (BBS) basic background subtraction algorithm, the W4, Single Gaussian Model (SGM), an adaptable mixture of multiple Gaussians (MGM). BBS was the easiest algorithm that detected objects by computing the difference between image background for each color channel and the current frame. The LOTS algorithm was applied to grey scale images and uses two image backgrounds with two per-pixel thresholds. Each pixel was treated differently by the per-pixel threshold image to allow the robustness of the detector as to localize noise in image regions with low size The performance of the algorithms was evaluated using the same dataset for all the algorithms. The results showed that the methods LOTS and SGM bring off better results as compared to MGM that uses complex background [7]. Tong et al. analyzed image pattern matching for detecting the target and the tracking in maritime radar images [8]. Automatic Radar Plotting Aid (ARPA) was added as a tracking feature in the radar [8]. Jing and Chaojian stated that existing algorithms for moving video detection included optical flow, background subtraction and frame difference [9]. Wan et al. proposed adaptive threshold algorithm based on improved Surendra algorithm of background subtraction and a gradient update algorithm to robustness in different videos [10]. A survey on object detection and tracking methods has been done, with the goal of presenting different algorithms on object detection, object classification, and object tracking. Most researchers indicated difficulties when detecting unknown objects and objects with difference in color, shape, and texture [11]. Guo et al. examined the usefulness of employing deep learning method to suppress sea clutter and perform target detection process. Deep convolutional auto-encoders (DCAEs) were used to filter out sea clutter and Logistic regression classifier was used to carry out target detection [12]. A novel military object detection algorithm was proposed based on fusing multi-channel CNNs [13]. Cascade architecture built on convolutional neural network (CNN) was proposed for face detection [14]. To improve moving object detection Tejada and

Rodriguez proposed Principal Component Pursuit (PCP) for pre-processing and R-CNN for detection [15]. In this research CNN is proposed for ships and boats detection in a maritime environment.

III. RESEARCH METHODOLOGY

In this study, empirical research was used. Empirical research incorporates the use of experiments to uncover and clarify facts and revise theories. It can be validated or invalidated based on observations and experiments [16]. In the context of this study empirical research was utilised experimentally and empirical evidence was acquired. This research produced empirical evidence as it involved training of data and testing which generated experimental results. Firstly, the research questions were formed, and the knowledge was acquired through experimentation which were in agreement with efficiency of the model. Questions on the existing methods for detecting objects in a maritime background and the performance of these methods in terms of reducing false positives in target detection were answered through experiment. More literature about target detection was revised, furthermore, experiments were implemented to analyse the results quantitatively.

A. The design of the study

The design contains all the methods for the improvement of target detection in maritime environment. Pre-trained faster R-CNN with inception v2 [17] was trained using labeled data containing images with objects labeled as a boat or ship. The experimental design contains five stages namely: **image labeling**, **converting files from XML to CSV**, **converting CSV to TFRecords** and **training and testing**. Fig. 1 presents the implementation steps which are discussed in the following subsections

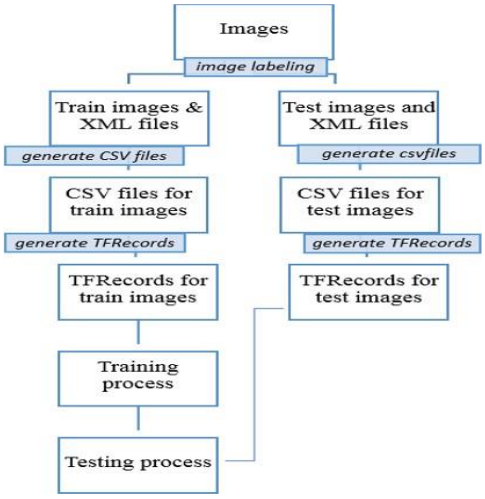

Fig. 1: *The implementation steps for this study.*

1) Dataset and image labelling

The dataset used in this research was made from included videos from Singapore maritime dataset [14] and images from maritime imagery within the visible and infrared spectrum [18]. The Singapore videos were captured using 70D cameras in Singapore waters. They were captured in the high definition (1080 x 1920). The dataset included videos which were captured by a fixed camera and a moving camera. The videos were taken during different times of the day, like in the morning, midday, afternoon, and evening [14]. The images from maritime imagery in the visible spectrum were used mostly for training in this study. Maritime environment videos were converted into frames using VLC. Video frames and images were used as initial sample for training and testing phase. The images were labeled using LablImg. During the labeling, each image was opened, and all possible ships and boats present in the image were rounded with rectbox and each image was saved. Fig. 2 shows the sample images with XML files. After the labeling all the images, each image was represented by its XML file. Each XML file consists of the name of the folder containing the image, image name, image path, image source, image size in terms of width, height and depth, and the name of all labeled objects together with their sizes.

There were 560 labeled images in the first labeling stage, 500 images were reserved for training and 60 images were reserved for testing. The first sample contained 100 labeled images, for the second training phase, the first sample was increased by 200 labelled images to make 300 labeled images, and these 300 train images were further increased by 200 to make up the third sample which contained 500 labeled images. There were challenges in proceeding with adding 200 new labelled images to the previous 500 train images, so the previous 500 train images were duplicated with 200 train images to form the fourth sample which contained 700 images and for fifth sample 500 train images which were used as third sample were duplicated with 400 train images to make 900 train images.

Fig. 2*: Sample images with XML files.*

2) Converting files from XML to CSV

The XML data was converted into CSV files which was further converted into TFRecords since tensorFlow required data in TFRecord format for training. The conversions were accomplished for each sample. CSV files for train labels and test labels were stored in a new directory. Each CSV file contains information for all labeled images. It encompassed filename, width, height, class, xminimum, yminimum, xmaximum and ymaximum. The conversion of XML files to CSV file was computed using python3.

3) Converting CSV files to TFRecords

Tesnsorflow records were generated using python3 and tensorflow. During the conversion from CSV files to TFRecords, train labels were taken as input to generate train TFRecords and test label was taken as input to generate test TFRecords. Image width, image height, filename, image source id, image format, image bounding box xminimum, image bounding box xmaximum, image bounding box minimum, image bounding box ymaximum, and image class label were considered during conversion. The train TFRecords and test TFRecords were generated as output and were put in the same folder as train and test labels.

4) Training

In this study supervised learning is utilized as a machine learning method for object detection. Faster R-CNN with inception v2, configured in MSCOCO (Microsoft Common Objects in Context) dataset was utilized to detect two object classes, boat, and ship. The faster R-CNN is widely used for detecting objects due to its high accuracy and minimum detection times [19]. Although the train sample size was small, transfer learning was adopted to improve the learning capability The training process was conducted for five sample data. sample one contained 100 train images, sample two contained 300 train images, sample three contained 500 train images, sample four contained 700 train images and sample five contained 900 train images. The TFRecords and label map were utilized as input. Each sample data was trained using the above configuration settings. A virtual environment called Detection was developed using the ubuntu 16 machine terminal. Fig. 3 shows the training process' overview.

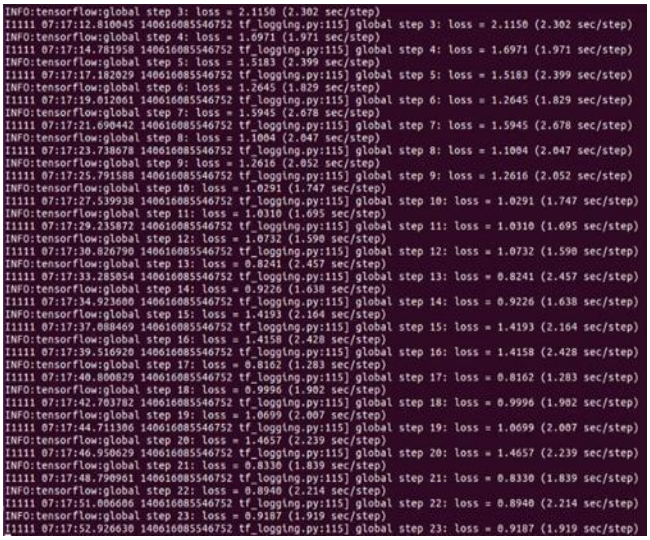

Fig. 3: *An overview of the training process.*

Fig. 3 presents the training process during the first few minutes. The training process started at global step 1 to global step 200000 on which the model has fully learned. While the training process was running, it recorded the time, global step number, the loss, and the number of seconds it took for each step to run. The training process took seven days until it reached global step 200000. Subsequently, the model was saved to disk. During and after the training phase, the performance of the training was recorded in the tensor board.

5) Testing

The saved models were tested using python3 on a Jupyter notebook. Each model was tested using the same dataset to track the performance of the models based on sample size. The test dataset contained 20 images and the output was recorded as results. The test images were excluded from the training dataset. The results were analyzed, and the information was recorded in using tables and graphs.

IV. RESULTS

The training process was conducted for five sample data. sample one contained 100 train images, sample two contained 300 train images, sample three contained 500 train images, sample four contained 700 train images and sample five contained 900 train images. TABLE 1 illustrates the detection potential of the faster R-CNN model with inception v2 using a sample of 100 images. Each image was observed to identify the number of detections, false negatives, false positives, and true positives. Image no depicts the order of images from image one to image twenty, total objects depict the number of objects present in each image, total detections portray the number of detections in each image, false positives denote false detection instances, true positives denote correct detection instances and false negative depicts the number of objects not detected. Each bounding box from each image shown in Fig. 4 represents the detection instance. The green bounding box denotes the ship instances, and the blue bounding box denotes the boat instances.

Fig. 4: *Results of the model trained with 100 images.*

TABLE 1: DETECTION POTENTIAL ON THE MODEL TRAINED WITH 100 IMAGES.

Image no	*1*	*2*	*3*	*4*	*5*	*6*	*7*	*8*	*9*	*10*	*11*	*12*	*13*	*14*	*15*	*16*	*17*	*18*	*19*	*20*
Objects	8	7	8	4	5	5	8	4	6	4	4	5	4	5	8	7	8	5	11	5
Detections	5	6	5	3	5	4	5	2	6	2	4	4	3	4	3	6	4	4	8	1
FP	1	1	3	0	0	1	1	0	1	1	1	0	1	0	0	1	1	2	1	0
TP	4	5	2	3	5	3	4	2	5	1	3	4	2	4	3	5	3	2	7	1
FN	3	2	3	1	0	1	4	2	0	2	1	1	1	1	5	2	4	1	3	4

V. EVALUATION

The detection performance of the proposed faster R-CNN was assessed in the testing phase. The test data contained 20 images with 121 objects in total. The same test data was used to test five models trained with different sample size. This study made use of binary classification method. The Confusion matrix was utilized to present the binary classification of results. The confusion matrix presented in TABLE 2 contains the possible outcomes which describe the detection performance. It depicts actual instances and predicted instances.

TABLE 2: THE CONFUSION MATRIX

	Actual positive	Actual Negative
Predicted positive	**True Positive (TP)**	**False Positive (FP)**
Predicted negative	**False Negative (FN)**	**True Negative (TN)**

- True Positive (TP): a boat instance was correctly detected and classified as a boat, or a ship instance was correctly detected as a ship.
- True Negative (TN): a non-boat instance was correctly classified as non-boat instance, or a non-ship instance was correctly classified as not ship instance.
- False Positive (FP): a non-boat instance was incorrectly detected and classified as a boat, or a non- ship instance was incorrectly detected and classified as a ship.
- False Negative (FN): a boat instance was incorrectly classified as non-boat, or a ship instance was classified as non-ship.

Fig. 5 shows the true positives based on increasing train sample size. The line graph presents that when the train sample size was 100 the number of true detections were 68, the number of true detections was 75 when the sample size was increased to 300 and when the data was further increased to 500 train images it jumped to 82 true detections. After 500 sample size graphs started to decrease in true detections due to the duplication of data. This means that by increasing sample size the number of true detections also increases

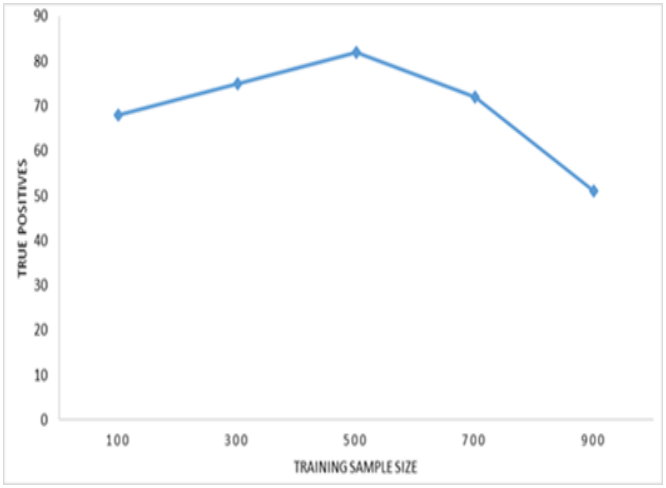

Fig. 5: *True positives based on train sample size*

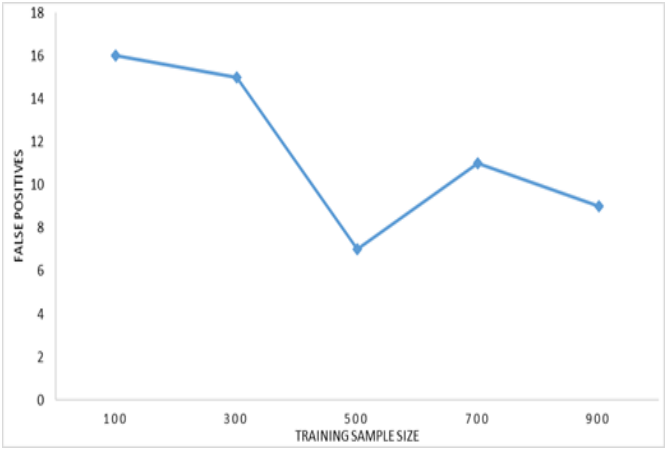

Fig. 6: *positives based on train sample size*

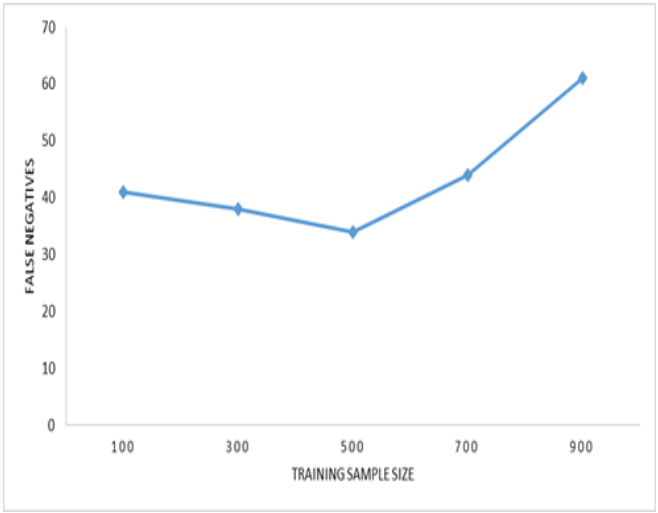

Fig. 7: False negatives based on train sample size

Fig. 6 shows false positives based on increasing train sample size. Considering the increased sample size, the number of false positives started from 16, but as the sample was increased to 500, false positives decreased to 7. The last two samples were duplicated so the false positives were affected.

Fig. 7 presents false negatives based on the increasing sample size. As the data was increased from 100 to 500 train images, the graph shows that in 100 sample size false negatives were 41, at 300 false negatives were 38 and at 500 train images false negatives were 34. This means that increasing the

false negatives. However, data duplication increased the false negatives.

The results obtained from faster R-CNN models trained with different sample size were added together for each entity. The 20 test images contained 121 objects and detected objects for each train sample were added together. All false positives, true positives, false negatives were added together for a model trained with 100 train images, a model 300 train images, a model trained with 500 images, a model trained with 700 images and a model trained with 900 images. False discovery rate (FDR), precision and recall were computed for results obtained from each model. The following formulas were utilized to determine false discovery rate, precision, and recall.

- False discovery rate is the correlation of false positive compared to total detected objects.

$$FDR = \frac{fp}{tp + fp}$$

- Precision is the proportion of all true positives compared to all objects detected.

$$PR = \frac{tp}{tp + fp}$$

- Recall is the proportion of all true positives compared to all possible detections.

$$RC = \frac{tp}{tp + fn}$$

TABLE 3: COMPARISON OF RESULTS FOR VARIOUS TRAIN SAMPLE SIZES

Trained images	*Total objects*	*Detected objects*	*False Positives*	*True Positives*	*False negatives*	*FDR*	*Precision*	*Recall*
100	121	84	16	68	41	0,190476	0,809524	0,623853
300	121	90	15	75	38	0,166667	0,833333	0,663717
500	121	89	7	82	34	0,078652	0,921348	0,706897
700	121	83	11	72	44	0,13253	0,86747	0,62069
900	121	66	9	51	61	0,15	0,85	0,455357

Looking at TABLE 3, based on increasing sample sizes, the number of false positives decreased as train sample increased and it was always lower than the number of true positives. Although the train sample size was very low, transfer learning improved the learning capability. Boats and ships were detected, and the number of false positives reduced as training data was increased.

Fig. 8 shows false discovery rate (FDR), precision and recall compared to the train sample size. False discovery rate (FDR) was utilized to predict the occurrence of false positives and compare the results with the results when the model was further re-trained with increasing sample size. From 100 to 500 train sample FDR ranges from 0.19 to 0.07, this means that it was decreased by increasing sample size. In this line graph the precision ranges from 0.81 to 0.92 with the first increasing sample and from 0.92 to 0.85 when the data was duplicated. This means that the precision rate increased with increasing sample size but was disturbed when the data was duplicated. The recall also increased with increasing data, ranging from 0.6 to 0.7 but decreased when data was duplicated.

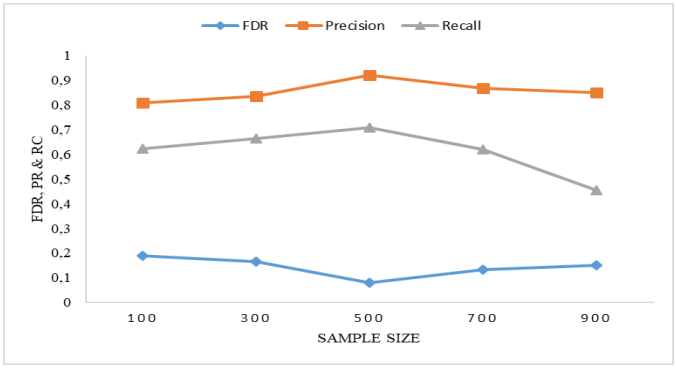

Fig. 8*: Detection performance compared to training size*

VI. CONCLUSION AND FUTURE WORK

This study aims to improve the implementation of object detection in maritime cluttered environment. Most of the algorithms for detecting the objects pose a lot of false positives due to the background clutter. Detecting objects produces a high detection rate, nevertheless, cluttered environments restrict the process leading to difficulties in detection. Slowly moving objects and stationary objects may not be detected. Background subtraction method poses a challenge when the camera is moving. In trying to solve the problem of ships and boats detection in a cluttered maritime environment, the faster R-CNN with inception v2will be employed.

There are many questions that are still not answered in this study. For instance, the detection was made for two different classes in a maritime environment, though there are many objects that are present in a maritime environment which can be a threat. The research only detected using images. A study can be done whereby all moving objects in a maritime video are detected and tracked. The data used in this research contained images with only the objects to be detected so the model was not familiar with negative examples, detection results can be improved with very large and relevant training data. It is recommended that the same research must be done using more than one algorithm.

ACKNOWLEDGMENT

The department of computer science in University of Fort Hare is acknowledged, and Council for Scientific and Industrial Research (CSIR) for dataset. Ballard, Dana H. "CM Brown Computer Vision." *NY: Prentice Hill* (1982).

Declaration

All the information in this paper, is based on Nosiphiwo Nkele's dissertation which is now online in the UFH library website.
https://vital.seals.ac.za/vital/access/services/Download/vital:40862/SOURCE1

REFERENCES

[1] Sonka, M., Hlavac, V. and Boyle, R., 2014. *Image processing, analysis, and machine vision*. Cengage Learning.

[2] D. H. Ballard and CM "Brown *Computer vision*. Prentice-Hall", 1982.

[3] F. Xu, J. Liu, M. Sun, D. Zeng, and X. Wang, "Optical Remote Sensing Imagery," pp. 1–23, 2017.

[4] Chan, L.A., Der, S.Z. and Nasarbadi, N.M., 2003. Automatic target detection. *Encyclopedia of Optical Engineering*, *1*, pp.101-113.

[5] A. Bachoo, B. Duvenhage, and J. De Villiers, "PRISM Project List," 2015.

[6] S. Kim and J. Lee, "Small infrared target detection by region-adaptive clutter rejection for sea-based infrared search and track," *Sensors (Switzerland)*, vol. 14, no. 7, pp. 13210–13242, 2014.

[7] Hall, D., Nascimento, J., Ribeiro, P., Andrade, E., Moreno, P., Pesnel, S., List, T., Emonet, R., Fisher, R.B., Victor, J.S. and Crowley, J.L., 2005, October. Comparison of target detection algorithms using adaptive background models. In *2005 IEEE International Workshop on Visual Surveillance and Performance Evaluation of Tracking and Surveillance* (pp. 113-120). IEEE.

[8] L. Tong, F. Heymann, and T. Noack, "Radar target detection based on methods of image pattern matching," vol. 36, no. 108, pp. 162–167, 2013.

[9] G. Jing and S. Chaojian, "Survey on Methods of Moving Object Video Detection in Marine Environment," vol. 51, no. Iccsit 2011, pp. 437–440, 2012.

[10] Songlin, W., Haodong, L., Taifang, W. and Zhi, C., 2013, November. Moving target detection algorithm research based on background subtraction method. In *3rd International Conference on Multimedia Technology (ICMT-13)* (pp. 1172-1179). Atlantis Press.

[11] U. K. J. 3 Himani S. Parekh1, Darshak G. Thakore 2, "A Survey on Object Detection and Tracking Methods," *Int. J. Innov. Res. Comput. Commun. Eng.*, vol. 2, no. 2, pp. 2970–2978, 2014.

[12] Guo, S., Zhang, Q., Shao, Y. and Chen, W., 2017. Sea clutter and target detection with deep neural networks. *DEStech Transactions on Computer Science and Engineering*, (aiea).

[13] S. Liu and Z. Liu, "Multi-Channel CNN-based Object Detection for Enhanced Situation Awareness," pp. 1–9, 2017.

[14] G. Li, Haoxiang and Lin, Zhe and Shen, Xiaohui and Brandt, Jonathan and Hua, "A Convolutional Neural Network Approach for Face Detection," *CVPR*, pp. 5325–5334, 2015.

[15] P. A. Rodriguez and E. D. Tejada, "moving object detection in videos using principal component pursuit and convolutional neural networks Enrique D . Tejada Pontificia Universidad Catolica del Peru Pontificia Universidad Catolica del Peru," pp. 793–797, 2017.

[16] I. S. MacKenzie, S. J. Castellucci, and Sigchi, "Empirical research methods for human-computer interaction," *32nd Annu. ACM Conf. Hum. Factors Comput. Syst. CHI EA 2014*, pp. 1–6, 2014.

[17] "Tensorflow detection model zoo," 2018. [Online]. Available: https://github.com/tensorflow/models/blob/master/research/object_detection/g3doc/detection_model_zoo.md. [Accessed: 07-Mar-2019].

[18] M. M. Zhang, J. Choi, K. Daniilidis, M. T. Wolf, and C. Kanan, "VAIS: A Dataset for Recognizing Maritime Imagery in the Visible and Infrared Spectrums," *Proc. IEEE Conf. Computer Vision and Pattern Recognition. Workshop (CVPRW).*, pp. 10–16, 1972

[19] Lokanath, M., Kumar, K.S. and Keerthi, E.S., 2017, November. Accurate object classification and detection by faster-RCNN. In *IOP Conference Series: Materials Science and Engineering* (Vol. 263, No. 5, p. 052028). IOP Publishing.

Nosiphiwo Nkele is an MSc graduate from the University of Fort Hare. This paper is from her dissertation entitled: Modelling false positive reduction in maritime object detection.

Nyashadzashe Tamuka is a PhD Computer Science student at University of Fort Hare.

A Lightweight Mutual Authentication Scheme for Cloud-Based Telecare Health Services

Philani Khumalo[1], Bakhe Nleya[2]

[1,2]*Department of Electronic Engineering/ Faculty of Engineering/ DUT*

[1] KhumaloPK@elec.durban.gov.za

[2]bakhen@dut.ac.za

Abstract— **The new version IPng (next-generation Internetworking Protocol), also referred to as IP version 6, lays the basis for interconnectivity among diverse entities in the present-day Internet of Things (IoT) network. The device-to-device (D2D) communication standard is also being incorporated to facilitate communication between devices (in proximity) without involving the core network, especially for critical mission services. Similarly, the same standard can facilitate network connectivity for devices that are out of network coverage by way of linking via neighboring peers within core network coverage. This development, coupled with advances in Fog-Cloud computing means that cloud-based Tele-care health services can now be deployed as D2D communication will enhance fail-safe connectivity. Implementing a Fog-Computing paradigm will also help maintain end-to-end latencies within acceptable bounds for such a service. However, privacy within such a service framework must be guaranteed. Similarly, the resource-constrained nature of devices such as medical sensors in terms of battery life and computing power secludes the direct implementation of legacy privacy and security measures. In this paper, we discuss a framework that enhances resilience in a Tele-care health service framework in terms of privacy and security. In this regard, we propose a scheme that is characterized by computational simplicity, privacy preservation as well as energy efficiency. Overall performance analysis demonstrates that the scheme is well suited for such a service framework.**

Keywords— **Telecare health, mutual authentication, D2D communication, privacy, security**

I. INTRODUCTION

The IoT network blends several technologies to facilitate connectivity among billions of objects and devices. [1], [2]. The health sector globally is taking advantage of the emergency of the IoT network to roll out Tele-care services that would effectively expand the s existing structures. Such a service will incorporate medical-related informational and multimedia coordination, as well as records processing. To satisfy, necessary privacy, as well as security in the form of availability, confidentiality as well as integrity in Telecare Health services and an enabling network, such as IoT, is required [3]. The network infrastructure will facilitate secure authentication and key exchange by key entities constituting the infrastructure of a Telecare health service. In this paper, it is assumed that the network supports D2D communication. Note that D2D communication is designed to support direct communication among proximity devices and objects. By design ensures fail-safe communications by way of facilitating interoperability between critical public safety and public network infrastructures, Its support for proximity-based communications leads to an improvement in spectrum efficiency as well as utilization, end-to-end throughput, and energy efficiency in existing networks.

Concurrently new and innovative services can be rolled out. Notably, D2D-communication compatible telecare health devices and objects are potentially a fail-safe backup infrastructure for critical mission networks should the public cellular networks become inaccessible. [4]. Thus in a typical Telecare health infrastructural service, usage of D2D communication compliant devices is necessary. At a local level, a 3rd Generation partnership project (3G-PP) IoT-enabled network architecture as well coverage is necessary [5]. Such a network incorporates key blocks such as a D2D communication server, a home subscriber server (HSS), and a mobility management entity (MME). The D2D communication server handles communications among proximity devices. The HSS retains attributes information of the devices as well as granting a set of necessary authenticating tokens.

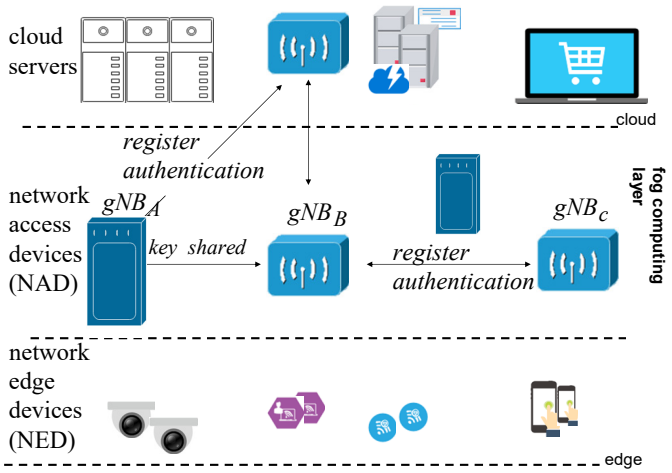

Figure. 1: Fog -Computing paradigm.

However, the base infrastructure just discussed cannot guarantee a high level of QoS and this is because of the limited computing (processing) capabilities of the devices themselves. The cloud computing paradigm is also being explored as an alternative. This is because it can render a better QoS to users with elastic resources despite its limitations. The key limitation is that of long round trip times. Besides, it cannot cope up with the low latency requirements of most health directly related services and applications.

Hence of recent the Fog Computing paradigm was introduced to directly respond to the latency minimization issue.

It exploits the fog layer, which is the interfacing layer between the core and peripheral network sections to drastically reduce latencies as well as boost the limited computing powers in resource-constrained devices. It can also provide network context information which ultimately is used by fog applications and services to optimize context awareness. Its support for location-awareness; means it can fully support device mobility which is a direct booster for location-based services and applications. Fog computing easily provides a local overview whereas a global overview will still be provided by cloud computing. Primarily a fog computing model comprises key elements such as (i) network edge device (NED), (ii) network access device (NAD), i.e., fog node, in the proximity of a NAD, and (iii) cloud server (CS). This is illustrated in Fig. 1.

II. TELECARE HEALTH FRAMEWORK DESCRIPTION

A typical Telecare health system will involve patients, a hospital, a cloud server as well as an enabling communication infrastructure as detailed in the previous section. As such, typical key communication components in the infrastructural network will include an HSS, normally incorporated in an evolved packet core (EPC), a few eNBs, as well as 3-GPP coverage. A patient will normally visit the nearest health canter such as a clinic or hospital for initial registration. It is at this stage that the patient will be Their furnished information will be used for authentication purposes in the future. E.g., authentication with the cloud server s mandatory before a patient's data can be uploaded or retrieved.

Likewise, at the device level, each patient's device performs the necessary mutual authentication with the CS before any data exchange sessions being sanctioned. Not all devices are within the 3-GPP coverage infrastructure. Only those within its coverage may use it to access the cloud server. Otherwise, those which are not within coverage ranges rely on D2D communication to perform mutual authentication, before dispatching any patient-related reports.

Relays will also assist other D2D devices to reach the cloud servers. Devices that connect directly to the 3GPP infrastructure may also utilize D2D communication for data exchanges with the cloud and other key parties. The medical personnel, namely medical doctors are also expected to mutually authenticate before gaining access to a patient's records.
We next summarize the mandatory details of the multi-phase mutual authentication between the various entities (including patients and devices) and the cloud server as follows: used.

III. PROPOSED PRIVACY SCHEME

We now proceed to describe, discuss as well as analyze the Group Authentication scheme in a D2D Communications-based telecare framework which among other things will involve as well as enable large volumes of confidential health-related data It was proposed in [6] and it is symmetric cryptography based.
We next summarize the mandatory details of the multi-phase mutual authentication between the various entities (including patients and devices) and the cloud server as follows: used.

A. Device Discovery Scheme

For the invoking of any service, which might include several devices, each of the group members must perform neighbor device discovery to identify collaborating devices within the vicinity. Each device does that via the HSS. The HSS will, in turn, verify whether its International Mobile Subscriber Identity (*IMSI*) matches the device records in its database and whether the device is indeed authorized (privileged) for the intended service, plus it is D2D communication compliant. Upon successful verification, the authorization will be relayed to an eNB and at the same time tagged with a timer.
Next, all verified devices belonging to a group can now mutually identify each other as belonging to that group by possibly using WLAN direct radio signals is sharing their attributes [7], [8].

B. Registration Phase

Key mutual authentication-related primitives are exchanged during this phase, The IMSI of each device must be registered in the HSS and normally this is done by the vendor. All key personnel and patients are registered to the cloud server via some identified secured channel. Each device is assigned a temporary identity.

$$TID_y = h_1(ID_y \| R_k) \quad (1)$$

where R_k is an arbitrary chosen random number that will remain mapped to their real identities ID_y ; h_1 is a hash function for the TID_y generation.

Both the real and temporary IDs will be furnished to the cloud server for storage and subsequent use in other authentication phases.

C. Hospital Uploading

This phase is exclusive to registered entities. At this stage, preparations are being made to mutually authenticate parties that will be involved in the updating of any data acquired from the patient. The authentication does not necessarily need to be done on a secured channel. Rather an unsecured channel is preferred for this purpose.

The phase commences with the would-be patient (user) paying a visit to his/her nearest health center for a health checkup. Alternatively, this could be due to some evident ailment. At the health center, the patient will be issued with login credentials which can now be used to access the service via a standard GSM handset (smartphone). The overall authentication at this phase is sequentially carried out as follows:
Using a randomly generated integer R_h and its real identity ID_h the hospital computes its message authentication code (MAC_h) as follows:

$$MAC_{hs} \rightarrow h_2(|ID_h|)(R_h) \quad (2)$$

Where, h_2 is a has function for generating the MAC. Later, the key primitives are relayed to the cloud server in the form of a time-stamped (T_h), message (m_1).;

$$m_1 \rightarrow (TID_h, R_h, MAC_{hs}) \quad (3)$$

Upon receiving m_1 together with T_h from the Hospital the cloud server performs the necessary validations by initially computing:

$$MAC_{hs}' \rightarrow' h_2(ID_h \,//\, R_h) \quad (4)$$

Note that the validation of (4) above is done using the real and temporary identities furnished by the hospital at the registration phase. It, therefore, suffices to compares its own computed MAC and that contained in m_1

$$MAC_{hs}' \rightarrow MAC_{hs} \quad (5)$$

Upon successful authentication, it goes on to select a random number R_{sh} before computing;

$$MAC_{sh} = h_2(ID_h \,//\, R_{sh}) \quad (6)$$

This will now be sent as a time-stamped (T_s) confirmation message (m_2) back to the hospital.

$$\text{m2} \rightarrow (MAC_{sh}, R_{sh}) \quad (7)$$

Upon receiving the time-stamped message m_2 from the server, likewise, the hospital performs all the necessary validations as follows:

First, it checks that the validity of the received timestamp. This is followed by a re-computing of the following.

$$MAC_{sh}' \rightarrow' h_2(ID_h \,//\, R_h) \quad (8)$$

After which it verifies that the two MACs match.

$$MAC_{sh}' \rightarrow MAC_{sh} \quad (9)$$

Subject to the validity of (9), the next step would be to generate a common session key.

$$K_{hs} = h_3(ID_h \,//\, R_{h\,//\,R_{sh}}) \quad (10)$$

Where h_3 once again is a MAC generation function; R_{sh} is a randomly generated number by the cloud and sent to the hospital. A session key validator is also computed, with the help of a session key generator hash function h_4 as follows:

$$C_{hs} = h_4(K_{hs}) \quad (11)$$

The session key is used to cipher the patient's records before uploading to the server in the form of a message $m_3 = M_{rp}$;

$$M_{rp} \rightarrow E_{K_{hs}}(patient\ record, TID_h, C_{hs}) \quad (12)$$

The message m_3 is then time-stamped from the hospital side before dispatching it to the cloud server.

Upon receipt of m_3 and T_h the cloud server computes the session key

$$K_{hs} \rightarrow h_3(ID_h \,//\, R_h \,//\, R_{sh}) \quad (13)$$

and deciphers the patient's report.

$$(patient's\ record, TID_R, C_{hs}) \rightarrow D_{K_{hs}} \quad (14)$$

Ultimately it computes, $C_{hs} = h_4(K_{hs})$ and validates:

$$C_{hs}' = C_{hs} \quad (15)$$

Only then will the records be admitted to the Cloud server's database.

D. Patient Uploading

This involves uploading all acquired patient's health-related data via sensors to be uploaded to the cloud server. This can be done over a generally insecure channel since most patients are scattered around the countryside and with insufficient network (3G-GPP) coverage. This data will thus be encrypted for confidentiality's sake. The patient's main device will prompt all sensors within the vicinity (around his/her body) to release the data to it. Authentication is necessary before the data collection by the main patient's device initiates. It is important to note that all associated devices must be initially successfully authenticated with the available 3G-PP network.

If they are to utilize the D2D communication mode, then a random number R_p is generated by the patient's device. It uses this same number to compute a hash of its $IMSI$.

$$Auth_p = h_1(IMSI_p \| R_p \quad (16)$$

Ultimately the hash is sent to the HSS for use in the authentication verification according to:

$$Auth_p^{'} = hi(IMSI_p \ \| R_p) = Auth_p \quad (17)$$

Once authenticated by the HSS the patient's device can perform discovery with peer proximity devices using their temporary devices as well. It is also possible for a device that is outside a 3GPP coverage area to rely on close-by devices to access the 3GPP network coverage range and ultimately authenticate with the cloud server [8].

E. Prescriptions

Once again the two parties involved; the medical specialist and cloud server must mutually authenticate. Ultimately a session key will be generated and used to cipher all patients' reports, body sensor measurements as well as the overall diagnosis. The procedures taken are as follows.

The medical specialist must initiate the authentication with the server by generating a random number R_d as well as providing a temporary ID (TID_d). The two will be used to generate:

$$MAC_{ds} = h_2(ID_d \,//\, R_d) \quad (18)$$

Which is now time-stamped (T_d) and dispatched to the server in the form of a message m_1.

$$m_1 = (TID_d, R_d, MAC_{ds}) \quad (19)$$

Upon receiving both m_1 and T_d the server validates them before further computing:

$$MAC_{ds}' = h_2(ID_d \,//\, R_d) \quad (20)$$

and ultimately verifying;

$$MAC_{ds}' = MAC_{ds} \quad (21)$$

Should the verification succeed, the server once again opts for a random integer R_{sd} and uses it to compute the MAC and session key:

$$MAC_{sd} = h_2(ID_d \,//\, R_{sd}) \quad (22)$$

$$K_{ds} = h_3(ID_d \,//\, R_d \,//\, R_{sd}) \quad (23)$$

$$C_{ds} = h_4(K_{ds}) \quad (24)$$

The server uses the session keys to cipher the patients records it retrieves from the database:

$$M_{RpMS} = E_{KHC}(p\_RR, sensor, TID_p C_{ds}) \quad (25)$$

Finally, it timestamps (T_s) the records and sends them in the form of a message m_2 to the medical specialist.

$$m_2 = (MAC_{sd}, R_{sd}, M_{RpMS}) \quad (26)$$

Upon receiving m_2 and T_s, the medical specialist validates them and ultimately generates a session key:

$$K_{ds} = h_3(ID_d // R_d \,//\, R_{sd}) \quad (27)$$

He will then decipher the received patient records before sending a time-stamped confirmation message (m_3) back to the cloud server. The latter will have to positively validate m_3 otherwise this is a malicious activity of the side of the medical specialist (i.e., a hacker is attempting to infiltrate the system).

IV. SCHEME'S EVALUATION

In this section, we summarily analyze the protocol in terms of security requirements as well as performance. The performance is restricted to computational simplicity, communications overhead as well as energy efficiency [9], [10], [11].

A. Security Analysis

Mutual authentication: As mentioned earlier, it is mandatory that all parties (including medical specialists, patients, and other entities) that are D2D communications compliant mutually authenticate with the 3GPP network using the supported AKA authentication framework. Once accomplished connection requests can securely be channeled among all parties within the framework as it is now guaranteed that they are legitimate (since authentication with the 3GPP network succeeded). Note that the connection request message has the remote SG devices' broadcasted HMAC code. The 3GPP network will use a locally stored HMAC key to verify the legitimacy of the broadcasting entity (device). The system also facilitates peer parties to mutually authenticate via an unsecured available channel. To accomplish that, a randomly generated HMAC key is also distributed from the 3GPP network to the devices involved. As this key once-off key is only exchanged via secure channels, attackers are unable to mislead a responding device by replaying previously exchanged messages, neither can a legitimate SG device be impersonated using another set of DHKE messages.

Secure data transmission: In our proposal, we have assumed that data is exchanged only after sessions have been authenticated. As the session keys are generated by ECDH and only transmitted via secured channels privacy-compromising is ruled out Note that ECDH is based on Computational Diffie-Hellman (CDH) problem, adversaries cannot find the symmetric key used. Hence only legitimized parties can read content messages but even an intermediary like the 3GPP network will not have knowledge of the actual key used. for the particular session.

Session key backward/ forward secrecy: The scheme guarantees that attackers cannot retrieve keys from previous or future sessions. This is to guard against situations where a party has exited the SG and then afterward be used for malicious actions in the SG. Similarly, new entrants may not be able to exploit previous transactions. We note that the session key backward/forward secrecy is consolidated by the fact that the stored HMAC keys are only used for message authentication and verification purposes.

Device anonymity: The scheme uses device pseudo identities. As such attackers may only be aware that live sessions exist on the network, but would not be able to decode that sender and destination's real identities and locations.

Traceability: The scheme requires that a confirmation message be sent upon successful connection establishment. In that way, if too many failed attempts are detected on one particular point, that would serve as an indicator that attackers are attempting to infiltrate.

Message non-repudiation: It is procedural with the proposed scheme that messages be sent via a secured channel, or the insecure channel with either HMAC code or a sequence number appended: the broadcast message, DHKE request message, and DHKE response message are protected using HMAC code. In that way, message non-repudiation is guaranteed and ensured.

B. Performance Analysis

In this subsection, we analyse the performance of the protocol. In this regard, we carry out a comparative performance analysis of the computational demands (intensities), communication overheads as well as energy efficiencies [14], [15] of the proposed versus similar protocols presented in [6] and [12].

The evaluation of computational costs of the protocols is solely based on an estimate of the time-lapses required to accommodate the execution of operations, which are regarded as an integral part of the messages exchanged in the various phases of each protocol. Provided in Table 1 are example

operations and associated computational costs of the proposed protocol.

Table 1. Various operations execution times (normalized)

symbol	*defination*	$\cos t(\sec s)$
T_p	patient's pairing	0.051
Ts	sign. between entities	0.052
T_E	encrypting/decrypting	0.0076
T_H	simplex hash operation	0.00495

For the proposed scheme, the total computational load will be aggregated from the 4 phases described in the preceding section.

$$C_{total} = 12nT_E + 30nT_H \equiv 0.051n \quad (28)$$

For [6], the total computational load is given by:

$$C_{total} = 4nT_s + 9nT_E + 35T_H = 0.021n \quad (29)$$

For [12], we have.

$$C_{total} = 5nT_s + 11nT_p + 8nT_E + 32nT_H \quad (30)$$

We now compare the computational loads of the three schemes namely the proposed, and two others proposed in [6] and [12] respectively. The number of devices per BAN is varied.

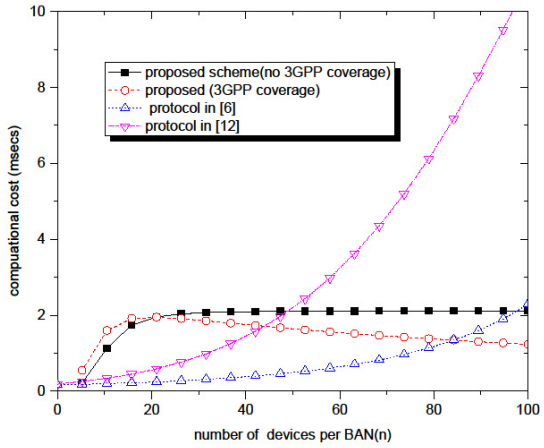

Fig. 2 Computational cost comparison

Fig. 2 plots the relative computational costs in which we see that the proposed requires the lowest computational cost.
With regards to communication overheads comparison, it is noted that in general, D2D communication cost metrics are depended on the volumes of exchanged signaling data over insecure channels. The communication cost and required transmission bandwidth are directly proportional. Associated parameters corresponding costs are shown in the table below.

Table 2. Communication costs

action	overhead
Timestamping, random integer, TID	6 bytes
Hash function/ pairing	2. bytes
Session key	16 bytes
Signature	64 bytes

The total overheads in bytes required by each scheme are as follows:

For the proposed scheme.

$$comm_{total} = 384n + 66m - 26 \quad (31)$$

Where n is the number of active devices in a BAN or wide BAN (WBAN) and m would be the number of messages that were exchanged The protocol proposed in [6] requires $384n$ bytes overhead whereas its equivalent in [12] requires $865n$ bytes. Plots of the communication overheads for the three protocols as a function of the number of active devices in either BAN or WBAN are provided in Fig. 3. From the same graph, it can be deduced that the proposed protocol generates relatively low communication overheads hence it is best suited for adaptation to D2D communication.

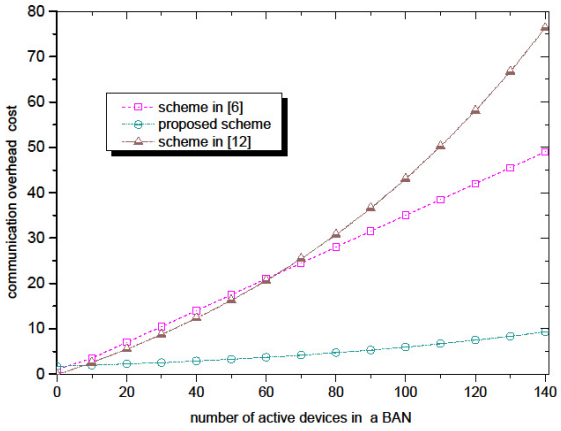

Fig. 3. Communication cost comparison

The other two schemes incur relatively much higher communication overheads since they involve the exchanging of quite a few costly signature parameters, for their mutual authentication. As we gradually move towards energy-efficient aware networking and protocol design, [15], [17]. It is necessary to minimize the operational energy requirements of any protocol thereof. Besides most of the devices are resource-constrained in terms of power supply. Most of the energy consumption is incurred by the CPUs of the respective devices.

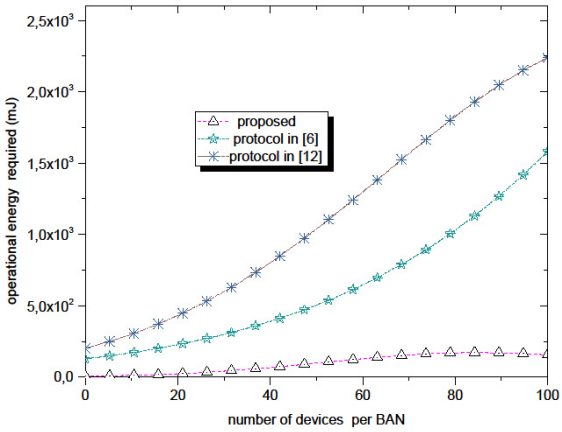

Fig. 4. Energy cost comparison

The normalized energy cost for the various protocols are calculated as set out in the next three following formulae:

For the proposed protocol:

$$E_{total} = 12nT_E + 33nT_H \quad (32)$$

For [6]

$$E_{total} = 4nT_s + 9nT_E + 35nT_H \quad (33)$$

For [12]

$$E_{total} = 5nT_s + 11nT_p + 8nT_E + 32nT_H \quad (34)$$

A plot of the operational energy requirements for the 3 different schemes is provided in Fig 4. By comparison, the proposed scheme is more energy efficient.

VI CONCLUSION

This paper proposes a D2D communication-based authentication and key agreement Tele-care scheme that ensures both privacy and security for patients who have enrolled in the service. The fact that the authentication can be done via an insecure link means that even in the absence of 3GPP network coverage, patients would still be able to link with the nearest health care center and medical specialists, thus making the scheme both resilient and robust. This is because D2D communication supports direct device linking of proximity devices and thus an affected device would still reach the nearest peer that is within sufficient coverage range.

The paper uses lightweight message authentication that is meant to reduce computational and communication loads, as well as operating in an energy-efficient manner. Its efficacy in terms of ensuring both security and privacy was explored. Overall, we conclude that the scheme would be quite viable in the practical implementation of telecare as most of the devices are resource-constrained in terms of computational as well as operating power requirements.

REFERENCES

[1] M. Pasha and S.Shah, “Framework for e-health systems in IoT-based environments” Wireless Communications and Mobile Computing Volume 2018.

[2] P. Świątek and A. Rucinski, "IoT as a service system for eHealth," 2013 IEEE 15th International Conference on e-Health Networking, Applications and Services (Healthcom 2013), 2013, pp. 81-84, doi: 10.1109/HealthCom.2013.6720643.

[3] K. Monteiro, É. Rocha, É. Silva, G. L. Santos, W. Santos and P. T. Endo, "Developing an e-Health System Based on IoT, Fog and Cloud Computing," 2018 IEEE/ACM International Conference on Utility and Cloud Computing Companion (UCC Companion), 2018, pp. 17-18, doi: 10.1109/UCC-Companion.2018.00024.

[4] J. Lee and J. H. Lee, "Performance Analysis and Resource Allocation for Cooperative D2D Communication in Cellular Networks With Multiple D2D Pairs," in IEEE Communications Letters, vol. 23, no. 5, pp. 909-912, May 2019, doi: 10.1109/LCOMM.2019.2907252.

[5] S. Fang, Y. Gao, C. Zhang and X. Hei, "Achieving 3GPP Fairness for LTE-U and WiFi Coexisting Networks in Unlicensed Spectrum," 2019 IEEE International Conference on Consumer Electronics - Taiwan (ICCE-TW), 2019, pp. 1-2.

[6] M, Wang, and Z., Yan, “Privacy-preserving authentication and key agreement protocols for D2D group communications”, IEEE Transactions on Industrial Informatics, vol.14, no.8, pp.3637-3647, 2018.

[7] R. H., Hsu, J., Lee, T. Q., Quek, and J. C., Chen, “GRAAD: Group Anonymous and Accountable D2D Communication in Mobile Networks.”, IEEE Transactions on Information Forensics and Security, vol.13, no.2, pp.449-464, 2018.

[8] A. Nauman, M. A. Jamshed, Y. Ahmad, R. Ali, Y. B. Zikria and S. Won Kim, "An Intelligent Deterministic D2D Communication in Narrow-band Internet of Things," 2019 15th International Wireless Communications & Mobile Computing Conference (IWCMC), Tangier, Morocco, 2019

[9] P. Kushwaha, "Towards the equivalence of Diffie-Hellman problem and discrete logarithm problem for important elliptic curves used in practice," 2017 ISEA Asia Security and Privacy (ISEASP), Surat, 2017, pp. 1-4, doi: 10.1109/ISEASP.2017.7976981.

[10] M. Gomba and B.. Nleya, "Architecture and security considerations for Internet of Things," 2017 Global Wireless Summit (GWS), Cape Town, 2017, pp. 252-256, doi: 10.1109/GWS.2017.8300477.

[11] L. P. Bopape, B. Nleya and P. Khumalo, "A Privacy and Security Preservation Framework for D2D Communication Based Smart Grid Ser-vices," 2020 Conference on Information Communications Technology and Society (ICTAS), Durban, South Africa, 2020, pp. 1-6, doi: 10.1109/ICTAS47918.2020.233995.

[12] L. Chiou, S., Ying, Z. and Liu, J., "Improvement of a privacy authentication scheme based on a cloud for the medical environment”, Journal of medical systems, v. 40, n. 4, pp.101, 2016.

[13] Mohit, P., Amin, R., Karati, A., Biswas, G. P., Khan, M. K., "A standard mutual authentication protocol for cloud computing-based health care system.", Journal of medical systems, v.41, n. 4, pp. 50, 2017.

[14] B. Nleya and C. Mulangu, "An Overview of GREEN Networking and Power Savings in Optical Backbone Networks," 2018 International Conference on Advances in Big Data, Computing and Data Communication Systems (icABCD), Durban, South Africa, 2018, pp. 1-6, doi: 10.1109/ICABCD.2018.8465402.

[15] B. Nleya and R. Chidzonga, "Overview of power-aware — RWA in optical backbone supported networks," 2017 IEEE AFRICON, Cape Town, 2017, pp. 446-449, doi: 10.1109/AFRCON.2017.8095523.

[16] C. Yang, F. Wu, S. Tsai and W. Kuo, "E-Health Services for Elderly Care Based on Google Cloud Messaging," 2015 IEEE International Conference on Smart City/SocialCom/SustainCom (SmartCity), Chengdu, China, 2015, pp. 9-12, doi: 10.1109/SmartCity.2015.39.

[17] P. Khumalo and B. Nleya, "Sleep-Mode/Traffic Grooming Versus Device Reliability Overview," 2018 International Conference on Advances in Big Data, Computing and Data Communication Systems (icABCD), Durban, 2018, pp. 1-5.

Philani Khumalo is currently a D. Eng student in the Department of Electronic and Computer Engineering of the Durban University of Technology. He is working on cyber security in Smart grids. He completed an M. Eng in the same Department and discipline some 4 years back. Research interests are in the fields of privacy and security in networked systems.

Limited Range Communications

Golden Code Deep Learning-Aided Sphere-Decoding With Sorted Detection Subsets

Bhekisizwe Mthethwa[#], Hongjun Xu[#]

[#]*School of Engineering, University of KwaZulu-Natal, Durban, 4041, South Africa*

[1]tshomie2020@yahoo.com

[2]xuh@ukzn.ac.za

Abstract—**Golden code is a full-rate full-diversity non-orthogonal space-time block coding (STBC) scheme which has spatial multiplexing gain over the famous Alamouti half-rate full-diversity orthogonal STBC scheme. The Alamouti scheme has been widely implemented in modern wireless standards such as the LTE 3GPP and Wi-Fi IEEE 802.11n standards. This is because it offers full diversity at a lower detection complexity compared to the non-orthogonal STBC schemes such as Golden code. Recently, a low complexity Golden code detection algorithm called sphere-decoding with sorted detection subsets (SD-SDS) was proposed in literature. In this study, we showcase the power of recurrent neural networks (RNN) by training an RNN to learn how to predict the sorted detection subset (SDS) sequences of the SD-SDS detection algorithm. The study shows that the RNN can generate the SDS sequences accurately for lower modulation orders, $M \leq 16$, but at the cost of increased detection latency at the high signal-to-noise ratio regions. It is observed that the RNN SDS technique can be used as an alternative in situations where the wireless transmitter uses low modulation orders, $M \leq 16$, and the MIMO configuration is very large, $i.e\ N_t \gg 2$, which makes the SD-SDS search radius and search depth very large.**

***Keywords*— space-time coding, WiMAX, Golden code, sphere-decoding, recurrent neural networks, deep learning.**

I. INTRODUCTION

Due to the recent high demand for real-time multimedia streaming through online multimedia conferencing applications, online learning video streaming, online movie and music streaming, wireless communication infrastructure is under pressure to deliver high data throughputs and link reliability. Multiple-input multiple-output (MIMO) wireless architectures have been developed to solve these challenges by offering spatial multiplexing gain and high link reliability. The high link reliability is delivered through the existence of multiple receiver antennas in the MIMO configuration. This offers receiver diversity on the wireless signal and improves the received signal-to-noise ratio (SNR) and thus the error rate performance or link reliability. Wireless link reliability can be further enhanced using the open loop transmit diversity schemes such as the space-time block coding (STBC) scheme.

Golden code [1] is a non-orthogonal STBC scheme which exhibits full-rate and full-diversity whilst having very high detection complexity. Golden code exhibits spatial multiplexing gain over the half-rate full-diversity orthogonal STBC scheme called Alamouti [2]. The coding rate in this paper is defined as the number of symbols transmitted per transmit antenna per timeslot. The Alamouti is an orthogonal STBC which means that it has a simple linear maximum likelihood (ML) detector due to its orthogonality property in slow fading channels [3]. Because of this low detection complexity and full diversity, it is incorporated in many modern wireless standards as an STBC scheme of choice namely in IEEE 802.11n wireless fidelity (WiFi) standard [4], IEEE 802.11ah low power WiFi [5] and the long-term evolution (LTE) 3GPP standard [6]. Golden code is a non-orthogonal STBC so it lends itself to non-linear ML detection complexity which in literature is known to be in the order of $\vartheta(M^4)$ where M is the M-QAM modulation order. Golden code is implemented in the now-defunct WiMAX IEEE 802.16e standard [7]. Its adoption in modern wireless communication standards is limited by its high detection complexity despite its spatial multiplexing gain property. High detection complexity has negative consequences to Telco companies because it drives up the energy costs and carbon footprint from an environmental sustainability point of view.

Recently, the wireless research community has gained interest in the application of recurrent neural networks (RNN) in solving wireless communication related research problems. In [8], the authors propose a novel gated recurrent residual neural network (GRRNet) for feature-based automatic modulation classification (AMC). The GRRNet model is shown to outperform the deep learning-based AMC models proposed in literature. The authors in [9] propose a hierarchical RNN architecture with grouped auxiliary memory to deal with the challenge of diminishing gradients for long temporal or spatial inputs when using long-short-term memory (LSTM) cells. The proposed hierarchical RNN architecture is shown to improve the AMC classification accuracy relative to the LSTM [10] and gated recurrent unit (GRU) [11] RNNs. The GRU is better suited for short temporal inputs [11], whilst the LSTM is suited for longer temporal inputs to a certain degree [10]. In [12-13], the authors develop RNN models to improve the classification accuracy of AMC. The authors in [14] develop a novel fading channel predictor using LSTM and GRU RNNs. It uses the strong temporal prediction capabilities of the GRU and LSTM RNNs to predict the channel fading. The prediction of channel fading helps to alleviate outdated channel state information (CSI).

Due to the benefits of delivering high spatial multiplexing gain over the Alamouti scheme, Golden code has the potential of being an STBC scheme of the future wireless standards provided the detection complexity can be reduced such that it is comparable or less than that of the Alamouti linear ML detector. Recently in [15], the authors propose sphere-decoding with sorted detection subsets (SD-SDS) to lower the detection complexity of Golden code. The SD-SDS algorithm is shown in [15] to have a detection complexity that is lower

than the detection complexity of the Schnorr-Euchner sphere-decoder (SE-SD) [16] and the sphere-decoding with increasing radius search (SD-IRS) [17].

Based on this, no literature has investigated the generation of the SD-SDS algorithm sorted detection subset (SDS) sequences using RNNs. It is interesting to investigate if it is possible for an RNN to learn how to generate accurate SDS sequences with marginal effect on the decoding latency of SD-SDS. This is what our paper will investigate and illuminate in this study. The accuracy of the SDS sequences will be tested using the bit-error-rate (BER) performance of the SD-SDS-DNN detection algorithm and decoding latency will be used to assess complexity.

The paper is organised as follows: Section II will present the system model, Section III will present the SD-SDS algorithm overview from [15], Section IV will exhibit the RNN algorithm architecture and training phase of the RNN, Section V is the simulation results and discussion of the paper, and Section VI concludes the paper.

Notation: Bold lowercase letters are used for vectors and bold uppercase for matrices. $(.)^T$ $(.)^H$, $\|.\|$ and $\|.\|_F$ represent the Transpose, Hermitian, Euclidean and Frobenius norm operations, respectively. The functions $\Re(.)$ and $\Im(.)$ are the real and imaginary components of a complex number, respectively. j is a complex number. The statistical average is represented by the expectation function $E(.)$. The function $(\cdot)^*$is the complex conjugate of a complex number.

II. SYSTEM MODEL

We consider a Golden code STBC system that operates over an $N_t \times N_r$ wireless MIMO configuration where $N_t = 2$ and $N_r \geq N_t$. The parameters N_t and N_r are the number of transmit and receive antennas in the MIMO configuration, respectively. The way Golden code operates is that information bitstreams are separated into 4 parallel streams. Each stream has bits packaged into $\log_2 M$ bit length words and mapped onto the M-QAM complex signal constellation Ω_M. This generates 4 M-QAM complex symbols that are transmitted over the air after being transformed into the following Golden code symbols.

Let x_{11}, x_{12}, x_{21} and x_{22} be the transmitted Golden Code symbols in which $x_{11} = \frac{\alpha}{\sqrt{5}}(x_1 + x_2\theta)$ and $x_{12} = \frac{\alpha}{\sqrt{5}}(x_3 + x_4\theta)$ and $x_{21} = \frac{\bar{\alpha}}{\sqrt{5}}(x_1 + x_2\bar{\theta})$ and $x_{22} = j\frac{\bar{\alpha}}{\sqrt{5}}(x_3 + x_4\bar{\theta})$. The scalar parameters $\alpha, \bar{\alpha}, \theta$ and $\bar{\theta}$ are defined as follows: $\alpha \triangleq 1 + j\,\bar{\theta}$, $\bar{\alpha} \triangleq 1 + j\,\theta$, $\theta = \frac{1+\sqrt{5}}{2}$ and $\bar{\theta} = \frac{1-\sqrt{5}}{2}$. The complex M-QAM symbols are $x_1, x_2, x_3, x_4 \in \Omega_M$, where Ω_M is an arbitrary M-QAM signal constellation. The average M-QAM symbol power is set to 1, $E\left(|x_q|^2\right) = 1, \forall q \in [1:4]$. Our research and results are limited to the square M-QAM signal constellation where $M = 2^{2n}\ \forall\ n \geq 1$.

Now we let the Golden Code transmission vector for timeslot $i, i \in [1:2]$ be $\boldsymbol{x}_i = [x_{i1}\ x_{i2}]^T$. Let $\boldsymbol{H}_i$ be the channel matrix for timeslot $i, i \in [1:2]$, where $\boldsymbol{H}_i \in \mathbb{C}^{N_r \times N_t}$ is a fast frequency-flat fading wireless channel which is perfectly estimated at the receiver side. The fast fading implies that the wireless channel changes for every transmission timeslot. The wireless channel fading gain is Rayleigh distributed and the complex fading gains are independent and identically distributed (i.i.d) according to the complex Gaussian distribution $\mathbb{C}N(0,1)$. The received signal vectors for timeslot $i, i \in [1:2]$ are given by

$$\boldsymbol{y}_i = \boldsymbol{H}_i\boldsymbol{x}_i + \boldsymbol{n}_i \tag{1}$$

where $\boldsymbol{y}_i \in \mathbb{C}^{N_r \times 1}$ is the received signal vector for timeslot i and $\boldsymbol{n}_i \in \mathbb{C}^{N_r \times 1}$ is the noise vector for timeslot i. Each entry of the complex Gaussian noise vectors, $\boldsymbol{n}_i$, is distributed according to $\mathbb{C}N(0, \sigma^2)$ where the average noise power $\sigma^2 = \frac{N_t}{\bar{\gamma}}$ and $\bar{\gamma}$ is the average SNR at each receive antenna.

III. GOLDEN CODE SD-SDS OVERVIEW

In [15], SD-SDS is introduced as a low complexity detection scheme for multiple complex symbol Golden code (MCS-GC). MCS-GC involves transmitting 2 or more complex M-QAM symbols inside a Golden code symbol over 2 or more timeslots. In our case, we are only dealing with the transmission of 2 M-QAM complex symbols per Golden code symbol over 2 timeslots. In [15], the authors propose representing the system model in an alternative form using 4 M-QAM symbols as the transmitted symbols per timeslot instead of 2 Golden code symbols. The Golden code Golden ratio θ, together with its algebraic conjugate and the scalar parameters α and $\bar{\alpha}$ are represented internally within the wireless channel matrices based on the equivalence relation shown in (2).

$$\boldsymbol{H}_i\boldsymbol{x}_i = \boldsymbol{H}_i\begin{bmatrix} x_{i1} \\ x_{i2} \end{bmatrix} = \widetilde{\boldsymbol{H}}_i\boldsymbol{u} \tag{2}$$

where $\boldsymbol{u} = [x_1 \quad x_2 \quad x_3 \quad x_4]^T$, $\widetilde{\boldsymbol{H}}_1 = \frac{1}{\sqrt{5}}\boldsymbol{H}_1\begin{pmatrix} \alpha & \alpha\theta & 0 & 0 \\ 0 & 0 & \alpha & \alpha\theta \end{pmatrix}$ and $\widetilde{\boldsymbol{H}}_2 = \frac{1}{\sqrt{5}}\boldsymbol{H}_2\begin{pmatrix} \bar{\alpha} & \bar{\alpha}\bar{\theta} & 0 & 0 \\ 0 & 0 & j\bar{\alpha} & j\bar{\alpha}\bar{\theta} \end{pmatrix}$. Wireless channel matrix $\widetilde{\boldsymbol{H}}_i \in \mathbb{C}^{N_r \times 2N_t}$ is the modified wireless channel matrices, for timeslot 1 and 2, that include the Golden code scalar parameters based on the equivalence relations in (2). The received signal vectors in (1), over timeslot 1 and 2, are combined using the methodology as determined in [15] to produce (3)

$$\boldsymbol{y} = \widetilde{\boldsymbol{H}}\boldsymbol{u} + \boldsymbol{n} \tag{3}$$

where $\widetilde{\boldsymbol{H}} = \left[\widetilde{\boldsymbol{H}}_1\ \widetilde{\boldsymbol{H}}_2\right]^T \in \mathbb{C}^{2N_r \times 2N_t}$, $\boldsymbol{y} = [\boldsymbol{y}_1\ \boldsymbol{y}_2]^T \in \mathbb{C}^{2N_r \times 1}$, and $\boldsymbol{n} = [\boldsymbol{n}_1\ \boldsymbol{n}_2]^{\boldsymbol{T}} \in \mathbb{C}^{2N_r \times 1}$.

To decode the transmitted M-QAM symbols x_1, x_2, x_3, x_4, SD-SDS is used based on the system model presented in (3). QR factorization is first performed on the modified wireless channel matrix $\widetilde{\boldsymbol{H}}$ such that we get (4)

$$\widetilde{\boldsymbol{H}} = \widetilde{\mathbf{Q}}\widetilde{\mathbf{R}} \tag{4}$$

The matrix $\widetilde{\mathbf{Q}} \in \mathbb{C}^{2N_r \times 2N_r}$ is a unitary matrix and matrix $\widetilde{\mathbf{R}} = \left[\widetilde{\boldsymbol{R}}_1\ \widetilde{\boldsymbol{R}}_2\right]^T \in \mathbb{C}^{2N_r \times 2N_t}$ has an upper triangular matrix $\widetilde{\boldsymbol{R}}_1 \in \mathbb{C}^{2N_t \times 2N_t}$ and also a zero matrix $\widetilde{\boldsymbol{R}}_2 \in \mathbb{R}^{(2N_r - 2N_t) \times 2N_t}$. The vector $\mathbf{z} = \widetilde{\mathbf{Q}}^H \boldsymbol{y} \in \mathbb{C}^{2N_r \times 1}$ is the modified received signal vector over 2-timeslots, which is given by (5)

$$\mathbf{z} = \widetilde{\mathbf{R}}\mathbf{u} + \widetilde{\mathbf{Q}}^H \boldsymbol{n} \tag{5}$$

SD-SDS Algorithm:

Step 1: *Determine the complex M-QAM symbol estimates using QR-decomposition. Estimate $\hat{x}_q$ where $q \in [1:4]$.*

$$\hat{x}_q = \frac{\boldsymbol{z}_q}{\widetilde{\boldsymbol{R}}_{q,q}}, q = 4$$
$$\hat{x}_q = \frac{\boldsymbol{z}_q - \sum_{l=q+1}^{4} \widetilde{\boldsymbol{R}}_{q,l} * \hat{x}_l}{\widetilde{\boldsymbol{R}}_{q,q}}, \forall q \in [3:1] \tag{6.1}.$$

where $\boldsymbol{z}_q$ is the q[th] scalar element stored in vector $\boldsymbol{z}$ and $\widetilde{\boldsymbol{R}}_{q,q}$ is the scalar element stored in the q[th] row and q[th] column of the matrix $\widetilde{\boldsymbol{R}}$.

Step 2: *Determine the Fixed SD-IRS initial radius*

From [15], the initial radius is calculated based on Equation. (28) in [17].

Step 3: *Create the sorted detection subsets*

Using the M-QAM estimates found in (6.1), sort the M-QAM signal constellation order for the symbols based on the Euclidean distance squared as shown in (6.2)

$$\mathrm{m}_q(\mathrm{i}) = \left|\hat{\mathrm{x}}_q - \mathrm{u}_i\right|^2, \forall\, \mathrm{i} \in [1:\mathrm{M}], \mathrm{u}_i \in \Omega_{\mathrm{M}} \tag{6.2}.$$

This implies that for each estimated M-QAM symbol, $\hat{\mathrm{x}}_q$, we need to find their associated sorted M-QAM symbol order of the $M - 1$ nearest neighbours. The symbol order is found by sorting, in ascending order, the whole M-QAM constellation symbol order based on the metric in (6.2). Furthermore, depending on the average SNR, a subset of the sorted M-QAM constellation symbol order is used for detection. The subset lengths (L) are determined in [15, Table 2]. In pseudo-code notation this is translated as follows in (6.3):

$$\mathrm{S_q} = sort\left(\mathrm{m_q(i)}\right)[1:\mathrm{L}] \tag{6.3}$$

where $\mathrm{S_q}, \forall q \in [1:4]$, are the L-dimensional sorted subsets used in the detection of the optimal estimated transmitted symbols $\mathrm{x}_1, x_2, \mathrm{x}_3$ and x_4.

Step 4: *Perform SD-IRS to determine candidates in hypersphere*

The lattice point candidates which are being searched for, using SD-IRS [17], must lie inside the hypersphere stated in (6.4)

$$\left\|\mathbf{z} - \widetilde{\mathbf{R}}\mathbf{u}\right\|_{\mathrm{F}}^2 \leq \mathrm{r}^2 \tag{6.4}$$

where r is the fixed initial radius determined in Step 2. The SDS found in Step 3 are used to search for these lattice point candidates that satisfy (6.4).

IV. SD-SDS-DNN DETECTION ALGORITHM

In this section, we train an RNN to learn how to accurately generate the SDS sequences determined in Step 3 of Section III of the SD-SDS algorithm. The RNN will act as a function approximator, $\boldsymbol{\epsilon} = f(\boldsymbol{\pi})$, that will predict the SDS integer sequences, given by vector $\boldsymbol{\epsilon}$, based on a given input vector $\boldsymbol{\pi}$. The RNN model's objective is to be a function approximator that takes, as an input, any estimated M-QAM complex symbol from Step 1 of the SD-SDS algorithm, i.e $\hat{x}_q\ \forall q \in [1:4]$, and then predict the sorted sequence of all the M-QAM symbols in the constellation for each estimated M-QAM symbol presented as an input.

For the RNN architecture, we choose a unidirectional RNN architecture because the ordered M-QAM symbol indices generated in Step 3 of Section III have an association relationship amongst them. When an M-QAM symbol index is chosen as the first element in an ordered list, the indices chosen subsequently after that cannot include previously chosen indices because the indices are unique in the ordered list. Thus, the RNN must only remember the previously chosen symbol indices and avoid re-choosing them when coming up with the ordered integer list. This association relation is only in one direction as the already chosen symbol indices do not have knowledge of the indices that will be chosen in future,

The RNN is trained over a wide range of SNR values with the estimated M-QAM complex symbols used as training inputs. Because we are dealing with predicting an ordered sequence of M-QAM symbol indices, this problem is a sequence-to-sequence prediction problem. The various neural network architectures which were entertained to attempt to solve this sequence-to-sequence prediction problem were as follows:

1. GRU [11] neural network architecture
2. LSTM [10] neural network architecture
3. Temporal Convolutional Network (TCN) architecture [18]

We found from experimentation that for our specific problem, the GRU yields better validation accuracy performance than the LSTM and TCN neural networks for modulation orders that are less than or equal to 16-QAM modulation. For the 64-QAM case, we found that the LSTM performs better than the TCN and GRU architectures for predicting 30 sorted sequences of M-QAM symbol indices. For training the sequence-to-sequence architectures above, in the case of M-QAM modulation, a $T \times 2$-dimensional input training matrix is created. Because the estimated complex M-QAM symbols experience complex fading and noise perturbations from i.i.d complex Gaussian processes, we train the RNN using input data from an arbitrary complex M-QAM symbol. We choose the estimated complex M-QAM symbol $\hat{x}_1$ as input without loss of generality. Recall that the estimated M-QAM symbol $\hat{x}_1$ is a complex number which represents the distorted M-QAM signal amplitude and phase.

It is known that an RNN only takes real numbers as an input and the in-phase (Real component) and quadrature (Imaginary component) components of the estimated complex M-QAM symbol $\hat{x}_1$ are on the same scale. As a result, no input data scaling is necessary. The input matrix of the RNN is comprised of the real and imaginary components of the estimated complex M-QAM symbol $\hat{x}_1$, repeated T times, to form the $T \times 2$-dimensional input matrix shown in (7)

$$\boldsymbol{\pi} = [[\Re(\hat{x}_1), \Im(\hat{x}_1)]_1, \cdots, [\Re(\hat{x}_1), \Im(\hat{x}_1)]_T] \in \mathbb{R}^{T \times 2} \quad (7)$$

The dimension size of T is the number of timesteps in the RNN architecture. In our examples, we are training for $T = 4, T = 8$, $T = 16$ and $T = 30$ to cater for 4-QAM, 8-QAM, 16-QAM and 64-QAM sequence-to-sequence predictions, respectively. We use $T = 30$ for 64-QAM because of practical limitations of training a $T = 64$ LSTM on modest processor units. In [15, Table 2], 30 sorted index sequences are sufficient for near-optimal 64-QAM BER performances for 10dB to 22dB SNR. Since this is supervised learning, our output training labels are put into ordered sequences that match those of the sorted M-QAM symbol indices determined in Step 3 of the SD-SDS algorithm for each estimated M-QAM complex symbol. Each of the M-QAM integer symbol indices are converted into an M-dimensional one-hot-vector and added to a T-dimensional vector based on the sequence ordering. This then creates an output label $T \times M$ training integer matrix as shown in (8)

$$\boldsymbol{\beta} = [[0,0,0,1,0,0, \ldots, 0]_1 \ldots, [0,0,0,0,0,1, \ldots, 0]_T] \in \mathbb{Z}^{T \times M} \quad (8)$$

The real-valued input training matrix in (7) is fed into the RNN architecture shown in Table I. The output of the RNN is compared to the true output target ordered sequence matrix $\boldsymbol{\beta}$ in (8). The overall training data sample sizes for 4-QAM, 8-QAM, 16-QAM and 64-QAM are 4000, 8000, 16000 and 64000, respectively. The training sample is 75% of the overall training sample size and the remaining 25% unseen sample is the test sample. The RNN is trained from high SNR to low SNR ranges that cover the BER simulation SNR values for each of the modulation orders. Each M-QAM modulation order has its own independently trained RNN architecture based on Table I with the associated architecture values T and M set accordingly. M in this case is the M-QAM modulation order.

The RNN architecture in Table I is trained to minimize the categorical-cross-entropy loss function using the ADAM optimizer [19]. For our case, we are using the Table I architecture for 16-QAM or lower modulation orders ($M \leq 16$) with a GRU cell and for 64-QAM ($M = 64$) sorted detection subset predictions we use the Table I architecture with an LSTM cell. We know from the literature that GRU networks perform well in predicting short sequences [11], and LSTM networks perform better than GRU networks in predicting longer sequences [10]. The pseudo-random seed value, learning rate and batch size hyperparameters are tuned using a meta-heuristic agent based Genetic algorithm [20] with the fitness function reliant on the validation accuracy metric.

TABLE I
RNN SORTED DETECTION SUBSET PREDICTOR ARCHITECTURE

Layer	**Parameter Description**
Input	$T \times 2$ input data dimension
(Input Layer) (GRU or LSTM) + Hyperbolic Tangent (Return_Sequences=True)	$8 \times T$ units.
BatchNormalization	void
Dropout	Probability of 0.2
(Hidden Layer) (GRU or LSTM) + Hyperbolic Tangent (Return_Sequences=True)	$8 \times T$ units
BatchNormalization	void
Dropout	Probability of 0.2
(Output Layer) TimeDistributed+Dense+Softmax	M neurons with T timesteps
Batch Size=200, Learning Rate=0.00033, Seed Value=23, and Maximum Epochs=2000	

The trained RNN architecture in Table I is used in the SD-SDS algorithm in Section III to replace step 3 of the algorithm and this modified SD-SDS algorithm is named the SD-SDS-DNN.

V. SIMULATIONS AND DISCUSSIONS

The Monte-Carlo wireless simulation environment is setup as a 2×4 MIMO, where $N_t = 2$ and $N_r = 4$, with a wireless channel with Rayleigh frequency-flat fast fading in which the channel gain changes per transmission timeslot. The wireless transmit and receive antennas are sufficiently spaced enough such that the wireless channels are de-correlated. The information symbol modulation orders used in the simulation are the 4-QAM, 8-QAM, 16-QAM and 64-QAM. The average power constraint for the M-QAM symbols is set to 1. The SD-IRS fixed initial radius probability is set to ε=0.995 for 4-QAM, 8-QAM, 16-QAM and ε=0.9999 for 64-QAM. The Monte-Carlo simulation determines the BER and decoding latency performance, from low to higher M-QAM modulation orders, for the two detection algorithms SD-SDS and SD-SDS-DNN. The decoding latency is measured for the two detection algorithms under the same computer platform.

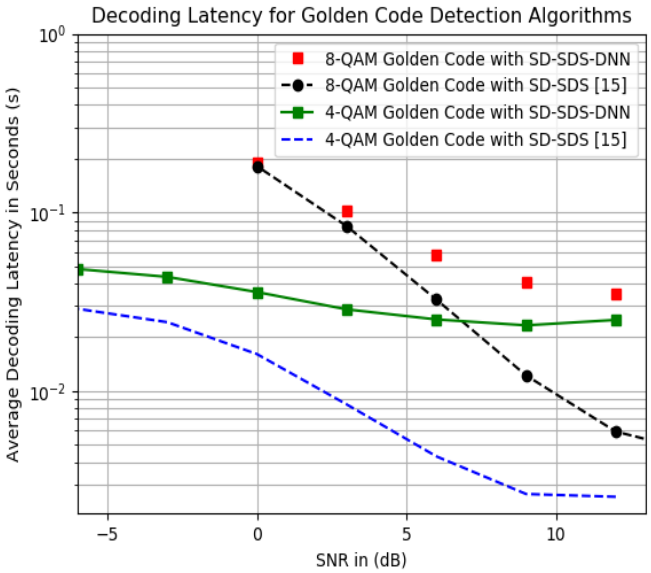

Figure 1: Decoding Latency of 2×4 MIMO 4-QAM and 8-QAM Golden Code Sphere-Decoding Detection Algorithms.

From Fig. 1, we can see that at high SNR, for both 4-QAM and 8-QAM baseband modulation, the decoding latency of the SD-SDS-DNN algorithm is orders of magnitude greater than that of the SD-SDS algorithm. This is because at high SNR, the search radius for the sphere-decoder is much smaller than at lower SNR values. The reason for a smaller search radius at higher SNR is because the search radius is directly proportional to the average noise variance [17] which is inversely proportional to the average SNR. The smaller the search radius is, the lower the number of lattice points that lie inside the hypersphere of the sphere-decoder [17]. The number of lattice points found inside the hypersphere is proportional to the detection complexity or latency of the sphere-decoding algorithm. Since the sphere-decoding detection latency is much lower at higher SNR, the source of the high detection latency for the SD-SDS-DNN algorithm is the propagation delay due to the RNN function approximator.

At lower SNR values, the sphere-decoding latency starts to increase drastically because the search radius is much larger at lower SNR values. This increases the resultant number of lattice points found inside the hypersphere and hence the decoding latency increases. At low SNR values, the dominant source of the high detection latency, for SD-SDS, is the sphere-decoder as opposed to the closed form SDS generator in Step 3 of Section III. That is the reason why the decoding latency of the SD-SDS algorithm, at low SNR, starts to dramatically increase approaching that of the SD-SDS-DNN algorithm.

If we look at Fig. 2, we see a tight BER performance between the SD-SDS and SD-SDS-DNN detection algorithms for 4-QAM and 8-QAM baseband modulation. This implies that the RNN function approximator was able to accurately predict the SDS sequences for both the 4-QAM and 8-QAM modulation.

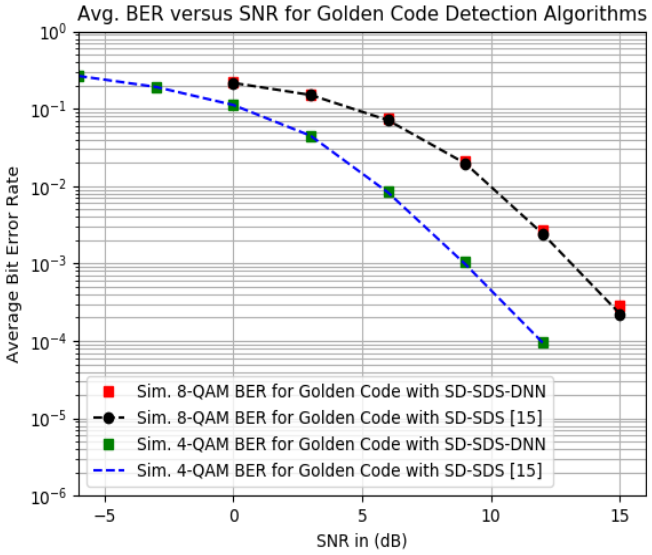

Figure 2: BER for 2×4 MIMO 4-QAM and 8-QAM Golden Code Sphere-Decoding Detection Algorithms.

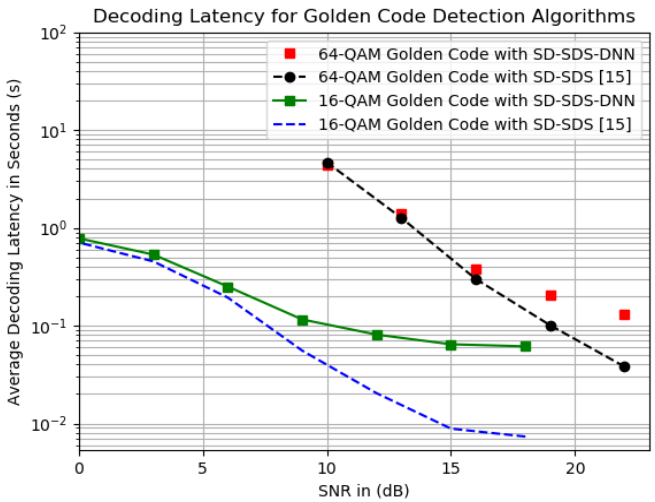

Figure 3: Decoding Latency of 2×4 MIMO 16-QAM and 64-QAM Golden Code Sphere-Decoder Detection Algorithms.

If we look at Fig. 3, we observe a similar trend to the detection latency results exhibited in Fig. 1. The SD-SDS detection latency approaches that of the SD-SDS-DNN algorithm at low SNR values for the same reasons advanced previously for the 4-QAM and 8-QAM case. What this tells us is that there is no detection latency difference between the SD-SDS and SD-SDS-DNN algorithms when the sphere-decoder detection complexity is much greater than that of the SDS RNN function approximator. This implies that we can use the SDS RNN function approximator when we either have higher dimensional MIMO ($N_t \gg 2$), which increases the sphere-decoder search depth and radius since $r^2 \propto \sigma^2$, and/or when the transmitter uses very high modulation orders like 512-QAM or 1024-QAM. The large modulation orders increase the sphere-decoder search breadth. Higher sphere-decoder search breadth or depth implies higher detection complexity. We also notice that at higher SNR values, for higher modulation orders, the detection latency gap between SD-SDS and SD-SDS-DNN is lower than at lower modulation orders. This further supports our argument that the SDS RNN function approximator can be used in situations where the sphere-decoder detection complexity is very large.

Fig. 4 shows a slight loss in diversity, at high SNR, for the 64-QAM modulation order because of the possibility of sub-optimal Genetic Algorithm hyperparameter tuning. For 16-QAM, the BER performance is tight between SD-SDS and SD-SDS-DNN and signifies that the RNN successfully generated accurate SDS sequences as per 4-QAM and 8-QAM.

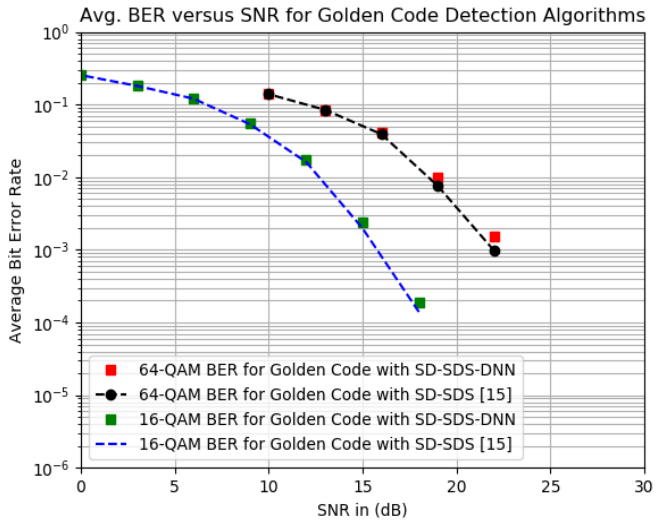

Figure 4: BER for 2×4 MIMO 16-QAM and 64-QAM Golden Code Sphere-Decoding Detection Algorithms.

VI. CONCLUSION

We showcased the power of RNN and its ability in predicting integer sorted detection subset sequences for lower to higher M-QAM modulation orders. The results show that the RNN accurately predicted the SDS sequences for lower modulation orders, $M \leq 16$, but at the cost of higher detection latency at high SNR regions. At lower SNR regions, the detection latency between SD-SDS and SD-SDS-DNN was comparable. At higher modulation orders, $M > 16$, there was a slight loss in diversity due to possible sub-optimal hyperparameter tuning. The RNN SDS technique can be used as an alternative in situations where the wireless transmitter uses lower modulation orders, $M \leq 16$, and the MIMO configuration is very large, $i.e\ N_t \gg 2$.

REFERENCES

[1] J. Belfiore, G. Rekaya and E. Viterbo, "The golden code: a 2 x 2 full-rate space-time code with non-vanishing determinants", International Symposium on Information Theory, ISIT 2004. Proceedings., Chicago, IL, 2004, pp. 310-310, 2004

[2] S. M. Alamouti, "A simple transmit diversity technique for wireless communications," IEEE Journ. Sel. Areas Commun., vol. 16, no. 8, pp.1451-1458, 1998.

[3] V. Torakh, H. Jafarkhani, A. R. Calderbank, "Space–Time Block Codes from Orthogonal Designs", IEEE Transactions on Information Theory, vol. 45, no 5, July 1999.

[4] F. Riera-Palou and G. Femenias, "Improving STBC Performance in IEEE 802.11n Using Group-Orthogonal Frequency Diversity", IEEE Wireless Communications and Networking Conference, Las Vegas, NV, pp. 193-198, 2008

[5] "IEEE Standard for Information technology--Telecommunications and information exchange between systems - Local and metropolitan area networks--Specific requirements," in IEEE Std 802.11ah-2016, vol., no., pp.1-594, 2017

[6] N. Sharma, "Space Time Block Code for Next Generation Multi-user MIMO System", 9th International Conference on Future Networks and Communications, Procedia Computer Science, pp. 172-179, 2014

[7] M. O. Sinnokrot and J. R. Barry, "Fast maximum-likelihood decoding of the Golden code", IEEE Trans.Wireless Commun., vol. 9, no. 1, pp. 26_31, 2010

[8] S. Huang *et al.*, "Automatic Modulation Classification Using Gated Recurrent Residual Network", IEEE Internet of Things Journal, vol. 7, no. 8, pp. 7795-7807, 2020

[9] K. Zang and Z. Ma, "Automatic Modulation Classification Based on Hierarchical Recurrent Neural Networks With Grouped Auxiliary Memory", IEEE Access, doi: 10.1109/ACCESS.2020.3039543.

[10] S. Hochreiter; J. Schmidhuber, "Long short-term memory", Neural Computation. **9** (8): 1735–1780, 1997

[11] C. Kyunghyun, V. Merrienboer, B. G. Caglar, B. Dzmitry, B. Fethi, S. Holger, B. Yoshua, "Learning Phrase Representations using RNN Encoder-Decoder for Statistical Machine Translation", arXiv:1406.1078, 2014

[12] D. Hong, Z. Zhang and X. Xu, "Automatic modulation classification using recurrent neural networks", 2017 3rd IEEE International Conference on Computer and Communications (ICCC), Chengdu, pp. 695-700, 2017.

[13] R. Utrilla, E. Fonseca, A. Araujo and L. A. Dasilva, "Gated Recurrent Unit Neural Networks for Automatic Modulation Classification with Resource-Constrained End-Devices", IEEE Access, vol. 8, pp. 112783-112794, 2020.

[14] W. Jiang and H. D. Schotten, "Deep Learning for Fading Channel Prediction", IEEE Open Journal of the Communications Society, vol. 1, pp. 320-332, 2020.

[15] H. Xu and N. Pillay, "Multiple Complex Symbol Golden Code", IEEE Access, vol. 8, pp. 103576-103584, 2020**.**

[16] L. Zhang, B. Li, T. Yuan, X. Zhang, and D. Yang, "Golden code with low complexity sphere decoder", in Proc. 18th Int. Symp. Pers. Indoor Mobile Radio Commun., pp. 1-5, 2007.

[17] B. M. Hochwald and S. ten Brink, "Achieving near-capacity on a multiple-antenna channel", IEEE Trans. on Commun., vol. 51, no. 3, pp. 389-399, 2003.

[18] S. Alla, S. K. Adari, "Temporal Convolutional Networks. In: Beginning Anomaly Detection Using Python-Based Deep Learning", Apress, Berkeley.

[19] D. B. J. Kingma, "Adam, a method for stochastic optimization", 2014.

[20] D. E. Goldberg, "Genetic Algorithms in Search, Optimization and Machine Learning", Reading, MA, USA: Addison-Wesley, 1989

Bhekisizwe Mthethwa received the BScEng Electronics degree from the University of KwaZulu-Natal in 2008 and the MScEng Electronics degree in 2013 from the same institution. He is currently pursuing his PhD in deep learning assisted wireless communications.

The Impact of Application-based Downlink Traffic in LoRaWANs

Jaco Morné Marais*, Adnan M. Abu-Mahfouz*†, Gerhard P. Hancke*‡
*Department of Electrical, Electronic and Computer Engineering, University of Pretoria, Pretoria 0028, South Africa
[1]jaco.marais@tuks.co.za
†Council for Scientific and Industrial Research, Pretoria 0084, South Africa
[2]a.abumahfouz@ieee.org
‡Nanjing University of Posts and Telecommunications, Nanjing 210023, China
[3]g.hancke@ieee.org

***Abstract*—A popular technology used for deploying Internet of Things (IoT) networks is Long Range Wide Area Network (LoRaWAN). These networks are designed for large scale deployments but the Quality of Service (QoS) levels achievable depends on the traffic volume and profile generated by the IoT use case(s). LoRaWANs are sensitive to the presence of downlink traffic (from a gateway to an end-device) which has two primary sources namely acknowledgements (ACKs), and application-based downlink traffic. This paper investigated the impact of application-based downlink traffic on the scalability of LoRaWANs. Simulations showed that confirmed traffic harms the performance of uplink traffic with both being dependent on the network packet arrival rate. The addition of application-based downlink traffic further decreases the performance of both unconfirmed and confirmed traffic. The packet size of generated application-based traffic did not have a major impact on unconfirmed traffic but larger packets did negatively influence the performance of confirmed traffic as gateway duty cycle limitations were reached quicker. This prevented gateways from sending ACKs when required.**

***Index Terms*—LPWAN, IoT, LoRaWAN**

I. Introduction

The LoRa Wireless Area Network (LoRaWAN) protocol has found favour with the Internet of Things (IoT) community due to its ability to provide city-wide coverage with only a few gateways [1]. This Low Power Wide Area Network (LPWAN) technology operates in the unlicensed Industrial, Scientific and Medical (ISM) bands and offers support for a variety of IoT use cases [2], [3].

A network's ability to support a large number of devices is dependant on overall traffic volumes with Downlink (DL) traffic (packets from a gateway to an end-device) having a large impact on scalability [4], [5]. Most IoT use cases generate mainly Uplink (UL) traffic (end-device to gateway) and thus the protocol was optimised to handle large volumes of this type of traffic.

LoRaWAN gateways are half-duplex, meaning that they cannot transmit and receive simultaneously. As a result, a gateway will miss uplink transmissions whilst it is sending any downlink traffic.

DL traffic is generated by three sources: network administration, sending of Acknowledgements (ACKs) to end-devices and messages to the end-device generated by the application server. The first source is unavoidable and consists of Medium Access Control (MAC) commands being exchanged between the Network Server (NS) and the MAC layer of an end-device [6]. The second source is dependent on whether any end-devices are configured to require ACKs for their uplink packets. The third source is the focus of this paper and consists of data that must be sent, potentially periodically, to applications on end-devices due to the IoT use case the network was deployed for.

In general, LoRaWAN research focuses on uplink only networks or the study of ACKs. Attention to the impact of application-based downlink traffic was however given in [7] and [4] which found that DL application traffic harms especially the success of confirmed UL traffic.

The work presented here seeks to further explore the impact of application-based downlink traffic on network performance as well as determine the factors that cause network performance to suffer. In small networks, the presence of downlink traffic is not an issue as gateway Duty Cycle (DC) restrictions are not easily reached. This paper thus focuses on the impact that this type of downlink traffic has on congested networks, i.e. large networks with high traffic volumes.

The paper is organised as follows. Related works are discussed in Section II, and a background on LoRaWANs are provided in Section III. Information on the simulator used and the scenario examined are given in Section IV. Results and discussions can be found in Section V. Finally, a conclusion is presented in Section VI.

II. Related Work

A scalability analysis of LoRaWANs was conducted in [4] for which an ns-3 module was developed. Matlab simulations were first conducted to develop an error model for the Long Range (LoRa) physical layer of these networks with simulations conducted with one, two and four gateway networks. Only one upstream channel was enabled for end-devices with end-devices sending eight byte payloads.

Analysis of simulations showed that the main cause of unconfirmed traffic not being delivered was collisions caused by the gateway already receiving a packet using the same data rate. The researchers noted that the packet delivery ratio of

confirmed traffic is not always higher than unconfirmed traffic as at higher traffic loads the gateway cannot transmit an ACK due to DC restrictions [4].

Application-based downlink data was investigated with eight bytes being sent, on average, either every ten or hundred upstream packets. As expected, the presence of application traffic negatively impacts the performance of confirmed traffic as the probability of conflict for a gateway's limited resources for downlink transmissions is increased. Unconfirmed traffic had an increase in transmissions that were not received, due to the gateway sending increased transmissions. Deploying more gateways was an effective solution as downlink responsibilities could be shared amongst them, allowing gateways to spend more time in receiving mode [4].

The impact of downlink traffic was also examined in [7] through the creation of LoRaWANSim. The impact of application downlink only, a percentage of device requiring ACKs and the combination of these two factors were studied.

Simulations of large networks showed that a gateway is often not able to transmit downlink packets due to DC restrictions. Furthermore, end-devices are recommended to switch to lower data rates when retrying confirmed messages. This will result in the corresponding ACK being sent at a lower data rate than was required by the distance between the gateway and the end-device, increasing the time on air of the response unnecessarily [7].

The authors also note that the optimum number of transmissions allowed (NbTrans) depends on the balance between a network's traffic load and energy consumption [7].

III. Background

LoRaWAN is an open MAC protocol developed by the LoRa Alliance for use with the LoRa physical layer employing a novel Chirp Spread Spectrum (CSS) modulation technique. LoRa enables these networks to have large link budgets with communication range dependent on several parameters such as Spreading Factor (SF), Bandwidth (BW) and Coding Rate (CR). The LoRaWAN protocol defines several Data Rates (DRs) which are combinations of these parameters and offers a trade-off between range, energy consumption and bit rate.

Due to a LoRaWAN gateway's multiple receiver paths, an SX1301 chip has eight, a gateway could potentially lose more than one uplink as any ongoing receptions will be aborted [4].

The LoRaWAN protocol offers three devices classes to accommodate different types of applications. Class A end-devices (the most common) will open two receive windows after sending a transmission. The gateway must send any scheduled downlink traffic, such as an ACK, in one of these two windows and would have to wait for the next uplink from this device if it was unable to do so. An end-device will retransmit a packet that requires confirmation if an ACK was not received and the maximum number of transmissions (NbTrans) has not yet been reached [6].

The first receive window is opened at the same frequency and, by default, at the same DR as the last uplink whilst the second window is opened at a fixed frequency and the lowest DR [8]. As a result, the first window is the preferred option as it is probable that a high DR can be used which minimises the duration of downlink transmissions. For both windows, duty cycles will apply to the sub-band used for downlink transmissions and could force a gateway to either have to use the second window or be unable to transmit at all.

The protocol does allow the data rate used by the second window to be changed using the RXParamSetupReq MAC command. Researchers have suggested that the protocol should not use the lowest DR as the default value as the use of the second window is more likely the result of DC restrictions rather than low link quality [4], [9].

LoRaWANs operate with a star-of-star topology with gateways forwarding packets to a central NS. This server is responsible for managing devices and is a two-way portal between an application server and the applications running on end-devices.

Supporting downlink traffic allows the LoRaWAN protocol to support a wide range of IoT use cases with unique Quality of Service (QoS) requirements [2], [5]. This allows not only acknowledgements to be sent for important data packets in use cases such as smart metering but also for position update requests to be sent in vehicle fleet tracking applications [10]. Additional application-based downlink traffic can occur when devices need to alerted that an event occurred or when updates to application parameters such as the sampling interval are required [4].

IV. Simulation setup and scenario

This work was conducted by adding support for application-based downlink unconfirmed traffic to the popular open-source ns-3 module LoRaWAN [11]. This simulator was chosen as it has been well-documented [12] and already supported downlink traffic in the form of ACKs [13].

The chosen simulation scenario is that of a single Gateway (GW) servicing 1200 end-devices who periodically generate packets with an equal period but with a random initial delay in the first period. This allows a simulation to target a specific overall network arrival rate (in packets per second) as results are presented for a range of traffic volumes. The network was configured for the European region and only uses the default channels. SF assignment was disabled and the module's SetSpreadingFactorsUp function allocated an optimum SF for each device based on distance. Results were gathered by averaging over 20 simulations using the "sem" framework for managing ns-3 simulation campaigns [14].

End-devices were configured to generate packets with an initial size of 10 Bytes to which a random additional value between 2 to 8 bytes was added. This was done so that simulations reflect a network in which not all devices necessarily send identical data. Devices only send unconfirmed traffic except in some simulations where 15 % percentage of devices

were chosen to rather only send confirmed traffic. Every time the NS received 5 uplink packets from a device, the application server would send the device a packet containing either 10 or 45 bytes of application data. These downlink packets were sent as unconfirmed downlinks (no ACK required from end-device).

An adaptation of the methods given in [15] was used to calculate performance metrics. With unconfirmed traffic, a packet was considered successful if it was received by a GW who forwarded it to the NS. Confirmed packet success has two elements namely whether the uplink packet was received successfully and the second being if the corresponding ACK was received by the end-device. As a result, a network's uplink performance could only be measured by examining unconfirmed traffic or by also measuring if confirmed packets were received.

For this work the two performance metrics used were:

- Confirmed Packet Success Ratio (CPSR): the probability that a confirmed uplink packet was received by a gateway and that the corresponding ACK was received by the end-device.
- Uplink Packet Ratio (ULPDR): the probability that an uplink unconfirmed packet was successfully received. Confirmed traffic is thus excluded (unlike the case in [15]).

The impact of application-based downlink traffic can only be seen in networks in which these additional transmissions have a measurable effect. A network must thus have sufficient traffic volumes so that uplink packets will be missed due to the half-duplex nature of GWs. Experimentation has shown that this volume is reached when packet arrival rates (λ) exceed 10^{-2} packets per second. Numpy's logspace function was used to generated arrival rates spaced evenly on a log scale. A summary of the simulation parameters as well as other details on simulation methodology is provided in Table I.

TABLE I
SIMULATOR PARAMETERS IN A "LORAWAN" MODULE SCRIPT.

Variable	Interval
Number of EDs	1200
Number of GWs	1
Radius (m)	6300,
Base packet size (Bytes)	10
Random element (Bytes)	[2, ..., 8]
Application downlink packet size (Bytes)	[10, 45]
Percentage of devices using confirmed traffic (%)	[0, 15]
Interval between application downlink packets	5 received
Simulation duration	50 periods
Realistic Channel Model used? (realisticChannelModel)	False
Number of Transmissions (NbTrans)	1

V. RESULTS AND DISCUSSION

Simulations were conducted to first investigate the impact of downlink traffic generated by ACKs before moving on to examining the impact of adding application-based traffic.

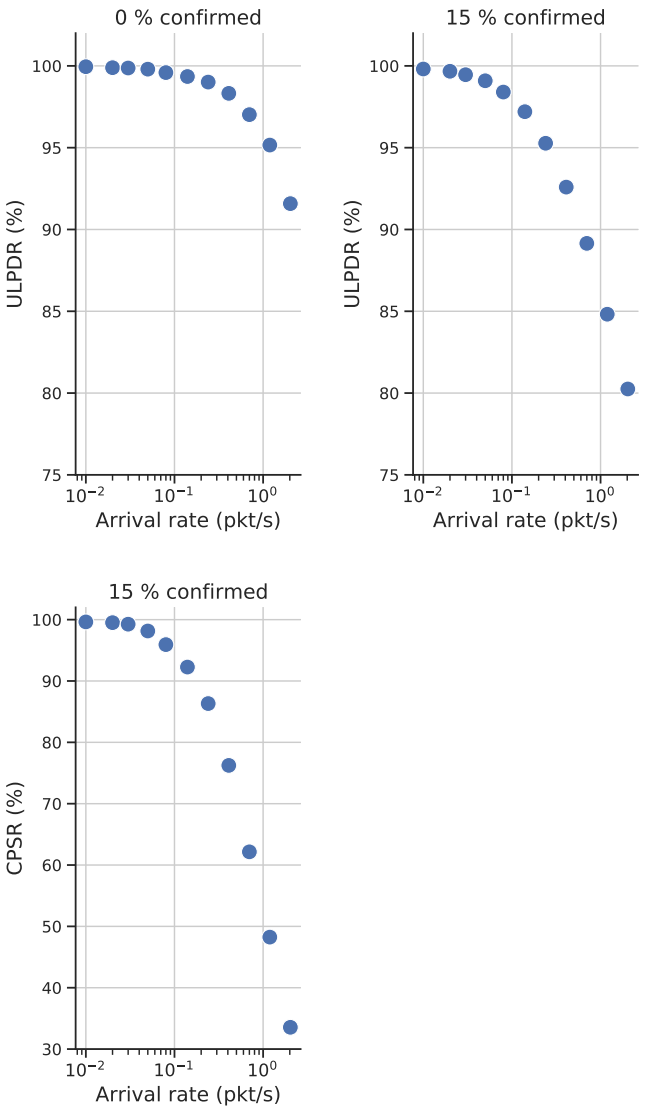

Fig. 1. Performance impact of adding confirmed traffic, examined over several arrival rates. Note that different y-axis were used.

A. Impact of Acknowledgements

Fig. 1 shows the impact of confirmed traffic on the success ratio of unconfirmed packets. The impact is minimal at low arrival rates but increases sharply as an increasing amount of uplink transmissions are missed due to gateway transmissions.

Simulations were conducted with NbTrans equal to one, and as a result, the performance of confirmed traffic drops sharply at arrival rates greater than $10^{-}1$. At these arrival rates, the gateway is frequently unable to transmit ACKs, due to DC restrictions. Devices are restricted to only one uplink transmission and thus their packets are recorded as unsuccessful.

B. Impact of various downlink application sizes

A decrease in the performance of unconfirmed and confirmed traffic due to application-based downlink traffic can be seen in Fig. 2. Note that the minor differences between 10 and 45 bytes in the case of zero application-based downlinks

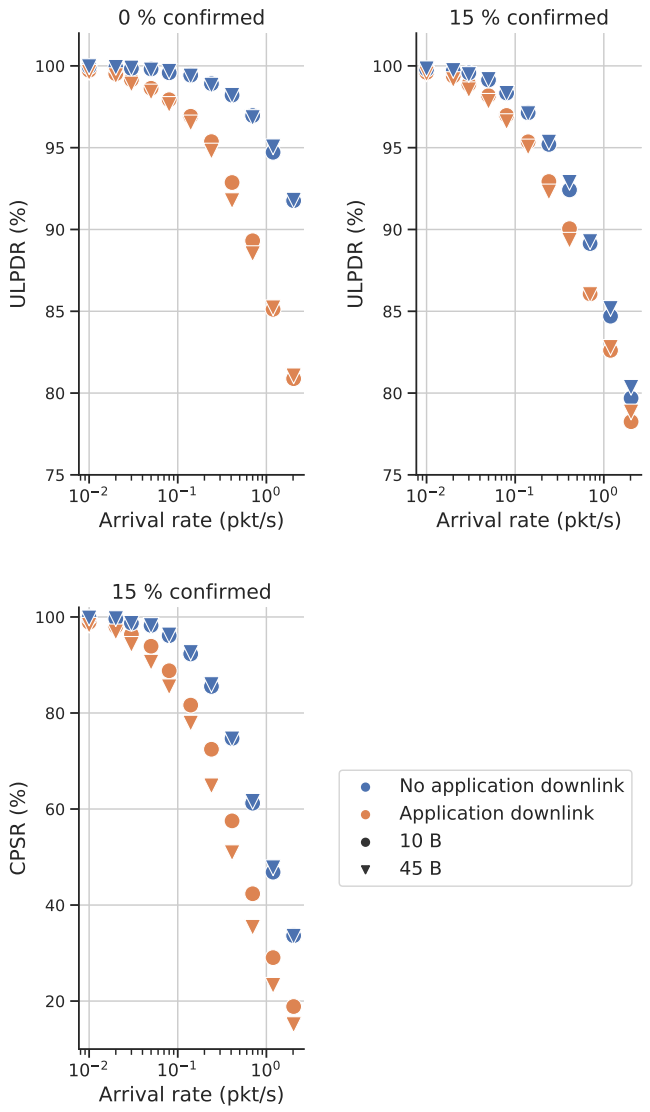

Fig. 2. Performance of the network when sending either 10 B or 45 B of application-based downlink packets for every 5 received uploads.

is due to variations in the distances between devices and the gateway between simulation runs. Averaging over a higher amount of simulations would further decrease this difference at the expense of requiring additional computational time.

For unconfirmed traffic only networks, downlink application packets in low arrival rate networks result in a minor decrease in performance as downlink transmissions remain infrequent. At higher arrival rates, uplink transmissions are increasingly lost due to gateway transmissions, i.e. less time being spend in receiving mode.

The addition of application-based downlink traffic results in a negative impact for both unconfirmed and confirmed traffic in the case of a network with 15% confirmed traffic. The NS will combine any pending application-downlink data with an ACK (if required) into one downlink packet scheduled for either the first or the second receive window. The first window would be preferred, as the packet is sent using the same data rate as the previous uplink packet. If no window is available, due to DC restrictions on either option's sub-channels, no transmission will be made and the uplink packet would be recorded as a failure if it was a packet that required confirmation.

The size of the data generated by the application server did not have a significant impact on ULPDR but did have a larger impact on the network's CPSR. Larger payloads require longer transmission times and result in DC restrictions being reached quicker. This can result in the gateway being forced to use window two as window one's subband is DC restricted. The use of window two is not ideal as for example, transmitting 45 bytes using SF12 (the lowest data rate) takes 2.6 s compared to only 113 ms using SF7 (the fast data rate). This will occur if the first window is unavailable or if the device was a considerable distance from the gateway and was thus required to use SF12 for all uplinks and downlinks.

Once a gateway has reached the DC restrictions in one or more sub-bands it would be unable to send some/all downlink traffic, allowing it to successfully receive more uplink traffic. This situation boosts the performance of ULPDR as packets are less likely to be lost due to gateway transmissions [16].

C. *Examining the cause of packet loss*

To better understand the decreases in performance, the causes of packet loss was plotted in Fig. 3. In the unconfirmed only network, higher arrival rates correspond to an increase in packets interfering with one another. Introducing downlink traffic in such a network causes uplink packets to be lost due to gateway transmissions even at low arrival rates. A reduction in packets being lost due to interference occurs at higher arrival rates, due to packets now rather being lost due to gateway transmissions.

In the 15% confirmed network's case, uplink packets are lost regardless of application downlink traffic due to the transmission of ACKs. The addition of application traffic increases packets lost due to increased transmissions with some packets still being lost due to interference. Larger application payloads result in more packets being lost due to their transmission at low arrival rates. At higher arrival rates, 10 byte payloads cause more packet losses compared to 45 byte payloads. This reversal is caused by the fact that the longer transmission times (for 45 bytes) cause DC restrictions to be reached earlier, resulting in the gateway transmitting fewer packets. This ultimately causes fewer packets to be lost due to transmissions.

Excessive downlink application traffic impacts the network as a whole as it impacts the sending of ACKs as well as other downlink messages required by the protocol such as LinkADRReqs.

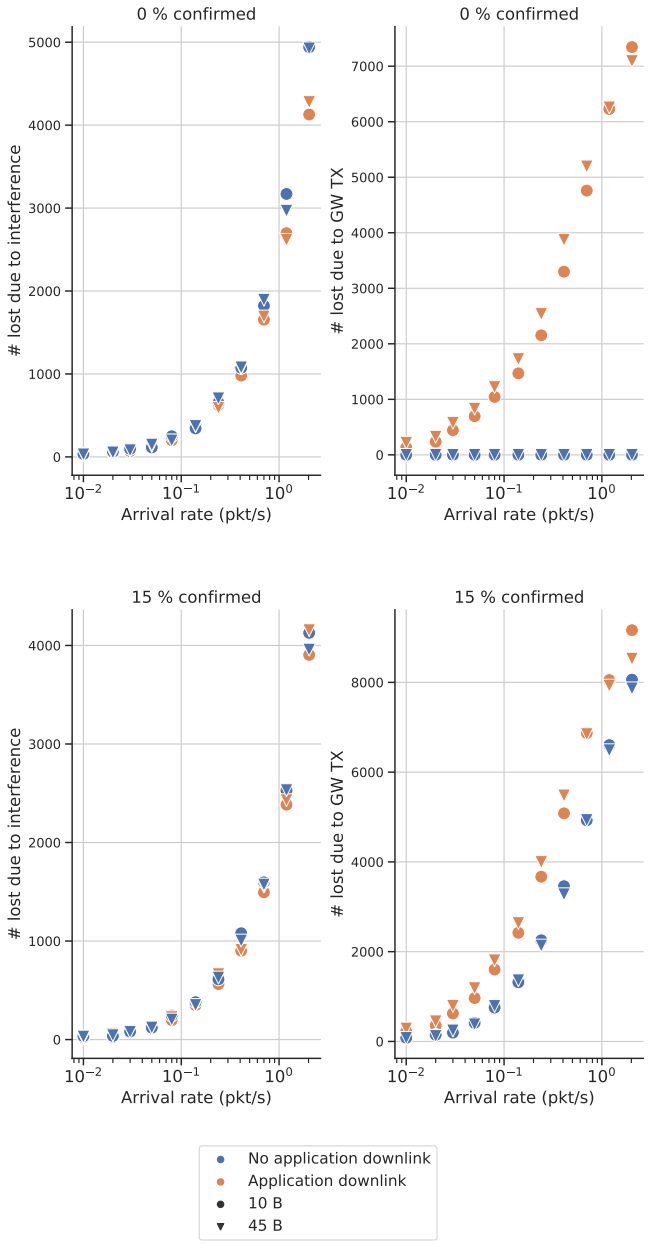

Fig. 3. The causes of packet loss in networks with application-based downlink traffic.

VI. Conclusion

This paper explored the performance impact of application-based downlink traffic in LoRaWANs. It was found that its impact was larger on confirmed traffic than unconfirmed as the additional downlink transmissions cause gateways to reach their DC restrictions sooner, thus limiting the time available for ACK transmissions. Unconfirmed traffic is still impacted, as packets are lost due to gateway transmissions resulting in gateways spending less time in receiving mode. The size of the application data does not significantly influence the reduction for ULPDR but for CPSR the larger packets further increase the airtime used by downlink transmissions.

In the future, this work could be expanded by investigating ways to reduce the negative impact of application-based downlink traffic. One suggestion is that the second receive window rather uses the same data rate as window one or a data rate derived from the most recently received packet's data rate. This would ease the impact of DL traffic on DC restrictions whilst still compensating for far away devices.

Acknowledgement

This research was supported by the Council for Scientific and Industrial Research, Pretoria, South Africa, through the Smart Networks collaboration initiative and IoT-Factory Program (Funded by the Department of Science and Innovation (DSI), South Africa). This work is based on the research supported in part by our industry partner Telkom. The grant holder acknowledges that opinions, findings and conclusions or recommendations expressed in any publication generated by this research are that of the author(s), and that our industry partners accept no liability in this regard.

References

[1] T. Janssen, N. Bnilam, M. Aernouts, R. Berkvens, and M. Weyn, "LoRa 2.4 GHz Communication Link and Range," *Sensors (Switzerland)*, vol. 20, no. 16, pp. 1–12, 2020.

[2] L. Feltrin, C. Buratti, E. Vinciarelli, R. De Bonis, and R. Verdone, "LoRaWAN: Evaluation of link- and system-level performance," *IEEE Internet of Things Journal*, vol. 5, no. 3, pp. 2249–2258, 2018.

[3] E. M. Torroglosa-Garcia, J. M. Calero, J. B. Bernabe, and A. Skarmeta, "Enabling Roaming across Heterogeneous IoT Wireless Networks: LoRaWAN MEETS 5G," *IEEE Access*, vol. 8, pp. 103 164–103 180, 2020.

[4] F. Van Den Abeele, J. Haxhibeqiri, I. Moerman, and J. Hoebeke, "Scalability analysis of large-scale LoRaWAN networks in ns-3," *IEEE Internet of Things Journal*, vol. 4, no. 6, pp. 2186–2198, 2017.

[5] J. M. Marais, A. M. Abu-Mahfouz, and G. P. Hancke, "A survey on the viability of confirmed traffic in a LoRaWAN," *IEEE Access*, vol. 8, pp. 9296–9311, 2020.

[6] LoRa Alliance, "LoRaWAN 1.1 Specification," pp. 1–101, 2017.

[7] A. I. Pop, U. Raza, P. Kulkarni, and M. Sooriyabandara, "Does Bidirectional Traffic Do More Harm Than Good in LoRaWAN Based LPWA Networks?" in *GLOBECOM 2017 - 2017 IEEE Global Communications Conference*, Singapore, Singapore, Dec. 2017, pp. 1–6. [Online]. Available: http://arxiv.org/abs/1704.04174

[8] LoRa Alliance, "LoRaWAN 1.1 Regional Parameters," *LoRa Alliance*, pp. 1–72, 2018.

[9] M. Capuzzo, D. Magrin, and A. Zanella, "Mathematical Modeling of LoRaWAN Performance with Bi-directional Traffic," in *IEEE Global Communications Conference, GLOBECOM 2018*, dec 2018, pp. 206–212.

[10] M. O. Farooq and D. Pesch, "Analyzing LoRa: A use case perspective," in *2018 IEEE 4th World Forum on Internet of Things (WF-IoT)*. Singapore, Singapore: IEEE, 2018, pp. 355–360.

[11] SIGNET Lab - DEI, University of Padova, "lorawan." [Online]. Available: https://github.com/signetlabdei/lorawan

[12] D. Magrin, "Network level performances of a LoRa system," Master's thesis, Università di Padova, Padua, Italy, 2016.

[13] M. Capuzzo, D. Magrin, and A. Zanella, "Confirmed traffic in LoRaWAN: Pitfalls and countermeasures," in *17th Annual Mediterranean Ad Hoc Networking Workshop, Med-Hoc-Net 2018*, Capri, Italy, June 2018, pp. 1–7.

[14] SIGNET Lab - DEI, University of Padova, "sem." [Online]. Available: https://github.com/signetlabdei/sem

[15] D. Magrin, M. Capuzzo, and A. Zanella, "A Thorough Study of LoRaWAN Performance Under Different Parameter Settings," *IEEE Internet of Things Journal*, vol. 7, no. 1, pp. 1–12, 2020.

[16] D. Magrin, M. Capuzzo, A. Zanella, and M. Zorzi, "A Complete LoRaWAN Model for Single-Gateway Scenarios," 2019. [Online]. Available: http://arxiv.org/abs/1912.01285

Jaco Morné Marais received BEng and MEng degrees from the University of Pretoria in 2015 and 2018 respectively and is currently completing his PhD at this university. His research interests include LoRaWAN, low power wide area networks, wireless sensor networks and embedded systems.

An Ad-Hoc Sensor Network for Vineyard Monitoring

Nicholas Nell*[1],Nathalie Mitton†[2],Thomas Niesler*[3],Riaan Wolhuter*[4]
*Department of Electronic Engineering, Stellenbosch University
†INRIA, Lille, France
[1]20165374@sun.ac.za [2]nathalie.mitton@inria.fr [3]trn@sun.ac.za [4]wolhuter@sun.ac.za

***Abstract*—This paper explores the use of an ad-hoc wireless sensor network in a vineyard-based environment to increase the effective range of sensor nodes without the use of high power communication techniques. Physical sensor and gateway nodes were developed in order to test the use of an adapted AODV routing protocol in a wireless sensor network. The network was deployed to a vineyard environment where the effectiveness of the strategy was evaluated based on the ability of the network to self-configure. First tests indicate that the protocol performs sufficiently well to be used in vineyard environments for data collection. We conclude that an ad-hoc sensor network is a feasible approach to low-power sensing over wide areas, as required for precision viticulture.**

***Index Terms*—Ad-hoc Networking, Wireless Sensor Networks, Short-Range Communication, Low-Power Operation, Vineyard Monitoring, Precision Agriculture**

I. Introduction

The collection and analysis of vineyard telemetry data can significantly contribute to viticultural efficiency and productivity. Such telemetry data can, for example, be used to increase the quality and amount of grapes produced in a vineyard, while at the same time minimising the risk of wasteful operations. This can contribute to increased efficiency by reducing the cost of production and increasing environmental sustainability [1]. Thus, an improvement in the effectiveness and ease of collecting such telemetry data will have a direct impact on the efficiency of the vineyard and allow methods of precision agriculture to be implemented.

Precision agriculture refers to the use of technology to make farming as efficient as possible by means of exact measurement. Generally, this is achieved by breaking farmland into smaller manageable sections, and then obtaining precise and continuous measurement data for each section. This allows for the determination of, for example, the variability in inter and intra-field condition of the plants and soil. If the exact conditions of every square meter of soil and every plant were known, the farmer could locally apply precisely the right quantity of water or fertiliser, thereby reducing waste and improving the quality of the produce. By using technology to virtually divide large areas of land into much smaller sections, the farmer is given far greater control over the crop. In the long term, this technology will also allow the collection and subsequent analysis of large sets of data, revealing trends that can be exploited for even more efficient farming and improved decision making [2].

Since these advances depend on the collection of telemetry data from the vineyards, a means must be developed to allow such data collection to be set up quickly, easily, at manageable cost and with reliable results. Currently, farmers must operate either without such data collection methods (especially in the case of small scale farms) or must use very labour-intensive approaches, such as on-site manual measurement and data collection. Where farmers have tried to deploy more advanced data collection methods, they have frequently been frustrated by the failure of traditional communication techniques. This could, for example, be due to a lack of cellular signal for GSM (Global System for Mobile Communications) enabled nodes or power usage demands which cannot be met due to a lack of grid-tied power, especially when using high power communication techniques such as satellite or GSM. Other difficulties arise in vineyards which are situated in mountainous or hilly landscapes, where direct line-of-sight between sensor nodes in a network is difficult.

On-the-go data collection is employed in situations where wireless sensor networks are not easily implemented. A relatively inexpensive data collection technique, on-the-go data collection is based on a sensor attached to pre-existing mobile farming equipment, and where the data is collected while the equipment is in use. Examples include sensors attached to tractors or irrigation systems [3]. A limitation associated with on-the-go sensors is that the equipment it is attached to has to be in use for data to be collected and that the data usually has to be manually retrieved by the farmer.

Many of these limitations can be overcome by using ad-hoc wireless sensor networks that use low power, short-range communication techniques in conjunction with in-situ environmental, soil and plant sensors. Ad-hoc networks are especially useful because it is not necessary to configure each sensor node individually. Low-power designs allow the nodes to be battery-powered, and can thus be placed anywhere in a vineyard. The use of short-range communication requires sensor nodes to communicate with their nearest neighbours, and automatically discover routes to a gateway node without manual intervention. This approach offers a practically feasible means of setting up a data collection system that can provide autonomously gathered real-time data to the farmer.

This paper will explore the design and implementation of such a low-power ad-hoc vineyard based wireless sensor network. A description of the network setup will be followed by the hardware design and implementation of the sensors.

This is followed by a description of the network protocol used. Finally, the results of the first practical test will be presented.

II. Hardware Implementation

Our sensor nodes consist of an MSP432p401r microprocessor (MCU) attached to several sensors and peripherals [4]. The use of an ultra-low-power processor allows the nodes to be battery-powered for extended periods.

Peripherals include a low-power RFM95W LoRa radio module, operating in the $868MHz$ frequency band [5]. This radio module is responsible for all inter-node communication.

Every node also includes a low-power Adafruit PA101D GPS (Global Positioning System) module [6]. This module supports multiple positioning systems, including GPS, GLONASS, GALILEO and QZSS. Besides providing each node with positional data, the most important function of the GPS module is to provide a stable, shared time base to all nodes. The accurate pulse-per-second signal, which commences when a positional lock is established, allows the MCU to synchronise its onboard real-time clock (RTC). This is critical to the operation of the network, as will be discussed in Section V.

To enable data transfer to cloud storage from the sensor network, the root node includes a GSM module based on the GL865-Quad [7]. The GSM module allows the gateway sensor node to periodically establish an HTTP connection to a web server and upload all received telemetry data.

Each node also includes a low-power BME280 temperature, pressure and humidity sensor. This integrated device simplifies the hardware design by avoiding the need for multiple separate sensors. For light intensity measurement, the MAX44009 light sensor is included, and to measure the volumetric water content of the soil, the EC-5 soil probe is used.

Lithium polymer (LiPo) batteries provide power to the nodes. This type of battery offers a high energy density and reliability. To regulate the voltage provided by the battery, a DC-DC regulator circuit was designed around the TPS63001 buck-boost converter [8].

All components were housed in an IP65 rated ABS enclosure to provide environmental protection and allow continuous operation in a vineyard, shown in Figure 1.

In the current prototype, the data collected by the network is uploaded to a web server running on a Raspberry Pi using the REST API.

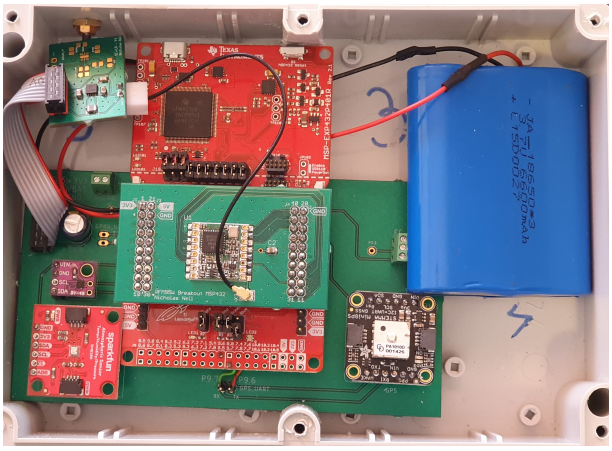

Fig. 1. Node hardware in enclosure.

III. Network Setup

Our sensor network consists of a mixture of edge nodes (nodes containing telemetry sensors) and gateway nodes (nodes that receive telemetry data from edge nodes). Edge nodes and gateway nodes have identical hardware, with the exception of the inclusion of the GSM module on the gateway nodes. The advantage of using the same underlying architecture for both node types is that it simplifies the maintenance of the hardware and makes it easy to increase the number of gateway nodes by simply adding a GSM module to an edge node.

Edge nodes primarily operate in a sleep state to conserve power. They are programmed to wake up periodically to collect telemetry data and to initiate a data transfer to a gateway node. Edge nodes also act as routing nodes when the need arises, for instance when there is no direct connection between an edge node and a gateway node. The network protocol will be discussed in greater detail in Section V.

In the current prototype, only a single gateway node is used. However, the network allows for the addition of multiple gateway nodes with no modification to the MAC or network layer protocols.

IV. MAC layer implementation

A. S-MAC

The MAC (Medium Access Control) layer protocol used by our network is an adaptation of the S-MAC protocol. S-MAC is specifically designed to reduce the power consumption of a wireless sensor network. It has been shown to perform well in situations where nodes have single tasks, are deployed in an ad-hoc fashion and where nodes spend most of their time in an inactive or sleep state [9]. The implemented protocol uses the GPS pulse-per-second signal to synchronise all network node in time. The nodes can then use time slots to synchronise communication. The use of time slots reduces the chance of message collisions on a shared communication medium. However, the main reason for the use of a time-slotted approach is to reduce node energy consumption. Careful synchronisation

TABLE I
DATAGRAM FORMAT

Data	Header	Data	Network Statistics	Total
Size (Bytes)	10	46	17	73

TABLE II
DATAGRAM HEADER FORMAT

	Next Hop	Local Source	Network Source	Network Destination	Hop Count	Tx Slot	Current Slot	Message Type
# Bytes	1	1	1	1	1	2	2	1

allows nodes to bring the onboard radio module out of its sleep state only within a specified time slot.

The implemented MAC protocol borrows a few key techniques from the S-MAC protocol. Neighbouring nodes share their transmission time slots, eliminating the need for nodes to listen to the shared communication channel in every time slot. Thus nodes can remain in a sleep state while not in their own, or a neighbouring node's, data transmission time slot. Another borrowed feature is that nodes will place their radio modules in a sleep state when overhearing a data message for which they are not the intended recipient. This happens when a node listens to the shared communication channel, expecting a message, but overhears a message with a different destination. It can then conserve power by entering a sleep state for the rest of the transaction. Synchronised global transmission time slots are used to allow the nodes of the network to perform the initial routing setup when there are no known routes or neighbours.

B. Datagram Structure

Messages sent using the MAC protocol consist of a header, followed by a data section and ended with a network statistics section as seen in Table I. The message header contains information about the route the packet is on, how many hops it has gone through, information about the sending node's transmission slot and current slot as well as a message type flag. The message type flag indicates to the receiving node how to interpret the data contained in the data section of the message. Finally, the network statistics section of the message is used only to analyse the performance of the network and is not necessary for network operation.

The message header structure is illustrated in Table II. The Next Hop byte contains the ID (Identification) of the next node along the route to the destination node, whose ID is contained in the Network Destination byte. The Local Source byte contains the ID of the node from which the message was most recently passed, while the Network Source byte contains the ID of the node from which the message originated. The two source ID's will be the same at the start of the lifecycle of a message, when it is generated. The TX (Transmission) Slot contains two bytes that indicate the transmission slot number of the local source node, while the Current Slot contains two bytes which indicate to the receiving node in which slot the message was sent by the local source node. This information is used to ensure that the network remains synchronised.

The data section of the message can be interpreted in one of three ways, depending on the value of the Message Type byte in the message header. First, it can be interpreted as telemetry data, thus containing all the sensor data dispatched by the source node. Second, the data can be interpreted as a route request and thirdly a route reply. The route reply and route request messages will be further discussed in Section V.

V. NETWORK PROTOCOL

A. AODV

AODV (Ad-hoc On-Demand Distance Vector Routing) was used to achieve routing within our network [10]. The advantages of AODV include loop-free route discovery, quick repair of broken links, and avoiding the need for individual nodes to store information about the entire network. AODV makes use of route request (RREQ) and route reply (RREP) messages to establish paths within the network. A node wanting to find a route to another node (in this implementation a gateway node), will broadcast an RREQ packet to all its neighbouring nodes, (A neighbouring node is classified as any node that can receive a radio message from the specified node). The nodes that receive the RREQ will check to see whether they have a valid and up-to-date route to the destination node. If they do, they unicast an RREP packet back to the source node. If they do not, they rebroadcast the RREQ to all of their neighbours, and store reverse-path information indicating the way to the source node if an RREP packet is later received. Once the RREQ packet reaches its destination, or reaches a node that knows a valid route to the destination, an RREP packet is unicast back to the source node along the reverse path stored by each of the intermediate nodes along which the RREQ had travelled. Each of these nodes in turn set up forward path information to the destination node. Each node along the path from the source node to the destination node will now have a route to the destination node.

B. AODV Modifications

Some simplification to the AODV protocol is possible based on the needs of the overall system. Gateway nodes will never have to initiate a route discovery, and will only receive data from edge nodes. Edge nodes only need to store routes to gateway nodes, and not to other edge nodes, as an edge node will never be the final destination of a data message. Nodes must however store information about all of their neighbours, including their TX slots and their ID. This is because a node will not know whether it is an intermediate node along a route from another edge node to a gateway node until it receives a data message that needs to be forwarded along the route. When an edge node initiates a data transfer to a gateway node, it will look up the route to the gateway node in its routing table, and then send the message in the appropriate transmission slot. The source node will wait for an acknowledgement message from the node on the next hop along the route, and will then assume the message has successfully been sent. This eliminates the need for acknowledgement messages to be routed back from the destination gateway node. If an acknowledgement is not

received from the next-hop node, the transaction will be re-attempted in the next available global transmission slot. This is repeated until either an acknowledgement is received or the maximum number of permitted retries per message has been reached. Once this maximum is reached, a dead route is assumed and deleted from the sending nodes routing table. Then, a new route discovery sequence is initiated.

Each route recorded by an edge node has an associated expiration timer. The route will have to be checked by the edge node when the timer expires to ensure that the route is still active. The use of an expiration timer on a route allows the quick discovery of broken routes. The edge node updates its routing information by sending out a new RREQ with which to discover a new route to the gateway node.

VI. Experimental Setup

For initial testing, several statistics regarding the performance of the sensor network were collected. These include the number of times a node had to initiate a route discovery, the message overhead that is required for successful data transfer from an edge node to a gateway node, and the time it takes a node to discover a route to a gateway node.

In our experiments the nodes are configured to collect and transmit sensor data once every twenty minutes, as the environmental data does not change rapidly. The gateway node will thus attempt to upload the data collected by all nodes at the start of the twenty-minute window. This is to reduce the risk of a node sending a data message during the GSM upload. If the GSM upload fails, the gateway will store the data messages that have not been uploaded, and retry the upload halfway through the twenty-minute window. Each of the GSM upload slots is limited to a maximum of one minute, to reduce the chance of messages arriving during the upload. When the gateway is in the process of uploading GSM data, it is unable to receive any messages over the radio channel due to the processor not being able to service both modules at the same time. This can be overcome in future by implementing a dedicated co-processor for the GSM communication.

A total of five nodes were installed in a hillside vineyard in Stellenbosch, South Africa. They were arranged in a star configuration so that each node can see the gateway node. The node placement is shown in Figure 2. This was done to test the loop-free nature of the routing protocol, as it is still possible for neighbouring nodes to respond to RREQ messages even if the node doing the route request has direct contact with the gateway node.

The gateway node was installed and activated first, after which the remaining nodes were enabled one by one. After a node is powered on, it waits for a GPS lock to synchronise the onboard RTC. Once the RTC is initialised, nodes will start the route discovery process. In each global transmission slot (global transmission slots are open every 10 seconds), each node is given a 20% chance to send an RREQ, if no routes to the gateway node are known, otherwise, if at least one route to the gateway is known, the edge nodes will listen in the global transmission slot. This is to reduce congestion at the start of the network's life, or when multiple nodes are activated and start the route discovery process at the same time.

Fig. 2. Node placement in the vineyard.

After the nodes were installed this way, they were left for 48 hours to both record vineyard telemetry and to monitor the stability of the network by means of the data that was uploaded to the webserver.

VII. Experimental Results

A. Initial Observations

As expected, it was found that the nodes that were activated directly after the gateway node found routes to the gateway node quickly and with a small number of RREQ messages. For example, The first node to be activated after the gateway (Node *AB*) found a route in 21 seconds with only 1 RREQ message. The second node (node *DE*) to be activated found a route to the gateway node after 31 seconds, also using a single RREQ. The remaining two nodes experienced the situation described below.

In situations where two edge nodes can both see the gateway, but one has a much stronger link to the gateway than the other, a direct route to the gateway is not always found. For example, for nodes *AB* and *BC* in Figure 2, AB sends an RREQ that is serviced with an RREP by both the gateway node and BC. Due to the capture effect present in LoRa demodulation, the source node AB would often only hear the stronger RREP from BC. This would cause AB to set up a route to the gateway node through node BC. This situation causes unnecessary traffic on the network, since a direct route to the gateway is in fact possible. To address this, a priority system was introduced, where all nodes other than gateway nodes would perform a brief carrier sense on the channel before sending an RREP. This allows the gateway node to always send an RREP first if it is in range.

Another addition that improved the route discovery rate of the network, is the introduction of periodic HELLO messages

sent out by the gateway node. When an edge node receives a HELLO message and does not yet know a route to the gateway, it can add a route to its routing table. The edge node that received the HELLO message then does not have to initiate a route discovery. It also further prevented the situation described above, because when a node hears a HELLO message from the root, it can replace any other route to the gateway node with a direct link, if the node had stored a previously inefficient route.

Another situation that led to incorrect or inefficient routing data, was the hidden node problem. In this situation, two nodes hear an RREQ and both respond to it with an RREP. However, the two nodes are not able to hear each other. This can cause the source node to receive incorrect routing data.

B. Network Results

After the changes mentioned above, all nodes were reset. The network performed noticeably better, with all edge nodes now finding the most direct route to the gateway node. A summary of the initial route discovery statistics is shown in Table III. Each edge node required only a single RREQ to discover a route to the gateway node, except for node *BC*. This node heard a HELLO message before it began route discovery and therefore did not have to perform this sequence. The gateway node sent out three RREQ messages, further confirming that it received each of the RREQ messages.

After the initial discovery, the edge nodes sent telemetry data to the gateway node once in every twenty-minute time window. The expiration time on routes was set to sixty minutes and did not reset even when a data message was successfully sent. This was done to test the situation where a node has to rediscover a route to the gateway node. This was found to occur successfully.

After 10 hours of operation, during which edge nodes performed route discovery every hour, the edge nodes had sent 131 data messages to the gateway, and 148 messages in total. This demonstrates that even with the artificially high incidence of broken links precipitated by not resetting the expiration timers the network protocol overhead was only 12.9%. The 148 messages were sent within a single one second time slot each, with 3540 global transmission slots available in the same 10 hour period. It is clear that with only 4 edge nodes and one gateway node, the network is far from capacity.

C. GSM Upload

During the testing period, we observed that it took the gateway node required up to 46 seconds to upload the five stored messages to the webserver. This delay occurs because the GSM module has to perform one push request to the web server for each message, and response time from the webserver is dependent on multiple uncontrollable factors. Thus, the blocking nature of the GSM uploads is a key limitation in the number of edge nodes a gateway node can accommodate in the current implementation.

TABLE III
STATISTIC GATHERED DURING NETWORK INITIAL ROUTE DISCOVERY

ID	*AB*	*BC*	*CD*	*DE*
RSSI	-91	-79	-81	-65
# RREQ To Route	1	0	1	1
Time To Route	21	42	82	32

VIII. CONCLUSION AND IMPROVEMENTS

We have presented the design of an ad-hoc sensor network intended for real-time viticultural monitoring that uses an adapted AODV routing protocol to allow easy installation without prior configuration. Once placed in the vineyard and enabled, nodes independently discover routes to the gateway node quickly and without excessive routing overhead. The telemetry data that was gathered by each node was successfully sent to the gateway node and uploaded to a web server, where it could be viewed on a dashboard [11].

The upload of data using the GSM module could be improved by better scheduling to avoid the transmission slots of neighbouring nodes, or by offloading the task to a dedicated co-processor to avoid blocking any inter-node data traffic.

The network can be improved by adding additional priority levels to nodes during the route discovery process, where nodes that are closer to the gateway node (and therefore have routes with fewer hops), have a higher priority in sending RREP messages back along a path to a source node that initiated an RREQ. Nodes with a higher priority would then have to perform carrier sensing on the channel for a shorter duration of time compared to nodes with lower priority levels, allowing them to transmit RREP messages sooner.

ACKNOWLEDGEMENT

We thank Albert Strever and Talitha Venter for arranging access to the test vineyard. This research was supported by the Wine Industry Network of Expertise and Technology (Winetech). We thank Telkom South Africa and the LIRIMA Agrinet project for additional support.

REFERENCES

[1] A. Modawal, The Softweb Solutions Website, [Online]. Available: https://www.softwebsolutions.com/resources/vineyard-management-system.html.
[2] S. Marios and J. Georgiou, "Precision agriculture: Challenges in sensors and electronics for real-time soil and plant monitoring," in *Proc. IEEE Biomedical Circuits and Systems Conference (BioCAS)*, 2017, pp. 1–4.
[3] V. Adamchuk, J. Hummel, M. Morgan, and S. Upadhyaya, "On-the-go soil sensors for precision agriculture," *Computers and Electronics in Agriculture*, vol. 44, no. 1, pp. 71–91, 2004.
[4] "MSP432p401r Product Page," Texas Instruments, [Online]. Available: https://www.ti.com/tool/MSP-EXP432P401R.
[5] "RFM95W Datasheet," HopeRF, [Online]. Available: https://www.hoperf.com/modules/lora/RFM95.html.
[6] "Adafruit Mini GPS Module," Adafruit, [Online]. Available: https://www.adafruit.com/product/4415.
[7] "GSM-Click Product Page," MikroElektronika, [Online]. Available: https://www.mikroe.com/gsm-click.
[8] "TPS63001 Datasheet," Texas Intruments, [Online]. Available: https://www.ti.com/product/TPS63001.

[9] W. Ye, J. Heidemann, and D. Estrin, "An energy-efficient mac protocol for wireless sensor networks," in *Proc.Twenty-First Annual Joint Conference of the IEEE Computer and Communications Societies*, vol. 3, 2002, pp. 1567–1576 vol.3.
[10] C. Perkins and E. Royer, "Ad-hoc on-demand distance vector routing," in *Proc. Second IEEE Workshop on Mobile Computing Systems and Applications (WMCSA)*, 1999, pp. 90–100.
[11] "ThingsBoard — Dashboard." [Online]. Available: http://meesters.ddns.net:8008/dashboard/a30f57f0-7d8b-11eb-9466-61843e0f4458?publicId=d7ab0d20-c43e-11eb-b1dd-0d4d650070a1

Nicholas Nell is currently a postgraduate research student at Stellenbosch University. He completed his undergraduate engineering degree at Stellenbosch University in 2019 and is currently studying the design of ad-hoc sensor networks for viticultural monitoring. His research interests include routing protocols, wireless sensor networks, and embedded software development.

Impact of the Packet Delivery Ratio (PDR) and Network Throughput in Gateway Placement LoRaWAN Networks.

Smangaliso Mnguni*, Pragasen Mudali*, Adnan Abu-Mahfouz†, Mathew Adigun*
*University of Zululand KwaDlangezwa, South Africa
[1]mngunismangaa@gmail.com
[2]mudalip@unizulu.ac.za
[4]adigunm@unizulu.ac.za
†Council for Scientific and Industrial Research Pretoria, South Africa
[3]a.abumahfouz@ieee.org

***Abstract*—Internet of Things (IoT) is a fast and rapidly growing environment with LoRa technology as a leading Low-Power Wide-Area Network (LPWAN). It is paramount important to understand the LoRaWAN limitations/drawbacks and capabilities in terms of its scalability, coverage, probability and network throughput while LoRa networks are being rapidly deployed across the globe. Therefore, this paper intends to evaluate the LoRa network performance through the use of improved LoRa gateway algorithm for a Long-Range transmission technology and FLoRa (Framework for LoRa) which is a simulation framework for carrying out end-to-end simulations for LoRa networks. More specific, this study analyse and present the results of data collected from the FLoRa simulator after implementing the gateway placement algorithm optimized. To characterize the coverage of every LoRa nodes in the network, packet delivery ratio (PDR) for each node has been calculated. The extensive results obtained shows that as few as two gateways deployed in the network is sufficient to cover an approximately 10 km radius of a dense urban area.**

***Index Terms*—IoT, LoRa Networks, PDR, LPWAN, FLoRa.**

I. Introduction

Internet of Things (IoT) is expected to grow exponentially such that devices connected to the internet reach 125 billion during the year 2030. For data transmission to the IoT end node devices rely on Gateways and to ensure coverage for IoT devices Gateways need to be optimally placed [1]. However, physical infrastructure and topography as features of the target area are essential for IoT gateway's optimal placement. Recently, Wireless Mesh Networks (WMN) has gained an important role in current communication technologies. It has been used in several applications such as surveillance and rescue systems. Network congestion can be minimized and throughput can be improved by placing many gateways but it can be very costly, deployment and interference will increase. Therefore, this work focuses on the gateway placement algorithms on the newly developed wireless technology called Long Range Wide Area Networks (LoRaWAN) protocol and its performance using matrices such as PDR, network throughput, and success probability of nodes.

Gateway placement is essential in long-range transmission of data for commercialization of the IoT technology due to its capability to facilitate data transmission in a long range,since demand for large amount of data transmission, low-power and long range (LoRa) arises. For a long-range and low power communication the LoRa technology is available but not suitable for transmission of large amount of data due to low transmission rate. The LoRa communication technology is a low power, long range wireless protocol developed by Semtech. High extendibility, low power consumption and high efficiency as compared to 3G/4G technologies are the main advantages of LoRa technology. However, low transmission rate is the notable disadvantage of LoRa technology [2].

Low Power Wide Area Network (LPWAN) provides Wireless connectivity, long-range transmission and increased power efficiency [3]. LoRa is the most promising technology with a lot of capabilities which is provided by LPWAN. LoRaWAN communication protocols/ standard are used by a lot of LoRa devices since they have a potential to improve power efficiency and it can sustain device batteries estimated up to 10 years. It is important to note that LPWAN consist of LoRa technology which uses LoRaWAN as the communication protocol. Furthermore, as a emerging wireless technology LPWANs compliments short range wireless technologies and traditional cellular to address requirements of IoT applications that are diverse. Not only short-range connectivity is offered by LPWAN technologies but also long-range connectivity with low rate and low power devices, not provided by ancient technologies. Applications that need low data rate, delay tolerant, and typically require the low consumption of power are specifically considered by LPWAN technologies [4].

The rest of this paper is organized as follows: Section II evaluates the importance of LoRaWAN protocol and gives a brief background on LoRa and LoRaWAN. Section III gives some details on a related work for this study. Section IV discusses the simulation procedure followed. Section V present the simulation results obtained. And Section VI concludes the paper.

II. The LoRaWAN protocol

Companies using the IoT devices are already benefiting from the use of LoRaWAN. There are two main components of LoRa network which is LoRa and LoRaWAN, each of these component in a protocol stack corresponds with different layer. In the other hand, LoRaWAN is describe by the LoRa Alliance as an open standard where LoRa physical layer is developed by Semtech which remains the only integrated LoRa circuit. Figure 1. represents protocol stack of network servers, IoT devices and gateways, while gateways acting as a middle man forwarding messages between sensors (i.e.. IoT devices) and the network server. The sensors are implemented on the application layer.

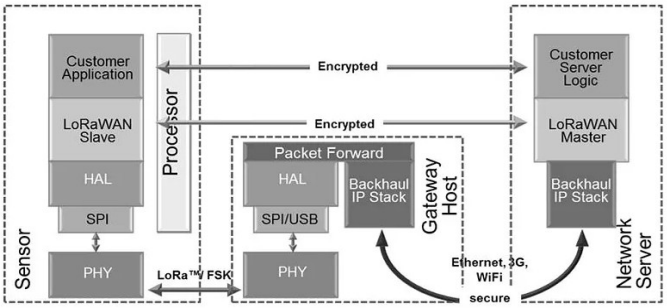

Fig. 1. Protocol stack in LoRaWAN with various devices.

A. LoRa

LoRa is a new promising and fast growing network designed for unlicensed,low power and long range operation. In order to meet the data and range requirements LoRa wireless uses a chip-spread-spectrum (CSS) modulation with options for different bandwidth (BW) and spreading factor (SF) for modulation optimization. 433 MHZ, 868 MHz and 915 MHz are all ISM band where LoRa operates depending on jurisdiction with the band divided up into channels [5]. In LoRa networks the combination of bandwidth and SF compromise speed for range. Other parameters affecting the communication range and data range includes center frequency, code rate and transmission power, not only SF and bandwidth.

The ratio between the chip rate and and data symbol rate is labelled as SF, therefore, tuning the reachable distance and the data rate is allowed through the configuration of SF. In fact, the higher the SF allows longer range at the expense of low data rate, and vice versa. The configuration of transmission power is mostly depends on the bandwidth and region used for transmission, whereas the code rate is regarded as forward error correction and it affects the data transmission airtime. The center frequency rely on the ISM band of chosen region. finally, the bandwidth plays a significance role in the data rate of transmission. 14dBm is the limited transmission power in Europe with the duty cycle of 1% for air time. However, the usage of these bands differs across the world [6].

B. LoRaWAN

LoRaWAN is a ALOHA based communication protocol and system architecture for LoRa physical layer used by the network. Using gateways to communicate over the air is the strongest ability of LoRaWAN due to gateways ability to facilitate communication amongst IoT devices and it involves LoRa wireless channels in a protocol stack, where gateways communicate with network servers and the communication between gateway and LoRa nodes are created by LoRa physical layer. To reduce the complexity of LoRa nodes in the network, LoRaWAN depends on ALOHA based MAC protocol [7].

LoRaWAN technology has the capability of adapting its principal parameters in order to optimize the energy consumption. Figure 2. shows the architecture of the LoRaWAN network, LoRa/LoRaWAN RF interface is used to facilitate communication between end nodes and the gateway. Ethernet,3G/4G, Wi-Fi and etc are all non-LoRaWAN network which are used by gateway to transmit frames to the network server and TCP/IP SSL is responsible for the protection of critical application from threat of attack.

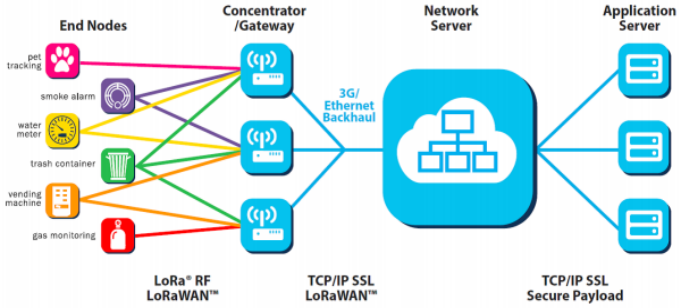

Fig. 2. The LoRaWANArchitecture [8]

III. Related work

Since LoRaWAN is an active study, network throughput, Packet Delivery Ratio (PDR) and success probability are being the main stand out matrices to evaluate the network performance especially in gateway placement. In [9] authors evaluated the scalability, coverage and throughput of LoRa LPWAN for Internet of Things, this was a simulation based study where custom-built simulator was used for characterization of LoRa network scalability under variety of network settings and traffic. The two measurements indoor and outdoor were conducted and to visualize the network coverage, PDR was imposed for the gateways on Google maps network coverage for a heatmap. A 95.3% of PDR was achieved at distance of $7.5km$ even though the gateways are placed close to the downtown area network coverage extends beyond the city edges.

Another authors in [10] evaluated LoRa LPWAN technology for remote health and wellbeing monitoring . A different of transmitting power, bandwidth and spreading factors were

used. The results obtained in this study gave insight on what can be covered by the single base station, since they obtain 96.7% of success packet delivery ratio. However, they never really looked at the LoRa gateway placement and its algorithms for different technologies but only the parameters that can be used.

In [11] scholars analysed the LoRa networks using certain case perspective, some of the cases that were considered includes areas like vehicle fleet tracking, smart street lights, smart parking and smart metering. This study was carried out using a simulator called LoRaSim, which is a packet-level discrete event simulator for LoRa networks. According to their findings, up to 380% packet delivery ratio was achieved through the fastest data rate correspond settings and uses 0.004 times the energy compared to other evaluated settings, while support IoT cases mentioned here.

LoRa/LoRaWAN study is categorized as follows throughput analysis, Interference analysis, Gateway coverage and latency analysis:

A. LoRa/LoRaWAN analysis of Throughput

The network throughput for LoRa that is analysed in [12], [6] and [13], which specifically focused on Class A devices revealed that, at the edge of the network throughput can be as low as 100 bps. Furthermore, although Aloha is used by LoRaWAN a 32% packet loss is convertible despite the increase of up to 1000 nodes per gateway which is caused by the LoRa's robustness modulation technique. In other words, a packets collision massively impact the network throughput in a low transmission rate. However, network throughput can also be impacted by the duty life cycle at a high rate transmission and Acknowledgement at a great extent especially in Class A device can reduce the achievable network throughput. The drawbacks of the existing study in the network throughput is that they only focus on few spreading factors which is SF7 and SF12 with 125KHz of bandwidth.

B. Interference analysis

In [14] and [15] a co-spreading factor interference and LoRa network interference analysis is presented. The use of multiple gateways and directional antennas were examined to combat interference from neighbouring LoRa networks. The results stated that, using multiple gateways to combat the LoRa networks interference is the better option as compared to the use of directional antennas since it increases the Packet Delivery Ration (PDR). Furthermore, it is observed that using one spreading factor drops the probability of successful packet due to high interfering signals.

C. Gateway coverage

In [16] and [17] the scalability and LoRa gateway coverage are being analysed some of the results shown that at least $2km$ of radius can be covered by a LoRa cell in a harsh propagation conditions, it was also observed that at the network edge the LoRa nodes are only guaranteed the lowest bit rate. The studies also revealed that with a 30 gateways deployed a metropolitan city of approximately $100km^2$ can be covered.

D. Latency analysis

In [18] and [19], an analytical model for uplink latency considering duty cycling regulation of Class A devices is presented. The results shown that for a given data load the impact on latency is caused by combining and sub-band selection. Furthermore, a large number of channels can help minimize the delays in the presence of networks that are heavily dominated by large number of nodes.

IV. Simulation procedure

To evaluate the performance of LoRa networks FLoRa was used. Furthermore, two network scenarios were created, the first one consisted a network of 100 LoRa nodes which were varied from 100 to 700 with a step of 100. The LoRa physical layer European environmental parameters were used as explained in Table I, and for both scenarios gateway varied from one to two. In the second network scenario 20 LoRa nodes with different gateways were deployed, where spreading factor and transmission power were arbitrarily picked by the nodes distributed within the permissible range.

TABLE I
Simulation Parameters

Parameters	Value(s)
Code Rate	4/8
Carrier Frequency	868 MHz
Spreading Factor	7 to 12
Transmission Power	2 dBm to 14 dBm
Bandwidth	125 kHz

In order to achieve zero packet loss with a transmission delay of 10ms, INET framework played a vital role to model the backhaul network. Sensing application was among the parameters considered in the simulation. With a mean of $1,000s$, each LoRa nodes were able to send a 20-byte packet after distribution time. In the first scenario, $500m$ x $500m$ was set as a size of deployment area and in the second scenario $10000m$ x $10000m$ was set. The square region was used to locate all LoRa devices deployed in the network in order to make sure nodes communicate with the gateway(s), since nodes were randomly place. The simulation process lasted exactly one day for both experiments and for the accuracy results purposes 10 iterations were done. LoRa networks performance was evaluated with and without Adaptive Data Rate (ADR). The mechanisms is disabled in the networks with no ADR for both at the LoRa nodes and network servers.

A. Simulation script

Algorithm 1. explain in details the main steps followed by the simulation script. A different scenarios are presented in different scripts for different purposes. LoRaNetworkTest.in and betTest.in files define the scenarios. Scenario consist of certain features including LoRaNodes, gateway(s), and a network server, for every network scenario created LoRaNodes

were randomly distributed in deployment area keeping in mind a radius. Transmission power and spreading factors are allocated for every nodes from available settings, in the nodes and network server ADR was disabled and enabled where necessary. 1 day was configured as the simulation time limit with a warm-up period of 5 hours, cloudDelay.xml file consist of backhaul network configuration and its link on package.ned file.

Algorithm 1 Simulation Script.

Input: Number of Gateways.
Input: Number of LoRaNodes.
Input: Radius for deployment area.
Assign UDPApps in LoRaGW, LoRaNodes, and Server.
Create parkert forwarder for all ports
Sim-time-limit = 1d
Warm-up period =5h
Create LoRaNodes features.
ADR inNode = True/False
InitialLoRaSF= (7,12)
InitialLoRaBW= (125KHz)
InitialLoRaCR= (4)
InitialLoRaTP= (2dBm + 3dBm * uniform (0,4))
Setup GW features
Start the simulation
Save the simulation results
return

V. Simulation Results

The various matrices used in this study are analysed in this section with the help of LoRa modules added to Framework for LoRa (FLoRa). The throughput for some performance network matrices such as Packet Delivery Ratio (PDR) and packet success probability were explored.

A. Packet Delivery Ratio (PDR)

To characterize the coverage of every LoRa nodes in the network, PDR for each node has been calculated. A ratio of a successfully received data packetsover a totally sent data packets is called PDR. Equation 3.1 is used to calculate PDR for each nodes:

$$PDR = \frac{Packetsreceived}{Packettransmitted} * 100 \quad (1)$$

In some cases the node disconnect from the network and try to reconnect at a later stage, most of these packet might not be successfully delivered to the gateway after failed to re-join the network. Therefore, equation 1. defines PDR solely focused on data packets and thus does not reflect in anyway the success ratio of join-request. Therefore, when the calculation is performed in the simulation using the equation a minor error will be observed compare of that simulation. PDR equation does not include join request because they have to be tracked manually in the LoRa nodes as gateway will be aware of any unsuccessful join request and only starts logging a LoRa nodes once it has successful joined.

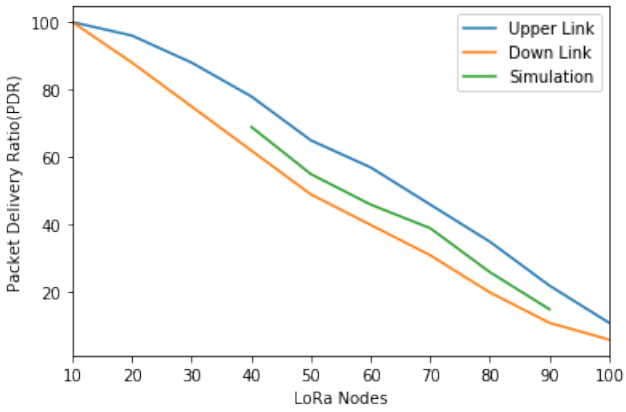

Fig. 3. Successful delivery ratio probability experimental dependence.

Figure 3. illustrate the experimental dependence of the probability of successful delivery on the number of devices. The simulation consist of two links upper and down links, the blue line represents upper link of theoretical value packet delivery ratio. The orange line represents the down link of theoretical value of packet delivery ratio. And the middle one, green in colour shows the experimental results of the actual results. From this simulation it is observed that the experimental value is slightly closed to upper link theoretical value due to congestion in the down link which leads to massive packet loss as the network expands.

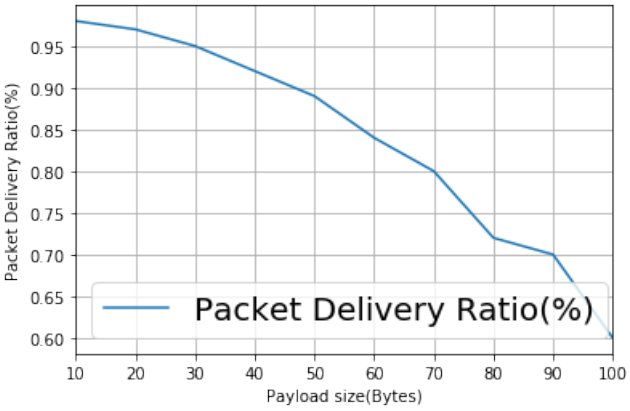

Fig. 4. Packet Delivery Ratio versus payload size for a 100 LoRa nodes.

The variation of the payload size ranged from 10 Bytes to 100 Bytes, with a transmission rate of 1 packet per second for each LoRa nodes deployed in the network. According to the results obtained as explained in Figure 4, it is observed that to obtain at least 90.0% of packet delivery ratio payload size should be kept under 45 Bytes with a 125 kHz bandwidth and coding rate of 4/5. This was a much better and improved performance in terms of PDR as compared to this study [20] which was done in a different environment with a change in parameters. This is an enormous improvement of the transmission rate by the algorithm implemented in this study as compared to the one existing, where most of them enables the network to reach percentage of 90.0% once the reporting time nearly

clocks 700 seconds with less LoRa nodes deployed in the networks compare of that 100 LoRa nodes used in this study.

B. Network performance evaluation

In this section we analyse and evaluate the network performance through the packet success probability and network throughput. These matrices used here are influenced by the LoRa modules added in FLoRa for LoRaWAN simulation networks. The first step, was to evaluate and visualize the results obtained for network throughput for performance purposes. The second step, was to actually evaluate the success probability of the packet sent for every network scenario created in a LoRaWAN communication protocol.

Throughput performance

The network throughput in this simulation campaign is characterized by S as a function offered by network traffic G where the function aims to evaluate network throughput. In this equation N denotes LoRa nodes placed around GW at a chosen radius r from the simulator. The value of radius is chosen based on SF=12, since r is the maximum range where LoRa nodes and GWs can be able to transmit packet using SF=12 and considering a propagation loss. Multiply LoRa channel was considered for this simulation section performed, for all simulations measuring throughput the gateway was configured to only have one receive path enabled.

It is supposed that LoRaNodes i=1..., for the computation of throughput. Where N generates every τ_i seconds a packet which occupies the channel for t_p,i in order to be transmitted. The duty cycle limitation for this simulation section is always 1% and when not specified it is not applied at all, the main aim is to test the LoRaWAN access scheme. The network offered traffic is computed as described in the equation below [21]:

$$\sum_{i=1}^{\mathrm{N}} \frac{t_{p,i}}{\tau_i} \tag{2}$$

The fraction of LoRa nodes packet transmission over time taken by the LoRa channel is called offered traffic as expressed in equation . The LoRa channel is underutilized if G<1 where no packet transmission or communication between the devices takes place in the network. However if G>1, it simple state that even during a free flowing transmission in the network some packets will attempt to use same channel simultaneous, which may lead to packet collision. Therefore now, throughput S is obtained through a given value of G as follows:

$$S{=}G{\cdot}P_{succ} \tag{3}$$

Again the total number of packet sent and total number of packet successfully received ratio in the simulation is said to be the approximation packet success probability denoted as P_{succ}. Perfect synchronization between LoRa devices inspired by a network offering of 1 can prevent the high packet loss during transmission by mitigating the probability of packet collision, and that will results into throughput of 1. of course, it is very difficult or impossible to achieve a 100 percent free flowing synchronization between the LoRa devices, so S<1 is expected.

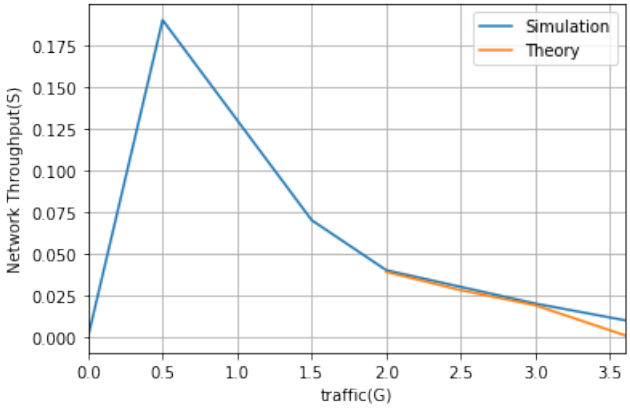

Fig. 5. Ideal packet collision and throughput of SF=7.

It is expected that a shape of the throughput becomes curved under ideal channel condition, and follow typically ALOHA network in a varying offered traffic G as shown in Figure 5. All LoRa nodes are configured to transmit using SF7 and all transmitted packet have the same time on air (ToA) provided payload length is fixed and gateway receives the packets at the same rate of power, these conditions takes place when the link measurement model is off. The number of LoRa nodes N plays a significant role in expressing the traffic offered by the network as shown below:

$$G{=}\tfrac{N{\cdot}t_7}{\tau_i} \tag{4}$$

This transmission happen at a fixed payload length for all packet using SF7 as a range of transmission, where t_7 is ToA.

Success probability performance

The aim of this simulation experiments is the estimation probability of successfully receiving a transmitted packet from LoRa nodes to LoRa gateway(s). Even though some network simulation scenarios featured more than one GW only LoRa devices are within the range covered were considered. Therefore, it is only LoRa nodes within the radius have their generated traffic considered for success probability [22].Figure 6. shows the decline of the probability success ratio as the network expands, all packets that arrives at the GW under the sensitivity are being ignored due to shadowing or massive building loss. Therefore, this eventually lead to a declining success probability because of path loss reception and interference of any different kind. In this scenario, 22% of LoRa nodes were unable to reach the gateway due to insufficient power.

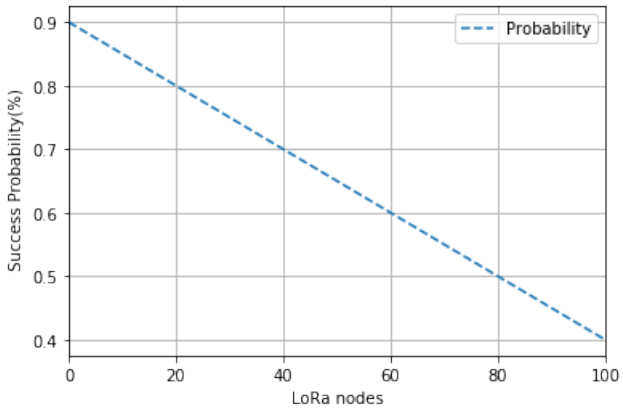

Fig. 6. Packet success probability as a function of LoRa devices.

The simulation actually lasted one day with 5 hours of warm up and the simulation was repeated 10 times for accuracy purposes. As the network increases the trend of the graph appears to be decreasing linear. The gateway(s) that were tasked to accommodate all the LoRa devices formed network scenarios were able to achieve a success probability of almost 91%.

VI. Conclusion

This study as a whole was set out to construct a LoRaWAN simulation with the purpose to execute a performance evaluation of the improve gateway placement algorithm in this new arising and fast developing technology. The results obtained through the simulation showed that for both upper link and down link the PDR percentage drops as the network expands at a different level including for that of simulation. Although this should be the trend for the calculated PDR of a network with different LoRa node our improved algorithm appears to give the better performance compare to other algorithms used before. However, in future the algorithm performance still need to be tested in a different environment such as testbed.

Acknowledgement

The authors wish to acknowledge the Computer Science department at the University of Zululand for a massive support. This research is sponsored by Department of Science and Innovation (DSI), South Africa collaborated with Council for Scientific and Industrial Research, Pretoria, South Africa through Smart Networks collaboration initiative and IoT-Factory program.

References

[1] J. M. Marais, R. Malekian, and A. M. Abu-Mahfouz, "Evaluating the lorawan protocol using a permanent outdoor testbed," *IEEE Sensors Journal*, vol. 19, no. 12, pp. 4726–4733, 2019.

[2] D. H. Kim, J. Y. Lim, and J. D. Kim, "Low-power, long-range, high-data transmission using wi-fi and lora," in *2016 6th International Conference on IT Convergence and Security (ICITCS)*. IEEE, 2016, pp. 1–3.

[3] D. Magrin, M. Centenaro, and L. Vangelista, "Performance evaluation of lora networks in a smart city scenario," in *2017 IEEE International Conference on Communications (ICC)*. ieee, 2017, pp. 1–7.

[4] A. M. Yousuf, E. M. Rochester, and M. Ghaderi, "A low-cost lorawan testbed for iot: Implementation and measurements," in *2018 IEEE 4th World Forum on Internet of Things (WF-IoT)*. IEEE, 2018, pp. 361–366.

[5] A. J. Wixted, P. Kinnaird, H. Larijani, A. Tait, A. Ahmadinia, and N. Strachan, "Evaluation of lora and lorawan for wireless sensor networks," in *2016 IEEE SENSORS*. IEEE, 2016, pp. 1–3.

[6] M. C. Bor, U. Roedig, T. Voigt, and J. M. Alonso, "Do lora low-power wide-area networks scale?" in *Proceedings of the 19th ACM International Conference on Modeling, Analysis and Simulation of Wireless and Mobile Systems*, 2016, pp. 59–67.

[7] A. S. Tanenbaum, D. Wetherall *et al.*, "Computer networks," pp. I–XVII, 1996.

[8] B. H. R. K. S. ZEADALLY and A. F. L. KHOUKHI, "Internet of things (iot) technologies for smart cities."

[9] A. M. Yousuf, E. M. Rochester, B. Ousat, and M. Ghaderi, "Throughput, coverage and scalability of lora lpwan for internet of things," in *2018 IEEE/ACM 26th International Symposium on Quality of Service (IWQoS)*. IEEE, 2018, pp. 1–10.

[10] J. Petäjäjärvi, K. Mikhaylov, M. Hämäläinen, and J. Iinatti, "Evaluation of lora lpwan technology for remote health and wellbeing monitoring," in *2016 10th International Symposium on Medical Information and Communication Technology (ISMICT)*. IEEE, 2016, pp. 1–5.

[11] M. O. Farooq and D. Pesch, "Analyzing lora: A use case perspective," in *2018 IEEE 4th World Forum on Internet of Things (WF-IoT)*. IEEE, 2018, pp. 355–360.

[12] F. Adelantado, X. Vilajosana, P. Tuset-Peiro, B. Martinez, J. Melia-Segui, and T. Watteyne, "Understanding the limits of lorawan," *IEEE Communications magazine*, vol. 55, no. 9, pp. 34–40, 2017.

[13] J. Haxhibeqiri, F. Van den Abeele, I. Moerman, and J. Hoebeke, "Lora scalability: A simulation model based on interference measurements," *Sensors*, vol. 17, no. 6, p. 1193, 2017.

[14] O. Georgiou and U. Raza, "Low power wide area network analysis: Can lora scale?" *IEEE Wireless Communications Letters*, vol. 6, no. 2, pp. 162–165, 2017.

[15] T. Voigt, M. Bor, U. Roedig, and J. Alonso, "Mitigating inter-network interference in lora networks," *arXiv preprint arXiv:1611.00688*, 2016.

[16] M. Centenaro, L. Vangelista, A. Zanella, and M. Zorzi, "Long-range communications in unlicensed bands: The rising stars in the iot and smart city scenarios," *IEEE Wireless Communications*, vol. 23, no. 5, pp. 60–67, 2016.

[17] J. Petajajarvi, K. Mikhaylov, A. Roivainen, T. Hanninen, and M. Pettissalo, "On the coverage of lpwans: range evaluation and channel attenuation model for lora technology," in *2015 14th International Conference on ITS Telecommunications (ITST)*. IEEE, 2015, pp. 55–59.

[18] R. B. Sørensen, D. M. Kim, J. J. Nielsen, and P. Popovski, "Analysis of latency and mac-layer performance for class a lorawan," *IEEE Wireless Communications Letters*, vol. 6, no. 5, pp. 566–569, 2017.

[19] M. Bor and U. Roedig, "Lora transmission parameter selection," in *2017 13th International Conference on Distributed Computing in Sensor Systems (DCOSS)*. IEEE, 2017, pp. 27–34.

[20] C. H. Barriquello, D. P. Bernardon, L. N. Canha, F. E. S. e Silva, D. S. Porto, and M. J. da Silveira Ramos, "Performance assessment of a low power wide area network in rural smart grids," in *2017 52nd international universities power engineering conference (UPEC)*. IEEE, 2017, pp. 1–4.

[21] N. F. Mhaidi, M. K. Ishak, and T. A. Alamiedy, "Backoff algorithms for embedded ethernet model in real-time system."

[22] S. Mnguni, P. Mudali, N. Sibeko, and M. O. Adigun, "Lora gateway placement at the university of zululand: A case study," in *2019 International Conference on Smart Applications, Communications and Networking (SmartNets)*. IEEE, 2019, pp. 1–6.

Smangaliso Mnguni is a Masters student in the Department of Computer Science at the University of Zululand. His research interest is under LoRa gateway placement in the Internet of Things (IoT) and Low Power Wide Area Networks(LPWAN).

Management

Topology-Aware Measurement Scheduling Strategies in Low Resource Networks

Taveesh Sharma*, Josiah Chavula†
Department of Computer Science, University of Cape Town
Cape Town, South Africa
*shrtav001@myuct.ac.za, †jchavula@cs.uct.ac.za,

***Abstract*—Community networks have been proposed by many networking experts and researchers as a way to bridge the connectivity gaps in rural and remote areas of the world. Many community networks are built with low-capacity computing devices and low-capacity links. Such community networks are examples of low resource networks. The design and implementation of computer networks using limited hardware and software resources has been studied extensively in the past, but scheduling strategies for conducting measurements on these networks remains an important area to be explored. In this study, the design of a Quality of Service monitoring system is proposed, focusing on performance of scheduling of network measurement jobs in different topologies of a low-resource network. Our results show that a graph colouring algorithm (AOSD) that arranges network measurement jobs in ascending order of their number of conflicts performs better than other scheduling algorithms like Round Robin (RR) and Earliest Deadline First (EDF).**

***Index Terms*—Internet Services, End User Applications, Internet Performance**

I. Introduction

Community networks are open, free and neutral network infrastructure built and maintained by citizens and organisations who pool their resources and coordinate their efforts [1]. These networks are often run by non-profit organizations. Further, community services like local networking, voice connections and internet access can be developed in cooperation with local stakeholders [2]. ITU statistics [3] for South Africa report that there were around 165.6 mobile-cellular subscriptions per 100 inhabitants as of 2019. Of these 165.6 subscriptions, around 102.2 correspond to mobile broadband subscriptions. Also, about 92.6% of total active internet users worldwide, and 94.7% of internet users in South Africa accessed internet through their mobile phones as of January 2021 [4]. The usage of smartphones as a computing and networking device thus presents an opportunity for constructing mobile crowdsourcing applications [5]. Such applications can be used as a platform to conduct research to improve community networks.

System architectures based on crowdsourcing are generally more complex as compared to systems where design, implementation and execution are centralized [5]. Other challenges arise due to adopting smartphones as an execution unit. It is difficult to precisely capture internet performance data through smartphones because the conditions, like location and bandwidth, are always changing over time, and as the subject moves with the device.

Although the load of executing measurements is shifted to smartphones in a crowdsourcing-based architecture, a centralized server should be able to allocate the measurements intelligently, given the availability of resources like network bandwidth and execution capacity of smartphones. If a large number of measurements are carried out using a limited number of vantage points, the obtained results could suffer from the observer effect [5], i.e a bias in the measurements due to the measurement infrastructure itself. Measurement processes that are executed in common points and links could contend for shared network resources. This contention for resources is also called measurement conflict problem [6]. Thus, scheduling and synchronization of measurements among the smartphones is important to ensure proper resource utilization and accuracy of results.

The costs associated with building large-scale active internet measurement platforms that provide open access to anonymized data to researchers are generally very high [7]. Networks may become overly congested and additional data costs on users' side may be incurred as a result of the injection of probing packets. A major reason behind this phenomena lies in the skewed distribution of measurement jobs towards a few vantage points. We posit that these costs can be reduced by ensuring proper scheduling and distribution of these measurements. Our study thus introduces mobile crowdsourcing in the context of a low cost monitoring system for low-resource networks with a focus on measurement scheduling strategies. In pursuit of finding the best possible design, we present an empirical analysis of alternative techniques for measurement scheduling and synchronization. These techniques are compared on the basis of evaluation metrics like platform delay, waiting time and node busy time ratio.

II. Related work

Most of the research on community networks has been done on the basis of Guifi.net [1], [8], [9] (the largest community network) or other interconnected European community networks [10]–[12]. Limited research has been performed on monitoring network characteristics in the context of community networks for developing regions [13]–[15], and measurement scheduling aspect of systems that characterize these networks has mostly been overlooked. In classical networks, the design and evaluation of measurement scheduling algorithms is based on computer simulations or synthetic testbeds. Also, these algorithms rely on the assumption that the execution

time of measurements is known in prior, contrary to a real-world scenario where it could vary because of several factors like signal strength, geolocation and time of the day. In our work, we make an attempt to apply the principles used in literature to develop a QoS measurement platform that can be used and tested in any real-world low resource network.

Scheduling of active internet measurements in classical networks has been studied by few researchers. Some of these works [16], [17] have not given much attention to conflicts between individual measurements. Calyam *et. al* [18] propose a novel enhanced-EDF heuristic that allows concurrent execution of measurements to address the measurement conflict problem. Scheduling algorithms for both periodic and on-demand jobs have been proposed in this work, and have been proven to perform better than existing algorithms through computer simulations as well as in an internet testbed. Qin *et. al* [6] compare the enhanced-EDF scheme with a novel graph-coloring based approach, and through computer simulations proves to achieve effective contention resolution and low execution delays. In addition to the graph coloring approach, the original Round Robin algorithm has also been modified by the authors to work well in a concurrent context. Two variants of the proposed graph coloring scheme are considered in our implementations - AOSD and DOSD, corresponding to ascending and descending order of subvertices' degree respectively. Both these schemes rely on a centralized point of scheme generation and task reporting, which according to Mathew Clegg [19], is a drawback. However, this could benefit our centralized measurement platform. In addition to proposing AOSD and DOSD algorithms, the original Round Robin algorithm has also been modified to run in a concurrent context.

III. Measurement system overview

This project will investigate strategies to measure under-resourced networks by deploying a containerized measurement system within iNethi [20], a localized content sharing and services platform being developed in Ocean View, a township in Cape Town, South Africa.

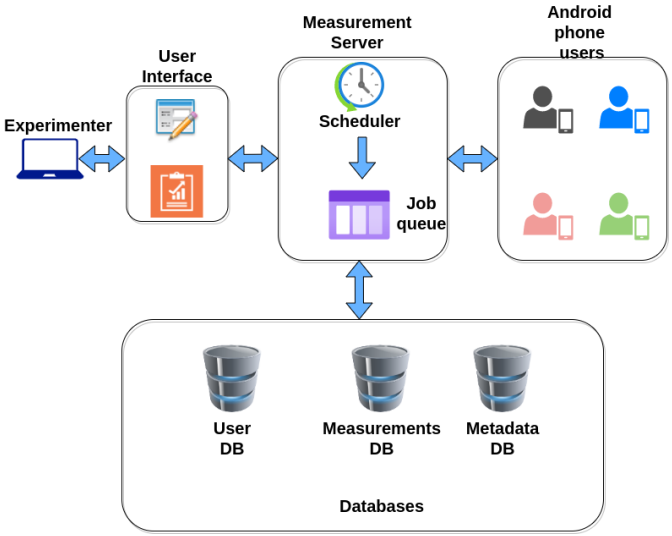

Fig. 1. A diagram showing the architecture of QoSMon, the proposed measurement system

Fig. 1 shows the architecture of the system. A key component in our architecture is a measurement server, which is responsible for orchestrating measurements like ping, DNS look-ups, HTTP downloads, and TCP throughput tests. For community network users, our system is capable of collecting and storing network usage data of applications in a phone. The data for apps is aggregated within a phone and sent to the server every 24 hours for storage. If the sending of usage data fails due to connectivity issues on a day, the data for this particular day is sent along with the batch for the next day. We implement this using a 3-step communication process. First, the phone sends a request to the server for a latest timestamp from which usage data is required for that phone. Second, the server responds with the desired timestamp. If no timestamp is returned, the phone sends usage data to the server for the last 24 hours. The measurement server is capable of running one of RR, EDF, AOSD and DOSD algorithms (Section II). Measurements are conducted in users' mobile phones distributed within the community network. Only Android phones are able to run the measurements in our current implementation. The communication between phones and measurement server is facilitated through HTTP websockets, whereby the server sends measurement jobs to the phones as and when they are ready to be dispatched. In addition to the server, a user interface is developed for community network administrators and researchers to schedule experiments, visualize the collected data and perform QoS analysis. Community network members will be able to visualize application usage through their phones.

IV. Implementation details

A. Conflict determination

Conflicts between individual job instances are first decided on the basis of target server. If two jobs are destined to the same target server, it is highly likely that they use common links in the network. Thus, we use a pairwise binary matrix for representing conflicts between active jobs. This binary matrix is then used to build an undirected conflict graph of the jobs and supplied to the scheduling algorithms as input.

Our system is also capable of addressing conflicts that arise due to the topology of the network. During initialization phase of the measurement server, we load the network topology as an undirected graph and then calculate the cost of scheduling on each measurement node. This cost is calculated by summing up the number of affected links in the network. We thus calculate all simple paths from a measurement node to the gateway access point and add the number of edges in the network graph. Fig. 2 shows an example of a network topology in which AP3 is the gateway access point. Requests from M4 to a target server anywhere on the internet can be routed through one of the paths in the set {M4 $\rightarrow$ AP6 $\rightarrow$ AP2 $\rightarrow$ AP4 $\rightarrow$ AP3, M4 $\rightarrow$ AP6 $\rightarrow$ AP2 $\rightarrow$ AP1 $\rightarrow$ AP3, M4 $\rightarrow$ AP6 $\rightarrow$ AP2 $\rightarrow$ AP1 $\rightarrow$ AP5 $\rightarrow$ AP3, M4 $\rightarrow$ AP6

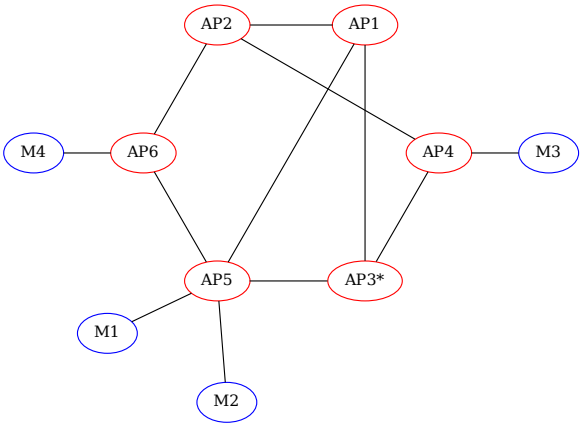

Fig. 2. A network topology with 6 access points and 4 measurement nodes. AP3 is chosen as the gateway access point, i.e, an access point having direct connection to the internet. All requests originating from other nodes in the network are routed through AP3.

$\rightarrow$ AP5 $\rightarrow$ AP3, M4 $\rightarrow$ AP6 $\rightarrow$ AP5 $\rightarrow$ AP1 $\rightarrow$ AP3$\}$. We calculate the scheduling cost by adding up the number of links in these paths irrespective of the number of times they appear in each path. Therefore, the scheduling cost for M4 is 20 in this example. We then assign the first available device with lowest value of scheduling cost to an executing job.

B. Job life-cycle

When a measurement job is requested to be scheduled, a unique identifier is assigned to the job by our system. After the job passes the criteria for a valid MobiPerf job, it gets stored into the metadata database. Next, the job is taken up by the scheduler service after which it is added into a global queue of active jobs. At this point, the job is assigned an instance number of 1. The time at which the job is added to the queue is recorded in the metadata database. A tracker thread executes within the server every 20 seconds that checks whether any of the jobs in the queue is ready to be fed to the underlying scheduling algorithm. This thread is also responsible for checking if a job is ready to be removed or reset. If a number of jobs are past their start time, they are supplied to the scheduling algorithm. The scheduling algorithm assigns a dispatch time and a mobile device to each job. A job is dispatched to the assigned device when the present time exceeds the dispatch time.

After the job finishes execution in the assigned mobile device, the job's results are sent to the measurement server through the websocket connection. The server checks the instance number of the job and records the time at which job's result was received. It also captures the execution time in milliseconds of the job in the mobile device. Starting from this time, when the tracker thread executes for the next time, it resets the job by updating the start time and incrementing the job's instance number. If the end time of the job is attained, it is removed from the job queue.

C. Device-Server communication

When our android application is installed in a phone, it establishes an HTTP websocket connection with the server. This connection is kept alive until the server is shut down manually or the app is manually stopped within the phone. Our android application is robust enough to handle connectivity changes in the community network. If the internet connectivity changes or the user switches to a different type of internet connection in the phone, the phone establishes a new websocket connection with the server. When new jobs are ready to be dispatched from the server, the server publishes the list of jobs to a fixed endpoint. The phone subscribes to this endpoint and receives jobs as and when they are made available.

V. Performance Evaluation

Before the deployment of our system in the community network, we performed evaluations in a lab setup. Fig. 3 and Fig. 4 show the testbeds of our measurement system. In the lab setup, four Android phones were used to conduct our experiments. We first conducted a set of preliminary experiments to determine the execution time of each job type and calibrate our scheduling algorithms. Then we assumed the maximum time across each job type as the expected value of execution time for any upcoming jobs in our system. We argue that the maximum value of execution time would be a good estimate so as to have a safe time window for the next job to execute when the previous job has not finished execution.

The target servers for ping, DNS lookup, traceroute and http were chosen uniformly from Alexa top 8 global websites [21]. TCP speed tests were run against a local speed test server running on the same test network. The periods of the jobs were chosen uniformly from the range [5, 10] minutes.

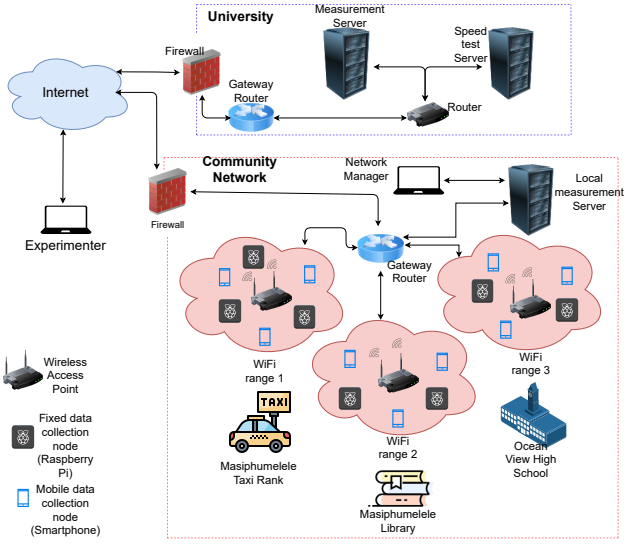

Fig. 3. A diagram showing the testbed for QoSMon set up in the iNethi community network

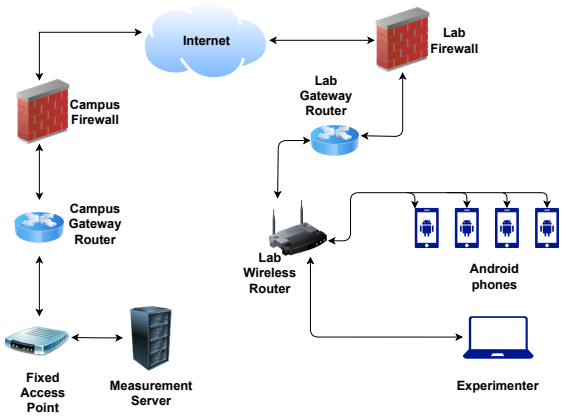

Fig. 4. A diagram showing the testbed for QoSMon set up in a lab environment

For our main experiments, we executed 20 periodic jobs with randomized network topologies containing 8 access points and 4 measurement nodes. Every topology had a conflict probability associated with it. A conflict probability of p indicates that there is an edge between any two access points with a probability of p. Topologies with lower value of conflict probability were likely to have more than one connected component. Therefore, we decided to randomly assign one gateway access point to each connected component in the generated topologies. All four scheduling algorithms were allowed to run with the same topology and set of jobs for 2 hours each. For the next iteration of our experiments, we changed the conflict probability and generated a new topology. The choice of p was made from the set $\{0.1, 0.5, 0.9\}$ so as to ensure that we could capture results for sparsely, moderately and densely connected topologies respectively.

Scheduling algorithms were first compared in terms of their job success rate. For a single periodic job, success rate is defined as:

$$JSR = \frac{Number\ of\ successful\ instances}{Total\ number\ of\ instances} \times 100 \quad (1)$$

For each 2-hour long iteration on a single topology, we calculated the average JSR over all 20 jobs and plotted it against the chosen conflict probability (Fig. 5(a)). Our first observation was that none of the algorithms achieved a 100% success rate for any given topology. This can be attributed to a few jobs missing their deadlines after being sent to the phones for execution. We argue that the job success rate for each algorithm can be improved by limiting the execution period to a fixed threshold of more than 10 minutes. This will allow the tracker thread to pick up less number of jobs at once and thus reduce the overall load on measurement nodes. Another way to improve JSR would be to increase the number of measurement nodes so that jobs can be distributed in a better way. We also observed that DOSD algorithm achieved the least job success rate of all algorithms and the rest of the

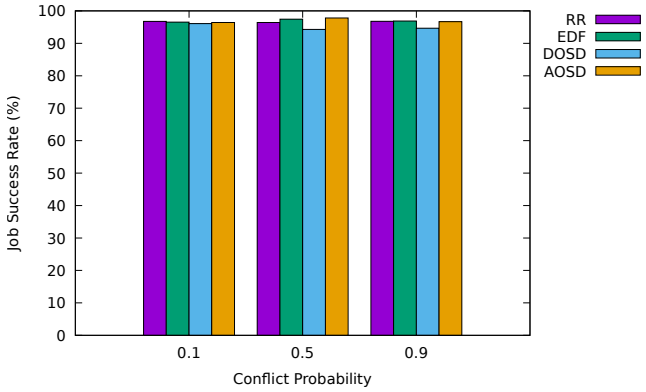

(a) Job success rate

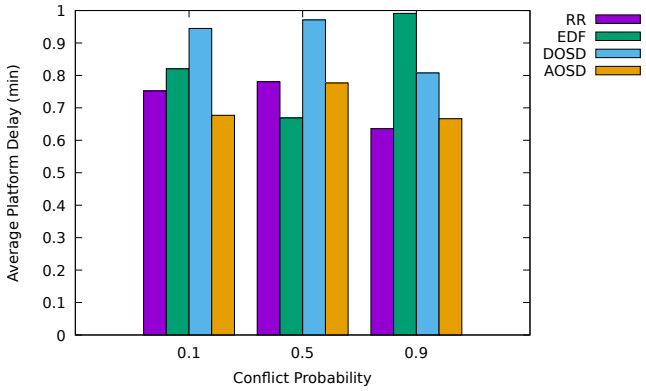

(b) Average platform delay

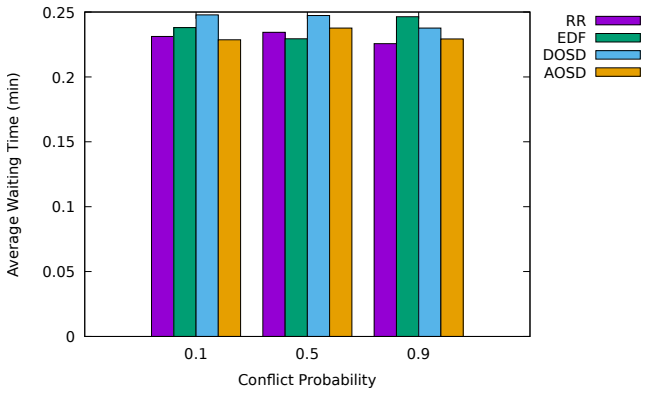

(c) Average waiting time

Fig. 5. Job evaluation metrics used in our experiments

algorithms had similar performance except for moderately connected topologies for which AOSD algorithm performed better than the rest.

We also calculated average platform delay for each periodic job and plotted it against conflict probability. Platform delay is defined as the time difference between actual and expected completion time of the job. For example, if a job's start time is 6:05 PM but its result is received on server end at 6:10 PM, then the platform delay for that particular instance of the job would be 5 minutes. We calculated average platform delay by averaging the platform delay over all instances of all 20 scheduled jobs (Fig. 5(b)). All four algorithms achieved

an average platform delay of less than 30 seconds, which confirms the absence of any implementation issues within our measurement server. AOSD algorithm outperformed the other algorithms for all three topologies except for the case of $p = 0.5$ where EDF performs slightly better. We argue that this is due to the randomized nature of our selection of jobs. We expected that an average over multiple job distributions would declare AOSD as a clear winner.

For determining the root cause behind platform delays, we calculated the waiting time of jobs in the queue (Fig. 5(c)). We observed that the waiting time of the jobs was almost unaffected by network's topology but it contributed quite significantly to the overall platform delay. We observed that 33% of the platform delay in AOSD algorithm was due to waiting time on an average. This percentage was 27%, 29% and 32% for DOSD, EDF and RR respectively. The remaining portion of platform delay was due to factors like network delay and scheduling delay within the phones due to uneven distribution of jobs.

In order to get an idea of the amount of load on the measurement nodes, we calculated their busy time ratios (Fig. 6). This metric translates directly into the energy efficiency of the scheduling algorithms. Better the distribution of jobs to the smartphones, lesser would be the chance of battery drainage. Node busy time ratio for i^{th} node, M_i is defined as:

$$NBTR_i = \frac{e_i}{\sum_{i=1}^{m} e_i} \times 100 \tag{2}$$

where e_i denotes the execution time in milliseconds of all job instances in M_i in a single iteration.

We observed a highly skewed distribution of jobs among the phones in the case of DOSD algorithm. RR and EDF had similar load distribution patterns while the best load distribution was achieved in AOSD, where one of the phones executed about 50% of the total job load in all three topologies. This confirmed that the higher contribution of external factors towards platform delay in RR, EDF and DOSD was indeed due to a skewed distribution of jobs among the phones.

VI. Conclusion

We compared our implementations of four network measurement scheduling algorithms on three different virtual network topologies. We designed our system to schedule network measurements by accounting for conflicts between individual jobs as well as conflicts that arise when active measurements route through common links and access points in wireless networks. Our results show that AOSD algorithm is superior than the rest of the chosen algorithms in terms of efficient distribution of jobs among measurement nodes and job success rate. A success rate as high as 97.3% is extremely useful in areas where internet connection is unstable due to a high proportion of wireless links in comparison to wired links. Our system thus has high applicability in wireless community networks, especially in communities where users access internet through their smartphones.

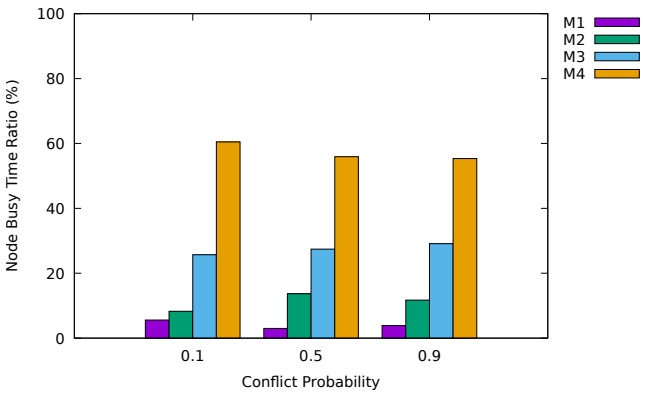

(a) RR

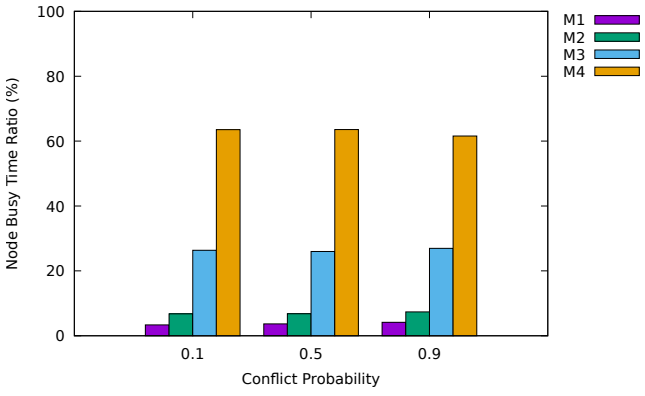

(b) EDF

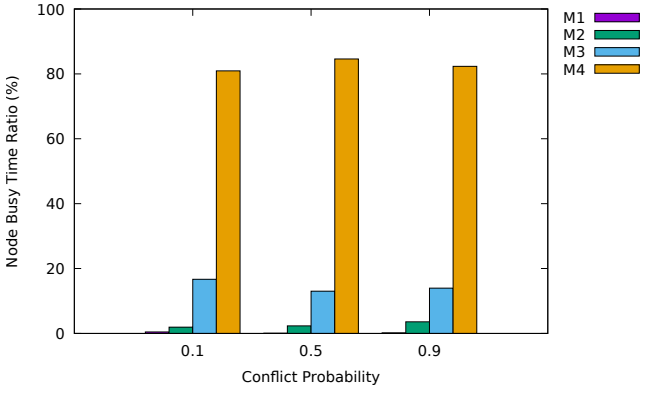

(c) DOSD

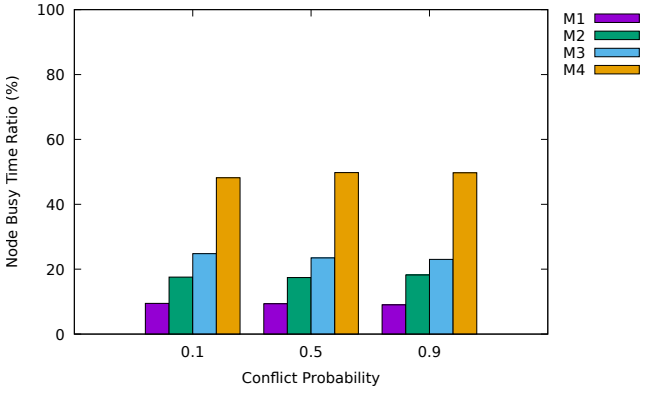

(d) AOSD

Fig. 6. Node busy time ratios for 4 mobile phones used in our experiments

VII. Future Work

In our current work, we make an attempt to find an effective scheduling strategy for low resource network measurements. In future work, the algorithms can be coupled with a job assignment algorithm to ensure even better allocation of jobs to the measurement nodes. A future implementation of our system can also be made to support fixed nodes, like Raspberry Pis coupled with a mininet-based implementation of the network topology. For performance evaluation, dependant variables like number of jobs, number of measurement nodes, time of the day and mobility of the devices etc. will be considered. Another interesting addition to this paper would be the support for on-demand measurements and the adjustment of job schedules in accordance with a custom priority order.

References

[1] R. Baig, R. Roca, L. Navarro, and F. Freitag, "guifi. net: A network infrastructure commons," in *Proceedings of the Seventh International Conference on Information and Communication Technologies and Development*, 2015, pp. 1–4.

[2] B. Braem, C. Blondia, C. Barz, H. Rogge, F. Freitag, L. Navarro, J. Bonicioli, S. Papathanasiou, P. Escrich, R. Baig Viñas *et al.*, "A case for research with and on community networks," 2013.

[3] (2020) Statistics. [Online]. Available: https://www.itu.int/en/ITU-D/Statistics/Documents/statistics/2020/MobileCellularSubscriptions_2000-2019.xlsx

[4] (2021) Internet users in the world 2021 — Statista. [Online]. Available: https://www.statista.com/statistics/617136/digital-population-worldwide/

[5] A. Faggiani, E. Gregori, L. Lenzini, V. Luconi, and A. Vecchio, "Smartphone-based crowdsourcing for network monitoring: opportunities, challenges, and a case study," *IEEE Communications Magazine*, vol. 52, no. 1, pp. 106–113, 2014.

[6] Z. Qin, R. Rojas-Cessa, and N. Ansari, "Task-execution scheduling schemes for network measurement and monitoring," *Computer communications*, vol. 33, no. 2, pp. 124–135, 2010.

[7] G. Aceto, A. Botta, W. De Donato, P. Marchetta, A. Pescapé, and G. Ventre, "Open source platforms for internet monitoring and measurement," in *2012 Eighth International Conference on Signal Image Technology and Internet Based Systems*. IEEE, 2012, pp. 563–570.

[15] M. R. Lorini, M. Densmore, D. Johnson, S. Hadzic, H. Mthoko, G. Manuel, M. Waries, and A. van Zyl, "Localize-it: Co-designing a community-owned platform," in *International Development Informatics Association Conference*. Springer, 2018, pp. 243–257.

[8] D. Vega, R. Baig, L. Cerdà-Alabern, E. Medina, R. Meseguer, and L. Navarro, "A technological overview of the guifi. net community network," *Computer Networks*, vol. 93, pp. 260–278, 2015.

[9] L. Cerda-Alabern, "On the topology characterization of guifi. net," in *2012 IEEE 8th International Conference on Wireless and Mobile Computing, Networking and Communications (WiMob)*. IEEE, 2012, pp. 389–396.

[10] L. Maccari and R. L. Cigno, "A week in the life of three large wireless community networks," *Ad Hoc Networks*, vol. 24, pp. 175–190, 2015.

[11] P. A. Frangoudis, G. C. Polyzos, and V. P. Kemerlis, "Wireless community networks: an alternative approach for nomadic broadband network access," *IEEE Communications Magazine*, vol. 49, no. 5, pp. 206–213, 2011.

[12] J. Avonts, B. Braem, and C. Blondia, "A questionnaire based examination of community networks," in *2013 IEEE 9th International Conference on Wireless and Mobile Computing, Networking and Communications (WiMob)*. IEEE, 2013, pp. 8–15.

[13] E. E. P. Pujol, W. Scott, E. Wustrow, and J. A. Halderman, "Initial measurements of the cuban street network," in *Proceedings of the 2017 Internet Measurement Conference*, 2017, pp. 318–324.

[14] C. Rey-Moreno, Z. Roro, W. D. Tucker, M. J. Siya, N. J. Bidwell, and J. Simo-Reigadas, "Experiences, challenges and lessons from rolling out a rural wifi mesh network," in *Proceedings of the 3rd ACM Symposium on Computing for Development*, 2013, pp. 1–10.

[16] R. L. Cottrell, C. Logg, and I.-H. Mei, "Experiences and results from a new high performance network and application monitoring toolkit," in *Passive and Active Measurement Workshop*, 2003.

[17] M. Luckie and A. McGregor, "Ipmp: Ip measurement protocol," in *Passive and Active Measurement Workshop*, 2002.

[18] P. Calyam, C.-G. Lee, P. K. Arava, and D. Krymskiy, "Enhanced edf scheduling algorithms for orchestrating network-wide active measurements," in *26th IEEE International Real-Time Systems Symposium (RTSS'05)*. IEEE, 2005, pp. 10–pp.

[19] M. Clegg, "Scheduling network performance monitoring in the cloud," 2017.

[20] "About the Object Management Group," accessed on October 15, 2020. [Online]. Available: https://www.inethi.org.za/

[21] "Alexa Internet," accessed on May 26, 2021. [Online]. Available: https://www.alexa.com/topsites

Taveesh Sharma is a Masters in Computer Science student at the University of Cape Town (UCT). His research topic is Investigating Optimal Internet Data Collection in Low Resource Networks. He obtained his honours degree from the Birla Institute of Technology and Science in India.

Josiah Chavula is a lecturer and researcher in Computer Science at the University of Cape Town. He received a PhD in Computer Science from UCT (2017), and an MSc in Networking and Internet Systems from Lancaster University (2011). His research focuses on performance of internet systems in Low Resource contexts.

Standards, Regulatory & Environmental

Development of Carbon Black/Graphite Filled Immiscible Polymer Blend for Application in Bipolar Plates for Fuel Cells

Oluwaseun Ayotunde Alo[1], Iyiola Olatunji Otunniyi[2], Johan Bekker[3]

[1,2]*Department of Chemical and Metallurgical Engineering, Vaal University of Technology, Vanderbijlpark, South Africa*

[3]*Centre for Alternative Energy, Vaal University of Technology, Vanderbijlpark, South Africa*

oluwaseuna@vut.ac.za

***Abstract*— Bipolar plates (BPs) constitute a key component of fuel cells (FCs), which are promising backup power supply for telecommunication and digital applications. Conductive polymer composites (CPCs) typically have good corrosion resistance required for FC BPs but there is usually a need for material compositions that provide maximized electrically conductive network. In this study, CPCs based on polyethylene (PE)-epoxy (EP) blend filled with graphite (as main filler) and highly conductive carbon black (CB) minor filler were produced. It was found that the PE-EP-G/CB composite with 80 wt% total filler content exhibited the lowest in-plane (≈0.01 Ω.cm) and through-plane (≈0.1 Ω.cm) resistivities. Also, the PE-EP-50G/CB composite exhibited superior electrical conductivity compared to the PE-EP-50G composite with no CB filler. The highest flexural strength and flexural modulus obtained were 30.17 MPa and 4.58 GPa, respectively, at 60 wt% total filler content and increase in filler content beyond 60 wt% caused a decrease in the flexural properties. The low resistivity values obtained for the PE-EP-G/CB composites could be attributed to bridging of the spaces between the larger graphite particles by the nano-sized CB particles as well as concentration of the fillers in one of the polymer phases in the blend. Combination of CB and graphite with immiscible blend of PE and EP has the potential to achieve CPCs with electrical and flexural performance that meet the requirements for BP application.**

Keywords- Fuel cell; bipolar plates; conductive polymer composite; electrical conductivity; carbon black.

I. INTRODUCTION

Fuel cell (FC) technology has emerged as a promising reliable energy solution to replace the problematic fossil fuel-based energy sources. In applications such as telecommunication infrastructures, data centers, and various digital technologies, FCs such as the polymer electrolyte membrane fuel cells (PEMFCs) offer an efficient and reliable backup power supply. FCs offer several benefits compared to other backup power sources such as batteries and generators. Contrary to batteries, FCs can operate for several years without a decline in capacity. They are also more durable and predictable than batteries. Compared to generators, FCs provide cleaner and quieter power generation, with less need for on-site maintenance [1-2].

The bipolar plate (BP) is one of the key components of FCs and its performance is critical to the overall performance of the FC stack. Fig. 1 shows a schematic of the PEMFC with anode and cathode sides of the BP. Therefore, the development of low-cost and high-performance materials for BP application has been a critical research issue. Due to the stringent low-cost, high performance and high durability requirements for BPs, the development of materials for commercial BP application remains a challenge. As a result of their low cost, light weight, good corrosion resistance, and good formability characteristics, conductive polymer composites (CPCs) have the potential to meet the above requirements [3]. However, to take full advantage of their benefits, problems associated with achieving high electrical conductivity in CPCs without compromising the mechanical strength beyond acceptable levels for FC BPs still need to be solved [4]. Decrease in mechanical strength of CPCs at the high filler content necessary to impart adequate electrical conductivity required for BP application is difficult to avoid. Therefore, the goal is often to make sure that the CPC retains enough flexural strength to meet the target set by the United States Department of Energy (DOE) for FC BPs (i.e., > 25 MPa), while simultaneously meeting the low electrical resistivity target of < 0.01 Ω.cm (in-plane) and < 0.05 Ω.cm (through-plane) [5].

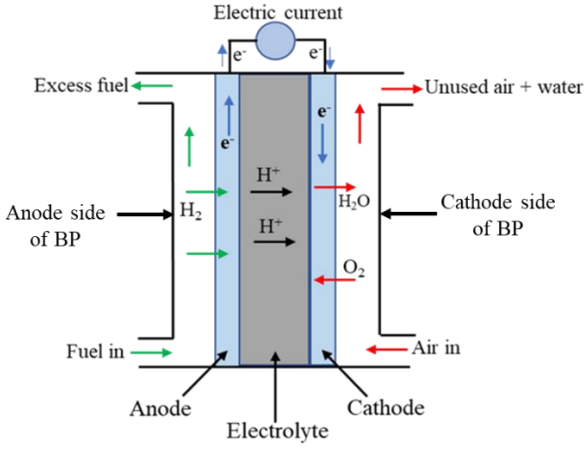

Figure 1: Schematic of a PEMFC

Meeting the high electrical performance requirement for CPC BPs requires material formulations that yield composites with maximized electrical conductive behaviour. Due to the high electrical conductivity of graphite and the small particle size (30 nm) of conductive carbon black (CB), CPCs in which graphite (G) is the main filler and CB is the minor filler have the potential to achieve high electrical performance for BP application. The nano-sized CB particles can fill the voids between the larger graphite particles, leading to more conductive networks and composites with high electrical conductivities. Lee et al. [6] reported higher electrical conductivity and lower amount of filler required to achieve a given conductivity level in polymer/G composites with CB as a secondary filler compared to the composites with no CB filler. Jiang and Drzal [3] also reported an improvement in the electrical conductivity of polyphenylene sulphide (PPS)/graphene nanoplatelets/CB composite as the CB content increased. Similar trends have been reported by other authors [7] - [9]. However, at certain critical concentrations of CB, which varied with the type of polymer matrix and conductive filler used, the electrical conductivity and mechanical strength of the composites decreased with increase in CB content due to poor filler wetting. Therefore, the electrical and mechanical behaviour of specific matrix-G/CB composite systems needs to be investigated and established. In a previous study by Alo et al. [10], the potential of graphite-filled immiscible polyethylene (PE)-epoxy (EP) blend for BP application has been reported. However, further improvement in electrical conductivity of the composite through incorporation of a secondary filler that can enhance the conductive network formation is necessary. Improvement in the electrical conductivity of G-filled polypropylene (PP)-EP blend by incorporating CB as secondary filler has been demonstrated [11]. Thus, it is expected that significant improvement in conductivity can be achieved with G/CB-filled PE-EP blends. Also, the water absorption characteristics of BP materials in the humid operating environment of the FC is critical to the overall performance of the FC stack.

Thus, the aim of the present work is to investigate the electrical, flexural, and water absorption properties of composites based on PE-EP blend filled with G/CB hybrid filler for potential application in BPs for FCs. It was expected that the small-sized CB would fill the spaces between the larger graphite particles. Therefore, the concentration of the CB minor filler was gradually increased as the graphite content increased.

II. EXPERIMENTAL

The high density PE 547999 (Melt index 2.2 g/10 min) and polyethylene-grafted-maleic anhydride 456632 (PE-g-MAH) compatibilizer used in this study were supplied by Sigma-Aldrich. The bisphenol-A epoxy resin (LR 30) and the amine-type hardener (LH 30) were supplied by AMT Composites, South Africa. The graphite powder (> 99% purity) used was donated by Graftech, South Africa while the highly conductive CB PRINTEX XE2-B (average particle size 30 nm) was supplied by Orion Engineered Carbons. The composites were melt-mixed in a Haake Rheomix OS mixer at 190 ^{o}C and 60 rpm for 10 minutes. After mixing, the samples were compression moulded at 200 ^{o}C at 6 metric tonnes for 10 minutes. Details of the composite formulations are shown in Table 1.

TABLE 1
FORMULATIONS OF THE PE-EP-G/CB COMPOSITES

Sample	Polymer	Filler	
		Graphite (wt%)	CB (wt%)
PE-50G/CB	PE	49	1
EP-50G/CB	Epoxy	49	1
PE-EP-50G	PE-EP	50	-
PE-EP-50G/CB	PE-EP	49	1
PE-EP-60G/CB	PE-EP	57	3
PE-EP-70G/CB	PE-EP	65	5
PE-EP-80G/CB	PE-EP	73	7

Measurements of the in-plane electrical resistivity were performed on samples with 50 × 13 mm dimensions using the four-point probe method according to the ASTM D4496. A Metronix 544B DC power supply was used to provide a constant current through the two outer probes while the voltage drop between the inner probes was measured with a Brymen TBM525 digital multimeter (Fig. 2). The electrical resistivity (ρ) was calculated using equation (1):

$$\rho = \frac{\pi}{ln2} \times t \times R \times f_1 f_2 \quad (1)$$

Where R is the measured resistance (Ω), f_1 and f_2 are finite thickness and width correction factors, respectively, and t is the thickness of the sample (cm). Based on the dimensions of the test specimens, the values f_1 and f_2 were obtained from data in literature [12], [13]. The mean resistivity was calculated from five measurements.

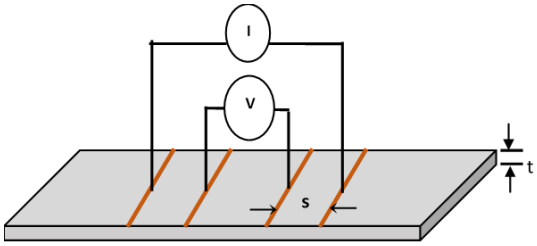

Figure 2: Schematic of experimental setup for measurement of in-plane electrical resistivity

The through-plane resistivity measurements were carried out on 30 mm × 30 mm samples, using the set-up shown in Fig. 3. As shown in Fig. 3a, the sample was placed between the carbon cloth gas diffusion layers (GDLs) to simulate contact situation between the BPs and the GDLs in a FC stack and ensure electrical contact between the sample and copper plate current collectors. Each sample was pressed between the copper plates under a constant pressure of 140 Ncm^{-2} and the total resistance was measured using a dual display LCR meter (Escort ELC-131D).

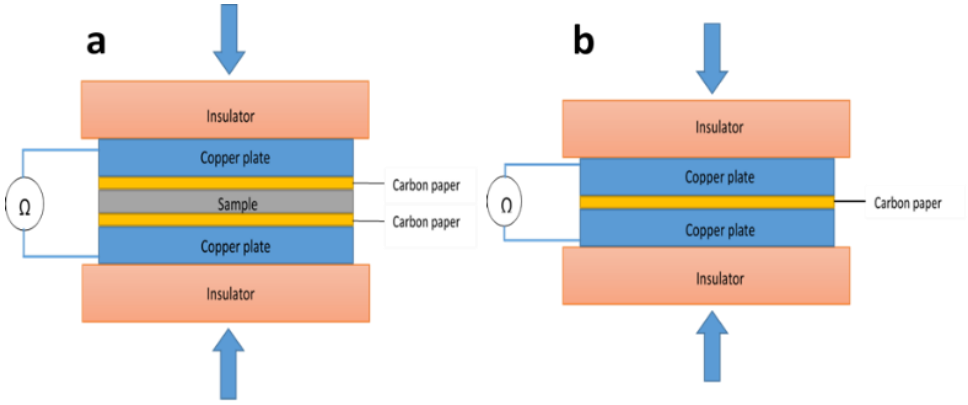

Figure 3: Schematic of set up for through-plane resistivity measurement

The total resistance of the set-up without the specimen (Fig. 3b) was also measured. The resistance of the sample was then calculated using Equation 2:

$$R = R_T - 2\,R_C \quad (2)$$

R, R_T and R_C are specimen resistance, measured system total resistance with specimen and total resistance of the system without the specimen, respectively. The volume resistivity was calculated using the following equation:

$$\rho(\Omega cm) = R_s(\Omega) \times \frac{A(cm^2)}{t(cm)} \quad (3)$$

A represents area of the specimen (cm^2) and t is thickness (cm). The flexural testing was carried out according to ASTM D 790-03 using a universal testing machine (Instron 5966). Water absorption measurements were carried out following the ASTM D570 procedure. Specimens having a dimension of 13 mm × 13 mm were weighed and then immersed in distilled water at 60 ºC for 24 hours. The specimens were then removed, wiped dry of excessive water, and weighed again. The water absorption of specimens was calculated according to the equation:

$$\text{Water absorption} = \frac{w_c - w_d}{w_d} \times 100\% \quad (4)$$

where w_c is the weight of the specimen at time t, and w_d is the weight of the dry specimen.

III. RESULTS AND DISCUSSION

A. Microstructure of Fillers and PE/EP/G/CB Composites

As shown in Fig. 4a, the graphite filler exhibits a flaky morphology. This type of morphology enhances contacts between the filler particles, thereby promoting formation of continuous conducting pathways within composites. Also, microstructure of the CB (Fig. 4b) shows agglomerated particles, which also favours formation of contacts between conductive filler particles, leading to improved electrical conductivity in CPCs. Fig. 4c shows the morphology of the PE-EP-G/CB with 50 wt% total filler. The graphite flakes are visible within the composite, but few distinct polymeric regions can be seen in the micrograph because of the high filler loading in the composite. Therefore, the composites will contain few regions in which the insulating polymeric phase is located in the gaps between the filler particles, which promotes high electrical conductivity.

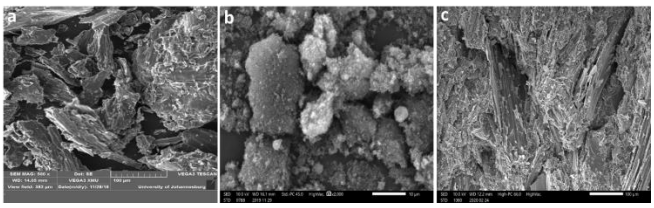

Figure 4: SEM micrographs of (a) graphite; (b) CB; (c) PE-EP-50G/CB composite

B. Electrical Conductivity of the PE-EP-G/CB Composites

The in-plane (Fig. 5) and through-plane (Fig. 6) electrical resistivity of the PE-EP-G/CB composites decreased from 0.0201 Ω.cm to 0.0098 Ω.cm and 1.9801 Ω.cm to 0.1016 Ω.cm, respectively, as the total filler concentration increased from 50 to 80 wt%. The electrical conductivity of CPCs is influenced by factors such as morphology of filler(s), dispersion state of filler(s), and contact between the filler particles [14], [15]. Increase in the concentration of fillers leads to more contacts between filler particles, which leads to reduced electrical resistivity. Also, the use of graphite and highly conductive CB would have a synergetic effect on the conductive network formation in the composite. Findings from previous studies have provided evidence that the improvement in electrical conductivity observed in polymer-G/CB composites compared to polymer-G composites with no CB addition is due to formation of more continuous conducting networks [8], [9], [16]. The nano-sized CB particles, with spherical geometry and high surface area, can effectively fill the gaps between the larger graphite platelets. Therefore, the decrease in electrical resistivity with increase in total filler concentration is due to formation of more conducting pathways within the composites. It is noteworthy that the concentration of the CB was increased in the formulations as the graphite content was increased in order to have more CB particles to fill the extra graphite-graphite interparticle spaces that would be present as a result of increased graphite contents. While the PE-EP-80G/CB composite exhibit in-plane resistivity that exceeds

the DOE target of < 0.01 Ω.cm, none of the composites meet the through-plane resistivity target of < 0.05 Ω.cm. However, the level of electrical performance achieved by the PE-EP blend-based composites is promising for further investigations for improvement.

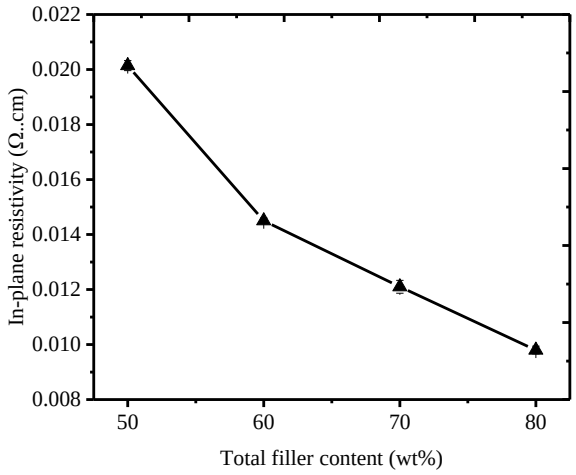

Figure 5: In-plane electrical resistivity of the PE-EP-G/CB composites

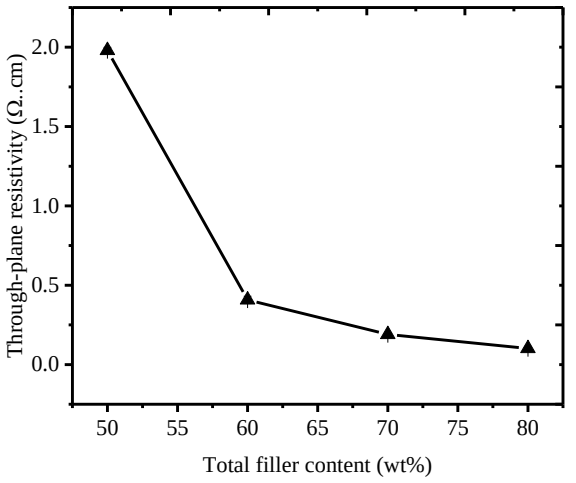

Figure 6: Through-plane electrical resistivity of the PE-EP-G/CB composites

The benefit of the G-CB hybrid filler on the conductivity behaviour of the composites is further revealed by the lower electrical resistivity of the PE-EP-50G/CB (0.02 Ω.cm) compared to the PE-EP-50G composite (0.04 Ω.cm) (Fig. 7).

In single polymer-conductive filler systems, depending on the filler type and processing conditions, fillers tend to be homogeneously distributed in the polymer matrix. However, in a composite having a matrix of immiscible polymer blend with co-continuous structure, selective distribution of filler within a segregated volume occurs [17]. In our previous studies [10], [18], it has been shown that the PE-EP blend exhibit a co-continuous morphology and selective distribution of filler in the epoxy occurred when the blend was filled with graphite particles. This type of filler dispersion, for a given filler content, favours formation of more contacts between filler particles, which leads to lower electrical resistivity. Therefore, as shown in Fig. 7, the PE-EP-G/CB with total filler content of 50 wt% has a lower in-plane electrical resistivity compared to the PE-G/CB composite and EP-G/CB composite, both with 50 wt% total filler content. This indicates the potential of combination of polymer blend matrix with hybrid conductive filler systems for achieving CPCs with high electrical performance for BP application.

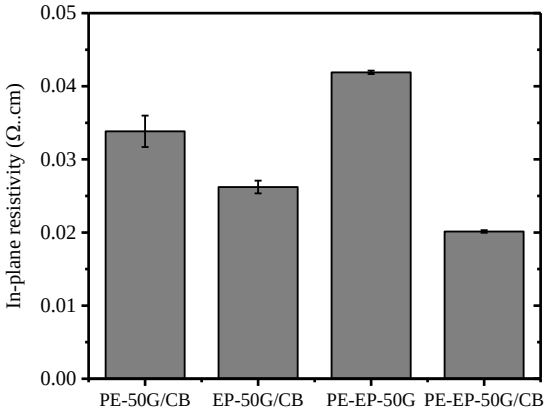

Figure 7: In-plane resistivity of G/CB-filled polymer blend and single polymers at 50 wt% filler content

C. Flexural Properties of the PE-EP-G/CB Composites

BPs must possess good mechanical strength to be able to withstand the high clamping forces in the FC stack and vibrations if applied in FC vehicles [19]. Fig. 8 shows the variation of the flexural properties of the composites with increase in total filler content. The flexural strength initially increased with increase in the total filler content up to a maximum value of 30.17 MPa at 60 wt% filler, which is above the DOE target of > 25 MPa. Further increase in filler concentration caused a decrease in the flexural strength. The decrease may be due to lack of enough polymers to wet the fillers, leading to poor matrix-filler adhesion. Also, as the amount of CB in the composites increased as the total filler content increased, there would be a greater tendency for agglomeration of the CB particles at higher total filler contents. When mechanical stress in applied during measurement of flexural properties, if the matrix-filler interaction is poor, agglomerates may cause stress concentrations, leading to reduced mechanical strength [20].

As the total filler content was increased, the flexural modulus of the composites increased from 2.96 GPa at 50 wt% filler to 4.58 GPa at 60 wt% total filler content. This can be attributed to much higher stiffness of the graphite main filler compared to the polymer matrix. However, increase in the total filler content beyond 60 wt% caused a decrease in the flexural modulus. At high filler concentration, the presence of air gap between the layered structure of the graphite as a result of insufficient polymer resin to wet the entire filler surface area could account for the reduced flexural modulus of the samples. Although, the PE-EP-60G/CB composite exhibit lower in-

plane and through-plane electrical conductivities compared to PE-EP-70G/CB and PE-EP-80G/CB composites (Fig. 5 and 6), it exhibits the best flexural performance.

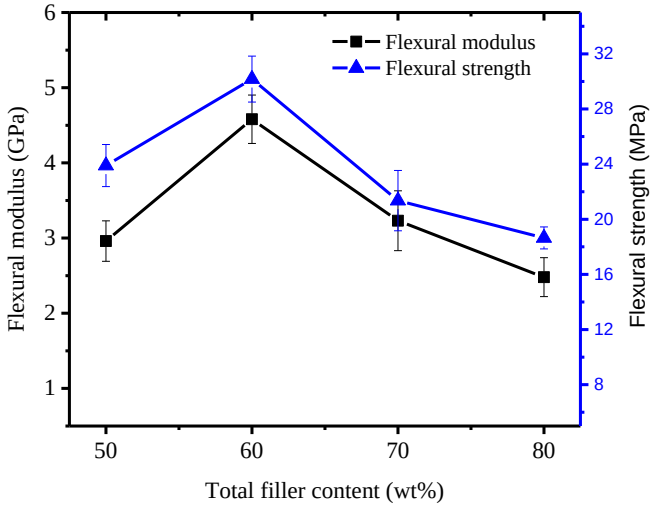

Figure 8: Flexural strength and modulus of the composites as a function of total filler content

D. Water absorption of the PE-EP-G/CB composites

Due to the hydrophobic nature and barrier effect of the platelet structure of graphite, graphite-filled polymer composites tend to exhibit resistance to absorption of moisture compared to the neat polymer [21], [22]. Therefore, to determine the effect of addition of CB secondary filler on the water absorption behaviour of the composites, water absorption tests were performed on both the PE-EP-G/CB composites and PE-EP-G composites with 50 to 80 wt% total filler concentration. The water absorption experiments were carried out at 60 ^{o}C to simulate the warm operating condition of the PEMFC. The variation of water absorption of the PE-EP-G/CB and PE-EP-G composites with increase in total filler content is shown in Fig. 9. As the total filler content increased from 50 to 80 wt%, the water absorption of the PE-EP-G composites increased slightly from 0.19% to 0.20% (≈5% increase) while the water absorption of the PE-EP-G/CB composites increased more considerably from 0.2% to ≈0.3% (50% increase). The slight increase in water absorption of the PE-EP-G composites can be attributed to increase in micro gaps as a result of reduced filler wetting, which counteract the barrier effect of the graphite platelets. In the case of the PE-EP-G/CB composites, the increase in water uptake is more significant. This can be attributed to the loose structure of CB secondary filler, which more than offset the effect of its hydrophobic nature and barrier effect of the graphite platelets. However, DOE water absorption target for PEMFC BP at 24 hours immersion is < 0.3% [23], and all the composites meet this target.

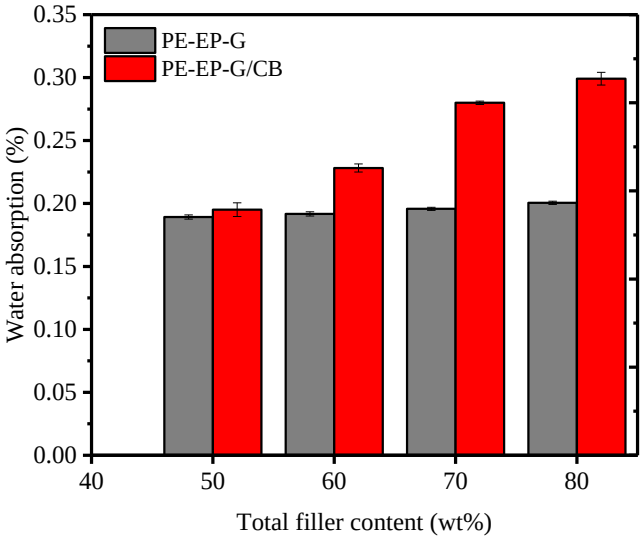

Figure 9: Variation of water absorption of PE-EP-Ge and PE-EP-G/CB composites with increasing total filler content.

IV CONCLUSION

CPCs based on PE-EP blend filled with G/CB hybrid filler were prepared by melt mixing followed by compression molding. The composites were then characterized in terms of electrical resistivity, flexural properties, and water absorption. The in-plane and through-plane electrical resistivities of the composites decreased as the total filler content increased. The PE-EP-G/CB composite with 80 wt% total filler exhibited the lowest in-plane and through-plane resistivities of ≈0.01 Ω.cm and ≈0.1 Ω.cm, respectively. The low resistivity of the PE-EP-G/CB composites could be attributed to bridging of the spaces between the larger graphite platelets by the nano-sized CB particles and the concentration of the fillers in one of the polymer phases in the blend. Both flexural strength and modulus of the composites initially increased with addition of the G/CB filler up to maximum values of 30.17 MPa and 4.58 GPa, respectively, and further increase in filler content caused a decrease in the flexural properties. The decline in flexural properties can be attributed to agglomeration of the CB and poor filler wetting at higher concentrations of the G/CB hybrid filler. Water absorption of the PE-EP-G/CB composites increased considerably as the filler content increased from 50 to 80 wt%. The loose structure of the CB filler, would more than offset the effect of its hydrophobic nature and barrier effect of the graphite platelets, leading to increase in water uptake. The properties exhibited by the PE-EP-G/CB composites show that combining G/CB hybrid filler with PE-EP blend is a promising approach to achieve CPC BPs that meet the DOE targets.

ACKNOWLEDGMENTS

The authors will like to thank the National Research Foundation of South Africa, Telkom Centre of Excellence, and Chemical and Metallurgical Engineering Department of the Vaal University of Technology for the financial support for the work.

REFERENCES

[1] Ghenai, C.; Bettayeb, M., Modelling and performance analysis of a standalone hybrid solar PV/Fuel Cell/Diesel Generator power system for university building. *Energy* **2019,** *171*, 180-189.

[2] Serincan, M. F., Reliability considerations of a fuel cell backup power system for telecom applications. *Journal of Power Sources* **2016,** *309*, 66-75.

[3] X. Jiang and L. T. Drzal, "Exploring the potential of exfoliated graphene nanoplatelets as the conductive filler in polymeric nanocomposites for bipolar plates," *Journal of Power Sources*, vol. 218, pp 297-306, 2012**.**

[4] M. Y. Zakaria, A. B. Sulong, J. Sahari and H. Suherman, "Effect of the Addition of Milled Carbon Fiber as a Secondary Filler on the Electrical Conductivity of Graphite/Epoxy Composites for Electrical Conductive Material," *Compos Part B: Eng.*,vol. 83, pp 75-80, 2015.

[5] A. Naji, B. Krause, P. Pötschke and A. Ameli, "Hybrid conductive filler/polycarbonate composites with enhanced electrical and thermal conductivities for bipolar plate applications,". *Polymer Composites*, vol. 40, issue 8, pp 3189-3198, 2019.

[6] J. H. Lee, Y. K. Jang, C. E. Hong, N. H. Kim, P. Li and H. K. Lee, "Effect of carbon fillers on properties of polymer composite bipolar plates of fuel cells," *Journal of Power Sources*, vol. 193, issue 2, pp 523-529, 2009.

[7] H. Suherman, J. Sahari and A. B. Sulong, "Effect of small-sized conductive filler on the properties of an epoxy composite for a bipolar plate in a PEMFC," *Cerami. Int.* vol. 39, issue 6, pp 7159-7166, 2013.

[8] D. Wu, Q. Lv, S. Feng, J. Chen, Y. Chen, Y. Qiu and X. Yao, "Polylactide composite foams containing carbon nanotubes and carbon black: Synergistic effect of filler on electrical conductivity," *Carbon*, vol. 95, pp 380-387, 2015.

[9] N. A. M. Radzuan, M. Y. Zakaria, A. B. Sulong and J. Sahari, "The effect of milled carbon fibre filler on electrical conductivity in highly conductive polymer composites," *Compos. Part B: Eng.*, vol. 110, pp 153-160, 2017.

[10] O. A. Alo, I. O. Otunniyi and C. Pienaar, "Exploring the Potential of Polyethylene/Epoxy/Graphite Composite as Bipolar Plate Material for Proton Exchange Membrane Fuel Cell," in 2020, AIP Conference Proceedings 2289, pp 020007-1 - 020007-5.

[11] O. A. Alo, I. O. Otunniyi, C. Pienaar and E. R. Sadiku, Electrical and mechanical properties of polypropylene/epoxy blend-graphite/carbon black composite for proton exchange membrane fuel cell bipolar plate. *Materials Today: Proceedings* 2021**,** *38*, 658-662.

[12] W. R. Runyan, *Semiconductor measurements and instrumentation*. McGraw-Hill: New York, 1975.

[13] D. K. Schroder, *Semiconductor material and device characterization*. Third ed.; John Wiley & Sons: New Jersey, 2015.

[14] X. Li, H. Deng, Q. Zhang, F. Chen and Q. Fu, "The effect of DBP of carbon black on the dynamic self-assembly in a polymer melt," *RSC Advances*, vol. 6, issue 30, pp 24843-24852, 2016.

[15] W. Fang, H. W. Jang and S. N. Leung, "Evaluation and modelling of electrically conductive polymer nanocomposites with carbon nanotube networks." *Composites Part B: Engineering*, vol. 83, pp 183-193, 2015.

[16] Y. Nakaramontri, S. Pichaiyut, S. Wisunthorn and C. Nakason, "Hybrid carbon nanotubes and conductive carbon black in natural rubber composites to enhance electrical conductivity by reducing gaps separating carbon nanotube encapsulates," *European Polymer Journal*, vol. 90, pp 467-484, 2017.

[17] T. Gong, S. P. Peng, R. Y. Bao, W. Yang, B. H. Xie and M. B. Yang, "Low percolation threshold and balanced electrical and mechanical performances in polypropylene/carbon black composites with a continuous segregated structure," *Composites Part B: Engineering*, vol. 99, pp 348-357, 2016.

[18] O. A. Alo and I. O. Otunniyi, "Graphite-Filled Polyethylene/Epoxy Blend for High-Conductivity Applications: The Immiscibility Edge," *Polym. Plast. Technol. Mater.*, pp 1-12, 2020.

[19] R. Taherian, "A review of composite and metallic bipolar plates in proton exchange membrane fuel cell: Materials, fabrication, and material selection," *J. Power Sources*, vol. 265, pp 370-390, 2014.

[20] B. Caglar, P. Fischer, P. Kauranen, M. Karttunen and P. Elsner, "Development of carbon nanotube and graphite filled polyphenylene sulfide based bipolar plates for all-vanadium redox flow batteries," *Journal of Power Sources*, vol. 256, pp 88-95, 2014.

[21] M Phuangngamphan, M. Okhawilai, S. Hiziroglu and S. Rimdusit, "Development of highly conductive graphite-/graphene-filled polybenzoxazine composites for bipolar plates in fuel cells," *J. Appl. Polym. Sci.*, vol. 136, issue 11, p. 47183, 2019.

[22] R. Plengudomkit, M. Okhawilai and S. Rimdusit, "Highly filled graphene-benzoxazine composites as bipolar plates in fuel cell applications," *Polym. Compos.*, vol. 37, issue 6, pp 1715-1727, 2016.

[23] R. K. Gautam and K. K. Kar, "Synergistic effects of carbon fillers of phenolic resin based composite bipolar plates on the performance of PEM fuel cell," *Fuel Cells*, vol. 16, issue 2, pp 179-192, 2016.

Oluwaseun Alo is a postdoctoral research fellow in the Department of Chemical and Metallurgical Engineering, Vaal University of Technology. He is currently working with the Additive Manufacturing Department at the Technology Transfer and Innovation (TTI) within the institution on polymer additive and advanced manufacturing.

Iyiola Otunniyi is an associate professor in the Department of Chemical and Metallurgical Engineering, Vaal University of Technology. His research interests include Physical Metallurgy, Mineral Processing and Extractive Metallurgy.

Johan Bekker completed his Ph.D in 2007, with focus on photovoltaic materials used to manufacture solar panels. He has a very keen research interest in Alternative Energy in general, currently is Associate Professor at the Vaal University of Technology, and head of the Centre for Alternative Energy.

Using Machine Learning to Predict Preeclampsia in Pregnant Women in South Africa

Nathan Smith[1], Prof Janet Wesson[2]

Department of Computing Sciences, Nelson Mandela University, Gqeberha, South Africa

[1]Nathan.Smith@Mandela.ac.za

[2]Janet.Wesson@Mandela.ac.za

***Abstract*— Preeclampsia is one of the leading causes of maternal mortality in South Africa and the world. Due to South Africa's poor antenatal care, the prediction of pregnant women at risk of developing preeclampsia is vital for allocating scarce resources. This paper proposes a machine learning model to predict preeclampsia using existing antenatal care datasets from South African hospitals. To the researcher's knowledge, this proposed model will be the first machine learning model for predicting preeclampsia using a South African dataset. A review of the literature and existing systems was performed to identify the eight risk factors. These risk factors are systolic blood pressure, diastolic blood pressure, maternal age, body mass index, diabetes status, hypertension history, nulliparity, and maternal disease. The proposed model will use supervised learning and will be evaluated using five evaluation metrics, namely classification accuracy, confusion matrix, logarithmic loss, area under curve, and F-Score.**

***Keywords*— Preeclampsia, Pregnancy, Predictions, Forecasting, Machine Learning, Supervised Learning, Proposed Model**

I. Introduction

Approximately 800 women die every day worldwide from preventable causes due to pregnancy and childbirth. Ninety-four per cent of these maternal deaths occur in low- to middle-income countries, with Sub-Saharan Africa accounting for two-thirds of these deaths [1]. Hypertensive disorders of pregnancy, such as preeclampsia, are the second leading causes of maternal death in South Africa [2]. Preeclampsia, usually diagnosed after 20 weeks' gestation, is the new onset of hypertension. It is a disorder characterised by high blood pressure, usually above 140/90, and the presence of proteinuria [3]. The mortality of pregnant women with preeclampsia is accompanied by increased foetal mortality and disability rates [4], [5]. The maternal complications associated with preeclampsia are acute kidney disease and placental abruption. In severe circumstances, preeclampsia can lead to low platelet count, elevated liver enzymes, haemolysis and eclamptic seizure.

Preeclampsia can be categorised into two groups, early- and late-onset. Early-onset preeclampsia develops before 34 weeks' gestation, and late-onset preeclampsia develops after 34 weeks' gestation. In South Africa, preeclampsia incidence is much higher than reported in other low- and middle-income studies. These statistics could be explained by South African women lacking access to antenatal and postnatal care, resulting in delays in seeking care [2]. If they can find a clinic, many pregnant women only attend their first session or attend it very late in their pregnancy [6]. South Africa has been fighting this ongoing battle with access to antenatal care and preeclampsia for decades, despite the availability of free antenatal care throughout the country [7], [6].

The importance of antenatal care for pregnant women with hypertensive disorders is echoed in a meta-analysis of the prevalence of hypertensive disorders of pregnancy, and pregnancy outcomes in Sub-Saharan Africa. The meta-analysis recommends future research in strategies to predict those women at greater risk of hypertensive disorders. Since there are no preventative measures for preeclampsia, clinics focus on early detection and surveillance. Early detection will allow for the prioritisation of preeclampsia patients, especially in low resource settings. Due to the large amounts of data the health sector produces, machine learning offers a useful way to extract meaning from this data [8]. The health sector has already seen the positive impact that machine learning has had on the accuracy of prediction in healthcare [9], [10]. This paper proposes a model that will predict if a pregnant woman is at risk of developing preeclampsia.

II. Related Work

Jhee et al. [11] developed a model to predict late-onset preeclampsia using machine learning-based methods. They included data from 11,006 women from the Yonsei University Healthcare Centre in China between 2005 and 2017. The preeclampsia development rate was 4.7% (n=474). The data included were: age, blood pressure, height, weight, gestational age, medical history, and biochemical laboratory data. The repeated-measures data, such as blood pressure, weight and laboratory data were delineated through pattern recognition and cluster analysis. Their model included a data split of 70% training and 30% testing, and two outcome categories, namely preeclampsia and no preeclampsia. Model development was programmed in R. The following six methods were used: logistic regression, decision tree model, naïve Bayes classification, support vector machine, random forest algorithm, and stochastic gradient boosting method. Jhee et al. [11] made use of the R programming language for all their models.

Pattern recognition and cluster analysis were used to determine the influence of each variable on prediction. Among the assessed variables, the 14 most influential factors were included in their prediction model. The most influential risk factor was systolic blood pressure. The C-statistic, a global measure of model discrimination, for all models used by Jhee et al [11], together with their respective calibration plots are shown in Fig. 1.

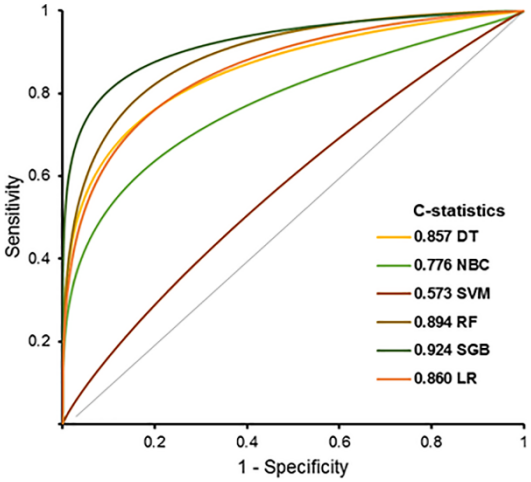

Figure 1: Jhee's Model's calibration plot with respective C-statistics [11]

When the prediction performances were compared among the prediction models, the stochastic gradient boosting (SGB) model had the best performance for predicting preeclampsia. The overall accuracy of the SGB model was 0.973, the false-positive rate was 0.009, and the detection rate reached 0.771. Jhee et al. [11] highlighted the use of mean values when dealing with prediction models in pregnancy. They agreed on the importance of taking fluctuation variability into account, and this is why they incorporated repeated measured values, and included the changing patterns as an analysable factor. These recommendations support the idea of incorporating smart devices, such as smartwatches, to automatically monitor fluctuation. Although Jhee et al. [11] could effectively predict late-onset preeclampsia, they faced several limitations. Many women only started the antenatal evaluation program early in the second trimester, resulting in unusable first trimester data. Acquiring large amounts of data will allow this study to overcome this limitation. When the data processing stage has been reached, all participants who started the antenatal care program late can be removed without affecting the model's performance. Jhee et al. [11] used a dataset containing 11,006 women; although this is a large sample an even larger sample may provide a more accurate model.

One simple prediction system currently used in South African clinics is the basic antenatal care approach (BANC). The BANC approach has been simplified to allow all postnatal care midwives to provide antenatal services to reduce maternal and perinatal deaths, while improving maternal health [12]. The BANC approach allows for better decision-making at the primary healthcare level. It achieves this by identifying high-risk pregnancies at an early stage. Although it is a very simple paper-based approach to predicting high-risk pregnancy, it has shown to be very effective.

In an article by Hofmeyr and Mentrop [15] in the South African Medical Journal, a case study is discussed that best describes the impact of poor antenatal care in South Africa, as follows: "A 22-year-old nulliparous woman was seen antenatally at 26 weeks' and 35 weeks' gestation and was well. Her blood pressure was 110/60 mmHg, urine tests were normal, and foetal movements were felt. Her next visit was booked for six weeks' later. After 23 days, she presented at 08h30 in labour with severe pulmonary oedema. Her blood pressure was 189/93 mmHg, and oxygen saturation was 70% on room air and 85% on 40% oxygen by mask. After stabilisation, a caesarean section was performed for foetal distress under general anaesthesia. A male baby was delivered at 09h50, with an Apgar score of 6/10 at 5 minutes. During the closure of the uterus, the mother had a cardiac arrest. Resuscitation was carried out, and she was transferred to the intensive care unit. Her condition deteriorated despite intensive care, and she died at 15h40. The most crucial avoidable factor was the long interval between routine BANC antenatal visits. Under the traditional antenatal model, she would have been seen two weeks after her visit at 35 weeks, and early preeclampsia would likely have been diagnosed and managed with delivery before she progressed to severe preeclampsia with pulmonary oedema" [13]. This case study illustrates the importance of proper antenatal care and proper management of resources.

Another study consulted was a systematic literature review and large meta-analysis [14]. The study identified publications investigating the association between preeclampsia and at least one risk factor in a previous pregnancy or the current pregnancy. Pubmed and Embase were searched for in English papers available from 2000 to June 2016. The pooled preeclampsia event rate for each risk factor was calculated using an arcsine transformation, followed by the derivation of a pooled relative risk (RR_{pooled}), and 95 per cent confidence intervals for each variable. Using the pooled relative risks, the population attributable fraction for each risk factor was calculated using the following formula:

$$PAF=[P_{epooled}\ (RR_{pooled}-1)]/[P_{epooled}(RR_{pooled}-1)+1]$$

Where $P_{epooled}$ is the number of women with a given risk factor in each study, divided by the total number of women in the study. Table I contains the pooled unadjusted risk for each risk factor.

TABLE I

RISK OF PREECLAMPSIA DETERMINED BY 16 WEEKS' GESTATION [14]

Risk Factor	No of women/No of studies	Pooled unadjusted risk (95% CI)
Prior IUGR	55,542/1	1.4(0.6 to 3.0)
SLE	2,413,908/2	2.5 (1.0 to 6.3)
Nulliparity	2,975,158/25	2.1 (1.9 to 2.4)
Maternal Age > 35	5,244,543/22	1.2 (1.1 to 1.3)
Maternal age > 40	4,260,202/16	1.5 (1.2 to 2.0)
Prior stillbirth	63,814/2	2.4 (1.7 to 3.4)
Chronic kidney disease	966,505/5	1.8 (1.5 to 2.1)
ART	1,463,529/20	1.8 (1.6 to 2.1)
Pre-pregnancy BMI>25	3,644,747/38	2.1 (2.0 to 2.2)
Pre-pregnancy BMI>30	5,921,559/40	2.8 (2.6 to 3.1)
Multifetal pregnancy	7,309,227/8	2.9 (2.6 to 3.1)
Prior placental abruption	291,134/3	2.0 (1.4 to 2.7)
Pregestational diabetes	2,553,117/19	3.7 (3.1 to 4.3)
Prior preeclampsia	3,720,885/20	8.4 (7.1 to 9.9)
Chronic hypertension	6,589,661/20	5.1 (4.0 to 6.5)
aPL	220,156/3	2.8 (1.8 to 4.3)

*IUGR=intrauterine growth restriction; SLE=systemic lupus erythematosus; ART=assisted reproductive technology; BMI=body mass index; aPL=antiphospholipid antibody syndrome

Prior preeclampsia had the most significant pooled relative risk, followed by chronic hypertension. Nulliparity had the greatest population attributable fraction for preeclampsia with pre-pregnancy BMI > 25 and prior preeclampsia in the second and third most. The study concluded by stating that all identified risk factors attributed to a heightened risk of preeclampsia. The most prominent risk factors were chronic hypertension, pre-gestational diabetes, prior preeclampsia, and BMI > 30.

The quality and quantity of data are some of the most influential factors regarding accurate predictions in machine learning models. While performing the literature review for this research, a clear gap in the accessibility of antenatal data for research purposes was identified. The Global Pregnancy Collaboration (CoLab) is a company currently striving to promote data accessibility and standardisation among research in preeclampsia [6]. Their goal is to create a large and powerful dataset by merging datasets from smaller studies worldwide. Standardised data is another key selling point for the COLLECT dataset. The time required to merge smaller datasets is significant, primarily due to data collection projects producing vastly different data sets. All projects currently using the COLLECT dataset are still in their data collection phase. Thus, this data cannot be used for this paper's proposed model. However, it is recommended that future research should use the COLLECT dataset for South African research in Preeclampsia [15].

III. Preeclampsia in Pregnant Women

Preeclampsia is a disorder associated with pregnancy, affecting 4.6% (95% confidence interval (CI), 2.7–8.2) of all pregnancies. It remains a leading cause of maternal and perinatal morbidity and mortality worldwide [16]. In the guidelines published by the National Institute for Health and Care Excellence (NICE) in 2019, a woman is classified at high risk of preeclampsia if there is a history of hypertensive disease during a previous pregnancy or a maternal disease, including chronic kidney disease, autoimmune diseases, diabetes, or chronic hypertension. Women are at moderate risk if they are [17][18]:

- Nulliparous
- ≥ 40 years of age
- Body mass index (BMI) ≥ 35 kg/m
- Family history of preeclampsia
- A multi-foetal pregnancy
- Pregnancy interval > 10 years

The presence of one high-risk factor, or two or more moderate risk factors, is used to help guide aspirin prophylaxis, which helps to reduce the risk of preeclampsia if administered before 16 weeks' gestation [19][20].

After consulting relevant literature, the following risk factors for preeclampsia were identified [11] – [19]:

- Systolic Blood Pressure
- Diastolic Blood Pressure
- Maternal Age
- BMI
- Diabetes Status
- Hypertension History
- Nulliparity
- Maternal Disease

However, pre-collected datasets may contain more or less features that were not explicitly highlighted. Therefore, these risk factors will be used as a guideline.

IV. Machine Learning for Prediction of Preeclampsia

The healthcare sector is always striving to achieve the Triple Aim, which improves outcomes, enhances patients' experience, and reduces healthcare costs to the public. Predictive modelling for real-time decision making is playing an essential role in achieving the Triple Aim. A clinical risk prediction model is defined as a model that combines several characteristics to predict the risk of disease presence and outcome occurrence in individuals [21]. Risk-prediction models as decision-making tools have long played an essential role in clinical practice. However, as times change, so do risk-prediction models. Two significant changes in risk prediction have been centred around advances in computer science. Firstly, we now live in a data-centric world where almost every aspect of our lives is digitally stored in some format. Secondly, there has been a sudden increase in the use of machine learning models to make predictions. The significant increase in data has led to an increasing need to analyse and interpret it [22]. Machine learning models allow for large amounts of data to be analysed and interpreted in a fraction of the time it would take a human. Thus, they save time and are immune to 'human error'. Machine learning is extensive and can include simple models such as the BANC model, or highly complex models such as Tesla's complex deep neural network for their autopilot [23].

V. Proposed Model

Machine learning models follow an iterative approach where a threshold is selected and, if not reached, will result in the model being adapted (Figure 2).

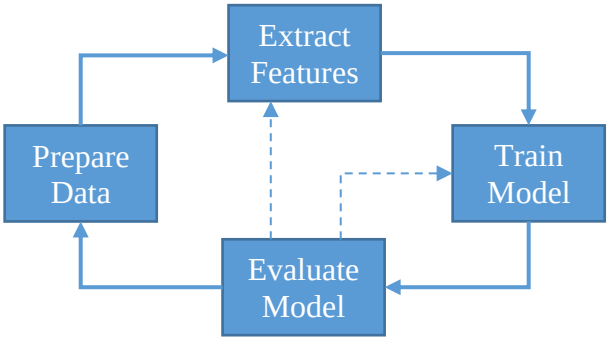

Figure 2: Iterative Machine Learning Process [24]

There are seven general steps to take when developing a machine learning model [25], [26]. These steps are:

1. Acquiring data
2. Preparing data
3. Choosing a suitable model

4. Training the model
5. Evaluating the model
6. Tuning the parameters
7. Making predictions

All seven steps will be described in detail in the following paragraph. The starting point for any machine learning model is the acquisition of data.

A. Data Acquisition

Clean and descriptive data is an essential aspect of a machine learning model, as without it, there is no way of making an accurate prediction. There are two main methods for acquiring data, either by performing the data collection or using an existing data set. Initially, the proposed model was going to make use of data collected from smartwatches of patients in South African clinics. However, due to the Covid pandemic, cost, logistics and time constraints, this proved unfeasible. Thus, an existing antenatal care dataset was needed.

The lack of customisation is a big disadvantage of using an existing dataset, and must be considered when selecting which dataset to use. Some risk factors that are crucial for making an accurate prediction may not be included in the dataset. Therefore, consulting many datasets to find which one suits the proposed model and contains most of the required features is very important. The researcher investigated many public dataset repositories for antenatal care or preeclampsia datasets. Unfortunately, no suitable public dataset could be found. Thus, another data source had to be explored, namely datasets directly from health institutions. Many hospitals in South Africa store their data and allow researchers to apply for access to the anonymised datasets. However, before applying for access to the data, ethical clearance from the Nelson Mandela University had to be obtained. This ethical clearance is currently underway, with the application awaiting review. Thereafter, applications for access to the hospitals' antenatal datasets will be submitted.

B. Data Preparation

Data preparation follows data acquisition, and the emphasis is on data quality. Data preparation is the transformation of raw data into a form suited for the machine learning model. Before handling the data, it is crucial to visualise it to highlight any relationships or data imbalances. The data preparation techniques used will depend on the specifics of the data. Generally, the first task is data cleaning. Data cleaning is the process of identifying and fixing systematic problems. General data operations performed in the data cleaning are:

- Use statistics to identify outliers by defining a 'normal' value;
- Identify and remove duplicates;
- Identify null values and replace them using statistics.

The next step is feature selection. Feature selection refers to the selection of a subset of input features that most affect the output. There is no 'best feature selection method'. Each specific problem will require experimentation of methods. The three most common feature selection methods for supervised learning problems are:

- *Wrapper:* The search for the best performing subset of features;
- *Filter:* The selection of a subset of features based on their relationship with the target variable
- *Intrinsic:* Algorithms that perform automatic feature selection during training, such as decision trees.

Once the optimal features have been selected, data transformation needs to begin. Data transformation is used to change the type of distribution of data. There are many different techniques, and only once the data has been thoroughly analysed will the suitable methods be identified. The final step in data preparation is feature engineering, which is the creation of new input variables from the existing available data. Feature engineering is used to add broader context to a single observation or to simplify a complex variable. This can be done by adding a Boolean flag, adding a summary statistic, or breaking down existing variables. An example of feature engineering for the proposed model would be adding a Boolean field that would be derived from the maternal age. Adding this field could potentially decrease the processing time of the model.

Once all these steps are performed the data will be randomly split into two sets, one being a training set equalling 70 per cent of the complete data set, and the remaining 30 per cent will be used as a testing set. Thus, the data will be ready to train and evaluate the model.

C. Model Selection

The three main types of machine learning models are supervised, unsupervised and semi-supervised learning. Supervised learning, which this paper's proposed model will use, requires all data to be labelled. The model then learns a mapping between input and output variables, and applies it to unseen data to predict the outputs [27]. Supervised learning can be broken down into two types of problems, namely classification and regression. A classification algorithm is used when you have a categorical outcome, such as true or false. A regression algorithm is used when you have a real value output, such as weight. Therefore, since the outcome for the proposed model will be either at risk of hypertension or not at risk, classification will be the selected algorithm. Women who developed preeclampsia will be categorised into the preeclampsia group, and those who did not, would be placed in the no preeclampsia group. Some of the fundamental algorithms that will be tested are:

- Support Vector Machine
- Naïve Bayes
- Decision Tree
- Artificial Neural Network

D. Model Training

Once the model is selected, the data will be used to train the model. Training a model requires the data to be supplied to the model to incrementally improve the model's ability to make predictions. Python will be the selected language due to the first author's familiarity with it, and that it is the most used language for programming machine learning models. The SciKit library will be used for creating and training the model [28].

E. Model Evaluation

After the model has been trained with the training dataset, the model will have to be evaluated. The evaluation phase uses

the testing dataset, which was set aside in the data processing phase. The following metrics are used to quantify the classification model's performance:

- *Classification accuracy* – number of predictions made as a ratio of all predictions made;
- *Confusion matrix* – A detailed breakdown of correct and incorrect classifications for each class;
- *Logarithmic Loss* – Performance of the model where the prediction probability diverges from the actual label. The goal is to minimise this value;
- *Area under curve* – A measure of the ability of a binary classifier to discriminate between positive and negative classes;
- *F-Measure (F-Score)* – Considers both the recall and the precision to compute a score for the model.

The overall performance of the proposed model can be evaluated using all the metrics.

F. Parameter Tuning

If the model's accuracy is not adequate, parameter tuning will be needed. It must be noted that before parameter tuning is performed, an attempt to improve the quality of data being input into the model must be performed. If the data cannot be improved, two methods for tuning the parameters will be used: a grid search and a random search. A grid search evaluates a model for each combination of parameters specified in a grid, whereas a random search samples each set of parameters from a distribution over a possible parameter value. Once the tuning is complete, the best configuration will be reported, and the necessary steps can be taken.

G. Performing Predictions

Finally, if the model's performance is satisfactory, the prediction model can be tested in a real-world scenario. When comparing studies with similar models, Jhee et al. achieved an overall accuracy on their SGB model of 0.973, a false positive rate of 0.009, and a detection rate of 0.771. This paper's proposed model will aim to perform equally or better than Jhee et al.'s SGB model.

VI. Discussion and Future Work

After performing the literature review and applying for ethics, the next step in developing the model is to apply for a usable data set. Thereafter, data preparation will begin (Section V-*B*). Figure 3 visualises the current status of the development of the proposed model.

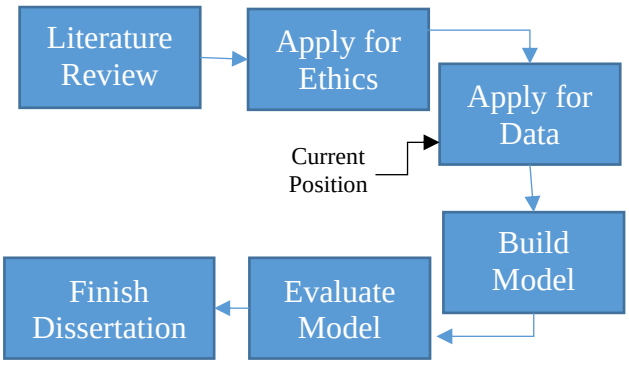

Figure 3: Visualisation of the proposed model development status

Once data preparation begins, the goal will be to use a South African hospital's antenatal dataset as the proposed model's primary data source. Once implemented, the model will be evaluated using all the methods outlined in Section V. The final step would be to implement the model in a South African clinic or hospital. If the model does not perform within acceptable thresholds, independent data collection will need to be considered. If data collection is needed, the COLLECT dataset and standards will be used.

The contribution of this paper is a proposed model for the prediction of preeclampsia using machine learning techniques. To the researcher's knowledge, this proposed model is the first of its kind in South Africa and the first to make use of a South African antenatal data set. Thus, the performance of different machine learning algorithms on South African antenatal data can be evaluated.

VII. Conclusion

Preeclampsia continues to affect pregnant South African women and their families. This paper proposes a model, which is the first of its kind in South Africa, for accurately predicting women at risk of developing preeclampsia, allowing clinics to assign their limited resources to women in critical need. The proposed model is planned to be the first preeclampsia prediction model that makes use of a South African Hospital's dataset. This paper plans to improve existing preeclampsia prediction models by increasing the sample size and exploring different prediction techniques. Future work will focus on the accessibility and standardisation of antenatal care data for future research into Preeclampsia.

Acknowledgements

This work was supported by the Telkom/NMU Centre of Excellence and the Nelson Mandela University Research Centre.

References

[1] "Maternal mortality." https://www.who.int/news-room/fact-sheets/detail/maternal-mortality (accessed Jun. 15, 2021).

[2] H. L. Nathan, P. T. Seed, N. L. Hezelgrave, A. De Greeff, E. Lawley, F. Conti-Ramsden, J. Anthony, W. Steyn, D. R. Hall, L. C. Chappell, and A. H. Shennan, "Maternal and perinatal adverse outcomes in women with pre-eclampsia cared for at facility-level in South Africa: A prospective cohort study," *J. Glob. Health*, vol. 8, no. 2, 2018, doi: 10.7189/jogh.08.020401.

[3] J. M. Roberts and H. S. Gammill, "Preeclampsia: Recent insights," *Hypertension*, vol. 46, no. 6. Lippincott Williams & Wilkins, pp. 1243–1249, Dec. 01, 2005. doi: 10.1161/01.HYP.0000188408.49896.c5.

[4] M. L. Rosser and N. T. Katz, "Preeclampsia: An Obstetrician's Perspective," *Advances in Chronic Kidney Disease*, vol. 20, no. 3. W.B. Saunders, pp. 287–296, May 01, 2013. doi: 10.1053/j.ackd.2013.02.005.

[5] S. Savaj and N. Vaziri, "An overview of recent advances in pathogenesis and diagnosis of preeclampsia.," 2012. https://escholarship.org/uc/item/3863p1k7 (accessed Aug. 04, 2020).

[6] J. Ebonwu, A. Mumbauer, M. Uys, M. L. Wainberg, and A. Medina-Marino, "Determinants of late antenatal care presentation in rural and peri-urban communities in South Africa: A cross-sectional study," *PLoS One*, vol. 13, no. 3, Mar. 2018, doi: 10.1371/journal.pone.0191903.

[7] L. Myer and A. Harrison, "Why do womn seek antenatal care late? Perspectives from rural South Africa," *J. Midwifery Women's Heal.*, vol. 48, no. 4, pp. 268–272, Jul. 2003, doi: 10.1016/S1526-9523(02)00421-X.

[8] R. Bhardwaj, A. R. Nambiar, and D. Dutta, "A Study of Machine Learning in Healthcare," in *Proceedings - International Computer Software and Applications Conference*, Sep. 2017, vol. 2, pp. 236–241. doi: 10.1109/COMPSAC.2017.164.

[9] L. Bottaci, P. J. Drew, J. E. Hartley, M. B. Hadfield, R. Farouk, P. W. R. Lee, I. M. C. MacIntyre, G. S. Duthie, and J. R. T. Monson, "Artificial neural networks applied to outcome prediction for colorectal cancer patients in separate institutions," *Lancet*, vol. 350, no. 9076, pp. 469–472, Aug. 1997, doi: 10.1016/S0140-6736(96)11196-X.

[10] J. D. Frizzell, L. Liang, P. J. Schulte, C. W. Yancy, P. A. Heidenreich, A. F. Hernandez, D. L. Bhatt, G. C. Fonarow, and W. K. Laskey, "Prediction of 30-day all-cause readmissions in patients hospitalized for heart failure: Comparison of machine learning and other statistical approaches," *JAMA Cardiol.*, vol. 2, no. 2, pp. 204–209, Feb. 2017, doi: 10.1001/jamacardio.2016.3956.

[11] J. H. Jhee, S. Lee, Y. Park, S. E. Lee, Y. A. Kim, S. W. Kang, J. Y. Kwon, and J. T. Park, "Prediction model development of late-onset preeclampsia using machine learning-based methods," *PLoS One*, vol. 14, no. 8, p. e0221202, Aug. 2019, doi: 10.1371/journal.pone.0221202.

[12] T. Sylvia Patience Ngxongo, "Basic Antenatal Care Approach to Antenatal Care Service Provision," in *Selected Topics in Midwifery Care*, IntechOpen, 2019. doi: 10.5772/intechopen.79361.

[13] G. J. Hofmeyr and L. Mentrop, "Time for 'basic antenatal care plus' in South Africa?'," *South African Medical Journal*, vol. 105, no. 11. South African Medical Association, pp. 902–903, Nov. 01, 2015. doi: 10.7196/SAMJ.2015.v105i11.10186.

[14] E. Bartsch, K. E. Medcalf, A. L. Park, J. G. Ray, Z. T. A. Al-Rubaie, L. M. Askie, H. Berger, J. Blake, L. Graves, J. C. Kingdom, G. Lebovic, S. J. Lord, J. L. Maguire, M. M. Mamdani, J. Meloche, M. L. Urquia, and V. Van Wagner, "Clinical risk factors for pre-eclampsia determined in early pregnancy: Systematic review and meta-analysis of large cohort studies," *BMJ*, vol. 353, Apr. 2016, doi: 10.1136/bmj.i1753.

[15] J. E. Myers, L. Myatt, J. M. Roberts, and C. W. G. Redman, "COLLECT, a collaborative database for pregnancy and placental research studies worldwide," *BJOG: An International Journal of Obstetrics and Gynaecology*, vol. 126, no. 1. Blackwell Publishing Ltd, pp. 8–10, Jan. 01, 2019. doi: 10.1111/1471-0528.15393.

[16] E. Abalos, C. Cuesta, A. L. Grosso, D. Chou, and L. Say, "Global and regional estimates of preeclampsia and eclampsia: A systematic review," *European Journal of Obstetrics and Gynecology and Reproductive Biology*, vol. 170, no. 1. Elsevier Ireland Ltd, pp. 1–7, Sep. 01, 2013. doi: 10.1016/j.ejogrb.2013.05.005.

[17] M. A. Brown, L. A. Magee, L. C. Kenny, S. A. Karumanchi, F. P. McCarthy, S. Saito, D. R. Hall, C. E. Warren, G. Adoyi, and S. Ishaku, "Hypertensive disorders of pregnancy: ISSHP classification, diagnosis, and management recommendations for international practice," *Hypertension*, vol. 72, no. 1. Lippincott Williams and Wilkins, pp. 24–43, Jul. 01, 2018. doi: 10.1161/HYPERTENSIONAHA.117.10803.

[18] "Hypertension in pregnancy: diagnosis and management NICE guideline," 2019. Accessed: Aug. 12, 2020. [Online]. Available: www.nice.org.uk/guidance/ng133

[19] L. M. Askie, L. Duley, D. J. Henderson-Smart, and L. A. Stewart, "Antiplatelet agents for prevention of pre-eclampsia: a meta-analysis of individual patient data," *Lancet*, vol. 369, no. 9575, pp. 1791–1798, May 2007, doi: 10.1016/S0140-6736(07)60712-0.

[20] E. Bujold, S. Roberge, Y. Lacasse, M. Bureau, F. Audibert, S. Marcoux, J. C. Forest, and Y. Giguère, "Prevention of preeclampsia and intrauterine growth restriction with aspirin started in early pregnancy: A meta-analysis," *Obstetrics and Gynecology*, vol. 116, no. 2. pp. 402–414, 2010. doi: 10.1097/AOG.0b013e3181e9322a.

[21] T. A. Alonzo, "Clinical Prediction Models: A Practical Approach to Development, Validation, and Updating: By Ewout W. Steyerberg," *Am. J. Epidemiol.*, vol. 170, no. 4, p. 2, Aug. 2009, doi: 10.1093/aje/kwp129.

[22] M. I. Jordan and T. M. Mitchell, "Machine learning: Trends, perspectives, and prospects," *Science*, vol. 349, no. 6245. American Association for the Advancement of Science, pp. 255–260, Jul. 17, 2015. doi: 10.1126/science.aaa8415.

[23] "Autopilot AI | Tesla." https://www.tesla.com/autopilotAI (accessed Jun. 17, 2021).

[24] "'Iterative Learning-InsideAIML.'" https://insideaiml.com/blog/Iterative-Learning-292 (accessed Jun. 15, 2021).

[25] B. Lantz, *Machine Learning with R*, 1st ed., vol. 1. Packt Publishing, 2013.

[26] M. Swamynathan, *Mastering Machine Learning with Python in Six Steps*. Apress, 2017. doi: 10.1007/978-1-4842-2866-1.

[27] P. Cunningham, M. Cord, and S. J. Delany, "Supervised learning," in *Cognitive Technologies*, 2008, pp. 21–49. doi: 10.1007/978-3-540-75171-7_2.

[28] F. Pedregosa FABIANPEDREGOSA, V. Michel, O. Grisel OLIVIERGRISEL, M. Blondel, P. Prettenhofer, R. Weiss, J. Vanderplas, D. Cournapeau, F. Pedregosa, G. Varoquaux, A. Gramfort, B. Thirion, O. Grisel, V. Dubourg, A. Passos, M. Brucher, M. Perrot andÉdouardand, andÉdouard Duchesnay, and Fré. Duchesnay EDOUARDDUCHESNAY, "Scikit-learn: Machine Learning in Python Gaël Varoquaux Bertrand Thirion Vincent Dubourg Alexandre Passos PEDREGOSA, VAROQUAUX, GRAMFORT ET AL. Matthieu Perrot," 2011. Accessed: Jun. 17, 2021. [Online]. Available: http://scikit-learn.sourceforge.net.

Nathan Smith is a second-year MSc student in the Department of Computing Sciences at the Nelson Mandela University. His research interests are machine learning, telemedicine, and smart spaces.

Multimode Optical Fibre for Converged Vibration Sensing and 10 Gbps Photonic Data with 1.7 GHz Wireless Transmission for Mining Applications

Vela Shumane, James Jena, Reinhard Karambera, Shukree Wassin, Andrew Leitch, Tim Gibbon

CBC lab, Department of physics, Nelson Mandela University

shumanev2@gmail.com

Abstract*— We propose and experimentally demonstrate a converged solution for high-speed data and accurate vibration sensing in mining applications. The solution is based on multimode fibre for connecting adjacent mining cavities, with wireless connectivity for machinery and users within cavities. Polarization-based vibration sensing over the multimode fibre is implemented to monitor vibrations and earth tremors leading to rock falls. Photonic data transmission over 100 m of multimode fibre is successfully achieved with a modal dispersion penalty of only 1.6 db. Wireless transmission at 1.7 GHz over 1 m is successfully demonstrated, while vibrations in the range 50 Hz to 1 kHz are accurately detected to within an error of 0.02%. The proposed technology has the potential to lower costs, increase productivity and improve safety across the mining sector.

Keywords- multimode fibre, photonic transmission, mining communication, vibration sensing

I. INTRODUCTION

A network operator can create tremendous value by offering tailored, industry-specific services in the age of the Fourth Industrial Revolution. The mining industry presents one such opportunity with big data-driven operations, remote wirelessly operated machinery, and safety considerations. The environment in the mining sector can be very harsh on the workers, as well as the longevity of the equipment responsible for the day to day running. These extremities have slowed down the innovation for mines when compared to other industry sectors. The complex and unpredictable geological conditions in an underground environment, form part of the major concerns during the design and construction phase of any underground excavation process. In the absence of a reliable geotechnical monitoring scheme, the event of an unexpected rock collapse due to excessive rock deformation may lead to catastrophic injuries, fatalities, and significant financial loss. According to a 2017 study of mining accidents, the most common mode of injury was hand tools/equipment (20%), falls of ground (15%), falling of material/rolling rock (14%), slipping, and falling (13%), and manual handling of material (11%). The most common tasks being performed by victims at the times of the accidents were drilling (25%), engineering tasks (24%), transportation of people (11%), and manual handling (11%). [1]

Optical fibre technology has made a significant contribution to transformation in the mining industry. High bandwidth and low latency create the platform for smart mines to emerge. Advancements in the optical fibre industry have inspired a lot more "fibre on the mine" research and implementation over the past decade [2][3]. With more research being conducted world-wide, the domination of more fibre optic-based solutions for mining catastrophes raises hope for a more efficient, productive, profitable, and safer workspace in the mines. Furthermore, these fibre optic-based solutions in mines contribute significantly to pressing matters such as environmental, employee, and equipment safety, and hence an increase in productivity leading to greater profits.

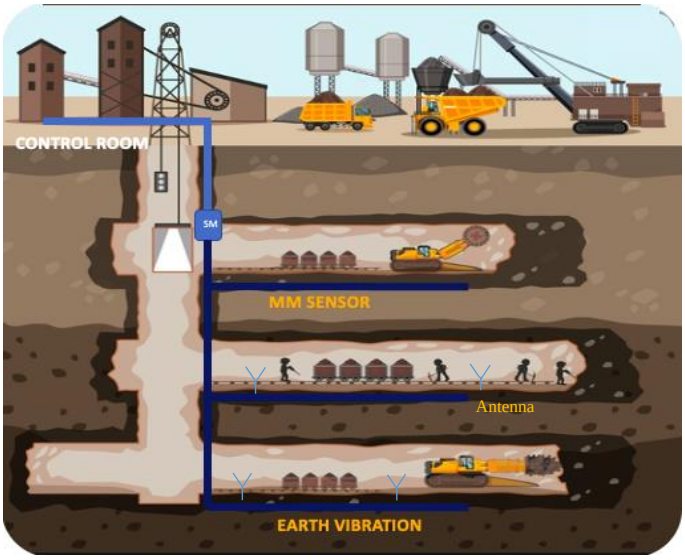

Figure 1: *Industrial underground mining illustration with proposed optical fibre connections [4]*

In this paper, a converged data and vibration sensing optical fibre system is proposed and experimentally demonstrated. The system features network components, transceivers, digital signal processing (DPS) algorithms and impairment mitigation. The OM4 multimode fibre used for 10 Gbps data transmission is simultaneously used as a polarization-based vibration sensor. The system lowers costs and adds value by offering converged data and vibration sensing over the same OM4 multimode fibre infrastructure. The use of optical fibre has the added benefit over copper of being non-spark thus preferable to mining environments with flammable gas and substances. As illustrated in Figure 1, conventional single mode (SM) fibre from the control room above the ground can be coupled to a multimode fibre interlink that leads to each individual mine cavity. Table 1 summarizes the advantages of multimode fibre over single mode fibre, particularly for shorter links where more cost-effective lasers and receivers are available at 850 nm. Figure 2 illustrates how the focus of our paper combines

aspects of High Speed Data, Vibration Sensing and Wireless in a single experiment.

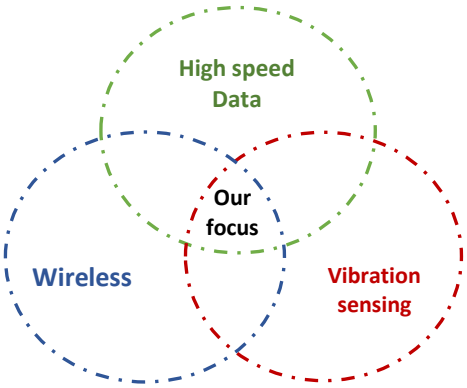

***Figure 2**: Representation of ideas behind our work*

The conventional SM fibre can easily interface with existing terrain networks, while multimode components tend to be cheaper for the short reach networks underground. Antennas would be placed in each respective mine cavity to carry out the data communication and controlling some of the equipment. It is proposed that 5G signal be used for faster data transmission within the cavity. Wireless 5G cannot easily penetrate dense rock, hence we propose multimode links for connecting adjacent cavities. In addition to vibration sensing and photonic 10Gbps data transmission, we thus also further include wireless transmission at 1.7 GHz

II. THEORY RELATING TO MULTIMODE FIBRE DATA TRANSMISSION AND POLARIZATION-BASED SENSORS

Multimode optical fibre (MMF) acts as a waveguide for 850 nm photonic signals. Data may be added through modulation of either the intensity of the light, the phase of the light, or both. Monitoring the polarization of the light transforms the optical fibre cable into an array of virtual sensing devices. Polarization sensing has the further advantage that it can easily be performed, without the need for fibre modification or costly equipment deployed along the link. Only a polarimeter and appropriate DSP are needed at the receiver end. This allows detection and monitoring of vibration near the cable, which alter the polarization of the light wave [5].

Polarization of light refers to the orientation and path traced out by the electric field over time. Light has three basic states of polarization (SOP) known to be linear, elliptical, and circular. These SOP's can be analysed and studied by representing them on a spherical surface known as a Poincare sphere, through one-on-one mapping systems. The Poincare sphere is orientated in Stokes's space, with an orthogonal set of axes S1, S2 and S3. A path is traced out on the surface of the Poincare sphere with changing polarization.

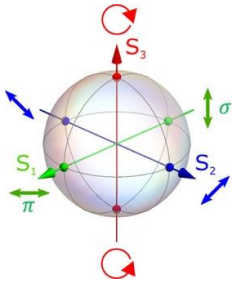

***Figure 3:** Poincare sphere with Cartesian coordinates, which represent three Stokes parameters namely S1, S2 and S3.* [7]

For communication and data transmission over optical fibre, a number of steps are required. These include: The electrical radio frequency (RF) data being transformed to a light wave carrier; transmission of the light pulse over an optical fibre network; and conversion of the light pulse back to a conventional RF digital signal.

TABLE 1: PROPERTIES OF SINGLE MODE AND MULTIMODE OPTICAL FIBRE.

	Single Mode Fiber Cable	Multimode Fiber Cable
Core Diameter	9/10µm	50/62.5µm
Transmission Mode	One mode	Multiple modes
Working Wavelengths	1310/1550nm	850/1310nm
Transmission Distance	Long(over 4km)	Short (1-2km)

Transmitting and receiving optical signals is accomplished through readily available transceivers that use devices such as light emitting diodes (LEDs) and photodetectors. Vertical cavity surface emitting lasers (VCSELs) are commonly used in fibre-optic transmission systems since modulation can be applied directly, at high bandwidth with low energy consumption.

VCSELs tend to lase at high powers in multiple transverse modes due to spatial hole burning (SHB). The complex transverse modal behaviour of VCSELs, the spontaneous emission noise and the intrinsic effects of the preceding bit pattern affect the performance of this type of lasers in datacom applications [6]. These effects limit performance by introducing impairments and a resultant power penalty. By managing the effects and including the power penalty in the link budget, VCSELs remain an attractive technology due to ease of direct modulation and relatively low cost.

III. EXPERIMENTAL PROCEDURE

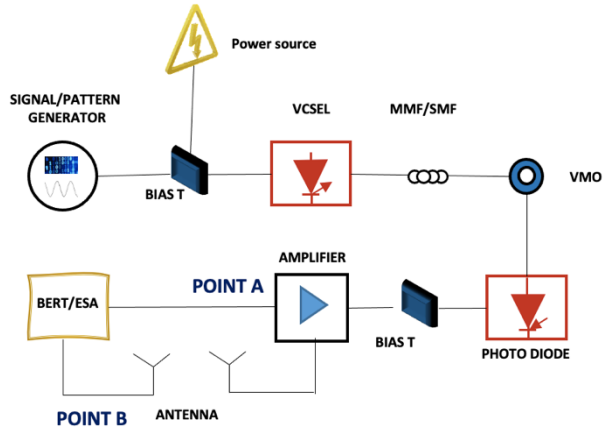

Figure 2: *Experimental procedure for converged data and sensing*

Figure 4 is a schematic representation of the experiment performed for this work. An 850 nm multimode VCSEL was directly modulated using a 10 Gbps 2^7-1 non-return-to-zero pseudorandom binary sequence (NRZ PRBS) from a programmable pattern generator (PPG). The maximum current for this 850 nm multimode VCSEL was specified at 10mA. The lasing threshold current is 1.5 mA. The VCSEL was biased at 5.5 mA, before adding the PRBS modulation. This bias point facilitates optimum modulation depth between the threshold current and non-linear output that occurs at 10 mA. The maximum output power of the VCSEL was -0.97dBm.
The PRBS, intensity modulated optical signal was subsequently transmitted over 100m OM4 multimode fibre. The attenuation of the fibre was 2.2dB /100m. The transmitted optical signal was detected using a PIN photodiode (PD) optimised for 850 nm. At point A in Figure 4 the eye diagram of the resultant electrical signal after the high- speed photodiode was analysed by using an Agilent Infinium 86100 high bandwidth oscilloscope with 10 GHz bandwidth in the time domain. Data transmission was also quantitatively measured through the bit error ratio (BER) performance for photonic transmission. The performance of the wireless antennae transmission was quantitatively investigated using the high bandwidth oscilloscope.

For the vibration sensing dimension of the experiment, a sine wave frequency synthesizer together with an audio speaker was used to generate applied external vibrations to the multimode fibre. The vibrations were applied approximately mid-span in the link. Once the data was acquired using a polarimeter, a series of digital signal processing (DSP) steps were applied. Step 1 involves the computation of the sample size, the total measurement time and the period of the SOP fluctuation. Step 2 involves the computation of the vibrational frequencies through a number of steps. This was realized by taking the FFT of the individual Stokes parameters SOP (S1, S2, S3) data collect by the polarimeter. From the resultant FFT data, the two sided and single sided spectrums were respectively computed. In doing so, the frequency spectra corresponding to the pre-selected vibrational frequencies were determined and the corresponding plots were generated.

IV. EXPERIMENTAL RESULTS

Data communication

The BER results for experiment with PRBS 7 at 10 GB/s are illustrated in Figure 5. These results were measured at point A in Figure 4. The graph illustrates a plot for the back to back and transmission signal through the 100 m multimode fibre. The back to back signal is represented in orange with lower power than the transmission signal represented in blue. The receiver sensitivities for the back to back and transmission signals were found to be -5.9dBm and -4.3dBm respectively. The difference between these two values is the power penalty, which is mainly due to the fibre impairments. In this this case the power penalty was found to be 1.6 dB, introduced mainly by modal dispersion. Modal dispersion occurs in multimode fibre since various modes follow unequal paths of propagation through the fibre. The value of 1.6 dB is within an acceptable dispersion budget of 2 dB, given that an overall link budget would be in the order of 8 dBm.

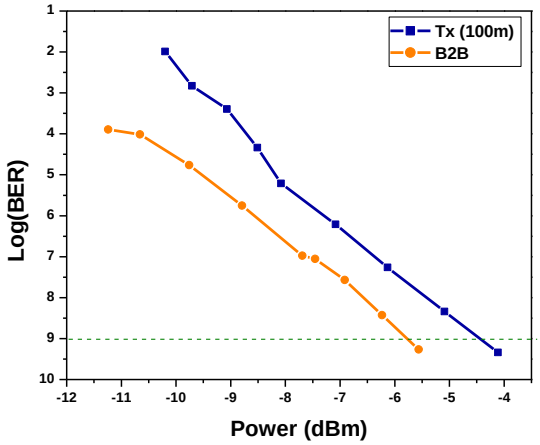

Figure 3*: Bit Error Rate (BER) of back-to-back (B2B) and transmitted (Tx) signal over 100m MMF.*

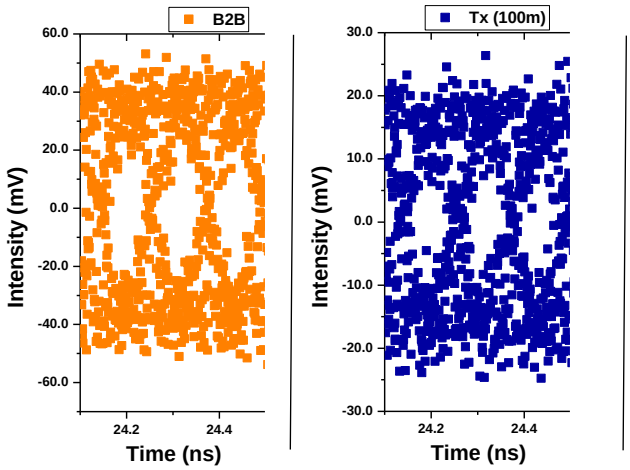

Figure 4: *The corresponding eye diagrams of the B2B and Tx*

Eye diagrams for the back to back and the transmission signals are presented in Figure 6. The bit pattern has been wrapped after every three bits. The eyes appear in both cases, with an error free decision threshold evident mid-level. The right-hand eye in Figure appears only slightly closed in comparison to the back-to-back eye. This corresponds to the small modal dispersion penalty of only 1.6 dB, as found in Figure 5.

Vibration sensing

The following results show how polarization changes in multimode fibre can be used to accurately sense vibrations in the range 50 Hz to 1 kHz. Broadband sensitivity corresponds well to measuring the response of rocks to drilling activities as well as early detection for ground tremors and rock falls.

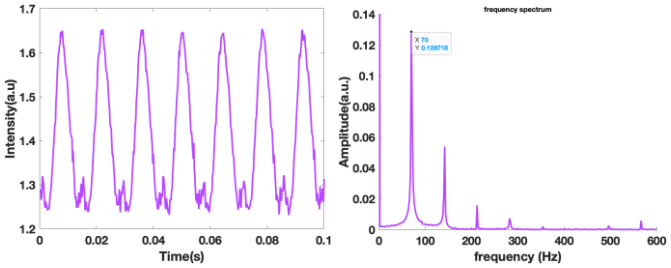

Figure 5*: Sine wave of speaker vibrating at a frequency of 70Hz and FFT showing the detected frequency*

A signal generator at 70 Hz was connected to a speaker in proximity of the multimode fibre link. Time series data of polarization data after transmission was collected. Figure 7 (left) shows the acquired sine wave of the Stokes parameter S1. Digital signal processing (DSP) through a fast Fourier transform (FFT) was then performed on the data to confirm the corresponding frequency that the polarimeter detected. . Figure 7 (right) shows the resultant frequency spectra. The fundamental frequency of the vibration, as well as the harmonics are clearly visible. The acquired frequency of 69.99 Hz from the FFT demonstrates successful operation.

The experiment was repeated for 50Hz, 100Hz, 200Hz, 300Hz, 500Hz and 1000Hz. The table below shows the results. All vibration frequencies were successfully experimentally measured to an error within less than 0.02%.

TABLE 2: TABULATION OF DIFFERENT VIBRATION FREQUENCIES SUCCESSFULLY MEASURES BY MM SENSOR.

Set frequency (Hz)	Acquired frequency (Hz)	Percentage error (%)
50.00	50.01	0.02
70.00	69.99	0.01
100.00	99.98	0.02
200.00	200.00	0.002
300.00	300.01	0.002
500.00	499.99	0.002
1000.00	999.98	0.001

Polarization fluctuations within the link have a negligible effect on data transmission performance. This is because short lengths of modern optical fibre have very small polarization mode dispersion (PMD). Furthermore, no components with significant polarization dependant loss (PDL) or relative intensity noise (RIN) are included in the experiment.

Wireless transmission

This part of the experiment focussed on measurements taken at Point B in the experimental setup of Figure 4. It demonstrates how the wireless signals can be transmitted and/or received at multimode nodes. This provides wireless 5G connectivity for machinery and users within mining cavities. In the experiment, two Omni directional antennas were used. The antennas were placed 1m apart for the duration of the experiment. The results on Table 3 show that wireless transmission was found to be optimal at a frequency of 1.7 GHz. The signal is observed to dwindle, and the SNR decreases as we switched to higher (2 GHz) and lower (1.4 GHz) frequencies. The combined results suggest that a 10 Gbps multimode mode fibre feed could be implemented to drive 10 or more wireless antennae, each transmitting at a bit rate of up to around 1 Gb/s.

TABLE 3: SINUSOIDAL WAVE TABULATION AT 1.4GHZ, 1.7GHZ AND 2.0GHZ FOR WIRELESS TRANSMISSION WITH ANTENNAS 1M APART.

Frequency (GHz)	Back-to-back	Transmission
1.4	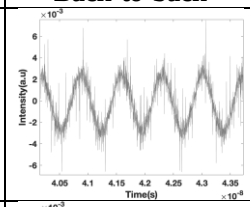	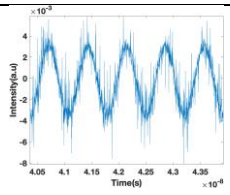
1.7	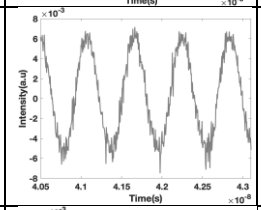	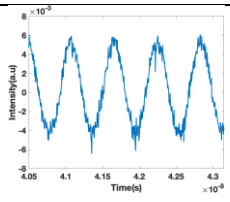
2.0	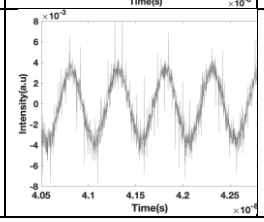	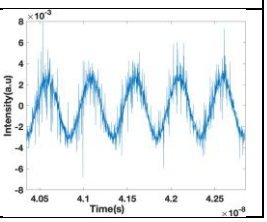

V. CONCLUSION

A solution for simultaneous data transmission and vibration sensing in the mining environment was proposed and experimentally demonstrated. Photonic transmission at 10 Gbps over 100 m of multimode fibre is shown to be ideal for connecting underground cavities, using the same multimode fibre, we implemented accurate vibration sensing in the range 50 Hz to 1 kHz. Antennae connecting to multimode modes and operating at 1.7 GHz are shown to be suitable for wireless data connectivity within cavities. The proposed technology has the potential to lower costs, increase productivity and improve safety in mining applications.

VI. REFERENCES

[1] A.A. Kelam, M.A. Kalem, A.M. Eker, H. Akgun, M. Kockar, "Optical fiber technology to monitor slope movement", Engineering Geology for Society and Territory, Volume 2, pp. 1425-1429, 2015.

[2] A.H. Hartog, "Raman sensors and their applications," Proc. SPIE 8421, (2012).

[3] Angloamerican.com, "Fibre optics: mining's unsung hero", 2018. [Online]. Available: https://www.angloamerican.com/futuresmart/stories/our industry/technology/fibre-optics-minings-unsung-hero [Accessed 15 August 2021].

[4] http://www.istockphoto.com

[5] A. Larsson, J.S. Gustavsson, P. Westbergh, "VCSEL design and integration for high-capacity optical interconnects", Optical Interconnects XVII; International Society for Optics and Photonics, 2017.

[6] J. Labuschagne, M. Ferentinou, M. Grobler, "Smart slope monitoring through the use of fibre optic sensors", Springer Series in Geomechanics and Geoengineering, 2019.

[7] N. Janev, K. Ivanov, V. Karagiozov, I. Starbanova, Y. Anastasova, "Opportunities for implementation of web interface in data base works in the mining industry", 50 Years University of Mining and Geology St. Ivan Rilski Annual, vol. 46, Part III, Sofia, pp 185-190, 2003.

[8] L. Tongyu, W. Yubin, G Song, Y. Li., J. Wang, Y. Ning, Y. Lu, "Advances of optical fibre sensors for coal mining safety monitoring applications", IEEE 2013 International Conference on Microwave and Photonics (ICMAP), India, 2013.

[9] M. Amanzadeh, S.M. Aminossadati, M.S. Kizil, A.D. Rakić, "Recent developments in fibre optic shape sensing", Measurement, vol 128, pp 119-137.

[10] C. Stratton, "Benefits of fiber optics for underground mine communications", White Paper, Industrial Market, AFL, 2015.

Vela Shumane is completing her MSc in Physics at Nelson Mandela University under the Center of Broadband Communication.

Investigating the Cost-effectiveness of Fibre Optic Technology Deployment in Rural Areas: a Case Study of Mdantsane

Olukayode Oki[#], Bathandwa Siyothula[#]

Department of Information Technology, Walter Sisulu University,

East London, 5241 South Africa

ooki@wsu.ac.za

Abstract—**Studies have shown that the majority of the global population are migrating from rural to urban areas. People are leaving rural areas due to poor services such as poor broadband service. Broadband speed and reliability are one of the most significant measures of service quality in rural areas Internet connectivity. Fibre optic technology has been introduced as a solution to the low and poor broadband quality. However, due to the unique characteristics of rural areas in South Africa, majority of the telecommunication operators are reluctant to invest in rural ICT networks because it tends to be much less profitable. Hence, the study of how cost effective it would be to deploy a fibre optic network in rural areas as compared to the current wireless (LTE) network remains an open issue. This study investigates the cost-effectiveness of deploying a fibre optic network in the rural area of Mdantsane township, by analysing the installation and operation costs of fibre optic networks in comparison to the cost of wireless (LTE) network. The finding of the study amongst others showed that while fibre optic networks seem to be great, however, they come at a cost. The cost of drilling and trenching associated with the deployment of fibre optic networks was reported as the key reason why the network deployment is costly. Hence, reducing the cost of drilling and trenching would reduce the cost significantly. The study recommends that in order to reduce the fibre optic deployment costs, the network operators should partner and share the costs using a customize pricing model that favours both the operators and internet users in the rural areas.**

Keywords— **Fibre optic, deployment, broadband, networking**

I. INTRODUCTION

The introduction of fibre optic networks in telecommunication access networks would be required in the upcoming years to cope with increasing network demands. Fibre-to-the-Home (FTTH) networks can offer higher bandwidth and thus new services for customers compared to current access networks [1]. Telecom is a fast-evolving market, in which new applications can quickly take over, offer ever richer services, but also require more and more bandwidth. Many existing access network infrastructures based on DSL (Digital Subscriber Line) or HFC (Hybrid Fibre Coax) technology run increasingly in bandwidth shortage problems. To offer the currently high-end services like HDTV, online video meetings, 3D TV, online gaming and especially to be ready for the future of more demanding services, an FTTH network that offers the most cost-effective solution is needed [2]. Fibre-to-the-home (FTTH) is a technology that connects the home to a high-speed network using an optical fibre cable to provide data, voice, and video services [3]. It is considered the broadband of choice because of the potential to improve bandwidth to the residential home and because it is a future-proof technology with improved network reliability and the advantage of enhancing the openness of the residential home [4].

Provisioning of high-speed rural Internet access is associated with higher incomes and decreased unemployment by expanding remote job opportunities and the potential to expand online brick and mortar businesses [5]. Although high monthly prices influence use, there are also questions regarding hardware prices, secret fees, transparency of pricing, quality of service, and availability [5].

The governments have a central role to play in ensuring universal access to Internet services, an enabling environment for infrastructure development and competition, and a policy framework that allows for the lowering of costs, the promotion of digital literacy and innovation [6]. As part of its obligations, company was mandated to implement public switch telephone network services in rural and semi-urban areas around the country, many of which would otherwise not have proved commercially viable to operators in a competitive environment [7]. Although, initially successful in its endeavours to connect the masses, the gravity of the situation soon came to the fore as the company was forced to disconnect over two million telephone lines owing to non-payment.

In South Africa, old townships are geographically, culturally, and economically diverse as a result of historical social compression in racially segregated areas. Many of the townships include middle and low income areas, especially larger townships, and also scattered middle-income houses. Yet, socio-economic statistics indicate that the majority of township residents are poor and that there is a very high unemployment rate [8].

[9] state that digital convergence (the incorporation of a combination of all forms of information such as data, voice, and video through convergence terminals and services) is expected to lead people to a smart society in which everyone can use customized services anywhere and anytime with the rapid growth of digital information technology. Unfortunately, when comparing urban and rural areas, there is an ever-growing gap in the infrastructures of information and communication technology (ICT), which is contributing immensely to the digital divides. Faster access to the Internet, security and making of calls while browsing the Internet are some of the perks. While distance, fragility, low power, higher access rates than dial-up, and lack of connectivity in remote areas are disadvantages [10].

Rural area development comes in different ways, different studies clearly showed that the majority of the global

population are migrating from rural to urban areas. People are leaving rural areas because of poor services (such as broadband) in the area. Broadband speed and reliability have been part of the most significant measures of service quality in rural areas. Poor broadband quality in a community indicates poor economic development and poor service delivery to the community.

Fibre optic technology have been introduced in the literature as a solution to the low and poor broadband quality. However, due to the unique characteristics of rural areas in the developing nations, the total deployment cost and economic viability of a fibre optic technology in rural areas remains an open issue. Hence, this study investigates the cost-effectiveness (for both the service provider and the end users) of deploying a fibre optic technology in rural areas as compare to their existing ADSL broadband connection. The study use Mdantsane township; one of the informal settlement in Eastern cape province of South Africa as a case study. In this study, the researchers explored two questions, which focuses on the major fibre optic network deployment component cost and how this deployment cost can be managed in a rural area environment.

The remainder of this paper is organized as follows: Section II presents the cost comparison for different network broadband in South Africa, while Section III describe the methodology that was used in this study. In section IV, the results of the analysis of data collected were presented, while the study's recommendations and conclusion are outline in Section V.

II. Cost Comparison of Network Broadband in South Africa

In providing internet connectivity and computing facilities within the South African context, several factors must be considered. These include finance, resources, and current facilities, as well as the desire of members of the community to embrace and use the amenities. To carry out fibre optic access network systems or configurations in remote areas, it is critical to investigate the most cost-effective systems or configurations. In the context of expected high capital costs, network operators considering installing fibre in rural areas must make the rollout as cost-effective as possible [11-12].

While prepaid mobile voice services in South Africa remain expensive by continental and global standards, the country's mobile data market, which is becoming a significant source of revenue for mobile operators, is fiercely competitive. Fixed-line packages are (surprisingly) more expensive than comparable mobile packages, according to analyses of prepaid and post-paid mobile and ADSL (fixed) broadband RIA price categories. Mobile data's appeal in South Africa is also boosted by its lower setup costs and more convenient prepaid charging options, which are especially appealing for low data use and uneven consumption [13].

In South Africa, the cost is still a barrier to widespread broadband acceptance and use. Uncapped Internet services, for example, are still prohibitively costly, and many consumers still rely on restricted plans with monthly data caps as low as 1GB for fixed-line connections and 10 MB for smartphone access. On Very-high-bitrate DSL (VDSL), speeds range from 1Mbps to 40Mbps; the latter is limited to certain areas, and each tier is more expensive. Long Term Evolution (LTE/4G) speeds on mobile networks can exceed 60Mbps in theory, but in reality are closer to 15Mbps [14].

Infrastructure innovation continues to deliver the best and most widespread broadband rollout, especially where cable networks have been formerly used mainly for broadcasting, and telco ADSL or fibre networks coexist. However, in areas where technology, let alone competitive infrastructure, is lacking, such as rural areas of Africa, different policy and regulatory decisions must be taken. Where the cost of duplicating networks is prohibitively high, regulatory action could concentrate on ways to improve service competition by providing equal access to a single network [15].

Public ADSL providers have traditionally avoided using usage pricing models, instead of providing internet coverage at a monthly fixed rate connected to a cumulative volume of data usage. Mobile providers all around the world are also providing usage-based pricing and other specialized packages [16]. When compared to the developing world or other countries with comparable economic and social characteristics to South Africa, it has been discovered that internet services in South Africa are very costly. Fixed-line broadband is also somewhat less expensive than mobile broadband, allowing it to retain other people and families that may otherwise have chosen mobile broadband [17]. It is believed that the low penetration in broadband access is as a result of inadequate investment in infrastructure due to limited state resources in public enterprises coupled with high risks that are primarily associated with sunk costs [18].

Optical fibre solves some of the limitations otherwise inherent with copper cables, including copper cables' susceptibility to external noise, lightning strikes, and signal loss when transmitting data over long distances. Optical fibre is therefore resistant to electrical noise while providing the ability to transmit huge amounts of data. These features have contributed to the use of optical fibres by telecommunication companies for their backbone networks.

Fig. 1 shows an overview of the different network parts with focus on utility (and telecom) access network infrastructures. On the horizontal level, we have foreseen four network lifecycle phases: deployment of the network, provisioning connection (pre-registration or later on) to the customer, and network operations. Upon this model, the actors involved for each party were mapped [1]. This study focus on the network parts where the different utility access infrastructure network owners could co-operate.

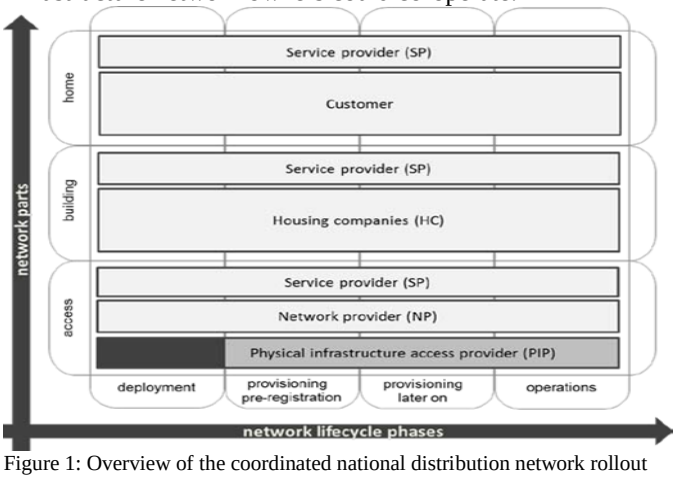

Figure 1: Overview of the coordinated national distribution network rollout

Three distinct cost categories can be identified when cost allocation is concerned; direct, shared and common costs [19]. Direct costs are specific for one actor and are typically borne by one actor and not divided between different actors. In infrastructure rollout projects, the cost of ducts, cables, and flexibility points are typical examples of direct costs. Shared and common costs can be divided among the different actors involved, and are thus of interest for the cost-sharing model.

The fibre operator might provide different offerings, packages of products, and services. The different products and offerings will have different markets, customers, and positions. In South Africa, several network providers have committed to rolling out FTTH in six of the metropolitan cities (Johannesburg, Durban, Port Elizabeth, Pretoria, Bloemfontein, and Cape Town). The mentioned cities are however fairly well developed, making it justifiable for network providers to design and implement these fibre access models. However, many South Africans still reside in rural communities, where fibre access infrastructure is hardly present because of socio-economic and geographical impediments. Hence, providing a customized broadband network that meets the rural demographics will help in bridging the digital divides and improve the life of the people in rural areas.

III. Research Methodology

To achieve the goal of this research, both qualitative and quantitative data were collected using structured survey questionnaire from 50 randomly selected Internet users' resident in Mdantsane and 5 Internet service providers; Herotel, Huge networks, EC Internet, Blaze and Internet Solutions, all of which are situated in East London area. Mdantsane is one of the townships located around East London in Eastern cape province of South Africa. Mdantsane township is an informal settlement, which is largely occupied by very low income and poor people. Hence, the number of Internet users in the area are very small. The questionnaires were distributed among the employed, unemployed, and students around the Mdantsane township.

The online surveys through a web link have been selected for use by the researcher as the method for data gathering. Surveys are more favourable for this study because they are one of the best in collecting data from a large sample of people, which is suitable for this study. Also, online survey was selected so as to be able to adhere to the government regulations on Covid-19 pandemic. In this study, the researcher used probability sampling method to reach the two groups of participants; the users in rural areas and Internet service providers (ISP) in East London. Probability samples are the gold standard in sampling methodology and for ensuring that the study results are generalizable to the target population. The term "probability sampling" is used to describe how each person in the population has an equal chance of being chosen for the study.

The method adopted in this study aimed to see whether fibre optic network provisioning is economically viable for both the service providers and Internet users in rural areas. To comment on the technology's cost-effectiveness in rural areas, its costs must be calculated and compared to the currently available broadband technology in this region, such as wireless long-term evolution (LTE). Hence, the price of the two broadband were compared so as to be able to understand their total deployment cost. This would help to recommend the solution that can be adopted in order to reduce the deployment costs.

The survey questionnaire is structured into two major categories; category one explains the opinion of Mdantsane Internet users with regards to their current connectivity and proposed fibre optic technology. While category two present the view of internet service providers regarding the cost of deployment of fibre optic technology in rural areas. The data collected were analysed by first grouping the respondent's answers all together. Thereafter, the validity test was carried out for each section of the questionnaire to ensure that the data collected are valid before carrying out a further analysis on the data. Lastly, the valid data collected was analysed and a statistical and graphical conclusion to the findings were presented.

IV. Results and Discussion

This section presents the results using three objectives; the respondents' opinion with regards to their current connectivity and proposed fibre optic technology, the Internet service providers' views regarding the total cost of deployment for both fibre optic and LTE technology in a rural area, and the comparison between the two deployment costs. The data was collected from 50 respondents who are employ, unemployed and students, residing in Mdantsane township. Also, data was collected from 5 Internet service providers in East London, which also covers the Mdantsane area. The results are presented in the form of figures and descriptive statistics.

Fig. 2 shows the age distribution of participants. It can be observed that 53.3% of the participants are under age 25 years, while 42.2% of the participants are age 25-34. 5% of the participants are between the age group 35 – 44 years. This result agrees with the previous study [20, 22], which says that the age between 18 – 35 years are the most population that utilizes the Internet connection more than any other age group. Also, this result can be attributed to the fact that majority of elderly people in the township/rural areas are mostly subsistence farmers or small scale traders. Hence, they seldom use Internet service.

The average amount of money spent by the participants on Internet data per week are presented in Fig. 3. It can be observed that 9% spend less than R50 per week on the internet data, while 31% spend between R50 – R100 on data

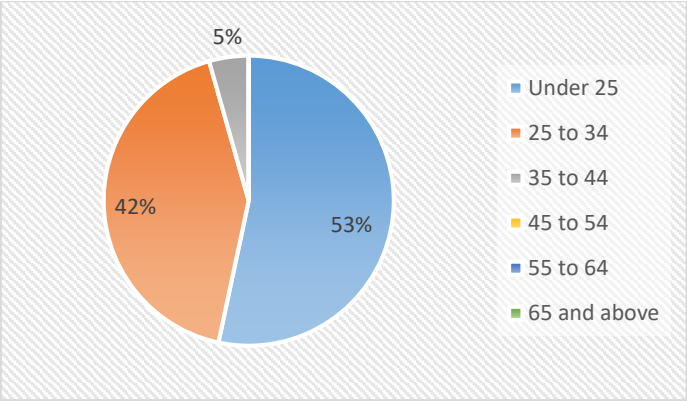

Figure 2: Respondents Age Group

per week. It can also be observed that 31% spend between R100 – R200 on weekly data, 20% spends between R200 – R300 per week on data. 7% are spending between R300 – R500 per week on data and only 2% claimed to be spending above R500 on Internet data per week. This result agrees with the existing work [21], which indicates that the cost of Internet data is high in South Africa as compared to other developing countries. Many of the respondents complained about the high cost, especially for people in rural areas, which majorly depends on government grant. However, due to the regulations around Covid-19 pandemic, they needed to be spending more on data, especially for the children that needs to attend and do their school works remotely.

Fig. 4 shows the participants rating in terms of internet services price satisfaction. It can be observed that, the 65% of the respondents are not satisfied (poor and very poor rating) with the amount of money they are paying for internet data, while 33% agreed on average rating. However, only 2% of the respondents are fine with the current price and 0% for very good price satisfaction rating. Although different reasons are being giving (both by the ICASA and telecommunication industry) as the reason for the current pricing. However, the high cost of internet data is still a big problem for South Africans, especially, the people in the rural areas.

The reliability of internet connection is one of the important factors usually considered by the Internet users when deciding on which network or service provider to choose for their connectivity. Hence, it is important to check whether the price that the users are paying commensurate with the connectivity reliability.

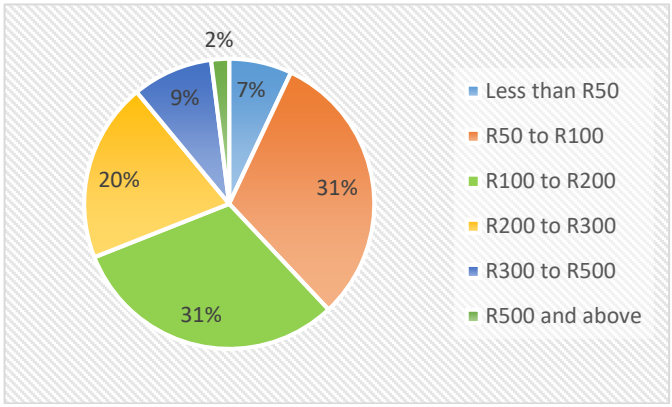

Figure 3: Average amount of money spent on Internet Data per week

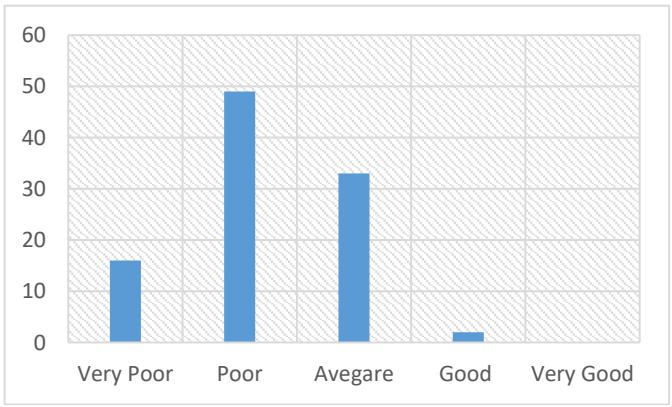

Figure 4: Current broadband Price satisfaction rating

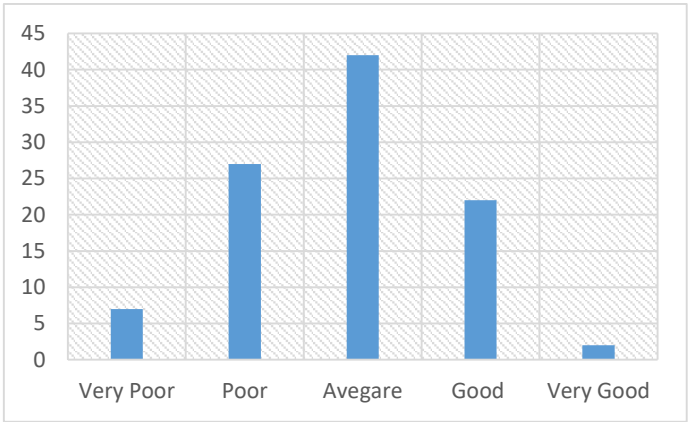

Figure 5: Current broadband Reliability satisfaction rating

Fig. 5 presents the participants rating in terms of Internet services reliability. It can be observed that the 34% of the respondents are not satisfied (poor and very poor rating) with their connection reliability, while 42% are averagely satisfied. 24% of the respondents are satisfied with their connection reliability. Although an average of 66% are satisfied with their connection reliability, however, it is important for the service providers to improve on their connection reliability, so as to increase the number of users that would select their Internet connection service.

Even though the reliability of an internet connection is an important factor, the Internet speed also plays an important role in determining the network provider to choose and in the amount of money the users would be ready to spend on internet services. Fig. 6 presents the participants level of satisfaction in terms of internet speed. It can be observed that the 70% of the respondents are not satisfied (poor and very poor rating) with their internet speed, especially when compare to the amount of money they are paying for internet data. 24% are averagely satisfied, while only 6% are satisfied with their internet speed. Although, the internet speed varies according to data packages, also the environment can affect the internet speed, especially in rural areas. However, a cost-effective deployment of fibre optic network in such rural areas will greatly enhance the internet speed and connection reliability, which in-turn will help to reduce the existing digital divides between the rural and urban areas.

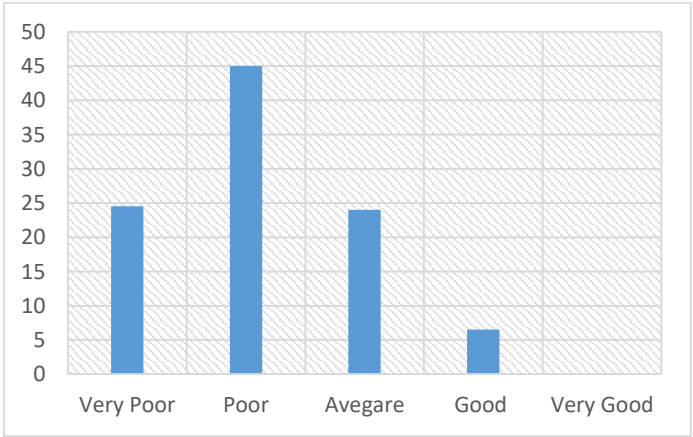

Figure 6: Current broadband Internet speed satisfaction rating

One of the factor that any service provider would want to check before investing in internet service provision is the probability of acceptance by the intending community or users. Here, this study investigates whether the participants would subscribe to fibre optic network if available in their community. Before the participants responded, the researcher explains the pros and cons of fibre optic network, especially in the context of rural areas. Fig. 7 shows that 36% would definitely subscribe, while 31% would probably subscribe. However, 33% of the participants are not sure whether or not they would subscribe to this very high-speed internet connection. This result aligns with that of the price and speed satisfaction rating, where an approximately 65% of the participants are not satisfied with the current price and speed. Hence, the service provider would need to give an affordable pricing model, so as to be able to convince the remaining 33% that were not sure of whether they would subscribe or not.

The installation and operational cost of both the fibre optic and wireless (LTE) networks were presented here. Also, the cost-effectiveness of fibre optic network deployment in the rural areas when compared with the existing wireless (LTE) network were presented. All the costs presented are expressed in South Africa million Rands (R). The estimated cost of installation and operation of both fibre optic and wireless (LTE) networks were obtained from the internet service providers in East London, which also covers the Mdantsane area.

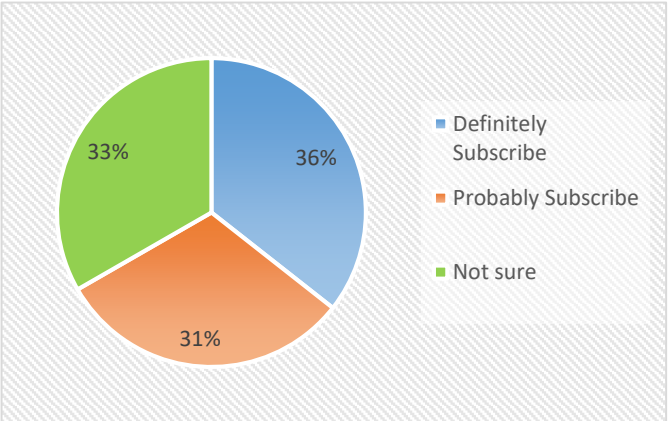

Figure 7: Users subscription to Fibre Optic network if available

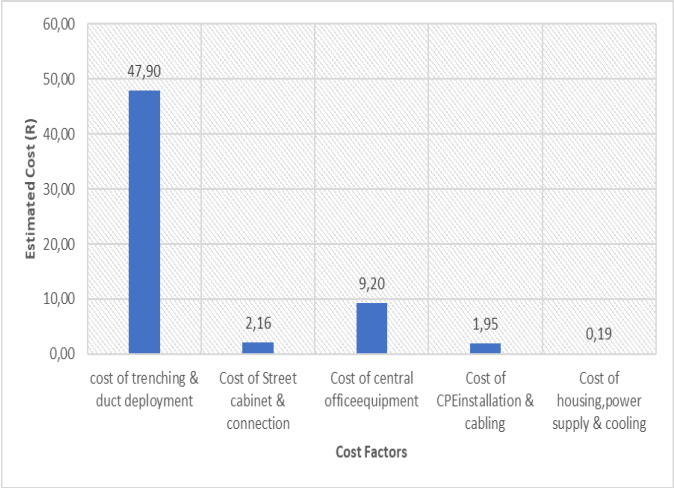

Figure 8: Fibre Optic installation cost

Fig. 8 presents the fibre optic installation costs factors and their respective estimated costs expressed in South Africa million Rand (R). It can be observed that the cost of trenching and duct deployment is the highest cost of the installation phase, estimated at R47,9 million. While the cost of housing, power supply, and cooling systems has the lowest costs in the installation phase, estimated at R0,19 million. Based on this result, the service provider can investigate different trenching and duct approaches that can be adopted, so as to reduce the installation cost significantly.

Fig. 9 presents the wireless (LTE) network installation costs factors and their respective estimated cost in Rand. It can be observed that the transmission and base station controller cost factor is the highest cost of the installation phase, estimated at R3,75 million. While the cost of licensing and spectrum has the lowest costs in the installation phase; estimated at R0,16 million. Based on this result, the service provider can investigate different trenching and duct approaches that can be adopted, so as to reduce the installation cost significantly. Although the cost factors of fibre optic and wireless (LTE) networks are different, however, based on total estimation from Figs. 8 and 9, the total installation cost for fibre optic and wireless (LTE) are R61,400,000 and R7,880,000 respectively.

The operation phase of the network deployment involves the monitoring and maintenance of different network conditions through day-to-day operations at possible minimal cost. The cost of operation phase for both fibre optic and wireless (LTE) networks are presented in Figs. 10 & 11 respectively. It can be observed from Fig. 10 that the cost of trenching and duct operation is the highest operation cost (R5,77 million), while the physical infrastructure has the lowest operation cost (R0,02 million) in fibre optic network operation phase.

In Fig. 11, it can be observed that the cost of base station equipment, transmission and controller is the highest operation cost (R2,56 million), while the base station civil works, standby power and cooling has the lowest operation costs (R0,1 million) in wireless (LTE) network operation phase. Based on Figs. 10 & 11, the total operational cost for fibre optic and wireless (LTE) networks are R11,150,568 and R2,867,900 respectively.

V. Conclusions and Recommendations

The main objective of this study was to investigate how cost effective it would be to deploy a fibre optic network in rural areas as compared to the current wireless (LTE) network. The Mdantsane township in Eastern cape province was used as a case study for this research. An analysis process was conducted to analyse the complete installation and operation costs of both the fibre optic and wireless (LTE) networks.
Established on the survey conducted amongst the residents of Mdantsane township and the internet service providers in East London, the findings show that while fibre optic networks seem to be great, however, they come at a cost.

Based on the findings of this study, installing a fibre optic access network in rural areas is not cost-effective as opposed to deploying a wireless (LTE) network. The cost of drilling and trenching associated with the deployment of fibre optic networks was reported as the key reason why the network is costly to install and operate. It is self-evident that reducing

the amount of drilling and trenching would decrease their high cost effectively. Hence, when implementing broadband in rural areas, it is firstly recommended that a mixed system, design, or even technology be considered. Secondly, it is recommended that the fibre optic cables could be used as backbone interconnection links with cellular networks using wireless mesh technology approach. Lastly, in order to lower the fibre optic network deployment costs, the network operators should partner and share fibre optic network installation and operation costs using a customize/differentiated pricing model, so as to be able to provide an affordable high-speed internet connectivity for the internet users in the rural areas.

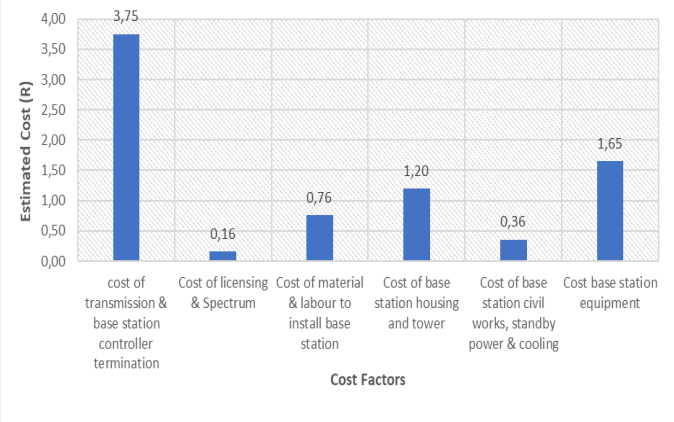

Figure 9: Wireless (LTE) installation costs

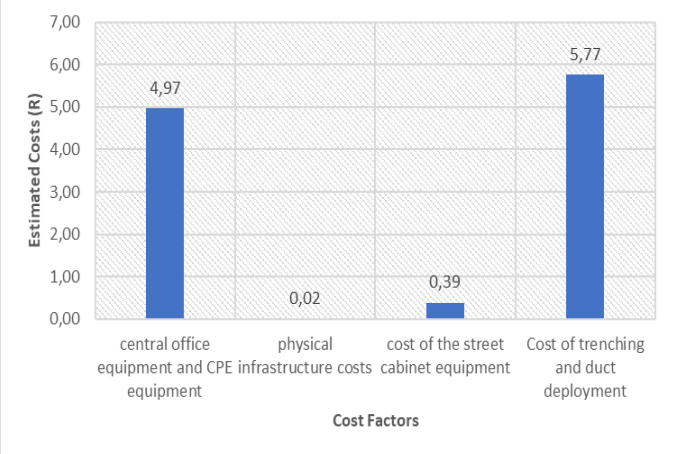

Figure 10: Fibre Optic operation phase cost

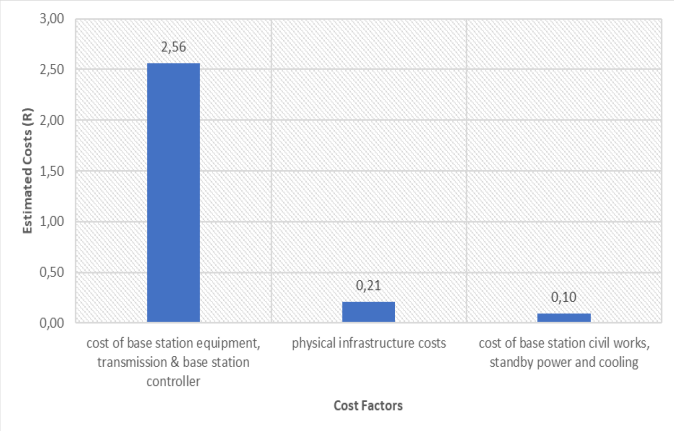

Figure 11: Wireless (LTE) operation phase cost

REFERENCES

[1] M. Tahon, J. Van Ooteghem, K. Casier, S. Verbrugge, D. Colle, M. Pickavet, and P. Demeester, "Improving the FTTH business case–A joint telco-utility network rollout model," *Telecommunications Policy*, 2015, 38(5-6), p. 426–437.https://doi.org/10.1016/j.telpol.2013.01.004

[2] S. Verbrugge, K. Casier, B. Lannoo, C.M. Machuca, T. Monath, M. Kind, and M. Forzati, "Research Approach towards the Profitability of Future FTTH Business Models," *Future Network & mobile summit*, 2017, pp. 1-10.

[3] K.H. Mohammadani, R.A. Butt, K.A. Memon, F. Hassan, A. Majeed, and R. Kumar, "Highest Cost First-Based QoS Mapping Scheme for Fibre Wireless Architecture," *Photonics 2020*, 7(4), 114. https://doi.org/10.3390/photonics7040114

[4] A. Ntsandeni, "Innovation-based competitive differentiation amongst South African fibre to the home (FTTH) operators," M. Man. Thesis, WITS, South Africa, 2018.

[5] B. Whitacre, R. Gallardo, and S. Strover, "Broadband contribution to economic growth in rural areas: Moving towards a causal relationship," *Telecommunications Policy*, 2014, 38, pp. 1011–1023. https://doi.org/10.1016/j.telpol.2014.05.005

[6] A. Goldstuck, (2017). "Internet Matters: The Quiet Engine of the South African Economy," pp. 38-50. [Online]: https://hsf.org.za/publications/focus/focus-66/AGoldstuck.pdf

[7] J.H. Beneke, *South Africa: The Long Walk to Broadband Freedom*, 2018, pp. 13-28.

[8] L. Pernegger, and S. Godehart, "Townships in the South African Geographic Landscape – Physical and Social Legacies and Challenges" TTRI, South Africa, 2007.

[9] C. Rametta, and G. Schembra, "Designing a Softwarized Network Deployed on a Fleet of Drones for Rural Zone Monitoring," *Future Internet*, 2017, 9(1), 8. https://doi.org/10.3390/fi9010008

[10] M. Al-Quzwini, "Design and Implementation of a Fibre to the Home FTTH Access Network based on GPON," *International Journal of Computer Applications*, 92(6), pp. 30–42, 2014. https://doi.org/10.5120/16015-5050

[11] S. Jay, K.H. Neumann, and T. Plückebaum, "Comparing FTTH access networks based on P2P and PMP fibre topologies," *Telecommunication Policy*, 2014, 38(5-6), pp. 415–425. https://doi.org/10.1016/j.telpol.2013.04.010

[12] S. Mamabolo, S.V. Solms, and A. Marnewick, 2019. University of Johannesburg 88.

[13] L.T. Gwaka, J. May, and W. Tucker, 2018. "Towards low-cost community networks in rural communities: The impact of context using the case study of Beitbridge, Zimbabwe," Electronic Journal of Information Systems in Developing Countries, 2018, 84(3). https://doi.org/10.1002/isd2.12029

[14] M. Chetty, S. Sundaresan, S. Muckaden, N. Feamster, and E. Calandro, "Measuring broadband performance in South Africa," In: 4th Annual Symposium on Computing for Development - ACM DEV-4 '13., Cape Town, South Africa, pp. 1–10, 2013.

[15] S. Esselaar, A. Gillwald, M. Moyo, and K. Naidoo, "South African ICT Sector Performance Review," *Towards Evidence-based ICT Policy and Regulation, 2010*, Vol. 2(6), 2010 2009/2010 46.

[16] A.J. Hoffman, and D.P. de Wet, "Broadband Internet access for rural Africa: finding a viable model," In: 2nd International Conference on applied informatics and computing theory, 2017.

[17] L.H. Moroeng, "Fixed-to-Mobile Broadband Substitution in South Africa," 2012.

[18] G. Alison, "Between two stools: Broadband policy in South Africa," *South African Journal of Information and Communication*, 2007(8), pp. 53-77, 2007. https://doi.org/10.23962/10539/19787

[19] G. Angelou, and A. Economides, "Broadband Business Opportunities for Utility-Based Firms in the New Era: Modeling the Competition," In: IEEE Fourth Balkan Conference on Informatics, Greece, 2009, pp. 209–214.

[20] L.F. Seymour, and M. Naidoo, "The Usage and Impact of Broadband: A South African Household analysis," *Electronic Journal of Information Systems Evaluation*, 16(2), pp. 223-234, 2013.

[21] M. Byanyuma, S. Kalolo, S.I. Mrutu, C. Nyakyi, and A. Sam, "Affordable broadband connectivity for rural areas," In Pan African International Conference on Information Science, Computing and Telecommunications (PACT), 2013 pp. 62–65. https://doi.org/10.1109/SCAT.2013.7055090

[22] G. Brian, "Community Fiber Broadband in North Carolina: A Comparative Analysis," MSc thesis, 2020. https://doi.org/10.17615/8ccv-bv14.

Interactive Visualisation of Energy Usage in a Smart Environment

Moreblessing Ngwenya, Janet L Wesson

[#]*Computing Sciences Department, Nelson Mandela University*

s215169511@mandela.ac.za

janet.wesson@mandela.ac.za

Abstract— **Saving electricity is a trending topic due to the electricity challenges that are being faced globally. Smart environments are environments that are equipped with physical objects, which include computers, sensors, actuators, smartphones, and wearable devices interconnected together through the Internet of Things. The Internet of Things provides a network to achieve communication and computation abilities to provide individuals with smart services anytime, and anywhere. Rapid developments in information technology have resulted in an increase in the number of appliances being used, leading to increased electricity usage. Devices and appliances in Smart environments continue to consume electricity even when not in use, because of the standby function. Problems arise as the electricity consumption of the standby function can accumulate to large amounts. Effective communication of the electricity consumption using visualisation can provide a viable solution to reduce the electricity usage. The aim of this research was to design and develop a visualisation tool that uses several visualisation techniques to effectively communicate electricity usage in a Smart environment to the user.**

Keywords— **Smart environment, energy, visualisation**

I. Introduction

A smart environment (SE) can be defined as an integrated environment where sensor-enabled technologies work together to make the life of the inhabitant more comfortable [1]. Smart refers to the advanced technologies that have some degree of artificial intelligence [2], which includes the ability to obtain and apply knowledge [1]. In [1] the authors concluded that a SE is an environment that can obtain and apply knowledge about its inhabitants and adapt the environment according to their needs.

Connectivity is possible anywhere and anytime in a SE, but comes at the cost of increased electricity consumption [3]. Continuous developments in data communication technology ensure connectivity of devices, however continuous connectivity contributes to a large portion of electricity consumption [4]. This consumption continues to increase as more developments occur [3].

Idle networked and connected smart devices in a SE contribute to electricity usage. The continuous connections, as is the case of smart devices, cause an increase in electricity usage, even when the devices are on standby mode [5]. Monitoring the electricity consumption, therefore, becomes essential to understand the sources of the electricity usage and take the appropriate action to save electricity [6].

Several systems have been developed to address monitoring and communication of the increase in electricity usage in SEs, however the effectiveness of their communication of the electricity usage to the user could be improved. Visualisation of data plays a vital role, as it can communicate findings in a way that is easily and quickly understood by the user [8]. It is important for users to understand their electricity usage, to know where they are wasting electricity, and what their consumption is in real-time [9]. The Design Science Research (DSR) methodology was used to design an information visualisation (IV) tool to increase the effectiveness of communication.

II. Research Methodology

The DSR methodology was used for this research. DSR has multiple activities, which are described below [7]:

- *Explicate problem*: This involve identifying and analysing the problem through a literature review [7] of SE, electricity usage and visualisation, as discussed in Sections III, IV, and V respectively. The problem for this research was how to save electricity in a SE by visualising the electricity consumption.
- *Define requirements*: Requirements of the proposed solution were gathered from the literature review [7] and summarised in Section VI.
- *Design and develop artefact:* This paper focuses on the design aspect of the activity, which is discussed in Section VI, involving multiple iterations of design and development of an artefact that addresses the problems and meets the specified requirements [7]. Each design iteration aimed to improve the previous one.
- *Demonstrate artefact:* The demonstrate artefact activity included using the developed artefact in an illustration or real-life case (proof of concept), to show the feasibility of the artefact [7]. The demonstration was done during the evaluations of the artefact, as discussed in Section VII.
- *Evaluate problem:* The evaluation activity determines the extent to which the developed artefact meets the specified requirements and solves the problem identified. A heuristic evaluation was conducted in Section VII and future work will include a user study.

III. Smart Environments

The Internet of Things (IoT) is a computing paradigm where every day physical objects are amplified by using computational and wireless communication capabilities [10]. The IoT provides open possibilities and flexibility in enabling unified and remote control of modern and old devices alike. IoT is viewed as a vital ingredient in developing SEs [11].

To understand what affects electricity usage in a SE, it is important to understand the architecture of SEs. The typical SE architecture is discussed in Section A.

A. Smart Environment Architecture

The SE architecture is a breakdown of the various technologies that can be found in a SE, separated into four layers, namely physical, context, adaptation, and application layer. A detailed description of each layer is given below.

1) Physical Layer: The first layer of a general SE has alternative names but was referred to as the physical layer for this research. The physical layer contains sensors, hardware devices [14], actuators, network interface, microcontroller, and sensing technologies [12]. The primary goal of this layer is to capture and gather outside information about the environment and transmit it to the context layer [13].

2) Context Layer: The context layer acts as the backbone of the entire architecture. It contains multiple components each having unique responsibilities related to the context [13]. This layer aims to provide a reliable, convenient, and complete infrastructure to enable sharing of data between users and devices in the SE [14].

3) Adaptation Layer: Adaptation refers to the ability to alter a service and provide another corresponding service to the SE [13]. This layer is aimed at adapting services according to the context identified by the context layer. The adaptation layer is responsible for analysing context and determining which actions to execute in response [13].

4) Application Layer: The application layer aims to support the business needs of the SE [14]. This layer includes all the applications subscribed to the user or exchange data-driven services of a SE [12]. The application layer is responsible for communication between the user and the system. It allows users to perform their required tasks, such as turning the television on/off or turning the lights on/off [15].

The investigation into the architecture of a SE provides a deeper understanding of the architecture of a SE and how it functions. The physical layer is important in monitoring as this is where the devices in the SE are located. It is vital to keep track of these devices and their respective electricity usage as when more devices are connected, more electricity is consumed [4]. In doing so, we can identify the sources of electricity consumption in a SE.

IV. Electricity usage in smart environments

Recent research has shown that, due to the global spread of climate change and electricity usage, electricity-saving has become a popular topic [41]. This provides a strong motivation for this research as we aim to reduce electricity wastage by using visualisation to communicate electricity usage to its users.

A. Electricity

Electricity is a universal currency that must be transformed to get anything done [16]. Electricity refers to the kinetic energy of moving electrons [16]. As global trends, such as technology developments, integration, technology transfer, and utilisation, continue to progress it also puts a high demand on electricity availability [17]. Electricity accounts for approximately 30% of global energy consumed, and this could be reduced by 15% by increasing awareness [18]. Understanding the source of electricity usage in an environment can help in finding ways to reduce electricity usage [5].

B. Sources of electricity in a smart environment

It is important to identify the source of electricity usage in a SE to find out how a SE impacts electricity usage.

1) Vampire power: Devices with standby mode consume electricity by maintaining an internal clock and waiting to receive remote signals from a device [19]. Research by [19] highlighted that the power used to maintain and control one device may be small, however, "vampire power" results in a lot of electricity usage as more devices are connected [20].

2) Smart environment sensing technologies: Multiple communication technologies can be used in a SE. For this research, the focus was placed on common technologies and their unique impact on electricity usage in a SE [21]. As seen in Table 1, different technologies have different levels of electricity consumption [21]. Depending on a selected technology, the levels of electricity consumption for specified data rate differs and can affect the overall electricity consumption.

TABLE I
TECHNOLOGIES THAT ARE COMMON IN SEs AND THEIR ATTRIBUTES [21]

Technology	Coverage Area Range	Data Rate	Electricity Consumption
Bluetooth	1-100m	1Mbps	15mV
ZigBee	10-20m	250Kbps	52.22mW
Wi-Fi	25-50m		
RFID	Depends on type of tag	Depends on type of tag	Depends on type of tag
WLAN	50-up to 250m	11.54-108Mbps	19.95mW

3) Smart environment devices and appliances: The IoT contains things that are connected anywhere and anytime ([10], [11]). There has been an increase in the number of devices being connected to the internet [24], and as a result, more devices can be included in a SE.

Problems in electricity usage continue to increase as the number of users rise and demand for electricity increases. Recent research by [23] found that as the number of devices passing through a SE increase, so does the electricity consumption. Section V discusses how the electricity consumed in a SE should be communicated to the user, which is the focus of this research.

V. Information Visualisation

Electricity usage can be 'invisible' as it is silent and cannot be touched [25]. It is therefore important to find ways to make electrical energy 'visible' to inform users of their consumption.

Many consumers do not clearly understand power and electricity, nor do they understand kilowatt (kW) and kWh. Electricity monitoring enables the possibility of understanding the usage of electricity and has thus become an important research topic.

Research conducted by [26] highlighted that vision allows us to obtain more information as compared to all other sensors combined. Visualisation refers to the graphical representation

of concepts or data; this enables users to make use of their user perception to achieve better analysis and understanding [27] of their electricity usage.

A. Objective

Data visualisation involves the illustration of data in a manner that allows the data to be easily understood by the user, without having to go into statistical details [28]. The main objective of IV involves using a visual perception of information to improve its reasoning abilities [29]. The main benefit of IV is the amount of information that can be quickly understood if presented well [26]. In addition, IV provides a platform for users to easily understand large amounts of data ([26], [29]).

Visualising electricity usage is important as it provides understandable and timely usage data allowing users to know when wastage occurs [30]. This paper aims to make use of visualisation to effectively communicate electricity usage to the user, and consequently lead to a reduction in electricity usage. Section B investigates various visualisation techniques, which can be implemented in the design and development of the IV tool.

B. Visualisation Techniques

Multiple techniques can be implemented to visualise data. We investigated visualisation techniques to find the most suitable techniques to use for visualisation of electricity usage. The techniques investigated [45] included: Bar graph including stacked and grouped bar graphs, Histogram, Donut chart, Scaled up number, Line chart, Box plot, Meter, Gauge, Pie chart and 3D visualisation.

The different chart types mentioned above each have a different role addressing a specific use case. The charts mentioned above all meet a similar criterion, which is to support the display of time series data, which is the basis of the selection of the chart types discussed.

For this paper, the aim was to use a dashboard to implement the various techniques. Dashboards and the design of dashboards are further discussed in Section VI.

VI. Dashboard Design

A dashboard can be referred to as a visual display of vital information, which includes graphics and text required to achieve one or more objectives; this information is combined and organized on a single screen so that it can be seen immediately [31]. Dashboards assist people in identifying patterns, trends, and anomalies, and subsequently guide users in effective decision making [32]. If designed properly, dashboards can effectively communicate large amounts of information [33].

A. Existing systems

A literature review was conducted on existing dashboards created to monitor electricity usage in SE. A few suggestions by researchers on the design of their electricity monitoring systems were identified and are discussed below.

Visual metaphors assist in easily understanding information and motivation to reach a certain target, such as the use of progress bars [41]. Allowing users to see different levels of details of their usage enables quicker decision making and intuitive understanding for the user [42]. Interaction between the user and the visualisation should be made possible. Relevant information should be displayed, and support provided for hover and zoom effects should be implemented [43].

These suggestions were considered in the design of the dashboard to make it as effective as possible in communicating electricity usage to the user.

B. Dashboard purpose, types, and requirements

The aim of the dashboard leads to choices in the visual design of the dashboard and its functionality [34]. Dashboards act as a means of communication, to effectively deliver a message to the user, the message needs to be concise, goal-oriented, and clear [35]. The different objectives of a dashboard include the ability to ensure consistency, planning, communication, and monitoring [31].

There are different types of dashboards, categorised by their different roles, namely strategic, analytical, and operational [36]. *Operational* dashboards [37] are focused on the current performance or day-to-day operations of an organisation. Operational dashboards make use of real-time or near real-time data [37]. *Analytical* dashboards are enabled with drill-down functionality, enabling users to explore data in detail [37]. Analytical dashboards can be used to show key data sets highlighted against previous data. *Strategic* dashboards aim to show key performance indicators of an organisation; [37]. The type of dashboard required for this research was a combination of all three types. The requirements were derived from the benefits of the existing systems and attempting to overcome the shortcomings.

The IV tool must: 1) Display total electricity usage of all devices for the hour, day, week, month, and year; 2) Display current electricity usage of selected devices; 3) Display total electricity usage of a selected device for the hour, day, week, month, and year; 4) Display current electricity usage of selected devices; 5) Display historical electricity usage of a selected device for a specific previous period (hour, day, week, month, year); 6) Enable the user to make comparisons of electricity usage between devices on selected dates; 7) Enable the user to make comparisons of electricity usage between category of devices on selected dates; 8) Alert the user of high electricity usage readings; 9) Display the device with the most or least electricity usage for specified period (hour, day, week, month, year); 10) Display the category of devices with the most or least electricity usage for a specified period (hour, day, week, month, year); and 11) Show which time of day the most electricity was consumed.

C. Design of dashboard

The design of the dashboard was repeated to refine the design of the IV tool, and the aim was to e develop more effective designs with each iteration.

To design advanced graphical user interfaces, Shneiderman [38] suggested the Visual Information Seeking Mantra as a starting point, which states: "*Overview first, zoom and filter, then details on demand*". The design of the dashboard followed this mantra, by showing the overview data first and then allowing the user to drill down to specific data.

The dashboard was designed for a Smart Lab in the Computing Sciences Department at Nelson Mandela University (NMU). The Smart Lab contains several devices,

which were categorised depending on their location in the Smart Lab, as shown below:

1) Kitchen: Toaster, fridge, and kettle

2) Study: Desktop monitor and desktop computer

3) Lounge: Television, google home, Wi-Fi router, intel NUC, vera smart home controller, Phillips's hue lamp, smart mirror, LED lighting

4) Other: Air conditioning, speakers, four roof stations each with a Raspberry pi, camera, speaker, and microphone.

The devices were connected to TP-Link HS100 smart Wi-fi plugs to capture their readings to a database, which will be displayed on the dashboard. Designs of the dashboard were created using the JustInMind prototyping tool. Some of the designs are shown in Figs. 1-4.

Figure 1 shows a home screen of the dashboard showing the overall usage of all devices in the Smart Lab. Figure 2 shows the usage of a specific category, in this case the kitchen. Figure 3 shows a single device usage, for this example, a fridge. Figure 4 shows the comparison screen between two devices.

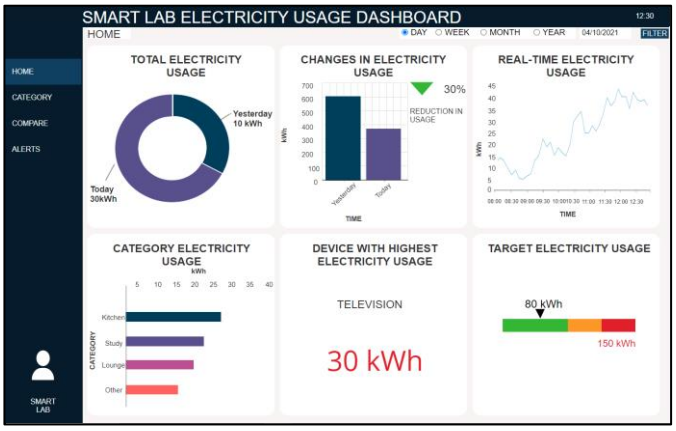

Figure 1: Dashboard (Overview)

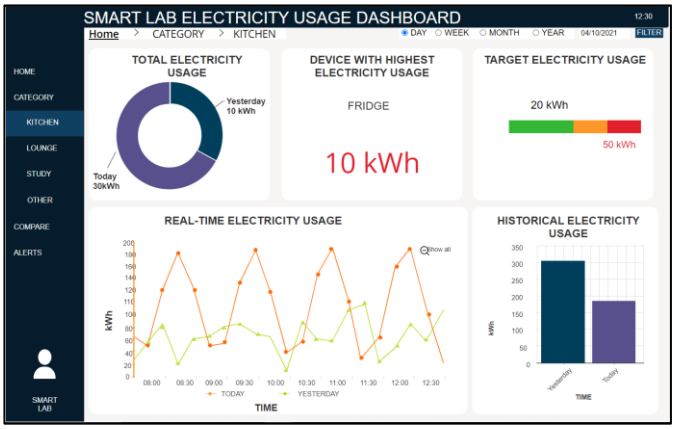

Figure 2: Category detail screen

VII. EVALUATION

There are different ways to test the usability of a product; a Formative Evaluation [39] was conducted for this research to focus on identifying ways to make improvements to the IV tool before it was released to actual users.

A. *Heuristic Evaluation*

A heuristic evaluation, a type of formative evaluation, was conducted on the designs to find issues in the design so they could be addressed as part of the iterative design activity in the DSR methodology. A heuristic evaluation includes having a small group of evaluators, usually, experts examining the user interface and judging the conformity with accepted usability standards [40].

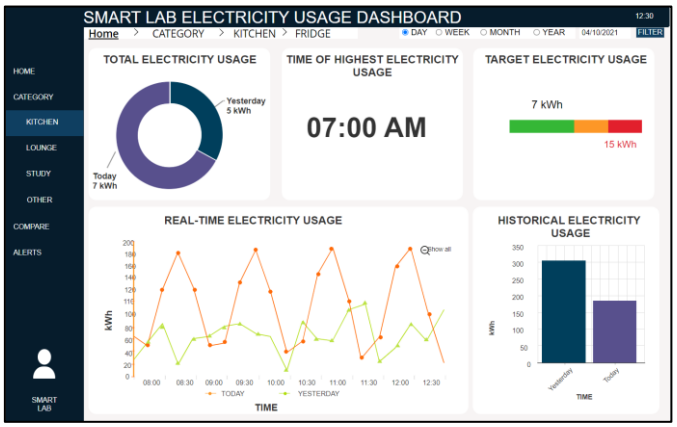

Figure 3: Single device details screen (Fridge)

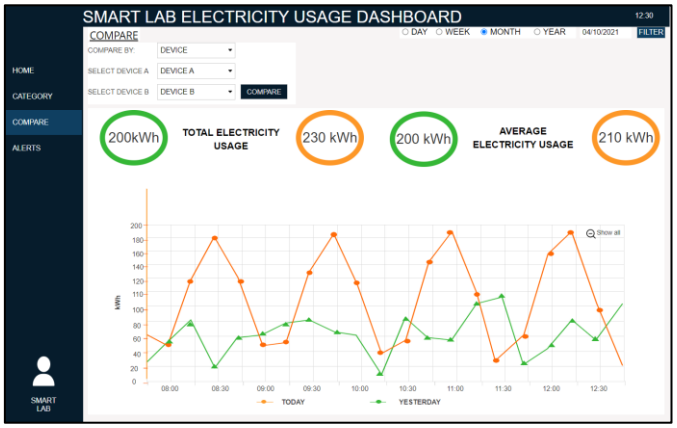

Figure 4: Comparison screen (Comparing Device A with Device B))

B. *Evaluation Process*

Evaluators were provided with dashboard designs and briefed on the research, its aims and requirements that had to be met for the design of the IV tool. For this evaluation, five people were selected as evaluation with five people allows for identification of nearly as many usability issues as testing with more individuals [40].

Evaluators were comprised of postgraduate students, graphic designers, and front-end designers. The evaluators were asked to evaluate the designs based on Nielsen's ten heuristics in order, namely visibility of system status, the match between system and real life, user control and freedom; consistency and standards; error prevention; recognition rather than recall; flexibility and efficiency of use; aesthetic and minimalist design; help users recognize, diagnose, and recover from errors; help and documentation.

After going through the designs, the evaluators completed a questionnaire, which included the heuristic questionnaire and additional open-ended questions on suggestions for design improvements.

C. Results and Discussion

All the heuristics mean scores were above 4, indicating that the usability problems identified with each heuristic were minor. Figure 5 shows the average rating of each heuristic principle.

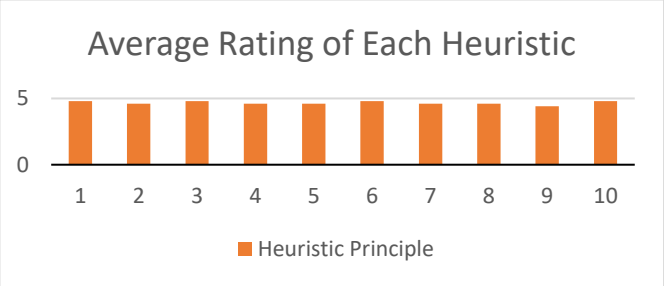

Figure 5: Average rating of each heuristic

TABLE 2
HEURISTIC REPORT

Issue	Description	Recommendation
Font	Font is not clear	Review and update font
Colour scheme	Colours used make it hard to read some text (e.g., blue colour)	• Review colour scheme • Use darker shade between grey and white cards
Filter	The filter labels (day, week, etc.) needs to be more visible to make comparison easier	• Need to improve the labels, make them clearer. • Use dropdown instead of radio button for filters (day, week, month, year)
Layout	White space and clarity of charts	• Line up grids with equal spacing • Stacking cads to show bigger graphs and remove white space.
Menu	Menu breadcrumbs	Add icons and add hover function
Charts	Replace bar chart with pie chart on showing historical usage as this improves clarity on reading	• Use pie chart instead of bar chart on historical electricity usage. • Total electricity usage show with bar graph instead of pie chart
Other	Compare screen is unclear (which figures belong to which device)	Need to improve the labels, make them clearer
	Logo	Add logo on top of menu

Table 2 shows the detailed problems that were identified by the evaluators from the responses in the questionnaire. In addition to the results in Table 2, the following additional positive comments were made on the design of the dashboard: "The design is simple and sleek, the infographics and data representation make for a good dashboard", "Visuals are crisp and make sense", and "Could be useful if combined with ambient notification systems".

VIII. CONCLUSION & FUTURE WORK

This research set out to design an effective IV tool to visualise the electricity usage of a SE. The aim of the research was to design a dashboard to effectively communicate the electricity usage of the SE, with the goal of reducing the overall electricity usage. A heuristic evaluation was conducted to identify usability issues with the dashboard design. The results showed that none of the issues identified were critical, meaning they would not affect the usability of the dashboard. Future work will include improving the designs based on the suggestions highlighted in the evaluations.

Implementation of the tool will be important so at to further test the usability of the IV tool. Future work involves implementation of the dashboard designs using ThingsBoard. ThingsBoard [44] is an open source IoT platform that allows rapid development, management, and scaling of IoT projects. Ambient visualisation could also be implemented as a support to the dashboard, to alert the user on critical or unusual electricity usage, or when a target electricity usage has been reached. An example of ambient visualisation could be the use of LED lights to indicate the level of electricity usage, using different colours. This could be used to prompt the user to further investigate the causes of the excessive electricity usage. In addition, enabling the IV tool to make decisions to turn devices on/off based on electricity usage.

ACKNOWLEDGMENT

The author would like to acknowledge the NMU/Telkom Centre of Excellence and the NMU Research Capacity Department for their financial assistance, as well as her supervisor Prof. Janet Wesson for her support throughout the process, without which this research would not be possible.

REFERENCES

[1] Ahmed, E., Yaqoob, I., Gani, A., Imran, M., & Guizani, M. (2016). Internet-of-things-based smart environments: State of the art, taxonomy, and open research challenges. *IEEE Wireless Communications*, *23*(5), 10–16. https://doi.org/10.1109/MWC.2016.7721736

[2] Marikyan, D., Papagiannidis, S., & Alamanos, E. (2019). A systematic review of the smart home literature: A user perspective. *Technological Forecasting and Social Change*, *138*(June 2018), 139–154. https://doi.org/10.1016/j.techfore.2018.08.015

[3] Li, J., Xiao, J., Nguyen, H. N. M., Hong, J. W. K., & Boutaba, R. (2014). Energy efficient Wi-Fi management for smart devices. *IEEE/IFIP NOMS 2014 - IEEE/IFIP Network Operations and Management Symposium: Management in a Software Defined World*. https://doi.org/10.1109/NOMS.2014.6838234

[4] Carroll, A., & Heiser, G. (2010). An Analysis of Power Consumption in a Smartphone. *USENIX Annual Technical Conference*.

[5] IEA. 2021. *More Data, Less Energy – Analysis - IEA.* [online] Available at: <https://www.iea.org/reports/more-data-less-energy> [Accessed 3 June 2021].

[6] Hertzog, P. E., & Swart, A. J. (2018). Non-Complex Cost-Effective Energy Monitoring using the Internet of Things. *2018 International Conference on Multidisciplinary Research*, *July*.

[7] Johannesson, P., & Perjons, E. (2014a). A Method Framework for Design Science Research. In *An Introduction to Design Science* (pp. 75–89). Springer International Publishing. https://doi.org/10.1007/978-3-319-10632-8_4

[8] Ambrose, M., & James, M. (2017). Dealing with energy efficiency data. *Energy Procedia*, *121*, 158–165. https://doi.org/10.1016/j.egypro.2017.08.013

[9] Fan, X., Qiu, B., Liu, Y., Zhu, H., & Han, B. (2017). Energy Visualization for Smart Home. *Energy Procedia*. https://doi.org/10.1016/j.egypro.2017.03.732

[10] Idongesit Efaemiode, E. (University of C., & Andrew, J. (2019). AN IOT-BASED SMART ENVIRONMENT SYSTEM. *Conference: 7th U6+ Consortium of African Universities Conference 2019*. https://www.researchgate.net/publication/343212530_AN_IOT-BASED_SMART_ENVIRONMENT_SYSTEM

[11] Gomez, C., Chessa, S., Fleury, A., Roussos, G., & Preuveneers, D. (2019). Internet of Things for enabling smart environments: A technology-centric perspective. *Journal of Ambient Intelligence and Smart Environments*, *11*(1), 23–43. https://doi.org/10.3233/AIS-180509

[12] Mokhtari, G., Anvari-Moghaddam, A., & Zhang, Q. (2019). A New Layered Architecture for Future Big Data-Driven Smart Homes. *IEEE Access*, *7*, 19002–19012. https://doi.org/10.1109/ACCESS.2019.2896403

[13] Belaidouni, S., Miraoui, M., & Tadj, C. (2016). Towards an efficient smart space architecture. *Ijascse*, *5*(1), 18–27.

[14] Liu, P., Fels, S., West, N., & Görges, M. (2019). Human Computer Interaction Design for Mobile Devices Based on a Smart Healthcare Architecture. 0–2. http://arxiv.org/abs/1902.03541

[15] Paredes-Valverde, M. A., Alor-Hernández, G., García-Alcaráz, J. L., Salas-Zárate, M. del P., Colombo-Mendoza, L. O., & Sánchez-Cervantes, J. L. (2020). IntelliHome: An internet of things-based system for electrical energy saving in smart home environment. *Computational Intelligence*. https://doi.org/10.1111/coin.12252

[16] Smil, V. (2019). Energy in world history. In *Energy in World History*. https://doi.org/10.4324/9780429038785

[17] Okakwu, I. K., Oluwasogo, E. S., Ibhaze, A. E., & Imoize, A. L. (2019). A comparative study of time series analysis for forecasting energy demand in Nigeria. *Nigerian Journal of Technology*, *38*(2), 465. https://doi.org/10.4314/njt.v38i2.24

[18] Floris, A., Meloni, A., Pilloni, V., & Atzori, L. (2015). A QoE-aware approach for smart home energy management. *2015 IEEE Global Communications Conference, GLOBECOM 2015*. https://doi.org/10.1109/GLOCOM.2014.7417799

[19] Kumar, A., Fathima, K., Saranya, T. M., & Hema, S. (2017). Methodology to reduce vampire power using PIC microcontroller. *ARPN Journal of Engineering and Applied Sciences*, *12*(13), 4027–4031.

[20] López-De-Armentia, J., Casado-Mansilla, D., & López-De-Ipiña, D. (2012). Fighting against vampire appliances through eco-aware things. *Proceedings - 6th International Conference on Innovative Mobile and Internet Services in Ubiquitous Computing, IMIS 2012*, 868–873. https://doi.org/10.1109/IMIS.2012.112

[21] Ahuja, K., & Khosla, A. (2019). Network selection criterion for ubiquitous communication provisioning in smart cities for smart energy system. *Journal of Network and Computer Applications*. https://doi.org/10.1016/j.jnca.2018.11.011

[22] Alaa, M., Zaidan, A. A., Zaidan, B. B., Talal, M., & Kiah, M. L. M. (2017). A review of smart home applications based on Internet of Things. In *Journal of Network and Computer Applications*. https://doi.org/10.1016/j.jnca.2017.08.017

[23] Agate, V., Concone, F., & Ferraro, P. (2018). WiP: Smart services for an augmented campus. *Proceedings - 2018 IEEE International Conference on Smart Computing, SMARTCOMP 2018*, 276–278. https://doi.org/10.1109/SMARTCOMP.2018.00056

[24] Zyrianoff, I., Heideker, A., Silva, D., Kleinschmidt, J., Soininen, J. P., Cinotti, T. S., & Kamienski, C. (2020). Architecting and deploying IoT smart applications: A performance–oriented approach. *Sensors (Switzerland)*, *20*(1). https://doi.org/10.3390/s20010084

[25] Nilsson, A., Wester, M., Lazarevic, D., & Brandt, N. (2018). Smart homes, home energy management systems and real-time feedback: Lessons for influencing household energy consumption from a Swedish field study. *Energy and Buildings*. https://doi.org/10.1016/j.enbuild.2018.08.026

[26] Ware, C. (2019). *Information Visualization: Perception for Design* (4th ed.). Elsevier Sciencev. https://books.google.co.za/books?id=3-HFDwAAQBAJ&dq=visualization&lr=&source=gbs_navlinks_s

[27] Ferreira, H., de Oliveira, G. P., Araújo, R., Dorça, F., & Cattelan, R. (2019). Technology-enhanced assessment visualization for smart learning environments. *Smart Learning Environments*. https://doi.org/10.1186/s40561-019-0096-z

[28] Grainger, S., Mao, F., & Buytaert, W. (2016). Environmental data visualisation for non-scientific contexts: Literature review and design framework. In *Environmental Modelling and Software*. https://doi.org/10.1016/j.envsoft.2016.09.004

[29] Hrabovskyi, Y., Brynza, N., & Vilkhivska, O. (2020). Development of information visualization methods for use in multimedia applications. *EUREKA, Physics and Engineering*, *2020*(1), 3–17. https://doi.org/10.21303/2461-4262.2020.001103

[30] Herrmann, Melanie Rosemarie. (2018). Smart energy feedback in the home: the effect of disaggregation and visualisation on householders' comprehension of electricity data. *Doctoral Thesis, UCL (University College London)*.

[31] Abduldaem, A., & Gravell, A. (2019). Principles for the Design and Development of Dashboards: Literature Review. *Proceedings of INTCESS 2019- 6th International Conference on Education and Social Sciences*.

[32] Toasa, R., Maximiano, M., Reis, C., & Guevara, D. (2018). Data visualization techniques for real-time information - A custom and dynamic dashboard for analyzing surveys' results. *Iberian Conference on Information Systems and Technologies, CISTI*, *2018-June*, 1–7. https://doi.org/10.23919/CISTI.2018.8398641

[33] Rahman, A. (2017). *Designing a Dashboard as Geo-Visual Exploration Tool for Origin-Destination Data*. 1–73. https://webapps.itc.utwente.nl/librarywww/papers_2017/msc/gfm/rahman.pdf

[34] Sarikaya, A., Correll, M., Bartram, L., Tory, M., & Fisher, D. (2019). What do we talk about when we talk about dashboards? *IEEE Transactions on Visualization and Computer Graphics*, *25*(1), 682–692. https://doi.org/10.1109/TVCG.2018.2864903

[35] Ergasheva, S., Ivanov, V., Khomyakov, I., Kruglov, A., Strugar, D., & Succi, G. (2020). InnoMetrics Dashboard: The Design, and Implementation of the Adaptable Dashboard for Energy-Efficient Applications Using Open Source Tools. *IFIP Advances in Information and Communication Technology*. https://doi.org/10.1007/978-3-030-47240-5_16\

[36] Sarikaya, A., Correll, M., Bartram, L., Tory, M., & Fisher, D. (2019). What do we talk about when we talk about dashboards? *IEEE Transactions on Visualization and Computer Graphics*, *25*(1), 682–692. https://doi.org/10.1109/TVCG.2018.2864903

[37] Toxboe, A. and Toxboe, A., 2021. *Dashboard design pattern*. [online] Ui-patterns.com. Available at: <http://ui-patterns.com/patterns/dashboard> [Accessed 27 March 2021].

[38] Shneiderman, B. (1996). Eyes have it: a task by data type taxonomy for information visualizations. *IEEE Symposium on Visual Languages, Proceedings*. https://doi.org/10.1016/b978-155860915-0/50046-9

[39] Tullis, T., & Albert, B. (2013). Measuring the User Experience: Collecting, Analyzing, and Presenting Usability Metrics: Second Edition. In *Measuring the User Experience: Collecting, Analyzing, and Presenting Usability Metrics: Second Edition*. https://doi.org/10.1016/C2011-0-00016-9

[40] Nielsen, J. (1994). *How to Conduct a Heuristic Evaluation*. https://www.nngroup.com/articles/how-to-conduct-a-heuristic-evaluation/

[41] Koroleva, K., Melenhorst, M., Novak, J., Herrera Gonzalez, S. L., Fraternali, P., & Rizzoli, A. E. (2019). Designing an integrated socio-technical behaviour change system for energy saving. *Energy Informatics*. https://doi.org/10.1186/s42162-019-0088-9

[42] Truong, H., Francisco, A., Khosrowpour, A., Taylor, J. E., & Mohammadi, N. (2017). Method for visualizing energy use in building information models. *Energy Procedia*, *142*, 2541–2546. https://doi.org/10.1016/j.egypro.2017.12.089

[43] Ali, S. M., Gupta, N., Nayak, G. K., & Lenka, R. K. (2016). Big data visualization: Tools and challenges. *Proceedings of the 2016 2nd International Conference on Contemporary Computing and Informatics, IC3I 2016*. https://doi.org/10.1109/IC3I.2016.7918044

[44] ThingsBoard. (2021). *What is ThingsBoard? | ThingsBoard Community Edition*. https://thingsboard.io/docs/getting-started-guides/what-is-thingsboard/

[45] Kirk, A. (2019). Data visualisation: a handbook for data driven design. In *SAGE Publications*.

Moreblessing Tafadzwa Ngwenya is a third-year master's student at Nelson Mandela University. She received her bachelor's and honours degrees in Computer Science and Information Systems at Nelson Mandela University. She is interested in information visualisation.

The Use of Fiber Bragg Grating Sensors (FBG) to Measure Movement and Internal Temperature During the Early Ages of Concrete

Musa Mbata[1], Mr JJ Bester[3], Mr M Grobler[2]

[1]*University of Johannesburg, Civil Engineering Science,* [2]*University of Johannesburg, Electrical & Electronics Science*

[1]musambatha75@gmail.com

[3]jannesb@uj.ac.za

[3]*University of Johannesburg, Civil Engineering Science, South Africa*

[2]michaelg@uj.ac.za

Abstract—**The use of structural health monitoring (SHM) systems in civil engineering structures has been a developing topic, that has allowed for a better understanding of structures' conditions and increasingly lead to more cost-effective management of those infrastructures. In this paper, the use of fiber optic sensors to measure early age movement has been studied. The possibility of monitor early age movement within construction is an advantage that fiber optic sensing provides to SHM systems. Fiber Bragg Grating sensors were embedded into a concrete slab (4040 mm x 1040 mm) and the FBG strain and temperature readings were recorded to provide immediate information with regards to internal concrete temperature, and movement after the final set.**

Keywords— **Fiber Bragg Grating, Structural Health Monitoring**

I. INTRODUCTION

The optical fiber field is experiencing a need for ever-increasing communication capacity and multiplexing techniques. This is also true for optical fiber sensors and the growing interest is in using simultaneous but different responses of optical modes in the optical waveguide to disturbances as a means to increase the sensitivity, capacity or limit of detection (LOD) of sensing systems [1]. Compared to conventional measuring techniques, optical fiber sensors have been used in a variety of applications due to their flexibility, ease of fabrication and immunity to electromagnetic disturbances [2]. Because of these advantages, multiple parameter measurements attracted extensive attention in many fields, such as the measurement of strain [3], temperature, refractive index (RI) [4], curvature, displacement and humidity [3]. In recent years, many optical fiber sensors based on various structures have been demonstrated to measure multiple parameters, particularly, strain, temperature and RI [5]. Simple to use, compact, rugged and especially inexpensive sensing technology with remote monitoring capabilities are needed to quickly assess important parameters in the field of structural health monitoring. Temperature and stress in loaded reinforced concrete structures is an important parameter in the design and maintenance of these structures. Conventional electrical sensors have limitations in noisy electromagnetic interference environments or flammable and explosive environments [1], [6].

Excessive early age of movement of reinforced concrete is known to have a significant influence on the overall performance of reinforced concrete structures, or elements within these structures [7]. The fundamental problem with early age movement in reinforced concrete is that it may cause undesirable stresses to development in these reinforced concrete structures, which may lead to undesirable cracking [8]. At this point in time it is important to point out that theoretically, concrete only reaches its specified characteristic strength after 28 days. Therefore, excessive movement of concrete in its early stages will have a negative effect on it [9]. According to Fulton's Concrete Technology, the temperature of concrete during casting should not exceed 70ºC, as anything above this temperature may cause detrimental effects on the young concrete, such as cracking [10]. Cracking in turn will lead to a reduction in strength, durability and serviceability of the reinforced concrete structure [11]. If the early age of concrete movement could be accurately predicted, then the detrimental effects of cracking, strength reduction and durability could be minimized and accounted for with better designs within the construction industry [8].

Construction practice is increasingly moving to better and more cost-effective societal demand and advances in the field of instrumentation and monitoring practices lead to a closing in the gap between theory and application [12]. Studies have been done to improve new techniques associated with the application of optical fiber sensors in reinforced concrete structures [4], [13]. Fiber Bragg gratings (FBGs) can be embedded directly into the concrete during the construction phase of a structure to provide immediate information with regards to internal concrete temperature directly after casting the fresh concrete, and movement after the final set occurs [11]. Measurements can be obtained as frequently as required, making them a more reliable alternative in measuring early age concrete temperature and movement [14].

II. BACKGROUND

Many materials used for civil engineering applications are impacted by changes in environmental factors, manufacturing practices and composition characteristics [15]. Concrete movement, for instance, changes its characteristics as it shrinks or expands. Concrete movement is a physical response that the concrete displays due to many different parameters, such as [14] water-to-cement ratio, coarse and fine aggregate proportions, cement type, compressive strength, curing temperatures, humidity and exposure time [3]. Understanding these

parameters and how they affect concrete movement at an early age is significant for concrete durability, the structure's serviceability and its structural design life [15].

Any sensing enterprise has to identify the variables to be measured and to quantify the sensing measurements into something useable. For new structures, the emphasis will be on early warning of structure deterioration such as strain and stress changes, excessive temperature changes, movement and crack development in concrete structures. For existing structures, the monitoring of an already deterioration process is important. This allows for the monitoring of the current condition of a structure and to assess the remaining structure-life [16].

Fiber optical sensors can detect strain, temperature changes, deformation and vibration in concrete structures. Strain and temperature measurements using an FBG are based on the principle of changes in the wavelength of the transmitted light waves as it passes through sensing element of the fiber [3]. When the light wave interacts with the reflection points making up an FBG, certain wavelengths will be reflected if they match the distance between these reflection points, hence the resulting wave at the other end will be transformed accordingly [17]. These changes allow for the variation of the Bragg wavelength to be established and measure strains and temperature changes within concrete [3].

III. STRUCTURAL HEALTH MONITORING

Structural health monitoring (SHM) in construction refers to the process of implementing a damaging diagnosis and identification strategy in a new or existing structure [4]. Current methods of the manual evaluation of a structure at fixed time intervals can be costly and labor-intensive [18]. The advances in sensor technologies, wireless communications, data processing techniques and artificial intelligence in conjunction with the ever-growing number of aging structures and the pressure to minimize maintenance costs, reducing in-service failures and unforeseen downtimes have led to the development of smarter measuring techniques, such as FBGs [18]. These developments have enabled the use of optic fiber sensors in reinforced concrete structures that could also provide monitoring capabilities from the moment the concrete is placed, and throughout its structural design life [3]. The FBG sensors could provide an in-depth analysis of the early age temperature changes and movement directly after the placing of concrete. This should enable designers and contractors to better understand early age movement of concrete, thereby allowing for better designs and improved site practice at reinforced concrete structures in the South African construction industry [19].

Fiber Bragg grating sensor systems can be permanently installed and are capable of continuous and systematic diagnosis, monitoring, and assessment of structural, environmental and durability conditions [19]. These variables are then used to assess key structural performance characteristics that may derive conclusions about the concrete movement performance of the infrastructure [20]. This process of monitoring can eventually help to establish a rational decision-making process within the civil engineering management field to optimize the maintenance decisions and preventing disastrous infrastructure failures [3]. Structural monitoring parameters such as strain and temperature can help to identify the source and the level of damage [3], [11]. Destructive techniques currently used, such as concrete core sampling [18] can be time-consuming, expensive and provide results only after laboratory investigation. This also leaves the owner of the structure with expensive repairs of the areas where the samples were taken [7].

A. Optical Fibre Sensors

An optical fiber sensor works by modulating one or more properties of a propagating light wave. The properties include polarization, wavelength or intensity in response to an environmental parameter being measured [21]. The structure of the optical fiber consists of three main layers and is shown in Fig. 1. The core is the medium through which light is transmitted. Cladding is used to ensure that the light traveling through the core does not escape. This will cause minimal loss of light, and is achieved by using a cladding material that has a refraction index that is lower than that of the core [3]. The fiber also has an outer layer, known as the buffer coating (not shown in the figure) to protect the fiber from external conditions that might cause damage to it [19]. Optical fibers can be characterized according to their sensor type. Extrinsic (hybrid) optical fiber sensors use the fiber mechanism only to transmit light to and from the sensing component, while an intrinsic optical fiber sensor uses the fiber itself as a measuring element. In this document, the focus will be on an intrinsic optical sensor called the FBG [21].

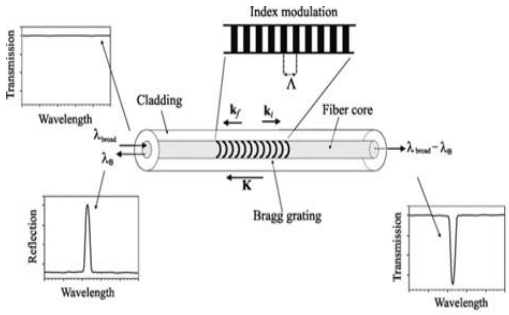

Figure 1: How an FBG works [21]

A fiber Bragg grating is a periodic modulation of the index of refraction along a short length of the fiber. FBGs are formed by exposing the core to an intense optical interference pattern, using UV illumination from a laser. The FBG reflects a wavelength that is called the Bragg wavelength, λ_B, and is given by (1):

$$\lambda_B = 2n_{\text{eff}}\Lambda, \quad (1)$$

Where n_{eff} is the refractive index of the modulated fiber and Λ is the grating period.

When the FBG is illuminated from a broadband source, λ_B is reflected while the rest of the broadband wavelengths of the source are transmitted, as shown in Fig.1. The strain and the temperature influence the periodicity of the FBG, resulting in

a shift of the Bragg wavelength which is given by equation (2) with the constants given in Table 1.

$$\frac{\Delta\lambda}{\lambda_O} = [\varepsilon(1 - P_e)] + [\Delta T(\alpha_\Lambda + \alpha_n)] \quad (2)$$

TABLE I
CONSTANTS USED IN THIS INVESTIGATION [3]

Quantity	Symbol	Value
Room Temperature	T_o	23.1
Thermo-optical coefficient	α_n	8.6×10^{-6} $^oC^{-1}$
Thermo-Expansion Coefficient	α_Λ	0.55×10^{-6} $^oC^{-1}$
Effective Refractive Index	$_{Neff}$	1.482
Grating Period	Λ	0.5229 µm
Effective Strain-Optic Constant	P_e	0.22

The first part of the expression, $[\varepsilon(1 - P_e)]$, describes the impact of strain on the wavelength shift, where P_e is the strain optic coefficient and ε is the strain experienced by the grating [13]. The second expression, $[\Delta T(\alpha_\Lambda + \alpha_n)]$, describes the impact of temperature on the wavelength shift. α_Λ is the expansion coefficient and α_n is the thermo-optic coefficient [11]. Because FBGs respond to both strain and temperature, when measuring strain, temperature compensation must be performed. [21, 13]. A separate sensor is embedded to measure only temperature (no strain is applied to the temperature measuring FBG) and its change in reflected wavelength (Δλ) reading is subtracted from the strain sensor wavelength change in wavelength values. This forces the second term of (2) to be zero and only the first term is considered [13].

B. Fabrication of FBG Sensors

Optical fiber sensors were fabricated in the Photonics Research Centre of the University of Johannesburg, employing the phase mask technique and an Nd:YAG laser. The fourth harmonic (266nm) is separated with dichroic mirrors from the fundamental harmonic of the laser and is used to imprint an FBG structure into a photosensitive fiber. The printed FBGs are then spliced into a single mode communication optical fibre. The wavelength spectrum for each FBG was measured with the HBM Bragg Meter FS22SI. The FBGs were calibrated for both strain and temperature. The temperature sensitivity was 9.13 pm/℃ for the FBG sensors and the strain sensitivity was 0.83µm/µε. The FBG's were printed in the 1540 to 1555 nm range.

IV. EXPERIMENTAL SETUP

Three optical fiber lines were used in this experiment. The first line consisted of 9 temperature FBG sensors, which was placed in copper tubing (Fig. 2 & Fig. 3). The second line consisted of a single temperature FBG sensor, which was placed in close proximity to the concrete slab to measure ambient temperature. The third line consisted of 4 strain sensors (S1, S2, S5, and S7 as indicated in Fig. 4. Strain sensor lines were tensioned to the slab mould (4040 x 1040 mm) of the concrete element before the fresh concrete was placed and is illustrated in Fig.2. The slab design in Fig. 2 was done following SANS 10100-2, for structural use of concrete, the cover of this concrete shall be 20mm for a slender slab with a length of 4040mm.

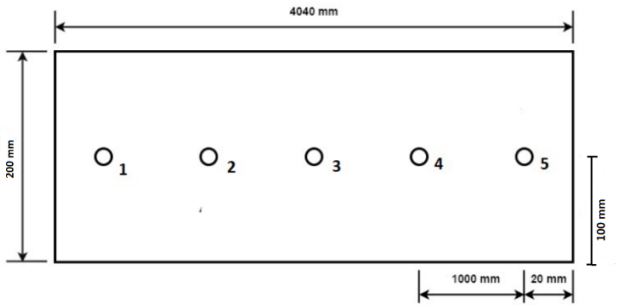

Figure 2: Front view of temperature copper tubing on the slab

All the temperature sensors were fitted into a 1mm diameter copper tube to isolate them from strain. TS1 and TS2 were installed in the first copper tube, marked as 1, TS3 and TS4 fitted into the copper tube marked as 2, TS5 into the copper tube marked as 3, TS6 and TS7 into the copper tube marked as 4 and, TS5 and TS6 into the copper tube, marked as 5 on the schematic diagram Fig. 2. These sensors were position as illustrated in Fig. 2 and Fig. 4

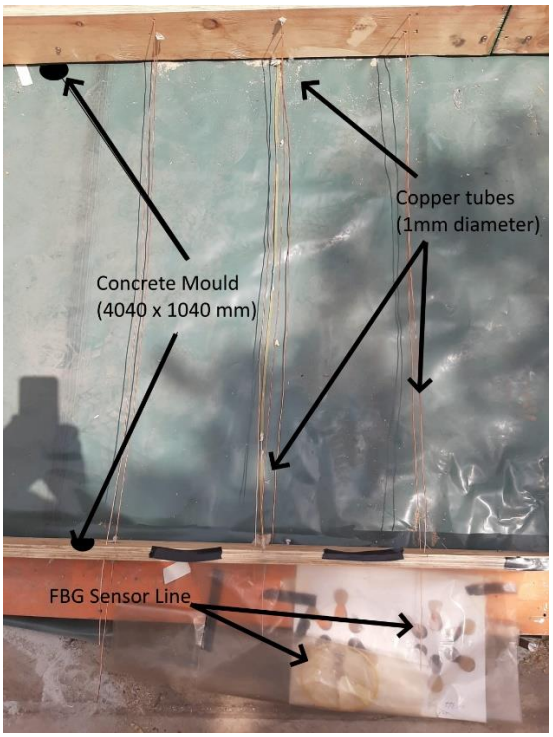

Figure 3: Concrete slab mould with top view of the copper tubing

The FBG sensors measuring temperature were spliced in one line, as shown in Fig. 3, to form one internal temperature system line. A wavelength response of the temperature sensors are shown in Fig 5 as measured by the HBM Bragg Meter. The loop had wavelengths varying with the wavelength range from 1542 nm to 1551 nm. This method used for strain sensors as well.

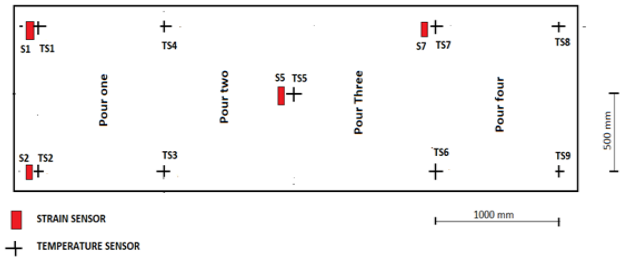

Figure 4: Top view of temperature and strain layout on the concrete slab

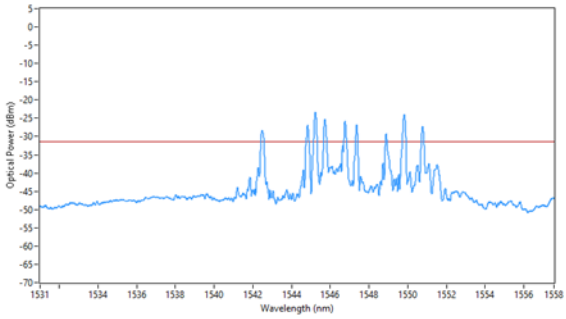

Figure 5: Internal Temperature FBG Sensor system line

C. *Concrete Mix Design*

Concrete was delivered by AfriSam and were prepared according to SANS 5861-3 with the mix design shown in Table 2. Fresh concrete was placed into four identical layers in the concrete mould. The strain sensors were pre-strained in the ends of the mould, to accommodate for expansion and shrinkage. The positions of the strain sensors were aligned with the position of the temperature sensors within the concrete slab.

TABLE II
CONCRETE MIX DESIGN

Material	**RD**	**Weight ($1m^3$)**	**Volume ($1m^3$)**	**Units**
Cement CEM I 52,5N	3,05	270	88	Kg
22mm Stone	2,7	670	248	Kg
9.5mm Stone	2,7	270	100	Kg
Crusher Sand	2,7	999	371	Kg
Chryso140AFR ZA	1,085	2,34	2,16	g
Water	**1**	**190**	190	**L**
Total		**2401**	**1000**	

V. RESULTS AND DISCUSSIONS

i. Temperature versus time

The wavelength shift of the embedded FBG sensors was recorded over a period of 40 hours. The first reading was taken at 14:38 on the 10th of October 2019, after the concrete was placed. As can be observed from Fig 6, the measured temperature increased rapidly within the first 4.75-11.25 hours after placement.

Furthermore, after 19 hours all temperature sensors reached their peak temperature. TS4 and TS5 reaching a maximum temperature of 59 ºC and 60 ºC respectively. The ambient temperature sensor ranged between 20°C and 30°C during the 40 hour period. The measurements in the concrete slab was taken for an additional 20.5 hours. During this time, it can be seen that there is a steady decrease in the internal temperature of the concrete, meaning that the heat of hydration is being dissipated into the environment. All sensors followed a similar trend [19].

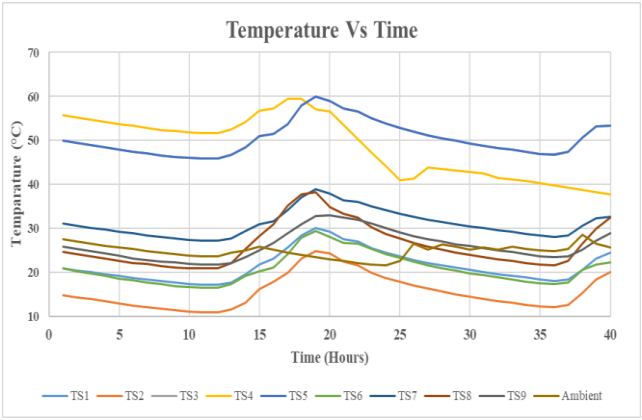

Figure 6: Temperature profile of the concrete slab during the 40 hours

ii. Microstrain Versus Time

Fig 7 shows that after 16 hours of measuring, ST5 and ST 7 gave similar microstrain values of 698 με and 730 με , and remain uniform with time, with the difference between the two about 31 με. This difference in microstrain indicating that the surface of the slab shrank more than the core. The microstrain change in the concrete is largely due to the evaporation of water from the concrete [3], thus leading to the outer part (ST2) of the concrete shrinking more than the core of the concrete slab [11]. The portion of the concrete slab, notably at the surface that is exposed to the ambient environment, experienced the greatest and fastest amount of shrinkage. On the other hand, at the core of the slab, since the water required a longer time to be transported to the surface via the pores, the shrinkage was smaller and slower than that of surface (ST1 sensor). As concrete hardens the surface of the concrete cools down faster than the core. This also induces micro strain on the surface and the core.

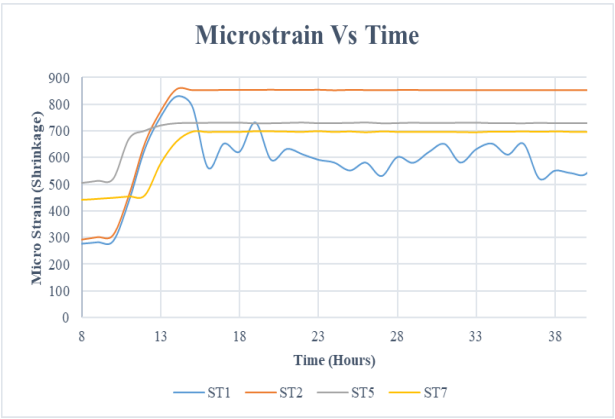

Figure 7: Shrinkage profile over 40 hours after placement

Although there was a difference in the strain measured between all the sensors in the slab, the differences are small.

The microstrain variations within the slab, and their shrinkage trends were very similar.

VI. CONCLUSION

The concrete movement and temperature changes were measured and investigated using embedded FBG sensors. The embedded FBG sensors yielded a similar trend over the measured period. FBG sensors can be used to monitor internal temperature to determine if the internal concrete temperature stays below prescribed limit of 70°C .The FBG sensors combine many advantages of the electrical and mechanical methods, notably they can be embedded directly into fresh concrete with minimal interference. The capability of multiplexing a large number of sensors in series along with a single optical fiber link, as well as taking measurements automatically from the locations, are the unique advantage of this type of fiber-optic sensor.

The results obtained from this experiment show that concrete movement and temperature at an early age varies. The movement occurring at the surface and core differ. The proposed FBG monitoring system will assist in structural health monitoring and real-time damage identification.

ACKNOWLEDGEMENT

This work has been supported by Telkom, the National Laser Centre (NLC), The Concrete Institute and AfriSam.

REFERENCES

[1] T. Guo, F. Liu, B. Guan and J. Albert, "Tilted fibre grating mechanical and biochemical sensors," *Optics and Laser Technology,* vol. 78, pp. 19-33, 2016.

[2] A. Fanella, "Concrete structures," in *Reinforced Concrete Structures*, New York, McGraw-Hill Education, 2016, pp. 216-222.

[3] C. Fernado , A. Bernier and S. Banerjee, "An Investigation of the Use of Embedded FBG Sensors to Measure Temperature and Strain Inside a Concrete Beam During the Curing Period and Strain Measurements Under Operational Loading," *Asia Pacfic Work on Structural Health Monitoring,* vol. 6(1), pp. 388-398, 14 Septemeber 2017.

[4] A. Barrias and J. Casas , "A Review of Distrubutesd Opitcal fiber Sensors For Civil Engineering Appplication," *Passaro VMN,* vol. 5, no. 1, pp. 96-104, 2016.

[5] S. Masri, "Expeimental Study of Embebbed Fiber Optic Sensors," *IEEE,* pp. 296-302, 2016.

[6] C. Hong, Y. Zhang, M. Zhang, L. Leung and L. Liu, "Application of FBG sensors for geotechnical health monitoring, a review of sensor design, implementation methods and packaging techniques," *Sensors and Actuators A: Physical,* no. 244, pp. 184-197, 2016.

[7] J. Farinhoto, "Controlled shrinkage within concretes Structures," *Congress of Construction, 3rd National Congress,.,* vol. 3, no. 1, pp. 234-239, 2016.

[8] R. Tarun , "Sustainability of Cement and Concrete," in *Global Construction*, Dundee, ASCE: Practice Periodical on Structural Design and Construction, 2015, pp. 254-266.

[9] B. Boshoff, R. Combrinck and G. van Zijl, "Strength and physical properties of hardened concrete," in *Funton's concrete technology*, 10th ed., M. Alexander, Ed., Midrand, South Africa, Cement & Concrete SA, 2021, pp. 233-259.

[10] H. MacDonald, "Casting large masses of concrete," in *Fulton's concrete technology,* 10th ed., M. Alexander, Ed., Midrand, South Africa, Cement & Concrete SA, 2021, pp. 627-639.

[11] P. Gaylard , L. Fatti and Y. Ballim, "Statistical modelling of the shrinkage behaviour of South African concretes," *South African Statistical Journal,* vol. 48, no. 1, pp. 103-110, 2014.

[12] K. Soga, "Understanding the real performance of geotechnical structures using an innovative fibre optic distributed strain measurement technology," *Rivista Italiana di Geotecnica,* vol. 48, pp. 7-48, 2014.

[13] M. I. Halim, M. Mbata, J. Bester and M. Grobler, "Implementation of an optical fiber sensor system to monitor the response of reinforced concrete due to formwork removal," *Embedded sensors, Continuous concrete monitoring, Fiber Bragg Gratings,* 2019.

[14] B. Person and P. Bentz, "Self-desiccation and its Importance in Concrete Technology," *National Institute of Standards and Technology,* vol. 2, no. 1, pp. 94-99, 2017.

[15] S. Nunes and T. Camoes, "Investigation on the Effect of Shrinkage Reducing Admixtures on Shrinkage and Durability of High-Performance Concrete," *High Performance Concrete,* vol. 46, no. 1, pp. 255-263, 2015.

[16] H. Zhu, A. Ho, J. Yin, H. W. Sun, H. Pei and C. Hong, "An optical fibre monitoring system for evaluating the performance of a soil nailed slope," *Smart Structures and Systems,* vol. 9, no. 5, pp. 393-410, 2012.

[17] A. Hadianfardc and Z. Yazdizadeha, "Monitoring of concrete shrinkage and creep using Fiber Bragg Grating sensors," *Construction and Building Materials,* pp. 505-512, 17 April 2017.

[18] T. Shima, "A review on Five Key Seonsors for monitoring Concrete Structures," in *Cnstruction and Buildings Materials,* 2019.

[19] C. Merzbacher, C. Kersey and D. Friebele, "Fiber optic sensors in concrete structures: a review," in *Optical Fiber Technology*, Boston MA, Spriger Link, 2016, pp. 1-24.

[20] G. Owens and B. Addis, "Deformation and volume change of hardened concrete," in *Fultons Concrete Technology*, 8. Edition, Ed., Midrand, Cement and Concrete Institute, 2001, pp. 147-152.

[21] T. Teng , "FBGs Technolgy," FBGs Tecnology, 14 October 2016. [Online]. Available: https://fbgs.com/references/. [Accessed 14 June 2021].

A methodology for sentiment analysis from Twitter feeds

Dumisani J. Solani*, Karen Bradshaw†
*Computer Science Department, Rhodes University, South Africa
[1]g16s2145@campus.ru.ac.za
[2]k.bradshaw@ru.ac.za

***Abstract*—This paper proposes using an automated methodology for Sentiment Analysis on Twitter feeds to help businesses like Telkom ascertain how their customers feel about their products and services. We provide a detailed explanation of what an Long Short-Term Memory (LSTM) network is and how it differs from a recurrent neural network. We explore what Sentiment Analysis is and how it can help businesses and the different ways businesses can make use of it. The paper discusses how the data is obtained from Twitter and the preprocessing that should be done on the data to remove noise and shaping the data in such a way that an LSTM network expects. The proposed model obtained 85.29% accuracy during training and had an area under the curve (AUC) of 0.9197, which is a good indication that the model is performing well.**

***Index Terms*—Sentiment Analysis, Machine learning, RNN, Long Term-Short Memory Network, LSTM**

I. Introduction

According to Stats [1], 30.01 million South Africans have access to social media and the number is projected to reach 40.77 million South Africans by the year 2026. With so many users, keeping track of how they feel about a company is a daunting task considering the rate at which data is generated daily. Nowadays, social media platforms have evolved to become a source of data that companies can use. This is due to the nature of the social media platforms that allow users to post real-time texts giving their opinions on various topics, discussing current or past issues, complaining, and/or expressing positive, neutral or negative sentiment about products they are using. For a business to be successful, it needs to maintain a good customer relationship and a good understanding of how customers feel about a product or a service. However, for a company to stay up-to-date with how their customers feel, it is near impossible to read every blog, tweet, or post due to the enormous volumes of data generated on social media.

As a possible solution, we could apply a process that scrapes data from the social media platforms and passes it to a model that can perform sentiment analysis on the data. The results of the analysis can then be used to make informed decisions that can help a business solve or identify a problem with either their goods or services.

Sentiment analysis is defined as the process of using natural language processing, text analysis and statistics to try and understand how customers feel about a product or a service [2]. As with many other fields, advancements in deep learning have brought sentiment analysis into the foreground. There are different types of machine learning algorithms that can be used for sentiment analysis, including the support vector machine (SVM), Naive Bayes, Artificial Neural Network (ANN), Convolutional Neural Network (CNN), Recurrent Neural Network (RNN), and long short-term memory network (LSTM).

In this paper, we investigate the use of Sentiment Analysis on Telkom, by presenting a methodology for sentiment analysis of data scraped from social media platforms. In particular, we use Twitter as the source of the sentiment data and an LSTM for classifying tweets as either positive, neutral or negative.

II. Background

This section introduces background concepts and terminologies essential to this paper. Topics covered include sentiment analysis, machine learning and natural language processing.

A. Sentiment Analysis

Sentiment analysis, also known as opinion mining, is one of the Natural Language Processing fields that is dedicated to the exploration of subjective opinions or feelings collected from various sources about a particular subject. Sentiment analysis is a machine learning technique that detects polarity within text as illustrated on 1. When put in business terms, sentiment analysis basically is a set of tools used to identify and extract opinions that can be used to benefit the business operations. Sentiment analysis can be used for brand monitoring, or analysis of customer service, for market research and analysis. Sentiment analysis for brand monitoring would help the company obtain a full 360 view of how the company as well as its brand and products are viewed by customers and stakeholders. By analyzing the product reviews and social reviews, key insights can be obtained into what is is being done correctly and what is not. Sentiment analysis can also be applied to new products, advertising campaigns or even recent company news on social media.

Sentiment analysis can also be used to assist in providing seamless customer service by for example, automatically sorting incoming user email into urgent or not urgent mail buckets based on the sentiment of the email. This would help the company deal with urgent issues timeously despite the vast amounts of emails being received on a daily basis.

Sentiment analysis is a classification algorithm aimed at finding an appointed point of view and its disposition and highlighting the information of interest in the process. Fig. 1, illustrates the sentiment analysis process as applied to tweets. The target of sentiment analysis is to reach sentiment polarity.

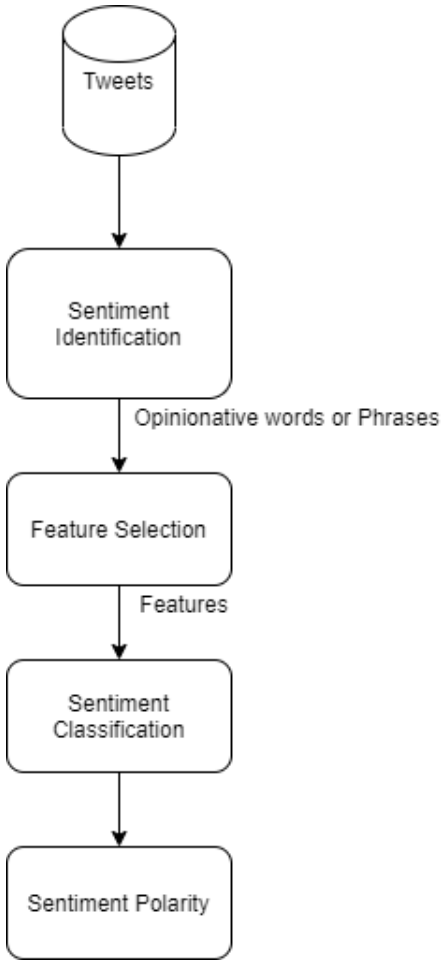

Fig. 1. Sentiment analysis process applied to Tweets

B. Artificial Neural Network

For us to understand what an LSTM is, we first need to look at what an artificial neural network (ANN) is. ANNs are the foundation of artificial intelligence and they try solve problems that would be considered impossible or difficult by human or statistical standards. ANNs are built like the human brain with neuron nodes interconnected like a web. The human brain has billions of cells called neurons, with each neuron made up of a body which is responsible for processing information towards and away from the brain. Just like the brain, the ANN has a many artificial neurons called processing units and these are interconnected by nodes. These artificial neurons are made up of input and output units. The input units receive various forms and structures of information based on the internal weighting system, and the neuron network attempts to learn about the information presented to produce an output report [3]. The ANN uses a set of rules called back-propagation [3], which is the essence of neural network training. It is the process of fine tuning the weights of a neural network based on the error rate obtained in the previous iteration (also known as an epoch). Having properly fine tuned weights will result in reduced error rates and make the model more reliable by increasing its generalization [4]. Back-propagation is the standard method of training artificial neural networks by calculating the gradient of loss with respect to the weights in the network.

An ANN first goes through training where it learns how to recognize patterns in data, whether visually, orally, or textually [5]. During training, the ANN is supervised and the network compares the output it generates to the output expected. The difference between the two outcomes is then used to adjust the weights using back-propagation. Back-propagation is when the network works backwards, going from the output unit to the input units to adjust the weights of the connections between the actual and the desired outcome until the network produces the lowest possible error [6].

The ANN forms the basis of all neural networks. A variation thereof is the RNN, which is a feed-forward neural network equipped with an internal memory [7]. RNNs are called recurrent because they perform the same task for every element of a sequence, with the output dependent on previous computations [8]. Theoretically, RNNs can make use of information in arbitrarily long sequences, but empirically, they are limited to looking back only a few steps. This capability allows RNNs to solve tasks such as unsegmented, connected handwriting recognition or speech recognition [8]. The RNN remembers what it knows from previous input using a simple loop. This loop takes the information from a previous time stamp and adds it to the input of the current time stamp. RNNs are not perfect as they suffer from a major drawback, known as the vanishing gradient problem. This problem prevents it from achieving a high accuracy score. The problem is that as the context length increases, layers in the unrolled RNN also increase. Consequently, as the network becomes deeper, the gradient flowing back in the back propagation step becomes smaller. As a result, the learning rate becomes really slow and makes it infeasible to expect long-term dependencies of the language. In other words, RNNs are not able to remember previous words far away in the sequence and is only able to make predictions based on the most recent words.

Over the years, researchers have developed more sophisticated types of RNNs to deal with this shortcoming of the standard RNN model and one of these models is the LSTM network.

III. Long Short-term Memory Network

An LSTM network is a modified version of the RNN, which makes it easier to remember past data in memory. The problem of having a vanishing gradient is solved here. Even though RNNs are in theory capable of handling long-term dependencies, they fall short when it comes to practical applications. This vanishing gradient decent problem was explored in depth by Bengio [9]. It was seen that a trade-off between gradient descent based learning and the time over which the information is held was required. Hochreiter [10] introduced the LSTM network where the LSTM units or

blocks are part of a RNN. The recurrent neural network uses long short-term memory blocks to provide context for the way the program receives inputs and creates outputs. The LSTM memory block is a complex unit with various components such as weighted inputs, activation functions, inputs from previous blocks and eventual outputs. The unit is called an LSTM block because the program is using a structure founded on short-term memory processes to create longer-term memory. These systems are often used, for example, in natural language processing [7].

The memory in an LSTM (called cells) takes as input the previous state and the current input. Internally, these cells decide what to keep in and what to eliminate from the memory. Then, they combine the previous state, the current memory, and the input. This process efficiently solves the vanishing gradient problem [11].

The central role of an LSTM is held by a memory cell known as a 'cell state'. This cell is responsible for maintaining the state over time. The cell state is the horizontal line that runs through the top of the diagram shown in Fig. 2. It can be visualized as a conveyor belt through which information flows unchanged [7]. The information can be added to or removed from the state in the LSTM and this is regulated by gates. These gates optionally let the information flow in and out of the cell.

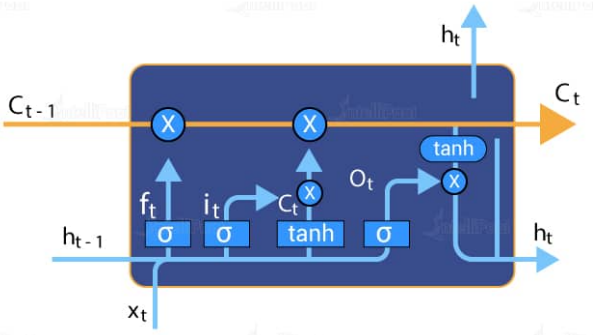

Fig. 2. Visual representation of the cell state, taken from [7]

An LSTM has three gates, namely, the input gate, forget gate and output gate [7] as illustrated in Fig. 3. The input gate is responsible for discovering which value from the input should be used to modify the memory. The gate uses the sigmoid function which decides which value to let through. The sigmoid layer gives out a number between 0 and 1, where 0 means nothing should be let through and 1 means everything should be let through. The $tanh$ function gives the weight-age to the values that are passed and deciding their level of importance ranging from -1 to 1. The formula for the input gate is:

$$i_t = \sigma(W_i.[h_{t-1}, x_t] + b_i)$$

$$C_t = tanh(W_C.[h_{t-1}, x_t] + b_C)$$

The forget gate has the responsibility of discovering what details should be discarded from the block. The decision is

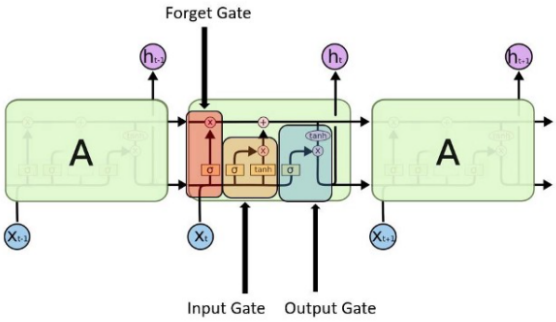

Fig. 3. LSTM gates, taken from [7]

made by the sigmoid function which looks at the previous state (h_{t-1}) and the current input (x_t). The end result is a number between 0 (which means forget this) and 1 (which means keep this), for each number in the cell state (C_{t-1}). The formula for the forget gate is given as:

$$f_t = \sigma(W_f.[h_{t-1}, x_t] + b_f)$$

The output gate is where the input and the memory of the block is used to decide the output. The sigmoid function decides which values to let through between 0 and 1 and the $tanh$ function gives the weight-age to the values which were passed giving them a number between -1 and 1. The value is then multiplied by the sigmoid value. The formula of the output gate is:

$$O_t = \sigma(W_o.[h_{t-1}, x_t] + b_o)$$

$$h_t = o_t * tanh(C_t)$$

IV. Methodology

This section describes the methodology designed for the automatic sentiment analysis.

A. Data Source

For this study, Twitter was chosen as the social platform from which to source data in the form of short messages. Twitter is a social networking platform that has different social communities and allows users to post real-time messages. The length of a message is restricted to 280 characters and these are called Tweets. Tweets can be short videos, or shorts text messages embedded with short hand and emojis. Fig. 4 show an example of a tweet that was made by a Telkom customer.

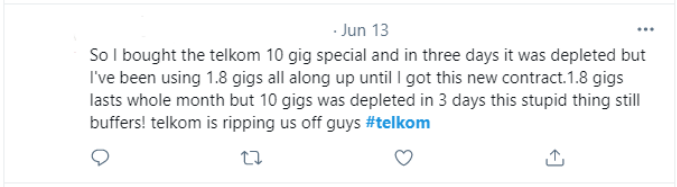

Fig. 4. A Telkom related tweet taken from Twitter with #telkom

B. Data Collection and Pre-Processing

Extraction of tweets from Twitter was carried out using a Python library called tweepy, which allows access to the Twitter API. Through the API, a program can connect to Twitter and stream tweets as they come in. Filters in tweepy allow the specification of which region or location the tweets should come from, what language the tweets should be in and which users should be included or excluded. This allows sourcing English tweets only from people in South Africa, and not those originating from the company itself (Telkom in this case). The reason behind the latter exclusion is that we wanted tweets from customers and not those from within the company or adverts. Due to the many South African languages, people tend mix vernacular languages and English. This becomes a problem if we try to tokenize the words since they will not be recognised as English words. A solution to this would to build a South African English corpora that will be able to tokenize the words appropriately. However, as this is beyond the scope of this research, all tweets containing non-English words are discarded and we focus purely on English tweets. A total of 3000 tweets were selected equally divided into 1000 tweets per category.

Pre-processing is done as the tweets are streaming in and this involves removing the @username, #hashtags , any emojies, URL links and punctuation and additional white spaces, and converting the tweets to lower case. The clean data then goes through a process of manual tagging, which involves reading each tweet and classifying manually whether it is positive or negative. This is done on all the training data that will be used to train the model. The manual tagging was done by a group of two people who read and labelled the tweets as either positive, negative or neutral. The positive tweets were stored in a positive tweets folder, negative and neutral tweets were also stored in negative and neutral tweets folders respectively. These tweets were then pulled from their folders using python, for feature extraction.

The next step after pre-processing the tweet is feature extraction, which is a process of reducing the dimensionality in the raw data so that it is more manageable for processing [12]. In other words, it is a technique for natural language processing that extracts the words (features) used in a sentence, document, tweet, etc. and classifies them by frequency of use. This process helps identify the features of the input that are more relevant and how to encode those features. The other reason for this is to avoid overfitting the model. The following process is tokenization.

Tokenization, is the process of breaking down a piece of text into small units called tokens [8]. A token can be a word or just characters like punctuation, but is has a known meaning. Tokenization is a fundamental task in natural language processing, but a difficult one because every language has its own grammatical constructs, which are often difficult to write down as rules.This is also one of the reasons why the model sticks strictly to English tweets. The reason for breaking up the long sentence into smaller tokens is because we can easily apply a small set of rules to combine them into some larger meaning. In short, it is done to present the computer with some finite set of symbols that can be combined to produce the desired result. Global Vectors for Word Representation (known as GloVe) [13] is an unsupervised learning algorithm for obtaining vector representations for words and was used to encode the tokens into a form that the LSTM model can accept. The output of this process is the representation of each individual review as a list of integer values acceptable to the LSTM when stored in a large list.

The final step is encoding the labels. Since our output can either be positive or negative, we assigned ”1” as positive, and ”0” as negative.

C. Implementing the LSTM Model

After completing the pre-processing and tokenization steps, the remaining data was padded to ensure that all tweets were of the same length in order to deal with both short and long reviews. The desired length is defined by the sequence length which is the same number of time steps for an LSTM layer. Padding for shorter reviews was done by appending 0s to the end of the review and truncating was done to long reviews, bearing in mind that each review is now represented by a list of integers.

Once the data was in a shape that the model could accept, training, validation and test sets were constructed. The training dataset is used as input for training the model, i.e. to teach the LSTM how to predict the result. This means that this data will be used to adjust the weights of the model. The reason it can be used to adjust the weights is because the data is passed into the LSTM with the label. The result obtained from the LSTM is then be compared to the expected result and through back-propagation the weights of the LSTM can be adjusted. If the data is not split into separate training and testing data, overfitting can happen, which occurs when a statistical model fits exactly against its training data [14], but cannot perform accurately against unseen data, thereby defeating its purpose.

The validation data is a portion of the dataset that is used to provide an unbiased evaluation of the model fit on the training data as it fine tunes the weights [4]. This helps to ascertain how well the model is learning from the training data. The model does not train on this data.

Test data is the data that is used to test how well a model is performing on unseen data. It is important that no observations from the training set are included in the test set. If the test set does contain examples from the training set, it will be difficult to assess whether the algorithm has learned to generalize from the training set or has simply memorized it. A program that generalizes well will be able to effectively perform a task with new data. In contrast, a program that memorizes the training data by learning an overly complex model could predict the values of the response variable for the training set accurately, but will fail to predict the value of the response variable for new examples.

The data was split into three datasets with 80% as training data, 10% as validation data and 10% as test data. Once the split was complete, the next step was to create dataloaders for

this data. Dataloaders are helper functions that help split the training data into batches to speed up the training process.

Once the dataloader function is in place, the next step would be to define the LSTM architecture. The LSTM has five layers, namely the emdedding layer, LSTM layer, fully connected layer, sigmoid activation layer and the output layer. The embedding layer, which converts the word tokens into embeddings of specific sizes, was defined using the built-in Keras Embedding Layer. The embedding layer maps the words to their embedding vectors from the embedding matrix. The embedding layer is used to map the words to their GloVe vectors, which become the inputs to the LSTM layer that follows.

The LSTM layer used was from the Tensorflow built-in Keras LSTM layer, which allowed us to specify which activation layer to use.

V. Training and Results

Once the model had been implemented, training was started. Using the Adam Keras optimizer with a learning rate of 0.0001, and 15 epochs, the model realised an accuracy of 85.29%. The results of each epoch are illustrated in Fig. 5.

```
Epoch 1/15
625/625 [==============================] - 535s 856ms/step - loss: 0.5792 - accuracy: 0.6890
Epoch 2/15
625/625 [==============================] - 536s 858ms/step - loss: 0.4912 - accuracy: 0.7663
Epoch 3/15
625/625 [==============================] - 535s 856ms/step - loss: 0.4715 - accuracy: 0.7778
Epoch 4/15
625/625 [==============================] - 532s 852ms/step - loss: 0.4393 - accuracy: 0.7995
Epoch 5/15
625/625 [==============================] - 534s 855ms/step - loss: 0.4141 - accuracy: 0.8141
Epoch 6/15
625/625 [==============================] - 529s 847ms/step - loss: 0.3913 - accuracy: 0.8253
Epoch 7/15
625/625 [==============================] - 524s 838ms/step - loss: 0.3788 - accuracy: 0.8336
Epoch 8/15
625/625 [==============================] - 520s 832ms/step - loss: 0.3727 - accuracy: 0.8354
Epoch 9/15
625/625 [==============================] - 516s 826ms/step - loss: 0.3643 - accuracy: 0.8416
Epoch 10/15
625/625 [==============================] - 511s 817ms/step - loss: 0.3614 - accuracy: 0.8418
Epoch 11/15
625/625 [==============================] - 524s 839ms/step - loss: 0.3523 - accuracy: 0.8462
Epoch 12/15
625/625 [==============================] - 518s 830ms/step - loss: 0.3485 - accuracy: 0.8480
Epoch 13/15
625/625 [==============================] - 523s 838ms/step - loss: 0.3454 - accuracy: 0.8499
Epoch 14/15
625/625 [==============================] - 519s 830ms/step - loss: 0.3434 - accuracy: 0.8496
Epoch 15/15
625/625 [==============================] - 523s 838ms/step - loss: 0.3382 - accuracy: 0.8529
```

Fig. 5. Results of LSTM model accuracy after each epoch during training

Since the model proved to have a good accuracy on the training data, the next step was to test the model on unseen data, i.e. the test data that was not used for training or validation. The test data is passed to the model with its label but this is only used to cross check if the desired outcome is a true label of the tweet passed in.

To evaluate the LSTM performance, we used the area under the receiver operating characteristic (ROC) curve (AUC), which measures the entire two-dimensional area underneath the ROC curve. The ROC is a graph showing the performance of a classification model at all classification thresholds [4]. The AUC ranges in value from 0 to 1 whereby a model whose predictions are 100% wrong has an AUC of 0.0, while one whose predictions are 100% correct has an AUC of 1.0. With the use of sklearn, which has a built-in function that can calculate the AUC, the AUC of our model was found to be 0.9197. This means that the model is performing well.

VI. Conclusion and Future Work

Based on the preliminary results, the proposed LSTM model appears to be performing well on unseen data. This means that Telkom (or any other company) could obtain automated sentiment analysis based on tweets from users, which could then assist in better marketing, advertising, and research on current issues. Moreover, the companies can keep up-to-date with current trends, and how their customers feel about their current products and services. Because we made use of the streaming tweet functionality of tweepy, real-time tweets can continuously be collected and analysed. As the model is presented with more and more new data, the accuracy is also likely to improve.

However, there are some drawbacks to the model. Due to the many South African languages in use, people often tend to use words from different languages in their tweets. As explained previously, the proposed model is limited to analysing only English words, and thus these mixed language tweets cannot currently be included in the sentiment analysis.

Going forward, collection of more data is required to further train the model and investigate whether the accuracy can be further improved. Further testing of the model is also needed as new tweets come in. Incorporating a South African English GloVe version to allow sentiment analysis on multi-lingual tweets like those found in South Africa, would improve the validity of the analysis.

Acknowledgement

This work was undertaken in the Distributed Multimedia CoE at Rhodes University, with the financial support from Telkom SA and Infinera. The authors acknowledge that opinions, findings and conclusions or recommendations expressed here are those of the author(s) and that non of the above mentioned sponsors accept liability whatsoever in this regards.

References

[1] Statisa. (2021, Sep.) Number of social network users in South Africa from 2017 to 2026. Https://www.statista.com/statistics/972776/number-of-social-network-users-in-south-africa/. [Online]. Available: https://www.statista.com/statistics/972776/number-of-social-network-users-in-south-africa/

[2] Q. T. Ain, M. Ali, A. Riaz, A. Noureen, M. Kamran, B. Hayat, and A. Rehman, "Sentiment analysis using deep learning techniques: a review," *Int J Adv Comput Sci Appl*, vol. 8, no. 6, p. 424, 2017.

[3] B. Kosko, *Neural networks and fuzzy systems: a dynamical approach to machine intelligence*. Prentice Hall, 1992.

[4] N. Buduma and N. Locascio, *Fundamentals of deep learning: Designing next-generation machine intelligence algorithms*. " O'Reilly Media, Inc.", 2017.

[5] A. B. Badiru and J. Cheung, *Fuzzy engineering expert systems with neural network applications*. John Wiley & Sons, 2002, vol. 11.

[6] A. Kattan, R. Abdullah, and Z. W. Geem, *Artificial neural network training and software implementation techniques*. Nova Science Publishers, Inc., 2011.

[7] K. Gopalakrishnan and F. M. Salem, "Sentiment Analysis Using Simplified Long Short-term Memory Recurrent Neural Networks," *arXiv preprint arXiv:2005.03993*, 2020.

[8] L. Nemes and A. Kiss, "Social media sentiment analysis based on covid-19," *Journal of Information and Telecommunication*, pp. 1–15, 2020.

[9] Y. Bengio, P. Simard, and P. Frasconi, "Learning long-term dependencies with gradient descent is difficult," *IEEE transactions on neural networks*, vol. 5, no. 2, pp. 157–166, 1994.
[10] S. Hochreiter and J. Schmidhuber, "Long short-term memory," *Neural computation*, vol. 9, no. 8, pp. 1735–1780, 1997.
[11] S. Khotijah, J. Tirtawangsa, and A. A. Suryani, "Using LSTM for context based approach of sarcasm detection in Twitter," in *Proceedings of the 11th International Conference on Advances in Information Technology*, 2020, pp. 1–7.
[12] E. Dumitrescu, S. Hue, C. Hurlin, and S. Tokpavi, "Machine Learning for Credit Scoring: Improving Logistic Regression with Non Linear Decision Tree Effects," Ph.D. dissertation, PhD thesis. Paris Nanterre University, University of Orleans, 2018.
[13] J. Pennington, R. Socher, and C. D. Manning, "Glove: Global vectors for word representation," in *Empirical Methods in Natural Language Processing (EMNLP)*, 2014, pp. 1532–1543. [Online]. Available: http://www.aclweb.org/anthology/D14-1162
[14] A. Yadav, C. Jha, A. Sharan, and V. Vaish, "Sentiment analysis of financial news using unsupervised approach," *Procedia Computer Science*, vol. 167, pp. 589–598, 2020.

Dumisani J. Solani is a Computer Science Masters student. He obtained his Information Systems honors degree in 2020 and his Bachelor of Science with majors in Computer Science and Information Systems in 2019. He is currently working part time with the Dictionary of South African English (DSAE) as a junior programmer.

Karen Bradshaw is an Associate Professor in the Department of Computer Science at Rhodes University. Her research interests lie in GPGPU, Computational thinking and Machine learning.